SCHOLARLY PUBLICATIONS

A CURRENT AWARENESS BULLETIN
OF RESEARCH OUTPUT

@DTU

(126th Edition)

JUNE 2023

BY: CENTRAL LIBRARY

DELHI TECHNOLOGICAL UNIVERSITY
(FORMERLY *DELHI COLLEGE OF ENGINEERING)*
GOVT. OF N.C.T. OF DELHI
SHAHBAD DAULATPUR, MAIN BAWANA ROAD
DELHI 110042

PREFACE

This is the **One Hundred Twenty Sixth** Issue of Current Awareness Bulletin started by Delhi Technological University, Central Library. The aim of the bulletin is to compile, preserve and disseminate information published by the faculty, students and alumni for mutual benefits. The bulletin also aims to propagate the intellectual contribution of Delhi Technological University (DTU) as a whole to the academia.

The bulletin contains information resources available in the internet in the form of articles, reports, presentations published in international journals, websites, etc. by the faculty and students of DTU. The publications of faculty and student which are not covered in this bulletin may be because of the reason that the full text either was not accessible or could not be searched by the search engine used by the library for this purpose.

The learned faculty and students are requested to provide their uncovered publications to the library either through email or in CD, etc. to make the bulletin more comprehensive.

This issue contains the information published during **June, 2023**. The arrangement of the contents is alphabetical. The full text of the article which is either subscribed by the university or available in the web is provided in this bulletin.

Central Library

CONTENTS

1. A CNN-OSELM Multi-Layer Fusion Network with Attention Mechanism for Fish Disease Recognition in Aquaculture, YO-PING HUANG and ***7.1.SIMON PETER KHABUSI***, CSE, DTU

2. A Comparative Study on Clickbait Detection using Machine Learning Based Methods, ***8.Kapil Kumar Yadav*** and ***3.Nipun Bansal***, CSE, DTU

3. A novel technique of schedule tracker for parabolic dish concentrator, Rajkumar Malviya, Akash Patel, Ayush Singh, Santosh Jagadev, Prashant Baredar and ***3.Anil Kumar***, Mechanical, DTU

4. A PSO optimized novel PID Neural Network model for Temperature Control of Jacketed CSTR: Design, Simulation, and a Comparative Study, ***6.Snigdha Chaturvedi***, ***3.Narendra Kumar*** and Rajesh Kumar, Electrical, DTU

5. A State-of-the-art Review on Micro Electro-Discharge Machining, ***6.Lakshya Prasad***, Mechanical, DTU

6. A Study Exploring the Psychological Perspective of Indian Managers on Employing Neurodiverse Talent, ***6.Elixir Sagar***, ***3.Dr. Shikha N. Khera*** and ***3.Dr. Naval Garg***, USME, DTU

7. A Synergistic Framework Leveraging Autoencoders and Generative Adversarial Networks for the Synthesis of Computational Fluid Dynamics Results in Aerofoil Aerodynamics, ***8.Tanishk Nandal***, ***8.Vaibhav Fulara*** and ***3.Raj Kumar Singh***, Mechanical, DTU

8. Accurate Disease Detection in Apple Fruit Images using Transfer Learning: A Novel Approach for Agricultural Sustainability, ***8.Piyush Agrawal***, ***8.Nishant Singh***, ***8.Nikunj Bansal*** and ***3.Anurag Goel***, CSE, DTU

9. AI based Approach for Solar PV Power Prediction with Varying Dust Accumulation Levels, ***7.Komal Singh*** and ***3.M. Rizwan***, Electrical, DTU

10. An Improved Hot Spot Mitigation Approach for Photovoltaic Modules Under Mismatch Conditions, ***6.Ranjeet Singh***, ***3.Vinod Kumar Yadav*** and ***3.Madhusudan Singh***, Electrical, DTU

11. ANALYSIS OF END LOSS AND ITS COMPENSATION IN SMALLER PARABOLIC TROUGHS: A COMPREHENSIVE STUDY, Lovebrat Saxena, ***3.Anil Kumar*** and Archana Soni, Mechanical and Environment, DTU

12. Analysis of Taxes through E-payment System for Transportation Services, Nesar Ahmad Ahmadi, Zalmai Zormatai, ***3.Samiullah Mehraban***, Khwaja Hedayetullah Sidiqi, Shafiullah Shinwari, Abdul Ghafaar and Mohammad Yonus, CSE, DTU

13. Application of Machine learning in predicting the yield strength of API steels, ***6.Gaurav Kumar***, ***3.Qasim Murtaza***, ***3.Ashutosh Bagchi***, ***3.G. Kumar*** and ***8.Darshan Lal***, Mechanical, DTU

14. APPROXIMATION BY APOSTOL-GENOCCHI SUMMATION-INTEGRAL TYPE OPERATORS, ***3.CHANDRA PRAKASH***, ***3.NAOKANT DEO***, AND DURVESH KUMAR VERMA, MATHEMATICS, DTU

15. Assessment of Stock Market Liquidity and Efficiency: Evidence from an Emerging Country, ***6.Reema Monga***, ***3.Deepti Aggrawal*** and Jagvinder Singh, USME, DTU+

16. Behaviour Analysis Using Machine Learning Algorithms In Health Care Sector, ***7.Anukriti Yadav***, ***6.Deepak Kumar*** and ***3.Yasha Hasija***, Biotechnology, DTU

17. Blood Cell Classification using Neural Network Models, ***8.Jagrit Mitra***, ***8.Kartik Vijayran***, ***8.Kartikeya Verma*** and ***3.Anurag Goel***, CSE, DTU

18. Breast Lesion Detection and Localization with VGG19 Optimized Vision Transformer, ***6.Kamakshi Rautela***, ***3.Dinesh Kumar*** and Vijay Kumar, ECE, DTU

19. Challenges of implementing industry 4.0 in achieving sustainable development goals: a case of Indian manufacturing organization, ***6.Abhishek Sahu***, ***3.Saurabh Agrawal***, and ***3.Girish Kumar***, Mechanical, Production and Industrial, DTU

20. Challenges, Impact and Integration of Machine Learning and Blockchain Technology in The Smart Healthcare Developments, Dr. Amiya Kumar Sahoo, Oluwadare Joshua OYEBODE, ***7.Kishor Kumar***, Dr Shakti Bhushan, Manjul Singla, Amanpreet Kaur and A Kakoli Rao, Applied Mathematics, DTU

21. Comparative Analysis of Single Classifier Models against Aggregated Fusion Models for Heart Disease Prediction, ***8.Naman Goel***, ***8.Nikhil Prabhat Yadav***, ***8.Prakarti*** and ***3.Dr.Anukul Pandey***, Electronics, DTU

22. Computational Analysis of Potential Flavonoids Targeting NSP14 of SARS-COV-2 : A Molecular Docking Approach, ***7.Khyati Rastogi***, ***7.Sanjoli Khare*** and ***3.Navneeta Bharadvaja***, Biotechnology, DTU

23. Coordination of circular supply chain for online recommerce platform in industry 4.0 environment: a game-theoretic approach, ***6.Dharmendra Kumar***, ***3.Saurabh Agrawal***, Rajesh Kumar Singh and ***3.Raj Kumar Singh***, Mechanical, Production & Industrial and DSM, DTU

24. CrisisHateMM: Multimodal Analysis of Directed and Undirected Hate Speech in Text-Embedded Images from Russia-Ukraine Conflict, ***8.Aashish Bhandari***, ***8.Siddhant B. Shah***, Surendrabikram Thapa, Usman Naseem and Mehwish Nasim, CSE, DTU

25. Debris failure susceptibility mapping using information value method, ***6.SANDEEP PANCHAL*** and ***3.AMIT KR SHRIVASTAVA***, Civil, DTU

26. Deep red emission from rare-earth-free calcium aluminozincate phosphor with the substitution of Cr3+ ion, ***6.Sumandeep Kaur***, ***6.Videsh Kumar*** and ***3.A. S. Rao***, Applied Physics, DTU

27. Design and Analysis of Vienna Rectifier considering System Parasitic for off-Board EV Charging, ***7.Kushank Singh*** and ***6.Vanjari Venkata Ramana***, Electrical, DTU

28. Design and Control of Fault-Tolerant Interleaved Buck Converter for Battery Charging Applications, ***7.Abhishek Chawla*** and ***3.Mayank Kumar***, Electrical, DTU

29. Design and Power Flow Control in Standalone PV System with Reduced Battery Current Ripple, ***6.Md. Modassir Masoom***, ***3.Narendra Kumar*** and ***3.Mayank Kumar***, Electrical, DTU

30. DESIGN AND STRUCTURAL ANALAYSIS OF KNUCKLE JOINT, ***8.Manish Kumar***, ***8.Kartik Bansal***, ***8.Lalit Mohan Sharma***, ***6.Neeraj kant*** and ***3.Pushpendra Singh***, Mechanical, DTU

31. Design Optimisation and Static Analysis of Non-Pneumatic Tyres, ***8.Divya Balchandani***, ***8.Shalini Nawariya***, ***8.Farzan Shahid*** and ***3.A.K Madan***, Mechanical, DTU

32. DETERMINING THE OPTIMAL RIDING FREQUENCY FOR AN ALL-TERRAIN VEHICLE (ATV) USING A COMPREHENSIVE MODEL OF A FOUR-WHEELED AUTOMOBILE, ***8.Risheek Arora***, ***8.Rishi Kabra***, ***8.Rishikesh Dubey*** and ***3.Prof. Atul Kumar Agarwal***, Mechanical, DTU

33. DIGITAL IMAGE ENCRYPTION USING 256-BIT ADVANCED ENCRYPTION STANDARD ALGORITHM, ***6.Jaideep kala***, ***3.Jeebananda Panda*** and ***3.Lavi Tanwar***, Electronics, DTU

34. Diospyros kaki's phytochemical mediated inhibition of GBM by targeting PDK-1: An in-silico docking and machine learning model, ***8.Harsh Aahra***, ***8.Nida E Falak*** and ***3.Dr. Asmita Das***, Biotechnology, DTU

35. DREAMVERSE: NFT MARKET PLACE, ***8.Aditya Kumar***, ***8.Anup Kumar*** and ***3.Bindu Verma***, IT, DTU

36. Driver's Drowsiness Detection using Mobile Net on Web, ***8.Shwetanshu Singh Bharti***, ***8.Rijul Mahajan***, ***8.Sonali Bhoriya*** and ***3.Dr. Aruna Bhat***, CSE, DTU

37. Early Detection of Alzheimer's Disease: The Importance of Speech Analysis, ***8.Kritesh Rauniyar***, ***8.Shuvam Thakur***, ***8.Aayush Nevatia*** and ***3.Prashant Giridhar Shambharkar***, CSE, DTU

38. Effectiveness of Vision Transformers in Human Activity Recognition from Videos, ***6.Rahul Kumar*** and ***3.Shailender Kumar***, CSE, DTU

39. Exploring the Observational Signatures of f(R, G, T) Gravity in FRW Universe, ***7.Himanshu Chaudhary***, Amine Bouali, Niyaz Uddin Molla, Ujjal Debnath and G.Mustafa, Applied Mathematics, DTU

40. Exploring the Potential Therapeutic Approach Using Ginsenosides for the Management of Neurodegenerative Disorders, ***6.Manju*** and ***3.Navneeta Bharadvaja***, Biotechnology, DTU

41. Fate of Jeratinine E as a potential compound to target NNMT protein in countering Parkinson's disease, ***7.Kumud Kaul*** and ***3.Pravir Kumar***, Biotechnology, DTU

42. FRN: Fusion and recalibration network for low-light image enhancement, ***8.Kavinder Singh***, ***8.Ashutosh Pandey***, ***8.Akshat Agarwal***, ***8.Mohit Kumar Agarwal***, ***8.Aditya Shankar*** and ***3.Anil Singh Parihar***, CSE, DTU

43. Graph theory-based EEG source connectivity for assessing biomechanical performance in transfemoral amputees with vibrotactile feedback, ***8.1.Saurabh Kumar***, Aayushi Khajuria and Deepak Joshi, Electrical, DTU

44. Ground Improvement Technique by Soil Nailing: A Theoretical Analysis, ***6.Prashant C. Ramteke*** and ***3.Anil Kumar Sahu***, Civil, DTU

45. Hate Speech Detection using Multimodal Meme Analysis, ***3.Aruna Bhat***, ***8.Vaibhav Vashisht***, ***8.Vaibhav Raj Sahni*** and ***8.Sumit Meena***, CSE, DTU

46. HIGHER ORDER DIFFERENTIAL SUBORDINATION FOR S∗, ***8.NEHA VERMA*** AND ***3.S. SIVAPRASAD KUMAR,*** APPLIED MATHEMATICS, DTU

47. Implementing Chaos Based Optimisations on Neural Networks for Predictions of Distributed Denial-of-Service (DDoS) Attacks, Anisha Jha, ***8.Avikal Goel***, ***8.Divansh Mahajan*** and ***3.Goonjan Jain***, Applied Mathematics, DTU

48. In-Silico medication of vitiligo by targeting 6AAH protein and riboflavin Ligand, ***7.Sakshi Rajesh Kumar***, ***7.Firoz Tyagi*** and ***3.Yasha Hasija***, Biotechnology, DTU

49. Machine Learning Health Assessment Model To Project Long-Term Degradation For A Pack Of Micro Gas Turbines, ***8.Mr. Vaibhav Prasad***, ***8.Mr. Yash Prasad*** and ***3.Prof. R.S. Mishra***, Mechanical, Production & Industrial and Automobile, DTU

50. Malware Classification using Malware Visualization and Deep Learning, ***8.Prabhpreet Singh***, ***8.Priyanshu*** and ***3.Aruna Bhat***, CSE, DTU

51. Microwave-based Transesterification of Waste Cooking Oil using Waste Aluminium Foil (NaOH/γ-Al2O3) as Catalyst, ***7.1.Naveen Kumar Garg*** and ***3.Amit Pal***, Mechanical, DTU

52. Mining Twitter for Insights into ChatGPT Sentiment: A Machine Learning Approach, ***7.Shivam Sharma***, ***8.Rahul Aggarwal*** and ***3.Manoj Kumar***, CSE, DTU

53. Modelling and Simulation of Crankcase Cover Manufacturing in the Automobile Industry, Sumit Chawla and ***3.Ranganath M Singari***, Mechanical, DTU

54. Modified Mutation based Rao-3 Algorithm for Design Optimization of Surface Inset PMSM via Multi-Echelon Strategy, ***6.Monika Verma***, ***6.Saket Gupta***, ***3.Prof. Madhusudan Singh***, ***3.Prof. Mini Sreejeth*** and ***3.Prof. Narendra Kumar***, Electrical, DTU

55. Multiple Replica Based Audinting of Outsourced Data: A Comprehensive Survey, ***6.Akhilesh Kumar Srivastava*** and ***3.Manoj Kumar***, CSE, DTU

56. NUMERICAL MODELLING OF GEOSYNTHETIC REINFORCED RETAINING WALL, ***3.Anil Kumar Sahu*** and ***6.Nikhil Gautam***, Civil, DTU

57. Numerical prediction of the proximity effects on wind loads of low rise buildings with cylindrical roofs, ***6.Deepak Sharma***, ***3.Shilpa Pal*** and ***3.Ritu Raj***, Civil, DTU

58. Obscenity detection transformer for detecting inappropriate contents from videos, ***6.Kamakshi Rautela***, ***6.Dhruv Sharma***, Vijay Kumar and ***3.Dinesh Kumar***, ECE, DTU

59. One step hydrothermal synthesis of MoS2–SnO2 nanocomposite for resistive switching memory application, ***7.Km. Komal***, ***3.Mukhtiyar Singh*** and ***3.Bharti Singh***, Applied Physics, DTU

60. Optimized deep neural network models for blood pressure classification using Fourier analysis-based time–frequency spectrogram of photoplethysmography signal, Pankaj, Ashish Kumar, ***3.Manjeet Kumar*** and Rama Komaragiri, Electronics, DTU

61. Phase Transition Material Modulated Hyper FET for Digital Applications, ***6.Ritika Sorot***, Anubha Goel and ***3.Sonam Rewari***, Electronics, DTU

62. Plant-based phytochemical mediated inhibition of breast cancer by targeting PLAT: An in-silico study, ***7.Akash Rana***, ***7.Amit*** & ***3.Navneeta Bharadvaja***, Biotechnology, DTU

63. Predicting Next Quarter Nifty 50 Price using Genetic Algorithm and Support Vector Regression, ***3.Mohit Beniwal***, ***3.Archana Singh*** and ***3.Nand Kumar***, DSM, DTU

64. PREDICTION OF SURFACE ROUGHNESS IN ADDITIVELY MANUFACTURED SAMPLES IN PLA+ POLYMER MATERIAL THROUGH MACHINE LEARNING, ***7.Anuj Saxena***, ***3.Qasim Murtaza*** and ***3.Paras Kumar***, Mechanical, DTU

65. Recoloring Grayscale Images using GAN, ***8.Aeshita Mathur***, ***8.Ameesha Dabas***, ***8.Parikshit Rana*** and ***3.Sanjay Kumar***, CSE, DTU

66. Small signal and noise analysis of T-gate HEMT with polarization doped buffer for LNAs, ***6.Megha Sharma***, ***6.Bhavya Kumar*** and ***3.Rishu Chaujar***, Applied Physics, DTU

67. Solar PV fed Non-Isolated DC-DC Multiport Converter, ***8.Kumood***, ***8.Krishan Kumar***, ***8.Jatin Dalal*** and ***3.Mayank Kumar***, Electrical, DTU

68. Structural and photoluminescence properties of Sm3+ ions doped Strontium Yttrium Tungstate Phosphors for Reddish-orange Photonic device applications, ***6.Sheetal Kumari***, ***3.A.S. Rao*** and ***3.R. K. Sinha***, Applied Physics, DTU

69. Study of Advancements of Solar Furnace Technology to Find Out Best Suitable Solar Furnace for Indian Conditions, ***8.Ashish Pal***, ***8.Abhiraj Kumar***, ***6.Deepak Kumar*** and ***3.Prof. J. P. Kesari***, Production and Industrial, DTU

70. Synthesis and characterization of novel xanthan gum-based pH-sensitive hydrogel for metformin hydrochloride release, ***7.Tushar***, ***7.Yash Saraswat***, ***6.Priyanka Meena*** and ***3.Sudhir G. Warkar***, Applied Chemistry, DTU

71. Temperature-based Numerical Simulation investigation of the analog performance of AlGaN/GaN MOS-HEMT, Mann Ruby, Sharma Shobha, ***3.Rewari Sonam*** and Gupta R. S, Electronics, DTU

72. Validation of the existential gratitude scale (EGS) in India and its relationship with spiritual well-being and distress, ***3.Naval Garg***, Nidhi Sharma and Jason Palframan, USME, DTU

73. Variation in Tensile Strength of 3D Printed PLA Parts by Varying Infill Density and Infill Pattern, ***8.Siddharth Garg***, ***8.Arko Sardar***, ***8.Rahul Srivastava***, ***8.Saksham Verma and 3.A. K. Madan,*** Mechanical***, DTU***

74. Wavelet Transform based Alzheimer's Disease detection using Grey Level Co-occurrence Matrix and Genetic Algorithm, ***6.Neha Garg***, ***3.Mahipal Singh Choudhry*** and Rajesh Mungasaji Bodade, Electronics, DTU

75. Wide Speed Range Control of PMSM Based on MTPA and Flux-Weakening Control, ***7.Abhishek Dalal*** and ***3.Mini Sreejeth***, Electrical, DTU

76. Word2Vec and LSTM based deep learning technique for context-free fake news detection, ***8.Abhishek Mallik*** and ***3.Sanjay Kumar***, CSE, DTU

1. *Vice Chancellor*
2. *Pro Vice Chancellor*
3. *Faculty*
4. *Teaching-cum-Research Fellow*
5. *Asst. Librarian*
6. *Research Scholar*
7. *PG Scholar*
8. *Undergraduate Student*

1.1. *Ex Vice chancellor*
2.1. *Ex Pro Vice Chancellor*
3.1. *Ex Faculty*
4.1. *Alumni*
5.1 *Others*
6.1. *Ex Research Scholar*
7.1. *Ex PG Scholar*
8.1. *Ex Undergraduate Student*

This article has been accepted for publication in IEEE Access. This is the author's version which has not been fully edited and content may change prior to final publication. Citation information: DOI 10.1109/ACCESS.2023.3280540

IEEE Access
Multidisciplinary | Rapid Review | Open Access Journal

Date of publication xxxx 00, 0000, date of current version xxxx 00, 0000.

Digital Object Identifier 10.1109/ACCESS.2022.Doi Number

A CNN-OSELM Multi-Layer Fusion Network with Attention Mechanism for Fish Disease Recognition in Aquaculture

YO-PING HUANG[1,2,3,4], *Fellow, IEEE*, and SIMON PETER KHABUSI[1], *Graduate Student Member, IEEE*

[1]Department of Electrical Engineering, National Taipei University of Technology, Taipei 10608, Taiwan
[2]Department of Electrical Engineering, National Penghu University of Science and Technology, Penghu 88046, Taiwan
[3]Department of Computer Science and Information Engineering, National Taipei University, Taipei 23741, Taiwan
[4]Department of Information and Communication Engineering, Chaoyang University of Technology, Taichung 41349, Taiwan

Corresponding author: Yo-Ping Huang (yphuang@gms.npu.edu.tw).

This work was partially funded by the National Science and Technology Council, Taiwan, under grants MOST108-2221-E-346-006-MY3 and MOST111-2221-E-346-002-MY3.

ABSTRACT The increasing global population has escalated the demand for fish products necessitating a stable supply. This can only be met through improved aquaculture practices. The automatic recognition of fish diseases from diseased underwater images is one of such practices that aims to control disease, improve fish production and optimize profits. However, due to lack of public fish disease dataset, there has been limited research towards fish disease recognition. Moreover, due to low quality of underwater images and complex underwater environments, traditional hand-designed feature extraction methods or convolutional neural networks (CNNs)-based classifiers cannot adequately recognize fish diseases in real underwater scenes. Therefore, this paper proposes a novel hybrid approach based on multilayer fusion, attention mechanism and online sequential extreme learning machine (OSELM) to recognize fish diseases in aquaculture. Feature extraction is enhanced by integrating same level features and focusing on salient features for fish disease recognition. The characteristic information of fish disease is refined by using strongly discriminative features of the infected fish regions and weakening regions of low interest using convolutional block attention module (CBAM). The module is added to the multilayer fusion network to sequentially infer attention maps along the channel and spatial dimensions for every intermediate feature map. Fish disease recognition is done by using OSELM for faster learning and improving classification performance. The models are trained, validated and tested on a custom dataset with image samples collected from various internet sources. The proposed method achieves 94.28% of accuracy, precision of 92.67%, recall of 92.17% and 92.42% of F1- score with background elimination. The proposed method can be used for fish identification in complex underwater environments in aquaculture.

INDEX TERMS Fish disease, aquaculture, multilayer fusion, extreme learning machines, attention mechanism.

I. INTRODUCTION

The global aquaculture production is a fast-growing agricultural practice that accounts for about 53% of total fish production. In 2019, the global production of Salmon fish from aquaculture had reached 2.6 million after a 7% increase [1]. The 2020 United Nations report on world fisheries and aquaculture showed a steady rise of global aquaculture production to 90.4 million tons in 2012 yielding US$ 144.4 billion in total revenue [2]. The annual growth rate is therefore estimated at 8.8% globally, making it the most dynamic food sector. However, the current annual growth can even be doubled with appropriate aquaculture practices including timely detection of diseases and control [3]. Fish diseases are one of the major threats to fish production, affecting both yield and quality of fish. Disease infestation on an aquarium result into increased

This work is licensed under a Creative Commons Attribution-NonCommercial-NoDerivatives 4.0 License. For more information, see https://creativecommons.org/licenses/by-nc-nd/4

This article has been accepted for publication in IEEE Access. This is the author's version which has not been fully edited and
content may change prior to final publication. Citation information: DOI 10.1109/ACCESS.2023.3280540

fish mortality, low breeding rates, reduced quality of fish and yield, and economic losses. The natural environment is no exception.

Fish diseases are caused by a variety of contagious parasitic organisms such as virus, bacteria and protozoa which are associated with at least 18 diseases that affect most of the fish species in fish farms [3]. The affected fishes develop physical and/or behavioral signs and symptoms that vary depending on the nature and stage of the disease. The fish recognition task presented in this paper focuses on physical characteristics of the fish to perform disease recognition using a custom fish disease dataset. In this paper, we focus on five fish diseases whose details are presented in Table I.

Fish disease recognition is a novel research area with very limited literature though very critical in the development of smart aquaculture systems. The recent trends in artificial intelligence and computer vision provide strong possibilities for the design of smart aquaculture systems for early recognition of fish diseases. Preliminary studies have employed classical methods for the detection of disease in aquaculture farms. These can be classified into biochemical, histological, and spatio-temporal studies. The biological studies involve the use of tests of antibiotic sensitivity for the detection of parasitic viruses and bacteria that cause diseases [6-7]. However, histological studies entail the microscopic analysis of fish cells and tissue structures [8-9]. Whereas the spatio-temporal studies use fish activity or movement to predict the fish's wellness, water environment for early prediction of possible disease invasion and fish appearance to diagnose fish disease presence. Some of the indirect approaches to fish detection have been reviewed in [10]. Behavior-based approaches include detection of anomalous behavior [11], prediction of water quality [12] and dissolved oxygen [13-17]. The direct approaches to fish disease detection which utilize the physical parameters or physical appearance of fish such as body texture, eye color, appearance of fish head, fish fins, scales, gills and tail are scanty. Moreover, their scope is limited to epizootic ulcerative syndrome (EUS) or redspot disease. This is attributed to various challenges such as unavailability of public dataset of fish disease, limited feature extraction and classification ability of baseline deep learning and machine learning models, complex underwater environments and tiny nature of visual presence of fish diseases limited by the quality of underwater images. The complex underwater environment is a source of various interferences caused by brightness imbalances, abrupt fish positional changes, movement of aquatic plants, fish texture and shape, and structure of the seabed [18] which are a major challenge to fish disease recognition.

This study therefore proposes a CNN-OSELM multilayer fusion network with attention mechanism for fish disease recognition in aquaculture. We develop a multilayer fusion network using same level composition (SLC) [19-21] and integrate attention mechanism to improve feature extraction and focus on strongly discriminative features of the infected fish regions while weakening regions of low interest. Classification is performed by the OSELM, instead of the dense layer, to improve the classification performance. OSELM algorithm utilizes the concepts of extreme learning machine (ELM) developed by [24]. The ELM algorithm was developed for single-hidden layer feedforward neural networks (SLFNs) and has shown to perform extremely fast and with good generalization performance.

TABLE I. OVERVIEW OF FISH DISEASES CONSIDERED IN THE STUDY

Disease	Preview	Description
EUS		- Caused by an oomycete scientifically referred to as Aphanomyces invadans [4]. - Manifests as ulcer or red spots. - Affects various fish species. - Conventional control is by adding lime to the aquarium and sun-drying.
Whitespot	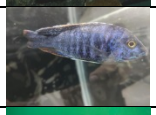	- Contagious viral disease caused by Ichyophthirius multifilis. It is also referred to as the white spot syndrome. - Parasite feeds on fish's body fluids and cells resulting into tissue damage and eventual death [6]. - Fish develop white spots on its skin and is prevalent among crustaceans of order decapoda such as shrimps, lobsters, prawns, and crabs though other fish species are also affected.
Argulus	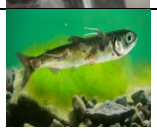	- Belongs to Argulidae family which are parasitic and disease-causing form of fish lice [5]. - The lice attach on the fish skin, suck blood and body nutrients leading to fish malnutrition and death. - Lice measures 7mm in length and 5mm in width but can be visually seen by a high-resolution underwater camera. - Affects both freshwater and marine fish.
Diplopstomiasis	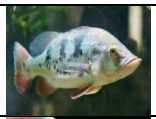	- Also known as black spot disease is a parasitic flatworm that attaches on fish fins and skin. - Manifests as tiny black spots. - The disease compromises the fish meat quality.
Hexamitiasis	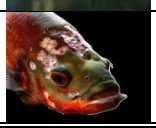	- Parasitic disease which affects fish in both salty/marine such as surgeonfish and fresh water such as goldfish. - It is also called "hole in the head" disease because the head and flanks develop lesions. - Might also cause erosion of the fish's head and lateral line (HLLE). - Fish's food consumption level drops significantly and the fish gets emaciated gradually and eventually dies.

This work is licensed under a Creative Commons Attribution-NonCommercial-NoDerivatives 4.0 License. For more information, see https://creativecommons.org/licenses/by-nc-nd/4

This article has been accepted for publication in IEEE Access. This is the author's version which has not been fully edited and
content may change prior to final publication. Citation information: DOI 10.1109/ACCESS.2023.3280540

The main contributions of this study are four-fold

1) Compared with the conventional backbone networks used for feature extraction in image recognition, this paper incorporates SLC structure to build CNN architecture which is less deep and with improved feature extraction.
2) To improve feature extraction and ultimately classification accuracy, this study includes the existing CBAM in the composite network.
3) This study incorporates OSELM for classification instead of the dense layer to reduce the training time and improve the classification. The OSELM network randomly sets the input weights and biases of the hidden layer and only updates the output weights.
4) This study is the first to apply the concept of SLC with background elimination to overcome the underwater interference for improving recognition of fish diseases.

The rest of the paper is organized as follows: The existing literature is given in Section II followed by the proposed approach in Section III. Section IV gives data preprocessing and experimentation. Section V presents and describes the study results. The paper is concluded in Section VI and the future direction of this work is suggested.

II. LITERATURE REVIEW

This section discusses the existing work on fish disease classification and detection, extreme learning machines, attention mechanism and mathematical basis of OSELM.

A. FISH DISEASE RECOGNITION

Using deep learning models for fish disease recognition is a novel research area with very limited existing literature. Among these is a binary classification method to classify salmon fish infected by EUS in aquaculture [27]. The proposed model was trained on a custom dataset and achieved an average accuracy of 92.8% and 94.3% on augmented data. Similar work has been done in [27], [28] to classify healthy fish that infected by EUS. The fish details were obtained by segregating fish images, morphological and edge detection operations and important features are determined by principal component analysis (PCA). The whitespot disease has also been studied and identified from a custom dataset through segmentation and achieved a test accuracy of 86% [29]. Moreover, fish disease recognition method using fish body surface features was proposed in [30]. In the study, structural segmentation and contour extraction were done using dual-threshold difference method. A precision value of 92.0% and recall value of 74.2% were achieved.

B. HYBRID CNN-ELM APPROACHES TO IMAGE CLASSIFICATION

The ELM algorithm developed by [24] has been reported to perform extremely fast and with better generalization performance compared to other methods that used batch training. Semi-supervised and active learning have been combined to discover hidden useful information from unlabeled samples in order to enhance classification performance in multiple class dataset [31]. Moreover, traffic sign recognition was proposed in [32] using CNN-ELM. CNN was used as a feature extractor and ELM as a classifier with 4,000 hidden nodes achieving a recognition rate of 99.23%. An extreme learning machine based on L1-norm minimization was proposed in [33] to detect disease on peach and strawberry leaves. The proposed algorithm, L1-ELM, was a feature-based detection method with higher generalization capability and lower learning compared to the conventional methods. The proposed approach achieved an overall accuracy of 98.5% on peach leaves and 97.7% on strawberry leaves compared to SVM which achieved accuracy of 93.0% on peach leaves and 92.3%, the highest amongst the conventional classifiers. Similar studies have been done for pneumonia classification in [34]. An ELM that adjusted output weights by increasing the output weight's corresponding column was proposed in [35]. Images of hyperspectral remote sensing were classified using ELM and based on hierarchical local-receptive-field [36].

Other related studies using composite kernels and ensemble learning have been implemented for both image classification and regression [37-41]. Moreover, a neural response approach on the basis of extreme learning machine has been proposed for image classification, tested on MNIST dataset, Caltech face dataset and CIFAR-10 dataset and achieved the highest accuracies of 99.18%, 93.93% and 42.43% (for 100 training images in every class), respectively, [42].

C. ATTENTION MECHANISM

There have been enormous efforts to improve the performance of CNNs in image recognition by integrating attention mechanisms into the backbone networks [25-26]. For example, a residual encoder/decoder attention network was proposed and used for feature map refinement [25]. In this regard, attention was a network engineering concept that aimed to utilize more important features and ignored the less important ones for improved classification, recognition or object detection performance.

To improve the recognition performance of fish disease, our work focuses on emphasizing important regions and weakening those that are less important by integrating attention mechanism in the proposed multilayer fusion network. CBAM has been integrated in the proposed network [44]. The 3-dimensional attention maps of CBAM are decomposed to learn separately via two modules: channel attention and spatial attention. The spatial and channel attention modules are placed sequentially between convolutional blocks starting with the channel attention. The feature map produced by the intermediate CNN blocks is refined adaptively at every block of the deep networks. This arrangement is adopted because it is reported to achieve better results [44].

This work is licensed under a Creative Commons Attribution-NonCommercial-NoDerivatives 4.0 License. For more information, see https://creativecommons.org/licenses/by-nc-nd/4

This article has been accepted for publication in IEEE Access. This is the author's version which has not been fully edited and
content may change prior to final publication. Citation information: DOI 10.1109/ACCESS.2023.3280540

For input $\boldsymbol{F} \in \mathbb{R}^{C\times H\times W}$ (CNN intermediary feature map) to the block, the module generates an attention map $\boldsymbol{M_c} \in \mathbb{R}^{C\times 1\times 1}$ (1-dimensional) and spatial attention feature map $\boldsymbol{M_s} \in \mathbb{R}^{1\times H\times W}$(2-dimensional). The process of attention is summarized as follows:

$$\boldsymbol{F'} = \boldsymbol{M_c}(F) \otimes \boldsymbol{F} \quad (1)$$

$$\boldsymbol{F''} = \boldsymbol{M_s}(\boldsymbol{F'}) \otimes \boldsymbol{F'} \quad (2)$$

The element-wise multiplication is denoted as $\otimes$. The multiplication process involves broadcasting (copying) the values of the attention maps accordingly. The values of the channel attention are copied along the spatial dimension and vice versa, generating $\boldsymbol{F''}$as the refined final output value as shown in Fig. 1.

In the channel attention module, the inter-channel relationships between the features are exploited to produce the channel attention maps. For a given input image, the channel attention focuses on the meaningful aspects of the image; hence, every channel of intermediate feature map is taken to be a detector of features of interest. The input feature map's spatial dimension is squeezed to achieve efficient computation of the channel attention. It is noted in the existing works that utilizing both max and average pooling considerably improves the representation ability of networks instead of using one separately. Therefore, CBAM uses both max and average pooling to aggregate the spatial information for a feature map. This generates two different descriptors of spatial context, $\boldsymbol{F^c_{max}}$ and $\boldsymbol{F^c_{avg}}$, the spatial features resulting from max and average pooling operations, respectively. The two spatial context features are then passed on to a fully connected shared network producing $\boldsymbol{M_c} \in \mathbb{R}^{C\times 1\times 1}$, which is channel attention map. The shared network is the multilayer perceptron (MLP) with a single hidden layer. The parameter overhead is reduced by setting activation size of the hidden layer to $\mathbb{R}^{C/r\times 1\times 1}$, where r is a reduction ratio. The MLP is then applied to each of the descriptors and feature vectors of the output are then merged by element-wise addition. In summary, computation of channel attention feature map is as follows:

$$M_c(\boldsymbol{F}) = \sigma\left(MLP\left(AvgPool(\boldsymbol{F})\right) + MLP\left(MaxPool(\boldsymbol{F})\right)\right) \quad (3)$$
$$= \sigma\left(\boldsymbol{W_1}\left(\boldsymbol{W_0}(\boldsymbol{F^c_{avg}})\right) + \boldsymbol{W_1}(\boldsymbol{W_0}(\boldsymbol{F^c_{max}}))\right)$$

The sigmoid function is denoted by σ, $\boldsymbol{W_0} \in \mathbb{R}^{C/r\times C}$ and $\boldsymbol{W_1} \in \mathbb{R}^{C\times C/r}$are MLP weights and are shared for both inputs. The activation function (ReLU) is followed by $\boldsymbol{W_0}$.

On the other hand, the spatial attention module produces the spatial attention map using inter-spatial relationships within features. The spatial attention concentrates on finding the informative part that is consistent with the channel attention. Computation of spatial attention involves the application of max and average pooling operations along channel axis and then the results are concatenated in order to obtain a systematic feature descriptor. A convolution layer is then applied on the feature descriptor to produce the spatial attention map $\boldsymbol{M_s}(\boldsymbol{F}) \in \boldsymbol{R}^{H\times W}$. The attention map encodes to suppress or emphasize the regions as shown in Fig. 1.

The channel information of the feature map is combined by max and average pooling operations. This generates two 2-dimensional feature maps, $\boldsymbol{F^s_{avg}} \in \mathbb{R}^{1\times H\times W}$ and $\boldsymbol{F^s_{max}} \in \mathbb{R}^{1\times H\times W}$. The two generated features are then concatenated and followed by convolutional operation using the standard convolutional layer. This produces the attention map of two dimensions. The computation of the spatial attention is given below.

$$\boldsymbol{M_s}(\boldsymbol{F}) = \sigma\left(f^{7\times 7}([AvgPool(\boldsymbol{F}); MaxPool(\boldsymbol{F})])\right) \quad (4)$$
$$= \sigma\left(f^{7\times 7}([\boldsymbol{F^s_{avg}}; \boldsymbol{F^s_{max}}])\right)$$

where σ is a sigmoid function and $f^{7\times 7}$ refers to convolution operation using 7×7 filter size. The overall stages undertaken in the study are shown in Fig. 1.

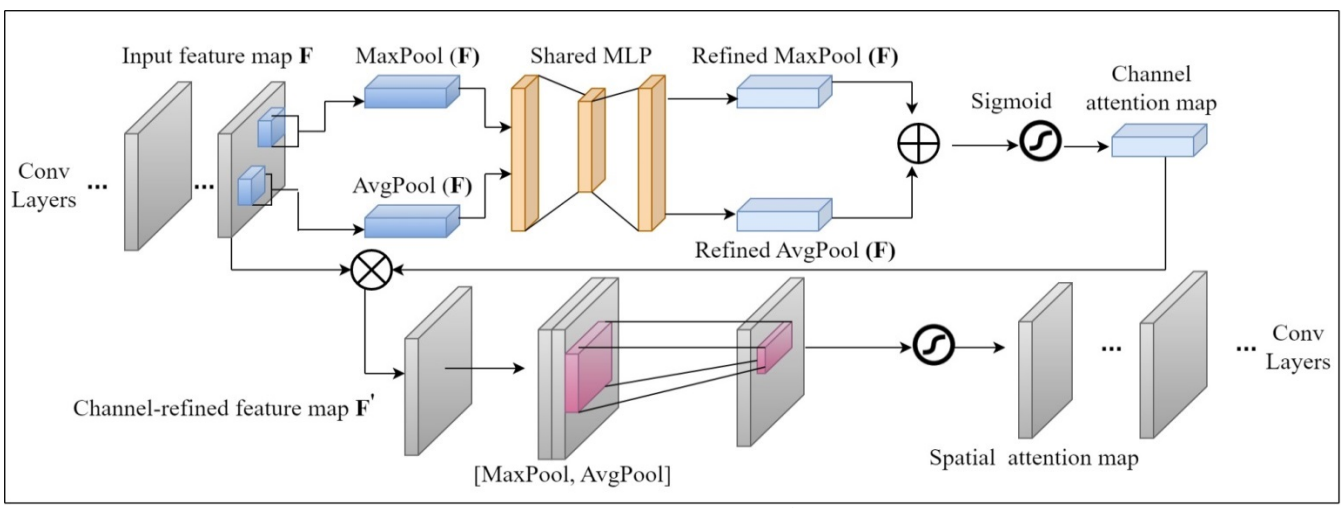

FIGURE 1. Architectural structure of CBAM.

D. ONLINE SEQUENTIAL EXTREME LEARNING MACHINE (OSELM)

This section presents the mathematical basis for single hidden layer feedforward neural network (SLFN) to give the foundation for the design of OSELM. The OSELM algorithm

This work is licensed under a Creative Commons Attribution-NonCommercial-NoDerivatives 4.0 License. For more information, see https://creativecommons.org/licenses/by-nc-nd/4

This article has been accepted for publication in IEEE Access. This is the author's version which has not been fully edited and
content may change prior to final publication. Citation information: DOI 10.1109/ACCESS.2023.3280540

was a sequential learning algorithm with higher versatility and achieved through four main operational principles. First, the training samples were presented in succession, one sample or one chunk at a time and the size was fixed or varied. Secondly, the learning process was done on the newly arrived single chuck or chunks of data samples at every single moment rather than on all the past data. Thirdly, a data sample or chuck was discarded immediately after the model completed learning from it. Lastly, the number of training observations was not known by the algorithm prior to training [23]. The OSELM was built on the operational basis of existing batch ELM [24].

Given a SLFN with x RBF or additive hidden nodes and P data samples, the representation of its output is given by:

$$f_x(l) = \sum_{i=1}^{x} \beta_i U(w_i, b_i, l), \quad l \in R^p, \ w_i \epsilon R^p \tag{5}$$

where w_i and b_i are the learning parameters of hidden nodes, β_i denotes the weight that connects the ith node of the hidden layer to the output node and $U(w_i, b_i, l)$ denotes the ith node of the hidden layer output with respect to its input l.

However, given additive hidden node with activation function $u(l): R \to R$ (such as sigmoid or threshold), $U(w_i, b_i, l)$ is given by:

$$U(w_i, b_i, l) = u(w_i . l + b_i), \quad b_i \in R \tag{6}$$

where w_i is the weight vector that connects the input layer to the ith hidden node and b_i is the bias of the ith hidden node. $w_i . l$ is the inner product of w_i and l vectors in R^p.

RBF network is a special kind of SLFN whose hidden layer consists of RBF nodes with a centroid and impact factor. The output of every node is given by a radially symmetric function of the distance between the input and the center of the node.

For the hidden node of RBF whose activation function is $u(l): R \to R$ (such as Gaussian), the hidden layer output with respect to its input l becomes:

$$U(w_i, b_i, l) = u(b_i \parallel l - w_i \parallel), \ b_i \in R^+ \tag{7}$$

where w_i denotes the center of ith node of the RBF network and b_i is its impact factor. R^+ denotes a set of all positive real values.

The ELM is a form of supervised learning algorithm. Suppose a dataset consists of P arbitrary distinct data points $\{(l(i), t(i))\}_{i=1}^{P}$, such that $l(i)$ is an input vector of dimension $p \times 1$ and $t(i)$ is a target vector of $m \times 1$ dimension. The standard SLFN with x number of hidden nodes and activation function $u(l)$ can be modeled such that:

$$f_x(l_j) = \sum_{i=1}^{x} \beta_i u(l(j)) w_i b_i = t_j, \ j = 1, \dots, P \tag{8}$$

When the SLFN outputs are equal to the targets, the following compact formulation is obtained:

$$\boldsymbol{H\beta} = \boldsymbol{T} \tag{9}$$

where

$$\boldsymbol{H}(w_1, \dots, w_x, b_1, \dots, b_x, l_1, \dots, l_P) = \begin{bmatrix} U(w_1, b_1, l_1) & \cdots & U(w_x, b_x, l_1) \\ \vdots & \dots & \vdots \\ U(w_1, b_1, l_P) & \cdots & U(w_x, b_x, l_P) \end{bmatrix}_{P \times x} \tag{10}$$

$$\beta = [\beta_1^T \dots \beta_x^T]_{x \times m}^T, \text{ and } T = [t_1^T \dots t_P^T]_{P \times m}^T \tag{11}$$

$\boldsymbol{H}$ is the output matrix of the hidden layer and superscript T denotes the transpose of the matrix.

The hidden nodes parameters can be assigned randomly when the training samples (P) and hidden layer nodes (x) are the same, i.e., when P=x. Then, output weights can be analytically calculated by merely inverting $\boldsymbol{H}$ which lowers the error rate to minimal value.

However, if the hidden layer nodes are less than the training samples, that is $x < P$, the hidden nodes parameters can nevertheless be randomly assigned. Conversely, the output weights can be calculated by using pseudoinverse of $\boldsymbol{H}$ which leads to a smaller training error $\epsilon > 0$. The training procedure is likewise reduced since the weights' calculation is done in a single step. The architecture of ELM is shown in Fig. 2.

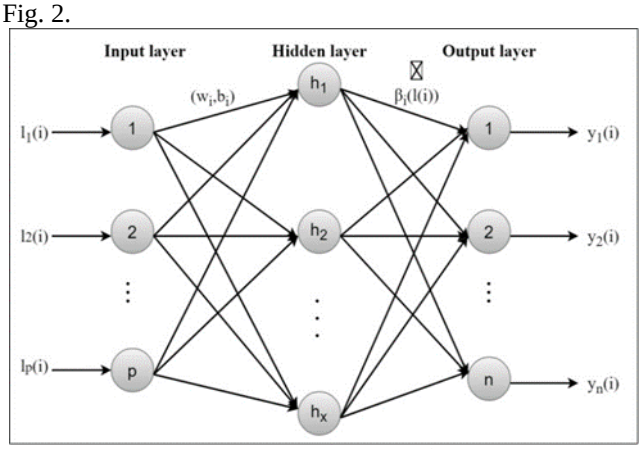

FIGURE 2. Architecture of ELM.

The OSELM algorithm is a two-phase algorithm consisting of the initialization phase and sequential learning phase. The initialization phase involves filling up the appropriate matrix $(H_0) = x$ to be used in the learning phase. The least number of data samples needed for filling up H_0 should be at least equal to the number of hidden nodes.

Given an initial training chuck of data $\rho_0 = \{(l_i, t_i)\}_{i=1}^{P_0}$ and $P_0 \geq x$, the target is to minimize $\|H_0\beta - T_0\|$ achieved by $\beta^{(0)} = K_0^{-1} H_0^T T_0$ where $K_0 = H_0^T H_0$.

$$H_0 = \begin{bmatrix} U(w_1, b_1, l_1) & \cdots & U(w_x, b_x, l_1) \\ \vdots & \dots & \vdots \\ U(w_1, b_1, l_{P_0}) & \cdots & U(w_x, b_x, l_{P_0}) \end{bmatrix}_{P_0 \times x}$$

$$T_0 = [t_1^T \dots t_{P_0}^T]_{P_0 \times m}^T \tag{12}$$

Suppose another chunk of training data $\rho_1 = \{(l_i, t_i)\}_{i=P_0+1}^{P_0+P_1}$ is given, where the number of observations in this chunk is P_1, the problem then requires to minimize (12) as follows.

$$\left\| \begin{bmatrix} H_0 \\ H_1 \end{bmatrix} \beta - \begin{bmatrix} T_0 \\ T_1 \end{bmatrix} \right\| \tag{13}$$

$$H_1 = \begin{bmatrix} U(w_1, b_1, l_{P_0+1}) & \cdots & U(w_x, b_x, l_{P_0+1}) \\ \vdots & \dots & \vdots \\ U(w_1, b_1, l_{P_0+P_1}) & \cdots & U(w_x, b_x, l_{P_0+P_1}) \end{bmatrix}_{P_1 \times x}$$

$$T_1 = \left[t_{P_0+1}^T \dots t_{P_0+P_1}^T\right]_{P_1 \times m}^T \tag{14}$$

This work is licensed under a Creative Commons Attribution-NonCommercial-NoDerivatives 4.0 License. For more information, see https://creativecommons.org/licenses/by-nc-nd/4

This article has been accepted for publication in IEEE Access. This is the author's version which has not been fully edited and content may change prior to final publication. Citation information: DOI 10.1109/ACCESS.2023.3280540

Equation (13) holds true, and when we consider the two chunks ρ_0 and ρ_1 of the training data sets, the output weight β evaluates to

$$\beta^{(1)} = K_1^{-1}\begin{bmatrix}H_0\\H_1\end{bmatrix}^T\begin{bmatrix}T_0\\T_1\end{bmatrix} \tag{15}$$

where

$$K_1 = K_1^{-1}\begin{bmatrix}H_0\\H_1\end{bmatrix}^T\begin{bmatrix}H_0\\H_1\end{bmatrix} \tag{16}$$

For sequential learning, output weight $\beta^{(1)}$ is expressed as a function of $\beta^{(0)}, K_1, H_1$, and T_1 and not that of chuck ρ_0 of training data. K_1 is rewritten as

$$K_1 = [H_0^T \;\; H_1^T]\begin{bmatrix}H_0\\H_1\end{bmatrix} = K_0 + H_1^T H_1 \tag{17}$$

$$\begin{aligned}\begin{bmatrix}H_0\\H_1\end{bmatrix}^T\begin{bmatrix}T_0\\T_1\end{bmatrix} &= H_0^T T_0 + H_1^T T_1\\ &= K_0 K_0^{-1} H_0^T T_0 + H_1^T T_1\\ &= K_0\beta^{(0)} + H_1^T T_1\\ &= (K_1 - H_1^T H_1)\beta^{(0)} + H_1^T T_1\\ &= K_1\beta^{(0)} - H_1^T H_1\beta^{(0)} + H_1^T T_1\end{aligned} \tag{18}$$

Combining (15) and (18), $\beta^{(1)}$ becomes

$$\begin{aligned}\beta^{(1)} &= K_1^{-1}\begin{bmatrix}H_0\\H_1\end{bmatrix}^T\begin{bmatrix}T_0\\T_1\end{bmatrix}\\ &= K_1^{-1}(K_1\beta^{(0)} - H_1^T H_1\beta^{(0)} + H_1^T T_1)\\ &= \beta^{(0)} + K_1^{-1}H_1^T(T_1 - H_1\beta^{(0)})\end{aligned} \tag{19}$$

where K_1 is given by

$$K_1 = K_0 + H_1^T H_1 \tag{20}$$

A recursive least squares algorithm is similar to the recursive updation algorithm for least squares solution. When the $(K+1)$th chunk, ρ_{k+1} is received,

$$\begin{aligned}&\rho_{k+1} = \{(l_i, t_i)\}_{i=(\sum_{j=0}^{k} P_j)+1}^{\sum_{j=0}^{k+1} P_j},\ K_{k+1} = K_k + H_{k+1}^T H_{k+1},\\ &\beta^{(k+1)} = \beta^{(k)} + K_{k+1}^{-1}H_{k+1}^T(T_{k+1} - H_{k+1}\beta^{(k)})\\ &H_{k+1} =\end{aligned} \tag{21}$$

$$\begin{bmatrix}U(w_1,b_1,l_{(\sum_{j=0}^{k} P_j)+1}) & \cdots & U(w_x,b_x,l_{(\sum_{j=0}^{k} P_j)+1})\\ \vdots & \ldots & \vdots\\ U(w_1,b_1,l_{\sum_{j=0}^{k+1} P_j}) & \cdots & U(w_x,b_x,l_{\sum_{j=0}^{k+1} P_j})\end{bmatrix}_{P_{k+1}\times x} \tag{22}$$

$$T_{k+1} = \left[t^T_{(\sum_{j=0}^{k} P_j)+1} \ldots t^T_{\sum_{j=0}^{k+1} P_j}\right]^{Transpose}_{P_{k+1}\times m} \tag{23}$$

Equation (22) and (23) hold.

Instead of K_{k+1}, K_{k+1}^{-1} is used for the computation of $\beta^{(k+1)}$ from $\beta^{(k)}$ in (21). The derivation for the updation formula for K_{k+1}^{-1} is made using Woodbury formula [52].

$$\begin{aligned}K_{k+1}^{-1} &= (K_k + H_{k+1}^T H_{k+1})^{-1}\\ &= K_k^{-1} - K_k^{-1}H_{k+1}^T\left(I + H_{k+1}K_k^{-1}H_{k+1}^T\right)^{-1} \times H_{k+1}K_k^{-1}\end{aligned} \tag{24}$$

Let $A_{k+1} = K_{k+1}^{-1}$, the updation equations for $\beta^{(k+1)}$ can then be rewritten as

$$A_{k+1} = A_k - A_k H_{k+1}^T(I + H_{k+1}A_k H_{k+1}^T)^{-1}H_{k+1}A_k$$

$$\beta^{(k+1)} = \beta^{(k)} + A_{k+1}H_{k+1}^T(T_{k+1} - H_{k+1}\beta^{(k)}) \tag{25}$$

Equation (25) gives the recursive formula for $\beta^{(k+1)}$.

III. PROPOSED METHOD

The existing transfer learning models are not sufficient in fish disease classification because they do not have the ability to emphasize salient features and weaken meaningless regions which lowers the classification performance. In fish disease classification task, the idea is to focus on key regions that present discriminative features for the various fish diseases. Additionally, the deep sequential networks do not have the ability to integrate and enrich the feature maps during feature extraction. This paper therefore uses the keras functional API that allows inputs which are a list of tensors of the same shape other than the concatenation axis, and concatenates them to return a single tensor. This strengthens the feature maps and improves feature extraction.

Given an input image, preprocessing is done to remove noise and make the image consistent with the neural network input specifications. The multi-layer fusion network then performs feature extraction whereas the attention module suppresses the meaningless regions and strengthens regions of higher interest for feature refinement. The output features are then flattened and fed to the OSELM network for classification. This flow of processes is shown in Fig. 3.

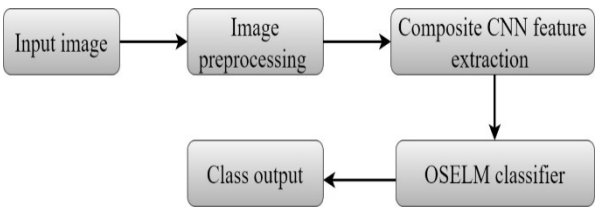

FIGURE 3. Process flow.

A. MODEL NETWORK STRUCTURE

The proposed method comprises of convolutional blocks that consist of Conv2D layers, pooling layers, dropout and batch normalization layers, ReLU, softmax activation and OSELM classification layer. The preprocessed image data is input to two parallel backbone networks. The output feature map is obtained by:

$$v_i^p = f\left(\sum_{i\in M_k} V_i^{p-1}.W_{ik} + b_i\right) \tag{26}$$

where p refers to the convolutional layers, W_{ik} is the convolutional kernel, b_i is the bias and V_i^{p-1} is the input channel map, and $f()$ represents the activation function. ReLU activation is used in the succeeding blocks since it is nonlinear and unsaturated. It can reduce training time, solve over fitting and provide fast convergence [46].

This work is licensed under a Creative Commons Attribution-NonCommercial-NoDerivatives 4.0 License. For more information, see https://creativecommons.org/licenses/by-nc-nd/4

This article has been accepted for publication in IEEE Access. This is the author's version which has not been fully edited and content may change prior to final publication. Citation information: DOI 10.1109/ACCESS.2023.3280540

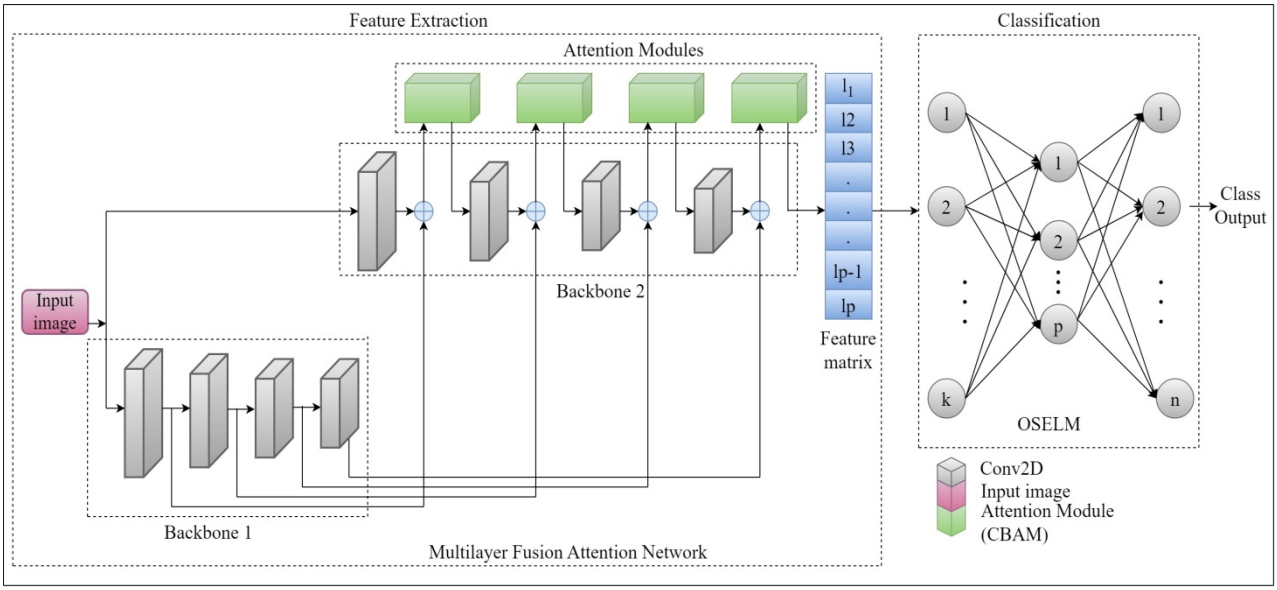

FIGURE 4. The proposed architecture.

The proposed network builds from parallel multiple backbones that are identical to each other. This enables the integration of same level features of the identical backbones for feature refinement. The features output by blocks $1, 2, \dots, n$ in backbone 1 are concatenated by the output features which are of the same size from the corresponding blocks in backbone 2 and refined by the corresponding attention block. Conventionally, the design procedure of most CNNs convolves channel maps of the input images into their respective intermediate features whose resolution is monotonically lower. In our network, the $(s+1)$th block of backbone 2 takes the refined feature map F_2^{att+1} resulting from the concatenation of output, x_1^s of the s-th block of backbone 1 and output x_2^s of the s-th block of backbone 2 and refined by attention block 1, that is:

$$F_2^{att+1} = F_1^s(x^s) \oplus F_2^s(x^s) \tag{27}$$

After the convolution operations, OSELM is then used for the classification of the 1-D vectors obtained after converting the output feature maps from the attention based multilayer convolutional network. The OSELM network randomly sets the input weights and biases of the hidden layer whereas only the output weights are updated. The input parameters are randomly generated and only the output weights are calculated during the model training stage. The entire process with no iteration operation generally improves the generalization ability of the neural network. The output 12544×1 of the CNN from the last layer is the input to the OSELM as elaborated in Table II.

Although it has been proven theoretically in [23] that so long as ELM models have as many nodes in the hidden layer as possible, they are able to make approximation of any continuous target functions with any degree of accuracy. It has been experimented that random addition of hidden layer nodes did not guarantee better performance of ELM [54]. The recommendation is to automatically determine the initial hidden layer node number by using incremental constructive techniques such as incremental extreme learning machine (I-ELM) [51] and enhanced incremental ELM (EI-ELM) [14], among others and then optimizing the initial model in order to obtain optimal network. In this study we adopt the number of hidden nodes as 16384 because it has been experimented with similar output size in [54] and proven to perform well. This also saves the computation cost and training time. The proposed architecture is shown in Fig. 4 and the expanded structure of the CNN network blocks is shown in Fig. 5. The proposed method is shown in Algorithm I.

TABLE II. DETAILS OF CONVOLUTIONAL OPERATIONS OF THE PROPOSED METHOD

Layers	**Backbone 1 Parameters**	**Backbone 1 Parameters**
Input	256 × 256 × 3	256 × 256 × 3
Block 1	Conv2D_1, 2 Filters: 3 × 3 *32 Shape: 224×224×32 MaxPool: 2×2 Shape: 112, 112, 32	Conv2D_1 Filters: 3 × 3 *32 Shape: 224×224×32 MaxPool: 2×2 Shape: 112, 112, 32
Block 2	Conv2D_1, 2 Filters: 3 × 3 *1*64 Shape: 112, 112, 64 MaxPool: 2×2 Shape: 56, 56, 64	Conv2D_1 Filters: 3 × 3 *1*64 Shape: 112, 112, 64 MaxPool: 2×2 Shape: 56, 56, 64
Block 3	Conv2D_1, 2,3,4 Filters: 3 × 3 *1*128 Shape: 56, 56, 128 MaxPool: 2×2 Shape: 28, 28, 128	Conv2D_1 Filters: 3 × 3 *1*128 Shape: 56, 56, 128 MaxPool: 2×2 Shape: 28, 28, 128
Block 4	Conv2D_1, 2,3,4 Filters: 3 × 3 *1*256 Shape: 28, 28, 256 MaxPool: 2×2 Shape: 7, 7, 256	Conv2D_1 Filters: 3 × 3 *1*256 Shape: 28, 28, 256 MaxPool: 2×2 Shape: 7, 7, 256
FC-1	(None, 12544)	(None, 12544)
Softmax OSELM		Input vector length: 16384 Hidden nodes: 8192
Output		Class Output

This work is licensed under a Creative Commons Attribution-NonCommercial-NoDerivatives 4.0 License. For more information, see https://creativecommons.org/licenses/by-nc-nd/4

This article has been accepted for publication in IEEE Access. This is the author's version which has not been fully edited and content may change prior to final publication. Citation information: DOI 10.1109/ACCESS.2023.3280540

ALGORITHM I. THE PROPOSED METHOD

Input: RGB image set $\{v_i, t_i\}, i = 1,2, \ldots, N$

Output: CNN feature extractor $f(v_i)$, output matrix H_k that maps channel and spatial features M_u of image v_i to its corresponding class label t_i.

1. Input RGB image of size 224×224.
2. Perform convolutional operations with attention to generate feature matrix $\{(l(i), t(i))\}_{i=1}^{P}$.
3. Remove the dense layers of feature extractor.
4. Initialize model learning using a small chunk of initial training sample matrix ρ_0 the training set.
5. Compute H_0, through (12) the output matrix of the hidden layer.
6. Estimate the initial output weight $\beta^{(0)}$ and set $k = 0$.
7. Calculate the output matrix H_{k+1} through (22) of for the $(k+1)th$ chunk of samples ρ_{k+1}.
8. Set $T_{k+1} = [t_{(\sum_{j=0}^{k} P_j)+1}, \ldots, t_{(\sum_{j=0}^{k+1} P_j)}]^T$.
9. Calculate the output weight $\beta^{(k+1)}$ though (25).
10. Set $k = k + 1$.

return the CNN feature extractor $f(v_i)$

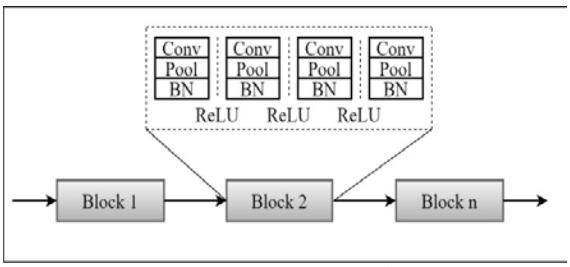

FIGURE 5. Detailed structure of CNN blocks.

B. PERFORMANCE EVALUATION METRICS

The classification performance has been determined using precision, accuracy, recall, and F-measure/score from the confusion matrix with TP, TN, FP, and FN, referring to true positive, true negative, false positive, and false negative, respectively. TP is prediction in which the predicted class label on the test data indeed correlates with the class of the ground truth image. FP refers to a prediction in which the predicted class does not belong to the class of the ground truth image. TN refers to a prediction in which the model predicts that a given test image does not belong to a given class and it is indeed true and FN refers to a prediction where the test image belongs to the ground truth image class but the model predicts it as not belonging to that class.

1) ACCURACY

This is one of the ways to evaluate model performance. It is the ratio of correctly predicted classifications to the overall number of predictions made.

$$Accuracy = \frac{TP+TN}{TP+TN+FP+FN} \quad (28)$$

2) PRECISION

This refers to the proportion of accurately classified samples in relation to the TP and FP values. In other words, it is a computation of the percentage of samples that are correctly classified.

$$Precision = \frac{TP}{TP+FP} \quad (29)$$

3) RECALL/SENSITIVITY

This refers to the ratio of TP to the sum of TP and FN.

$$Recall = \frac{TP}{TP+FN} \quad (30)$$

4) F1-SCORE

This is calculated as the symphonic mean of precision and recall.

$$F1 - score = \frac{2 \times Precision \times Recall}{Precision+Recall} \quad (31)$$

IV. DATASET AND PREPROCESSING

This section presents the details of the dataset used in the study and the preprocessing stages undertaken to make the data samples compliant with network specifications.

A. DATASET

The fish disease dataset is a custom dataset that has been collected from various internet sources. It includes a total of 649 low resolution images of infected fish and non-infected fish. The images have been captured in both aquariums and wild environments and are distributed into 6 classes, EUS, white spot disease, diplopstomiasis, argulus, hexamitiasis and healthy fish. The image samples have been augmented using rotation, flipping, and cropping to obtain a total of 5,165 image samples as shown in Table III.

TABLE III. DATASET DETAILS

Class	Training (60%)	Validation (20%)	Test (20%)
EUS	451	151	151
Whitespot	648	216	216
Argulus	353	117	117
Diplopstomiasis	538	180	180
Hexamitiasis	295	98	98
Healthy	814	271	271
Total	**3,099**	**1,033**	**1,033**

The complex background environment poses a major challenge during feature extraction and disease identification by the learning algorithms. A source domain backbone to learn background information features was proposed and used to subtract the source domain information from the feature map of the entire image [19]. However, the presented method was not feasible without having a mechanism to initially separate the background from the entire image. In this paper, we eliminate the image background before passing the image data to the neural network in order to overcome noise and improve feature extraction as discussed in the next subsection.

The interferences caused by complex underwater environment makes the classification task very challenging due to the following issues:

1) LOW-RESOLUTION UNDERWATER IMAGES

The fish's texture feature information is lost due to low quality images which make it challenging in identifying fish diseases with similar characteristics such as argulus and diplopstomiasis.

2) COMPLEX SEABED BACKGROUND

The various images collected from the internet are from diverse sources including onshore and offshore aquariums

This work is licensed under a Creative Commons Attribution-NonCommercial-NoDerivatives 4.0 License. For more information, see https://creativecommons.org/licenses/by-nc-nd/4

This article has been accepted for publication in IEEE Access. This is the author's version which has not been fully edited and
content may change prior to final publication. Citation information: DOI 10.1109/ACCESS.2023.3280540

with varying seabed and dynamic plant textures. This reduces the feature extraction ability of CNNs and make it difficult to identify fish disease.

3) CAMOUFLAGE COLOR

The appearance of some fish diseases on the body surfaces of the fish is identical with the colour of the background. The fish skin affected by disease blends well with such environments and makes it hard to extract important features.

4) OCCLUSION

The fish's texture feature information is considerably lost due to obstruction from various objects and light reflection. This affects fish disease identification and increases the number of false positive predictions.

5) FISH DIVERSITY

The fish images collected have a variety of fish species which presents different patterns in the learning process. For example, there are many fish types in the collection of EUS disease. It would be easier to classify EUS among fish of the same species.

6) COMPLEX AND CHANGEABLE UNDERWATER ENVIRONMENT

The images collected from internet sources were collected at various times, scenes, and light intensities using cameras of various pixel sizes. The collected images vary in quality and light intensities which were not conducive for model learning that reduced the generalization ability of the model.

B. DATA PREPROCESSING

1) BACKGROUND ELIMINATION

The complex image backgrounds are a source of noise which over fits the model and lowers the classification performance. These backgrounds also give varying contrasts to the fish disease features and further interfere with the identification of important features for classification. In this paper, the image backgrounds have been eliminated to give uniform background to all the sample images for accurate model training. There exist a number of background removal techniques in image processing which are classified into edge-based techniques such as canny edge detection; foreground detection and machine learning based approaches such as thresholding and clustering, and deep learning approaches. These approaches have been reported to perform well on grayscale images but not on RGB images and the foreground pixels using the mean absolute deviation (MAD) tends to generate some isolated pixels (holes) in the target object interiors. We enhance the RGB colour space algorithm for background subtraction by initially applying a foreground detection technique using machine learning selfie segmentation with media pipe [20][55]. The selfie segmentation function assigns a float number in the range of [0.0, 1.0] to every pixel of the output mask. When the number assigned to each pixel is closer to 1.0, it indicates greater confidence for the pixel to represent the object of interest which in this case is fish. By contrast, the closer the value to 0, the more the confidence that the given pixel belongs to the background and is eliminated. The selfie segmentation then produces an output mask of the same image size as the input. However, due to the nature of underwater diseased fish images, the backgrounds are not completely eliminated. The output images of selfie segmentation still have some sheds of the background. Therefore, these images are further input to the RGB color space algorithm for background elimination.

The RGB colour space algorithm starts by assuming $u = (u, v)$, and $p(u)$ is a pixel whose intensity is expressed as $\boldsymbol{L}(u)$:

$$\boldsymbol{I}(u) = [L^R(u), L^G(u), L^B(u)]^K \tag{32}$$

where L^R, L^G and L^B refers to the intensities of the RGB color components (red, green, and blue, respectively). For simplifying the notations, superscript C is used to represent R, G or B.

Suppose $[\boldsymbol{L}_1(u), \boldsymbol{L}_2(u), \dots, \boldsymbol{L}_T(u)]$ denotes K image frames, and $\boldsymbol{M}(\boldsymbol{u})$ denotes the image that contains each pixel's temporal median, for $0 \le \alpha < 1$, the $\alpha-$ metrically trimmed mean $\lambda_\alpha^C(u)$ of every RGB component for each pixel u is obtained by calculating temporal average of $I_k^C(u)$, disregarding the biggest $[\alpha K]$ deviations away from the median point. Note that [.] denotes the largest integer function. Formally, taking into consideration an ordering of the differences $\left|I_k^C(u) - M^C(u)\right|$, and defining a function $1 \le f(u,k) \le K$ which is an integer function that returns the position of $\left|I_k^C(u) - M^C(u)\right|$ in such ordering, the α-metrically trimmed mean $\lambda_\alpha^C(u)$ is given by:

$$\lambda_\alpha^C(u) = \frac{1}{K-[\alpha K]} \sum_{t \epsilon Z_\alpha(u)} I_k^C(u), \tag{33}$$

where $Z_\alpha(u) = \{k: f(u,k) \le K - [\alpha K]\}$. When α = 0, the trimmed mean becomes exactly the average and as α approaches 1, the trimmed mean tends towards the median value. The value of α is experimentally set to 0.3 [3]. Moving forward, $\lambda^C(u)$ then refers to the α- metrically trimmed value of mean for the pixel u using α = 0.3.

It is necessary to evaluate the distribution of noise around the value of the actual background. This is done using scale parameter such as the standard deviation. However, in the colour space algorithm, a more robust scale estimator, called the mean absolute deviation (MAD), is used. MAD is defined as:

$$MAD^C(u) = \underset{k \epsilon \{1, \dots, K\}}{median} \left\{\left|I_k^C(u) - M^C(u)\right|\right\} \tag{34}$$

If we assume additive Gaussian noise, the relation $\sigma^C(u) = 1.4826 MAD^C(u)$ gives the standard deviation estimate of each RGB component for every pixel. Pixels that belong to the foreground tend to be far from the distribution's estimated mean. The foreground pixels normally appear in blobs and not isolated in the image. Therefore, we analyze close neighborhoods of each pixel. A pixel u is assigned to the foreground if

$$\sum_{x \epsilon \Omega(u)} w(\boldsymbol{x}) \left|I_k^C(\boldsymbol{x}) - \lambda^C(x)\right| > h \sum_{x \epsilon \Omega(u)} w(\boldsymbol{x}) \sigma^C(\boldsymbol{x}), \tag{35}$$

This work is licensed under a Creative Commons Attribution-NonCommercial-NoDerivatives 4.0 License. For more information, see https://creativecommons.org/licenses/by-nc-nd/4

This article has been accepted for publication in IEEE Access. This is the author's version which has not been fully edited and
content may change prior to final publication. Citation information: DOI 10.1109/ACCESS.2023.3280540

where $\Omega(u)$ denotes a small close neighborhood with center u, $w(\boldsymbol{x})$ is a weighting mask for every pixel $\boldsymbol{u} = (u, v)$, h determines the maximum possible deviation away from the mean value with respect to the standard deviation and the weighted average mask is denoted by w, with a central point whose weight is 4, weight of horizontal and vertical neighbors being 2, and 1 for diagonal neighbors. The neighborhood is set to 3×3 for Ω and h = 3.

The implementation has been done in opencv library and the sample preprocessing results are presented in Table IV.

TABLE IV. SAMPLE IMAGE PREPROCESSING STAGES

Original image	Resized image (512×512)	Contrast enhancement	Background elimination
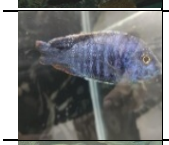	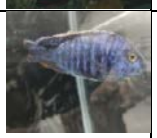		
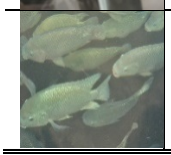			

2) PIXEL ENHANCEMENT

This is applied to enhance the image contrast by increasing the domain of pixel intensity values.

3) IMAGE RESIZE

All sample images are resized to a dimension of 512 × 512 × 3 to reduce the computational model complexity.

4) DATA AUGMENTATION

We augmented the data using rotation and flipping to increase the data samples.

5) LABELING

The image files were assigned class labels for the classification task.

V. RESULTS AND DISCUSSION

In this paper, 649 image samples from a custom dataset are augmented to obtain a total of 5,165 images and preprocessed for contrast enhancement, background elimination. The dataset is divided into training, validation and test sets in the ratio of 3:1:1, respectively. The training set uses 3,099 images, validation set uses 1,033 images and the test set uses 1,033 images as well. All image inputs to the neural networks are of size 224×224×3. The same dataset is used for all the models in our experiments. The hardware and software specifications of the training environment include; Intel Core CPU i7-4790 of 3.6GHz, RAM of 16GB and supported by GPU (NVIDIA GeForce RTX 2080 Ti), Tensorflow 2.4.0 and Keras 2.3.1 environment with the following parameters: batch size of 4, Adam optimizer, with default parameters β1=0.9, β2=0.999, α =0.001 and ϵ=10-7 and cross entropy loss.

The proposed model is trained for 800 epochs on our dataset with eliminated background. The testing accuracy, precision, recall and F-measure are compared with state-of-the-art models used in image classification. We fine tune and train 5 deeper pretrained models for 300 epochs. The models are validated and tested on the same validation and test sets, respectively. The test performance comparisons are given in Table V.

TABLE V. PERFORMANCE COMPARISON OF PROPOED METHOD WITH PRETRAINED MODELS WITH BACKGROUND ELIMINATION

Model	Acc. (%)	P (%)	R (%)	F (%)	Parameters
VGG19	92.04	90.60	91.00	90.80	143M
ResNet50	92.00	92.80	88.00	90.40	25.6M
EfficientNet	91.60	89.07	88.00	88.54	4.2M
Inceptionv3	90.55	89.00	88.82	88.91	22.2M
Xception	90.40	87.00	91.00	89.00	21.5M
Proposed	**94.28**	**92.67**	**92.17**	**92.42**	**4.7M**

Note: ***Acc.*** denotes *accuracy*, ***P*** denotes *precision*, ***R*** denotes *recall* and ***F*** denotes *F1-score*.

In comparison with the transfer learning models, the proposed model performs better with a top accuracy of 94.28% which is 2.2% higher than the accuracy of VGG19, the highest performing model in terms of accuracy among the pretrained models, precision of 92.67%, recall of 92.17% and F1-score of 92.42%. The proposed network is less deep which reduces feature information loss and reduces the vanishing gradient problem and learns well on limited data. The attention modules further suppress regions of low interest and focus on more meaningful regions to enhance the feature extraction process. This intimates that more deeper and important features are easily extracted. The addition of the OSELM in the place of the fully connected layer further strengthens the classification process by reducing the training time and loss. This is achieved because the input nodes to hidden node weights and biases are generated randomly and the output weights are determined analytically on the basis of the training samples arriving sequentially. The proposed network has much less parameters compared to the pretrained models.

To further ascertain the impact of our composite CNN-OSELM network in comparison to other attention-based networks, the deep pretrained models have been enhanced by integrating attention mechanism after the last convolutional layer. The models are trained for 500 epochs, validated and tested on the same dataset. The performance comparison with the proposed method is shown in Table VI.

TABLE VI. PERFORMANCE COMPARISON OF PROPOSED METHOD WITH ATTENTION-BASED PRETRAINED MODELS WITH BACKGROUND ELIMINATION

Model	Acc. (%)	P (%)	R (%)	F (%)
VGG19+CBAM	93.38	91.00	91.83	91.50
ResNet50+CBAM	93.81	92.67	89.83	91.25
EfficientNet+ CBAM	92.28	91.00	89.00	90.00
Inceptionv3+ CBAM	91.40	90.00	88.50	89.25
Xception+ CBAM	91.99	89.50	91.00	90.25
Proposed Model	**94.28**	**92.67**	**92.17**	**92.42**

The proposed model still outperforms the pretrained-attention models by over 0.47% accuracy. The multilayer

This work is licensed under a Creative Commons Attribution-NonCommercial-NoDerivatives 4.0 License. For more information, see https://creativecommons.org/licenses/by-nc-nd/4

This article has been accepted for publication in IEEE Access. This is the author's version which has not been fully edited and
content may change prior to final publication. Citation information: DOI 10.1109/ACCESS.2023.3280540

fusion network is less deep but wider, with two backbones that fuse features from the same level blocks. This refines the feature maps further and reduces loss that arises due to diminishing gradient problem commonly experienced in very deep networks. The OSELM further improves the classification performance and reduces the number of parameters. This is because only the number of hidden layers is selected and other parameters are automatically determined. To better appreciate the performance of the proposed method in comparison with the pretrained attention models, we present a detailed summary of the class-wise performance in Table VII.

TABLE VII. CLASS-WISE PERFORMANCE COMPARISON OF THE PROPOSED METHOD WITH ATTENTION-BASED PRETRAINED MODELS WITH BACKGROUND ELIMINATION. (UNIT: %)

Model	Parameter	EUS	WSS	Argulus	Diplopstomiasis	Hexamitiasis	Healthy
VGG19+CBAM	Accuracy	92.73	98.80	82.00	92.00	95.94	98.80
	Precision	92.00	98.00	79.00	90.00	92.00	95.00
	Recall	95.00	96.00	75.00	92.00	95.00	98.00
	F1-score	93.50	97.50	77.00	91.00	93.50	96.50
ResNet50+CBAM	Accuracy	94.44	98.70	82.50	92.40	96.22	98.60
	Precision	93.00	99.00	80.00	93.00	92.00	99.00
	Recall	91.00	96.00	68.00	90.00	96.00	98.00
	F1-score	92.00	97.50	74.00	91.50	94.00	98.50
EfficientNet+ CBAM	Accuracy	90.09	98.30	81.70	91.00	95.30	97.30
	Precision	92.00	97.00	79.00	89.00	93.00	96.00
	Recall	93.00	96.00	67.00	89.00	92.00	97.00
	F1-score	92.50	96.50	73.00	89.00	92.50	96.50
Inceptionv3+ CBAM	Accuracy	92.05	97.40	80.33	89.90	92.70	96.00
	Precision	89.00	98.00	78.00	88.00	92.00	95.00
	Recall	93.00	92.00	70.00	89.00	93.00	94.00
	F1-score	91.00	95.00	74.00	88.50	92.50	94.50
Xception+ CBAM	Accuracy	92.00	98.40	80.35	90.16	95.02	96.00
	Precision	90.00	95.00	73.00	88.00	93.00	98.00
	Recall	93.00	96.00	77.00	90.00	94.00	96.00
	F1-score	91.50	95.50	75.00	89.00	93.50	97.00
Proposed Model	Accuracy	93.58	99.20	82.90	92.16	98.84	99.00
	Precision	92.00	98.00	80.00	91.00	96.00	99.00
	Recall	95.00	100.00	75.00	92.00	96.00	95.00
	F1-score	93.00	99.00	77.00	91.00	96.00	97.00

The class-wise classification performance results presented in Table VIII show that our proposed model achieves the best results on overall for all the 6 classes, followed by attention-based ResNet50 and VGG19. However, in comparison with performance results of the baseline models depicted in Table VI, it shows that CBAM considerably improves the performance of the baseline models by an average of 1% on accuracy, 1.8% on precision, and 0.5% and 1.3% on recall and F1-score, respectively. The class-wise performance in Table VII reveals that the classification performance of whitespot disease was highest with an accuracy of 99.20% and F1-score of 99% followed by the healthy class with an accuracy of 99% and F1-score of 97%. This pattern is true in both the proposed method and the attention-based pretrained models. This is attributed to the physical characteristics of these two classes which makes them very distinct and easily identified. In Table VI, attention-based ReNet50 generally out competes its counterparts due to its ability to maintain a low error rate with skip connections that help to regularize layers in case of performance degradation. However, the classification performance of argulus was poorest with the proposed model achieving an accuracy of 82.90% and F1-score of 77%. Moreover, all the attention-based pretrained models also indicate a similar performance on the argulus class despite hexamitiasis class having the least number of training samples. The poor classification performance of argulus is associated with the nature of the disease. The argulus disease causing agent, Argulidae, tends to attach itself on the body of its host. However, the host will bear physical characteristics of the infestation after the disease has adversely progressed. The proposed approach bases the recognition ability on the presence of the Argulidae on the fish body which tends to resemble the colour of its host making it difficult to identify. The class-wise performance of the proposed method with background elimination is graphically illustrated in Fig. 6.

The image background are initially subtracted in the RGB color space from the training samples to reduce noise brought about by the unstable water environment due to multiple underwater scenes, complex underwater seabed, reflections, low contrast, low-resolution and blurring of images. To illustrate the relevancy of image background elimination in our study, we further trained, validated and tested the proposed model and the attention-based pretrained models on the original dataset without background elimination. In other words, the models were trained, tested and validated on the same number of data samples with their original background as opposed to the previous experiments. The summarized results are shown in Table VIII and the class-wise performance results are shown in Table IX. The results attained by all the models show a poor uniform

This work is licensed under a Creative Commons Attribution-NonCommercial-NoDerivatives 4.0 License. For more information, see https://creativecommons.org/licenses/by-nc-nd/4

This article has been accepted for publication in IEEE Access. This is the author's version which has not been fully edited and
content may change prior to final publication. Citation information: DOI 10.1109/ACCESS.2023.3280540

pattern of accuracy, precision, recall and F1-score though the proposed method still achieves better results compared to the attention based pretrained models.

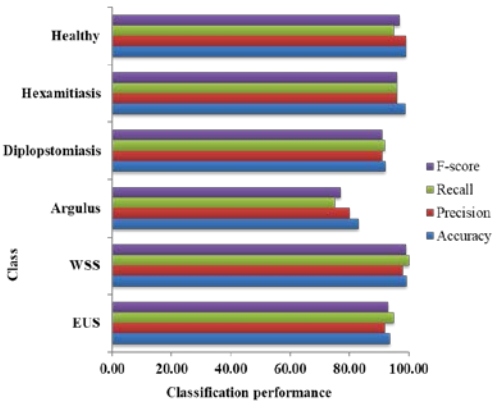

FIGURE 6. Class-wise performance of the proposed method with background elimination.

The performance of the proposed method without background removal is demonstrated graphically in Fig. 7 for a clearer overview. The class-wise performance without background elimination generally reveals an over-fitting problem and is generally poor with some classes having very low values of F1-score and accuracy and others having fairly higher accuracy values but with low precision and recall.

TABLE VIII. PERFORMANCE COMPARISON OF PROPOSED METHOD WITH ATTENTION-BASED PRETRAINED MODELS WITHOUT BACKGROUND ELIMINAION.

Model	Acc.	P	R	F
VGG19+CBAM	78.86	80.50	78.50	79.50
ResNet50+CBAM	81.25	83.33	74.50	77.50
EfficientNet+CBAM	78.79	77.50	82.50	79.17
Inceptionv3+CBAM	71.65	66.33	73.33	69.33
Xception+CBAM	69.59	66.17	67.50	66.50
Proposed	**86.11**	**82.00**	**89.00**	**84.00**

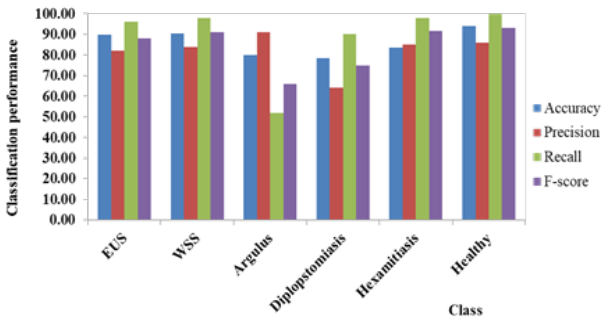

FIGURE 7. Class-wise performance of the proposed method without background removal.

TABLE IX. CLASS-WISE PERFORMANCE COMPARISON OF PROPOSED METHOD WITH ATTENTION-BASED PRETRAINED MODELS WITHOUT BACKGROUND ELIMINATION. (UNIT: %)

Model	Parameter	EUS	WSS	Argulus	Diplopstomiasis	Hexamitiasis	Healthy
VGG19+CBAM	Accuracy	60.44	84.32	81.00	75.62	85.00	86.79
	Precision	55.00	96.00	79.00	71.00	87.00	95.00
	Recall	52.00	85.00	71.00	80.00	92.00	91.00
	F1-score	54.00	90.50	75.00	75.00	89.50	93.00
ResNet50+CBAM	Accuracy	82.47	82.96	79.58	80.00	80.30	82.24
	Precision	77.00	80.00	95.00	59.00	92.00	97.00
	Recall	91.00	82.00	55.00	88.00	71.00	60.00
	F1-score	83.00	81.00	70.00	71.00	81.50	78.50
EfficientNet+ CBAM	Accuracy	78.34	82.96	67.00	79.06	80.99	84.40
	Precision	69.00	89.00	67.00	82.00	71.00	87.00
	Recall	52.00	94.00	86.00	69.00	100.00	94.00
	F1-score	60.00	91.50	75.00	75.00	83.00	90.50
Inceptionv3+ CBAM	Accuracy	60.00	83.00	42.79	69.22	84.91	90.00
	Precision	56.00	85.00	31.00	55.00	82.00	89.00
	Recall	65.00	90.00	50.00	70.00	79.00	86.00
	F1-score	60.00	87.50	39.00	62.50	80.00	87.00
Xception+ CBAM	Accuracy	66.79	81.30	56.00	62.00	71.47	80.00
	Precision	49.00	93.00	52.00	47.00	71.00	85.00
	Recall	61.00	88.00	46.00	60.00	71.00	79.00
	F1-score	55.00	90.00	49.00	52.00	71.00	82.00
Proposed Model	Accuracy	89.88	90.48	80.10	78.62	83.59	94.00
	Precision	82.00	84.00	91.00	64.00	85.00	86.00
	Recall	96.00	98.00	52.00	90.00	98.00	100.00
	F1-score	88.00	91.00	66.00	75.00	91.50	93.00

VI. CONCLUSION AND FUTURE WORK

This study proposed a multilayer fusion attention CNN-OSELM network for fish disease recognition in aquaculture. We built a more powerful feature extractor that integrated the output features from same level blocks to enhance feature extraction using SLC and multilayer fusion with CBAM. Classification was also improved by incorporating the OSELM at the fully connected layer. The dataset used in the study was collected from various internet sources and the image backgrounds were initially subtracted in the RGB colour space from the training samples to reduce noise brought about by interferences from multiple underwater scenes, complex underwater seabed background, low contrast, reflections, low-resolution and blurring of images. The network was trained, tested and validated on both the preprocessed dataset and the original dataset to appreciate the impact of background elimination in underwater fish disease

This work is licensed under a Creative Commons Attribution-NonCommercial-NoDerivatives 4.0 License. For more information, see https://creativecommons.org/licenses/by-nc-nd/4

This article has been accepted for publication in IEEE Access. This is the author's version which has not been fully edited and
content may change prior to final publication. Citation information: DOI 10.1109/ACCESS.2023.3280540

images. The pretrained backbone networks with and without attention mechanism were also trained, validated and tested on the same dataset for performance comparisons. The trained models were evaluated on the basis of accuracy, precision, recall and F1-score. The test results achieved by the proposed method were better compared to that of the pretrained models. The class-wise performance also indicated that whitespot disease and healthy had higher classification performance than the rest of the classes due to the distinctive and more visible nature of these infections.

In the future, fore training data were required to step up the classification performance of the remaining classes. The experimental results show a promising trend in the fish disease detection research.

REFERENCES

[1] G. Chamberlain, "Global aquaculture alliance annual report,' *Global aquaculture alliance*, New Hampshire, USA, pp.1-36, Dec. 2019.
[2] Q. Dongyu "The state of world fisheries and aquaculture report," *Food and Agricultural Organization (FAO) of the United Nations*, Rome, Italy, pp.1-73, Mar. 2020.
[3] M. Tavares-Dias and L. M. Maurı, "An overall estimation of losses caused by diseases in the Brazilian fish farms," *Journal of Parasitic Disease*, vol. 41, no. 4, pp.913-918, Oct. 2017.
[4] E. J. Noga, "*Fish Disease: Diagnosis and Treatment*," 2nd Edition, Wiley-Blackwell, ISBN: 978-0-813-80697-6, pp.1-544, Jun. 2010.
[5] G. Osman, M. M. Alam, S. M. I. Khalil, et al., "Identification of pathogenic bacteria from diseased stringing catfish Heteropneustis fossilis with their sensitivity to antibiotics," *Int. Journal of Fisheries and Aquatic Studies*, vol. 8, no. 1, pp.291-301, Dec. 2019.
[6] N. Steckler and R. P. E. Yanong, "Argulus (fish louse) infections in fish," *Univ. of Florida*, vol. 184, no. 1, pp.1-4, Jan. 2022.
[7] R. Wang et al., "Studies on the isolation of Photobacterium damselae subsp. piscicida from diseased golden pompano (Trachinotus ovatus Linnaeus) and antibacterial agents' sensitivity," *Veterinary Microbiology*, vol. 162, no. 1, pp.957-963, Sep. 2012.
[8] H. A. Alturkistani, F. M. Tashkandi, and Z. M. Mohammedsaleh, "Histological stains: A literature review and case study," *Global Journal of Health Science*, vol. 8, no. 3, pp.72-79, May 2016.
[9] A. E. Toranzo, B. Magarinos, and J. L. Romalde, "A review of the main bacterial fish diseases in mariculture systems," *Aquaculture Journal of Elsevier*, vol. 246, no. 1, pp.37-61, Dec. 2005.
[10] M. Sun, X. Yang, and Y. Xie, "Deep learning in aquaculture: A review," *Journal of Comp.*, vol. 31, no. 1, pp.294-319, Jan. 2020.
[11] J.-H. Wang, S.-K. LEE, Y.-C. Lai, et al., "Anomalous behaviors detection for underwater fish using AI techniques," *IEEE Access*, vol. 8, no. 1, pp.224372-224382, Dec. 2020.
[12] K. P. R. A. Haq and V. P. Harigovindan, "Water quality prediction for smart aquaculture using hybrid deep learning models," *IEEE Access*, vol. 10, no. 1, pp.60078-60098, Jun. 2022.
[13] S. P. Khabusi and Y.-P. Huang, "A deep learning approach to predict dissolved oxygen in aquaculture," in *Proc. of Int. Conf. on Advanced Robotics and Intelligent Systems (ARIS)*, Taipei, Taiwan, pp.1-6, Aug. 2022.
[14] L. Kuang, P. Shi, C. Hua, B. Chen, and H. Zhu, "An enhanced extreme learning machine for dissolved oxygen prediction in wireless sensor networks," *IEEE Access*, vol. 8, no. 1, pp.198730-198739, Nov. 2020.
[15] D. Li, J. Sun, H. Yang, and X. Wang, "An enhanced Naive Bayes model for dissolved oxygen forecasting in shell fish aquaculture," IEEE *Access*, vol. 8, no.1, pp.217917-217927, Dec. 2020.
[16] W.-C. Hu, L.-B. Chen, B.-K. Huang, and H.-M. Lin, "A computer vision-based intelligent fish feeding system using deep learning techniques for aquaculture," *IEEE Sensors Journal*, vol. 22, no. 7, pp.7185-7194, Apr. 2022.
[17] H. Yang, X. Wang, J. Sun, and D. Li, "Dissolved oxygen prediction using RBF network based on improved conjugate gradient method," in *Proc. of IEEE 11th Int. Conf. on Software Eng. and Service Sc.*, Beijing, China, pp.515-518, Oct. 2020.
[18] W.-H. Lin, J.-X. Zhong, S. Liu, T. Li, and G. Li, "ROIMIX: Proposal-fusion among multiple images for underwater object detection," in *Proc. IEEE Int. Conf. Acoust., Speech Signal Process. (ICASSP)*, Barcelona, Spain, pp.2588-2592, May 2020.
[19] Z. Zhao, Y. Liu, X. Sun, et al., "Composited FishNet: Fish detection and species recognition from low-quality underwater videos," *IEEE Trans. on Image Processing*, vol. 30, no. 1, pp.4719-4734, Apr. 2021.
[20] C. R. Jung, "Efficient background subtraction and shadow removal for monochromatic video sequences," *IEEE Trans. on Multimedia*, vol. 11, no. 1, pp.571-577, Apr. 2009.
[21] Y. Liu, Y. Wang, S. Wang, et al., "CBNet: A novel composite backbone network architecture for object detection," in *Proc. AAAI Conf. Artificial. Intelligence*, vol. 34, no. 7, pp.11653-11660, Apr. 2020.
[22] T. Liang, X. Chu, Y. Liu, et al., "CBNet: A composite backbone network architecture for object detection," *IEEE Trans. on Image Processing*, vol. 31, no. 1, pp.6893-6906, Oct. 2022.
[23] N.-Y. Liang, G.-B. Huang, P. Saratchandran, and N. Sundararajan, "A fast and accurate online sequential learning algorithm for feedforward networks," *IEEE Trans. on Neural Networks*, vol. 17, no. 6, pp.1411-1423, Nov. 2006.
[24] G.-B. Huang, Q.-Y. Zhu, and C.-K. Siew, "Extreme learning machine: Theory and applications," *Neurocomputing*, vol. 70, no. 1, pp.489-501, May 2006.
[25] F. Wang, M. Jiang, C. Qian, et al., "Residual attention network for image classification," *Cornell Univ. Rep*., pp.3156-3164, Apr. 2017.
[26] J. Hu, L. Shen, and G. Sun, "Squeeze-and-excitation networks," *Cornell Univ. Rep*., pp.1-13, May 2019.
[27] M. S. Ahmed, T. T. Aurpa, and M. A. K. Azad, "Fish disease detection using image-based machine learning technique in aquaculture," *Journal of King Saudi University*, vol. 34, no. 8, pp.5170-5182, May 2022.
[28] S. Malik, T. Kumar, and A. K. Sahoo, "Image processing techniques for identification of fish disease," in *Proc. of IEEE 2nd Int. Conf. on Signal and Image Processing*, Singapore, pp.55-59, Aug. 2017.
[29] V. Lyubchenko, R. Matarneh, O. Kobylin, and V. Lyashenko, "Digital image processing techniques for detection and diagnosis of fish diseases," *Int. Journal of Advanced Research in Computer Science and Software Engineering*, vol. 6, no. 7, pp.79-83, Jul. 2016.
[30] Y. Wang, H. Ye, and B. Li, "A research based on recognition algorithm of characteristics of body surface of infected fish," in *Proc. of World Automation. Congress*, Kobe, Japan, Sep. 2010.
[31] J. Liu, H. Yu, W. Yang, and C. Sun, "Combining active learning and semi-supervised learning based on extreme learning machine for multi-class image classification, "in *Proc. of Int. Conf. on Intelligent Sci. and Big Data Eng.*, Suzhou, China, pp. 163-175, Jun. 2015.
[32] Y. Zeng, X. Xu, Y. Fang, and K. Zhao, "Traffic sign recognition using deep convolutional networks and extreme learning machine," in *Proc. of Int. Conf. on Intelligent Sci. and Big Data Eng.*, Suzhou, China, pp.272-280, Jun. 2015.
[33] R. Dwivedi, T. Dutta, and Y.-C. Hu, "A leaf disease detection mechanism based on L1-norm minimization extreme learning machine," *IEEE Geoscience and Remote Sensing Letters*, vol. 19, no. 1, pp.8019905-8019905, Aug. 2022.
[34] Nahiduzzaman, O. F. Goni, et al., "A novel method for multivariate pneumonia classification based on hybrid CNN-PCA based feature extraction using extreme learning machine with CXR images," *IEEE Access*, vol. 9, no. 1, pp.147512-147526, Oct. 2021.
[35] X. Zhang and L. Qin, "An improved extreme learning machine for imbalanced data classification," *IEEE Access*, vol. 10, no. 1, pp.8634-8642, Jan. 2022.
[36] Q. Lv, X. Niu, Y. Dou, J. Xu, and Y. Lei, "Classification of hyperspectral remote sensing image using hierarchical local-receptive-field-based extreme learning machine," *IEEE Geoscience and Remote Sensing Letters*, vol. 13, no. 3, pp.434-438, Mar. 2016.
[37] Y. Bazi, N. Alajlan, F. Melgani, H. AlHichri, S. Malek, and R. R. Yager, "Differential evolution extreme learning machine for the classification of hyperspectral images," *IEEE Geoscience and Remote Sensing Letters*, vol. 11, no. 6, pp.1066-1070, Jun. 2014.
[38] G.-B. Huang, H. Zhou, X. Ding, and R. Zhang, "Extreme learning machine for regression and multiclass classification," *IEEE Trans. on*

This work is licensed under a Creative Commons Attribution-NonCommercial-NoDerivatives 4.0 License. For more information, see https://creativecommons.org/licenses/by-nc-nd/4

This article has been accepted for publication in IEEE Access. This is the author's version which has not been fully edited and
content may change prior to final publication. Citation information: DOI 10.1109/ACCESS.2023.3280540

Systems, Man, and Cybernetics-Part B: Cybernetics, vol. 42, no. 2, pp.513- 529, Apr. 2012.

[39] Y. Zhou, J. Peng, and C. L. P. Chen, "Extreme learning machine with composite kernels for hyperspectral image classification," *IEEE Journal of Selected Topics in Applied Earth Observations and Remote Sensing*, vol. 8, no. 6, pp.2351-2360, Jun. 2015.

[40] Y. Yang, and Q. M. J. Wu, "Extreme learning machine with subnetwork hidden nodes for regression and classification," *IEEE Trans. on Cybernetics*, vol. 46, no. 12, pp.2885-2898, Dec. 2016.

[41] X. Liu, Q. Hu, Y. Cai, and Z. Cai, "Extreme learning machine-based ensemble transfer learning for hyperspectral image classification," *IEEE Journal of Selected Topics in Applied Earth Observations and Remote Sensing*, vol. 13, no.1, pp.3892-3902, Jun. 2020.

[42] H. Li, H. Zhao, and H. Li, "Neural-response-based extreme learning machine for image classification," *IEEE Trans. on Neural Networks and Learning Systems*, vol. 30, no. 2, pp.539-552, Feb. 2019.

[43] T.-Y Lin, P. Dollar, R. Girshick, K. He, B. Hariharan, S. Belongie, "Feature pyramid networks for object detection," in *Proc. IEEE Conf. Computer Vision and Pattern Recognition (CVPR)*, Honolulu, USA, pp.2117-2125, Aug. 2017.

[44] S. Woo, J. Park, J.-Y. Lee, and I. S. Kweon, "CBAM: convolutional block attention module," *Cornell. Univ Rep.*, pp.1-17, Jul. 2018.

[45] P. K. Wong, C. M. Vong, X. H. Gao, and K. I. Wong, "Adaptive control using fully online sequential-extreme learning machine and a case study on engine air-fuel ratio regulation," *Mathematical Problems in Engineering, Hindawi*, vol. 1, no. 1, pp.1-11, Apr. 2014.

[46] A. Krizhevsky, I. Sutskever, and G. E. Hinton, "ImageNet classification with deep convolutional neural networks," in *Proc. of the Advances in Neural Information Processing Systems*, Lake Tahoe, NV, USA, pp.1097-1105, Dec. 2012.

[47] N. Wang, M. J. Er, and M. Han, "Generalized single-hidden layer feedforward networks for regression problems," *IEEE Trans. on Neural Networks and Learning Systems*, vol. 26, no. 6, pp.1161-1176, Jun. 2015.

[48] S. Tamura and M. Tateishi, "Capabilities of a four-layered feedforward neural network: Four layers versus three," *IEEE Trans. on Neural Networks*, vol. 8, no. 2, pp.251-255, Mar. 1997.

[49] G.-B. Huang, "Learning capability and storage capacity of two-hidden layer feedforward networks," *IEEE Trans. On Neural Networks*, vol. 14, no. 2, pp.274-281, Mar. 2003.

[50] C. R. Rao and S. K. Mitra, "Generalized inverse of a matrix and its applications," in *Proc. of the 6th Berkeley Symposium on Mathematical Statistics and Probability*, CA, USA, pp.601-620, Jul. 1971.

[51] G.-B. Huang, L. Chen, and C.-K. Siew, "Universal approximation using incremental constructive feedforward networks with random hidden nodes," *IEEE Trans. on Neural Networks*, vol. 17, no. 4, pp.879-892, Jul. 2006.

[52] G. H. Golub and C. F. V. Loan, *Matrix Computations*, 3rd Edition, Baltimore, MD: The Johns Hopkins Univ. Press, ISBN: 0-8018-5414-8, pp.1-723, 1996.

[53] G.-B. Huang et al., "On-line sequential extreme learning machine," in *Proc. Int. Conf. Computational Intelligence*, Calgary, Canada, pp.1-6, Jul. 2005.

[54] J. Sharma, O.-C. Granmo, and M. Goodwin, "Deep CNN-ELM hybrid models for fire detection in images," in *Proc. Artificial Neural Networks and Machine Learning (ICANN)*, Rhodes, Greece, pp.245-259, Sep. 2018.

[55] J. Ye, T. Gao, and J. Zhang, "Moving object detection with background subtraction and shadow removal," in *Proc. of 9th Int. Conf. on Fuzzy Systems and Knowledge Discovery (FSKD)*, Chongqing, China, pp.1859-1863, May 2012.

YO-PING HUANG (Fellow, IEEE) received the Ph.D. Degree in Electrical Engineering from Texas Tech University, Lubbock, TX, USA. He is currently the President of National Penghu University of Science and Technology, Penghu, Taiwan. He is also a Chair Professor in the Department of Electrical Engineering, National Taipei University of Technology, Taipei, Taiwan, where he served as the Secretary General. He was a Professor and the Dean of Research and Development, the Dean of the College of Electrical Engineering and Computer Science, and the Department Chair with Tatung University, Taipei. His current research interests include fuzzy system design and modeling, deep learning modeling, intelligent control, medical data mining, and rehabilitation systems design. Dr. Huang received 2021 Outstanding Research Award from Ministry of Science and Technology, Taiwan. He is Fellows of IET, CACS, TFSA, and an International Association of Grey System and Uncertain Analysis. He serves as the IEEE SMCS VP for Conferences and Meetings and the Chair of the IEEE SMCS Technical Committee on Intelligent Transportation Systems. He was the IEEE SMCS BoG, the President of the Taiwan Association of Systems Science and Engineering, the Chair of the IEEE SMCS Taipei Chapter, the Chair of the IEEE CIS Taipei Chapter, and the CEO of the Joint Commission of Technological and Vocational College Admission Committee, Taiwan.

SIMON PETER KHABUSI (Graduate Student Member, IEEE) received the B.S. Degree in Computer Engineering from Busitema University, Tororo, Uganda in 2016 and the M.Tech. Degree in Computer Science and Engineering from Delhi Technological University, Delhi, India in 2020. He is currently pursuing the Ph.D. Degree in Electrical Engineering from the National Taipei University of Technology, Taipei, Taiwan. Before joining the doctoral program, he was working as a systems administrator at Uganda Heart Institute, Mulago National Referral Hospital, Kampala, Uganda and part-time Assistant Lecturer at Ernest Cook Ultrasound Research and Education Institute, Mengo Hospital, Kampala, Uganda. His research interests include machine learning, deep learning and computer vision and their applications in aquaculture, network and information security, medical image analysis and health informatics.

This work is licensed under a Creative Commons Attribution-NonCommercial-NoDerivatives 4.0 License. For more information, see https://creativecommons.org/licenses/by-nc-nd/4

A Comparative Study on Clickbait Detection using Machine Learning Based Methods

Kapil Kumar Yadav
Department of Computer Science Delhi Technological University,
New Delhi, India
singhkapil347@gmail.com

Nipun Bansal
Department of Computer Science Delhi Technological University,
New Delhi, India
Nipunbansal@dtu.ac.in

2023 International Conference on Disruptive Technologies (ICDT) | 979-8-3503-2388-7/23/$31.00 ©2023 IEEE | DOI: 10.1109/ICDT57929.2023.10150475

Abstract—Clickbait is a type of providing false content, intended to attract a variety of users and get engagement and monetary benefits. It makes users curious to click the link and follow the content in various formats like audio, video, text, and images. Clickbait detection is a critical and difficult task. Many researchers have proposed various techniques using deep learning techniques and machine learning techniques like Logistic Regres- sion, Linear Support Vector Machine, Adaboost, Multilayer Per- ceptron, Random Forest, Convolution Neural Networks(CNN), and Recurrent Convolutional Neural Networks (RCNN). To give a clear overview of the efficient algorithms, we went through some existing studies from 2016–2022, which proposed various clickbait detection methods. This review gives an exhaustive study of existing methods and also suggests some recommendations for further enhancements to be done by combining the various deep learning techniques and machine learning techniques.

Keywords— Clickbait, Natural Language Processing, Deep Learning, Machine Learning.

I. INTRODUCTION

In today's world, with all the advancements in technology and a significant increase in the number of users accessing the internet and online resources, there is also an increase in vulnerable and clickbait data on the internet. Clickbait is simply poor content with no meaning or value-added data, which is fed to the user by exciting them with catchy textual and non-textual data. The purpose of clickbait is to get more views on their sites, which will lead to more revenue via advertisements and other sources. These clickbait articles or news feeds create an irrelevant experience for humans and sometimes distract them to favour a particular agenda. Clickbaits can be categorized into eight types: teasing, ambiguous, formatting, inflammatory, wrong, graphic, exaggeration, and bait-and-switch [23].

Fig. 1. Some News Headlines

In Fig. 1, some headlines were given, and they were taken from pop- ular news websites. As we can see, the headlines seem so promising and exciting that there is a high probability of clicking the headlines to read the complete news. In recent years, clickbait has become extremely popular. People in this domain want early success, and for that, they do whatever they feel will increase their business. A lot of research has been already done to detect clickbait, and Facebook in 2014 took action to remove the clickbaits as per El-Arini and Tang [24]. Reis et al. [25] took a dataset of 69,000 headlines and observed the polarity of sentiments found in these headlines and extremities in the gained popularity. Headlines are the first impressions of the news and decide whether the user will read it or not, as per Digirolamo and Hintzman [26]. Loewenstein [27] also explained the information gap theory, according to him, what we know and what we wish to know vary, and this difference has emotional consequences. Users become curious about these gaps. Not knowing makes us uncomfortable. Natural Language Processing (NLP) has gained more popularity to find context and is very frequently used in the below models. To understand the context better, convolutional neural networks (CNN) have been used in many models to improve accuracy, as per Kim [28].

Pothast et al. [29] were one of the first, to work on detecting clickbait on Twitter, but the problem was not limited to Twitter, the same problem exists with other social media platforms as well. Gianotto and Alison [30] came up with approaches like "down-worthy," which transforms the headlines into something more garbage-ish after applying a predefined set of words to identify clickbait. Using the dataset created by Chakraborty et al. [2], recurrent neural networks were used in an experiment by Anand et al. [19] to recognise clickbait news. They adopted a bi-directional RNN. Fig. 2 depicts the model architecture and the output of the model.

Fig. 2. Bi-Directional RNN architecture for clickbait detection [19]

Rony et al. [31] analysed the millions of Facebook posts from several organizations. Deep learning approaches have recently achieved suc- cess in text categorization, so they built their algorithms utilising distributed sub-word embeddings rather than bags of words and trained their systems using this dataset. They were able to achieve 98.3% accuracy. Lie et al. [32] utilised Integer Linear Programming, the addition of the relationship between the images and the text in the technique is what distinguishes their study apart from the competition.

The paper is divided into various sections. The relevant studies and existing clickbait detection methods are presented in Section 2. The conclusion, based on all the previous studies taken into consideration in the survey, is found in Section 3. The research gap and future research directions identified by these investigations are provided in Section 4, along with the conclusions.

II. RELATED WORK

To identify clickbait, Amol Agrawal [1] has presented a deep learning-based methodology. He used Convolution Neural Net- works(CNN) with one layer of convolution, the first layer was used for word embedding, During his experiments, he used both word embeddings created from scratch as well as word embeddings explored using an unsupervised neural model [12][13]. Word Vectors were then

Authorized licensed use limited to: DELHI TECHNICAL UNIV. Downloaded on June 28,2023 at 06:28:23 UTC from IEEE Xplore. Restrictions apply.

trained on billion words of google 1 news[14].In the next layer, convolutions over word vectors are produced using filters of various sizes (3, 4, and 5). A new feature is produced by each operation. A feature map is created using all the newly generated features. The feature map is subjected to a max-over-time pooling process [15], and the feature chosen for that particular feature map is the one having the highest value. These generated features from the filters constitute the subsequent layer, which is the penultimate layer. After that, a fully linked softmax layer receives these features and outputs the probability distribution over labels. He has used 5-fold cross-validation in his experiments. He compares both the scratch and the non-static word2vec models,and the click-word2vec beats the scratch model. He was able to get the highest F1-Score of 0.86, a precision of 0.85, an accuracy of 0.90, and a recall of 0.88.

In [2], A. Chakraborty et al. proposed a method by selecting N-gram features, Word Patterns, Sentence Structure, and Clickbait Languages. They used two approaches, one based on topical similarity and another based on linguistic patterns. They have done experiments using three prediction models - Decision Trees, Random Forests, and Support Vector Machines. They have done 10-fold cross-validation, out of all 3 prediction models, SVM performs the best, with the F1- score of 0.93, recall of 0.90, precision of 0.95, accuracy of 0.93, and ROC-AUC of 0.97 for all features.

TABLE I. PERORMANCE OF SVM CLASSIFER

SVM					
Features Used	ROC-AUC	Acc.	F1-Score	Prec.	Rec.
Sentence Structure	0.84	0.77	0.77	0.79	0.75
N-gram Features	0.9	0.89	0.89	0.92	0.85
Clickbait Language	0.88	0.86	0.85	0.88	0.82
Word Patterns	0.91	0.84	0.84	0.84	0.84
All features	**0.97**	**0.93**	**0.93**	**0.95**	**0.90**

They performed pattern-based, topic-based, and hybrid blocking approaches, and pattern-based approaches gave better results, so they implemented them into the browser extension. They offered a feature where users could examine the websites that the extensionhad blocked and provide feedback, whether it was clickbait or not.On average, around 89% of the time, the extension correctly blocked the clickbait sites.

[a] 1https://code.google.com/p/word2vec/

TABLE II. PERORMANCE OF BLOCKING APPROACHES

Approach	F1-Score	Acc.	Prec.	Rec.
Topic Based	0.74	0.75	0.769	0.74
Pattern Based	**0.79**	**0.81**	**0.834**	**0.76**
Hybrid	0.72	0.72	0.766	0.682

In [3], A. Gec¸kil et al. demonstrated the model by referencing the Potthast et al. [17] model. In [17], the authors selected 215 elements from among three groups: meta information, linked web pages, and teaser messages. Out of 215 features from the Potthast et al. [17] model, the last four features related to the metadata and the first 19 features of the teaser message were chosen. They classified the data according to the confidence index and decided whether the given headline was clickbait or not. When compared to the non- Clickbait word list, the frequency consistency of the news headline with the Clickbait word list should be higher than 0.08 and lower than 0.02, then the headline is considered a Clickbait headline. Using the TextRank algorithm, an unsupervised technique put forth by Rada Mihalcea and Paul Tarau [18], a summary of the titles has been generated. They were able to get a precision of 0.899, a F-Score of 0.920, a recall of 0.941, and an accuracy of 0.865.

In [4], S. Chawda et al. utilized the context of the titles and preferred Recurrent Convolutional Neural Network (RCNN) for text classifica- tion. They further enhanced the proposed model using LSTM and Gated Recurrent Unit (GRU) for better accuracy than the previous models. They used the pre-trained word2vec and randomly initiated word embeddings as input for RCNN. RCNN considers the left and right contexts of a given word. GRU and LSTM are further used to capture long-term dependencies. SVM in [2] gives an accuracy of 0.93, whereas using RCNN, the accuracy went to 0.950. Now, for further improvements, using LSTM with RCNN, the accuracy increased a bit and reached 0.9586. RCNN, when used with GRU, gave an accuracy of 0.9667, and finally, the proposed method of RCNN + GRU + Word2Vec gave an optimum accuracy of 0.9776.

S. Kaur et al. [5] proposed a method for textual as well as non- textual texts. They experimented using a two-phase hybrid CNN- LSTM biterm model and performed it on three different datasets. The first dataset was obtained from A. Chakraborty et al. [2], which contains 32,000 headlines from various news articles. The second dataset was taken from Khater et al. [20], which contains 12,000 headlines. The third dataset was created by the authors themselves and primarily contains the headlines from Reddit and Facebook pages. Word embedding is done using GloVe and Word2Vec. LSTM was used to capture the long-term sequences. CNN is used to extract high-level sequences of word features. Data pre-processing is done on non-textual data, where the image is converted into grayscale, noise removal, text extraction, and auto-correction are done, and the pre-processed data is fed into the proposed model. The performance of the proposed model is shown in Table 3.

In [6], P. Rajapraksha et al. demonstrated a model using transfer learn- ing models like XLNET, BERT, and RoBERTa to detect clickbait. They have taken the training dataset from Webis Clickbait Corpus 2017 2 and the testing dataset from Kaggle 'Train a clickbait detector' 3. They used these three models with different cases by fine-tuning them to categorize whether it was clickbait or not. They used 3 fine tuning strategies, model generalization, model expansion, and model compression. According to their experiments, the results for RoBERTa were far better than BERT and XLNet in many cases.

[b] 2https://webis.de/data/webis-clickbait-17.html

[c] 3https://www.tira.io/task/clickbait-detection/dataset/clickbait17-test-

[d] 170720/

TABLE III. PERORMANCE OF BLOCKING APPROACHES

Approach	Dataset	ROC-AUC	Acc	Prec.	F1-Score	Rec.
Without Pre-trained vectors	Dataset 1	0.87	0.81	0.82	0.81	0.79
	Dataset 2	0.81	0.78	0.80	0.79	0.78
	Dataset 3	0.87	0.84	0.84	0.82	0.80
With Word2vec pre-trained vectors	Dataset 1	0.97	0.93	0.92	0.85	0.80
	Dataset 2	0.89	0.84	0.90	0.85	0.81
	Dataset 3	0.94	0.89	0.91	0.88	0.85

Authorized licensed use limited to: DELHI TECHNICAL UNIV. Downloaded on June 28,2023 at 06:28:23 UTC from IEEE Xplore. Restrictions apply.

With GloVe pre-trained vectors	Dataset 1 Dataset 2 Dataset 3	0.99 0.94 0.98	0.95 0.89 0.94	0.91 0.95 0.95	0.88 0.92 0.93	0.85 0.89 0.91

In [7], B. Gamage et al. used a combination of deep learning models. Their approach is inspired by Zannettou et al. [21]. The idea ofthe authors is to use the different features of a YouTube video to classify it, and Zannettou et al. [21] focused more on user features such as titles, tags, statistics, and comments, whereas B. Gamage et al. considered an audio transcript along with the above features for evaluation. They used the same dataset as Zannettou et al. [21], which consists of 14000 videos, where 5,049 videos weren't clickbait and 8,591 videos were clickbait. The division of the dataset is donein 81% in training, 9% in validation, and 10% in testing. A multi- model deep learning architecture is built to classify whether the video is clickbait or not. An audio transcript is generated from the YouTube videos using the youtube-transcript API [22]. A separate model is applied to each of the features (title, thumbnail, comments, audio transcript, tags, statistics) and later combined into a single one. After combining, transfer learning is applied to the model, where dense layers were trained and fine-tuning was done throughout the entire model. Their model was successful in obtaining an accuracy of92.4%. but it cannot be considered the same with different datasets,as a result, the model was not able to give more than 85% of accuracyfor different datasets.

In [8], D. Varshney et al. proposed a similar method to B. Gamageet al. [7], but they categorized the features into three categories - Video-Content based features, user-profile-based features, and humanconsensus-based features. Video-based features contain speech-title similarity, dislike-like ratio, number of likes, and number of dislikes. In speech-to-title similarity, first, the audio is extracted from thevideo and an audio transcript is generated, later, the audio transcript and the title are compared using the cosine similarity formula, to find the similarity between them. Human consensus-based features include the number of comments, positive polarity, negative polarity,Fake comment count ratio, etc. User profile features consist of the total number of videos, subscribers-to-age ratio, subscriber count, channel views, and registration age. Various classifiers like SVM, Random Forest, Decision-Tree, SVM, and Logistic Regression were used to experiment, and the Random Forest outperformed them all. The authors were able to get the F1-score of 0.77, a recall of 0.78,and a precision of 0.84.

A. A. Balan et al. [9] presented a method using deep learning models, especially recurrent neural networks like Long short-term memory (LSTM). They used 32,000 headlines, including clickbaitas well as non-clickbait news. The data was taken from popularwebsites like 'ViralNova', 'BuzzFeed', 'Scoopwhoop', 'Thatscoop' etc. Preprocessing is done where text is converted to lowercase, punctuation is removed, and stop words are removed. Word2vec word embedding was used to convert text into word vectors. 20% of the dataset was used for testing, and the remaining 80% was used for training. LSTM was trained multiple times to improve efficiency. The most accurate LSTM units were 50 and 50. Different classifiers were compared with LSTM, like Naive Bayes, and LSTM performed betterthan Naive Bayes. The authors were able to get the F1 score of 0.96 with a recall of 0.96, a precision of 0.96, and an accuracy of 0.96.

In [10], S. Regina, K. Purwandari, et al used Natural Lan- guage Processing (NLP) methods along with supervised-learning methods like K-Nearest Neighbor, Decision trees, and Bidirec- tional Long Short-Term Memory. The dataset was taken from DATA INDONESIA.xlsx.Text preprocessing is done, and steps like stemming, folding, and tokenization have been performed on the data.Word2Vec is used for text embedding. The dataset was divided into 3:1:1 for training, validation, and testing. When a word or phrase may have many interpretations, bi-LSTM is more beneficial. The performance of Bi-LSTM, KNN, and decision trees is shown in Table-IV. Out of all the classifiers, Bi-LSTM performed better than others.

TABLE IV. PERORMANCE OF BLOCKING APPROACHES

Approach	Acc.	F1-Score	Prec.	Rec.
Bi-LSTM	**0.71**	**0.65**	**0.67**	**0.69**
KNN	0.577	0.388	0.51	0.313
Decision Tree	0.56	0.49	0.49	0.49

In [11], Y.-W. Ma et al. proposed an approach based on feature engineering and artificial intelligence. They had done data collection, feature extraction, text preprocessing, feature evaluation, etc. Their model used 18 format-based or lexicon features including title starts−with number, title− of exclamation,Number of inputs, Number of tags, etc. They have taken a dataset containing 6,000 non-clickbait and 6,000 clickbait headlines. A hybrid model is built using a neural network schema. CNN and LSTM are used to improve accuracy. Softmax activation function was used in the model, and an input layer and 100-D vectors of the title text are used in the embedding process. ANOVA is used for feature selection and extraction. They were able to get to a precision of 93.25% and an accuracy of 88.5%.

III. COMPARATIVE ANALYSIS OF EXISTING MODELS

Table V shows a summary of existing models like Random For- est, SVM, Decision Tree, Logistic Regression, Convolution Neural Network (CNN), Naive Bayes, RCNN, LSTM, CNN-LSTM, etc. to detect whether the given headline is clickbait or not. Among all these approaches, some models performed really well. Different textual features are extracted using NLP tools like N-gram, word patterns, and lexical features, and words are used like word2vec to enhance the performance of the classifiers. Different authors used different datasets to perform their experiments, but the majority of the data was collected using articles, social media sites, YouTube videos, etc. A. Chakraborty et al. [2]. The dataset was used by many researchers for their classifiers. In the given table, we have taken different performance evaluation parameters like accuracy, precision, F1-score, ROC-AUC, and recall and compared the models.

TABLE V. SUMMARY OF EXISTING MODELS

Author Name	Year	Approach	Dataset	Performance Evaluation Parameters	Result
Amol Agrawal et al.	2016	Word2vec and CNN with one layer of convolution	News articles Reddit, Facebook an- Different	Accuracy, ROC-AUC,	Accuracy = 0.90,

Authorized licensed use limited to: DELHI TECHNICAL UNIV. Downloaded on June 28,2023 at 06:28:23 UTC from IEEE Xplore. Restrictions apply.

A. Chakraborty et al.	2016	Features Selected - Sentence Structure, Clickbait Language, N-gram features, Word Patterns, Models used - SVM,Decision Tree, Random Forest	Non-clickbait data - Extracted headlines from 18,513 wikinews articles , Clickbaits - Collected arti-cles from ’Buzzfeed’, ’Upworthy’, ’Scoopwhoop’ etc.	F1-Score, Recall, Precision	F1-Score = 0.86
	2018		News Headlines from BBC Turkish, Anadolu Agency,Hurriyest,Newspaper Vatan	Accuracy, ROC-AUC,	Recall = 0.88,
A. Geçkil et al.	2019	Features Selected - Meta Information,Teaser Message(N-grams,bag of words) Models Used - Naive Bayes, Logistic Regression, Random Forest	A. Chakraborty et al [2].	Precision, F1-Score,Recall	ROC-AUC = 0.90
				Accuracy, F1-Score, Recall, Precision, Accuracy	Precision = 0.85, Accuracy = 0.93, ROC-AUC = 0.97
S. Chawda et al.	2020	Recurrent Convolution Neural Network (RCNN) + Gated Recurrent Unit (GRU) + Word2Vec	Dataset-1 : A. Chakraborty et al [2] Dataset-2 :S. R. Khater[20]	Accuracy, ROC-AUC,	Precision = 0.92,
		A Hybrid CNN-LSTM Biterm model with Glove and Word2vecpre-trained vectors and also without pre-trained vectors	Dataset-3 : Created a corpus fromReddit and Facebook of 1800 headlines.	Recall, F1-Score, Precision	F1-Score = 0.934
S. Kaur et al.	2021	Transfer Learning Models like BERT, RoBERTa and XLNet with fine-tuning with different cases	Webis Clickbait Corpus 2017, Kaggle dataset ’Train a clickbait’detector’	Recall, Accuracy, F1-Score,Precision Accuracy	Recall = 0.95, F1-Score = 0.920
P. Rajapaksha et al.	2021	Features selected - Title, comments, audio transcript, Tags, Statistics	Zannettou et al. [21]	Recall, Precision, F1-Score	Precision = 0.899, Accuracy = 0.865,
		Deep Learning Models - LSTM, CNN	Created a Dataset using Youtube Rest API v3. contains 987 videos,474 Cickbait, 513 Non-Clickbait		Recall = 0.941,
B. Gamage et al.	2021	Features selected - Title, comments, audio transcript, Tags, Statistics Model Used - SVM, Random Forest, Decision-Tree, logistic-Regression	Created a Dataset of 32000 headlines containing clickbaits and non-clickbaits from websites like ’BuzzFeed’, ’Upworthy’,’Scoopwhoop’	Accuracy, Precision, Recall, F1-Score	Accuracy = 0.9776
D. Varshney et al.	2022	Word Embedding using Word2Vec, Model Used - LSTM, Naive Bayes	Created a Dataset containing 15000 clickbaits and non-clickbaits from websites like ’Liputan6’, ’detikNews’,’Okezone’	Accuracy, F1-Score, Recall, Precision	Table - III
			Crawled data from websitescontaining 6000 clickbaits and 6000 non-clickbaitsheadllines	F1-Score, Accuracy, Recall, Precision	
A. A. Balan et al.	2022	Word Embedding using Word2Vec, Models Used- Bi-LSTM, KNN, Decision Tree			Precision = 0.73, Accuracy = 0.85,
		Lexicon and format-based features Model Used - CNN-LSTM			F1-Score = 0.69
S. Regina et al.					Recall = 0.87, Accuracy = 0.85
Y.-W. Ma et al.					Precision = 0.84, F1-Score = 0.77
					Recall = 0.78,
					Precision = 0.96, Accuracy = 0.96, F1-Score = 0.96
					Recall = 0.96, Table-IV
					Accuracy = 0.88, F1-Score = 0.98
					Recall = 0.98, Precision = 0.93,

Authorized licensed use limited to: DELHI TECHNICAL UNIV. Downloaded on June 28,2023 at 06:28:23 UTC from IEEE Xplore. Restrictions apply.

IV. CONCLUSION AND FUTURE WORK

Clickbait detection is a really difficult task, as in a world full of the internet, a lot of news headlines float from here to there, and sometimes it's very difficult to find the origin of the news as it takes time to actually detect whether it is confirmed news or not. That's why there is no fixed dataset used in the various models included in our study because news and headlines keep on changing, and publishers are getting more and more intelligent after every such detection model, so we need to keep improvising our models with a different dataset. In this study, we reviewed the existing models in the domain of clickbait detection and observed that machine learning algorithms have a very significant role in clickbait detection and that NLP tools are really important to understand the context of the data. In the future, clickbait detection can be identified by browser extensions as well as mobile applications. Until now, the experiment was performed on datasets with only a few languages; in the future, larger datasets with multiple languages will be collected by news websites and socialmedia sites. Future work also includes (1) finding important features that are more useful, (2) using the latest word embedding techniques, and (3) clickbait detection for thumbnails and video frames.

REFERENCES

[1] A. Agrawal, 'Clickbait detection using deep learning', in 2016 2nd international conference on next generation computing technologies (NGCT), 2016, pp. 268–272.

[2] A. Chakraborty, B. Paranjape, S. Kakarla, and N. Ganguly, 'Stop clickbait: Detecting and preventing clickbaits in online news media', in 2016 IEEE/ACM international conference on advances in social networks analysis and mining (ASONAM), 2016, pp. 9–16.

[3] A. Gec¸kil, A. A. Mu¨ngen, E. Gu¨ndogan, and M. Kaya, 'A clickbait detection method on news sites', in 2018 IEEE/ACM International Conference on Advances in Social Networks Analysis and Mining (ASONAM), 2018, pp. 932–937.

[4] S. Chawda, A. Patil, A. Singh, and A. Save, 'A novel approach for clickbait detection', in 2019 3rd International Conference on Trends in Electronics and Informatics (ICOEI), 2019, pp. 1318–1321.

[5] S. Kaur, P. Kumar, and P. Kumaraguru, 'Detecting clickbaits using two-phase hybrid CNN-LSTM biterm model', Expert Systems with Applications, vol. 151, p. 113350, 2020.

[6] P. Rajapaksha, R. Farahbakhsh, and N. Crespi, 'BERT, XLNet or RoBERTa: The Best Transfer Learning Model to Detect Clickbaits', IEEE Access, vol. 9, pp. 154704–154716, 2021.

[7] B. Gamage, A. Labib, A. Joomun, C. H. Lim, and K. Wong, 'Baitradar: A Multi-Model Clickbait Detection Algorithm Using Deep Learning', in ICASSP 2021-2021 IEEE International Conference on Acoustics, Speech and Signal Processing (ICASSP), 2021, pp. 2665–2669.

[8] D. Varshney and D. K. Vishwakarma, 'A unified approach for detection of Clickbait videos on YouTube using cognitive evidences', Applied Intelligence, vol. 51, no. 7, pp. 4214–4235, 2021.

[9] A. A. Balan, P. Anoop, and A. S. Mahesh, 'Clickbait Detection Using Long short-term memory', in 2022 Second International Conference on Interdisciplinary Cyber Physical Systems (ICPS), 2022, pp. 159–163.

[10] S. Regina, K. Purwandari, F. I. Kurniadi, and Others, 'Clickbait Headline Detection Using Supervised Learning Method', in 2022 IEEE Inter- national Conference on Internet of Things and Intelligence Systems (IoTaIS), 2022, pp. 408–412.

[11] Y.-W. Ma, J.-L. Chen, L.-D. Chen, and Y.-M. Huang, 'Intelligent Clickbait News Detection System Based on Artificial Intelligence and Feature Engineering', IEEE Transactions on Engineering Management, 2022.

[12] R. Collobert, J. Weston, L. Bottou, M. Karlen, K. Kavukcuoglu, and P. Kuksa, 'Natural language processing (almost) from scratch', Journal of machine learning research, vol. 12, no. ARTICLE, pp. 2493–2537, 2011.

[13] R. Socher, J. Pennington, E. H. Huang, A. Y. Ng, and C. D. Manning, 'Semi-supervised recursive autoencoders for predicting sentiment distri- butions', in Proceedings of the 2011 conference on empirical methods in natural language processing, 2011, pp. 151–161.

[14] T. Mikolov, K. Chen, G. Corrado, and J. Dean, 'Efficient estimation of word representations in vector space', arXiv preprint arXiv:1301. 3781, 2013.

[15] R. Collobert, J. Weston, L. Bottou, M. Karlen, K. Kavukcuoglu, and P. Kuksa, 'Natural language processing (almost) from scratch', Journal of machine learning research, vol. 12, no. ARTICLE, pp. 2493–2537, 2011.

[16] V. Piek et al., "Newsreader: How semantic web helps natural language processing helps semantic web," Special Issue Knowledge Based Systems, Elsevier.

[17] M. Potthast, S. Ko¨psel, B. Stein, and M. Hagen, 'Clickbait detection', in European conference on information retrieval, 2016, pp. 810–817.

[18] R. Mihalcea and P. Tarau, 'Textrank: Bringing order into text', in Proceedings of the 2004 conference on empirical methods in natural language processing, 2004, pp. 404–411.

[19] A. Anand, T. Chakraborty, and N. Park, 'We used neural networks to detect clickbaits: You won't believe what happened next!', in European Conference on Information Retrieval, 2017, pp. 541–547.

[20] S. R. Khater, O. H. Al-sahlee, D. M. Daoud, and M. S. A. El-Seoud, 'Clickbait detection', in Proceedings of the 7th international conference on software and information engineering, 2018, pp. 111–115.

[21] S. Zannettou, S. Chatzis, K. Papadamou, and M. Sirivianos, 'The good, the bad and the bait: Detecting and characterizing clickbait on youtube', in 2018 IEEE Security and Privacy Workshops (SPW), 2018, pp. 63–69.

[22] Jonas Depoix, youtube-transcript-api : YouTube Transcript/Subtitle API (including automatically generated subtitles and subtitle translations), 2020, Available at : https://pypi.org/project/youtube-transcript-api/

[23] P. Biyani, K. Tsioutsiouliklis, and J. Blackmer, '" 8 amazing secrets for getting more clicks": detecting clickbaits in news streams using article informality', in Thirtieth AAAI conference on artificial intelligence, 2016.

[24] K. El-Arini and J. Tang, 'News feed fyi: Click-baiting', Facebook Newsroom, 2014.

[25] J. Rieis, F. de Souza, P. V. de Melo, R. Prates, H. Kwak, and J. An, 'Breaking the news: First impressions matter on online news', in Proceedings of the international AAAI conference on web and social media, 2015, vol. 9, pp. 357–366.

[26] G. J. Digirolamo and D. L. Hintzman, 'First impressions are lasting impressions: A primacy effect in memory for repetitions', Psychonomic Bulletin & Review, vol. 4, no. 1, pp. 121–124, 1997.

[27] G. Loewenstein, 'The psychology of curiosity: A review and reinterpre- tation', Psychological bulletin, vol. 116, no. 1, p. 75, 1994.

[28] K. Yoon, 'Convolutional Neural Networks for Sentence Classification [OL]', arXiv Preprint, 2014.

[29] M. Potthast, S. Ko¨psel, B. Stein, and M. Hagen, 'Clickbait detection', in European conference on information retrieval, 2016, pp. 810–817.

[30] A. Gianotto, 'Downworthy: A browser plugin to turn hyperbolic viral headlines into what they really mean', downworthy. snipe. net, 2014.

[31] M. M. U. Rony, N. Hassan, and M. Yousuf, 'Diving deep into clickbaits: Who use them to what extents in which topics with what effects?', in Proceedings of the 2017 IEEE/ACM international conference on advances in social networks analysis and mining 2017, 2017, pp. 232–239.

[32] W. Li and H. Zhuge, 'Summarising news with texts and pictures', in 2014 10th International Conference on Semantics, Knowledge and Grids, 2014, pp. 100–107.

Authorized licensed use limited to: DELHI TECHNICAL UNIV. Downloaded on June 28,2023 at 06:28:23 UTC from IEEE Xplore. Restrictions apply.

Environmental Science and Pollution Research
https://doi.org/10.1007/s11356-023-27934-x

RESEARCH ARTICLE

A novel technique of schedule tracker for parabolic dish concentrator

Rajkumar Malviya[1] · Akash Patel[1] · Ayush Singh[1] · Santosh Jagadev[1] · Prashant Baredar[1] · Anil Kumar[2]

Received: 25 December 2022 / Accepted: 19 May 2023
© The Author(s), under exclusive licence to Springer-Verlag GmbH Germany, part of Springer Nature 2023

Abstract

Tracking is important in a system that harnesses solar energy. Single axis tracking mechanism is cheaper and simple to develop but because of the limitation of tracking axis, this system is less efficient than dual axis. Dual-axis tracking systems necessitate a large number of equipment, sensors, motors, and a lengthy computer program to function properly. Therefore, in the present study, a novel method of solar tracking has been discussed where each tracking point has the impact of both the azimuth and altitude angle at a single point. This method is an average axis tracking method (AATM). HelioScope software was used to extract the hourly solar altitude and azimuth angles for each day and month for the site of Bhopal, India. The average method was then used to get the hourly average solar tracking angle (ASTA) for each month. The parabolic dish concentrator was designed in SolidWorks to apply and simulate the newly developed tracking points on SolTrace software. The graphical analysis was presented along with proper validation of the proposed method, and the single and dual axes were compared with AATM. The graphical study shows that the average axis tracking points have a smoother slop of wave than the single axis. From June to September, the proposed method's error was estimated between 0.85 and 0.95. It can be concluded that by making slight adjustments to the seasonal angle, this error could be minimized and the concept could be successfully applied to a parabolic dish or a solar PV system.

Keywords Solar energy · Sun tracking · Parabolic dish concentrator · Schedule technique · SolTrace · HelioScope

Nomenclature

D	diameter of dish (mm)
Ar	receiver area (mm^2)
A_d	aperture area of dish (mm^2)
H	depth (mm)
F	focal length (mm)
S	arc length of dish (mm)
Ψ_{rim}	rim angle (deg.)
$\varnothing$	altitude angle
γ_s	solar azimuth angle
θ_z	zenith angle
α	average solar tracking angle (ASTA)

Abbreviations

AATM	average axis tracking method
ASTA	average solar tracking angle
CSP	concentrated solar power
PDC	parabolic dish concentrator
PV	photovoltaic
NREL	National Renewable Energy Laboratory

Responsible Editor: Philippe Garrigues

✉ Akash Patel
aks.bpl91@gmail.com

Rajkumar Malviya
er.rajkmalviya@gmail.com

Ayush Singh
singh.ayush1024@gmail.com

Santosh Jagadev
santoshjagadev123@gmail.com

Prashant Baredar
prashantbaredar@gmail.com

Anil Kumar
anilkumar76@dtu.ac.in

[1] Energy Centre, Maulana Azad National Institute of Technology, Bhopal, M.P 462003, India

[2] Department of Mechanical Engineering, Delhi Technological University, Delhi 110042, India

Introduction

The shift from traditional energy to sustainable, renewable energy sources is currently the most pressing global task. Over the last decade, some countries have seen a rapid expansion of renewable energy sources. Among the sustainable energy sources, solar energy is the most appealing

Published online: 05 June 2023

and abundant (Srinivasarao et al. 2021; Bishoyi and Sudhakar 2017). Solar energy receives special attention because it is freely accessible regardless of location and can be used as an energy source for a variety of autonomous systems (Ahmet et al. 2021; Tukymbekov et al. 2019). Numerous studies have shown that solar tracking systems, depending on the installation mechanism and operating algorithms, boost the efficiency of concentrating technology. Solar tracking systems are classified into two types based on their design and operation principles: single-axis and dual-axis solar trackers. Single-axis solar trackers have only one rotational axis for orienting to the sun. Depending on the tracker location coordinates, the axis of rotation might be horizontal, vertical, or with a fixed angle of rotation. However, such solar tracking systems cannot properly track the sun's journey during the day (Nadia et al. 2020). Dual-axis trackers feature two axes of rotation. Such trackers have several advantages to single-axis trackers, but they are more difficult to implement and cost more (Shufat et al. 2019; Fahad et al. 2019).

In concentrating solar power CSP technology, the parabolic dish collector is the most efficient way to convert solar energy. A parabolic reflector (dish) and a solar thermal receiver situated at the focal point comprise a parabolic dish concentrator. The parabolic dish has high-temperature applications and could be beneficial for solar thermal steam generation and solar thermal power generation (Bijarniya et al. 2016; Malviya et al. 2021). A tracking system is used to continuously track the sun's direction to capture the reflected solar energy from the dish to the receiver. Depending on the degree of movement, there are two types of solar tracking systems. The single-axis solar tracking systems track the sun from one side to the other by rotating a single pivot point, and the dual-axis solar tracking systems monitor the sun along two independent axes by rotating two pivot points. Thus, the tracking system is critical to the operation of CSP-based systems for effective collection and concentration of sunlight onto the receiver for conversion into a useable form of energy (Natarajan et al. 2019; Sahu et al. 2022; Kumar et al. 2022; Malik and Alahmer 2022). The importance of tracking in solar thermal and solar PV are discussed by many authors in the past, the recent 5-year articles with their key contributions in the field of solar tracking are discussed in Table 1.

Some of the authors had previously made significant contributions in the field of solar tracking systems, which were deemed to be necessary to review for the current investigation. Fatha Badi (2016) discusses the application of maximum power point tracking (MPPT) in a sensor-less biaxial tracker. When compared to present practices, the principal benefit of using the suggested solar tracking system is an increase in the energy efficiency of 28.8–43.6%, depending on the season (Fatha Badi 2016). Khlaichom and Sonthipermpoon (2016) developed a sun-tracking system with a two-axis (altitude and azimuth) control loop that was closed-loop controlled by a genetic algorithm (GA). According to the results of the tests, a tracking system with GA boosted output voltage by 7.084% over a system without GA (Khlaichom and Sonthipermpoon 2016). Skouras (2018) conducted a comparative evaluation of the design and construction of sun-tracking systems for collar parabolic concentrator displacement (created at the Centre of Energy, Tunisia). It was discovered that one of the three pilot sun-tracking systems had a tracking error of less than 0.2° (Skouras 2018). Sadeque and Ahsan (2014) provided an algorithm for detecting the sun's location and implementing this control approach on a single-axis solar tracking system to obtain the maximum quantity of solar energy. The highest absolute error is about 2.4°. A comparison was done between the measured and actual azimuth angles (Sadeque and Ahsan 2014). Eke and Senturk (2012) compared the performance of a double-axis sun tracking system and a latitude tilt fixed system. When the double-axis sun-tracking system is compared to the latitude tilt fixed system, the double-axis sun-tracking system produces 30.79% more PV electricity (Eke and Senturk 2012). Ponniran and Ali Munir (2011) developed and tested a method for automatically tracking the sun's motion through the sky to increase the quantity of solar power gathered. This concept was intended for private dwellings and was developed for a single axis (Ponniran and Ali Munir 2011). Bakos (2006) performed an experiment to investigate the effect of two-axis tracking on the amount of solar energy harvested, which is also based on the combination of photo-resistors and the programming method for controlling them. The two-axis sun tracking system was created with a simple and low-cost electromechanical setup that required little maintenance and was simple to set up and use (Bakos 2006).

According to the mentioned research review, a schedule tracker is more efficient than a system without a tracker. A single axis examines either azimuth or altitude tracking, whereas dual tracking considers both axes. As a result, single and dual trackers require one and two motors, respectively, to align the PDC with the sun. Independent parameters are explicitly followed for each axis in either method of tracking. If an optimum parameter including the effect of both azimuth and altitude angles can be discovered, then the effects of both angles are determined by a single parameter. As a result, a single motor can produce the effect of both angles. This paper presents an innovative schedule tracker algorithm that combines the azimuth and altitude parameters into a single attribute. A novel solar tracking angle has been introduced named average solar tracking angle (ASTA). The objective of the present work is to identify the tracking error of ASTA using different software tools and graphical analysis. The average solar tracking method shows promising results after being analyzed graphically with proper validation.

Table 1 Literature survey of some solar tracking methods proposed by other researchers in recent 5 years

Authors (year)	Proposed work with a tracking mechanism	Implemented technology	Result
Karabiber and Güneş (2023)	The asymmetric sun tracker (AST) is a single-motor, dual-axis solar tracking system. The adjustable asymmetrical platform that holds the PV panels is AST's most significant innovation.	PV system	Because of its asymmetrical stand, AST can track the sun in both axes while moving on only one. AST increases the daily electrical energy produced by PV panels by 25 to 38% when compared to a fixed solar system.
Mohammed and Mohammed (2022)	An astronomical formula is used to compute the sun's altitude and azimuth based on the given latitude and longitude coordinates.	PV system	The daily increase in power generation from fixed to tracked panel structure is 17.3%. The excess electricity generated is spread out during the period between solar noon.
Tchao et al. (2022)	A computer vision-based dual-axis solar tracking algorithm is presented and constructed, which includes a vision controller, camera, light sensor, Arduino microcontroller, two stepper motors, a stick, and a transparent plate.	Heliostats field for CSP	The suggested technology is not reliant on location and can be put in a single heliostat or in a group of heliostats.
Henriques et al. (2021)	The control of angle deviation within a (polar) single axis setup is the basis for this work.	PV system	According to the proposed model, total gathered energy would be around 96.5% of a dual axis system on a yearly average basis.
Saymbetov et al. (2021)	A dual-axis schedule tracker and a dual-axis schedule tracker with an adaptive algorithm are evaluated in terms of performance.	PV system	The developed dual-axis method of tracking the sun outperforms the dual-axis schedule tracker by 41%.
Barbón et al. (2021)	A new open-loop solar tracking system with three movements for a small-scale linear Fresnel reflector has been conceived, constructed, and simulated.	Linear Fresnel reflector	The proposed system produces 16.64% more energy, has a 78.46% higher energy-to-area ratio, and has a 4.62% lower levelized cost of energy.
Kuttybay et al. (2020)	In varied weather circumstances, a stationary photovoltaic system, as well as single-axis solar trackers based on schedule and light-dependent resistor (LDR) photosensors, was assessed.	PV system	In varied weather situations, a schedule-based solar tracking system outperforms LDR solar trackers by 4.2%.
Zhu et al. (2020)	The tilted-rotating axis tracking (TR-axis tracking) structure is a unique single-axis tracking structure.	PV system	This system rotates a tracked panel along a slanted axis of rotation, with the panel angled relative to the axis of revolution. The suggested tracked panel's annual solar radiation incidence is 96.40% larger than that incident on a dual-axis tracked panel.
Sahu et al. (2021)	Design and development of an experimental study manual tracking on dual-axis.	Parabolic dish concentrator	According to the economic analysis, it is more cost effective than the other existing dish concentrators in the literature, which cost 6877.00 per square meter.
Kuttybay et al. (2019)	Intelligent automated solar tracking control system with adaptive algorithm based on experimental data.	PV system	The proposed method collects 18% more energy with a biaxial solar tracker.
Batayneh et al. (2019)	Using the isotropic and HDKR anisotropic models, investigate the effect of discrete three-positional single-axis solar tracking.	PV system	During the summer season, tracking the sun in three optimum angle movements produced around 91–94% of solar energy collection as a continuous single-axis solar tracker that moved three times an hour based on solar calculations.
Rahimoon et al. (2019)	Using Arduino, create a dual-axis tracking system for a parabolic solar dish.	Parabolic dish concentrator	The Arduino dual-axis tracking system is installed with the PDC, confirming the higher efficiency as a result of the proposed PDC combined PV system.
Arif et al. (2019)	Created a microcontroller-based sun tracker control system for solar cell systems.	PV system	Rather than fixed systems, the generated power increased in the tracking system.
Natarajan et al. (2019)	Create a dual-axis tracking system for a solar parabolic dish concentrator and test its performance experimentally.	Parabolic dish concentrator	In comparison to a standard solar PV panel, the suggested tracking system's positioning precision improves the short circuit current of 0.11 A by 86%.
Yang et al. (2017)	An open looped altitude and azimuth tracking system were investigated for the Fresnel lens module, which focuses sunlight on the heating head of a Stirling engine.	Linear Fresnel reflector	Under cloudless conditions, the temperature of the heating head reaches roughly 900 °C.
Nsengiyumva et al. (2018)	Examine the most commonly used ST and find systems that provide advantages such as increased efficiency, increased tracking accuracy, ease of installation, and cost-effectiveness.	PV and CSP both	According to the study, when compared to fixed PV panels, double axis ST in the form of polar-axis and azimuth/elevation with solar movement models and dynamic closed loop feedback control are the most successful, providing more than a 40% increase in energy return.
Sidek et al. (2017)	An open-loop automatic positioning dual-axis solar tracking system	PV system	The solar tracker can autonomously position itself based on the sun path trajectory algorithm with an accuracy of 0.5°.

The rest of this paper is organized as follows. The complete methodology of the proposed work has been discussed in the "Methodology" section, and "Methods" section deals with the implemented methods to design PDC and calculate ASTA. Both software and graphical analysis results with validation are presented in the "Results and discussion" section and "Conclusions and recommendations" section concludes the paper.

Methodology

Proposed parabolic dish concentrator (PDC)

This paper presents an innovative schedule tracker algorithm that combines the azimuth and altitude parameters into a single attribute. For this analysis, a PDC was designed in SolidWorks 2020 software considering design parameters shown in Table 2. The complete PDC is designed in 3 parts: (1) parabolic dish with receiver, (ii) table with bearing arrangement, and (iii) connecting rod with pivot joints.

First, a parabolic dish with receiver was designed, considering specifications as shown in the Fig. 1a. The receiver area was considered as 17,671.46 mm^2, and the surface area of parabolic dish was 2,057,626.28 mm^2. A parabolic dish was design with a pivot joint at the bottom which would move the dish according to the predefined set of data points with the help of connecting rod. Then, this dish is connected to the connecting rod using the pivot joint provided in the connecting rod as shown in Fig. 1b. The connecting rod helps the PDC to rest at a position without significant wear and tear. The connecting rod and dish assemble is connected to the pivot table using the bearing arrangement provided in the table, as shown in Fig. 1c. The designed table had a bearing arrangement to provide the required angular movement to the PDC. The table height is constant. The complete 3D model of the proposed PDC assembly is shown in Fig. 1d.

Table 2 Design parameters of PDC

Design parameters	Units	Specification
Diameter of dish (D)	mm	1400
Receiver area (Ar)	mm^2	17,671.46
Aperture area of dish (A_d)	mm^2	2,057,626.28
Depth (H)	mm	450
Focal length (F)	mm	272
Reflectivity	–	0.82
Intercept factor	–	0.98
Rim angle	deg.	45
Arc length of a dish (S)	mm	1542.26

Proposed methodology

The study is performed in the geographical location of Bhopal, India (Shukla et al. 2015). To develop and simulate an innovative schedule tracker algorithm that combines the azimuth and altitude parameters into a single attribute, one new angle has been introduced which is named average solar tracking angle (ASTA). This angle allows the movement of PDC on a single axis which combines the effect of both azimuth and altitude. First of all, the average of all hourly azimuth and altitude angles is calculated, then the daily average for respective angles has been calculated. Then, after calculating the daily average for individual angles, the average of both angles is calculated for each month. The complete calculation of angles is performed in Microsoft Excel. The complete methodology of the present work is briefly explained using a flow diagram shown in Fig. 2.

Tracking parameters

The altitude ($\varnothing$) and azimuth (γ) measurements, as well as their specifications, are functions of the geographical location under consideration. The solar azimuth angle (γ_s) denotes the tilt angle between solar radiation and the north as measured clockwise. The zenith angle (θ_z) depicts the angle between the solar radiation beam and the normal the horizontal surface (Nsengiyumva et al. 2018). The three tracking angles are shown in Fig. 3.

Software used in the analysis

HelioScope

The monthly azimuth and altitude angles of Maulana Azad National Institute of Technology (MANIT), Bhopal, are imported from HelioScope software. HelioScope is a piece of software designed exclusively for PV system design and analysis. HelioScope analyzes solar energy, including losses caused by weather (Milosavljević et al. 2022; Shukla and Saroj Rangnekar 2015). These data were imported to Excel to analyze and calculating the average of these points was used. Table 3 illustrates the monthly daily average azimuth and altitude angle calculated for January month. These points are the positional angle of PDC due north.

SolidWorks 2020

A parabolic dish was designed in SolidWorks (Solidworks 2018). A detailed description of the design and specification of the model is given in the "Proposed

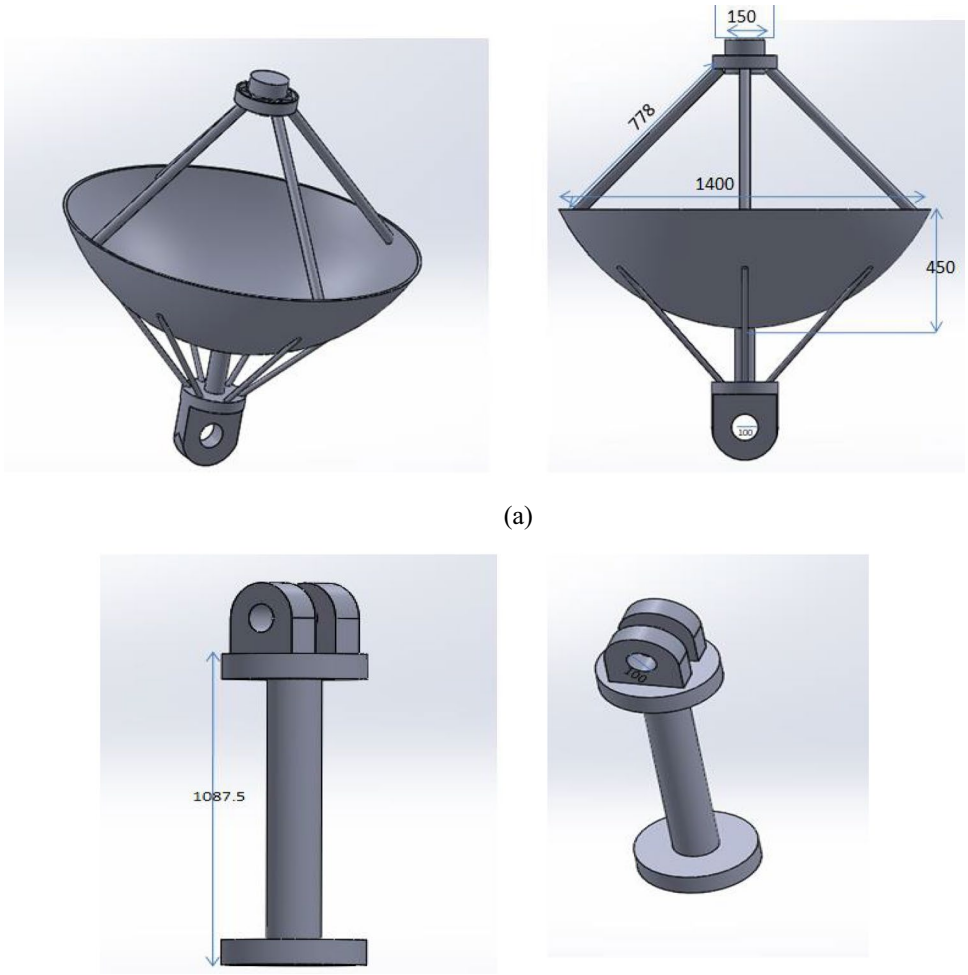

Fig. 1 **a** 3D model of parabolic dish with receiver. **b** 3D model of connecting rod with pivot arrangement. **c** 3D model of pivot table for PDC. **d** Assembly of parabolic dish concentrator (PDC)

parabolic dish concentrator (PDC)" section. The proposed methodology of average axis tracking is applied to this designed model of PDC.

SolTrace

For analysis of average azimuth and altitude angle data, it is required to observe the sun ray tracing at these new tracking points in SolTrace software. After calculating the new set of data points, to analyze and compare with dual axis points at PDC was designed in SolTrace software, and its ray tracing was performed. SolTrace is one such optical analysis tool developed at the National Renewable Energy Laboratory (NREL) beginning in early 2003 and is currently in use. SolTrace is an optical modeling tool for CSP systems developed to investigate optical systems used in CSP. SolTrace uses Monte Carlo ray tracing method to trace the rays received by the PDC which are generated from the sun. Optical performances such as flux distribution and interception factor are some results that can be observed in SolTrace. One thing is necessary that the receiver's position is also needed to be adjusted according to the position of the PDC and if the ray does not concentrate on the receiver, then the receiver will not show in the simulation process (Wendelin 2003).

Methods

Method for determining specifications of PDC

The mathematical models adopted for evaluating several parameters associated with the dish concentrator are mentioned in the following equations and the estimated values are depicted in Table 1.

The aperture area of the dish is calculated using Eq. 1.

$$A_d = \frac{\pi}{4} D^2 \tag{1}$$

The height of the dish is calculated using Eq. 2 (Leonard 1989).

Fig. 1 (continued)

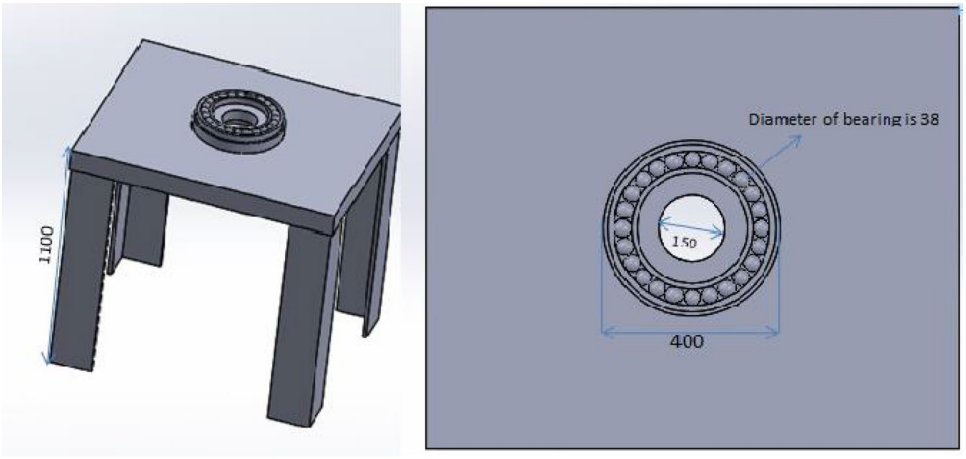

(c)

(d)

$$H = \frac{D^2}{16F} \tag{2}$$

Here, F is the focal length and D is the diameter of the dish. The focal length is determined using Eq. 3 (Leonard 1989).

$$F = \frac{D}{4.\tan\left(\Psi_{rim}\right)} \tag{3}$$

Arc length of the dish can be calculated using Eq. 4 (Leonard 1989).

$$S = \left[\frac{D}{2}\sqrt{\left(\frac{4H}{D}\right)^2 + 1}\right] + 2.F.\ln\left[\frac{4H}{D}\sqrt{\left(\frac{4H}{D}\right)^2 + 1}\right] \tag{4}$$

Method used for calculating ASTA

Latitude and longitude for the MANIT location are 23.22983° N and 77.41183° E (Patel et al. 2022; Anupama et al. 2021). The average azimuth and altitude angle data imported from Heliostat for MANIT location is then simulated using various methods which are Pythagoras theorem, 3 days moving average, and simple average of data points. First, Pythagoras theorem was implemented, but it was found that the azimuth and altitude angles are not perpendicular to each other, this method did not resemble the dual or single axis tracking points, therefore this method was discarded. The next method was the moving average method. The moving average of 3 h was calculated for each month

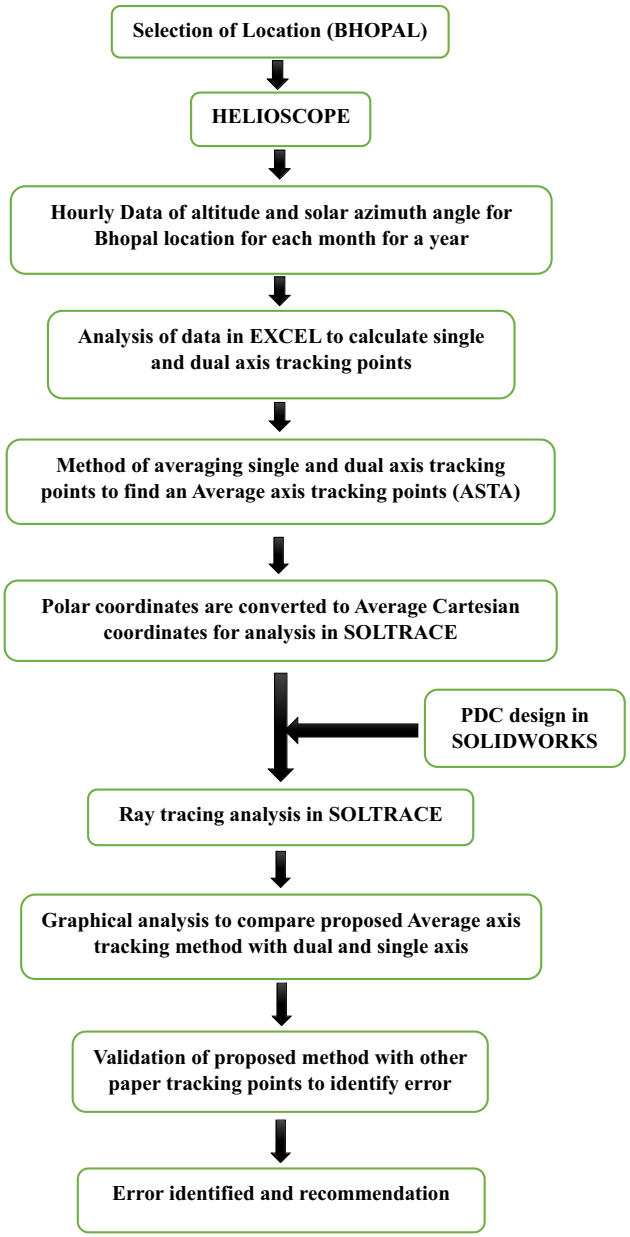

Fig. 2 Flow chart of complete methodology adopted in present research work

for a whole year. The moving average was calculated and a graph was plotted against it. It was found that the hourly variation in coordinates of PDC was very less concerning the hourly variation of sun. Since these variations were very less, it was not feasible in a practical scenario. Therefore, in the present simulation, simple average method of calculating the average of azimuth and altitude monthly for the whole year has been adopted. After calculating the new set of data points, to analyze and compare with dual axis points at PDC,

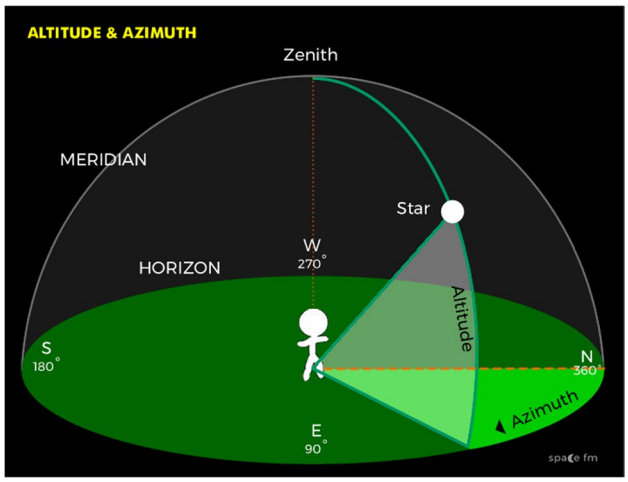

Fig. 3 Altitude and azimuth (Duffie and Beckman 2013)

it was designed in SolTrace software and its ray tracing was performed.

Estimation of tracking points (Cartesian coordinates of ASTA)

Table 3 shows the daily average azimuth and altitude angle calculated for each month of 2022. These points are actually the positional angle of PDC due north.

For analysis of these data, first need to observe the ray tracing at these new tracking points. SolTrace software has been used to do the simulation and observe the ray tracing points. To perform the ray tracing simulation in SolTrace, it is required to provide the Cartesian position of the PDC rather than the angular position. Hence, angular positions (tracking points) have been converted to Cartesian 3D position of PDC with respect to sun. Cartesian coordinates were calculated for single axis, dual axis, and average axis. To calculate all the Cartesian values, all angles are converted to radians as shown in Fig. 4.

(a) Cartesian coordinates for single axis tracking

In a single axis tracking, the PDC follows the azimuth angle of the sun, and PDC is fixed for other axes, hence here only one tracking parameter is defined which is the azimuth angle (γ_s).

Equations to convert polar to Cartesian coordinate system:

$$X = r.\cos\gamma_s \tag{5}$$

$$Y = r.\sin\gamma_s \tag{6}$$

Table 3 Average axis (ASTA) data for each month

Time (hours)	Month											
	Jan.	Feb.	Mar.	Apr.	May	June	July	Aug.	Sep.	Oct.	Nov.	Dec.
6:00	50.61722	47.71671	44.66754	34.50165	41.90843	40.08989	39.8921	42.28556	47.30828	57.20329	53.7428	53.33199
7:00	59.9004	57.3715	54.54488	44.23058	51.05598	48.92035	48.9004	51.7838	57.22793	67.40034	63.28829	62.53935
8:00	69.55964	67.37718	64.70919	53.90066	60.17683	57.57845	57.79377	61.38331	67.53153	78.30794	73.28825	72.15185
9:00	79.76677	78.02845	75.57384	63.78325	69.49466	66.12445	66.70566	71.44042	78.75582	90.40775	83.96499	82.3014
10:00	90.6686	89.72081	87.88192	74.33105	79.57034	74.61548	75.9034	82.82121	91.98803	104.0261	95.47557	93.03528
11:00	102.1219	102.745	102.9235	86.63661	93.22420	83.1815	86.54973	98.79001	109.2745	118.1165	107.457	104.005
12:00	113.1182	116.2169	120.8882	104.1748	152.3647	178.3669	150.5344	134.1261	130.4619	129.5333	118.2955	114.0321
13:00	121.7431	127.03	135.6555	134.3159	166.0236	173.5931	169.9522	156.5433	143.7691	135.6436	125.8097	121.456
14:00	126.7162	132.8731	142.3561	151.8713	163.6848	168.3486	166.5281	158.1359	147.1639	137.0591	129.347	125.4698
15:00	128.3061	134.4544	143.2648	154.3226	159.5611	163.1935	161.9359	155.5043	146.0917	135.6585	129.7415	126.4731
16:00	127.4522	133.3295	141.3464	152.313	155.0766	158.2549	157.2113	151.6593	143.1488	133.3559	128.0469	125.2912
17:00	108.6107	130.6247	138.1084	148.8129	150.6780	153.6601	152.6718	147.4889	139.9312	133.566	127.547	122.5459

Here, r is the distance between the PDC and sun, which is 1 AU. Therefore, r is considered as constant "1" (Sahu et al. 2021). Cartesian coordinates for a single axis are shown in Table 4. First day of each month has been selected and yearly average data has been calculated to determine the Cartesian coordinate of a given time in a day.

(b) Cartesian coordinates for dual axis tracking

In the dual axis, two tracking parameters vary with time: (i) zenith angle (θ_z) and (ii) azimuth angle (γ_s). Figure 4a shows the two-tracking angle which the PDC can track.

Equations to convert the spherical to Cartesian coordinate system are:

$$X' = r.\sin\gamma_s.\cos\theta_z \tag{7}$$

$$Y' = r.\sin\gamma_s.\sin\theta_z \tag{8}$$

$$Z' = r.\cos\gamma_s \tag{9}$$

From Fig. 1, it is visible that θ is the complementary angle of altitude angle ($\varnothing$), therefore it can be calculated as:

$$\theta_z = 90° - \textit{Altitude angle}\ (\varnothing) \tag{10}$$

X', Y', and Z' are calculated for each month from January to December then the yearly average X and Y axis data has been determined.

$$X = \textit{Average of}\ X' \tag{11}$$

$$Y = \textit{Average of}\ Y' \tag{12}$$

The dual-axis tracking increases the optical efficiency of any tracking system but to operate the system on two different axes two individual motors are required. Utilizing two motors and a different program for each motor increases the error in tracking the sun, therefor in the proposed methodology new method of tracking is introduced in this paper where single-axis tracking has defined the impact of both the azimuth and altitude angle. This method is an average axis tracking method (AATM) in which PDC is used to track the sun on a single axis, reducing tracking error and increasing optical efficiency over single-axis tracking.

(iii) Cartesian coordinates for average axis tracking (ASTA)

The Cartesian coordinates for average axis tracking include only a single tracking parameter which is the average solar tracking angle (ASTA) (α) as shown in Fig. 4b. The

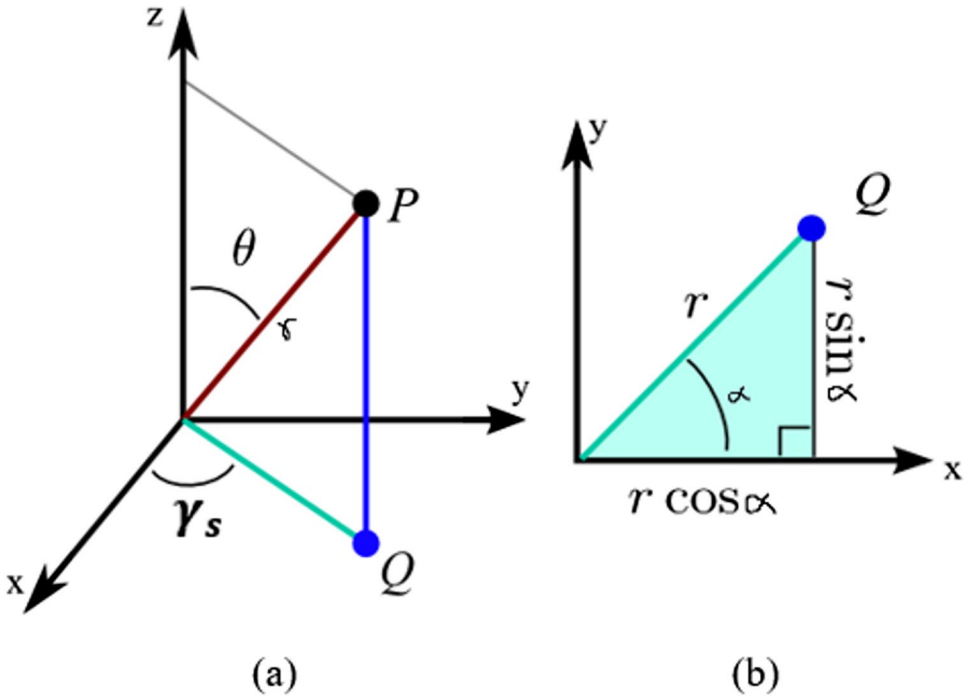

Fig. 4 **a** Dual axis parameter and **b** average axis parameter

X and Y coordinates of the average axis tracking method can be determined using the following equation:

$$X = r.\cos\alpha \tag{13}$$

$$Y = r.\sin\alpha \tag{14}$$

In this method, the azimuth angle varies with time throughout the day. The average angle data for each month are given in Table 3. The yearly average estimated Cartesian coordinates for average axis are shown in Table 4.

Results and discussion

Optical simulation of calculated and predefined positions of PDC

The optical design is one of the most significant aspects of the overall system. Physically building and testing the many possible preliminary prototypes as part of the product development path is not practicable since optical systems for CSP applications could be very sophisticated with various parameters to tweak. Computer techniques are applied to simulate and forecast these systems' optical behavior and performance. Figure 5a illustrates the ray tracing of PDC in SolTrace, indicating the rays falling perpendicular to the PDC. So, depending on the latitude, day, and time the sun's position is determined and the position of PDC is given by calculated X, Y, and Z coordinates. This procedure is followed for June and the ray tracing is compared for dual, single, and average axis. The heat flux generated or the flux mapping of the receiver shows the flux distribution on the receiver. Ray tracing simulations were done for June, the result shows that the single-axis and dual-axis tracking points show the proper tracking and the reflected rays concentrate at the focal point as shown in Fig. 5b and c, respectively.

Figure 5b shows the ray tracing simulation for single axis data of June at 11:00 am. The simulation indicates that the rays concentrate at the receiver, which is located near the PDC's focal point. The position of PDC at this time in single-axis tracking is mentioned in Table 5. Figure 5c shows the ray tracing simulation for dual axis data of June at 11:00 hours. The simulation shows that the rays concentrate at the receiver placed at the focal point of the PDC. The position of PDC at this time in dual-axis tracking is mentioned in Table 5. The z coordinate is not considered since the PDC height is constant and can be considered any value since it does not affect the tracking. Figure 5d shows the ray tracing simulation for the average axis data of June at 11:00 hours. The figure demonstrates that the rays are not received at the receiver position. Understandably, the rays are not roughly parallel to the PDC at these data points that is the reason the rays do not concentrate at the receiver. As the rays are not getting received at the receiver, they are not visible in the simulation shown in Fig. 5d. This indicates that the data points derived from the average axis data were not tracing the sun correctly. This effect represents that the proposed method of average axis point tracking has an error. Therefore, to identify this error, a graphical analysis has been performed.

Table 4 Cartesian coordinates of PDC for single, dual, and average axis parameters

Time	Single axis			Dual axis						Average axis		
	Azimuth (γ_s) (radian)	X	Y	Azimuth (γ_s) (radian)	Altitude ($\varnothing$) (radian)	X′	Y′	X	Y	ASTA (α) (radian)	X	Y
05:00												
06:00	1.5589	0.0119	0.9999	1.9528	1.7031	−0.1224	0.9198	−0.1306	0.9348	0.8838	0.6342	0.7732
07:00	1.6657	−0.0947	0.9955	2.0541	1.4845	0.0763	0.8822	0.0763	0.9027	1.0459	0.5011	0.8654
08:00	1.7886	−0.2161	0.9764	2.1818	1.2786	0.2359	0.7843	0.2467	0.8090	1.2145	0.3488	0.9372
09:00	1.9518	−0.3718	0.9283	2.3481	1.0931	0.3277	0.6330	0.3513	0.6601	1.3928	0.1771	0.9842
10:00	2.2049	−0.5924	0.8056	2.5677	0.9402	0.3201	0.4385	0.3559	0.4662	1.5831	−0.0123	0.9999
11:00	2.6507	−0.8819	0.4714	2.8496	0.8382	0.1925	0.2140	0.2313	0.2403	1.7831	−0.2107	0.9776
12:00	3.3550	−0.9773	−0.2118	3.1764	0.8067	−0.0241	−0.0251	−0.0013	−0.0020	1.9751	−0.3934	0.9194
13:00	3.9395	−0.6982	−0.7159	3.4975	0.8535	−0.2291	−0.2626	−0.2339	−0.2442	2.1257	−0.5268	0.8500
14:00	4.2555	−0.4411	−0.8974	3.7672	0.9673	−0.3323	−0.4822	−0.3579	−0.4697	2.2125	−0.5986	0.8011
15:00	4.4430	−0.2661	−0.9639	3.9751	1.1280	−0.3172	−0.6689	−0.3524	−0.6633	2.2403	−0.6206	0.7842
16:00	4.5758	−0.1362	−0.9907	4.1326	1.3184	−0.2089	−0.8101	−0.2467	−0.8117	2.2254	−0.6088	0.7933
17:00												

Graphical analysis and comparison of single, dual, and average axis tracking methods

Initially to compare the proposed algorithm of average axis tracking (ASTA) the month of June is selected because the sunny days in the northern hemisphere are longer in June therefore receiving maximum solar radiation in a day. Also, the summer solstice occurs in June on the 21st marking the beginning of longer days and shorter nights. Then, in the second case, the graphical analysis is performed for September because this is the month of change of season in India which directly affects the position coordinates of the sun-earth geometry at the location of Bhopal. In addition, September heralds the end of the monsoon season and the advent of fall.

Analysis for June

Figure 6a, b, and c show the graphical analysis for single axis, dual axis, and average axis tracking points of the proposed schedule tracker respectively for June. Figure 6a shows that the wave of the single-axis tracing point starts from X = 0.44 and Y = 0.89 and intersects the X-axis at 0.0256. The curve drastically decreases from X = 0.0325 and Y = 0.99 to X = 0.0256 and Y = 0. The time for this drastic change is between 11 am and 12 noon. This represents that between 11 am and 12 noon, the tracking points change from positive Y to negative Y coordinates. But the waveform of a single axis tracking system is having a step-like shape which shows that the PDC is not properly tracking the sun throughout the day and only azimuthal tracking is possible.

In Fig. 6b, it is seen that the waveform of a dual axis is smooth which shows proper tracking of the sun's trajectory throughout the day without any delay. This curve intersects the X-axis at X = 0.984 and Y = 0 at the intersection. The time of intersection is between 11:30 and 12 noon. Figure 6c shows the waveform of the average axis tracking method. It has been seen that the waveform of the average axis tracking method and single-axis tracking method is similar which is a step-like shape. This represents that the proposed average axis tracking method will perform just like the single axis method. But the difference is that the curve of average axis tracking is having little slots starting from X = 0.85 and Y = 0.515 reaching its maximum point at X = 0.11 and Y = 0.99. This represents the PDC in average axis tracking points following the sun trajectory smoothly with less delay. As compared to single-axis tracking points, the only difference was that the X-axis at Y = 0 was intercepted by both dual and single-axis tracking points but not by the average-axis tracking points. This difference is identified in Fig. 6d, which shows the comparison of 3 graphs with time in a day. It is seen that the average axis tracking plot does not intersect

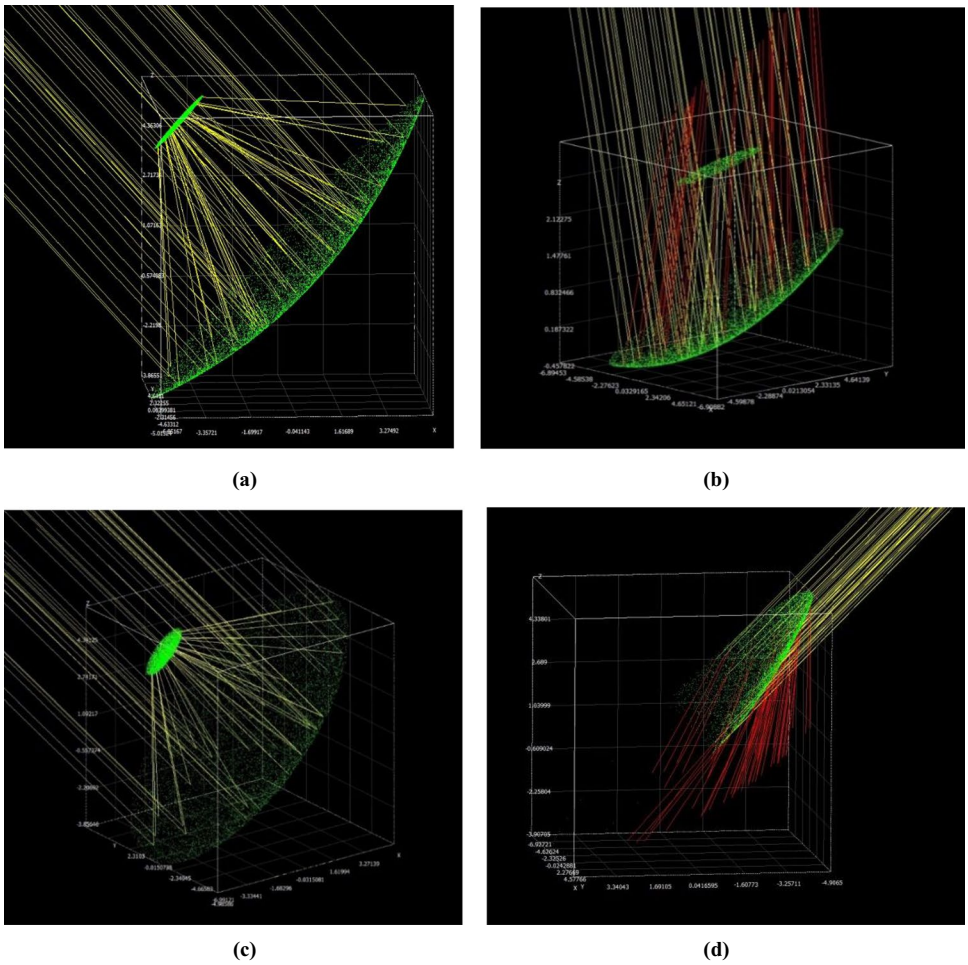

Fig 5 **a** Ray tracing of PDC in SolTrace. **b** Single axis ray tracing for June at 11:00 am. **c** Dual axis ray tracing for June at 11:00 am. **d** Average axis ray tracing for June at 11:00 am

Table 5 X-Y positions input to SolTrace for single axis, dual axis, and average axis tracking

Time	Single axis		Dual axis		Average axis	
	X	Y	X	Y	X	Y
5	0.4400	0.8980	0.0278	0.8977	0.8570	0.5154
6	0.3518	0.9361	−0.1769	0.9193	0.7649	0.6442
7	0.2760	0.9612	−0.3907	0.8782	0.6568	0.7540
8	0.2092	0.9779	−0.5934	0.7773	0.5358	0.8443
9	0.1485	0.9889	−0.7677	0.6233	0.4043	0.9146
10	0.0914	0.9958	−0.8996	0.4268	0.2648	0.9643
11	0.0325	0.9995	−0.9783	0.2013	0.1181	0.9930
12	−0.0187	−0.9998	0.9862	−0.0355	−0.9996	0.0272
13	0.0547	−0.9985	0.9604	−0.2722	−0.9939	0.1104
14	0.1112	−0.9938	0.8643	−0.4903	−0.9796	0.2008
15	0.1690	−0.9856	0.7182	−0.6749	−0.9576	0.2880
16	0.2311	−0.9729	0.5336	−0.8135	−0.9293	0.3694
17	0.3002	−0.9539	0.3256	−0.8965	−0.8967	0.4427
18	0.3793	−0.9253	0.1125	−0.9183	−0.8629	0.5054

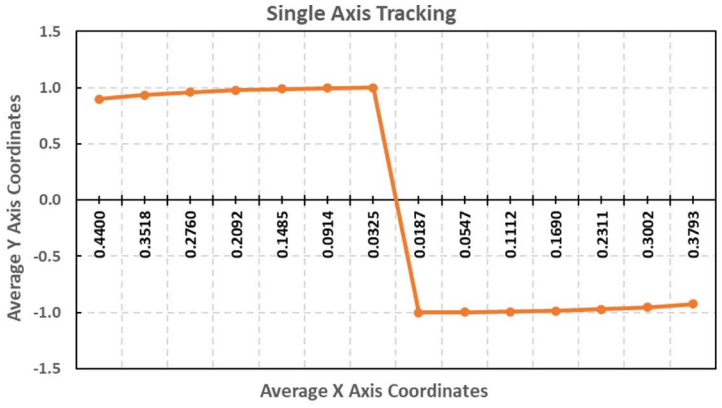

(a)

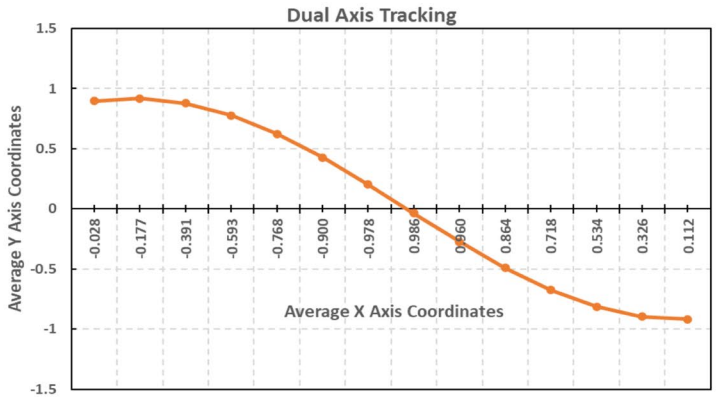

(b)

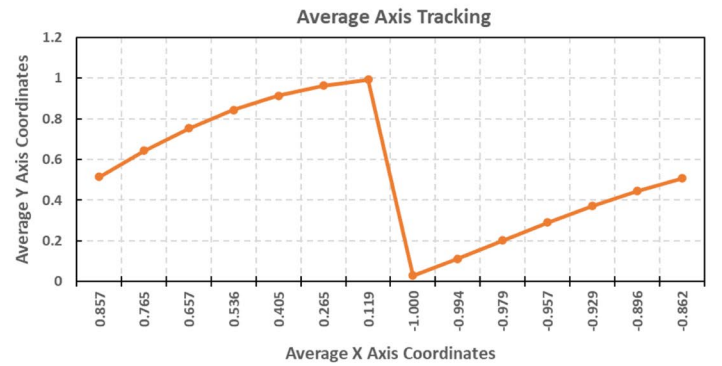

(c)

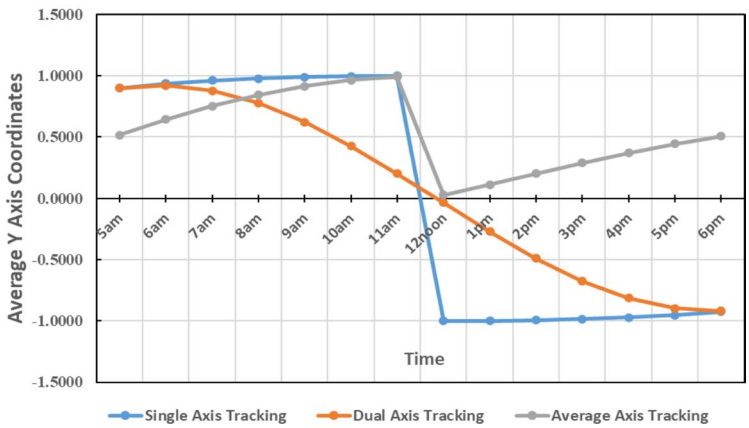

(d)

Fig. 6 **a** Graphical analysis for the month of June for single axis tracking points. **b** Graphical analysis for the month of June for dual axis tracking points. **c** Graphical analysis for the month of June for average axis tracking points. **d** Comparison of single, dual, and average axis data plots variation with time

the X-axis at Y = 0 and during noon, whereas the single and dual axis intersects at 12 noon and enters in negative Y-axis coordinate system after 12 noon. The graph represents the error of approximately 0.95 at Y-axis at 12 noon.

Since the waveform was similar to that of the single axis, it implies that the equations describing the single and average axes are similar. Although, on shifting the plot by offsetting the Y = 0 intercept using any mathematical tool, then the average plot can be equivalent to that of a single axis. To confirm the analysis, similar plots were plotted for September.

Graphical analysis for September

Figure 7a, b, and c show the tracking points of single, dual, and average axis tracking methods for September. In Fig. 7a, it can be seen that the waveform of the single-axis tracking method for September is different from the waveform of June month. This is because of the change in angular coordinates of September month. The waveform in September shows better results as compared to June month. It intersects the X-axis at X = 0.901. Figure 7b again shows the waveform of the dual-axis system is smoother than the waveform of the single-axis system. It intersects the X-axis at X= −0.3755. Figure 7c shows that the waveform of average axis tracking for September is smoother than the waveform in June. Again, a similar error has been observed in September also. The waveform of the average axis tracking system does not intersect the X-axis. This again represents the presence of error in tracking points of an average axis tracking system. Between 11 am and 12 noon, the tracking points change their path from a positive Y axis to a negative Y axis in the case of single and dual axis tracking systems. Figure 7d depicts that in the case of the average axis tracking system, the tracking points show an error of 0.633 at the Y axis. This error in the tracking point is 0.317 less than the error in June. This represents that the error in tracking point decreases as the month proceeds from June.

Validation

To validate the method of average axis, data from a reference paper was taken. In the reference paper, a single axis tracking system design and implementation is done for a solar PV panel for a specific region. To compare the method discussed in this work, the same process is implemented with the data points of the work presented by Sadeque and Ahsan (2014).

Sadeque and Ahsan (2014) proposed a control algorithm for the detection of the position of the sun and its single-axis tracking (azimuth tracking). The experiment was performed at the location of Dhaka, Bangladesh, in March. The data that has been extracted from the paper was also for March as identified using HelioScope software (Sadeque and Ahsan 2014). The solar azimuth angle has been extracted for the given location and the Cartesian coordinates were calculated for single and dual-axis systems. The tracking point of the experiment over the proposed system was taken from the paper. First, the single-axis tracking points have been drawn for theoretical (software) data and experimental data of the proposed system. Figure 8 shows that the error in the theoretical and experimental tracking points of the single axis tracking method is very less because the curves of theoretical and experimental tracking points overlap each other. This represents that the extracted values from HelioScope software are correct for the proposed system by Sadeque and Ahsan (2014). After confirming this, the average axis tracking points have been calculated using the method proposed in the present paper which is graphically shown in Fig. 8. From Fig. 8, it has been identified that the proposed method of average axis tracking has an error of around 0.85 when it is applied to the tracking points of Sadeque and Ahsan (2014) for both theoretical and experimental data. The error was indicated at 12 noon as the curve of the single axis system intersects the X-axis at 12 noon.

Practical implication

The graphical analysis calculated by the average method in Fig. 8 confirms that the average axis tracking can provide promising results if some additional mathematical calculations are performed to solve the axis alignment problem. These adjustments can then be practically implemented in a PDC.

From the graphs plotted for different axes, it was understood that the axis adjustment was necessary for the average axis plot. This adjustment in the practical scenario can be any of the adjustments like:

- Rather than considering the angular movement concerning north, we can consider the movement concerning north east or north west.
- Tilt can be offset by the addition or subtraction of a constant value.
- All the points can be offset by addition or subtraction of a constant value.

If any of the above adjustments would work, then the average axis tracking data points could give promising results.

Solar trackers capture solar energy and channel it into the PV system and solar concentrators, increasing their overall efficiency. In single and biaxial tracking systems, each axis rotation needs a motor to rotate the desired angular movement. As the number of axes increases, the

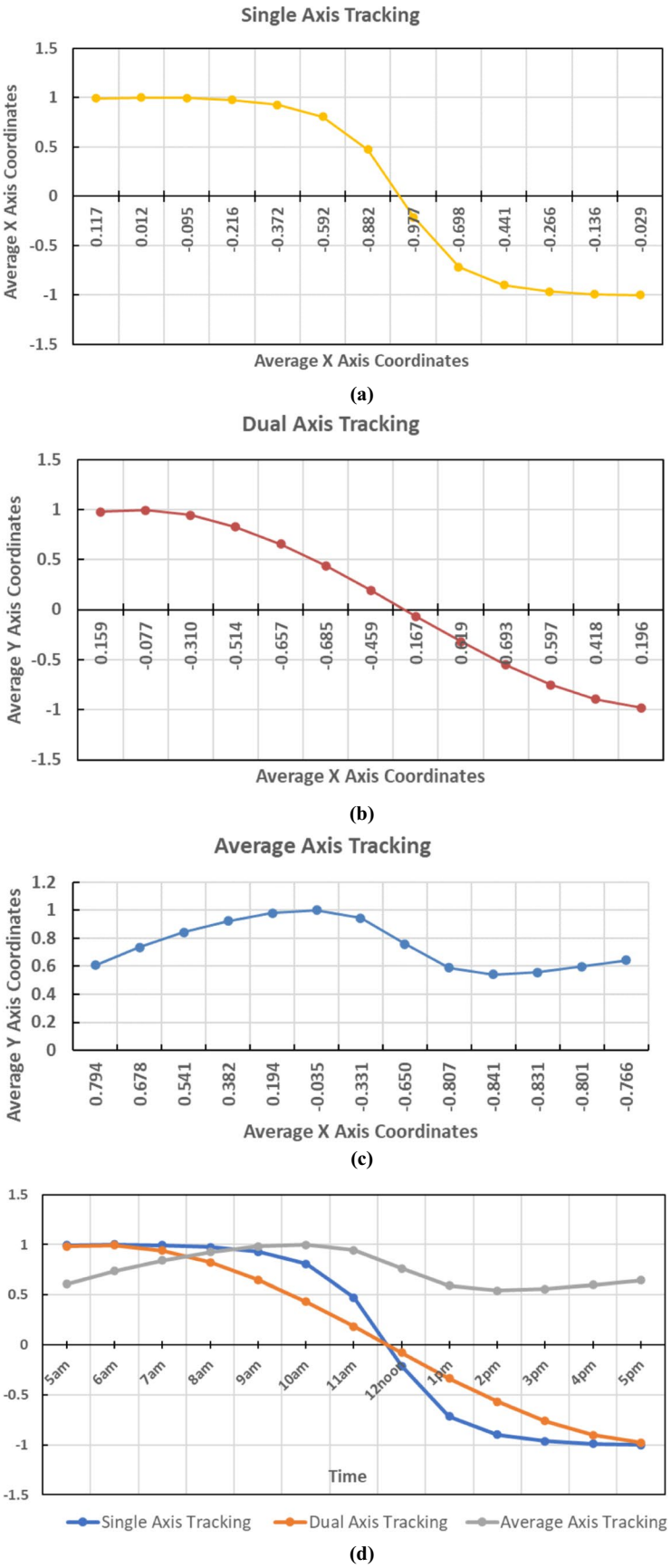

Fig. 7 **a** Graphical analysis for the month of September for single axis tracking points. **b** Graphical analysis for the month of September for dual axis tracking points. **c** Graphical analysis for the month of September for average axis tracking points. **d** Comparison of single, dual, and average axis tracking points variation with time in a day for the month of September

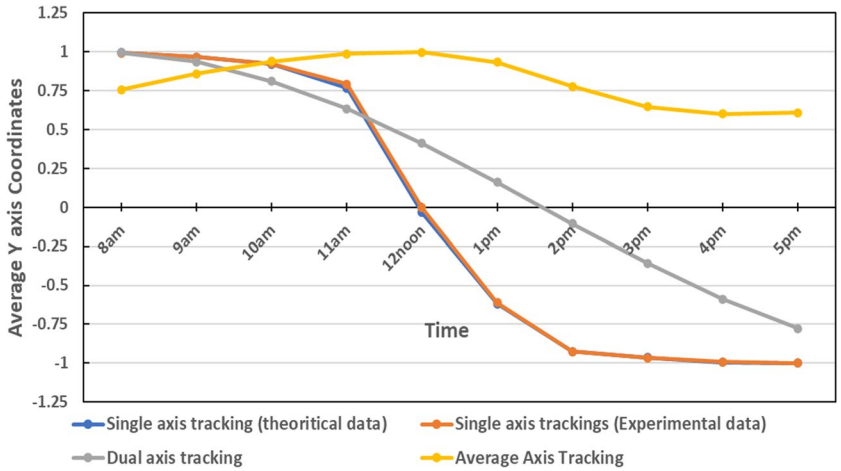

Fig. 8 Graphical representation of Sadeque and Ahsan (2014) with comparison of single, dual, and average axis tracking method

number of degrees of freedom of the system increases and hence the number of motors increases, which need more electrical energy to work. Therefore, this paper demonstrates a novel schedule tracking point that has the effect of both the axes, i.e., azimuth and altitude tracking at a single point. In this way, the system will act as a single-axis tracking system with the effect of dual tracking angles. The present system can also be applied to solar PV modules for tracking the sun on a single axis. The results of the present simulation show that the new tracking points have an error of 0.85 to 0.95 at noon for the month between June and September. This could be adjusted by adjusting the concentrators or modules manually for seasonal change, especially in September. This method can be further improved by comparing with the proposed results of Skouri et al. (2016), who found that one of the three pilot sun-tracking systems produced less than 0.2° tracking error. Skouri et al. (2016) did a comparative study of the design and construction of sun-tracking systems for collar parabolic concentrator displacement. As the proposed method in the present paper is the novel solar tracking method, no one in the past has adopted this method. Some authors have developed tracking algorithms for either single-axis or dual-axis tracking systems which has been discussed in Table 1.

Conclusions and recommendations

Tracking is an important component in the system that harnesses solar energy. The single axis tracking mechanism is cheaper and simple to develop as it has to track the sun on a single axis only. However, because of the limitation of the tracking axis, this system has less efficiency as compared to dual-axis tracking systems. Dual-axis tracking systems necessitate a large number of equipment, sensors, motors, and a lengthy computer program to function properly. Therefore, in the present study, a novel method of solar tracking has been discussed where each tracking point has an impact on both azimuth and altitude angle at a single point. This method is an average axis tracking method (AATM). A new tracking parameter has been introduced named average solar tracking angle (ASTA). The following important findings have been drawn from the software and graphical examination of the proposed system:

- The simplicity of the changes required with the data points was made possible by the similarity of the graphs of the single and average axes.
- From June to September, the error in the tracking method was observed to be between 0.95 and 0.85.
- After evaluating the graphs for different months, it is advised that an offset of around "−0.8" units can make the graph intersect at the Y = 0 axis. But similarly, other data will also get affected, so it needs to be taken care of while experimenting.
- In single and biaxial tracking systems, each axis rotation needs a motor to rotate the desired angular movement. As the number of axes increases, the number of degrees of freedom of the system increases and hence the number of motors increases. Gear and shaft arrangements also become more complex so the proposed tracking system, if it successfully works in the future after the required calculation and adjustments are done, will have an impact on both the azimuth and altitude, i.e., both daily and seasonal movement of the sun, on a single tracking point.
- It may be possible that the system's efficiency will also lie between the dual axis and single axis tracking systems.
- The type of tracker discussed in this paper is a schedule tracker. When output data is used directly in a controller such as Arduino, the system becomes independent of the light sensors, which lowers the overall cost of the system.

In future work, the system's complete performance will be examined to determine its suitability. The proposed method will be used in the proposed PDC experimental model. Following experimentation, more meaningful results can be achieved, which will aid in cost analysis. The proposed innovative tracking approach can be tested with sensor and sensor-less tracking mechanisms in the experimental model.

Acknowledgements The authors wish to acknowledge the faculties of Energy Centre, MANIT Bhopal, for providing the resources and facilities for successfully conducting the analysis. The authors are grateful to the reviewers for their valuable time and suggestions, which helped to improve the quality of the paper.

Author contribution R Malviya: conceptualization, methodology; A Patel: writing—original draft preparation; A Singh: writing—review and editing; S Jagadev: review and editing, resources, software; P Baredar: supervision, validation; A Kumar: supervision, validation.

Data availability The datasets used and/or analyzed during the current study are available from the corresponding author on reasonable request.

Declarations

Ethics approval and consent to participate Not applicable.

Consent for publication Not applicable.

Competing interests The authors declare no competing interests.

References

Ahmet S, Mekhilef S, Kuttybay N et al (2021) Dual-axis schedule tracker with an adaptive algorithm for a strong scattering of sunbeam. Solar Energy 224:285–297, ISSN 0038-092X. https://doi.org/10.1016/j.solener.2021.06.024

Anupama KS, Seema S, Sudhakar K, Energy, economic and environmental performance assessment of a grid-tied rooftop system in different cities of India based on 3E analysis, *Clean Energy*, Volume 5, Issue 2, June 2021, Pages 288–301, https://doi.org/10.1093/ce/zkab008

Arif EMH, Hossen J, Ramana Murthy G, Jesmeen MZH, Emerson Raja J (2019) An efficient microcontroller based sun tracker control for solar cell systems. International. J Electric Comput Eng 9(4):2743–2750. https://doi.org/10.11591/ijece.v9i4.pp2743-2750

Bakos GC (2006) Design and construction of a two-axis Sun tracking system for parabolic trough collector (PTC) efficiency improvement. Renew Energy 31(15):2411–2421. https://doi.org/10.1016/j.renene.2005.11.008

Barbón A, Fernández-Rubiera JA, Martínez-Valledor L, Pérez-Fernández A, Bayón L (2021) Design and construction of a solar tracking system for small-scale linear Fresnel reflector with three movements, Applied Energy, Volume 285, 116477, ISSN 0306-2619, https://doi.org/10.1016/j.apenergy.2021.116477.

Batayneh W, Bataineh A, Soliman I et al (2019) Investigation of a single-axis discrete solar tracking system for reduced actuations and maximum energy collection. Autom Constr 98:102–109, ISSN 0926-5805. https://doi.org/10.1016/j.autcon.2018.11.011

Bijarniya JP, Sudhakar K, Baredar P (2016) Concentrated solar power technology in India: a review. Renew Sust Energ Rev 63:593–603, ISSN 1364-0321. https://doi.org/10.1016/j.rser.2016.05.064)

Bishoyi D, Sudhakar K (2017) Modeling and performance simulation of 100MW PTC based solar thermal power plant in Udaipur India. Case Stud Ther Eng 10:216–226, ISSN 2214-157X. https://doi.org/10.1016/j.csite.2017.05.005

Duffie JA, Beckman WA (2013) Solar engineering of thermal processes. John Wiley & Sons

Eke R, Senturk A (2012) Performance comparison of a double-axis sun tracking versus fixed PV system. Sol Energy 86(9):2665–2672. https://doi.org/10.1016/j.solener.2012.06.006

Fahad HM, Islam A, Islam M, Hasan MF, Brishty WF, Rahman MM (2019) Comparative analysis of dual and single axis solar tracking system considering cloud cover, 2019 international conference on energy and power engineering (ICEPE), Dhaka, Bangladesh, 2019, pp. 1-5, https://doi.org/10.1109/CEPE.2019.8726646.

Fatha Badi H (2016) Novel high accurate sensor less dual-axis solar tracking system controlled by maximum power point tracking unit of photovoltaic systems. Appl Energy 173:448–459. https://doi.org/10.1016/j.apenergy.2016.03.109

Henriques M, Campos DS, Tiba C (2021) npTrack: a n-position single axis solar tracker model for optimized energy collection. Energies 14(4):925

Karabiber, A., and Güneş, Y. (February 14, 2023). "Single-motor and dual-axis solar tracking system for micro photovoltaic power plants." ASME. *J. Sol. Energy Eng*. October 2023; 145(5): 051004. https://doi.org/10.1115/1.4056739.

Khlaichom P, Sonthipermpoon K (2016) Optimization of solar tracking system based on genetic algorithms.

Kumar KH, Daabo AM, Karmakar MK et al (2022) Solar parabolic dish collector for concentrated solar thermal systems: a review and recommendations. Environ Sci Pollut Res 29:32335–32367. https://doi.org/10.1007/s11356-022-18586-4

Kuttybay N, Mekhilef S, Saymbetov A, Nurgaliyev M, Meiirkhanov A, Dosymbetova G, Kopzhan Z (2019) An automated intelligent solar tracking control system with adaptive algorithm for different weather conditions. 2019 IEEE international conference on automatic control and intelligent systems, I2CACIS 2019 - proceedings, 315–319. https://doi.org/10.1109/I2CACIS.2019.8825098

Kuttybay N, Saymbetov A, Mekhilef S, Nurgaliyev M, Tukymbekov D, Dosymbetova G, Meiirkhanov A, Svanbayev Y (2020) Optimized single-axis schedule solar tracker in different weather conditions. *Energies 13*:5226. https://doi.org/10.3390/en13195226

Leonard D (1989) Jaffe, Test results on parabolic dish concentrators for solar thermal power systems. Sol Energy 42(2):173–187, ISSN 0038-092X. https://doi.org/10.1016/0038-092X(89)90144-8

Malik, I. Al-Amayreh, Ali Alahmer, On improving the efficiency of hybrid solar lighting and thermal system using dual-axis solar tracking system, Energy Reports, Volume 8, Supplement 1, 2022, 841-847, ISSN 2352-4847, https://doi.org/10.1016/j.egyr.2021.11.080

Malviya, R., Baredar, P.V. Kumar, A. (2021). Thermal performance improvement of solar parabolic dish system using modified spiral coil tubular receiver. Intl J Photoenergy, 2021, https://doi.org/10.1155/2021/4517923

Milosavljević DD, Kevkić TS, Jovanović SJ (2022) Review and validation of photovoltaic solar simulation tools/software based on case study. Open Physics 20(1):431–451. https://doi.org/10.1515/phys-2022-0042

Mohammed GA, Mohammed ZS (2022) Modeling horizontal single axis solar tracker upon sun-earth geometric relationships. Tikrit Journal of. Eng Sci 29(3):43–48. https://doi.org/10.25130/tjes.29.3.5

Nadia AL-R, Isa NAM, Desa MKM (2020) Efficient single and dual axis solar tracking system controllers based on adaptive neural fuzzy inference system. J King Saud Univ Eng Sci 32(7):459–469, ISSN 1018-3639. https://doi.org/10.1016/j.jksues.2020.04.004

Natarajan SK, Thampi V, Shaw R et al (2019) Experimental analysis of a two-axis tracking system for solar parabolic dish collector. Int J Energy Res 43:1012–1018. https://doi.org/10.1002/er.4300

Patel A, Soni A, Baredar P, Malviya R (2022. Analysis of temperature distribution over pipe surfaces of air-based cavity linear receiver for cross-linear concentration solar power system. Springer-Verlag GmbH Germany, part of Springer Nature 2022. https://doi.org/10.1007/s11356-022-24036-y

Ponniran A, Ali Munir H (2011) A design of single axis sun tracking system. 978-1-4577-0353-9/11/$26.00 ©2011 IEEE

Rahimoon AA, Abdullah MN, Soomro DM, Nassar MY, Memon ZA, Shaikh PH (2019) Design of parabolic solar dish tracking system using Arduino. Indonesian Journal of Electrical Engineering and Computer. Science 17(2):914–921. https://doi.org/10.11591/ijeecs.v17.i2.pp914-921

Sadeque, F., Ahsan, Q. (2014). Design and implementation of a single-axis automatic solar tracking system. Gub J Sci Eng, Volume 1, Issue 1, July 2014

Sahu SK, Arjun Singh K, Natarajan SK (2021) Design and development of a low-cost solar parabolic dish concentrator system with manual dual-axis tracking. Int J Energy Res 45(4):6446–6456. https://doi.org/10.1002/er.6164

Sahu SK, Kopalakrishnaswami AS, Natarajan SK (2022) Historical overview of power generation in solar parabolic dish collector system. Environ Sci Pollut Res 29:64404–64446. https://doi.org/10.1007/s11356-022-21984-3

Saymbetov A, Mekhilef S, Kuttybay N, Nurgaliyev M, Tukymbekov D, Meiirkhanov A, Dosymbetova G, Svanbayev Y (2021) Dual-axis schedule tracker with an adaptive algorithm for a strong scattering of sunbeam. Sol Energy 224:285–297. https://doi.org/10.1016/j.solener.2021.06.024

Shufat SAA, Kurt E, Hançerlioğullari A (2019) Modeling and design of azimuth-altitude dual axis solar tracker for maximum solar energy generation. Intl J Renew Energy Dev IJRED 8(1):7–13

Shukla KN, Rangnekar S, Sudhakar K (2015) Mathematical modelling of solar radiation incident on tilted surface for photovoltaic application at Bhopal, M.P., India, International Journal of Ambient Energy, DOI: https://doi.org/10.1080/01430750.2015.1023834

Shukla KN, Saroj Rangnekar K (2015) Sudhakar, Comparative study of isotropic and anisotropic sky models to estimate solar radiation incident on tilted surface: a case study for Bhopal, India. Energy Rep 1:96–103, ISSN 2352-4847. https://doi.org/10.1016/j.egyr.2015.03.003

Sidek MHM, Azis N, Hasan WZW, Ab Kadir MZA, Shafie S, Radzi MAM (2017) Automated positioning dual-axis solar tracking system with precision elevation and azimuth angle control. Energy 124:160–170, ISSN 0360-5442. https://doi.org/10.1016/j.energy.2017.02.001

Skouras, G. N. (2018). Design and analysis of a parabolic trough solar concentrator.

Solidworks, S. F. S. (2018). Technical reference. Solidworks Corporation, Waltham.

Srinivasarao P, Peddakapu K, Mohamed MR, Deepika KK, Sudhakar K (2021) Simulation and experimental design of adaptive-based maximum power point tracking methods for photovoltaic systems, Computers & Electrical Engineering, Volume 89, 106910, ISSN 0045-7906, https://doi.org/10.1016/j.compeleceng.2020.106910

Tchao E, Simon Atuah Asakipaam, Yesuenyeagbe Atsu Kwabla Fiagbe, Bright Yeboah-Akowuah, Ramde E, Andrew Selasi Agbemenu, Kommey B (2022) An implementation of an optimized dual-axis solar tracking algorithm for CSP plants deployment, Scientific African, Volume 16, e01228, ISSN 2468-2276, https://doi.org/10.1016/j.sciaf.2022.e01228.

Tukymbekov, D., Saymbetov, A., Nurgaliyev, M., Kuttybay, N., Nalibayev, Y., & Dosymbetova, G. (2019). Intelligent energy efficient street lighting system with predictive energy consumption," 2019 international conference on smart energy systems and technologies (SEST), Porto, Portugal, pp. 1-5, https://doi.org/10.1109/SEST.2019.8849023

Nsengiyumva W, Chen SG, Hu L, Chen X (2018) Recent advancements and challenges in solar tracking systems (STS): a review, Renewable and Sustainable Energy Reviews, Volume 81, Part 1, Pages 250-279, ISSN 1364-0321, https://doi.org/10.1016/j.rser.2017.06.085

Wendelin T (2003) SolTRACE: a new optical modeling tool for concentrating solar optics. Proceedings of the ISEC 2003: international solar energy conference, 15-18 March 2003, Kohala Coast, Hawaii. New York: American Society of Mechanical Engineers, pp. 253-260; NREL Report No. CP-550-32866

Yang C-K, Cheng T-C, Cheng C-H, Wang C-C, Lee C-C (2017) Open-loop altitude-azimuth concentrated solar tracking system for solar thermal applications. Sol Energy 147:52–60

Zhu Y, Liu J, Yang X (2020) Design and performance analysis of a solar tracking system with a novel single-axis tracking structure to maximize energy collection. Appl Energy 264:114647. https://doi.org/10.1016/j.apenergy.2020.114647

Publisher's note Springer Nature remains neutral with regard to jurisdictional claims in published maps and institutional affiliations.

Springer Nature or its licensor (e.g. a society or other partner) holds exclusive rights to this article under a publishing agreement with the author(s) or other rightsholder(s); author self-archiving of the accepted manuscript version of this article is solely governed by the terms of such publishing agreement and applicable law.

Research Square

Preprints are preliminary reports that have not undergone peer review.
They should not be considered conclusive, used to inform clinical practice,
or referenced by the media as validated information.

A PSO optimized novel PID Neural Network model for Temperature Control of Jacketed CSTR: Design, Simulation, and a Comparative Study

Snigdha Chaturvedi (snigdha0chaturvedi@gmail.com)
Delhi Technological University https://orcid.org/0000-0002-7729-7063
Narendra Kumar
Delhi Technological University
Rajesh Kumar
Delhi Technological University

Research Article

Keywords: Backpropagation, Neural network, PID controller, CSTR, Particle swarm optimization

Posted Date: June 6th, 2023

DOI: https://doi.org/10.21203/rs.3.rs-2851632/v1

License: This work is licensed under a Creative Commons Attribution 4.0 International License.
Read Full License

Title page

A PSO optimized novel PID Neural Network model for Temperature Control of Jacketed CSTR: Design, Simulation, and a Comparative Study

Snigdha Chaturvedi [a, *], Narendra Kumar [b], Rajesh Kumar [c]

[a] Delhi Technological University, Shahbad Daulatpur, Main Bawana Road, Delhi-110042, India

[b] Delhi Technological University, Shahbad, Daulatpur, Main Bawana Road, Delhi-110042, India

[c] National Institute of Technology, Kurukshetra-136119, India

Email address: snigdha_2k17phdee07@dtu.ac.in, narendrakumar@dtu.ac.in, rajeshmahindru23@nitkkr.ac.in

Corresponding Author details:

Snigdha Chaturvedi

Delhi Technological University, Shahbad Daulatpur, Main Bawana Road, Delhi-110042, India

Email address: snigdha_2k17phdee07@dtu.ac.in

A PSO optimized novel PID Neural Network model for Temperature Control of Jacketed CSTR: Design, Simulation, and a Comparative Study

Abstract

This paper proposes a Particle Swarm Optimization (PSO) tuned novel Proportional Integral Derivative (PID) like neural network (PID-NN). The structure of proposed PID-NN is very simple having only 3 neurons in the hidden layer and a single output neuron. The proportional, integral, and derivative gains of the PID controller are represented by the three weights in the neural network's output layer, respectively. The suggested approach uses the PSO method to optimize the output layer weights, which correspond to PID gains. The non-linear Continuous Stirred Tank Reactor (CSTR) plant, one of the most popular chemical industry processes, is utilized to test the suggested approach. A jacketed CSTR's temperature is controlled via a Particle Swarm Optimization tuned PID like neural network (PSO-NN-PID) controller. In terms of time domain specifications, the performance of the PSO-based NN-PID controller, the back propagation-based NN-PID controller (BP-NN-PID), and the conventionally tuned PID controller are compared. Mean square error is the objective function used in PSO-NN-PID and BP-NN-PID to optimize PID settings. The results show that the overshoot decreases from 44.13% in case of Zeigler- Nichols tuned PID controller to 26.33% in case of BPNN-PID controller, and further reduces to 23.13% in case of proposed PSO-based NN-PID controller. The decrease in rise time is observed from 0.2727 seconds in case of BPNN tuned PID to 0.1283 seconds in case of proposed PSO-NN-PID controller.

Keywords: Backpropagation, Neural network, PID controller, CSTR, Particle swarm optimization

1. Introduction

Most of the linear control problems have been solved because of intensive study on linear control systems during the past few decades. However, most systems in the real world including those that govern vehicles, biological systems, aircrafts, and robots are inherently nonlinear in nature. In recent years, nonlinear control issues have received a lot of attention. Certain laws, like superposition and homogeneity, are observed only in linear systems. A nonlinear system does not operate uniformly according to a common law. A nonlinear system displays various behavior in several operating regions[1]. Therefore, it becomes difficult to develop an effective controller for non-linear system. In industrial applications, the PID controller has perhaps been the most successful controller. Despite the development of numerous nonlinear system control strategies, such as artificial neural networks, fuzzy logic control, adaptive control, and model predictive control. 90% of industrial controllers are PID controllers. The controller's ongoing success serves as evidence that in engineering, simplicity and ease of use are most important aspect. The crucial step while implementing a PID controller is the effective tuning of three gains, K_p proportional gain, K_i integral gain and K_d derivative gain[2]. A study found that 30% of installed controllers employ manual PID tuning and that 65% of them are improperly tuned. Numerous adjustments are performed to account for the nonlinear effects when employing a PID controller on a nonlinear system. In past few decades several intelligent optimization techniques have been used to tune PID gains. A lot of research has been done on controlling linear systems with PID controllers and in most cases, we attain desirable results[3]. But the problem arises when PID controller is applied to a nonlinear system. Many researchers have addressed this problem and proposed various methods of handling the nonlinear effects. Some of the methods used in past are linearizing the plant

around a stable operating point, gain scheduling, anti-reset windup etc. [4]. Following are the four primary divisions of classical PID tuning methods: The first method involves analytically calculating the PID parameters from algebraic equations between the plant and the performance objectives. Analytical tuning methods include lambda tuning and internal model control. These may produce a straightforward formula that can be used for online tuning, but the model must be accurate, and the objective must take the form of an analytical formula. Among the methods used in the second category are Zeigler Nichols[5] tuning, Cohen Coon tuning[5], and other heuristic PID tuning strategies. Once more, these can be employed as a formula or rule-based system for online use, frequently with trade-off design goals.

Because of the above-mentioned challenges while applying PID controller, hybrid form of PID parameter adjustments is becoming more popular. The advantages of simple PID and soft computing techniques can be combined to tune PID parameters effectively. This method can improve robustness of the system. With the development of AI techniques in few decades, application of these methods to the PID parameter tuning has proved to be efficient than conventional methods. To address this problem in past few decades, a lot of researchers have applied different optimization algorithms to tune PID parameters. The ANN is used as an intelligent controller for modelling and control of nonlinear system. Fuzzy logic has also been used as controller for tuning PID parameters. The fuzzy controller uses error and change in error to obtain PID gain values. However, fuzzy logic requires expert knowledge to determine appropriate membership functions[6]. Therefore, NN can solve the problem because they have high computational speed and have been used in past for determining PID parameters efficiently. Metaheuristic algorithms have also been used to address complex nonlinear problems. With the research of several algorithms like GA, PSO, ACO, CSA etc. They suffer from the drawback of right selection of parameters and slow computational speed. These algorithms mostly do not give desired results because it becomes difficult to choose several parameters correctly. So, there is a need to develop hybrid method combining NN and PSO. PSO being an algorithm widely used for lot of complex problems has proved its efficiency[7]–[11]. Neural network can be utilized for tuning PID gains. A Back propagation neural network can be modified as a PID like structure and provide with the advantages of both BP neural network and PID control. This technique has been utilized and being applied to several nonlinear problems[6], [12]–[14].

In this study a novel hybrid approach is proposed utilizing Particle swarm optimization for weight initialization and optimization for PID like neural network structure. The above proposed technique is compared with the BP-NN-PID, and conventionally tuned Zeigler Nichols tuned PID controller. The proposed controllers are applied on temperature control of a Jacketed CSTR which is a nonlinear benchmark control problem.

The structure of the paper is as follows: section 1 contains the introduction, literature review, research gaps identified and contributions of the paper, section 2 describes the problem statement, section 3 describes the mathematical modelling of the CSTR temperature control, section 4 discusses the proposed PSO based NN -PID structure and algorithm, section 5 describes the classical Back propagation tuned NN-PID controller, section 6 describes the simulation results and finally conclusion is given in section 7.

Literature Review

In past a lot of researchers have done a substantial amount of research in PID controller tuning. Earlier classical tuning methods like Zeigler Nichols[5], Cohen coon and IMC type tuning[15] was mostly used for PID tuning. In [16] authors, have reviewed the various issues and problems while tuning of PID controller. In [2] authors, have discussed various problems in tuning PID controller when multi objectives are to be achieved. The intelligent methods were proposed to tune PID controller. In [3], authors proposed an extended PID controller while controlling nonlinear systems with uncertainty. In [17], authors have presented an review of various conventional and intelligent tuning methods and

compared their performance on an level control system. In [18] authors have proposed tuning method for an AVR system using chaotic optimization method and compared the performance in terms of rise time, settling time and overshoot. In [8], authors have applied PSO and TLBO algorithm to tune PID controller for concentration and temperature control of CSTR. In [7], authors have used cuckoo search algorithm to tune PID parameters of quadrotor. The simulation results proved that this method is more efficient than classical tuned methods. In [19], authors have used fuzzy logic to tune PID parameters applied to control airway pressure of respiratory system. The fuzzy logic based PID controller proved better as compared conventionally tuned methods in terms of rise time, overshoot, settling time etc. In [20], authors have applied PSO to tune PID gains of an artificial ventilation system. The results proved that PSO tuned controller gave better response as compared to conventional methods. In [21], authors proposed an improved teaching learning based optimization algorithm by adding concept of number of teachers, teaching factor adaptability etc. The improved teaching learning-based optimization algorithm was tested on benchmark functions. The results showed its superiority. In [22], authors have compared hybrid genetic algorithm type fractional order PID controller, Fmincon based pattern search based PID controller and hybrid MPC controller. Hybrid genetic algorithm based FOPID gives better response in terms of performance indices. In [23], authors have proposed gravitational search based fuzzy logic control for controlling position of nonlinear ball and beam system. The results showed that the results were better as compared to conventional controller. In [24] proposed a new algorithm to optimize PID parameters by combining swarm algorithms and learning processes. The proposed algorithm was better as compared to GA, PSO and NN tuned controllers. In [25], authors described the methods to develop fuzzy controllers for tuning PID gains. In [26], authors proposed a multi-objective fuzzy based fractional order PID controller tuned by evolutionary algorithms to control a hydraulic turbine governing system. In [27], authors applied an arithmetic optimization algorithm called empirical identification algorithm to find best PID values. In [28], authors have implemented hybrid optimization algorithms combining PSO with GWO and GSA to tune PID parameters. The proposed controllers were implemented to three bench mark nonlinear problems. The hybrid optimization techniques proved to be faster and less convergence error as compared to earlier used evolutionary algorithms. In [29], authors have proposed a new intelligent controller design based on sequential quadratic programming to derive the transfer function.

Research Gaps

PID tuning is a challenging process when applied to a nonlinear system, according to the literature review. To adjust PID controllers, several researchers have used a variety of techniques. Numerous AI techniques, including neural networks, fuzzy logic, and bio-inspired algorithms, are used to fine-tune PID controllers. The AI-based tuning techniques have been shown to be superior to the traditional techniques. The neural network based intelligent methods have the advantage of high computational speed whereas, the evolutionary algorithms can be easily applied to any non-linear system and gives accurate results. So, there is a need to combine the advantages of both the techniques and develop hybrid controllers.

Contributions of the paper

The main contributions of the paper are summarized as below:

1. A novel PSO tuned PID like neural network is proposed. The structure of PID like neural network is kept simple having only three neurons in the hidden layer. Therefore, the implementation of the controller is very easy.
2. The proposed controller is compared with the BP based NN-PID controller and ZN tuned PID controller.
3. The controller developed is tested for robustness under the disturbance application and is found to perform better than BP based NN-PID controller and ZN tuned PID controller.

2. Problem Statement

The structure of the proposed control scheme is shown in Fig.1. In the Figure 1, e(k) is the error between actual output and desired reference input. The optimized PID like neural network is connected in cascade with the non-linear jacketed CSTR plant. The neural network weights are adjusted with PSO algorithm to obtain P, I and D parameters.

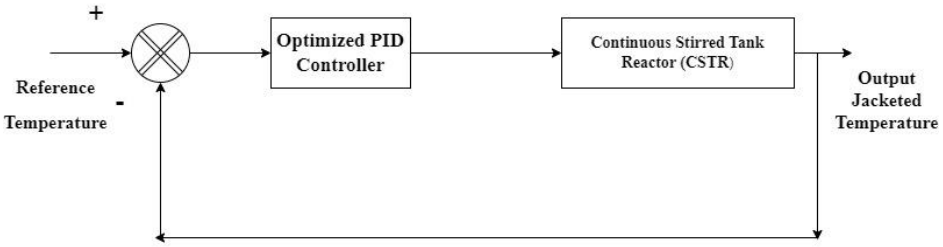

Figure 1 Structure of the proposed control scheme

The cost function is calculated after each iteration. The objective of the controller is to minimize the cost function:

$$E_c = \frac{1}{2}\sum_{k=1}^{T}(r(k) - y_{act}(k))^2 \quad (1)$$

Where, $r(k)$ is the desired reference input and $y_{act}(k)$ is the actual output.

3. Mathematical Modelling of a Jacketed CSTR

Continuous Stirred tank Reactor (CSTR) is reactor mostly used in chemical industries. It is generally used in processes where continuous flow of product is required to reach a product. Chemical reactors have a lot of effect on the output due to heat, so it is important to control heat in a chemical reactor. In a jacketed CSTR temperature control can be done by controlling the temperature of jacket around the reactor. The jacket temperature can be controlled by a coolant flowing in it. It operates with the following assumptions:

1. The reactor volume is kept constant V_R.
2. It is operated under steady state conditions with perfect mixing

In the CSTR considered we consider a simple reaction $A \xrightarrow{yields} B$. The concentration of the feed flown initially of product A is donated as C_{AR0}, the initial temperature of the product A is T_{R0} and it is assumed that there is a constant flow rate q_R. Irreversible reactions take place inside the reactor. The final products generated have a concentration C_{AR} and temperature T_R. The heat produced in the exothermic reaction is controlled by flowing a coolant in the jacketed layer of the reactor. The coolant temperature is T_{CRO} and its flow rate is q_{CR}.

The material balance of jacketed CSTR can be given as:

$$\frac{dV_o\rho_o}{dt} = q_{in}\rho_{in} - q_{out}\rho_{out} \quad (2)$$

Where, V_o is the reactor volume, ρ_o is the density of reactor, ρ_{in} is the density of feed flow input, q_{in} and q_{out} is the flow rates of input and output feed. In this case as per the assumptions $\rho_{in} = \rho_{out} = \rho_o$. The flow rates are also equal.

The balance equation for component A is given as,

$$V_o \frac{dC_{AR}}{dt} = q_R(C_{AR0} - C_{AR})V_R - V_o r_A \quad (3)$$

Where, C_{AR} is the concentration of component A in the reactor, r_A is the rate of reaction and is given as,

$$r_A = K_{R0}\exp\left(\frac{-E_R}{RT_R}\right)C_{AR}$$

Where, K_{R0} is the frequency factor, E_R is the activation energy and T_R is the reactor temperature

The energy balance equations for the reactor considering above given assumptions and neglecting kinetic and potential energy are given as,

$$V_R\rho_R C_P \frac{dT_R}{dt} = q_R\rho_R C_P(T_R - T) - (-\Delta H)V_R r_A + \rho_{CR}C_{PC}q_{CR}\left[1 - \exp\left(\frac{-hA}{\rho_{CR}C_{PC}q_{CR}}\right)\right](T_R - T) \quad (4)$$

In Equation 3 RHS represents heat accumulation in the reactor, in LHS the first term represents energy in and out due to flow of component A, the second term represents the heat due to reaction in the reactor and the third term represents heat transferred to the jacket. Where, T_R is the reactor temperature and T is the jacket temperature.

The above equations can be presented in the state variable form choosing C_{AR} and T_R as state variables,

$$\frac{dC_{AR}}{dt} = \frac{q_R}{V_R}(C_{AR0} - C_{AR}) - K_{R0}\exp\left(\frac{-E_R}{RT_R}\right)C_{AR} \quad (5)$$

$$\frac{dT_R}{dt} = \frac{q_R}{V_R}((T_{RO} - T_R) - \left(\frac{-\Delta H}{\rho_R C_P}\right)K_{R0}\exp\left(\frac{-E_R}{RT_R}\right)C_{AR} + \left(\frac{\rho_{CR}C_{PC}}{\rho_R V_R C_P}\right)q_{CR}\left[1 - \exp\left(\frac{-hA}{\rho_{CR}C_{PC}q_{CR}}\right)\right](T_{RO} - T_R) \quad (6)$$

The steady state solutions can be obtained by putting the two equations 5 & 6 to zero. For this study the parameters of jacketed CSTR chosen are shown in Table 1.

Table 1 Parameters of Jacketed CSTR

Parameters	Values
C_{AR} Concentration of input feed component A	**0.0882 mol/l**
Reactor temperature T_R	**441.2 K**
Flow rate of the coolant q_{CR}	**100 l/min**
Feed flow rate q_R	**100 l/min**
Input Feed temperature T_O	**350 K**
Jacket temperature T	**350 K**
Volume of reactor V_R	**100 l**

Coefficient of heat transfer hA	**$7\times 10^5\ cal/(minK)$**
Reaction rate constant K_R	**7.2×10^{10} min-1**
Activation Energy $\frac{E_R}{R}$	**1×10^4 K**
Heat produced in Reaction $(-\Delta H\ )$	**$-2\times 10^5\ cal/mol$**
C_H, C_{HC} Specific heat	**1 Cal (g/K)**
Densities, $\rho_{R,}\rho_{CR}$	**$1\times10^3 g/l$**

3. Structure of NN Based PID Controller

The structure of BPNN Based PID Controller consists of input layer, hidden layer, and output layer. There is a single node in the input layer, three nodes in the hidden layer and one node in the output layer. The three nodes of the hidden layer correspond to three PID parameter gains, proportional Kp, integral gain Ki and derivative gain Kd. The activation functions used are all linear in nature. To produce the integral action the integral nodea_1 is taken as feedback by using delaying effect. To produce the derivative effect the derivative node a_3 is given activation feedback. The proportional node a_2 is the general node without any feedback. The BPNN based PID structure is shown in Figure 2,

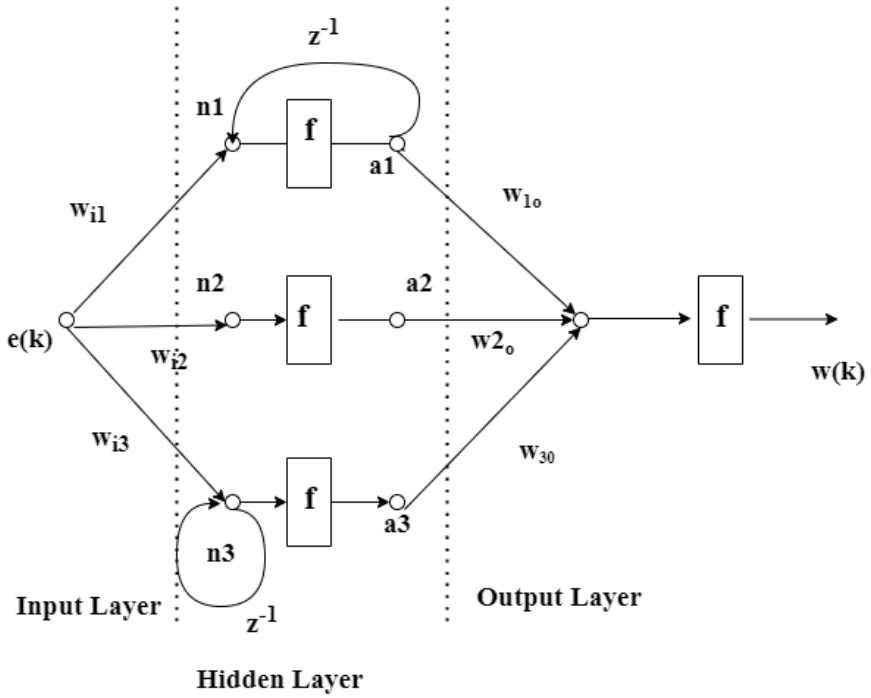

Figure 2 Structure of BPNN Based PID controller

The outputs of the hidden layer $a_1, a_2\ and\ a_3$ at sampling times k may be given as,

$$a_1(k) = e(k)w_{i1}(k) + a_1(k-1) \tag{7}$$

$$a_2(k) = e(k)w_{i2}(k) \tag{8}$$

$$a_3(k) = e(k)w_{i3}(k) - w_{i3}(k-1)e(k-1) \tag{9}$$

The output of the neural network-based controller is,

$$u(k) = \sum_{j=1}^{3} w_{jo}(k)a_j(k) = w_{1o}(k)a_1(k) + w_{2o}(k)a_2(k) + w_{30}(k)a_3(k) \tag{10}$$

In the first node z^{-1} is added as delay. So, $a(k-1) = a(k)z^{-1}$

Then, $e(k-1) = z^{-1}e(k)$ (11)

The output of the first hidden layer is

$$a_1(k) = \frac{w_{i1}(k)e(k)}{1-z^{-1}} \tag{12}$$

This equation represents an integral relationship. Therefore, this node generates a gain proportional to the integral of the error. The derivative action was produced by the derivative node using activation feedback.

$$a_3(k) = w_{i3}(k)e(k)[1 - z^{-1}] \tag{13}$$

This equation represents differential mode of operation. It is evident from the control output u(k) is that the neural network-based controller produces output like a PID controller. The second node of the neural network produces action like proportional control, the first node produces output like an integral action and third node produces output like a derivative control. A conventional BP based NN is complex having several layers, but a PID NN proposed here is simple structure where the output layers produce the sum or controller output. In this way by training the weights of PID based NN we can easily tune the PID parameters to obtain desired results.

4. PID Like Neural Network tuned by PSO

In this paper, a novel method is proposed to tune PID NN using PSO. PSO is an evolutionary algorithm which is inspired by bird flocking or fish schooling. A random population of particles is initialized in a search space. The particles have certain velocity and position. The particles fly in search space to the global best position after certain iterations. After each iteration, the particles position and velocity are adjusted in accordance with the value of fitness function.

*4.1 **Mathematical Formulation***

PSO is used to tune weights of PID like NN proposed in the study. The position of particles represents the weights in each iteration. The dimensionality of PSO algorithm chosen is equal to the total number of weights i.e., six. There are three weights used connecting input layer to hidden layer and three weights connecting hidden layer to output layer. Let the position vector of particles with S search space be defined as,

$$x_p = [x_{pi1}, x_{pi2}, \dots\dots\dots, x_{piS}]^T \tag{14}$$

And the velocity vector denoted as,

$$v_p = [v_{pi1}, v_{pi2}, \dots\dots\dots\dots v_{iS}]^T \tag{15}$$

The optimization is done by PSO and not by classical Back propagation algorithm. The objective function used for tuning NN based PID controller weights is Mean square error. Each particle moves in accordance to minimize the fitness function. The local best position of the particles is given by,

$$P_{abestij} = [P_{abesti1}, P_{abesti2} \dots\dots\dots\dots\dots\dots P_{absetiS}]^T \quad (16)$$

The global best position is denoted by,

$$G_{obestij} = [G_{obesti1}, G_{obesti2} \dots\dots\dots\dots\dots\dots G_{obsetiS}]^T \quad (17)$$

The particles change their position by updating the synaptic weights of the neural network to reduce the value of fitness function. The process of updating velocity after each iteration k is given by the following equation,

$$v_{ij}(k+1) = w_o v_{ij}(k) + c_1 r_1 \left[P_{abestij}(k) - x_{ij}(k)\right] + c_2 r_2 [G_{obestij}(k) - x_{ij}(k)] \quad (18)$$

Where, w_o is the weight of the algorithm, c_1 and c_2 are social factors and r_1 and r_2 are random numbers in interval [0,1].

The position of particles at $(k+1)^{th}$ iteration is,

$$x_{ij}(k+1) = x_{ij}(k) + v_{ij}(k) \quad (19)$$

After the updating the velocity and position, the values of P_{abesti} and G_{obesti} vectors also change accordingly. The two vectors are updated by the following law,

$$P_{abesti}(k+1) = \begin{cases} P_{abesti}(k) \; if \; f(x_i(k) \geq f(P_{abest}(k) \\ x_i(k) \qquad\qquad\qquad\qquad\qquad else \end{cases} \quad (20)$$

$$G_{obesti}(k+1) = \min [P_{abesti}(k+1) \quad (21)$$

The flowchart of the PSO Algorithm is shown in Figure 3.

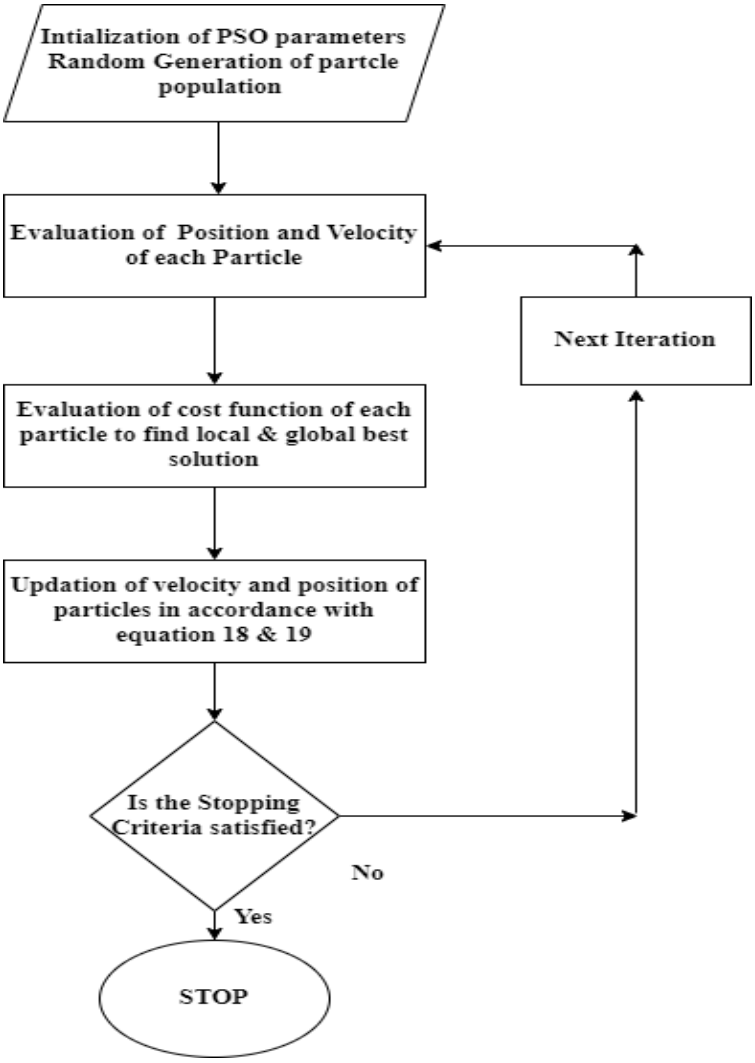

Figure 3 Flowchart of PSO

Despite of the development of several metaheuristic algorithms, PSO remains one of the most widely used algorithm to solve various non-linear problems. The main advantages of PSO are its simple structure, ease of implementation, fast computational efficiency, and robustness to the selection of parameters. The block diagram explaining the function of PSO-NN-PID is shown in Figure 4.

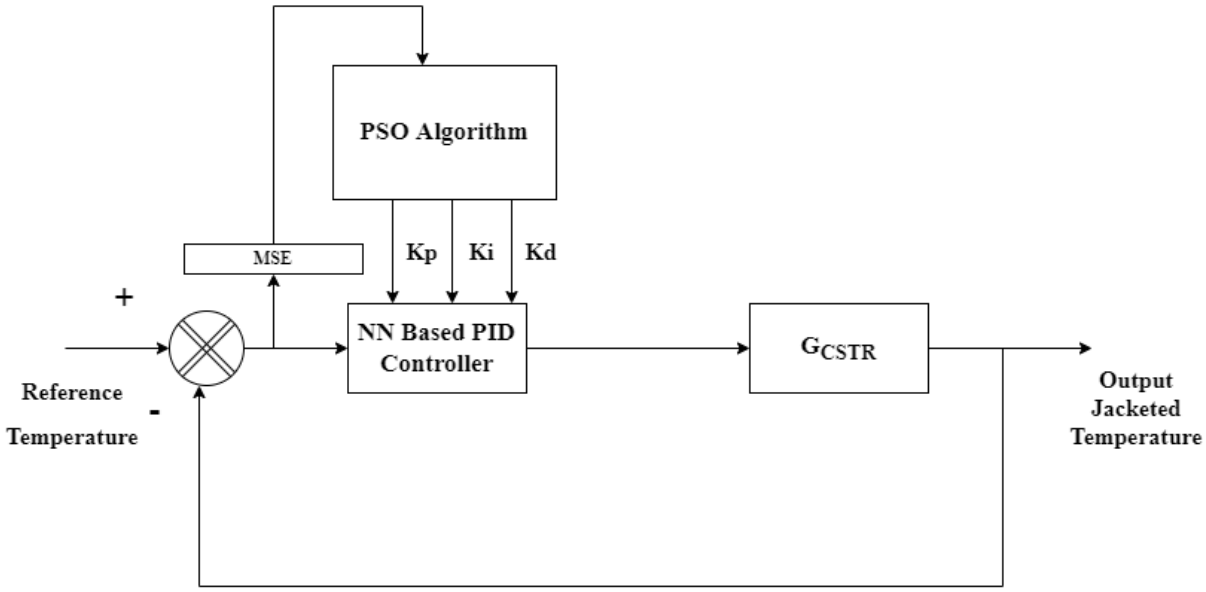

Figure 4 Block Diagram of PSO based novel NN-PID controller

It can be seen in the Figure 2 that the NN like PID controller parameters are tuned by PSO. The objective function used is mean square error (MSE). The PSO tuned NN based PID controller then gives the control signal to the Jacketed CSTR for temperature control. The algorithm of proposed PSO tuned NN-PID Controller is described below:

4.2 Algorithm of the proposed PSO tuned NN-PID Controller

1. Define PID like neural network having one neuron in the input layer, three neurons in the hidden layer and one neuron in the output layer.
2. Initialize random weights within the range [-1,1].
3. PSO is initialized with dimension size 3, population size 25 and maximum number of iterations as 50.
4. The fitness function is chosen as Mean square error.
5. For all particles do
6. Calculation of the control law $u(k)$ by initial weights.
7. Calculation of output $y_i(k)$
8. Evaluate current position and velocity in the search space
9. Calculate the value of objective function for the current iteration
10. If current position gives best objective function, then,
11. $P_{abesti} = w_i^k$
12. Else If the current objective function is the best overall objective function, then,
13. $G_{abesti} = w_i^k$
14. Endif
15. Move the particles in the search space
16. Update the position and velocity of the particles,
17. Do until stopping criteria is met
18. END

5. Classical Back propagation algorithm for tuning NN PID controller

The objective of the controller is to minimize the error between the actual output and the desired reference input. The output error can be written mathematically as,

$$error_i(k) = r_i(k) - yout_i(k) \quad (22)$$

Where, I = 1,2,….S and $yout_i(k)$ are the output variables measured and $r_i(k)$ is the reference input

The fitness function MSE is given as,

$$MSE(k) = \sum_{i=1}^{S} MSE_i(k) \quad (23)$$

Now, we state the rules for updating weights of neural network controller

$$\frac{\partial MSE(k)}{\partial w_{ij}(k-1)} = \sum_{i=1}^{S} \left[\frac{\partial MSE_i(k)}{\partial yout_i(k)} . \frac{\partial yout_i(k)}{\partial u(k-1)}\right] \frac{\partial u(k-1)}{\partial w_{ij}(k-1)} \quad (24)$$

$$\frac{\partial yout_i(k)}{\partial u(k-1)} \approx \frac{\Delta yout_i(k)}{\Delta u(k-1)} \approx \frac{yout_i(k) - yout_i(k-1)}{u(k-1) - u(k-2)} \quad (25)$$

We use sign function to find the result. The final rule of updating weights is,

$$\Delta w_{ij}(k-1) = -\alpha_{rij} \frac{\partial MSE(k)}{\partial w_{ij}(k-1)} = \alpha_{rij} \sum_{i=1}^{S} error_i(k) . sign \frac{\Delta yout_i(k)}{\Delta u(k-1)} . error_i(k-1) \quad (26)$$

Where, j=1,2,3

Weights of output layer are,

$$w_{oi} = 1, i = 1,2,3 \quad (27)$$

The function of back propagation based NN PID controller is shown in Figure 6.

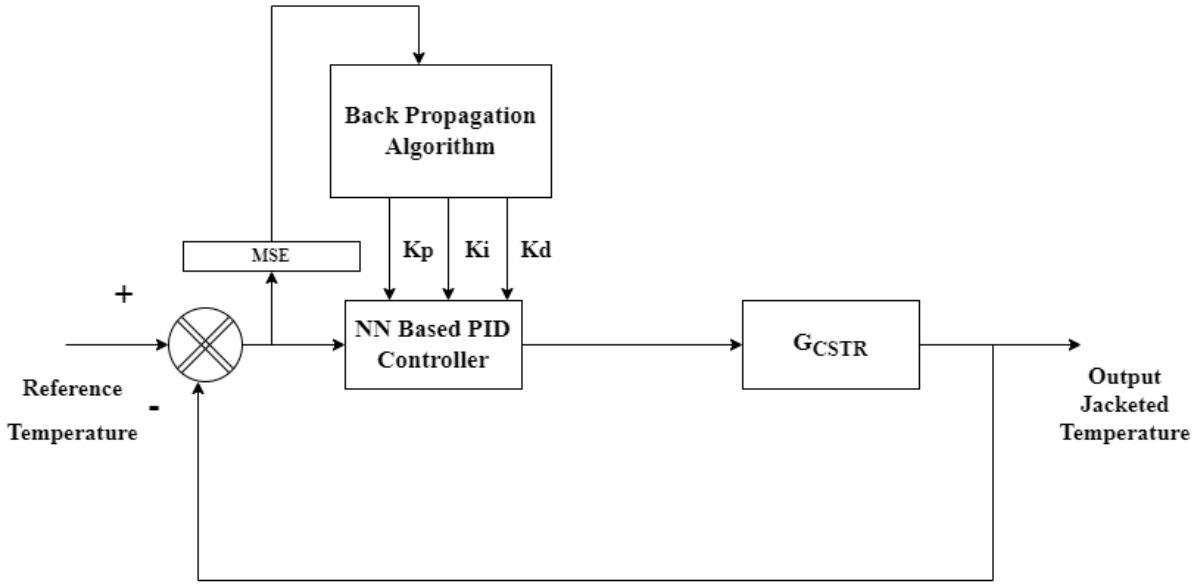

Figure 2 Block Diagram of BP-NN based PID controller

The BP based NN like PID controller shown in the Figure 3 gives the optimized PID parameters. The NN based PID controller gives the control signal to control the temperature of jacketed CSTR.

6. Simulation Results

The proposed hybrid PSO-NN technique is implemented to tune PID parameters for temperature control of jacketed CSTR and compared with BPNN-PID and ZN-PID tuning method. The parameters chosen while applying PSO algorithm are presented in Table 2

Table 2 PSO Parameters

S.no.	Parameters	Values
1.	C_1&C_2 Acceleration Constants	2
2.	w_{max}	0.9
3.	w_{min}	0.4
4.	Maximum no. of Iterations	50

The comparative step responses for various controllers for temperature control of jacketed CSTR is given in Figure 7.

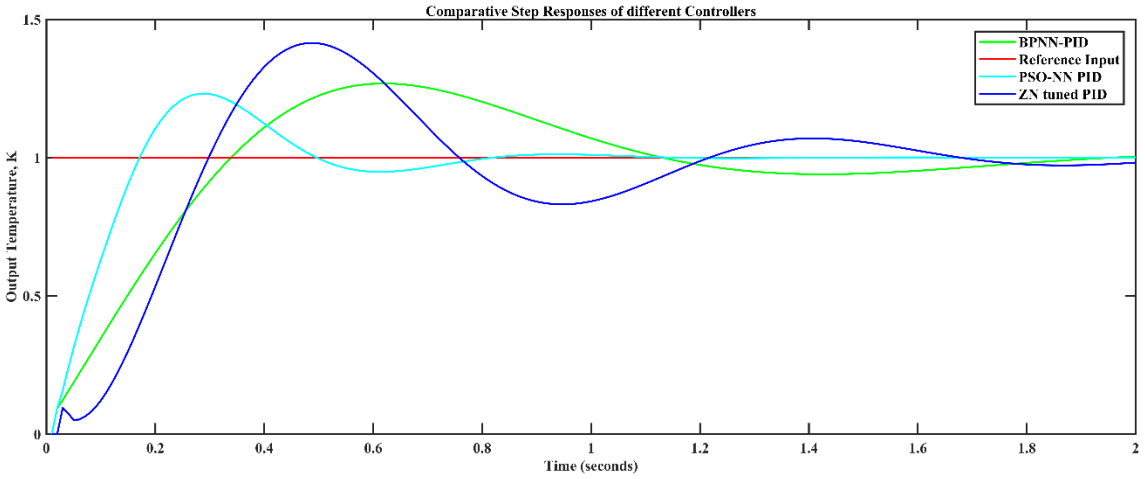

Figure 3 Comparative Step responses of Various Controllers

The performance indices explaining the step responses quantitatively is presented in Table 3.

Table 3 Comparative Step performance indices of various Controllers

S.no.	**Method used**	**Rise time (in secs)**	**Overshoot %**	**Peak time (in secs)**	**Settling time (in secs)**
1.	Zeigler Nichols	0.1810	44.08	0.4900	1.6731
2.	BPNN-PID	0.2727	26.33	0.6200	1.8194
3.	PSO-NN-PID	**0.1283**	**23.13**	**0.2900**	**0.7480**

It is evident from Figure 4 and Table 3 that rise time, tr is lowest 0.1283 in case of PSO-NN-PID tuned controller as compared to BPNN-PID and ZN tuned PID. The maximum overshoot has also reduced from 44.08% in ZN tuned PID to 26.33% in BPNN-PID and has further reduced to 23.13% in PSO-NN-PID. The settling time is also lowest 0.7480 in case of PSO-NN-PID controller. The values of different optimized PID gains Kp, Ki and Kd is given in Table 4.

Table 4 K_p, K_i and K_d parameters of various Controllers

S.no.	Method Used	K_p	K_i	K_d
1.	ZN Tuned	4.0795	0.8703	12.019
2.	PSO-NN-PID	**9.9000**	**2.0272**	**9.4000**
3.	BPNN-PID	4.3300	0.3100	6.1100

The proposed controller is also tested for disturbance rejection. The comparative step responses of different controllers in case of disturbance application from time=1 second to time=2 seconds is presented in Figure 8. The performance indices of the responses presented in Figure 5 are quantitatively compared in Table 5.

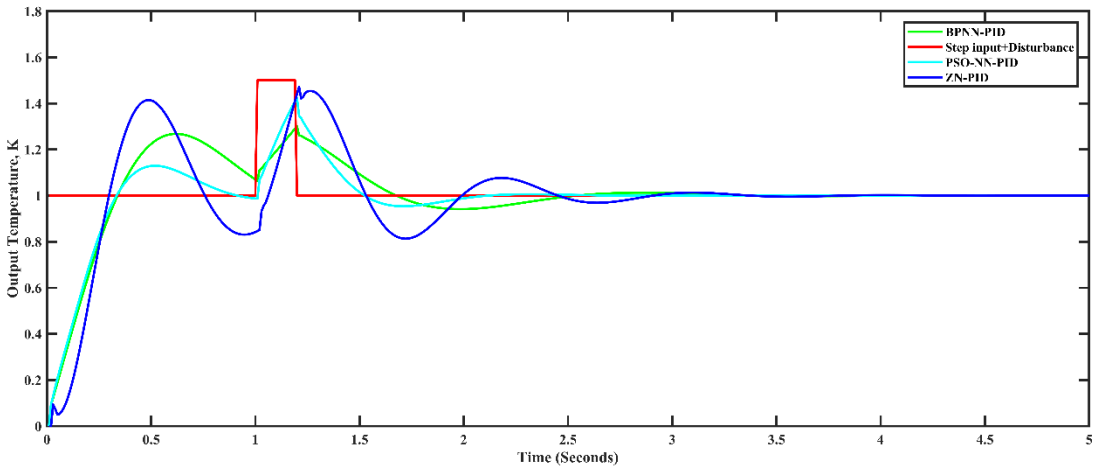

Figure 4 Comparative Step responses of various controllers under disturbance application

Table 5 Comparative Step performance indices of various controllers under disturbance application

S.no.	Method used	Rise time (in secs)	Overshoot %	Peak time (in secs)	Settling time (in secs)
1.	Zeigler Nichols	0.1839	47.03	1.21	2.77
2.	BPNN-PID	0.2713	30.00	1.21	2.36
3.	PSO-NN-PID	**0.1289**	50.00	**1.20**	**1.88**

The Table 5 shows that the PSO-NN-PID has the best rise time of 0.1289 seconds as compared to 0.2713 seconds in BPNN-PID and 0.1839 seconds in ZN-PID. There is slight increase in maximum overshoot in case of PSO-NN-PID controller but if we compare the settling time, it shows that the controller efficiently reduces the effect of disturbance quickly. Settling time is lowest 1.88 seconds in case of PSO-NN-PID controller. The values of controller gains are given in Table 6.

Table 6 K_P, K_i and K_d parameters of various Controllers under disturbance application

S.no.	Method Used	K_P	K_i	K_d
1.	ZN Tuned	4.0795	0.8703	12.019
2.	PSO-NN-PID	9.9000	1.9983	9.4000
3.	BPNN-PID	4.2145	0.2909	6.2350

The comparative analysis of the performance indices is shown in the Figure 9.

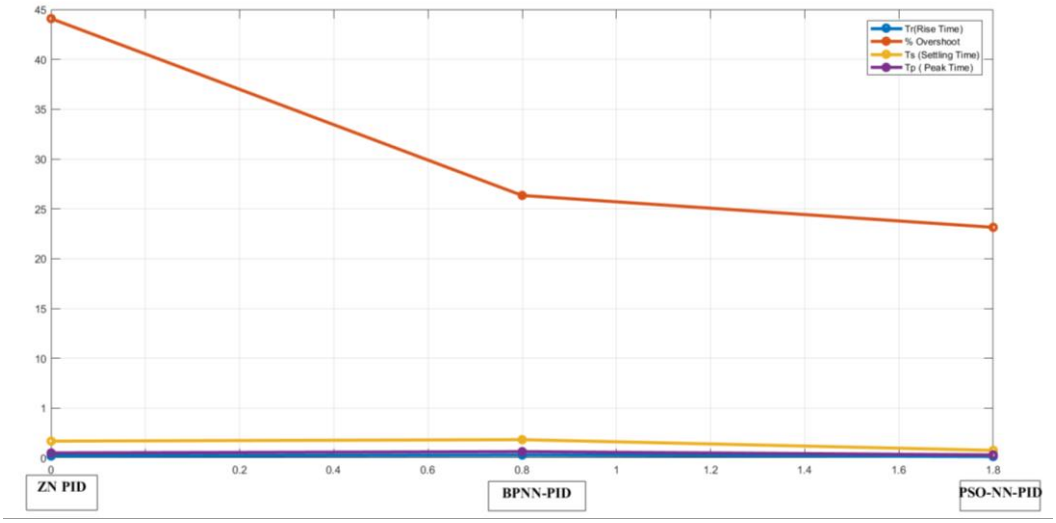

Figure 5 Comparative graph of rise time, overshoot, peak time and settling time for various controllers

The control signal u(t) and error signal e(t) are shown in Figure 10 & 11.

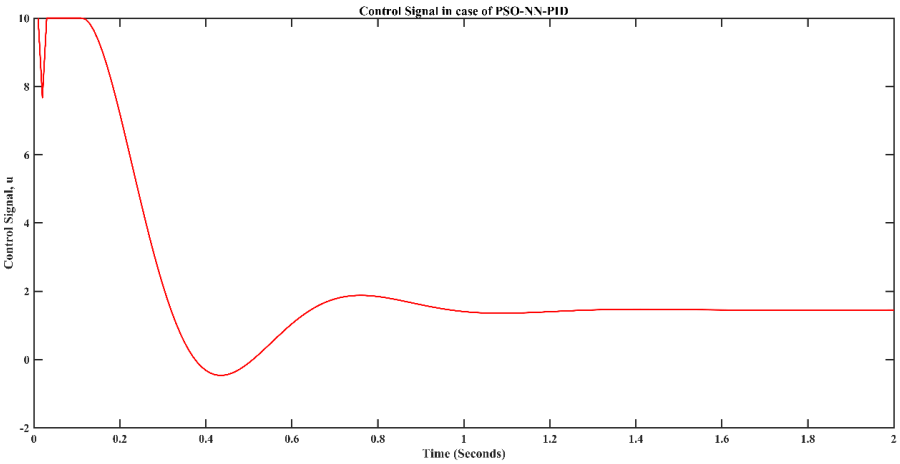

Figure 6 Control Signal in case of PSO-NN-PID controller

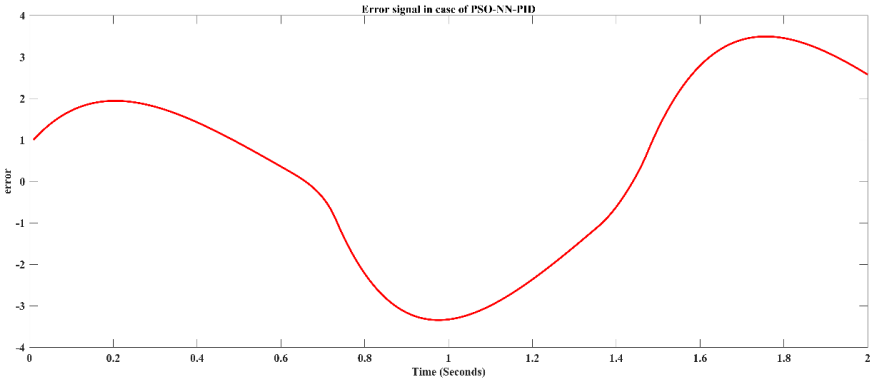

Figure 7 Error Signal in case of PSO-NN-PID controller

The graph showing variation in Kp, Ki and Kd with respect to time is shown in Figure 12.

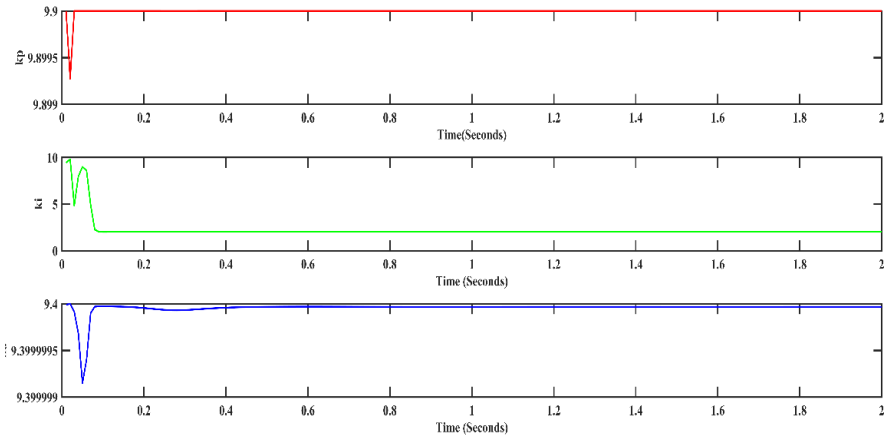

Figure 8 Variation or Kp, Ki and Kd values with time

The comparative bar graph of MSE in the case of three controllers, ZN-PID, BPNN-PID and PSO-NN-PID is shown in Figure 13.

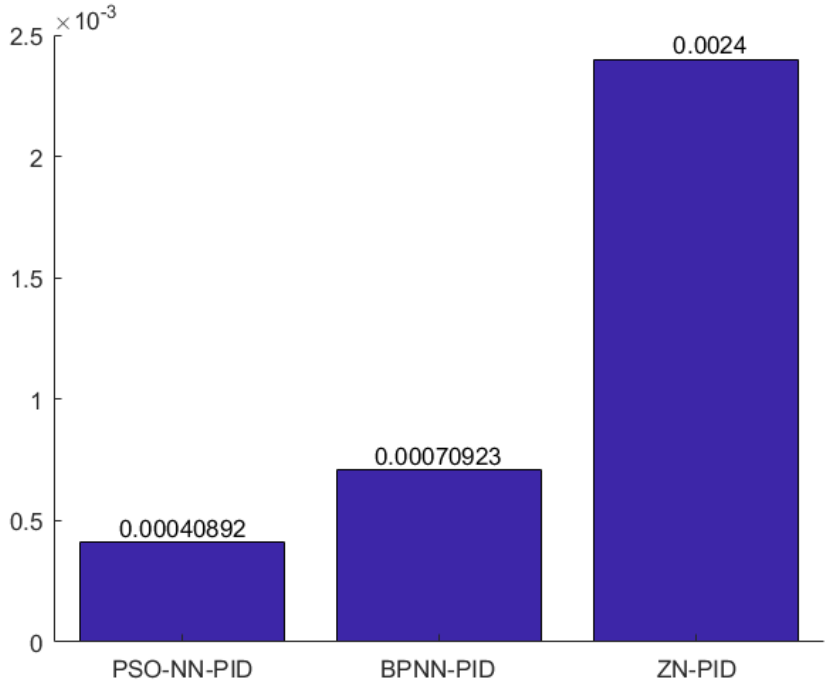

Figure 9 Comparative bar graph of MSE values for various controllers

6.1 Discussion

A comparison of simulation results of the three controllers are presented in the above section. ZN- tuned PID, BP tuned PID-NN and PSO tuned PID-NN are compared on a non-linear jacketed CSTR plant. From the results it is evident that in case of PSO tuned PID-NN controller there is a decrease of 33% in rise time and 47.7% in overshoot. To test the robustness of the proposed scheme a disturbance signal of amplitude 1.5 was applied. In case of PSO tuned PID-NN controller there is slight increase in overshoot but it can be observed that the controller was able to subside the disturbance quickly in 1.88 seconds as compared to ZN tuned PID taking 2.77 seconds and BP tuned PID-NN taking 2.36 seconds. Figure 6 shows a comparative graph of rise time, peak time, overshoot, peak time and settling time. It can be seen from the graph that there is a reduction in rise time, overshoot and settling time in case of PSO-PID-NN. Figure 8 & 9 represent the variation of control signal and error signal with time in case of PSO-PID-NN. Figure 10 represents the variation of $K_p, K_i \; and \; K_d$ with respect to time in case of PSO-PID-NN. Figure 11 shows a comparative bar graph of different controllers. The value of cost function MSE is least in case of PSO-PID-NN and largest in case of ZN tuned PID.

7. Conclusion

The study proposes a novel NN based PID controller based on PSO tuning method. The two techniques used combine the advantage of high computational speed, in case of neural network and accuracy in case of PSO. The NN is modified as a PID like structure where the hidden layer has three neurons and the output layer has three weights which are proportional to P, I and D gains respectively. The weights are optimized using PSO algorithm. The proposed technique is compared with Back propagation algorithm tuned NN-PID controller. The simulation results show that overshoot reduces to 23.13% to

44.08% in case of PSO-NN-PID. The rise time also reduces from 0.18 seconds to 0.1283 seconds. The controller developed was also tested for robustness under the application of disturbance and is found to be better than BP based NN-PID controller and conventionally tuned PID controller.

8. Statements and Declarations

Compliance with Ethical Standards

Ethical Approval

Not Applicable

Funding

The authors declare that no funds, grants, or other support were received during the preparation of this manuscript.

Conflict of interest

The authors certify that there is no conflict of interest with any individual/organization for the present work.

Informed Consent

Not Applicable

Authorship Contributions

All authors have contributed significantly in the study. The study conception and design were performed by Snigdha Chaturvedi and Narendra Kumar. Analysis and interpretation of results were done by Rajesh Kumar. Draft manuscript preparation was done by Snigdha Chaturvedi, Narendra Kumar and Rajesh Kumar. All authors reviewed the results and approved the final version of the manuscript

9. References

[1] J. Kang, W. Meng, A. Abraham, and H. Liu, "An adaptive PID neural network for complex nonlinear system control," *Neurocomputing*, vol. 135, pp. 79–85, 2014, doi: 10.1016/j.neucom.2013.03.065.

[2] K. H. Ang, G. Chong, S. Member, and Y. Li, "PID Control System Analysis , Design , and Technology," vol. 13, no. 4, pp. 559–576, 2005.

[3] C. Zhao and L. Guo, "Control of Nonlinear Uncertain Systems by Extended PID," vol. 9286, no. c, pp. 1–8, 2020, doi: 10.1109/TAC.2020.3030876.

[4] "1-0-1-k-j-astrom-pid-controllers-theory-design-and-tuning-2ed.pdf." .

[5] N. Method, "Ziegler - Nichols Method : Ziegler - Nichols Tuning Chart :," vol. 25, no. 10, pp. 1–2, 2015.

[6] R. Kumar, S. Srivastava, and J. R. P. Gupta, "Artificial Neural Network based PID controller for online control of dynamical systems," *1st IEEE Int. Conf. Power Electron. Intell. Control Energy Syst. ICPEICES 2016*, pp. 1–6, 2017, doi: 10.1109/ICPEICES.2016.7853092.

[7] S. E. I. Hasseni, L. Abdou, and H. E. Glida, "Parameters tuning of a quadrotor PID controllers by using nature-inspired algorithms," *Evol. Intell.*, vol. 14, no. 1, pp. 61–73, 2021, doi: 10.1007/s12065-019-00312-8.

[8] V. Srivastava and S. Srivastava, "Control of continuous stirred tank reactor (CSTR) using nature inspired algorithms," *Journal of Information and Optimization Sciences*, vol. 40, no. 2. pp. 329–338, 2019, doi: 10.1080/02522667.2019.1578092.

[9] S. Chatterjee and V. Mukherjee, “PID controller for automatic voltage regulator using teaching-learning based optimization technique,” *Int. J. Electr. Power Energy Syst.*, vol. 77, pp. 418–429, 2016, doi: 10.1016/j.ijepes.2015.11.010.

[10] A. W. Lins and R. Krishnakumar, “Tuning of PID controller for a PV-fed BLDC motor using PSO and TLBO algorithm,” *Applied Nanoscience (Switzerland)*. 2022, doi: 10.1007/s13204-021-02272-x.

[11] B. Abdollahzadeh, F. S. Gharehchopogh, and S. Mirjalili, “African vultures optimization algorithm: A new nature-inspired metaheuristic algorithm for global optimization problems,” *Comput. Ind. Eng.*, vol. 158, no. January, p. 107408, 2021, doi: 10.1016/j.cie.2021.107408.

[12] R. K. Mandava and P. R. Vundavilli, “An adaptive PID control algorithm for the two-legged robot walking on a slope,” *Neural Computing and Applications*, vol. 32, no. 8. pp. 3407–3421, 2020, doi: 10.1007/s00521-019-04326-2.

[13] G. Q. Zeng, X. Q. Xie, M. R. Chen, and J. Weng, “Adaptive population extremal optimization-based PID neural network for multivariable nonlinear control systems,” *Swarm Evol. Comput.*, vol. 44, pp. 320–334, 2019, doi: 10.1016/j.swevo.2018.04.008.

[14] T. Varshney and S. Sheel, “Improved NN-PID control of MIMO systems with PSO-based initialisation of weights,” *Int. J. Autom. Control*, vol. 8, no. 2, pp. 158–172, 2014, doi: 10.1504/IJAAC.2014.063362.

[15] S. Bennett, “Development of the PID Controller,” *IEEE Control Syst.*, vol. 13, no. 6, pp. 58–62, 1993, doi: 10.1109/37.248006.

[16] O. Ayokunle, K. Akingbade, and F. Dahunsi, “Annual Reviews in Control The dilemma of PID tuning ☆,” *Annu. Rev. Control*, no. May, 2021, doi: 10.1016/j.arcontrol.2021.05.002.

[17] J. M. S. Ribeiro, M. F. Santos, M. J. Carmo, and M. F. Silva, “Comparison of PID Controller Tuning Methods : Analytical / Classical Techniques versus Optimization Algorithms,” pp. 533–538, 2017.

[18] L. dos Santos Coelho, “Tuning of PID controller for an automatic regulator voltage system using chaotic optimization approach,” *Chaos, Solitons and Fractals*, vol. 39, no. 4, pp. 1504–1514, 2009, doi: 10.1016/j.chaos.2007.06.018.

[19] I. M. Mehedi, H. S. M. Shah, U. M. Al-Saggaf, R. Mansouri, and M. Bettayeb, “Fuzzy PID Control for Respiratory Systems,” *J. Healthc. Eng.*, vol. 2021, 2021, doi: 10.1155/2021/7118711.

[20] A. T. Yimchunger, D. Acharya, and D. K. Das, “Particle Swarm Optimization based PID-Controller Design for Volume Control of Artificial Ventilation System,” *2020 IEEE Calcutta Conf. CALCON 2020 - Proc.*, vol. C, pp. 278–282, 2020, doi: 10.1109/CALCON49167.2020.9106480.

[21] R. V. Rao and V. Patel, “An improved teaching-learning-based optimization algorithm for solving unconstrained optimization problems,” *Sci. Iran.*, vol. 20, no. 3, pp. 710–720, 2013, doi: 10.1016/j.scient.2012.12.005.

[22] S. Sakthiya Ram, C. Kumar, A. Ramesh Kumar, and T. Rajesh, “Hybrid optimization techniques based automatic artificial respiration system for corona patient,” *Automatika*, vol. 63, no. 2. pp. 226–243, 2022, doi: 10.1080/00051144.2022.2031538.

[23] M. J. Mahmoodabadi and N. Danesh, “Gravitational search algorithm-based fuzzy control for a nonlinear ball and beam system,” *J. Control Decis.*, vol. 5, no. 3, pp. 229–240, 2018, doi: 10.1080/23307706.2017.1403864.

[24] J. Pongfai, X. Su, H. Zhang, and W. Assawinchaichote, “A novel optimal PID controller

autotuning design based on the SLP algorithm," *Expert Syst.*, vol. 37, no. 2, pp. 1–15, 2020, doi: 10.1111/exsy.12489.

[25] H. B. Kazemian, "Developments of fuzzy PID controllers," *Expert Syst.*, vol. 22, no. 5, pp. 254–264, 2005, doi: 10.1111/j.1468-0394.2005.00316.x.

[26] T. Piraisoodi, W. I. Maria Siluvairaj, and M. A. K. Kappuva, "Multi-objective robust fuzzy fractional order proportional–integral–derivative controller design for nonlinear hydraulic turbine governing system using evolutionary computation techniques," *Expert Syst.*, vol. 36, no. 2, pp. 1–15, 2019, doi: 10.1111/exsy.12366.

[27] M. Issa, "Enhanced Arithmetic Optimization Algorithm for Parameter Estimation of PID Controller," *Arab. J. Sci. Eng.*, 2022, doi: 10.1007/s13369-022-07136-2.

[28] Srivastava, V., Srivastava, S., Chaudhary, G., & Blanco Valencia, "Performance improvement and Lyapunov stability analysis of nonlinear systems using hybrid optimization techniques," *Expert Syst.*, 2022.

[29] C. N. Huang and A. Chung, "An Intelligent Design for a PID Controller for Nonlinear Systems," *Asian J. Control*, vol. 18, no. 2, pp. 447–455, 2016, doi: 10.1002/asjc.1074.

ResearchGate

See discussions, stats, and author profiles for this publication at: https://www.researchgate.net/publication/371685311

A State-of-the-art Review on Micro Electro-Discharge Machining

Article · June 2023

CITATIONS
0

READS
5

1 author:

Lakshya Prasad
Delhi Technological University
1 PUBLICATION **0** CITATIONS

SEE PROFILE

All content following this page was uploaded by Lakshya Prasad on 19 June 2023.

The user has requested enhancement of the downloaded file.

A State-of-the-art Review on Micro Electro-Discharge Machining

Lakshya Prasad

Department of Mechanical Engineering,

Delhi Technological University, New Delhi-110092, India

Abstract

Electro-Discharge Machining (EDM) is one of the non-conventional machining processes available, in which the material removal takes place due to melting and vaporisation of electrode materials. Micro Electro-Discharge Machining (μ-EDM) is a variant of EDM, is playing an important role in generation of micro features on difficult to machine conducting materials. In this paper, authors carried out an extensive literature study to give a complete description on μ-EDM process, its requirements, performance and applications. More than fifty papers were referred and the details were categorized into five major areas, namely, experimental setups and its subsystems, experimental studies and optimization methods, generated micro features, modeling and simulation approaches and applications.

Keywords: μ-EDM ; dielectric fluid; micro features; modeling, optimization, tool feed mechanism

1. Introduction

EDM also referred to as spark machining is a manufacturing process whereby a required shape of an object is obtained as a mirror image of the tool. The material removal from the workpiece occurs by a series of rapidly recurring spark discharges between the two electrodes, which, results in extremely high temperature usually in the order of 8,000 ^{0}C to 12,000 ^{0}C causing vaporisation of the material at the point of discharge. The vapourized material is dispersed into the space surrounding the electrodes. Melting and vaporization of the material leads to the formation of tiny craters on the work surface. EDM has proved to be an effective method to machine metals irrespective of their hardness and other mechanical properties. But thermal properties such as melting point, boiling point, heat conduction efficiency and heat capacitance influences the process only to a very small extent, as the temperature generated by the electrical discharges exceeds the boiling point of any material on earth [1]. µ-EDM has capability to machine microstructures of varying complexity levels on difficult to cut metals and alloys. According to College International pour la Recherche en Productique (CIRP) Scientific Technical Committee Paper, the term micro-machining defines the processes that machine dimensions in the range of 1 m to 999 m [2]. µ-EDM has gained importance because of its ability to produce stress free micro sized cavities of desires shapes on conducting and semi conducting materials. Even though the principles of conventional EDM and µ-EDM are the same, there are some differences between the two processes, which arise due to the scaling effect. Table 1 shows the major differences between the conventional EDM and µ-EDM.

Table 1. Major differences between the conventional EDM and µ-EDM.

Parameters	Conventional EDM	µ-EDM
Size of the tool	Greater than 999 µm	Lesser than 999 µm
Inter electrode gap	10 to 500 µm	Less than 10 µm
Open circuit voltage	4 - 400 V	10 - 120 V
Peak current	Greater than 3 A	Lesser than 3 A
Pulse on-time	0.5 to 8 ms	50 ns to 100 µs
Specific energy	High	Low

μ-EDM process can be divided into four categories based on the type of tool and tool kinematics. They are μ- wire EDM, μ- die sinking EDM, μ-milling EDM and μ-EDM drilling [3]. In this, paper a complete review of ongoing/completed research in the field of μ-EDM and its possibilities are presented.

1.1. Principle of μ-EDM

The working principle of conventional EDM, various components, subsystems, applications etc are detailed in text books [4, 5]. In μ-EDM, the two electrodes-workpiece (anode) and tool (cathode) separated by dielectric fluid are supplied with pulsed voltage. Figure 1 shows the schematic representation of μ-EDM cell.

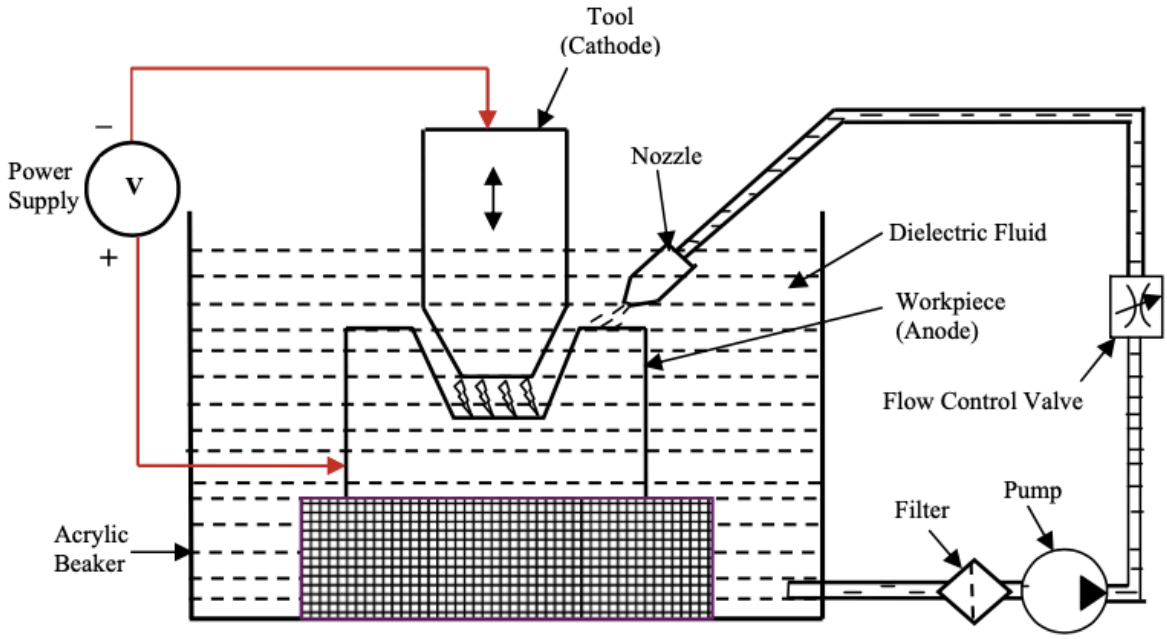

Fig. 1. Schematic representation of EDM cell.

The workpiece and tool are brought closer until the dielectric in the media breaks down and allow current to pass through it which appears as sparks. By varying the electrical process parameters such as voltage, frequency,

current, duty cycle etc., it is possible to control the energy of sparks**.** Application of pulsed voltage at discharge energies in the range of few micro joules that result in continuous material removal in µ-EDM. µ-EDM provides immense possibilities to produce tiny features, micro components and even fabrication of Micro Electro Mechanical System (MEMS) devices.

2. Review on µ-EDM process

This section focuses on the reviewed literatures of research areas and the current trends in µ-EDM. Figure 2 shows the classification of research papers.

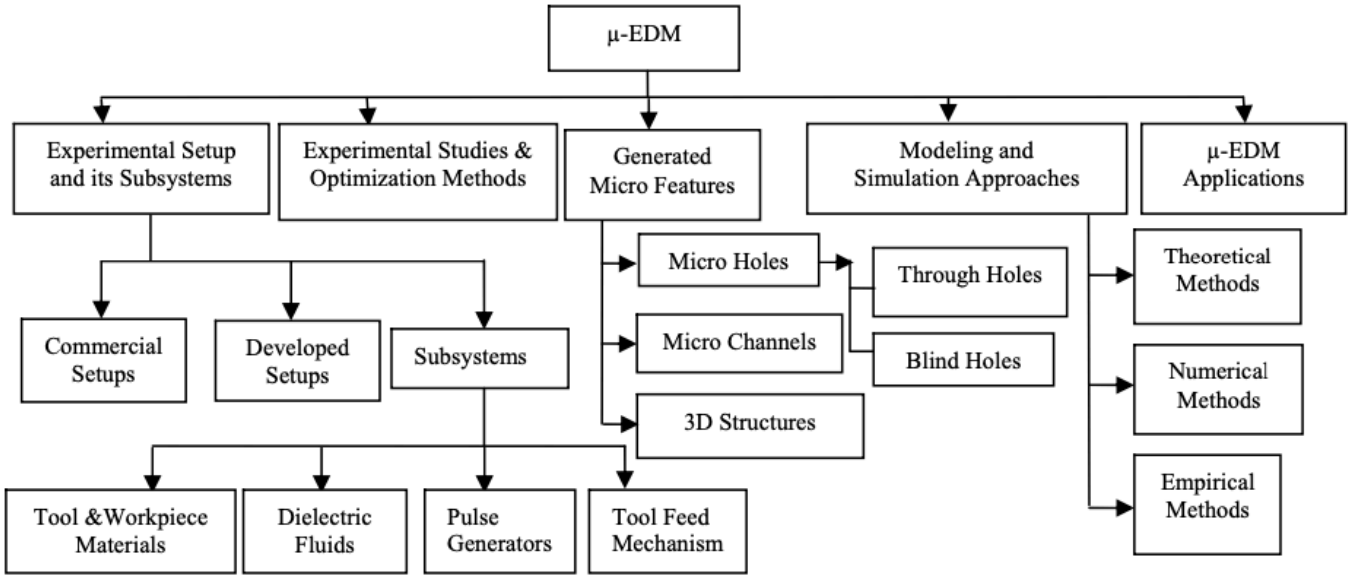

Fig. 2. Classification of research papers.

2.1. Experimental setups and its subsystems

Most of the research work carried so far on µ-EDM is on commercial available µ-EDM machines. There are only a very few manufacturers supplying µ-EDM machines. Some of the researchers utilized these commercial available machines such as SARIX [6, 7, 8, 9], Panasonic Factory Automation, Pacific Controls and SmalTec. Details of the

commercial available µ-EDM systems and their capabilities were collected and summarized [10, 11].

At the same time, a large number of researchers have focused on development of µ-EDM setups that suit their requirements to conduct experiments. **Higuchi et al.** [12] developed a pocket sized EDM with a volume of one thousandth than that of the conventional ones having the performance same as a conventional EDM. **Lim et al.** [13] developed a µ-EDM, which is energized by a pulse generator that can be switched to both transistor type and RC- type. **Gang et al.**[14] developed a precision µ-EDM which consists of high precision XYZ stages with the resolution of 0.1 µm driven by linear motor, a high speed rotary spindle with rotation accuracy within 1 µm, high precision granite base, small energy power unit and video microscopic system with high enlargement factor which is used to monitor the state of machining online. Fig. 3 shows the developed µ-EDM machine. **Chow et al.** [15] modified a conventional EDM machine by fitting a rotating disk as the electrode to machine micro slits. **Leera et al.** [16] proposed an indigenously developed µ-EDM setup. The schematic diagram of the proposed µ-EDM experimental setup is shown in Fig. 4.

It consists of copper plate as workpiece electrode, copper wire as tool electrode of diameter 300 – 800 µm, peizoactuated tool feed mechanism, transistor based pulse generation circuit, deionized water as dielectric fluid, and ultasonicator containing the dielectric fluid. µ-EDM subsystems are categorised into workpiece electrodes, tool electrodes, dielectric fluids, pulse generation circuits, tool feed mechanism and its circuits.

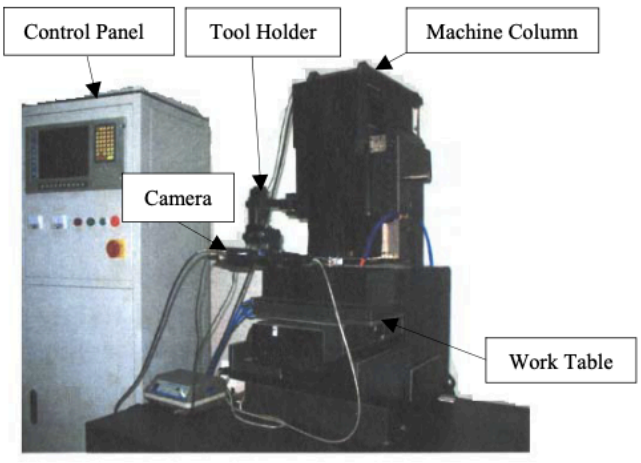

Fig. 3. Developed µ-EDM setup [12].

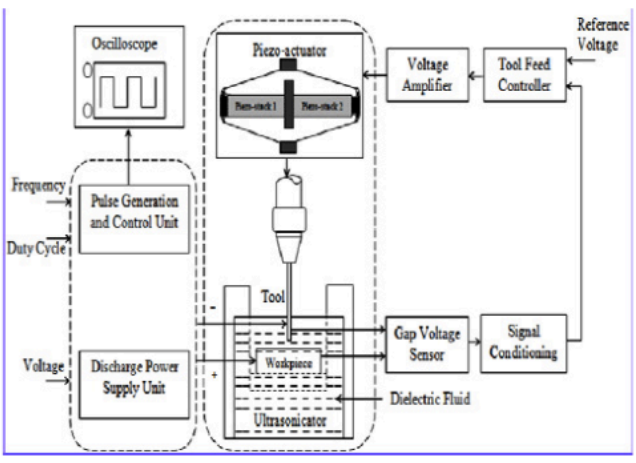

Fig. 4. Schematic diagram of the proposed µ-EDM setup.

The detailed explanations of these components are elaborated below:

1. Workpiece materials: A variety of metals and alloys can be machined using μ-EDM setup. The various materials machined using μ-EDM found in literature are copper [16, 17, 18] titanium alloy Ti-6Al-4V [19, 20], SK3 carbon tool steel [21], SS304 [22, 23], high nickel alloys [24], tungsten carbide [25, 26], ceramics [8, 10].

2. Tool materials: Selection of tool in μ-EDM is a critical factor, as the accuracy and shape of the micro feature machined largely depends on the tool. Tungsten electrodes [27, 28] and tungsten carbide electrodes [20, 21, 26] are the preferred tool materials in μ-EDM. To complement this widely used expensive material, cost effective materials namely brass [23], copper[16, 29], graphite and stainless steel are also tried as tool electrodes.

3. Dielectric fluids: The commonly used dielectric fluids are deionized water [30] and kerosene [28, 21]. Total EDM 3 oil [23], hydro carbide dielectric liquids [31] etc are the other dielectric fluids used in μ-EDM process. Researchers have added micro molybdenum di-sulphide (μ-MoS_2) powder in dielectric fluid and using ultrasonic vibration during μ-EDM processes to improve surface finish and MRR [28].

4. Pulse generators: The commonly used pulse generators in μ-EDM are RC type, transistor-type and transistor- type iso-pulse generators. In RC type of generators, the capacitor stores the energy and this energy is discharged during the machining process. Whereas in transistor type pulse generators, the capacitor is replaced by a transistor which switches the pulses to generate rectangular pulses between 0V and 60 V, supply voltage. RC type generators are preferred to transistor type because of high discharge frequency and low discharge energy [17]. In most cases, transistor-type generator has been used to supply the discharge energy which is good for conventional EDM [32]. **Jahan** [25] studied, RC-type circuit could be more suitable for fabricating microstructures in tungsten carbide, where accuracy and surface finish are of prime importance.

5. Tool feed mechanisms: For interrupted machining the gap between the tool electrode and the workpiece electrode should be maintained constant. The function of tool feed mechanism is to raise or lower the tool by sensing the voltage fluctuations in the inter electrode gap, so that a constant inter electrode gap is maintained. Servo feed control mechanism is used in most of the setups [32, 33]. Whereas some researchers used

different technology based micro actuators to impart the tool movements and these have proved to be more efficient compared to the conventional servo controlled tool feed mechanisms. **Han et al.** [32] proposed a new servo control tool feed mechanism that senses the average gap voltage and uses it as the feedback signal to control the feed, so that the electrode gap is maintained constant. **Mahendran et al.** [34] developed a μ-EDM system with directly mounted APA 400MML Actuator as the tool feed mechanism. **Li et al.** [35] have proposed an inchworm type micro feeding mechanism. Impact drive mechanism [12] and direct drive method [34] based on piezoelectric actuation were also proposed and elaborated. **Leera et al.** [16] developed a μ-EDM system with a piezoactuated tool feed mechanism to maintain a constant gap between the electrodes.

2.2 Experimental studies and optimization techniques

μ-EDM is a thermal process, where in electrical power supplied creates the thermal effect to remove material. Therefore, the input electrical power is a matter of significance. The electrical input conditions generally consist of several parameters such as current, voltage, frequency, pulse on-time, pulse off-time, duty cycle etc. Most of the papers have focused on tuning these process parameters to achieve optimum performance measures like MRR and TWR. The process parameters are classified as electric and non-electric parameters to study their effects on machining. The electrical parameters are voltage, frequency, pulse on-time, pulse off-time, discharge energy, duty cycle etc. The non-electrical parameters are dielectric fluid, flushing pressure, frequency of induced vibrations addition of some particles of micro and nano size to enhance the machining rate etc. Two performance measures that greatly judges efficiency of μ-EDM process are Material Removal Rate (MRR) and Tool Wear Rate (TWR). Surface roughness, dimensional accuracy, taper, overcut (OC) etc are the performance measures of quality of the machined feature mainly holes and channels. The parameters are analysed and optimized using various diagnostic studies like grey relational analysis, Taguchi method, multi objective optimization, ANOVA, Genetic Algorithm (GA) etc. The available literatures on this area are as follows. **Tiwary et al.** [19] carried out a study on the influence of various process parameters on MRR, TWR, OC, and taper angle while machining of Ti–6Al–4V. To perform the experimentation, they have utilized Central Composite Design (CCD) to design the experiments and Response Surface Methodology (RSM) to map the relationship between the input process parameters with the resulting

process response. **Lin et al.** [21] also used RSM based on the CCD for evaluation of the characteristics Electrode Wear Rate (EWR), MRR and OC. **Natarajan et al.** [36] carried out optimization of multiple performance characteristics - MRR, TWR and OC, using Taguchi method and Grey relational analysis. The parameters selected by them were pulse on-time, discharge current and gap voltage. **Meena et al.** [20] carried out multi objective optimization of μ-EDM machining parameters of Ti-6Al-4V alloy by the grey relational analysis and analysis of variance (ANOVA). **Mehfuz et al.** [37] investigated the influence of process parameters, feed rate, capacitance, and voltage. The response variables were average surface roughness (Ra), maximum peak-to-valley roughness height (Ry), TWR and MRR. **Pandey et al.** [22] carried out studies on optimization of the process parameters using RSM and GA. **Leera et al.** [17] studied the interaction effects of process parameters on width, OC and surface roughness of micro channels machined on μ-EDM using Taguchi method and RSM.

2.3 Generated micro features

The micro features of interest in machining using μ-EDM are micro holes-blind and through holes, micro channels, micro grooves, micro slits, three dimensional structures and textured surfaces. These promising features that can be machined with a high level of accuracy using μ-EDM have a great demand in industry. This section discusses the literature corresponding to machining of such micro features.

Micro holes are common features of many micro products – catheters, injection needles, nozzles, cooling holes on turbine blades, dies etc. μ-EDM is very effective to machine any kind of holes such as small diameter holes down to 10 m and blind holes with an aspect ratio of 20. **Maity et al.** [28] observed that circularity error, recast layer formation and longer machining time during micro hole machining was mainly due to the effect of capacitance value used. **Jahan et al.** [26] conducted experimental investigations on μ-EDM for obtaining high-quality micro- holes in WC with small spark gap, better dimensional accuracy, good surface finish and circularity. **Rajurkar et al.** [38] reported that μ-EDM can be easily used to produce a hole of depth equivalent to five times the bore diameter. **Yeo et al.** [39] investigated feasibility of a magnetic field to obtain higher aspect holes on hardened tool steel using μ-EDM process. **Natarajan et al.** [23] carried out a study on machinability and accuracy of microholes machined

on grade 304 stainless steel using μ-EDM. **Tahsin et al.** [31] studied the shape and dimensional geometry of blind micro holes machined on plastic mold steel using μ-EDM. **Ekmekci et al.** [40] experimentally investigated the geometry and subsurface damage of blind micro-holes produced by μ-EDM on plastic mold steel to explore the relational dependence with respect to pulse energy. **Liu et al.** [24] investigated the feasibility of machining high nickel alloy using μ-EDM, and they were successful in doing it. Micro channel is one of the most necessary feature in many micro devices and systems and have found research interest in a wide range of sectors including biomedical, energy, chemical, micro fluidics, micro molding etc. **Murali et al.** [41] demonstrated the fabrication of micro channels of width 25 μm and surface roughness with R_a value 0.4 μm on titanium alloys. **Modica et al.** [6] conducted a study on process optimization during machining of micro channels. **Hung et al.** [42, 43] used μ-EDM method to produce micro channels with aspect ratio 1.2 on metallic bipolar plates. **Oscar et al.** [44] proposed a new system to machine micro channels using an oscillating electrode by designing an electrode holder capable of getting required oscillation. **Schubert et al.** [45] successfully demonstrated μ-EDM milling of non-conductive ZrO_2 ceramics by creating an electrically conducting starting layer. **Ali** [27] compared micro end milling and micro electrical discharge milling for the fabrication of micro channels on metals. **Tong et al.** [46] machined non-circular cross section microstructure using a vibration assisted EDM process. A novel multiprocessing μ-EDM technique was used to fabricate complex 3D structures like micro lollipop end mills [47].

2.4 Modeling and simulation approaches

The various process parameters affecting the μ-EDM process as mentioned in section 2.2 are voltage, current, capacitance, feed rate etc. Researchers have tried various modelling and simulation approaches to study the effect of various parameters on MRR, TWR, surface finish etc. The models are broadly classified as analytical models for mathematical analysis, numerical models using Finite Element Method (FEM) as tool and empirical models from experimental studies to relate the effect of parameters on various responses. **Murali et al.** [48] developed a mathematical model based on heat transfer principle for the simulation of single spark machining during μ-EDM of titanium alloy. **Dhanik et al.** [49] developed a comprehensive model to predict the material removal in a

single discharge in μ-EDM using the basics of EDM models. **Sarikavak et al.** [50] developed a 3 D transient model for single discharge to calculate the MRR and radius of the crater formed. **Wang et al.** [51] suggested a thermo- physical model for μ-EDM deposition process. FEM was used for the numerical analysis of single spark deposition. **Tan et al.** [52] conducted a new heat conduction analysis of μ-EDM with FEM. They have also proposed a new approach for predicting the effects of multiple discharges on machining performance. **Tan et al.** [53] proposed a numerical model based on the multiple discharge approach to predict the thicknesses of the recast layer produced using the μ-EDM process. **Somashekhar et al.** [54] developed a numerical model based on Finite Volume Method (FVM) to solve the micro-EDM model equations so that the effect of spark ratio on the temperature distribution in the material can be predicted. **Pradhan et al.** [55] developed an Artificial Neural Network (ANN) model using a back-propagation neural network algorithm, which was trained with response values obtained from the experimental results. Empirical models for optimization based on RSM were developed to predict the response parameters for any arbitrarily input parameters.

2.5 Application areas

μ-EDM finds wide applications in inkjet nozzles of printers, cooling holes in turbine blades, micro channels in micro fluidic analysis, micro moulds, honeycomb structures etc. Some of the research works from literature are as follows: **Allen et al.** [56] used μ-EDM process to machine inkjet nozzles. **Tong et al.** [57] used μ-EDM process to drill high quality drilling spray holes on diesel injector nozzles. **Oliaei et al.** [47] fabricated tungsten carbide and Poly Crystalline Diamond (PCD) ball end mills using μ-EDM process. **Sahu et al.**[58] generated nano particles of mean diameter less than 10 nm using μ-EDM finds its application as an efficient coolant in automobile sector. A novel experimental approach-Ultrasonic technique for concentration characterization of copper nanofluids is elaborated [59]. **Liu et al.** [60] demonstrated the applications of two and three-dimensional microstructures on different types of materials such as a stainless steel micro-compressor and a ceramic miniature gas turbine.

3. Conclusions

μ-EDM is one of the important non-conventional machining methods that can find wide application. In this connection, authors reviewed many papers on μ-EDM and concluded that there are large research potentials in this area. The outcome of this review makes the reader to think in the direction of various issues as discussed in the paper as:

- Experimental setups and its subsystems
- Experimental studies and optimization techniques
- Generated micro features
- Modelling and simulation approaches
- Application areas

REFERENCES

[1] Masuzawa T. State of the art micromachining. Ann. CIRP Manuf. Technol 2000; 49 (2): 473-488.

[2] Masuzawa T and Tonshoff HK. Three-dimensional micromachining by machine tools. Annuals of the CIRP 1997; 46, 2: 621-628.

[3] Singh S and Bhardwaj A. Review to EDM by Using Water and Powder-Mixed Dielectric Fluid. Journal of Minerals & Materials Characterization & Engineering 2011; 10: 2-199-230.

[4] Production Technology, HMT Banglore, *Tata Mc Graw Hill*, 1980.

[5] Production Engineering Sciences, PC Pandey and CK Singh, *Standard Publishers Distributors*, 1989.

[6] Francesco Modica, Valeria Marrocco, Giacomo Copani and Irene Fassi. Sustainable MicroManufacturing of Micro-Components via Micro Electrical Discharge Machining, Sustainability 2011; 3: 2456-2469.

[7] Opoz TT, Ekmekci B and Erden A. An Experimental Study on the Geometry of Microholes in Microelectric Discharge Machining. Materials and Manufacturing Processes 2009; 24, 12:1236-1241.

[8] Schubert A, Zeidler H, Hahn M, Hackert-Oschätzchen M and Schneider J. Micro-EDM milling of electrically nonconducting zirconia ceramics, Procedia 2013; CIRP 6: 297-302.

[9] Ekmekci B, Sayar A, Opoz TT and Erden A. Geometry and surface damage in micro electrical discharge machining of micro-holes. J.Micromech. Microeng. 2009; 19-105030 (16pp).

[10] Kun LIU; Micro electrical discharge machining of ceramic materials and composites; Thesis, Chapter 2 pg 60.

[11] Moylan SP, Chandrasekar S and Benavides GL. High-Speed MicroElectro-Discharge Machining, Sandia Report, Sandia National Laboratories, 2005; SAND2005-5023, Printed September.

[12] Higuchi T, Furutani K, Yamagata Y and Takeda K. Development of pocketsize electro discharge machine. Annals of the CIRP 1991;40,1:203-6.

[13] Lim HS, Wong YS, Rahman M and Lee EMK. A study on the machining of high-aspect ratio micro-structures using micro EDM. J. Mater. Process. Technol. 2003; 140:318-325.

[14] Gang LI, Wanshengt ZHAO, Fuqiang HU and Zhang Y. Development and application of a prototype micro edm machine. International Technology and Innovation Conference 2006; 14-18.

[15] Chow HM, Yan BH and Huang FY. Micro slit machining using electro-discharge machining with a modified rotary disk electrode (RDE). Journal of Materials Processing Technology 1999; 91:161-166.

[16] Raju L, Sakthi SV, Somashekhar SH and Singaperumal M. Effect of Process Parameters on Quality of Micro Holes Machined on Copper Plate using Developed μ-EDM Setup. Applied Mechanics and Materials 2014; 592-594: 229-233.

[17] Leera R and Somashekhar SH. Study of micro channels machined on copper plates using micro-electro discharge machining process. Proceedings of the International Conference on Materials, Design and Manufacturing Process ICMDM ’16; 5070, 605-609.

[18] Leera R and Somashekhar SH. Study of micro channels machined on copper plates using micro-electro discharge.machining process. Proceedings of the International Conference on Materials, Design and Manufacturing Process ICMDM ’16; 5070, 605-609.

[19] Tiwary AP, Pradhan BB and Bhattacharyya B. Study on the influence of micro-EDM process parameters during machining of Ti– 6Al–4V superalloy. Int J Adv Manuf Technol 2015; 76:151-160.

[20] Meena VK and Azad MS. Grey Relational Analysis of Micro-EDM Machining of Ti-6Al-4V Alloy, Materials and Manufacturing Processes. 2012; 27: 973-977.

[21] Lin YC, Tsao CC, Hsu CY, Hung SK and Wen DC. Evaluation of the characteristics of the microelectrical discharge machining process using response surface methodology based on the central composite design. Int J Adv Manuf Technol. 2012; 62:1013-1023.

[22] Pandey AK, Tiwari K and Dubey AK. Optimization of the Process Parameters in Micro-Electric Discharge Machining Using Response Surface Methodology and Genetic Algorithm. International Journal of Scientific and Research Publications 2014; 4: Issue 9.

[23] Natarajan N and Suresh P. Experimental investigations on the microhole machining of 304 stainless steel by micro-EDM process using RC-type pulse generator. Int J Adv Manuf Technol. 2015; 77:1741-1750.

[24] Liu HS, Yan BH, Huang FY and Qiu KH. A study on the characterization of high nickel alloy micro-holes using microEDM and their application, Journal of Materials Processing Technology 2005; 169: 418-426.

[25] Hyun-Seok TAK, Chang-Seung HA, Dong-Hyun KIM, Ho-Jun LEE, Hae-June LEE and Myung-Chang Kang. Comparative study on discharge conditions in micro-hole electrical discharge machining of tungsten carbide (WC-Co) material, Transactions of non-ferrous materials Society of China 2009;19 s114-s118.

[26] Jahan MP, Wong YS and Rahman M. A study on the quality micro-hole machining of tungsten carbide by micro-EDM process using transistor and RC-type pulse generator; Journal of materials processing technology 2009; 209:1706-1716.

[27] Ali MY. Fabrication of microfluidic channel using micro end milling and micro electrical discharge milling. International Journal of Mechanical and Materials Engineering (IJMME) 2009; 4 : 1, 93-97.

[28] Maity KP and Singh RK. An optimisation of micro-EDM operation for fabrication of micro-hole. Int J Adv Manuf Technol 2012; 61:1221-1229.

[29] Prihandana GS, Mahardika M., Hamdi M., Wong YS and Mitsui K. Effect of micro-powder suspension and ultrasonic vibration of dielectric fluid in micro-processes-Taguchi approach. International Journal of Machine Tools & Manufacture 2009; 49: 1035-1041.

[30] Pradhan BB and Bhattacharya B. Improvement in microhole machining accuracy by polarity changing technique for microelectrode discharge machining on Ti-6Al-4V. Proc. IMechE Part B: J. Engineering Manufacture 2008; 222: 163-173.

[31] Opoz TT , Ekmekci B and Erden A. An Experimental Study on the Geometry of Microholes in Microelectric Discharge Machining. Materials and Manufacturing Processes 2009; 24: 1236-1241.

[32] Han F, Wachi S and Kunieda M. Improvement of machining characteristics of micro-EDM using transistor type isopulse generator and servo feed control. Precis. Eng. 2004; 28: 378-385.

[33] Han F, Chen L and Yu DW. Basic study on pulse generator for micro-EDM. The International Journal of Advanced Manufacturing Technology 2007; 33: 474-479.

[34] Mahendran S, Fazli Ismail and S. Thinesh Chander. Development of Micro EDM with Directly Mounted APA 400MML Actuator as Tool Feed Mechanism. Advanced Materials Research 2011; 314-316: 1811-1817.

[35] Li Y, Guo M, Zhou Z and Hu M. Micro electro discharge machine with an inchworm type of micro feed mechanism. Precision engineering 2002; 26: 7-14.

[36] Natarajan N and Arunachalam RM. Optimization of micro-EDM with multiple performance characteristics using Taguchi method and Grey relational analysis. Journal of Scientific and Industrial Research 2011; 70: 500-505.

[37] Mehfuz R and Ali MY. Investigation of machining parameters for the multiple-response optimization of micro electrodischarge milling. Int J Adv Manuf Technol. 2009; 43:264-275.

[38] RajurkarKPandYuZY.Micro-EDMcanproducemicroparts.ManufEng2000;11:68-75

[39] Yeo SH, Murali M and Cheah HT. Magnetic field assisted micro electro-discharge machining. J. Micromech. Microeng.2004; 14, 1526-1529

[40] Ekmekci B, Sayar A, Opoz TT and Erden A. Geometry and surface damage in micro electrical discharge machining of micro-holes. J.Micromech. Microeng. 2009; 19-105030 (16pp).

[41] Murali M and Yeo SH. Rapid biocompatible micro device fabrication by micro-electro discharging. Biomedical Devices 2004; 6:1; 41-45.

[42] Hung JC, Yang TC and Li KC. Studies on the fabrication of metallic bipolar plates—Using micro electrical discharge machining milling. Journal of Power Sources196 2011; 2070-2074.

[43] Hung JC, Chang DH and Chuang Y. The fabrication of high-aspect-ratio micro-flow channels on metallic bipolar plates using die- sinking micro-electrical discharge machining. Journal of Power Sources 2012; 198 : 158-163.

[44] Oscar Chaídes, Horacio Ahuett-Garza and Allen Y Yi. Implementation of a microchannel manufacturing system based on micro- Electro Discharge Machining. Ingeniería mecánica tecnología y desarrollo 2014, Vol. 4 : 6 , 229-238.

[45] Schubert A, Zeidler H, Hahn M, Hackert-Oschätzchen M and Schneider J. Micro-EDM milling of electrically nonconducting zirconia ceramics. Procedia CIRP 2013, 6: 297-302.

[46] Tong H, Li Y and Wang Y. Experimental research on vibration assisted EDM of micro-structures with non-circular cross-section. Journal of materials processing technology 2008; 208: 289-298.

[47] Oliaei SNB, Özdemir C and Karpat Y. Fabrication of Micro Ball End Mills Using Micro Electro Discharge Machining. 7th International Conference and Exhibition on Design and Production of MACHINES and DIES/MOLDS 2013; 20-23.

[48] Murali MS and Yeo SH. Process simulation and residual stress estimation of micro electric discharge machining using finite element method. J Appl Phys 2005; 44(7A):5254–526.

[49] Dhanik S, Joshi SS, Ramakrishnan N and Apte PR, Evolution of EDM process modeling and development towards the modelling of micro EDM process. Int J Manuf Technol Manag 2005; 7:157-180.

[50] Sarikavak Y and Cogun C. Single discharge thermo-electrical modeling of micromachining mechanism in electric discharge machining. Journal of Mechanical Science and Technology 2012; 26 (5): 1591-1597.

[51] Wang YK, Xie BC, Wang ZL and Peng ZL. Micro EDM deposition in air by single discharge thermo simulation. Transcations Non Ferrous Metals Society of China 2011; 21: 450-455.

[52] Tan PC and Yeo SH. Modelling of overlapping craters in micro-electrical discharge machining. J. Phys. D: Appl. Phys.2008; 41, 205302 (12pp).

[53] Tan PC and Yeo SH. Modeling of Recast Layer in Micro-Electrical Discharge Machining. Journal of Manufacturing Science and Engineering 2010, 132: 031001-1.

[54] Somashekhar KP, Panda S, Mathew J and Ramachandran N. Numerical simulation of micro-EDM model. Int J Adv Manuf Technol 2015; 76: 83-90.

[55] Pradhan BB and Bhattacharya B. Modelling of micro-electro discharge machining during machining of titanium alloy Ti–6Al–4V using response surface methodology and artificial neural network algorithm. Proceedings of the Institution of Mechanical Engineers, Part B: Journal of Engineering Manufacture 2009; 223: 683-693.

[56] Allen DM and Lecheheb A. Micro electro-discharge machining of ink jet nozzles: optimum selection of material and machining parameters. Journal of Materials Processing Technology 1996; 58:53- 66.

[57] Tong H, Li Y, Zhang L and Li B. Mechanism design and process control of micro EDM for drilling spray holes of diesel injector nozzles. Precision Engineering 2013; 37: 213-221.

[58] Sahu RK, Somashekhar SH, Manivannan PV and Singaperumal M. Generation and Characterization of Copper Nanoparticles Using Micro-Electrical Discharge Machining. Materials and Manufacturing Processes 2014; 29: 477-486.

[59] SahuRK,SomashekharSHandManivannanPV.Ultrasonictechniqueforconcentrationcharacterization ofcoppernanofluids synthesized using -EDM: A novel experimental approach. Powder Technology 2015; 284: 429-436.

[60] Liu K, Lauwers B and Reynaerts D. Process capabilities of Micro-EDM and its applications. Int J Adv Manuf Technol 2010; 47:11-19.

View publication stats

Journal for Re Attach Therapy and Developmental Diversities
eISSN: 2589-7799
2023 May; 6 (5s): 524-531

A Study Exploring the Psychological Perspective of Indian Managers on Employing Neurodiverse Talent.

[1]Elixir Sagar, [2]Dr. Shikha N. Khera, [3]Dr. Naval Garg
[1]Research Scholar, Delhi Technological University, Rohini, New Delhi
[2]Assistant Professor, Delhi Technological University, Rohini, New Delhi
[3]Assistant Professor,USME Delhi Technological University(East Campus),New Delhi

Received: 20- March -2023
Revised: 15- April -2023
Accepted:21-May-2023

Abstract

Introduction: This study explores the psyche of Indian managers when faced with the prospect of hiring a neurodivergent employee in an Indian business organization. Ten Indian managers were interviewed and thematic analysis was used to extract different themes and subthemes from the collected data. Two main themes comprising of several subthemes emerged from the collected data. The first theme was 'neurodiversity awareness among Indian managers'. It includes two subthemes: a) little awareness and unfavourable attitude; b) Apprehension regarding competence of neurodiverse employees. The second theme highlights readiness of Indian managers to employ neurodiverse people in their organizations. Subthemes included are a) reasonable workplace accommodations; b) legal aspect of employing neurodiverse individuals; c) fear of ridicule; d) resistance from neurotypical employees.

Objectives: The principle objective of the study was to understand Indian managers perspectives on hiring neurodiverse employees and their apprehensions regarding the same.

Methods: Semi structured interview questionnaires were prepared based on comprehensive review of literature, consultation with neurodiverse individuals and social workers involved in aiding neurodiverse employees to get gainfully employed. Thereafter thematic analysis based on Braun and clarkes(2006) approach to qualitative thematic analysis was deployed to analyse the data.

Results: Two main themes comprising of several subthemes emerged from the collected data. The first theme was 'neurodiversity awareness among Indian managers'. It includes two subthemes: a) little awareness and unfavourable attitude; b) Apprehension regarding competence of neurodiverse employees. The second theme highlights readiness of Indian managers to employ neurodiverse people in their organizations. Subthemes included are a) reasonable workplace accommodations; b) legal aspect of employing neurodiverse individuals; c) fear of ridicule; d) resistance from neurotypical employees.

Conclusions: The results have implications for Indian organizations looking to employ neurodiverse talent. Indian managers and employees must be made aware of neurodiversity through organization wide initiative like seminars, lectures and so on,Team building and sensitivity training exercises must be performed to encourage empathy towards neurodiverse individuals. Future researches can look into providing workplace accommodations to neurodiverse employs, employing neurodiverse women in Indian organizations.

Keywords: Neurodiverse talent, managers, India, disability, Managerial psychology

1.Introduction

Neurodiversity is loosely defined as a naturally occurring variation in neurological wiring in human beings. Neurodivergent individuals lie at the edges of the bell curve as far as neurological functioning is concerned. The term neuroatypical is often used interchangeably with the term neurodivergent to describe individuals with people on the autism spectrum (ASD), those with attention-deficit/hyperactivity disorder and dyslexia. As opposed to this, neurotypical is a person of typical and normal cognitive, developmental and intellectual capabilities (Brusie, 2017). Since, neurodiverse people has different set of neurological wiring than neurotypical people, they have a different approach, style, and perception of a situation. They have a unique way of thinking and savant abilities with systems like computer programming, software testing and mathematics. Also, they are blessed with high levels of creative talents, indifference to peer pressure to conform to social norms that are not in tune with their own personal idea of happiness, musical abilities, above-average levels of attention to detail, strong visual-spatial skills, and remarkable abilities in art and design (Austin & Pisano, 2017). Yet despite having off the charts abilities in some aspects of their lives, these neurodiverse individuals often struggle to find

and sustain a job (Pesce, 2019) due to their socially ineptitude, their sensory overload issues and an inability to thrive in an unsuitable work environment that is designed keeping in mind neurotypical employees (Bellini, 2006).

The neurodiversity approach to the evolution of the human mind views neurological developments that have previously been considered as an anomaly or as a diagnosable disorder, such as autism or dyslexia (Jaarsma &Welin, 2012). People who stand by this perspective argue that many neurodiverse individuals are talented and are capable of functioning productively in an organization. But they are not able to get work opportunities that match their talents (Robison, 2013). The main issue is conventional hiring methods that have a very narrow definition of talent, and mostly rely on job interviews, which are biased against people with atypical manners of interaction (Baldwin and Costley, 2015; Eckerd, 2020). Hence diversity is not the problem. And real challenge lies with proper management of diversity in an organizational context (Härtel & Fujimoto, 2000). Despite the slow acceptance of this alternative inclusive view of diversity in countries like India, its validity is being established with major companies like Microsoft, JP Morgan and chase, Ford and DXC. These companies have started pro-neurodiverse employment initiatives like placing less emphasis on interviews in favor of inclusive recruiting practices that have lead to greater success in hiring neurodiverse individuals.

Researchers, practitioners, and neurodiverse activists have highlights a dearth of studies in the domain of the employment of neurodiverse individuals in modern workplaces in countries like India (Chaudary et al., 2008; Barua, 2007; Sharma et al., 2013). Although research exploring experiences of individuals who are in the minority group with respect to their race, gender, sexual orientation has only grown in the recent years, scant research exists to study the workplace experiences of Indian individuals who are minorities due to their variant neurology. Even less research exists to explore employer perspectives on employing neurodiverse employees at the workplace. Although in recent years a few big MNC's like SAP, Microsoft, Google, JP Morgan Chase, Hewlett Packard etc have started recruiting neurodiverse workers owing to their unique abilities in problem solving, software testing and other domains (Austin & Pisano, 2017; Moran, 2019). Yet, little research exists exploring the perspectives of Indian managers on employing neurodiverse individuals. Through this research, we study Indian managers' when faced with the prospect of employing neurodiverse talent.

In the recent times, researchers have started using the term autism spectrum condition to paint a holistic picture of heterogeneous autistic traits (Krzeminska, Austin, Bruyere, & Hedley, 2019; Haywards, Mcvillya, & Stokes, 2018). It suggests that autistics are "wired" differently in a way they process information differently rather than having an illness to be cured. They opined that the term disorder is correlated to disability which has a negative connotation (Lai & Baron-Cohen, 2015). The neurodiversity movement has shifted the focus from viewing autism as a pathological condition to one that doesn't need a cure. Proponents of neurodiversity movement feel that there is no right or wrong way to function in society. The "right" way is just a social construction and is in no way more correct than thinking there is a "right" gender. Thus the main issue with autism is not with autism but rather with the lack of awareness, acceptance and accommodations to how a neurodiverse individual functions, that causes unwarranted stress and rejection for neurodiverse individuals. As opposed to neurodiverse, a "neurotypical" person is one with a neurocognitive style considered as "normal." and hence accepted by society. Neurodiversity movement opines that there are various neurological profiles (like Autism, Dyslexia etc) as well as "normal" or "neurotypical." The "neurodiversity movement" is a social justice movement for and by autistic individuals. Through this movement, they aim to get the same level of inclusion and respect as neurotypicals. Additionally, understanding autism requires listening to the experiences of autistic individuals, rather than those of neurotypical "experts" who have not lived through the autistic experience.

One of the most notable studies on employing a neurodiverse workforce was conducted by Rebholz (2012). The findings of the study suggest that the academic success of an autistic individual was tied with the level of stability of their childhood home environment. It also reported that the autistic workers found it difficult to maintain interpersonal relationships. Autistic employees gauged their level of success in terms of intellectual challenges, achievements and recognition received due to the achievement (Rebholz, 2012). The study also found that autistic employees might be ill adapted to solve open ended problems because of lack of context and difficulties in generalizing, thus, increasing their chance of failure. This may make their manager wrongly believe that the autistic worker is less intellectually competent than his peers (Rebholz, 2012). Also, all individuals on the spectrum were found to have sensory issues such as heightened sensitivity to certain smells, bright lights, etc. It leads to physical and mental anguish among autistic people, which decreases their productivity. Most individuals on the spectrum may make constant social blunders in meetings and their social interactions with peers due to their overtly blunt and honest comments. They also express their inability to understand context and sub context. It may lead to a label of "difficult" by their peers.

They also fail to understand contextual cues in communication (Geurts et al., 2019). Most autistic individuals display varied levels of difficulty in understanding non-literal uses of language like sarcasm, irony, and metaphor (Austin & Pisano, 2017). While this in no way implies that an autistic individual cannot think in abstract; it merely implies that they take language literally, to mean exactly what has been said (Annabi, Sunderesan, & Zolyomi, 2017). Confusion regarding non-literal language leads to them committing a social faux pas. Autistic individuals have deficits understanding another person's thought process or cognitive empathy but not necessarily emotional empathy (Harmsen, 2019). It may lead autistic individuals to become emotionally overwhelmed by cognitive, emotional, behavioral, or sensory demands. This may make them "shut down", withdraw, or have an emotional outburst called a "meltdown." To a neurotypical, these outbursts may seem to happen "out of the blue" but it is not usually the case. They are preceded by extended periods of sensory overload (Eckerd, 2020). Autistic individuals experience extreme levels of distress even when asked to accommodate small changes in their daily routine and neurotypical expectation of accepting a different way to solve a problem.

Despite the above shortcomings, there are countless benefits to hiring neurodiverse talent. Rebholz (2012) suggested that autistic employees are far more loyal to their company and specific manager than people not on the spectrum. Additionally, it is observed that neurodiverse employees are blessed with inherent abilities to observed and analyze minute and complex information and data. Autistic employee may derive a workable solution through analyzing such information, which may seem insignificant or useless to neurotypical people Rebholz (2012) also pointed out that they persevere on difficult assignments long after their peers have given up, due to their need to demonstrate their intellectual capability and their need to help people in their workplace teams. Also, they contribute more to a company's finances than people not on the autistic spectrum, because they typically do not spend time socializing (Rebholz, 2012).

Powers (2018) stresses upon the fact that attracting and supporting neurodiverse talent requires that companies overcome their unconscious bias. It requires work in three specific areas i.e., different hiring process, workplace accommodation for autistic employees, and anti-bullying policies. Firstly, modern firms are required to make necessary and vital changes in their recruitment and selection process. Normally used hiring processes could gauge into performance and potential of neurotypical people. They fail to judge special abilities and talent of autistic people. Experts suggest a pragmatic change from resumes and interviews to task-based hiring processes. Work sampling, vestibule training, and practical assignment are ideal way to gauge into their competency level (Delaney, 2019). For inference, at Cockroach labs, autistics candidates are given creative tasks like take home projects, presentations, case studies, etc, that allows the candidate to show what they are abilities and talent. Additionally, focus is on open source interviews, wherein , candidate is aware of the general outline of the interview process and certain "curveball" questions are used to differentiate candidates who think on their feet from the average one (Delaney, 2019).

The major issues of workplace accommodation emerges post recruitment of a neurodiverse worker. These impending challenges include maximization of the performance and potential of autistic employee. Another emerging issue arises with retention of neurodiverse employees. Researchers suggest specific autistic-friendly adjustments to accommodate their concerns (Waisman-Nitzan et al., 2018). They also reported that employers were ready to consider providing workplace accommodations to the workers as long as it was economical and could also improve the productivity levels of neurodiverse employees. Vogus and Taylor (2018) listed desirable changes to accommodate autistic workplace. A workplace climate must appreciate and promote diversity. It allows respect and mutual understanding of workers of different community, race, colour, caste, region, and religion. Although modern workplaces have started to appreciate physical and geographically differences, the variations-based on different neurological wiring are yet to be acknowledged. Another desirable workplace changes in favour of accommodation of neurodiverse employees is ensuring psychological safety climate (Vogus and Taylor, 2018). Such, a climate promotes psychological well-being and capital of the employees, which include hope, optimism, self-efficacy, and resilience. At Ultranauts, autistic workers are allowed a flexible schedule, remote work, doing away of personal meetings in lieu of slack (an instant messaging app), having a concrete agenda for each meeting, doing away with open plan offices, doing away with interviews, and providing a career alternative to promotion to the post of a manager (Doyle, 2019).

Although workplace accommodation, anti bullying/anti harassment policies are much needed to sustain autistic workers. It is far more important to put formal and informal structures in place at work that prevent bullying of neurodiverse individuals particularly for asking for workplace accommodations, their social ineptitude, their shyness and inability to deal with office politics (Mellifont, 2019). It is also observed that neurodiverse people hesitate in reporting workplace bullying incidences. They find no benefit to approach seniors to complaint

against bullies, as neurotypical senior fails to recognize the uncivil behaviour of neurotypical employees. They evaluate such behaviour as normal and part-and-parcel of workplace life. In some cases, neurodiverse workers experience victimization or harassment after reporting any unprofessional act of neurotypical colleague. The need of the hour is to educate and aware employees regarding the plight, conditions, and special requirements of neurodiverse employees. Legal guidelines are already in place in certain countries but they are underutilized in reality (Mellifont, 2019).

Above-discussed literature suggests a growing need to explore the intricacies of employment of autistic employee especially in country like India, wherein autism is still considered as a social stigma. Researchers and practitioners have advocated studies from different point of views, i.e., from autistics workers, managers, colleagues, and customers' perspectives. This paper investigates Indian managers' perspective on diverse issues related to employment of neurodiverse employees.

2.Objective

The main objective of the study was to understand Indian managers psyche when faced with the prospective of employing and managing neurodiverse talent. As a subset of this objective we aimed to identify the source of their apprehensions towards employing a neurodiverse worker and how they can become more receptive of employing neurodiverse talent.

3.Methods

Participants

A total of 10 Indian managers participated in the research. Recruitment took place in Delhi and Bombay. Relevant snippets of the interviews were included as quotations in the 'results' section. To preserve the identity of the study participants, each participant was given a pseudonym consisting of an alphabet and a number. Participants were addressed using this pseudonym throughout the study.

Interview protocol

Study participants took part in a semi structured interview lasting between forty five minutes to an hour. Interview questions centered on neurotypical employers awareness of neuroatypicality as a form of diversity, ease of employing neurodiverse talent, readiness of Indian managers to provide workplace accommodations to neurodiverse employees.

Data analysis

The data from semi structured interviews has been analyzed thematically based on the work of Braun and Clarke (2006). An inductive approach has been adopted to analyze data. Data has been experientially oriented and the theoretical perspective adopted has been a critical realist one (Braun & Clarke, 2012), to systematically examine Indian managers subjective accounts of their experiences with neurodiverse employees. Direct quotes from the participants were used in illustrating the themes that had been identified. Authors read and re-read the transcripts of interviews, which helped in observation of recurring themes in the data. A coding framework was developed and used to code the data. Finally, entire transcripts was read, observed and categorized in different themes and subthemes.

4.Results

Two main themes emerged from the data. 1) Neurodiversity awareness among Indian managers , dealt with Indian managers perception of and (lack of)awareness of Neurodivergence as a phenomenon in human beings. Subthemes included a)Indian managers attitude towards ASD and other neurodivergent conditions b)Indian managers perceptions regarding competence of neurodiverse employees 2) Readiness to employ autistic talent dealt with Indian managers willingness to employ neurodiverse talent. Subthemes included a) reasonable workplace accommodations b)Legal aspect of employing neurodiverse individuals c)Fear of ridicule d)Resistance from neurotypical employees.

Theme 1: Neurodiversity awareness among Indian managers

Majority of Indian managers interviewed reported having little to no awareness about the term neurodiverse, although when they were illuminated about its link with autism spectrum disorders, ADHD and dyslexia quite a few of them reported being aware of it. However, awareness of neurodiversity was still only limited to examples of neurodivergent individuals depicted in mainstream Indian cinema.

Subtheme 1: Little awareness and unfavourable attitude

"Oh you mean someone like Ishann Awasthi in Taare Zameen par... I do know a few people who have children like that. I imagine it would be quite tough to bring them up. I wouldn't wish such an experience on my worst enemy" P07

"India is no country for the disabled. Resources are few, population density is too much." P02

Subtheme 2: Apprehension regarding competence of neurodiverse employees

The interviewers made the managers aware of the unique strengths and talents of neurodiverse individuals yet they still expressed disbelief at the competence of neurodiverse employees.

"Well you say they're great at software testing …I'd still have my doubts about their abilities until I get to see it for myself" P01

P02 who was a manager in a software company revealed that he had met a few employee who fit the definition of ASD and while he acknowledged that they were skilled at their jobs, he expressed apprehensions about their ability to be team players and fit in with their neurotypical colleagues.

"Yeah I have a guy like that in my team…pretty brilliant chap …spots bugs in codes that would go unnoticed by others, yet he is quite eccentric, not very sociable , always twiddling his thumbs or playing with his shirt buttons. Not very presentable too, definitely not a team player. I don't see him moving up the ladder anytime soon"P02

"My nephew is mentally disabled or autistic …whatever you call it. While he is good at numbers and as much as I would like to help him and other kids like him, we simply don't have the requisite resources or awareness at this point to employ them with other "normal" employees."P05

Theme 2: Apprehension regarding competence of neurodiverse employees

Subtheme 1: Reasonable workplace accommodations

This subtheme dealt with Indian manager's readiness to provide workplace accommodations to neurodiverse employees. The employers were ready to provide workplace accommodations to neurodiverse workers as long as it did not involve commitment of extra resources and did not disturb the existing status quo in the organization.

"Allowing him (neurodiverse employee) to work from home some days of the week is possible..can be done but we simply don't have the infrastructure to give him a separate corner office…besides this might infuriate other employees who might see this as preferential treatment" P01

Subtheme 2: Legal aspect of employing neurodiverse individuals

All managers interviewed stated being aware of the persons with disability act in India but only a few were aware of the intricacies of the act. They further expressed apprehensions in employing neurodiverse talent for fear of any legal repercussions.
"Well…as much as I would like to employ a person like that …I fear not being able to provide him the environment in which he can thrive and then…what if he complains against me or the company…it could become a human rights issue and taint our image"P08

Subtheme 3: Fear of ridicule
Owing to the deep stigma associated with autism and other mental disorders in India , managers expressed concern over being the subject of ridicule for employing autistic talent.

"My friends would definitely laugh at me behind my back…they might say stuff like…couldn't you get anyone better to do the job"P10

"It might make our organization seem incompetent…we are answerable to our stakeholders…employing them seems good from CSR perspective …but we have to meet our targets at the end of the day , we can't risk facing embarrassment because of them" P08

Subtheme 4: Fear of resistance from neurotypical employees

Indian managers expressed apprehensions over neurodiverse individual's ability to blend into the company culture and bond with their neurotypical peers.
"Well like I said…we can't give preferential treatment to some employs…especially when they look "normal" on the surface. Other employees may not understand …they would face problems fitting in with the team"P01

"He might get covertly bullied or boycotted by his colleagues …we won't be able to help him in such a situation" P06

5.Discussion

Data collected through interviews with ten Indian managers helped shed light on the neurodiversity awareness and the readiness to employ neurodiverse talent among Indian managers. Two main themes emerged. Theme 1 deals with neurodiversity awareness among Indian managers. It highlights an important issue of lack of awareness regarding condition, status, special requirement, workplace accommodation facilities, and bullying-related issues of autistic employees. Subthemes dealt with Indian mangers unfavourable attitude towards neurodivergent individuals and Indian managers' apprehension regarding competence of neurodiverse individuals. It was found that majority of Indian managers interviewed lacked the requisite awareness about autism and related mental disorders and also held a negative perception towards the competence level of neurodiverse individuals. The first theme and its associated subthemes highlight important issues of lack of awareness, unfavourable attitude, and managers' apprehension towards competency of autistic employees. It reflects a need to acclimatize and customize the managers and employees towards different set of 'wiring' of the neurodiverse workers. The budding managers during their MBA or other management courses must be made aware of autistic employees and their special requirements.
Theme 2 deals with Indian managers' apprehension towards employment of neurodiverse talent. Subthemes deals with Indian managers readiness to provide reasonable workplace accommodations to autistic individuals, legal aspects of employing neurodiverse individuals, fear of ridicule and fear of resistance form neurotypical colleagues, it was found that majority of Indian managers interviewed were open to providing low investment workplace accommodations like schedule flexibility and working from home which did not disturb the status quo of the organization and did not require extensive commitment of resources. Indian managers also expressed apprehensions about the legal aspect of employing neurodiverse individuals as they felt that any perceived misdemeanor towards neurodiverse employees on their part would open the organization up to public scrutiny.
This is the first in depth study to examine Indian manager's attitude towards employing neurodiverse individuals in the context of Indian organizations. Due to the Covid -19 lockdown , the data collection for this study took place through online interviews conducted over Google meet, Zoom, E-mail and instant messaging yet, this helped us collect data from geographically diverse locations within India.
The results have implications for Indian organizations looking to employ neurodiverse talent. Indian managers and employees must be made aware of neurodiversity through organization wide initiative like seminars. Team building and sensitivity training exercises must be performed to encourage empathy towards neurodiverse individuals. Future researches can look into providing workplace accommodations to neurodiverse employs, employing neurodiverse women in Indian organizations.

References

1. Akundi, S. (2020, March 16). Retrieved January 20, 2021, from www.thehindu.com: https://www.thehindu.com/sci-tech/health/do-indian-workplaces-need-to-be-more-neurodiverse/article31083213.ece
2. Allison, C., Auyeung, B., & Baron-Cohen, S. (2012). Toward Brief "Red Flags" for Autism Screening: The Short Autism Spectrum Quotient and the Short Quantitative Checklist in 1,000 Cases and 3,000 Controls. Journal Of The American Academy Of Child &Amp; Adolescent Psychiatry, 51(2), 202-212.e7. https://doi.org/10.1016/j.jaac.2011.11.003

3. Austin, R. D., & Pisano, G. P. (2017, May-June). Neurodiversity as a competitive advantage . Harvard Business Review .
4. Bannerjee, G. (1975). Another calendar calculator. Indian Journal of Psychiatry, 17, 144-146.
5. Barker, C., Elliott, R., & Pistrang, N. (2016). Research methods in clinical psychology. John Wiley & Sons.
6. Barua, M., & Daley, T. C. (n.d.). Retrieved november 24, 2020, from www.rehabcouncil.nic.in: http://www.rehabcouncil.nic.in/writereaddata/autism.pdf
7. Bruyere, S., Sonnenfeld, J., Cunningham, T., Giannantonio, C., Griffiths, A., & Hamdani, M. et al. (2019). Autism in the Inclusive Organization: Implications for Research and Practice. Academy Of Management Proceedings, 2019(1), 14216. https://doi.org/10.5465/ambpp.2019.14216symposium
8. Buescher, A., Cidav, Z., Knapp, M., & Mandell, D. (2014). Costs of Autism Spectrum Disorders in the United Kingdom and the United States. JAMA Pediatrics, 168(8), 721. https://doi.org/10.1001/jamapediatrics.2014.210
9. Baldwin, S., & Costley, D. (2015). The experiences and needs of female adults with high-functioning autism spectrum disorder. Autism, 20(4), 483-495. https://doi.org/10.1177/1362361315590805
10. Bargiela, S., Steward, R., & Mandy, W. (2016). The Experiences of Late-diagnosed Women with Autism Spectrum Conditions: An Investigation of the Female Autism Phenotype. Journal Of Autism And Developmental Disorders, 46(10), 3281-3294. https://doi.org/10.1007/s10803-016-2872-8
11. Barua, M. (2007). Lessons from Neeraj, My Son with Autism. Journal Of Religion, Disability &Amp; Health, 11(2), 29-40. https://doi.org/10.1300/j095v11n02_05
12. Cassidy, S., Robertson, A., Townsend, E., O'Connor, R., & Rodgers, J. (2020). Advancing Our Understanding of Self-harm, Suicidal Thoughts and Behaviours in Autism. Journal Of Autism And Developmental Disorders, 50(10), 3445-3449. https://doi.org/10.1007/s10803-020-04643-9
13. Chaudhary, D., Siitholey, P., Aggarwal, V., Gupta, N., & Kumar, P. (2008). Adult manifestations of childhood autism. Delhi psychiatry journal .
14. Chen, M., Wei, H., Chen, L., Su, T., Bai, Y., & Hsu, J. et al. (2015). Autistic spectrum disorder, attention deficit hyperactivity disorder, and psychiatric comorbidities: A nationwide study. Research In Autism Spectrum Disorders, 10, 1-6. https://doi.org/10.1016/j.rasd.2014.10.014
15. Couderc, S., Cousson-Gélie, F., Pernon, E., Porro, B., Miot, S., & Baghdadli, A. (2021). Burnout among direct support workers of adults with autism spectrum disorder and intellectual disability. Scandinavian Journal Of Caring Sciences. https://doi.org/10.1111/scs.13008
16. Doyle, N. (2019). Making the invisible visible : supporting neurodiversity at the workplace. personneltoday .
17. Goel, S. (2018). Third generation sexism in workplaces: Evidence from India. Asian Journal Of Women's Studies, 24(3), 368-387. https://doi.org/10.1080/12259276.2018.1496616
18. Hedley, D., Uljarević, M., Bury, S., & Dissanayake, C. (2019). Predictors of mental health and well-being in employed adults with autism spectrum disorder at 12-month follow-up. Autism Research, 12(3), 482-494. https://doi.org/10.1002/aur.2064
19. Hurlbutt, K., & Chalmers, L. (2004). Employment and Adults With Asperger Syndrome. Focuson Autism and Other Developmental Disabilities, 19(4), 215–222. https://doi.org/10.1177/10883576040190040301
20. Jacob, A., Scott, M., Falkmer, M., & Falkmer, T. (2015). The Costs and Benefits of Employing an Adult with Autism Spectrum Disorder: A Systematic Review. PLOS ONE, 10(10), e0139896. https://doi.org/10.1371/journal.pone.0139896
21. Kamerāde, D., Wang, S., Burchell, B., Balderson, S., & Coutts, A. (2019). A shorter working week for everyone: How much paid work is needed for mental health and well-being?. Social Science &Amp; Medicine, 241, 112353. https://doi.org/10.1016/j.socscimed.2019.06.006
22. Kemper, T., & Bauman, M. (1998). Neuropathology of Infantile Autism. Journal Of Neuropathology And Experimental Neurology, 57(7), 645-652. https://doi.org/10.1097/00005072-199807000-00001
23. Kendall, H. (2014). Autism Spectrum Disorder in an Indian Context: Impact of Socioeconomic Factors on the Experiences of Individuals with ASD and Their Families. SIT Graduate Institute/SIT Study Abroad SIT Digital Collections.
24. Knapp, M., Romeo, R., & Beecham, J. (2009). Economic cost of autism in the UK. Autism, 13(3), 317-336. https://doi.org/10.1177/1362361309104246

25. Krauss, M. W., Seltzer, M. M., & Jacobson, H. T. (2005). Adults with autism living at home orin non-family settings: positive and negative aspects of residential status. Journal of Intellectual Disability Research, 49(2), 111–124. https://doi.org/10.1111/j.1365-2788.2004.00599.x
26. Krzeminska, A., Austin, R. D., Bruyère, S. M., & Hedley, D. (2019). The advantages andchallenges of neurodiversity employment in organizations. Journal of Management &Organization, 25(04), 453–463. https://doi.org/10.1017/jmo.2019.58
27. Lai, M. C., & Baron-Cohen, S. (2015). Identifying the lost generation of adults with autismspectrum conditions. The Lancet Psychiatry, 2(11), 1013–1027. https://doi.org/10.1016/s22150366(15)00277-1
28. Lawer, L., Brusilovskiy, E., Salzer, M., & Mandell, D. (2008). Use of Vocational Rehabilitative Services Among Adults with Autism. Journal Of Autism And Developmental Disorders, 39(3), 487-494. https://doi.org/10.1007/s10803-008-0649-4
29. Markram, H. (2007). The intense world syndrome – an alternative hypothesis for autism.Frontiers in Neuroscience, 1(1), 77–96. https://doi.org/10.3389/neuro.01.1.1.006.2007
30. Nesbitt, S. (2000). Why and why not? Factors Influencing Employment for Individuals with Asperger Syndrome. Autism, 4(4), 357-369. https://doi.org/10.1177/13623613000040040
31. Oomen, D., Nijhof, A., & Wiersema, J. (2021). The psychological impact of the COVID-19 pandemic on adults with autism: a survey study across three countries. Molecular Autism, 12(1).https://doi.org/10.1186/s13229-021-00424-y
32. Orsmond, G. I., Krauss, M. W., & Seltzer, M. M. (2004). Peer Relationships and Social and Recreational Activities Among Adolescents and Adults with Autism. Journal of Autism and Developmental Disorders, 34(3), 245–256. https://doi.org/10.1023/b:jadd.0000029547.96610.df
33. Pan, P., Bölte, S., Kaur, P., Jamil, S., & Jonsson, U. (2020). Neurological disorders in autism: A systematic review and meta-analysis. Autism, 25(3), 812-830. https://doi.org/10.1177/1362361320951370
34. Patton, E. (2019). Autism, attributions and accommodations. Personnel Review, 48(4), 915-934. https://doi.org/10.1108/pr-04-2018-0116

A Synergistic Framework Leveraging Autoencoders and Generative Adversarial Networks for the Synthesis of Computational Fluid Dynamics Results in Aerofoil Aerodynamics

[1]Tanishk Nandal [2]Vaibhav Fulara, [3]Raj Kumar Singh
[1] Delhi Technological University ,[2] Delhi Technological University [3] Delhi Technological University
[1] tanishknandal_2k19me252@dtu.ac.in,[2] vaibhavfulara_2k19me262@dtu.ac.in, [3]rajkumarsingh@dtu.ac.in

Abstract*— In the realm of computational fluid dynamics (CFD), accurate prediction of aerodynamic behaviour plays a pivotal role in aerofoil design and optimization. This study proposes a novel approach that synergistically combines autoencoders and Generative Adversarial Networks (GANs) for the purpose of generating CFD results. Our innovative framework harnesses the intrinsic capabilities of autoencoders to encode aerofoil geometries into a compressed and informative 20-length vector representation. Subsequently, a conditional GAN network adeptly translates this vector into precise pressure-distribution plots, accounting for fixed wind velocity, angle of attack, and turbulence level specifications. The training process utilizes a meticulously curated dataset acquired from JavaFoil software, encompassing a comprehensive range of aerofoil geometries. The proposed approach exhibits profound potential in reducing the time and costs associated with aerodynamic prediction, enabling efficient evaluation of aerofoil performance. The findings contribute to the advancement of computational techniques in fluid dynamics and pave the way for enhanced design and optimization processes in aerodynamics.

Index Terms— Autoencoders, Computational Fluid Dynamics, Deep learning, Generative Adversarial Networks

I. INTRODUCTION

In aerospace engineering, Computational Fluid Dynamics (CFD) plays a paramount role in predicting the aerodynamic behavior of an aircraft. Traditional CFD approaches involve using wind tunnels and simulation tools to test the aerodynamics of various aerofoils. However, these methods are time-consuming and expensive, making it challenging to perform tests on a large number of aerofoils. Hence, there is a need for faster and more efficient methods to predict aerodynamic performance.

Deep Learning (DL) has recently shown tremendous potential in various applications, including CFD. DL algorithms can learn from a large dataset of aerodynamic simulations to predict the aerodynamic behavior of an aerofoil for different wind velocities, angles of attack, and turbulence levels. However, the prediction accuracies are totally dependent on the quality of training data.

To address this problem, we propose a novel approach that combines an autoencoder and a Generative Adversarial Network (GAN) for the generation of CFD results for a given aerofoil geometry. Our GAN model takes a 20-length vector as input, generated by an autoencoder, designed primarily to encode the aerofoil geometry in a compressed form. The GAN then converts the input vector into an output result pressure-distribution plot for a fixed wind velocity, angle of attack, and turbulence level.

The training data for our model has been acquired from JavaFoil software, which simulates the flow over an aerofoil section using a viscous-inviscid interaction technique. We trained our model on a dataset of 4096 simulations, each with a different aerofoil geometry, out of which 3276 simulation samples are used for training, and the remaining 820 samples are used for validation.

Our model has the potential to significantly reduce the time and cost involved in predicting the aerodynamic performance of an aerofoil. While the traditional CFD approaches can be reserved for later screening of the shortlisted aerofoils, our model can be used for initial shortlisting, thereby reducing the overall testing time and cost. The approach can be extended to other areas of aerospace engineering, such as wing design, propeller design, and flight control systems, to name a few.

Our work highlights the potential of combining ML with CFD to predict the aerodynamic behavior of an aerofoil. This approach provides a faster and more efficient method of predicting aerodynamic performance, which could significantly impact the aerospace industry.

In recent years, the application of machine learning in CFD has garnered significant attention due to its potential to enhance the simulations. Researchers have explored various machine learning techniques to accelerate simulations, reduce computational costs, and improve the accuracy of fluid flow predictions. Ling et al. [1] proposed a deep neural network as an alternative to traditional turbulence models in CFD simulations. By training the network using a Reynolds-averaged Navier-Stokes (RANS) simulations dataset, they achieved notable advancements in turbulence prediction, surpassing the capabilities of conventional RANS models. Kutz et al. [2] introduced machine learning techniques to model fluid flows within a low-dimensional state space. Their method involved combining dynamic mode decomposition with sparse regression to identify the governing equations of fluid dynamics. This approach exhibited promising results in accurately predicting flow behavior and showed potential for reducing the computational burden associated with CFD simulations.

Building upon these ideas, Wang et al. [3] proposed a hybrid approach that combined machine learning algorithms with numerical simulations to model turbulent flow over

aerofoils. By leveraging a convolutional neural network, they successfully learned the intricate features of the flow field and improved the accuracy of numerical simulations. This integration of machine learning and traditional simulation methods showcased enhanced performance in capturing the complex phenomena associated with turbulent flows.

Another study by Wang et al. [4] focused on leveraging machine learning algorithms to optimize the design of microfluidic mixers. Their approach involved employing a genetic algorithm to generate initial design parameters and training a neural network to predict mixer performance. The results indicated a significant improvement over the traditional trial-and-error approach, highlighting the potential of machine learning in enhancing the efficiency and effectiveness of fluid system design.

Exploring alternative avenues, researchers have also delved into generative adversarial networks (GANs) to generate CFD results. Lapeyre et al. [5] proposed employing GANs to generate realistic turbulent flow fields by conditioning the GAN on input parameters such as Reynolds number and pressure gradient. This conditional GAN framework demonstrated the capability to generate highly accurate and realistic flow fields, offering promising possibilities for various CFD applications. Similarly, Jin et al. [6] applied GANs to create the pressure distribution on aerofoils, focusing on parameters such as angle of attack and Mach number. The GAN-based approach successfully generated precise pressure distributions across a wide range of input parameters, highlighting its potential for optimizing aerodynamic design and analysis.

In addition to turbulence modeling and flow field generation, researchers have explored the application of machine learning algorithms for improving the accuracy of turbulence models. Wang et al. [7] proposed a machine learning algorithm to correct errors in RANS turbulence models. By training a neural network to learn the required corrections, they achieved improved accuracy and better agreement with experimental data.

Expanding the scope of machine learning in CFD, Smith et al. [8] investigated machine learning for unmanned aerial vehicle (UAV) aerodynamic performance prediction. Their approach showcased the potential of machine learning in optimizing UAV design and enhancing flight efficiency. Zhang et al. [9] explored the use of deep learning for flow pattern recognition in multiphase flows. Training deep neural networks on large datasets achieved accurate flow pattern identification, contributing to a better understanding and analysis of multiphase flow phenomena.

Chen et al. [10] applied recurrent neural networks (RNNs) for improved turbulence modeling. The sequential nature of RNNs allowed them to capture temporal dependencies in flow data, resulting in enhanced turbulence predictions. Liu et al. [11] focused on combining machine learning and data assimilation techniques for weather forecasting. By assimilating observational data into a machine learning-based weather model, they achieved improved forecasting accuracy, which has important implications for weather-dependent industries and emergency preparedness.

Guo et al. [12] investigated the application of deep reinforcement learning for aerodynamic shape optimization. Their work demonstrated the potential of using reinforcement learning algorithms to autonomously optimize aerodynamic shapes, leading to enhanced performance and efficiency in aerospace engineering.

In another direction, Li et al. [13] explored the use of transfer learning in CFD simulations. By transferring knowledge from pre-trained models to new domains or tasks, they achieved accelerated simulations without sacrificing accuracy, offering a promising avenue for reducing computational costs in CFD. Also, Wang et al. [14] proposed a hybrid approach that integrated physics-based models with machine learning techniques for multiphase flow simulations. By combining the strengths of both systems, they demonstrated improved accuracy and efficiency in simulating complex multiphase flows.

These studies collectively emphasize the significant potential of machine learning in various aspects of CFD, ranging from turbulence modeling and flow pattern recognition to optimization, weather forecasting, and simulation efficiency improvements. By integrating machine learning techniques, researchers continue to pave the way for advancements in CFD, fostering a deeper understanding of fluid dynamics and enabling more efficient and accurate simulations.

II. METHODOLOGY

A. Autoencoders

Autoencoders are neural networks expected to learn a compressed input data representation. These networks chiefly consist of two main parts: an encoder and a decoder. The encoder is fed the input data and produces a compressed representation using the input, often referred to as a "latent code". The decoder then uses this to produce an output that tries to reconstruct the original input data.

Autoencoders are often used for dimensionality reduction, where the high-dimensional input data is reduced to a lower-dimensional representation that still preserves the critical features of the input data. They can also be used for data compression and denoising. The input data is corrupted with noise, and the autoencoder learns to remove the noise to reconstruct the original data.

In recent years, autoencoders have become an essential tool in ML and have been applied to a wide range of applications, such as anomaly detection [15], natural language processing, and image and speech recognition [16]-[17]. Variants of autoencoders, such as denoising [18] and variational autoencoders [19], have also been developed to improve their performance and applicability to various tasks.

In recent years, autoencoders have become an essential tool in ML and have been applied to a wide range of applications, such as anomaly detection [15], natural language processing, and image and speech recognition [16]-[17]. Variants of autoencoders, such as denoising [18] and variational autoencoders [19], have also been developed to improve their performance and applicability to various tasks.

B. Dataset

JavaFoil uses a panel approach to discretize the aerofoil into a sequence of panels and determine the flow field at each panel to solve the potential flow equations. The flow around the aerofoil is computed by superimposing the effects of each panel, which is viewed as a source of possible flow.

Additionally, the approach meets the no-slip boundary requirement at the aerofoil surface. After calculating the flow field, JavaFoil applies the Bernoulli equation to determine the aerofoil surface's pressure coefficient at each location. We sample 4096 aerofoils based on NACA 4-digit profiles by changing the aerofoil geometry parameters to train the proposed model. The thickness t/c ranges from 0.1 to 0.18, with the Camber f/c ranging between 0 to 0.08. The Camber location x_f/c is varied from 0.4 to 0.6. Pressure coefficient C_p field around the aerofoil for the 4096 samples is simulated using Javafoil. The raw geometry image and the CFD results are then used for training.

C. Convolutional Autoencoder

Let x represent a vector of input data in the high-dimensional space X. The encoder function $f(x)$ converts the input value x to a latent representation z with a lower dimension, learning a mapping $f : x \to z$. The decoder function $g(z)$ maps z back to a reconstruction x' in the original high-dimensional space X, mapping $g : z \to x'$. The autoencoder is trained to minimise the reconstruction error, which is commonly expressed as the mean squared error, between the original data x and the reconstructed data x'. A simple representation of an autoencoder is shown in Fig. 1.

The core operation of a convolutional layer is the convolution operation. It involves sliding a filter over the input data and computing the dot product between the filter and the corresponding input region at each position. The kernel acts as a window or template that extracts certain features or characteristics from the input. Given an input image and a kernel, this process generates a feature map, which represents the presence of specific elements or patterns in the input data, given by:

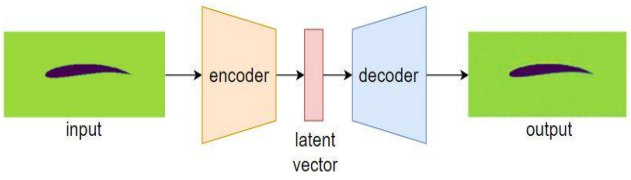

Fig 1: A simple representation of the Autoencoder network

$$F(i,j) = \sum_x \sum_y I(x,y) * K(i-x, j-y) \qquad (1)$$

In our model, the autoencoder is designed to take in a matrix of size $164 \times 364 \times 1$ which is a binary representation of the input geometry. The autoencoder is trained to learn a representation of this geometry as a latent vector of dimension 20. It is then reconstructed back to the original dimensions of $164 \times 364 \times 1$. The encoder part of the network consists of two 2D convolutional layers with kernel size 3, each followed by a max pooling and a ReLU activation. It is then flattened and passed into a linear layer that forms the latent layer.

The decoder part of the network does the opposite; it attempts to reconstruct the original image using the latent vector obtained at the end of the encoder network. It consists of three 2D convolution layers and ReLU activation, two of which are preceded by upsampling layers that scale their inputs by a factor of 2 using nearest neighbor interpolation.

Mean squared error (MSE) is used as the loss function for the autoencoder, which minimizes the average squares of differences between the original image and its reconstruction:

$$MSE = \frac{1}{n}\sum_{1}^{n}\left(p_i - p'_i\right)^2 \qquad (2)$$

where p represents pixels of the original image and p' represents pixels of the reconstructed image, and $n = h \times w \times c$ is the total number of pixels for an image of height h, width w, having c channels. The detailed autoencoder architecture is shown in Fig. 2.

D. Generative Adversarial Networks

Generative Adversarial Networks (GANs) are deep-learning neural networks capable of generating synthetic data similar to real-world data. These image generators are composed of a generator and a discriminator. The former takes in a random noise vector as input and generates fake data samples, while the latter tries to distinguish between the developed models and actual samples. The generator attempts to trick the discriminator into accepting the generated samples as correct while these two components are being trained together in a minimax game. The discriminator, on the other hand, aims to categorize the real and fake samples appropriately.

The key advantage of a GAN is that it can generate data samples that are indistinguishable from actual data, which can be helpfully used for various purposes, including, but not limited to, image generation, video generation, and even data augmentation. GANs have also been effective in unsupervised learning tasks, where the network is trained on unlabeled data and can learn valuable data representations. However, GANs are challenging to train and can suffer from problems similar to mode collapse, wherein the generator can produce just a limited set of outputs, and vanishing gradients, where the gradients in the training process become too small to be useful. Despite these challenges, GANs have proven to be a powerful tool in the field of deep learning and continue to be an active area of research.

Given random noise z, and real data x, the vanilla GAN objective can be formulated as follows:

$$min_G max_D \mathcal{L}_{vGAN}(G,D) = \mathbb{E}_x[logD(x)] + \mathbb{E}_z\left[\log\left(1 - D\left(G(z)\right)\right)\right] \qquad (3)$$

The Generator G tries to minimize this objective while the Discriminator D tries to maximise it, leading to a two player minimax game.

Conditional Generative Adversarial Networks (cGANs) are an extension of GANs that allow for the conditional generation of data. The critical distinction between GANs and cGANs is that cGANs incorporate additional conditioning information, such as class labels or other structured metadata, to produce more precise and regulated outputs for both the generator and discriminator. cGANs may generate data samples that adhere to specific qualities or characteristics by conditioning the generator on this information, making them especially helpful for applications like image and video synthesis, text-to-image translation, and style transfer.

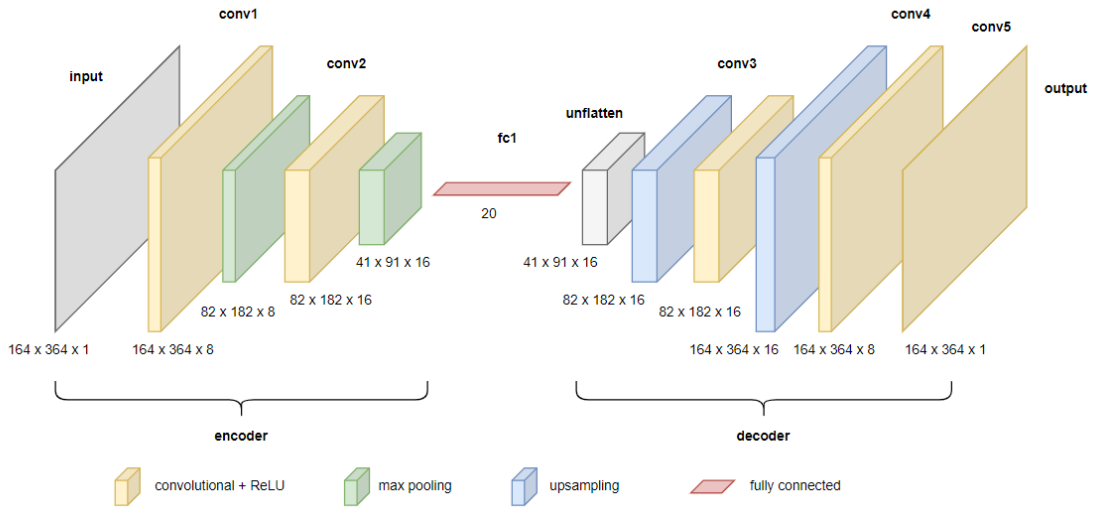

Fig 2: Autoencoder network architecture

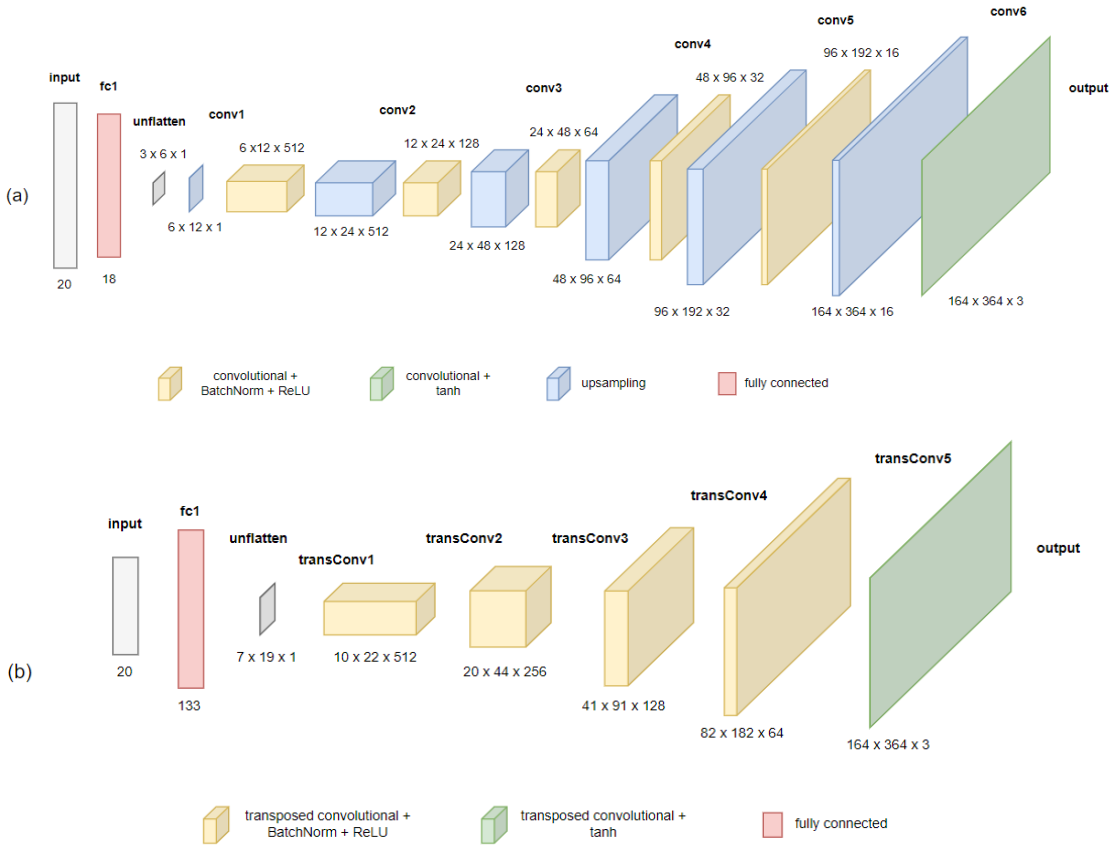

Fig. 3 (a) upsample-Generator and (b) transConv-Generator network architectures

In the context of CFD simulations, cGANs have shown promise in generating more accurate and high-fidelity results by conditioning the generator on relevant simulation parameters such as Reynolds number, angle of attack, and turbulence intensity. This allows the generator to produce pressure distribution plots tailored to specific flow conditions and geometries. By incorporating such conditional information into the training process, cGANs can learn to generate more realistic and physically meaningful CFD results, significantly reducing the computational cost and time required for traditional CFD simulations.

In a cGAN architecture, the generator G takes random noise z and the conditional information y as input and generates synthetic samples. The discriminator D takes both real samples x and their corresponding conditional information y as input and tries to distinguish between real and synthetic samples. Objective for the cGAN can be formulated as:

$$min_G max_D \mathcal{L}_{cGAN}(G, D) = \mathbb{E}_{x,y}[logD(x, y)] + \mathbb{E}_{y,z}\left[\log\left(1 - D\left(G(y, z)\right)\right)\right] \quad (4)$$

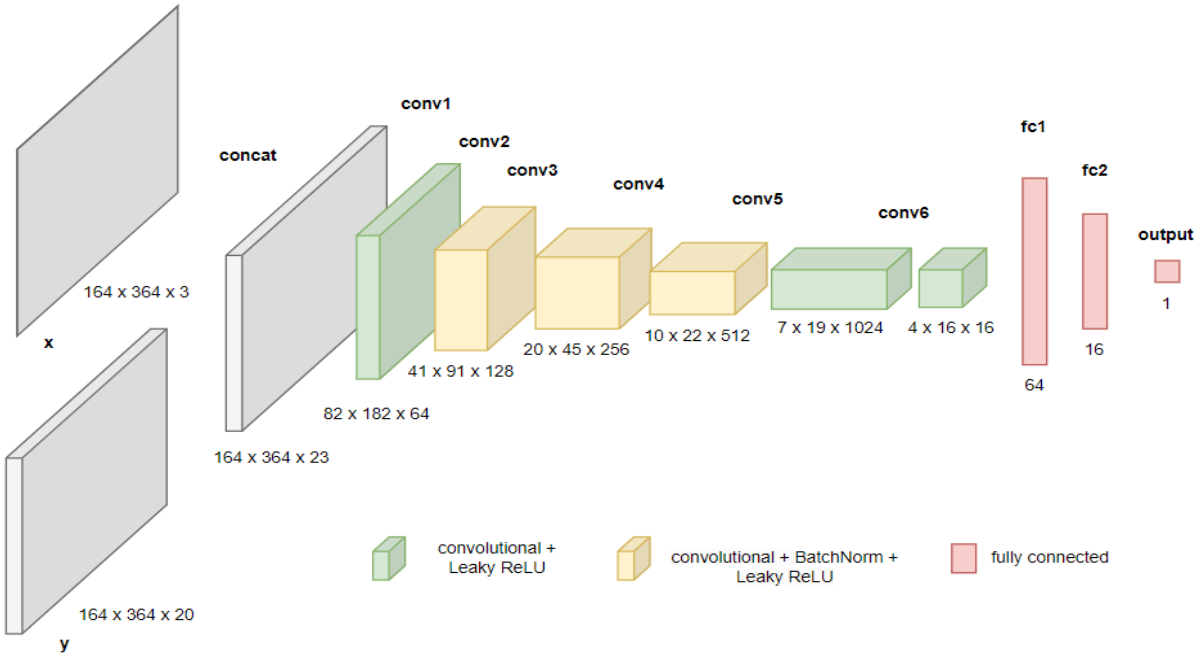

Fig 4: Discriminator network architecture

In our implementation, the GAN is formulated in a fashion similar to the cGAN, which is conditioned to generate an output based on a specific class. Instead of taking noise as an input as done traditionally, the Generator G takes in the latent vector y generated by the autoencoder as the input, which acts as the conditional information. This vector y is also passed into the discriminator after resizing, and is concatenated with the input, which is either the real data x, or the generated data $G(y)$. The objective function for this GAN formulation can be expressed as:

$$min_G max_D \mathcal{L}_{GAN}(G,D) = \mathbb{E}_{x,y}[logD(x,y)] + \mathbb{E}_y\left[\log\left(1 - \mathrm{D}(\mathrm{G}(\mathrm{y}))\right)\right] \quad (5)$$

An L1 loss term between the generated image and the expected image output is added to the Generator loss, which measures the average absolute pixel-wise difference between the corresponding pixels of the two images. The L1 loss encourages the generator to produce outputs that closely match the target image in pixel intensities. This loss term can be expressed as:

$$\mathcal{L}_{L1}(G) = \mathbb{E}_{x,y}[\|x - G(y)\|_1] \quad (6)$$

The final objective now becomes:

$$\mathcal{L}(G,D) = min_G max_D \mathcal{L}_{GAN}(G,D) + \lambda \mathcal{L}_{L1}(G) \quad (7)$$

where λ is a hyperparameter denoting the weight of the L1 loss. Two variants of the generator are proposed: one with upsampling layers (upsample-Generator) and the other with 2D transposed convolution layers (transConv-Generator).

The upsampler-generator uses five upsampling layers followed by 2D convolution layers, along with ReLu activations (except tanh after the last layer) and batch normalization. The transConvranspose-generator uses transposed convolutions to replace upsampling + 2D convolution layers. The two network architectures are given in Fig. 3.

The Discriminator D consists of convolutional layers, batch normalization and LeakyReLU activation. It ends up with a single output with sigmoid activation, which gives a probability that classifies the given input as either real or fake. The discriminator is constructed keeping the guidelines given by Radford et al. [20] in mind. Strided convolution, as opposed to pooling, is recommended for downsampling because it allows the network to develop its own pooling function. Additionally, healthy gradient flow is promoted by batch norm and leaky ReLU functions, which are essential for both the Generator G and the Discriminator D's learning processes. Fig. 4 shows the Discriminator network architecture.

During training, a sample first passes through the autoencoder, which extracts its important features in the form of a 20-dimensional vector, and this vector can now be used as an input to the GAN. The Generator G takes in this vector and generates an output which is supposed to be a mapping to the input's pressure coefficient field. Such fake samples, along with the true samples are passed to the Discriminator D, with their corresponding extracted feature vectors reshaped to the shape [batch_size, 164, 364, 20]. This shape is the same height and width as the field but with 20 channels instead of 3. Inside the network, these are concatenated and passed through the subsequent layers to give a classification result finally. As formulated before, the generator loss combines the usual adversarial loss and the L1 reconstruction loss between the true and the generated image, as formulated

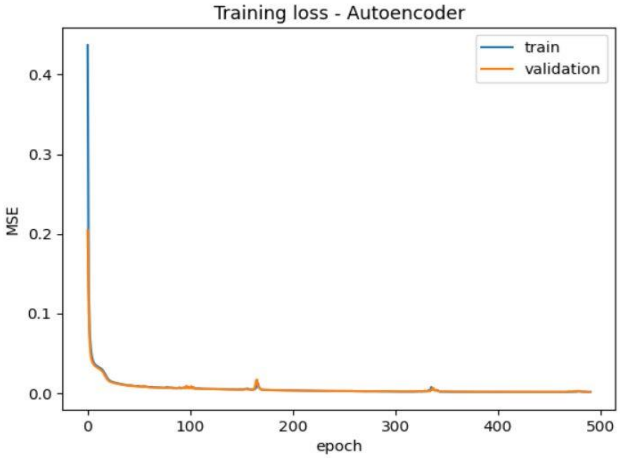

Fig. 5 Autoencoder loss

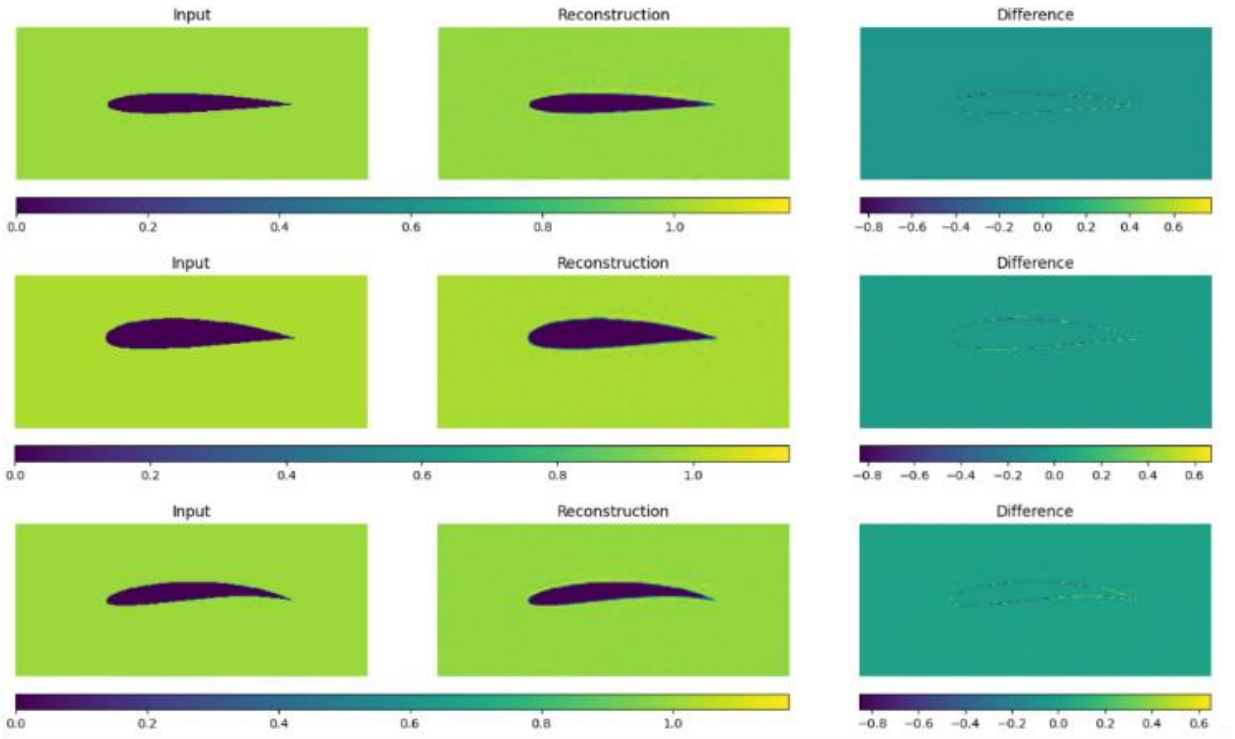

Fig. 6 Autoencoder reconstructions on some test samples

before. The hyperparameter λ is the weight applied to the L1 reconstruction loss term, and is chosen as 500 after tuning.

III. RESULTS AND DISCUSSION

A. Autoencoder

The autoencoder, consisting of 2D convolutional layers, max pooling, dense layers, and ReLU activations, learns to reconstruct the input geometry of shape [164x364x1], passing it through a bottleneck. A latent vector of size 20 seemed sufficiently capable of reconstructing the inputs. This latent vector attempts to capture the essential features of the geometry represented by the input to reconstruct the output based on this compressed feature representation. The training was done using 4096 samples, of which 3276 were used as training samples and 820 as validation samples. The network weights were updated using the Adam optimizer, which computes individual adaptive learning rates for different parameters from estimates of the first and second moments of the gradients. A learning rate of 1e-3 and a batch size of 16 were used. The MSE loss between the original input and the reconstruction is minimized, during which a meaningful latent representation of the input is derived in the bottleneck.

The Autoencoder model is trained for 500 epochs, after which the training and validation losses converge. Fig. 5 shows the Autoencoder loss while training. The results of the reconstructions on some test samples are shown in Fig. 6. The reconstructions agree with the respective inputs fairly; however, a slight difference is observable along the boundary of the aerofoil. Despite this, the model has generalized well

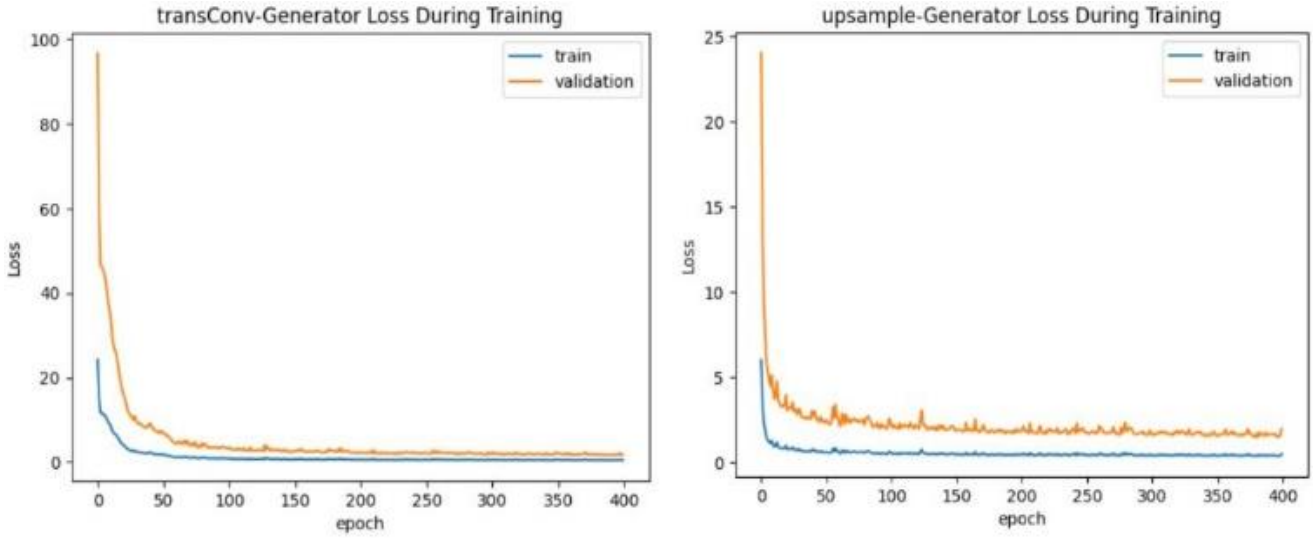

Fig. 7 (a) transConv-Generator loss and (b) Upsample-Generator loss during training

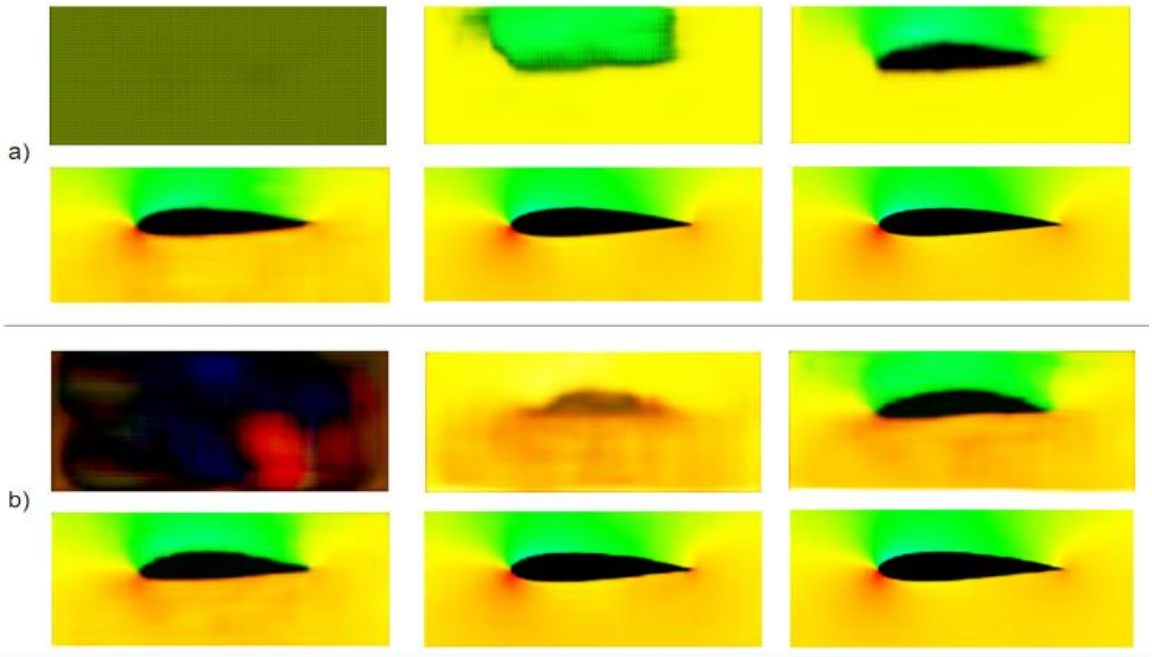

Fig. 8 (a) transConv-Generator and (b) Upsample-Generator generating the field for a test sample

for different aerofoil thicknesses, camber, and camber locations. Hence the encoder can now be detached and used as an independent compressor, which can convert a [164x364x1] raw input to its compressed representation of size [20].

B. Conditional GAN

Two variants of the GAN are trained, consisting of batch normalization, dense layers and ReLU activations, along with upsample + 2D convolutional layers or 2D transposed connvolutional layers. The Generator *G*, conditioned on the input latent vector, learns to generate pressure field corresponding to the input. At the same time the discriminator *D* aims to classify between real and fake images, again looking at the expanded latent vector representation of the aerofoil along with the pressure field. In both the networks, the weights were updated using the Adam optimizer, and a learning rate of 1e-3 was used. The dataset was passed in with a batch size of 16.

The networks are trained together for 400 epochs, by the end of which the losses converge. Fig. 7 shows the Generator losses for the two variants while training. The generation of a validation sample as the model trains is shown in Fig. 8. In the initial epochs, the transConv-Generator exhibits artifacts which are generally caused by "uneven overlap" of the convolution kernel [19] but they diminish by the end of 400 epochs. Overall by the end of 400 epochs, both the generators

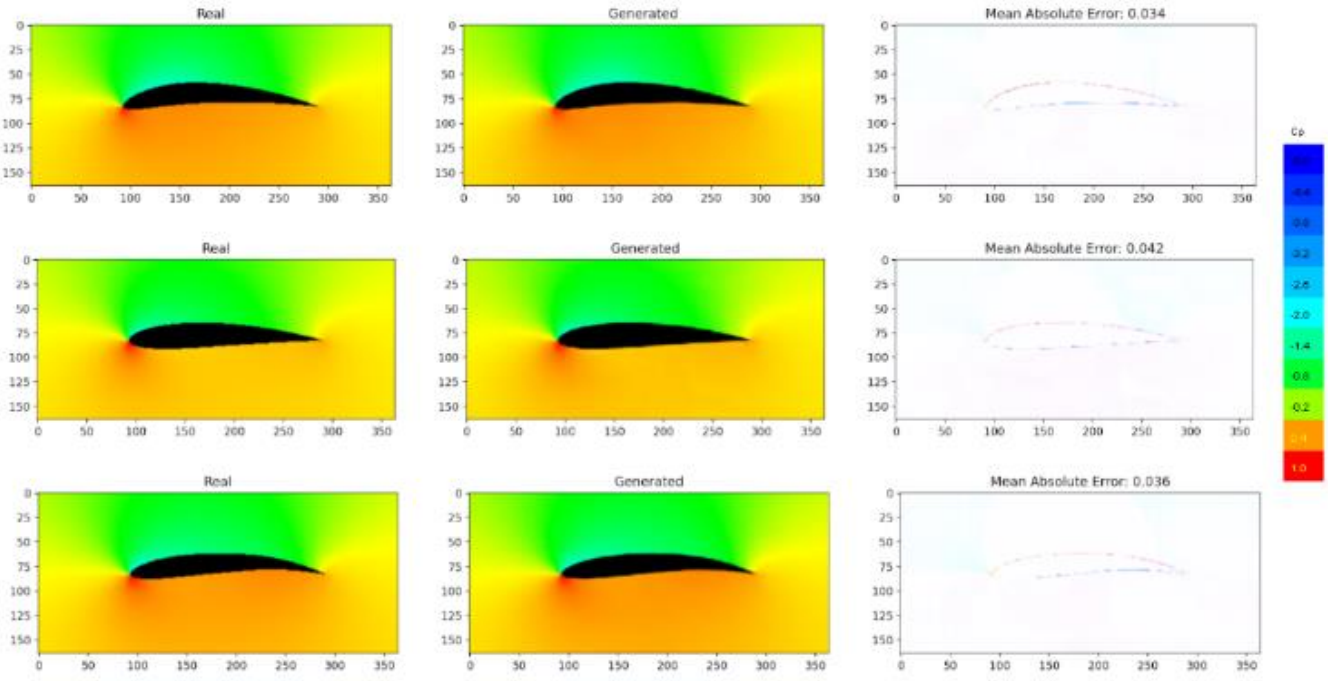

Fig. 9 Real and Generated test samples using upsample-Generator

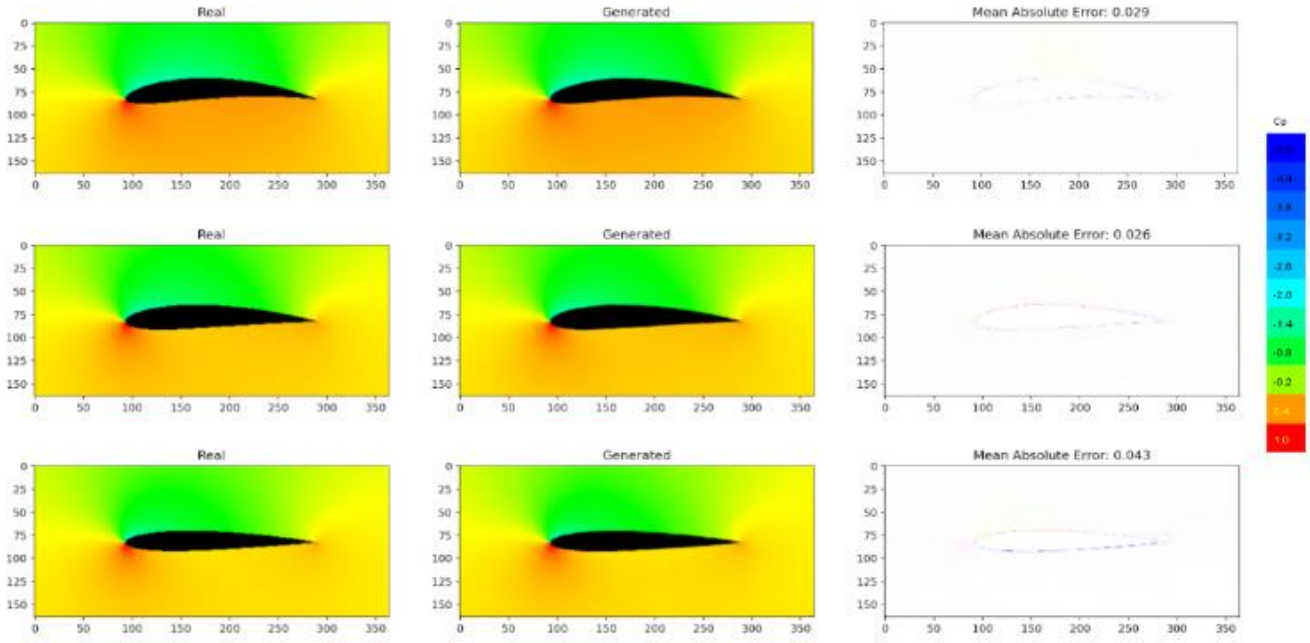

Fig. 10 Real and Generated test samples using transConv-Generator

achieve similar results. However, the aerofoil surface in the case of transConv-Generator looks smoother as compared to the upsample-Generator.

C. Pressure field prediction

The encoder and generator weights saved after training completion are used to test the results of the combined model. The input geometry of size [164x364x1] is passed into the encoder, which outputs a vector of size 20. This vector is then resized and passed into the Generator G which generates an output of size [164x364x3], conditioned on the input vector. The predictions using the upsample-Generator are shown in Fig. 9, and using the transConv-Generator are shown in Fig. 10. It can be seen that there is a good match between the real and the generated pressure fields with sufficiently low mean absolute error (MAE) values. Higher values of error are concentrated along the aerofoil boundary, and seem less pronounced in the regions with lower C_p values. It is evident from the results that the combined AE+GAN model can generate predictions with a high degree of accuracy over varying geometry parameters like thickness, camber, and camber location, accommodating various aerofoil profiles.

The performance of the two generator variants on a set of test samples is compared in figure 11. It can be observed that the MAE values in case of the transConv-Generator are almost always lower than when upsample-Generator is used. This is likely due to the fact that the transposed convolutional layers, being trainable, can learn the spatial upsampling. MAE for the value of the pressure coefficient ranges for the transConv-Generator ranges from 0.025 to 0.043, while for the upsample-Generator lies between 0.031 and 0.052. Overall, the real and predicted fields are in good agreement, with consistent predictions around varying aerofoil geometry.

IV. CONCLUSIONS

The study results demonstrate that the combined AE+GAN model successfully generates predictions with high accuracy. The generated pressure fields closely match the real pressure fields, as indicated by the low MAE values. The errors observed primarily occur along the aerofoil boundary and are

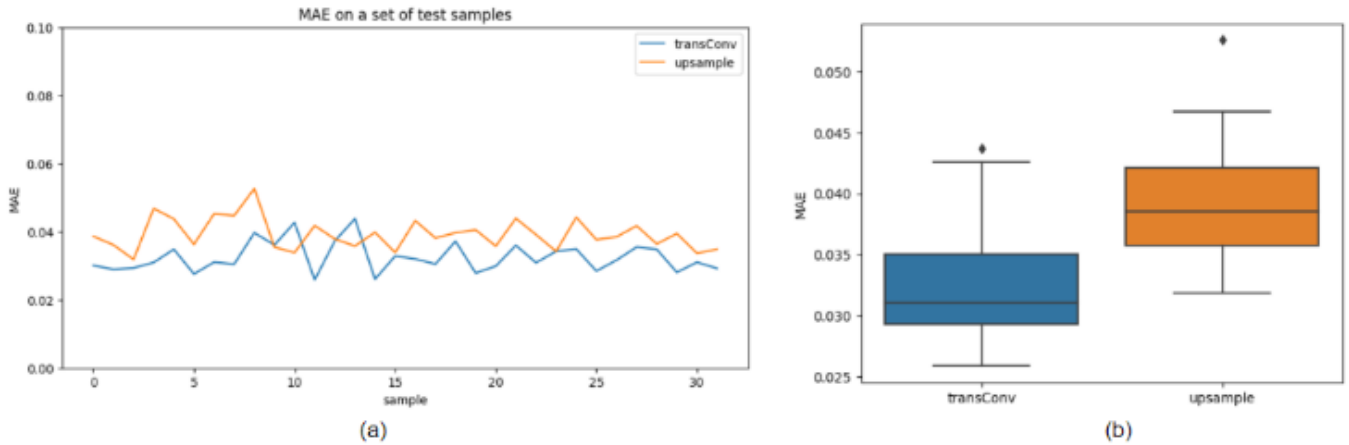

Fig. 11 Comparison of MAE for the two Generator variants

less pronounced in regions with lower Cp values. Nevertheless, the model accommodates various aerofoil profiles, including varying geometry parameters such as thickness, camber, and camber location.

This research contributes significantly to the advancement of computational techniques in fluid dynamics, specifically in the domain of aerodynamics. By leveraging the synergistic power of autoencoders and GANs, the proposed approach demonstrates the potential to reduce the time and costs associated with aerodynamic prediction. The efficient evaluation of aerofoil performance facilitated by this approach opens up new avenues for enhanced design and optimization processes in aerodynamics.

Further refinements and investigations can be conducted to enhance the model's performance and address the observed errors along the aerofoil boundary. Additionally, exploring the scalability and applicability of this approach to more complex aerodynamic scenarios and real-world applications could be a valuable direction for future research.

V. REFERENCES

[1] LingJ., Kurzawski, A., & Templeton, J. (2016). Reynolds averaged turbulence modelling using deep neural networks with embedded invariance. Journal of Fluid Mechanics, 807, 155-166.

[2] Kutz, J. N., Brunton, S. L., Brunton, B. W., & Proctor, J. L. (2017). Dynamic mode decomposition-based reduced-order modelling of complex fluid flows. Proceedings of the Royal Society A: Mathematical, Physical and Engineering Sciences, 473(2201), 20160499.

[3] Wang, Q., Zhang, X., Xie, Y., & Zhang, X. (2019). Optimization of a microfluidic mixer using genetic algorithm and machine learning. Computers & Chemical Engineering, 126, 218-227.

[4] Lapeyre, C. J., Hickey, J. E., & Brenner, M. P. (2018). Artificial neural networks trained on DNS data for turbulent flow reconstruction and prediction. Journal of Computational Physics, 366, 29-48.

[5] Jin, J. M., Zhang, W. W., Liu, L., & Shao, X. M. (2018). A generative adversarial network for generating synthetic data of unsteady turbulent flows. Journal of Computational Physics, 366, 1-15.

[6] Wang, Q., & Ling, J. (2020). Machine learning of accurate turbulence models from DNS data. Journal of Computational Physics, 404, 109105.

[7] Smith, R., Zhu, Y., & Eldred, M. S. (2017). Machine learning for UAV aerodynamic performance prediction. Journal of Aircraft, 54(2), 712-725.

[8] Zhang, M., Li, J., & Li, Z. (2018). Flow pattern recognition in multiphase flows using deep learning. Computers & Fluids, 173, 189-199.

[9] Chen, Z., Hu, X., Huang, P., & Wang, L. (2019). Recurrent neural networks for turbulence modelling. Journal of Fluid Mechanics, 878, 708-731.

[10] Liu, L., Zhang, W. W., Jin, J. M., & Ling, J. (2020). Data assimilation with machine learning for weather forecasting. Journal of Computational Physics, 408, 109287.

[11] Guo, Z., Shi, X., Zhang, L., Zhao, L., & Jiang, Z. (2021). Deep reinforcement learning for aerodynamic shape optimization. Aerospace Science and Technology, 111, 106546.

[12] Li, H., Ling, J., & Perdikaris, P. (2022). Transfer learning accelerated computational fluid dynamics. Journal of Computational Physics, 455, 110965.

[13] Wang, X., Zhang, J., Cao, W., & Kang, Q. J. (2022). Hybridizing physics-based models with machine learning for multiphase flow simulations. Journal of Computational Physics, 452, 110993.

[14] Wang, Q., Perdikaris, P., Karniadakis, G. E., & Koumoutsakos, P. (2018). A deep learning approach for turbulence modelling in complex flows. Physics of Fluids, 30(5), 055109.

[15] S. Chen, B. Mulgrew, and P. M. Grant, "A clustering technique for digital communications channel equalization using radial basis function networks," IEEE Trans. on Neural Networks, vol. 4, pp. 570-578, July 1993.

[16] J. U. Duncombe, "Infrared navigation—Part I: An assessment of feasibility," IEEE Trans. Electron Devices, vol. ED-11, pp. 34-39, Jan. 1959.

[17] C. Y. Lin, M. Wu, J. A. Bloom, I. J. Cox, and M. Miller, "Rotation, scale, and translation resilient public watermarking for images," IEEE Trans. Image Process., vol. 10, no. 5, pp. 767-782, May 2001.

[18] Vincent, P., Larochelle, H., Bengio, Y., & Manzagol, P. A. (2008, July). Extracting and composing robust features with denoising autoencoders. In *Proceedings of the 25th international conference on Machine learning* (pp. 1096-1103).

[19] Kingma, D. P., & Welling, M. (2013). Auto-encoding variational bayes. *arXiv preprint arXiv:1312.6114*.

[20] Radford, A., Metz, L., & Chintala, S. (2015). Unsupervised representation learning with deep convolutional generative adversarial networks. *arXiv preprint arXiv:1511.06434*.]

[21] Odena, A., Dumoulin, V., & Olah, C. (2016). Deconvolution and checkerboard artifacts. Distill, 1(10), e3.

Proceedings of the Second International Conference on Applied Artificial Intelligence and Computing (ICAAIC 2023)
IEEE Xplore Part Number: CFP23BC3-ART; ISBN: 978-1-6654-5630-2

Accurate Disease Detection in Apple Fruit Images using Transfer Learning: A Novel Approach for Agricultural Sustainability

Piyush Agrawal
Dept. of Computer Science and Engineering
Delhi Technological University
New Delhi, India
piyush18agrawal@gmail.com

Nishant Singh
Dept. of Computer Science and Engineering
Delhi Technological University
New Delhi, India
nishantsinghdtu@gmail.com

Nikunj Bansal
Dept. of Computer Science and Engineering
Delhi Technological University
New Delhi, India
nikunjbansal037@gmail.com

Anurag Goel
Dept. of Computer Science and Engineering
Delhi Technological University
New Delhi, India
0000-0003-2660-7540

2023 2nd International Conference on Applied Artificial Intelligence and Computing (ICAAIC) | 978-1-6654-5630-2/23/$31.00 ©2023 IEEE | DOI: 10.1109/ICAAIC56838.2023.10141138

***Abstract*—Apple fruit disease poses a significant challenge to the agriculture industry due to its negative impact on orchard yield and economic growth. The current method of identifying diseased apples is a manual inspection process that is time-consuming and requires significant labor. To address this issue, the proposed work focuses on transfer learning based models namely ResNet, MobileNet, Inception, EfficientNet and Xception, to detect disease in apple images. The transfer learning based approaches aim to quickly identify infections and prevent further spread caused by environmental factors, allowing for efficient selection of healthy fruits while also replacing the manual inspection system to speed up the process and improve accuracy and efficiency. The transfer learning models are evaluated on apple images dataset. The obtained research results show that the Xception model outperforms the rest of the transfer learning models with significant margin.**

***Index Terms*—Apple Disease Detection, Convolutional Neural Network, Deep Neural Network, Transfer Learning.**

I. Introduction

Apples are highly valued and nutritious fruit in our society, and they have been cultivated for many years. However, apple cultivation is complicated by the multitude of diseases that can affect apple trees, leading to a reduction in fruit quality and quantity. To ensure high-quality produce, apple farmers must manually sort through each apple to separate healthy ones from those that are diseased or damaged. This process is laborious and time-consuming, requiring constant supervision to ensure the accuracy of the sorting.

The aim of this research is to explore the feasibility of utilizing image processing techniques to differentiate between healthy and defective apples. The study entails analyzing images of apple to detect and segregate those that exhibit signs of disease or damage from those that are healthy.

The utilization of deep learning and Internet of Devices (IoT) advancements can be harnessed to enhance apple growth and production, reducing the reliance on human supervision and labor and ultimately resulting in a decrease in production costs for apple industries and agricultural economies. This work implemented a transfer learning based methodology - Xception Net for the classification of healthy and unhealthy apples after carefully analyzing and simplifying the apple images. The Xception Net has the potential to significantly decrease the human supervision and effort required for detecting apple fruit diseases, leading to improved production efficiency and reduced costs for both apple industries and agricultural economies.

II. Literature Review

To forecast fruit disease infection, Milos et al. [1] used mathematical algorithms and data mining approaches. Six weather factors, a time variable, the month of the sickness, are chosen as the prediction variables in the model. This work predicted two serious cherry fruit illnesses with the aid of data mining tools.

Paul et. al. [2] employed image processing to find and avoid pests. The suggested method found illnesses and pests in the leaves of pistachio trees. In [3], Decision Trees are used to identify illnesses in apple plants. using the aid of Deep Convolutional Neural Network (CNN).

[4] proposed a novel method to identify ten prevalent rice illnesses. In order to categorize banana leaves as healthy or unhealthy, [5] used transfer learning and the LeNet architecture. To distinguish between the groups of apple leaf pathogens, Liu, Bin et al. [6] developed a special Deep CNN structure based on AlexNet and trained the proposed model on 13000 images of sick apple leaves.

Bingze Dai, Tian Qiu, [7] employed various deep learning models including DenseNet, ResNet [8], and GoogleNet [9]

Authorized licensed use limited to: DELHI TECHNICAL UNIV. Downloaded on June 14,2023 at 05:00:06 UTC from IEEE Xplore. Restrictions apply.

to extract features using trained CNNs and Histogram of Gradients (HoG), followed by transfer learning methods and Support Vector Machine (SVM).

S. Melike et al. [10] recommended a Faster Region-based CNN (Faster R-CNN) in their study to classify apple leaf diseases. The Inception v2 architecture served as the basis for the model. [11] conducted research on the tomatoes in which processed tomato images are investigated using Magnetic Resonance Imaging (MRI) to distinguish between healthy and diseased tissue in the tomato samples. By linking the pixels in the MRI images with their corresponding healthy or affected tissue, the researchers were able to gain significant knowledge about the disease's characteristics and how it develops.

The current methods for processing hyperspectral data using neural networks were evaluated by Golhani et al. [12] with discovering plant diseases as the main goal. Jiang et al. [13] suggested CNNs as a method for identifying illnesses in apple leaves. They developed an enhanced CNN model that can diagnose diseases in real-time from complex real-life photographs and laboratory images. The dataset was pre-processed by annotating and enhancing the images before training and testing the CNN model using a hold-out test strategy. While fruit disease detection is still an ongoing research topic, transfer learning algorithms are also valuable machine learning techniques for identifying fruit illnesses, in addition to neural networks [14]. Transfer learning approaches are proved to be effective for several applications [15, 16]. Therefore, this work investigated transfer learning techniques for diagnosing apple illness.

III. Methodology Used

1) ResNet: Kaiming et al. [17] residual learning framework, which permits the construction of much deeper networks than those previously employed, was offered as a solution to this problem. Instead of learning unreferenced functions, the Resnet technique reformulates the layers to train residual functions for the reference layer inputs. The notion that these residual networks are easier to optimise and increase accuracy with depth is supported by empirical evidence provided by the author. The first two layers of ResNet are the same as the GoogLeNet layers. ResNet structure is more straightforward and flexible than GoogleNet, despite the fact that their respective core architectures are identical. ResNet captures and models very complex features in the data but ResNet deep architecture and large number of parameters can make its training computationally expensive. The ResNet architecture is shown in Figure 1.

2) MobileNet: Howard et al. [19] proposed the MobileNet architecture for image classification. The architecture of MobileNet is based on depth-separable convolutions, where exception is the first layer which is convolutional wholly. ReLU activation function is applied on all the layers except the last layer which has no non-linearity and connects directly to a softmax layer for the classification purposes. Rectified Linear Unit (ReLU) activation function plays a critical role in enhancing the model's efficiency and performance. ReLU is mathematically represented as follows:

$$f(x) = max(0, x)$$

ReLU introduces non-linearity into the network while simultaneously maintaining computational simplicity. As a primary component of the MobileNet architecture, ReLU is employed following each depthwise and pointwise convolution operation. Its incorporation results in the suppression of negative activations while retaining positive ones, promoting sparse activation patterns. This sparsity contributes to the reduction of computational complexity, enabling faster inference times without compromising model accuracy.ReLu is fostering both computational efficiency and performance. Through the introduction of non-linearity and sparsity, ReLU enables the model to achieve rapid inference times and robust generalization, making it suitable for resource-constrained mobile and embedded applications. A factorization layer, which applies depth convolution, batch norm, and ReLU after each convolutional layer, is contrasted with a regular convolution layer as shown in Figure 2. MobileNet applies stretched convolutions to the first layer and depth crown for downsampling. To lower the spatial resolution to 1, a last average pooling layer is applied before the entirely linked layer. The 28 layers of MobileNet perform deep and point convolutions separately. In deep convolution, large size kernel filters are used for convolution while the point convolution is performed using the 1×1 sized kernel filters. MobileNet's great efficiency and cheap computational cost make it an asset for picture classification, making it perfect for use on mobile devices with constrained computational power. With fewer factors and less computational complexity, it still achieves high precision because of the depthwise separable convolutions. In comparison to other models with standard convolutions, MobileNet's depthwise separable convolutions can result in a loss of accuracy, particularly on tasks that call for fine-grained categorization. By deepening the model or adding more regularisation methods, this can be resolved. The MobileNet architecture is shown in Figure 3.

3) Inception-v3: Inception-v3 [21] is an improvement over the earlier version, Inception-v1, which was introduced in 2014 as GoogLeNet. The Inception-v3 model, released in 2015, has 42 layers and achieves a lower rate of error compared to its ancestor. The major changes in Inception-v3 architecture are as follows:

a) Smaller Convolution Factorization: The computation is less expensive as a result of the fewer parameters. The proportional advantage from this reduction of bigger convolutions into smaller ones is 28%.

b) Spatial decomposition into asymmetric convolutions: Large convolutions can be broken down into smaller ones. Asymmetric convolution is even more efficient alternative to further increase model efficiency. Asymmetric convolution has a mathematical shape of $n \times 1$, which is less expensive than using 2×2 convolutions. Actually, using the same number of output filters with the same number of input and output

Authorized licensed use limited to: DELHI TECHNICAL UNIV. Downloaded on June 14,2023 at 05:00:06 UTC from IEEE Xplore. Restrictions apply.

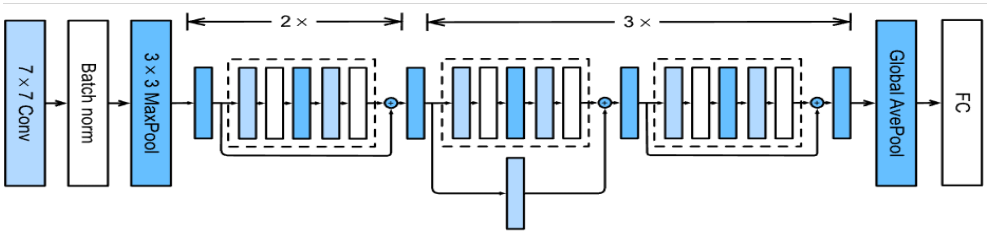

Fig. 1. Resnet Architecture [18]

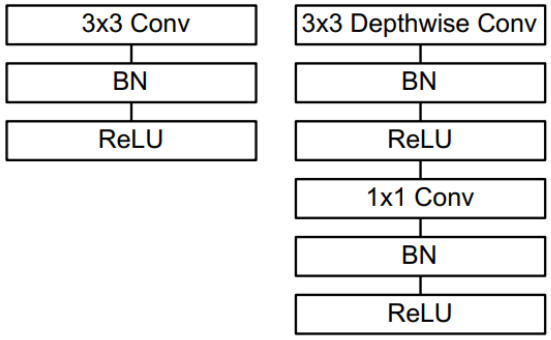

Fig. 2. (i) Left: ReLU Activation and Batch Normalization for a Standard Convolutional Layer (ii) Right: Batch normalisation, ReLU activation, Depthwise Separable Convolutions using Depthwise and Pointwise Layers [19]

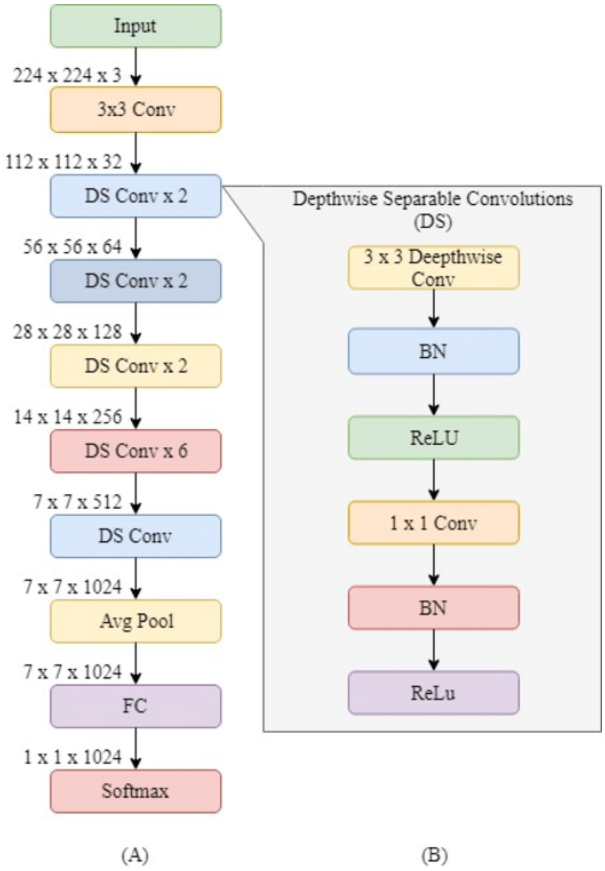

Fig. 3. MobileNet Architecture [20]

filters costs 33% more than using the two-layer technique with asymmetric convolution.

c) Auxiliary classifiers: To speed up the convergence of deep neural networks, auxiliary classifiers are utilized. The network's intermediate layers are where the auxiliary classifiers are introduced as new branches. These branches are made up of a fully connected layer with softmax activation, a fully connected layer with global average pooling, and a 1×1 convolution layer. Each auxiliary classifier produces a chance distribution over the classes as its output. The primary classifier loss and the auxiliary classifier loss are combined with a coefficient to create the final loss function during training. As a result, the intermediate layers capture more distinguishing characteristics that are helpful for classification. These classifiers are useful in addressing the issue of leakage gradients in extremely deep networks. At the start of training, no significant improvement is seen with auxiliary classifiers. In the end, the Inception-v3 model that includes auxiliary classifiers achieves higher accuracy compared to the one without them. As a result, the design of the Inception-v3 model acts as a regulator due to the presence of the auxiliary classifier.

d) Efficient Reduction of Grid Size: One common method for reducing the grid size of feature maps in neural networks is through maximum and average clustering. In the original V3 model, an extension of the network filter activation dimension was utilized to effectively decrease the grid size.

Using its inception modules, which blend multiple convolutional layers of various sizes in parallel, Inception-v3 excels at classifying images by successfully capturing and modelling complicated patterns and characteristics in the data. As a result, it can successfully complete a variety of image classification jobs with high precision.

Due to its deep design and numerous parameters, Inception-v3 has a weakness that may make it less appropriate for implementation on devices with constrained processing resources:

Authorized licensed use limited to: DELHI TECHNICAL UNIV. Downloaded on June 14,2023 at 05:00:06 UTC from IEEE Xplore. Restrictions apply.

a comparatively high computational cost. Furthermore, compared to simpler models, its complicated architecture might be more challenging to comprehend and alter. The Inception-v3 architecture is shown in Figure 4.

4) EfficientNet: Tan et al. [24] proposed EfficientNet architecture for image classification. When developing a convolutional neural network, this is done at a fixed resource cost. These networks are then scaled to achieve greater accuracy as more resources become available. A ResNet-18 model can be extended to ResNet-200 model by adding more layers to the original model. In most cases, this scaling technique can provide better accuracy on most benchmark data sets. But traditional model scaling techniques are very random. Some models are scaled in depth and some in width. Some models simply capture higher resolution images for better results. This random model scaling technique requires manual tuning and many hours of work, often resulting in little or no performance improvement. The EfficientNet authors propose to extend CNN models to achieve greater accuracy and efficiency in a more ethical way.

Using a technique called compound coefficients, EfficientNet adjusts models in a simple but effective way. Instead of scaling width, depth, or resolution at random, compound scaling uniformly scales each measure using a predetermined set of scaling factors.

The authors create effective models in seven different dimensions using a scaling and AutoML method, outperforming the most advanced convolutional neural networks in accuracy and efficiency. A core network called EfficientNet was created using the AutoML MNAS framework and is built on research into neural architecture.

The network is set up to provide the highest level of accuracy, but if it uses a lot of processing power, there will be a cost. It is also penalised for slow inference times when the network makes predictions slowly. With more FLOPS than MobileNet-v2, the architecture employs moving inverse bottleneck convolutions, which are larger in size. This fundamental model is scaled up to produce the EfficientNet family.

EfficientNet's high efficiency and scalability, which enable it to accomplish state-of-the-art precision on a variety of image classification tasks while utilising fewer factors and less computational resources than other models, are one of its strengths in image classification. In order to combine precision and computational speed, the model's depth, width, and resolution are adjusted using a compound scaling technique.

EfficientNet's architecture could be more complex and difficult to understand than simpler models, which could make training and refining it more difficult. Additionally, because the design of the model makes use of a large number of scaling factors and hyperparameters, it might be more difficult to fine-tune the model for specific tasks. The EfficientNet architecture is shown in Figure 5.

5) Xception: The Xception model was proposed by François Chollet [25] which uses CNNs to make judgements about inputs like language or images. To speed up the pre-processing stage, the system employs the Xception model, a 71-layer CNN. Animals, keyboards, mice, and pencils are just a few of the 1000 different object categories that the Xception model can classify photos into. More than a million photos from the ImageNet collection served as its pretraining. For a wide range of photos, the network now offers a comprehensive feature representation. A picture with a resolution of 299 by 299 pixels is sent to the network as input.

Deep Neural Networks employ less pre-processing than traditional picture categorization methods, allowing the network to incorporate measures that were manually held in earlier methods. The neural network's convolution layers perform a decent job of extracting features from the input photos. These kinds of networks have been successful at classifying images due to the complex extraction and sophisticated features of vision made possible by the presence of several layers of convolution. Additionally, network resistance to changes in the unappealing texture of the fruit in the image is caused by the levels of integration and normalization. By receiving fruit photos, the network eventually labels the visuals as healthy or unhealthy in its output.

Xception's ability to accurately capture and model complex features in the data while keeping a relatively shallow architecture in comparison to other models is one of its strengths in the area of image classification. This is accomplished by swapping out the conventional convolutional layers for depthwise separable convolutions, which results in a decrease in processing and the number of parameters. The Xception architecture is shown in Figure 6.

IV. Experimental Setup

A. Dataset Collection

Apple fruit disease picture dataset from Gembloux Agro-Bio Tech i.e. ULG [13], Belgium is used for evaluating the models. The CAPA apple fruit images dataset is a collection of high-quality digital images of apples captured under controlled conditions. The dataset has been specifically curated and designed to be utilized in the domain of computer vision research, particularly in the area of apple fruit detection and recognition. In the dataset, there are 3279 images which were divided into 80% as training set, 10% as validation set and 10% as test set. The dataset includes multispectral images of infected and healthy apples at wavelengths of 450, 500, 750, and 800 nm. The bi-color photos are manually segmented for the areas that are diseased. In contrast, we divided the images into two groups: clean and contaminated. The flaws come in four separate categories and include, among others, decay, flesh injury, bruising, and forest damage.

B. Data Pre-Processing

Convolution networks along with transformer models are trained using images from a training set. Due to the graphics requirement, the image size is reduced in dimensions. It improves accuracy as well, and also does not lower the convolutional neural networks and transformer's classification accuracy for images or the training process precision. Healthy

Authorized licensed use limited to: DELHI TECHNICAL UNIV. Downloaded on June 14,2023 at 05:00:06 UTC from IEEE Xplore. Restrictions apply.

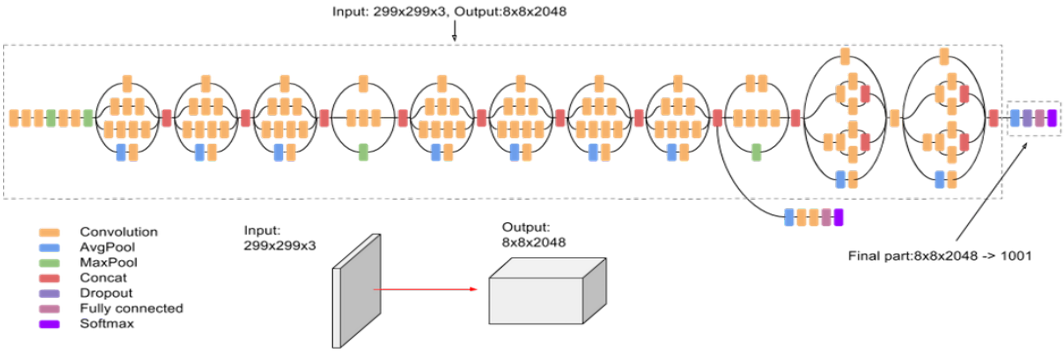

Fig. 4. Inception-v3 Architecture [22]

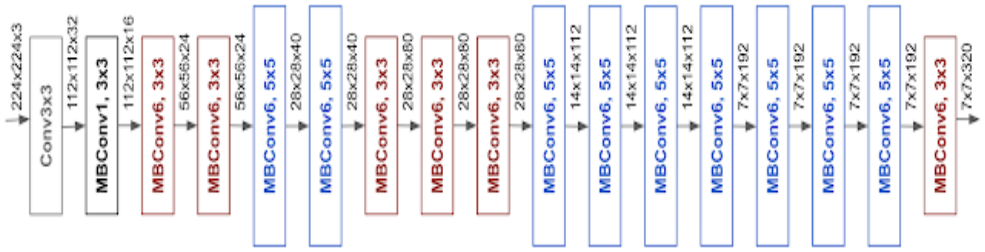

Fig. 5. EfficientNet Architecture [23]

tissues and redundant information make up the majority of the image-related size, while non-healthy tissues are only present in a very small percentage of the images. Together, these elements explain this performance. On the other hand, when image size decreases, the number of parameters in the network likewise decreases, hastening and streamlining the network training process.

C. Data Augmentation

With a bigger and more diversified dataset, deep neural networks' performance must be improved. Data augmentation is a technique used to increase the amount of data available for training the model without the need for new data collection. Variations of the training set images that the model might see while being taught are created using this technique. By expanding the dataset while consuming less memory, data augmentation can boost the model's ability to generalise to fresh, unstudied data. Data augmentation is also useful since it helps the model be more resilient to different fluctuations and distortions in the input data.

D. Test Train Split

The dataset is divided into three parts: 80% for training, 10% for validation, and 10% for testing the models. Prior to conducting the split, the full dataset must be randomly generated. This is done to make sure the split is impartial and to remove any potential impact from the data's initial ordering.

E. Metrics used

The four outcomes commonly used to assess the effectiveness of any strategy are T True Positive (TP), True Negative (TN), False Positive (FP), and False Negative (FN). The transfer learning models are evaluated using standard classification namely Precision, Recall, F1-score and Accuracy.

$$Precision(P) = \frac{TP}{TP + FP} \tag{1}$$

$$Recall(R) = \frac{TP}{TP + FP} \tag{2}$$

$$F1\ score = 2 \times \frac{P \times R}{P + R} \tag{3}$$

V. Results Analysis

The accuracy of the various transfer learning models namely ResNet, MobileNet, Inception-v3, EfficientNet & Xception are shown in Table I. The Xception model has the highest accuracy of 90.09% followed by EfficientNet and Inception-v3 while the ResNet model shows the least accuracy. The classfication metrics scores for the Xception model are shown in Table II

Figure 7 and 8 show the Principal Component Analysis (PCA) plot and T-SNE plot of the output of Xception model on the test set respectively. In specific, patterns and connections between various classes or clusters of images can be found using PCA. PCA also discloses how various features add to

Authorized licensed use limited to: DELHI TECHNICAL UNIV. Downloaded on June 14,2023 at 05:00:06 UTC from IEEE Xplore. Restrictions apply.

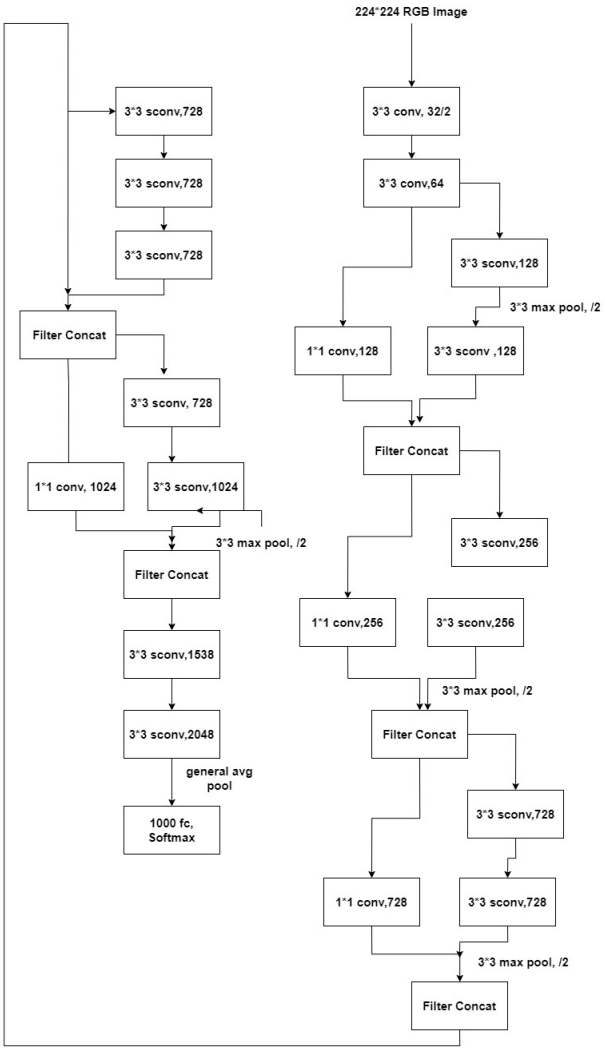

Fig. 6. Xception Architecture

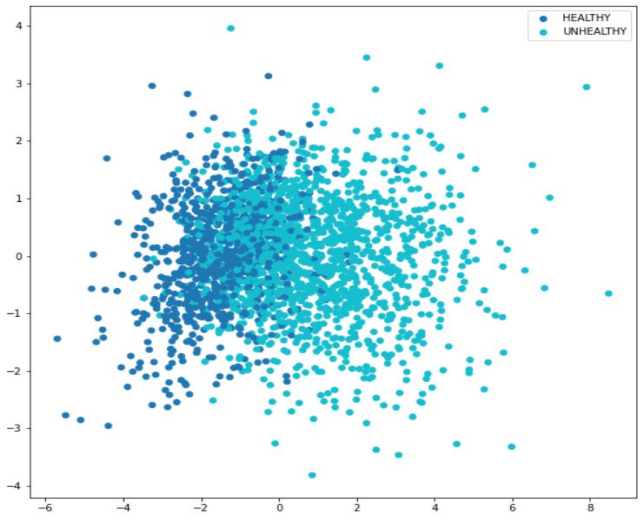

Fig. 7. Xception Model: PCA plot

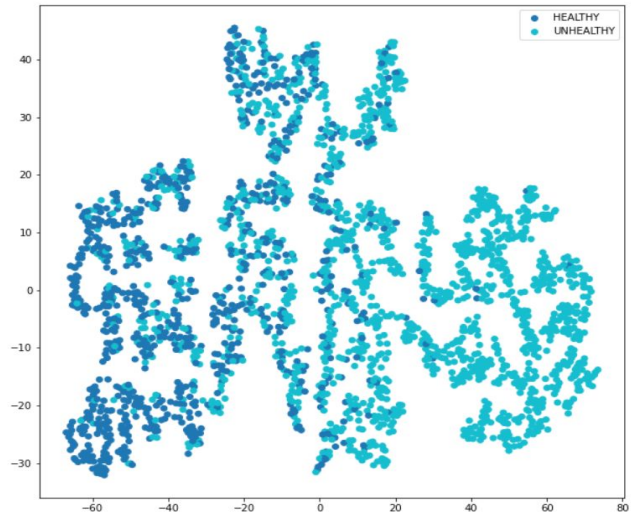

Fig. 8. Xception Model: T-SNE plot

TABLE I
ACCURACY OF TRANSFER LEARNING MODELS

Models	Accuracy
ResNet	76
MobileNet	82
Inception-v3	83.71
EfficientNet	84.49
Xception	90.09

TABLE II
XCEPTION MODEL CLASSIFICATION METRICS

Metric	Accuracy	Recall	Precision	F1-Score
Value	0.9009	0.9145	0.8761	0.8897

the classification of images and how they can be optimised to increase the accuracy of the image classification model by looking at the distribution of the feature vectors on the graph. In order to visualise the condensed feature space and aid in better grasping the connections between the features and the images, PCA plots can be used.

Xception model outperforms rest of the transfer learning models since Xception utilizes depthwise separable convolutions, which are a type of convolution that separates the spatial and channel-wise filtering. This makes the model more efficient and reduces the number of parameters, which can help to prevent overfitting. The deep architecture of Xception captures more complex features in the data. The model has over 20 layers, which helps it to learn more abstract and nuanced features that are important for image classification.

Authorized licensed use limited to: DELHI TECHNICAL UNIV. Downloaded on June 14,2023 at 05:00:06 UTC from IEEE Xplore. Restrictions apply.

VI. Conclusion

Precise disease diagnosis in apple fruit is very crucial to reduce the financial loss of the apple agriculture. In this paper, transfer learning based approaches are used to precisely detect apple diseases. The transfer learning models used in this work are ResNet, MobileNet, Inception-v3, EfficientNet and Xception. The transfer learning based models are evaluated on a standard apple fruit images dataset. The results demonstrate that the Xception model outperforms rest of the models with a significant margin, followed by EfficientNet, Inception-v3, MobileNet and ResNet model has the lowest accuracy.

References

[1] Milos Ilic, Sinisa Ilic, Srdjan Jovic, and Stefan Panic. Early cherry fruit pathogen disease detection based on data mining prediction. *Computers and Electronics in Agriculture*, 150:418–425, 2018.

[2] Paul Boissard, Vincent Martin, and Sabine Moisan. A cognitive vision approach to early pest detection in greenhouse crops. *Computers and Electronics in Agriculture*, 62(2):81–93, 2008.

[3] Prakhar Bansal, Rahul Kumar, and Somesh Kumar. Disease detection in apple leaves using deep convolutional neural network. *Agriculture*, 11(7):617, June 2021.

[4] Yang Lu, Shujuan Yi, Nianyin Zeng, Yurong Liu, and Yong Zhang. Identification of rice diseases using deep convolutional neural networks. *Neurocomputing*, 267:378–384, 2017.

[5] Y. Lecun, L. Bottou, Y. Bengio, and P. Haffner. Gradient-based learning applied to document recognition. *Proceedings of the IEEE*, 86(11):2278–2324, 1998.

[6] Peng Jiang, Yuehan Chen, Bin Liu, Dongjian He, and Chunquan Liang. Real-time detection of apple leaf diseases using deep learning approach based on improved convolutional neural networks. *IEEE Access*, 7:59069–59080, 2019.

[7] Bingze Dai, Tian Qiu, and Kai Ye. Foliar disease classification (2020).

[8] Kaiming He, Xiangyu Zhang, Shaoqing Ren, and Jian Sun. Deep residual learning for image recognition. In *Proceedings of the IEEE Conference on Computer Vision and Pattern Recognition (CVPR)*, June 2016.

[9] Christian Szegedy, Wei Liu, Yangqing Jia, Pierre Sermanet, Scott Reed, Dragomir Anguelov, Dumitru Erhan, Vincent Vanhoucke, and Andrew Rabinovich. Going deeper with convolutions. In *Proceedings of the IEEE Conference on Computer Vision and Pattern Recognition (CVPR)*, June 2015.

[10] Melike Sardoğan, Yunus Özen, and Adem Tuncer. Detection of apple leaf diseases using faster r-cnn. *Düzce Üniversitesi Bilim ve Teknoloji Dergisi*, 8(1):1110 – 1117, 2020.

[11] Lu Zhang and Michael J. McCarthy. Measurement and evaluation of tomato maturity using magnetic resonance imaging. *Postharvest Biology and Technology*, 67:37–43, 2012.

[12] Kamlesh Golhani, Siva K. Balasundram, Ganesan Vadamalai, and Biswajeet Pradhan. A review of neural networks in plant disease detection using hyperspectral data. *Information Processing in Agriculture*, 5(3):354–371, 2018.

[13] He Jiang, Xiaoru Li, and Fatemeh Safara. Iot-based agriculture: Deep learning in detecting apple fruit diseases. *Microprocessors and Microsystems*, page 104321, 2021.

[14] Sanjay Kumar, Abhishek Mallik, Akshi Kumar, Javier Del Ser, and Guang Yang. Fuzz-clustnet: Coupled fuzzy clustering and deep neural networks for arrhythmia detection from ecg signals. *Computers in Biology and Medicine*, page 106511, 2023.

[15] Sanjay Kumar, Abhishek Mallik, and BS Panda. Influence maximization in social networks using transfer learning via graph-based lstm. *Expert Systems with Applications*, 212:118770, 2023.

[16] Sanjay Kumar and Abhishek Mallik. Covid-19 detection from chest x-rays using trained output based transfer learning approach. *Neural processing letters*, pages 1–24, 2022.

[17] Kaiming He, Xiangyu Zhang, Shaoqing Ren, and Jian Sun. Deep residual learning for image recognition. *CoRR*, abs/1512.03385, 2015.

[18] Aston Zhang, Zachary C. Lipton, and Mu Li. Resnet, 2021.

[19] Andrew G. Howard, Menglong Zhu, Bo Chen, Dmitry Kalenichenko, Weijun Wang, Tobias Weyand, Marco Andreetto, and Hartwig Adam. Mobilenets: Efficient convolutional neural networks for mobile vision applications. *CoRR*, abs/1704.04861, 2017.

[20] Alok Chakraborty, Soumyajit Dey, Subhadip Mukhopadhyay, and Sugata Sanyal. Food image classification with improved mobilenet architecture and data augmentation, 2019.

[21] Christian Szegedy, Vincent Vanhoucke, Sergey Ioffe, Jonathon Shlens, and Zbigniew Wojna. Rethinking the inception architecture for computer vision. *CoRR*, abs/1512.00567, 2015.

[22] OpenGenus IQ. Inception-v3 model architecture, 2021.

[23] Mingxing Tan and Quoc V. Le. Efficientnet: Improving accuracy and efficiency through automl and model scaling, 2019.

[24] Mingxing Tan and Quoc V. Le. Efficientnet: Rethinking model scaling for convolutional neural networks. *CoRR*, abs/1905.11946, 2019.

[25] François Chollet. Xception: Deep learning with depthwise separable convolutions, 2016.

Authorized licensed use limited to: DELHI TECHNICAL UNIV. Downloaded on June 14,2023 at 05:00:06 UTC from IEEE Xplore. Restrictions apply.

2023 International Conference on Recent Advances in Electrical, Electronics & Digital Healthcare Technologies (REEDCON) | 978-1-6654-9382-6/23/$31.00 ©2023 IEEE | DOI: 10.1109/REEDCON57544.2023.10150800

AI based Approach for Solar PV Power Prediction with Varying Dust Accumulation Levels

Komal Singh
Department of Electrical Engineering
Delhi Technological University
Delhi, India
komalsingh2581998@gmail.com

M. Rizwan
Department of Electrical Engineering
Delhi Technological University
Delhi, India
rizwan@dce.ac.in

***Abstract*— Energy demand and concerns over greenhouse gases have made the integration of solar PV into the grid imperative. Solar power forecasting models must have a high prediction accuracy to address the intermittent nature of solar irradiation. Solar PV power is significantly affected by the dust deposited on the PV panel surface. The amount of dust deposited on PV panel as one of the input parameters to predict solar PV power and solar irradiation is performed in this paper. Multivariate analysis of three deep learning techniques that is LSTM (Long short-term memory), 1D CNN (Convolution Neural Network) and BilSTM (Bidirectional Long short-term memory) to predict the solar PV power and solar irradiation with varying dust accumulated levels for the 335 watt PV module installed on the rooftop of the lab at Delhi Technological University is presented. An artificial dust scenario is created by continually incrementing the dust level by 1.258 mg/cm^2.**

Keywords*— *1D CNN (Convolution Neural Network), LSTM (Long short-term memory), Bilateral LSTM, Dust levels, Multivariate forecasting, Solar PV

I. INTRODUCTION

According to government data, India's power consumption increased by 13.6% year on year to 112.81 billion units in November 2022. Approximately 770 million tonnes of coal equivalent (MTCE) will be consumed by 2030, rising annually thereafter before reaching a peak in the early 2030s in India. Over the next decade, coal is expected to continue to increase in definite terms, reaching a peak around 2030. However, its contribution to electricity generation is projected to drop from just under 75 percent to just under 55 percent. More than 60 percent of the growth in power demand will come from renewable energy sources, and 35 percent of electricity will come from renewable sources by 2030 - solar PV alone will account for more than 15 percent of the energy mix [1]. With such a high contribution of solar PV, the efficiency of solar PV in power production plays a crucial role.

The stochastic, volatile, and variable nature of solar power generation threatens the economic viability and stability of energy systems as well as its use as a renewable resource [2]. Solar source is irregular in nature as a result, PV power is intermittent and is highly dependent on irradiance, temperature level and other atmospheric parameters [3]. There are various factors affecting the power output of PV modules such as partial shading [4], dust [5], hotspots [6] and faults. Dust is a varying factor that can significantly affect PV power production. Smart grids may suffer from grid stability and reliability issues due to the high penetration of solar PV. Therefore, solar PV power forecasting plays a vital role in integrating renewable energy generation efficiently and reducing volatility in distributed generation systems [7].

There are various factors affecting the solar PV power forecast accuracy such as forecasting horizon, input parameters, weather classification etc [8]. There are two major approaches to predict solar PV output such as direct and indirect approach. The direct approach involves directly calculating the PV system's power output, whereas the indirect approach begins with calculating the solar irradiation, then uses a PV performance model to determine the PV system's power output. Cloud imagery and numerical weather prediction techniques are used in the indirect method, whereas machine learning is used in the direct method [9].

Solar forecasting can be accomplished using various statistical models such as ARIMA (autoregressive integrated moving average) [10], ARMA (autoregression and moving average) [11], VAR (vector autoregression); machine learning models [12] such as linear regression, SVM (support vector machine), KNN (K nearest neighbor) etc.; deep learning models [13] such as LSTM (long short-term memory), GRU (gated recurrent unit), autoencoders, Conv1D or CNN-1D (convolutional neural network). The irradiance can be predicted using machine learning techniques and statistical models such as artificial neural networks (ANN), support vector machines (SVM), vector autoregressive (VAR), autoregressive moving average (ARMA) and many more. However, they lack accuracy because they cannot capture long-term dependency [14]. Bi-LSTM is comprised of basically two LSTMs: a forward LSTM that utilizes past information and a backward or reverse LSTM that takes future information into use. Bi-LSTM achieves more accurate performance than LSTM and RNN (recurrent neural network) in general because it can use both past and future information [15].

This paper presents solar power and irradiation forecasting of the 335 watt module that is installed on the rooftop of the lab at Delhi Technological University. The parameters such as temperature (^{0}C), irradiation (W/m^2), PV power (W) and dust (g/cm^2) are collected. The temperature, irradiation and PV power are measured using a solar system PV analyzer. The dust level is incremented daily at regular levels by 1.258 mg/cm^2. PV power and solar irradiation prediction is performed using three ANN models: LSTM, BiLSTM and 1D CNN. The data is preprocessed using standardization and then passed through the ANN models for analysis. Dust accumulation on PV panels has a significant adversative impact on the solar cells' performance, especially in hot and arid regions [16]. Dust as a factor for solar PV forecasting is rarely done in the literature. The novelty of this paper lies in considering dust as an input parameter for predicting solar PV power and solar irradiation. An overview of ANN models, data preprocessing techniques and statistical indicators is presented in Section II. Section III describes the solar PV forecasting system. Sections IV and V constitute the results and conclusion, respectively.

Authorized licensed use limited to: DELHI TECHNICAL UNIV. Downloaded on June 28,2023 at 06:36:31 UTC from IEEE Xplore. Restrictions apply.

II. METHODOLOGY

A. LSTM (Long Short-term Memory)

LSTM is a recurrent type of neural network that can resolve the problem associated with vanishing and exploding gradients. Each unit of the LSTM contains information about the previous state. Instead of the same feedback loop connection, LSTM uses different paths for long and short-term memories. Unlike basic vanilla recurrent neural networks, LSTM is based on a much more complicated unit. The lack of weights allows long-term memories to flow through a series of unrolled units without causing the gradient to explode or vanish. At various stages, the sigmoid activation function determines the amount that LSTM remembers. A cell that acts as a memory can store, read or write information. In-coming information is stored when the cell reads, writes, or erases through the opening and closing of the gates. There are four neural network layers in the LSTM instead of one, each of which interacts with the others in a unique manner.

$$i_k = \sigma\,(W_i[h_{k-1}, \Psi_k] + b_i \quad (1)$$

$$f_k = \sigma\,(W_f[h_{k-1}, \Psi_k] + b_f \quad (2)$$

$$O_k = \sigma\,(W_o[h_{k-1}, \Psi_k] + b_o \quad (3)$$

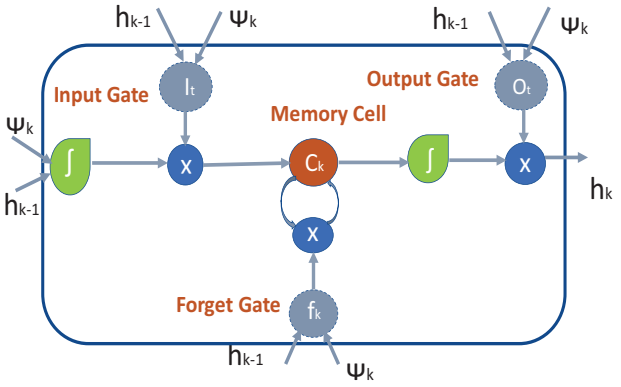

Fig.1. LSTM Structure

$$C'_k = tanh\,(W_C\,[h_k - 1, \Psi_k] + b_c \quad (4)$$

$$C_k = f_k * C_{k-1} + i_k * C'_k \quad (5)$$

$$h_k = O_k * tanh(C_k) \quad (6)$$

i_k = input gate, f_k = forget gate, O_k = Output gate

σ = sigmoid function,

Ψ_k = input at current timestamp ,

W_x = weight of the respective (x) gate neurons

$h_k - 1$ = output of the previous LSTM Block

b_x = bias of the respective gates (x)

C_k = Cell state (memory) at timestamp k

C'_k = represents candidate for cell state at timestamp k

The Cell state is the core concept of the LSTM technique LSTM networks comprise of different gates that contain information about the previous state. The first step of the long short-term memory unit is forget gate that determines what percentage of the long term memory is to be remembered. The second step is the input gate that determines how often long-term memory needs to be updated. The final stage of the LSTM updates the short-term memory, as this short-term memory is the output from this entire LSTM unit; this stage is known as the output gate.

Bidirectional LSTM encodes a sequence in both forward and backward directions and concatenates the results from both forward and backward LSTMs. In bidirectional LSTM, two models are trained. The first model learns the sequence of the input data samples provided, and the second model tries to learn the reversed sequence in the backward direction.

The merge step involves combining of both models; Merging can be done with one of the following operations:

- Concatenation (default)
- Sum
- Multiplication
- Averaging

B. 1D CNN (Convolutional Neural Network)

For handling 1-dimensional data, 1D-CNN or Conv1D is a suitable approach. Under identical conditions, the computational complexity of 1D-CNN is lower than that of its 2D counterpart. The types of layers present in a CNN architecture are CNN layers, flatten layers, dropout layers, fully connected dense layers or MLP (multilayer perceptron) layers. Configuration of a 1 D CNN comprises of a number of hidden CNN and MLP neurons, filter size and subsampling factor in each CNN layer and the choice of pooling and activation function.

A feature map can be obtained by using the filtering operation repeatedly on the layers. A feature map specifies the different attributes linked to the data samples. Convolution is a linear operation involving the multiplication of inputs with a certain set of weights. In 1D CNN, the inputs are multiplied by the kernel, that is a 1D array of weights. Executing this multiplication operation returns a unique value with each go, and with number of passes or go's, multiple values are obtained constituting a feature map.

After the feature map is obtained, each component is passed through an activation function. The ReLU activation function can be used to improve the performance of the model and also to overcome the problem of the vanishing gradient.

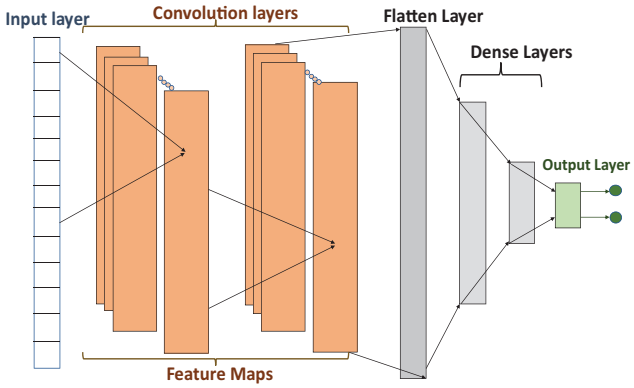

Fig.2. CNN Architecture

For aa 1D input sequence $X \in R^n$ and a filter $k \in R^{2m+1}$, the convolution operation is as shown in equation (7)

$$h(t) = x * z(t) = \sum_{z=-m}^{m} x(t-z).k(z) \quad (7)$$

Authorized licensed use limited to: DELHI TECHNICAL UNIV. Downloaded on June 28,2023 at 06:36:31 UTC from IEEE Xplore. Restrictions apply.

C. Data Preprocessing

Feature scaling is an important step in data preprocessing. Daily solar PV data is bell-shaped in nature, so standardization is a suitable preprocessing approach. ANN models perform better when the predictors are on the same scale. In Standardization, all features follow the reduced central normal distribution.

$$X_{standarized} = \frac{X-\mu}{\sigma} \quad (8)$$

μ = Mean

σ = Standard deviation

X = feature

D. Statistical Indicators

The statistical indices are used to test and examine the performance of the models. The performance metrics used are MAE (Mean Absolute Error), R^2 (R Squared Error), RMSE (Root Mean Square Error) and R_a^2 (Adjusted R squared error).

$$MAE = \frac{1}{N} \sum_{i=1}^{n} |Y_i - Y_i'| \quad (9)$$

Where Y_i is the actual result, Y_i' is the predicted result and N is the number of samples.

$$RMSE = \sqrt{\frac{1}{N} \sum_{i=1}^{n} (Y_i - Y_i')^2} \quad (10)$$

RMSE is the square root of the average of squared residuals. Residuals are estimated by subtracting the predicted value from the actual value.

$$R^2 = 1 - \frac{Mean\ Squared\ Error\ (Model)}{Mean\ Squared\ Error\ (Baseline)} \quad (11)$$

R squared error is another popular metric used for the evaluation of regression models, also known as the coefficient of Determination. The R-squared indices allow us to assess the performance of the model to a constant baseline. To determine a constant baseline, the mean of the data is taken and, a line is drawn through it.

As the number of input features is increasing the R^2 score is improved, even if the model is not improving. It may mislead the researchers; hence adjusted R^2 can also be calculated.

To overcome the problem of R square, adjusted R squared is used, which always returns a lower value than R2. This is due to the fact that it adjusts the values of increasing predictors and only shows improvement if there is a genuine improvement.

$$R_a^2 = 1 - [\frac{n-k}{n-k-1} * (1 - R^2)] \quad (12)$$

'n' is the number of data points and 'k' denotes the number of features or independent variable.

III. SYSTEM DESCRIPTION

The setup present on the rooftop of the laboratory is shown in fig. 3.

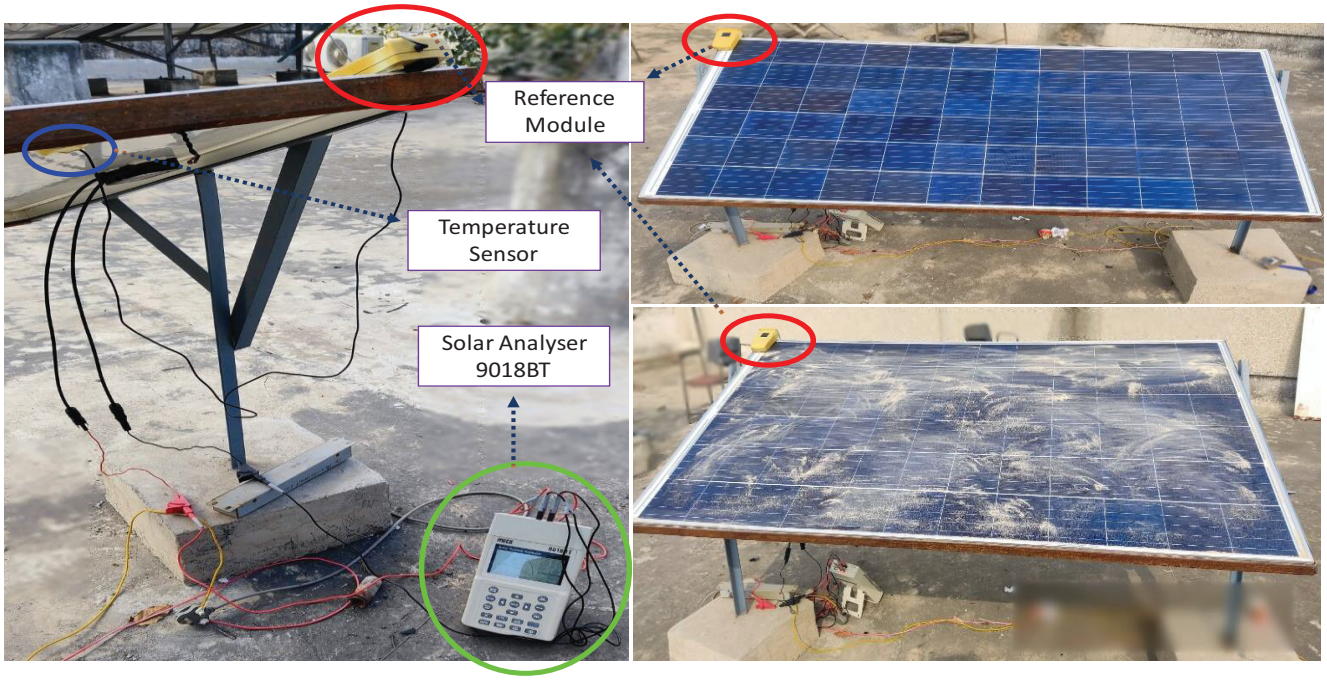

Fig. 3. Experimental Setup of solar forecasting with dust as input parameter

Fig. 3 shows the experimental setup for solar PV forecasting with dust as one of the input parameters. The 335 watt PV module is located on the rooftop of the laboratory and the data is collected from the solar system analyzer at intervals of 1 minute, and a total of around 2000 samples are collected.

The remote solar detector (reference module) measures the incident solar irradiation on the 335 watt module and the cell temperature. The considered parameters for the forecasting model are solar irradiation incident on the module (W/m^2), cell temperature (^0C), module output power (W) and dust (mg/cm^2).

Authorized licensed use limited to: DELHI TECHNICAL UNIV. Downloaded on June 28,2023 at 06:36:31 UTC from IEEE Xplore. Restrictions apply.

The dust is varied with an increment of 1.258 mg/cm^2 at regular intervals. The ratings of the 335 watt module are shown in the below table: -

TABLE I. 335 Wp MODULE RATINGS AT STC

Cell type	Polycrystalline
Rated output (P_{mpp})	335 Wp
Rated voltage (V_{mpp})	35 V
Rated current (I_{mpp})	7.10 A
Open Circuit Voltage (V_{oc})	40 V
Short circuit current (I_{sc})	7.5 A
Tolerance	± 8 %
Number of Cells	60
Module Area	1.9878 m^2
Bypass diode rating	10 A

The above table shows the ratings of the reference 335 watt module

IV. RESULTS

Fig. 4. and Fig. 5. show the solar irradiation (W/m^2) and solar power (W) data.

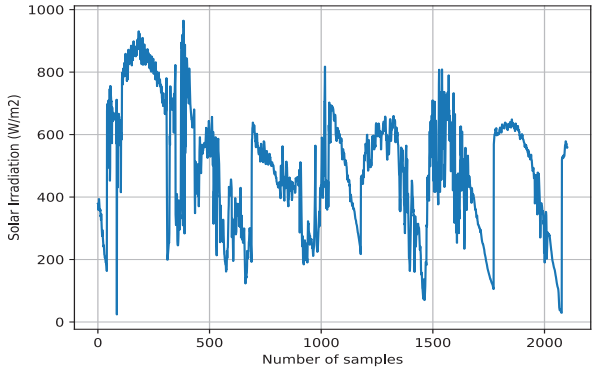

Fig. 4. Solar Irradiation (W/m^2) V/S Number of samples

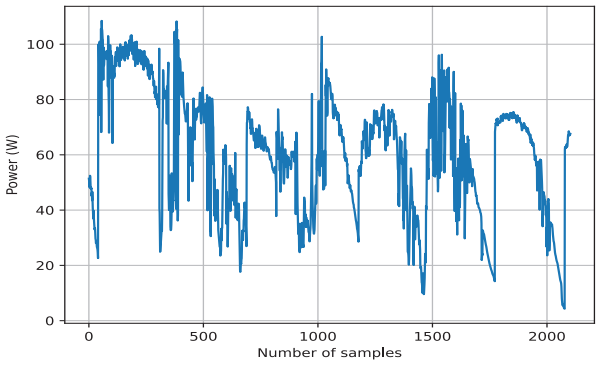

Fig. 5. Power (W) V/S Number of samples

The data is forecasted for three deep learning models; LSTM, 1D CNN and BiLSTM using a python jupyter environment. Multivariate forecasting is used to predict results for irradiation and power with other features as input parameters. The parameters for each model are shown in Table II

TABLE II. MODEL PARAMETERS

		1D CNN	LSTM	BiLSTM
Total Features		4 and 3	4 and 3	4 and 3
Layers	Number of Hidden layer /Neurons/ Activation function	1/64/ ReLU	1/64/ ReLU	1/64/ ReLU
	Number of Dense layer/Neurons/ Activation function	1/8/ ReLU + 1/1/ linear	1/8/ ReLU + 1/1/ linear	1/8/ ReLU + 1/1 /linear
	Number of flatten layer	1	1	1
Kernel Size		2	Not valid	Not valid
No. of Trainable Parameters		2641	18,193	36, 369
Epochs		50	50	50
Optimizer/ learning rate		Adam/ 0.001	Adam/ 0.001	Adam/ 0.001

Table II shows the model parameters; total number of features is considered as 4 for the case that considers dust as the input parameter and for the case without dust as the input parameter, the total number of features is 3. The parameters for all three models are kept equal to compare them at a level.

The Fig. 6. shows the comparison of all three models, with dust as an input parameter denoted with 'D' and without dust as an input parameter denoted as 'WD' with the actual results and it can be observed that the predictions are significantly improved for with dust as the input parameter case than as compared to the case that does not consider dust as input parameter for all three models.

As can be seen from Fig. 7, Fig. 8, Table III and Table IV, the BiLSTM model has the highest prediction accuracy compared to LSTM and Conv1D (1D Convolution neural network) models. The Conv1D model also gives very close results to the BilSTM model. Conv1D model has the least number of trainable parameters, and hence it takes the least time to get executed. As can be seen from Table III and Table IV, RMSE and MAE is least for BiLSTM for all cases, whereas RMSE is highest for BiLSTM compared to other models.

Authorized licensed use limited to: DELHI TECHNICAL UNIV. Downloaded on June 28,2023 at 06:36:31 UTC from IEEE Xplore. Restrictions apply.

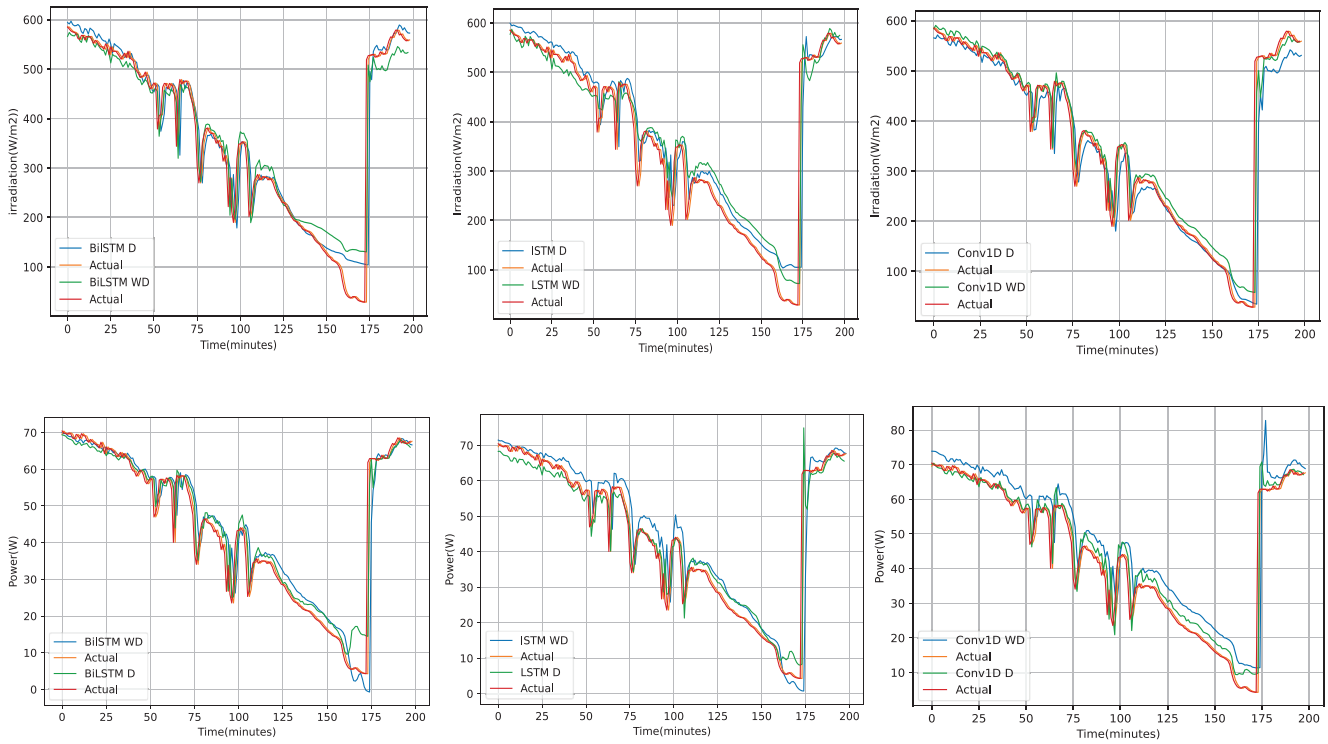

Fig. 6. Comparison of WD (Without dust as an input parameter) and D(with Dust as an input parameter) for different models

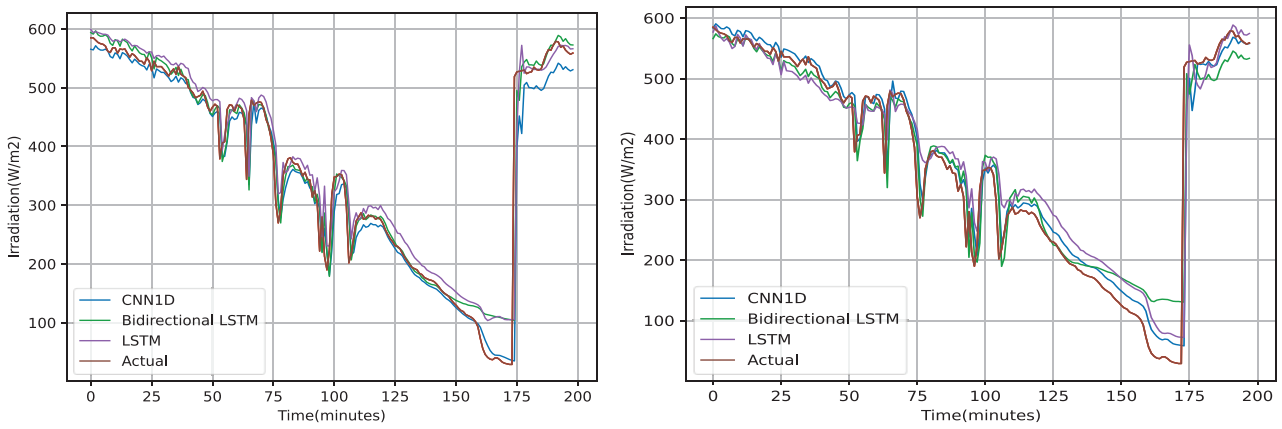

a)with dust as an input parameter b)without dust as an input parameter

Fig. 7. Comparison of different models for predicting irradiation with the actual irradiation results

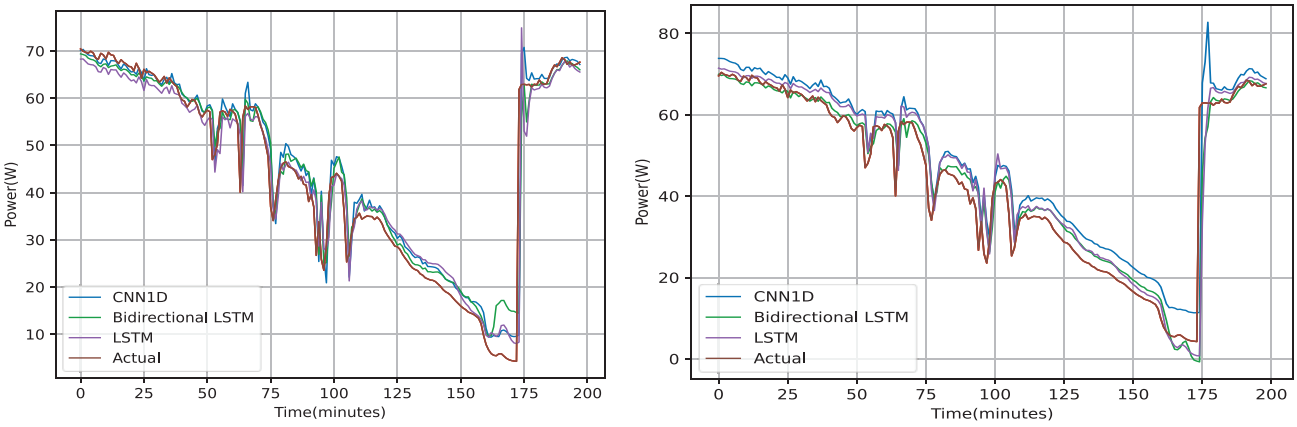

a)with dust as an input parameter b)without dust as an input parameter

Fig. 8. Comparison of different models for predicting power with the actual power results

Authorized licensed use limited to: DELHI TECHNICAL UNIV. Downloaded on June 28,2023 at 06:36:31 UTC from IEEE Xplore. Restrictions apply.

TABLE III. PERFORMANCE COMPARISON OF VARIOUS MODELS FOR PREDICTING POWER (W)

Power (W)		RMSE (W)	MAE (W)	R^2	Adjusted R^2
Dust	CNN 1D	5.35	5.12	0.937	0.89
	LSTM	5.35	4.8	0.931	0.86
	BiLSTM	5.32	4.65	0.94	0.90
Without Dust	CNN 1D	6.74	5.6	0.891	0.80
	LSTM	6.36	5.23	0.903	0.82
	BiLSTM	5.8	5.15	0.919	0.85

TABLE IV. PERFORMANCE COMPARISON OF VARIOUS MODELS FOR PREDICTING IRRADIATION (W/m^2)

Irradiation(W)		RMSE (W/m^2)	MA (W/m^2)	R^2	Adjusted R^2
Dust	CNN – 1D	42.7	33.8	0.938	0.89
	LSTM	44.84	35.2	0.932	0.87
	BiLSTM	40.3	31.3	0.944	0.91
Without Dust	CNN – 1D	43.09	33.9	0.937	0.88
	LSTM	49.62	33.0	0.9174	0.84
	BiLSTM	42.4	32.7	0.92	0.86

V. CONCLUSION

Dust is a significant factor affecting the performance of PV panels. Solar forecasting accuracy can be improved by considering dust as one of the parameters. The BiLSTM model has the highest forecasting accuracy but also has the highest number of trainable parameters, hence it will take more time to get executed, on the other hand 1D CNN has good accuracy but has a smaller number of trainable parameters so 1D CNN can be a preferable model to opt for in case of execution time constraints.

Future Scope of the work may include-

- Dust IQ meters can give more accurate dust measurements and thus can be used for solar power forecasting in future research.
- Hybrid artificial neural network techniques can also be tested for better prediction accuracy.

REFERENCES

[1] International Energy Agency, World energy outlook 2022. OECD, 2022.

[2] H. Wang et al., "Taxonomy research of artificial intelligence for deterministic solar power forecasting," Energy Convers. Manag., vol. 214, no. 112909, p. 112909, 2020.

[3] M. K. Behera, I. Majumder, and N. Nayak, "Solar photovoltaic power forecasting using optimized modified extreme learning machine technique," Eng. Sci. Technol. Int. J., vol. 21, no. 3, pp. 428–438, 2018.

[4] S. Rezazadeh, A. Moradzadeh, K. Pourhossein, M. Akrami, B. Mohammadi-Ivatloo, and A. Anvari-Moghaddam, "Photovoltaic array reconfiguration under partial shading conditions for maximum power extraction: A state-of-the-art review and new solution method," Energy Convers. Manag., vol. 258, no. 115468, p. 115468, 2022.

[5] F. Ekinci, A. Yavuzdeğer, H. Nazlıgül, B. Esenboğa, B. Doğru Mert, and T. Demirdelen, "Experimental investigation on solar PV panel dust cleaning with solution method," Sol. Energy, vol. 237, pp. 1–10, 2022

[6] R. Aman and M. Rizwan, "Power Enhancement and Hotspot Reduction of a Rooftop Solar PV Array Using MOSFETs," 2022 International Conference on Electrical, Computer, Communications and Mechatronics Engineering (ICECCME), Maldives, Maldives, 2022, pp. 1-6

[7] A. Kumar, M. Rizwan, and U. Nangia, "A hybrid intelligent approach for solar photovoltaic power forecasting: Impact of aerosol data," Arab. J. Sci. Eng., vol. 45, no. 3, pp. 1715–1732, 2020.

[8] R. Ahmed, V. Sreeram, Y. Mishra, and M. D. Arif, "A review and evaluation of the state-of-the-art in PV solar power forecasting: Techniques and optimization," Renew. Sustain. Energy Rev., vol. 124, no. 109792, p. 109792, 2020.

[9] C. Voyant et al., "Machine learning methods for solar radiation forecasting: A review," Renew. Energy, vol. 105, pp. 569–582, 2017.

[10] R. Perdomo, E. Banguero and G. Gordillo, "Statistical modeling for global solar radiation forecasting in Bogotá," 2010 35th IEEE Photovoltaic Specialists Conference, 2010, pp. 002374-002379

[11] B. Singh and D. Pozo, "A Guide to Solar Power Forecasting using ARMA Models," 2019 IEEE PES Innovative Smart Grid Technologies Europe (ISGT-Europe), 2019, pp. 1-4

[12] L. Huang, J. Kang, M. Wan, L. Fang, C. Zhang, and Z. Zeng, "Solar radiation prediction using different machine learning algorithms and implications for extreme climate events," Front. Earth Sci., vol. 9, 2021.

[13] P. Kumari and D. Toshniwal, "Deep learning models for solar irradiance forecasting: A comprehensive review," J. Clean. Prod., vol. 318, no. 128566, p. 128566, 2021.

[14] Alzahrani, A., Shamsi, P., Dagli, C., & Ferdowsi, M. (2017). Solar irradiance forecasting using deep neural networks. Procedia Computer Science, 114, 304–313.

[15] Y.-L. He, L. Chen, Y. Gao, J.-H. Ma, Y. Xu, and Q.-X. Zhu, "Novel double-layer bidirectional LSTM network with improved attention mechanism for predicting energy consumption," ISA Trans., vol. 127, pp. 350–360, 2022.

[16] H. Abuzaid, M. Awad, and A. Shamayleh, "Impact of dust accumulation on photovoltaic panels: a review paper," Int. J. Sustain. Eng., vol. 15, no. 1, pp. 264–285, 2022.

Authorized licensed use limited to: DELHI TECHNICAL UNIV. Downloaded on June 28,2023 at 06:36:31 UTC from IEEE Xplore. Restrictions apply.

This article has been accepted for publication in IEEE Transactions on Industrial Electronics. This is the author's version which has not been fully edited and content may change prior to final publication. Citation information: DOI 10.1109/TIE.2023.3281684

An Improved Hot Spot Mitigation Approach for Photovoltaic Modules Under Mismatch Conditions

Ranjeet Singh, Vinod Kumar Yadav, *Senior Member IEEE,*
and Madhusudan Singh, *Senior Member IEEE*

***Abstract*—The reduction of photogenerated current in photovoltaic (PV) cells due to various degradation mechanisms leads to hot spot (HS) generation, resulting in serious safety and reliability concerns. This article presents a novel hot spot mitigation circuit (HSMC), which effectively counters HS formation in cells under mismatch situations, improving the reliability of the entire PV arrangement. The effectiveness of the proposed HSMC is compared extensively with the conventional bypass diode (BPD) through experimentation on a 3×1 PV string and a 3×3 series-parallel (SP) PV array in an outdoor setting. Detailed thermographic analysis showed that the maximum temperature of the PV module under low shading levels reached 119.16 % and 54.11 % higher with the traditional BPD than with the proposed HSMC when tested on a 3×1 PV string and 3×3 SP PV array, respectively. This indicates that the mismatched cell was subjected to elevated temperatures with BPD. Moreover, the experimental results confirm that the proposed HSMC resulted in enhanced power output and a significant reduction of power loss in the bypass path of the shaded module under increased shading levels compared to the traditional BPD. The proposed HSMC reduced mismatch loss by up to 89.82 % when tested on a 3×1 PV string.**

***Index Terms*— Bypass circuit, hot spot, partial shading, power MOSFETs, PV system reliability, thermal imaging.**

I. INTRODUCTION

DUE to continued investment and ongoing innovation in photovoltaic (PV) technology over the past several years, commercial and residential PV installations are rapidly evolving globally [1]. Photovoltaic modules are renowned for their reliability, with a potential operational lifetime of over 30 years [2]. However, PV cells often experience malfunctioning or partial shading conditions (PSCs) that impede the optimal utilization of the modules and degrade the entire PV installation performance [3]. One such common abnormality in present-day PV installations is the formation of hot spots (HS) in PV cells[4], [5]. It was first observed in satellite power systems in the late 1960s and still exists today, which is highly detrimental to the operating lifetime of the module [6]–[9]. HS formation has severe implications for the reliability of the module and the system at large [10]. If allowed to persist for extended periods, HS formation in PV cells initiates accelerated thermal aging of the module with consequent irreversible damage.

Numerous other reliability issues govern the performance of PV modules in addition to HS generation. The occurrence of faults in maximum power extraction units coupled to string/modules is common in sizeable PV installations [11]. Potential induced degradation (PID) causes serious performance degradation to modules operating under field conditions [12]. Cell cracking, encapsulant delamination and discoloration, insulation weakening, solder bond failure and permanent soiling are some of the many performance defects associated with PV systems [13]. However, this article strictly addresses the issue of hot spot degradation in PV modules under PSCs and proposes counter measure to improve system performance.

The behavior of PV modules and their constituent materials response under actual stressed outdoor environmental conditions is the principal indicator of reliability, longevity, durability, and safety over the entire operating period. The reliability of PV modules is verified in accordance to the panel qualification standards laid down by European Standard EN61215 [14]. Under this certification procedure, before commercialization, the HS tolerant behavior of modules is tested by subjecting them to the worst expected operating scenarios through various HS endurance tests. Despite that, localized overheating resulting in module failure is a persistent reported phenomenon [15], [16].

Commercial PV module manufacturers provide bypass diodes (BPDs) that offer an alternative path for the string current to flow when certain cell(s) within a module generate reduced current owing to PSCs [17]. In most of the early reported works for HS mitigation, BPDs, have been exclusively employed as the only defense system against thermal overloads

Ranjeet Singh is with the Department of Electrical Engineering, Delhi Technological University, Delhi 110042, India (Email: ranjeetsingh_2k20phdee502@dtu.ac.in

Vinod Kumar Yadav is with the department of Electrical Engineering, Delhi Technological University, Delhi 110042, India (email: vinodkumar@dtu.ac.in)

Madhusudan Singh is with the department of Electrical Engineering, Delhi Technological University, Delhi 110042, India (email: madhusudan@dce.ac.in)

Authorized licensed use limited to: DELHI TECHNICAL UNIV. Downloaded on June 14,2023 at 05:30:41 UTC from IEEE Xplore. Restrictions apply.
© 2023 IEEE. Personal use is permitted, but republication/redistribution requires IEEE permission. See https://www.ieee.org/publications/rights/index.html for more information.

This article has been accepted for publication in IEEE Transactions on Industrial Electronics. This is the author's version which has not been fully edited and content may change prior to final publication. Citation information: DOI 10.1109/TIE.2023.3281684

in PV module design, a passive protection approach [18]. BPDs are connected in parallel across certain serially connected cells (standard industrial practice is to have a BPD across every $1/3^{rd}$ of the total module cells). A general misconception is that BPDs can counter localized thermal stress and evade it. However, previous studies have shown that BPDs are inadequate for countering HS formation, and severe damage can still occur even in their presence. The PV panels are typically rated for temperatures much lower than attained by the cells at the time of the HS event, which often causes the weakening of electrical joints with consequent initiation of the arc that increases the possibility of fire and poses serious safety issues [9]. Recently, active protection methods have drawn much interest among researchers [19],[20]-[23].

In [20], a cool bypass switch (CBS) is proposed. The protection circuit consists of a power MOSFET that is controlled by a controller, which is responsible for charging a storage capacitor. The MOS parasite diode is used during shading conditions. Unfortunately, the leakage current turns off the power MOS and affects the storage cycle of the capacitor. In [21], the proposed circuit relies on the function of only two NMOSTs to enable or disable the bipolar transistor device automatically. This circuit can be employed concurrently with the module integrated BPD. However, the circuit complexity increases manifold due to many devices operating in tandem to bring down the power dissipation significantly during increased shading events. In [22] and [23], a series connected MOSFET and IGBT is respectively used for subtracting the reverse voltage from the obscured cell and pushes the operating region of the shaded cell away from the thermal breakdown point. A significant reduction in the hot spot temperature of the shaded module was observed due to the transfer of reverse voltage applied on to the shaded cells from well illuminated cells to series MOSFET and IGBT switch.

Though these methods successfully cooled down the shaded cell temperature, the activation of the prevalent BPD during the onset of the shading condition was not elaborately discussed concerning shading ratio (SR). Additionally, none of the aforementioned techniques were tested using various PV module connections, and the majority of them were only experimentally validated for a single module or a PV string. The mitigation techniques that were reported, specifically those outlined in [22] and [23], did not address the issue of power loss caused by conduction of BPD during bypass events, nor did they discuss the power contribution to the existing PV arrangement post implementation. Additionally, complete gate driving circuits for the switches were not provided.

The following are the significant contributions of the proposed work:

1) An improved HS mitigation approach to counter module localized heating with enhanced power extraction under PSCs is proposed. The experimental analysis presented here is hence remarkably aligned with the improvement of PV reliability.

2) The reverse breakdown behavior and actual power loss in a completely shaded cell of a scaled-down PV module exhibiting HS condition is quantified.

3) The further objective of this article is to demonstrate the inability of the standard BPD to counter localized heating under low shading situations which is highly detrimental to the module's reliability.

4) Module-integrated BPDs conduct a significant portion of the string current during increased shading events. In this article, a power loss analysis is presented for both the conventional BPD and the proposed approach during these events.

The remainder of this article is organized as follows: The underlying theoretical aspects of PV behavior under non-ideal conditions supported by experimental analysis on a scaled-down PV module are presented in Section II. Section III deals with theoretical considerations of the proposed hot spot mitigation circuit (HSMC) and the experimental setup developed for validation of theoretical findings. Section IV focuses on the results and discussions of the experimental work performed for examining the hot spot endurance efficacy of the shaded portion of the module with the proposed HSMC. Finally, conclusions are drawn in Section V.

II. PV Response Analysis Under Non-Ideal Conditions

Analysis of PV behavior under mismatch conditions is extremely crucial for the utmost energy harvest from the PV installation and the system reliability.

A. Analysis of Power Loss in a Shaded Cell Exhibiting HS Behavior

Fig. 1(a) shows the PSC on one of the cells in a module. The respective I-V characteristics are displayed under each cell. As string current is increased from zero to the optimum point, the operating point of each PV cell shifts. Since all the cells are connected in series, each cell operating point in the module is obtained by the intersection of the individual cell I-V curves with the operational line horizontal to the x-axis. The operating point shifts as specified, $c_I \rightarrow b_I \rightarrow a_I$ for cell *I*, $c_{II} \rightarrow b_{II} \rightarrow a_{II}$ for cell *II* and $c_{III} \rightarrow b_{III} \rightarrow a_{III}$ for cell *III* .When the operating line corresponds to O_c, the shaded cell *III*, operates at its maximum power operating point (MPOP), c_{III} . However fully illuminated cells, *I* and *II* still do not operate at their MPOPs. As the operation line shifts to O_b, fully illuminated cells, *I* and *II* generates power at corresponding points b_1 and b_{II} . The new string current corresponding to this operation line (indicated by a solid line in Fig. 1(a)) happens to be higher in magnitude than the short circuit current of the shaded cell *III*, causing the reverse voltage across this cell. Since the voltage polarity is reversed with current still flowing in the same direction, cell *III* now acts as a sink of power instead of a power source. If allowed to operate under this condition for a prolonged duration, cell *III* acting as a load will dissipate substantial power as heat, thus immensely causing the cell's local temperature to rise. At O_a, the reverse voltage impressed on the shaded cell, *III* increases with cells *I*, *II* and *III* operating respectively at points a_I, a_{II} and a_{III}. Interestingly, although PV cells *I* and *II* generate

Authorized licensed use limited to: DELHI TECHNICAL UNIV. Downloaded on June 14,2023 at 05:30:41 UTC from IEEE Xplore. Restrictions apply.
© 2023 IEEE. Personal use is permitted, but republication/redistribution requires IEEE permission. See https://www.ieee.org/publications/rights/index.html for more information.

This article has been accepted for publication in IEEE Transactions on Industrial Electronics. This is the author's version which has not been fully edited and content may change prior to final publication. Citation information: DOI 10.1109/TIE.2023.3281684

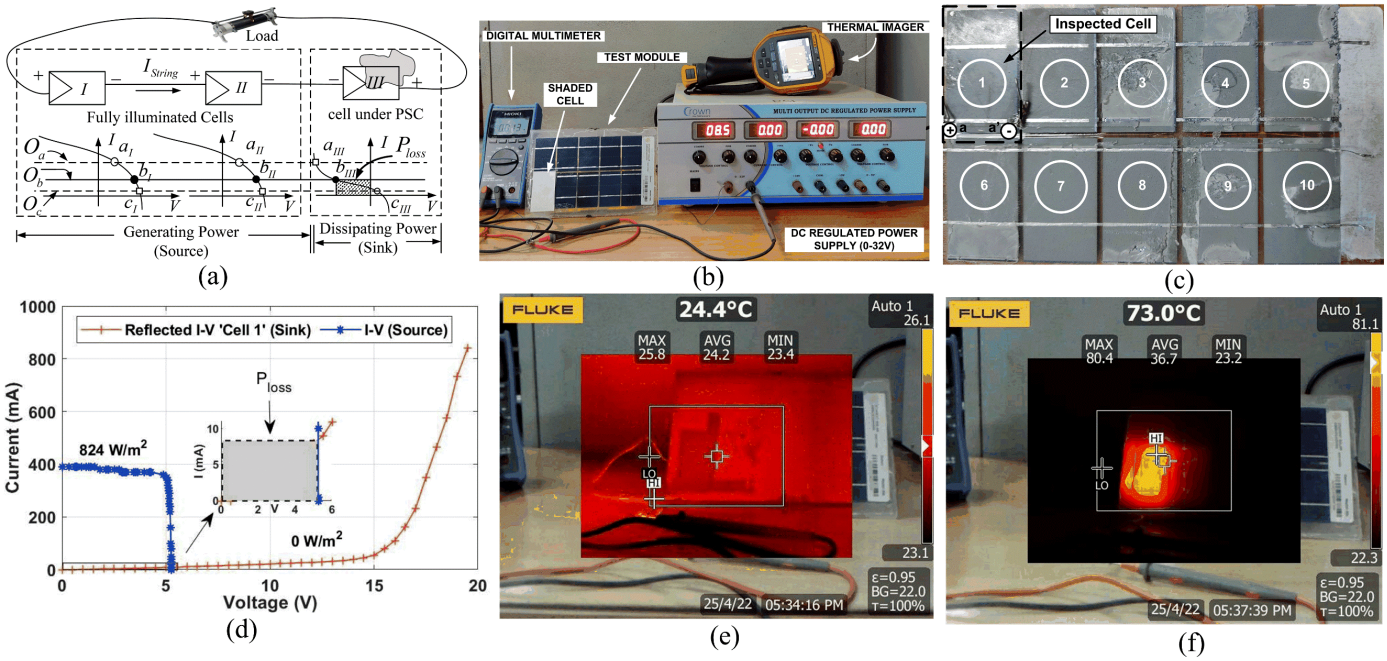

Fig. 1. (a) Typical response of PV cells under PSC (b) experimental arrangement to examine reverse characteristics (1 cell shaded) (c) rear view of the disintegrated module (d) measured power loss, P_{loss} of a completely shaded cell (cell '1') (e) thermographic behavior of a test module under normal condition (f) thermographic behavior of the same module exhibiting HS condition under reverse bias.

power at their respective MPOPs, the shaded cell, *III* dissipates tremendous power as heat, downgrading the overall system efficiency heavily and posing serious safety and reliability concerns. To practically validate the theoretical considerations presented here, a scaled-down PV module (2.5 Wp rating) was employed as a test module to estimate the impact of completely shading one cell. Fig.1 (b) shows the experimental setup for analyzing the power loss in a completely obscured cell exhibiting HS. The PV module was disintegrated for accessing the shaded cell (cell '1') terminals marked by '+' and '–' (see Fig.1(c)). Reverse characteristics of a completely shaded cell (cell '1', acting as load) were estimated by gradually varying the reverse bias applied to the cell and measuring the resultant current at various instants. At natural solar irradiance of 824 W/m^2, the forward I-V characteristics of the unshaded cells (acting as source) were measured. To determine the power loss in the shaded cell, the measured reverse characteristics were reflected and superimposed on the forward I-V curve of the source in the first quadrant. The operating point of the PV module is the point of intersection of the I-V characteristics of the source (9 unshaded cells) and the sink (1 shaded cell) (see Fig. 1(d)). The shaded area is the measure of power loss occurring in the completely shaded cell, with the remainder of the cells generating power (maximum power of 1.764 W @ 824 W/m^2). The power loss, P_{loss} is estimated to be 52.54 mW, accounting for 2.98 % of the maximum generated power output at the specified irradiance. Interestingly, this loss further intensifies as the cell area under the shading ambit reduces. The number of cells connected in series for the inspected module is 10 (see Fig 1(c)) and the cumulative open circuit voltage of the module is merely 6 V. The shaded cell is compelled to dissipate substantial power as heat causing significant localized temperature leading to an extremely inefficient system as the

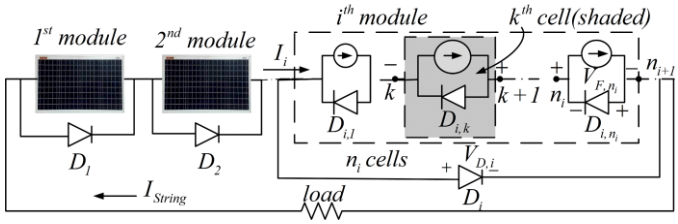

Fig. 2. PV string behavior under mismatch condition.

number of series connected cells increases. Infrared (IR) images (see Fig. 1(e) and Fig. 1(f)) revealed that the temperature of the examined cell increases by over 200 % (80.4 ^0C) from the normal conditions (25.8 ^0C) even on gradual application of reverse bias within 3 minutes, indicating that the cell has entered the avalanche breakdown region beyond -15 V. Hence, there is a need to devise effective technological solutions to mitigate this localized generated heat in the affected cell to prevent unwanted damage and consequential economic loss.

B. Reverse Voltage Across a Shaded cell: Mathematical Analysis

Consider n_i number of series cells forming the module. For the PV configuration under observation (3×1 string), n_i equals 36. To keep the analysis simple, the ideal single diode circuit model (Rsh=∞, Rs=0) of the participant cells of the module is considered [24] (see Fig. 2). The reverse voltage imposed upon the obscured cell of the module can be quantified by employing Kirchhoff's voltage rule on the loop through individual module integrated BPD. Due to the virtual disconnection of the series circuit at the k^{th} node of the i^{th} module in the string because of the mismatch event at the k^{th} cell, the current is forced to pass through the intrinsic diode, $D_{i,j}$ of individual cells, thus incurring a voltage drop of $V_{F,j}$ The voltage between k^{th} and

Authorized licensed use limited to: DELHI TECHNICAL UNIV. Downloaded on June 14,2023 at 05:30:41 UTC from IEEE Xplore. Restrictions apply.
© 2023 IEEE. Personal use is permitted, but republication/redistribution requires IEEE permission. See https://www.ieee.org/publications/rights/index.html for more information.

This article has been accepted for publication in IEEE Transactions on Industrial Electronics. This is the author's version which has not been fully edited and content may change prior to final publication. Citation information: DOI 10.1109/TIE.2023.3281684

$(n_i+1)^{th}$ terminal of any shade affected i^{th} module can be estimated as:

$$v_k^{n_i+1} = -V_{D,i} - \sum_{j=1}^{k-1} V_{F,j} \quad \left\{ \begin{array}{l} \forall\ i = 1,2,3\ (module\ indices) \\ \forall\ j = 1,2,3,\ldots n_i\ (cell\ indices\ of\ the\ shaded\ module) \end{array} \right\} \quad (1)$$

where $V_{D,i}$ is the forward voltage drop of the i^{th} module integrated BPD, D_i and $V_{F,j}$ is the forward voltage drop of the intrinsic diode, $D_{i,j}$ corresponding to the j^{th} cell. It must be noted that the i^{th} module integrated BPD, D_i conducts only when condition (2) is met.

$$I_{String} > I_i \quad (2)$$

where I_{String} is the total current of the PV string and I_i is the current of the i^{th} module. The voltage across $(k+1)^{th}$ and $(n_i+1)^{th}$ terminal of the i^{th} module in the string can be calculated as:

$$v_{k+1}^{n_{i+1}} = \sum_{j=k+1}^{n_i} V_{F,j} \quad (3)$$

Using (1) and (3), the voltage across the k^{th} mismatched cell of the i^{th} module of the string can be determined as:

$$v_k^{k+1} = v_k^{n_{i+1}} - v_{k+1}^{n_{i+1}} = -\left(V_{D,i} + \sum_{j=1}^{k-1} V_{F,j} + \sum_{j=k+1}^{n_i} V_{F,j} \right) \quad (4)$$

To have good reliability in the design, the value of n_i should be kept sufficiently low to avoid entering the breakdown region of the shaded cell. The following voltage condition (5) must be met for any arbitrary shaded cell, *k*, at all times to evade any premature aging and subsequent damage due to the elevated temperature operation for a prolonged duration:

$$v_k^{k+1} = -\left(V_{D,i} + \sum_{j=1}^{k-1} V_{F,j} + \sum_{j=k+1}^{n_i} V_{F,j} \right) << V_{BV,k} \quad (5)$$

where $V_{BV,k}$ is the breakdown voltage of the k^{th} cell. Substituting the forward voltage drop, for the intrinsic diode $D_{i,j}$ ($V_{F,j} = 0.6\,V$) and standard BPD ($V_{D,i} = 0.5V$), the peak value of the reverse voltage across the mismatched cell may be realized as 21.5 V for the module under inspection (single BPD per module). Following the same rationale, the peak reverse voltage across non-productive cells may also be estimated for other commercially available modules viz; 60 cells (11.9 V) and72 cells (14.3 V) having BPD across each one-third of the cells in module. As discussed in the preceding section, the magnitude of reverse bias across PV cells dominates the cell operating temperature under shading conditions. The avalanche breakdown behavior is expected from the alkaline, and acidic texturized PV cells at -15 V to -20 V for the former and -13 V for the latter [21]. One approach to safeguard masked cells is to have BPD across each cell body. However, this is not an economical option from manufacturer's point of view and may result in complexity and extended power losses with more diodes being in conduction and is highly unlikely to be incorporated in the immediate future. Another approach would be to employ short string lengths that enhance HS mitigation effectiveness using BPDs. Again, module manufacturers do not accept this solution commercially because of the involved costs.

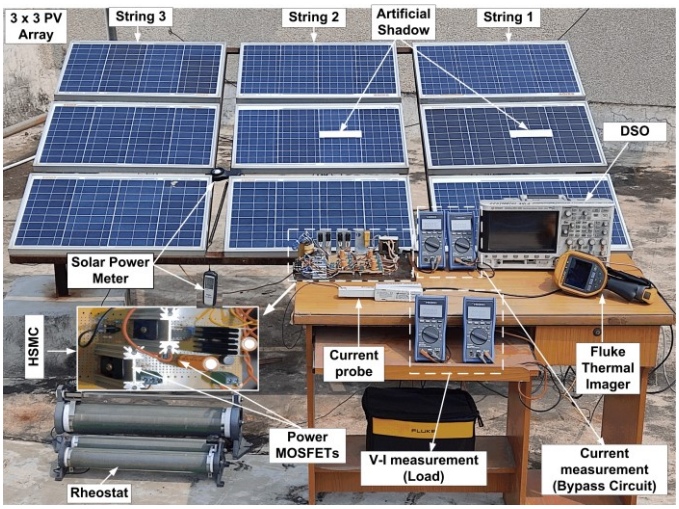

Fig. 3. Experimental setup for assessing the thermal reliability of the module under PSC.

TABLE I
SPECIFICATIONS OF THE EXPERIMENTAL PLATFORM

Equipment	Parameter	Value
PV module	Maximum Power	40 W
	Open-circuit voltage	22.18 V
	Voltage at MPP	18.00 V
	Current at MPP	2.22 A
	Short circuit current	2.40 A
	Number of cells	36(=9×4)
	Tolerance	+ 0 to 5W
Thermal Imager	Type	FLUKE Ti400
	Detector resolution	320 × 240 pixels
	Thermal Sensitivity (NETD)	≤0.05 °C at 30 °C target temp (50 mK)
	Accuracy	±2 °C or 2%
	Frame rate	60 Hz
	IFOV (spatial resolution)	1.31 mRad
Solar Power meter	Make: MECO instruments	
Rheostats	Rating 100 Ω /5 A (2 units in series connection)	
Multimeters	2 units (Type: FLUKE 101)	
Digital Storage Oscilloscope	4 Channel (Type: KEYSIGHT DS0-X 2024A, 200Mhz)	

II. PROPOSED HSMC AND EXPERIMENTAL SETUP

A. Experimental Setup

In the present work, an analysis and validation of the MOSFETs-based HSMC approach is described in detail. Fig. 3 shows the developed experimental set-up which consists of nine identical PV modules mounted on the same supporting frame, aligned in the same direction and at the same inclination. This arrangement enables them to be tested at exactly similar time

Authorized licensed use limited to: DELHI TECHNICAL UNIV. Downloaded on June 14,2023 at 05:30:41 UTC from IEEE Xplore. Restrictions apply.
© 2023 IEEE. Personal use is permitted, but republication/redistribution requires IEEE permission. See https://www.ieee.org/publications/rights/index.html for more information.

This article has been accepted for publication in IEEE Transactions on Industrial Electronics. This is the author's version which has not been fully edited and content may change prior to final publication. Citation information: DOI 10.1109/TIE.2023.3281684

and conditions. The electrical characteristics of the PV modules under standard test conditions (STC) and the critical specifications of the thermal imager to access the HS are reported in Table I. The 3×1 PV string and 3×3 series-parallel (SP) array was examined under the effect of the artificial shadow of varying SR (1 cell-shaded: 2.77% and 2 cell-shaded: 5.55%) under the same operating and ambient conditions. Here SR is computed as the ratio of number of shaded cells to the total number of cells in the module. For instance, the total number of cells in the considered module are 36. So, 1 cell shading corresponds to a SR of 0.027 (or 2.77 %) and likewise. The artificial shadow-infected module was examined with both standard BPD and integration with the proposed HSMC. Thermal imaging measurements of the shaded cell were performed to quantify the impact of the mismatch effect in the PV system under examination since detecting HS using thermal imaging is a universal approach. The key outcomes of the experimental analysis with detailed discussions are presented in Section IV.

B. Proposed HSMC Topology

The proposed approach is based on dual power MOSFET configuration. MOSFET Q_1 is connected serially between the module and the load whereas MOSFET Q_2 is connected across the module, as shown in Fig 4(a). In the event of PSC, Q_2 is driven into conduction, offering a near short circuited path across the affected module, thus providing bypass, whereas Q_1 provides a reduction in reverse voltage across the shaded cell, which is reflected as an improved temperature reduction of the shaded cell than the standard BPD circuit. As discussed in the preceding section, *II.B*, the maximum reverse voltage impressed on the k^{th} shaded cell of any i^{th} module is the sum of intrinsic diode forward voltage drop, V_F of the remaining unshaded cells and forward voltage drop of the conducting BPD, V_D. To bring the temperature of the shaded cell well within the safe limits, the reverse voltage imposed on the cell needs to be pushed sufficiently low to prevent the mismatched cell from reaching the avalanche breakdown region. Under normal operation ((Mode I: Unshaded condition), the switch Q_1 is in conduction having low value of drain to source voltage, $V_{DS,1}$ while the switch Q_2 is not conducting any current. So, the string current I_{String}, coincides with the drain current of the MOSFET Q_1, i.e. $I_{String} = I_{DS,1}$ and the corresponding system output includes generation from all the three PV sources . Under PSC (Mode II: ≥ 1 cell shading), the switch Q_1, stops conduction, and the bypass circuit involving the switch Q_2 gets activated. Thus, the string current, I_{String} equals the drain current of the switch Q_2 i.e. $I_{String} = I_{DS,2}$ with the consequence that the affected module is effectively bypassed (see Fig. 4(a)). Interestingly, the current through the switch, Q_1 is decreased, and the corresponding operating point shifts to a higher value of drain to source voltage, $V_{DS,1}$. The modified reverse voltage across the k^{th} shaded cell of the i^{th} module using the proposed HSMC can be estimated similarly as discussed in section *II.B*.

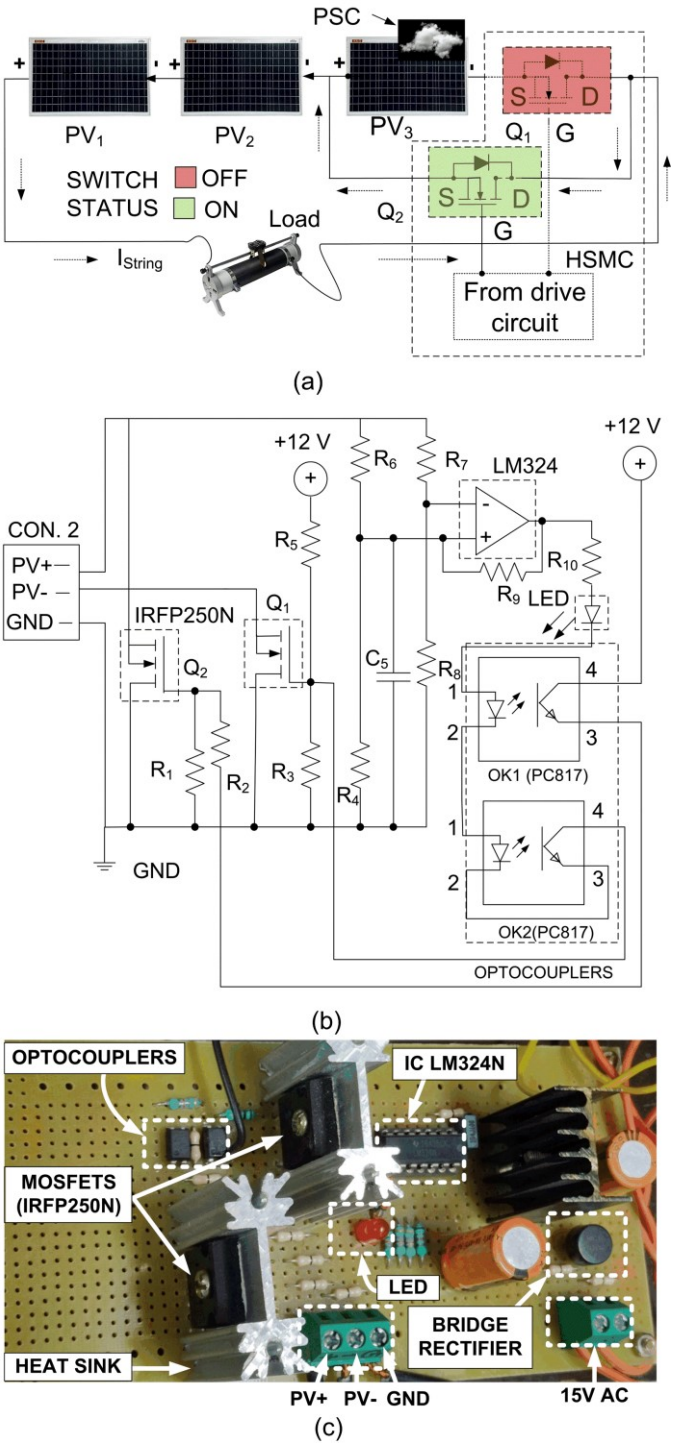

Fig.4. Proposed HSMC: (a) Operation mechanism of the proposed HSMC under mode II: PSC. (b) circuit arrangement (c) hardware prototype for experimental validation.

$$v_k^{k+1} = -\left(V_{DS,2,i} + \sum_{j=1}^{k-1} V_{F,j} + \sum_{j=k+1}^{n_i} V_{F,j} \right) + V_{DS,1,i} \qquad (6)$$

where $V_{DS,1,i}$ and $V_{DS,2,i}$ are the drain to source voltages across switches Q_1 and Q_2 respectively of the proposed circuit integrated to the i^{th} module. On comparing (4) and (6), an apparent reduction in the reverse voltage appearing across the mismatched cell can be ascertained. Thus, the proposed HSMC

Authorized licensed use limited to: DELHI TECHNICAL UNIV. Downloaded on June 14,2023 at 05:30:41 UTC from IEEE Xplore. Restrictions apply.
© 2023 IEEE. Personal use is permitted, but republication/redistribution requires IEEE permission. See https://www.ieee.org/publications/rights/index.html for more information.

This article has been accepted for publication in IEEE Transactions on Industrial Electronics. This is the author's version which has not been fully edited and content may change prior to final publication. Citation information: DOI 10.1109/TIE.2023.3281684

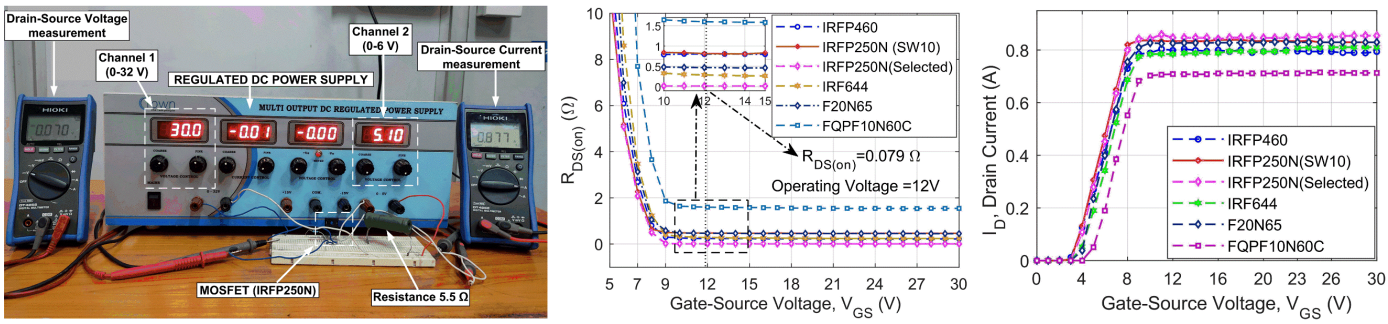

Fig. 5. Experimental investigation of different MOSFETs for HSMC: (a) Experimental test set up (b) determination of drain-source on-state resistance (c) Gate-to-source Vs drain current characteristics.

performs significantly better in reducing the voltage imposed on the shaded cell under PSC with the consequent shift of the operating point to a safe value, much lower than the avalanche breakdown region of the cell, thus ensuring safe and reliable operation. The complete circuit arrangement showing the gate driver circuits for the individual switches, Q_1 and Q_2 along with the complete hardware realization is shown in Fig. 4(b) & (c) respectively. The 15 V AC supply is drawn from a step-down transformer (not shown in the circuit) fed from a 230 V, 50 Hz single phase source. To reduce the on-state power losses of HSMC, a meticulous selection of switches from a variety of available MOSFET ratings is carried out through extensive initial experimental analysis on a laboratory setup before their deployment into operation, as depicted in Fig. 5(a). MOSFETs (IRFP250N) having low on-state drain-source resistance $R_{DS(on)} = 0.079\,\Omega$ is selected for HSMC [25]. The operating gate-to-source voltage, V_{GS} for the proposed circuit, is 12 V. The variation of on-state drain-source resistance $R_{DS(on)}$ and drain current, I_D for different values of gate-to-source voltage, V_{GS} for various examined MOSFETs, are also shown in Fig. 5(b) and (c). A generalized flowchart depicting various operational stages of the conventional BPD and the proposed HSMC approach is shown in Fig. 6.

IV. Results and Discussion

To corroborate the practical workability of the proposed control approach, key measurements and thermal inspection of 3×1 PV string system were carried out after intentionally shading the different number of cells under similar operating and ambient conditions. A 3×3 PV array configured in a SP arrangement is also considered for experimental analysis and thermographic inspection for testing the performance of the proposed HSMC extensively.

A. Experimental Measurements (Electrical characteristics, Dynamic response, and Power loss estimation)

1) Electrical Characteristics: The solar irradiance varied from 700-815 W/m^2 during the entire experimental investigation. The PV system's electrical characteristics were measured under various operating conditions, viz. normal condition (NC) (unshaded), PSC (No Bypass: 1 cell shaded (HSMC 'OFF')), bypass with standard BPD ((2 cells shaded) &

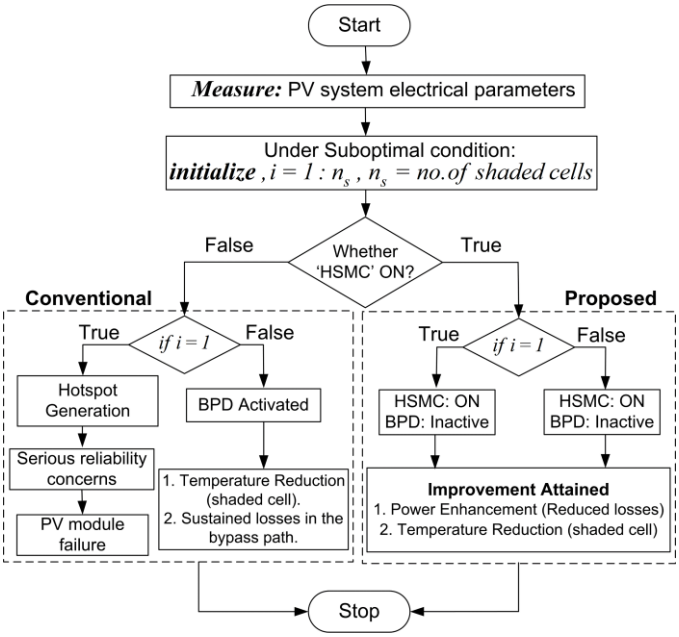

Fig.6. Flow chart summarizing the various stages of the conventional and the proposed HS mitigation approach.

(HSMC 'OFF')) and lastly bypass with proposed HSMC (≥ 1cell shaded) by performing the complete scan of the operating region achieved through variation of a resistive load. The measured P-V and I-V characteristics at 700 W/m^2 for 3×1 PV string system under predefined conditions are shown in Fig. 7(a) and (b) respectively. A maximum power enhancement of 5.0 % under 2 cells shading condition is attained with the proposed HSMC. The variation of current through the bypass circuits with string voltage was also measured as depicted in Fig. 7(c). Under 1-cell shading, BPD is not activated, since negligible current flows through it, as a result, HS formation is inevitable for all the operating points of the affected module located in between the short circuit region and close to MPOP region. The shaded area in Fig.7(c) represents the hot spot-prone region for the shade-affected module under 1-cell shading (protected through traditional BPD). As the shading area is increased to 2 cells, BPD starts to conduct string current though not completely. On the contrary, the HSMC completely bypassed the affected module even at the slightest of the shading event ensuring safe operation. The P-V and I-V curves for a 3×3 SP PV array under different operating conditions are shown in Fig. 8(a) and (b) respectively. On integration with proposed HSMC, a maximum power enhancement of 2.42 % is observed when one of the modules of the array is subjected to

Authorized licensed use limited to: DELHI TECHNICAL UNIV. Downloaded on June 14,2023 at 05:30:41 UTC from IEEE Xplore. Restrictions apply.
© 2023 IEEE. Personal use is permitted, but republication/redistribution requires IEEE permission. See https://www.ieee.org/publications/rights/index.html for more information.

This article has been accepted for publication in IEEE Transactions on Industrial Electronics. This is the author's version which has not been fully edited and content may change prior to final publication. Citation information: DOI 10.1109/TIE.2023.3281684

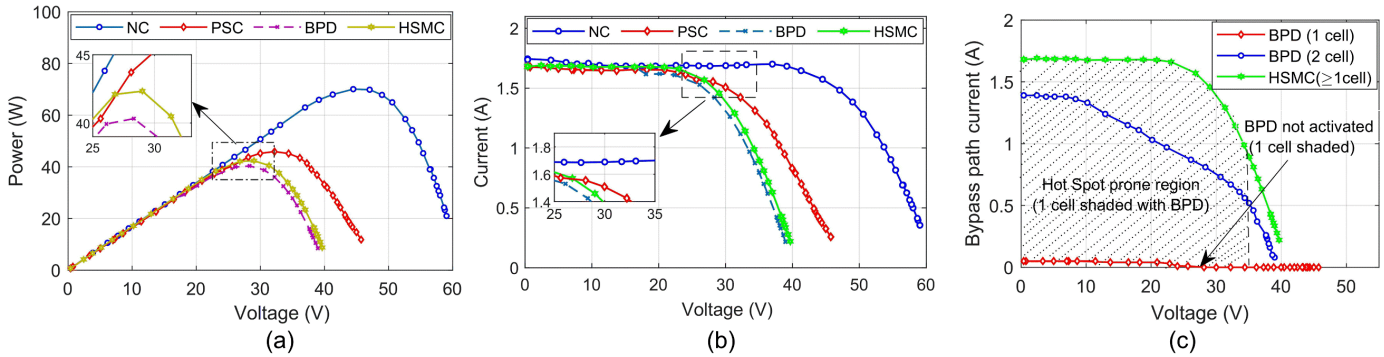

Fig.7. Measured electrical characteristics of 3×1 PV string. (a) power-voltage curves (b) current-voltage curves (c) PV string voltage vs bypass path current.

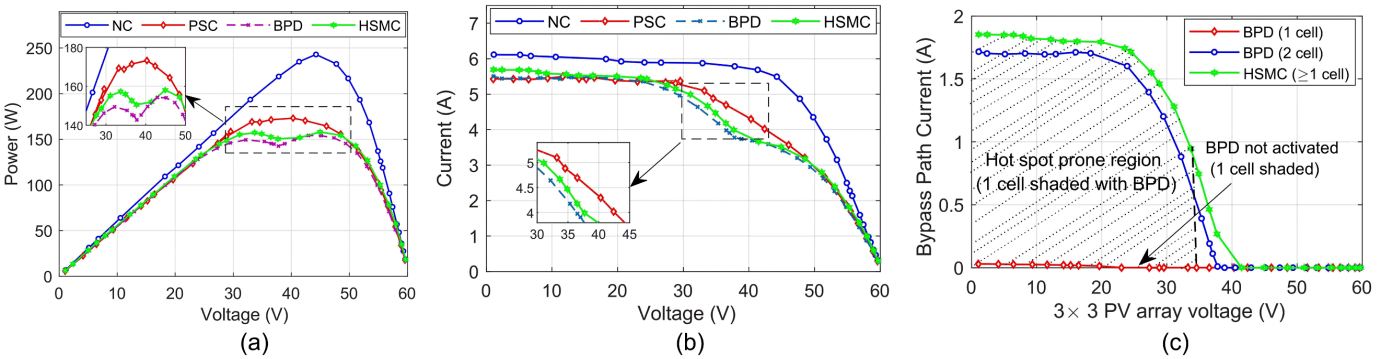

Fig. 8. Measured electrical characteristics of 3×3 SP PV array (a) power-voltage curves (b) current-voltage curves (c) PV array voltage vs bypass path current.

2 cell shading conditions. Similar experimental measurements were carried out as done on 3×1 PV string system to examine the response of the bypass circuit to varying shading conditions. As before, conventional BPD completely failed in bypassing the shade-affected module under 1-cell shading. The hot spot-prone region under 1-cell shading for the module protected through BPD is depicted in Fig. 8 (c).

To extensively investigate the behavior of BPD during 1 cell shading conditions, series of experiments were conducted on three 3×1 PV strings, each comprising of different ratings of PV modules viz. M1: 50 W, M2: 10 W, M3: 40 W respectively. Experimental results confirm that BPD failed to conduct during 1 cell shading even close to the short circuit conditions (refer Fig. 9) in all the three considered PV string systems subjecting the mismatched cell to elevated temperatures.

2) Dynamic response analysis of the PV system: To better analyze the various operating modes of the PV systems, the dynamic response is captured on a Digital Storage Oscilloscope (DSO). Clear transitions among different functional stages of 3×1 PV string system and 3×3 SP PV array are respectively observed through experimental waveforms recorded as shown in Fig. 10(a) and (b). A complete scan of the system operation is carried out using DSO for a total duration of 50 s and the system response at various transitions are captured for the 3×1 PV string and the 3×3 SP PV array. For the initial 12 s, the system is operating under NC (unshaded), with the operating voltage and current of the PV string being 56.56 V and 0.690 A, respectively as shown in Fig. 10 (a). The onset of PSC (1 cell completely obscured) occurs at t=12 s, string voltage, and current dip and settles to new values of 43.2 V and 0.52 A, respectively. Under this condition, no bypass

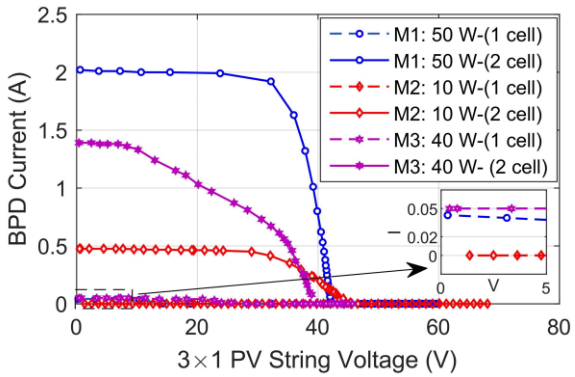

Fig. 9. BPD current vs. String voltage under 1 cell and 2 cell shading for different rating modules.

circuit is active. At t=22 s, BPD gets activated (under 2- cell shading) and provides a bypass path to the string current. Under this condition, the string voltage and current recorded were 37.2 V and 0.479 A respectively. Interestingly, BPD activation starts only for ≥ 2 cell shading conditions, thus exposing the mismatched cell to thermal degradation over time for low (<2 cell) shading conditions and hence may initiate irreversible failure of the module. At t=32 s, shading is reduced to 1 cell again, and the proposed HSMC is activated resulting in immediate activation of the bypass circuit with the corresponding string voltage and current values being 37.9 V and 0.489 A respectively. The system is left unattended for a further 10 s, and at t = 42 s, the artificial shading is withdrawn. The system restores to normal condition with corresponding string voltage and current values being 56.56 V and 0.690 A, respectively. The corresponding system parameters are listed in Table II. For brevity, since the same workflow was observed with the 3×3 SP PV array (near MPOP region) (see Fig. 10(b)),

Authorized licensed use limited to: DELHI TECHNICAL UNIV. Downloaded on June 14,2023 at 05:30:41 UTC from IEEE Xplore. Restrictions apply.
© 2023 IEEE. Personal use is permitted, but republication/redistribution requires IEEE permission. See https://www.ieee.org/publications/rights/index.html for more information.

This article has been accepted for publication in IEEE Transactions on Industrial Electronics. This is the author's version which has not been fully edited and content may change prior to final publication. Citation information: DOI 10.1109/TIE.2023.3281684

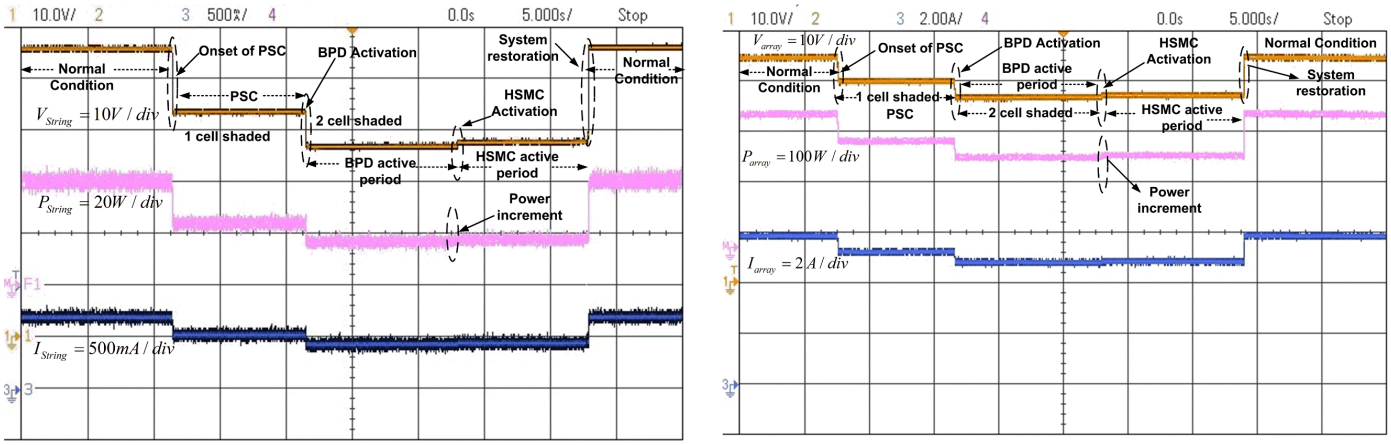

(a) (b)

Fig. 10. Experimental waveforms showing PV system dynamic response (a) 3×1 PV string (b) 3×3 SP PV array.

hence it is not presented here in detail but is listed for reference in Table III.

3) Estimation of Power Loss (3×1 PV String): The power loss, $P_{byp,loss}$ occurring in the bypass path of the shaded module protected through the conventional BPD and the proposed HSMC for the 3×1 PV string is measured for different shading cases for the entire operating zone of the PV string as depicted in Fig. 11. It is observed that since under 1 cell shading, the standard panel integrated BPD does not go into conduction, the $P_{byp,loss}$ is therefore apparently the least. However, as the number of shaded cells is increased and BPD goes into full conduction, significant power loss occurs in the bypass path of the module. The $P_{byp,loss}$ is computed for the conventional bypass circuit and the proposed HSMC as shown in (7) and (8) respectively.

$$\underbrace{P_{byp,loss}}_{BPD} = V_D \times I_{String} \tag{7}$$

$$\underbrace{P_{byp,loss}}_{HSMC} = {I_{String}}^2 \times R_{DS(on)} = {I_{DS,2}}^2 \times R_{DS(on)} \tag{8}$$

where V_D represents the forward voltage drop of the BPD which varied from 0.667 to 1 V as the string current is increased and $R_{DS(on)}$ is the drain-source on-state resistance of MOSFET (IRFP250N) switches used in proposed HSMC having the value of 0.079 Ω. It is observed that at the MPOP of the PV string, $P_{byp,loss}$ of the shade-affected module on application of proposed HSMC circuit is reduced to 88.65 % and 89.82 % under 2-cell and 3-cell shading respectively in comparison to module integrated BPD.

B. Thermographic Inspection

Thermal inspection of the shade-affected module is done considering two prominently employed PV connection topologies viz. series (S) and series-parallel (SP) connection.

1) 3×1 PV String: To obtain a precise evaluation of the thermal performance of a module affected by shading, thermal measurements were taken from two identical 3×1 PV strings. One of the strings had its middle module equipped with the proposed HSMC (String1, Panel 2), while the same module in the other string (String 2, Panel 2) was fitted with a traditional BPD. Each PV string's middle module was thoroughly examined using a high-resolution thermal imager to capture the thermal behavior of the shaded module. The use of different middle modules from distinct PV strings with different bypass strategies was employed to prevent any disturbances in the thermal measurements of the shaded module during its operation. Furthermore, assessing the PV string's behavior with the same shading pattern simultaneously guaranteed the accurate capture of the thermal behavior of the shade-affected module, allowing for a comparison of the two different bypass strategies. IR images of the inspected module (String 1: Panel 2 (with HSMC), String 2: Panel 2(with BPD)) were captured at various instants during the entire system operation. Under normal unshaded conditions, the maximum temperature of the middle panel for string 1 and string 2 was observed to be 42.4

TABLE II
PARAMETERS OF THE 3×1 PV STRING UNDER ALL OPERATING CONDITIONS (CLOSE TO OPEN CIRCUIT)

	String Voltage	String Current	String Power
Condition 1: NC (Unshaded)	56.56 V	0.690 A	39.02 W
Condition 2: PSC	43.2 V	0.52 A	22.46 W
Condition 3: Bypass with standard BPD ((2 cells shaded) (HSMC 'OFF'))	37.2 V	0.479 A	17.81 W
Condition 4: Bypass with HSMC (1 cell shaded)	37.9 V	0.489 A	18.53 W
Condition 5: System Restoration	56.56 V	0.690 A	39.02 W

TABLE III
PARAMETERS OF THE 3×3 SERIES PARALLEL (SP) PV ARRAY UNDER ALL OPERATING CONDITIONS (CLOSE TO MPOP)

	Array Voltage	Array Current	Array Power
Condition 1: NC (Unshaded)	44.25 V	5.91 A	261.51 W
Condition 2: PSC	40.2 V	5.12 A	205.82 W
Condition 3: Bypass with standard BPD ((2 cells shaded) (HSMC 'OFF'))	37.2 V	4.79 A	178.18 W
Condition 4: Bypass with HSMC (1 cell shaded)	37.9 V	4.98 A	188.53 W
Condition 5: System Restoration	44.25 V	5.91 A	261.51 W

Authorized licensed use limited to: DELHI TECHNICAL UNIV. Downloaded on June 14,2023 at 05:30:41 UTC from IEEE Xplore. Restrictions apply.
© 2023 IEEE. Personal use is permitted, but republication/redistribution requires IEEE permission. See https://www.ieee.org/publications/rights/index.html for more information.

This article has been accepted for publication in IEEE Transactions on Industrial Electronics. This is the author's version which has not been fully edited and content may change prior to final publication. Citation information: DOI 10.1109/TIE.2023.3281684

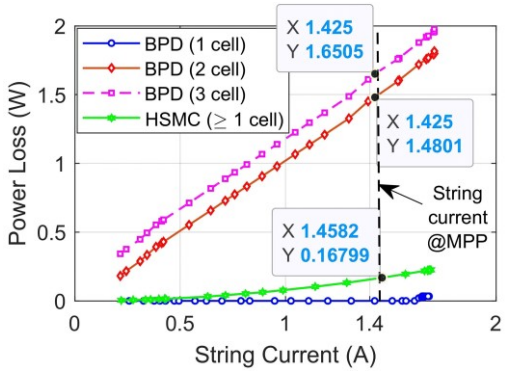

Fig. 11. Power loss estimation under different shading cases for the conventional BPD circuit and the proposed HSMC.

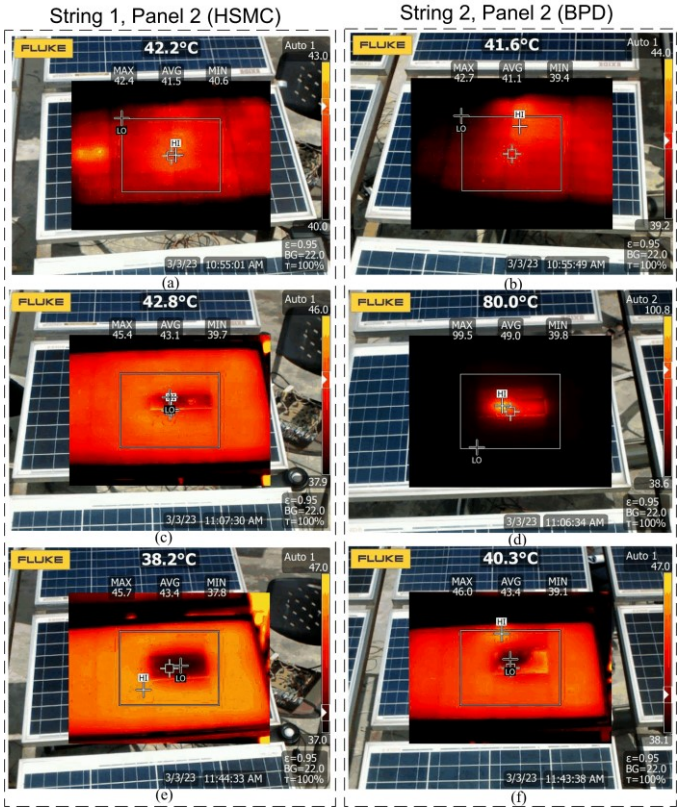

Fig. 12. Thermographic analysis (near MPOP) of the shaded module of two 3×1 PV strings under consideration: (a), (b) Normal condition (Unshaded) (c) 1 cell shaded (with HSMC) (d) 1 cell shaded (with BPD): No bypass (c) 2 cells shaded (with HSMC) (d) 2 cells shaded (with BPD).

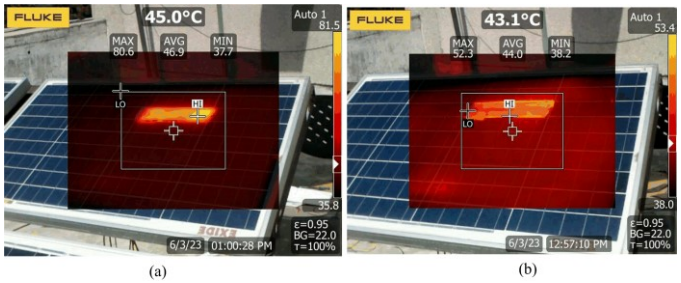

Fig. 13. Thermographic behavior (near MPOP) of the shaded module of 3×3 SP PV array under 1 cell shading: (a) with BPD (b) with HSMC.

^0C and 42.7 ^0C respectively under full exposure to the incoming irradiance as shown in Fig. 12(a) and (b). The middle modules in the respective PV strings were kept unattended under 1 cell shading condition for approx. 12 minutes. This resulted in a rise in the temperature of the shaded cell of the panel 2 (String 2) to 80 ^0C with the consequent initiation of the localized heating of the shaded cell to exceedingly high temperatures of up to 99.5 ^0C as shown in Fig. 12(d). This condition must not be sustained for a significant time, otherwise, it may lead to cell destruction and irreversible module failure. It was observed that the standard BPD failed to counter the localized temperature rise in the shaded cell due to its inability to get into conduction for low shading conditions (< 2 cells). On the contrary, the maximum temperature of the shaded cell of panel 2 (String 1) protected through HSMC under the 1-cell shading scenario was recorded to be 45.4 ^0C, as shown in Fig. 12(c) which is well within the safe limits. As the number of shaded cells increases, BPD goes into conduction under 2 cells shading scenario, thus bypassing the affected module. The PV strings were again left unattended for approx. 37 minutes. It is observed that the maximum temperature reached in the shaded cells for the respective modules under 2 cell shading for both the bypass strategies is respectively 45.7 ^0C and 46 ^0C (refer Fig. 12(e) and (f)) which falls within the safe operating limit of the individual shaded modules.

2) 3×3 SP PV array: Different modules of the array were shaded. The maximum temperature of the module equipped with BPD on shading with 1 cell reached 80.6 ^0C (refer Fig. 13(a)). On the contrary, the maximum temperature of the HSMC protected module was recorded to be 52.3 ^0C under 1 cell shading (refer Fig. 13(b)). As the shading area is increased, the thermal behavior of both the shaded modules shows similar nature. This confirms that BPD performs satisfactorily when the shading area is higher than close to 2 cells leading to safe operation, however, it completely failed under low shading conditions posing a serious threat to the system's reliability. The key experimental measurements of 3×3 SP PV array under different operating conditions are reported in Table IV.

TABLE IV
RESPONSE OF THE CONVENTIONAL BPD AND THE PROPOSED HSMC TO ONE CELL SHADING SCENARIO (3×3 SP PV ARRAY)

Bypass mechanism	String Voltage	String Current	Bypass current	Operation Status
Case I: Near Open circuit condition				
With BPD	60.1 V	0.298 A	0.0 A	Safe operation
With HSMC	60.1 V	0.298 A	0.0 A	Safe operation
Case II: Near Short circuit condition				
With BPD	1.125 V	5.31 A	0.191 A	HS formation
With HSMC	1.166 V	5.35 A	1.72 A	Safe operation
Case III: Intermediary Condition				
With BPD	30.58 V	4.59 A	0.068 A	HS (Fig. 13(a))
With HSMC	31.28 V	4.63 A	1.31 A	Safe (Fig. 13(b))

V. CONCLUSION

The present work proposes an alternative and improved solution to address the inadequacy of BPDs for HS mitigation. It proposed a novel HS alleviation circuit based on a dual-power MOSFET configuration, which can be easily integrated with any number of series-connected cells. Integrating the proposed

Authorized licensed use limited to: DELHI TECHNICAL UNIV. Downloaded on June 14,2023 at 05:30:41 UTC from IEEE Xplore. Restrictions apply.
© 2023 IEEE. Personal use is permitted, but republication/redistribution requires IEEE permission. See https://www.ieee.org/publications/rights/index.html for more information.

This article has been accepted for publication in IEEE Transactions on Industrial Electronics. This is the author's version which has not been fully edited and content may change prior to final publication. Citation information: DOI 10.1109/TIE.2023.3281684

HSMC with 3×1 PV string and 3×3 SP PV array resulted in maximum power enhancement of 5 % and 2.42 %, respectively, when shading increased from 1 cell to 2 cells. Under low shading events ($\leq$1 cell), the maximum temperature of the shaded cell of the module protected using BPD was 119.16 % and 54.11 % higher, respectively, when compared to the module protected with proposed HSMC on a 3×1 PV string and 3×3 SP PV array. Additionally, compared to the traditional module integrated BPD, the proposed HSMC significantly reduced power loss to 88.65 % and 89.82 % in the bypass path under 2 cells and 3 cells shading, respectively, when the PV string operated near its MPOP. The experimental analysis revealed that compared to the prevalent BPD, the proposed HSMC not only successfully countered excessive localized heating within the faulty cells for low shading events but also offered maximum power enhancement under high shading scenarios.

REFERENCES

[1] S. Ghosh and R. Yadav, "Future of photovoltaic technologies: A comprehensive review," *Sustain. Energy Technol. Assessments*, vol. 47, no. June, p. 101410, 2021.

[2] W. L. Shaoshuai Li and B. X. Shan Hu, "A method for determining the applicable geographical regions of PV modules field reliability assessment results based on regional clustering of environmental factors and their weights," *Sustain. Energy Technol. Assessments*, vol. 53, no. Part C, 2022.

[3] V. M. R. Tatabhatla, A. Agarwal, and T. Kanumuri, "Performance Improvement by Mitigating the Effects of Moving Cloud Conditions," *IEEE Trans. Power Electron.*, vol. 36, no. 4, pp. 4214–4223, 2021.

[4] C. Cheng, M. Liu, H. Yi, G. Ran, and H. Chen, "Slow Manifold Analysis-Based Detection of Hot Spots in Photovoltaic Systems," *IEEE Trans. Instrum. Meas.*, vol. 71, 2022.

[5] C. Cheng, M. Liu, H. Yi, J. Wang, and H. Chen, "Tendency-Aided Data-Driven Method for Hot Spot Detection in Photovoltaic Systems," *IEEE J. Emerg. Sel. Top. Ind. Electron.*, vol. 3, no. 4, pp. 901–910, 2022.

[6] A. Wang and Y. Xuan, "Close examination of localized hot spots within photovoltaic modules," *Energy Convers. Manag.*, vol. 234, no. February, p. 113959, 2021.

[7] K. A. Kim and P. T. Krein, "Reexamination of Photovoltaic Hot Spotting to Show Inadequacy of the Bypass Diode," *IEEE J. Photovoltaics*, vol. 5, no. 5, pp. 1435–1441, 2015.

[8] C. E. Clement, J. P. Singh, E. Birgersson, Y. Wang, and Y. S. Khoo, "Hotspot development and shading response of shingled PV modules," *Sol. Energy*, vol. 207, no. May, pp. 729–735, 2020.

[9] L. Xia, Z. Wen, K. Liao, J. Chen, Q. Li, and X. Luo, "Unveiling the Failure Mechanism of Electrical Interconnection in Thermal-Aged PV Modules," *IEEE Trans. Device Mater. Reliab.*, vol. 20, no. 1, pp. 24–32, 2020.

[10] S. Ghosh, V. K. Yadav, and V. Mukherjee, "Improvement of partial shading resilience of PV array though modified bypass arrangement," *Renew. Energy*, vol. 143, pp. 1079–1093, 2019.

[11] M. Dhimish, "Assessing MPPT techniques on hot-spotted and partially shaded photovoltaic modules: Comprehensive review based on experimental data," *IEEE Trans. Electron Devices*, vol. 66, no. 3, pp. 1132–1144, 2019.

[12] M. Dhimish and J. Kettle, "Impact of Solar Cell Cracks Caused during Potential-Induced Degradation (PID) Tests," *IEEE Trans. Electron Devices*, vol. 69, no. 2, pp. 604–612, 2022.

[13] B. Bora *et al.*, "Failure Mode Analysis of PV Modules in Different Climatic Conditions," *IEEE J. Photovoltaics*, vol. 11, no. 2, pp. 453–460, 2021.

[14] J. Y. Hartley *et al.*, "Effects of Photovoltaic Module Materials and Design on Module Deformation under Load," *IEEE J. Photovoltaics*, vol. 10, no. 3, pp. 838–843, 2020.

[15] D. P. Winston, "Efficient Output Power Enhancement and Protection Technique for Hot Spotted Solar Photovoltaic Modules," *IEEE Trans. Device Mater. Reliab.*, vol. 19, no. 4, pp. 664–670, 2019.

[16] K. Ayache, A. Chandra, and A. Chériti, "An Embedded Reconfiguration for Reliability Enhancement of Photovoltaic Shaded Panels against Hot Spots," *IEEE Trans. Ind. Appl.*, vol. 56, no. 2, pp. 1815–1826, 2020.

[17] M. Kumar, "Enhanced Solar PV Power Generation under PSCs Using Shade Dispersion," *IEEE Trans. Electron Devices*, vol. 67, no. 10, pp. 4313–4320, 2020.

[18] P. Changmai, S. Kumar, S. K. Nayak, and S. K. Metya, "Maximum Power Estimation of Total Cross-Tied Connected PV Cells in Different Shading Conditions for High Current Application," *IEEE J. Emerg. Sel. Top. Power Electron.*, vol. 10, no. 4, pp. 3883–3894, 2022.

[19] S. Tang, Y. Xing, L. Chen, X. Song, and F. Yao, "Review and a novel strategy for mitigating hot spot of PV panels," *Sol. Energy*, vol. 214, no. July 2020, pp. 51–61, 2021.

[20] G. Acciari, D. Graci, and A. La Scala, "Higher PV module efficiency by a novel CBS bypass," *IEEE Trans. Power Electron.*, vol. 26, no. 5, pp. 1333–1336, 2011.

[21] V. D'Alessandro, P. Guerriero, and S. Daliento, "A Simple Bipolar Transistor-Based Bypass Approach for Photovoltaic Modules," *IEEE J. Emerg. Sel. Top. power Electron.*, vol. 4, no. 1, pp. 405–413, 2014.

[22] S. Daliento, F. Di Napoli, P. Guerriero, and V. d'Alessandro, "A modified bypass circuit for improved hot spot reliability of solar panels subject to partial shading," *Sol. Energy*, vol. 134, pp. 211–218, 2016.

[23] S. Ghosh, V. K. Yadav, and V. Mukherjee, "A Novel Hot Spot Mitigation Circuit for Improved Reliability of PV Module," *IEEE Trans. Device Mater. Reliab.*, vol. 20, no. 1, pp. 191–198, 2020.

[24] E. I. Batzelis and S. A. Papathanassiou, "A Method for the Analytical Extraction of the Single-Diode PV Model Parameters," *IEEE Trans. Sustain. Energy*, vol. 7, no. 2, pp. 504–512, 2016.

[25] IRFP250N MOSFET Datasheets, [Online] Available: www.alldatasheet.com/datasheetpdf/pdf/68504/IRF/IRFP250N.html.

Ranjeet Singh received the B.Tech. degree in Electrical Engineering from G.B. Pant Engineering College Ghurdauri, Pauri Garhwal, India, in 2011, the M.Tech. degree in Renewable Energy Systems from National Institute of Technology, Kurukshetra, India, in 2016. He is currently working toward the Ph.D. degree with Delhi Technological University, Delhi, India. His research interests include modeling and characterization of solar cells, diagnostic and monitoring techniques for photovoltaic devices and systems, PV reconfiguration for enhanced performance and output power yield.

Vinod Kumar Yadav (Senior Member, IEEE) received the B.Tech. degree in electrical engineering from the Institute of Engineering and Technology, Bareilly, India, in 2003, the M.Tech. degree in power system engineering from the National Institute of Technology, Jamshedpur, India, in 2005, and the Ph.D. degree in power system engineering from the Indian Institute of Technology, Roorkee, India, in 2011. His research interests include renewable energy systems, power system planning and optimization, distributed generations, and smart grid.

Madhusudan Singh (Senior Member, IEEE) was born in Ghazipur, India, in 1968. He received the B.Sc. degree in electrical engineering from the Faculty of Technology, Dayalbagh Educational Institute, Dayalbagh, Agra, India, in 1990, the M.E. degree from the University of Allahabad, Allahabad, India, in 1992, and the Ph.D. degree from the Faculty of Technology, University of Delhi, New Delhi, India, in 2006. His research interests include modelling and analysis of electrical machines, power quality in power systems, renewable energy systems, voltage control aspects of self-excited induction generators, power electronics, drives.

Authorized licensed use limited to: DELHI TECHNICAL UNIV. Downloaded on June 14,2023 at 05:30:41 UTC from IEEE Xplore. Restrictions apply.
© 2023 IEEE. Personal use is permitted, but republication/redistribution requires IEEE permission. See https://www.ieee.org/publications/rights/index.html for more information.

JOURNAL OF AERONAUTICAL MATERIALS
ISSN: 1005-5053

Vol. 43, Issue-01, 2023
pp. 890-905

ANALYSIS OF END LOSS AND ITS COMPENSATION IN SMALLER PARABOLIC TROUGHS: A COMPREHENSIVE STUDY

Lovebrat Saxena[a], Anil Kumar[b,c] and Archana Soni[a]

[a]Energy Centre, Maulana Azad National Institute of Technology, Bhopal -462 003 (India)

[b]Department of Mechanical Engineering, Delhi Technological University, Delhi -110 042 (India)

[c]Centre for Energy and Environment, Delhi Technological University, Delhi -110042 (India)

Abstract

Parabolic trough collector (PTC) based concentrated solar power (CSP) systems for industrial process heat (IPH) are small size systems due to space constraints and lower temperature requirements. These system uses solar radiations to heat thermal fluid, which transports heat to process applications. End loss in line concentrating systems is proportionally greater in smaller troughs as compared to larger trough systems. To quantify end loss, a multi-variate numerical model was studied in the present work. In this study, optics of a PTC has been numerically estimated and experimentally validated, focusing on end loss. End losses are observed 5% for less than 280 incidence angles and also they are limited to 15% between 280 and 600 incidence angles. However, end loss increases exponentially for greater than 600 incidence angles. Uncertainty in skipped length measurements is found 2.3%. Whereas propagation of uncertainty in the calculation of end loss factor was found to be 4.15%. Estimating end loss forehand to installation will enable a designer to select a site-specific design to minimize the end loss and enhance the heat collection through the system.

Keywords: Parabolic trough collector; Optical analysis; End loss analysis; Skipped length

1. Introduction

21st century is surrounded by significant threats like global warming, climate change, pollution and depletion of fossil fuels, etc., which adversely impact environment and human life. The scientific community is developing new and sustainable ways to tackle the threats arising from increasing energy demands amid the energy crisis without degrading the environment (E. Xu et al., 2015). The usability of renewable energy in transportation, domestic and industrial applications is proven as the best alternative to fossil fuel based energy for sustainable development. Among all renewable sources, solar energy is a vast, clean, economical, convenient, and safer source of energy, overcoming its diluted nature. It has proven itself as a potential alternative to conventional energy, to deal with the environmental problems like CO2 emission, energy crisis and climate change (Luo et al., 2015). According to an estimate, the amount of solar energy received annually is twice the energy obtained from all the fossil based energy sources combined, shows the vast availability of the energy resource (Hermann, 2006). Practically, solar energy is an abundant source of energy with a vast potential (Zhu et al., 2019). An investigation to assess the capability of power producing limit of CSP in Libya shows that CSP innovation is techno-monetarily practical in Libya (Belgasim et al., 2018). Islam et al. carried out an investigation on techno-financial aspects of different CSP advancements, and inferred that PTC and ST plants were most appropriate for the considered Malaysian locales

(Islam et al., 2019). The techno-economic impact of design changes in TES (Thermal Energy System) was studied and it was reported that type of storage tank used greatly affects cost of system (Andika et al., 2017). Purohit and Purohit examined the techno-monetary plausibility of CSP in India. CSP technology is fairly feasible in India and monetarily, north-western piece of India (Rajasthan and Gujarat) (Purohit & Purohit, 2010).

Fig. 1. Classification of CSP

Most of the research work has been done for analysis and performance of PTC, including simulations and experimental investigations, whereas end loss is a subject kept less addressed. End loss depends upon the angle of incidence and is independent of length of trough. Therefore, for high solar radiation collection, it becomes insignificant. In a smaller trough, specifically used in industrial applications, end loss plays a significant role. Considering the importance of endloss in the overall efficiency of PTC, a detailed analysis of endloss and investigation of its compensation techniques were required. On the other hand, much literature is available on thermal models of a PTC and their characteristics, as discussed by (Al-Sulaiman et al., 2015; de Oliveira Siqueira et al., 2014; S. A. Kalogirou, 2012; Lu et al., 2013; Nolte et al., 2015; Salgado Conrado et al., 2017; Sun et al., 2015).

Optical losses in PTC collectors during receipt of solar energy and conversion process are less addressed. End loss and cosine effect combinedly hold the maximum share in losses. An investigation on the seasonal effect of endloss with compensation suggests 20% increment in the instantaneous efficiency of LFR (Ma & Chang, 2018). Relative end loss formulation is done and results were compared for linear Fresnel reflector (LFR) and parabolic trough collector. Annual optical efficiency values for PTC and LFR were 58% and 43% with ECOSTAR approach and 57% and 43% with COLSIM approach (Morin et al., 2012). Theoretical and experimental analysis for examining the effect of end loss with and without a heat insulator and a coil heater was performed for a 50MW PTS in China (Lei et al., 2013). Optical analysis for arbitrary oriented and short PTC is also addressed with the three compensation techniques (Li et al., 2015; Zou et al., 2016). Diameter of HTF receiver should be chosen, considering the aperture width of the trough. Small diameter receiver with high aperture width trough suffers larger endloss at a constant incident angle. Hence, sunshade largely affects the performance of PTC and should be considered in practice (Zou et al., 2017). A new design with a rotatable axis is presented with an emphasis on end losses and cosine loses. Results were compared with a traditional single-axis system (Peng et al., 2013). Compensation of endloss in LFR using extended receiver, displaced receiver and their combination yields 50.3%, 20.2% and 48.7% enhancement in the yearly performance. Study suggests the use of extended receiver compensation techniques over other techniques (Bellos et al., 2019).

The objective of this study is to develop a mathematical model for assessing end losses for a parabolic trough placed at any inclination, location, date and time. The findings of numerical simulation based on a developed mathematical model have been validated with experimental observations. Experimentation was carried out on an indoor setup of the scaled-down model of Poly Trough 1800. The developed model is useful for researchers designing PTC based CSP systems for process heat applications.

2. Mathematical formulation of end loss

The problem consists of a PTC, a receiver and incoming beam radiations from the sun. Solar radiations falling on the surface of the collector are reflected and intercepting the receiver. Problem consists of multiple variables that have direct or indirect relation with the objective function, hence for simplification following set of assumptions were taken into consideration.

- For optical analysis, the reflector surface is considered to be smooth.
- Reflection coefficient is taken to be unity.
- Only beam radiations are taken into consideration; hence rays striking at the critical points of the trough are assumed parallel to each other.
- Single ray is used to derive the expressions.
- Since the parabolic trough employs single-axis tracking, thus facing the sun directly all the time.
- Real time tracking is assumed.
- Deflection of radiations from the sharp edges is not considered.

Physical factors are shown in Table 1 affect the amount of end loss occurring in a parabolic trough at any instant of time. Their dependency and ranges are also illustrated in tabular form.

Table 1- Characteristics of quantities affecting end loss

Declination angle (δ) and the angle of incidence (θ) are not independent variables. However, for the simplicity of expression, these are used and calculated separately.

Fig. 2. Schematic diagram for parabolic trough

Side view of a parabolic trough in Fig. 2. depicts the solar radiation falling at an angle, θ. Solar radiation falling on point A gets reflected and strikes the Heat Collecting Element (HCE) at point C. As per trigonometry, the relation between focal length (x) and skip length (d/2) can be expressed as:

$$\frac{d}{2} = x\,Tan\,\theta \qquad (1)$$

Skip length is considered d/2 to reduce the complexity of equations.

Aperture length of the trough, which contributes the thermal energy to heat transfer fluid, can be calculated as:

$$Sin(90-\theta) = \frac{y}{\left(l-\frac{d}{2}\right)}$$

$$y = \left(l - \frac{d}{2}\right) Cos\,\theta \qquad (2)$$

In a Parabolic Trough, the reflected radiation that does not concentrate over the receiver accounts for end loss. Length of trough participating in end loss depends upon the angle at which radiation is falling over the trough surface.

From properties of similar triangles ΔAEF and ΔAGD, the aperture length of collector involved in end loss can be expressed as:

$$z = y\left(\frac{d}{2l-d}\right) = \frac{d}{2}cos\,\theta \qquad (3)$$

Aperture area of the collector (Ael,ap) is responsible for end loss. It is obtained with the product of ineffective collector length (z) from Eq. (3) and the aperture width (w) of the parabolic trough and expressed as:

$$A_{el,ap} = w\left(\frac{d}{2}\right) Cos\,\theta \qquad (4)$$

Fraction of collector area involves in instantaneous end loss phenomenon, which is represented as the ratio of end loss aperture area to the total aperture area of the trough, is given as end loss factor:

$$\mu = \frac{\left\{\frac{d}{2} * \cos\theta\right\}}{z+y} \quad (5)$$

'd' is a dependent variable and it is a function of theta, whereas l is a constant for a trough under consideration.

Although angle of incidence (θ) can be directly measured, while in the case of a comprehensive model of end loss for any arbitrary set of condition, θ can be calculated if the given set of parameters in Table 2 are known (Duffie & Beckman, 2013; Tiwari & Tiwari, 2017).

$$Cos\,\theta = Sin\,L\,Sin\,\delta\,Cos\,\beta - Cos\,L\,Sin\,\delta\,Sin\,\beta\,Cos\,a_s + Cos\,L\,Cos\,\delta\,Cos\,\omega\,Cos\,\beta + Sin\,L\,Cos\,\delta\,Cos\,\omega\,Sin\,\beta\,Cos\,a_s + Cos\,\delta\,Sin\,\omega\,Sin\,\beta\,Sin\,a_s \quad (6)$$

For parabolic trough systems, the angle between the aperture surface and the horizontal plane β is generally kept 00. It is to avoid the formation of long shadows when the sun is at a lower altitude. Collector should be oriented in N-S orientation to collect maximum solar radiation. Hence, the surface azimuth angle (as) will become 00. Expression of incidence angle in Eq. (8). is reduced to (R. Xu & Wiesner, 2015):

$$Cos\,\theta = Sin\,L\,Sin\,\delta + Cos\,L\,Cos\,\delta\,Cos\,\omega$$

$$\theta = \cos^{-1}(Sin\,L\,Sin\,\delta + Cos\,L\,Cos\,\delta\,Cos\,\omega) \quad (7)$$

Earth's axis is tilted by 23.45o, therefore throughout the year declination angle varies between positive or negative magnitude. Declination angle for a particular day in a year can be calculated as (Page, 2018):

$$\delta = 23.45\,Sin\left[\left(\frac{360}{365}\right)(284+n)\right] \quad (8)$$

Hour angle ( ) for a particular instant or for a period of observation can be estimated as [43]:

$$\omega = (ST - 12)15^0 \quad (9)$$

Solar time (ST) or apparent solar time is a reckoning of the passage of time concerning the position of the sun in the sky. The relation between solar time and local time is established as (Duffie & Beckman, 2013; Page, 2018):

$$Standard\,time = ST - 4(L_{st} - L_{loc}) + E \quad (10)$$

where, E represents the equation of time (minutes) as:

$$E = 229.2(0.000075 + 0.001868\,Cos\,B - 0.032077\,Sin\,B - 0.014615\,Cos\,2B - 0.04089\,Sin\,2B) \quad (11)$$

The substitution of B, in Eq. (11). can be calculated through,

$$B = (n-1)\left(\frac{360}{365}\right) \quad (12)$$

Solar radiations loss due to end loss over a period of time can be calculated as:

$H_{loss} = \sum_{i=0}^{N} H_i * z_i$, when values have taken at regular intervals. (13)

$H_{loss} = \int_0^T H(t) * z(t)dt$, when analog time is considered. (14)

where,

Hi, H(t) = instantaneous value of DNI.(W/m2)

zi, z(t) = Instantaneous value of Aperture length of collector involved in end loss.

The end loss factor can be calculated for any parabolic trough with an arbitrary set of parameters given in Table 1 from the Eq. (1, 2, 3, 5, 6, 7, 8, 10, 11 and 12). The set of Eq. (1, 2, 3, 5, 6, 7, 9, 10, 11 and 12) can be used for parabolic trough placed horizontally on the surface and long axis oriented towards N-S direction. Moreover, instantaneous power loss, daily variation, daily average, annual variation and an annual average of energy loss due to end loss can be easily calculated using the appropriate beam radiation data arranged from credible data distribution centers and monitoring stations. Synthetic beam radiation data can also be generated for a particular location using computer algorithms.

In general, receiver length is kept equal to collector length in a parabolic trough. In order to collect the concentrated radiations that skip the interaction with the receiver due to oblique incidence of radiations, length of receiver can be extended with length, Δl as shown in Fig. 2. It would be advantageous in a smaller trough, as the end loss factor is much more significant than larger troughs.

3. Design of Experimental Setup

An indoor experimental set up is fabricated to emulate different angle of incidence over a parabolic trough and the length skipped by the ray after getting reflected from the trough is measured. Poly Trough - 1800 by NEPSOLAR is a commonly used commercial model of a parabolic trough for plant design, is taken as reference (Freeman et al., 2015). A miniature model is fabricated by scaling down the geometry.

Table 2- Specifications of Poly Trough - 1800 and Experimental Trough (NEP SOLAR AG, 2012)

Focal length and width of aperture are constructional feature and remains unchanged for any particular PTC. Incidence angle varies with time and respective to sun's position. Therefore, to design an experimental setup to evaluate the end losses, incidence angle is the only parameter that can be made variable.

Reflector substrate is constructed using aluminum sheet of 3 mm thickness. Metallized PET film, which is manufactured by depositing a thin layer of aluminum over the surface of PET substrate film to realize a bright metallic effect, is pasted over the Aluminum sheet, as shown in Fig. 3(a). The reflectivity of PET film is 95%, can be used up to 1200C for five years. The reflective tape has constant reflection over the visual range. Toy LASER lights of 650 nm with output power rated 5mW were chosen and arranged in array to create beam radiations. LASER has a collimated beam. Hence after getting reflected, it doesn't disperse as given in Fig. 3(b).

Fig. 3. (a) Metallized PET reflector film, (b) Schematic diagram of setup

Instead of a heat collecting element (HCE), transparent meter rulers are used to measuring the skipped length of the trough after the reflection of incident ray. Point of interception was identified with the center of the bright red spot on the ruler. 6 repeated observations of skipped length were recorded for angle of incidence with a step of 2o to improve measurement accuracy. A movable arm controls the incidence angle of LASER beam with a degree of freedom of 700. For performing the complete analysis of 900, trough support structure was designed to allow the adjustment in the inclination of the trough.

The indoor experiments were carried out from 20 -27 December 2019 at Solar Energy Lab, Energy Centre, Maulana Azad National Institute of Technology (MANIT), Bhopal, India. All the experiments were performed at night to ensure the location of LASER spots on the scale.

4. Experimental Uncertainty

Uncertainty plays a vital role in any experimentation. There are sources of error like systematic errors and random errors, which alter the outcome of measurements. Therefore, to get reliable measurement data, uncertainty analysis provides the range of possibly induced error in measurement. Uncertainty calculation of independent variables and calculated parameters are of much importance. The calculated uncertainties are given in Table 3. The total uncertainty in end loss factor (δEF) can occur from the skipped length, total length of trough and angle of incidence (Bevington et al., 1993; Taylor & Thompson, 1998). The uncertainty for the measurement in experimental setup should be minimum and can be estimated as (Chauhan et al., 2018):

$$\delta\mu = \sqrt{\left(\left(\frac{\partial\mu}{\partial z}.\delta z\right)^2 + \left(\frac{\partial\mu}{\partial l}.\delta l\right)^2 + \left(\delta\theta\ \frac{\cos\theta}{\sin\theta}\right)^2\right)} \quad (15)$$

Table 3- Uncertainties in variables and parameters

5. Results and discussions

Numerical simulation suggests that, as the angle of incidence increases, the skip length increases gradually in starting. However, a steeper upslope can be seen, which signifies the portion of trough providing end loss. All radiations at an angle greater than 84.8o skip the receiver tube due to the limited trough length. Hence, there is always critical angle for any arbitrary trough, after which all the radiations falling over the trough do not reflect on receiver. This critical incident angle holds much lower values for smaller troughs. Hence, compensation techniques must be employed in case of smaller troughs. Receiver extension is the most simple, effective and economical compensation method. It can be seen that, with receiver extension of 14 cms, end loss occurring for all the values of incidence angle below 40o can be eliminated. The discussed method of compensation can largely prevent end loss with the presented set of equations.

5.1 End loss simulation results

Analysis and calculations have been done for the mathematical model presented above and are presented in this section. The variables that directly affect the skip length are given in Table 2 and used in the analysis. Other variables that are used can be found in the abbreviation section in the last. Fig 4. shows the variation of declination for a year. It shows that by what angle the equatorial plane of the earth has been shifted w.r.t the line joining the center of earth and sun. Latitude (L), Hour angle (ω) and Declination angle (δ) jointly controls the angle of incidence (θ) for the case of parabolic trough.

Fig. 4. Declination angle (δ) over a year

Fig 5. shows the trend comparison between skip length (d/2), aperture of skip length (z) and aperture of total length of trough (z+y). The variation of the above variables has been noted w.r.t the angle of incidence (θ).

Fig. 5. Variation of trough length variables with θ

According to Eq. (1, 2, 3), the angle of incidence increases, the skip length increases gradually in starting, but a steeper upslope can be seen, which signifies the portion of trough providing end loss. All radiations falling over the surface of the trough at an angle greater than 84.8o

could not be collected at the receiver tube. Also, the aperture of skip length and total aperture length crossover point in Fig. 5 states the same phenomenon.

Fig. 6. Variation of end loss factor (%) with θ

The fraction of beam radiations skipping the receiver as the incidence angle of radiations falling over the surface increases is shown in Fig. 6. The incidence angle has been varied from 0o to 90o. The reason for the variation being non-linear is that the cosine effect and end loss effect are actions simultaneously. The cumulative percentage of radiation loss with the corresponding angle of incidence is shown in Table 4.

Table 4- Loss trend with angle of incidence

None of the radiation is reflected on the receiver for all the angles above 84.8o (Table 4). The first reason is the short length of receiver tube, which does not allow the reflected radiations to fall upon the receiver when the sun reaches lower altitudes. The second reason is long focal length of the parabolic trough. Longer the focal length of the trough, complete radiation loss will take place at lower angle of incidence.

Fig. 7. Impact of extended Receiver length on end loss due to incidence angle, θ

Radiation skipping the receiver after getting reflected from the collector surface results end loss. These skipping radiations can be collected by elongating the receiver tube. Fig. 7. shows the compensation of end loss (for a range of incidence angle) when receiver is extended with a certain length. It can be seen that, with receiver extension of 14 cms, end loss occurring for all the values of incidence angle below 40o can be eliminated. The length extension per degree of incidence angle is not constant as the dependency is non-linear in nature or the presented compensation technique, longitudinal tracking of focal line extremities is expensive and requires a reliable control system. Hence location-based length optimization of receiver tube is a better alternative.

5.2 Numerical simulation validation

Sun continuously ascends with time from sunrise till sunset in space fabric. The movement is well reflected in its azimuth and altitude angles when seen through a location on earth. For N-S orientation of trough altitude angle causes end loss. At the same time, azimuth is tracked with a single axis tracking mechanism. End loss model is developed to predict the end loss factor of any size of trough placed at any geographical location and orientation. Numerical model has also been validated with experimental values. The simulated and experimental results of end loss factor are presented in Fig. 8.

Fig. 8. Measured and Predicted skipped length with θ

End loss factor is 0% when the angle of incidence is 00 with respect to the normal surface (Fig. 8). End loss factor is limited to 5% when the incidence angle is lower than 280. Whereas for angles between 280 to 600, trough experience end loss between 5% and 15%. The end loss turns violent and increases exponentially above 600 incidence angles. However, trough length is a design feature and considers constant for a particular case. Still, the reflected radiations intercept the receiver, depending on the balance between the focus (x) and the trough length (l). Further, the predicted end loss factor exceeds 100% at an angle 84.80 due to the short trough length and practically impossible to measure it in experimentation.

Fig. 9. Error in skipped length measurement

The difference between predicted and experimental values of skipped trough length and end loss factor are in the range of -2.8 mm to 6.9 mm and -0.158 and 0.388, respectively, as shown

in Fig. 9. The predicted values of skipped length and end loss factor are also well matched with the experimental values. Therefore, prediction shows a fair agreement with the experimental observations.

Since the trend in error changing after 650, this is because of the high rate of skipped length and end loss factor with respect to the angle of incidence. It is an important design parameter and should always consider designing a parabolic trough field to limit the end loss.

6. Conclusion

The conclusions drawn based on end loss modeling and characteristics are:

i. End loss model covers a wide range of variables and is useful to analyze end loss variation with local time, solar time, latitude, dimensions of a trough and the angle of incidence of incoming beam radiations.

ii. End loss is dominantly dependent on the incidence angle and is non-linear. End loss factor is limited to 5% for values of incidence angle till 28%. For the angles between 28% and 60%, end loss factor was limited to 5% to 15%. End loss factor increases drastically for the angles over 60%.

iii. The difference between predicted and experimental values of skipped trough length and end loss factor are in the range of -2.8 mm to 6.9 mm and -0.158 and 0.388.

iv. Due to the limited length of trough, all radiations falling at higher inclination angles (near to 900) collected by the trough aperture skips the receiver. In such a case end loss factor will reach 100%, and for the present specimen, this phenomenon is occurring at 830.

v. Uncertainty measurement of skipped length was found to be 2.3 %, which is within the acceptable limit.

vi. Total uncertainty propagated in the calculation of end loss factor was 4.15 %. Therefore, the model is well validated with the experimental results obtained from the indoor setup.

It will make a more economically viable parabolic trough array setup for industrial applications. It could also enable readers to analyze end loss for non-standard sized troughs. Also, compensation of end loss using receiver extension can be personalized for different locations on the globe.

Acknowledgment

Authors are highly thankful to Maulana Azad National Institute of Technology -Bhopal (India) and Delhi Technological University, Delhi (India), for providing the necessary facilities for conducting this research work.

References

Agyekum, E. B., & Velkin, V. I. (2020). Optimization and techno-economic assessment of concentrated solar power (CSP) in South-Western Africa: A case study on Ghana. Sustainable Energy Technologies and Assessments, 40. https://doi.org/10.1016/j.seta.2020.100763

Al-Sulaiman, F. A., Zubair, M. I., Atif, M., Gandhidasan, P., Al-Dini, S. A., & Antar, M. A. (2015). Humidification dehumidification desalination system using parabolic trough solar air collector. Applied Thermal Engineering, 75. https://doi.org/10.1016/j.applthermaleng.2014.10.072

Andika, R., Kim, Y., Yoon, S. H., Kim, D. H., Choi, J. S., & Lee, M. (2017). Techno-economic assessment of technological improvements in thermal energy storage of concentrated solar power. Solar Energy, 157. https://doi.org/10.1016/j.solener.2017.08.064

Belgasim, B., Aldali, Y., Abdunnabi, M. J. R., Hashem, G., & Hossin, K. (2018). The potential of concentrating solar power (CSP) for electricity generation in Libya. In Renewable and Sustainable Energy Reviews (Vol. 90). https://doi.org/10.1016/j.rser.2018.03.045

Bellos, E., Tzivanidis, C., & Moghimi, M. A. (2019). Reducing the optical end losses of a linear Fresnel reflector using novel techniques. Solar Energy, 186. https://doi.org/10.1016/j.solener.2019.05.020

Bermejo, P., Pino, F. J., & Rosa, F. (2010). Solar absorption cooling plant in Seville. Solar Energy, 84(8). https://doi.org/10.1016/j.solener.2010.05.012

Bevington, P. R., Robinson, D. K., Blair, J. M., Mallinckrodt, A. J., & McKay, S. (1993). Data Reduction and Error Analysis for the Physical Sciences. Computers in Physics, 7(4). https://doi.org/10.1063/1.4823194

Brooks, M. J. (2005). Performance of a parabolic trough solar collector.

Chauhan, P. S., Kumar, A., Nuntadusit, C., & Banout, J. (2018). Thermal modeling and drying kinetics of bitter gourd flakes drying in modified greenhouse dryer. Renewable Energy, 118. https://doi.org/10.1016/j.renene.2017.11.069

Clark, J. A. (1982). An analysis of the technical and economic performance of a parabolic trough concentrator for solar industrial process heat application. International Journal of Heat and Mass Transfer, 25(9). https://doi.org/10.1016/0017-9310(82)90136-3

de Oliveira Siqueira, A. M., Gomes, P. E. N., Torrezani, L., Lucas, E. O., & da Cruz Pereira, G. M. (2014). Heat transfer analysis and modeling of a parabolic trough solar collector: An analysis. Energy Procedia, 57. https://doi.org/10.1016/j.egypro.2014.10.193

Duffie, J. A., & Beckman, W. A. (2013). Solar Engineering of Thermal Processes: Fourth Edition. In Solar Engineering of Thermal Processes: Fourth Edition. https://doi.org/10.1002/9781118671603

El-Kassaby, M. M. (1994). Prediction of optimum tilt angle for parabolic trough with the long axis in the north-south direction. International Journal of Solar Energy, 16(2). https://doi.org/10.1080/01425919408914269

El-Kassaby, M. M., & Hassab, M. A. (1995). Effect of parabolic trough solar collector orientation on its collection efficiency. International Journal of Solar Energy, 16(3). https://doi.org/10.1080/01425919508914275

El-Swify, M. E. (2001). Orientation and Tilt angle of parabolic trough solar concentrator at different latitudes. Journal of the Institution of Engineers (India), , 82(1), 10–18.

Freeman, J., Hellgardt, K., & Markides, C. N. (2015). An Assessment of Solar-Thermal Collector Designs for Small-Scale Combined Heating and Power Applications in the United Kingdom. Heat Transfer Engineering, 36(14–15). https://doi.org/10.1080/01457632.2015.995037

Gong, G., Huang, X., Wang, J., & Hao, M. (2010). An optimized model and test of the China's first high temperature parabolic trough solar receiver. Solar Energy, 84(12). https://doi.org/10.1016/j.solener.2010.08.003

Hafez, A. Z., Attia, A. M., Eltwab, H. S., ElKousy, A. O., Afifi, A. A., AbdElhamid, A. G., AbdElqader, A. N., Fateen, S. E. K., El-Metwally, K. A., Soliman, A., & Ismail, I. M. (2018).

Design analysis of solar parabolic trough thermal collectors. In Renewable and Sustainable Energy Reviews (Vol. 82). https://doi.org/10.1016/j.rser.2017.09.010

Hermann, W. A. (2006). Quantifying global exergy resources. Energy, 31(12). https://doi.org/10.1016/j.energy.2005.09.006

Islam, M. T., Huda, N., & Saidur, R. (2019). Current energy mix and techno-economic analysis of concentrating solar power (CSP) technologies in Malaysia. Renewable Energy, 140. https://doi.org/10.1016/j.renene.2019.03.107

Kalogirou, S. (1998). Use of parabolic trough solar energy collectors for sea-water desalination. Applied Energy, 60(2). https://doi.org/10.1016/S0306-2619(98)00018-X

Kalogirou, S. A. (2002). Parabolic trough collectors for industrial process heat in Cyprus. Energy, 27(9). https://doi.org/10.1016/S0360-5442(02)00018-X

Kalogirou, S. A. (2004). Solar thermal collectors and applications. In Progress in Energy and Combustion Science (Vol. 30, Issue 3). https://doi.org/10.1016/j.pecs.2004.02.001

Kalogirou, S. A. (2012). A detailed thermal model of a parabolic trough collector receiver. Energy, 48(1). https://doi.org/10.1016/j.energy.2012.06.023

Kumar, S., Agarwal, A., & Kumar, A. (2021). Financial viability assessment of concentrated solar power technologies under Indian climatic conditions. Sustainable Energy Technologies and Assessments, 43. https://doi.org/10.1016/j.seta.2020.100928

Lei, D., Li, Q., Wang, Z., Li, J., & Li, J. (2013). An experimental study of thermal characterization of parabolic trough receivers. Energy Conversion and Management, 69. https://doi.org/10.1016/j.enconman.2013.02.002

Li, M., Xu, C., Ji, X., Zhang, P., & Yu, Q. (2015). A new study on the end loss effect for parabolic trough solar collectors. Energy, 82. https://doi.org/10.1016/j.energy.2015.01.048

Lu, J., Ding, J., Yang, J., & Yang, X. (2013). Nonuniform heat transfer model and performance of parabolic trough solar receiver. Energy, 59. https://doi.org/10.1016/j.energy.2013.07.052

Luo, N., Yu, G., Hou, H. J., & Yang, Y. P. (2015). Dynamic Modeling and Simulation of Parabolic Trough Solar System. Energy Procedia, 69. https://doi.org/10.1016/j.egypro.2015.03.137

Ma, J., & Chang, Z. (2018). Understanding the effects of end-loss on linear Fresnelcollectors. IOP Conference Series: Earth and Environmental Science, 121(5). https://doi.org/10.1088/1755-1315/121/5/052052

Mohammadi, K., Khanmohammadi, S., Immonen, J., & Powell, K. (2021). Techno-economic analysis and environmental benefits of solar industrial process heating based on parabolic trough collectors. Sustainable Energy Technologies and Assessments, 47. https://doi.org/10.1016/j.seta.2021.101412

Morin, G., Dersch, J., Platzer, W., Eck, M., & Häberle, A. (2012). Comparison of Linear Fresnel and Parabolic Trough Collector power plants. Solar Energy, 86(1). https://doi.org/10.1016/j.solener.2011.06.020

NEP SOLAR AG. (2012, December). NEP-Solar-Polytrough1800_Datasheet. Https://Serv.Spf.Ch/Spftesting/Collectors/Pdfs/Scf1549en.Pdf.

Nolte, H. C., Bello-Ochende, T., & Meyer, J. P. (2015). Second law analysis and optimization of a parabolic trough receiver tube for direct steam generation. Heat and Mass Transfer /Waerme- Und Stoffuebertragung, 51(6). https://doi.org/10.1007/s00231-014-1465-3

Ouagued, M., Khellaf, A., & Loukarfi, L. (2013). Estimation of the temperature, heat gain and heat loss by solar parabolic trough collector under Algerian climate using different thermal oils. Energy Conversion and Management, 75. https://doi.org/10.1016/j.enconman.2013.06.011

Page, J. (2018). The role of solar-radiation climatology in the design of photovoltaic systems. In McEvoy's Handbook of Photovoltaics: Fundamentals and Applications. https://doi.org/10.1016/B978-0-12-809921-6.00016-1

Peng, S., Hong, H., Jin, H., & Zhang, Z. (2013). A new rotatable-axis tracking solar parabolic-trough collector for solar-hybrid coal-fired power plants. Solar Energy, 98(PC). https://doi.org/10.1016/j.solener.2013.09.039

Purohit, I., & Purohit, P. (2010). Techno-economic evaluation of concentrating solar power generation in India. Energy Policy, 38(6). https://doi.org/10.1016/j.enpol.2010.01.041

Salgado Conrado, L., Rodriguez-Pulido, A., & Calderón, G. (2017). Thermal performance of parabolic trough solar collectors. In Renewable and Sustainable Energy Reviews (Vol. 67). https://doi.org/10.1016/j.rser.2016.09.071

Sun, J., Liu, Q., & Hong, H. (2015). Numerical study of parabolic-trough direct steam generation loop in recirculation mode: Characteristics, performance and general operation strategy. Energy Conversion and Management, 96. https://doi.org/10.1016/j.enconman.2015.02.080

Tagle-Salazar, P. D., Nigam, K. D. P., & Rivera-Solorio, C. I. (2020). Parabolic trough solar collectors: A general overview of technology, industrial applications, energy market, modeling, and standards. In Green Processing and Synthesis (Vol. 9, Issue 1). https://doi.org/10.1515/gps-2020-0059

Taylor, J. R., & Thompson, W. (1998). An Introduction to Error Analysis: The Study of Uncertainties in Physical Measurements. Physics Today, 51(1). https://doi.org/10.1063/1.882103

Tiwari, G. N., & Tiwari, A. (2017). Handbook of solar energy. Singapore. Springer.

Valizade, M., Heyhat, M. M., & Maerefat, M. (2020). Experimental study of the thermal behavior of direct absorption parabolic trough collector by applying copper metal foam as volumetric solar absorption. Renewable Energy, 145. https://doi.org/10.1016/j.renene.2019.05.112

Xu, C., Chen, Z., Li, M., Zhang, P., Ji, X., Luo, X., & Liu, J. (2014). Research on the compensation of the end loss effect for parabolic trough solar collectors. Applied Energy, 115. https://doi.org/10.1016/j.apenergy.2013.11.003

Xu, E., Zhao, D., Xu, H., Li, S., Zhang, Z., Wang, Z., & Wang, Z. (2015). The Badaling 1MW Parabolic Trough Solar Thermal Power Pilot Plant. Energy Procedia, 69. https://doi.org/10.1016/j.egypro.2015.03.096

Xu, R., & Wiesner, T. F. (2015). Closed-form modeling of direct steam generation in a parabolic trough solar receiver. Energy, 79(C). https://doi.org/10.1016/j.energy.2014.11.004

Zhu, S., Yu, G., Ma, Y., Cheng, Y., Wang, Y., Yu, S., Wu, Z., Dai, W., & Luo, E. (2019). A free-piston Stirling generator integrated with a parabolic trough collector for thermal-to-electric conversion of solar energy. Applied Energy, 242. https://doi.org/10.1016/j.apenergy.2019.03.169

Zou, B., Dong, J., Yao, Y., & Jiang, Y. (2016). An experimental investigation on a small-sized parabolic trough solar collector for water heating in cold areas. Applied Energy, 163. https://doi.org/10.1016/j.apenergy.2015.10.186

Zou, B., Yang, H., Yao, Y., & Jiang, Y. (2017). A detailed study on the effects of sunshape and incident angle on the optical performance of parabolic trough solar collectors. Applied Thermal Engineering, 126. https://doi.org/10.1016/j.applthermaleng.2017.07.149

Rawani, A. T. W. A. R. I., S. P. Sharma, and K. D. P. Singh. "Comparative performance analysis of different twisted tape inserts in the absorber tube of parabolic trough collector." International Journal of Mechanical and Production Engineering Research and Development 8.1 (2018): 643-656.

Senthil, R., and A. P. Nishanth. "Optical and thermal performance analysis of solar parabolic concentrator." International Journal of Mechanical and Production Engineering Research and Development 7.5 (2017): 367-374.

Senthil, R. A. M. A. L. I. N. G. A. M., M. U. K. U. N. D. Gupta, and C. H. I. N. M. A. Y. A. Rath. "Parametric analysis of a concentrated solar receiver with Scheffler reflector." International Journal of Mechanical and Production Engineering Research and Development 7.5 (2017): 261-268.

Senthil, R. "Effect of secondary reflector on thermal performance of linear fresnel concentrated solar collector." International Journal of Mechanical and Production Engineering Research and Development 8.4 (2018).

Kumar, M., B. Veerabhadra Reddy, and P. Venkateshwar Reddy. "Experimental Comparison of Solar Paraboloid Collector with and without Mirror in Aluminum Foil as Reflectors." International Journal of Mechanical and Production Engineering Research and Development (IJMPERD) 8.2 (2018): 1117-1124.

Parveen, M., and O. H. Mohideen. "A Study on Financial Performance of Pharmaceutical Company Using Five Power Analyses." International Journal of Business Management & Research (IJBMR) 1.4 (2014): 45-50.

Annexure:

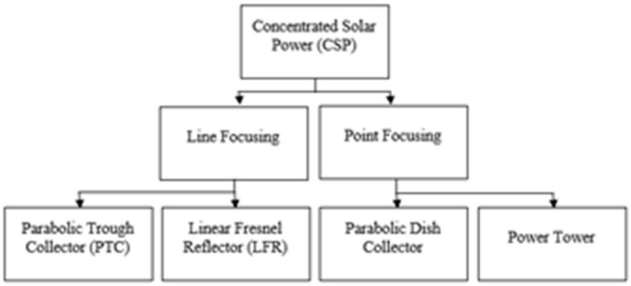

FIGURE 1. Classification of CSP

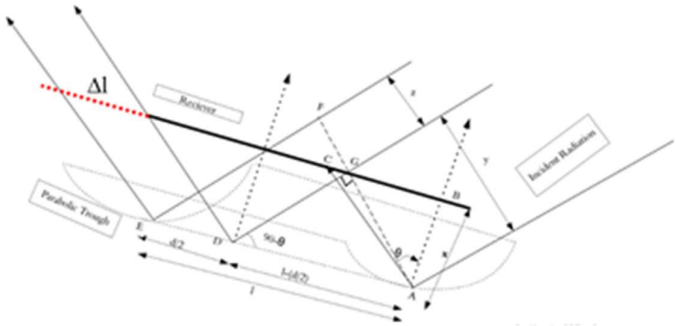

FIGURE 2. Schematic diagram for parabolic trough

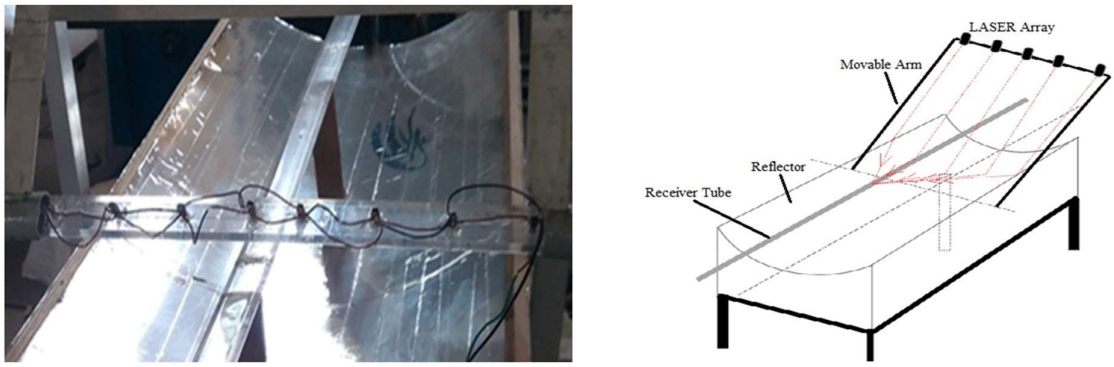

(a) (b)

FIGURE 3. (a) Metallized PET reflector film, (b) Schematic diagram of setup

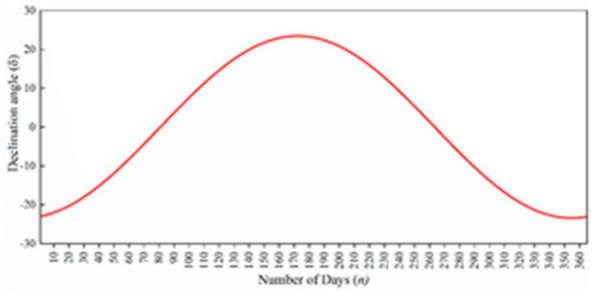

FIGURE 4. Declination angle (δ) over a year

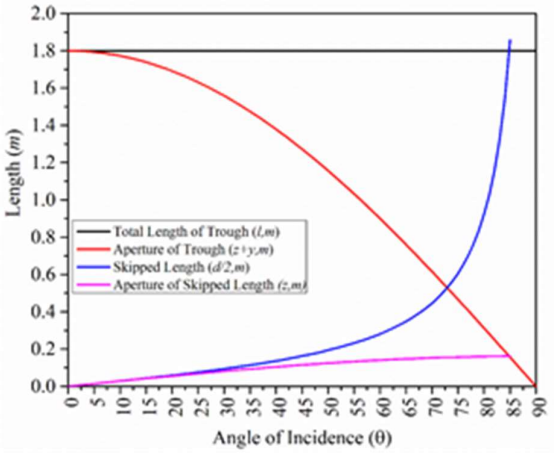

FIGURE 5. Variation of trough length variables with θ

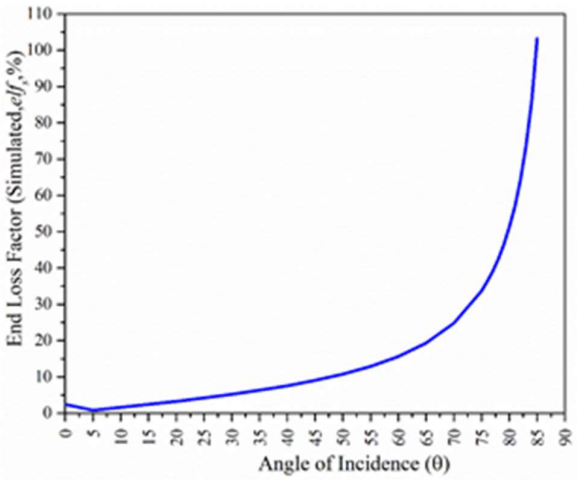

FIGURE 6. Variation of end loss factor (%) with θ

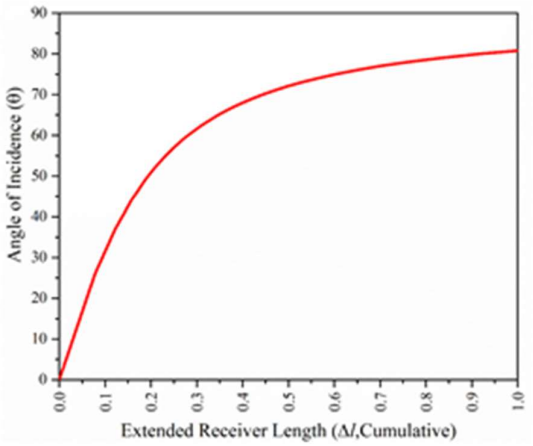

FIGURE 7. Impact of extended Receiver length on end loss due to incidence angle, θ

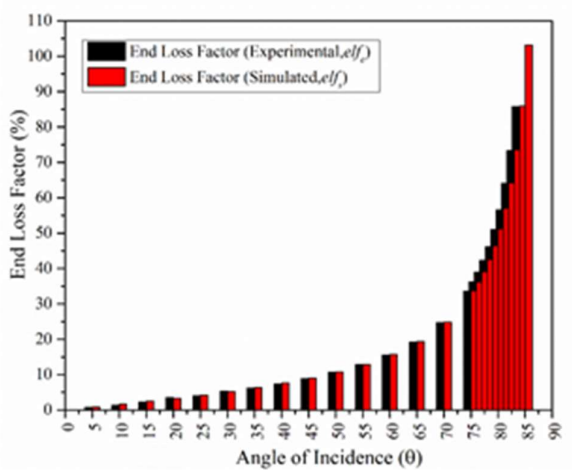

FIGURE 8. Measured and Predicted skipped length with θ

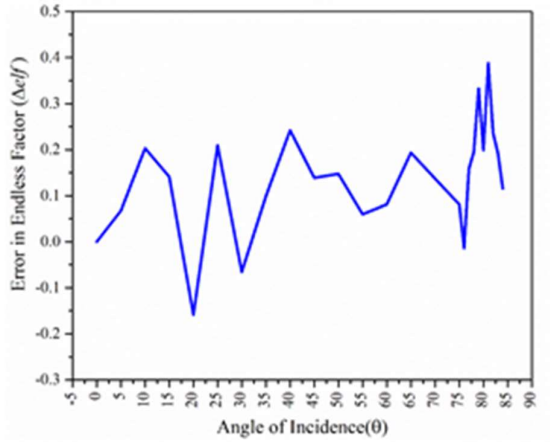

FIGURE 9. Error in skipped length measurement

Table 1- Characteristics of quantities affecting end loss

S. No.	Symbol	Parameter	Dependency	Range	Reference
1.	θ	Angle of incidence	f (L, δ, a_s, β, ω)	$-90^0 \le \theta \le 90^0$	Ouagued et al., 2013
2.	L	local latitude	independent	90^0 N ≤ L ≤ 90^0 S	Ouagued et al., 2013
3.	δ	declination angle	f(n)	$-23.45^0 \le \delta \le 23.45^0$	Ouagued et al., 2013
4.	a_s	surface azimuth angle	f(a_f)	0^0 to 360^0 due south	Page., 2012
5.	β	surface tilt angle from horizontal surface	independent	$0^0 \le \beta \le 90^0$	Ouagued et al., 2013

6.	ω	hour angle	f(ST)	0 to 24 hours	Mghouchi et al., 2016
7.	θ_z	solar zenith angle	independent	$0^0 \leq \theta_z \leq 90^0$	Ouagued et al., 2013
8.	n	day of the year	independent	$1 \leq n \leq 365$	Page., 2012
9.	w	aperture width of the trough	Depends upon design and trough profile	NA	

Table 2- Specifications of Poly Trough - 1800 and Experimental Trough [Dataset]

S.No	Specification	Poly Trough - 1800	Experimental Model
1.	Aperture Area, A_{ap}	36.9 m^2	0.94 m^2
2.	Length, l	20.9 m	1.8 m
3.	Width, w	1.845 m	0.52 m
4.	Focal Length, x	0.65 m	0.1625 m
5.	Rim Angle, r	71^0	71.6^0
6.	Concentration ratio (geometric), C_{geo}	54	-----

(Source: http://www.nep-solar.com/wp-content/uploads/2013/11/NEP-Solar-Polytrough1800_Datasheet.pdf)

Table 3- Uncertainties in variables and parameters

S.No.	Quantity	Uncertainty
1.	Skipped Length (d/2)	± 0.002 m
2.	Angle of Incidence (θ)	± 1^0
3.	Length of Trough (l)	± 0.001 m
4.	Solar Radiation (H)	± 10 W/m^2
5.	Aperture of skipped length (z)	2.3%
6.	Aperture of length of trough (z+y)	1.86%
7.	End loss factor (μ)	4.15%

Table 4- Loss trend with angle of incidence

Angle of Incidence, θ	**0°**	**10°**	**20°**	**30°**	**40°**	**50°**	**60°**	**70°**	**80°**	**84.8°**	**90°**
End loss Factor (%)	0 %	1.6 %	3.28 %	5.21 %	7.57 %	10.75 %	15.63 %	24.80 %	51.19 %	100 %	NA

ResearchGate

See discussions, stats, and author profiles for this publication at: https://www.researchgate.net/publication/370984375

Analysis of Taxes through E-payment System for Transportation Services

Article · May 2023

CITATIONS
0

READS
18

7 authors, including:

Samiullah Mehraban
Delhi Technological University
7 PUBLICATIONS **8** CITATIONS

SEE PROFILE

Some of the authors of this publication are also working on these related projects:

Hybrid SDN Network View project

All content following this page was uploaded by Samiullah Mehraban on 24 May 2023.

The user has requested enhancement of the downloaded file.

WWW.IJRPR.COM

International Journal of Research Publication and Reviews

Journal homepage: www.ijrpr.com ISSN 2582-7421

Analysis of Taxes through E-payment System for Transportation Services

Nesar Ahmad Ahmadi [a], Zalmai Zormatai [b], Samiullah Mehraban [c], Khwaja Hedayetullah Sidiqi [d], Shafiullah Shinwari [e], Abdul Ghafaar [f], Mohammad Yonus [g]

[a] *Researcher, Bakhtar University*
[b] *Assistant Professor, Bakhtar University*
[c] *PhD scholar, Delhi Technological University*
[d] *Researcher, Bakhtar University*
[e] *Dean of Faculty, Bakhtar University*
[f] *Assistant Professor, Bakhtar University*
[g] *Vice Chanceler, Bakhtar University*

A B S T R A C T

The use of Information and Communication Technology (ICT) in governmental procedures has become a typical marvel in ongoing years. With the extraordinary improvement of Information and Communication Technologies (ICT) and growing attention to Electronic Governance's advantages, ICT empowered the transformation procedure of administration forms to become an essential part of national strategies in the developing world. For a long time, tax policy has been one of the dominant methods for financing a country's administration. Tax collection provides a financial basis for every country to offer public services to its citizens. Since the Ministry of Transport, especially the Land Transportation Regulation General Directorate is responsible for managing and regulating the transport services so, one of the essential tasks of the institution is to collect transport taxes. These institutions face various challenges in this regard while they use the common manual system. We developed the concept based on evaluating the current processes, interviews with relevant authorities, analysing technologies for electronic tax collection, researching this field, and considering Afghanistan's current situation. The purpose of this thesis is to evaluate concepts and technologies for an electronic payment system for Afghanistan's transportation taxes and make a recommendation considering Afghanistan' situation. Furthermore, the concept aims to provide advancement for the Ministry of Transport, especially the Land Transportation Regulation General Directorate, to have an effective and transparent collection of national or local transportation

Keywords: Taxes, Transportation, E payment, ICT

1. Introduction

The use of Information and Communication Technology (ICT) in governmental procedures has become a typical marvel in ongoing years. In the late 1990s, ICT presented a unique concept for the government (e-Government) in public administration. With the dramatic improvement of Information and Communication Technologies (ICT) and expanding attention to the advantages of Electronic Governance, ICT empowered the transformation procedure of administration forms to become an essential part of national strategies in the developing world.

The development of data and correspondence innovation has altered customary frame- works of payment. People would now be able to do numerous exchanges for products and enterprises utilizing new techniques rather than traditional strategies for money and cheques. This wonder of a cashless installment is known as e-Payment. With e- Payment frameworks, people can pay for merchandise and ventures over the counter and through the Internet without money utilization. E-Payment frameworks have different properties, including convenience, safety, transparency, time, and cost investment funds of exchanges. The installment arrangement of a nation assumes a pivotal job in its economy, as this is the empowering channel for the progression of budgetary resources.

Modern ICT and e-business systems support operations that include ordering, booking, billing, charging tariffs, customs clearance, insurance claims, bill of lading, tracing, and payment. If we are going to refer to the effect of e-business on transport services, keep it in mind that the transport industry has, over the decades, been undergoing organizational and technological changes. These have been independent of any influence from e-commerce, particularly the Internet, which in this respect, is quite a recent phenomenon.

In the last 16 years, Afghanistan has seen significant telecommunications, information technology, and energy resources. By attracting extensive investments in the telecommunications industry, the national fiber optic ring, and the expansion of internet connectivity, the country has seen substantial

achievements in enabling its people to become digitally linked with the rest of the world. Despite the country's tech industry's achievements, there are still problems that need to be addressed to provide a basis for a digitally empowered Afghanistan and connected society.

These include the lack of a cohesive plan, a regulatory and institutional framework for digital transformation, a lack of infrastructure capabilities, lengthy and outdated government processes, and technology procurement and deployment

Besides, duplicate and non-prioritized efforts, insufficient cooperation between government agencies in the implementation of technology, lack of a coherent system for information and data governance, limited human capital and skills, limited use of technology in the provision of public services, and the absence of necessary research and development practices to support digital transformation.

2. Literature Review

Transportation

For economic and social activities such as traveling, producing, distributing goods, or supplying energy, passenger and freight transport mobility is considered fundamental. There is an intent, an origin, a possible collection of intermediate locations, and a destination for each movement. Transport networks consisting of infrastructures, modes, and terminals are supported and powered by mobility. They enable people, organizations, companies, regions, and nations to communicate and consider economic, social, cultural, or political activities. Mobility-providing transport networks are closely connected to socioeconomic shifts. There are likely to be economic opportunities where transportation networks will ensure access to markets and services. Economic development has affected the world differently. Both international, regional, and local transport networks have become essential components of economic activity. Thus, an increasing proportion of wealth is connected to trade and delivery. However, there are also negative effects, such as pollution, injuries, and mobility inequalities, even though transportation has a positive effect on socioeconomic structures. Transportation is also a business activity derived from operational characteristics such as expense, power, efficiency, reliability, and speed. Transportation networks are emerging within a complex collection of links between the supplies of transport, representing the network's operating ability, the demand for transport, and the economy's mobility requirements. [6]

Revenues and Taxation

For a long time, taxation has been one of the dominant methods for financing a country's administration. Tax collection provides a financial basis for every country to offer public services to its citizens. Furthermore, this process plays a useful role in the social welfare and economic development of a society. Today's governments collect taxes in various ways and spend it on current affairs, making it one of the safest ways for the country to progress [7]. Therefore, appropriate, reliable, and transparent methods should be adopted so that as many taxpayers as possible are encouraged to pay taxes voluntary.

For this reason, it is recommended to refer, during the development and operation of the project, to the financial resources of public infrastructure and construction projects, which are primarily supplied by taxation, so that taxpayers can be fully aware of the type of tax expenditure by looking at the above projects [7].

Afghanistan is a country that earns its income from internal and external sources. One of these sources is tax collection, which plays a vital role in government revenue generation. Since the establishment of the current government and the new political system in Afghanistan in 2001, many attempts have been made to develop their financial and economic structure. Thus, many governmental institutions designed a series of reforms and have implemented them to increase internal revenue [8].

Although the use of technology in Afghanistan's governmental institutions as a means for electronic governance, better and effective administration is not yet wholly utilized. However, the government and especially the Ministry of Finance have used technology to improve governmental institutions' transparency and credibility.

Finance and taxation are the backbones of any country's economy. Therefore, it needs to be transparent and credible so that the citizens and donors feel committed to the development process. With this in mind, the government has decided to implement the Afghanistan Financial Management Information System (AFMIS) and Standard Integrated Government Tax Administration System (SIGTAS), with the help of the Public Financial Management Reform (PFMR), which is a project implemented by the ministry of Finance [8].

Transport Taxes in Afghanistan

The Ministry of Transport, to provide better transport services to the people and regulate the country's transport affairs, collects a certain percentage of the freight for the transport of commercial cargo or passengers as transport tax from companies and means of transportation.

According to the Land Transportation Regulation law, the internal transportation companies and vehicles must pay five percent of the total fare as a transport tax to the Ministry of Transport. The same is for the external companies and vehicles but with an increase in the tax amount, which is ten percent of the total fare.

By exploiting the mentioned revenues, the Ministry of Transport spends the collected transportation taxes for building transport terminals for passengers and trucks, Creating repairing workshops for vehicles, and improving and enhancing its transportation system.

Ministry of Transport

The Ministry of Transport is responsible for regulating air and ground transport, operations at airports, international routes, and other government enterprises involved in transport transactions. The main focus is on strengthening the regulatory and monitoring capabilities and improving the country's transport infrastructure. As the development of the transport sector is of particular importance in improving the public's well-being, it continues to have a positive impact on the Afghan economy.

Most importantly, it enhances the growth of a balanced economy across the country and facilitates trade, increases government revenues, creates opportunities for personal investment, and improves the safety, security, credibility, and efficiency of both air and ground transportation.

The Ministry of Transport's primary mission is to design, regulate, oversee, and man- age, with full engagement and participation of the private sector, transportation systems that are efficient, safe, easily accessible, environment-friendly, equitable, affordable, mod- ern, high quality, and are stimulants of the economic growth of the country [9].

Ministry of Transport's Services

The Ministry of Transport has five central authorities that provide different services, namely as follows:

1. National Road Authority
2. Traffic Authority
3. Land Transport Authority
4. Afghanistan Railway Authority
5. Civil Aviation Authority

Land Transportation Authority

Land Transport Authority is one of the vital service and revenue departments in the Ministry of Transport's organizational structure. Their main objectives are to design, regulate, monitor, and manage the road transport system effectively, safe, accessible, environmentally friendly, and economical to provide better services at the national and international level. And it is in cooperation with companies and the private sector for the economic growth of the country. The authority is responsible for preparing transportation facilities and manage all land traffics, including cargo trucks, passenger buses, and private vehicles through Afghanistan, especially on the highways and regional routes [9].

Vehicles Registration

Another essential process in the General Directorate of Land Transport is the vehicle registration process at this directorate. After the contract with the transport companies and to operate in the countries transport system, vehicle owners must submit their application to the vehicle registration department of the General Directorate of Land Transport to receive a vehicle transport card. For this purpose, the vehicle owners must submit their application and some necessary documents such as the approval of the transport company, driving license, identity card, and driver's license. This process includes some sub-processes, which are explained as follows

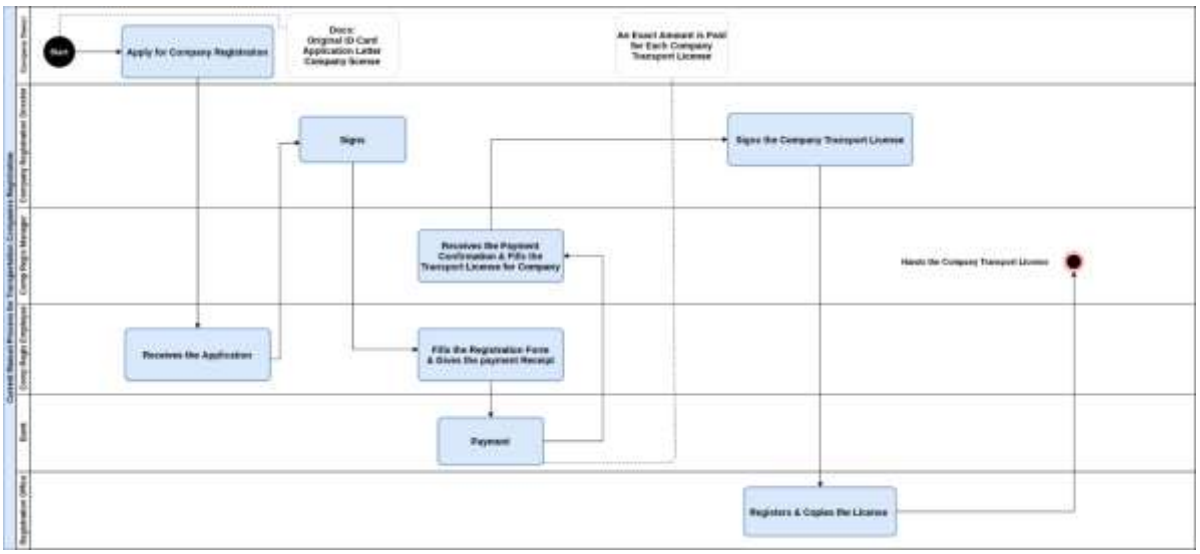

Figure: Current Manual Process for Transportation Companies Registration

Route Determination

After the vehicle registration procedure in a transport company, the route determination procedure is needed to be done. In this procedure, the route determination process is done based on the demands and needs of different local regions in the country. For instance, we can say that Afghanistan's central districts do not have an adequate number of transport vehicles, so the route for the new vehicles is assigned to that region.

Transport Card Distribution

When a vehicle is registered in this phase, and the route is assigned, the vehicle registration department hands in the vehicle owner's transport card. This card contains information about the vehicle, driver, Transportation Company, and the determined route. Cite interview for a better understanding of the vehicles registration process, the following activity diagram illustrates the whole vehicles registration processes, including the route determination and transport card distribution processes:

Table: Requirement description for Vehicles & Drivers Registration.

Steps	**8**
Required Documents	Original ID Card, Application Letter, Transport Company Confirmation, Driving Licenes, Driving Permit
Process Fee	-
Required Time	1-2 day

For a better understanding of the transport company registration process, the follow- ing activity diagram illustrates the transport company's registration processes:

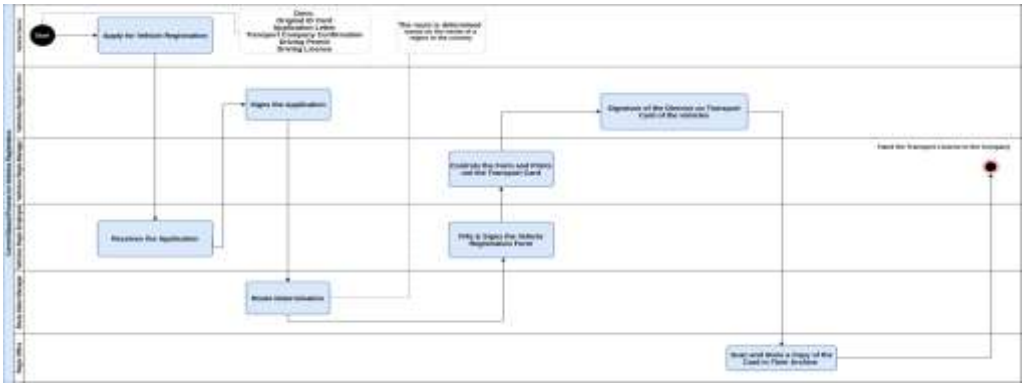

Figure: Current Manual Process for Vehicle Registration

Tax Collection

This is the most critical and essential process being done under the land transportation general directorate's management. It is the primary process that can get digitally- enabled after this system is developed. In the tax payment process, when a vehicle arrives in a transportation port, they have to pay the transport tax, which differs due to the type of vehicles that are for public services or are transferring commercial properties. The transport tax is determined after the identification of the vehicle type. The tax definition is a predetermined process by the Ministry of Transport in which the taxes are assigned or determined based on the type of vehicle and the route distances covered by the vehicles.

After that, the port operators write down the amount of tax that has to be paid by the driver of the vehicle in a slip called transportation tax invoice. The tax amount is gathered in cash by the responsible employees of the transportation port, and then the invoice is given to the driver. This invoice is checked during the route which the vehicles pass, and in case they do not have this invoice, they have to pay an additional amount of money as a fine.[11] For a better understanding of the transportation tax payment process, the following activity diagram illustrates the whole processes, including the route determination and amount of the transportation tax processes:

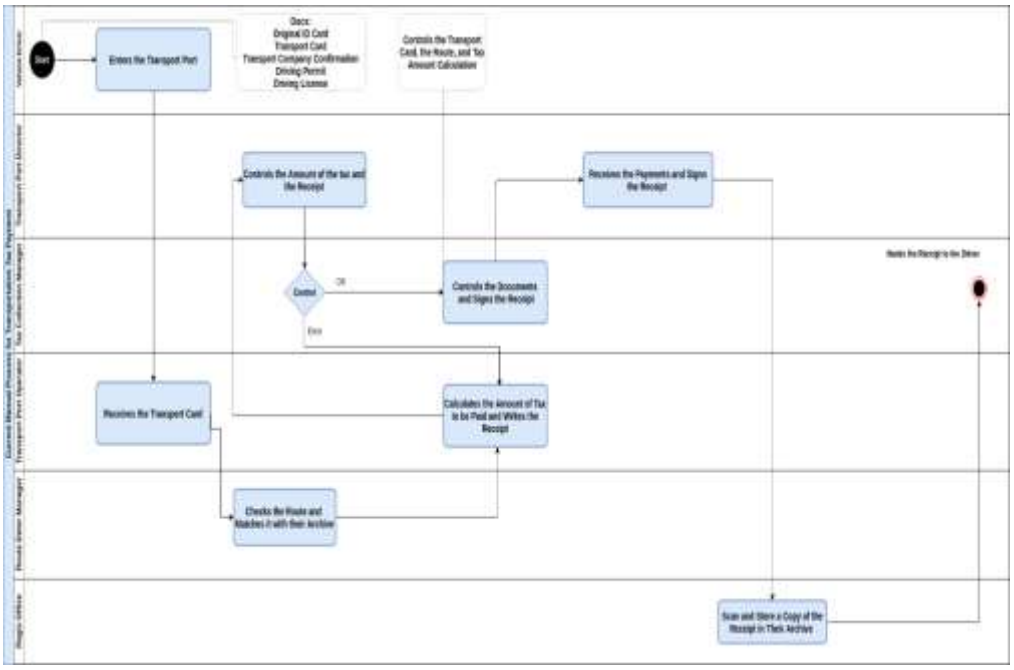

Figure: Current Manual Process for Tax Collection

The primary purpose of this research is to implement an electronic payment system for transportation taxes in Afghanistan. Considering the significant and dramatic advances in technology over the past few decades have had a significant and positive impact on the economy, different industries like construction, health care, education, and trans- partition.

Digitization and utilization of technology today serve as the main driver of economic growth and improve the population's quality of life. Since there are various developed and developing countries around the world where the electronic payment systems or transport toll collection systems have been implemented [12].

Although we will not achieve a complete implementation of these approaches in Afghanistan due to different aspects such as infrastructure, economic or costs, poli- cies, and IT literacy, lessons can be learned from their implementation experiences to solve issues and challenges.

This chapter will look at two different electronic payment systems for transportation taxes including GPS-based electronic payment system, and RFID-based electronic payment system, used in countries such as the Czech Republic, Srilanka, and India. The most suitable approaches, experiences, and best practices could be used as part of the lessons learned for developing an electronic payment system for transportation taxes in Afghanistan. Before addressing the mentioned technologies, we will briefly explain e- governance, e-government in developed and developing countries, and electronic payment.

3. Methodology and Research Work

Proposed Concept

The challenges mentioned earlier have built support for a new concept for an electronic transport tax payment system in Afghanistan. In general, some several technologies and methods make it possible to Change the common system into an automated and electronic system. Different methods from both developed and developing countries have been explored to recommend the concept. The proposed system must be designed and implemented following the relevant depart- ment's requirements and taking into account the needs of that organization, to address all the existing problems and challenges of the current system.

By studying the current situation, modern technologies for the collection of trans- port taxes, the challenges facing them in Afghanistan, and the current situation in Afghanistan, we concluded that it is currently hard and challenging to implement any of these technologies in Afghanistan.

We suggest a management information system for collecting transport taxes in Afghanistan, taking into account all the aspects that have already been addressed in detail in previous chapters. We have proposed this system for several reasons, each of which is discussed below [30].

First, Afghanistan has enough capacity to implement the proposed system. In con- trast, the adaptation of any existing technology, such as GPS or RFID, has its prereq- uisites and modern equipment. In Afghanistan, these conditions are not available, as mentioned in the previous chapter.

Second , in terms of economics and time, this system needs less budget and less time. Simultaneously, it will be time-consuming and expensive for Afghanistan to implement any of the modern technologies.

Third , given the country's existing technological capability, the introduction of this proposed system is much simpler than new technologies that require skilled personnel.

The system will store information related to transport companies, driver information, payments information, payments tracking, and report generation for better management and provide statistics to the relevant authorities.

In the following, we will more discuss the proposed system, and its design aspects.

System Architecture

A system is described as a set of multiple elements that collaborate to achieve a common goal. The objective of a system is to accept input, manipulate or transform such input into output. Therefore, a system is expected to have inputs, processing mechanisms, outputs, and feedback. As mentioned in the previous section, our proposed system is a management information system for transport taxes. Based on web-based manage- ment information systems principles, the overall system architecture is illustrated in the following diagram.

As illustrated in the above diagram, the system architecture consists of three layers: each is explained shortly in the following. The data tier executes a set of commands to allow access to the data storage stored in a database and uses a DBMS to do so. We need a DBMS, such as a MySQL server, to add, view, or process the stored data in the database.

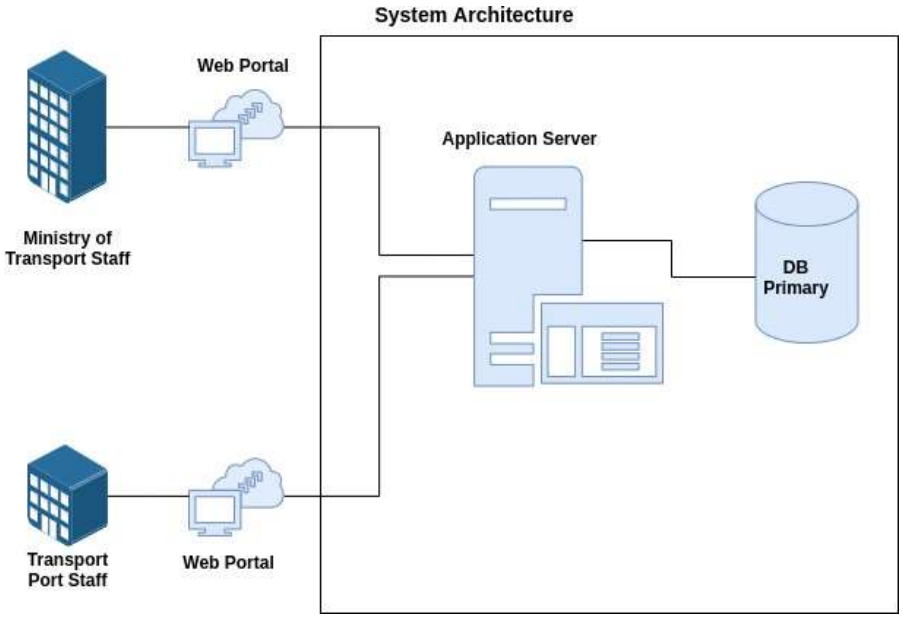

Figure: System Architecture

The middle-tier business logic tier contains scripts and system features representing the interface between the database tier and the presentation tier. After converting to a SQL query, this tier sends the request to the database tier. This layer is physically located on the web services host server.

The presentation tier is the architecture's front-end portion responsible for delivering the user interface, physically located on the client computer. The presentation layer focuses on converting the business logic layer's outcome into a user-friendly and readable output.

Use Cases

A use-case diagram is simply the representation of interactions between the intended users and the system. The use-case shows the work of a specific user who does use the system [31]. Concerning the system's requirements, especially concerning MOT's administrative structure, differentiation of roles and responsibilities is a crucial task in the system. The privacy of data and data flow requires different roles to be considered in the system. Based on the requirements analysis, the actors and their interactions are visualized in the following use-case diagram:

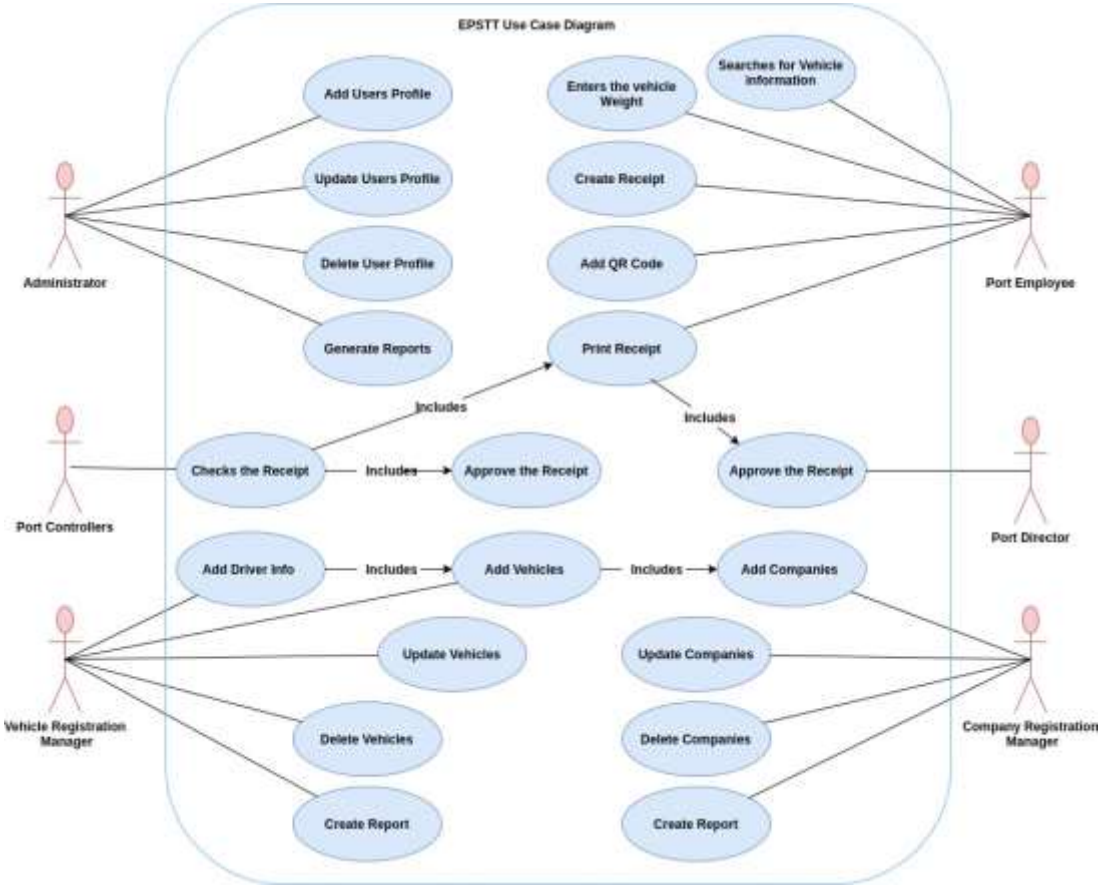

Figure: Use-case Diagram

Based on the user's requirements and the rules of the MOT tax collection procedure, there are different users involved with the system who are doing different tasks. Everyone has to login into the system, the system only allows authorized users to perform their particular tasks, and no one has to influences other users of the system.

The variety of users, according to the transportation tax collection process at MOT, can be categorized into the following types: Administrator, Vehicles registration user, Transportation Companies registration data entry user, Port employee data entry user, Port director user, and port controller user.

Company Registration Manager: The company registration manager is re- sponsible for adding, updating, and if needed deleting transportation companies' information from the system. Another major rule of the company registration manager is creating reports that differ based on its needs. The number of these users is limited to two or three employees, including the company registration, general manager.

Vehicles Registration Manager: The vehicle registration manager is responsible for adding, updating, deleting vehicle information from the system, and adding the driver's information. Furthermore, the vehicle registration manager can create reports that differ based on the authority's needs. The number of these users is limited to two or three employees, including the vehicle's registration general manager.

Port Manager: The port manager is one of the system's primary users. They are responsible for browsing the vehicle information by entering the Plate number, adding the vehicle weight from the Ministry of Public Works' document, creating the receipts for tax payments, adding the QR code to, and printing out the receipts. Another significant rule of the Port manager is creating reports that differ based on the authorities' needs, and the number of these users are different due to the load on a transport port, which rises to more than three employees.

Port Director: The Port director is another user of the system responsible for approving the receipts created by the port managers. If there are some mistakes in receipts, then the port director can update the receipts information as well, and the number of these users are limited to one user per each transport port in every region.

Port Controller: Port controllers are other users of the system responsible for checking and approving the receipts created by the port managers. This controlling can be done in each transport port, and if the vehicles do not have the receipt, the port controllers perform the same processes as the port managers do while they can add fines to the receipts.

It is essential to be considered that the port controllers have the same rules as the port managers have, which means that the same user policies are applied to the port controller users by the system administrator.

System Administrator: Besides all the users who were discussed above, the system administrator is responsible for doing all administrative staff regarding the system users. The system administrator adds, updates, and deletes users and their rules based on the institution's needs and provides some reports for the authorities.

Data Model

A class diagram is one of the fundamental building blocks for object oriented software development (MVC development model in the context). It describes the structure of the whole system by describing the classes involved. It shows basic operations, attributes, and relationships between the classes [32]. Based on the requirements anlysis, the classes and their relationships are visualized in the following class diagram.

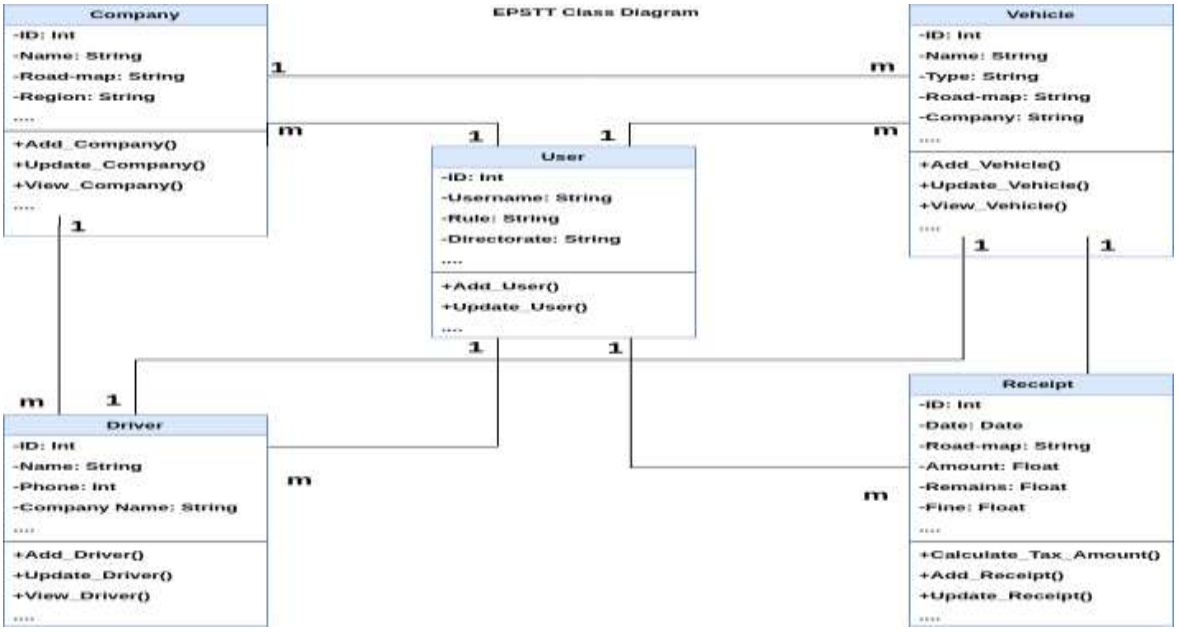

Figure: Class Diagram

Because of the large number of attributes and methods, few attributes and methods are presented in the diagram above. The most important information stored in the sys- tem will be the transportation companies' information, vehicle information, the drivers' information, and receipts information. The basic class elements and their relationship in the mentioned diagram are briefly described as following:

Company: Transport company information such as ID, name, region, road map, number of vehicles, and other required information will be stored in the system. The relevant user is also allowed to add, correct, and, if needed, delete the in- formation of a company. As illustrated in the diagram, the company class has a relation with vehicle, driver, and user classes.

Vehicle: Vehicle information such as ID, name, type, road map, plate number, company name, permissible weight, number of allowed passenger in case it is a public vehicle, and other required information will be stored in the system, and the relevant manager is also allowed to add, correct and if necessary delete the information of a vehicle. As illustrated in the diagram, the vehicle class has a relation with the company, receipt, and user classes.

Driver: The driver information such as ID, name, last name, license number, license type, company name, belonging vehicle, plate number, and other required information will be stored in the system. Furthermore, the relevant user is also allowed to add, correct, and delete the driver's information. As illustrated in the diagram, the driver class has a relation with vehicle, company, and user classes.

Receipt: The receipt information such as ID, date, tax amount, road map, the weight of trucks, number of the passengers(in case it is a public vehicle), remains, fines, plate number, related company name, port name in which the payment was issued, and other required information is stored in the system. The relevant user is also allowed to add, correct, and, if needed, delete the information of a company. As illustrated in the diagram, the receipt class has a relation with vehicle and user classes.

User: Necessary information of the system users, including username password, rules, directorate name, will be stored in the system. As illustrated in the diagram, the user class has a relationship with all other system classes.

4. Core Functionalities

Based on observations as well as interviews, the core tasks are identified. As mentioned in the outcomes of requirements analysis in chapter four, the concept will digitize the transportation tax collection processes. It should be emphasized that these core functionalities are specified based on the ministry

of transport's need to have an electronic system for the processes that are part of the transportation taxes collection. The most essential and core functionalities, which will be provided by the proposed concept, are listed as following:

Transportation Companies Registration: As mentioned in the second chap- ter, the transport companies' registration process was the first step to collect transportation taxes. Furthermore, considering the ministry of transport's re- quirements, one of the main tasks of the proposed system is to register and store information on transportation companies. It includes standard CRUD functional- ities for the transportation companies. Based on their rules, the responsible users can add, view, edit, and, if necessary, delete the information of the transportation companies (See Flow-Chart here: 59).

Vehicles Registration: As previously described in Chapter Two, it is necessary to have information related to vehicles to regulate the transportation tax collection process. Thus, one of the proposed system's main tasks is to register all vehicles that are active in the transport sector and store their needed information in the system. It includes standard CRUD functionalities for the vehicles, and the re- sponsible users, based on their rules, can add, view, edit, and, if necessary, delete the vehicles' information(See Flow-Chart here: 60).

Drivers Registration: Another important task of this system is to record and store the necessary information for drivers specified by the related authorities and the land transport regulating law. As mentioned in previous processes, this in- cludes standard CRUD functionalities for the vehicles. Based on their rules, the responsible users can add, view, edit, and, if necessary, delete the information of the vehicles.

Tax Payments and Tracking: The process of storing and tracking the transport tax payments is one of this system's main tasks. All tax payment steps, including tax calculation based on available vehicle information in the system, tax amount, payment status, payments receipts generation and printing, and other related is- sues, should be stored. Moreover, as standard, the users will perform the CRUD functionalities on the system's tax payment and tracking function based on their rules(See Flow-Chart here: 61).

Reports Generation: Another important task of the system is to prepare reports based on users' demands, who prepare and submit quarterly, semi-annual and annual reports.

5. Risk Analysis

Considering the requirements of relevant institutions in Afghanistan, after providing a detailed concept, the system could face some threats after successful implementation. To understand the strengths, weaknesses, and risks that may threaten the system, as a precaution for these threats and providing some strategic plans for overcoming the weaknesses, we will conduct a comprehensive SWOT analysis and point out some critical risk analysis of the proposed system. It will assist us in having some predefined strategies to deal with upcoming threats. The SWOT analysis focuses on the system's four elements (Strengths, Weaknesses, Opportunities, and Threats). The first two elements, strengths, and weaknesses are identified as internal factors, and two other elements are identified as external factors that affect the system [33]. In the following, we have prepared a SWOT analysis of the proposed system.

Strengths

The proposed system can have good performance, and the following are the system's strengths compared to the current manual system.

- Well organized data regarding the transport companies and vehicles.
- Improves the tax collection processes.
- Improves the payments trucking.
- Improves reporting and customized reports.
- Availability.
- Accessibility.
- Time Efficiency.

Weaknesses

The followings are the system's weaknesses, which are derived from the challenges to- wards the implementation of the system.

- Lack of ICT infrastructure, which may slow down the implementation process.
- Human capital problems, which is a problem towards the adoption of the system.
- Lack of Political willingness, which may disturb the implementation process.
- Electricity dependency.

Opportunities

The proposed system will provide some opportunities after a successful implementation, which are listed as follows:

- It will enhance the highways of transport authorities to have better transport management.

- It will provide the opportunity of payment trucking that provides the ability for the related authorities to enforce the people to pay the transport taxes.

- Provides efficient information and reports which can help the authorities for better planning and management of the transport sectors.
- The system will help the ministry of Transport to increase incomes by transport ports.
- The system will provide the opportunity to increase transparency and, by the time, decrease corruption.

Threats

Some threats may threaten the system, which is listed as follows:

- Fraud in the payment process.
- System failure or downtime.
- Connectivity problems.
- Infrastructure Security.

Strategic Plans to overcome the threats

To deal with the weaknesses and threats that exist for the system, we will provide some plans and strategies in two separate sections to address the weaknesses and deal with the risks and threats.

Recommendations to Overcome the Weaknesses

We need collaboration, commitment, and intention at the national level to solve these problems to eliminate the system's weaknesses pointed out earlier. The way will be paved for the implementation of this system once this collective intention has emerged, and we have the full support of the government.

For this purpose, we must consider the following issues:

Gain government officials' trust by introducing the benefits of the system and describing the opportunities that the system creates. It helps to attract their support and work with them to eliminate other weaknesses of the system.

Assessment and upgrade of the IT infrastructure of participating national and local government units. We can provide the necessary infrastructure and sufficient power for the system by gaining government funding and a certain budget.

We can address the human capital development issue by launching on-location training courses to improve workers and system users' ability.

Recommendations to Overcome the Threats and Risks

To deal with the threats and risks, we considered strategies and plans for each of the previously stated threats that could threaten the system, which is listed as follows.

Fraud Detection:

The system will face two unique problems concerning fraud in payment systems, as stated in the current system problems and challenges related to the tax collection process. First, some vehicles could, cross the port from subways or via smuggling routes without tax payments. Second, some vehicles will carry out the payments, but it is not the real sum. Due to the apparent existence of administrative corrup- tion, they do not pay the actual amount.

It could happen with the proposed system as described in the threat portion of our swot analysis, and that is why we have considered some precautionary plans to overcome these problems.

A: The proposed system is designed so that the information of all vehicles active in the field of transport services will be entered into the system. Therefore, any vehicle that is active in any part of the country can be tracked by the system and reported, which means with the help of the system, we can identify these vehicles and collect taxes from them. Therefore, no device that is included in the system can evade paying taxes. However, in the case of vehicles that are not registered in the system, we can identiand register them with law enforcement agencies' cooperation so that they can be registered and taxed according to the law.

B: In the case of payment fraud, which can often occur due to corruption in trans- port ports, As we described in the system's design and functionality, the variables necessary to calculate the amount of tax, such as road-map, vehicle weight, are already included in the system. The tax is calculated based on those variables. It will avoid fraud and changes in the amount of tax because, except in the case of a formal request, not every user has the rule to change these variables.

System Failure and Connectivity: In the case of system failure and connec- tivity issues, we will use the method and technique of replication to resolve the problems described.

The following diagram shows how the replica nodes are distributed country-wide and how the associated provincial sites communicate with and support them. All the country's provinces are divided into five separate zones, as seen in the illustra- tion, and one control center controls all of these zones. Each

zone comprises many provinces that usually have all their transactions with the appropriate zone server. It is the responsibility of the control center located in Kabul to synchronize the servers of all zones.

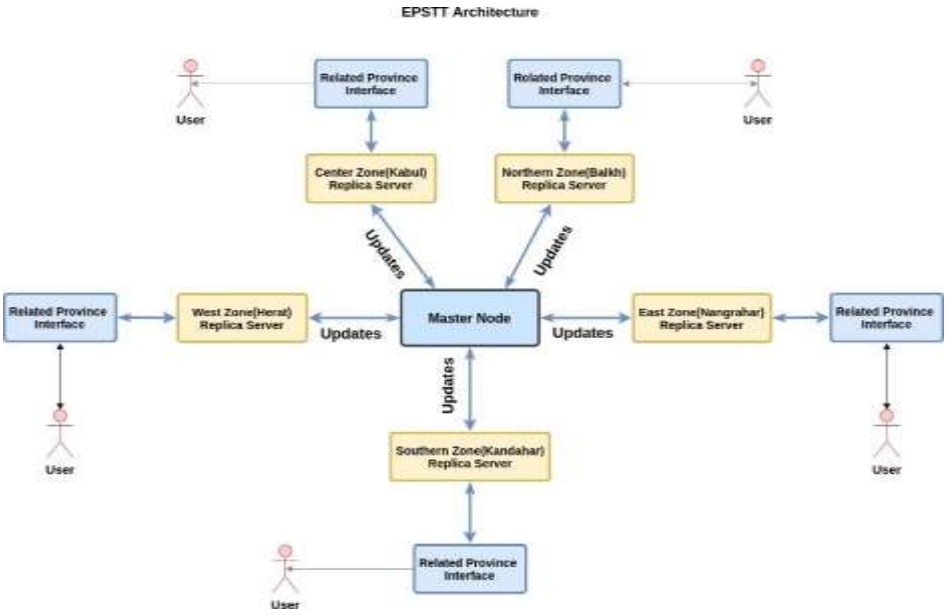

Figure: Replication Architecture Diagram

It is worth mentioning for data replication, and we will use the transactional method because users receive full initial copies of the transactional replication database and then receive updates as the data changes. Data is copied in real- time from the publisher to the receiving node in the same order as it occurs with the publisher, so transactional consistency is guaranteed in this type of replication. In server-to-server environments, transactional replication is typically employed. It does not merely copy the changes in the data but instead replicates each change consistently and accurately[34].

With this strategy, we can achieve system availability, high performance, and pro- tect the system failure; however, it may require more budget and equipment.

Infrastructure Security

Infrastructure security is one of the other threats that may impact the system, especially in a country like Afghanistan. In the current situation that we have many security issues in Afghanistan, we can not be assured to prevent this risk from happening completely. However, there are some practices that we can do to minimize the risk of damaging the infrastructure. Locate the infrastructure in a secure area and ask the related authorities to cooperate with the Ministry of Transport to achieve this goal.

7. Conclusion

The work presented has shown that collecting transportation taxes in Afghanistan can be improved by conducting different actions and applying different methods and tech- nologies. The proposed concept, which is developed based on the current situation analysis, the analysis of the available concurrent technologies for the electronic collection of trans- portation taxes, and the requirements analysis for the proposed concept, has led us to three following major phases. A literature review on the current situation and the current situation analysis was initially carried out. Subsequently, the systems and technologies available for the electronic collection of transport taxes are being introduced and reviewed to derive the elements and sample design for the proposed concept.

The requirements analysis was performed through face-to-face interviews back in Afghanistan to understand and assess the proposed concept's requirements. Initially, the definitions of fundamentals and terminology are defined, then the current processes for the collection of transportation taxes are analyzed. The problems and challenges of the current manual system for collecting transportation taxes are described and discussed in the last part of this section. Observations of current processes, as well as interviews, are instruments to identify the core tasks.

In this section, we introduced and discussed the available technologies in the field of transportation tax collection. Two modern technologies, including GPS and RFID, have been analyzed in-depth, taking all aspects into accounts, such as structure, components, and work processes. Finally, after reviewing the mentioned technologies, the benefits and challenges of implementing them in Afghanistan were explained in detail.

Derived from the current situation analysis findings and how the users might use the system, both functional and non-functional requirements are specified in this section. Additionally, we have conducted the system's stakeholder analysis and prepared a de- tailed use-case diagram to represent the core tasks in a more precise structure.

We proposed an electronic payment system that is practically a management information system to digitize the current manual system, taking into account the requirements, reviewing the available technologies, and related challenges in Afghanistan, as this was the main objective of this study.Different aspects of the proposed system was discussed in this section, such as usage, system architecture, core features, and risk analysis.

References

1. B. Majeed, H. A. K. Niazi, and N. Sabahat, "E-government in developed and devel- oping countries: A systematic literature review," in *2019 International Conference on Computing, Electronics Communications Engineering (iCCECE)*, pp. 112–117.
2. "Z. Fang, "E-Government in Digital Era: Concept, Practice, and Develop- ment," vol. 10, p. 22, 2002. - Google Search."
3. *Review of information and communications technology and development. Issue no. 1*. UN,, 2003.
4. "Digital Foundation – Strategy For Afghanistan, [Online]. Available: http://digital.af."
5. S. F. Starr, A. Kuchins, Central Asia-Caucasus Institute and Silk Road Studies Program, and D. Center for Strategic and International Studies (Washington, *The key to success in Afghanistan: modern Silk Road strategy*. Central Asia-Caucasus Institute, in cooperation with the Center for Strategic and International Studies ; Silk Road Studies Program, Institute for Security and Development Policy. OCLC: 981845692.
6. P. Jones, "The evolution of urban mobility: The interplay of academic and policy perspectives," vol. 38, no. 1, pp. 7–13.
7. "taxation | definition, principles, importance, & types." Library Catalog: www.britannica.com.
8. "Afghanistan customs department, [online]. Available: https://mof.gov.af/dr ´´´
9. "Ministry of Transport | AfGOV, [Online]. Available: https://mot.gov.af/en/."
10. "NAZARI, AHMAD JAWID: Technical Employee, land Transportation Regulation General Directorate, Face-to-Face Interview, August 2019."
11. "Tax Collection Manager, kabul West Transportation Port, Face-to-Face Interview, August 2019."
12. S. Chattoraj, S. Bhowmik, K. Vishwakarma, and P. Roy, "Design and implemen- tation of low cost electronic toll collection system in india," in *2017 Second In- ternational Conference on Electrical, Computer and Communication Technologies (ICECCT)*, pp. 1–4.

View publication stats

Application of Machine learning in predicting the yield strength of API steels

Gaurav Kumar*, Qasim Murtaza, Ashutosh Bagchi, G. Kumar, Darshan Lal

Department of Mechanical Engineering, Delhi Technological University, New Delhi 110042

Email*: gauravkumar2k19.me090@gmail.com

Abstract:

Machine learning has become increasingly important in various fields, including the mechanical industry. API steels being a subgroup of high-strength low-alloy (HSLA) steels have been designed for use in the petroleum industry. In this research, the application of machine learning models to estimate the mechanical properties of API steels was explored. Both non-linear and linear machine learning models were employed to predict the yield strength of API steels. The models were evaluated using different performance metrics on test samples, which produced promising results. Random forest model proved to be effective in estimating the yield strength of API steels with a R2 Score of 0.95. The results exhibit the effectiveness of machine learning techniques in predicting mechanical properties, making them a valuable tool for researchers and engineers in the materials industry.

Keywords: Machine Learning, API steels, Data analysis, Yield Strength

1. Introduction:

API steels are a type of high-strength low-alloy (HSLA) steel [1] primarily developed for use in the petroleum industry [2]. A mixture of alloying elements, such as chromium, molybdenum, and nickel are present in these steels, which impart enhanced strength and corrosion resistance to them [3]. Their design is specifically aimed at enduring extreme temperatures, pressures, and corrosive environments [4,5] that are frequently encountered in the oil and gas sector. API steels are graded accordingly to maintain the quality of the steels used for the production of pipes and other equipment. The most widely used API grade classifications are API 5L for seamless and welded pipes, API 5CT and API 5B for casing and tubing, and API 5D for drill pipe [6]. Given their exceptional strength and toughness, API steels are extensively used in various applications, such as pipelines, offshore platforms, and drilling equipment, to withstand challenging industry conditions.

Machine learning, a branch of artificial intelligence, enables computers to learn from data and make decisions or predictions without human intervention. The three primary types of machine learning include reinforcement learning, unsupervised learning, and supervised learning. In supervised learning, labeled data is used to teach the algorithm in order to predict new data. Unsupervised learning entails discovering relationships and patterns in unlabeled data, while reinforcement learning involves learning through trial and error in a dynamic environment. Machine learning has widespread applications, including fraud detection, speech and image recognition, autonomous vehicles, predictive maintenance, natural language processing, and

recommendation systems. With the continuous growth in data generation, machine learning is gaining importance in making sense of and extracting insights from the vast amount of data [7].

The utility of machine learning in production engineering and material science is diverse and extensive. One of its primary applications is the optimization of manufacturing processes, which is achieved through the prediction of defects, monitoring of equipment performance, and enhancement of product quality. In material science, machine learning techniques are used to expedite the discovery of new materials, predict their properties and performance, and optimize their processing [8]. Furthermore, machine learning algorithms are leveraged for predicting the fatigue life of materials [9], analyzing fracture patterns [10], and detecting material defects [11]. Additionally, predictive maintenance is another area where machine learning is used to identify potential equipment failures before they occur, thereby ensuring uninterrupted operations and reducing downtime [12].

This research aims to devise and compare several machine learning models to predict the minimum yield strength (in ksi) of API steels based on their mechanical properties and chemical composition. The dataset consisted of API steels with confirmed target values of yield strength, which were used to train and evaluate the models. The objective of this study is to determine the most precise and dependable ML model to anticipate the yield strength of API steels.

2. Methodology:

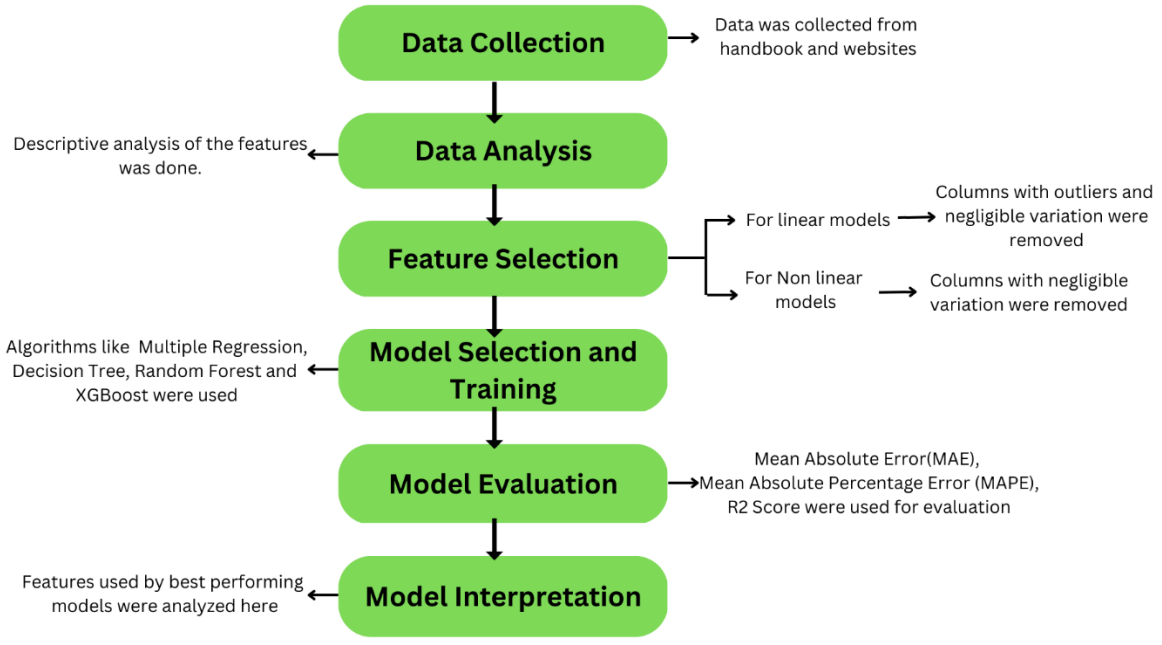

Figure 1: Flowchart of the steps followed in the analysis

This study utilized machine learning techniques to estimate the yield strength of API steels. As depicted in Figure 1, Initially a dataset of API steels was gathered, and their chemical composition, physical properties, and mechanical properties were recorded. Since the variation in physical properties was negligible, they were eliminated from the analysis. Subsequently, the dataset was divided into two sets, one having 87% of the data was allocated for training and another having 13% for testing. In the case of Linear models, data were subjected to feature scaling or normalization, while it was deemed unnecessary for nonlinear models. Also, Features like Cr and Ni having a high number of outliers were removed from the analysis while using Linear models in order to improve their performance [13]. Multiple regression, multiple regression with L1 regularization, multiple regression with L2 regularization, decision tree, and random forest models were established using the training data. The models' performance was assessed using R2 score, mean absolute percentage error (MAPE), and mean absolute error (MAE) metrics, which were later compared and have been summarized in Table 1.

2.1 Artificial Intelligence Models:

This study explores various machine learning models to estimate the yield strength of API steels on the basis of their chemical compositions and mechanical parameters. The aim is to achieve accurate prediction by implementing and evaluating several regression-based models, including random forest, decision tree, and multiple regression. This section provides a detailed overview of each of these models, including their underlying principles and performance metrics.

2.1.1. Multiple Regression:

Multiple regression is an analytical method used to analyze the relationship between multiple independent variables and an outcome variable. It helps to estimate the outcome variable based on the values of multiple independent features [14]. In multiple regression, a regression equation is created that estimates the value of the outcome variable based on the values of the independent variables.

The expression of multiple regression is given as:

$$\hat{y} = \alpha_0 + \alpha_1 x_1 + \alpha_2 x_2 + \cdots + \alpha_n x_n$$

here, $\hat{y}$ = Dependent Variable (Yield Strength(min)).

x_1 to x_n = independent variables (Chemical composition and mechanical properties)

E = Irreducible/ Prediction error

Hence the equation of the predicted yield strength can be given as:

$$Predicted\ yield\ strength = \alpha_0 + \alpha_1(C) + \alpha_2(Mn) + \alpha_3(Si) + \alpha_4(Mo) + \alpha_5(Cu) + \alpha_6(V) + \alpha_7(N) + \alpha_8(S) + \alpha_9(P) + \alpha_{10}(Fe) + \alpha_{11}\big(Hardness(HB, min)\big) + \alpha_{12}\big(Hardness(HB, max)\big) + E \quad (1)$$

α_0= y-intercept

α_n = Slope of the line, where n = 1,2, 3...

$$\alpha_0 = \frac{(\sum y)(\sum x^2) - (\Sigma x)(\Sigma xy)}{n(\sum x^2) - (\sum x)^2} \quad (1a)$$

$$\alpha_n = \frac{n(\sum xy) - (\sum x)(\Sigma y)}{n(\sum x^2) - (\sum x)^2} \quad (1b)$$

The above equations are solutions to the cost function of Multiple regression using the Ordinary Least Square method [15].

The cost function for Multiple regression:

$$\text{Minimize } \theta = Minimize \sum_{i=1}^{n} (y_i - \hat{y}_i)^2 \quad (2)$$

where y_i = actual values and $\hat{y}_i$ = predicted values

As per our case, it can be written as:

θ = Summation of ((Actual Yield Strength – Predicted Yield strength)^2) for all records

However, in some cases, multiple regression models can be prone to overfitting, especially when there are many independent variables. This can result in models that are overly complex and have poor predictive power. Regularization is a method that can help in the prevention of overfitting by adding a penalty term to the regression equation [16].

L1 and L2 regularization are two commonly used techniques for regularized multiple regression. In the case of L1 regularization, a penalty term is added to the cost function that is proportional to the absolute value of the coefficients. This technique is also known as Lasso regression. On the other hand, in the case of L2 regularization, also called Ridge regression, a penalty term is added which is proportional to the square of the coefficients [17].

.

The cost function in case of L1 regularization:

$$\theta = \sum_{i=1}^{n} (y_i - \hat{y}_i)^2 + \lambda * (Sum\ of\ absolute\ values\ of\ coefficients)$$

$$\theta = \sum_{i=1}^{n} (y_i - \hat{y}_i)^2 + \lambda * \sum_{i=1}^{n} |\alpha_i| \quad (2a)$$

The cost function in case of L2 regularization:

$$\theta = \sum_{i=1}^{n} (y_i - \hat{y}_i)^2 + \lambda * (Sum\ of\ square\ of\ coefficients)$$

$$\theta = \sum_{i=1}^{n} (y_i - \hat{y}_i)^2 + \lambda * \sum_{i=1}^{n} (\alpha_i)^2 \quad (2b)$$

The penalty term (λ) in regularization helps to control the size of the coefficients in the regression equation, preventing them from becoming too large and reducing the impact of irrelevant or redundant independent variables. By doing so, it helps improve the model's accuracy and stability [18].

Regularized multiple regression techniques like L1 and L2 regularization have proven to be effective in improving the multiple regression model's performance, particularly when dealing with large datasets with many independent variables.

2.1.2. Decision Tree:

Decision tree is a popular machine learning technique used for both regression and classification tasks. The basic idea behind this algorithm is to recursively partition the input data into smaller subsets, on the basis of the values of the input features, until each subset contains only one type of output (in classification) or a single value (in regression). Each partition is made using a decision rule that splits the data based on the value of a single feature [19].

The CART (Classification and Regression Trees) algorithm is a popular algorithm used to construct decision trees. The CART algorithm works by recursively splitting the data into two subsets, where each subset is split along a single feature. The feature and the splitting threshold are chosen to maximize the increase in homogeneity or reduction in impurity in the resulting subsets. The impurity of a subset is calculated using a measure of the variability of the output values in that subset. For classification tasks, commonly used impurity measures are entropy and Gini impurity, whereas for regression tasks, mean squared error (MSE) is typically used [20]. Equation 4, given below shows the cost function that the CART algorithm uses to minimize, to find the best split of a given node.

$$J = \frac{n_{left}}{n} MSE_{left} + \frac{n_{right}}{n} MSE_{right} \quad (3)$$

Where,

$$MSE_{node} = \frac{\sum_{i \in node} \left(\hat{y} - y^{(i)}\right)^2}{n}$$

And,

$$\hat{y} = \frac{1}{n} \sum_{i \in node} y^{(i)}$$

In the above equations:

n = Records in the dataset

n_{left} = Records in the left subtree

n_{right} = Records in the right subtree

The CART algorithm begins with a single root node that represents the complete dataset. At each level of the tree, the algorithm chooses the feature and the splitting threshold that minimize the impurity or increase the homogeneity of the resulting subsets. The algorithm continues to split the data into smaller subsets until it reaches a stopping criterion, such as a minimum number of samples in each leaf node or a maximum tree depth [21].

Once the tree is constructed, it becomes feasible to make predictions on new data by traversing the tree from the root node to a leaf node. At each node, the decision rule corresponding to the splitting feature is applied, and the algorithm follows the appropriate branch based on the value of the feature in the input data. The prediction is then made based on the output value associated with the leaf node. Figure 2 given below, shows the visualization of decision tree generated by training the decision tree model on training data.

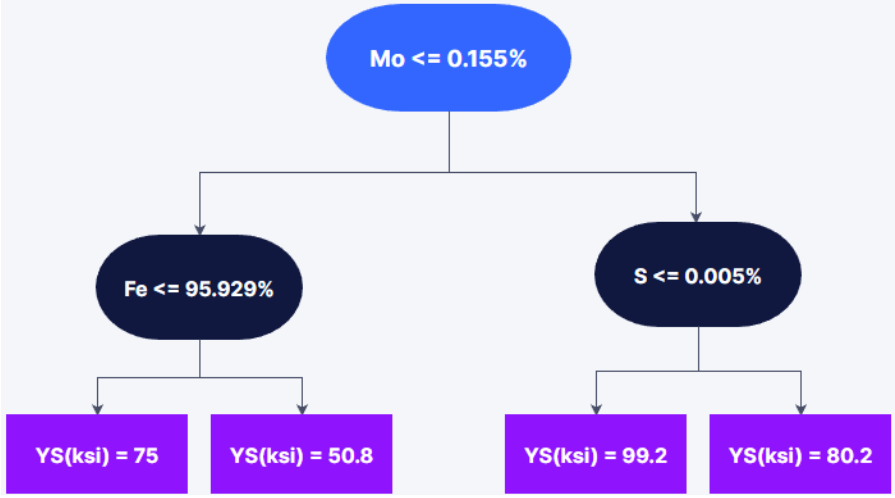

Figure 2: Decision Tree for Yield strength

2.1.3. Random Forest:

Random Forest is a widely used algorithm in machine learning used for both regression and classification tasks. It leverages the power of collective intelligence that works by constructing multiple decision trees and averaging their predictions [22] as shown in Figure 3.

In Random Forest regression, each tree in the ensemble is constructed using a random subset of the training data and a random subset of the input features [23]. This helps to improve the model's performance by reducing the correlation between the trees. The prediction of the Random Forest model is then obtained by averaging the predictions of all the individual trees [24].

Random Forest has several advantages over other regression models, including its capability to handle large datasets with many input variables, its capability to detect and handle relationships that are non-linear between input features and the target feature, and its capability to handle outliers and missing data [25]. On the other hand, it is not interpretable [26] and requires more training time and memory [27] due to the number of decision trees being generated.

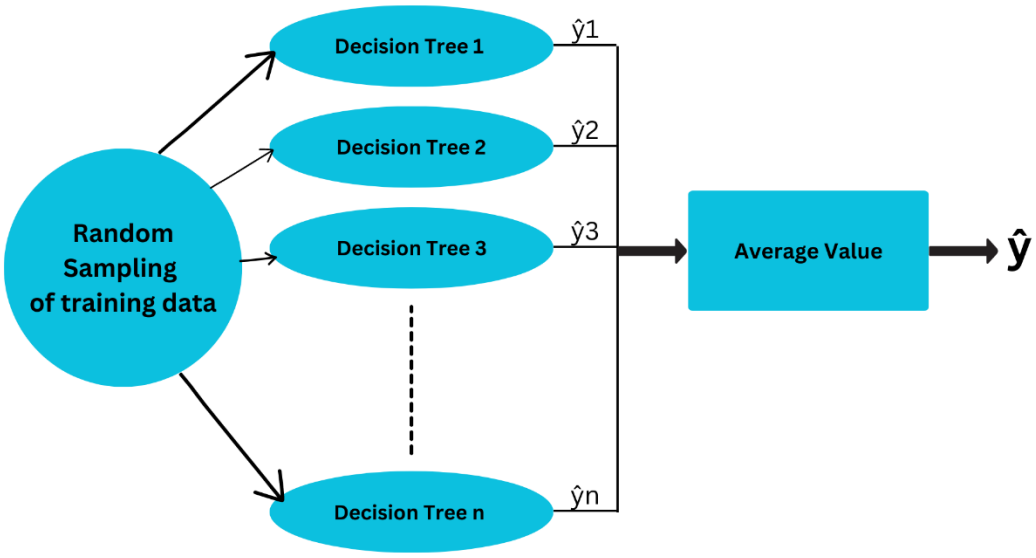

Figure 3: Random Forest flow diagram

2.2. Performance Metrics:

To judge the performance of our machine learning models, several evaluation criteria or performance metrics which are commonly used in regression problems were used. Each criterion provides a unique aspect of the model's performance, and together they give a detailed picture of how well the model is able to predict the yield strength of API steels.

Mean Absolute Error (MAE): MAE indicates that on average, how far the predicted values are from actual values, without taking their direction into consideration. It is calculated by taking the absolute difference between the real and estimated values and then averaging them. MAE has the same units as the variable being estimated. The lower the value of MAE, the better the model's performance, since it means that the model's predictions are closer to the actual values [28].

$$MAE = \frac{\sum_{i=1}^{n} |y_i - \hat{y}_i|}{n} \tag{4}$$

Mean Absolute Percentage Error (MAPE): MAPE is a metric that quantifies the average percentage difference between the predicted and true values. To calculate the MAPE, the absolute percentage difference between the estimated and true values is obtained, and the resulting values are averaged. MAPE is expressed as a percentage. The lower the value of MAPE, the better the model's performance, since it shows that the model's predictions are closer to the real values in percentage terms [29].

$$MAPE = \frac{100\%}{n} \sum_{i=1}^{n} \left| \frac{y - \hat{y}}{y} \right| \tag{5}$$

R-squared (R2) Score: The R2 score evaluates how much of the variability in the target variable can be accounted for by the independent variables incorporated in the model, ranging between 0 and 1. A higher R2 value indicates a better model's performance. The calculation of R2 involves subtracting the ratio of the sum of squares of the residuals to the total sum of squares from 1. A R2 score of 1 denotes that the model fits the data perfectly, whereas a score of 0 indicates that the model fails to explain any variation in the target variable [30].

$$R^2 = 1 - \frac{\sum_{i=1}^{n}(y_i - \hat{y})^2}{\sum_{i=1}^{n}(y_i - \bar{y})^2} \quad (6)$$

These performance metrics were calculated for each of the machine learning models used in this study, which include Multiple Regression, Multiple Regression with L1 and L2 Regularization, Decision Tree, and Random Forest. The results are summarized in Table 1 and shown in Figure 9.

3. Results and Discussions:

In this section, the results of the study are presented, aimed at predicting the yield strength of API steels using various machine learning models. The performance of multiple regression, multiple regression with L1 and L2 regularization, decision tree, and random forest models was evaluated separately to predict yield strength. The test data was used to calculate the mean absolute percentage error (MAPE), mean absolute error (MAE), and R-squared (R2) score for each model. The following subsections present the results obtained to predict the yield strength of the API steels along with the interpretation of those results using feature importance.

Feature importance is a concept in machine learning that helps to identify the most important variables or features that are contributing the most to the model's prediction [31]. The importance of features is calculated based on the effect of that feature on a dependent variable. The higher the importance of a feature, the more significant its impact on the model's prediction accuracy [32]. Feature importance helps in identifying the relevant features that are driving the predictions, which can be useful to comprehend the existing relationships and making better decisions [33].

3.1. Prediction of AI models:

Based on the results obtained, the multiple regression model had a high MAE of 50.047 and a MAPE of 52.73%, indicating a poor performance in predicting yield strength. The Lasso regression model performed better than the multiple regression model with a MAE of 13.806 and a MAPE of 14.66%. The Ridge regression model also showed good performance with a MAE of 10.717 and a MAPE of 12.06%. The decision tree model had a MAE of 12.955 and a MAPE of 14.36%, indicating a slightly poorer performance than the Ridge regression model. Finally, the random forest model gave the best performance, with a MAE of 3.297 and a MAPE of 3.73%, and a R2 score of 0.9524.

In summary, the results imply that the random forest model is the most fruitful in predicting the yield strength of API steels, followed by Ridge regression, decision tree, lasso regression, and multiple regression.

3.1.1. Multiple regression:

In the multiple regression model, the feature importance for the prediction of yield strength can be interpreted based on the magnitude of the corresponding coefficients. Among the input variables, the ones with the highest magnitude coefficients have the most significant impact on the predicted yield strength. The coefficients show how the change in the independent variables will impact the dependent variable. For instance, As shown in Figure 4, a one-unit increase in Mn and Si will lead to a decrease in yield strength by 61.02 and 7.33 ksi respectively. Similarly, a one-unit increase in P and Mo will increase the yield strength by 56.25 and 33.30 ksi respectively. On the other hand, Fe and Hardness(HB, max) have a negative impact on yield strength, where a one-unit increase in these variables results in a decrease of 18.15 ksi and 17.56 ksi respectively.

The performance of the multiple regression model for yield strength prediction was evaluated using several metrics, including MAE, MAPE, and R2 score. The MAE of the model was found to be 50.047, indicating an average error of 50.047 ksi in the predicted yield strength values. The MAPE was 52.73%, suggesting that the model predictions were, on average, off by 52.73% of the actual yield strength values. The R2 score was -8.276, indicating that the model has poor predictive power and explains very little of the variance in the yield strength data. Overall, the model's performance needs to be improved to make accurate predictions of the yield strength of API steels.

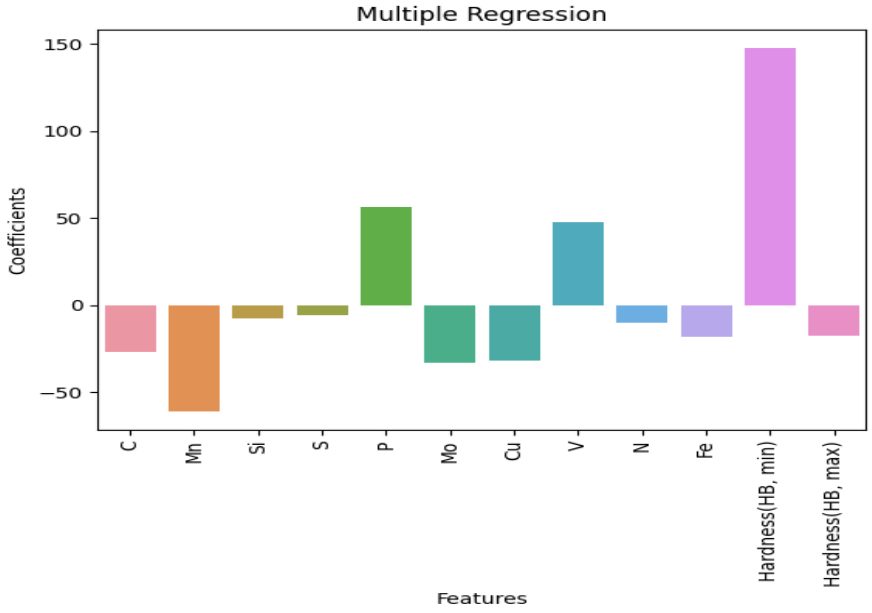

Figure 4: Feature importance w.r.t Multiple Regression Model

3.1.2. Multiple Regression with L1 regularization:

According to multiple regression with L1 regularization or Lasso regression, the important features for predicting yield strength having positive coefficients are the Hardness(HB, min) and Hardness(HB, max), i.e., one unit increase in their values would increase the yield strength by 1.8-65.43 ksi whereas the increment of one unit in the values of Mn, Cu, and S having negative coefficients would decrease the value of yield strength by 3.66-6.98 ksi, while other variables have coefficients close to 0, which means they have little or no influence on yield strength. Figure 5, suggests that the hardness, manganese, and copper content are important factors that affect the yield strength of API steels.

The evaluation of the model using the mean absolute percentage error (MAPE) and mean absolute error (MAE) shows a significant improvement in performance over the unregularized model. The MAE decreased from 50.047 to 13.806, while the MAPE decreased from 52.73% to 14.66%. The R2 score also improved from -8.276 to 0.1622. These results suggest that the L1 regularization technique has effectively reduced overfitting in the model and improved its predictive accuracy for yield strength prediction.

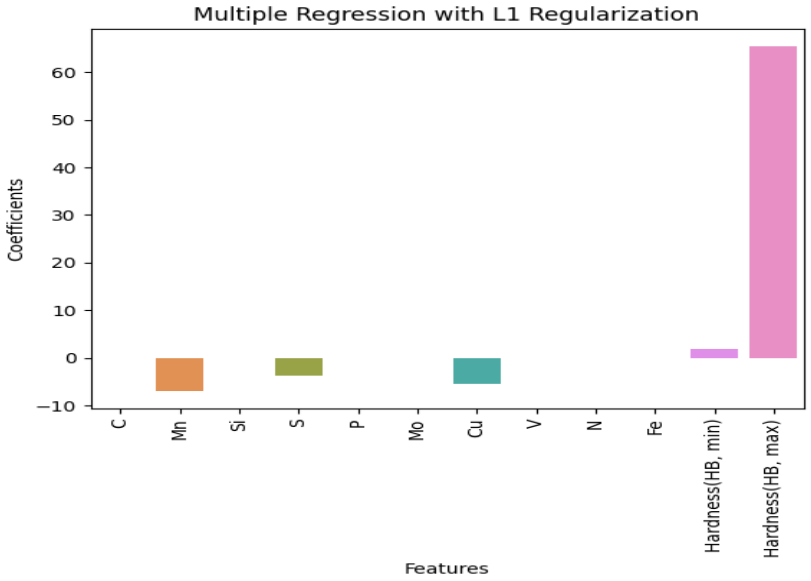

Figure 5: Feature importance w.r.t Lasso regression

3.1.3. Multiple Regression with L2 regularization:

In multiple regression with L2 regularization, also known as Ridge regression, as shown in Figure 6, the most important features having a positive impact on yield strength according to their coefficients are the Hardness(HB, max), Hardness(HB, min), C, Mo, N, and V ,i.e., one unit change in their value would increase yield strength by 1.8-23.6 ksi. On the other hand, Mn, Si, S, P, Cu, and Fe have negative coefficients, indicating that an increment in their values leads to a decrement in the predicted variable in the range of 1.03-11.33 ksi.

It has also been observed that the performance of the multiple regression model improved significantly after applying L2 regularization with a low MAE of 10.717, low MAPE of 12.06%, and higher R2 score of 0.6217.

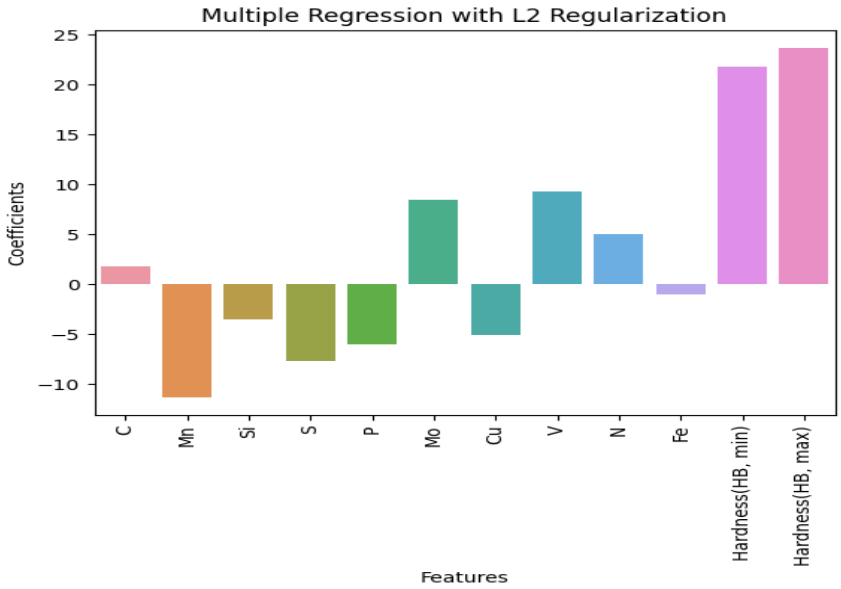

Figure 6: Feature importance w.r.t Ridge regression

3.1.4. Decision Tree:

In the decision tree model, the feature importance is calculated based on how much the feature contributes to the overall decision-making process of the model. The importance score of a feature is calculated by summing up the reduction in impurity [32] gained by splitting on that feature across all nodes in the tree. In this case, as shown in Figure 7, the feature importance values indicate that the 'Mo' is the most important feature for predicting yield strength, followed by the 'S' and 'Fe' features.

In terms of performance evaluation, the decision tree model achieves a mean absolute percentage error (MAPE) of 14.36% and a mean absolute error (MAE) of 12.955 which suggests that the model is capable of predicting the yield strength of API steel with reasonable accuracy. Additionally, the R2 score of 0.4813 indicates that the model explains a moderate proportion of the total variance in the yield strength of the API steel. Overall, the decision tree model provides good results, but its performance is not better than the Ridge regression.

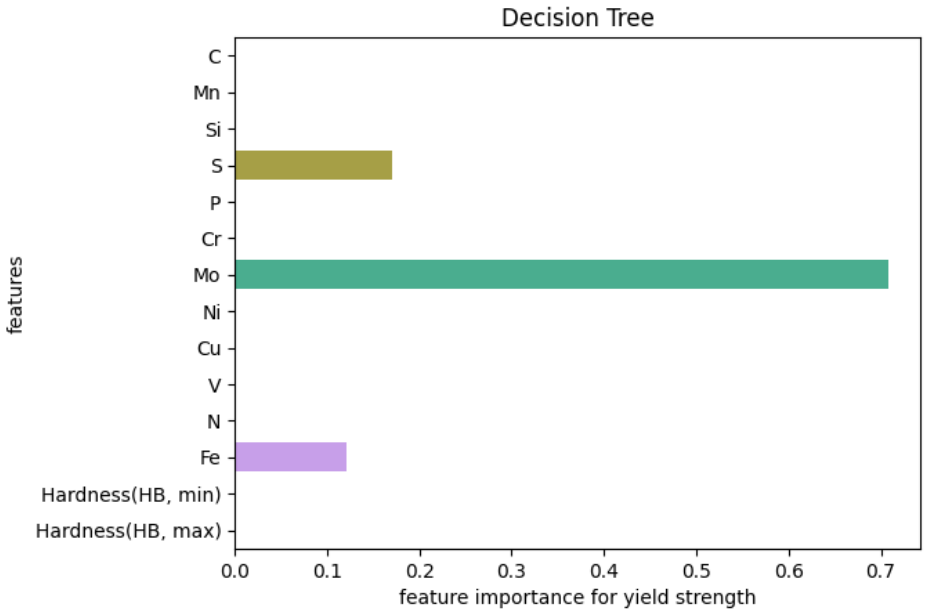

Figure 7: Feature importance w.r.t Decision Tree

3.1.5. Random Forest:

The feature importance for the Random Forest regression model indicates the relative importance of each feature in predicting the target variable. The feature importance is obtained based on the reduction in impurity (measured as mean squared error) achieved by splitting on a given feature over all trees in the forest. Specifically, for each tree, the decrease in impurity (impurity before split minus impurity after split) is computed for each feature that was used in the tree and then averaged over all trees in the forest [34].

Features that result in a high decrease in impurity when used for splitting tend to be more important, as they have a greater impact on reducing the error of the forest. The resulting feature importance values are normalized, to sum up to 1, so they can be interpreted as relative importance scores. In the case of yield strength, P is the most important, followed by Hardness (HB, min), and S, which has been shown in Figure 8.

In terms of model performance evaluation, the Random Forest regression model has a lower MAE and MAPE as 3.29 and 3.73% respectively, than the other models for yield strength, indicating that it is more accurate in predicting yield strength. The R2 score is 0.952 which is also higher, indicating that the Random Forest model explains more of the variance in yield strength. Overall, the Random Forest regression model showed promising results to estimate yield strength, with P, S, and Hardness (HB, min) being the most important features.

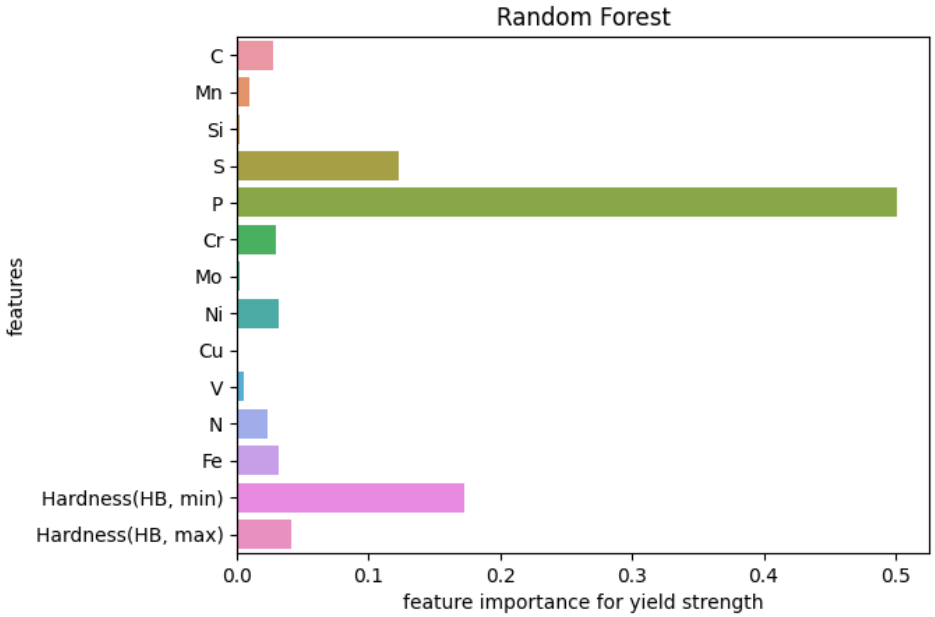

Figure 8: Feature importance w.r.t Random Forest model

Models	Yield Strength		
	MAE	MAPE	R2 Score
Multiple regression	50.047	52.73	-8.276
Lasso Regression	13.806	14.66	0.1622
Ridge Regression	10.717	12.06	0.6217
Decision Tree	12.955	14.36	0.4813
Random Forest	3.297	3.73	0.9524

Table 1: Models' Performance

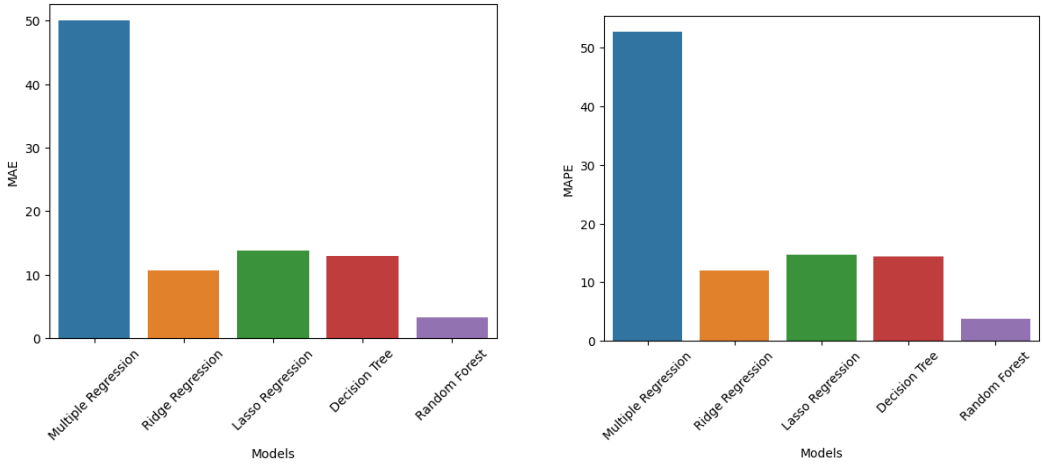

Figure 9: Visualization of models' performance

4. Conclusions:

In conclusion, the analysis conducted in this study has demonstrated that:

- The models developed in this study were implemented successfully and provided valuable insights into predicting the yield strength of API steels using machine learning techniques.
- The non-linear model (random forest) outperformed linear models in predicting the mechanical properties of API steels, specifically Yield strength.
- For the prediction of yield strength, the Random Forest model gave the most promising results with a MAE of 3.29, a MAPE of 3.73, and a R2 score of 0.95.

References:

1. Ananta Nagu, G. & G Namboodhiri, T. K. Effect of heat treatments on the hydrogen embrittlement susceptibility of API X-65 grade line-pipe steel. *Bull. Mater. Sci* **26**, 435–439 (2003).
2. Das, A. K. The present and the future of line pipe steels for petroleum industry. *Center for Bioinformatics and Molecular Biostatistics* **25**, 14–19 (2010).
3. 5 Common Alloying Elements. https://www.metalsupermarkets.com/5-common-alloying-elements/.
4. W.E. White & G. I. Ogundele. Influences of Dissolved Hydrocarbon Gases and Variable Water Chemistries on Corrosion of an API-L80 Steel. *CORROSION* **43**, 665–673 (1987).
5. Elgaddafi, R., Ahmed, R. & Shah, S. Modeling and experimental studies on CO2-H2S corrosion of API carbon steels under high-pressure. *J Pet Sci Eng* **156**, 682–696 (2017).
6. A brief introduction of API 5L, API 5B, API 5CT and API 5D. https://www.worldironsteel.com/news/a-brief-introduction-of-api-5l-api-5b-api-5c-12677821.html.
7. In depth guide to machine learning. https://www.techtarget.com/searchenterpriseai/definition/machine-learning-ML#:~:text=Machine%20learning%20(ML)%20is%20a,to%20predict%20new%20output%20values.
8. Meng, L. *et al.* Machine Learning in Additive Manufacturing: A Review. *JOM* **72**, 2363–2377 (2020).
9. Gan, L., Wu, H. & Zhong, Z. Fatigue life prediction considering mean stress effect based on random forests and kernel extreme learning machine. *Int J Fatigue* **158**, (2022).
10. Nasiri, S. & Khosravani, M. R. Machine learning in predicting mechanical behavior of additively manufactured parts. *Journal of Materials Research and Technology* **14**, 1137–1153 (2021).
11. Sah, A. K., Agilan, M., Dineshraj, S., Rahul, M. R. & Govind, B. Machine learning-enabled prediction of density and defects in additively manufactured Inconel 718 alloy. *Mater Today Commun* **30**, (2022).
12. Carvalho, T. P. *et al.* A systematic literature review of machine learning methods applied to predictive maintenance. *Comput Ind Eng* **137**, (2019).
13. Moeedlodhi. How Outliers Can Pose a Problem in Linear Regression. https://medium.com/swlh/how-outliers-can-pose-a-problem-in-linear-regression-1431c50a8e0 (2020).

14. Wagner, M. M., Moore, A. W. & Aryel, R. M. Combining Multiple Signals for Biosurveillance. in *Handbook of Biosurveillance* 235–242 (Academic Press, 2006).
15. Induraj. How to derive B0 and B1 in Linear Regression- Part2. https://induraj2020.medium.com/how-to-derive-b0-and-b1-in-linear-regression-4d4806b231fb (2020).
16. Ying, X. An Overview of Overfitting and its Solutions. *J Phys Conf Ser* **1168**, (2019).
17. L.E. Melkumova & S.Ya. Shatskikh. Comparing Ridge and LASSO estimators for data analysis. *Procedia Eng* **201**, 746–755 (2017).
18. How do you explain the impact of regularization on the bias-variance trade-off in linear regression? https://www.linkedin.com/advice/0/how-do-you-explain-impact-regularization-bias-variance
19. S. B. Kotsiantis. Decision trees: A recent overview. *Artif Intell Rev* **39**, 261–283 (2013).
20. Roman Timofeev. Classification and Regression Trees (CART) Theory and Applications. (Humboldt University, 2004).
21. Max Bramer. Avoiding Overfitting of Decision Trees. in *Principles of Data Mining* 119–134 (Springer, 2007).
22. Breiman, L. Random Forests. **45**, 5–32 (2001).
23. Aurélien Géron. *Hands-on Machine Learning with Scikit-Learn, Keras, and TensorFlow*. (2019).
24. Mark R. Segal. Machine Learning Benchmarks and Random Forest Regression. *Center for Bioinformatics and Molecular Biostatistics* 1–14 (2004).
25. Rodriguez-Galiano, V. F., Ghimire, B., Rogan, J., Chica-Olmo, M. & Rigol-Sanchez, J. P. An assessment of the effectiveness of a random forest classifier for land-cover classification. *ISPRS Journal of Photogrammetry and Remote Sensing* **67**, 93–104 (2012).
26. Ziegler, A. & König, I. R. Mining data with random forests: Current options for real-world applications. *Wiley Interdiscip Rev Data Min Knowl Discov* **4**, 55–63 (2014).
27. Santur, Y., Karaköse, M. & Akın, E. Random Forest Based Diagnosis Approach for Rail Fault Inspection in Railways. *National Conference on Electrical, Electronics and Biomedical Engineering (ELECO)* 714–719 (2016).
28. Mean absolute error. https://en.wikipedia.org/wiki/Mean_absolute_error.
29. Mean absolute percentage error. https://en.wikipedia.org/wiki/Mean_absolute_percentage_error.
30. Coefficient of determination. https://en.wikipedia.org/wiki/Coefficient_of_determination.
31. Mirka Saarela & Susanne Jauhiainen. Comparison of feature importance measures as explanations for classification models. *SN Appl Sci* **3**, (2021).
32. Jason Brownlee. How to calculate feature importance with python. https://machinelearningmastery.com/calculate-feature-importance-with-python/ (2016).
33. Aaron Fisher, Cynthia Rudin & Francesca Dominici. All Models are Wrong, but Many are Useful: Learning a Variable's Importance by Studying an Entire Class of Prediction Models Simultaneously. *Journal of Machine Learning Research* **20**, 1–81 (2019).
34. Christine Dewi & Rung-Ching Chen. Random forest and support vector machine on features selection for regression analysis. *International Journal of Innovative Computing, Information and Control* **15**, 2027–2037 (2019).

Miskolc Mathematical Notes
Vol. 24 (2023), No. 1, pp. 369–382

HU e-ISSN 1787-2413
DOI: 10.18514/MMN.2023.3848

APPROXIMATION BY APOSTOL-GENOCCHI SUMMATION-INTEGRAL TYPE OPERATORS

CHANDRA PRAKASH, NAOKANT DEO, AND DURVESH KUMAR VERMA

Received 21 May, 2021

Abstract. In the present paper, we proposed a new sequence of summation-integral type operators involving Apostol-Genocchi polynomials. We study some approximation results of the proposed operators using first and second-order modulus of continuity, the global rate of convergence using Voronovskaja-type asymptotic theorem, Lipschitz-type space, and Ditzian-Totik modulus of smoothness. Lastly, we study the weighted approximation.

2010 *Mathematics Subject Classification:* 41A25; 41A30; 41A36

Keywords: Apostol-Genocchi polynomials, rate of convergence, Ditzian-Totik modulus of smoothness, Voronovskaja-type asymptotic formula, Lipschitz-type space, weighted approximation

1. Introduction

The Appell polynomial $A_n(x)$ is defined by

$$e^{xt}f(t)=\sum_{n=0}^{\infty}A_n(x)\frac{t^n}{n!},$$

where $f(t)$ be a formal power series in t. This polynomial found stunning applications in several field of mathematics, see [7, 21, 22]. One special case known as Genocchi polynomials $G_n(x)$ are defined by

$$\frac{2te^{xt}}{e^t+1}=\sum_{n=0}^{\infty}G_n(x)\frac{t^n}{n!},\ |t|<\pi.$$

In this case the Genocchi numbers G_n have many applications in number theory, special functions, combinatorics and numerical analysis, where

$$\frac{2t}{e^t+1}=\sum_{n=0}^{\infty}G_n\frac{t^n}{n!},\ |t|<\pi.$$

The Apostol-Genocchi polynomials $G_k^{\alpha}(x;\beta)$, $\beta\in\mathbb{C}$, of order α (non negative integers) are defined and found some results in [7].

Recently, Prakash et al. [15] proposed a sequence of operators involving Apostol-Genocchi polynomials given in (1.1). They studied some approximation results using

© 2023 Miskolc University Press

second-order modulus of continuity, Voronovskaja-type theorem and weighted approximation theorem for these operators. They also proposed the Kantorovich form of (1.1), and discussed some approximation results. Many researchers have worked on new modifications of various operators and deliberate the approximation properties ([1, 3, 9, 10, 16, 17, 19, 22–24]). The operators discussed in [15] are given as follows. For $f \in C[0,\infty)$,

$$\mathcal{M}_n^{\alpha,\beta}(f;x) = e^{-nx}\left(\frac{1+e\beta}{2}\right)^{\alpha}\sum_{k=0}^{\infty}\frac{G_k^{\alpha}(nx;\beta)}{k!}f\left(\frac{k}{n}\right), \tag{1.1}$$

where $G_k^{\alpha}(x;\beta)$ are the generalized Apostol-Genocchi polynomials, with the generating function of the form

$$\left(\frac{2t}{1+\beta e^t}\right)^{\alpha}e^{xt} = \sum_{k=0}^{\infty}G_k^{\alpha}(x;\beta)\frac{t^k}{k!}, \qquad (\beta \in \mathbb{C}, \alpha \in \mathbb{N}\cup 0, |t| < \pi).$$

For more information about the Apostol-Genocchi polynomials and their properties, readers should refer articles [6, 8, 11, 12, 14, 18, 20].

In 2007, Srivastava et al. proposed a family of summation-integral type operators and estimated rate of convergence and function having derivative of bounded variation [20]. Here we refer to some more articles related to summation-integral type operators for the readers ([4, 5, 13]). Motivated by the above work, for non negative integer α and $f \in L_1[0,\infty)$ we propose the integral-type generalization of the operators (1.1) as follows:

$$T_{n,\rho}^{\alpha,\beta}(f,x) = e^{-nx}\left(\frac{1+e\beta}{2}\right)^{\alpha}\left(G_0^{\alpha}(nx;\beta)f(0) + \sum_{k=1}^{\infty}\frac{G_k^{\alpha}(nx;\beta)}{k!}\int_0^{\infty}\Theta_{n,k}^{\rho}(t,c)f(t)dt\right), \tag{1.2}$$

where $\rho > 0$, and

$$\Theta_{n,k}^{\rho}(t,c) = \begin{cases} \dfrac{n\rho}{\Gamma(k\rho)}e^{-n\rho t}(n\rho t)^{k\rho-1}, & c = 0, \\ \dfrac{\Gamma\left(\frac{n\rho}{c}+k\rho\right)}{\Gamma(k\rho)\Gamma\left(\frac{n\rho}{c}\right)}\dfrac{c^{k\rho}t^{k\rho-1}}{(1+ct)^{\frac{n\rho}{c}+k\rho}}, & c = 1,2,3,\ldots \end{cases}$$

It can be easily observed by simple computation that

$$\int_0^{\infty}\Theta_{n,k}^{\rho}(t,c)t^r dt = \begin{cases} \dfrac{\Gamma(k\rho+r)}{\Gamma(k\rho)}\dfrac{1}{\prod_{i=1}^{r}(n\rho-ic)}, & r \neq 0 \\ 1, & r = 0. \end{cases} \tag{1.3}$$

2. Lemmas

In this section we deal with some useful lemmas and results.

Lemma 1 ([15]). *For $\mathcal{M}_n^{\alpha,\beta}(t^i;x)$, $i = \overline{0,4}$, we have $\mathcal{M}_n^{\alpha,\beta}(1;x) = 1$;*

$\mathcal{M}_n^{\alpha,\beta}(t;x) = x + \dfrac{\alpha}{n(1+e\beta)}$;

$$\mathcal{M}_n^{\alpha,\beta}(t^2;x) = x^2 + \frac{(1+2\alpha+e\beta)}{n(1+e\beta)}x + \frac{\alpha^2-2\alpha e\beta-\alpha e^2\beta^2}{n^2(1+e\beta)^2};$$

$$\mathcal{M}_n^{\alpha,\beta}(t^3;x) = x^3 + \frac{(3+3\alpha+3e\beta)}{n(1+e\beta)}x^2 + \frac{\left(3\alpha^2+3\alpha+e^2\beta^2-3\alpha e^2\beta^2-3\alpha e\beta+2e\beta+1\right)}{n^2(1+e\beta)^2}x + \frac{\left(\alpha^3-6\alpha^2 e\beta-3\alpha^2e^2\beta^2-5\alpha e\beta-4\alpha e^2\beta^2-\alpha e^3\beta^3\right)}{n^3(1+e\beta)^3};$$

$$\begin{aligned}\mathcal{M}_n^{\alpha,\beta}(t^4;x) &= x^4 + \frac{(3+2\alpha+3e\beta)}{n(1+e\beta)}x^3 + \frac{\left(6\alpha^2+25e^2\beta^2-50e\beta-6\alpha e^2\beta^2+12\alpha+25\right)}{n^2(1+e\beta)^2}x^2\\ &+ \frac{x}{n^3(1+e\beta)^3}(4\alpha^3+6\alpha^2+42e\beta+48e\alpha\beta-18e\alpha^2\beta+42e^2\beta^2+6e^2\alpha\beta^2\\ &- 12e^2\alpha^2\beta^2+14e^3\beta^3-10e^3\alpha\beta^2+40\alpha+14)\\ &+ \frac{1}{n^4(1+e\beta)^4}(16\alpha^4-1056e\alpha\beta+256e\alpha^2\beta-192e\alpha^3\beta-1888e^2\alpha\beta^2\\ &+224e^2\alpha^2\beta^2-96e^2\alpha^3\beta^2-1312e^3\alpha\beta^3+128e^3\alpha^2\beta^3-304e^4\alpha\beta^4\\ &+48e^4\alpha^2\beta^4+288\alpha^2-80\alpha).\end{aligned}$$

Lemma 2. *The moments of the proposed operator* $T_{n,\rho}^{\alpha,\beta}\left(t^i,x\right)$, $i=\overline{0,3}$, *we have*

$$T_{n,\rho}^{\alpha,\beta}(1,x) = 1;$$

$$T_{n,\rho}^{\alpha,\beta}(t,x) = \frac{n\rho}{(n\rho-c)}x + \frac{\alpha\rho}{(n\rho-c)(1+e\beta)};$$

$$\begin{aligned}T_{n,\rho}^{\alpha,\beta}\left(t^2,x\right) &= \frac{n^2\rho^2}{(n\rho-c)(n\rho-2c)}x^2 + \frac{n\rho^2+2n\alpha\rho^2+n\rho^2e\beta}{(n\rho-c)(n\rho-2c)(1+e\beta)}x\\ &+ \frac{\alpha^2\rho^2-2\alpha\rho^2e\beta-\alpha\rho^2e^2\beta^2}{(n\rho-c)(n\rho-2c)(1+e\beta)^2};\end{aligned}$$

$$\begin{aligned}T_{n,\rho}^{\alpha,\beta}\left(t^3,x\right) &= \frac{n^3\rho^3}{(n\rho-c)(n\rho-2c)(n\rho-3c)}x^3\\ &+ \frac{3n^2\rho^2+3n^2\rho^3+3\alpha n^2\rho^3+3n^2\rho^2e\beta+3n^2\rho^3e\beta}{(n\rho-c)(n\rho-2c)(n\rho-3c)(1+e\beta)}x^2\\ &+ \frac{x}{(n\rho-c)(n\rho-2c)(n\rho-3c)(1+e\beta)^2}\left[n\alpha^2\rho^3+9n\alpha\rho^2\right.\\ &\left.+n\rho^2e^2\beta^2(3-2n\rho)+3n\alpha\rho^2e\beta+n\rho(1+e\beta)^2+8n\rho^2e\beta+3n\rho^2+n\rho\right]\\ &+ \frac{1}{(n\rho-c)(n\rho-2c)(n\rho-3c)(1+e\beta)^3}\left[\alpha^3\rho^3+3\alpha^2\rho^2e\beta(1-2\rho-\rho e\beta)\right.\\ &\left.+3\alpha^2\rho^2-5\alpha\rho^3e\beta-\alpha\rho^2e^2\beta^2(4\rho+\rho e\beta+9e\beta+3)-6\alpha\rho^2e\beta+2\alpha\rho\right.\\ &\left.+2\alpha\rho e^2\beta^2+4\alpha\rho e\beta\right].\end{aligned}$$

The proof the above lemma follows from (1.2), (1.3) and Lemma 1.

Remark 1. From Lemma 2 and simple estimation, we have

$$T_{n,\rho}^{\alpha,\beta}(t-x,x) = \frac{cx}{(n\rho-c)} + \frac{\alpha\rho}{(n\rho-c)(1+e\beta)};$$

$$T_{n,\rho}^{\alpha,\beta}\left((t-x)^2,x\right) = \frac{n\rho c+2c^2}{(n\rho-c)(n\rho-2c)}x^2 + \frac{n\rho^2+n\rho^2 e\beta+4c\alpha\rho}{(n\rho-c)(n\rho-2c)(1+e\beta)}x + \frac{\alpha^2\rho^2-2\alpha\rho^2 e\beta-\alpha\rho^2 e^2\beta^2}{(n\rho-c)(n\rho-2c)(1+e\beta)^2}.$$

Remark 2. For the central moments $T_{n,\rho}^{\alpha,\beta}((t-x)^m;x)$ for $m=1,2$, we have

$$\lim_{n\to\infty} nT_{n,\rho}^{\alpha,\beta}((t-x);x) = \frac{xc}{\rho} + \frac{\alpha}{(1+e\beta)};$$

$$\lim_{n\to\infty} nT_{n,\rho}^{\alpha,\beta}((t-x)^2;x) = \frac{x(cx+\rho)}{\rho}.$$

For $n\in\mathbb{N}$, $T_{n,\rho}^{\alpha,\beta}((t-x)^2;x) \le \frac{2\phi^2(x)}{n\rho}$, where $\phi(x)=\sqrt{x(cx+\rho)}$.

Let $C_B[0,\infty)$ be the set of all continuous and bounded functions on $[0,\infty)$ endowed with the norm $\|f\| = \sup\{|f(x)| : x\in[0,\infty)\}$.

Lemma 3. *Let $f\in C_B[0,\infty)$, $0\le x<\infty$ and $n\in\mathbb{N}$, then*

$$|T_{n,\rho}^{\alpha,\beta}(f;x)| \le \|f\|,$$

where $\|.\|$ is the uniform norm on $[0,\infty)$.

Proof. We have $T_{n,\rho}^{\alpha,\beta}(e_0;x)=1$, so $|T_{n,\rho}^{\alpha,\beta}(f;x)| \le T_{n,\rho}^{\alpha,\beta}(e_0;x)\|f\| = \|f\|$. □

3. Direct Results

In this section we establish the uniform convergence of the operators (1.2) using the Bohman-Korovkin theorem, the rate of convergence with the aid of different kind of modulus of smoothness and for functions in Lipschitz-type spaces, and a Voronovskaja-type asymptotic theorem.

Theorem 1. *Let $f\in C[0,\infty)$ and an adequately large n, then the sequence $\{T_{n,\rho}^{\alpha,\beta}(f,.)\}$ converges uniformly to f in $[a,b]$, where $0\le a<b<\infty$.*

Proof. From Lemma 2 we have $T_{n,\rho}^{\alpha,\beta}(1,x)=1$ for every $n\in\mathbf{N}$,

$$T_{n,\rho}^{\alpha,\beta}(t,x) = \frac{n\rho}{(n\rho-c)}x + \frac{\alpha\rho}{(n\rho-c)(1+e\beta)}$$

tends to x and

$$T_{n,\rho}^{\alpha,\beta}\left(t^2,x\right)=\frac{n^2\rho^2}{(n\rho-c)(n\rho-2c)}x^2+\frac{n\rho^2+2n\alpha\rho^2+n\rho^2e\beta}{(n\rho-c)(n\rho-2c)(1+e\beta)}x+\frac{\alpha^2\rho^2-2\alpha\rho^2e\beta-\alpha\rho^2e^2\beta^2}{(n\rho-c)(n\rho-2c)(1+e\beta)^2}$$

tends to x^2 as $n\to\infty$, similarly $T_{n,\rho}^{\alpha,\beta}\left(t^3,x\right)$ tends to x^3 uniformly on every compact subset of $[0,\infty)$. Hence, by Bohman-Korovkin theorem the required result holds. □

Consider the K-functional

$$K_2(f,\delta)=\inf_{j\in W^2}\{\|f-j\|+\delta\|j''\|\},\tag{3.1}$$

where $\delta>0$ and $W^2=\{j\in C_B[0,\infty):j',j''\in C_B[0,\infty)\}$. For a constant $C>0$ such that

$$K_2(f,\delta)\le C\,\omega_2(f,\sqrt{\delta}),\tag{3.2}$$

where $f\in C_B[0,\infty)$ and

$$\omega_2(f,\sqrt{\delta})=\sup_{0<h\le\sqrt{\delta}}\sup_{x\in[0,\infty)}|f(x+2h)-2f(x+h)+f(x)|$$

is the second order modulus of smoothness.

Theorem 2. *Let $f\in C_B[0,\infty)$ and $x\in[0,\infty)$. Then we have*

$$\left|T_{n,\rho}^{\alpha,\beta}(f,x)-f(x)\right|\le C\omega_2\left(f,\sqrt{\delta_n}\right)+\omega\left(f,|\alpha_2|\right),$$

where C is a positive constant, $\delta_n=\frac{1}{2}[\alpha_1+\alpha_2^2]$, $\alpha_1=T_{n,\rho}^{\alpha,\beta}\left((t-x)^2,x\right)$ and

$$\alpha_2=\left(\frac{cx}{n\rho-c}+\frac{\alpha\rho}{(n\rho-c)(1+e\beta)}\right).$$

Proof. Define the auxiliary operators $L_{n,\rho}^{\alpha,\beta}:C_B[0,\infty)\to C_B[0,\infty)$ as follows:

$$L_{n,\rho}^{\alpha,\beta}(f,x)=T_{n,\rho}^{\alpha,\beta}(f,x)-f\left(\frac{n\rho}{(n\rho-c)}x+\frac{\alpha\rho}{(n\rho-c)(1+e\beta)}\right)+f(x).\tag{3.3}$$

These operators are linear and $L_{n,\rho}^{\alpha,\beta}(t-x,x)=0$.

Let $j\in W^2$ and $x,t\in[0,\infty)$. By Taylor's series expansion

$$j(t)=j(x)+(t-x)j'(x)+\int_x^t(t-u)j''(u)du.$$

Applying the operator $L_{n,\rho}^{\alpha,\beta}$ on above, we obtain

$$L_{n,\rho}^{\alpha,\beta}(j;x)=j(x)+j'(x)L_{n,\rho}^{\alpha,\beta}((t-x);x)+L_{n,\rho}^{\alpha,\beta}\left(\int_x^t(t-u)j''(u)du;x\right)$$

implying that

$$\begin{aligned}\left|L_{n,\rho}^{\alpha,\beta}(j,x)-j(x)\right| &\leq L_{n,\rho}^{\alpha,\beta}\left(\left|\int_x^t (t-u)j''(u)du\right|,x\right)\\ &\leq T_{n,\rho}^{\alpha,\beta}\left(\left|\int_x^t (t-u)j''(u)du\right|,x\right)\\ &\quad+\left|\int_x^{\frac{n\rho}{(n\rho-c)}x+\frac{\alpha\rho}{(n\rho-c)(1+e\beta)}}\left(\frac{n\rho}{(n\rho-c)}x+\frac{\alpha\rho}{(n\rho-c)(1+e\beta)}-u\right)j''(u)du\right|\\ &\leq \frac{1}{2}T_{n,\rho}^{\alpha,\beta}\left((t-x)^2,x\right)||j''||\\ &\quad+\left|\int_x^{\frac{n\rho}{(n\rho-c)}x+\frac{\alpha\rho}{(n\rho-c)(1+e\beta)}}\left(\frac{n\rho}{(n\rho-c)}x+\frac{\alpha\rho}{(n\rho-c)(1+e\beta)}-u\right)du\right||j''||\end{aligned}$$

$$\begin{aligned}\left|L_{n,\rho}^{\alpha,\beta}(j,x)-j(x)\right| &\leq \frac{1}{2}\left[T_{n,\rho}^{\alpha,\beta}\left((t-x)^2,x\right)+\left(\frac{n\rho}{(n\rho-c)}x+\frac{\alpha\rho}{(n\rho-c)(1+e\beta)}-x\right)^2\right]||j''||\\ &\leq \frac{1}{2}\left[T_{n,\rho}^{\alpha,\beta}\left((t-x)^2,x\right)+\left(\frac{c}{n\rho-c}x+\frac{\alpha\rho}{(n\rho-c)(1+e\beta)}\right)^2\right]||j''||\\ &\leq \frac{1}{2}\left[\alpha_1+\alpha_2^2\right]||j''||=\delta_n||j''||. \qquad (3.4)\end{aligned}$$

Since

$$\begin{aligned}\left|T_{n,\rho}^{\alpha,\beta}(f,x)\right| &\leq e^{-nx}\left(\frac{1+e\beta}{2}\right)^{\alpha}\left(G_0^{\alpha}(nx;\beta)\,|f(0)|+\left|\sum_{k=1}^{\infty}\frac{G_k^{\alpha}(nx;\beta)}{k!}\int_0^{\infty}\Theta_{n,k}^{\rho}(t,c)\,f(t)dt\right|\right)\\ &\leq ||f||.\end{aligned}$$

Now by (3.3), we have

$$||L_{n,\rho}^{\alpha,\beta}(f,.)|| \leq ||T_{n,\rho}^{\alpha,\beta}(f,.)||+2||f|| \leq 3||f||,\ f\in C_B[0,\infty). \qquad (3.5)$$

Using (3.3), (3.4) and (3.5), we have

$$\begin{aligned}\left|T_{n,\rho}^{\alpha,\beta}(f,x)-f(x)\right| &\leq \left|L_{n,\rho}^{\alpha,\beta}(f-j,x)-(f-j)(x)\right|+\left|L_{n,\rho}^{\alpha,\beta}(j,x)-j(x)\right|\\ &\quad+\left|f\left(\frac{n\rho}{(n\rho-c)}x+\frac{\alpha\rho}{(n\rho-c)(1+e\beta)}\right)-f(x)\right|\\ &\leq 4||f-j||+\delta_n||j''||+\left|f(x)-f\left(\frac{n\rho}{(n\rho-c)}x+\frac{\alpha\rho}{(n\rho-c)(1+e\beta)}\right)\right|\\ &\leq 4||f-j||+\delta_n||j''||+\omega(f,\alpha_2).\end{aligned}$$

Taking infimum over all $j\in W^2$, and using (3.2), we get the required result. □

Our next result is the Voronovskaja-type asymptotic formula.

Theorem 3. *Let f be a bounded and integrable function on $[0,\infty)$ such that $f''(x)$ exists at $0 \le x < \infty$, then*

$$\lim_{n\to\infty} n\left[T_{n,\rho}^{\alpha,\beta}(f,x) - f(x)\right] = \left[\frac{cx}{\rho} + \frac{\alpha}{(1+e\beta)}\right] f'(x) + \left[\frac{c}{\rho}x^2 + x\right]\frac{f''(x)}{2!}.$$

Proof. Using the well known Taylor's series expansion

$$f(t) = f(x) + (t-x)f'(x) + \frac{(t-x)^2}{2!}f''(x) + \sigma(t,x)(t-x)^2,$$

where $\sigma(t,x) \to 0$ as $t \to x$ and the function ρ is bounded on $[0,\infty)$. Now,

$$\begin{aligned}
&n\left[T_{n,\rho}^{\alpha,\beta}(f,x) - f(x)\right] \\
&= n\left[T_{n,\rho}^{\alpha,\beta}(t-x,x)f'(x) + \frac{T_{n,\rho}^{\alpha,\beta}\left((t-x)^2,x\right)}{2!}f''(x) + T_{n,\rho}^{\alpha,\beta}\left(\sigma(t,x)(t-x)^2,x\right)\right] \\
&= n\left[\left(\frac{cx}{(n\rho-c)} + \frac{\alpha\rho}{(n\rho-c)(1+e\beta)}\right)f'(x) + \frac{n\rho c + 2c^2}{(n\rho-c)(n\rho-2c)}\frac{x^2}{2!}f''(x)\right. \\
&\quad \left. + \frac{n\rho^2 + n\rho^2 e\beta + 4c\alpha\rho}{(n\rho-c)(n\rho-2c)(1+e\beta)}\frac{x}{2!}f''(x) + \frac{\alpha^2\rho^2 - 2\alpha\rho^2 e\beta - \alpha\rho^2 e^2\beta^2}{2!(n\rho-c)(n\rho-2c)(1+e\beta)^2}f''(x)\right] \\
&\quad + \hbar(n,x),
\end{aligned}$$

where

$$\begin{aligned}
\hbar(n,x) &= e^{-nx}\left(\frac{1+e\beta}{2}\right)^{\alpha} \\
&\quad \cdot \left(G_0^{\alpha}(nx;\beta)\,\sigma(0,x)(-x)^2 + \sum_{k=1}^{\infty}\frac{G_k^{\alpha}(nx;\beta)}{k!}\int_0^{\infty}\Theta_{n,k}^{\rho}(t,c)\,\sigma(t,x)(t-x)^2dt\right).
\end{aligned}$$

Now it is sufficient to show that $\hbar(n,x) \to 0$ as large n. Since $\sigma(t,x) \to 0$ as $t \to x$, for a given $\varepsilon > 0$, there exists $\delta > 0$ such that $|\sigma(t,x)| < \varepsilon$, whenever $-\delta < t-x < \delta$,

$$\begin{aligned}
|\hbar(n,x)| &\le e^{-nx}\left(\frac{1+e\beta}{2}\right)^{\alpha}\sum_{k=1}^{\infty}\frac{G_k^{\alpha}(nx;\beta)}{k!} \\
&\quad \left[\int_{|t-x|<\delta}\Theta_{n,k}^{\rho}(t,c)\,|\sigma(t,x)|(t-x)^2dt + \int_{|t-x|\ge\delta}\Theta_{n,k}^{\rho}(t,c)\,|\sigma(t,x)|(t-x)^2dt\right] \\
&\quad + e^{-nx}\left(\frac{1+e\beta}{2}\right)^{\alpha}G_0^{\alpha}(nx;\beta)\,\sigma(0,x)(-x)^2.
\end{aligned}$$

By using Remark 1, we have $I_1 = \sigma O(1)$ and for $m \ge 2$, we obtain

$$\begin{aligned}
I_2 &\le Ce^{-nx}\left(\frac{1+e\beta}{2}\right)^{\alpha}\left(G_0^{\alpha}(nx;\beta)\,\sigma(0,x)(-x)^2 + \sum_{k=1}^{\infty}\frac{G_k^{\alpha}(nx;\beta)}{k!}\int_0^{\infty}\Theta_{n,k}^{\rho}(t,c)\,\frac{(t-x)^{2m}}{\delta^{2m-2}}dt\right) \\
&= O(n^{-m+1}),
\end{aligned}$$

where $C = \sup_{t\in[x,\infty)} |\sigma(t,x)|$. Due to arbitrariness of $\varepsilon > 0$, $\hbar(n,x) \to 0$ for sufficiently large n, the proof is completed. □

In the following theorem, we succeed the rate of convergence of the proposed operators (1.2) for functions in Lipschitz-type spaces.

Suppose that $x \in (0,\infty)$, $t \in [0,\infty)$, and consider the Lipschitz-type space defined as

$$Lip^*_M(\sigma) = \left\{ f \in C[0,\infty) : |f(t) - f(x)| \leq M \frac{|t-x|^\sigma}{(t+x)^{\frac{\sigma}{2}}} \right\},$$

where $M > 0$ is a constant and $0 < \sigma \leq 1$.

Theorem 4. *Let $f \in Lip^*_M(\sigma)$ and $0 < \sigma \leq 1$. Then for each $x \in (0,\infty)$, we have*

$$|T^{\alpha,\beta}_{n,\rho}(f(t);x) - f(x)| \leq M \left(\frac{T^{\alpha,\beta}_{n,\rho}((t-x)^2;x)}{x} \right)^{\frac{\sigma}{2}}.$$

Proof. Let $f \in Lip^*_M(\sigma)$ and $x \in (0,\infty)$, $t \in [0,\infty)$, we have

$$\begin{aligned} |T^{\alpha,\beta}_{n,\rho}(f(t);x) - f(x)| &\leq T^{\alpha,\beta}_{n,\rho}(|f(t) - f(x)|;x) \\ &\leq M \cdot T^{\alpha,\beta}_{n,\rho}\left(\frac{|t-x|^\sigma}{(t+x)^{\frac{\sigma}{2}}};x \right) \\ &\leq \frac{M}{x^{\frac{\sigma}{2}}} T^{\alpha,\beta}_{n,\rho}(|t-x|^\sigma;x). \end{aligned} \tag{3.6}$$

Taking $p = \frac{2}{\sigma}$ and $q = \frac{2}{2-\sigma}$ and applying Hölder's inequality, we obtain

$$\begin{aligned} T^{\alpha,\beta}_{n,\rho}(|t-x|^\sigma;x) &\leq \left\{ T^{\alpha,\beta}_{n,\rho}(|t-x|^2;x) \right\}^{\frac{\sigma}{2}} \cdot \left\{ T^{\alpha,\beta}_{n,\rho}(1^{\frac{2}{2-\sigma}};x) \right\}^{\frac{2-\sigma}{2}} \\ &\leq \left\{ T^{\alpha,\beta}_{n,\rho}(|t-x|^2;x) \right\}^{\frac{\sigma}{2}}. \end{aligned} \tag{3.7}$$

Using (3.6) and (3.7), we get the required result

$$|T^{\alpha,\beta}_{n,\rho}(f(t);x) - f(x)| \leq M \left(\frac{T^{\alpha,\beta}_{n,\rho}((t-x)^2;x)}{x} \right)^{\frac{\sigma}{2}}.$$

□

Here, we estimate the convergence using the first order Ditzian-Totik modulus of smoothness $\omega_{\phi^\gamma}(f;t)$ and The Peetre $K-$functional $K_{\phi^\gamma}(f;t)$, $0 \leq \gamma \leq 1$. The Ditzian-Totik modulus of smoothness is defined as

$$\omega_{\phi^\gamma}(f;t) = \sup_{0<h\leq t} \left\{ \left| f\left(x + \frac{h\phi^\gamma(x)}{2} \right) - f\left(x - \frac{h\phi^\gamma(x)}{2} \right) \right|, x \pm \frac{h\phi^\gamma(x)}{2} \in [0,\infty) \right\},$$

where $\phi^2(x) = x(cx+\rho)$ and $f \in C[0,\infty)$.

The Peetre $K-$functional is defined as

$$K_{\phi^\gamma}(f;t) = \inf_{j\in W_\gamma}\{\|f-j\| + t\|\phi^\gamma j'\|\}\,(t>0),$$

where $W_\gamma[0,\infty) = \{j : j \in AC_{loc}[0,\infty),\ \|\phi^\gamma j'\| < \infty\}$ and $AC_{loc}[0,\infty)$ is the class of the locally absolutely continuous functions. In [2], (Theorem 2.1.1), there is a relation between K-functional and the Ditzian-Totik first order modulus of smoothness

$$C^{-1}\omega_{\phi^\gamma}(f,t) \le K_{\phi^\gamma}(f;t) \le C\omega_{\phi^\gamma}(f;t), \tag{3.8}$$

where $C>0$ is a constant.

Theorem 5. *For $f \in C_B[0,\infty)$ and $x \in (0,\infty)$, we have*

$$|T_{n,\rho}^{\alpha,\beta}(f(t);x) - f(x)| \le C\omega_{\phi^\gamma}\left(f; \frac{\phi^{1-\gamma}(x)}{\sqrt{n\rho}}\right),$$

for sufficiently large n and constant $C>0$, which is independent of f and n.

Proof. For $j \in W_\gamma$, we get

$$j(t) = j(x) + \int_x^t j'(u)du. \tag{3.9}$$

Applying $T_{n,\rho}^{\alpha,\beta}$ in (3.8) and using Hölder's inequality, we obtain

$$\begin{aligned}
|T_{n,\rho}^{\alpha,\beta}(j(t);x) - j(x)| &\le T_{n,\rho}^{\alpha,\beta}\left(\int_x^t |j'|du;x\right)\\
&\le \|\phi^\gamma j'\| T_{n,\rho}^{\alpha,\beta}\left(\left|\int_x^t \frac{du}{\phi^\gamma(u)}\right|;x\right)\\
&\le \|\phi^\gamma j'\| T_{n,\rho}^{\alpha,\beta}\left(|t-x|^{1-\gamma}\left|\int_x^t \frac{du}{\phi(u)}\right|^\gamma;x\right).
\end{aligned} \tag{3.10}$$

Take $A = \left|\int_x^t \frac{du}{\phi(u)}\right|$, we find

$$\begin{aligned}
A &\le \left|\int_x^t \frac{du}{\sqrt{u}}\right|\left|\left(\frac{1}{\sqrt{cx+\rho}} + \frac{1}{\sqrt{ct+\rho}}\right)\right|\\
&\le 2|\sqrt{t}-\sqrt{x}|\left(\frac{1}{\sqrt{cx+\rho}} + \frac{1}{\sqrt{ct+\rho}}\right)\\
&\le 2\frac{|t-x|}{\sqrt{x}+\sqrt{t}}\left(\frac{1}{\sqrt{cx+\rho}} + \frac{1}{\sqrt{ct+\rho}}\right)\\
&\le 2\frac{|t-x|}{\sqrt{x}}\left(\frac{1}{\sqrt{cx+\rho}} + \frac{1}{\sqrt{ct+\rho}}\right).
\end{aligned} \tag{3.11}$$

Using the inequality $|a+b|^{\gamma} \leq |a|^{\gamma}+|b|^{\gamma}$, $0 \leq \gamma \leq 1$ and (3.11), we get

$$\| \int_x^t \frac{du}{\phi(u)} \|^{\gamma} \leq 2^{\beta} \frac{|t-x|^{\gamma}}{x^{\frac{\gamma}{2}}} \left(\frac{1}{(cx+\rho)^{\frac{\gamma}{2}}} + \frac{1}{(ct+\rho)^{\frac{\gamma}{2}}} \right). \tag{3.12}$$

From (3.10), (3.12) and using Cauchy inequality, we get

$$\begin{aligned} |T_{n,\rho}^{\alpha,\beta}(j(t);x) - j(x)| &\leq \frac{2^{\gamma}\|\phi^{\gamma} j'\|}{x^{\frac{\gamma}{2}}} T_{n,\rho}^{\alpha,\beta} \left(|t-x| \left(\frac{1}{(cx+\rho)^{\frac{\gamma}{2}}} + \frac{1}{(ct+\rho)^{\frac{\gamma}{2}}} \right); x \right) \\ &\leq \frac{2^{\gamma}\|\phi^{\gamma} j'\|}{x^{\frac{\gamma}{2}}} \left(\frac{1}{(ct+\rho)^{\frac{\gamma}{2}}} (T_{n,\rho}^{\alpha,\beta}((t-x)^2;x))^{\frac{1}{2}} \right. \\ &\quad \left. + (T_{n,\rho}^{\alpha,\beta}\left((t-x)^2;x\right))^{\frac{1}{2}} . (T_{n,\rho}^{\alpha,\beta}\left((ct+\rho)^{-\gamma};x\right))^{\frac{1}{2}} \right). \end{aligned}$$

If n is adequately large, then we get

$$\left(T_{n,\rho}^{\alpha,\beta}\left((t-x)^2;x\right) \right)^{\frac{1}{2}} \leq \sqrt{\frac{2}{n\rho}} \phi(x), \tag{3.13}$$

where $\phi(x) = \sqrt{x(cx+\rho)}$.

For each $x \in (0,\infty)$, $T_{n,\rho}^{\alpha,\beta}((ct+\rho)^{-\gamma};x) \to (cx+\rho)^{-\gamma}$ as $n \to \infty$. For $\varepsilon > 0$, there exists $n_0 \in \mathbb{N}$ such that

$$T_{n,\rho}^{\alpha,\beta}\left((ct+\rho)^{-\gamma};x\right) \leq (cx+\rho)^{-\gamma} + \varepsilon, \ \forall\, n \geq n_0 = n_0(c,x,\rho,\beta).$$

By choosing $\varepsilon = (cx+\rho)^{-\gamma}$, we obtain

$$T_{n,\rho}^{\alpha,\beta}\left((ct+\rho)^{-\gamma};x\right) \leq 2(cx+\rho)^{-\gamma}, \ \forall\, n \geq n_0. \tag{3.14}$$

From (3.10) to (3.14), we get

$$\begin{aligned} |T_{n,\rho}^{\alpha,\beta}(j(t);x) - j(x)| &\leq 2^{\gamma}\|\phi^{\gamma} j'\| \sqrt{\frac{2}{n\rho}} \phi(x) \left(\phi^{-\gamma}(x) + \sqrt{2} x^{\frac{-\gamma}{2}} (cx+\rho)^{\frac{-\gamma}{2}} \right) \\ &\leq 2^{\gamma+\frac{1}{2}} (1+\sqrt{2}) \|\phi^{\gamma} j'\| \sqrt{\frac{2}{n\rho}} \phi^{1-\gamma}(x). \end{aligned} \tag{3.15}$$

We may write

$$\begin{aligned} |T_{n,\rho}^{\alpha,\beta}(f(t);x) - f(x)| &\leq |T_{n,\rho}^{\alpha,\beta}(f(t)-j(x);x)| + |T_{n,\rho}^{\alpha,\beta}(j(t);x) - j(x)| + |j(x)-f(x)| \\ &\leq 2\|f-j\| + |T_{n,\rho}^{\alpha,\beta}(j(t);x) - j(x)|. \end{aligned} \tag{3.16}$$

From (3.15) to (3.16) and for adequately large n, we get

$$|T_{n,\rho}^{\alpha,\beta}(f(t);x) - f(x)| \leq 2\|f-j\| + 2^{\gamma+\frac{1}{2}} (1+\sqrt{2}) \sqrt{\frac{2}{n\rho}} \phi^{1-\gamma} \|\phi^{\beta} j'\|$$

$$\leq m_1 \left\{ \|f-j\| + \frac{\phi^{1-\gamma}(x)}{\sqrt{n\rho}} \|\phi^{\gamma} j'\| \right\}$$
$$\leq CK_{\phi^{\gamma}} \left(f, \frac{\phi^{1-\gamma}(x)}{\sqrt{n\rho}} \right), \tag{3.17}$$

where $m_1 = \max(2, 2^{\gamma+\frac{1}{2}}(1+\sqrt{2})\sqrt{2})$, from (3.8) and (3.17) we obtain the result. □

4. Weighted Approximation

In this section, we will examine the weighted estimation hypothesis. Let $B_{x^2}[0,\infty) = \{f : \text{for every } x \in [0,\infty), |f(x)| \leq \varphi_f(1+x^2), \varphi_f \text{ is a constant depending on } f\}$. Here $C^*_{x^2}[0,\infty)$, denotes the subspace of all continuous functions belonging to $B_{x^2}[0,\infty)$ and satisfying the condition $\lim_{x\to\infty} \frac{f(x)}{1+x^2}$ is finite. The norm on $C^*_{x^2}[0,\infty)$ is given by $||f||_{x^2} = \sup_{x\in[0,\infty)} \frac{f(x)}{1+x^2}$.

Theorem 6. *For each $f \in C^*_{x^2}[0,\infty)$ and $n > 2c$, we have*

$$\lim_{n\to\infty} ||T^{\alpha,\beta}_{n,\rho}(f) - f||_{x^2} = 0.$$

Proof. Using Lemma 2, we see that it is sufficient to verify the conditions

$$\lim_{n\to\infty} ||T^{\alpha,\beta}_{n,\rho}(t^r, x) - x^r||_{x^2} = 0, \; r = 0,1,2. \tag{4.1}$$

Since $T^{\alpha,\beta}_{n,\rho}(1,x) = 1$, for $r = 0$, (4.1) holds. For $n\rho > c$, we have

$$||T^{\alpha,\beta}_{n,\rho}(t,x) - x||_{x^2} = \sup_{x\in[0,\infty)} \frac{|T^{\alpha,\beta}_{n,\rho}(t,x) - x|}{1+x^2}$$
$$= \sup_{x\in[0,\infty)} \frac{1}{1+x^2} \left| \frac{n\rho x}{(n\rho - c)} + \frac{\alpha\rho}{(n\rho-c)(1+e\beta)} - x \right|$$
$$\leq \left[\frac{n\rho}{(n\rho-c)} - 1 \right] \sup_{x\in[0,\infty)} \frac{x}{1+x^2} + \frac{\alpha\rho}{(n\rho-c)(1+e\beta)} \sup_{x\in[0,\infty)} \frac{1}{1+x^2},$$

condition (4.1) holds for $r = 1$ as $n \to \infty$. Again $n\rho > 2c$, we have

$$||T^{\alpha,\beta}_{n,\rho}(t^2,x) - x^2||_{x^2} = \sup_{x\in[0,\infty)} \frac{|T^{\alpha,\beta}_{n,\rho}(t^2,x) - x^2|}{1+x^2}$$
$$= \sup_{x\in[0,\infty)} \frac{1}{1+x^2} \left| \frac{n^2\rho^2}{(n\rho-c)(n\rho-2c)} x^2 \right.$$
$$\left. + \frac{n\rho^2(1+2\alpha+e\beta)}{(n\rho-c)(n\rho-2c)(1+e\beta)} x \right.$$

$$
\begin{aligned}
&+\frac{\rho^2(\alpha^2-2\alpha e\beta-\alpha e^2\beta^2)}{(n\rho-c)(n\rho-2c)(1+e\beta)^2}-x^2\Bigg| \\
&\leq\left[\frac{n^2\rho^2}{(n\rho-c)(n\rho-2c)}-1\right]\sup_{x\in[0,\infty)}\frac{x^2}{1+x^2} \\
&+\frac{n\rho^2(1+2\alpha+e\beta)}{(n\rho-c)(n\rho-2c)(1+e\beta)}\sup_{x\in[0,\infty)}\frac{x}{1+x^2} \\
&+\frac{\rho^2(\alpha^2-2\alpha e\beta-\alpha e^2\beta^2)}{(n\rho-c)(n\rho-2c)(1+e\beta)^2}\sup_{x\in[0,\infty)}\frac{1}{1+x^2}.
\end{aligned}
$$

Condition (4.1) holds for $r=2$ as $n\to\infty$. This completes the proof of the theorem. □

Corollary 1. *For each $f\in C_{x^2}[0,\infty)$, and $\alpha>0$, we have*

$$\lim_{n\to\infty}\sup_{x\in[0,\infty)}\frac{|T_{n,\rho}^{\alpha,\beta}(f;x)-f(x)|}{(1+x^2)^{\alpha}}=0.$$

Proof. For any fixed $x_0>0$,

$$
\begin{aligned}
\sup_{x\in[0,\infty)}\frac{|T_{n,\rho}^{\alpha,\beta}(f;x)-f(x)|}{(1+x^2)^{1+\alpha}} &\leq \sup_{x\leq x_0}\frac{|T_{n,\rho}^{\alpha,\beta}(f;x)-f(x)|}{(1+x^2)^{1+\alpha}}+\sup_{x\geq x_0}\frac{|T_{n,\rho}^{\alpha,\beta}(f;x)-f(x)|}{(1+x^2)^{1+\alpha}} \\
&\leq \|T_{n,\rho}^{\alpha,\beta}(f;.)-f\|_{C[0,x_0]}+\|f\|_{x^2}\sup_{x\geq x_0}\frac{|T_{n,\rho}^{\alpha,\beta}(f;x)-f(x)|}{(1+x^2)^{1+\alpha}} \\
&\quad+\sup_{x\geq x_0}\frac{|f(x)|}{(1+x^2)^{1+\alpha}}.
\end{aligned}
$$

From Theorem 2, in the above inequality first term tends to zero and by Lemma 2 for any fixed x_0 it can be easily seen that

$$\sup_{x\geq x_0}\frac{|T_{n,\rho}^{\alpha,\beta}(1+t^2;x)-f(x)|}{(1+x^2)^{1+\alpha}}\leq\frac{\varphi}{(1+x_0^2)^{\alpha}}.$$

Constant $\varphi>0$ is independent of x, and choose adequately large x_0 the right-hand side of the earlier inequality and last part can be made small, we get the required result. □

ACKNOWLEDGEMENTS

The authors are extremely thankful to the referee for his valuable suggestions and useful remarks.

REFERENCES

[1] N. Deo *et al.*, "Integral modification of Apostol-Genocchi operators," *Filomat*, vol. 35, no. 8, pp. 2533–2544, 2021, doi: 10.2298/FIL2108533N.

[2] Z. Ditzian and V. Totik, *Moduli of smoothness*, ser. Springer Series in Computational Mathematics. Springer-Verlag, New York, 1987, vol. 9, doi: 10.1007/978-1-4612-4778-4.

[3] A. D. Gadžiev, "Theorems of the type of P. P. Korovkin's theorems," *Mat. Zametki*, vol. 20, no. 5, pp. 781–786, 1976.

[4] N. K. Govil, V. Gupta, and M. A. Noor, "Simultaneous approximation for the Phillips operators," *Int. J. Math. Math. Sci.*, pp. Art. ID 49 094, 9, 2006, doi: 10.1155/IJMMS/2006/49094.

[5] V. Gupta, R. N. Mohapatra, and Z. Finta, "A certain family of mixed summation-integral type operators," *Mathematical and Computer Modelling*, vol. 42, no. 1-2, pp. 181–191, 2005, doi: 10.1016/j.mcm.2004.02.042.

[6] V. Gupta and H. M. Srivastava, "A general family of the Srivastava-Gupta operators preserving linear functions," *European Journal of Pure and Applied Mathematics*, vol. 11, no. 3, pp. 575–579, 2018, doi: 10.29020/nybg.ejpam.v11i3.3314.

[7] Y. He, S. Araci, H. M. Srivastava, and M. Abdel-Aty, "Higher-order convolutions for Apostol-Bernoulli, Apostol-Euler and Apostol-Genocchi polynomials," *Mathematics*, vol. 6, no. 12, p. 329, 2018, doi: 10.3390/math6120329.

[8] Y. He, S. Araci, H. Srivastava, and M. Acikgoz, "Some new identities for the Apostol–Bernoulli polynomials and the Apostol–Genocchi polynomials," *Applied Mathematics and Computation*, vol. 262, pp. 31–41, 2015, doi: 10.1016/j.amc.2015.03.132.

[9] H. S. Jung, N. Deo, and M. Dhamija, "Pointwise approximation by Bernstein type operators in mobile interval," *Applied Mathematics and Computation*, vol. 244, pp. 683–694, 2014, doi: 10.1016/j.amc.2014.07.034.

[10] P. P. Korovkin, "On convergence of linear positive operators in the space of continuous functions," *Doklady Akad. Nauk SSSR (N.S.)*, vol. 90, pp. 961–964, 1953.

[11] Q.-M. Luo, "Extensions of the Genocchi polynomials and their Fourier expansions and integral representations," *Osaka Journal of Mathematics*, vol. 48, no. 2, pp. 291–309, 2011.

[12] Q.-M. Luo and H. M. Srivastava, "Some generalizations of the Apostol-Genocchi polynomials and the Stirling numbers of the second kind," *Applied Mathematics and Computation*, vol. 217, no. 12, pp. 5702–5728, 2011, doi: 10.1016/j.amc.2010.12.048.

[13] C. P. May, "On Phillips operator," *Journal of Approximation Theory*, vol. 20, no. 4, pp. 315–332, 1977, doi: 10.1016/0021-9045(77)90078-8.

[14] H. Ozden and Y. Simsek, "Modification and unification of the Apostol-type numbers and polynomials and their applications," *Applied Mathematics and Computation*, vol. 235, pp. 338–351, 2014, doi: 10.1016/j.amc.2014.03.004.

[15] C. Prakash, D. K. Verma, and N. Deo, "Approximation by a new sequence of operators involving Apostol-Genocchi polynomials," *Mathematica Slovaca*, vol. 71, no. 5, pp. 1179–1188, 2021, doi: 10.1515/ms-2021-0047.

[16] R. Pratap and N. Deo, "Rate of convergence of Gupta-Srivastava operators based on certain parameters," *Journal of Classical Analysis*, vol. 14, no. 2, pp. 137–153, 2019, doi: 10.7153/jca-2019-14-11.

[17] H. M. Srivastava, "Some formulas for the Bernoulli and Euler polynomials at rational arguments," *Math. Proc. Cambridge Philos. Soc.*, vol. 129, no. 1, pp. 77–84, 2000, doi: 10.1017/S0305004100004412.

[18] H. M. Srivastava, M. A. Özarslan, and C. Kaanoğlu, "Some generalized Lagrange-based Apostol-Bernoulli, Apostol-Euler and Apostol-Genocchi polynomials," *Russ. J. Math. Phys.*, vol. 20, no. 1, pp. 110–120, 2013, doi: 10.1134/S106192081301010X.

[19] H. M. Srivastava and A. Pintér, "Remarks on some relationships between the Bernoulli and Euler polynomials," *Appl. Math. Lett.*, vol. 17, no. 4, pp. 375–380, 2004, doi: 10.1016/S0893-9659(04)90077-8.

[20] H. Srivastava, Z. Finta, and V. Gupta, "Direct results for a certain family of summation–integral type operators," *Applied Mathematics and Computation*, vol. 190, no. 1, pp. 449–457, 2007, doi: 10.1016/j.amc.2007.01.039.

[21] H. Srivastava, M. Masjed-Jamei, and M. R. Beyki, "A parametric type of the Apostol-Bernoulli, Apostol-Euler and Apostol-Genocchi polynomials," *Appl. Math. Inf. Sci*, vol. 12, no. 5, pp. 907–916, 2018, doi: https://dx.doi.org/10.18576/amis/120502.

[22] H. Srivastava, M. Masjed-Jamei, and M. Beyki, "Some new generalizations and applications of the Apostol-Bernoulli, Apostol-Euler and Apostol-Genocchi polynomials," *Rocky Mountain Journal of Mathematics*, vol. 49, no. 2, pp. 681–697, 2019, doi: 10.1216/RMJ-2019-49-2-681.

[23] S. Varma and F. Taşdelen, "Szász type operators involving Charlier polynomials," *Math. Comput. Modelling*, vol. 56, no. 5-6, pp. 118–122, 2012, doi: 10.1016/j.mcm.2011.12.017.

[24] D. K. Verma and V. Gupta, "Approximation by a new sequence of operators involving Charlier polynomials with a certain parameter," in *Modern mathematical methods and high performance computing in science and technology*, ser. Springer Proc. Math. Stat. Springer, Singapore, 2016, vol. 171, pp. 25–34, doi: 10.1007/978-981-10-1454-3_3.

Authors' addresses

Chandra Prakash
Delhi Technological University, Department of Mathematics, Bawana Road, 110042 Delhi, India
E-mail address: chandu.math.bhu@gmail.com

Naokant Deo
(**Corresponding author**) Delhi Technological University, Department of Mathematics, Bawana Road, 110042 Delhi, India
E-mail address: naokantdeo@dce.ac.in

Durvesh Kumar Verma
Miranda House, University of Delhi, Department of Mathematics, 110007 Delhi, India
E-mail address: durvesh.kv.du@gmail.com

Vilnius University Press

Contents lists available at Vilnius University Press

Organizations and Markets in Emerging Economies
2023, vol. 14, no. 1(27), pp. 6–25

ISSN 2029-4581 eISSN 2345-0037
DOI: https://doi.org/10.15388/omee.2023.14.80

Assessment of Stock Market Liquidity and Efficiency: Evidence from an Emerging Country

Reema Monga

University School of Management and Entrepreneurship, Delhi Technological University, India
https://orcid.org/0000-0001-9619-0205
reemamonga23@gmail.com

Deepti Aggrawal (corresponding author)

University School of Management and Entrepreneurship, Delhi Technological University, India
https://orcid.org/0000-0003-1899-1570
deeptiaggrawal@dtu.ac.in

Jagvinder Singh

Department of Operational Research, University of Delhi, India
https://orcid.org/ 0000-0002-4558-5220
jagvinder.singh@gmail.com

Abstract. *The study examines the market efficiency, multi-dimensions of liquidity, and their interconnectedness in the emerging Indian stock market. In contrast to the existing literature, the current study aims to fill the gap by testing market liquidity considering multi-dimensions such as depth, breadth, immediacy, tightness, and resilience. Second, the study used a battery of tests to determine efficiency, including the Ljung and Box, the runs test, the Bartels test, Variance Ratio, and the BDS tests. To the best of the authors' knowledge, this is also the primary study to assess how market efficiency and liquidity are related in the Indian equity market. The results of the study show that during the pandemic, the Indian stock market was proven to be efficient, suggesting that there are no abnormal returns. Moreover, the research demonstrates that during the COVID-19 pandemic, large volumes of securities were traded quickly and at a lower price effect, but with higher trading costs for completing a market transaction. However, it is worth noting that increased liquidity equates to greater efficiency, while lower liquidity equates to inefficiency. The study has underlined the most significant implications for policymakers,*

Received: 14/9/2022. **Accepted:** 17/2/2023
Copyright © 2023 Reema Monga, Deepti Aggrawal, Jagvinder Singh. Published by Vilnius University Press. This is an Open Access article distributed under the terms of the Creative Commons Attribution Licence, which permits unrestricted use, distribution, and reproduction in any medium, provided the original author and source are credited.

market regulators, investors and other stakeholders who are monitoring the asset allocations and risk management.

Keywords: *COVID-19, market liquidity, efficiency, Indian stock market, multi-dimensional approach, country lockdown*

1. Introduction

Since the beginning of 2020, the ongoing COVID-19 pandemic has slowed the global and national economies (Goodell, 2020; Ozili & Arun, 2020; Chowdhury et al., 2021; Khan et al., 2021, Su et al., 2021). The novel coronavirus has triggered an infectious disease crisis worldwide, resulting in the loss of human lives and other tangible and financial losses. To limit the spread of the virus, governments around the world have implemented several containment measures, including workplace and school closures, public event cancellations, travel restrictions, home isolations, quarantines, social distancing, and mask wear (Hale et al., 2020; WHO, 2020). However, this endeavor has resulted in a substantial global economic downturn (Ashraf, 2020; Baker et al., 2020; Janiak et al., 2021). The entire economic climate and operational activities become depressed with the outbreak and the growth in COVID-19 cases over time. In particular, hysteria has disrupted the market by preventing customers and businesses from engaging in normal consumption patterns.

The initial wave of the COVID-19 pandemic (early 2020) sparked alarm and compelled the temporary closure of nearly all economies. However, various economies are particularly more vulnerable to the second wave of pandemic (early 2021). The first occurrence of infection in India was reported on January 30th, 2020, as a result of an overseas connection. Despite having the world's second-largest population and inadequate health-care infrastructure, India had fared well in its initial struggle against COVID-19 compared to countries that are significantly more developed and equipped. However, the scenario is totally disastrous, and it had spread to become a terrifying pandemic during its second hit. The second wave of coronavirus was spreading like a tsunami, and COVID-19 cases in India had surpassed 15.9 million as of April 23rd, 2021, with 185,000 deaths. As a result, this invasion has resulted in a large number of afflicted people and, unfortunately, a high fatality rate.

Big events such as natural disasters, disease outbreaks, and political upheavals influence market conditions. With the onset of COVID-19, several studies have identified adverse stock reactions, surge in market volatility, higher systematic risk, and decreased market liquidity and stability (Al-Awadhi et al., 2020; Ashraf, 2020; Zhang et al., 2020; Baig et al., 2021). It is quite evident that investors are considered rational, fully informed, and base their investment decisions on publicly available information under normal circumstances. However, a crisis like COVID-19 can cause market overreaction, causing investors' decision-making processes to be disrupted. During a

worldwide shock, informational market efficiency is critical for investors and other market participants to make effective trading decisions and achieve profitable results. Furthermore, liquidity is an essential indicator of market health because a liquidity shortage can lead to a financial crisis (Munteanu, 2012) and market degradation (Amihud et al., 1990).

Financial research has long focused on the stock markets in the aftermath of previous extraordinary extreme occurrences and catastrophes, such as the SARS pandemic of 2002–2004, the global financial crisis of 2008, and the H1N1 virus (Dimitriou et al., 2013; Peckham, 2013; Chang et al., 2020; Shehzad et al., 2020). In line with the idea, the novel COVID-19 outbreak allows us to examine the two crucial dimensions, i.e., liquidity and efficiency, because these are the key policy areas that tend to be adverse in challenging market conditions, such as crises and pandemics. Brunnermeier and Pedersen (2009) argued that liquidity plays a vital role in market functioning during a financial crisis. Notably, a lack of market liquidity impairs the ability to execute purchase and sell transactions – potentially jeopardizing financial stability. Moreover, with the outbreak of the COVID-19 pandemic, the argument over the validity of informational market efficiency in financial markets has been reignited.

This research is essential for investors, market regulators, and policymakers to understand market liquidity and efficiency during intense turbulence like COVID-19. Furthermore, emerging markets have more information asymmetry and less liquidity (Hu & Prigent, 2019; Mdaghri et al., 2020; Yildiz, 2021). As a result, any unexpected global economic shock that strikes emerging economies creates uncertainty and has a detrimental influence on their financial markets (Tran et al., 2018).

We contribute to the literature in a number of different ways. First, as India is one of the most important components of emerging economies, this article examines the market efficiency of the Indian stock market during the pandemic. Second, several authors point out the limitations of using a single measure or proxy to assess liquidity, i. e., there is no consensus over the ideal metric for gauging liquidity. Therefore, we used the multi-faceted concept of liquidity, which encompasses five different multi-dimensions of liquidity: depth, breadth, immediacy, tightness, and resilience. Further, there is a paucity of research regarding the connectedness of market liquidity and efficiency, thus, in this study, the Efficient Market Hypothesis (EMH) is being tested on the returns of several stocks that have been sorted for market liquidity.

The remainder of this research is outlined as follows. The literature is examined in Section 2. Section 3 delves into the data and methodology. The empirical results are reported in Section 4. Section 5 concludes the paper. Finally, Section 6 presents the implications and future scope of research.

2. Review of Literature

Major events such as financial crises, pandemics, and natural catastrophes have been labeled as "black swan" events that have induced uncertainty in the financial markets (Burch et al., 2016; Ahmad et al., 2021; Antipova, 2021; Yarovaya et al., 2022). Global financial markets have been severely disrupted as the world deals with the enormous economic and social instability caused by COVID-19. To put in another way, the stock market has plummeted as a result of the economic slowdown caused by the COVID-19 outbreak (Topcu & Gulal, 2020; Chowdhury et al., 2021; Okorie & Lin, 2021; Sadiq et al., 2021; Bannigidadmath et al., 2022; Chopra & Mehta, 2022; Nguyen & Nguyen, 2022).

It is evident that the uncertainty surrounding the COVID-19 cases, in particular, could serve as a warning to the financial markets and their participants about the pandemic's progression. Liu et al. (2020) investigated the impact of the Coronavirus outbreak on 21 major stock markets. They found that equity markets fell precipitously following the pandemic, with the negative impact being more significant in Asian countries than in other countries. Ozili and Arun (2020) investigated the impact of Covid-19 on the global economy. They found that efforts to control the virus resulted in the closure of corporate enterprises, business events, and global financial markets, which halted the economies. Given the severity of the pandemic, Firzli (2020) and IMF (2020b) marked this pandemic as "the Great Financial Crisis." IMF (2020a) also stated that the COVID-19 put the entire world into the biggest crisis of the century, even worse than the 2007–2008 Financial Crisis.

Pandemics can cause extraordinary disruptions in the financial markets, affecting stock market's liquidity, volatility, and returns (Baker et al., 2020; Mdaghri et al., 2020). With the commencement of the COVID-19 pandemic, financial markets have been influenced by panic and uncertainty, which has been mirrored in global equity markets (Khan et al., 2020; Berberet al., 2021). Baker et al. (2020) concluded that stock market volatility in the US peaked at its greatest level in history due to the outbreak. Zaremba et al. (2020) found that COVID-19 has affected the financial market and resulted in aberrant trading behavior, and destabilizing most of the financial markets. Mdaghri et al. (2020) reported that the pandemic has reduced stock market liquidity in the MENA region in terms of depth and tightness dimensions. Dev and Sengupta (2020) investigated the impact of Covid-19 on the Indian economy, concluding that the economy decelerated due to the nationwide lockdown, global economic crisis, and concomitant disruption of demand and supply networks.

Ozkan (2020) examined the impact of COVID-19 on the efficiency of six developed countries: the United States, the United Kingdom, Spain, France, Italy, and Germany, using a wild bootstrap automated variance-ratio and the automatic portmanteau test. The author found that during the COVID-19 pandemic, markets became more inefficient, implying a higher likelihood of predictability and abnormal returns. Baig

et al. (2021) concluded that the COVID-19-related lockout impairs the stability and liquidity of the US stock market. Vasileiou (2021) investigated the efficiency of the US stock market and found that the market was inefficient during the pandemic. The Coronovirus Fear Index was also employed in the study, which demonstrated that fear had a detrimental impact on the performance of the US stock market. Nguyen et al. (2021) looked at the influence of the COVID-19 pandemic on the stock returns and liquidity of the financial services industry in Vietnam. They discovered that as the COVID-19 scenario worsens, stock returns and market liquidity suffer significantly. Using the automatic variance ratio and portmanteau test, Bhatia (2022) looked into how the pandemic affected the efficiency of the Indian stock market. The author came to the conclusion that the Indian stock market displayed a divergence from market efficiency, suggesting anomalous gains. Monga et al. (2021, 2022) tested different factor based and optimization based investment strategies in the emerging Indian equity market and found evidence of better risk-adjusted performance and diversification.

Despite several studies on the influence of COVID-19 on various economies, geographies, and sectors, research on emerging equity markets remains scarce. Also, the related literature covers areas like return; volatility; proxies of liquidity such as depth and immediacy. However, this study addresses the gap by examining multi-dimensions of stock market liquidity: depth, breadth, immediacy, tightness, and resilience in the emerging Indian equity market. This research further emphasizes the role of liquidity as an important consideration for market efficiency. In other words, adequate liquidity may be a critical condition for the Efficient Market Hypothesis; thus, our study comprises testing the linkage between market liquidity and efficiency. Finally, our findings add to current research on the market efficiency during the COVID-19 pandemic.

3. Data and Methodology

For this study, we chose 500 stocks from the NIFTY 500 index of the NSE (National Stock Exchange) of India. However, we used a dataset of 485 stocks available during the study period of January 30th, 2020–December 28th, 2021. This time span encompasses both when India first reported a COVID-19 case and when cases began to decline amid the devastating second wave of the pandemic. All the daily data on closing share prices, the number of shares outstanding, trading volume, bid and ask prices were retrieved from Bloomberg. The daily return for the stock is calculated as follows:

$$R_t = lnP_t - lnP_{t-1} \quad (1)$$

where R_t is the daily stock return at time t; lnP_t and lnP_{t-1} are the natural logarithm of the closing price at time t and $t - 1$ respectively.

3.1 Framework of the Study

Figure 1

Model for Testing Market Liquidity and Efficiency

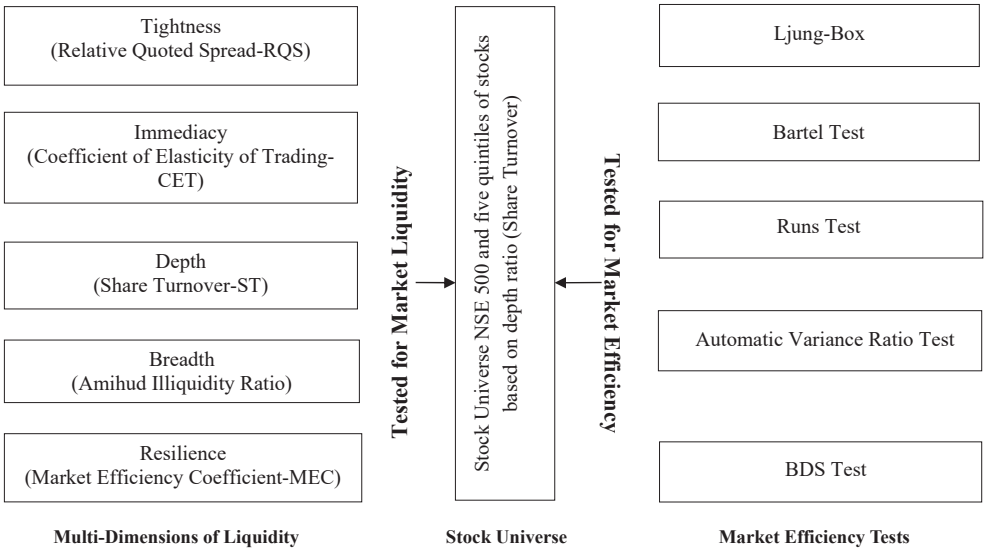

3.2 Multi-dimensions of Liquidity

The nature of market liquidity has been conceptualized variably in the literature (Sarr & Lybek, 2002; Bhattacharyaet al., 2019; Diaz & Escribano, 2020; Naik et al., 2020; Naik & Reddy, 2021; Le & Gregoriou, 2020), and hence measuring market liquidity accurately was a difficult issue for previous studies. It is observed from the previous literature that there is no consensus to quantify liquidity, and as a result, various authors employed different measures for the same. Therefore, given the heterogeneous characteristics of market liquidity, we used a multi-dimensional approach proposed by Sarr and Lybek (2002) to measure market liquidity, which encompasses the five dimensions: depth, tightness, immediacy, breadth, and resilience. The proxies to represent various dimensions are listed below.

Tightness: It is a characteristic of transaction costs that is represented by the difference in ask and bid prices. To accomplish so, we used the Closing Percent Quoted Spread (CPQS), which was developed by Chung and Zhang (2014). It is calculated using daily closing bid-ask prices and is recognized as the most widely utilized proxy measure for the effective bid-ask spread by previous studies (Fong et al., 2017; Diaz & Escribano, 2020; Le & Gregoriou, 2020; Naik et al., 2020).

$$\text{Relative Quoted Spread } \left(RQS\right) = \frac{\text{Ask Price}_{it} - \text{Bid Price}_{it}}{\left(\text{Ask Price}_{it} + \text{Bid Price}_{it}\right)/2} \quad (2)$$

Immediacy: It refers to the simplicity and speed with which the process of trade can be well-accomplished and settled (Tripathi et al., 2019). It displays the settlement structure, coherence of trading systems, and the speed at which orders are executed. In other words, it relates to the amount of time both parties will need to complete the stated quantity of a security at the agreed-upon price.

To quantify market immediacy, Wanzala (2018) and Naik et al. (2020) used the Coefficient of Elasticity of Trading (COE), which accurately portrays the speed with which a trade is executed. The following formula is used to calculate it:

$$\text{Coefficient of Elasticity of Trading } \left(CET\right) = \frac{\%\Delta T}{\%\Delta P} \quad (3)$$

where, $\%\Delta T$ and $\%\Delta P$ represent the percentage changes in daily trading volume, and closing price, respectively.

Depth: It demonstrates the market's ability to accommodate a vast number of orders to maintain stock price equilibrium. In this approach, the number of stocks traded in the entire market is critical for the survival of a deeper market (Naik et al., 2020). It is calculated using Equation 4:

$$\text{Share Turnover } \left(ST\right) = \frac{VO_t}{SO_t} \quad (4)$$

where, VO_t and SO_t represents the volume of stocks and shares outstanding at time *t,* respectively.

Breadth: It refers to the capacity of the market to seamlessly facilitate the trading of a certain amount of securities without significantly impacting their share prices. In analyzing the dimension of breadth, we utilize the Amihud Illiquidity Ratio, which was proposed by Amihud (2002) and was considered the best price impact metric by earlier studies (Diaz & Escribano, 2020; Le & Gregoriou, 2020; Naik et al., 2020). This ratio shows how the price of a security changes when its volume changes. It is calculated as follows:

$$\text{Amihud Illiquidity Ratio} = \frac{\left|R_{it}\right|}{Vol_{it}} \quad (5)$$

where R_{it} stands for absolute return on day *t* for stock *i*, and Vol_{it} represents Volume value.

Resilience: It is a market characteristic in which new trade orders flow quickly to fix trading imbalances, and prices tend to revert to intrinsic value. Hasbrouck and Schwartz (1988) suggested the Market Efficiency Coefficient (MEC) as a way to discern short-term price changes from long-term price changes, i. e., the variances of two returns with distinct time duration. Following Sarr and Lybek (2002) and Bhattacharyaet al.

(2019), we considered five day-returns as a longer period and daily returns as a short term, and thus T equals 5 for our study. In efficient liquid markets, the statistic is close to one, but large deviations from one indicate a lack of liquidity. The following formula is used to compute MEC:

$$\text{Market Efficiency Coefficient}=\frac{\text{Long period log return variance}}{\text{T}\times\text{Short period log return variance}} \tag{6}$$

where *T* stands for the number of short periods within each longer period.

3.3 Testing of Efficient Market Hypotheses

The study of EMH, as proposed by Fama (1970), is a critical concept in finance. An efficient market is one in which asset values are not predictable since the prices already represent the information and quickly respond to any new information.

In the current study, the analysis of EMH has been carried out with a battery of tests (Urquhart, 2016) including the Ljung and Box test, runs test, the Bartels test, the Variance ratio test, and the BDS test.

The weak-form efficiency has been examined using two hypotheses, which are as follows:

H_0: *Return series follows a random walk, i. e., market is weak-form efficient.*

H_1: *Return series does not follow a random walk, i. e., market is weak-form inefficient.*

The autocorrelation test is a useful and accurate tool for determining the independence of a set of random variables, with a null hypothesis of no correlation ($p = 0$). Statistically, positive autocorrelation is indicated by $p > 0$, and negative autocorrelation is shown by $p < 0$. If autocorrelation exists, returns are influenced by their preceding values. However, when the returns are independent, the series shows no signs of autocorrelation, signaling that the time series follows a random walk process. We use the Ljung-Box (Ljung & Box, 1978) test to look at the autocorrelation of returns:

$$\text{Q}=\text{n}\left(n+2\right)\sum_{k=1}^{h}\frac{\hat{p}_k^2}{n-k} \tag{7}$$

where $\hat{p}_k$ indicates the autocorrelation of order k, *k* is the number of lags, and *n* denotes the sample size.

Second, the runs test is employed as a non-parametric technique for determining the randomness of time series, particularly those that are not normally distributed. The test looks to see if the direction of one observation impacts subsequent observations. The idea behind this test is that if the time series is randomly fluctuating and independent, the number of actual runs in the series should be identical to the expected number of runs. The following formula is used to compute the number of expected runs:

$$\text{Expected Number of Runs}=\frac{2PN\left(P+N\right)}{\left(P+N\right)}+1 \tag{8}$$

where P represents positive runs and N indicates negative runs.

The variance is computed as follows:

$$\sigma^2=\frac{2PN\left(2PN-P-N\right)}{\left(P+N\right)^2\left(P+N-1\right)} \tag{9}$$

Furthermore, to determine the randomness of the series, the third test is the Bartels (1982) test, which is a rank variant of von Neumann's Ratio Test for Randomness. This non-parametric test is equivalent to the Run test but is considered to be more effective. It uses independence as the null hypothesis, i.e., determining whether returns are independent. If the null hypothesis is rejected in any of these tests, it is likely that stock returns can be forecast using historical data, which would indicate that weak-form market efficiency is not being followed.

In addition to the tests listed above, the Variance Ratio (VR) Test, created by Lo and Mackinlay (1988), is the most often used econometric instrument to evaluate the random walk hypothesis. It is a common approach for examining serial independence with the null hypothesis of random walk or martingale, i.e., the returns is serially uncorrelated. To implement the VR test, we utilize the Choi (1999) automatic variance test (AVR) in conjunction with wild bootstrap Kim (2009) to improve the small sample properties.

$$\text{VR}\left(K\right)=1+2\sum_{j=1}^{k-1}\left(1-\frac{j}{k}\right)p_j \tag{10}$$

where k represents the holding period, p_j denotes the autocorrelation of return in order j.

Next, we employed the BDS test for serial dependence, which is one of the most prominent and extensively used non-parametric tests (Brock et al., 1996). The null hypothesis asserts that data generation mechanisms are "independent and uniformly distributed," whereas the alternative hypothesis holds that "the model is unspecified." Following Lim (2013) and Urquhart (2016), we chose embedding dimension (m) ranging from 2 to 5, and ε/σ is 1, i.e., 1 times the standard deviation of the returns.

$$\text{W}_{m,n}\left(\varepsilon\right)=\sqrt{n}\frac{T_{m,n}\left(\varepsilon\right)}{V_{m,n}\left(\varepsilon\right)} \tag{11}$$

where $W_{m,n}(\varepsilon)$ is the BDS statistics, n is the sample size, m is the embedding dimension, and (ε) is the metric bound, the largest difference between the observation pairs considered while calculating the correlation integral.

Thereafter, our study involves examining the connectedness of market liquidity and efficiency, i.e., the Efficient Market Hypothesis (EMH) is being tested on the returns

of several stocks that have been sorted for market liquidity. The tests used to examine market efficiency closely follow those of Urquhart (2016) and Wei (2018).

Firstly, we followed the methodology based on the work of Naik et al. (2020) to divide the stock universe into five quintiles based on the Depth ratio, with the 1st Quintile (upper quintile) being the most liquid and the 5th Quintile (lower quintile) being the least liquid. This procedure is used to evaluate how closely liquidity and efficiency are related. Additionally, the weak-form of efficiency is examined for five different quintiles that are classified by depth ratio in order to ascertain the linkage between liquidity and efficiency. We closely follow Wei (2018) for a set of statistical tests for randomness and note the quintile-based p-values for each of the efficiency tests for the five stock groups arranged by liquidity.

During the sample period, each quintile included a total of 97 stocks, with each quintile allowed to vary based on the yearly rankings of their share turnover (ST) ratio. To compute aggregate market liquidity, we converted daily stock-specific data into cross-sectional averages that were weighted depending on the daily market capitalization of the stocks. These daily averages of liquidity metrics were converted to natural log values to eliminate outliers. Finally, the aggregate market liquidity results were calculated using these log values.

4. Analysis of Findings and Discussion

Table 1 shows the return statistics for the entire sample and for the different quintiles, which are divided into five groups depending on the Depth ratio, with group 1 being the most liquid and group 5 being the least liquid. The results indicate that, on aver-

Table 1

Descriptive Statistics of Returns Sorted by Liquidity

Sort by Liquidity			Return Characteristics						
	Group	Depth	Mean	Median	Maximum	Minimum	SD	Skewness	Kurtosis
	Full Sample	-	0.0012	0.0036	0.0705	-0.1287	0.0163	-2.1049	18.3768
High liquidity	1st Quintile	0.0111	0.0014	0.0043	0.0719	0.1762	0.0140	-2.2705	17.0161
	2nd Quintile	0.0048	0.0013	0.0041	0.0834	-0.1445	0.0149	-1.8239	15.9930
	3rd Quintile	0.0026	0.0011	0.0026	0.0689	-0.1239	0.0171	-1.6190	15.0737
	4th Quintile	0.0017	0.0008	0.0021	0.0818	-0.1255	0.0189	-1.7279	22.4100
Low Liquidity	5th Quintile	0.0009	0.0015	0.0025	0.0541	-0.0914	0.0220	-1.5877	12.6931

age, the stock market had positive returns based on the entire sample period and the quintiles. Notably, the findings also imply an illiquidity premium, as indicated by the highest mean return for the 5th quintile, signifying that equity investors must expect a premium to retain illiquid stocks. However, considering the standard deviation, the 5th quintile has the most extensive volatility, while the 1st quintile has the lowest. This is in line with the premise that pricing efficiency is higher in liquid markets with more active traders, resulting in lower volatility.

Table 2 summarizes the descriptive statistics for the liquidity measurements. Compared to other measures, the log mean values show that CET is greater and AR is lower, indicating that huge volumes of securities may be traded quickly and at a lower price effect. It further shows that the high log mean value of MEC indicates that order imbalances are better corrected throughout the outbreak. Next, in terms of market depth, the value of ST indicates that the market is deeper, implying that market has a significant number of orders to keep price equilibrium. Furthermore, it is notable that RQS is higher than ST and AR, indicating higher trading costs for completing a market transaction. In other words, the findings demonstrate that the market is less tight during COVID-19, implying that trading is more expensive during the pandemic.

Table 2

Descriptive Statistics for Liquidity Measures for the Full Sample

	AR	ST	CET	ROS	MEC
Mean	-7.154	-5.618	4.526	-3.386	-0.400
Median	-7.227	-5.606	4.495	-3.468	-0.399
Maximum	-5.098	-4.737	7.434	-1.589	-0.027
Minimum	-8.001	-7.534	1.601	-4.253	-0.891
Std. Dev.	0.388	0.227	0.660	0.324	0.139
Skewness	1.695	-1.620	0.295	1.861	-0.289
Kurtosis	7.202	17.760	5.858	8.219	3.760

Table 3 shows that the upper and lower quintile groups have a substantial gap in share turnover (almost 56 percent). Furthermore, AR is smaller in the upper quintile (most liquid), meaning that heavily traded equities have less price influence due to their trading consistency. Notably, the MEC for the top quintiles is particularly high, implying a better correction of order imbalances for highly traded stocks. Furthermore, the upper quintile has a greater CET, indicating a speedy flow of order transactions. Unlike other indicators, the dimension of tightness suggests that stocks in the lower quintile have lower spreads (as measured by RQS) than those in the upper quintile. This means that trading in low-volume equities is less expensive during the pandemic than trading in high-volume ones.

Table 3

Descriptive Statistics for Liquidity Measures for the Quintiles

	1st Quintile					2nd Quintile					3rd Quintile				
	RQS	CET	ST	AR	MEC	RQS	CET	ST	AR	MEC	RQS	CET	ST	AR	MEC
Mean	-3.193	4.733	-4.544	-7.279	-0.405	-3.334	4.581	-5.369	-7.239	-0.436	-3.408	4.226	-5.996	-7.167	-0.408
Median	-3.257	4.025	-4.536	-7.026	-0.379	-3.382	4.219	-5.354	-7.187	0.405	-3.564	4.104	-5.977	-7.339	-0.394
Maximum	-1.439	7.359	-3.907	-4.897	-0.049	-1.521	8.888	-4.548	-5.082	0.042	-1.626	7.722	-4.823	-5.249	0.250
Minimum	-8.166	-0.362	-9.589	-12.110	-4.825	-8.264	-0.181	-10.49	-11.88	-4.902	-8.582	0.691	-11.15	-12.37	-5.006
Std. Dev.	0.447	0.836	0.382	0.5243	0.286	0.427	0.869	0.368	0.495	0.296	0.449	0.818	0.410	0.522	0.315
Skewness	-3.208	-0.080	-7.016	-2.020	-10.96	-3.713	0.041	-8.281	-1.771	-10.18	-3.459	0.585	-6.165	-1.938	-9.142
Kurtosis	48.333	6.399	91.884	30.108	168.50	55.432	7.166	113.99	28.344	153.19	51.413	6.336	76.998	29.566	135.44

	4th Quintile					5th Quintile				
	RQS	CET	ST	AR	MEC	RQS	CET	ST	AR	MEC
Mean	-3.456	4.159	-6.468	-7.123	-0.434	-3.503	4.039	-7.096	-6.964	-0.421
Median	-3.531	4.530	-6.476	-7.297	0.4230	-3.442	4.687	-7.131	-7.217	-0.422
Maximum	-1.657	7.999	-3.889	-5.136	-0.0001	-1.661	8.452	-5.673	-5.406	0.235
Minimum	-8.190	0.651	-11.506	-12.164	-5.002	-8.014	-0.080	-11.855	-11.576	-5.202
Std. Dev.	0.420	0.849	0.408	0.477	0.299	0.389	0.781	0.390	0.463	0.300
Skewness	-3.222	0.149	-4.925	-2.216	-10.502	-4.027	-0.054	-5.195	-1.844	-11.791
Kurtosis	50.965	6.102	75.899	37.293	161.746	61.222	8.7225	68.841	26.905	189.866

Table 4 displays the efficiency results for the entire sample and five different quintiles. Except for non linear BDS testing, all tests show a sign of efficiency for the entire sample. This indicates that the market does not support return projection, implying that there is lack of possibility of earning abnormal profits during the pandemic. Further, considering the results of quintiles, the p-values of the lowest quintile (with the least liquidity) reject the null hypothesis of randomness in all tests at a 5% significance level. To put it another way, the quintiles with the least liquidity diverge the most from market efficiency. However, higher liquidity quintiles exhibit higher average p-values, showing that high-liquid markets are more efficient. The findings are noteworthy because they suggest a linkage between market liquidity and market efficiency, signaling that stronger liquidity is associated with greater efficiency.

Table 4

Results for Weak-Form of Market Efficiency Sorted by Liquidity

Sort by Liquidity		**p- values**					
	Group	Depth	Ljung-Box	Bartels test	Runs test	AVR	BDS
	Full Sample	-	0.118	0.129	0.103	0.45	0.0163*
High liquidity	1st Quintile	0.011	0.871	0.74	0.103	0.846	0.022*
	2nd Quintile	0.005	0.128	0.139	0.09	0.41	0.018*
	3rd Quintile	0.003	0.043*	0.057*	0.058*	0.031*	0.017*
	4th Quintile	0.002	0.024*	0.044*	0.046*	0.048*	0.015*
Low Liquidity	5th Quintile	0.001	0.017*	0.015*	0.035*	0.021*	0.014*

Note. * denotes significance at a 5% level.

Throughout human history, epidemic diseases have had catastrophic social consequences (deaths of millions of people) and tremendous economic and financial consequences. Compared to the previous pandemics, COVID-19 has a massive effect on global economies (Baker et al., 2020; Jorda, 2020; Ma et al., 2021). It is apparent that most of the world's stock markets have been affected by COVID-19, and among all, India is one of the countries afflicted by the pandemic. Considering this, the research intends to evaluate the two crucial dimensions, i.e., market liquidity and efficiency in the emerging Indian stock market. We looked at market liquidity from multiple perspectives, including depth, immediacy, breadth, tightness, and resilience. The findings of the study indicate that the Indian stock market has been efficient during the pandemic, suggesting that there are no abnormal returns. The study also shows that large amounts of securities can be swiftly traded with a minimal price effect despite increasing trading costs required to execute a market transaction. Finally, it is important to note that increased liquidity equates to greater efficiency, whereas lower liquidity is associated with inefficiency.

The research also tested the market efficiency using a list of tests including the Ljung and Box, the runs test, the Bartels test, the Variance ratio test, and the BDS test. The results show that over the study period, the emerging Indian stock market supported the EMH, suggesting that returns are unpredictable. Also, it was worth checking the linkage with liquidity and efficiency for such analysis, five stock quintiles were formed with 1st Quintile (upper quintile) being the most liquid and the 5th Quintile (lower quintile) being the least liquid. The findings demonstrate that the higher liquidity quintiles exhibit efficiency, showing that high-liquid markets are more efficient. Overall, the study suggests a linkage between market liquidity and market efficiency, implying that higher liquidity is associated with greater market efficiency.

5. Conclusion

The COVID-19 pandemic is the ideal test scenario for assessing key components of the stock market as these unfolding events were completely unknown to participants in the financial market. Particularly, the rapid spread of the COVID-19 pandemic has had an unfathomable impact on the worldwide community, culminating in devastating economic and human costs. We contribute to the literature by looking at multi-dimensions of market liquidity and market efficiency over the evaluation period from January 30th, 2020 to December 28th, 2021. The findings show that the market is less tight during the pandemic, as seen by higher trading costs for executing a market transaction. Also, as indicated by CET and AR, there is a high degree of immediacy and a lower price impact, implying that large volumes of securities are traded quickly with a lower price effect.

The study also investigated multi-dimensions of liquidity for various quintiles based on the criteria of market depth. According to the findings, the top quintile with a deeper market has more RQS than the bottom quintile, implying that high liquidity equities are more expensive to trade. Considering the dimension of market breadth, AR is smaller in the top quintile, meaning that actively traded equities have less price influence due to their trading consistency. The MEC for the top quintiles is very high, showing that high-liquid equities handle order imbalances better than low-liquid stocks. Empirically, the upper quintile has a greater CET, indicating a speedy flow of trading orders.

Using five tests— the Ljung and Box, runs tests, the Bartels test, the Variance ratio test, and BDS— the study also examined the market efficiency during the COVID-19 outbreak. The findings reveal that the weak-form of efficiency is supported by the emerging Indian stock market across the whole sample period, implying that returns are unpredictable. Previous research has shown that there are no definitive findings on the interconnectedness of market liquidity and efficiency (Cajueiro & Tabak, 2004; Bariviera, 2011). Therefore, we used the approach of five different quintiles based on market depth to evaluate the linkage between these two dimensions. According to the analysis, higher liquidity quintiles exhibit efficiency, showing that high-liquid markets

are more efficient. However, it is worth noting that increased liquidity associates with greater efficiency, while lower liquidity is linked to inefficiency.

6. Implications and Future Scope of Research

COVID-19 is a worldwide pandemic that is affecting both developed and developing nations. To the best of our knowledge, this is one of the early initiatives to investigate the stock market efficiency, liquidity and their interconnectedness during the COVID times. Notably, a shortage of market liquidity limits the ability to undertake buy-and-sell transactions, putting financial stability at risk. Furthermore, the debate over the validity of informational market efficiency in financial markets has been revived with the onset of the COVID-19 pandemic. As a result, analyzing these dimensions is critical for regulatory authorities and market players, particularly during crises and pandemics.

Given the severity of the pandemic, the study has highlighted the most significant implications for policymakers, investors, market regulators, and other stakeholders who are monitoring the asset allocations and risk management during the outbreak. The findings of the study suggest that the Indian stock market has higher trading costs during the COVID-19, implying that trading is more expensive. Furthermore, the results supported that the market is efficient, i.e., no exploitable trading opportunities exist, and thus, there is a lack of possibility of earning abnormal profits. Lastly, the study provides empirical evidence that the liquidity and efficiency are linked, i. e., greater liquidity resulting in higher market efficiency.

The findings of the study could be useful for both academicians as well as managers of corporate houses. The results can help the academicians to understand the stock market's response to the pandemic (Covid-19 in this case). The study can also serve as a base for future researchers to determine the numerous elements that need to be addressed in the event of a global issue or pandemic, which will enable better handling of such circumstances. The outcome of the study will be helpful to the market players as well since they could take necessary strategic decisions and adapt to the changes in the market. They may also take measures to reduce the risk or uncertainties prevalent in the stock market owing to these pandemic and other challenges that may occur in the future. Furthermore, these insights are also critical for other market stakeholders since they actively participate in the market and therefore better comprehend the market's situation during such catastrophic events.

Further research could focus on a time-varying approach to market efficiency, particularly during the catastrophic events. Testing the efficiency and multi-dimensions of liquidity in other asset classes and among different emerging economies could be another area of investigation.

Declaration of Conflicting Interests

The Authors declare that there is no conflict of interest.

References

Ahmad, W., Kutan, A. M., & Gupta, S. (2021). Black swan events and COVID-19 outbreak: Sector level evidence from the US, UK, and European stock markets. *International Review of Economics & Finance*, *75*, 546–557. https://doi.org/10.1016/j.iref.2021.04.007

Al-Awadhi, A. M., Alsaifi, K., Al-Awadhi, A., & Alhammadi, S. (2020). Death and contagious infectious diseases: Impact of the COVID-19 virus on stock market returns. *Journal of Behavioral and Experimental Finance*, *27*, 100326. https://doi.org/10.1016/j.jbef.2020.100326

Amihud, Y. (2002). Illiquidity and Stock Returns: Cross-Section and Time-Series Effects. *Journal of Financial Markets*, *5*(1), 31–56. https://doi.org/10.1016/S1386-4181(01)00024-6

Amihud, Y., Mendelson, H., & Wood, R. (1990). Liquidity and the 1987 stock market crash. *Journal of Portfolio Management*, *16*(3), 65–69. https://doi.org/10.3905/jpm.1990.409268

Antipova, T. (2020). Coronavirus Pandemic as Black Swan Event. In T. Antipova (Ed.), *Integrated Science in Digital Age 2020, ICIS 2020* (pp. 356–366). Springer, Cham. https://doi.org/10.1007/978-3-030-49264-9_32

Ashraf, B. N. (2020). Stock markets' reaction to COVID-19: Cases or fatalities?. *Research in International Business and Finance*, *54*, 101249. https://doi.org/10.1016/j.ribaf.2020.101249

Baig, A. S., Butt, H. A., Haroon, O., & Rizvi, S. A. R. (2021). Deaths, panic, lockdowns and US equity markets: The case of COVID-19 pandemic. *Finance Research Letters*, *38*, 101701. https://doi.org/10.1016/j.frl.2020.101701

Baker, S. R., Bloom, N., Davis, S. J., Kost, K., Sammon, M., & Viratyosin, T. (2020). The Unprecedented Stock Market Reaction to COVID-19. *The Review of Asset Pricing Studies*, *10*(4), 742–758. https://doi.org/10.1093/rapstu/raaa008

Bannigidadmath, D., Narayan, P. K., Phan, D. H. B., & Gong, Q. (2022). How stock markets reacted to COVID-19? Evidence from 25 countries. *Finance Research Letters*, *45*, 102161. https://doi.org/10.1016/j.frl.2021.102161

Bariviera, A. F. (2011). The influence of liquidity on informational efficiency: The case of the Thai Stock Market. *Physica A: Statistical Mechanics and its Applications*, *390* (23–24), 4426–4432. https://doi.org/10.1016/j.physa.2011.07.032

Bartels, R. (1982). The Rank Version of von Neumann's Ratio Test for Randomness. *Journal of the American Statistical Association*, *77*(377), 40–46. https://doi.org/10.2307/2287767

Berber, E., Sumbria, D., & Çanakoğlu, N. (2021). Meta-analysis and comprehensive study of coronavirus outbreaks: SARS, MERS and COVID-19. *Journal of Infection and Public Health*, *14*(8), 1051–1064. https://doi.org/10.1016/j.jiph.2021.06.007

Bhatia, M. (2022). Stock Market Efficiency and COVID-19 with Multiple Structural Breaks: Evidence from India. *Global Business Review, 0*(0).https://doi.org/10.1177/09721509221110372

Bhattacharya, S. N., Bhattacharya, M., & Basu, S. (2019). Stock market and its liquidity: Evidence from ARDL bound testing approach in the Indian context. *Cogent Economics & Finance,* *7*(1), 1586297. https://doi.org/10.1080/23322039.2019.1586297

Broock, W. A., Scheinkman, J. A., Dechert, W. D., & LeBaron, B. (1996). A test for independence based on the correlation dimension. *Econometric Reviews*, *15*(3), 197–235. https://doi.org/10.1080/07474939608800353

Brunnermeier, M. K., & Pedersen, L. H. (2009). Market Liquidity and Funding Liquidity. *The Review of Financial Studies*, *22*(6), 2201–2238. https://doi.org/10.1093/rfs/hhn098

Burch, T. R., Emery, D. R., &Fuerst, M. E. (2016). Who Moves Markets in a Sudden Marketwide Crisis? Evidence from 9/11. *Journal of Financial and Quantitative Analysis*, 51(2), 463–487. https://doi.org/10.1017/S0022109016000211

Cajueiro, D. O., & Tabak, B. M. (2004). Ranking efficiency for emerging markets. *Chaos, Solitons & Fractals*, *22*(2), 349–352. https://doi.org/10.1016/j.chaos.2004.02.005

Chang, C. L., McAleer, M., & Wang, Y. A. (2020). Herding behaviour in energy stock markets during the Global Financial Crisis, SARS, and ongoing COVID-19. *Renewable and Sustainable Energy Reviews*, *134*, 110349. https://doi.org/10.1016/j.rser.2020.110349

Choi, I. (1999). Testing the Random Walk Hypothesis for Real Exchange Rates. *Journal of Applied Econometrics*, *14*(3), 293–308. https://doi.org/10.1002/(SICI)1099-1255(199905/06)14:3<293::AID-JAE503>3.0.CO;2-5

Chopra, M., & Mehta, C. (2022). Is the COVID-19 pandemic more contagious for the Asian stock markets? A comparison with the Asian financial, the US subprime and the Eurozone debt crisis. *Journal of Asian Economics*, 101450. https://doi.org/10.1016/j.asieco.2022.101450

Chowdhury, E. K., Khan, I. I., & Dhar, B. K. (2021). Catastrophic impact of Covid-19 on the global stock markets and economic activities. *Business and Society Review, 127*(3). https://doi.org/10.1111/basr.12219

Chung, K. H., &Zhang, H. (2014). A simple approximation of intraday spreads using daily data. *Journal of Financial Markets*, *17*(C), 94–120. https://doi.org/10.1016/j.finmar.2013.02.004

Dev, S. M., & Sengupta, R. (2020). *Covid-19: Impact on the Indian economy*. (Indira Gandhi Institute of Development Research, Mumbai Working Papers 2020-13). https://ideas.repec.org/p/ind/igiwpp/2020-013.html

Díaz, A., & Escribano, A. (2020). Measuring the multi-faceted dimension of liquidity in financial markets: A literature review. *Research in International Business and Finance*, *51*, 101079. https://doi.org/10.1016/j.ribaf.2019.101079

Dimitriou, D., Kenourgios, D., & Simos, T. (2013). Global financial crisis and emerging stock market contagion: A multivariate FIAPARCH–DCC approach. *International Review of Financial Analysis*, *30,* 46–56. https://doi.org/10.1016/j.irfa.2013.05.008

Fama, E. F. (1970). Efficient Capital Markets: A Review of Theory and Empirical Work. *The Journal of Finance*, *25*(2), 383–417.https://doi.org/10.2307/2325486

Firzli, M. N. (2020). Financial Market impact of the COVID-19 pandemic. https://en.wikipedia.org/wiki/Financial_market_impact_of_the_COVID-19_pandemic

Fong, K. Y., Holden, C. W., &Trzcinka, C. A. (2017). What Are the Best Liquidity Proxies for Global Research?. *Review of Finance, 21*(4), 1355–1401. https://doi.org/10.1093/rof/rfx003

Goodell, J. W. (2020). COVID-19 and finance: Agendas for future research. *Finance Research Letters*, *35*, 101512. https://doi.org/10.1016/j.frl.2020.101512

Hale, T., Angrist, N., Kira, B., Petherick, A., Phillips, T., & Webster, S. (2020). Variation in Government Responses to COVID-19. (Working Paper BSG-WP-2020/032).HTTPS://WWW.BSG.OX.AC.UK/RESEARCH/PUBLICATIONS/VARIATION-GOVERNMENT-RESPONSES-COVID-19.

Hasbrouck, J., & Schwartz, R. A. (1988). Liquidity and execution costs in equity markets. *Journal of Portfolio Management*, *14*(3), 10–16. https://doi.org/10.3905/jpm.1988.409160

Hu, Y., & Prigent, J. L. (2019). Information asymmetry, cluster trading, and market efficiency: Evidence from the Chinese stock market. *Economic Modelling, 80,* 11–22. https://doi.org/10.1016/j.econmod.2018.04.001

International Monetary Fund (IMF). (2020a, March 23). *IMF managing director Kristalina Georgieva's statement following a G20 ministerial call on the coronavirus emergency* [Press Release

No. 20/98]. https://www.imf.org/en/News/Articles/2020/03/23/pr2098-imf-managing-director-statement-following-a-g20-ministerial-call-on-the-coronavirus-emergency

IMF. (2020b, June 20). A Crisis Like No Other, An Uncertain Recovery. *World Economic Outlook Update*. https://www.imf.org/en/Publications/WEO/Issues/2020/06/24/WEOUpdateJune2020

Janiak, A., Machado, C., & Turén, J. (2021). Covid-19 contagion, economic activity and business reopening protocols. *Journal of Economic Behavior &Organization, 182,* 264–284. https://www.sciencedirect.com/science/article/pii/S1544612321002269#bib0020

Jordà, Ò., Singh, S. R., & Taylor, A. M. (2020). *Longer-Run Economic Consequences of Pandemics* (NBER working paper No. 26934). National Bureau of Economic Research. https://doi.org/10.3386/w26934

Khan, A., Khan, N., & Shafiq, M. (2021). The Economic Impact of COVID-19 from a Global Perspective. *Contemporary Economics*, *15*(1), 64–76. https://go.gale.com/ps/i.do?id=GALE%7CA653470027&sid=googleScholar&v=2.1&it=r&linkaccess=abs&issn=20840845&p=AONE&sw=w&userGroupName=anon%7E86a28113

Khan, K., Zhao, H., Zhang, H., Yang, H., Shah, M. H., & Jahanger, A. (2020). The Impact of COVID-19 Pandemic on Stock Markets: An Empirical Analysis of World Major Stock Indices. *The Journal of Asian Finance, Economics, and Business*, 7(7), 463–474. https://doi.org/10.13106/jafeb.2020.vol7.no7.463

Kim, J. H. (2009). Automatic variance ratio test under conditional heteroskedasticity. *Finance Research Letters*, *6*(3), 179–185. https://doi.org/10.1016/j.frl.2009.04.003

Le, H., & Gregoriou, A. (2020). How do you Capture Liquidity? A Review of the Literature on Low-Frequency Stock Liquidity. *Journal of Economic Surveys*, *34*(5), 1170–1186. https://doi.org/10.1111/joes.12385

Lim, K. P., & Hooy, C. W. (2013). Non-Linear Predictability in G7 Stock Index Returns. *The Manchester School, 81*(4), 620–637. https://doi.org/10.1111/j.1467-9957.2012.02303.x

Liu, H., Manzoor, A., Wang, C., Zhang, L., & Manzoor, Z. (2020). The COVID-19 Outbreak and Affected Countries Stock Markets Response. *International Journal of Environmental Research and Public Health*, *17*(8), 2800. https://doi.org/10.3390/ijerph17082800

Ljung, G. M., & Box, G. E. (1978). On a Measure of Lack of Fit in Time Series Models. *Biometrika, 65*(2), 297–303.https://doi.org/10.1093/biomet/65.2.297

Lo, A. W., & MacKinlay, A. C. (1988). Stock market prices do not follow random walks: Evidence from a simple specification test. *The Review of Financial Studies*, *1*(1), 41–66. https://doi.org/10.103/rfs/1.1.41

Ma, C., Rogers, J. H., & Zhou, S. (2021). Modern Pandemics: Recession and Recovery. Available at SSRN: https://dx.doi.org/10.2139/ssrn.3565646

Mdaghri, A. A., Raghibi, A., Thanh, C. N., &Oubdi, L. (2020). Stock market liquidity, the great lockdown and the COVID-19 global pandemic nexus in MENA countries. *Review of Behavioral Finance*, *13*(1), 51–68. https://doi.org/10.1108/RBF-06-2020-0132

Monga, R., Aggrawal, D., & Singh, J. (2021). Exploring new frontiers in indexing strategies: an optimization-based risk-efficient solution. *International Journal of System Assurance Engineering and Management*, 1–13. https://doi.org/10.1007/s13198-021-01138-3

Monga, R., Aggrawal, D., & Singh, J. (2022). Smart Beta Investing: An Alternative Investment Paradigm in Emerging Indian Equity Market. *Organizations and Markets in Emerging Economies, 13*(1), 209–237.https://doi.org/10.15388/omee.2022.13.77

Munteanu, I. (2012). Bank Liquidity and its Determinants in Romania. *Procedia Economics and Finance*, *3*, 993–998. https://doi.org/10.1016/S2212-5671(12)00263-8

Naik, P., Poornima, B. G., & Reddy, Y. V. (2020). Measuring liquidity in Indian stock market: A dimensional perspective. *PloSOne, 15*(9), e0238718. https://doi.org/10.1371/journal.pone.0238718

Naik, P., & Reddy, Y. V. (2021). Stock Market Liquidity: A Literature Review. *Sage Open*, *11*(1), 2158244020985529. https://doi.org/10.1177/2158244020985529

Nguyen, C. T., Hai, P. T., & Nguyen, H. K. (2021). Stock market returns and liquidity during the COVID-19 outbreak: evidence from the financial services sector in Vietnam. *Asian Journal of Economics and Banking*,*5*(3), 324-342. https://doi.org/10.1108/AJEB-06-2021-0070

Nguyen, V. C., & Nguyen, T. T. (2022). The Effect of Covid 19 Pandemic on the Financial Market's Performance: Evidence from Top ASEAN Stock Markets. In N. Mansour & L.M.B. Vadell (Eds.), *Finance, Law, and the Crisis of COVID*-19 (pp.139–155). Springer, Cham.https://doi.org/10.1007/978-3-030-89416-0_9

Okorie, D. I., & Lin, B. (2021). Stock markets and the COVID-19 fractal contagion effects. *Finance Research Letters*, *38*, 101640.https://doi.org/10.1016/j.frl.2020.101640

Ozili, P. K., & Arun, T. (2020). *Spillover of COVID-19: Impact on the Global Economy.*Available at SSRN: http://dx.doi.org/10.2139/ssrn.3562570

Ozkan, O. (2021). Impact of COVID-19 on stock market efficiency: Evidence from developed countries. *Research in International Business and Finance*, *58*, 101445. https://doi.org/10.1016/j.ribaf.2021.101445

Peckham, R. (2013). Economies of contagion: financial crisis and pandemic. *Economy and Society*, *42*(2), 226–248. https://doi.org/10.1080/03085147.2012.718626

Sadiq, M., Hsu, C. C., Zhang, Y., & Chien, F. (2021). COVID-19 fear and volatility index movements: Empirical insights from ASEAN stock markets. *Environmental Science and Pollution Research*, *28*(47), 67167–67184. https://doi.org/10.1007/s11356-021-15064-1

Sarr, A., & Lybek, T. (2002). *Measuring Liquidity in Financial Markets.* Available at SSRN 880932. https://www.imf.org/en/Publications/WP/Issues/2016/12/30/Measuring-Liquidity-in-Financial-Markets-16211#:~:text=The%20measures%20include%20bid%2Dask,depth%2C%20breadth%2C%20and%20resiliency.

Shehzad, K., Xiaoxing, L., & Kazouz, H. (2020). COVID-19's disasters are perilous than Global Financial Crisis: A rumor or fact? *Finance Research Letters*, *36*, 101669. https://doi.org/10.1016/j.frl.2020.101669

Su, C. W., Dai, K., Ullah, S., & Andlib, Z. (2021). COVID-19 pandemic and unemployment dynamics in European economies. *Economic Research-EkonomskaIstraživanja*, 1–13, 1226469. https://www.tandfonline.com/doi/full/10.1080/1331677X.2021.1912627

Topcu, M., & Gulal, O. S. (2020). The impact of COVID-19 on emerging stock markets. *Finance Research Letters*, *36*, 101691. https://doi.org/10.1016/j.frl.2020.101691

Tran, L. T. H., Hoang, T. T. P., & Tran, H. X. (2018). Stock liquidity and ownership structure during and after the 2008 Global Financial Crisis: Empirical evidence from an emerging market. *Emerging Markets Review*, 37, 114–133. https://doi.org/10.1016/j.ememar.2018.07.001

Tripathi, A., & Dixit, A. V. (2019). Liquidity of financial markets: A review. *Studies in Economics and Finance*, *37*(2), 201–227.https://doi.org/10.1108/SEF-10-2018-0319

Urquhart, A. (2016). The inefficiency of Bitcoin. *Economics Letters*, *148*, 80–82. https://doi.org/10.1016/j.econlet.2016.09.019

Vasileiou, E. (2021). Behavioral finance and market efficiency in the time of the COVID-19 pandemic: Does fear drive the market? *International Review of Applied Economics*, *35*(2), 224-241. https://doi.org/10.1080/02692171.2020.1864301

Wanzala, R. W. (2018). Estimation of market immediacy by Coefficient of Elasticity of Trading three approach. *The Journal of Finance and Data Science*, *4*(3), 139–156. https://doi.org/10.1016/j.jfds.2018.02.006

Wei, W. C. (2018). Liquidity and market efficiency in cryptocurrencies. *Economics Letters*, *168*, 21–24. https://doi.org/10.1016/j.econlet.2018.04.003

World Health Organization. (2020). Overview of public health and social measures in the context of COVID-19: Interim guidance, 18 May 2020 (No. WHO/2019-nCoV/PHSM_Overview/2020.1).

Yarovaya, L., Matkovskyy, R., & Jalan, A. (2022). The COVID-19 black swan crisis: Reaction and recovery of various financial markets. *Research in International Business and Finance*, *59*, 101521. https://doi.org/10.1016/j.ribaf.2021.101521

Yildiz, Y. (2021). Foreign institutional investors, information asymmetries, and asset valuation in emerging markets. *Research in International Business and Finance, 56*, 101381. https://doi.org/10.1016/j.ribaf.2021.101381

Zaremba, A., Aharon, D. Y., Demir, E., Kizys, R., & Zawadka, D. (2021). COVID-19, government policy responses, and stock market liquidity around the world: A note. *Research in International Business and Finance, 56*, 101359. https://doi.org/10.1016/j.ribaf.2020.101359

Zhang, D., Hu, M., & Ji, Q. (2020). Financial markets under the global pandemic of COVID-19. *Finance Research Letters, 36*, 101528. https://doi.org/10.1016/j.frl.2020.101528

2023 International Conference on Advancement in Computation & Computer Technologies (InCACCT) | 979-8-3503-9648-5/23/$31.00 ©2023 IEEE | DOI: 10.1109/InCACCT57535.2023.10141829

Behaviour Analysis Using Machine Learning Algorithms In Health Care Sector

Anukriti Yadav
Department of Biotechnology Engineering, Delhi Technological University, Shahbad Daulatpur, Main Bawana Road, Delhi 110042, India
anukritiyadav454@gmail.com

Deepak Kumar
Department of Biotechnology Engineering, Delhi Technological University, Shahbad Daulatpur, Main Bawana Road, Delhi 110042, India
deeepak545@gmail.com

Yasha Hasija*
Department of Biotechnology Engineering, Delhi Technological University, Shahbad Daulatpur, Main Bawana Road, Delhi 110042, India
yashahasija06@gmail.com

***Abstract* - A behavioral analytics approach uses big data analytics in combination with machine learning (ML) to identify patterns, trends, aberrations, and other useful insights. The behavior of an individual can be analyzed by expressions, postures, and activity levels. Using ML algorithms could revolutionize the way clinicians make decisions in health care sector. Studies of human behavior have been conducted in a range of scientific disciplines (e.g sociology, psychology, computer science). ML algorithms have the potential to transform the way doctors and instructors make choices. This methodology has been slow to be adopted by behavior analysis experts to maximize its application to practical issues and to aid them in learning more about human behavior. ML algorithms are dominating the healthcare industry. Recent researches have indicated that these techniques can be used to anticipate disease based on health data. Our study examines several machine learning algorithms used in early disease detection and identifies key trends in their performance. The analysis suggests that human behavior may play a role in a variety of conditions, including diabetes, cancer, heart disease, autism, mental illness, Alzheimer's, and others. A number of daily habits are associated with this behavior, including food, respiration rate, blood pressure, voice output, social abnormalities, insomnia, and so on. A few examples of ML applications integrated into healthcare services are naive bayes (NB), support vector machines (SVM), random forest (RF), and convolutional neural networks (CNN). In a variety of cancer classification applications, these models are proved to be highly efficient in diagnosing various cancer types. This review includes a number of research investigations that employ ML to analyze behavioral data. As we gain further insights into the factors influencing organisms' behavior, we are able to create computational models which allow disease prediction and management to become more accurate.**

Keywords— Behavioral analytics, Machine learning, Algorithm, accuracy, healthcare services

I. INTRODUCTION

Patients with neurological diseases, head traumas, and mental illnesses benefit greatly from behavioral analysis in the health sector It is helpful to determine the root cause of a disease by analyzing the patient's behavior. There are many challenges associated with patient behavioral analysis in traditional healthcare [1]. Through the development of smart healthcare, it is possible to analyze patient behavior more easily. Using ML for human behavior recognition has become a new topic of analysis due to the issues relating to potency and accuracy of conventional artificial feature-extraction behavior identification. **Figure 1** shows different type of machine learning algorithms that are used behavioral analysis

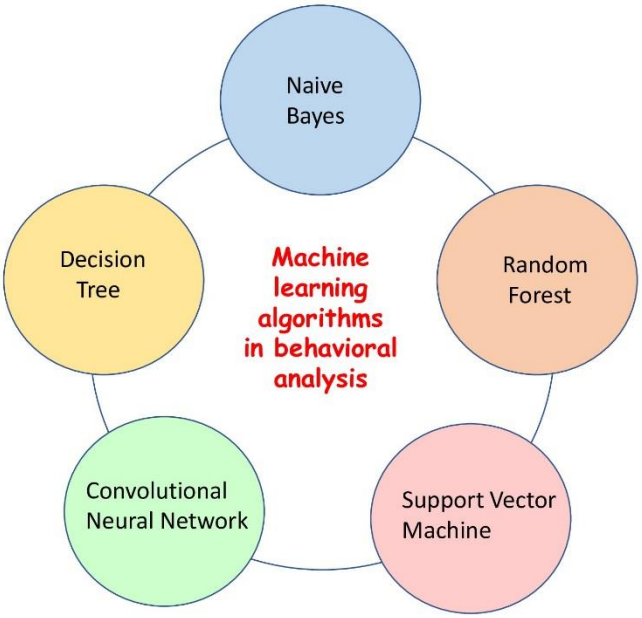

Fig. 1. Different type of machine learning algorithms in behavioral analysis

Research investigators used ML tools to detect behavioral patterns for different patient groups based on the experimental case study they conducted such as pattern analysis for anxiety and depression level [2], assessing patients who have been diagnosed with autism and those who have not [3]. In spite of extensive instrumental as well as scoring noise, ML is capable of detecting interactions that are complex, high-dimensional and, non-linear that may notify prognosis [4]. *Figure 2 depicts how behavioral analysis is carried out using machine learning algorithms. Many biology and behavioral research laboratories, however, find it strenuous to implement these advanced analyses, which may explain why they have not yet been widely adopted. In this article, we have reviewed about various machine learning techniques (like* SVM, CNN, Decision tree, Random forest, Naive bayes) *to study behavior analysis in healthcare sector.*

ISBN: 979-8-3503-9648-5/23/$31.00 ©2023 IEEE

Authorized licensed use limited to: DELHI TECHNICAL UNIV. Downloaded on June 14,2023 at 05:11:15 UTC from IEEE Xplore. Restrictions apply.

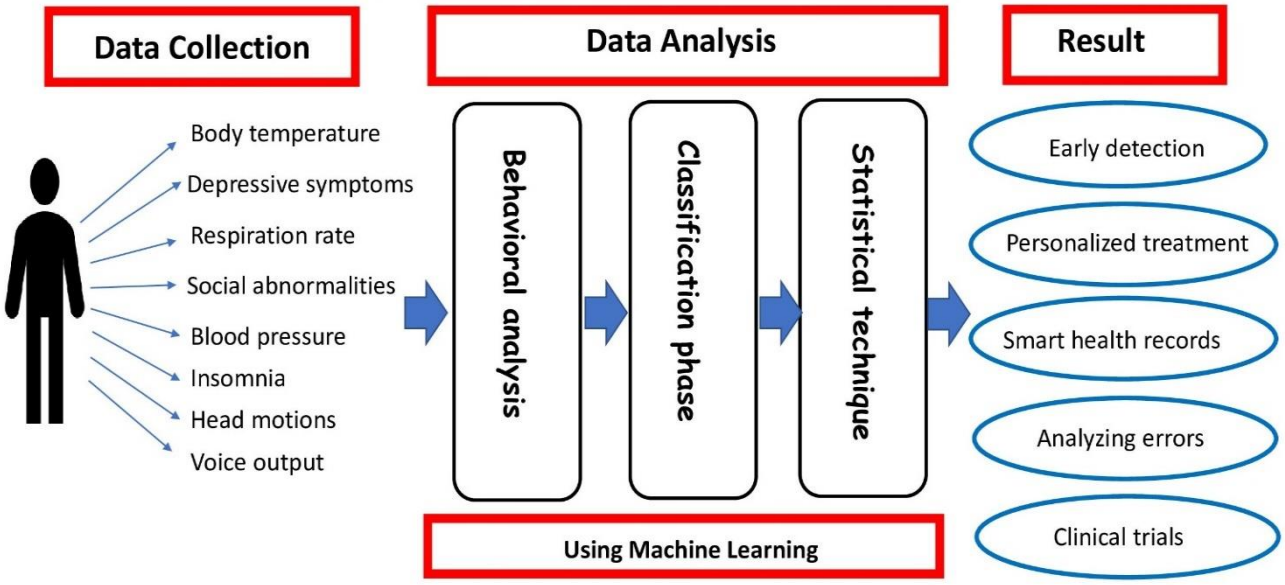

Fig. 2. Use of machine learning algorithm in behavioral analysis

II. Algorithms in Detecting Behavioural Analysis

A. Naive bayes

The Naive Bayes algorithm is a statistical classifier which predicts the likelihood that a given tuple belongs to a given class in accordance with Bayesian analysis theorem [5]. A naive bayes method is used in healthcare to assess a patient's behavior, such as their mental health, using a multiclass classification approach and probilistic algorithm. Radwan Qasrawi et al used an empirical Bayesian approach to investigate the factors associated with depression and anxiety in school-aged children. A total of 3984 West Bank students from 5th to 9th grades, age ranging 10-15 years, were studied in refugee and community schools. During the academic year 2013-2014 data was assembled using the health behaviors of school children examination to identify risk variables related to student mental health symptoms. ML was then used to analyze the data. An analysis of 5 ML algorithms, including RF, neural networks, decision trees, SVMs, and NB were used and it was concluded that NB had the best accuracy in predicting depressive disorders (87.1) and anxiety (72.7) [6]. As a tool for predicting how a person's body will behave if she/he contracts Covid-19, Rabie et al. developed the Covid-19 Prudential Expectation Strategy (CPES). In this method there are three steps: Outlier Rejection Phase (ORP), Feature Selection Phase (FSP), and Classification Phase (CP). CPES makes use of a Statistical Naive Bayes (SNB) classifier, CP, to categorize people according to their body's reaction to Covid-19 infection. There were 2215 persons that filled out the form in total. Compared to current classification algorithms, Prudential Expectation Strategy performs better in accuracy, precision, error and recall, measuring 0.87, 0.84, 0.13 and 0.79, respectively [7].

B. SVM (Support Vector Machine)

A support vector network is the most prevailing supervised learning model which uses deep learning algorithms to map data into a high-dimensional feature space for classifying and predicting data from two groups. SVM increases effectiveness and makes healthcare more convenient and personalized for patients in a healthcare institution. The algorithm is utilized in several healthcare practices to anticipate if a patient has a particular heath issue. Its high classification accuracy, sensitivity, and specificity make it an excellent option for diagnosing diseases like heart disease, stress, and influenza. Athira et al. [8] used SVM technique for development of multi-parameter for monitoring patients health. The researchers developed a multi parameter system based on IOT which had four parameters including heart rate, hotness and coldness, pulse rate, and oxygenation are observed using analogous sensors and in case of emergency an email is conveyed to patient's guardian. They achieved classification accuracy to 95 percent of the mpm system (Multi-Parameter Patient Monitor) by improving the algorithm of SVM. Using behavioral risk as a predictor of cervical cancer, Degrimenci [9] investigated KNN, Random Forest, and SVM algorithms for their potential role in cervical cancer prediction. The information utilized in this study was collected from the UCI Machine Learning Repository (a library of data on cervical cancer behavior risk). A total of 72 indonesians were recruited to provide the samples. Result showed that 21 were in danger (positive) and the remaining 51 were not in danger (negative). The facts that were collected related to cervix cancer behavior which includes 19 characteristics, such as diet, hygiene practices, sexual risk, emotion, etc. Out of all the approaches that were tested, the SVM technique had the most appreciative accuracy (91.67% with sigmoid-SVM).

C. Random Forest

Random Forest (RF) algorithm is an ensemble classifier that uses a variety of decision tree models to improve presaging accuracy. Based on the set of training data, it generates several classification trees that are each trained using

Authorized licensed use limited to: DELHI TECHNICAL UNIV. Downloaded on June 14,2023 at 05:11:15 UTC from IEEE Xplore. Restrictions apply.

bootstrap sampling [10]. Random forests are effective at estimating variable significance with neural networks. Their ability to handle huge data sets with hundreds of variables makes them an excellent approach for dealing with missing data. Probabilities of contracting a disease can be forecast using a random forest model based on past diagnoses. The concept may be useful for managing risks, communicating customized health inforation, and assisting with healthcare decisions [11]. Khalilia et al. [12] trained random forest classifiers for predicting diseases using HCUP (Healthcare Cost and Utilization Project) data from National Inpatient Sample (NIS). To predict the threat of 8 chronic disease, they evaluated the effectiveness of SVM, bagging, boosting, and RF ensemble learning hinge on the Area Under the ROC Curve (AUC). Additionally, RF calculates the significance of each and every variable in the classification procedures, which helped them overcome the class imbalance issue. An average AUC of 88.79% was calculated for eight disease types using the HCUP data set and found to be promising in disease prediction. Kazuya et al. [13] conducted a study in Japan to show a link between stroke-related search behavior and stroke-related mortality. The regression analysis used a number of characteristics as predictors, including sex, lifespan, hospitalizations, progress, strokes, etc. They identified 9476 abstracts from Japanese literature relating to stroke symptoms and signs and a score of 89.94% was achieved using age-adjusted mortality from stroke in the RF analysis. It revealed that the query with high relevance score was stroke, and that it was associated with Japan's age-adjusted mortality rate.

D. CNN (CONVOLUTED NEURAL NETWORK)

CNN is a kind of artificial neural network which uses mathematical operations that it is typically employed in image recognition, segmentation, classification and has one or more convolutional layers, and other correlated tasks. As CNN categorizes hundreds of pictures each minute, it could be useful because new photos could be categorized instantly. Photos are sent for grading to physicians when a patient comes in for screening, but they are not appropriately rated. A trained CNN is capable of making a rapid diagnosis and responding to a patient immediately. In similar fashion, the network produced these results using only one image per eye. Oliveira et al. [14] developed a CNN method to detect the wandering movements of Alzheimer's patients based on data gathered from non-intrusive sensors around the house (**Figure 3).** 220 paths were generated in the dataset. This data was identified by CNN using visual features (such as loops or random movements). The data was compared with 60 min and 30 min datasets and the 30 min datasets had a precision difference of 55.57%, a recall difference of 20% and a F1 score difference of 17.86%.

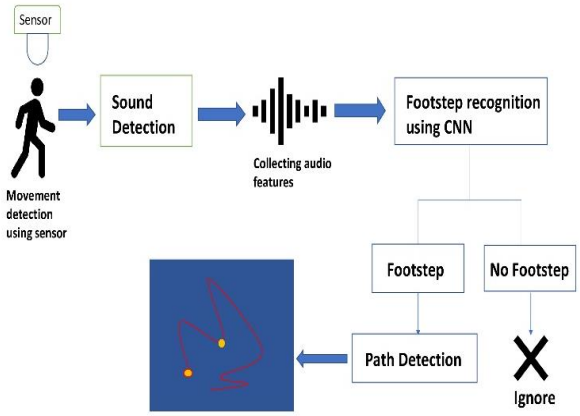

Fig. 3. An illustration of how data filtering works

Pratt et al. [15] carried out a CNN based model for the classification of 5 classes of diabetic retinopathy disease. They took 80000 images from the Kaggle through which state-of-the-art DR stage classification technique was put together by utilizing complex DR characteristics such as transude on the retina, MAS, and HEMS, they employed a CNN architecture with expansion of data to designate 5 degrees of diabetic retinopathy severity.

D. Decision Tree

Decision tree is a type of supervised machine learning technique which predicts and processes data using classification and regression analogies based on real life [5]. Health systems can use decision trees to determine the initial course of treatment for behavior problems and to implement empirically validated treatment procedures [16]. In a study by Cohen et al. [17] behavioral profiles of children with Autism Spectrum Disorder are used to guide treatment decisions through CART decision trees. They compared the PDDBI with the ADOS-2 to determine its criterion-related validity. A total of 110 candidates were selected between 1.5 and 6.9 years age and grouped into 2 behavioral aspects: Receptive/Expressive Social Communication Abilities (REXSCAs) and Approach Withdrawal Problems (AWPs). Based on T-scores, various cut-off scores was evaluated in this study for domains such as sensory behaviors, traditions, repetition of language, offensive behaviour, and ability to express. Using a decision tree algorithm, Batterham et al. analysed depression outcomes. This study showed that environmental factors are associated with various social factors that are related to depression. After 4 weeks of follow-up, patients were allowed to begin taking new antidepressants; 25% of placebo patients and 7% of zuranolone patients received new antidepressants in the phase 2 study. Decision trees were discovered to have higher susceptibility and selectivity than logistic regressions when analogous predictors were used [18].

Table I. Recent Studies Conducted on Behavior Analysis with The Help of ML for the Treatment of Various Disease

S. No	Technique	Paper	Worked on	Accuracy	Year
1	Naïve Bayes	Radwan Qasrawi et al. [6]	Depression and anxiety	87.1%(depression) 72.7%(anxiety)	2022
		Rabie et al. [7]	Covid	87%	2022
2	SVM	Degirmenci [9]	Cervical cancer	91.67%	2022

Authorized licensed use limited to: DELHI TECHNICAL UNIV. Downloaded on June 14,2023 at 05:11:15 UTC from IEEE Xplore. Restrictions apply.

		Athira et al. [8]	Heart rate, temperature, respiration rate, oxygen and saturation	95%	2020
3	Random Forest	Khalilia et al. [12]	8 chronic diseases	88.79%	2011
		Kazuya et al. [13]	Stroke	89.94%	2022
4	CNN	Pratt et al. [15]	Daibetic retinopathy disease	-	2016
		Oliveira et al. [14]	Alzheimer disease	82.65%	2022
5	Decision Tree	Cohen et al. [17]	Autisum spectrum disorder	-	2019
		Batterham et al. [18]	Depression	-	2009

III. CONCLUSION

As machine learning becomes more prevalent, it is being used for diagnosing diseases in multiple industries. A number of scientists have discussed the benefit of machine learning-based disease diagnostics (MLBDD) in terms of time and cost efficiency. Traditionally, diagnostic techniques are labor-intensive, expensive, and require human involvement frequently. According to WHO estimates, lifestyle changes are responsible for 30% of all deaths worldwide. These deaths can be avoided by correctly identifying the risk factors that go along with them and developing behavior modification strategies. Prevention of potentially fatal consequences requires changes in health-related behavior. Life expectancy will be increased if early diagnosis, prevention assistance, and appropriate treatment are provided as soon as possible. Machine learning algorithms will be implemented to further investigate methods like sensor based feature extraction, such as Electrocardiogram (ECG), Electroencephalogram (EEG) etc, for the diagnosis of early-stage diseases from human behavior on various platforms. The idea behind automated patient and disease monitoring activities are to conserve time and fill in when all doctors are busy, like during an emergency. The deployment of smart technology in this industry can help save lives during pandemics, such as the COVID-19 epidemic.

REFERENCES

[1] F. Yao, "Deep learning analysis of human behaviour recognition based on convolutional neural network analysis," *Behav. Inf. Technol.*, vol. 0, no. 0, pp. 1–9, 2020, doi: 10.1080/0144929X.2020.1716390.

[2] T. Richter, B. Fishbain, A. Markus, G. Richter-Levin, and H. Okon-Singer, "Using machine learning-based analysis for behavioral differentiation between anxiety and depression," *Sci. Rep.*, vol. 10, no. 1, pp. 1–12, 2020, doi: 10.1038/s41598-020-72289-9.

[3] D. P. Wall, R. Dally, R. Luyster, J. Y. Jung, and T. F. DeLuca, "Use of artificial intelligence to shorten the behavioral diagnosis of autism," *PLoS One*, vol. 7, no. 8, 2012, doi: 10.1371/journal.pone.0043855.

[4] B. Kanchanatawan, S. Thika, S. Sirivichayakul, A. F. Carvalho, M. Geffard, and M. Maes, "In Schizophrenia, Depression, Anxiety, and Physiosomatic Symptoms Are Strongly Related to Psychotic Symptoms and Excitation, Impairments in Episodic Memory, and Increased Production of Neurotoxic Tryptophan Catabolites: a Multivariate and Machine Learning," *Neurotox. Res.*, vol. 33, no. 3, pp. 641–655, 2018, doi: 10.1007/s12640-018-9868-4.

[5] M. Srividya, S. Mohanavalli, and N. Bhalaji, "Behavioral Modeling for Mental Health using Machine Learning Algorithms," *J. Med. Syst.*, vol. 42, no. 5, 2018, doi: 10.1007/s10916-018-0934-5.

[6] R. Qasrawi, S. P. V. Polo, D. A. Al-Halawa, S. Hallaq, and Z. Abdeen, "Assessment and Prediction of Depression and Anxiety Risk Factors in Schoolchildren: Machine Learning Techniques Performance Analysis," *JMIR Form. Res.*, vol. 6, no. 8, pp. 1–15, 2022, doi: 10.2196/32736.

[7] A. H. Rabie, N. A. Mansour, A. I. Saleh, and A. E. Takieldeen, "Expecting individuals' body reaction to Covid-19 based on statistical Naïve Bayes technique," *Pattern Recognit.*, vol. 128, no. April, 2022, doi: 10.1016/j.patcog.2022.108693.

[8] A. Athira, T. D. Devika, K. R. Varsha, and S. S. Bose, "Design and Development of IOT Based Multi-Parameter Patient Monitoring System," *2020 6th Int. Conf. Adv. Comput. Commun. Syst. ICACCS 2020*, pp. 862–866, 2020, doi: 10.1109/ICACCS48705.2020.9074293.

[9] A. Degirmenci, "Performance Comparison of kNN , Random Forest and SVM in the Prediction of Cervical Cancer from Behavioral Risk," vol. 7, no. 10, pp. 71–79, 2022.

[10] W. Mao and F.-Y. Wang, "Cultural Modeling for Behavior Analysis and Prediction," *Adv. Intell. Secur. Informatics*, pp. 91–102, 2012, doi: 10.1016/b978-0-12-397200-2.00008-7.

[11] G. Biau and E. Scornet, "A random forest guided tour," *Test*, vol. 25, no. 2, pp. 197–227, 2016, doi: 10.1007/s11749-016-0481-7.

[12] M. Khalilia, S. Chakraborty, and M. Popescu, "Predicting disease risks from highly imbalanced data using random forest," *BMC Med. Inform. Decis. Mak.*, vol. 11, no. 1, 2011, doi: 10.1186/1472-6947-11-51.

[13] K. Taira and S. Fujita, "Prediction of Age-Adjusted Mortality from Stroke in Japanese Prefectures: Ecological Study Using Search Engine Queries," *JMIR Form. Res.*, vol. 6, no. 1, 2022, doi: 10.2196/27805.

[14] R. Oliveira, R. Feres, F. Barreto, and R. Abreu, "CNN for Elderly Wandering Prediction in Indoor Scenarios," *SN Comput. Sci.*, vol. 3, no. 3, pp. 1–11, 2022, doi: 10.1007/s42979-022-01091-3.

[15] H. Pratt, F. Coenen, D. M. Broadbent, S. P. Harding, and Y. Zheng, "Convolutional Neural Networks for Diabetic Retinopathy," *Procedia Comput. Sci.*, vol. 90, no. July, pp. 200–205, 2016, doi: 10.1016/j.procs.2016.07.014.

[16] V. Podgorelec, P. Kokol, B. Stiglic, and I. Rozman, "Decision trees: An overview and their use in medicine," *J. Med. Syst.*, vol. 26, no. 5, pp. 445–463, 2002, doi: 10.1023/A:1016409317640.

[17] I. L. Cohen and M. J. Flory, "Autism Spectrum Disorder Decision Tree Subgroups Predict Adaptive Behavior and Autism Severity Trajectories in Children with ASD," *J. Autism Dev. Disord.*, vol. 49, no. 4, pp. 1423–1437, 2019, doi: 10.1007/s10803-018-3830-4.

[18] P. J. Batterham, H. Christensen, and A. J. Mackinnon, "Modifiable risk factors predicting major depressive disorder at four year follow-up: A decision tree approach," *BMC Psychiatry*, vol. 9, pp. 4–11, 2009, doi: 10.1186/1471-244X-9-75.

Authorized licensed use limited to: DELHI TECHNICAL UNIV. Downloaded on June 14,2023 at 05:11:15 UTC from IEEE Xplore. Restrictions apply.

2023 2nd International Conference on Smart Technologies and Systems for Next Generation Computing (ICSTSN) | 979-8-3503-4800-2/23/$31.00 ©2023 IEEE | DOI: 10.1109/ICSTSN57873.2023.10151543

Blood Cell Classification using Neural Network Models

Jagrit Mitra
Dept. of Computer Science and Engineering
Delhi Technological University
New Delhi, India
jagritmitra08@gmail.com

Kartik Vijayran
Dept. of Computer Science and Engineering
Delhi Technological University
New Delhi, India
vijayrankartik@gmail.com

Kartikeya Verma
Dept. of Computer Science and Engineering
Delhi Technological University
New Delhi, India
kartikeyav1726@gmail.com

Anurag Goel
Dept. of Computer Science and Engineering
Delhi Technological University
New Delhi, India
anurag@dtu.ac.in

***Abstract*— Blood cells classification is a crucial aspect in medical diagnosis. Several machine learning models have been proposed under various researches for classification of blood cells in recent years. However, the traditional machine learning algorithms are limited in the accurate detection of abnormal cells. In this study, we propose deep learning based approach for blood cell classification and evaluate the efficiency of multi-layer neural network model built for the classification of the various types of White Blood Cells using Convolutional Neural Networks (CNN) and Recurrent Neural Networks (RNN) in combination. The proposed method leverages the strengths of both CNN and RNN and gives better results.**

Keywords — White Blood Cells (WBCs), Blood Cell Classification, Convolutional Neural Network (CNN), Recurrent Neural Network (RNN), Long Short-Term Memory (LSTM).

I. INTRODUCTION

White Blood Cells (WBCs) are an important constituent of human blood. Sometimes called leukocytes, they play a critical function in the immunological system of the human body. Their production occurs in the bone marrow, and can be classified into several types, including lymphocytes, monocytes, neutrophils and eosinophils. One crucial component of medical diagnostics is how these blood cells are classified. The detection of abnormal cells can provide crucial information for the early diagnosis of various diseases, including cancer. The proposed method aims to categorize the WBCs using the hidden characteristics of their images. Each type of WBCs has distinct features, including variations in texture, color, size, and shape. By utilizing these underlying features of their images, the proposed approach aims to accurately classify the various classes of WBCs.

II. RELATED WORK

Characterizing and identifying a patient's blood sample is crucial for the diagnosis of blood-related disorders. In [1], Deep CNNs are implemented for separating the subclasses of WBCs. In [2], Pierre at. al. implemented multi-scale CNNs acting at different resolutions for vision based cell classification. Region-Based CNN (R-CNN) is used to classify WBCs in [3,4]. These approaches do not focus on utilizing the long-term dependency between key features. Recurrent Neural Networks are considered excellent in mapping input and output sentences in recognition/prediction problems. Although, difficulties are reported when sequence spans over long intervals. The storing information over extended time interval involves the problem of decaying error backflow, to resolve this a gradient-based method is Long Short Term Memory (LSTM) [5,6].

Besides neural network, statistical pattern analysis analysis has been utilised [7] for classification of WBCs. It is based on con- trolled watershed algorithm to segment the nuclei from its microscopic image. Then their discriminating potentiality has been calculated using kernel density function. Morphological characteristics of cells have also been utilised for classification as in [8] . It was tested over gray scale images with outline feature being the outer contour of the cell. Architectures with combination of CNN and RNN are unable to produce results in case of multiple overlap cells. A Canonical Correlation Analysis (CCA) process was proposed in [9] which solved the above problem.

Segmentation algorithms are used for segmentation of WBCs in [10] using multiple features of including geometrical features, LDP features and color features using three different neural network based classifiers. Classification of Red Blood Cells (RBCs) helps in diagnosing many diseases. CNNs are used in [11], to classify various types of RBCs. Some works have combined CNN and RNN to classify WBCs [12, 13, 14].

III. METHODOLOGY USED

A. Convolutional Neural Network (CNN)

CNNs are based on shared weight architecture of convolutional kernels which slide upon features to generate feature maps. They are generalized multi- layer perceptrons CNNs are very popular for vision imagery tasks. CNN has the following layers:

1. Convolutional layer: This is responsible for creation of the activation map, simply it convolves the input and passes it on very similar to the neuron in visual cortex.
2. Pooling layer: Dimensionality is reduced by pooling layers by clustering outputs at next layer. These mainly is max pooling or can be average pooling.
3. Dropout: It is primarily utilized as a regularisation method. Since these are prone to overfitting, it is essential to be taken care of. At this layer some cells

Authorized licensed use limited to: DELHI TECHNICAL UNIV. Downloaded on June 28,2023 at 06:27:06 UTC from IEEE Xplore. Restrictions apply.

are dropped/ignored to reduce the network complexity.

B. Recurrent Neural Network (RNN)

RNNs are the artificial neural networks where sequential data is utilized, a cycle is created allowing outputs from node to affect subsequent inputs on same node, thus inducing temporally dynamic behaviour. Developed on feedforward networks, parameter is shared across each layer of network. There are following variants of RNNs:

1. Long Short Term Memory (LSTM): LSTMs are invented in 1997. LSTMs solve the problem when the previous state influences the current prediction and leads to inaccuracy. To control the flow, LSTM has three gates: an input gate, an output gate and a forget gate. The Forget gate allows some information to be removed from current state
2. Bidirectional LSTM: In this variant, as the name suggests, the information from both sides is utilized. A finite sequence is used to predict based on elements' future as well as past context by concatenating opposite working layers.

RNN is mainly used for sequential data. Although, the blood cells do not have any sequential information in general but [12, 13, 14] have shown the applicability of RNN for WBCs classification. Therefore, we have also implemented RNN in this work.

C. Proposed Approach

The proposed model is an ensemble model of RNN and CNN.

The CNN model has the following architecture as shown in Figure 1.

1. Input layer: The input image is changes by this layer into 3-dimensional tensor.
2. Convolutional layer: An initial convolutional layer with 32 kernel filters is used for producing output of dimension 58*76*32. On top of this, two convolutional layers with 64 kernel filters are used along with max pooling layers embedded in between to reduce the number of features.
3. Dropout layer: This layer is added for reducing the dimensionality and overfitting.
4. Flatten layer: This layer is required to feed the output to the fully connected layer.

A dropout layer is sandwiched between the dense layers for ensuring the features are learned without overfitting. Adadelta optimizer is used. The architecture is shown in Figure 1.

The RNN model layers are described as follows:

1. Input layer: This layer converts the input image into 3-dimensional tensor.
2. Lambda layer: This layer is used to implement the customized functions. Here, it converts the tensor into single channel of dimension 60*80.
3. Bidirectional LSTM: This layer connects two opposite layers to common output, thus allowing the receiving of information from both past and future states. Two Bidirectional LSTM layers with 64 units are used.
4. Dropout layer: Dropout layer is added to avoid the issue of overfitting and to speed up the process.
5. Dense layer: The last layer is a fully-connected dense layer which produces the `final` output.

Adadelta optimizer is used to avoid the continuous decay of learning rate. The architecture displayed in Figure 2.

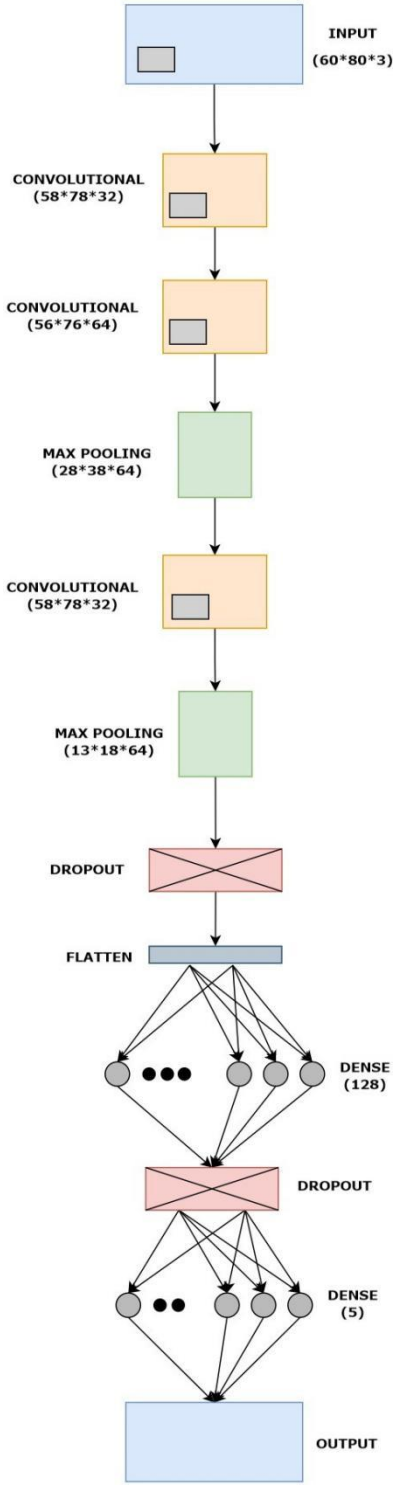

Figure 1. CNN Architecture

Authorized licensed use limited to: DELHI TECHNICAL UNIV. Downloaded on June 28,2023 at 06:27:06 UTC from IEEE Xplore. Restrictions apply.

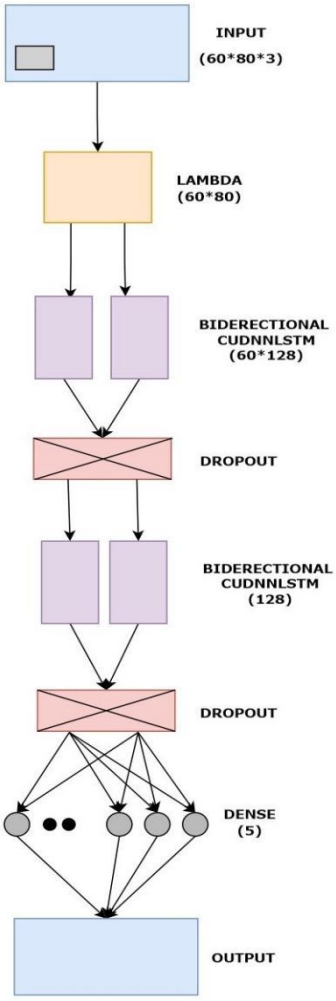

Figure 2. RNN Architecture

The concatenated ensemble model consists of the following layers:

1. Input layer: This layer converts the input image into 3-dimensional tensor, which is then fed into CNN and RNN units.
2. CNN Unit: CNN unit is the sequential model which comprises of a convolutional layer initially of 32 units and kernel size of 3*3. This was followed by two more convolutional layers along with corresponding max-pooling layers. Following that, a fully- connected layer receives the output and results are later flattened.
3. RNN Unit: This unit starts with a Lambda layer for reducing the dimensionality followed by two Bi-directional LSTMs with their corresponding dropout layers.
4. Fully-connected layer: The results from two individually working units: CNN and RNN, are concatenated and provided for this fully-connected layer's input.
5. Output layer: For obtaining the final output, two another fully-connected layers are used with reduced dimensions along with dropout layer to avoid overfitting.

The architecture is shown in Figure 3.

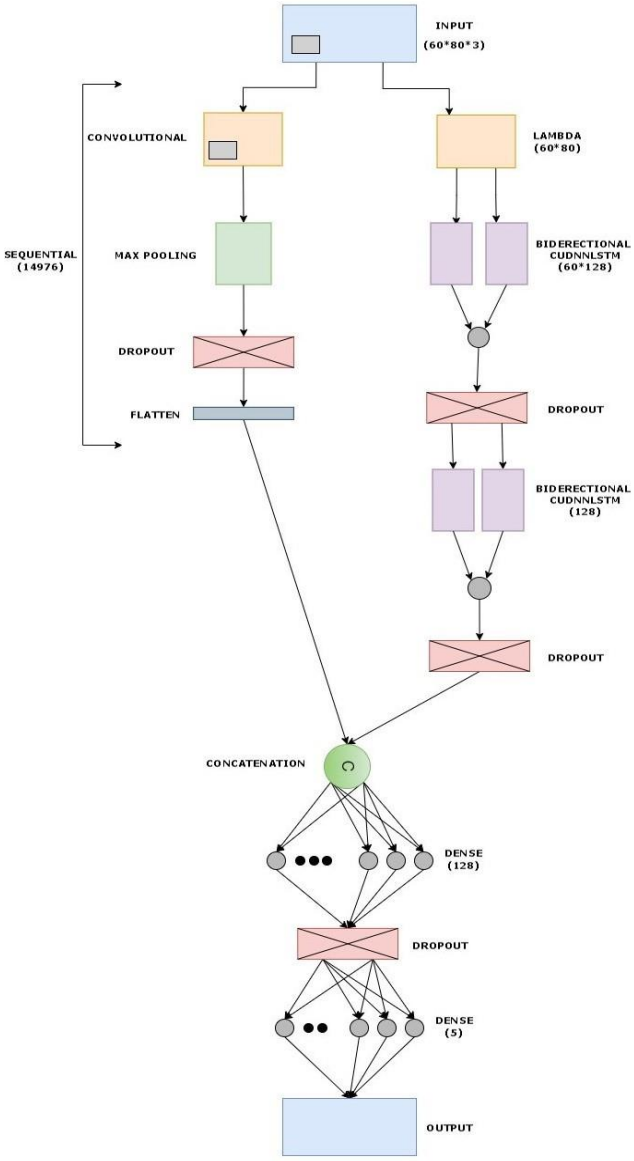

Figure 3. CNN+RNN Ensemble Model

IV. Implementation

A. Dataset

It is frequently necessary to identify and characterize blood cell samples for diagnosis of blood-based illness. The original raw data is available as BCCD Dataset. The processed blood cell dataset publicly available on Kaggle [15] consists of 12500 JPEG images of size 480*640*3 with their labels. There are four classes namely Lymphocyte, Monocyte, Eosinophil, Neutrophil. The entire dataset includes approximately 3000 sample images of each class. Besides we have 410 images with sub-type labels and corresponding bounding boxes (JPEG + XML). Four-way classification classifies cells among the four classes of WBCs namely Lymphocyte, Monocyte, Eosinophil, and Neutrophil. This classification is based upon the actions that the cells conduct against pathogens in the body, they do also possess differences in physical structures. On the other hand, two-way classification classifies WBCs in two broader categories i.e. Mono-nuclear and Poly-nuclear. Monocytes and

Authorized licensed use limited to: DELHI TECHNICAL UNIV. Downloaded on June 28,2023 at 06:27:06 UTC from IEEE Xplore. Restrictions apply.

Lymphocytes are major mono-nuclear cells while Eosinophil and Neutrophil fall into the category of poly-nuclear cells.

B. Data Pre-Processing

One-hot encoding is used to normalize the cell types into four dimensional vectors. This allows utilizing the Softmax loss function for evaluation. The input mages have been downscaled to 80*60 for reducing the computation time without significantly losing the accuracy. This is done without scaling transformations as size of nuclei is important for classification. A sample blood cell image with labels is shown in Figure 4.

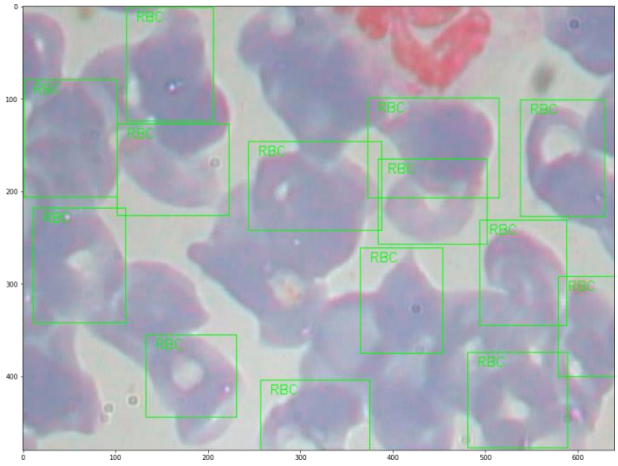

Figure 4. Blood Cell Image with Labels

V. RESULTS

The ensemble model is tested with CNN-only and RNN-only models under same conditions. Furthermore, we improved upon the models by making changes to the hidden layers and number of epoch values, referred to as Modified CNN and Modified CNN+RNN. Table 1 and Table 2 shows the results of two-way classification and four-way classification respectively.

The accuracy plots of Modified CNN for two-way classification and four-way classification are shown in Figure 5 and 6 respectively. The accuracy plots of Modified ensemble CNN+RNN model for two-way classification and four-way classification are shown in Figure 7 and 8 respectively.

Table 1: Results: Two-way Classification

Models	Two-Way Classification			
	Precision	Recall	F1-Score	Accuracy
RNN only	0.51	0.48	0.49	49.65%
CNN only	0.95	0.94	0.94	93.76%
RNN+CNN	0.95	0.94	0.95	94.53%
Modified CNN	0.96	0.95	0.95	95.13%
Modified RNN+CNN	**0.99**	**0.97**	**0.96**	**96.05%**

Table 2: Results: Four-way Classification

Models	Four-Way Classification			
	Precision	Recall	F1-Score	Accuracy
RNN only	0.30	0.25	0.27	25.13%
CNN only	0.90	0.87	0.88	86.81%
RNN+CNN	0.89	0.87	0.88	87.05%
Modified CNN	**0.90**	**0.88**	**0.89**	**87.85%**
Modified RNN+CNN	**0.90**	**0.88**	0.88	87.57%

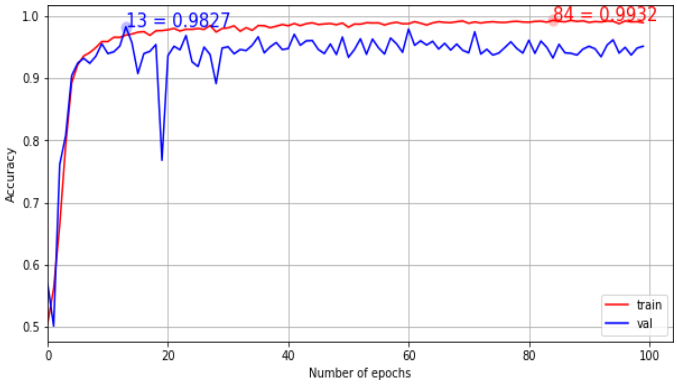

Figure 5. Accuracy Plot of Modified CNN for Two-way Classification

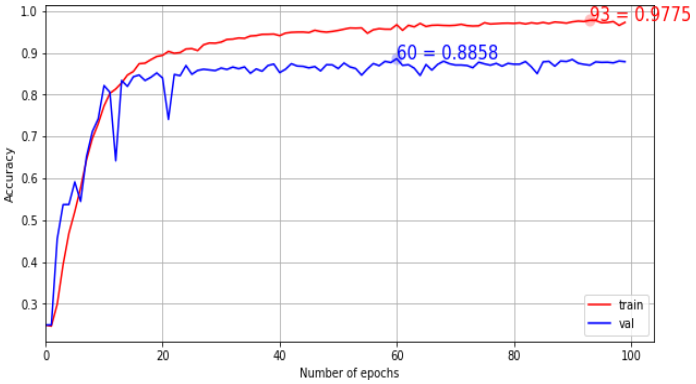

Figure 6. Accuracy Plot of Modified CNN for Four-way Classification

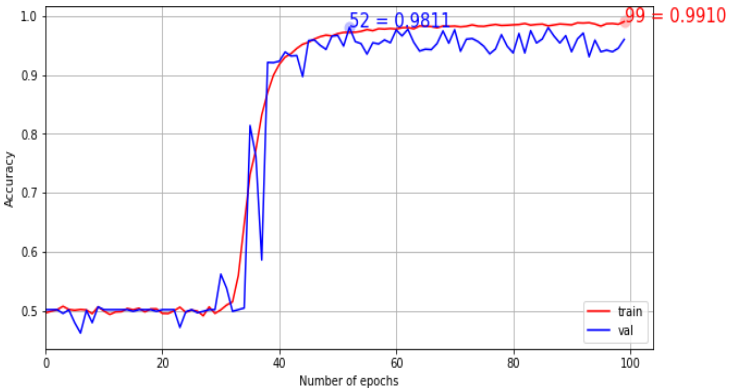

Figure 7. Accuracy Plot of Modified Ensemble CNN+RNN Model for Two-way Classification

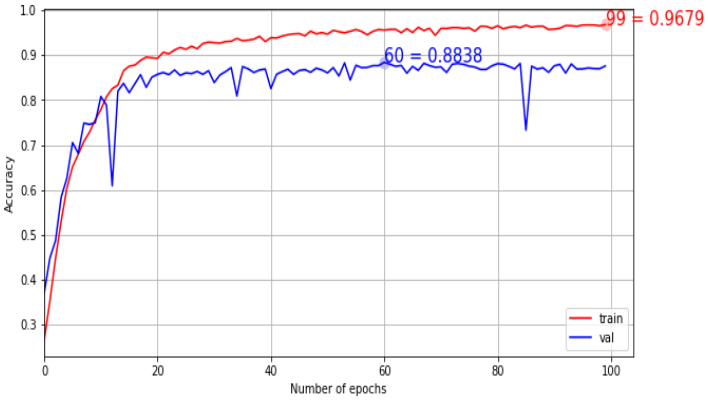

Figure 8. Accuracy Plot of Modified Ensemble CNN+RNN Model for Four-way Classification

Authorized licensed use limited to: DELHI TECHNICAL UNIV. Downloaded on June 28,2023 at 06:27:06 UTC from IEEE Xplore. Restrictions apply.

VI. Conclusion

In this paper, we have implemented an ensemble model combing CNN and RNN for WBCs classification. The results show that the ensemble model of CNN+RNN achieves better accuracy as compared to the traditional CNN only and RNN only models under both the cases of two-way and four-way classification. We can also notice an increase of approximately 1% across both the CNN only and the ensemble model after tuning the number of epochs and the total number of hidden layers. The modified ensemble model outperforms the rest of the models.

References

[1] Togacar, Mesut, Burhan Ergen, and Mehmet Emre Sertkaya. "Subclass separation of white blood cell images using convolutional neural network models." Elektronika ir Elektrotechnika 25, no. 5 (2019): 63-68.

[2] Buyssens, Pierre, Abderrahim Elmoataz, and Olivier Lézoray. "Multiscale convolutional neural networks for vision–based classification of cells." In Computer Vision–ACCV 2012: 11th Asian Conference on Computer Vision, Daejeon, Korea, November 5-9, 2012, Revised Selected Papers, Part II 11, pp. 342-352. Springer Berlin Heidelberg, 2013.

[3] Kutlu, Hüseyin, Engin Avci, and Fatih Özyurt. "White blood cells detection and classification based on regional convolutional neural networks." Medical hypotheses 135 (2020): 109472.

[4] Dhieb, Najmeddine, Hakim Ghazzai, Hichem Besbes, and Yehia Massoud. "An automated blood cells counting and classification framework using mask R-CNN deep learning model." In 2019 31st international conference on microelectronics (ICM), pp. 300-303. IEEE, 2019.

[5] Hochreiter, Sepp, and Jürgen Schmidhuber. "Long short-term memory." Neural computation 9, no. 8 (1997): 1735-1780.

[6] Bengio, Yoshua, Patrice Simard, and Paolo Frasconi. "Learning long-term dependencies with gradient descent is difficult." IEEE transactions on neural networks 5, no. 2 (1994): 157-166.

[7] Ghosh, Madhumala, Devkumar Das, Subhodip Mandal, Chandan Chakraborty, Mallika Pala, Ashok K. Maity, Surjya K. Pal, and Ajoy K. Ray. "Statistical pattern analysis of white blood cell nuclei morphometry." In 2010 IEEE Students Technology Symposium (TechSym), pp. 59-66. IEEE, 2010.

[8] Bikhet, Sawsan F., Ahmed M. Darwish, Hany A. Tolba, and Samir I. Shaheen. "Segmentation and classification of white blood cells." In 2000 IEEE International Conference on Acoustics, Speech, and Signal Processing. Proceedings (Cat. No. 00CH37100), vol. 4, pp. 2259-2261. IEEE, 2000.

[9] Patil, A. M., M. D. Patil, and G. K. Birajdar. "White blood cells image classification using deep learning with canonical correlation analysis." Irbm 42, no. 5 (2021): 378-389.

[10] Su, Mu-Chun, Chun-Yen Cheng, and Pa-Chun Wang. "A neural-network-based approach to white blood cell classification." The scientific world journal 2014 (2014).

[11] Parab, Mamata Anil, and Ninad Dileep Mehendale. "Red blood cell classification using image processing and CNN." SN Computer Science 2, no. 2 (2021): 70.

[12] Liang, Gaobo, Huichao Hong, Weifang Xie, and Lixin Zheng. "Combining convolutional neural network with recursive neural network for blood cell image classification." IEEE access 6 (2018): 36188-36197.

[13] Ghosh, Indraneel, and Siddhant Kundu. "Combining Neural Network Models for Blood Cell Classification." arXiv preprint arXiv:2101.03604 (2021).

[14] Meenakshi, A., J. Anitha Ruth, V. R. Kanagavalli, and R. Uma. "Automatic classification of white blood cells using deep features based convolutional neural network." Multimedia Tools and Applications 81, no. 21 (2022): 30121-30142.

[15] Blood Cell Images Dataset: https://www.kaggle.com/datasets/paultimothymooney/blood-cells.

Authorized licensed use limited to: DELHI TECHNICAL UNIV. Downloaded on June 28,2023 at 06:27:06 UTC from IEEE Xplore. Restrictions apply.

ResearchGate

See discussions, stats, and author profiles for this publication at: https://www.researchgate.net/publication/366174962

Breast Lesion Detection and Localization with VGG19 Optimized Vision Transformer

Conference Paper · December 2022

DOI: 10.1109/AIST55798.2022.10065355

CITATIONS
0

READS
40

3 authors:

Vijay Chahar
Dr B R Ambedkar National Institute of Technology Jalandhar
230 PUBLICATIONS **7,085** CITATIONS
SEE PROFILE

Kamakshi Rautela
Delhi Technological University
15 PUBLICATIONS **11** CITATIONS
SEE PROFILE

Dinesh Kumar
Delhi Technological University
87 PUBLICATIONS **1,027** CITATIONS
SEE PROFILE

Some of the authors of this publication are also working on these related projects:

Occlusion invariant three dimensional face recognition system View project

Tox2020: Toxicity Prediction of pre clinical trial drug using Physicochemical Properties and Machine Learning Approaches View project

All content following this page was uploaded by Kamakshi Rautela on 13 April 2023.

The user has requested enhancement of the downloaded file.

Breast Lesion Detection and Localization with VGG19 Optimized Vision Transformer

Kamakshi Rautela
Department of Electronics and Communication Engineering
Delhi Technological University
Delhi, India
kamakshi_2k19phdec06@dtu.ac.in

Dinesh Kumar
Department of Electronics and Communication Engineering
Delhi Technological University
Delhi, India
dineshkumar@dtu.ac.in

Vijay Kumar
Department of Computer Science Engineering
National Institute of Technology
Hamirpur, India
vijaykumarchahar@nith.ac.in

***Abstract*— In many different medical imaging tasks, convolutional neural networks have been extensively used. However, due to the inherent locality of convolution operation, CNNs typically aren't good at modelling long-range dependencies, which are crucial for correctly mapping or identifying corresponding breast lesion features. This encourages us to use the Vision Transformer block with VGG19 for breast cancer detection. We also suggested an effective model to combine global and local features. Finally, the model is trained separately on two different modalities of datasets i.e., INbreast and Database for Mastology Research (DMR). We used transfer learning for training, 80% of the data from both the datasets are used to train the model and rest 20% is used to test. The network was trained using a batch size of 50 and a learning rate of 0.01 over the course of 100 epochs. The test accuracy obtained for INbreast and DMR dataset are 98% and 89.9%, respectively. The results obtained for digital mammogram are very are high but for thermal image dataset it is marginally low.**

Keywords*— *Breast Cancer, Global Features, Local Features, Mammogram, Thermogram, VGG19, Vision Transformer

I. INTRODUCTION

One of the most prevalent cancers in women globally is breast cancer, as per the reports from the WHO (World Health Organization) (accessed on 24 May 2022 at https://www.who.int/news-room/factsheets/ detail/breast-cancer). According to the WHO, the number of breast cancer cases has reached 2 million (representing approximately 24.5% of all represented new cancer cases) [1]. It has been recorded in both males and females, although its prevalence in females is considerably very high. So, the development of a breast cancer imaging tool is essential for early diagnosis and treatment of breast cancer. According to National Centre for Disease Informatics and Research (NCDIR) National Cancer Registry Program, the estimated breast cancer cases and mortality in females in India [2].

When breast tumor begins to grow malignantly, it does this inside the duct, where it is unlikely to spread to other body parts and usually doesn't cause symptoms. This type of tumor is metastasis. Breast tumor in-situ have the potential to enlarge and encroach into surrounding tissue before distant metastasizing to nearby lymph nodes. This is known as distant metastasis. Notably, the most common cause of death in people with breast cancer is distant metastasis [3]. Therefore, early detection of breast cancer is necessary to lower mortality rate. Many nations around the world have created programs that regularly screen women. Ultrasound imaging, magnetic resonance imaging and mammography are the currently employed clinical breast cancer screening techniques.

In recent years, medical image analysis applications like image classification, have used convolutional neural networks (CNNs) as their most popular network type [5]. Earlier, the traditional image segmentation algorithms were the main building blocks of the medical image analysis systems, which included threshold-based methods, edge detection-based methods and region-based methods. However, complex texture, low contrast, and blurred boundary areas are frequently present in medical images, which restricts the effectiveness and practicality of such image segmentation algorithms. Currently, the most widely used model in the field of natural language processing (NLP) is the Transformer architecture, which was presented by Vaswani et al. [4]. The advancement of self-attention centred deep neural networks served as inspiration for the author of [6] when they introduced the Vision Transformer architecture for the classification of image. For those models, the general training procedure is based on treating each embedded patch in the input image as a word in natural language processing. In order to learn the relationship between these embedded patches, these models employ self-attention modules [5].

Hence, this paper makes use of Transformers in medical image analysis and investigates how self-attention based architectures are used to categorize breast cancer images. For automatic and precise breast tumor, a model based on VGG19 optimized vision transformer is used. The proposed model captures local and global data using transformer and convolution blocks, respectively, and combines them using a cross-attention fusion mechanism with both local and global feature mechanisms.

II. METHODOLOGY

This section would help to highlight the overall framework of our strategy as shown in Fig. 1. The proposed model is the parallel module based on VGG19 and vision transformer. We

XXX-X-XXXX-XXXX-X/XX/$XX.00 ©20XX IEEE

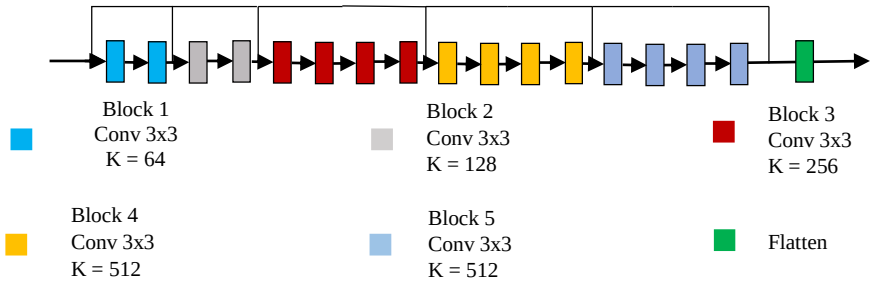

Fig. 2. Architecture of VGG19

first extract the information from a dataset with $H \times W \times D \times 4$ input size and down-sample it using the convolution Block. The extracted information is passed down to two models VGG19 and vision transformer. Both the models extract the important features to distinguish cancerous and non-cancerous data from breast cancer datasets. The information obtained from both the dataset is fused together to make the classification better.

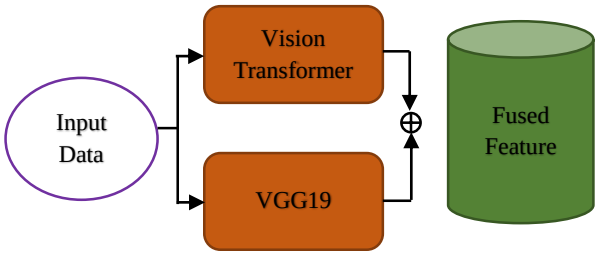

Fig. 1. Basic architecture of proposed model

We create a parallel module from the vision transformer and VGG19 to extracts global and local features, respectively. Additionally, to combine local and global features with significant semantic variations, we used cross-attention fusion.

A. Local feature extraction via VGG19

VGG19, an improved version of VGG16, first created in [7]. Max pooling and convolutional layers, also referred to as feature extractors, make up VGG19 i.e., deep CNN. Following these layers is at least one FC (fully connected) layer, which works as the classifier. Fig. 2 shows the basic architecture of VGG19. A softmax takes over the output layer. This activation function defines the type of cancer, with the input layer's size set to 64x64. Without spending all that time manually inspecting them, it is simple to find the features that can differentiate different cancer type thanks to the feature extraction capability of VGG19.

B. Global feature extraction via Vision Transformer

An innovative work for transformers to be used directly on images is called Vision Transformer [9]. The main factor contributing to the high computational cost of the transformer is the multi-head self-attention (MSA), refer Fig. 3. The complexity of the computation is inversely correlated with the number of tokens in this case. Unlike conventional transformers, the one being proposed uses window-based MSA to reduce computation.

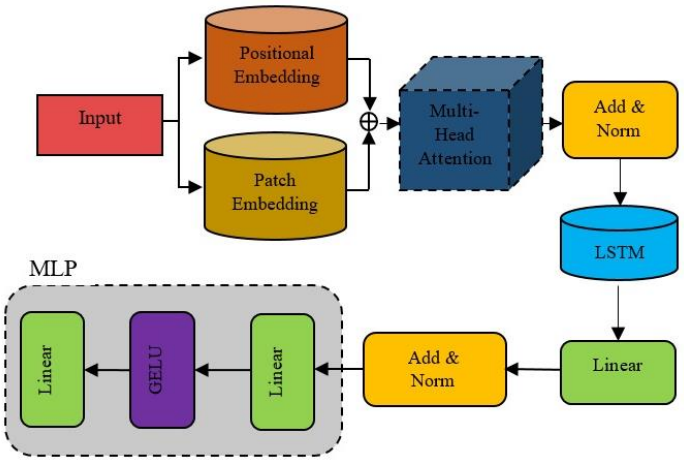

Fig. 3. Block diagram of Vision Transformer

With MLP and multi head attention approach, Vision Transformer layers can be written as:

$$V_T^{'} = MHA(L_N(V_T^{n-1}) + V_T^{n-1} \quad (1)$$

$$V_T = MLP(L_N(V_T^{'n-1}) + V_T^{'n-1} \quad (2)$$

$V_T^{'}$ and V_T represents the MHA and MLP module's respective output global features in the proposed Vision Transformer block. Layer normalization and the multilayer perceptron module, respectively, are abbreviated as MLP and LN [8][9][11]. The masked self-attention in MHA can be expressed as follows using the masked attention map (M_{mask}):

$$M_{attention} = soft\max\left(\frac{KQ^T}{\sqrt{r}} + M_{mask}\right) \quad (3)$$

Where $M_{attention}$ stands for the masking attention matrix. Query, key, and value matrices are denoted as Q, K, and V. T stands for transpose and Q/K dimension is r.

C. Fusion of local and global features

We propose a fusion with local and global feature with semantic differences, which is inspired by many literatures on multimodal feature fusion with the help of attention mechanism [10-14]. Auxiliary (I_1) and master input (I_2) are features of the fusion, that can be expressed as follows:

$$M_{attention} = soft\max\left(\frac{z_1(I_1)z_2(I_2)}{\sqrt{r}}\right) \quad (4)$$

$$F_{fuse} = M_{attention}(z_3)(I_2) \quad (5)$$

$$Output = z_4(F_{fuse}) + (I_2) \quad (6)$$

Here, z_1 , z_2 , z_3 and z_4 are depth-wise convolution. The attention matrix ($M_{attention}$) reflects how important the master features are in comparison to the auxiliary features, and then by using Equation (5) fused features are obtained. Finally, by adding I_2 and F_{fuse} , we obtain the *Output* , which enables effective backpropagation during training.

III. Description of Datasets

TABLE I.
DESCRIPTION OF DATASETS USED

Dataset	Explanation	Source
DMR [15]	There are images in this database that our research team has collected, including thermal and mammography images (32 healthy and 32 unhealthy). The accuracy was 100% for a sample of 64 breasts.	Database for Research Mastology The database contains the Infrared images, attainable via the website http://visual.ic.u .br/dmi
IN breast [13]	The Breast Center at CHSJ in Porto authorized the photographs to be taken between 2008 and 2010, and the National Committee for Data Protection also gave their approval.	IN Breast database requests can be made online at http://medicalresear ch.inescporto.pt/breast research/index.php/Ge tINbreastDatabase.

Table I gives the detailed description of the datasets used for the proposed technique.

Identify applicable funding agency here. If none, delete this text box.

IV. Result and Discussion

The model is trained and tested on two different datasets which are discussed above i.e., INbreast and DMR. We are using transfer learning here, 80% of the data from both the datasets are used for training the model and rest 20% is used to test. The network was trained using a batch size of 50 and a learning rate of 0.01 over the course of 100 epochs. Adam is chosen as the optimization function for this network. The model parameters with the best performance were selected and applied to the testing images after 100 epochs in order to assess the network's overall performance.

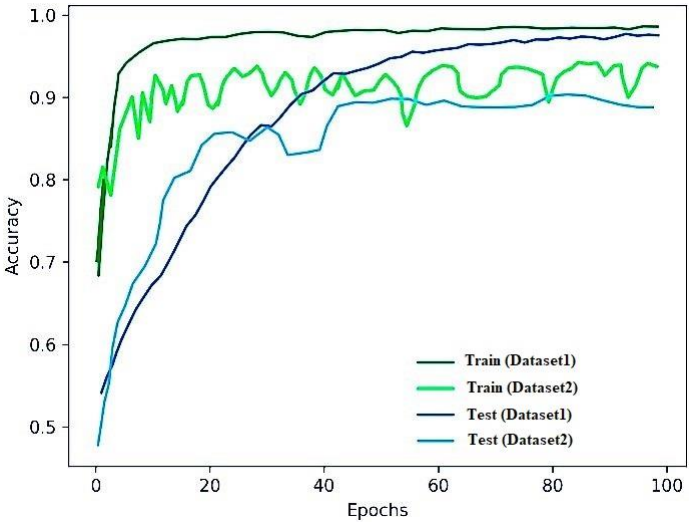

Fig. 4. Accuracy obtained for INbreast and DMR Dataset

Following network training, images from the respective dataset are tested, and performance is assessed using overall accuracy. Fig. 4. Shows the overall accuracy obtained for the proposed model for both the datasets. From the graph obtained Dataset1 is the INbreast dataset and Dataset2 is the DMR dataset. The accuracy during training and testing of Dataset1 was 0.988 and 0.98, respectively. While for Dataset2, the accuracy during training and testing was 0.949 and 0.899, respectively.

TABLE II.
SUMMARY OF OBTAINED ACCURACY FOR BOTH THE DATASETS

	Epoch	Accuracy	
		Dataset1	Dataset2
Train	25	0.953	0.942
	50	0.975	0.933
	100	0.988	0.949
Test	25	0.887	0.878
	50	0.941	0.90
	100	0.98	0.899

Table II provides a summary of the train and test results for both the datasets. As can be seen, there is little difference between train and test results, indicating that the proposed model is not overfitting. From the results obtained it is clear that the model worked best for INbreast dataset and slightly less for DMR dataset.

TABLE III.
COMPARISION WITH RECENT WORKS ON BREAST CANCER DETECTION

Ref	Year	Dataset	Ac	Sen	Spec
[16]	2021	Thermal	91.42±2.93	5.87	4.90
[17]	2021	Thermal	87.96	NA	NA
[18]	2022	Mammogram	(MIAS)98.50 (DDSM)97.55	97.579	98.217
[19]	2021	Mammogram	NA	84.07	NA
Proposed		Thermal Mammogram	INbreast: Train Ac 98.8 Test Ac 98 DMR: Train Ac 94.9 Test Ac 89.9	96.2	95.4

Table III gives the comparison of the proposed work with the recent work done on breast cancer detection. It shows that the model works good on mammogram data in comparison to thermal image data. Our model obtained the best possible outcome for mammogram and thermal data when compared to the work done on the respective datasets.

V. CONCLUSION

For the purpose of detecting breast cancer, we proposed a parallel model made up of the vision transformer and the VGG19. Additionally, we proposed an efficient model to fuse global and local features, which was motivated by numerous studies of multimodal feature fusion. The experimental result on Dataset1 and Dataset2 show that the proposed model achieved good accuracy score on Dataset1 and marginally low for Dataset2. It proves that transformer based networks may achieve good performance for any medical image modality.

Insufficient datasets are a medical image's main drawback. In the future, we plan to experiment with using some self-supervised new learning techniques in addition to transformer for cancer early detection.

REFERENCES

1. Union for International Cancer Control's - International Agency for Research on Cancer WHO. https://www.uicc.org/news/globocan2020-new-global-cancer-data. [Online; accessed 1-March-2020].
2. National Cancer Registry Programme, "Report of population based cancer registries 2020 national cancer registry programme.," National Centre for Disease Informatics and Research. and Indian Council of Medical Research.
3. Mannu, G.S.; Wang, Z.; Broggio, J.; Charman, J.; Cheung, S.; Kearins, O.; Dodwell, D.; Darby, S.C. Invasive breast cancer and breast cancer mortality after ductal carcinoma in situ in women attending for breast screening in England, 1988–2014: Population based observational cohort study. BMJ 2020, 369, m1570.
4. Ashish Vaswani, Noam Shazeer, Niki Parmar, Jakob Uszkoreit, Llion Jones, Aidan N Gomez, Łukasz Kaiser, and Illia Polosukhin, "Attention is all you need," in Advances in neural information processing systems, 2017, pp. 5998–6008.
5. Ali Hatamizadeh, Dong Yang, Holger Roth, and Daguang Xu, "Unetr: Transformers for 3d medical image segmentation," arXiv preprint arXiv:2103.10504, 2021.
6. Alexey Dosovitskiy, Lucas Beyer, Alexander Kolesnikov, Dirk Weissenborn, Xiaohua Zhai, Thomas Unterthiner, Mostafa Dehghani, Matthias Minderer, Georg Heigold, Sylvain Gelly, et al., "An image is worth 16x16 words: Transformers for image recognition at scale," arXiv preprint arXiv:2010.11929, 2020.
7. Simonyan, K. and Zisserman, A., 2014. Very deep convolutional networks for large-scale image recognition. arXiv preprint arXiv:1409.1556.
8. Liu Z, Lin Y, Cao Y, Hu H, Wei Y, Zhang Z, Lin S, Guo B. Swin transformer: Hierarchical vision transformer using shifted windows. arXiv preprint arXiv:210314030 2021.
9. Dosovitskiy A, Beyer L, Kolesnikov A, Weissenborn D, Zhai X, Unterthiner T, Dehghani M, Minderer M, Heigold G, Gelly S. An image is worth 16x16 words: Transformers for image recognition at scale. arXiv preprint arXiv:201011929 2020.
10. Gao P, Jiang Z, You H, Lu P, Hoi SC, Wang X, Li H, editors. Dynamic fusion with intra-and inter-modality attention flow for visual question answering. Proceedings of the IEEE/CVF Conference on Computer Vision and Pattern Recognition; 2019.
11. Liu Z, Ning J, Cao Y, Wei Y, Zhang Z, Lin S, Hu H. Video swin transformer. arXiv preprint arXiv:210613230 2021.
12. Song X, Guo H, Xu X, Chao H, Xu S, Turkbey B, Wood BJ, Wang G, Yan P. Cross-modal Attention for MRI and Ultrasound Volume Registration. arXiv preprint arXiv:210704548 2021.
13. Moreira, I.C., Amaral, I., Domingues, I., Cardoso, A., Cardoso, M.J. and Cardoso, J.S., 2012. Inbreast: toward a full-field digital mammographic database. Academic radiology, 19(2), pp.236-248.
14. Xu X, Wang T, Yang Y, Zuo L, Shen F, Shen HT. Cross-Modal Attention With Semantic Consistence for Image-Text Matching. IEEE Trans Neural Netw Learn Syst 2020;31:5412-25.
15. Visual Lab. A Methodology for Breast Disease Computer-Aided Diagnosis using dynamic thermography. Available Online: http://visual.ic.uff.br/en/proeng (accessed on 11 July 2019).
16. Pereira, J., Santana, M.A., Gomes, J.C., de Freitas Barbosa, V.A., Valença, M.J.S., de Lima, S.M.L. and dos Santos, W.P., 2021. Feature selection based on dialectics to support breast cancer diagnosis using thermographic images. Research on Biomedical Engineering, 37(3), pp.485-506.
17. da Silva, A.L.R., de Santana, M.A., de Lima, C.L., de Andrade, J.F.S., de Souza, T.K.S., de Almeida, M.B.J., da Silva, W.W.A., de Lima, R.D.C.F. and dos Santos, W.P., 2021. Features selection study for breast cancer diagnosis using thermographic images, genetic algorithms, and particle swarm optimization. International Journal of Artificial Intelligence and Machine Learning (IJAIML), 11(2), pp.1-18.

View publication stats

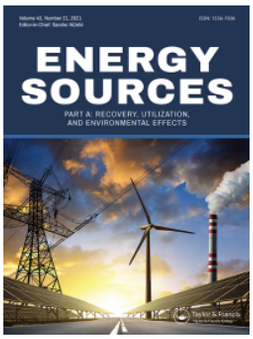

Taylor & Francis
Taylor & Francis Group

Energy Sources, Part A: Recovery, Utilization, and Environmental Effects

ISSN: (Print) (Online) Journal homepage: https://www.tandfonline.com/loi/ueso20

Challenges of implementing industry 4.0 in achieving sustainable development goals: a case of Indian manufacturing organization

Abhishek Sahu, Saurabh Agrawal & Girish Kumar

To cite this article: Abhishek Sahu, Saurabh Agrawal & Girish Kumar (2023) Challenges of implementing industry 4.0 in achieving sustainable development goals: a case of Indian manufacturing organization, Energy Sources, Part A: Recovery, Utilization, and Environmental Effects, 45:3, 8125-8139, DOI: 10.1080/15567036.2023.2226098

To link to this article: https://doi.org/10.1080/15567036.2023.2226098

View supplementary material

Published online: 19 Jun 2023.

Submit your article to this journal

Article views: 65

View related articles

View Crossmark data

Full Terms & Conditions of access and use can be found at
https://www.tandfonline.com/action/journalInformation?journalCode=ueso20

ENERGY SOURCES, PART A: RECOVERY, UTILIZATION, AND ENVIRONMENTAL EFFECTS
2023, VOL. 45, NO. 3, 8125–8139
https://doi.org/10.1080/15567036.2023.2226098

Taylor & Francis
Taylor & Francis Group

Check for updates

Challenges of implementing industry 4.0 in achieving sustainable development goals: a case of Indian manufacturing organization

Abhishek Sahu[a], Saurabh Agrawal[b], and Girish Kumar[a]

[a]Department of Mechanical, Production and Industrial Engineering, Delhi Technological University, Delhi, India; [b]Delhi School of Management, Delhi Technological University, Delhi, India

ABSTRACT

The purpose of this study is to identify the implementation challenges of Industry 4.0 and circular supply chain during a pandemic in order to achieve sustainable development goals. Based on the literature review and discussion with experts, combined challenges of implementing Industry 4.0 for developing a circular supply chain were identified. A combination of ANP and Fuzzy TOPSIS approaches has been adopted for the proposed research as the network model with dependence and feedback improves rankings derived from the alternatives and can make better decisions for optimal challenges. The ANP approach has been utilized to evaluate the weights of the criteria using Super Decisions software 2.10 version for reliability and accuracy of the results, while Fuzzy TOPSIS approach has been used to prioritize the alternatives. A case example of an XYZ barrel manufacturing organization has been selected for the illustration of the proposed research. Four experts from the manufacturing organization were selected to review the preliminary draft of the questionnaire. The main findings are identifying and prioritizing 5 major challenges and 15 criteria for implementing Industry 4.0 technologies in circular supply chain during the pandemic. The results of the study demonstrate that organizational is the major challenge, while sustainable development challenge is the least prioritized. Data security and privacy, technological development and big data and analytics are the essential criteria for implementing Industry 4.0 and circular supply chain principles. The findings of the research may help academicians, researchers, and industrialists in their decision-making to ensure the smooth implementation of Industry 4.0 and to develop a circular supply chain.

ARTICLE HISTORY
Received 31 January 2023
Revised 9 June 2023
Accepted 10 June 2023

KEYWORDS
Sustainable Development Goals; industry 4.0; circular supply chain; analytic network process; Fuzzy TOPSIS

Introduction

In recent years, disruptions triggered by the coronavirus pandemic have generated unprecedented challenges for businesses throughout the world. As a result, manufacturing organizations are confronting unsustainable production and consumption issues, such as lack of availability of raw materials, insufficient supply chain processes, and inadequate implementation of emerging technologies in the present production process. Its impact on the global manufacturing industry includes automobile, aviation, textile, electronics, and food-beverage industry. According to the report of IMF, the impact of a pandemic on the World economy will be worse than the economic crisis of 1929 (Singh et al. 2020). The Ministry of Statistics 2020 declared that the estimated impact of the pandemic on the Indian growth in the fourth quarter of the financial year 2020 had been down to 3.1%. Further, the unplanned lockdown causes a shortage of raw materials, workforce, and distribution logistics, eventually leading to supply chain disruptions in the manufacturing process.

CONTACT Abhishek Sahu er.abhisheksahu2012@gmail.com Department of Mechanical, Production and Industrial Engineering, Delhi Technological University, Delhi, India
Supplemental data for this article can be accessed online at https://doi.org/10.1080/15567036.2023.2226098
© 2023 Taylor & Francis Group, LLC

In India, the socio-economic effect of the pandemic includes an increased unemployment rate, risk to healthcare workers and lower GDPs. These challenges gradually affect manufacturing industries, business environment and entire economies. Consequently, the production rate decreases, and the cost of production increases with each passing day, which produces an unsustainable environment. Further, the lack of implementation of modern technologies and unavailability of essential information related to product development, which increases resource consumption and material wastage. To overcome such manufacturing issues, circular supply chain (CSC) plays an essential character in managing available resources by reducing, recycling, and redesigning the unusual wastage using the application of Industry 4.0 technologies. Further, the implementation of Industry 4.0 and CSC has the potential to achieve circular strategies and sustainable development goals (SDGs). The implementation of Industry 4.0 technologies in CSC provides automation, real-time data exchange, optimal resource management, and a circular business model that handles environmental and managerial disruptions caused by pandemic (Centobelli, Cerchione, and Ertz 2020). Therefore, the current manufacturing system needs to integrate Industry 4.0 with CSC to address unsustainable production and consumption issues. The research also supports the suggestions of Yadav et al. (2020), Tseng et al. (2018), Sahu, Agrawal, and Kumar (2022), Ozkan-Ozen, Kazancoglu, and Kumar (2020), and Kristoffersen et al. (2020), where they have developed a relationship among Industry 4.0, CSC, and sustainable supply chain and proposed the several research positions. The main objective of the work is to identify and prioritize the major challenges faced by the present manufacturing organization during the pandemic and provide the basis for future research directions. In this viewpoint, CSC's major role is to utilize the principle of Industry 4.0-based technologies and improve resource circularity, business processes, and ecological performance at various stages of the supply chain. In addition, XYZ manufacturing organization is selected to establish the proposed research. The present organization was selected since it is the largest manufacturer of Steel Barrels in India. The identified challenges of the present organization will be prioritized using multi-criteria decision marking (MCDM) approaches for achieving sustainability orientation in a resilient and sustainable supply chain. The proposed study attempts to capitalize on analytic network process (ANP) and fuzzy TOPSIS approach. In the previous studies, AHP (Analytic Hierarchy Process), ANP, Delphi, DEMATEL, and Fuzzy TOPSIS approaches are applied individually in Industry 4.0 and CSC problems. However, a combination of ANP and Fuzzy TOPSIS approach has received less attention in the literature. Therefore, the combination of ANP and Fuzzy TOPSIS approaches have been taken in this study for the selection of important challenges of Industry 4.0 and CSC. Moreover, the criteria weights have been calculated using ANP approach, while the alternative challenges of Industry 4.0 and CSC have been calculated using fuzzy TOPSIS approach. Further, Super Decisions software 2.10 version is utilized to check the weights of the criteria for reliability and accuracy of the results. Therefore, it is essential to address the following research questions:

Q1. What are the CSC challenges in the Industry 4.0 implementation?
Q2. How can these challenges be prioritized from the Industry 4.0 and CSC perspective?

The remaining structure of the paper is as follows: Section 2 explores the current literature review on Industry 4.0 and CSC, including implementation challenges. In Section 3, research methodology and the stepwise procedure of ANP and Fuzzy TOPSIS approaches are mentioned. A numerical example of the Indian manufacturing organization along with modeling the problem is provided in Section 4. Section 5 includes the results and discussion, and finally, Section 6 provides conclusions along with the implications and limitations of the present study.

Literature review

The literature review on Industry 4.0 and CSC are described in the following sub-sections.

Industry 4.0 and circular supply chain overview

Digitalization is measured as a principal enabling force of Industry 4.0. Its implication for SDGs has received a lot of consideration from the viewpoints of the triple bottom line, sustainable business models, and the CSC. Yadav et al. (2020) identified core technologies of Industry 4.0, such as Internet of Things, Cyber-Security, Cyber-Physical-Systems, Big Data, and Cloud Computing. These technologies have the potential to reduce energy consumption, resource utilization, and machine utilization to improve sustainable manufacturing operations (Palsodkar, Yadav, and Nagare 2023). On the other hand, CSC proposes a sustainable outcome through its transformation from the traditional linear economy to a circular formation by reforming waste into a recycled product Yadav et al. (2020). It aims to develop an economic eco-system that provides a closed-loop network by reducing and recycling waste products or raw materials. Moreover, the implementation of Industry 4.0 provides the infrastructure and platforms that facilitate CSC approaches, particularly in business and service sectors. Tseng et al. (2018) utilized big data analytics and proposed the cross-industrial networks from the perspective of Industry 4.0 and CSC. Sahu, Agrawal, and Kumar (2023) established the interrelationship between circular economy and value engineering and developed a circular business model that reduces or recycles industrial waste.

Implementation challenges of industry 4.0 and circular supply chain

The combined challenges of Industry 4.0 and CSC are identified from the detailed literature review, which is shown in Table 1. Five major challenges and fifteen criteria are identified in this study. The effect of these challenges and criteria are described comprehensively in Table 1.

Research methodology

The selection of the implementation challenges of Industry 4.0 and CSC is dependent on the various criteria and sub-criteria. Several MCDM approaches, such as AHP, Delphi, DEMATEL, and Fuzzy TOPSIS are available to address such problems (Kumar, Singh, and Dwivedi 2020; Rajput and Singh 2019). If the parameters are independent, TOPSIS and AHP are used, which is not the case in the presented problem. When using the AHP approach, it is assumed that the criteria are independent of one another, which is not feasible in real-life applications. Similarly, ANP has some advantages and disadvantages. According to Saaty (1996), the ANP approach provides a hierarchical relation between criteria and sub-criteria and decision-making with feedback and dependence. A combination of ANP and Fuzzy TOPSIS multi-criteria approaches have been adopted for estimating the weights of the criteria and ranking of the alternatives, respectively. The following research path taken in this study is shown in Figure 1.

Analytic network process

ANP is one of the most commonly used MCDM approaches, which is an extension of AHP. According to Saaty (1996), the ANP approach has replaced hierarchies of AHP approach by the network. Further, it is used to estimate all inner and outer dependence criteria and feedback in decision-making problems. AHP, ANP, DEMATEL, PROMETHEE, and ELECTRE are among the most widely used MCDM methods for Industry 4.0 and CSC challenges. The ANP provides its own set of benefits and has developed excellent results in a variety of disciplines. In the current study, ANP approach has been utilized to estimate the criteria weight of the Industry 4.0 and CSC challenges for selecting the best alternatives. The stepwise procedure of ANP approach by utilizing the geometric mean technique is explained in the following sub-section.

Table 1. Combined challenges of industry 4.0 and CSC in the context of pandemic.

Challenges	Criteria	Descriptions	Authors
Technological (A1)	Technological development (C1)	Lack of IT infrastructure, high initial disposal cost, insufficient network facilities, inadequate recycling technologies, and lack of resources for R&D.	Kristoffersen et al. (2020); Yadav et al. (2020)
	Complexity in collaboration (C2)	Lack of skillset, lack of understanding, and lack of collaboration and data sharing procedure, and limited knowledge about the Industry 4.0 technologies.	Rajput and Singh (2019); Sahu, Agrawal, and Kumar (2022)
	Data security and privacy (C3)	Data transparency, data theft and lack of data management issues are present in the existing system.	Ozkan-Ozen, Kazancoglu, and Kumar (2020); Sahu, Agrawal, and Kumar (2022)
Operational (A2)	Data management (C4)	Lack of data analysis, data mining and cleansing, data and information sharing, lack of effective reverse logistic system, quality compromise of the secondary material and product technology improvement.	Kumar, Singh, and Dwivedi (2020); Tesch da Silva et al. (2020)
	Big data and analytics (C5)	Data integration complexity, higher data growth, lack of data analytics, insufficient and data acquisition.	Singh et al. (2021); Agrawal, Sahu, and Kumar (2022)
	Strategic development (C6)	Lack of operational strategies for a sustainable CSC, traditional rules and regulations, poor leadership and management, poor R&D on Industry 4.0 and CSC implementation, and lack of adequate government planning and support.	Schneider (2018); Luthra and Mangla (2018); Ozkan-Ozen, Kazancoglu, and Kumar (2020)
Organizational (A3)	Employment disruption (C7)	Unemployment and fear of disruption to the existing job by replacing the workforce with machines.	Rajput and Singh (2019); Ozkan-Ozen, Kazancoglu, and Kumar (2020)
	Collaborative model (C8)	Poor organizational culture, lack of collaboration and coordination with supply chain partners, lack of human and machine interaction, and lack of social and ethical policies.	Rajput and Singh (2019); Sahu, Agrawal, and Kumar (2022)
	Decision-making ability (C9)	The complex and uncertain nature of CSC needs high decision-making ability to integrate with a smart production system that manages resources sustainably and self-determination, social, and skilled workforce capabilities.	Luthra and Mangla (2018); Yadav et al. (2020)
Managerial (A4)	Management support (C10)	Anticipating market demand, lack of top management and stakeholder support, conservative attitude of existing workers, lack of availability of skilled workers, and lack of proficiency to lead digitalization initiatives.	Kumar, Singh, and Dwivedi (2020); Sahu, Agrawal, and Kumar (2022); Ozkan-Ozen, Kazancoglu, and Kumar (2020)
	Analysis and strategy (C11)	Lack of planning and implementation, ineffective take-back mechanism, lack of information management system, lack of risk management infrastructure, lack of availability of recycling/reuse products and deficiency of circular design strategies.	Schneider (2018); Centobelli, Cerchione, and Ertz (2020); Sahu, Agrawal, and Kumar (2022)
	Human resource (C12)	Lack of competencies, lack of skilled workers and safety facilities for sustainable operation, lack of attention towards legal and ethical issues.	Schneider (2018); Ozkan-Ozen, Kazancoglu, and Kumar (2020)
Sustainable development (A5)	Social (C13)	Minimal involvement of top management authorities and competitive pressure towards the implementation of SDGs leads to failures and non-consideration of social implications.	Luthra and Mangla (2018); Kumar, Singh, and Dwivedi (2020)
	Economic (C14)	Lack of financial feasibility, lack of economic inducement, and fear of low economic returns.	Rajput and Singh (2019); Singh et al. (2020)
	Environmental (C15)	Lack of ecological protocols and massive automation produce adverse impacts on the environment, which include huge power expenditure, depletion of natural resources, CO2 emission, and e-waste generation.	Palsodkar, Yadav, and Nagare (2023); Sahu, Agrawal, and Kumar (2023)

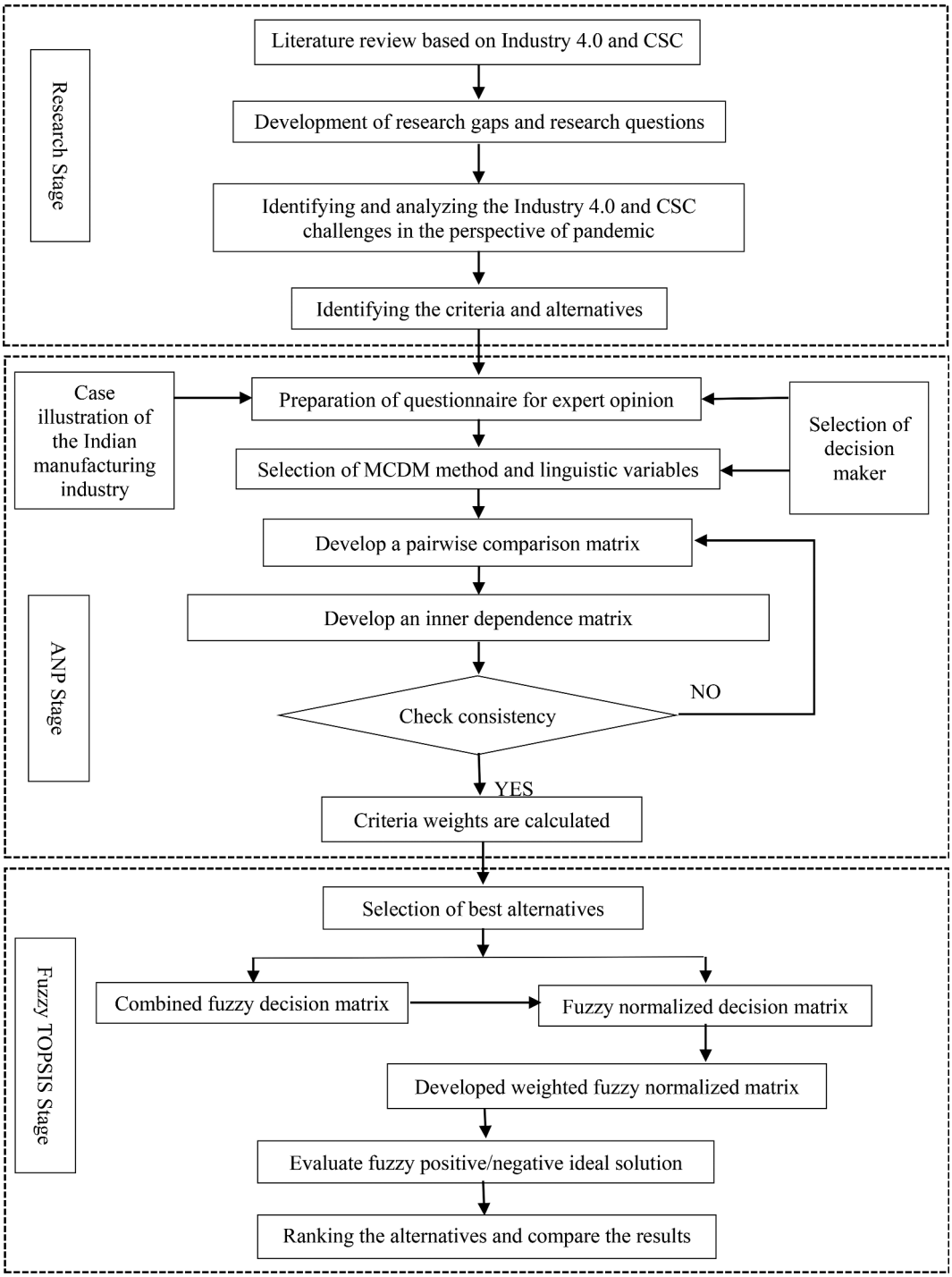

Figure 1. Research path of the present study.

Sub-step 1. Construct a model and structure the problem.
Sub-step 2. Develop a pairwise comparison matrix (A) and local priority vector. The pairwise comparison matrix is constructed using a nine-point preference scale, as shown in Table A.1 (Appendix A). Each element aij (i, j = 1, 2,. . ., n) in the judgment matrix A, is the proportion of weights of the criteria as presented below:

$$A = \begin{bmatrix} a_{11} & \cdots & a_{12} & \ldots & a_{1n} \\ \vdots & & \vdots & & \vdots \\ a_{21} & \cdots & a_{22} & \ldots & a_{2n} \\ \vdots & & \vdots & & \vdots \\ a_{31} & \cdots & a_{32} & \ldots & a_{3n} \end{bmatrix}, \quad a_i i = 1, a_i j = \frac{1}{a_{ij}}, a_i j \neq 0 \tag{1}$$

Sub-step 3. The weights of the criteria are estimated based on the limited supermatrix using Super Decision software. In the last step, obtained criteria weights are approved by a group of experts.

Sub-step 4. Check the consistency through a pairwise comparison matrix. In case of triangular fuzzy number, the consistency check through the largest Eigenvalue (λ_{max}).
The CR value is calculated by applying the following relation:

$$\text{Consistency ratio(CR)} = \frac{\text{CI}}{\text{RI corresponding to n}} \tag{2}$$

Where, CI is the consistency index that can be estimated through the following relation:

$$\text{Consistency index(CI)} = \frac{(\lambda_{\text{ max}} - \text{n})}{(\text{n} - 1)} \tag{3}$$

Further, random index (RI) may be obtained through Table A.2 (Appendix A).
Sub-step 5. Selection of important alternatives.

Fuzzy TOPSIS

The TOPSIS approach was initially introduced by Chen and Hwang (1992). This approach is founded on the notion that the selected alternative should have the shortest geometric distance from the positive ideal solution that minimizes the cost and maximizes the benefit and extreme distance from the negative ideal solution. Moreover, the existing TOPSIS approach implies that criteria weights and rankings are in a crisp number that is not adequate in the real-time situation. To overcome these situations, the fuzzy set theory was introduced (Xu and Chen 2007). Zadeh (1976) introduced the fuzzy set theory into the TOPSIS for dealing with the uncertainty and vagueness of the human decisions. In the Fuzzy TOPSIS approach, a five-point linguistic scale was used to rank the alternatives and criteria weights, sub-criteria, and alternatives. The following sub-steps are used in the Fuzzy TOPSIS method.

Sub-step 1: Choose the best alternatives for identifying the decision matrix using linguistic terms based on the expert respondent. The five-point scale has linguistic terms as shown in Table A.3 (Appendix A). These linguistic terms mentioned each criterion (C) associated with each alternative (A) using Eq. (4).
C_1 A_1 A_n

$$D = \begin{bmatrix} X_{11} & \cdots & X_{1n} \\ \vdots & \ddots & \vdots \\ X_{m1} & \cdots & X_{mn} \end{bmatrix} \tag{4}$$

C_m

Sub-step 2: Evaluate combined fuzzy decision matrix x_{ij} through Eq. (5), Eq. (6), and Eq. (7).

$x_{ij} = (a_{ij}, b_{ij}, c_{ij})$

Where,

$$aij = \frac{\min}{k}\left\{a_{ij}^{k}\right\} \tag{5}$$

$$b_{ij} = \frac{1}{k}\sum\nolimits_{k=1}^{k}\frac{b_{ij}{}^{k}}{k} \tag{6}$$

$$Cij \;=\; \max\{C_{ij}\}, \tag{7}$$

where, k is the decision-maker number and x_{ij} is fuzzy opinion.

Sub-step 3: Constructed fuzzy normalized decision matrix $[r_{ij}]_{m\times n}$ through vector normalization technique for the beneficial criteria (see Eq. 8).

$$r_{ij} = \frac{x_{ij}}{\left(\sum_{i=1}^{m} x_{ij}^{2}\right)^{1/2}}, \tag{8}$$

where, i = 1, . . . , m and j = 1, . . . , n.

Sub-step 4: Evaluate weighted fuzzy normalized decision matrix $[v_{ij}]_{m\times n}$ through Eq. (9).

$$\widetilde{Vij} = \widetilde{rij} \;\times\; \widetilde{w}j, i \in [1,m] \text{and} j \;\in\; [1, n] \tag{9}$$

where, wj (j∈n) is the weight of j^{th} criteria or attribute.

Sub-step 5: Evaluation of the fuzzy positive ideal solution (FPIS, A^+) and fuzzy negative ideal solution (FNIS, A^-).

$$A^{+} = \left\{\widetilde{V_1^*}, \widetilde{V_2^*}, \ldots . \widetilde{V_n^*}\right\}, \text{where} \widetilde{V_j^*} = \text{maxi}\left\{V_{ij3}\right\} \tag{10}$$

$$A^{-} = \left\{\widetilde{V_1^-}, \widetilde{V_2^-}, \ldots . \widetilde{V_n^-}\right\}, where \widetilde{V_j^-} = max_i\left\{V_{ij1}\right\} \tag{11}$$

Sub-step 6: Evaluation of the sum of distance (D_i^+ and D_i^-) from a positive and negative ideal solution, respectively, for each alternative through the vertex method (see Eq. (12) and Eq. (13)).

$$Di+ = \sum\nolimits_{j=1}^{n}(Vij - Vij*), \;\; i \;\in\; [1, m] \tag{12}$$

$$Di- = \sum\nolimits_{j=1}^{n}(Vij - Vij*), \;\; i \;\in\; [1, m] \tag{13}$$

The distance between two triangular fuzzy numbers is evaluated through vector algebra $d(\widetilde{a},\widetilde{b})$ defined by Eq. (14). Where $a = (a_1, a_2, a_3)$ and $b = (b_1, b_2, b_3)$.

$$d\left(\tilde{a}, \tilde{b}\right) = \sqrt{\frac{1}{3}\left[(a_1 - a_2)^2 + (b_1 - b_2)^2 + \;(c_1 - c_2)^2\right]} \tag{14}$$

Sub-step 7: Evaluate the value of closeness coefficient (CC_i) of each alternative to the ideal solution. The CC_i value is evaluated using Eq. (15) to evaluate the rank of each alternative. Further, the CCi value with respect to A^+ is expressed as: Closeness coefficient

$$(CCi) = \frac{D_i^-}{D_i^- + D_i^+}, \; i = 1, 2, \ldots, m \tag{15}$$

Sub-step 8: Ranking the alternatives based on the highest value of CCi.

Case illustration

A barrel manufacturing organization XYZ has been selected to illustrate the proposed methodology. The present organization is selected because of the largest manufacturer of steel barrels in developing economies like India. XYZ is a market leader in steel barrels manufacturing with a total 45% market camp. The organization has an annual turnover is more than 500 million INR. The organization has a primary objective to become a leading industry in Asia and is placed among the top ten organizations in the global market for manufacturing steel barrels. Moreover, organization produces a huge amount of waste at the end of product's life. The organization has primarily centered on lean manufacturing, continuous improvement, green culture, and waste reduction. Currently, the organization faces major challenges in the execution of Industry 4.0 and CSC in its manufacturing division. Therefore, the study identifies and analyzes the most influencing challenges in the steel barrels manufacturing organization to implement Industry 4.0 applications for the continuing and large-scale waste retrieval of barrel scrap. Four experts from the organization were selected to review the preliminary draft of questionnaire. The first decision-maker is an operations manager who has 10 years of experience. The second decision-maker is a production engineer with 12 years of experience, and the third decision-maker is a supply chain manager who has 15 years of experience. Finally, the fourth decision-maker is a plant head of the selected organization having 16 years of industrial experience. These experts were asked to discuss the multiple objectives and decisions that chose the critical challenge in this research. The questionnaire was developed to evaluate the essential criteria. The criteria were analyzed and rated in decision-making processes. The following steps were taken to develop an Industry 4.0 and CSC decision-making model.

Modeling the problem as a hierarchy

The main purpose of this section is to identify the research objectives, including evaluation criteria and alternatives. Therefore, objectives are placed at the upper level, criteria are placed at the middle level, and alternatives are placed at the bottom level. Based on expert judgments, it was concluded that these five alternative challenges do not vary in any of the fifteen criteria. All five challenges appeared to satisfy the standards of the nine criteria stated for the important Industry 4.0 and CSC objectives. The remaining six criteria looked to differentiate for the alternative Industry 4.0 and CSC challenges; the following six criteria are: C1, C3, C5, C9, C10, and C14. Only these six criteria are employed in the calculation, and a decision hierarchy and network were developed accordingly. A decision network is organized with the identified alternative of Industry 4.0 and CSC and criteria are provided. A hierarchy level for the selection of important challenges is shown in Figure 2. Further, interdependence relationship among selected criteria is shown in Figure 3.

Development of pairwise comparison matrices

A nine-point scale of preference is used to explain the relative importance of criteria to develop a pairwise comparison matrix. The opinions of expert panels are collected using the scale provided in Table A.1 (Appendix A). A group of experts having vast experience in production, supply chain and R&D were requested to compare each of the criteria with others and then compute a combined decision matrix. A final pairwise comparison matrix with a consensus is obtained by estimating geometric mean values found from individual estimations. Based on the final comparison matrix, criteria weights are estimated. The obtained criteria weights are approved by a group of experts.

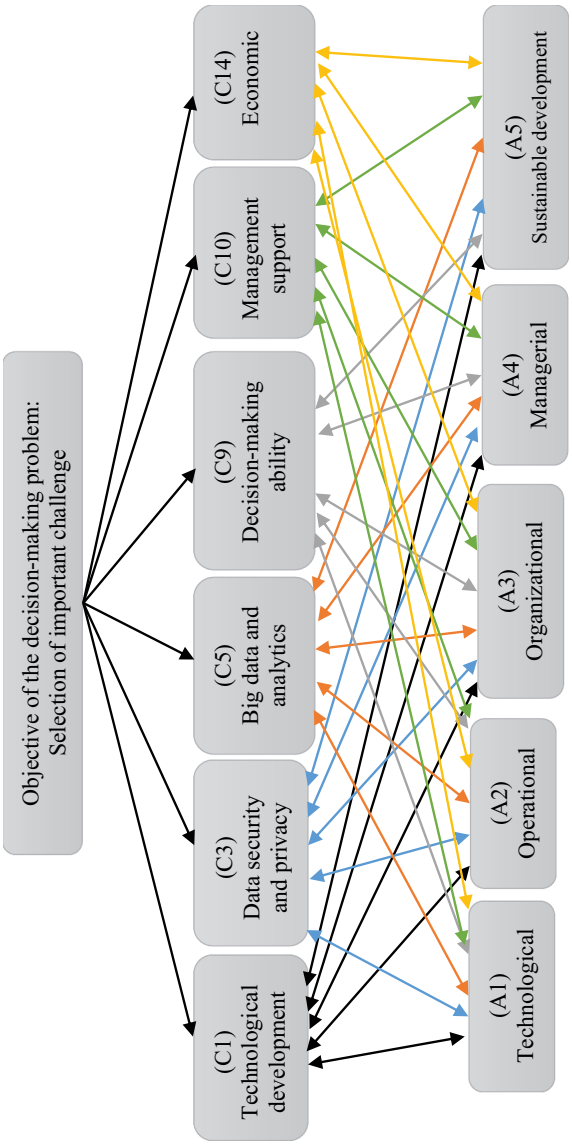

Figure 2. A hierarchy level for the selection of important challenges.

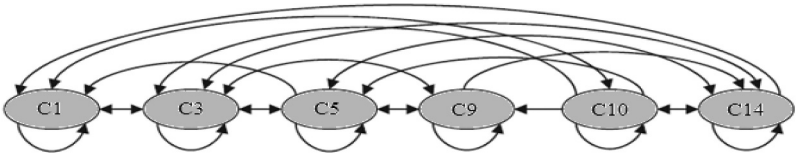

Figure 3. Inner dependence relationship among selected criteria.

Estimations of the triangular fuzzy weights

In this step, a fuzzy linguistic scale is utilized to estimate alternative challenges. Table A.3 (Appendix A) shows a triangular fuzzy linguistic scale. The opinions of expert panels are entered using linguistic variables. Therefore, outcomes will be more sophisticated than crisp judgment. The fuzzy decision matrix is constructed using (l, m, n) values of each decision-maker.

Tested the consistency in the pairwise comparison matrix

The value of RI is taken from Table A.2 (Appendix A), that is, 1.59 (no. of criteria $n = 15$), and using RI value, CI value is calculated. The value of consistency ratio is calculated which is less than 0.1.

Evaluate the weight of the criteria

After developing the decision hierarchy, criteria weights are estimated using the ANP approach. In this stage, expert's opinion is collected to form the pairwise matrix in ANP through a nine-point scale of preference. Further, geometric mean values are calculated to get the pairwise matrix in ANP. Based on expert opinion, inner dependence relationship among selected criteria is shown in Figure 3. It is found that some inner dependence relationship is considered in weighting of criteria. For example, C1 has an inner dependence relationship with C1, C3, and C10. The final inner dependence matrix of evaluation criteria is shown in Table A.4 (Appendix A). Further, weights of criteria found on limited supermatrix from the Super Decision Software in ANP are shown in Table A.5 (Appendix A). The C3, C1, C5, C9, and C14 are estimated as the five most significant criteria in the selection of Industry 4.0 and CSC challenge by ANP. It is found that C3 has a maximum weight (0.301) among all considered criteria followed by C1, C5, C9, C14, and C10.

Estimation of alternatives and decide the final rank using Fuzzy TOPSIS

Four experts with vast experience in the industry as well as R&D are used to generate a decision matrix for alternatives. These experts were used to rate the importance of the aforementioned Industry 4.0 and CSC challenges on a five-point scale. Further, with the help of a questionnaire, these experts compare the Industry 4.0 and CSC challenges on a five-point linguistic scale presented in Table A.3 (Appendix A). Additionally, we evaluated a combined fuzzy decision matrix (x_{ij}) using Eqs. (5), (6), and (7), which are presented in Table A.6 (Appendix A). A fuzzy normalized matrix is evaluated using the vector normalization method (see eq. 8) for the beneficial criteria, shown in Table 2. The weighted normalized matrix is estimated using Eqs. (9), which is presented in Table 3. Equations (10) and (11) are used to estimate fuzzy positive and negative solutions, which are also shown in Table 3. The sum of distance (D_i^+ and D_i^-) from a positive and negative ideal solution for each alternative is estimated through the vertex technique (see Eqs. (12) and Eq. (13)) and is shown in Table 4. The closeness coefficient value is estimated using Eqs. (15), which is also shown in Table 4. The maximum value of closeness coefficient indicates a superior ranking. Therefore, alternatives are ranked in order of organizational (0.575) > operational (0.526) > technological (0.500) > managerial (0.470) and sustainable development (0.457).

Table 2. Fuzzy normalized matrix using vector normalization technique.

	A1	A2	A3	A4	A5
C1	(0.416, 0.589, 0.693)	(0.371, 0.557, 0.743)	(0.433, 0.541, 0.721)	(0.267, 0.535, 0.802)	(0.424, 0.566, 0.707)
C3	(0.424, 0.566, 0.707)	(0.324, 0.487, 0.811)	(0.277, 0.484, 0.830)	(0.381, 0.524, 0.762)	(0.258, 0.580, 0.773)
C5	(0.085, 0.513, 0.854)	(0.424, 0.566, 0.707)	(0.371, 0.557, 0.743)	(0.424, 0.566, 0.707)	(0.362, 0.588, 0.724)
C9	(0.267, 0.535, 0.802)	(0.371, 0.557, 0.743)	(0.213, 0.479, 0.852)	(0.162, 0.566, 0.808)	(0.381, 0.524, 0.762)
C10	(0.218, 0.436, 0.873)	(0.267, 0.535, 0.802)	(0.207, 0.518, 0.830)	(0.416, 0.589, 0.693)	(0.424, 0.566, 0.707)
C14	(0.305, 0.571, 0.762)	(0.416, 0.589, 0.693)	(0.424, 0.566, 0.707)	(0.424, 0.566, 0.707)	(0.424, 0.566, 0.707)

Table 3. Weighted fuzzy normalized decision matrix.

	A1	A2	A3	A4	A5	(FPIS, A*)	(FNIS, A-)
C1	(0.086, 0.121, 0.143)	(0.076, 0.115, 0.153)	(0.089, 0.111, 0.149)	(0.055, 0.110, 0.165)	(0.087, 0.117, 0.146)	(0.055, 0.110, 0.165)	(0.055, 0.110, 0.165)
C3	(0.128, 0.170, 0.213)	(0.098, 0.147, 0.244)	(0.083, 0.146, 0.250)	(0.115, 0.158, 0.229)	(0.078, 0.175, 0.233)	(0.083, 0.146, 0.250)	(0.078, 0.175, 0.233)
C5	(0.016, 0.095, 0.158)	(0.078, 0.105, 0.131)	(0.069, 0.103, 0.137)	(0.078, 0.105, 0.131)	(0.067, 0.109, 0.134)	(0.016, 0.095, 0.158)	(0.016, 0.095, 0.158)
C9	(0.035, 0.071, 0.106)	(0.049, 0.074, 0.098)	(0.028, 0.063, 0.112)	(0.021, 0.075, 0.107)	(0.050, 0.069, 0.101)	(0.028, 0.063, 0.112)	(0.021, 0.075, 0.107)
C10	(0.017, 0.033, 0.066)	(0.020, 0.041, 0.061)	(0.016, 0.039, 0.063)	(0.032, 0.045, 0.053)	(0.032, 0.043, 0.054)	(0.017, 0.033, 0.066)	(0.016, 0.039, 0.063)
C14	(0.030, 0.057, 0.076)	(0.042, 0.059, 0.069)	(0.042, 0.057, 0.071)	(0.042, 0.057, 0.071)	(0.042, 0.057, 0.071)	(0.030, 0.057, 0.076)	(0.030, 0.057, 0.076)

Table 4. Sum of the distances to the ideal solution and final results.

Alternatives	D_i^+	D_i^-	CC_i	Ranking position
A1	0.112	0.112	0.5	3rd
A2	0.092	0.102	0.526	2nd
A3	0.065	0.088	0.575	1st
A4	0.09	0.08	0.47	4th
A5	0.107	0.09	0.457	5th

Results and discussion

The main purpose of the study is to identify the implementation challenges of Industry 4.0 and CSC on sustainable development in the Indian manufacturing organization. The proposed findings help to obtain a more comprehensive understanding of the outcome of Industry 4.0 technologies on CSC for long-term growth. The combination of ANP and Fuzzy TOPSIS approaches has prioritized the current manufacturing challenges of the pandemic. The ANP approach has been utilized to find the relative weights of criteria to address the given organization problem. Further, Fuzzy TOPSIS approach has been utilized to prioritize alternative challenges. To prioritize the alternatives of Industry 4.0 and CSC, five challenging factors were identified and considered in this study. These factors are technological, operational, organizational, managerial, and sustainable development. Additionally, these factors were prioritized on the basis of beneficial criteria.

The study analyses that "Data security and privacy" (C3) and "Technological development" (C1) acquired the highest weightage criteria. Data security and privacy are found to be the most important criteria that highlight data transparency and privacy issues. It may be an important aspect to protecting databases and crucial product design or information from unauthorized access and cyberattacks. Consequently, the manufacturing organization should focus more on data security and privacy compared to other criteria. Technological development is the second important criteria found that includes insufficient development of sensor technology, modern IT infrastructure and improper communication and network facilities that may be used to monitor and predict the product consumption pattern. Further, the use of latest technologies, such as IoT, RFID, and EDI in CSC may be

useful to collect the waste product information through real-time product tracking and identify failures and errors in the existing supply chain processes. Moreover, the initial cost of adopting these technologies in present Indian manufacturing industries is challenging, however these technologies have capabilities to increase the efficiency and rate of the production process (Kumar, Singh, and Dwivedi 2020). The contemporary work reveals that "Organizational (A3)" is the highest-ranked challenge while implementing Industry 4.0 technologies on CSC during the pandemic. Moreover, findings reveal that "Operational (A2)" and "Technological (A1)" challenges have ranked in 2nd and 3rd position, respectively. The further challenges with the highest priority are "Managerial (A4)" and "Sustainable development (A5)," challenges that manufacturing industries should initially implement. Luthra and Mangla (2018) identified that organizational challenge (A3) is one of the important aspects in implementing the sustainable development of supply chains within Industry 4.0 in the Indian manufacturing organization. Moreover, sophisticated and vagueness environment of CSC needs a high decision-making strategy and a smart manufacturing system that manages resources sustainably. The organizational dimension has the capability to develop a more resilient supply chain and decision-making strategies to address future challenges without disrupting SDGs. "Operational (A2)" challenge obtains the next important priority level. Operational challenges consist of many factors, including data and information sharing, lack of data analytics in the supply chain, and lack of adequate government planning and support for implementing Industry 4.0 and a sustainable environment. "Technological challenge (A1)" is the next important aspect of present manufacturing. The effect of technological challenges consists of many factors, including lack of IT infrastructure and internet facilities, lack of data sharing protocols and cloud network issues, and lack of transparency and privacy. The technological challenge is concerned with technology itself. It includes both internal and external technology in the organization, which affects the overall production rate. In the present Indian manufacturing industry, the technological challenge plays an important role in developing circular strategies and sustainable development. It includes the challenges of lack of information about the latest technology and automation, smart manufacturing systems, sourcing and retaining IT talent, and lack of capital for R&D. According to Kumar, Singh, and Dwivedi (2020), Indian industrial organizations need to be aware of the financial benefits of IoT to effectively implement Industry 4.0. It can be understood as amongst the most promising technologies with massive potential implications. "Managerial (A4)" challenge acquires the subsequent level of the priority list. Schneider (2018) suggested that management support provides the decision-making support and strategic transformation path for developing a new business model. The advancement of the present manufacturing industry may cause unemployment and fear of disruption from the existing jobs. Further, a lack of collaboration with supply chain partners and human-machine interaction may cause a delay in production and breakdown due to the unavailability of modern machine parts and maintenance skills. "Sustainable development (A5)" is considered the last most important challenge of the current manufacturing industries. In the present condition, sustainable development plays a substantial character in strengthening the CSC. It fulfills the various objectives of the sustainable supply chain. Yadav et al. (2020) suggested that sustainable development is getting significant in the Indian manufacturing sectors, as there are growing considerations from stakeholders for resource consumption and reducing environmental degradation. The present study considers the manufacturing industry as the most important source of employment in India. The developing economies like India in which a total of 16% contributions of the GDP is from the manufacturing sector (Kumar, Singh, and Dwivedi 2020). The literature review reveals that very limited studies have considered the application of Industry 4.0 in CSC implementation during the pandemic. According to Sahu, Agrawal, and Kumar (2023), organizations must consider socio-economic, environmental, legal, and human rights-related steps while developing their strategies for sustainable development. Additionally, a sustainable supply chain mitigates risks and uncertainties caused by the pandemic, such as bottlenecks in the logistics process restricting the information flow, capital flow, and visibility of the production. Consequently, business stability and distribution process improve, which can reduce production and delivery delays and costs.

Conclusions and future directions in field

The contemporary study has identified and analyzed the effect of Industry 4.0 technologies on CSC from a COVID-19 perspective. The pandemic considerably affects the global trade, including manufacturing sectors of several developed and developing economies. Since most trade routes are disrupted or redirected due to this, the logistic process is directly affected by the supply and demand of the raw material. Therefore, it is necessary to adopt a sustainable and resilient logistic system that can resolve the indeterminate corporate environment of COVID-19 pandemic. The application of Industry 4.0 technologies has the capability to develop a decentralized manufacturing system. The study has analyzed the perception of a barrel manufacturing industry regarding the effect of Industry 4.0 technologies on CSC from the SDGs viewpoint. In this study, two research questions were asked: To answer the first research question (Q1), five challenges and 15 criteria that affected such challenges were identified from the expert opinion and literature review. For the second research question (Q2), a combined ANP and Fuzzy TOPSIS approaches was used to prioritize these challenges. The study shows that data security and privacy, technological development, and big data analytics are essential criteria while implementing Industry 4.0 and CSC perceptions. Furthermore, organizational is the highest-ranked challenge in the considered organization, followed by operational, technological, managerial, and sustainable development, which XYZ manufacturing organization should initially resolve. The paper provides significance of Industry 4.0 for the sustainable performance of CSC and makes the following contributions.

- The article discusses a statistical model and numerical findings to better understand the pandemic effect and formulate resilient and sustainable supply chain strategies. In such circumstances, managers and industrialists need to consider the sustainable development perspective in manufacturing industries while adopting the modern technologies of Industry 4.0 and CSC.
- In the proposed methodology, ANP Fuzzy-TOPSIS has been utilized, which provides a realistic and comprehensive understanding of the current challenges in the implementation of Industry 4.0 and CSC.
- The major challenges identified in this case study are focused on sustainable development, which provides direction to the organizations for alternative selection according to their managerial requirements.
- The XYZ barrel manufacturing organization has made significant contributions to the economic growth of developing countries, while it is limited because of low return on investment, high operational budget, and unbalanced cash flow. Organizations should pay more attention to the circular strategies and lean manufacturing to achieve SDGs.

The present study has a couple of limitations. The number of experts considered in the analysis is limited. Therefore, when the vaccination for COVID-19 will completed, more responses from different industries could be collected. Further, this study has considered only the Indian manufacturing sector. As time passes, these analyses may consider the other sector such as healthcare, automobile, tyre recycling, food processing and textiles industries, and so on. The authors have considered five challenges and 15 criteria for implementing Industry 4.0 technologies during the pandemic to develop a CSC. Future researchers could explore other factors affecting this implementation, such as legal and ethical effects, human-machine collaboration, and sustainable effects, and so on. In addition, the identified challenges can be investigated further in the future research to determine their causal and dependent relations. The present study has utilized combined ANP and Fuzzy TOPSIS approaches; as time passes, future research could be compared to these approaches with other MCDM approaches, which may suggest the best method to consider these factors. In the future research, sensitivity analysis may also be conducted. Finally, organizations must design and develop circular business models to deal with managerial and environmental disruptions due to the pandemic using Industry 4.0 applications.

Disclosure statement

No potential conflict of interest was reported by the author(s).

Notes on contributors

Abhishek Sahu is currently a research scholar in Delhi Technological University in the Department of Mechanical Engineering.

Saurabh Agrawal is an Associate Professor in Delhi School of Management at Delhi Technological University, Delhi.

Girish Kumar is a Processor in the Department of Mechanical Engineering at Delhi Technological University.

ORCID

Abhishek Sahu http://orcid.org/0000-0001-6481-6728

References

Agrawal, S., A. Sahu, and G. Kumar. 2022. A conceptual framework for the implementation of Industry 4.0 in legal informatics. *Sustainable Computing: Informatics and Systems* 33:100650. doi:10.1016/j.suscom.2021.100650.

Centobelli, P., R. Cerchione, and M. Ertz. 2020. Managing supply chain resilience to pursue business and environmental strategies. *Business Strategy and the Environment* 29 (3):1215–46. doi:10.1002/bse.2428.

Chen, S. J., and C. L. Hwang. 1992. *Fuzzy multiple attribute decision making methods*, 289–486. Berlin: Springer Berlin Heidelberg. doi:10.1007/978-3-642-46768-4_5.

Kristoffersen, E., F. Blomsma, P. Mikalef, and J. Li. 2020. The smart circular economy: A digital-enabled circular strategies framework for manufacturing companies. *Journal of Business Research* 120:241–61. doi:10.1016/j.jbusres.2020.07.044.

Kumar, R., R. K. Singh, and Y. K. Dwivedi. 2020. Application of industry 4.0 technologies in SMEs for ethical and sustainable operations: Analysis of challenges. *Journal of Cleaner Production* 275:124063. doi:10.1016/j.jclepro.2020.124063.

Luthra, S., and S. K. Mangla. 2018. Evaluating challenges to Industry 4.0 initiatives for supply chain sustainability in emerging economies. *Process Safety and Environmental Protection* 117:168–79. doi:10.1016/j.psep.2018.04.018.

Ozkan-Ozen, Y. D., Y. Kazancoglu, and M. S. Kumar. 2020. Synchronized barriers for circular supply chains in industry 3.5/industry 4.0 transition for sustainable resource management. *Resources Conservation & Recycling* 161:104986. doi:10.1016/j.resconrec.2020.104986.

Palsodkar, M., G. Yadav, and M. R. Nagare. 2023. Integrating Industry 4.0 and agile new product development practices to evaluate the penetration of sustainable development goals in manufacturing industries. *Journal of Engineering, Design & Technology*. doi:10.1108/JEDT-02-2022-0101.

Rajput, S., and S. P. Singh. 2019. Industry 4.0–challenges to implement circular economy. *Benchmarking: An International Journal* 28 (5):1717–39. doi:10.1108/BIJ-12-2018-0430.

Saaty, T. L. 1996. Decision making with dependence and feedback: The analytic network process. RWS publications 4922.

Sahu, A., S. Agrawal, and G. Kumar. 2022. Integrating Industry 4.0 and circular economy: A review. *Journal of Enterprise Information Management* 35 (3):885–917. doi:10.1108/JEIM-11-2020-0465.

Sahu, A., S. Agrawal, and G. Kumar. 2023. Triple bottom line performance of manufacturing Industry: A value engineering approach. *Sustainable Energy Technologies and Assessments* 56:103029. doi:10.1016/j.seta.2023.103029.

Schneider, P. 2018. Managerial challenges of Industry 4.0: An empirically backed research agenda for a nascent field. *Review of Managerial Science* 12 (3):803–48. doi:10.1007/s11846-018-0283-2.

Singh, R. K., S. Agrawal, A. Sahu, and Y. Kazancoglu. 2021. Strategic issues of big data analytics applications for managing health-care sector: A systematic literature review and future research agenda. *The TQM Journal* 35 (1):261–91. doi:10.1108/TQM-02-2021-0051.

Singh, S., R. Kumar, R. Panchal, and M. K. Tiwari. 2020. Impact of COVID-19 on logistics systems and disruptions in food supply chain. *International Journal of Production Research* 59 (7):1993–2008. doi:10.1080/00207543.2020.1792000.

Tesch da Silva, F. S., C. A. da Costa, C. C. D. Paredes, and R. da Rosa Righi. 2020. Looking at energy through the lens of Industry 4.0: A systematic literature review of concerns and challenges. *Computers & Industrial Engineering* 143:106426. doi:10.1016/j.cie.2020.106426.

Tseng, M., R. R. Tan, A. S. F. Chiu, C. Chien, and T. Chi. 2018. Circular economy meets industry 4.0: Can big data drive industrial symbiosis? *Resources, Conservation and Recycling* 131:146–47. doi:10.1016/j.resconrec.2017.12.028.

Xu, Z. S., and J. Chen. 2007. An interactive method for fuzzy multiple attribute group decision making. *Information Sciences* 177 (1):248–63. doi:10.1016/j.ins.2006.03.001.

Yadav, G., A. Kumar, S. Luthra, J. A. Garza-Reyes, V. Kumar, and L. Batista. 2020. A framework to achieve sustainability in manufacturing organisations of developing economies using industry 4.0 technologies' enablers. *Computers in Industry* 122:103280. doi:10.1016/j.compind.2020.103280.

Yadav, G., S. Luthra, S. K. Jakhar, S. K. Mangla, and D. P. Rai. 2020. A framework to overcome sustainable supply chain challenges through solution measures of industry 4.0 and circular economy: An automotive case. *Journal of Cleaner Production* 254:120112. doi:10.1016/j.jclepro.2020.120112.

Zadeh, L. A. 1976. A fuzzy-algorithmic approach to the definition of complex or imprecise concepts. *International Journal of Man-Machine Studies* 8 (3):249–91. doi:10.1016/S0020-7373(76)80001-6.

Challenges, Impact and Integration of Machine Learning and Blockchain Technology in The Smart Healthcare Developments

Dr. Amiya Kumar Sahoo
Associate Professor, Department of Computer Science & Engineering, Aryan Institute of Engineering and Technology, Bhubaneswar

Oluwadare Joshua OYEBODE
Civil and Environmental Engineering, Afe Babalola University Ado-Ekiti, Ekiti State, Nigeria

Kishor Kumar
M.Sc Applied Mathematics, Department of Applied Mathematics, Delhi Technological University, Delhi.

Dr Shakti Bhushan
Department of Pharmacy Research officer, Central Ayurveda Research Institute Kolkata

Manjul Singla
Assistant Professor, Gulzar Group of Institutions, Khanna (Ludhiana), Punjab

Amanpreet Kaur
Assistant Professor, Gulzar Group of Institutes, Khanna, Punjab

A Kakoli Rao

Lloyd Institute of Engineering and Technology, Greater Noida, India

Abstract

Over the past ten years, the growth of blockchain technology has been significant. Given as the basis for cryptographic forms of money like Bitcoin, it quickly found use in other fields thanks to its security and protection features. In the healthcare industry, blockchain has been used for a variety of tasks, including secure data logging, trades, and maintenance via smart contracts. To combine the greatest features of the two technological developments, incredible work has been done to make blockchain smart by integrating computerized reasoning (man-made intelligence). Undoubtedly one of the most important revelations and inventive developments that is significantly influencing the professional present is blockchain technology. Blockchain technology is actively pushing for change and disruption. This study aims to investigate the application of blockchain technology in smart healthcare, lay out a

progressive hypothetical structure for smart healthcare, determine the influence of blockchain on smart healthcare, and then create a better application setup for smart healthcare under the blockchain based on partner hypothesis. However, such an advanced hypothetical system should consider not just the fundamental traits and the connections between various viewpoints and attributes, but also the various partners' functions.

Keywords: *Machine Learning, Blockchain, Technology, Smart Healthcare, Developments, Integration*

1. Introduction

Modern technology is driven by frameworks based on machine learning (ML) and computerized reasoning (artificial intelligence). Increased research and testing are being done in several domains of artificial intelligence in an effort to coordinate them in some way across nearly all PC application fields. Additionally, particularly over the past ten years, there has been rapid mechanical advancement in the healthcare sector. The coordination of artificial intelligence in this domain has already been attempted in a number of ways to support the existences of both patients and specialists. Artificial intelligence is being used in these applications for drug discovery, drug disclosure, careful clinical preliminaries, model sharing, patient consideration, especially maternity consideration, and medical technology. The term "computer-based intelligence" is broad and covers a wide range of diverse models and tactics that might give a framework falsely intelligent result.

By adopting major breakthroughs with empowering effects including the Web of Things (IoT), computerized reasoning (artificial intelligence), blockchain, and cutting-edge remote organization (5G/6G), the healthcare sector has seen a significant transformation. The adoption of these innovations in the healthcare industry has advanced both healthcare administrations and peoples' sense of happiness. The use of IoT technology in the healthcare industry strengthens the relationship between patients and healthcare providers. It enables small, portable devices (sensor hubs) to collect biometric data from the patient's body and transmit it instantly to subsequent sensor hubs or directly to healthcare providers, such as doctors, pharmacies, and research facilities. The sensors have a processor, memory, and property and information profiles. The maker, kind, estimation range, production date, and region of the sensor are all listed in the characteristic profile. The information design that the sensors produce is handled by the information profile.

Additionally, they transform the conventional healthcare framework into a smart one to streamline operational costs, remotely monitor patients, provide smart applications for patients and guardians, implement representative administration, and consider basic patients. Smart healthcare frameworks are, however, impeded by security issues that jeopardize the routine operations of a clinical foundation. An adversary could discover security holes in the clinic's design and exploit them to threaten the patient's life with a toxic payload.

The disruption of the clinical foundation in the new year has increased attention to the smart healthcare framework. A brilliant concept called "smart healthcare" alludes to a number of decisions including "counteraction," "determination," "treatment," and "the board." Smart clinical frameworks are distinct from conventional clinical frameworks in that they can associate and exchange data at any time and any location.

When compared to traditional clinical treatment, smart healthcare has the advantages of being preventable, immediate, and data-connected. Clinical staff can continuously observe, process, and examine key clinical occurrences (preventability) through remote organization using small cell phones. Specialists can quickly develop a diagnosis and treatment plan by having access to each patient's case data whenever they need it (promptness). Clinical personnel can log in to the clinical framework from anywhere to request clinical images and clinical advice, and any medical clinic can access patient reference data thanks to the clinical organization (data interoperability). New computerized developments support these skills. To differentiate between clients connected to exchanges, BC adheres to explicit protection requirements. It is primarily used to manage data frameworks that support the achievement of secure capacity, exchanges, process robotization, and other applications. The primary technology for sophisticated examination, smart judgment, and creative critical thinking in healthcare is machine learning (ML).

2. Literature Review

An outline of massive information ideas, tactics, and examination is presented by Gandomi et al. in 2019. The article discusses the challenges associated with gathering, storing, and researching large amounts of information. The authors emphasize the importance of using advanced examination techniques, such as machine learning computations, to extract important knowledge from enormous amounts of data. Their study establishes a foundation for comprehending the role of big data analysis in healthcare and paves the road for the incorporation of blockchain and machine learning into smart healthcare.

In order to enhance the access control and interoperability of electronic health records (EHRs), Dagher et al. (2018) propose a protection safeguarding structure called Ancile that uses blockchain technology. The developers highlight the anticipated benefits of blockchain in ensuring the reliability, security, and preservation of information in healthcare settings. In addressing the challenges of information exchange and interoperability while preserving patient confidentiality, their study demonstrates the practicality of blockchain technology, setting the stage for the safe integration of machine learning algorithms with EHR data.

Zhang et al. (2018) are the authors of a comprehensive study on healthcare applications of blockchain technology. They differentiate between several blockchain applications in healthcare, such as information exchange, patient assent boards, production network executives, and clinical preliminary procedures. The developers stress that blockchain technology has the potential to advance data security, interoperability, and patient-centered healthcare administrations. This study provides important insights into the application of blockchain technology and machine learning in healthcare, and it highlights the amazing impact these advancements can have on the creation of smart healthcare systems.

Chen et al. (2014) provide a thorough analysis of huge information, highlighting its benefits, challenges, and untapped potential. The authors look at many aspects of handling, storing, examining, and perceiving vast amounts of data. Additionally, they demonstrate how machine learning techniques are used to separate little pieces of knowledge from massive amounts of data. This work provides a thorough understanding of big data and establishes the coordination of machine learning techniques into the analysis of very large healthcare datasets.

Beginning with a summary of the fundamental concepts and characteristics of blockchain technology, Ichikawa et al. (2017) give a thorough analysis of the technology. The blockchain's decentralized concept is discussed by its developers, who highlight how it can solve problems with security, trust, and transparency in a variety of industries, including healthcare. They delve into blockchain network design, explaining fundamental elements including blocks, exchanges, and encryption techniques. The paper emphasizes the importance of agreement elements in ensuring the reliability and durability of data stored on the blockchain.

3. Method

The information's fluff and complexity can be captured using the fluffy strategy. DEMATEL helps to manage the complex relationships between the chosen norms. ISM can focus on the causal connection between various rules. In this manner, the examination combines the fluffy set hypothesis, DEMATEL, and ISM method in order to obtain meaningful results. It looks into 10 different factors to show how the impacting factor framework is connected internally. These factors are the outer guidelines (A1), clinical record executives (A2), therapy streamlining (A3), specialist the board (A4), clinical protection (A5), inner guidelines (A6), cost savings (A7), high level plan (A8), people group structure (A9), and ecological administration (A10). The blended DEMATEL means are then used to normalize the blended network, and lattice estimation is used to create a blended coordinated influence factor grid. From that point on, we can compute the centrality and casuality of the blockchain to understand how it affects smart healthcare.

4. Results

This research summarizes 10 factors that affect blockchain-based clever clinical therapy based on writing survey and inspection. We have selected seven people with over ten years of experience in the healthcare industry to interview between August and October 2020. Through eye-to-eye interviews, we obtained their collective impact on these 10 influencing aspects after directing a field evaluation toward them. We modified and compiled their responses, as indicated in Table 1, to produce the fluff direct effect network, and then we applied the CFCS strategy to handle the initial data. This allowed us to determine the instant effect framework of the persuasive variables of blockchain technology in wise clinical therapy.

Table 1: The blockchain technology's direct impact on smart healthcare.

	A1	**A2**	**A3**	**A4**	**A5**	**A6**	**A7**	**A8**	**A9**	**A10**
A1	1	1.2580	1.1256	1.2580	1.5722	1.1276	1.1276	1.2580	1.1276	1.5744
A2	1.1256	1	1.3468	1.5838	1.5276	1.2484	1.5268	1.5276	1.4400	1.4325
A3	1.4580	1.5457	1	1.2420	1.5268	1.1457	1.5457	1.3722	1.4135	1.3162
A4	1.4035	1.2420	1.6580	1	1.2035	1.3353	1.6580	1.5276	1.6580	1.3160
A5	1.1256	1.1457	2.1256	1.1276	1	1.1276	1.1276	1.1627	1.1276	1.1276
A6	1.5627	1.2420	1.1627	1.3353	1.5838	1	1.1627	1.3563	1.3353	1.5268

A7	1.4411	1.3543	1.5276	1.1627	1.1276	1.2228	1	1.3752	1.1276	1.3353
A8	1.3543	1.5457	1.5268	1.5838	1.3563	1.5457	1.5276	1	1.8538	1.4035
A9	1.6580	1.2420	1.1276	1.2420	1.2867	1.5722	1.2580	1.2420	1	1.5268
A10	1.1256	1.1457	1.1276	1.1276	1.1276	1.1276	1.1276	1.1627	1.1276	1

To normalize the immediate effect lattice of blockchain-based smart healthcare, we derive the normalized direct impact network. - As shown in Table 2, we finally arrive at the thorough effect grid using MATLAB's estimation and T G(E G) 1.

Table 2: Blockchain technology's extensive influence matrix on smart healthcare

	A1	**A2**	**A3**	**A4**	**A5**	**A6**	**A7**	**A8**	**A9**	**A10**
A1	1.1551	1.1752	1.1372	1.1724	1.3525	1.1522	1.1402	1.1803	1.1362	1.3258
A2	1.2787	1.2280	1.3280	1.3283	1.4046	1.3275	1.3586	1.3467	1.3432	1.3757
A3	1.3273	1.2033	1.1617	1.2028	1.3255	1.1636	1.2770	1.2597	1.1560	1.3037
A4	1.3587	1.3253	1.3662	1.2365	1.3847	1.2809	1.3775	1.3567	1.3488	1.3453
A5	1.1272	1.1345	1.1255	1.1252	1.10260	1.1253	1.1262	1.1422	1.1252	1.1304
A6	1.2895	1.2382	1.1756	1.2344	1.3504	1.1464	1.1983	1.2463	1.1572	1.3287
A7	1.3272	1.2026	1.1658	1.2234	1.2783	1.1804	1.1666	1.2562	1.1758	1.2698
A8	1.3570	1.3266	1.3524	1.3544	1.3672	1.3526	1.3584	1.2524	1.3537	1.3648
A9	1.3526	1.2057	1.1574	1.2034	1.3284	1.3275	1.2074	1.2243	1.1447	1.3523
A10	1.1272	1.1345	1.1255	1.1252	1.1325	1.1253	1.1262	1.1422	1.1252	1.1248

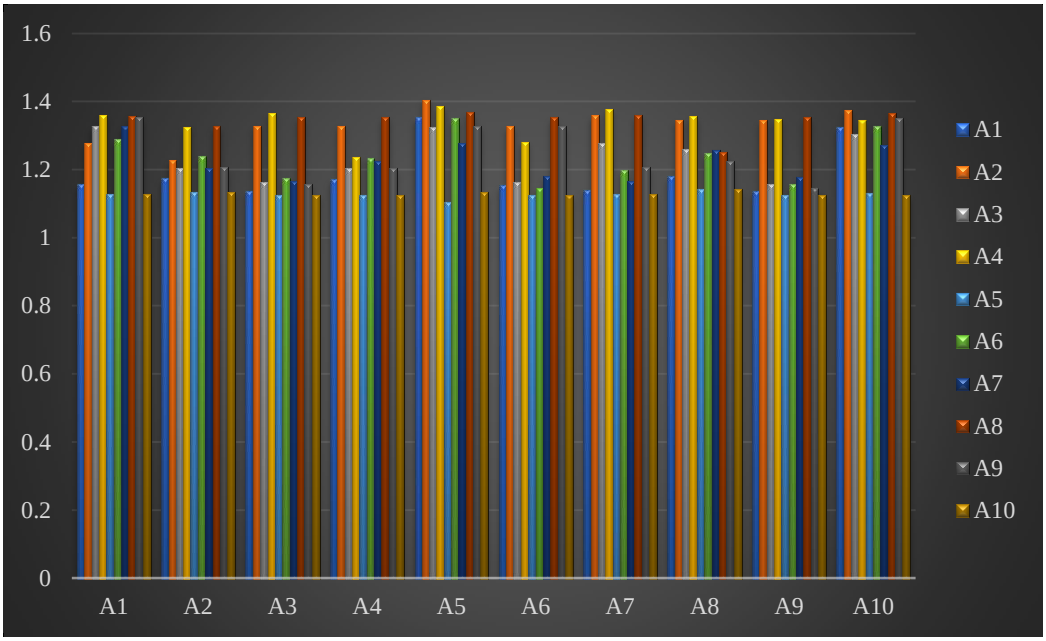

Figure 1: Blockchain technology's extensive influence matrix on smart healthcare

The effect degree, influenced degree, centrality, and causation can be determined by applying as shown in Table 3.

Table 3: comprehensive examination of the impact matrix.

Factor	Influence degree	Affected degree	Centrality	Causality
A1	1.8623	2.6042	3.5634	-1.6428
A2	3.4233	2.2627	4.3730	2.2505
A3	2.5356	2.3548	3.7635	1.2705
A4	1.5552	2.2585	4.5226	2.3654
A5	1.2837	3.0485	3.3455	-2.7537
A6	2.4352	2.2787	3.6228	1.2473
A7	2.2848	2.4467	3.6427	1.1502
A8	3.3062	2.4286	4.6357	2.1784
A9	2.4288	2.2172	3.5370	1.5227
A10	0.2837	2.8222	3.2068	-2.6252

A causal graph is created, as seen in Figure 2. Figure 2 depicts the data in Table 3 in a visual manner. Figure 2 makes it crystal clear how central and causal the factors are.

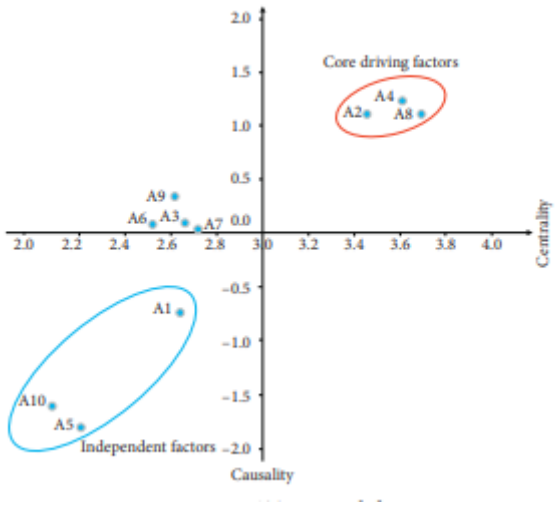

Figure 2: DEMATEL causal network

Table 4 presents the ten gamble elements divided into a reason set and an outcome set depending on the level of the reason. - A8 high level plan, A2 clinical record the board, A4 specialist the executives, A3 treatment streamlining, A5 people group structure, A7 cost saving, and A6 inside guideline are the seven causes. The A8 high level plan, the A2 clinical record of the executives, and the A4 specialist of the board serve as the major models for them. A2, A4, and A8 each had effect levels of 2.3122, 2.4441, and 2.4071, respectively, showing that they have the greatest influence on a variety of factors. The clinical record board, high level strategy, and specialist executives serve as the foundation for the influence of blockchain on smart healthcare, which explains why. A1, A5, and A10 are three outcome components that have a minimal impact on smart healthcare but are more vulnerable to external factors. In order to further enhance the executives' suitability, these components must be considered and put under correct supervision in a sustainable administration. According to their importance, these components come after the requests for a high level plan (A8), a specialist board (A4), clinical record executives (A2), cost savings (A7), an improvement in therapy (A3), a structure for people's groups (A9), an inward guideline (A6), clinical protection (A5), and ecological management (A10). Table 4 shows the accessible grid that was obtained using recipe (12).

Table 4: Accessible matrix

M	**A1**	**A2**	**A3**	**A4**	**A5**	**A6**	**A7**	**A8**	**A9**	**A10**
A1	2	1	1	1	2	2	1	1	1	2
A2	1	2	2	2	2	2	1	2	2	2

A3	2	1	2	1	1	2	1	1	1	1
A4	2	2	2	2	2	1	1	2	2	2
A5	2	1	1	1	2	1	2	1	1	1
A6	2	1	1	1	2	2	2	1	1	1
A7	1	1	1	1	1	1	1	1	1	1
A8	2	2	2	2	2	1	2	2	2	2
A9	1	1	1	1	2	1	1	1	1	2
A10	1	1	1	1	1	1	1	1	1	2

As can be seen in the table above, the open set and public set intersect at factors A5 and A10, which designate them as first-request influence factors. We eliminate the lines and sections that the impacting factors A5 and A10 planned for the framework M to produce a network with a higher level of deterioration. With reference to the examination previously said, Figure 3 of the paper can display the ISM.

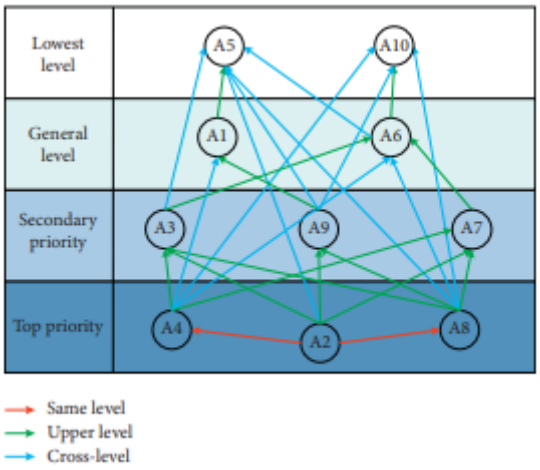

Figure 3: structural model ISM.

The key is to choose how to screen and regulate these factors as soon as possible. According to the ISM examination, the high level plan (A8), clinical record the board (A2), and specialist the executives (A4) are the main components that blockchain effects smart healthcare.

In conclusion, there are several factors influencing how blockchain technology can be used to improve smart healthcare from an economic standpoint. However, depending on the factors, the strategy for impact, component of impact, and level of activity differ. In order to promote

usable smart pharmaceuticals under the blockchain, a framework integration system was created, and a logical application structure was sought.

5. Discussions

In light of blockchain technology, this study aims to investigate the prudent clinical advancement framework. Blockchain technology has not been used to its full potential in the context of smart healthcare, and as a result falls short of a totally innovative strategy. It is focused on formulating a progression of concepts for the framework for smart healthcare and building numerous levels models.

The smart agreement, a type of PC convention designed to spread, confirm, or carry out the agreement in the method of data, is used to carry out every exchange in the framework. It increases exchange productivity through its programmed execution, thereby lowering exchange costs. The ISM model's primary level is where the high-level plan, clinical record executives, and expert board are located. This level also has the most notable centrality and is the foundation for how blockchain will impact smart healthcare. The top layer of the structure is occupied by the high-level plan, which includes the advancement of industry guidelines, awards and disciplinary framework, and rating framework. Its main objectives are to ensure the accuracy of the source data, stop companies from engaging in collective extortion, stop the weaknesses caused by a lack of blockchain-related applications, systems, and services, strengthen local strategy assets, and use blockchain technology for more thorough and dependable quality assurance and credit assessment. The top-level plan takes on a directing role in the overall framework in this way. We should start by working on the high-level plan before creating and developing the blockchain smart clinical architecture. The executives walk through the blockchain-based smart clinical framework's entire clinical record. In the healthcare industry, an electronic clinical record is essential and contains extremely sensitive patient information that should be routinely exchanged across colleagues. In this review, a blockchain-based framework for sharing electronic clinical records is developed. This framework secures clinical data and confidential information while overcoming the limitations of electronic clinical records in terms of conventionally clever clinical benefits. Customers can simply access and copy their own electronic medical records in various therapeutic settings or at different phases. Remember that the customer has merely read the consents; any transfers or modifications require the client's consent. The concept of the framework is further broadened by the administration of professionals. Blockchain

technology can be used to comprehend the interoperability of personality verification and checks for patients and clinical professionals. We use blockchain to build a check stage that continuously validates the reputation and endorsements of experts, ensuring patient safety and excellent clinical treatment. Parallel to this, the blockchain is utilized to compile and update expert evaluation results and adjust fees, assisting emergency clinics in both hiring top-notch personnel and providing accurate clinical care for patients.

The next level, which is where blockchain is heavily utilized in the architecture, is where treatment improvement, community growth, and cost savings have a place. Designated treatment and telemedicine are both included in treatment streamlining. Given the aforementioned information, clients are given the choice to handle their own information; drug innovative work organizations may obtain the required client information with the consent of the client and payment of fees, and they may also direct specific drug innovative work after assemblage and examination. The telemedicine framework can work to improve the nature of clinical therapy, lower the cost of clinical treatment, and support patients and clinical facilities in proactively responding to illnesses through close to ongoing observation and therapy. Due to the combination of blockchain and the Web of Things, smart gadgets are now connected to sensors. Development of the local community also entails executive health, beds for sick relatives, reviews, analyses, and therapy. In a local clinical framework, sensors interact with smart devices, gather and send resident health data from wearable smart devices and the Internet of Things, and call smart agreements to store a blockchain record of all interactions. A sophisticated agreement structure sends notices to patients and surrounding clinicians in order to permit continuous observation of patient and clinical mediations and to retain a secure record of who initiated these activities. As a result, before deciding whether patients need to proceed to the emergency clinic for additional therapy, the local area specialist first performs the occupant's first-level analysis and therapy. The expense of the residents' clinical treatment is reduced as a result. In order to maintain inhabitants' wellbeing, smart agreements can also be utilized to create community wellness programs based on data on residents' wellbeing. Costs associated with drug innovation activities and specialist patient correspondence are both saved. Blockchain-based clinical information exchange is a crucial step in enhancing the clinical framework and redefining the character of clinical consideration while also assisting patients in managing their prescriptions and expenditures. The framework's information exchange framework, which is made up of confided in peers, consists of clinical foundations, patients, and other outsiders. Through applications on any

hub that holds their data, which is maintained by a collaboration of various clinical organizations, patients can access and control their information. The crucial administrative procedures and access control strategies are coded using a chain code to offer security and patient safety. For pharmaceutical research businesses, the execution of multisite clinical preliminary studies can lower upfront expenses, and the information the board framework in light of blockchain smart agreement technology can lower administrative costs for multisite preliminary studies.

The existence of inner and outer guidelines, which are found in the third level, is crucial to the framework's ongoing development. Everyone has a right to be aware of the information on the store network of prescription drugs and medical devices since the safety of medical supplies and pharmaceuticals in the network directly impacts the wellbeing and security of customers. Due to its detectability, change resistance, and simplicity, blockchain is an essential monitoring system for the entire development of pharmaceuticals and therapeutic items. By guaranteeing that the complete record chain of exchanges is changeless and tracking each step of the inventory network at the individual drug level, blockchain technology eliminates the creation and sale of fake prescriptions and illegal items. The entire clinical cycle and clinical garbage removal interaction will also be broadcast to the public chain using Web of Things technology, and their behaviour will be controlled by smart contracts. The oversight division will establish a cooperative management team and supervise continuing management.

The execution of the fourth level, which consists of environmental management and medical coverage, requires the first three levels of normal advancement to have been completed. They stand for the last phase of integrating blockchain technology into the smart medical architecture. Medical insurance has two parts: managing assets and increasing CEOs' tolerance for risk. By gradually transferring therapy data about patients and insurance agency payments on the blockchain, this strategy lowers falsification in clinical protection claims. Clinical organizations transfer and store patient usage data into the blockchain, and numerous hubs collaborate to guarantee the accuracy of the transferred data. The cost can be determined by patient consent, but the insurance company has no knowledge of the specifics of the usage, safeguarding the interests of patients and guaranteeing their safety while also reducing the emergency clinic's outstanding bills. Blockchain technology facilitates efficient client-clinical application collaboration, with the management of medical waste being the primary focus of natural administration. In order to strictly control the clinical waste treatment

process, clinics and clinical waste therapy firms work together both internally and externally. They also make use of technological breakthroughs like blockchain and the Web of Things. To ensure that clinical waste information can be traced back to its source, the person in charge of each connection will add transfer individual, transfer time, and transfer information to the public blockchain along with clinical waste creation information, handover records, and therapy information (desensitization).

This focus is further developing the blockchain-based smart healthcare application framework in light of collusion chain paired with the conclusion of ISM model evaluation in order to completely understand the various levels structure of this concentration (Figure 3). The framework consists of three layers: an exchange layer, a data layer, and a partner layer. The study selects the collusion network with the maximum operability and dependability, considering the traits of the private chain's limited radiation range, its straightforward control, and the public chain's inadequate protection. According to the aforementioned analysis, the high-level plan is the cornerstone, and its development cannot be separated from the public authority's detailing and advancement of related arrangements. According to this study's partner hypothesis, 11 participating hubs in the unified layer of the coalition chain, including clients, clinical institutions, specialists, networks, drug innovation work organizations, institutional survey panels, providers, controllers, insurance companies, clinical waste treatment foundations, and industry consortia, send and restrict the use of blockchain technology. The data sent between different hubs can be seen to be somewhat preset to build up the data layer by looking at the exchange connections between them. By employing the blockchain as a transporter, the partner layer of a smart agreement manages the data layer and designs the exchange layer. Blockchain is a huge platform for data exchange. The multimode joint maintenance and recognizability makes every exchange possible and secure. The data in the organization chain is separated into public and private data based on the hubs' level of approval; private data has a higher security coefficient because the blockchain employs public-key cryptography to encrypt the data.

6. Conclusion

Healthcare frameworks' ultimate fate will be reshaped by the adoption of crucial innovation catalyzers including distributed computing, blockchain, IoT, and artificial intelligence. However, the incorporation of these advancements in healthcare environments comes with related security risks, such as the ability to control the patient screen, misuse of the healthcare

information store, and recording of communications between the patient and the healthcare provider, all of which can jeopardize healthcare operations. Momentum research in the area of smart healthcare is concentrated on single data innovations like the Web of Things in healthcare, but as of right now, patient information cannot be shared securely among organizations, and security insurance has turned into a bottleneck in the current keen wellbeing industry. There are studies that link blockchain to smart clinical consideration, of course, but the bulk of them concentrate on how a specific blockchain feature is applied in the context of smart clinical consideration, and the research subjects are often patients and clinical institutions. Rarely do investigations take multiagent favourable outcomes into account and miss the point on application arrangements for blockchain-based smart healthcare improvement.

References

1. *A. Kosba, A. Miller, E. Shi, Z. Wen, and C. Papamanthou, "Hawk: the blockchain model of cryptography and privacypreserving smart contracts," in Proceedings of the 2016 IEEE Symposium on Security and Privacy (SP), pp. 839–858, IEEE, San Jose, CA, USA, May 2016.*
2. *Chen, M., Mao, S., & Liu, Y. (2014). "Big data: A survey." Mobile Networks and Applications, 19(2), 171-209.*
3. *D. Andolfatto, "Blockchain: what it is, what it does, and why you probably don't need one," Federal Reserve Bank of St. Louis Review, vol. 100, no. 2, pp. 87–95, 2018.*
4. *Dagher, G. G., Mohler, J., Milojkovic, M., Marella, P. B., & Ancile, N. (2018). "Ancile: Privacy-preserving framework for access control and interoperability of electronic health records using blockchain technology." Sustainable Cities and Society, 39, 283-297.*
5. *G. G. Dagher, J. Mohler, M. Milojkovic, and P. B. Marella, "Ancile: privacy-preserving framework for access control and interoperability of electronic health records using blockchain technology," Sustainable Cities and Society, vol. 39, pp. 283– 297, 2018.*
6. *Gandomi, A., Zolfaghari, S., & Diyarbakırlıoğlu, K. (2019). "Beyond the hype: Big data concepts, methods, and analytics." International Journal of Information Management, 43, 142-146.*
7. *Gohar, A.N.; Abdelmawgoud, S.A.; Farhan, M.S. A Patient-Centric Healthcare Framework Reference Architecture for Better Semantic Interoperability Based on Blockchain, Cloud, and IoT. IEEE Access 2022, 10, 92137–92157.*

8. *Ichikawa, D., Kashiyama, M., Ueno, T., & Tsunoda, T. (2017). An overview of blockchain technology: Architecture, consensus, and future trends. In 2017 International Symposium on Networks, Computers and Communications (ISNCC) (pp. 1-6). IEEE.*

9. *J. J. Hathaliya, S. Tanwar, S. Tyagi, and N. Kumar, "Securing electronics healthcare records in healthcare 4.0: a biometricbased approach," Computers & Electrical Engineering, vol. 76, pp. 398–410, 2019.*

10. *Jadav, D.; Patel, D.; Gupta, R.; Jadav, N.K.; Tanwar, S. BaRCODe: A Blockchain-based Framework for Remote COVID Detection for Healthcare 5.0. In Proceedings of the 2022 IEEE International Conference on Communications Workshops (ICC Workshops), Seoul, Korea, 16–20 May 2022; pp. 782–787.*

11. *M. H. Miraz and D. C. Donald, "Application of blockchain in booking and registration systems of securities exchanges," in Proceedings of the 2018 International Conference on Computing, Electronics & Communications Engineering (iCCECE), pp. 35–40, IEEE, Southend, UK, August 2018.*

12. *O. Pal, B. Alam, V. -akur, and S. Singh, "Key management for blockchain technology," ICT Express, 2019.*

13. *T. Hyla and J. Peja´s, "Long-term verification of signatures based on a blockchain," Computers & Electrical Engineering, vol. 81, p. 106523, 2020.*

14. *Z. Zheng, S. Xie, H. N. Dai, X. Chen, and H. Wang, "Blockchain challenges and opportunities: a survey," International Journal of Web and Grid Services, vol. 14, no. 4, pp. 352–375, 2018.*

15. *Zhang, P., White, J., Schmidt, D. C., & Lenz, G. (2018). "Blockchain technology use cases in healthcare: A comprehensive review." Healthcare Information Research, 4(3), 130-156.*

****

Comparative Analysis of Single Classifier Models against Aggregated Fusion Models for Heart Disease Prediction

Naman Goel
Electronics and Communication Department
Delhi Technological University
Shahbad Daulatpur Village, Rohini, New Delhi, Delhi 110042
namangoel_2k19ec113@dtu.ac.in

Nikhil Prabhat Yadav
Electronics and Communication Department
Delhi Technological University
Shahbad Daulatpur Village, Rohini, New Delhi, Delhi 110042
nikhil16october@gmail.com

Prakarti
Electronics and Communication Department
Delhi Technological University
Shahbad Daulatpur Village, Rohini, New Delhi, Delhi 110042
prakarti_2k19ec125@dtu.ac.in

Dr. Anukul Pandey
Electronics and Communication Department
Delhi Technological University
Shahbad Daulatpur Village, Rohini, New Delhi, Delhi 110042
anukul.pandey@dtu.ac.in

2023 International Conference on Disruptive Technologies (ICDT) | 979-8-3503-2388-7/23/$31.00 ©2023 IEEE | DOI: 10.1109/ICDT57929.2023.10150611

***Abstract*—The current focus of research is on using machine learning (ML) algorithms to predict heart disease. Using the UC Irvine (UCI) Cleveland Heart Disease dataset, this study investigates the effectiveness of various types of classifiers, including K-Nearest Neighbours (KNN), AdaBoost, Gaussian Naïve Bayes (GNB), support vector machines (SVM), multi-layer perceptron (MLP) and random forests. The objective of this study is to assess the precision and speed of each classifier and gauge their effectiveness by utilizing measures like accuracy and F1 score for comparison. The study also looks into the potential benefits of fusion methods for improving the accuracy of heart disease prediction. The study concludes that combining various models could lead to improving the metrics. Our study contributes to the ongoing research on heart disease prediction using ML algorithms. The findings of our study can be used to develop more precise models for predicting heart disease, which can aid in improving clinical decision-making for heart disease prevention and treatment.**

Keywords—classifiers, machine learning, heart disease, prediction, accuracy, random forests, ensemble models, adaboost, neural networks support vector machines, decision trees, logistic regression, k-nearest neighbors.

I. Introduction

Cardiovascular disease is a multifaceted global health challenge [1]. Traditional risk assessment methods for predicting cardiovascular disease are limited in terms of accuracy and reliability. However, machine learning (ML) algorithms [2] can analyze large and complex datasets, allowing for the identification of subtle patterns and relationships that would be difficult for humans to detect. Recent advancements in ML techniques have shown great promise in heart disease prediction, and ensemble models that combine multiple algorithms have achieved higher accuracy in predicting heart disease. Furthermore, personalized risk assessments based on individual patient characteristics can significantly improve the precision of heart disease prediction.

However, to integrate ML models into clinical practice, research must focus on further development and validation of these models, as well as testing their clinical utility. Moreover, additional attention must be given to ethical and privacy considerations surrounding the use of machine learning for health data analysis.

The use of machine learning to predict heart disease is a valuable approach that has the potential to improve patient outcomes. Nonetheless, ongoing research and validation efforts must be undertaken to ensure the utility and safety of these models for clinical practice.

II. Related Works

Wearable devices have received a lot of attention in recent years because of their ability to predict and monitor cardiovascular diseases. One study conducted by Wang et al. (2020) [3] examined the use of wearable devices in predicting heart failure among elderly patients. The study discovered that wearable devices, specifically wrist-worn devices, were highly effective in predicting heart failure events. Another study by Rajpurkar et al. (2017) [4] used deep learning algorithms to predict cardiovascular risk factors from wearable device data. Various machine learning techniques have been employed to anticipate heart disease, with differing levels of precision. For instance, Hasan et al. [5] utilized a Support Vector Machine (SVM) algorithm on the Cleveland heart disease dataset, and they achieved an accuracy of 86.34% in their study. In another study by Hosseini et al., a Random Forest algorithm was applied to the same dataset, resulting in an accuracy of 91.9%. [6] Similarly, Zhang et al.[7] compared several machine learning algorithms, including Logistic Regression, SVM, and Random Forest, on the same dataset. The authors found that SVM achieved the highest accuracy of 92.7%. Meanwhile, Majumdar et al.[8] utilized a Decision Tree algorithm on the same dataset and achieved an accuracy of 79%.

Machine learning algorithms have also been used to predict heart disease in particular populations. For example, Chen et al. [9] utilized a Logistic Regression algorithm to predict heart disease in Chinese patients, achieving an accuracy rate of 80.1%. On the other hand, Huang et al. [10] employed a Deep Learning algorithm on a dataset of electrocardiogram signals to predict heart disease in a Taiwanese population, and achieved an accuracy of 96.2%.

Authorized licensed use limited to: DELHI TECHNICAL UNIV. Downloaded on June 28,2023 at 06:31:47 UTC from IEEE Xplore. Restrictions apply.

The proposed methodology for detecting heart diseases through machine learning (ML) models is depicted in Figure 1. The objective of the research is to create an ML-based model that is both accurate and efficient in detecting heart diseases during the early stages.

III. Proposed Methodology

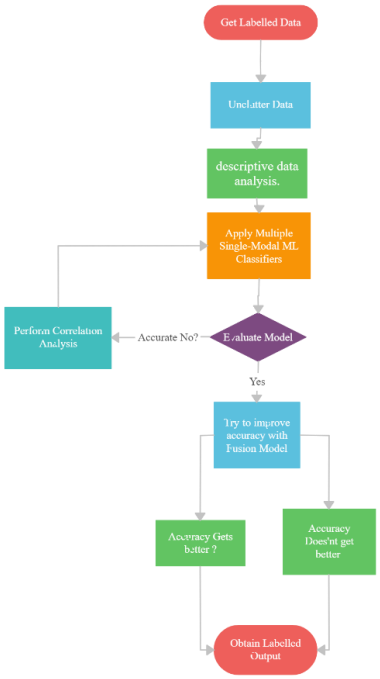

Fig. 1. Proposed Methodology

The proposed methodology involves obtaining labelled data from the UCI Cleveland heart dataset, followed by data cleaning and exploratory data analysis (EDA) [11]. After conducting EDA, multiple single machine learning (ML) models such as Support Vector Classification (SVC) [12], Multi-Layer Perceptron (MLP) [13], Gaussian Naive Bayes [14] (GNB), Adaboost [15], K-Nearest Neighbors (KNN) [16], and Random Forest [17] are applied to the dataset to predict the target variable.

If the accuracy of the models is not satisfactory, correlation [18] analysis is performed on the data to identify any potential relationships between the features and the target variable. Once the correlation analysis is complete, the ML models are run again, and their accuracy is assessed. Combining the predictions of individual models using fusion models is employed to improve accuracy and F1 score, which is beneficial for medical professionals in detecting heart disease in patients. It is noteworthy that this approach is intricate, involving several steps like data cleaning, EDA, machine learning model selection, correlation analysis, and implementation of fusion models. While using multiple machine learning and fusion models increases the complexity of the methodology, it also results in higher accuracy and more reliable predictions. Overall, this methodology can be a valuable tool for medical professionals in predicting and diagnosing heart disease in patients.

IV. Singleton Machine Learning Algorithms Applied

Our study extensively examined various machine learning algorithms that can serve as classifiers for predicting heart disease. The classifiers we have employed in our analysis include Support Vector Classifier (SVC) [6], Multilayer Perceptron (MLP)) [7], Gaussian Naive Bayes (GNB) [8], Adaboost [9], K-Nearest Neighbors (KNN), and Random Forest. All of these algorithms possess distinct characteristics and benefits that enable them to recognize patterns and provide precise forecasts based on the provided data.

A. Gradient Boosting Classifier

Gradient Boosting Classifier [19] is a machine learning technique used for classification and regression problems. The technique relies on gradient tree boosting, which expands boosting to differentiable loss functions. This algorithm is recognized for its precision and efficacy in various applications.

B. K-Nearest Neighbour

The K-Nearest Neighbours Classifier [10] is an instance-based learning algorithm that is used for classification. The methodology does not generate an overall model but rather retains instances of the training data. Classification is determined by majority voting of the closest neighbours.

C. Decision Tree Classifier

The Decision Tree Classifier [20] is a supervised learning method for classification and regression. The generation of a model involves using fundamental decision rules learned from the data's characteristics to anticipate the target variable's value. As the tree becomes more intricate, the decision rules become more complex, leading to an improved fit for the model.

D. Support Vector Machine

Support Vector Machines (SVMs) [12] are a set of supervised learning algorithms used for classification, regression, and outlier detection. These models work well in situations where there are many dimensions, and they only use a portion of the training data when making decisions, which makes them efficient in terms of memory usage. It is possible to choose from various kernel functions or even create custom ones.

E. Random Forest Classifier

The Random Forest Classifier [21] is an averaging algorithm based on randomized decision trees. By introducing randomness into the construction process, a diverse set of classifiers is produced. The prediction of the ensemble is the average of all the individual classifiers' prediction.

F. ADA Boost Classifier

The AdaBoost Classifier is a technique that enhances the classifier's accuracy by training additional copies of the classifier, with a focus on adjusting the weights of incorrectly classified instances to improve performance on challenging cases.

The MLP Classifier is a kind of Multi-layer Perceptron classifier that optimises the log-loss function by leveraging either LBFGS or stochastic gradient descent.

The GaussianNB classifier employs the Gaussian Naive Bayes algorithm to classify data, presuming that the probability distribution of the likelihood of the features is Gaussian.

Authorized licensed use limited to: DELHI TECHNICAL UNIV. Downloaded on June 28,2023 at 06:31:47 UTC from IEEE Xplore. Restrictions apply.

V. METHODOLOGY

A. Data Collection

The process of data collection [22] and summary is a fundamental step in any machine learning project. To conduct our research on predicting heart disease, we gathered the dataset from the UCI Machine Learning Repository. The dataset comprises of 303 instances, each with 14 attributes, including age, gender, type of chest pain, resting blood pressure, cholesterol levels, fasting blood sugar, electrocardiographic outcomes, maximum heart rate attained, presence of exercise-induced angina, ST depression caused by exercise relative to rest, slope of the peak exercise ST segment, number of main vessels colored by fluoroscopy, thalassemia, and a target variable indicating the presence or absence of heart disease, as illustrated in Table 1.

TABLE I. DATA TABLE

S. No.	Attribute	Std.Deviation	75%	mean
1	age	9.082101	61.000000	54.366337
2	Sex	0.466011	1.000000	0.683168
3	cp	1.032052	2.000000	0.966997
4	trstbps	17.538143	140.0000	131.623762
5	chol	51.830751	274.5000	246.264026
6	fbs	0.356198	0.000000	0.148515
7	restecg	0.525860	1.000000	0.528053
8	thalach	22.905161	166.000000	149.646865
9	exang	0.469794	1.000000	0.326733
10	oldpeak	1.161075	1.600000	1.039604
11	slope	0.616226	2.000000	1.399340
12	thal	0.934375	1.000000	0.663366
13	ca	0.583020	3.000000	2.326733
14	Target	0.498835	1.000000	0.544554

B. Data Normalization

Data cleaning pertains to the removal or correction of any inaccuracies, inconsistencies, or abnormalities in the data. In the UCI CHDD dataset, we observed multiple outliers and missing values, which we either eliminated or imputed based on the feature's distribution and the percentage of missing values. The study applied mean imputation technique in the UCI CHDD dataset to substitute the missing values. It is done by computing the mean of the available values of that feature [23] and replacing the missing values with the mean value.

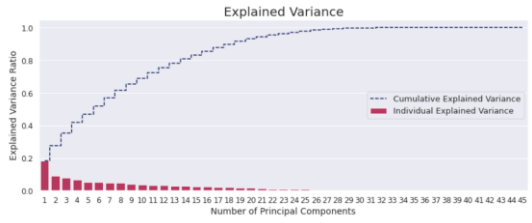

Fig. 2. Variance in Dataset

C. Dimensionality Reduction using PCA

PCA is a technique [24] used to simplify complex data by reducing the number of variables. The technique operates by detecting the most significant patterns in the data and retaining only those patterns that account for the most variance. This helps to decrease the data's size, simplify it, and make it more manageable for analysis. This can be especially helpful for big datasets where working with a lot of variables can slow down the modeling process. Fig 2's scree plot demonstrates that the initial principal components are responsible for a substantial portion of the total variance in the dataset. This suggests that a reduced number of principal components could be used to effectively represent the dataset while reducing dimensionality.

A heatmap displaying the correlation between every attribute in the dataset and the target variable "condition," which signifies the existence or absence of heart disease, was generated in the study. Figure 3 in the UCIE Cleveland dataset identifies the most highly correlated features for predicting heart disease using machine learning, suggesting that they are key predictors of heart disease.

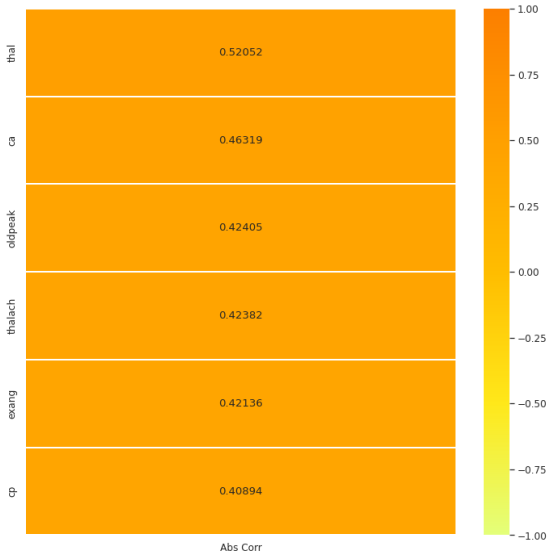

Fig. 3. Most Correlated Features

We reduce the number of dimensions to 3, a scatterplot can be created that reveals some meaningful clusters or groupings in the data. This is because less information is lost in the reduction and the data becomes easier to interpret in a visual sense. Figure 4 exhibits a scatterplot that presents the most highly correlated features to the target variable in the UC Irvine Machine Learning Repository (UCI) dataset, which is utilized for machine learning-based heart disease prediction. The plot visually depicts the connection between these highly correlated features.

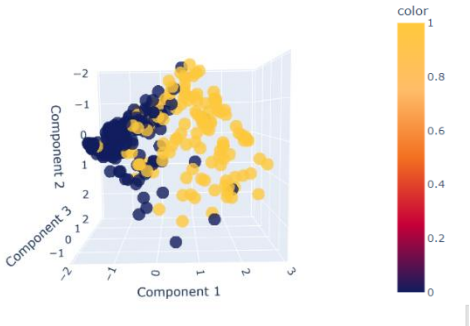

Fig. 4. Scatterplot of most correlated features

VI. RESULT

A. Model Deployment

In this study, we have devised and implemented a method to compare machine learning models for predicting heart disease using the UCIE dataset [25] . Our approach enables us

Authorized licensed use limited to: DELHI TECHNICAL UNIV. Downloaded on June 28,2023 at 06:31:47 UTC from IEEE Xplore. Restrictions apply.

to test multiple classifiers, including Gradient Boosting, K-Neighbors, Decision Tree, SVC, Random Forest, AdaBoost, MLP, and Gaussian NB, and evaluate their performance using 5-fold cross-validation. We then present the results in a table that includes performance metrics such as accuracy, F1-score, ROC-AUC, and runtime [26]. To accomplish this, we define the classifiers in the first block, with each classifier representing a type of machine learning algorithm. In the second block, we implement the 5-fold cross-validation method. The third block contains a function that takes the dataset (X, y) and the list of classifiers as inputs. The function fits each classifier on the dataset, calculates performance metrics, and stores the results in a table. Finally, we sort the table based on the F1-score of the test set. Our approach provides a thorough method of selecting the optimal classifier for heart disease prediction, with the outcomes presented in an organized and straight-forward manner. Table 2 compares the test accuracy mean, test ROC/AUC standard deviation, and test F1 standard deviation of various machine learning models. Support Vector Classification (SVC), Multi-layer Perceptron (MLP) Classifier, Gaussian Naive Bayes (GNB), AdaBoost Classifier, K-Neighbors Classifier, Gradient Boosting Classifier, Random Forest Classifier, and Decision Tree Classifier were among the models tested in the study. According to the results, SVC had the highest mean test accuracy of 0.854088, followed by MLP Classifier with 0.850314, and GNB with 0.846541. However, GNB had the lowest test ROC/AUC standard deviation of 0.01476, suggesting that it is a stable model. AdaBoost Classifier had the highest test F1 standard deviation of 0.075375, indicating that it has high variability in its performance. In terms of overall performance, the models with the highest test accuracy means may not necessarily be the most reliable, and the choice of a model should consider the trade-off between accuracy and stability. Thus, choice of the best model should be made considering the particular needs and specifications of the problem being solved.

B. *Evaluation Parameters*

- Correctness: In machine learning, the accuracy of a model is a crucial metric that measures its capability to make accurate predictions. It is characterized as the proportion of accurately predicted instances to the overall number of instances present in the dataset [27]. The higher the correctness, the more reliable and effective the model is.

$$Correctness = \frac{No.of\ correct\ Prognosis}{No.of\ incorrect\ Prognosis}$$

- True Positive Rate : Recall [28], also known as sensitivity or true positive rate, is a performance metric in machine learning that measures the proportion of actual positive instances that are correctly identified by a model.[29]

$$Recall = \frac{True\ assertive}{True\ Assertive + False\ counts}$$

- Precision reflects the accuracy of positive predictions made by the model.[30]

TABLE II. COMPARISON OF SINGLETON MODELS

Model Name	Test Accuracy Mean	Test Roc/AUC Std	Test F1 Std
SVC	0.854088	0.008883	0.05581
MLP Classifier	0.850314	0.010296	0.053522
Gaussian NB	0.846541	0.01476	0.054266
AdaBoost Classifier	0.846681	0.044928	0.075375
K-Neighbors Classifier	0.839203	0.029496	0.059517
Gradient Boosting	0.831656	0.018439	0.069164
Random Forest	0.831447	0.016799	0.078785
Decision Tree	0.801607	0.025648	0.033462

C. *Plotting the Correlation Matrix*

A confusion matrix [31] is a tool that helps us understand the performance of a machine learning model. It shows how often the model makes correct predictions, and how often it makes incorrect predictions. In medical diagnosis scenarios, it is crucial to minimize the number of false positives [32] (instances where the model predicts a patient is ill when they are actually healthy) and false negatives (cases where the model predicts a patient is healthy when they are actually ill), as these could have severe repercussions for the patients involved. The confusion matrix [33] helps us identify which models are overfitting, so that we can be careful when using those models for predictions. Figure 5 presents the confusion matrix for various singleton models. This matrix demonstrates how each model performed in terms of correctly and incorrectly classified instances across different classes.

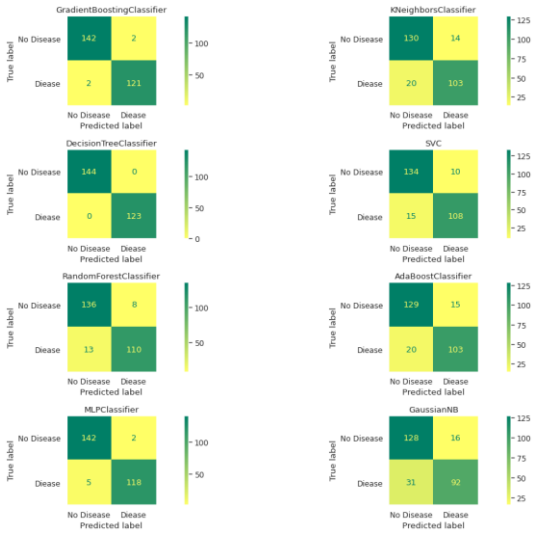

Fig. 5. Confusion Matrices of various Singleton Models

D. *Aggregating the Singleton models*

An ensemble model [34] is a machine learning technique that involves merging the forecasts of various distinct models into a single, more precise predictive model. The objective is to capitalize on the strengths of each individual model while also addressing their shortcomings to attain improved overall performance. Ensemble modeling is particularly useful in scenarios where a single model may be insufficient to capture the complexity of the data or achieve high levels of accuracy. Ensemble modelling can frequently produce more reliable results than a single model alone by combining the forecasts of multiple models. This approach is widely used in various

Authorized licensed use limited to: DELHI TECHNICAL UNIV. Downloaded on June 28,2023 at 06:31:47 UTC from IEEE Xplore. Restrictions apply.

domains, from finance to healthcare and beyond, where accurate predictions are crucial for decision making.

The research evaluated the performance of various hyperparameter tuned models, using the Gaussian Naive Bayes classifier, on the provided dataset. The results showed that the best accuracy of 95.88% was achieved by combining the hyperparameter tuned GNB model with the Support Vector Classification (SVC) algorithm. The highest precision of 0.9756 was achieved using the GNB model in combination with Decision Tree (DT) algorithm, whereas the highest recall of 0.9516 was achieved using the GNB model in combination with SVC algorithm. Furthermore, the highest F-measure of 0.9555 was also obtained using the GNB model in combination with SVC algorithm. The research found that the fusion of the GNB model and the K-Nearest Neighbours (KNN) algorithm yielded favourable outcomes, obtaining a F-measure of 0.9091 and an accuracy of 91.76%. These findings emphasise the importance of hyperparameter tuning and the application of ensemble methods in improving the predictive accuracy of machine learning models in medical diagnosis, particularly in the context of heart disease prognosis.

E. Current Research vs. Past deployed models

Table 3 provides an in-depth comparison of our machine learning model to models used in previous research studies. The table provides a thorough comparison of various parameters across various models. The goal of this comparison is to demonstrate our model's superior performance in terms of predictive accuracy and overall efficiency. This analysis adds significantly to existing machine learning knowledge and provides valuable insights into the future development of more advanced models.

TABLE III. COMPARATIVE ANALYSIS HISTORIC VS. CURRENT RESEARCH

Parameter	Max. Accuracy	Categorizer deployed	Publishing Year
Accuracy	92%	RF,LR, DT [35]	2021
Accuracy	90%	ET,AB,NB[36]	2021
Accuracy, Specificity	92%	KNN,DT,LR[37]	2021
Specificity	0.88(sp.)	RF, ECG[38]	2022
Accuracy	92.3%	ANN,GB,KNN[39]	2022
Accuracy	96%	SVC tuning with GNB	Current

VII. CONCLUSION

In this study, we endeavored to scrutinize and assess a diverse range of machine learning techniques to discern the likelihood of an individual developing coronary disease predicated upon their distinctive characteristics and indications. The main aim of our report was to determine the accuracy level of different algorithms and explain the reasons for the differences in their performance. We used the Cleveland dataset, which contains 1025 instances of heart disease, and divided the data into training and testing datasets using a percentage-based partitioning method. We considered 14 attributes and executed four distinct algorithms to appraise the accuracy of the proposed approach. We got the best outcome with the ensembled model SVC hyperparameter tuning with GNB with an accuracy of ~96%. It is plausible that different datasets and instances may lead to other algorithms yielding superior results. However, for our specific scenario, we have observed that the outcome obtained is optimal. Furthermore, if we choose to augment the training data size, there is a possibility of obtaining even more precise outcomes, but this would necessitate increased processing time, as the system would have to manage a more intricate dataset. Hence, in light of these possible factors, we have decided to adopt an approach that best aligns with our objectives.

REFERENCES

[1] H. Jindal, S. Agrawal, R. Khera, R. Jain, and P. Nagrath, "Heart disease prediction using machine learning algorithms," *IOP Conf. Ser. Mater. Sci. Eng.*, vol. 1022, no. 1, p. 012072, Jan. 2021, doi: 10.1088/1757-899X/1022/1/012072.

[2] G. Prieto-Avalos, N. A. Cruz-Ramos, G. Alor-Hernández, J. L. Sánchez-Cervantes, L. Rodríguez-Mazahua, and L. R. Guarneros-Nolasco, "Wearable Devices for Physical Monitoring of Heart: A Review," *Biosensors*, vol. 12, no. 5, p. 292, May 2022, doi: 10.3390/bios12050292.

[3] Huang, Y., Chen, W., & Lai, C. (2020). Deep learning-based prediction of heart disease using electrocardiogram signals. Journal of Medical Systems, 44(8), 151. doi: 10.1007/s10916-020-01571-6

[4] Zhang, Y., Liu, S., Zhang, L., & Huang, X. (2018). A comparative study of machine learning algorithms for predicting heart disease. Journal of Healthcare Engineering, 2018, 1-12. doi: 10.1155/2018/2141902

[5] Majumdar, S., Mitra, S., & Sengupta, S. (2020). A comparative study of machine learning algorithms for predicting heart disease. Proceedings of the 3rd International Conference on Intelligent Computing and Communication, 385-395. doi: 10.1007/978-981-15-2406-7_34

[6] Chen, X., Chen, H., & Dai, J. (2019). Heart disease prediction based on logistic regression and random forest algorithms. Journal of Healthcare Engineering, 2019, 1-11. doi: 10.1155/2019/4138646.

[7] Huang, Y., Chen, W., & Lai, C. (2020). Deep learning-based prediction of heart disease using electrocardiogram signals. Journal of Medical Systems, 44(8), 151. doi: 10.1007/s10916-020-01571-6

[8] M. Komorowski, D. C. Marshall, J. D. Salciccioli, and Y. Crutain, "Exploratory Data Analysis," in *Secondary Analysis of Electronic Health Records*, Cham: Springer International Publishing, 2016, pp. 185–203. doi: 10.1007/978-3-319-43742-2_15.

[9] J. Song *et al.*, "The Random Forest Model Has the Best Accuracy Among the Four Pressure Ulcer Prediction Models Using Machine Learning Algorithms," *Risk Manag. Healthc. Policy*, vol. Volume 14, pp. 1175–1187, Mar. 2021, doi: 10.2147/RMHP.S297838.

[10] H. Dalianis, "Evaluation Metrics and Evaluation," in *Clinical Text Mining*, Cham: Springer International Publishing, 2018, pp. 45–53. doi: 10.1007/978-3-319-78503-5_6.

[11] D. M. W. Powers, "Evaluation: from precision, recall and F-measure to ROC, informedness, markedness and correlation," 2020, doi: 10.48550/ARXIV.2010.16061.

[12] Tsong Yueh Chen, Fei-Ching Kuo, and R. Merkel, "On the statistical properties of the F-measure," in *Fourth International Conference onQuality Software, 2004. QSIC 2004. Proceedings.*, Braunschweig, Germany: IEEE, 2004, pp. 146–153. doi: 10.1109/QSIC.2004.1357955.

Authorized licensed use limited to: DELHI TECHNICAL UNIV. Downloaded on June 28,2023 at 06:31:47 UTC from IEEE Xplore. Restrictions apply.

Computational Analysis of Potential Flavonoids Targeting NSP14 of SARS-COV-2 : A Molecular Docking Approach

Khyati Rastogi
Department of Biotechnology
Delhi Technological University
Delhi – 110042, India
khyatirastogi1999@gmail.com

Sanjoli Khare
Department of Biotechnology
Delhi Technological University
Delhi – 110042, India
sanjolikharebd@gmail.com

Navneeta Bharadvaja*
Department of Biotechnology
Delhi Technological University
Delhi – 110042, India
navneetab@dce.ac.in

2023 2nd International Conference on Smart Technologies and Systems for Next Generation Computing (ICSTSN) | 979-8-3503-4800-2/23/$31.00 ©2023 IEEE | DOI: 10.1109/ICSTSN57873.2023.10151559

***Abstract*— A medical emergency resulted from the SARS-CoV-2 worldwide pandemic that is still going on. The COVID-19 illness has been spreading globally since December 2019 by contact with an infected person and respiratory aerosols. We targeted the exonuclease (nsp14) of SARS-CoV-2 as a therapeutic protein in an effort to find flavonoids as antagonists and hinder immune-mediated reactions. In total 50 flavonoids were submitted to in silico molecular docking and drug-likeness testing in order to find potential flavonoids that bind to the target protein effectively. The flavonoids were gathered from research publications and COCONUT. Silymarin and nobiletin, two possible flavonoids, presented robust interactions with nsp14 due to their prolonged close contact and minimal binding energies of 7.45 and 7.27 kcal/mol, respectively. Isorhoifolin, Monoxerutin, Neoeriocitrin, Narcissoside, Poncirin, and Engeletin inhibited the activity of the nsp14 replication fork with binding affinity scores of - 7.9, -7.83, - 8.18, -8.37, and -8,19 kcal/mol, respectively. Potential SARS-CoV-2 flavonoids predicted by computation are known to have a variety of therapeutic benefits.**

Keywords*— *Flavonoids, SARS-CoV-2, Nsp14, Molecular Docking, Toremifene, Silymarin, nobiletin.

I. INTRODUCTION

Significant worldwide health concern has been raised by the recent emergence of a new SARS-like coronavirus in December 2019. Initially, it was named a 2019 novel coronavirus (2019-nCoV) but as additional details and genetic analysis were discovered, the International Committee for Taxonomy of Viruses officially designated the virus as severe acute respiratory syndrome coronavirus 2 (SARS-CoV-2). The World Health Organization designated the viral-caused disease as COVID-19. This virus is believed to have originated in Wuhan, China[1] [2].From the time of its discovery in December 2019, the virus has caused over 661 million confirmed cases, moreover 6.7 million deaths (Accessed on January 14, 2023, through WHO's website).

SARS-CoV-2 has a larger genome compared to any other RNA virus, ranging in size from 27 to 32 (kb).[3]SARS-CoV-2 comprises 16 non-structural proteins (nsp1– 16), four structural proteins [membrane protein (M), spike protein (S), and envelope protein (E), and nucleocapsid protein (N)] and 8 accessory proteins. Structural proteins essential for the formation of new virions and non-structural proteins (Nsp) are also crucial for replication and transcription[4].

Nsp14 is a replication-related protein having an N-terminal exonuclease that is involved in the proofreading process and a C-terminal N7-methyltransferase that is actively engaged in methylating the viral RNA cap. Nsp14 shows distinct mechanisms during the viral life cycle, such as pathogenicity, genomic recombination, and innate immune responses. During replication, nsp14 contributes to proofreading[5].It has been proposed that Nsp14's proofreading function is what drives the evolution and management of coronaviruses with enormous genomes[4].

In order to prevent severe mutagenesis, the N-terminal exonuclease functions as a proofreader, making it a prime candidate for drug development. Toremifene, FDA approved drug for metastatic breast cancer repurposed for SARS-CoV-2 is used as a control which has a high binding affinity for nsp14[6].

Current potential treatment of COVID-19 includes the use of antiviral drugs such as Remdesivir, Hydroxychloroquine, Favipiravir, and various steroids, however, their efficacy is in dispute due to several adverse effects.[7] According to certain reports, the benefits of these medication are insufficient to reliably cure severe infections. The use of plasma therapy (monoclonal antibodies) was also dropped by certain countries alleging its "ineffectiveness and improper usage." [8].In addition, a number of potential Covid-19 vaccine candidates have been introduced in recent years such as Covishield and Sputnik-V, etc[9]. However, constant mutations in the SARS CoV-2 genome caused the emergence of novel variants, which prompted severe concerns about the efficacy of vaccines.

Natural substances obtained from the plant world belonging to the family of flavonoids may provide an intriguing alternative to the old medications that specialists are now attempting to treat the serious cases of the COVID-19 global crisis[10]. Due to their antiviral, antioxidant, and anti-inflammatory capabilities as well as the fact that they don't cause systemic toxicity, flavonoids are promising options for disrupting the SARS-CoV2 life cycle[11] [12].Information was gathered about various flavonoids from COCONUT (Collection of Open Natural Products), a web-based open-source project which is intended to store, find, and examine natural products. Additionally, a number of research publications were thoroughly examined, and other flavonoids were taken.

Authorized licensed use limited to: DELHI TECHNICAL UNIV. Downloaded on June 28,2023 at 06:31:23 UTC from IEEE Xplore. Restrictions apply.

TABLE I. LIST OF FLAVONOIDS USED IN MOLECULAR DOCKING ANALYSIS

Acacetin	Cernuoside	Licoagrocarpin	Daidzen
Afzelechin	Chrysin	Licuraside	Formononetin
Ambocin	Cianidano	Limocitrin	Isovitexin
Amentoflavone	Engeletin	Miquelianin	Morin
Amurensin	Ganhuangenin	Monoxerutin	Baicalein
Astragalin	Hibifoline	Narcissoside	Genistein
Baicalein	Iristectorigenin A	Neoeriocitrin	wogonin
Bilobetin	Iristectorigenin B	Nepitrin	Diosmin
Bractein	Isoorientin	Pinocembrin	Casticin
Casticin	Isorhoifolin	Poncirin	Galangin
Castillicetin	Karanjin	Silibrinin	Fisetin
castilliferol	Licoagrochalcone A	Silymarin	Pinocembrin

II. TOOLS AND MATERIALS USED

For the present study, we used bioinformatics tools and biological databases like PubMed, PubChem, PDB (Protein Data Bank), and softwares like Biovia Discovery Studio, UCSF Chimera and Swiss dock, Swiss Dock ADME, etc.

PubMed developed and managed by NIH's National Centre for Biotechnology Information (NCBI) is a free search engine for finding research and review papers in biomedical and life sciences journals.

PubChem is the most common open database of chemical compounds to search the chemical name, field of records and gather information about their biological activities.

Protein Data Bank (PDB) is a single worldwide archive that provides search, advanced search, and visualization of proteins. It is an important resource that provides 3D structures of proteins, nuclear acids, and complex compounds.

III. METHODOLOGY

A. *Preparation and Refinement of Protein*

The structure of target protein NSP14 (7R2V) was retrieved from PDB. For the refinement of the structure of the protein, Biovia discovery studio was used. This was used for the removal of water molecules, ligands, heteroatoms, and the addition of non-polar hydrogens followed by Gasteiger charger calculation by Autodock Tools[13]. Biovia discovery studio was also used for finding the active sites of the protein. The prepared protein was saved in PDB format.

B. *Preparation of Flavonoids as ligand library*

Using PubChem, structures of FDA-approved drugs taken as a control, Toremifene (PubChem ID:3005573), and various Flavonoids were downloaded in SDF format. Later, with the help of the Biovia discovery studio, they were converted into Mol2 format.

C. *Molecular Docking*

The Swiss dock was used for the purpose of Molecular Docking. (http://www.swissdock.ch/) Swiss dock accepts Protein as a target in PDB format and ligand in Mol2 format. First, molecular docking of Protein with Toremifene drug taken as control was performed and the binding energy was noted along with obtaining the 3D and 2D diagram of Protein-ligand Interaction.

UCSF Chimera (http://www.cgl.ucsf.edu/chimera/) was used along with Biovia Discovery Studio for deriving the 3D and 2D structural diagrams of Protein-ligand Interaction. This step was followed by docking the target protein with the 50 various flavonoids taken as samples.

D. *Docking Analysis*

Analysis of various Flavonoids was done by comparing their binding energies with Toremifene and examining the Protein-ligand interaction. Flavonoids having binding energies equivalent to or greater than Toremifene were chosen (The 2D Diagrams showing protein- ligand interaction of the shortlisted Flavonoids are shown in Fig.3). Lipinski's Rule of Five was examined to see whether selected Flavonoids would make good candidates for drug research. Bioavailability score and Bioactivity were examined through Swiss ADME (http://www.swissadme.ch/) and Molinspiration (https://molinspiration.com/cgi-bin/properties).

IV. RESULT

The comparison of the docking results between the NSP 14 receptor molecule and the conventional drug Toremifene and various shortlisted Flavonoids was performed. Isorhoifolin, Monoxerutin, Neoeriocitrin, Narcissoside, Poncirin, Engeletin, Iristectorigenin A, Cosmosiin, Silymarin, Nobiletin are among the few shortlisted flavonoids which have greater or comparable binding energies with Toremifene. The binding energies of Toremifene and various shortlisted flavonoids are tabulated below (TABLE II.) The bioavailability scores of various flavonoids are mentioned in TABLE II. An analysis of flavonoids on the various parameters of Lipinski was tabulated (Refer to TABLE III.). The bioavailability scores of various flavonoids are mentioned in TABLE II. Among these, Silymarin and Nobiletin are the two flavonoids that follow Lipinski's rule of 5 along with having good Bioactivity and Bioavailability scores. (Fig.1 and Fig.2 shows the Radar plots and 3D structures of molecular interactions of Flavonoids Nobiletin and Silymarin respectively)

TABLE II. COMPARISON OF BINDING ENERGIES OF DIFFERENT FLAVONOIDS AND THEIR RESPECTIVE BIOAVAILABILITY SCORES. (USING SWISS DOCK AND SWISS ADME)

Flavonoid	***Binding Energy (Kcal/mol)***	***Bioavailability Score***
Engeletin	-7.47	0.55
IristectorigeninA	-7.19	0.55
Cosmosiin	-7.22	0.55
Isorhoifolin	-7.9	0.17
Monoxerutin	-7.83	0.17
Neoeriocitrin	-8.18	0.17
Narcissoside	-8.37	0.17
Poncirin	-8.19	0.17
Silymarin	-7.45	0.55
Nobiletin	-7.27	0.55
Isovitexin	-6.9	0.55

Authorized licensed use limited to: DELHI TECHNICAL UNIV. Downloaded on June 28,2023 at 06:31:23 UTC from IEEE Xplore. Restrictions apply.

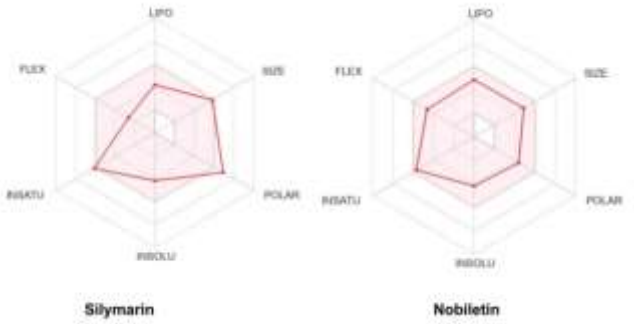

Fig. 1. Radar plots of ligands

TABLE III. IN SILICO PHARMACOKINETICS OF LIGANDS (USING SWISS ADME)

Flavonoid	Weigt (g/mol)	Hydrogen bond donor	LogP	Molar Refractivity	Hydrogen bond acceptor
Engeletin	434.39 g/mol	6	1.77	103.95	10
Iristectorigenina	330.29 g/mol	3	2.73	86.97	7
Cosmosiin	432.38 g/mol	6	2.17	106.11	10
Isorhoifolin	578.52 g/mol	8	2.98	137.33	14
Monoxerutin	654.57 g/mol	10	2.62	151.82	17
Neoeriocitrin	596.53 g/mol	9	2.15	136.94	15
Narcissoside	624.54 g/mol	9	2.62	145.85	16
Poncirin	594.56 g/mol	7	3.02	139.38	14
Silymarin	482.44 g/mol	5	2.79	120.55	10
Nobiletin	402.39 g/mol	0	3.96	106.87	8
Isovitexin	432.38 g/mol	7	1.94	106.61	10

TABLE IV. BIOACTIVITY OF FLAVONOIDS (USING MOLINSPIRATION)

Flavonoid	GPCR ligand	Ion Channel modulator	Kinase inhibitor	Nuclear receptor ligand	Protease inhibitor	Enzyme inhibitor
Engeletin	0.1	0.05	0.03	0.11	0.17	0.34
Iristectorigenin A	-0.22	-0.62	0.01	0.04	-0.67	0.03
Isorhoifolin	0.05	-0.32	-0.01	-0.03	0.01	0.24
Monoxerutin	-0.25	-0.9	-0.42	-0.53	0.17	-0.16
Neoeriocitrin	0.07	-0.5	-0.3	0.04	0.07	0.17
Narcissoside	-0.12	-0.66	-0.23	-0.36	-0.13	0.02
Poncirin	0.05	-0.52	-0.31	-0.08	0.06	0.15
Silymarin	0.07	-0.05	0.01	0.16	0.02	0.23
Nobiletin	-0.13	-0.04	0.09	0	-0.22	0.11
Isovitexin	0.12	0.02	0.15	0.23	0.04	0.47

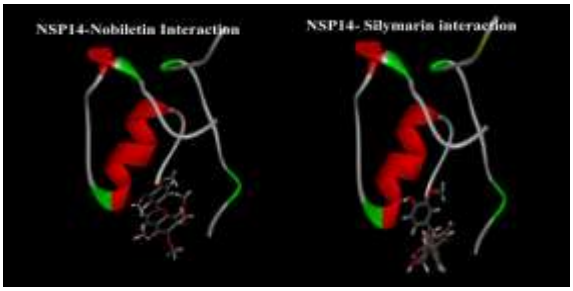

Fig. 2. Molecular Interactions of Flavonoids Nobiletin and Silymarin with target protein. (Source- UCSF Chimera)

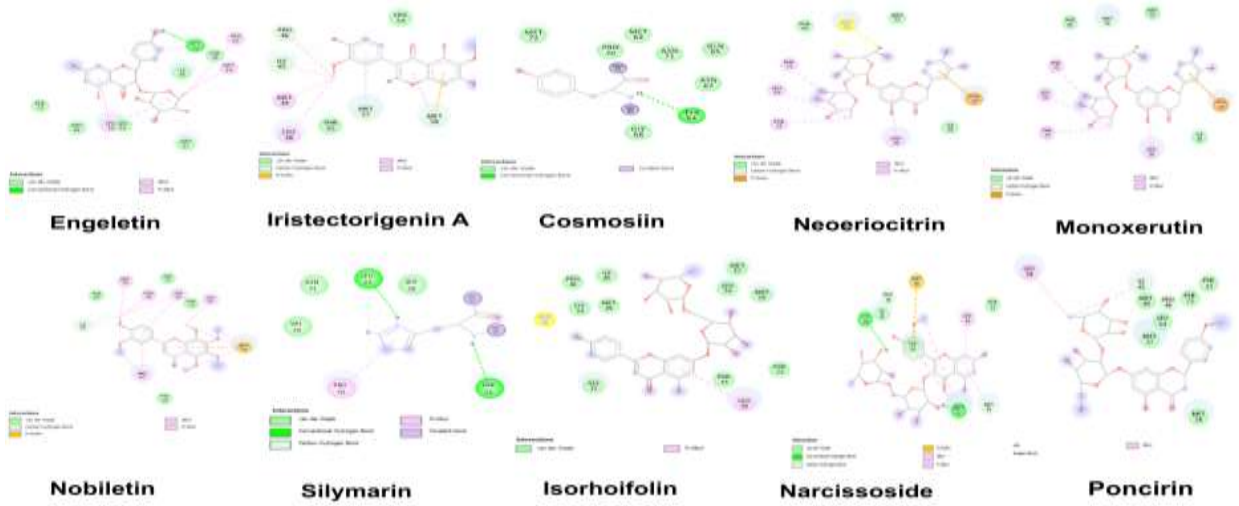

Fig. 3. Showing Protein-ligand Interaction of different Flavonoids (Using UCSF Chimera and Biovia Discovery Studio)

Authorized licensed use limited to: DELHI TECHNICAL UNIV. Downloaded on June 28,2023 at 06:31:23 UTC from IEEE Xplore. Restrictions apply.

V. CONCLUSION

When engineering drugs with a structural basis the protein ligand interaction is crucial. In the present work, the receptor of NSP14 of SARS CoV-2 were taken, followed by identification of various flavonoids which have higher binding energies than already approved repurposed drug Toremifene. Further the flavonoids which were showing high binding energies were examined under various pharmacokinetic and drug likeness parameters. Two flavonoids, Silymarin and Nobiletin, satisfied all pharmacokinetic and binding energy requirements, making them potential therapeutic agents. As flavonoids are phytochemicals with a wholly natural origin, there aren't much possibilities of causing any kind of harm. They are beneficial for health in a variety of ways, including by having anti-inflammatory, antioxidant, antibacterial, and antiviral effects. And hence, compared to the pharmaceuticals that are currently available on the market, flavonoids derived from natural sources can be thought of as a superior prospective therapeutic drug target for the treatment of COVID-19.

VI. REFERENCES

[1] S. Ludwig and A. Zarbock, "Coronaviruses and SARS-CoV-2: A Brief Overview," *Anesth Analg*, vol. 131, no. 1, pp. 93–96, Jul. 2020, doi: 10.1213/ANE.0000000000004845.

[2] A. Shannon *et al.*, "Remdesivir and SARS-CoV-2: Structural requirements at both nsp12 RdRp and nsp14 Exonuclease active-sites," *Antiviral Res*, vol. 178, p. 104793, Jun. 2020, doi: 10.1016/j.antiviral.2020.104793.

[3] M.-Y. Wang, R. Zhao, L.-J. Gao, X.-F. Gao, D.-P. Wang, and J.-M. Cao, "SARS-CoV-2: Structure, Biology, and Structure-Based Therapeutics Development," *Front Cell Infect Microbiol*, vol. 10, Nov. 2020, doi: 10.3389/fcimb.2020.587269.

[4] R. Arya *et al.*, "Structural insights into SARS-CoV-2 proteins," *J Mol Biol*, vol. 433, no. 2, p. 166725, Jan. 2021, doi: 10.1016/j.jmb.2020.11.024.

[5] B. Canal *et al.*, "Identifying SARS-CoV-2 antiviral compounds by screening for small molecule inhibitors of nsp14/nsp10 exoribonuclease," *Biochemical Journal*, vol. 478, no. 13, pp. 2445–2464, Jul. 2021, doi: 10.1042/BCJ20210198.

[6] W. R. Martin and F. Cheng, "Repurposing of FDA-Approved Toremifene to Treat COVID-19 by Blocking the Spike Glycoprotein and NSP14 of SARS-CoV-2," *J Proteome Res*, vol. 19, no. 11, pp. 4670–4677, Nov. 2020, doi: 10.1021/acs.jproteome.0c00397.

[7] L. Forchette, W. Sebastian, and T. Liu, "A Comprehensive Review of COVID-19 Virology, Vaccines, Variants, and Therapeutics," *Curr Med Sci*, vol. 41, no. 6, pp. 1037–1051, Dec. 2021, doi: 10.1007/s11596-021-2395-1.

[8] M. Gavriatopoulou *et al.*, "Emerging treatment strategies for COVID-19 infection," *Clin Exp Med*, vol. 21, no. 2, pp. 167–179, May 2021, doi: 10.1007/s10238-020-00671-y.

[9] I. Hadj Hassine, "Covid-19 vaccines and variants of concern: A review," *Rev Med Virol*, vol. 32, no. 4, Jul. 2022, doi: 10.1002/rmv.2313.

[10] G. A. Gyebi *et al.*, "Antimalarial phytochemicals as potential inhibitors of SARS-CoV-2 guanine N7-methyltransferase (nsp 14): an integrated computational approach," *J Biomol Struct Dyn*, pp. 1–23, May 2022, doi: 10.1080/07391102.2022.2078408.

[11] M. Russo, S. Moccia, C. Spagnuolo, I. Tedesco, and G. L. Russo, "Roles of flavonoids against coronavirus infection," *Chem Biol Interact*, vol. 328, p. 109211, Sep. 2020, doi: 10.1016/j.cbi.2020.109211.

[12] C. Liu, X. Zhu, Y. Lu, X. Zhang, X. Jia, and T. Yang, "Potential treatment with Chinese and Western medicine targeting NSP14 of SARS-CoV-2," *J Pharm Anal*, vol. 11, no. 3, pp. 272–277, Jun. 2021, doi: 10.1016/j.jpha.2020.08.002.

[13] G. M. Morris *et al.*, "AutoDock4 and AutoDockTools4: Automated docking with selective receptor flexibility," *J Comput Chem*, vol. 30, no. 16, pp. 2785–2791, Dec. 2009, doi: 10.1002/jcc.21256.

Authorized licensed use limited to: DELHI TECHNICAL UNIV. Downloaded on June 28,2023 at 06:31:23 UTC from IEEE Xplore. Restrictions apply.

Operations Management Research
https://doi.org/10.1007/s12063-023-00384-x

Coordination of circular supply chain for online recommerce platform in industry 4.0 environment: a game-theoretic approach

Dharmendra Kumar[1] · **Saurabh Agrawal**[2] · **Rajesh Kumar Singh**[3] · **Raj Kumar Singh**[1]

Received: 19 November 2022 / Revised: 26 February 2023 / Accepted: 21 May 2023
© The Author(s), under exclusive licence to Springer Science+Business Media, LLC, part of Springer Nature 2023

Abstract

In today's customer-oriented sustainable business environment, Industry 4.0 technologies may improve supply chain coordination, although their applicability in recommerce circular supply chain has not been thoroughly explored. The mobile application-based refurbishment company acquires end-of-life/end-of-use items from customers, refurbishes them, and resell them to end-users using an online recommerce platform. This study investigates the effects of extending product life and resource value of end-of-life/end-of-use products on channel performance in the era of industry 4.0. The issue of channel conflicts, pricing of refurbished products, and improving the quality of refurbished items with a warranty has been addressed. A Stackelberg game model is created to find the best supply chain decisions. In addition, we build four alternative scenarios: centralized, decentralized, revenue-sharing, and two-part tariff contract models and compared results to decide which of the scenario is the best. To assess the influence of relevant parameters on decisions, we present a numerical illustration and sensitivity analysis. We analyzed that decentralized channel needs further improvements and can achieve a win–win situation, but not in perfect coordination with a revenue-sharing contract. Our results also showed two-part tariff contract as a perfect coordination scenario i.e., most effective contracting approach for implementing extended producer responsibility regulation in the circular economy.

Keywords Circular economy · Sustainability · Industry 4.0 · Mobile technology · Extended producer responsibility · Coordination

Abbreviation

CE	Circular economy
SC	Supply chain
CSC	Circular supply chain
ORP	Online recommerce platform
WP	Wholesale price
RS	Revenue sharing
TPT	Two-part tariff
MABRC	Mobile application-based refurbishment company
Model C	Centralized model
Model D	Decentralized model
Model R	Revenue sharing contract model
Model T	Two-part tariff contract model

1 Introduction

Circular economy (CE) models aided by industry 4.0 technologies turn end-of-life goods into new, distinct products (Mastos et al. 2021). CE maximizes the value of resources and things by extending their useful lives and extracting the greatest value from them by reusing and recovering them at the end of their useful lives (Mishra et al. 2022b; Bressanelli et al. 2019). CE shifts towards using refurbished products with a warranty that may compete with new products. Implementing a CE relies heavily on circular thinking in SC management is called a circular supply chain (CSC) (Maranesi and De Giovanni 2020). The purpose of a CSC is to recycle

✉ Dharmendra Kumar
dharmendra.research@gmail.com

Saurabh Agrawal
agrawals.iit@gmail.com

Rajesh Kumar Singh
rajesh.singh@mdi.ac.in

Raj Kumar Singh
rajkumarsingh@dce.ac.in

[1] Mechanical, Production & Industrial Engineering Department, Delhi Technological University, Delhi, India

[2] Delhi School of Management, Delhi Technological University, Delhi, India

[3] Management Development Institute, Gurgaon, India

Published online: 24 June 2023

end-of-life/end-of-use products and turn them into new ones or to refurbish them and resell them (Taghikhah et al. 2019). Even, practitioners indicate that circularity fell from 9.1% in 2018 to 7.2% in 2023 due to rising material extraction. This indicates that over 90% of supplies are wasted, lost, or unusable (Economy 2023). Due to which use of the circular economy approach may boost economic expansion and increase gross domestic product (Knäble et al. 2022). A circular economy growth route might deliver India yearly benefits of US$ 624 billion in 2050, equal to 30% of India's GDP (Foundation 2016). Even, Government of India's E-waste Management guidelines 2016 indicates the procedure for collecting, channelizing, and disposing of e-waste in an environmentally responsible manner. Under E-waste (Management) Rules, 2016, manufacturers, e-retailers, and refurbishers have all been placed under the umbrella of extended producer responsibility (Arya and Kumar 2020). Because of the numerous benefits of a CSC, including economic value, research in this field is critical.

Utilizing the technological benefits of industry 4.0, online platforms (also called recommerce) allows buying and resale of used/refurbished items, like mobile phones (Bag et al. 2023; Chen et al. 2022). An online recommerce platform (ORP) utilizes a "product value extension" approach via refurbishing and a "resource value extension" strategy through recycling (Zucchella 2019). Implementing industry 4.0 technology at the individual level makes the SC less coordinated and results in inefficient resource usage (Singh et al. 2019). SCs should be carefully coordinated to make the most of these digital technologies (Ran et al. 2020). Decentralized industry 4.0 SC dominates the industry in sustainability when coordinated (Toktaş-Palut 2022). Coordination will also assist in performing specialized activities such as refurbishment (Whalen et al. 2018). A CSC requires close coordination to achieve a formal alliance (Berlin et al. 2022).

A major obstacle to implementing CSC is a lack of coordination among members (Ozkan-Ozen et al. 2020). For example, just 5% of the value of used plastic packaging gets captured (Agenda 2016). Coordination has become a key element in achieving a successful CE because it involves the consistent decision-making of various participants in the CSC to achieve common goals (Sudusinghe and Seuring 2022). Coordination is underrepresented in CE literature, implying a missed opportunity for implementing CE (Velenturf and Purnell 2021). The coordination issues of SCs in the context of the CE have become a new research paradigm (Fang et al. 2021; Li et al. 2021). A contract is an agreement made to control circular material flows. The agreement's revenue model determines the contract type (Fischer and Pascucci 2017). A relevant study topic could be designing coordination contracts to improve circular business models (Vegter et al. 2020). In this study, widely used coordination contracts, e.g., wholesale price (WP) contract, revenue sharing (RS) contract, and two-part tariff (TPT) contract, are applied (Cao and Zhang 2020; Darbari et al. 2019; Chen et al. 2021).

Refurbished products with quality and warranty service have relieved consumers from performance-related risks (Van Weelden et al. 2016). Although some papers (e.g., Chen et al. 2022; Sharifi and Shokouhyar 2021) investigated the selling price, warranty period, and quality level in the SC context, they have not been discussed in the coordination context. Some researchers (e.g., Hosseini-Motlagh et al. 2018; Ma et al. 2013) have focused on channel management with selling price, quality improvement, and warranty period. However, they did not consider the circularity of resources. One of the major barriers to CE is a lack of funding for undertaking investments for implementation of CE mandate (Scarpellini et al. 2019).

Therefore, to bridge existing research gaps, this research aims to find an effective method for coordinating decisions such as selling price, quality level, and warranty periods under various decision-making structures, as well as to investigate the consequences of these decisions on the performance of CSC in the industry 4.0 era. To achieve this objective, this study answers the following questions:

RQ1. Which contract structure most efficiently encourages the mobile application-based refurbishment company (MABRC) to focus on quality, motivates the ORP to provide warranty service, and optimizes SC profit?
RQ2. Is there a contract that can perfectly coordinate the CSC in the era of industry 4.0?
RQ3. How do the warranty period sensitivity coefficient and warranty investments parameter affect the key decision variables (e.g., retail price, warranty period, quality level, and profitability of players and entire SC?

This study contributes to the literature on CSC coordination in the age of industry 4.0, considering closing the resource loop by leveraging refurbishment and recycling processes. We start with the simplest and most popular contract type, i.e., the WP contract though it results in an inefficient solution. It is found that the problem under the WP contract in the decentralized channel can be improved. Subsequently, we have considered an RS contract and a TPT contract to achieve the system's optimal performance. We show that the RS contract can achieve a win–win outcome but cannot perfectly coordinate the channel. However, the TPT contract achieves both channel coordination and a win–win situation. Further, the contributions of this study are as follows:

- The study implements industry 4.0 technology to coordinate the CSC.

- Our study used recommerce business model of CE, which is rising rapidly at the current time (Tang and Chen 2022).
- This paper focused on coordinating mechanisms when demand is influenced by the selling price, quality level, and warranty duration of refurbished products.
- Studies on CSCs (e.g., Farooque et al. 2019; Lahane et al. 2020) have recommended that coordination contracts be developed to optimize the CSC in the era of industry 4.0. Our research is focused on selecting the most appropriate contract for effectively coordinating the CSC.
- We investigate the impacts of the warranty period sensitivity coefficient and warranty investment parameter on channel decisions and the profitability of channel players.

The remaining sections of the article are organized as follows. A review of related literature is discussed in Section 2, and the research methodology is described in Section 3. In Section 5, a description of the problem is provided. Discussion of results is carried out through the numerical illustration and sensitivity analysis in Section 6. In Section 7, managerial implications are discussed. Finally, Section 7 defines research results, limitations, and guidelines for future research.

2 Literature review

This study investigates CSC coordination by implementing circular economy business model strategies in the era of industry 4.0 using a game-theoretic framework wherein demand is a function of the selling price, warranty time, and refurbished product quality. The literature is summarized in the following sub-sections:

2.1 Implementation of circular models for ORP in the industry 4.0 age

Circularity, digitization, and industry 4.0 promote sustainability (Prajapati et al. 2022a; Dwivedi and Paul 2022; Mishra et al. 2022a). Adopting a circular economy is difficult since most organizations depend on a linear growth model (Husain et al. 2021). The role of industry 4.0 technologies in improving sustainability has been explained by various researchers (e.g., Patidar et al. 2022; Jamwal et al. 2021a, b). Some researches (Hettiarachchi et al. 2022; Khan et al. 2022; Bhattacharya 2021; Dev et al. 2020) have suggested using Industry 4.0 and CE concepts together to achieve sustainability. Bocken et al. (2016) proposed three business development strategies: limiting resource flows by utilizing fewer resources per product, slowing resource loops by prolonging product life or designing long-life products, and completing the loop by recycling. Previous studies (e.g., den Hollander and Bakker 2016; Whalen 2019; Han et al. 2020) suggested various CE business models, including recommerce model, to capture product system value. Many industries have used the recommerce business model of circular economy, including consumer electronics, digital devices, and fashion (Tang et al. 2022; Tang and Chen 2022; Slaton and Pookulangara 2022). Companies like Gazelle, Yerdle, Thredup, rebuy, and Loopster utilizes ORPs (Matsui 2022; Chu et al. 2021; Caro et al. 2020).

Some studies have considered recommerce business (e.g., Chu et al. 2021; Yrjölä et al. 2021). ORPs facilitate extending the usable life of an end-of-life/end-of-use/customer-returned product (Ertz et al. 2019). Exploiting leftover value is done by extending the useful life of goods through designing for refurbishment in recommerce business (Nußholz 2017). Refurbished consumer electronics items are sold in the secondary market at a lower price after minor cleanup and repackaging operations (Pan and Huynh 2022; Jauhari et al. 2020). Ripanti et al. (2016) deliberated the application of CE concepts for designing product refurbish operations. Giri et al. (2018) have considered refurbishing pre-owned products after their useful life for the smooth functioning of the channel and making appropriate decisions. Schlosser et al. (2021) have mentioned that recycling is also a key activity on the CE platform. Santana et al. (2021) discussed the refurbishment and recycling of cell phones to achieve sustainability goals. Accordingly, recommerce business model of CE has been used for the present study.

2.2 Application of industry 4.0 technologies in SC coordination

Digital technology may improve supply chain performance and encourage sustainable initiatives, according to industry (Akbari and Hopkins 2022; Mukherjee et al. 2022). Numerous researchers have investigated SC coordination in the context of various technologies considered under industry 4.0 (e.g., Big data (Hu et al. 2022), Block chain (Ding and Bai 2022; De Giovanni 2020), and Internet of things (Yadav et al. 2022)). Coordination contracts are typical coordination strategies. Blockchain, Big data, and IoT are the most debated technologies allowing such strategies. Digital technologies, particularly mobile phones, help in effective implementation of Industry 4.0 (Gallego-García et al. 2022; Agnusdei et al. 2022; Shahin et al. 2020). Some literature (e.g., Bai et al. 2020; Zhou et al. 2021; Nascimento et al. 2019; Wang and Wang 2019) emphasized that mobile technology may be useful for recycling purposes to achieve sustainability goals. Accordingly, in this study, mobile technology has been considered. Industry 4.0 technology helps construct a coordinated CSC (Gebhardt et al. 2022; Kumar and Singh 2021; Tiwari 2021). Accordingly, CSC coordination with industry 4.0 technology is considered in the present study; however, it has not been studied earlier.

2.3 Application of game theory for channel coordination in CSC

To achieve different objectives related to the CE (such as economic growth, environmental sustainability and social responsibility), the players' strategies must be coordinated (Maranesi and De Giovanni 2020). Coordination is critical because a business entity cannot have all in-house processing arrangements. Some of the literature (e.g., Mangla et al. 2018; Ozkan-Ozen et al. 2020) found that one of the major barriers to successful CSC management is a lack of coordination among SC participants. Leal Filho et al. (2019) also marked the same reason for poor textile recycling. The game-theoretic paradigm has been used to address CSC challenges in the CE (Choi et al. 2020; Cao and Zhang 2020). In a CE approach, the game theory may facilitate agreement among stakeholders and the settlement of disputes (Palafox-Alcantar et al. 2020). The optimum SC decisions are obtained using a Stackelberg game model. It is widely used to investigate SC decision-making behaviors (Cheng et al. 2018).

Some literature has also used smart contracts based on Blockchain technology (e.g., De Giovanni 2020). However, some literature has demonstrated that an RS contract could not coordinate the sustainable SC (Xu et al.. 2016), but the TPT contract can perfectly coordinate the same (Kuiti et al. 2019; Chen et al. 2017). The Stackelberg model was used in the majority of previous literature. According to the analysis, the RS contract and the TPT contract will be employed in Stackelberg game model to coordinate the current investigation.

2.4 Pricing, warranty, and quality strategies for refurbished products

Many recent studies have recommended that selling price, warranty period, and quality level are important factors for a refurbished product from a customer perspective (e.g., Chen et al. 2022; Sharifi and Shokouhyar 2021; Nasiri and Shokouhyar 2021). Several studies (e.g., Ovchinnikov 2011; Yoo and Kim 2016; Zhang et al. 2019b) have investigated the optimal prices for new and refurbished products. Sadeghi et al. (2019) and Li et al. (2010) investigated the pricing decision of refurbished products in different channel structures. Zhang et al. (2019b) looked at new and refurbished products' quality and pricing decisions. Niu and Xie (2020) investigated the impact of quality uncertainty of refurbished products on Green SC. Pinçe et al. (2016) considered an allocation problem in choosing whether refurbished consumer returns would be used to fulfill warranty claims or remarketed as refurbished products to extract maximum value over the product's lifecycle.

Consumers who buy used/refurbished goods are concerned about product quality and warranty service (Esmaeilian et al. 2021; Liu et al. 2018; Oraiopoulos et al. 2012). Van Weelden et al. (2016) described that refurbished products with quality and warranty service would relieve consumers from performance-related risk. Nasiri and Shokouhyar (2021) explored two perceived consumer values, i.e., incentive and quality, including product warranty of refurbished smartphones. Sharifi and Shokouhyar (2021) identified four influential factors: (i) price, (ii) warranty, (iii) quality, and (iv) retailer reputation for promoting the refurbished mobile phone. On the basis of the above discussion, pricing, warranty, and quality strategies for refurbished products have been considered in this proposal.

2.5 Research gaps

The emphasis of the studies mentioned above was on the price of new and refurbished items. Some papers have highlighted the importance of quality and warranty issues on consumer purchase behavior. Some literature has discussed coordination issues utilizing game-theoretical settings in the industry 4.0 context. However, they did not use CE strategies (e.g., Toktaş-Palut 2022; Liu and De Giovanni 2019). Some literature has discussed coordination issues utilizing game theoretical settings and circular economy strategies. However, they did not use industry 4.0 technologies and did not consider end-of-use/end-of-life/customer-returned products for their study (e.g., Li et al. 2021; Fang et al. 2021). CSC coordination in the era of industry 4.0 technology has not been considered in the earlier study; however, it has a major obstacle to implementing CSC (Ran et al. 2020; Ozkan-Ozen et al. 2020). The above discussions demonstrate that our research challenges are significant yet unexplored. The discrepancy between our study and the most relevant research is shown in Table 1.

3 Research methodology

This paper investigates a two-echelon CSC consisting of a mobile application-based refurbishment company (MABRC) and an online recommerce platform (ORP) in the era of industry 4.0. The decision variables are wholesale price and quality level for the MABRC and the warranty period and selling price for ORP, respectively.

The game-theory models are made using different channel powers (Agrawal et al. 2022b). Firstly, the decentralized channel under the Stackelberg model has been analyzed (Zhang et al. 2019c). In a decentralized channel scenario, the MABRC and ORP make their own decisions under wholesale price contracts to increase

Table 1 the comparison between our study and the most related studies

Literature	Coordination mechanism	Types of SC	Modeling technique	Types of industry 4.0 technology
Hu et al. (2022)	Zero WP-side-payment contract and greedy WP-side-payment contract	Forward supply chain (FSC)	Stackelberg game model (SGM)	Big data (BD)
Ding and Bai (2022)	Hybrid contract based on benefit-sharing and cost-sharing (CS)	FSC	SGM	Blockchain technology (BT)
De Giovanni (2020)	Smart WP contract and Smart RS contract	FSC	SGM	BT
Yadav et al. (2022)	IoT-oriented coordinating mechanism	FSC	Interpretive Structural model and Fuzzy DEMATEL model	Internet of things
Li et al. (2021)	WP contract, CS contract and RS contract	FSC	SGM	-
Fang et al. (2021)	WP contract	Closed loop SC	Newsboy model and Stackelberg model	-
Toktaş-Palut (2022)	RS contract	FSC	Stackelberg model and Nash bargaining	Industry 4.0 technology (in general but not specific)
Liu and De Giovanni (2019)	WP contract and RS contract	FSC	Differential game model	Industry 4.0 technology (in general but not specific)
Our paper	WP contract, RS contract and TPT contract	CSC	Stackelberg game	Mobile technology

revenues. To compare the performance of this model, a benchmark model in a centralized channel setting is to be built. In the centralized channel, the MABRC and the ORP are vertically integrated, and they aim to optimize the whole channel's profit. Therefore, the goal is to evaluate the optimum values of the decision variables that maximize the total profit of the whole channel. Studies have demonstrated that a centralized approach works better than a decentralized one (Raj et al. 2018). But the players won't always be able to work as a unified unit. Therefore, decentralized models need effective coordination structures.

To that, a coordination contract is designed from the perspective of the MABRC, the game's leader, and offers a contract to the ORP. The MABRC has offered an RS contract to the ORP to decide the best choices for maximizing the entire supply chain's revenues. The ORP has agreed to share the revenue to be received from refurbished goods re-market under this contract. Under the RS contract, the MABRC will use a lower wholesale price to induce the ORP to share sale revenue. It will increase overall channel efficiency compared to the decentralized channel model; however, SC couldn't be perfectly coordinated.

Further, to coordinate perfectly, a TPT contract is designed. Finally, numerical demonstration and sensitivity analysis are used to test the proposed model. Figure 1 summarizes the steps of the research methodology.

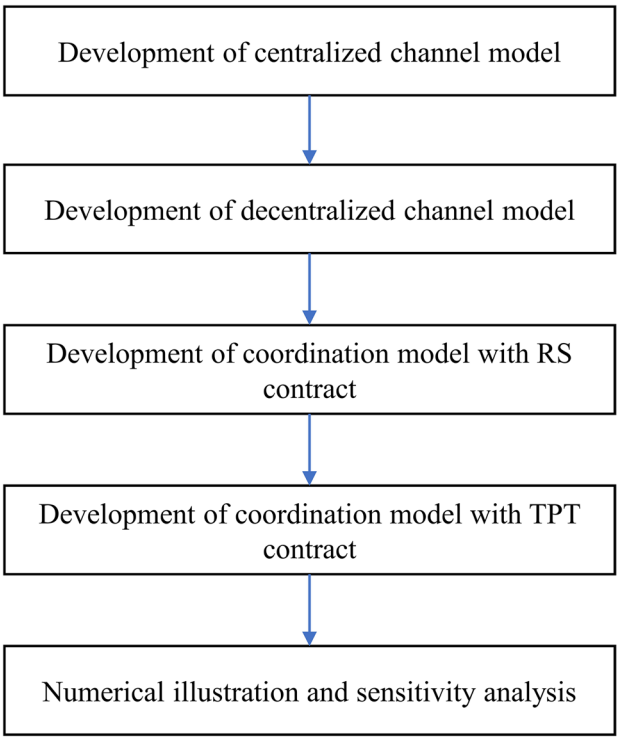

Fig. 1 Methodology steps

4 Model development

This section describes the model's assumptions, notations, description, formulation, and analysis. The centralized, decentralized, and coordinating models are built to examine equilibrium decisions using the technique described in the preceding section.

4.1 Assumptions

We use the following assumptions to ensure analytical consistency and agreement with previous work: -

1. A two-echelon CSC has a mobile application-based refurbishment company (MABRC) and an online recommerce platform (ORP) (Liu et al. 2022) that sells a single type of refurbished product on the secondary market through online retailing in the era of industry 4.0 technology.
2. The same information is accessed by both the members of the SC who are risk-neutral (Rong and Xu 2020).
3. The linear deterministic market demand dependent on the selling price, warranty period, and quality level of the refurbished product is considered for channel decisions (Panda et al. 2017; Zhang et al. 2019a).
4. All used products collected can be categorized into refurbishable and non-refurbishable products. Refurbishable products are sold in the secondary market after refurbishment (Oraiopoulos et al. 2012). Non-refurbishable products are sold to a recycler as e-waste (Yoo and Kim 2016).
5. It is assumed that the unit cost of refurbishment and salvage value is constant for all refurbishable and non-refurbishable products, respectively (Reimann 2016). The unit cost of refurbishment includes cost along with transportation, cleaning, inspection, and other indirect costs.
6. There will be no shortages (Mishra et al. 2020).

4.2 Notations

The parameters used in this paper are explained as follows:p: Unit retail price for a refurbished product to the end-user in the secondary market$c$: Unit acquisition cost of the end-of-life/end-of-use products$q$: Wholesale price of recycler$t$: Refurbishing cost of the MABRCd: Secondary market demand for refurbished goods, where $d \geq 0$. The demand function is illustrated as:

$$d = a - bp + kw + ly \tag{1}$$

a Demand potential for a refurbished item. Note: a > 0.

b Price sensitivity of demand. Note: b > 0

w Warranty period.

k Warranty period sensitivity coefficient. Note: $k > 0$.

y Quality level of refurbished products

l Quality level sensitivity coefficient. Note: $l > 0$.

z Recovery rate of end-of-use/end-of-life item that can be refurbished

g Items procured by the recycler. The expression of g is expressed as:

$$g = d/z \tag{2}$$

s Salvage price of a non-refurbishable item. Note: $s < c$.

π_O^I Profitability function of a participant O in the SC model I.

I Superscript, $I = D, C, R, T$ Where D: decentralized channel, C: centralized channel, R: RS contract model, T: TPT contract model.

O Subscript, $O =$ Ref (MABRC), Rec (ORP), Csc (CSC).

$*$ Indicates optimal model parameter values.

F Lump sum fee under the TPT contract model.

u Warranty investment parameter

x Quality investment parameter

The warranty cost is assumed to be a strictly convex function, which is represented as uw^2. Note: $u > 0; w > 0$.

It is also believed that the quality improvement cost is a strictly convex function, which is written as xy^2. Note: $x > 0; y > 0$.

4.3 Problem description

A CSC consisting of a mobile application-based refurbishment company (MABRC) and an online recommerce platform (ORP) is considered in the industry 4.0 era. The

MABRC collects used items through the mobile-based application from end-users or retailers/OEMs that have collected used items through various schemes such as an exchange program/buyback program to fulfill the direction laid down under extended producer responsibility in the implementation of e-waste (Management) Rules, 2016. These collected products are inspected and sorted into two categories: refurbishable and non-refurbishable (Prajapati et al. 2022b; Resmi and Fasila 2017). Products categorized as refurbishable are processed for data sanitization to clean the hard drives. After inspection and data cleansing, the item is subjected to extensive testing to see if repairs are necessary.

To ensure adequate quality, the product has been transported for quality control. If it passes the quality check, they are cleaned to restore the original look as much as possible. MABRC makes efforts to improve the quality of refurbished quality. Accordingly, the MABRC makes decisions towards investment for the quality level of refurbished items. Finally, they are repackaged with new wrapping material enclosing all accessories. Products that fail during the inspection process are categorized as non-refurbishable. They are sent as electronic waste to a material recycler, who then uses the recycling process to recover the valuable recyclable material.

The MABRC works with the ORP operating in the secondary market. The MABRC sells the refurbished products at the wholesale price to the ORP, which then sells these products along with a warranty to the final customers in the secondary market at the retail price through online retailing. Customers will be provided free after-sales warranty services by the ORP and decide on warranty investment accordingly. The material flow in CSC is shown pictorially in Fig. 2. The area inside the dotted line is the focus of the analysis.

4.3.1 Model development

As the refurbishment firm leads the SC, the following series of events is predicted by the Stackelberg game approach. First, the MABRC determines the wholesale price q and quality level y. Then ORP places an order of quantity g with the actual output of refurbished products is $d = gz$ and decides the warranty period w and unit retail price p of the refurbished product.

Considering the scenario mentioned above:

Total refurbished goods for sale = gz.

Quantity of items that cannot be refurbished = $(1 - z)g$.

Total expenditures for refurbishment = zgt.

Revenue generated from the sale of non-refurbishable items = $(1 - z)gs$.

The expression of profit for the MABRC is given as: $gzq - gc + g(1 - z)s - gzt - xy^2$.

The expression of profit for the ORP is given as: $gzp - gzq - uw^2$.

The overall profit function of the SC is stated as: $gzp + (1 - z)gs - gzt - gc - uw^2 - xy^2$.

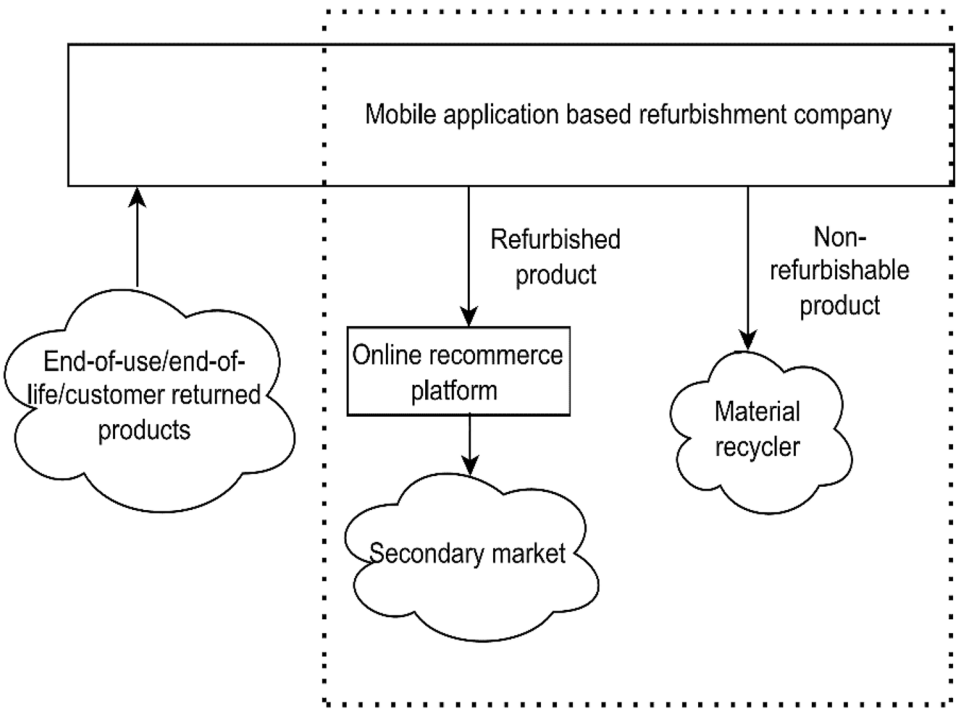

Fig. 2 Investigated model of circular supply chain

4.3.2 Decentralized channel model (model D)

In a decentralized channel scenario, the MABRC and ORP make their own decisions to increase their profits. In this setting, the MABRC sells the refurbished products to the ORP at wholesale price. A Stackelberg game model led by the MABRC is developed, and the solution is obtained through a WP contract. First, the MABRC offers a contract to the ORP. ORP determines whether to accept or reject a contract offer. The dynamic game order is as follows: firstly, a refurbishing determines the unit wholesale price q and quality level y, then the ORP reacts to determine the retail price p and warranty period w. Using the inverse induction method, first solve the profit function of the ORP.

The profit function for the ORP is expressed as:

$$\pi_{\text{Rec}}^{D} = gzp - gzq - uw^2 \tag{3}$$

After substituting the result of Eq. (2) into Eq. (3), the expression for π_{Rec}^{D} is obtained as:

$$\pi_{\text{Rec}}^{D} = (p-q)(a - bp + kw + ly) - uw^2 \tag{4}$$

Solving the first-order condition of Eq. (4) with respect to p and w, the following expressions obtained:

$$\frac{\partial \pi_{\text{Rec}}^{D}}{\partial p} = -b(2p - q) + ly + kw + a = 0 \tag{5}$$

$$\frac{\partial \pi_{\text{Rec}}^{D}}{\partial w} = k(p - q) - 2uw = 0 \tag{6}$$

Solving the second-order conditions of Eq. (4) with respect to p, w and y, the following expressions obtained:

$$\frac{\partial^2 \pi_{\text{Rec}}^{D}}{\partial p^2} = -2b \tag{7}$$

$$\frac{\partial^2 \pi_{\text{Rec}}^{D}}{\partial p \partial w} = k \tag{8}$$

$$\frac{\partial^2 \pi_{\text{Rec}}^{D}}{\partial w \partial p} = k \tag{9}$$

$$\frac{\partial^2 \pi_{\text{Rec}}^{D}}{\partial w^2} = -2u \tag{10}$$

The expression of the Hessian matrix corresponding to the profit function for the ORP under the decentralized channel is

$$H(p, w) = \begin{pmatrix} -2b & k \\ k & -2u \end{pmatrix}$$

Thus, the ORP's profit function is jointly concave in p and w if the Hessian $H(p, w)$ is negative definite. This results in the following conditions:

$$H_{11} = -2b < 0$$

$$H_{22} = 4bu - k^2 > 0$$

Solving Eqs. (5) and (6), we get the value of p and w as:

$$p = \frac{2luy + q(2bu - k^2) + 2au}{4bu - k^2} \tag{11}$$

$$w = \frac{kly - bkq + ak}{4bu - k^2} \tag{12}$$

The profit function for the MABRC is expressed as:

$$\pi_{\text{Ref}}^{D} = gzq + g(1 - z)s - gc - gzt - xy^2 \tag{13}$$

Substituting g's value from Eq. (2) into Eq. (13), we get the equation for π_{Ref}^{D} is as:

$$\pi_{\text{Ref}}^{D} = (zq + (1 - z)s - c - zt)\left(\frac{a - bp + kw + ly}{z}\right) - xy^2 \tag{14}$$

First, taking the value of p and w from Eqs. (11) and (12) in Eq. (14), and then solving the first-order condition of Eq. (14) with respect to q and y, the expressions obtained as follows:

$$\frac{\partial \pi_{\text{Ref}}^{D}}{\partial q} = -\frac{2bu(z(b(2q - t - s) - ly - a) + b(s - c))}{(4bu - k^2)z} = 0 \tag{15}$$

$$\frac{\partial \pi_{\text{Ref}}^{D}}{\partial y} = -\frac{((8bu - 2k^2)xy + (2blt + 2bls - 2blq)u)z + (2bcl - 2bls)u}{(4bu - k^2)z} = 0 \tag{16}$$

Equations (15) and (16) have been solved, and optimal values of q and y have been found; then, taking this optimal value in Eqs. (11) and (12), we get the following proposition 1.

Proposition 1 *The optimal solution that maximizes the decentralized channel profit is achieved at*

$$q^{D*} = \frac{(((4b^2t + 4b^2s + 4ab)u - bk^2t - bk^2s - ak^2)x + (-bl^2t - bl^2s)u)z + ((4b^2c - 4b^2s)u + bk^2s - bck^2)x + (bl^2s - bcl^2)u}{((8b^2u - 2bk^2)x - bl^2u)z} \tag{17}$$

$$y^{D*} = -\frac{(blt + bls - al)uz + (bcl - bls)u}{((8bu - 2k^2)x - l^2u)z} \tag{18}$$

$$p^{D*} = \frac{((2b(b(t+s)+3a)u - bk^2t - bk^2s - ak^2)x - bl^2(t+s)u)z - b(s-c)(2bu-k^2)x + bl^2(s-c)u}{b(2(4bu-k^2)x - l^2u)z} \tag{19}$$

$$w^{D*} = -\frac{(kx((b(t+s)-a)z - b(s-c)))}{(2(4bu-k^2)x - l^2u)z} \tag{20}$$

$$\pi_{\text{Rec}}^{D*} = \frac{u(4bu-k^2)x^2((b(t+s)-a)z - b(s-c))^2}{(2(4bu-k^2)x - l^2u)^2z^2} \tag{21}$$

$$\pi_{\text{Ref}}^{D*} = \frac{ux((b(t+s)-a)z - b(s-c))^2}{(2(4bu-k^2)x - l^2u)z^2} \tag{22}$$

$$\pi_{\text{Csc}}^{D*} = \frac{(ux(3(4bu-k^2)x - l^2u)((b(t+s)-a)z - b(s-c))^2)}{((2(4bu-k^2)x - l^2u)^2z^2)} \tag{23}$$

Optimal demand under decentralized channel:

$$d^{D*} = -\frac{(2bux((b(t+s)-a)z - b(s-c)))}{((2(4bu-k^2)x - l^2u)z)} \tag{24}$$

Proposition 1 gives the optimal wholesale price, retail price, warranty period, quality level, and profits of the MABRC and ORP in the decentralized setting under the WP contract. It is also observed that the expected profit under the centralized channel is higher than the decentralized channel because the double marginal behavior reduces total profit under the decentralized channel (*Raj et al.* 2018). *Accordingly, to compare the performance of the decentralized channel, we have developed a benchmark model in a centralized channel setting in the following section.*

4.3.3 Centralized channel model (model C)

In this part, we investigate the scenario where a decision-maker may choose the optimal retail price, quality level, and warranty duration to build the study's benchmark. To optimize the expected profit of the whole SC, the centralized channel's decision-maker is a viable approach. In this case, the equilibrium decisions will be optimized globally. The equilibrium results will be a reference point for subsequent discussion (Biswas et al. 2018).

The profit function for the whole SC is expressed as

$$\pi_{\text{Csc}}^{C} = gzp + g(1-z)s - gc - gzt - uw^2 - xy^2 \tag{25}$$

After taking the value of g from Eq. (2) into Eq. (25), the expression for Π_{Csc}^{c} is given as:

$$\pi_{\text{Csc}}^{C} = (zp + (1-z)s - c - zt)(\frac{(a - bp + kw + ly)}{z}) - uw^2 - xy^2 \tag{26}$$

After solving the first-order condition of Eq. (26) with respect to p, w and y, we get the following expressions:

$$\frac{\partial \pi_{\text{Csc}}^{C}}{\partial p} = (-b(2p - t - s) - \frac{b(s-c)}{z} + ly + kw + a) = 0 \tag{27}$$

$$\frac{\partial \pi_{\text{Csc}}^{C}}{\partial w} = (\frac{k(-tz + pz + s(1-z) - c)}{z} - 2uw) = 0 \tag{28}$$

$$\frac{\partial \pi_{\text{Csc}}^{C}}{\partial y} = (\frac{l(-tz + pz + s(1-z) - c)}{z} - 2xy) = 0 \tag{29}$$

After solving the second-order conditions of Eq. (26) with respect to p, w and y, we get the following expressions:

$$\frac{\partial^2 \pi_{\text{Csc}}^{C}}{\partial p^2} = -2b \tag{30}$$

$$\frac{\partial^2 \pi_{\text{Csc}}^{C}}{\partial p \partial w} = k \tag{31}$$

$$\frac{\partial^2 \pi_{\text{Csc}}^{C}}{\partial p \partial y} = l \tag{32}$$

$$\frac{\partial^2 \pi_{\text{Csc}}^{C}}{\partial w \partial p} = k \tag{33}$$

$$\frac{\partial^2 \pi_{\text{Csc}}^{C}}{\partial w^2} = -2u \tag{34}$$

$$\frac{\partial^2 \pi_{\text{Csc}}^{C}}{\partial w \partial y} = 0 \tag{35}$$

$$\frac{\partial^2 \pi_{\text{Csc}}^{C}}{\partial y \partial p} = l \tag{36}$$

$$\frac{\partial^2 \pi_{\text{Csc}}^{C}}{\partial y \partial w} = 0 \tag{37}$$

$$\frac{\partial^2 \pi_{\text{Csc}}^{C}}{\partial y^2} = -2x \tag{38}$$

To prove the concavity of profit function of the centralized channel with respect to p, w and y, Hessian matrix is found as follows:

$$\begin{pmatrix} -2b & k & l \\ k & -2u & 0 \\ l & 0 & -2x \end{pmatrix}$$

If the Hessian Matrix's principal minors are alternately negative and positive, the function will be concave (Modak et al. 2019). Accordingly, the following conditions are obtained:

$$H_{11} = -2b < 0$$

$$H_{22} = 4bu - k^2 > 0$$

$$H_{33} = -8bux + 2k^2x + l^2u < 0$$

Solving Eqs. (27) to (29), we get proposition 2, which is as follows.

Proposition 2 *The optimal solution that maximizes the centralized channel profit is achieved at.*

$$p^{C*} = \frac{(((t(2bu-k^2)+s(2bu-k^2)+2au)x - l^2tu - l^2su)z + (c(2bu-k^2)+s(k^2-2bu))x + l^2su - cl^2u)}{((4bu-k^2)x - l^2u)z} \tag{39}$$

$$w^{C*} = -\frac{((bkt+bks-ak)xz + (bck-bks)x)}{((4bu-k^2)x - l^2u)z} \tag{40}$$

$$y^{C*} = -\frac{((bltu+blsu-alu)z - blsu + bclu)}{((4bu-k^2)x - l^2u)z} \tag{41}$$

The optimal profit under the centralized channel is achieved as follows:

$$\pi_{\text{Csc}}^{C*} = \frac{(ux((b(t+s)-a)z - b(s-c))^2)}{(((4bu-k^2)x - l^2u)z^2)} \tag{42}$$

Optimal demand under centralized channel:

$$d^{C*} = -\frac{(2bux((b(t+s)-a)z - b(s-c)))}{((4bu-k^2)x - l^2u)z} \tag{43}$$

Proposition 2 gives the optimal retail price, warranty period, quality level, and SC profit in the centralized setting. The centralized scenario merely raises the profit of the entire SC and cannot ensure that each member will make a satisfactory profit (*Heydari and Rafiei 2020*). *To address the disadvantages of the centralized and decentralized channels under WP contract, a coordination model using the RS contract is presented in the next subsection.*

4.3.4 RS contract model (model R)

The RS contract is formulated to improve the effectiveness of the decentralized model (Sharma et al. 2022; Rong and Xu 2020). The MABRC has offered an RS contract under which the ORP shares its revenue received through remarketing of refurbished items with the MABRC. It is considered that the ORP retains a portion j of the selling price and shares the remaining $(1-j)$ with the MABRC. A Stackelberg game model led by the MABRC is developed. The MABRC first determines the wholesale price q and quality level y, and then on this basis, the ORP determines the retail price p and warranty period w. Finally, the online recommerce platform determines the revenue fraction j. Initially, the profit function for the online recommerce platform is solved using the reverse induction approach.

The profit function for the online recommerce platform is expressed as:

$$\pi_{\text{Rec}}^{R} = jgzp - gzq - uw^2 \tag{44}$$

After substituting the value of g using Eq. (2) into Eq. (44), the expression for π_{Rec}^{R} is:

$$\pi_{\text{Rec}}^{R} = (jp-q)(a-bp+kw+ly) - uw^2 \tag{45}$$

Solving the first-order condition of Eq. (45) with respect to p and w, the following expressions obtained:

$$\frac{\partial \pi_{\text{Rec}}^{D}}{\partial p} = j(ly+kw+a) - b(2jp-q) = 0 \tag{46}$$

$$\frac{\partial \pi_{\text{Rec}}^{D}}{\partial w} = k(jp-q) - 2uw = 0 \tag{47}$$

Solving Eqs. (46) and (47), we get the value of p and w, as:

$$p = \frac{(u(j(2ly+2a)+2bq) - jk^2q)}{j(4bu-jk^2)} \tag{48}$$

$$w = -\frac{(bkq - jk(ly+a))}{(4bu-jk^2)} \tag{49}$$

The profit function for the MABRC is expressed as:

$$\pi_{\text{Ref}}^{R} = (1-j)p(a-bp+kw+ly) + gzq + g(1-z)s - gc - gzt - xy^2 \tag{50}$$

After taking the value of g from Eq. (2) into equations of (50), the expression of π_{Ref}^{R} is given as:

$$\pi_{\text{Ref}}^{R} = ((1-j)pz + (zq + (1-z)s - c - zt))\left(\frac{(a-bp+kw+ly)}{z}\right) - xy^2 \tag{51}$$

First, taking the value of p and w from Eqs. (48) and (49) in Eq. (51), and then solving the first-order condition of Eq. (51) with respect to q and y, the following expressions obtained:

We put Eqs. (54)–(57) into Eq. (45) and then obtain the first derivative of j:

$$\frac{\partial \pi^{R}_{Ref}}{\partial q} = -\frac{\begin{array}{l}(2bu(2b(2b(j+1)u - jk^2)zq - j(4bjluy - jk^2ly + 4b^2tu + 4b^2su + 4abju - bjk^2t - bjk^2s - ajk^2)z + \\ 4b^2j(s-c)u - bj^2k^2s + bcj^2k^2))\end{array}}{(j^2(4bu - jk^2)^2z)} = 0 \tag{52}$$

$$\frac{\partial \pi^{R}_{\mathrm{Ref}}}{\partial y} = -\frac{\begin{array}{l}(2(((4bu - jk^2)^2x + 4b(j-1)l^2u^2)zy + blu(4(b(t+s-q) + a(j-1))u - \\ k^2(j(t+s) - q))z - 4b^2l(s-c)u^2 + bjk^2l(s-c)u))\end{array}}{((4bu - jk^2)^2z)} = 0 \tag{53}$$

Equations (52) and (53) have been solved, and optimal values of q and y have been found; then, taking this optimal value in Eqs. (48) and (49), we get the following expressions for q,y, p and w:

$$\frac{\partial \pi^{R}_{\mathrm{Rec}}}{\partial j} = -\frac{(2u^2x^2((b(t+s)-a)z - bs + bc)^2((8b^2ux - k^2l^2)j - 8b^2ux + 2bl^2u))}{(z^2(2(2bu - k^2)xj + 4bux - l^2u)^3)} \tag{58}$$

$$q = \frac{\begin{array}{l}(((((u(t(bjl^2 - 4b^2jx) + s(bjl^2 - 4b^2jx) - 4abj^2x) + bj^2k^2tx + bj^2k^2sx + aj^2k^2x)z + \\ u(s(4b^2jx - bjl^2) - 4b^2cjx + bcjl^2) - bj^2k^2sx + bcj^2k^2x))\end{array}}{((b((u(-4bjx - 4bx + l^2) + 2jk^2x)z))))} \tag{54}$$

$$y = \frac{((blt + bls - al)uz + (bcl - bls)u)}{((u(-4bjx - 4bx + l^2) + 2jk^2x)z)} \tag{55}$$

$$p = \frac{\begin{array}{l}((2b(b(t+s) + a(2j+1))u - bjk^2t - bjk^2s - ajk^2)x - bl^2(t+s)u)z - \\ b(s-c)(2bu - jk^2)x + bl^2(s-c)u\end{array}}{b(2(2b(j+1)u - jk^2)x - l^2u)z} \tag{56}$$

$$w = -\frac{(jkx((b(t+s)-a)z - b(s-c)))}{(2(2b(j+1)u - jk^2)x - l^2u)z} \tag{57}$$

We set the first derivative equal to zero and obtain the optimal value of j is as:

$$j^{R*} = \frac{(8b^2ux - 2bl^2u)}{(8b^2ux - k^2l^2)} \tag{59}$$

After substituting the optimal value of j, we get the following proposition 3.

Proposition 3 *The optimal solution that maximizes the decentralized channel profit after applying the coordination model mechanism, namely the RS contract, is achieved as*

$$p^{R*} = \frac{\begin{array}{l}((8b(2b^2tu + 2b^2su + 6abu - bk^2t - bk^2s - ak^2)x^2 - 8bl^2(b(t+s) + a)ux + k^2l^4t + k^2l^4s)z - \\ 8b^2(s-c)(2bu - k^2)x^2 + 8b^2l^2(s-c)ux - k^2l^4s + ck^2l^4)\end{array}}{(4bx - l^2)(16b^2ux - 4bk^2x - k^2l^2)z} \tag{60}$$

$$w^{R*} = -\frac{(2bkx((b(t+s)-a)z - b(s-c)))}{(16b^2ux - 4bk^2x - k^2l^2)z} \tag{61}$$

$$q^{R*} = \frac{(2bu(4bx - l^2)((2(b(t+s)+a)(4bu - k^2)x - k^2l^2t - k^2l^2s)z - 2b(s-c)(4bu - k^2)x + k^2l^2s - ck^2l^2))}{(8b^2ux - k^2l^2)(4b(4bu - k^2)x - k^2l^2)z} \tag{62}$$

$$y^{R*} = -\frac{(l(8b^2ux - k^2l^2)((b(t+s)-a)z - b(s-c)))}{(4bx - l^2)(16b^2ux - 4bk^2x - k^2l^2)z} \quad (63)$$

$$\pi_{\text{Ref}}^{R*} = \frac{(x(8b^2ux - k^2l^2)((b(t+s)-a)z - b(s-c))^2)}{((4bx - l^2)(16b^2ux - 4bk^2x - k^2l^2)z^2)} \quad (64)$$

$$\pi_{\text{Rec}}^{R*} = \frac{(4b^2ux^2((b(t+s)-a)z - b(s-c))^2)}{((4bx - l^2)(16b^2ux - 4bk^2x - k^2l^2)z^2)} \quad (65)$$

Proposition 3 gives the optimal wholesale price, retail price, warranty period, quality level, and profits for MABRC and ORP in the decentralized setting under the RS contract. In the next section, we use the TPT contract to perfectly coordinate the CSC.

4.3.5 TPT contract model (model T)

A TPT contract is a simple and effective mechanism widely used to coordinate SC systems (Mahdiraji et al. 2022). To ensure both firms participate in the contract, their profits should not be less than those in the decentralized model. In this contract, the MABRC will charge a lesser wholesale price q to the ORP to motivate them to decrease their retail price p, to be equal to the one under the centralized setting (Kuiti et al. 2019). This procedure increases market demand and raises the ORP's profit. Then, the ORP (benefited player) pays a lump sum fee, F, to the MABRC (losing player) for compensating the loss of the MABRC (Chen et al. 2021). The TPT contract can coordinate the channel, and the optimal decisions regarding the retail price p, quality level y, and warranty period w are the same as the centralized scenario (Wang et al. 2019).

The Profit function of the ORP is:

$$\pi_{\text{Rec}}^{T} = gzp - gzq - uw^2 - F \quad (66)$$

After taking the value g from Eq. (2) into Eq. (66), the expression for π_{Rec}^{T} is as:

$$\pi_{\text{Rec}}^{T} = (p-q)(a - bp + kw + ly) - uw^2 - F \quad (67)$$

The profit function of the MABRC is:

$$\pi_{\text{Ref}}^{T} = gzq + g(1-z)s - gc - gzt - xy^2 + F \quad (68)$$

After taking the value g from Eq. (2) into Eq. (68), the expression for π_{Ref}^{T} is as:

$$\pi_{\text{Ref}}^{T} = (zq + (1-z)s - c - zt)\left(\frac{(a - bp + kw + ly)}{z}\right) - xy^2 + F \quad (69)$$

Differentiating Eq. (66) with respect to p and equated with zero, we get the optimal value of p as

$$p = \frac{ly + kw + bq + a}{z} \quad (70)$$

Now substitute the value of p, w and y as p^{C*}, w^{C*} and y^{C*} respectively into Eq. (70) and simplify them for q. Now we get the following proposition 4.

Proposition 4 *To ensure the implementation of the contract, wholesale price q under the TPT contract and a feasible range of lump-sum fee F is achieved as*:

$$q = \frac{(t+s)z - s + c}{z} \quad (71)$$

Now, substituting the above values of p, w and y as p^{C*}, w^{C*} and y^{C*} respectively and Eq. (71) and simplifying Eq. (67), we get as

$$\pi_{\text{Rec}}^{T} = \frac{(u(4bu - k^2)x^2((b(t+s)-a)z - b(s-c))^2)}{(((4bu - k^2)x - l^2u)^2z^2)} - F \quad (72)$$

Along similar lines as above, we get the expression for π_{Ref}^{T} as given below:

$$\pi_{\text{Ref}}^{T} = -\frac{(l^2u^2x((b(t+s)-a)z - b(s-c))^2)}{(((4bu - k^2)x - l^2u)^2z^2)} + F \quad (73)$$

To ensure proper SC coordination, the profits earned by participants of the channel using the TPT contract model mustn't be lower than those acquired using the WP contract in the decentralized approach. Thus, the profit of the MABRC follows: $\pi_{\text{Ref}}^{T} \geq \pi_{\text{Ref}}^{D*}$.

From Eqs. (22) and (73), we get,

$$\pi_{\text{Ref}}^{T} = \left(-\frac{(l^2u^2x((b(t+s)-a)z - b(s-c))^2)}{(((4bu - k^2)x - l^2u)^2z^2)} + F\right) \geq \frac{(u(4bu - k^2)x^2((b(t+s)-a)z - b(s-c))^2)}{((2(4bu - k^2)x - l^2u)^2z^2)} \quad (74)$$

From Eq. (74), we get the minimum value of the lump-sum fee F_{Min} as:

$$F_{Min} = \frac{(u(4bu - k^2)^2x^3((b(t+s)-a)z - b(s-c))^2)}{(((4bu - k^2)x - l^2u)^2(2(4bu - k^2)x - l^2u)z^2)} \quad (75)$$

On similar lines, we get, $\pi_{\text{Rec}}^{T} \geq \pi_{\leq\text{Rec}}^{D*}$.

From Eqs. (21) *and* (72), *we get*

$$\pi_{\text{Rec}}^{T} = \left(\frac{(u(4bu-k^2)x^2((b(t+s)-a)z-b(s-c))^2)}{(((4bu-k^2)x-l^2u)^2z^2)} - F\right) \geq \frac{(u(4bu-k^2)x^2((b(t+s)-a)z-b(s-c))^2)}{((2(4bu-k^2)x-l^2u)^2z^2)} \tag{76}$$

From Eq. (76), *we get the maximum value of the lump sum fee* F_{Max} *as*:

$$F_{Max} = \frac{(u(4bu-k^2)^2x^3(3(4bu-k^2)x-2l^2u)((b(t+s)-a)z-b(s-c))^2)}{(((4bu-k^2)x-l^2u)^2(2(4bu-k^2)x-l^2u)^2z^2)} \tag{77}$$

A specific lump sum fee determines the split of the surplus earnings between the MABRC and ORP. The maximum amount of the lump sum fee (F_{Max}) *guarantees that the ORP will engage in the contract. Furthermore, the minimum value of the lump sum charge* (F_{Min}) *prohibits the TPT contract from being negative. Now the concern is how the MABRC and ORP may decide the value of the lump sum fee. In reality, the channel members used to bargain to obtain a resolution. The TPT contract is the result of SC members' negotiation. When the ORP and MABRC agree to split the SC's overall profit, they negotiate the value of the contract parameter F, which is transferred from the ORP to the MABRC. The lump-sum charge F can be easily determined by members' relative channel bargaining power using the Nash bargaining model, which is not considered in this model. The following section presents a numerical illustration wherein we have considered the symmetric Nash bargaining concept for sharing the surplus profit as a lump sum fee, considering the negotiation power of the channel players is equal.*

5 Result and discussions

Through numerical demonstration and sensitivity analysis, we analyze the optimal outcomes of the present study in this section.

5.1 Numerical illustration

In this sub-section, a numerical illustration is used to analyze the performance of the established model. It facilitates achieving a managerial perspective. Table 2 shows the data (in appropriate units) for the parameters to analyze the performance. The optimal values of decision variables, demand, and profit functions of CSC and its channel members under the different scenarios, viz. centralized model (model C), decentralized model (model D), RS contract model (model R), and TPT contract model (model T), are shown in Table 3.

From Table 3, optimal decision variables, demand, and profit functions of decentralized and centralized channels can be compared, summarized in the following proposition 5.

Proposition 5 *The quality level, warranty period, retail price, and market demand for refurbished products, as well as channel profit for the centralized channel and the decentralized channel, are related as follows*:

The channel profit for the centralized channel is greater than the total channel profit for the decentralized channel, i.e., $\pi_{\text{Csc}}^{C*} > \pi_{\text{Csc}}^{D*}$. *Compared to the centralized channel, the retail price in the decentralized channel will be higher, i.e.,* $p^{C*} < p^{D*}$. *In the decentralized channel, quality level, warranty period, and market demand for refurbished products are lower than in the centralized channel, i.e.* $y^{C*} > y^{D*}$, $w^{C*} > w^{D*}$ *and* $d^{C*} > d^{D*}$. *Thus, the channel cannot be coordinated using a decentralized model. This result aligns with the findings of Agrawal et al.* (2022*a*). *According to these findings, there is potential for the issue to be solved more effectively.*

From Table 3, *the impact of the implementation of the RS contract for coordinating the decentralized channel considering decisions for quality level, warranty period, and retail price of refurbished products has been observed, summarized in the following proposition* 6.

Proposition 6 *The RS contract can achieve a win–win outcome but cannot perfectly coordinate the channel.*

Table 2 Data of parameters

Parameter	a	b	c	k	l	s	t	u	x	z
Value	120000	20	800	50	30	100	400	100	80	0.6

Table 3 Optimal values under different scenarios

Parameters	Model D	Model C	Model R	Model T
p	5835.44	5628.57	5767.94	5628.57
q	4080.17	-	3751.1	1666.67
w	438.82	990.476	420.84	990.476
y	329.12	742.857	335	742.857
d	35105.5	79328	35733.2	79328
π_{Csc}	118425466	171682539.7	119862785.7	171682539.7
π_{Ref}	76061884.67		77421744	102690421.5
π_{Rec}	42363581.33		42441041.7	68992118.2
j			0.942	
F_{Min}				120208823.44
F_{Max}				173465897
$F_{Avg}[=(F_{Min}+F_{Max})/2]$				146837360.2

The retail price under the RS contract model is more than that under a centralized channel setting and less than that under a decentralized channel, i.e., $p^{C*} < p^{R*} < p^{D*}$. The quality level under the RS contract model is lower than that in the centralized channel and higher than that in the decentralized channel setting, i.e., $y^{C*} > y^{R*} > y^{D*}$. The order of warranty period under different models is as follows: $w^{C*} > w^{D*} > w^{R*}$. The total channel profit under the RS contract is greater than that under the decentralized channel but lesser than that under the centralized channel, i.e., $\pi_{\text{Csc}}^{C*} > \pi_{\text{Csc}}^{R*} > \pi_{\text{Csc}}^{D*}$. The profits of individual players, i.e., ORP and MABRC under the RS contract model, are more than that in the decentralized channel setting, i.e., $\pi_{\text{Rec}}^{R*} > \pi_{\text{Rec}}^{D*}$ and $\pi_{\text{Ref}}^{R*} > \pi_{\text{Ref}}^{D*}$. These findings suggest that the RS contract model can create a win–win situation. This result agrees with the findings of Giri et al. (2018). However, because the total profit under Model R is less than that in model C, thus model R cannot lead to perfect coordination. As a result, there is still an opportunity for improvement regarding the issue, i.e., a more attractive contract mechanism should be developed.

From Table 3, the impact of the TPT contract on optimal decisions, market demand, and channel profits in CSC coordination has been observed, summarized in the following proposition 7.

Proposition 7 *The TPT contract achieves both channel coordination as well as a win–win situation.*

The retail price, quality level, warranty period, and market demand under model T are the same as in model C. The profits of individual players, i.e., the ORP and MABRC under model T, are more than that found in model D, i.e., $\pi_{\text{Rec}}^{T*} > \pi_{\text{Rec}}^{D*}$ and $\pi_{\text{Ref}}^{T*} > \pi_{\text{Ref}}^{D*}$. The Sum of profits of the ORP and MABRC under model T is equal to the profit under model C, i.e., $\pi_{\text{Rec}}^{T*} + \pi_{\text{Ref}}^{T*} = \pi_{\text{Csc}}^{C*}$. These findings suggest that the TPT contract can create a win–win situation and lead to perfect coordination. Thus, the TPT contract is an effective mechanism for coordinating the CSC. This result agrees with the one obtained by Hosseini-Motlagh et al. (2022) and Xu et al. (2016).

This model has used the concept of refurbishment and recycling used items and ultimately achieved zero waste. These actions positively influence the environment by reducing the use of fresh raw materials. The strategy also enhances social performance by providing jobs in the ORP.

5.2 Sensitivity analysis

In this section, a sensitivity analysis is presented to study the effect of key parameters on the optimal decisions and profits of the proposed model. It is performed by keeping all key parameters constant except one parameter whose effects are to be observed. The sensitivity of the parameters k and u are shown in Figs. 3, 4, 5 and 6. In the following subsections, the effects of warranty period sensitivity coefficient k and warranty investment parameter u on the channel parameters like retail price, wholesale price, warranty period, quality level, and profits of SC players under the various channel structures, i.e., centralized model (model C), decentralized model (model D), RS contract model (model R) and TPT contract model (model T), are examined. To illustrate the effects of key parameters, we have taken the average value of the lump sum fee under a two-part tariff contract.

5.2.1 Effects of warranty period sensitivity coefficient

To illustrate the effects of the warranty period sensitivity coefficient k, the values of key parameters are taken as

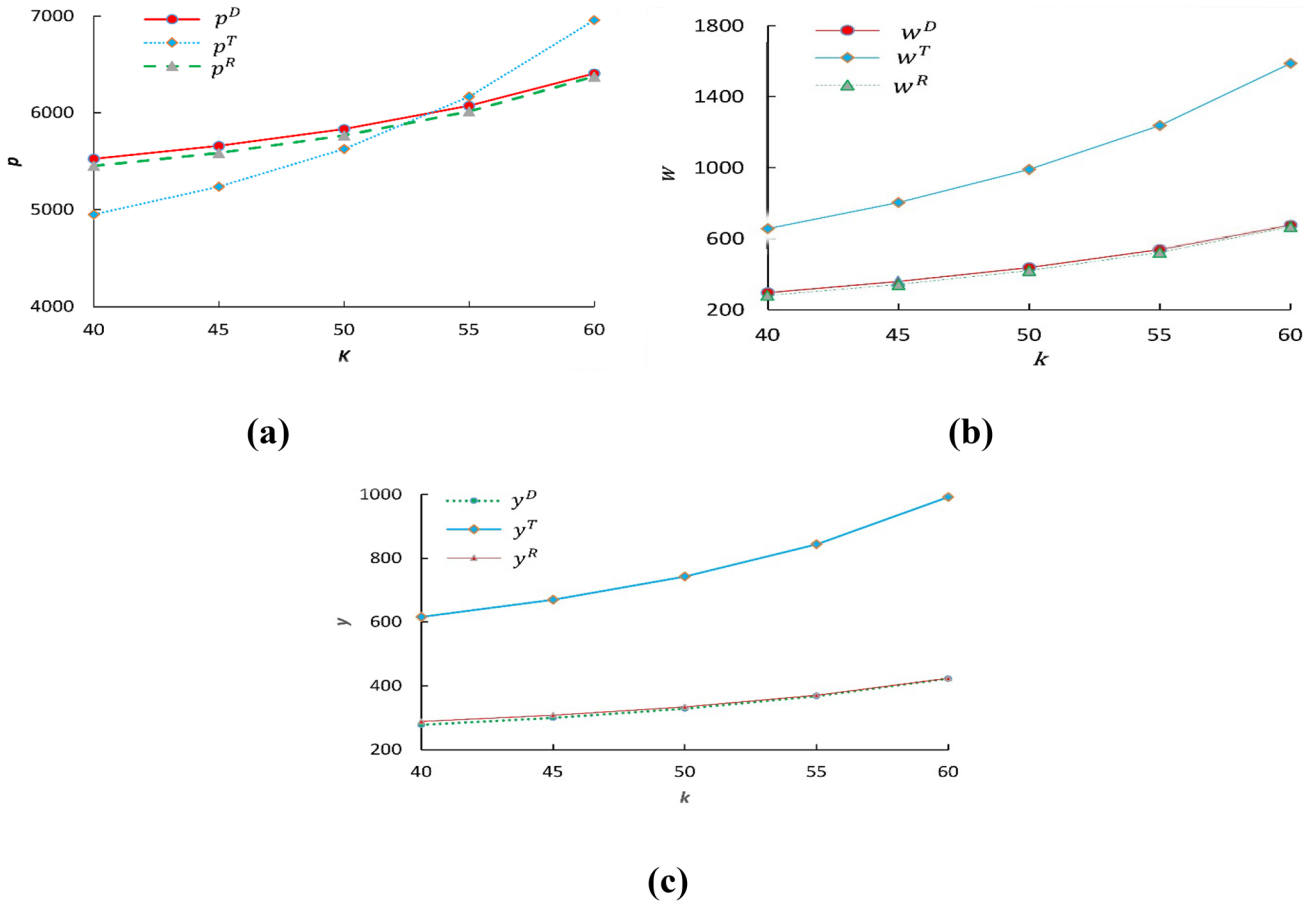

Fig. 3 Impact of the warranty period sensitivity coefficient k on **a** retail price, **b** warranty period, and **c** quality level

discussed in Table 2. To study the effects of k, its value varied from 40 to 60, and the effects are shown in Figs. 3 and 4.

Figure 3a shows that the retail price increases with an increase in the warranty period sensitivity coefficient k for all scenarios. However, it is observed that the retail price in model T/model C may be lower or higher than in the Model D and model R. When the warranty period sensitivity coefficient is large, the optimal retail price in model T/model C is higher than in the model D and model R, while the optimal retail price in model T/model C is lower than that in the model D and model R when the warranty investment parameter is low. Figure 3b also shows that the warranty period increases with the sensitivity coefficient k for all scenarios. That is, the increase in warranty period sensitivity coefficient positively impacts customers. Figure 3b validates the conclusion of proposition 6, i.e., $w^{C*} > w^{D*} > w^{R*}$.This is because with an increase in warranty period sensitivity coefficient, consumer preference towards refurbished products with warranty increases. This motivates the ORP to improve the warranty period.

Meanwhile, the warranty period rankings are in descending order: model T/model C, model D, and model R, demonstrating that model T may provide a longer warranty period. In Fig. 3c, we have compared optimal quality levels against the warranty period sensitivity coefficient k for different channel structures. Like an optimal warranty period, the quality level increases with an increase in the warranty period sensitivity coefficient k. The quality level is the highest for model T, equal to model C, and the lowest for Model d. Comparison of quality levels yields: $y^{C*} > y^{R*} > y^{D*}$. The result is consistent with Proposition 5.

According to Fig. 4a, the MABRC's profit increases with the warranty period sensitivity coefficient k in all settings. The MABRC's profit is highest under model T and lowest under model D. Comparison of the MABRC's profit in different channel structure yields: $\pi_{\text{Ref}}^{T*} > \pi_{\text{Ref}}^{R*} > \pi_{\text{Ref}}^{D*}$. The result is consistent with Propositions 6 and 7. In Fig. 4b, the ORP's profit is compared under different models and has a similar trend to the MABRC's profit. In Fig. 4c, the CSC's profit is compared under different models and has a similar trend to the MABRC's profit. The warranty period sensitivity coefficient favors total SC profitability and channel performance, as shown in the numerical study scenario above. The

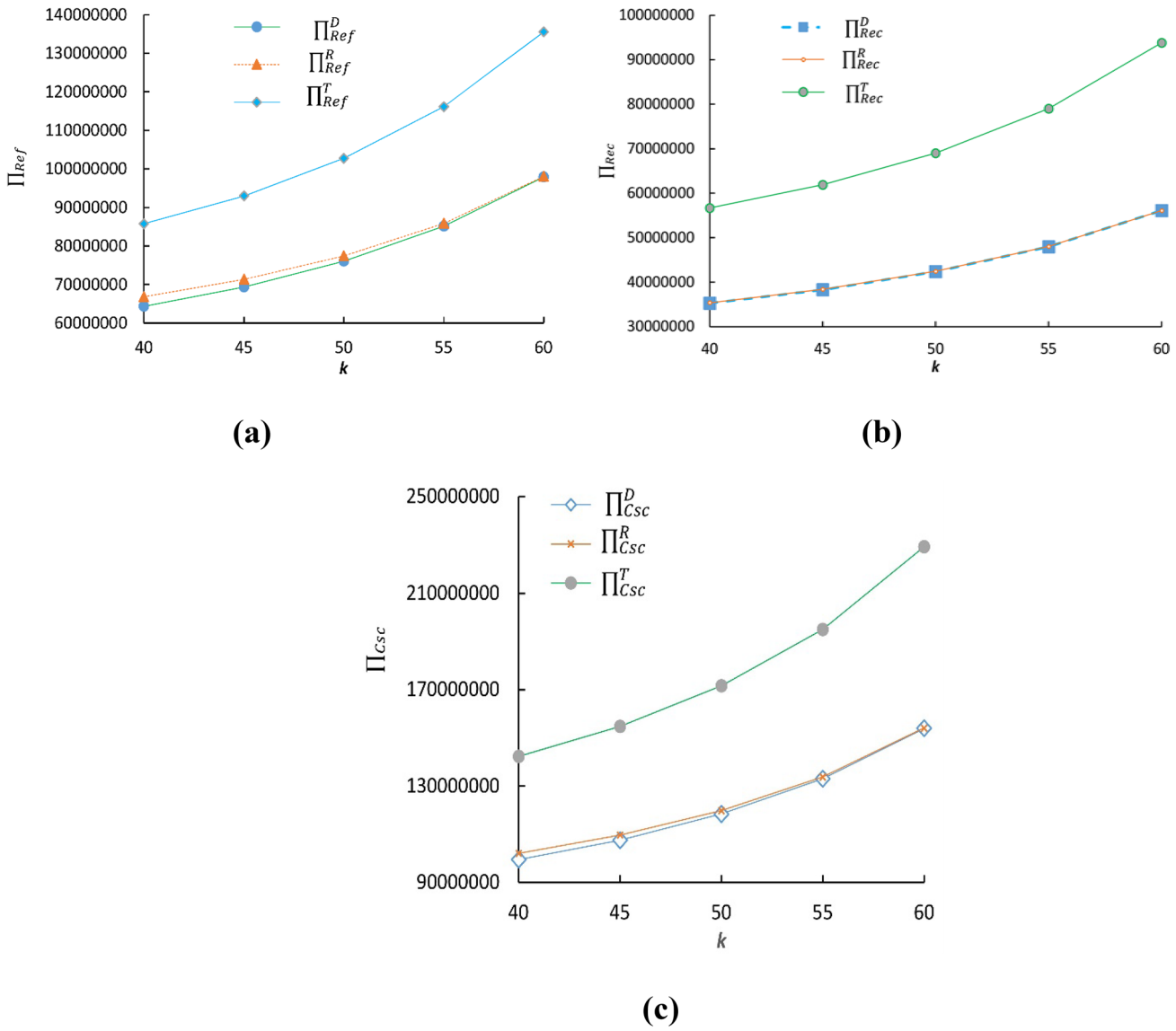

Fig. 4 Impact of the warranty period sensitivity coefficient k on **a** the profit of MABRC, **b** the profit of ORP, and **c** the profit of CSC

increased warranty time encourages buyers to purchase more items, increasing market demand.

As a consequence, the channel players' earnings increase. The numerical study also reveals that the RSC model may enhance the product quality level but not the warranty period compared to the decentralized model; therefore, the SC cannot be coordinated. TPT contracts have the potential to boost channel performance through optimizing channel decisions as well as also improve channel player profitability. This fact demonstrates that the warranty and quality preferred consumer market offers chances for CSC participants to deliver warranty and quality level products, which will bring more advantages to SC members if the coordination system is designed appropriately. Similar results were found by Nouri-Harzvili et al. (2022), Ji et al. (2021), and Qu et al. (2021).

5.2.2 Effects of warranty investment parameter

To illustrate the effects of the warranty investment parameter u, the values of key parameters are taken as discussed in Table 2. To study the effects of u, its value varied from 80 to 120, and the effects are shown in Figs. 5 and 6.

Figure 5a shows that the retail price decreases with an increase in the warranty investment parameter u for all scenarios. This is because the more expensive warranty investment becomes less desirable to the ORP, resulting in reduced customer demand. To attract more customers, the

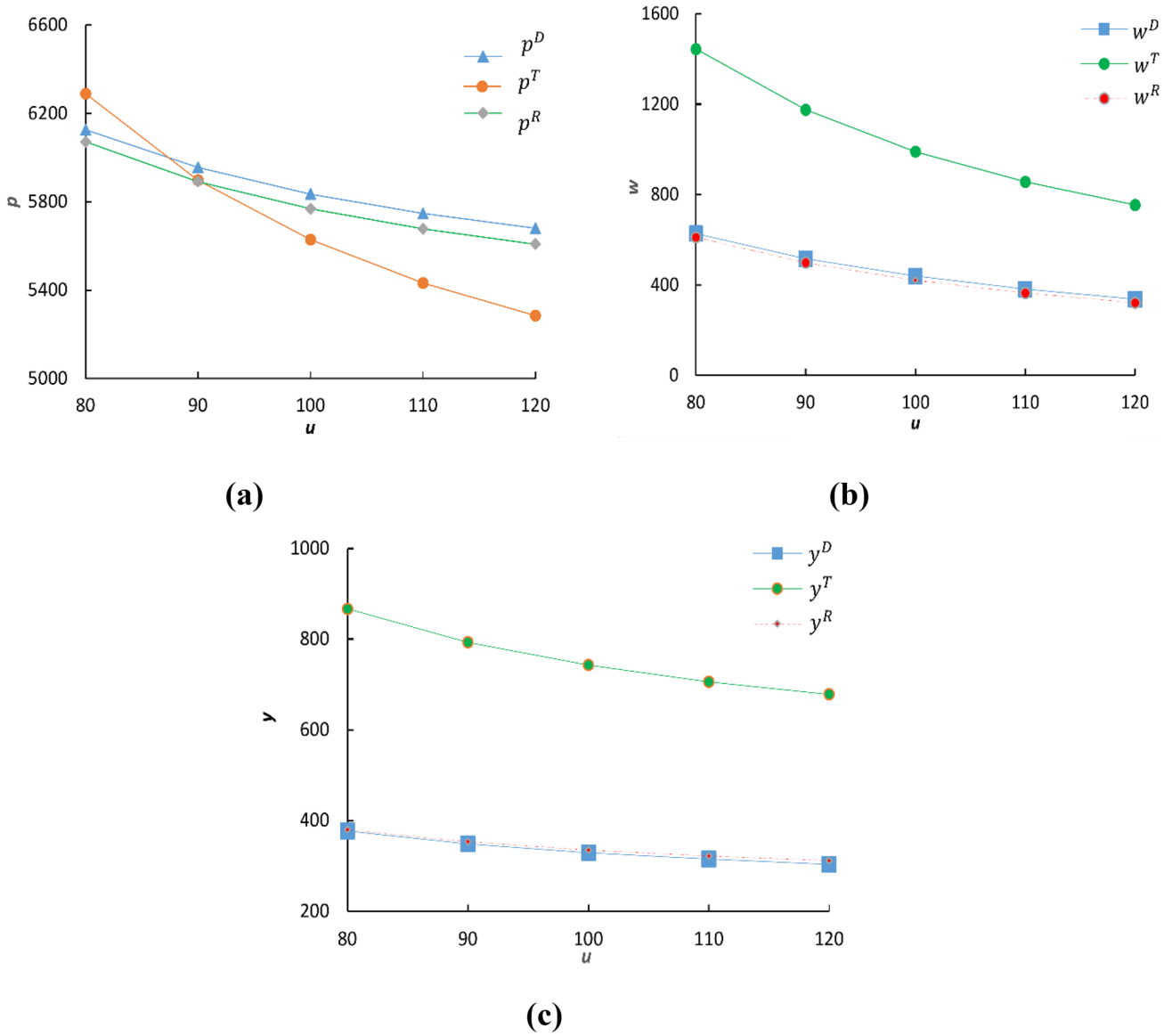

Fig. 5 Impact of the warranty investment parameter u on **a** retail price, **b** warranty period, and **c** quality level

ORP lowers the pricing. However, an interesting observation is that retail price in a centralized channel may be lower or higher than in a decentralized and RSC model. When the warranty investment parameter is large, the optimal retail price in a centralized channel is lower than that in the decentralized channel and RSC model, while the optimal retail price in centralized channel is higher than that in the decentralized channel and RSC model when the warranty investment parameter is low. Figure 5b also shows that the warranty period decreases with an increase in the warranty investment parameter u for all scenarios. That is, the warranty investment parameter has a negative impact on customers. This is because with an increase in warranty investment parameter, the cost of warranty increases, so, to compensate for the profit by ORP, the warranty period decreases. The warranty period is highest in model T and equal to that of model C, followed by model D and model R. Comparison of warranty level for all scenarios is: $\omega^{C*} > \omega^{D*} > \omega^{R*}$. In Fig. 5c, we have compared optimal quality levels against the warranty investment parameter for different channel structures. Like the optimal warranty period, the quality level also decreases with an increase in the warranty investment parameter u. The quality level is highest for model T, equal to that of model C, and lowest for model D. Comparison of quality levels yields: $y^{C*} > y^{R*} > y^{D*}$. The result is consistent with Proposition 5.

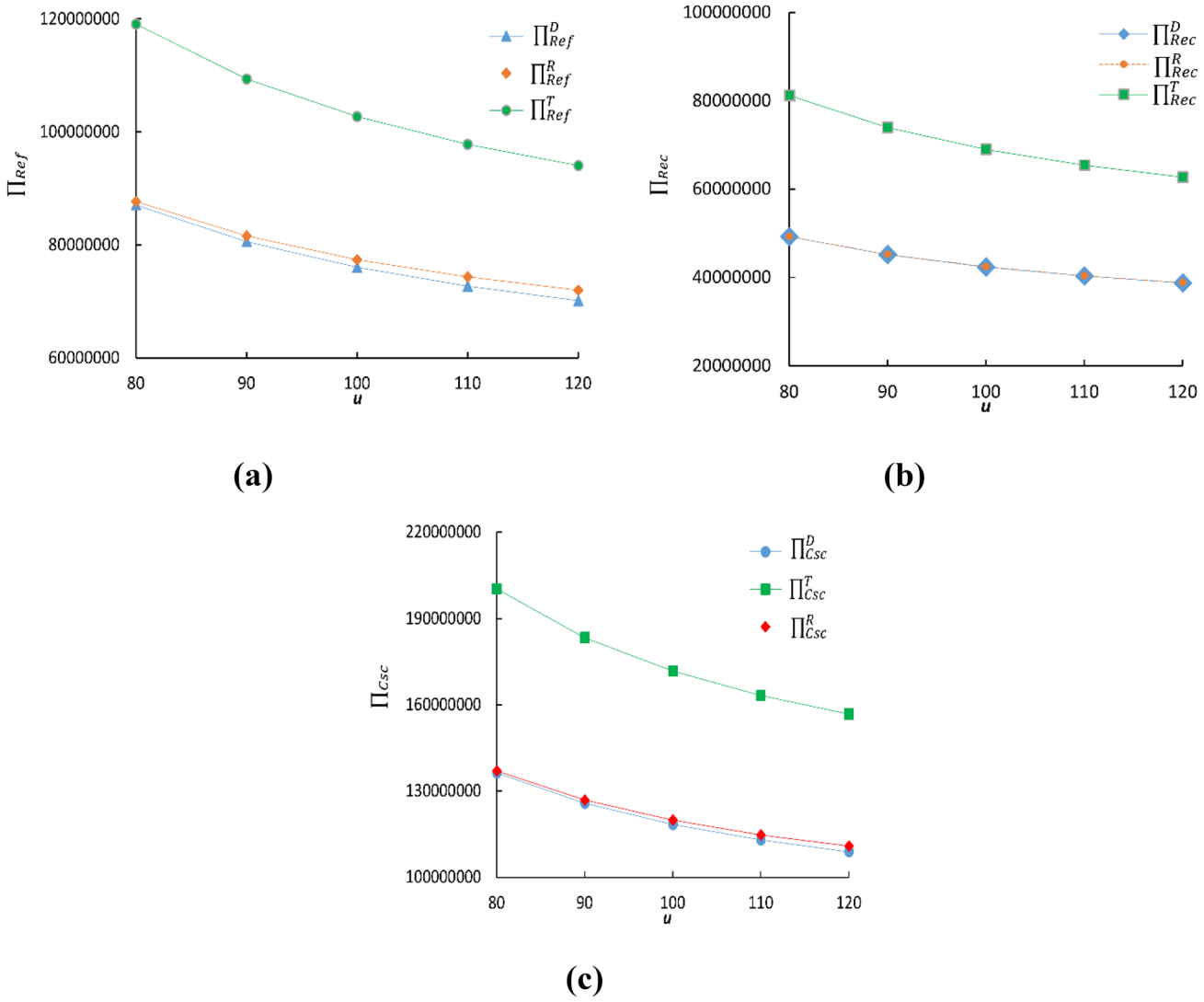

Fig. 6 Impact of the warranty investment parameter u on **a** profit of MABRC **b** profit of ORP, and **c** profit of CSC

According to Fig. 6a, the MABRC's profit decreases with the warranty investment parameter in all settings. As mentioned in the above para, the demand reduces with an increase in warranty investment parameter, so the profits of channel players decrease. The MABRC's profit is highest under model T and lowest under model D. Comparison of the MABRC's profit in different channel structures yields: $\pi_{\mathrm{Ref}}^{T*} > \pi_{\mathrm{Ref}}^{R*} > \pi_{\mathrm{Ref}}^{D*}$. In Fig. 6b, the ORP's profit is compared under different models and found a similar trend as in the MABRC's profit. In Fig. 6c, the CSC's profit is compared under different models and found a similar trend as in the MABRC's profit. Similar results were found by Qu et al. (2021). The result is consistent with Propositions 6 and 7.

6 Managerial implications

Our research has immediate practical implications for businesses under extended producer responsibility. The findings have several implications for SC managers and policymakers operating within a circular economy framework in the era of industry 4.0. First, managers must find a solution to process end-of-use products due to potential cost savings, technology innovation, global environmental consciousness, and stringent regulatory restrictions. Firms may wish to consider our findings while addressing these concerns. Second, we find that the mobile technology of industry 4.0 may be used for coordination purposes. So SC managers engaged in recommece business may use this technology

in collection work wherein circular economy strategies are considered. Third, refurbishment and recycling strategies may use SC managers, wherein sustainability is the goal of stakeholders. Fourth, we find that key parameters (e.g., pricing, warranty period, and quality of refurbished goods) critically impact the CSC's performance. To increase SC surplus, policymakers should address the interplay between these parameters to promote commercially viable product reuse and environmentally acceptable e-waste disposal. Fifth, our results imply that all channel members can coordinate to maximize the profitability of the CSC by applying particular coordination contracts (Zheng et al. 2021). Generally, organizations will profit from adopting a CSC approach. This allows businesses to save money and take advantage of new business opportunities while being environmentally and socially responsible.

6.1 Managerial insights

The results give key management insights for the two-echelon circular supply chain to meet circularity objectives when the refurbishing firm leads and carries expanded producer responsibility.

Firstly, the results prompt businesses to rethink their refurbished product price. The retail price rises with the warranty term sensitivity coefficient. When the warranty investment parameter is low, the optimum retail price in TPT contract model is lower than in the decentralized model and RS contract model, but when the warranty period sensitivity coefficient is high, it is higher (see Fig. 3a). Second, our study assists refurbishment companies in comprehending the function of refurbished product quality in regulating demand. Thirdly, this study assists recommerce companies in maintaining the product warranty of refurbished products for the purpose of influencing demand and retail pricing. A high quality standard and lengthy guarantee duration might raise the demand for refurbished products on the market. Profit levels are significantly influenced by circularity. Thus, it is worthwhile to examine realistic pricing-quality-guarantee recommerce circular supply chain strategies. Finally, our analysis (see Figs. 4 and 6) reveals that the usage of a TPT contract may make the whole supply chain more profitable and place each CSC member in a win–win scenario, as opposed to a WP contract.

7 Conclusion, limitations, and scope for future research

This study uses a game-theoretic method to address the coordination issue in a CSC in the era of industry 4.0, where market demand is a function of the retail price, warranty period, and quality of refurbished items. We discovered that the TPT contract structure is most effective in encouraging refurbishment companies to focus on quality, motivating ORPs to offer warranty service, and maximizing SC profits. We also found that the TPT structure can perfectly coordinate the CSC with zero-waste in the industry 4.0 era. We discovered that the warranty period sensitivity coefficient and the warranty investments parameter impact the major decision parameters.

We construct four scenarios – centralized, decentralized, revenue-sharing contract, and two-part tariff contract models. Comparing the outcomes of four scenarios, we find that the decentralized scenario yields a lower profit than the centralized option. The centralized scenario increases the profit of the whole SC, but cannot guarantee that each member will earn an acceptable profit. Under the RS contract model, the overall profit is lower than under the centralized approach. CSC's earnings under the TPT contract are equivalent to its profits under the centralized model. We conduct a numerical illustration and sensitivity analysis to determine the effect of important parameters on the decisions. We observe that the decentralized channel under the WP contract has opportunities for improvement. The channel can reach a win–win situation, but not perfect coordination with an RS contract. The quality level has been improved; however, the warranty period is decreased under the RS contract. The TPT contract has resulted in perfect coordination. The quality level and the warranty period have been improved under the TPT contract. The warranty period sensitivity coefficient positively impacts channel decisions (e.g., selling price, warranty period, and quality level of refurbished product) and the profit of channel players of CSC in various channel structures. In contrast, the warranty investment parameter has a negative impact.

This study may be expanded in several ways. First, we restrict the scope of the investigation to the MABRC and the ORP. A CSC is a multi-player network in reality. Therefore, a scenario involving several stakeholders might be a future research extension of the study. Second, we assumed information symmetry in this model. In practice, information is seldom symmetrical, influencing final decisions and the SC coordination approach. Analyzing models with asymmetric information is exciting. Third, during an examination, we accounted for a constant refurbishment rate. In actuality, the pace of refurbishment is seen to be random. Therefore, it may be advantageous for future research to examine the variable refurbishing rate. Fourth, it is believed that the cost of refurbishing and the salvage value of non-refurbishable commodities are stable and predictable. To expand on this concept, the cost of refurbishing and the salvage value of non-refurbished items may rely on industry issues such as product quality and consumer willingness. Though, internet-of-things technologies (i.e., Electronic product code encoded radio frequency identification) have a huge potential to apply

to monitor the return management of goods (Mo et al. 2009), however we have not used. Development of an internet-of-things-based coordination paradigm should be the focus of future study.

Acknowledgements Authors would like to express sincere thanks to Editor and reviewers for providing constructive comments to improve quality of this manuscript.

Data availability The authors confirm that the data supporting the findings of the study are available within the article.

Declarations

Conflict of interest There are no relevant financial or non-financial interests to report for the authors. The authors don't have any competing interests that are important to the content of this article that they need to disclose. All contributed authors have been mentioned.

References

Agenda I (2016) The new plastics economy rethinking the future of plastics. World Econ Forum 36

Agnusdei GP, Gnoni MG, Sgarbossa F, Govindann K (2022) Challenges and perspectives of the Industry 4.0 technologies within the last-mile and first-mile reverse logistics: A systematic literature review. Res Transp Bus Manag. https://doi.org/10.1016/j.rtbm.2022.100896

Agrawal S, Kumar D, Singh RK, Singh RK (2022a) Analyzing coordination strategy of circular supply chain in re-commerce industry: A game theoretic approach. Bus Strat Environ

Agrawal S, Kumar D, Singh RK, Singh RK (2022b) Coordination issues in managing the reverse supply chain: a systematic literature review and future research directions. Benchmark Int J. https://doi.org/10.1108/bij-08-2021-0467

Akbari M, Hopkins JL (2022) Digital technologies as enablers of supply chain sustainability in an emerging economy. Oper Manag Res 15(3–4):689–710. https://doi.org/10.1007/s12063-021-00226-8

Arya S, Kumar S (2020) E-waste in India at a glance: Current trends, regulations, challenges and management strategies. J Clean Prod 271:122707. https://doi.org/10.1016/j.jclepro.2020.122707

Bai C, Dallasega P, Orzes G, Sarkis J (2020) Industry 4.0 technologies assessment: A sustainability perspective. Int J Prod Econ 229:107776. https://doi.org/10.1016/j.ijpe.2020.107776

Bag S, Dhamija P, Singh RK, Rahman MS, Sreedharan VR (2023) Big data analytics and artificial intelligence technologies based collaborative platform empowering absorptive capacity in health care supply chain: An empirical study. J Bus Res 154:113315

Berlin D, Feldmann A, Nuur C (2022) Supply network collaborations in a circular economy: A case study of Swedish steel recycling. Resour Conserv Recycl. https://doi.org/10.1016/j.resconrec.2021.106112

Bhattacharya A (2021) Achieving sustainability in supply chain operations in the interplay between circular economy and Industry 4.0. Prod Plan Control 0(0):1–3. https://doi.org/10.1080/09537287.2021.1981032

Biswas I, Raj A, Srivastava SK (2018) Supply chain channel coordination with triple bottom line approach. Transp Res Part E Logist Transp Rev 115:213–226

Bocken NMP, De Pauw I, Bakker C, Van Der Grinten B (2016) Product design and business model strategies for a circular economy. J Ind Prod Eng 33(5):308–320

Bressanelli G, Perona M, Saccani N (2019) Challenges in supply chain redesign for the Circular Economy: A literature review and a multiple case study. Int J Prod Res 57(23):7395–7422

Cao Q, Zhang J (2020) Gray market's product quality in the circular economy era. Int J Prod Res 58(1):308–331

Caro F, Gürhan Kök A, Martínez-De-Albéniz V (2020) The future of retail operations. Manuf Serv Oper Manag 22(1):47–58. https://doi.org/10.1287/msom.2019.0824

Chen X, Wang X, Chan HK (2017) Manufacturer and retailer coordination for environmental and economic competitiveness: A power perspective. Transp Res Part E Logist Transp Rev 97:268–281

Chen Z, Fang L, Su S-II (2021) The value of offline channel subsidy in bricks and clicks: an O2O supply chain coordination perspective. Electron Commer Res 21(2):599–643

Chen Z, Hong S, Ji X, Shi R, Wu J (2022) Refurbished products and supply chain incentives. Ann Oper Res 310(1):27–47. https://doi.org/10.1007/s10479-021-04016-0

Cheng Y, Sun H, Jia F, Koh L (2018) Pricing and low-carbon investment decisions in an emission dependent supply chain under a carbon labelling scheme. Sustainability 10(4):1238

Choi T-M, Taleizadeh AA, Yue X (2020) Game theory applications in production research in the sharing and circular economy era. Int J Prod Res 58(1):118–127. Taylor & Francis

Chu X, Wen Z, Chen J (2021) Optimal grading policies in the online acquisition of used products. J Syst Sci Syst Eng 30(1):29–43

Darbari JD, Kannan D, Agarwal V, Jha PC (2019) Fuzzy criteria programming approach for optimising the TBL performance of closed loop supply chain network design problem. Ann Oper Res 273(1):693–738

De Giovanni P (2020) Blockchain and smart contracts in supply chain management: A game theoretic model. Int J Prod Econ 228(June):107855. https://doi.org/10.1016/j.ijpe.2020.107855

den Hollander M, Bakker C (2016) Mind the gap exploiter: circular business models for product lifetime extension. Electronics Goes Green 2016+: Inventing Shades of Green 1–8

Dev NK, Shankar R, Qaiser FH (2020) Industry 4.0 and circular economy: Operational excellence for sustainable reverse supply chain performance. Resour Conserv Recycl 153(November 2019):104583. https://doi.org/10.1016/j.resconrec.2019.104583

Ding J, Bai S (2022) Optimal decision and coordination of organic food supply chain from the perspective of blockchain. Discrete Dyn Nat Soc. https://doi.org/10.1155/2022/6050185

Dwivedi A, Paul SK (2022) A framework for digital supply chains in the era of circular economy: Implications on environmental sustainability. Bus Strat Environ 31(4):1249–1274. https://doi.org/10.1002/bse.2953

Economy C (2023) The circularity gap report 2023. https://admin.circl.nl/wp-content/uploads/2023/01/Circularity-Gap-Report-2023.pdf

Ertz M, Leblanc-Proulx S, Sarigöllü E, Morin V (2019) Made to break? A taxonomy of business models on product lifetime extension. J Clean Prod 234:867–880. https://doi.org/10.1016/j.jclepro.2019.06.264

Esmaeilian B, Onnipalayam Saminathan P, Cade W, Behdad S (2021) Marketing strategies for refurbished products: Survey-based insights for probabilistic selling and technology level. Resour Conserv Recycl 167(April 2020):105401. https://doi.org/10.1016/j.resconrec.2021.105401

Fang C, Ma X, Zhang J, Zhu X (2021) Personality information sharing in supply chain systems for innovative products in the circular economy era. Int J Prod Res 59(19):5992–6001

Farooque M, Zhang A, Thürer M, Qu T, Huisingh D (2019) Circular supply chain management: A definition and structured literature review. J Clean Prod 228:882–900

Fischer A, Pascucci S (2017) Institutional incentives in circular economy transition: The case of material use in the Dutch textile industry. J Clean Prod 155:17–32

Foundation EM (2016) Circular economy in India: Rethinking growth for long-term prosperity. Ellen MacArthur Foundation

Gallego-García S, Groten M, Halstrick J (2022) Integration of improvement strategies and industry 4.0 Technologies in a dynamic evaluation model for target-oriented optimization. Appl Sci (Switzerland) 12(3):1–21. https://doi.org/10.3390/app12031530

Gebhardt M, Kopyto M, Birkel H, Hartmann E (2022) Industry 4.0 technologies as enablers of collaboration in circular supply chains: a systematic literature review. Int J Prod Res 60(23):6967–6995. https://doi.org/10.1080/00207543.2021.1999521

Giri BC, Mondal C, Maiti T (2018) Analysing a closed-loop supply chain with selling price, warranty period and green sensitive consumer demand under revenue sharing contract. J Clean Prod 190:822–837. https://doi.org/10.1016/j.jclepro.2018.04.092

Han J, Heshmati A, Rashidghalam M (2020) Circular economy business models with a focus on servitization. Sustainability (Switzerland) 12(21):1–17. https://doi.org/10.3390/su12218799

Hettiarachchi BD, Seuring S, Brandenburg M (2022) Industry 4.0-driven operations and supply chains for the circular economy: a bibliometric analysis. Oper Manag Res 15(3–4):858–878. https://doi.org/10.1007/s12063-022-00275-7

Heydari J, Rafiei P (2020) Integration of environmental and social responsibilities in managing supply chains: A mathematical modeling approach. Comput Ind Eng 145(August 2019):106495. https://doi.org/10.1016/j.cie.2020.106495

Hosseini-Motlagh SM, Nematollahi M, Ebrahimi S (2022) Tri-party reverse supply chain coordination with competitive product acquisition process. J Operat Res Soc 73(2):382–393. https://doi.org/10.1080/01605682.2020.1824550

Hosseini-Motlagh SM, Nematollahi M, Nouri M (2018) Coordination of green quality and green warranty decisions in a two-echelon competitive supply chain with substitutable products. J Clean Prod 196:961–984. https://doi.org/10.1016/j.jclepro.2018.06.123

Hu H, Li Y, Li M (2022) Decisions and coordination of green supply chain considering big data targeted advertising. J Theor Appl Electron Commer Res 17(3):1035–1056. https://doi.org/10.3390/jtaer17030053

Husain Z, Maqbool A, Haleem A, Pathak RD, Samson D (2021) Analyzing the business models for circular economy implementation: a fuzzy TOPSIS approach. Oper Manag Res 14(3–4):256–271. https://doi.org/10.1007/s12063-021-00197-w

Jamwal A, Agrawal R, Sharma M, Giallanza A (2021a) Industry 4.0 technologies for manufacturing sustainability: A systematic review and future research directions. Appl Sci (Switzerland) 11(12). https://doi.org/10.3390/app11125725

Jamwal A, Agrawal R, Sharma M, Kumar V, Kumar S (2021b) Developing A sustainability framework for Industry 4.0. Procedia CIRP 98:430–435. https://doi.org/10.1016/j.procir.2021.01.129

Jauhari WA, Adam NAFP, Rosyidi CN, Pujawan IN, Shah NH (2020) A closed-loop supply chain model with rework, waste disposal, and carbon emissions. Oper Res Perspect. https://doi.org/10.1016/j.orp.2020.100155

Ji Y, Yang H, Qu S, Nabe M (2021) Optimal strategy for a closed-loop supply chain considering recycling and warranty channels. Arab J Sci Eng 46(2):1585–1601. https://doi.org/10.1007/s13369-020-04751-9

Khan SAR, Piprani AZ, Yu Z (2022) Digital technology and circular economy practices: future of supply chains. Oper Manag Res 15(3–4):676–688. https://doi.org/10.1007/s12063-021-00247-3

Knäble D, de Quevedo Puente E, Pérez-Cornejo C, Baumgärtler T (2022) The impact of the circular economy on sustainable development: A European panel data approach. Sustain Prod Consump 34:233–243. https://doi.org/10.1016/j.spc.2022.09.016

Kuiti MR, Ghosh D, Gouda S, Swami S, Shankar R (2019) Integrated product design, shelf-space allocation and transportation decisions in green supply chains. Int J Prod Res 57(19):6181–6201. https://doi.org/10.1080/00207543.2019.1597292

Kumar P, Singh RK (2021) Application of Industry 4.0 technologies for effective coordination in humanitarian supply chains: a strategic approach. Ann Oper Res (Issue 0123456789). Springer US. https://doi.org/10.1007/s10479-020-03898-w

Lahane S, Kant R, Shankar R (2020) Circular supply chain management: A state-of-art review and future opportunities. J Clean Prod 258:120859. https://doi.org/10.1016/j.jclepro.2020.120859

Leal Filho W, Ellams D, Han S, Tyler D, Boiten VJ, Paço A, ... Balogun AL (2019) A review of the socio-economic advantages of textile recycling. J Clean Prod 218:10–20. https://doi.org/10.1016/j.jclepro.2019.01.210

Li G, Wu H, Sethi SP, Zhang X (2021) Contracting green product supply chains considering marketing efforts in the circular economy era. Int J Prod Econ. https://doi.org/10.1016/j.ijpe.2021.108041

Li W, Lai M, Zeng G, Cao E, Nie K (2010) Pricing decision for remanufactured and refurbished products about WEEE. Int Conf Logist Syst Intell Manag (ICLSIM) 3:1391–1395

Liu B, De Giovanni P (2019) Green process innovation through Industry 4.0 technologies and supply chain coordination. Ann Oper Res. https://doi.org/10.1007/s10479-019-03498-3

Liu H, Lei M, Huang T, Leong GK (2018) Refurbishing authorization strategy in the secondary market for electrical and electronic products. Int J Prod Econ 195(October 2017):198–209. https://doi.org/10.1016/j.ijpe.2017.10.012

Liu Z, Wan MD, Zheng XX, Koh SCL (2022) Fairness concerns and extended producer responsibility transmission in a circular supply chain. Ind Mark Manag 102:216–228. https://doi.org/10.1016/j.indmarman.2022.01.014

Ma P, Wang H, Shang J (2013) Contract design for two-stage supply chain coordination: Integrating manufacturer-quality and retailer-marketing efforts. Int J Prod Econ 146(2):745–755. https://doi.org/10.1016/j.ijpe.2013.09.004

Mahdiraji HA, Kamardi AA, Beheshti M, Hajiagha SHR, Rocha-Lona L (2022) Analysing supply chain coordination mechanisms dealing with repurposing challenges during Covid-19 pandemic in an emerging economy: a multi-layer decision making approach. Oper Manag Res. https://doi.org/10.1007/s12063-021-00224-w

Mangla SK, Luthra S, Mishra N, Singh A, Rana NP, Dora M, Dwivedi Y (2018) Barriers to effective circular supply chain management in a developing country context. Prod Plan Control 29(6):551–569. https://doi.org/10.1080/09537287.2018.1449265

Maranesi C, De Giovanni P (2020) Modern circular economy: Corporate strategy, supply chain, and industrial symbiosis. Sustainability (Switzerland) 12(22):1–25. https://doi.org/10.3390/su12229383

Mastos TD, Nizamis A, Terzi S, Gkortzis D, Papadopoulos A, Tsagkalidis N, Ioannidis D, Votis K, Tzovaras D (2021) Introducing an application of an industry 4.0 solution for circular supply chain management. J CleanProd. https://doi.org/10.1016/j.jclepro.2021.126886

Matsui K (2022) Optimal timing of acquisition price announcement for used products in a dual-recycling channel reverse supply chain. Eur J Oper Res 300(2):615–632. https://doi.org/10.1016/j.ejor.2021.08.010

Mishra M, Hota SK, Ghosh SK, Sarkar B (2020) Controlling waste and carbon emission for a sustainable closed-loop supply chain management under a cap-and-trade strategy. Mathematics 8(4). https://doi.org/10.3390/math8040466

Mishra R, Naik BKR, Raut RD, Paul SK (2022a) Circular economy principles in community energy initiatives through stakeholder perspectives. Sustain Prod Consump 33:256–270. https://doi.org/10.1016/j.spc.2022.07.001

Mishra R, Singh RK, Govindan K (2022b) Barriers to the adoption of circular economy practices in micro, small and medium enterprises: instrument development, measurement and validation. J Clean Prod 351:131389. https://doi.org/10.1016/j.jclepro.2022.131389

Mo JPT, Lorchirachoonkul W, Gajzer S (2009) Enterprise system design for RFID enabled supply chains from experience in two national projects. Int J Eng Bus Manag 1(2):1–6. https://doi.org/10.5772/6780

Modak NM, Kazemi N, Cárdenas-Barrón LE (2019) Investigating structure of a two-echelon closed-loop supply chain using social work donation as a Corporate Social Responsibility practice. Int J Prod Econ 207:19–33. https://doi.org/10.1016/j.ijpe.2018.10.009

Mukherjee AA, Singh RK, Mishra R, Bag S (2022) Application of blockchain technology for sustainability development in agricultural supply chain: justification framework. Oper Manag Res 15(1–2):46–61. https://doi.org/10.1007/s12063-021-00180-5

Nascimento DLM, Alencastro V, Quelhas OLG, Caiado RGG, Garza-Reyes JA, Lona LR, Tortorella G (2019) Exploring Industry 4.0 technologies to enable circular economy practices in a manufacturing context: a business model proposal. J Manuf Tech Manag 30(3):607–627. https://doi.org/10.1108/JMTM-03-2018-0071

Nasiri MS, Shokouhyar S (2021) Actual consumers' response to purchase refurbished smartphones: Exploring perceived value from product reviews in online retailing. J Retail Consum Serv 62(June):102652. https://doi.org/10.1016/j.jretconser.2021.102652

Niu B, Xie F (2020) Incentive alignment of brand-owner and remanufacturer towards quality certification to refurbished products. J Clean Prod 242:118314. https://doi.org/10.1016/j.jclepro.2019.118314

Nouri-Harzvili M, Hosseini-Motlagh SM, Pazari P (2022) Optimizing the competitive service and pricing decisions of dual retailing channels: A combined coordination model. Comput Ind Eng 163(October 2020):107789. https://doi.org/10.1016/j.cie.2021.107789

Nußholz JLK (2017) Circular business models: Defining a concept and framing an emerging research field. Sustainability (Switzerland) 9(10):14–17. https://doi.org/10.3390/su9101810

Oraiopoulos N, Ferguson ME, Toktay LB (2012) Relicensing as a secondary market strategy. Manag Sci 58(5):1022–1037. https://doi.org/10.1287/mnsc.1110.1456

Ovchinnikov A (2011) Revenue and cost management for remanufactured products. Prod Oper Manag 20(6):824–840. https://doi.org/10.1111/j.1937-5956.2010.01214.x

Ozkan-Ozen YD, Kazancoglu Y, Kumar Mangla S (2020) Synchronized barriers for circular supply chains in industry 3.5/industry 4.0 transition for sustainable resource management. Resour Conserv Recycl. https://doi.org/10.1016/j.resconrec.2020.104986

Palafox-Alcantar PG, Hunt DVL, Rogers CDF (2020) The complementary use of game theory for the circular economy: A review of waste management decision-making methods in civil engineering. Waste Manag 102:598–612. https://doi.org/10.1016/j.wasman.2019.11.014

Pan W, Huynh CH (2022) Optimal operational strategies for online retailers with demand and return uncertainty. Oper Manag Res. https://doi.org/10.1007/s12063-022-00321-4

Panda S, Modak NM, Cárdenas-Barrón LE (2017) Coordinating a socially responsible closed-loop supply chain with product recycling. Int J Prod Econ 188:11–21. https://doi.org/10.1016/j.ijpe.2017.03.010

Patidar A, Sharma M, Agrawal R, Sangwan KS (2022) Supply chain resilience and its key performance indicators: an evaluation under Industry 4.0 and sustainability perspective. Manag Environ Qual Int J. https://doi.org/10.1108/MEQ-03-2022-0091

Pinçe Ç, Ferguson M, Toktay B (2016) Extracting maximum value from consumer returns: Allocating between remarketing and refurbishing for warranty claims. Manuf Serv Oper Manag 18(4):475–492. https://doi.org/10.1287/msom.2016.0584

Prajapati D, Jauhar SK, Gunasekaran A, Kamble SS, Pratap S (2022a) Blockchain and IoT embedded sustainable virtual closed-loop supply chain in E-commerce towards the circular economy. Comput Ind Eng 172(PA):108530. https://doi.org/10.1016/j.cie.2022.108530

Prajapati D, Pratap S, Zhang M, Huang GQ (2022) Sustainable forward-reverse logistics for multi-product delivery and pickup in B2C E-commerce towards the circular economy. International Journal of Production Economics 253(August):108606. https://doi.org/10.1016/j.ijpe.2022.108606

Qu S, Yang H, Ji Y (2021) Low-carbon supply chain optimization considering warranty period and carbon emission reduction level under cap-and-trade regulation. Environ Dev Sustain 23(12):18040–18067. https://doi.org/10.1007/s10668-021-01427-8

Raj A, Biswas I, Srivastava SK (2018) Designing supply contracts for the sustainable supply chain using game theory. J Clean Prod 185:275–284. https://doi.org/10.1016/j.jclepro.2018.03.046

Ran W, Wang Y, Yang L, Liu S (2020) Coordination mechanism of supply chain considering the bullwhip effect under digital technologies. Math Probl Eng. https://doi.org/10.1155/2020/3217927

Reimann M (2016) Accurate response with refurbished consumer returns. Decis Sci 47(1):31–59

Resmi NG, Fasila KA (2017) E-waste management and refurbishment prediction (EMARP) model for refurbishment industries. J Environ Manag 201:303–308. https://doi.org/10.1016/j.jenvman.2017.06.065

Ripanti EF, Tjahjono B, Fan I (2016) Circular economy in reverse logistics: formulation and potential design in product refurbish. Prod Oper Manag 6:1

Rong L, Xu M (2020) Impact of revenue-sharing contracts on green supply chain in manufacturing industry. Int J Sustain Eng 13(4):316–326

Sadeghi R, Taleizadeh AA, Chan FTS, Heydari J (2019) Coordinating and pricing decisions in two competitive reverse supply chains with different channel structures. Int J Prod Res 57(9):2601–2625. https://doi.org/10.1080/00207543.2018.1551637

Santana JCC, Guerhardt F, Franzini CE, Ho LL, Júnior SERR, Cânovas G, Yamamura CLK, Vanalle RM, Berssaneti FT (2021) Refurbishing and recycling of cell phones as a sustainable process of reverse logistics: A case study in Brazil. J Clean Prod 283:124585

Scarpellini S, Portillo-Tarragona P, Aranda-Usón A, Llena-Macarulla F (2019) Definition and measurement of the circular economy's regional impact. J Environ Plan Manag 62(13):2211–2237. https://doi.org/10.1080/09640568.2018.1537974

Schlosser R, Chenavaz RY, Dimitrov S (2021) Circular economy: Joint dynamic pricing and recycling investments. Int J Prod Econ 236:108117

Shahin M, Chen FF, Bouzary H, Krishnaiyer K (2020) Integration of Lean practices and Industry 4.0 technologies: Smart manufacturing for next-generation enterprises. Int J Adv Manuf Technol 107(5–6):2927–2936. https://doi.org/10.1007/s00170-020-05124-0

Sharifi Z, Shokouhyar S (2021) Promoting consumer's attitude toward refurbished mobile phones: A social media analytics approach. Resour Conserv Recycl 167(March):105398. https://doi.org/10.1016/j.resconrec.2021.105398

Sharma V, Raj A, Chakraborty A (2022) Analysis of power dynamics in sustainable supply chain under non-linear demand setup. Oper Manag Res. https://doi.org/10.1007/s12063-022-00268-6

Singh RK, Kumar P, Chand M (2019) Evaluation of supply chain coordination index in context to Industry 4.0 environment. Benchmarking 28(5):1622–1637. https://doi.org/10.1108/BIJ-07-2018-0204

Slaton K, Pookulangara S (2022) Collaborative consumption: An investigation into the secondary sneaker market. Int J Consum Stud 46(3):763–780. https://doi.org/10.1111/ijcs.12725

Sudusinghe JI, Seuring S (2022) Supply chain collaboration and sustainability performance in circular economy: A systematic literature review. Int J Prod Econ. https://doi.org/10.1016/j.ijpe.2021.108402

Taghikhah F, Voinov A, Shukla N (2019) Extending the supply chain to address sustainability. J Clean Prod 229:652–666. Elsevier Ltd. https://doi.org/10.1016/j.jclepro.2019.05.051

Tang Z, Chen L (2022) Understanding seller resistance to digital device recycling platform: An innovation resistance perspective. Electron Commer Res Appl 51(November 2021):101114. https://doi.org/10.1016/j.elerap.2021.101114

Tang Z, Zhou Z, Warkentin M (2022) A contextualized comprehensive action determination model for predicting consumer electronics recommerce platform usage: A sequential mixed-methods approach. Inf Manag 59(3):103617. https://doi.org/10.1016/j.im.2022.103617

Tiwari S (2021) Supply chain integration and Industry 4.0: a systematic literature review. Benchmarking 28(3):990–1030. https://doi.org/10.1108/BIJ-08-2020-0428

Toktaş-Palut P (2022) Analyzing the effects of Industry 4.0 technologies and coordination on the sustainability of supply chains. Sustain Prod Consump 30:341–358. https://doi.org/10.1016/j.spc.2021.12.005

Van Weelden E, Mugge R, Bakker C (2016) Paving the way towards circular consumption: Exploring consumer acceptance of refurbished mobile phones in the Dutch market. J Clean Prod 113:743–754. https://doi.org/10.1016/j.jclepro.2015.11.065

Vegter D, van Hillegersberg J, Olthaar M (2020) Supply chains in circular business models: processes and performance objectives. Resour Conserv Recycl. https://doi.org/10.1016/j.resconrec.2020.105046

Velenturf APM, Purnell P (2021) Principles for a sustainable circular economy. Sustain Prod Consump 27:1437–1457. Elsevier B.V. https://doi.org/10.1016/j.spc.2021.02.018

Wang XV, Wang L (2019) Digital twin-based WEEE recycling, recovery and remanufacturing in the background of Industry 4.0. Int J Prod Res 57(12):3892–3902. https://doi.org/10.1080/00207543.2018.1497819

Wang Y, Wang Z, Li B, Liu Z, Zhu X, Wang Q (2019) Closed-loop supply chain models with product recovery and donation. J Clean Prod 227:861–876. https://doi.org/10.1016/j.jclepro.2019.04.236

Whalen KA (2019) Three circular business models that extend product value and their contribution to resource efficiency. J Clean Prod 226:1128–1137. https://doi.org/10.1016/j.jclepro.2019.03.128

Whalen KA, Milios L, Nussholz J (2018) Bridging the gap: Barriers and potential for scaling reuse practices in the Swedish ICT sector. Resour Conserv Recycl 135:123–131. https://doi.org/10.1016/j.resconrec.2017.07.029

Xu J, Chen Y, Bai Q (2016) A two-echelon sustainable supply chain coordination under cap-and-trade regulation. J Clean Prod 135:42–56. https://doi.org/10.1016/j.jclepro.2016.06.047

Yadav S, Luthra S, Garg D (2022) Internet of things (IoT) based coordination system in Agri-food supply chain: development of an efficient framework using DEMATEL-ISM. Oper Manag Res 15(1–2):1–27. https://doi.org/10.1007/s12063-020-00164-x

Yoo SH, Kim BC (2016) Joint pricing of new and refurbished items: A comparison of closed-loop supply chain models. Int J Prod Econ 182:132–143. https://doi.org/10.1016/j.ijpe.2016.07.017

Yrjölä M, Hokkanen H, Saarijärvi H (2021) A typology of second-hand business models. J Mark Manag 37(7–8):761–791. https://doi.org/10.1080/0267257X.2021.1880465

Zhang J, Zhao S, Cheng TCE, Hua G (2019a) Optimisation of online retailer pricing and carrier capacity expansion during low-price promotions with coordination of a decentralised supply chain. Int J Prod Res 57(9):2809–2827. https://doi.org/10.1080/00207543.2018.1516901

Zhang M, Fu Y, Zhao Z, Pratap S, Huang GQ (2019b) Game theoretic analysis of horizontal carrier coordination with revenue sharing in E-commerce logistics. Int J Prod Res 57(5):1524–1551. https://doi.org/10.1080/00207543.2018.1492754

Zhang Y, He Y, Yue J, Gou Q (2019c) Pricing decisions for a supply chain with refurbished products. Int J Prod Res 57(9):2867–2900. https://doi.org/10.1080/00207543.2018.1543968

Zheng B, Chu J, Jin L (2021) Recycling channel selection and coordination in dual sales channel closed-loop supply chains. Appl Math Model 95:484–502. https://doi.org/10.1016/j.apm.2021.02.022

Zhou J, Jiang P, Yang J, Liu X (2021) Designing a smart incentive-based recycling system for household recyclable waste. Waste Manag 123:142–153. https://doi.org/10.1016/j.wasman.2021.01.030

Zucchella A (2019) Value propositions and business models for circular entrepreneurship. Circ Entrep 61–88. Springer

Publisher's Note Springer Nature remains neutral with regard to jurisdictional claims in published maps and institutional affiliations.

Springer Nature or its licensor (e.g. a society or other partner) holds exclusive rights to this article under a publishing agreement with the author(s) or other rightsholder(s); author self-archiving of the accepted manuscript version of this article is solely governed by the terms of such publishing agreement and applicable law.

This CVPR workshop paper is the Open Access version, provided by the Computer Vision Foundation.
Except for this watermark, it is identical to the accepted version;
the final published version of the proceedings is available on IEEE Xplore.

CrisisHateMM: Multimodal Analysis of Directed and Undirected Hate Speech in Text-Embedded Images from Russia-Ukraine Conflict

Aashish Bhandari[1§], Siddhant B. Shah[1§], Surendrabikram Thapa[2§], Usman Naseem[3], Mehwish Nasim[4, 5]
[1]Department of CSE, Delhi Technological University, India
[2]Department of Computer Science, Virginia Tech, USA
[3]School of Computer Science, The University of Sydney, Australia
[4]School of Physics, Mathematics and Computing, The University of Western Australia, Australia
[5]College of Science and Engineering, Flinders University, Australia

Abstract

Text-embedded images are frequently used on social media to convey opinions and emotions, but they can also be a medium for disseminating hate speech, propaganda, and extremist ideologies. During the Russia-Ukraine war, both sides used text-embedded images extensively to spread propaganda and hate speech. To aid in moderating such content, this paper introduces CrisisHateMM, a novel multimodal dataset of over 4,700 text-embedded images from the Russia-Ukraine conflict, annotated for hate and non-hate speech. The hate speech is annotated for directed and undirected hate speech, with directed hate speech further annotated for individual, community, and organizational targets. We benchmark the dataset using unimodal and multimodal algorithms, providing insights into the effectiveness of different approaches for detecting hate speech in text-embedded images. Our results show that multimodal approaches outperform unimodal approaches in detecting hate speech, highlighting the importance of combining visual and textual features. This work provides a valuable resource for researchers and practitioners in automated content moderation and social media analysis. The CrisisHateMM dataset and codes are made publicly available at https://github.com/aabhandari/CrisisHateMM.

1. Introduction

The widespread usage of social media has resulted in a significant increase in multimodal data [1]. This data type includes various forms of content, such as text, images, and video. The volume of such data has grown substantially, with a 3% increase in social media users from 2022 to 2023, bringing the total number of users to 4.76 billion worldwide [2]. However, along with the growth in usage, the amount of offensive and hateful data has also increased. The rise of offensive and hateful content on social media poses several challenges for detecting and moderating such content [3]. Traditional approaches to content moderation, such as manual review and filtering, are no longer effective due to the sheer volume of data. Therefore, automated approaches are needed to detect and remove offensive and hateful content. Apart from making content moderation easier, automated hate speech moderation can also reprieve social media moderators from over-exposure to hateful content, which can be psychologically damaging [4]. However, one significant challenge is the development of algorithms that can recognize different forms of multimodal data. Most current algorithms are designed to analyze text-based content and struggle to identify and moderate images and video [5]. To address this issue, researchers need to develop new algorithms to analyze multiple data forms, such as image recognition and audio analysis. However, the limited data available to train algorithms has impeded the ability to detect and moderate content automatically, especially during political events like invasions.

The Russia-Ukraine conflict that started on February 24, 2022, triggered a wave of social media activity [6, 7]. The conflict saw polarized opinions, with one side supporting the Russian invasion and the other opposing it. Social media provided a platform for people to express their views on the conflict, but it also led to the spread of hateful content. Text-embedded images were widely used to disseminate hate speech on social media. Russian state media and pro-Russian separatists used such images to portray Ukrainians as fascists and Nazis, while Ukrainian activists and supporters used them to highlight Russian aggression

[§]The authors contributed equally and are joint first authors. The ordering of authors is alphabetical.
WARNING: SOME EXAMPLES PRESENTED IN THIS PAPER CONTAIN HATEFUL CONTENT AND MIGHT BE OFFENSIVE.

(a) No Hate (b) Undirected Hate (c) Target: Individual (d) Target: Organization (e) Target: Community

Figure 1. Examples of text-embedded images labeled for hate speech and sub-classes from CrisisHateMM dataset. Text-embedded images for directed hate speech were further annotated for target classes, as shown in the figure.

and human rights violations, as shown in Figure 1. Such hate speech can exacerbate ongoing tensions and potentially incite more violence. Therefore, it is essential to identify instances of hate speech, especially in determining whether it is directed towards a particular target, to address the issues that arise from such content. Detecting targets would help protect vulnerable groups and plan for specific interventions. However, despite the severity of this issue, there has been limited research on hate speech detection during political events such as the Russia-Ukraine war.

Bridging this gap, we investigate hate speech in text-embedded images in social media and the internet. We annotate a unique dataset related to the Russia-Ukraine crisis to address three main tasks: (i) **Task A:** Detecting whether a given text-embedded image is hateful or not. (ii) **Task B:** Detecting whether the hate speech is directed or undirected. (iii) **Task C:** Detecting the targets of directed hate speech in given text-embedded images. Our main contributions are:

- We create and release a dataset of 4,723 text-embedded images manually annotated to identify hate speech, the direction of hate speech, and the targets of directed hate speech.
- We do a preliminary analysis of the data and benchmark the dataset with various textual, visual, and multimodal algorithms.
- Our experiments show that multiple modalities are important to better understand hate speech in text-embedded images.

2. Related Work

In recent years, the identification of hate speech on social media has become an important research topic in the field of computational linguistics [15]. However, one of the main challenges in this area has been the lack of relevant data, which has hindered the development of effective methods for detecting hate speech. To tackle this problem, researchers have been curating novel datasets with the purpose of aiding the identification of hate speech on social media. Fortuna et al. [8] proposed a dataset of 5,668 tweets annotated into 81 categories of hate speech in the Portuguese language. Similarly, Pereira-Kohatsu et al. [9] curated a dataset of 6,000 Spanish tweets on hate speech along with an unlabeled corpus of 2 million tweets.

Political events may have a significant impact on society as they often have the ability to sway public opinion on a large scale. Thus, it is important to curate datasets that have a relevant political context. Kumar et al. [10] proposed TweetBLM, a dataset related to the Black Lives Matter movement, which was manually annotated for hate speech. Similarly, Grimminger et al. [11] introduced a dataset consisting of 3,000 tweets related to the 2020 US elections, categorized them according to their political stance toward a candidate, and further classified those tweets as offensive and non-offensive.

While the vast majority of research in hate speech detection remains limited to unimodal methods, the research in text-embedded images is equally important because of the ease of sharing such content. Most research accounts for either visual or textual information for detecting hate speech in text-embedded images. Leveraging multimodal information, typically the combination of textual and visual information, has proven to robustly detect hate speech in social media for multimodal content [16]. Liu et al. [17] introduced Figmemes, a multimodal dataset consisting of 5,141 politically-opinionated memes annotated according to the figurative language used in them. Similarly, Gasparini et al. [12] collected multimodal data of 800 memes categorized into misogynistic, ironic, and aggressive content.

The Russia-Ukraine conflict emphasizes the role social media plays in modern-day warfare. Alongside the conflict in the physical environment, there was an active conflict in the information environment. This prompted numerous research efforts to monitor user trends and moderate hate speech. Smart et al. [18] collected a dataset of over $5Mn$ tweets, to quantify how bots were influencing people in the online conversation around the Russia-Ukraine conflict. Hasan et al. [19] collected a dataset containing 10,861 Bengali comments regarding the Russia-Ukraine crisis posted on YouTube news channels and annotated them into three categories: 'Pro-Ukraine', 'Pro-

Table 1. Summary of datasets used in the literature related to hate speech detection. CrisisHateMM (our dataset) is multimodal and has different sub-classes. It is the first dataset annotating text-embedded images that has the context of the Russia-Ukraine crisis.

Work	Data Source	Multimodal	Sub-classes	Size	Context
Fortuna et al. [8]	Twitter	✗	✓	5668	✗
Pereira-Kohatsu et al. [9]	Twitter	✗	✗	6000	✗
Kumar et al. [10]	Twitter	✗	✗	9165	BLM movement
Grimminger et al. [11]	Twitter	✗	✓	3,000	2020 US Elections
Gasparini et al. [12]	Facebook, Twitter, Instagram, Reddit	✓	✗	800	Online Misogyny
Kiela et al. [13]	Self Generated	✓	✗	10,000	✗
Thapa et al. [14]	Twitter	✓	✗	5,680	Russo-Ukraine War
CrisisHateMM (Ours)	Twitter, Facebook, Reddit	✓	✓	4,723	Russo-Ukraine War

Russia', and 'Neutral'. Similarly, Toraman et al. [20] curated a dataset containing 5,284 English and 5,064 Turkish tweets pertaining to recent topics such as the Russia-Ukraine war, COVID-19, and Refugees, where the misinformation propagated by the tweets was analyzed. Thapa et al. [14] curated a multimodal dataset containing 5,680 image-caption text pairs obtained from tweets regarding the Russia-Ukraine conflict. They categorized their data into two classes: Hate and Non-Hate, and their experiments reflected the superiority of multimodal algorithms over unimodal visual and text methods. However, such image-caption pairs may have a lower degree of congruence between visual and textual data than text-embedded images, which may cause processing systems to capture inaccurate contextual information. Furthermore, existing datasets are restricted solely to one social media platform, and thus they may only represent the opinions of a small percentage of the population. Moreover, existing works suffer from limitations such as a lack of subclassing during annotation, reliance on unimodal data, and using single-platform data. To fill this void, we annotate text-embedded images from various platforms for different sub-categories. We hope that our comprehensively annotated dataset acts as a stepping stone toward robust and cross-platform content moderation on social media. Table 1 provides a detailed comparison of the hate speech datasets used in the literature. Unlike other existing datasets, which are either unimodal or lack sub-classes and context, our dataset is multimodal with hierarchical annotation of sub-classes.

3. Dataset

Text-embedded images refer to images that contain textual information within the image itself. This text can be used to provide additional context, or explanation, or to convey a specific message related to the image. Examples of text-embedded images include infographics, social media posts, memes, news snippets, and posters. For our dataset, we curated text-embedded images starting from February 24, 2022, the day the president of Russia, Vladimir Putin, announced the initiation of a special military operation in Ukraine, to March 3, 2023. This section provides the specifications of the data collection process along with the annotation guidelines that were used to annotate the text-embedded images. A schematic overview of the data collection, along with the hierarchical annotation process, is shown in Figure 2.

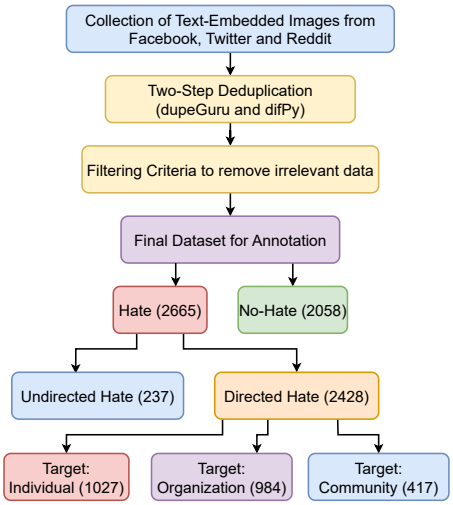

Figure 2. Flow diagram of the data acquisition process

3.1. Data Collection and Deduplication

We collected data from the social media platforms Twitter, Reddit, and Facebook. The Twitter API[1] was used to collect images from Twitter, while manual curation was performed for Reddit and Facebook. We selected several keywords, namely *putin*, *zelensky*, *kremlin*, *ukraine*, *russia*, *kyiv*, *kiev*, *nato*, *russian*, *ukrainian*, *moscow*, *kharkiv*, *donbas*, and *himars* to define our area of interest in data collection. These keywords were chosen to capture relevant text-embedded images of the Russia-Ukraine conflict.

[1] https://developer.twitter.com/en/docs/twitter-api

For data obtained through Twitter, we used tesseract-OCR[2] to identify text-embedded images which were subjected to manual filtering by using robust filtering criteria mentioned in section 3.2. While collecting images from Facebook and Reddit, the same filtering guideline was used to collect text-embedded images for the curation of the dataset.

Since the data was collected by different individuals from multiple sources, duplicates were encountered. Duplicate data can lead to errors in analysis and negatively impact the quality of results, making it crucial to remove duplicates before analyzing the dataset. We sequentially employed two deduplication tools viz. dupeGuru[3] and Duplicate Image Finder (difPy) python package[4]. Our two-step deduplication helped remove duplicate images by preserving the image with the highest resolution from each batch of duplicates. Google OCR Vision API[5] was used to extract textual content from the images, enabling us to process the data further. By using these tools and techniques, we ensured that the data collection process was clean and consistent.

3.2. Filtering Criteria

Filtering is an essential precursory task to remove data that might potentially skew analysis results. To ensure the relevance and quality of our dataset, we filtered the images based on the following criteria:

- **Non-text or only-text images**: We removed images that did not contain any text or contained only text, such as online articles or images of newspapers.
- **Non-English text**: We manually excluded images that had a considerable amount of non-English words. However, we retained images that had a few commonly used non-English words or phrases such as "Ukraini".
- **Irrelevant Images**: We removed images that were not pertinent to the Russia-Ukraine conflict both visually and textually, such as advertisements, spam, images devoid of context, or images focusing on other unrelated topics.
- **Low-Quality Images**: We eliminated images that had a substantial amount of distortion, blurriness, graininess, or other types of degradation, resulting in incomprehensible text.

Figure 3 shows examples of images that were eliminated during the filtering process. The resulting dataset consists of 4,723 manually annotated images, each with textual and visual content relevant to the Russia-Ukraine conflict.

[2] https://github.com/tesseract-ocr/tesseract
[3] https://github.com/arsenetar/dupeguru
[4] https://github.com/elisemercury/Duplicate-Image-Finder
[5] https://cloud.google.com/vision/docs/ocr

3.3. Annotation Schema

Accurate annotation of data is essential to ensure the consistency, reliability, and validity of the dataset [21]. Furthermore, annotations are also responsible for conveying the underlying patterns within a dataset, which can greatly affect the conclusions drawn from the data. A team of *three annotators* with excellent fluency in the English language annotated the data. The annotators had prior experience annotating and had varying educational qualifications, political beliefs, and backgrounds. Inaccurately or inconsistently labeled data can lead to the distortion of analysis methods and model development. Therefore, we follow a three-phase annotation scheme to ensure that the annotators are well-acquainted with the annotation scheme. To measure the inter-annotator agreement quantitatively, we used Cohen's Kappa (κ) as a measure of the inter-rater agreement. Figure 1 shows examples of annotated images.

3.3.1 3-Phase Annotation

The annotation was initiated with a set of clear and unambiguous instructions. The instructions were further revised in an iterative manner until all annotators were clear about them. As a measure to further eliminate ambiguity and ensure consistency, we followed a three-phase annotation scheme.

- **Pilot Run**: The first phase of annotation involved a pilot run of 50 images to ensure that the annotation instructions were understood by all annotators. Our exhaustively annotated dataset required annotators to have a collective understanding of what constitutes hate speech. During the pilot run, there were slight disagreements among annotators, mainly regarding the targets of hate speech, after which the instructions were revised to address all discrepancies.
- **Revised Instructions**: In the second phase, 200 images were annotated by each annotator to ensure that the revised set of instructions was explicit enough. During this phase, the annotators followed the revised set of instructions to annotate the images. The results of this phase further helped to revise instructions and ensured that annotators were consistently able to identify hate speech.
- **Consolidation Phase**: The third annotation phase involved annotating 50 images in a group meeting by all annotators, during which they discussed discrepancies in their annotation in the second phase and reached a consensus. This phase ensured that all annotations were consistent, helped make instructions more apparent to the annotators, and provided an opportunity to uncover any further ambiguities in the instructions.

(a) Non-text image

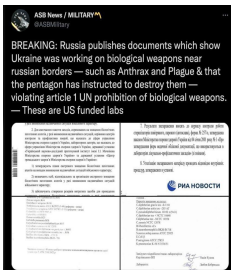

(b) Only-text image

(c) Non-English text

(d) Irrelevant Image

(e) Degraded Image

Figure 3. Examples of posts removed during the filtering process. Our robust filtering criteria were applied to remove irrelevant text-embedded images.

3.3.2 Annotation Guidelines

In order to make annotation consistent, we devised detailed annotation guidelines for annotators. The guidelines are mentioned in this section.

Hate Speech: A text-embedded image is classified as hateful if it contains visual or textual hateful content such as threats, personal attacks, slander, or abuse.

- **Targeted language**: Hate speech attributed to the Russia-Ukraine conflict often targets specific groups based on affiliations, political beliefs, or origin. If there is a use of language that degrades, dehumanizes, or demeans a particular organization, a community of people, or an individual, it is labeled as 'Hate Speech'.
- **Hostility and aggression**: If the text-embedded image contains language that promotes hostility, incites aggression, or glorifies violence towards a political organization or individual, it is labeled as 'Hate Speech'.
- **Use of Hateful memes and images**: Hateful memes and images are often used to disseminate harmful language that degrades, dehumanizes, or demeans a particular political organization, a community of people, or an individual.

Hate speech can be masked through sarcasm and satire, making hate more subtle and harder to detect. The annotators were guided to detect sarcasm and satire in images and understand the context in which it is used. They were also trained to differentiate the intent of sarcasm and satire between humor and hate. The annotation guidelines were supplanted with examples of sarcastic and satiric images and how they express hate speech.

No Hate Speech: A text-embedded image is considered non-hateful if it reports events or objectively reports others' opinions in a non-hateful manner. To make guidelines clear, the following points were discussed as significant identifiers of non-hateful speech.

- **Constructive criticism**: Non-hate speech includes constructive criticism of political organizations, policies, parties, and the individuals affiliated with them. This may also include criticism of political events and happenings around the Russia-Ukraine war.
- **Factual and informative**: Non-hate speech includes factual and informative content such as news, reports, updates, and analyses about political proceedings.
- **Respectful and civil**: Non-hate speech during political events remains civil and respectful and does not use hateful symbols or derogatory language.
- **Lack of hostility**: Non-hate speech during the Russia-Ukraine conflict should not express hostility or aggression towards any political group or individual.

Hate speech was further divided into two categories on the basis of direction: 'Directed hate' and 'Non-directed hate'. The annotation guidelines for the direction of hate speech are the following:

- **Directed hate**: Hateful memes and images that are directed towards a particular political organization, a community of people, or an individual.
- **Undirected hate**: Hateful memes and images that do not have a specific target but instead focus on general societal themes or abstract topics, such as war and capitalism, are considered undirected hate. This type of hate speech may also use ambiguous pronouns like "they" or "you" to refer to abstract targets.

Directed hate speech was further divided into three categories based on their intended targets: 'Individual', 'Organization', and 'Community'.

- **Individual**: An individual refers to an autonomous entity involved in politics in any manner. This can include politicians, political candidates, activists, journalists, and other individuals who are involved in political discourse or have a stake in the outcome of the election. Some of the most frequently mentioned individuals in the context of our dataset are "Vladimir Putin", "Volodymyr Zelenskyy", and "Joe Biden".

- **Organization**: An organization refers to a structured group of individuals who come together for a purpose such as a business, non-profit, or government agency. An organization has a clear leadership structure, a specific goal, and a defined membership. Examples of organizations in our dataset include "NATO", "Republican Party", and the "United Nations".
- **Community**: A community refers to a group of people who share a commonality, such as geographical location, culture, or interest. A community does not have a clear leadership structure, and membership is loosely defined. Examples of communities in our dataset include "Russians", "Ukrainians", and "Liberals".

The annotation guidelines were exhaustive, and the annotators regularly communicated the problems in annotations to each other. Some resolutions were made through regular meetings and group annotation sessions. Resolutions were also made through meetings with senior researchers involved in drafting annotation guidelines.

3.3.3 Inter-Annotator Agreement

Table 2. Cohen's Kappa (κ) for annotation during different phases by three annotators

Annotation Phase	Annotators	κ_{taskA}	κ_{taskB}	κ_{taskC}
Pilot Phase	α_1 and α_2	0.64	0.59	0.58
	α_1 and α_3	0.65	0.61	0.60
	α_2 and α_3	0.61	0.54	0.54
Final Phase	α_1 and α_2	0.81	0.77	0.78
	α_1 and α_3	0.82	0.79	0.78
	α_2 and α_3	0.78	0.74	0.72

To assess the consistency of the annotations, Cohen's Kappa (κ) was used as a statistical measure [22]. The inter-annotator agreement was high, with a Cohen's Kappa of 0.78 for Task A, which was a 2-class annotation (κ_{taskA}) of 'Hate' vs 'Non-Hate'. For Task B, a 2-class annotation (κ_{taskB}) of 'Directed' vs 'Undirected', we obtained a Cohen's Kappa of 0.72. Similarly, the Cohen's Kappa for Task C i.e. 3-class annotation (κ_{taskC}) of 'Individual', 'Organization', and 'Community' is 0.71. The annotator agreement for different annotation phases are shown in Table 2.

3.4. Dataset Statistics

Our dataset comprises 4,723 text-embedded images, which have been categorized into two classes: 'Hate' and 'No Hate'. Of these, 2,665 images (56.43%) have been labeled as 'Hate', while 2,058 (43.57%) have been labeled as 'No Hate'. Additionally, the images labeled as hate speech have been further classified into two subcategories, namely, 'Directed hate speech' and 'Undirected Hate Speech'. The 'Directed' category consists of 2,428 (91.11%) images, whereas 'Undirected' consists of 237 (8.89%) images. The directed hate speech was further divided into 'Individual', 'Organization', and 'Community'. The 'Individual' category contains 1,027 images (38.54%), while the 'Organization' category contains 984 images (36.92%). The 'Community' category contains 417 (15.65%). These data figures, along with the average character count and average word count, are presented in Table 3.

Table 3. Statistics for CrisisHateMM. After preprocessing the text embedded in images, the average value of characters per tweet (Avg. Char) and words per tweet (Avg. Words) are determined.

Problem	Labels	Text-embedded images	Avg. Char	Avg. words
Hate Speech	Hate	2,665	200.42 (151.84)	33.34 (28.64)
	Non-Hate	2,058	318.22 (238.70)	51.94 (43.99)
Target	Individual	1,027	194.81 (148.64)	32.39 (28.05)
	Organization	984	201.53 (151.64)	33.45 (28.50)
	Community	417	224.37 (168.22)	37.32 (31.83)
Direction	Directed	2,428	202.67 (153.26)	33.68 (28.89)
	Undirected	237	177.27 (137.32)	29.88 (26.12)

3.5. Exploratory Data Analysis

Table 4 presents the top 10 most frequently occurring words in the hate, direction, and target classes for our dataset. To evaluate the significance of each word in the dataset, we employed the TF-IDF (Term Frequency-Inverse Document Frequency) statistical approach. TF-IDF calculates the weight for each word based on its frequency in a document (TF) and the number of documents in the collection that contain the word (IDF) [23, 24]. The final score of a word is the product of its TF and IDF scores. TF-IDF scores assist in giving useful insights into the patterns and trends that appear in hate speech text. When a word has a high TF-IDF score, it is considered more relevant and meaningful in the context of the document. Table 4 shows that certain words, such as 'Ukraine', 'Russia', and 'Putin', have a high level of significance across most of the subclasses within our dataset. Additionally, Table 4 gives a helpful visual summary of all the words along with TF-IDF scores which may be beneficial in understanding the links between different keywords and the general language used in the dataset.

Similarly, the number of characters in each class is shown in a histogram in Figure 4, whereas, Figure 5 shows a histogram of the number of words in each category. Results without text preprocessing as well as the results with text preprocessing are given in the figures. The preprocessing steps are explained in section 4.2.

4. Results and Discussion

We used various techniques to establish the baselines, employing both unimodal and multimodal approaches.
Unimodal methods: In the unimodal process, we utilized various unimodal textual and visual methods:

Table 4. Top-10 most frequent words (from text extracted using OCR) in each class. Each word is provided with the TF-IDF scores.

All Posts		Hate Speech Posts		Target: Individual		Target: Organization		Target: Community		Direction: Directed		Direction: Undirected	
Words	**TF-IDF**	**Words**	**TF-IDF**	**Words**	**TF-IDF**	**Words**	**TF-IDF**	**Words**	**TF-IDF**	**Words**	**TF-IDF**	**Words**	**TF-IDF**
ukraine	0.3222	ukraine	0.2863	ukraine	0.2764	ukraine	0.3127	ukraine	0.2508	ukraine	0.2816	ukraine	0.2991
russia	0.2025	russia	0.2139	putin	0.2636	russia	0.3048	russian	0.2165	russia	0.2152	russia	0.1856
russian	0.1448	putin	0.1527	russia	0.1400	russian	0.1471	russia	0.1682	putin	0.1597	war	0.1490
putin	0.1244	russian	0.1377	russian	0.0923	nato	0.0991	ukrainian	0.1344	russian	0.1394	russian	0.1155
war	0.0928	war	0.0899	war	0.0866	war	0.0847	putin	0.0924	war	0.0838	putin	0.0719
ukrainian	0.0915	ukrainian	0.0745	biden	0.0688	ukrainian	0.0699	war	0.0835	ukrainian	0.0768	news	0.0586
news	0.0851	nato	0.0555	president	0.0561	putin	0.0558	people	0.0717	nato	0.0587	ukrainian	0.0545
president	0.0493	world	0.0448	ukrainian	0.0552	world	0.0540	military	0.0394	world	0.0443	world	0.0503
world	0.0475	news	0.0447	vladimir	0.0529	news	0.0419	news	0.0336	biden	0.0436	people	0.0496
nato	0.0472	president	0.0388	news	0.0468	military	0.0396	world	0.0335	news	0.0433	president	0.0292

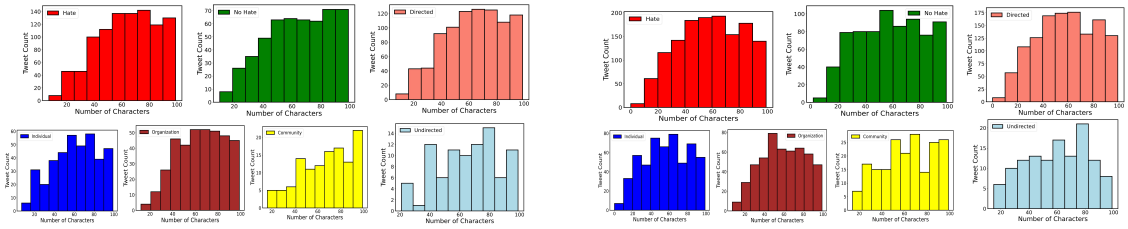

(a) Without Preprocessing (b) With Preprocessing

Figure 4. Histogram of number of characters per text-embedded image before and after preprocessing

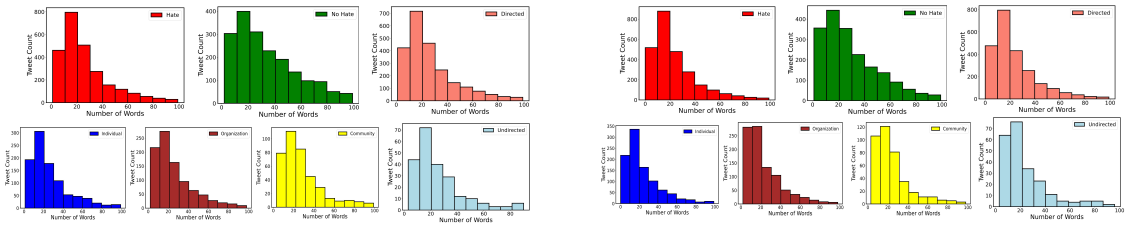

(a) Without Preprocessing (b) With Preprocessing

Figure 5. Histogram of number of words per text-embedded image before and after preprocessing

- **Textual methods**: The textual models used include BERT [25], DistilBERT [26] and DistilRoBERTa [26].
- **Visual methods**: For the visual unimodal baseline methods, we used DenseNet [27], Visformer [28], MViTv2 [29] and VGG19 [30].

Multimodal methods: As we have text-embedded images, we explored using multimodal models to capture the data's visual and textual information. We implemented the state-of-the-art model CLIP (Contrastive Language-Image Pre-training) [31], and GroupViT (Grouping Vision Transformer), a pre-trained vision-language transformer [32].

4.1. Implementation Details

For baselines, we trained the models on a Tesla T4 with 25 GB of dedicated memory and assessed their performance by using accuracy, F1-score (macro), and MMAE (Macro Mean Absolute Error) as performance metrics. We imported the pre-trained transformer models from the hugging face[6] library for the unimodal text and multimodal tasks [33]. Similarly, for the visual models, we employed pre-trained models from the PyTorch Image Models library (timm) [34]. All the tested models, where applicable, used the Adam optimizer [35]. The hyperparameters and models required to replicate the experiments are listed in Table 5.

4.2. Preprocessing

Text preprocessing is an important step in NLP tasks. The text retrieved from OCR was preprocessed along with the image filtering criteria. We removed non-alphanumeric elements, including special characters, hyperlinks, symbols, and non-English characters that may contribute to noise in the data, which could ultimately distort analysis results. Further, non-English words were removed using the English corpus from the NLTK library [36]. Our preprocessing step ensures data quality so that only meaningful text is retained for further analysis.

4.3. Performance Analysis and Insights

Table 6 shows the performance of different algorithms in **Task A**- Hate classification, **Task B**- Direction classification, and **Task C**- Target classification. When using uni-

[6] https://huggingface.co/

Table 5. Implementation Details of the Experiments. Experiments were conducted using a train/test/validation split ratio of 70/15/15.

Modality	Models	Batch Size	Epochs	Learning Rate	Parameters	Image Encoder	Text Encoder
Textual	BERT	8	3	5×10^{-5}	110M	-	bert-base-uncased
	DistilBERT	8	3	5×10^{-5}	67M	-	distilbert-base-uncased
	DistilRoBERTa	8	3	5×10^{-5}	82M	-	distilroberta-base
Visual	DenseNet-161	16	5	10^{-5}	26.5M	densenet161	-
	Visformer_small	16	5	10^{-5}	39.5M	visformer_small	-
	MViTv2_base	16	5	10^{-5}	50.7M	mvitv2_base	-
	VGG19	16	5	10^{-5}	139.6M	vgg19	-
Multimodal	CLIP	4	5	10^{-3}	63M	ViT-Large-Patch14	
	GroupViT	8	5	10^{-3}	-	GroupViT (Hugging Face)	

Table 6. Performance of different unimodal and multimodal algorithms on our dataset

Modality	**Model**	**Hate Classification**			**Direction Classification**			**Target Classification**		
		Accuracy ↑	**F1-score** ↑	**MMAE** ↓	**Accuracy** ↑	**F1-score** ↑	**MMAE** ↓	**Accuracy** ↑	**F1-score** ↑	**MMAE** ↓
Textual	BERT	0.779	0.767	0.240	0.928	0.591	0.427	0.629	0.427	0.998
	DistilBERT	0.754	0.750	0.247	0.925	0.532	0.473	0.637	0.423	1.008
	DistilRoBERTa	0.777	0.769	0.233	0.912	0.578	0.447	0.654	0.440	0.919
Visual	DenseNet-161	0.741	0.739	0.259	0.704	0.487	0.514	0.538	0.425	0.774
	Visformer_small	0.741	0.739	0.257	0.605	0.458	0.461	0.451	0.407	0.772
	MViTv2_base	0.731	0.726	0.276	0.908	0.476	0.500	0.576	0.422	0.657
	VGG19	0.686	0.686	0.305	0.908	0.476	0.500	0.525	0.395	0.785
Multimodal	CLIP	**0.798**	**0.786**	**0.204**	**0.936**	**0.609**	**0.407**	**0.684**	**0.615**	**0.579**
	GroupViT	0.792	0.785	0.214	0.877	0.467	0.500	0.598	0.451	0.763

modal text, DistilRoBERTa performs the best at task A and task C with an F-1 score of 0.769 and 0.440, respectively, despite being a smaller model than BERT. For task B, BERT performs the best with an F-1 score of 0.591. When using unimodal images, DenseNet-161 performs the best with F-1 scores of 0.739, 0.487, and 0.425 for tasks A, B, and C, respectively. For task A, Visformer_small is tied with DenseNet-161 for performance. For unimodal images, the smaller models seemed to perform the best. Among the multimodal models, CLIP outperformed all unimodal and multimodal models, with F-1 scores of 0.786, 0.609, and 0.615 for tasks A, B, and C, respectively. The proportionally higher scores of multimodal models reflect their superiority over unimodal methods, suggesting that multimodal models should be explored more to classify hate speech efficiently. By looking at a few cases of misclassification by models, we can infer that sarcastic images were misclassified. Figure 6 shows an example of such a case.

The misclassification of sarcastic images that pose as harmless memes but carry a more profound meaning through combining visual and textual cues indicates the need to develop multimodal models that better leverage the interplay between visual and textual modalities.

5. Conclusion

The Russia-Ukraine crisis is a delicate and multifaceted problem that has given rise to many conflicting viewpoints. Identifying hate speech and its targets is essential for protecting prejudiced communities, creating safe spaces, and promoting conflict resolution. In conclusion, this paper presents CrisisHateMM, a novel multimodal dataset of text-embedded images from the Russia-Ukraine conflict annotated for hate and non-hate speech with further sub-classes. Future work could include expanding the CrisisHateMM dataset to include more text-embedded images from other conflicts and social media platforms. Additionally, further research could be conducted to improve the performance of multimodal algorithms for detecting hate speech in text-embedded images.

Figure 6. Label: **Hate** Predicted: **No Hate**. Seemingly sarcastic, yet hate speech content is classified as no hate by models.

Acknowledgments

MN acknowledges partial financial support from South Australian DIP – Collaborative Research Funds.

References

[1] Ganesh Chandrasekaran, Tu N Nguyen, and Jude Hemanth D. Multimodal sentimental analysis for social media applications: A comprehensive review. *Wiley Interdisciplinary Reviews: Data Mining and Knowledge Discovery*, 11(5):e1415, 2021. 1

[2] DataReportal. *DIGITAL 2023: GLOBAL OVERVIEW REPORT*. Web page: https://datareportal.com/reports/digital-2023-global-overview-report. Accessed March 2023. 1

[3] Anil Singh Parihar, Surendrabikram Thapa, and Sushruti Mishra. Hate speech detection using natural language processing: Applications and challenges. In *2021 5th International Conference on Trends in Electronics and Informatics (ICOEI)*, pages 1302–1308. IEEE, 2021. 1

[4] Sarah T Roberts. *Behind the screen: The hidden digital labor of commercial content moderation*. University of Illinois at Urbana-Champaign, 2014. 1

[5] Anusha Chhabra and Dinesh Kumar Vishwakarma. A literature survey on multimodal and multilingual automatic hate speech identification. *Multimedia Systems*, pages 1–28, 2023. 1

[6] Om Prakash Choudhary, AbdulRahman A Saied, Rezhna Kheder Ali, Sazan Qadir Maulud, et al. Russo-ukrainian war: An unexpected event during the COVID-19 pandemic. *Travel Medicine and Infectious Disease*, 48:102346, 2022. 1

[7] Alexander Shevtsov, Christos Tzagkarakis, Despoina Antonakaki, Polyvios Pratikakis, and Sotiris Ioannidis. Twitter dataset on the Russo-Ukrainian war. *arXiv preprint arXiv:2204.08530*, 2022. 1

[8] Paula Fortuna, Joao Rocha da Silva, Leo Wanner, Sérgio Nunes, et al. A hierarchically-labeled Portuguese hate speech dataset. In *Proceedings of the third workshop on abusive language online*, pages 94–104, 2019. 2, 3

[9] Juan Carlos Pereira-Kohatsu, Lara Quijano-Sánchez, Federico Liberatore, and Miguel Camacho-Collados. Detecting and monitoring hate speech in Twitter. *Sensors*, 19(21):4654, 2019. 2, 3

[10] Sumit Kumar and Raj Ratn Pranesh. TweetBLM: A hate speech dataset and analysis of black lives matter-related microblogs on Twitter. *arXiv preprint arXiv:2108.12521*, 2021. 2, 3

[11] Lara Grimminger and Roman Klinger. Hate towards the political opponent: A Twitter corpus study of the 2020 US elections on the basis of offensive speech and stance detection. *arXiv preprint arXiv:2103.01664*, 2021. 2, 3

[12] Francesca Gasparini, Giulia Rizzi, Aurora Saibene, and Elisabetta Fersini. Benchmark dataset of memes with text transcriptions for automatic detection of multi-modal misogynistic content. *Data in brief*, 44:108526, 2022. 2, 3

[13] Douwe Kiela, Hamed Firooz, Aravind Mohan, Vedanuj Goswami, Amanpreet Singh, Pratik Ringshia, and Davide Testuggine. The hateful memes challenge: Detecting hate speech in multimodal memes. *Advances in Neural Information Processing Systems*, 33:2611–2624, 2020. 3

[14] Surendrabikram Thapa, Aditya Shah, Farhan Jafri, Usman Naseem, and Imran Razzak. A multi-modal dataset for hate speech detection on social media: Case-study of Russia-Ukraine conflict. In *Proceedings of the 5th Workshop on Challenges and Applications of Automated Extraction of Socio-political Events from Text (CASE)*, pages 1–6, 2022. 3

[15] Pinkesh Badjatiya, Shashank Gupta, Manish Gupta, and Vasudeva Varma. Deep learning for hate speech detection in tweets. In *Proceedings of the 26th International Conference on World Wide Web Companion*, pages 759–760, 2017. 2

[16] Fan Yang, Xiaochang Peng, Gargi Ghosh, Reshef Shilon, Hao Ma, Eider Moore, and Goran Predovic. Exploring deep multimodal fusion of text and photo for hate speech classification. In *Proceedings of the Third Workshop on Abusive Language Online*, pages 11–18, 2019. 2

[17] Chen Liu, Gregor Geigle, Robin Krebs, and Iryna Gurevych. Figmemes: A dataset for figurative language identification in politically-opinionated memes. In *Proceedings of the 2022 Conference on Empirical Methods in Natural Language Processing*, pages 7069–7086, 2022. 2

[18] Bridget Smart, Joshua Watt, Sara Benedetti, Lewis Mitchell, and Matthew Roughan. #IStandWithPutin versus #IStandWithUkraine: The interaction of bots and humans in discussion of the Russia/Ukraine war. In *Social Informatics: 13th International Conference, SocInfo 2022, Glasgow, UK, October 19–21, 2022, Proceedings*, pages 34–53. Springer, 2022. 2

[19] Mahmud Hasan, Labiba Islam, Ismat Jahan, Sabrina Mannan Meem, and Rashedur M Rahman. Natural Language Processing and sentiment analysis on Bangla social media comments on Russia-Ukraine war using transformers. *Vietnam Journal of Computer Science*, 2023. 2

[20] Cagri Toraman, Oguzhan Ozcelik, Furkan Şahinuç, and Fazli Can. Not good times for lies: Misinformation detection on the Russia-Ukraine war, COVID-19, and refugees, 2022. 3

[21] Rion Snow, Brendan O'connor, Dan Jurafsky, and Andrew Y Ng. Cheap and fast–but is it good? evaluating non-expert annotations for natural language tasks. In *Proceedings of the 2008 Conference on Empirical Methods in Natural Language Processing*, pages 254–263, 2008. 4

[22] Matthijs J Warrens. Five ways to look at cohen's kappa. *Journal of Psychology & Psychotherapy*, 5(4):1, 2015. 6

[23] Sang-Woon Kim and Joon-Min Gil. Research paper classification systems based on TF-IDF and LDA schemes. *Human-centric Computing and Information Sciences*, 9:1–21, 2019. 6

[24] Surabhi Adhikari, Surendrabikram Thapa, Usman Naseem, Priyanka Singh, Huan Huo, Gnana Bharathy, and Mukesh Prasad. Exploiting linguistic information from nepali transcripts for early detection of Alzheimer's disease using Natural Language Processing and machine learning techniques. *International Journal of Human-Computer Studies*, 160:102761, 2022. 6

[25] Jacob Devlin, Ming-Wei Chang, Kenton Lee, and Kristina Toutanova. BERT: Pre-training of deep bidirectional transformers for language understanding. *arXiv preprint arXiv:1810.04805*, 2018. 7

[26] Victor Sanh, Lysandre Debut, Julien Chaumond, and Thomas Wolf. DistilBERT, a distilled version of BERT: smaller, faster, cheaper and lighter. *arXiv preprint arXiv:1910.01108*, 2019. 7

[27] Gao Huang, Zhuang Liu, Laurens Van Der Maaten, and Kilian Q Weinberger. Densely connected convolutional networks. In *Proceedings of the IEEE Conference on Computer Vision and Pattern Recognition*, pages 4700–4708, 2017. 7

[28] Zhengsu Chen, Lingxi Xie, Jianwei Niu, Xuefeng Liu, Longhui Wei, and Qi Tian. Visformer: The vision-friendly transformer. In *Proceedings of the IEEE/CVF International Conference on Computer Vision*, pages 589–598, 2021. 7

[29] Yanghao Li, Chao-Yuan Wu, Haoqi Fan, Karttikeya Mangalam, Bo Xiong, Jitendra Malik, and Christoph Feichtenhofer. MViTv2: Improved multiscale vision transformers for classification and detection. In *Proceedings of the IEEE/CVF Conference on Computer Vision and Pattern Recognition*, pages 4804–4814, 2022. 7

[30] Karen Simonyan and Andrew Zisserman. Very deep convolutional networks for large-scale image recognition. *arXiv preprint arXiv:1409.1556*, 2014. 7

[31] Alec Radford, Jong Wook Kim, Chris Hallacy, Aditya Ramesh, Gabriel Goh, Sandhini Agarwal, Girish Sastry, Amanda Askell, Pamela Mishkin, Jack Clark, et al. Learning transferable visual models from natural language supervision. In *International Conference on Machine Learning*, pages 8748–8763. PMLR, 2021. 7

[32] Jiarui Xu, Shalini De Mello, Sifei Liu, Wonmin Byeon, Thomas Breuel, Jan Kautz, and Xiaolong Wang. GroupViT: Semantic segmentation emerges from text supervision. In *Proceedings of the IEEE/CVF Conference on Computer Vision and Pattern Recognition*, pages 18134–18144, 2022. 7

[33] Thomas Wolf, Lysandre Debut, Victor Sanh, Julien Chaumond, Clement Delangue, Anthony Moi, Pierric Cistac, Tim Rault, Rémi Louf, Morgan Funtowicz, et al. Huggingface's transformers: State-of-the-art Natural Language Processing. *arXiv preprint arXiv:1910.03771*, 2019. 7

[34] Adam Paszke, Sam Gross, Francisco Massa, Adam Lerer, James Bradbury, Gregory Chanan, Trevor Killeen, Zeming Lin, Natalia Gimelshein, Luca Antiga, et al. PyTorch: An imperative style, high-performance deep learning library. *Advances in Neural Information Processing Systems*, 32, 2019. 7

[35] Sebastian Bock, Josef Goppold, and Martin Weiß. An improvement of the convergence proof of the adam-optimizer. *arXiv preprint arXiv:1804.10587*, 2018. 7

[36] Edward Loper and Steven Bird. NLTK: The Natural Language Toolkit. *arXiv preprint cs/0205028*, 2002. 7

Sādhanā (2023)48:119
https://doi.org/10.1007/s12046-023-02167-3
© Indian Academy of Sciences

Debris failure susceptibility mapping using information value method

SANDEEP PANCHAL* and AMIT KR SHRIVASTAVA

Delhi Technological University, Main Bawana Road, Samaypur Badli, Delhi, India
e-mail: 2290sandy@gmail.com

MS received 20 February 2022; revised 23 February 2023; accepted 11 April 2023

Abstract. The heavy rainfall during the rainy season triggers slope failures and causes debris failure and runouts in hilly regions. During the monsoon period, the flooding conditions and debris failures caused huge damage to the properties, roads, and bridges in the Rampur sub-division, Shimla, Himachal Pradesh (H.P.), India. So, it is necessary to prepare a debris failure susceptibility map for the region for planning and management of disaster. The aim of this study is to prepare a debris failure susceptibility map for the Rampur sub-division in Himachal Pradesh (H.P.) province in India. A statistical approach i.e. Info value is used to prepare the debris failure susceptibility map in geographic information system (GIS). Nine causative factors responsible for the occurrence of debris failures were identified i.e. slope, aspect, relative relief, topographic wetness index (TWI), lithology, drainage density, distance from roads, and faults and land use of the region. A landslide inventory containing more than 400 debris slides, debris failure, and subsidence events is prepared using previous literature, news items, and inventories. The weightage to each factor and sub-factor is assigned using the information value method. The debris failure susceptibility map is prepared by overlaying the weighted layers of causative factors. The debris failure susceptibility map is divided into four categories based on the debris failure susceptibility index (DFSI). The debris failure susceptibility index varies from − 8.072 to 4.246. The results of the study can be used by planners and engineers for planning and mitigation of debris failures in the study area.

Keywords. Debris failure; debris failure susceptibility mapping; GIS; remote sensing; info value.

1. Introduction

The hilly terrain is always prone to natural disasters. Debris failures may be defined as the downslope movement of coarse material mixed with water under the effect of gravity [1]. Debris failures cause severe threats to the infrastructure and human lives. Debris failures and run-outs are the most disastrous type of landslides [2]. The risk of disaster is the highest in case of debris failures, run-outs, and avalanches [3–5]. Human interference and engineering activities disturb the natural slopes which becomes more prone to failure [6, 7]. Debris failure susceptibility maps show the probability of the occurrence of debris failures in the region [8, 9]. It is important to determine the potential of natural hazards like landslides, avalanches, debris failures, etc. for risk assessment of the hazards.

Geographic information system (GIS) has emerged as an efficient tool for the planning and management of disasters [10]. The debris failure mapping was performed in the GIS environment by many researchers [5, 8, 9]. Qualitative and quantitative techniques are used widely for overall landslide susceptibility mapping [11–15]. Qualitative models like the analytic hierarchy process (AHP), analytic network process, fuzzy logic, etc. are used to perform landslide susceptibility mapping [16–21]. In quantitative techniques frequency ratio, bivariate statistical method, multivariate methods, and probabilistic methods are used for susceptibility mapping [21–24]. The quantitative approach establishes a relationship between the occurrence of landslides and causative factors [6, 7].

The study area selected in this study is the Rampur sub-division situated in Shimla district, Himachal Pradesh (H.P.), India. The landslide susceptibility mapping for the whole Shimla region has been undertaken using frequency ratio, Shannon's entropy, and analytic hierarchy process (AHP), but the Rampur sub-division is more susceptible to debris failure [7]. The monsoon season has a great impact on the occurrence of debris failures in the region. National Highway 5 was blocked due to a massive landslide in September 2021 [25]. Cracking of rocks, debris failures, and debris slides are common in the study area. So, there is a need to prepare a debris failure susceptibility map for the area which can help the planners and risk managers to mitigate the hazards.

Landslide susceptibility mapping is performed in different areas of the world and debris failures are considered

*For correspondence
Published online: 24 June 2023

with all other types of landslides, but debris failures are more disastrous and frequent in rainy seasons. So, there is a need of considering the debris failures separately. The aim of this study is to prepare a debris failure susceptibility map for the Rampur sub-division in the Shimla district using the information value method. Previously, landslide susceptibility maps are prepared for the whole Shimla region using frequency ratio, Shannon's entropy, and the AHP technique [7]. In this study information value technique is used for debris failure susceptibility mapping of the region. The debris failure susceptibility map has not been prepared for the study area before. The results of the study can help planners and risk managers for understanding the debris failure hazard in a better way.

2. Study area

Rampur is the sub-division in the Shimla district of Himachal Pradesh (H.P.) province in India. The study area lies in the north-western range of the Himalayas. Rampur town is located along the bank of the Satluj River [26]. Figure 1 shows the study area. The failure of the Satluj River changes drastically during monsoon season causing the cutting and erosion of the soil along its banks. The study area lies between longitudes 77° 29′ E and 77° 57′ E and latitudes 30° 15′ N and 31° 43′ N.

The average elevation of the Rampur sub-division is 4429 feet above mean sea level [26]. The changes in vegetation can be observed as the elevation of the study area changes. The precipitation remains maximum during August month. The monthly average precipitation is 1575 ml [27]. Snowfall takes place in the region during December, January, and even up to mid-February. The study area lies in Zone 4 as per earthquake hazard zonation. The region is under the high-damage risk zone [27]. The increasing number of tourists, climate change, and anthropogenic activities make the study area more vulnerable to natural hazards.

2.1 *Debris failure inventory*

A debris failure inventory provides details about the historical debris failure cases. The inventory consists of

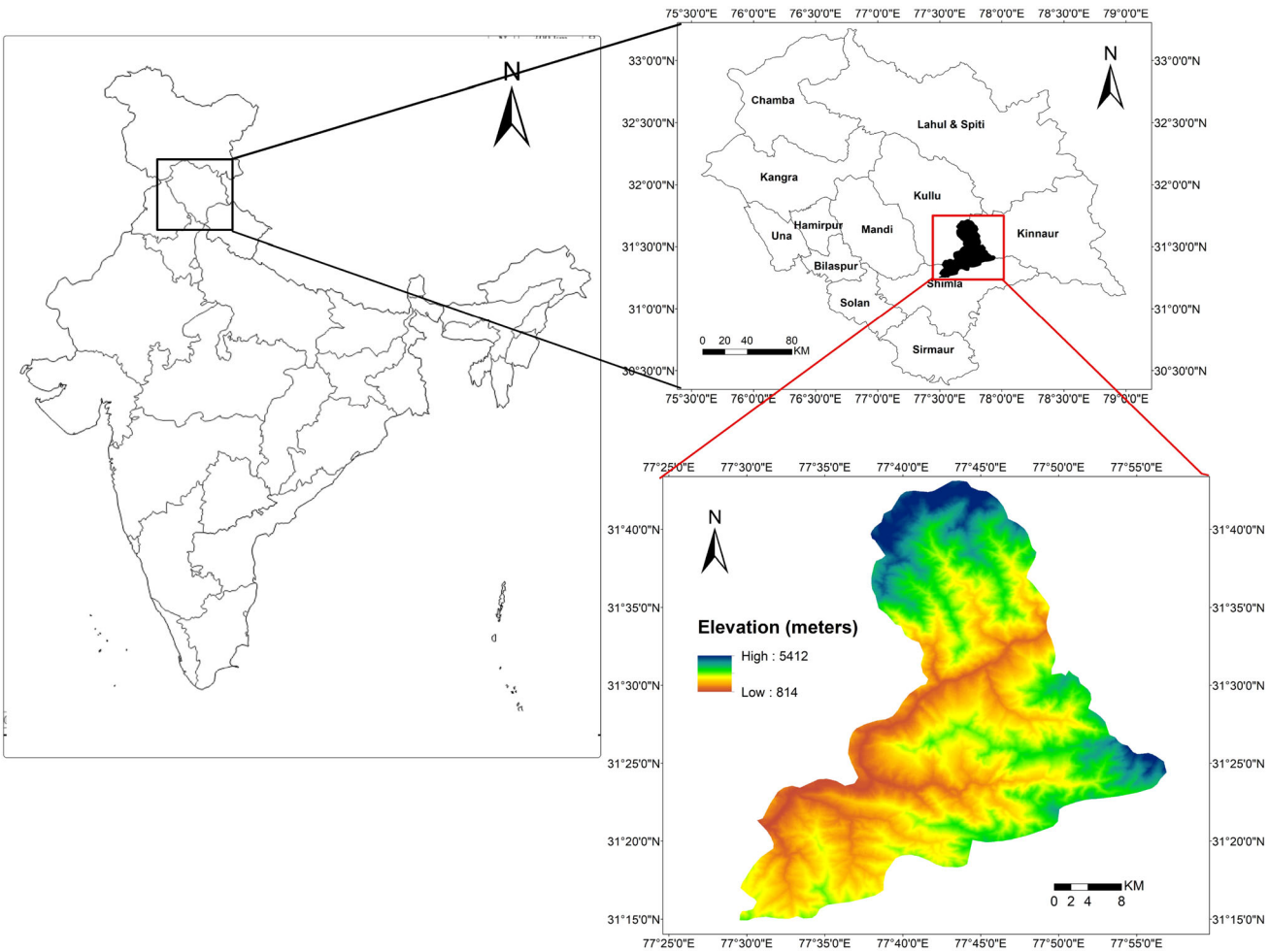

Figure 1. Study area.

information about the type of failure, location of the failure, impact of failure, activity, date of occurrence, etc. A debris failure inventory containing more than 400 debris failure cases is prepared using previous literature, newspaper articles, the Bhukosh portal, Survey of India (SOI) factsheets, and field surveys. The inventory consists of debris failures, debris slides, and subsidence events. The debris failures are mapped as polygons. The inventory is used for mathematical modeling and validation of the results.

2.2 *Parameters of debris failure*

The occurrence of debris failures depends on the various causative factors. There are three kinds of causative factors considered in this study i.e. topographic factors, geological factors, hydrological factors, land use of the region, and anthropogenic causative factors. The causative factors of debris failure are explained briefly. Figure 2 shows the details of causative factors.

2.2.1 *Topographic factors* Topography plays an important role in the occurrence of debris failures [28]. The factors related to the topographical characteristics of the region are considered in this study. The first topographical factor considered is the slope gradient. The slope gradient represents the angle of inclination of soil mass or rock mass. Steeper slopes are more prone to failure [24, 27]. The major area (more than 70%) of the region is covered with slopes of more than 65°.

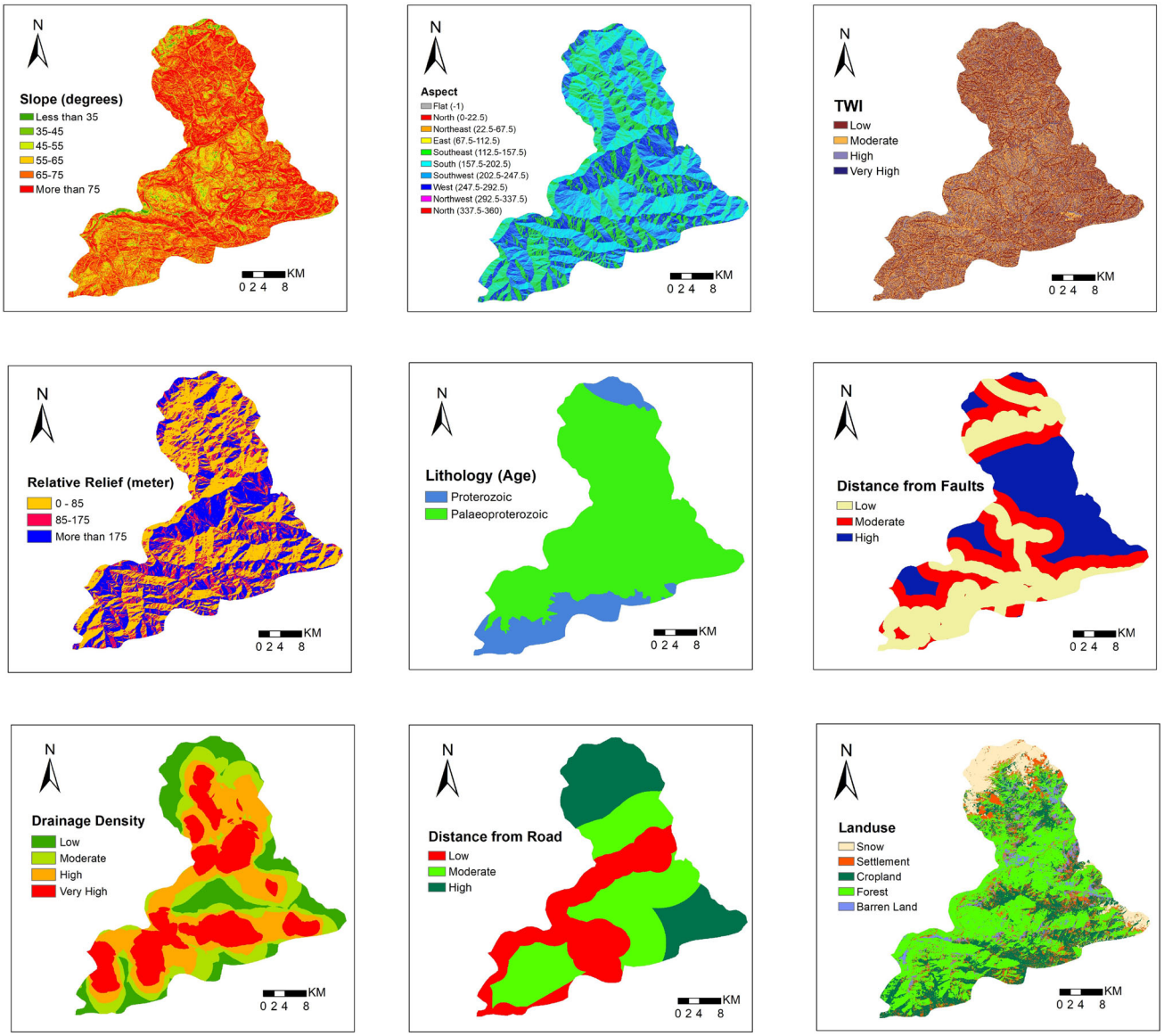

Figure 2. Causative factors of the debris failure.

The slope aspect is the second topographic factor that is considered in this study. The aspect shows the direction of the maximum slope. The direction of the slope considers the impact of exposure to sunlight, winds, and rainfall indirectly [29]. So, it becomes an important causative factor.

The topographic wetness index (TWI) is also an important causative factor of debris failures. It is also known as the compound topographic index [30, 31]. It shows the control of topography over the hydrological process. Indirectly it shows the impact of moisture on the occurrence of debris failure. It represents the moisture-retaining capacity of the soil. TWI establishes a relationship between the specific catchment area (SCA) and slope angle. TWI acts on the principle of the mass balance equation. Specific catchment area (SCA) represents the tendency of receiving the water while slope angle shows the tendency of draining out of the water. Lower TWI values are more prone to the occurrence of landslides.

Relative relief shows the variation of elevation. As the relief changes, the type of vegetation and topography changes which impacts the occurrence of debris failures [29]. The relative relief of the region varies from 0 m to 254 m. The relative relief is extracted from the digital elevation model (DEM). The relative relief of the region is divided into three categories i.e. 0–85 m, 85–175 m, and more than 175 m. More than 40% of the total study area lies under low relief (0–85 m).

2.2.2 *Geological and hydrological factors* The geology of the region impacts the occurrence of debris failures [32]. The region's lithology is the first geological factor that affects the occurrence of debris failures. The age of lithological deposits is considered a causative factor of debris failures. The study area is covered with two types of lithological units i.e. Proterozoic and Palaeo-proterozoic. More than 80% of the study area is covered with Palaeo-proterozoic deposits. Proterozoic deposits consist of deposits of schist, amphibolite, and quartzite belonging to the Taradevi formation while the palaeo-proterozoic deposits consist of deposits of white-green quartzite, phyllite belonging to the Manikaran formation.

Fault distance is the second geological parameter considered in this study. The region near faults is more prone to failure [33–35]. The distance from faults is divided into three categories i.e. low, moderate, and high.

Hydrological characteristics of the area have a significant impact on the occurrence of debris failures [36]. Drainage density shows the impact of stream channels on the occurrence of debris failures. The erosion caused by rivers and streams triggers the failures along their banks [37, 38]. As the drainage density increases, the slopes become more prone to failure. The drainage density is divided into four categories.

2.2.3 *Miscellaneous causative factors* Human interference and unplanned construction activities in the hilly region are considered the main causative factors for the occurrence of debris failures. The impact of human interference is considered using the factor distance from roads. The slopes along the roads are more prone to failure. Due to excessive cutting and filling operations, the slopes near roads become unstable [39–44]. The distance from the road is divided into three categories.

Land use and land cover is also an important causative factor for this study. The Land use map is derived from Landsat 8 data. More than 40% of the region is covered with forests while 28% of the study area is covered with agricultural land. The land use of the region has been changing significantly due to the development of the study area. Land use has a significant impact on the occurrence of debris failures [45–47].

3. Mathematical modelling

The various causative factors are identified. The digital elevation model (DEM) is used to extract topographic factors. The faults and roads are digitized from Survey of India (SOI) maps. The causative factors and sub-factors are modeled according to information value using the reclassification tool. The layers are added using the raster calculator. Figure 3 shows the workflow of the study.

The information value method is used for the calculation of the weightage of causative factors and sub-factors. The information value method is a probabilistic approach that comes under the category of bivariate statistical techniques. The information value method is used widely for mapping landslide susceptibility but very rarely used for debris failure susceptibility mapping [14, 48–50]. The technique establishes a relationship between the occurrence of debris failures and causative factors.

The information value is defined as the natural logarithm of the ratio of conditional probability to the prior probability. The weightage of causative factors can be calculated using the following equation:

$$Info\ Value\ (IV) = \ln\left(\frac{Conditional\ Probability\ (CP)}{Prior\ Probability\ (PP)}\right)$$
$$Info\ Value\ (IV) = \ln\left(\frac{\frac{\text{Ndlpix}}{\text{Ncpix}}}{\frac{\text{Ntdlpix}}{\text{Ntcpix}}}\right) \quad (1)$$

Here, conditional probability (CP) is the ratio between the number of pixels covered by debris failure events in a particular class to the number of pixels covered by that class. The prior probability is the ratio between pixels covered by total debris failures to the number of pixels

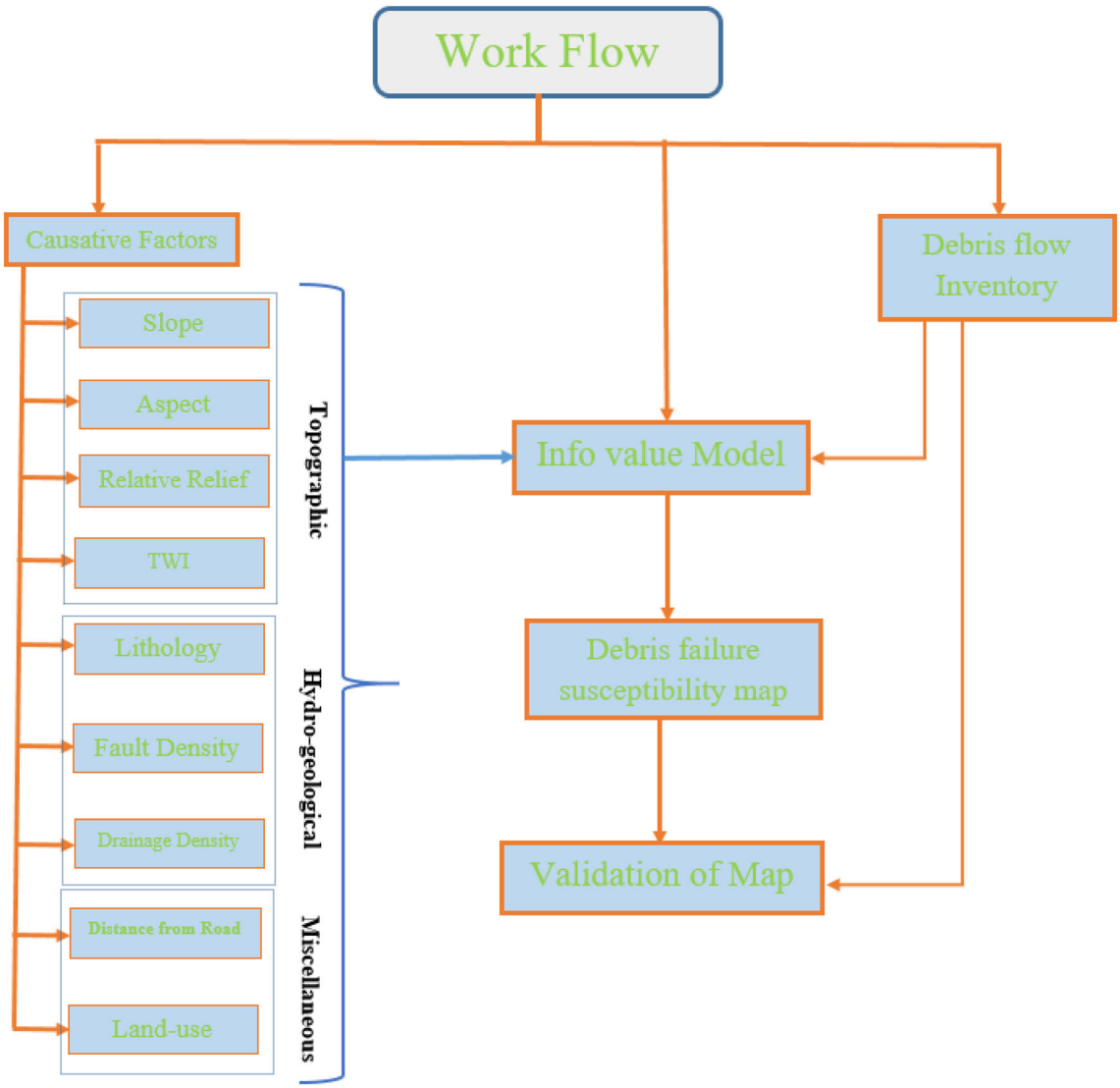

Figure 3. Workflow of the study.

covered by the total study area. Table 1 shows the values obtained from the information value technique. Positive information values show a high correlation of causative factors with the occurrence of landslides while negative information values show a lesser correlation.

4. Results and discussion

The relative importance of the causative factors and sub-factors are evaluated based on the weightage calculated using the information value technique. There is a negligible number of debris failures for the regions where slopes are less than 45° slopes. The slopes up to 45° show a negative correlation with the occurrence of debris failures. More than 45% of the study area is covered with slopes with slope angles of 65°–75°, and more than 37% of the total debris failure events occur in these regions. Slopes with more than 75° slope angle are highly susceptible to debris failures as 53.19% of the debris failures occur in such regions but such slopes cover only 27.96% of the total study area.

Flat, northwest, and west aspect directions show a very high negative correlation with the occurrence of debris failures while east, northeast, and southeast aspect directions show a positive correlation. East facing aspect covers 10.9% of the total area but 24.43% of the total debris failures occur in this area. Similarly, the northeast and southeast aspect covers around 21% of the total area but are responsible for the occurrence of 32.32% of the total debris failures. The northwest aspect covers more than 12% of the study area but only 4% of the total debris failures occur in this region.

Table 1. Info value weightage.

Conditioning factor	Classes	Pixels of class (Ncpix)	Pixels of landslides (Ndlpix)	% Pixel of landslides (pps)	% Area class (ppa)	Info value (IV)
Slope (°)						
	Less than 45	49347	50	0.00842	0.04104	− 1.584
	45–55	66715	140	0.02357	0.05549	− 0.856
	55–65	202163	390	0.06566	0.16815	− 0.940
	65–75	547813	2200	0.37037	0.45564	− 0.207
	More than 75	336245	3160	0.53199	0.27967	0.643
		1202283	**5940**			
Aspect						
	Flat	135643	230	0.03872	0.11282	− 1.069
	North	118623	549	0.09242	0.09866	− 0.065
	Northeast	106502	960	0.16162	0.08858	0.601
	East	131163	1451	0.24428	0.10909	0.806
	South East	147135	960	0.16162	0.12238	0.278
	South	157869	821	0.13822	0.13131	0.051
	South West	123612	412	0.06936	0.10281	− 0.394
	West	131033	274	0.04613	0.10899	− 0.860
	North West	150703	283	0.04764	0.12535	− 0.967
		1202283	**5940**			
Relative relief						
	0–85	528152	4380	0.73737	0.43929	0.518
	85–175	281043	960	0.16162	0.23376	− 0.369
	More than 175	393088	600	0.10101	0.32695	− 1.175
		1202283	**5940**			
TWI						
	Low	530866	3017	0.50791	0.44155	0.140
	Moderate	479044	2057	0.34630	0.39845	− 0.140
	High	165306	823	0.13855	0.13749	0.008
	Very high	27067	43	0.00724	0.02251	− 1.135
		1202283	**5940**			
Lithology						
	Proterozoic (Undiff)	206588	686	0.11549	0.17183	− 0.397
	Palaeoproterozoic	995695	5254	0.88451	0.82817	0.066
		1202283	**5940**			
Drainage density						
	Low	232575	415	0.06987	0.19344	− 1.018
	Moderate	247741	1436	0.24175	0.20606	0.160
	High	373654	2075	0.34933	0.31079	0.117
	Very high	348313	2014	0.33906	0.28971	0.157
		1202283	**5940**			
Distance from road						
	Low	373093	1077	0.18131	0.31032	− 0.537
	Moderate	489898	1632	0.27475	0.40747	− 0.394
	High	339292	3231	0.54394	0.28221	0.656
		1202283	**5940**			
Distance from faults						
	Low	461135	2511	0.42273	0.38355	0.097
	Moderate	357849	1783	0.30017	0.29764	0.008
	High	383299	1646	0.27710	0.31881	− 0.140
		1202283	**5940**			
Landuse/landcover						
	Snow	111264	1753	0.29512	0.09254	1.160
	Settlement	136274	210	0.03535	0.11335	− 1.165
	Agricultural land	340077	960	0.16162	0.28286	− 0.560
	Forest	541299	2880	0.48485	0.45023	0.074
	Barren Land	73369	137	0.02306	0.06102	− 0.973
		1202283	**5940**			

The relative relief is divided into three categories. 43.92% of the total area is covered with low relative relief (0–85 m) which is responsible for 73.73% of the total debris failures. Lower relief values establish a positive correlation with the occurrence of debris failures while high relative relief (more than 175 m) establishes a negative correlation. High relief covers 32.69% of the total study area but is responsible for the occurrence of 10.1% of the total debris failures.

The topographic wetness index (TWI) is divided into four categories. Lower values of TWI showed a positive correlation with the occurrence of debris failures. Low TWI covers 44.15% of the total area while contributing to 50.791% of the total debris failures. Very high values of TWI show a high negative correlation (− 1.135) towards the occurrence of debris failures.

Lithology is divided into two categories i.e. Proterozoic and Palaeo-proterozoic. Palae-oproterozoic lithological deposits show a positive correlation with the occurrence of debris failures. More than 80% of the total region is covered with Palaeo-proterozoic deposits which are responsible for the occurrence of more than 88% of the total debris failures. Proterozoic deposits cover 17.18% of the total study area but only 11.54% of the total debris failures occur in such regions.

Lower drainage densities show a negative correlation with the occurrence of debris failures while higher drainage densities show a positive correlation. Very high drainage density region is 28.97% of the total study area and 33.9% of the total debris failures occur in such regions. As the drainage density increases, the potential for debris failure increases. 19.34% of the total study area lies under the low drainage density category and faces only 6.98% of the total debris failures.

Distance from the roads is divided into three categories. The low distance from the roads shows a negative correlation while the large distance from the roads shows a positive correlation with the occurrence of debris failures. It is because there is less number of roads in the study area. High distances from roads cover 28.22% of the total study area but 54.39% of the total debris failures occur in this region.

As the proximity to the faults increases, the proneness towards debris failure increases. 38.35% of the total study area is highly proximate to the faults and 42.27% of the total debris failures occur in this region. Around 32% of the

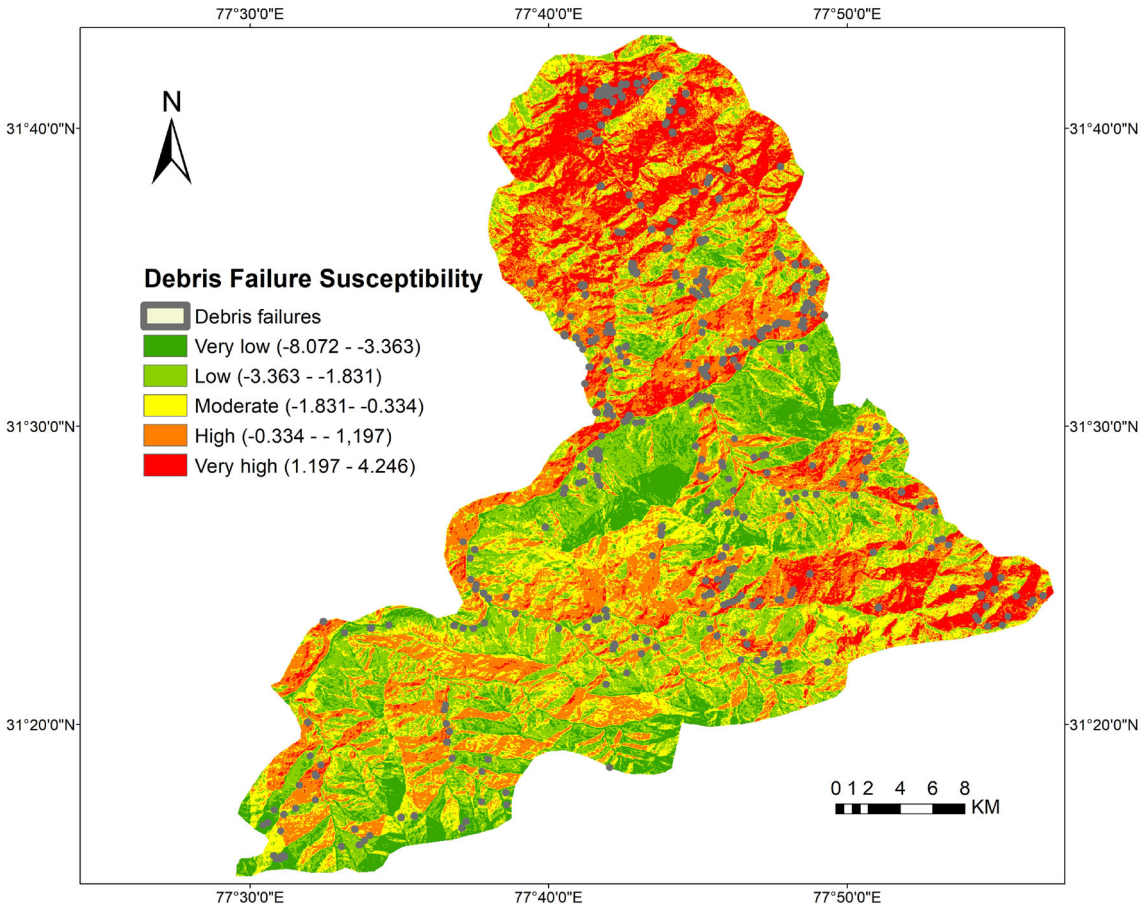

Figure 4. Debris failure susceptibility map.

total area falls under the high distance from faults category and around 27% of the total debris failures take place in such regions.

The region covered with snow shows a positive correlation with the occurrence of debris failures. The region covered with snow is only 9.25% of the total study area but more than 29% of the total debris failure events occur in this region. Forests cover around 45% of the total study area and the forest-covered region faces around 49% of the total debris failures. The causative factors are prepared in different thematic layers. The info value weightage is assigned to the sub-factors using the reclassification tool. The thematic layers are overlaid to obtain the debris failure susceptibility map. The debris failure susceptibility map is divided into five categories i.e. very low (− 8.072 to − 3.363), low (− 3.363 to − 1.831), moderate (− 1.831 to − 0.334), high (− 0.334 to 1.197), very high (1.197–4.246). Figure 4 shows the debris failure susceptibility map. The area which is very low and low susceptible to the occurrence of debris failure covers 11.81% and 21.93% of the total study area respectively and faced only around 11% of the total debris failures in total. The region which is moderately susceptible to the occurrence of debris failures covers 22.62% of the total area and faced around 12% of the total debris failures. 28.32% of the total study area lies under high susceptibility towards debris failures and faced 32.55% of the total debris failures. Only 15.29% of the total study area lies under very high susceptibility towards debris failure and 44.19% of the total debris failures occur in very high susceptibility zone. Figure 5 shows the graphical representation of the distribution of debris failures with respect to the debris failure susceptibility zones. The receiver's operation characteristics curve is used for validation of the final map.

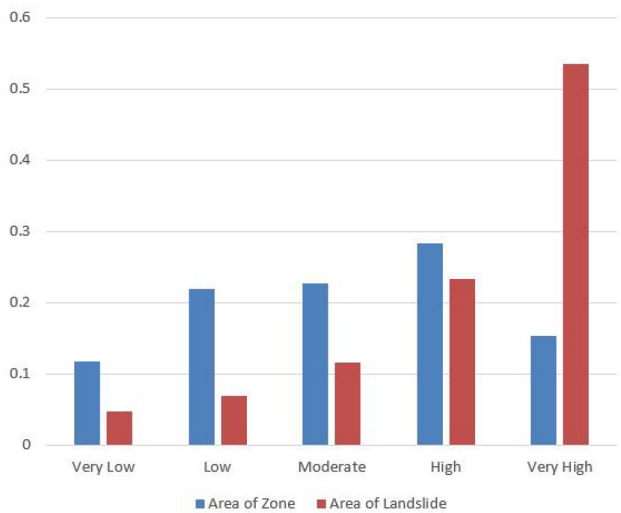

Figure 5. Distribution of debris failure versus area of zones.

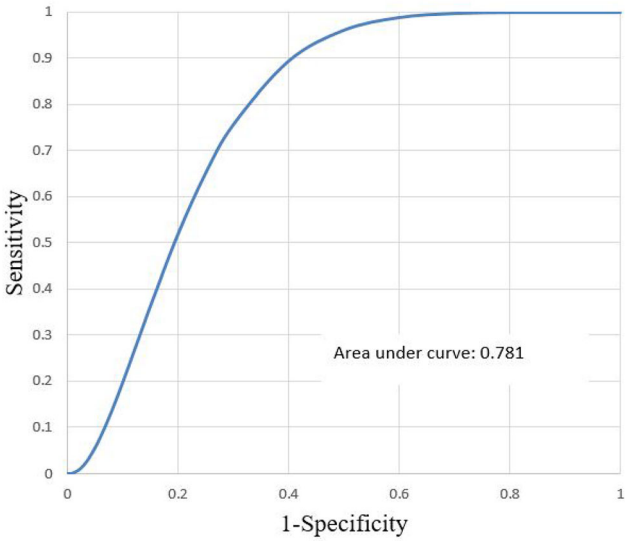

Figure 6. ROC curve.

The ROC curve is shown in figure 6. The curve shows an accuracy of 0.781 which is good at the regional level. The accuracy of the final map depends upon the causative factors and the accuracy and distribution of debris failure inventory. The accuracy can be further improved by identifying the realistic causative factors.

5. Conclusion

The debris failure susceptibility map for the study area is prepared using the information value model in GIS environment. This statistical model has given very encouraging results showing an accuracy of 0.781. The region lying under high and very high susceptibility show evidence of debris slides, debris flows, and subsidence. The impact of slope, curvature and drainage density has a significant impact on the occurrence of debris failures while the distance from the road has less impact on the occurrence of debris failures. The planners and risk managers can use the output of this study. The results of the study can help in better planning of the facilities in the region which can help in mitigating debris disasters.

Acknowledgement

The first author is thankful to his wife Mrs. Anjali for her cooperation during the study.

Funding No funding is obtained for this work.

Data availability All the data generated or analyzed during this study are included in this published article.

Declarations

Conflict of interest No potential conflict of interest was reported by the author(s).

References

[1] Berzi D, Jenkins J T and Larcher M 2010 Debris failures: recent advances in experiments and modelling. *Adv. Geophys.* 52: 103–108. https://doi.org/10.1016/S0065-2687(10)52002-8

[2] Nohani E, Moharrami M, Sharafi S, Khosravi K, Pradhan B, Pham B T, Lee S, Asseffa M M 2019 Landslide susceptibility mapping using different GIS-based bivariate models. *Water* 11: 1402. https://doi.org/10.3390/w11071402

[3] Ryou K, Chang H and Lee H 2021 Laboratory analysis of debris flow characteristics and berm performance. *Water* 13: 2223. https://doi.org/10.3390/w13162223

[4] Sassa K, and Wang G (n.d.) 2005 Mechanism of landslide-triggered debris flows: liquefaction phenomena due to the undrained loading of torrent deposits. In: *Debris-Flow Hazards and Related Phenomena*. Springer Berlin Heidelberg, pp. 81–104. https://doi.org/10.1007/3-540-27129-5_5

[5] Wang C, Esaki T, Xie M and Qiu C 2006 Landslide and debris-flow hazard analysis and prediction using GIS in Minamata-Hougawachi area, Japan. *Environ. Geol.* 51(1): 91–102. https://doi.org/10.1007/s00254-006-0307-0

[6] Panchal S and Shrivastava A K 2020 Application of analytic hierarchy process in landslide susceptibility mapping at regional scale in GIS environment. *J. Stat. Manag. Syst.* 23(2): 199–206. https://doi.org/10.1080/09720510.2020.1724620

[7] Panchal S and Shrivastava A K 2021 A comparative study of frequency ratio, Shannon's entropy and analytic hierarchy process (AHP) models for landslide susceptibility assessment. *ISPRS Int. J. Geo-Inf.* 10: 603. https://doi.org/10.3390/ijgi10090603

[8] Qin S, Lv J, Cao C, Ma Z, Hu X and Liu FF, Qiao S, Dou Q 2019 Mapping debris flow susceptibility based on watershed unit and grid cell unit: a comparison study. *Geomat. Nat. Hazards Risk* 10(1): 1648–1666. https://doi.org/10.1080/19475705.2019.1604572

[9] Polat A and Erik D 2020 Debris flow susceptibility and propagation assessment in West Koyulhisar, Turkey. *J. Mt. Sci.* 17(11): 2611–2623. https://doi.org/10.1007/s11629-020-6261-6

[10] Gokceoglu C and Aksoy H 1996 Landslide susceptibility mapping of the slopes in the residual soils of the Mengen region (Turkey) by deterministic stability analyses and image processing techniques. *Eng. Geol.* 44: 147–161. https://doi.org/10.1016/s0013-7952(97)81260-4

[11] Lee S, Ryu J-H, Won J-S and Park H-J 2003 Determination and application of the weights for landslide susceptibility mapping using an artificial neural network. *Eng. Geol.* 71: 289–302. https://doi.org/10.1016/s0013-7952(03)00142-x

[12] Yeon Y-K, Han J-G and Ryu K H 2010 Landslide susceptibility mapping in Injae, Korea, using a decision tree. *Eng. Geol.* 116: 274–283. https://doi.org/10.1016/j.enggeo.2010.09.009

[13] Pourghasemi H R, Mohammady M and Pradhan B 2012 Landslide susceptibility mapping using index of entropy and conditional probability models in GIS: Safarood Basin, Iran. *Catena* 97: 71–84. https://doi.org/10.1016/j.catena.2012.05.005

[14] Singh K and Kumar V 2018 Hazard assessment of landslide disaster using information value method and analytical hierarchy process in highly tectonic Chamba region in bosom of Himalaya. *J. Mt. Sci.* 15: 808–824. https://doi.org/10.1007/s11629-017-4634-2

[15] Gautam P, Kubota T, Sapkota L M and Shinohara Y 2021 Landslide susceptibility mapping with GIS in high mountain area of Nepal: a comparison of four methods. *Environ. Earth Sci.* 80: 359. https://doi.org/10.1007/s12665-021-09650-2

[16] Hasekioğulları G D and Ercanoglu M 2012 A new approach to use AHP in landslide susceptibility mapping: a case study at Yenice (Karabuk, NW Turkey). *Nat. Hazards* 63: 1157–1179. https://doi.org/10.1007/s11069-012-0218-1

[17] Kayastha P, Dhital M and De Smedt F 2013 Application of the analytical hierarchy process (AHP) for landslide susceptibility mapping: a case study from the Tinau watershed, west Nepal. *Comput. Geosci.* 52: 398–408. https://doi.org/10.1016/j.cageo.2012.11.003

[18] El Jazouli A, Barakat A and Khellouk R 2019 GIS-multicriteria evaluation using AHP for landslide susceptibility mapping in Oum Er Rbia high basin (Morocco). *Geoenviron. Disasters* 6: 3. https://doi.org/10.1186/s40677-019-0119-7

[19] Sujatha E R and Sridhar V 2017 Mapping debris flow susceptibility using analytical network process in Kodaikkanal Hills, Tamil Nadu (India). *J. Earth Syst. Sci.* 126: 116. https://doi.org/10.1007/s12040-017-0899-7

[20] Lee S 2006 Application and verification of fuzzy algebraic operators to landslide susceptibility mapping. *Environ. Earth Sci.* 52: 615–623. https://doi.org/10.1007/s00254-006-0491-y

[21] Pradhan B 2010 Landslide susceptibility mapping of a catchment area using frequency ratio, fuzzy logic and multivariate logistic regression approaches. *J. Indian Soc. Remote Sens.* 38: 301–320. https://doi.org/10.1007/s12524-010-0020-z

[22] Kavzoglu T, Sahin E K and Colkesen I 2014 An assessment of multivariate and bivariate approaches in landslide susceptibility mapping: a case study of Duzkoy district. *Nat. Hazards* 76: 471–496. https://doi.org/10.1007/s11069-014-1506-8

[23] Akgun A and Erkan O 2016 Landslide susceptibility mapping by geographical information system-based multivariate statistical and deterministic models: in an artificial reservoir area at Northern Turkey. *Arab. J. Geosci.* 9: 165. https://doi.org/10.1007/s12517-015-2142-7

[24] Ram P, Gupta V, Devi M and Vishwakarma N 2020 Landslide susceptibility mapping using bivariate statistical method for the hilly township of Mussoorie and its surrounding areas, Uttarakhand Himalaya. *J. Earth Syst. Sci.* 129: 167. https://doi.org/10.1007/s12040-020-01428-7

[25] Bodh A 2021 Himachal Pradesh: landslide at Jeori blocks Shimla-Kinnaur highway, The Times of India, available on https://timesofindia.indiatimes.com/city/shimla/himachal-pradesh-landslide-at-jeori-blocks-shimla-kinnaur-highway/articleshow/85970060.cms

[26] Mathews R P 2013 Ground information water booklet Shimla district, Himachal Pradesh, Ministry of water resources, Central ground water board, Government of India accessed on 01/04/2021 available on http://cgwb.gov.in/District_Profile/HP/Shimla.pdf

[27] District Survey Document Shimla, accessed on 03/05/2021 available on https://emerginghimachal.hp.gov.in/miningstone/survay_docs/shimla.pdf

[28] Nakileza B R and Nedala S 2020 Topographic influence on landslides characteristics and implication for risk management in upper Manafwa catchment, Mt Elgon Uganda. *Geoenviron. Disasters* 7(1). https://doi.org/10.1186/s40677-020-00160-0

[29] Singh K and Kumar V 2017 Landslide hazard mapping along national highway-154A in Himachal Pradesh, India using information value and frequency ratio. *Arab. J. Geosci.* 10(24): 539. https://doi.org/10.1007/s12517-017-3315-3

[30] Pourghasemi H R, Mohammady M and Pradhan B 2012 Landslide susceptibility mapping using index of entropy and conditional probability models in GIS: Safarood Basin, Iran. *Catena* 97. https://doi.org/10.1016/j.catena.2012.05.005

[31] Akgun A and Erkan O 2016 Landslide susceptibility mapping by geographical information system-based multivariate statistical and deterministic models: in an artificial reservoir area at Northern Turkey. *Arab. J. Geosci.* 9(2): 165. https://doi.org/10.1007/s12517-015-2142-7

[32] Ali S, Haider R, Abbas W, Basharat M and Reicherter K 2021 Empirical assessment of rockfall and debris flow risk along the Karakoram Highway, Pakistan. *Nat. Hazards* 106(3): 2437–2460. https://doi.org/10.1007/s11069-021-04549-4

[33] Chen X, Chen H, You Y and Liu J 2015 Susceptibility assessment of debris flows using the analytic hierarchy process method: a case study in Subao river valley, China. *J. Rock Mech. Geotech. Eng.* 7(4): 404–410. https://doi.org/10.1016/j.jrmge.2015.04.003

[34] Li Y, Wang H, Chen J and Shang Y 2017 Debris flow susceptibility assessment in the Wudongde dam area, China based on rock engineering system and fuzzy C-means algorithm. *Water* 9(9). https://doi.org/10.3390/w9090669

[35] Di B, Zhang H, Liu Y, Li J, Chen N, Stamatopoulos C A, Luo Y, Zhan Y 2019 Assessing susceptibility of debris flow in Southwest China using gradient boosting machine. *Sci. Rep.* 9(1). https://doi.org/10.1038/s41598-019-48986-5

[36] Cabral V C, Reis F A G V, D'Affonseca F M, Lucía A, dos Santos Corrêa C V, Veloso V, Gramani M F,Ogura A T, Lazaretti A F, Vemado F, Filho A J P, Santos C C, Lopes E S S, Rabaco L M R, Giordano LC, Zarfl C 2021 Characterization of a landslide-triggered debris flow at a rainforest-covered mountain region in Brazil. *Nat. Hazards* 108(3): 3021–3043. https://doi.org/10.1007/s11069-021-04811-9

[37] Raja N B, Çiçek I, Türkoğlu N, Aydin O and Kawasaki A 2017 Landslide susceptibility mapping of the Sera River Basin using logistic regression model. *Nat. Hazards* 85(3): 1323–1346. https://doi.org/10.1007/s11069-016-2591-7

[38] Chen J, Chen X, Wang T, Zou Y and Zhong W 2014 Types and causes of debris flow damage to drainage channels in the Wenchuan earthquake area. *J. Mt. Sci.* 11(6): 1406–1419. https://doi.org/10.1007/s11629-014-3045-x

[39] Zhang Y, Ge T, Tian W and Liou Y-A 2019 Debris flow susceptibility mapping using machine-learning techniques in Shigatse area, China. *Remote Sens.* 11(23): 2801. https://doi.org/10.3390/rs11232801

[40] Singh K and Sharma A 2022 Road cut slope stability analysis at Kotropi landslide zone along NH-154 in Himachal Pradesh, India. *J. Geol. Soc. India* 98(3): 379–386. https://doi.org/10.1007/s12594-022-1989-y

[41] Hussain G, Singh Y, Singh K and Bhat G M 2019 Landslide susceptibility mapping along national highway-1 in Jammu and Kashmir State (India). *Innov. Infrastruct. Solut.* 4(1): 59. https://doi.org/10.1007/s41062-019-0245-9

[42] Panchal S and Shrivastava A K 2020 Landslide susceptibility mapping along highway corridors in GIS environment. In: *Smart Cities: Challenges and Opportunities*, *Lecture Notes in Civil Engineering*, pp. 79–89. https://doi.org/10.1007/978-981-15-2545-2_8

[43] Singh K and Kumar V 2021 Slope stability analysis of landslide zones in the part of Himalaya, Chamba, Himachal Pradesh, India. *Environ. Earth Sci.* 80(8): 332. https://doi.org/10.1007/s12665-021-09629-z

[44] Panchal S and Shrivastava A K 2022 Landslide hazard assessment using analytic hierarchy process (AHP): a case study of National Highway 5 in India. *Ain Shams Eng. J.* 13(3): 101626. https://doi.org/10.1016/j.asej.2021.10.021

[45] Yesilnacar E and Süzen M L 2006 A land-cover classification for landslide susceptibility mapping by using feature components. *Int. J. Remote Sens.* 27(2): 253–275. https://doi.org/10.1080/0143116050030042

[46] Swetha T V and Gopinath G 2020 Landslides susceptibility assessment by analytical network process: a case study for Kuttiyadi river basin (Western Ghats, southern India). *SN Appl. Sci.* 2(11). https://doi.org/10.1007/s42452-020-03574-5

[47] Roccati A, Paliaga G, Luino F, Faccini F and Turconi L 2021 GIS-based landslide susceptibility mapping for land use planning and risk assessment. *Land* 10(2). https://doi.org/10.3390/land10020162

[48] Sarkar S, Roy A K and Martha T R 2013 Landslide susceptibility assessment using Information Value Method in parts of the Darjeeling Himalayas. *J. Geol. Soc. India* 82(4): 351–362. https://doi.org/10.1007/s12594-013-0162-z

[49] Chen T, Niu R and Jia X 2016 A comparison of information value and logistic regression models in landslide susceptibility mapping by using GIS. *Environ. Earth Sci.* 75(10): 867. https://doi.org/10.1007/s12665-016-5317-y

[50] Du G, Zhang Y, Iqbal J, Yang Z and Yao X 2017 Landslide susceptibility mapping using an integrated model of information value method and logistic regression in the Bailongjiang watershed, Gansu Province, China. *J. Mt. Sci.* 14(2): 249–268. https://doi.org/10.1007/s11629-016-4126-9

RSC Advances

PAPER

View Article Online
View Journal | View Issue

Check for updates

Cite this: *RSC Adv.*, 2023, **13**, 16663

Deep red emission from rare-earth-free calcium aluminozincate phosphor with the substitution of Cr^{3+} ion

Sumandeep Kaur, Videsh Kumar and A. S. Rao *

Chromium-doped calcium aluminozincate phosphor with a distinct amount of chromium was prepared *via* the sol–gel technique. The phase analysis and morphological study along with optical properties were conducted on the prepared material. The room temperature luminescent traits of the sample were studied in detail under 540 nm excitation wavelength. The deep red emission was confirmed from the CIE coordinates calculated using emission data. The decay curves were recorded to calculate the lifetime values for the aforementioned powder samples. The temperature-dependent luminescent characteristics were also investigated to identify the activation energy and thermal stability. The quantum yield was also calculated using luminescence spectra and found to be relatively good for the present phosphor. All of the investigated studies specified above signify that the synthesized phosphor is well suited as a red emitter in lighting and display devices.

Received 31st March 2023
Accepted 14th May 2023

DOI: 10.1039/d3ra02129g

rsc.li/rsc-advances

Open Access Article. Published on 02 June 2023. Downloaded on 6/14/2023 6:39:21 AM.
This article is licensed under a Creative Commons Attribution-NonCommercial 3.0 Unported Licence.

1. Introduction

Inorganic materials incorporated with transition metal or rare earth ions, also known as phosphors, exhibit luminescence. These luminescent materials find applications in various fields, *e.g.*, sensors, solar cells, plant growth, display, lighting, biophotonic applications, and anti-counterfeiting.[1–7] Usually, rare earth ions such as Eu^{3+}, Tb^{3+}, Sm^{3+}, and Dy^{3+} ions are widely used in lighting applications. However, there are some limitations of using these rare earths as dopants in luminescent materials. These rare earths are quite expensive and require some harsh conditions such as high temperature and high pressure[8] to synthesize phosphors. Also, these rare earths have high photon re-absorption in the visible region owing to various transition levels available in rare earth ion doped phosphors and decline the output of the phosphors. Moreover, they have narrow and weak absorption bands due to parity-forbidden transitions, which reduce the absorption efficiency.[9] All of these drawbacks provide an opportunity for the development of rare-earth-free phosphors for different applications.

The alternative approach of designing a color emitter in the hue of the visible electromagnetic spectrum is to use transition metal ions, such as Bi^{3+}, Cr^{3+}, Mn^{4+}, and Mn^{2+} as dopants in the inorganic material as these ions possess blue, red, and green emissions, respectively.[9–14] There are many reports on the Cr^{3+} and Mn^{4+}-doped luminescent materials developed for wLEDs as a red component, which is required to improve the color rendering index of wLEDs.[8] The transition metals have a tendency to give variable color emission based on different hosts, as the transitions that take place in the transition metal ion-doped phosphors are influenced by the crystal field environment, including the type of ligand coordination, variation in functional groups, and covalency.[15,16] The energy levels in the transition metal ions are described by the Tanabe–Sugano diagram. The vacant d-orbital of Cr^{3+} ($3d^3$) provides the arrangement of energy levels based on the crystal field and site occupation in such a way that it can give red and near infrared emission.[12,17,18] Qiang M. *et al.* reported on ceramic phosphor $ZnAl_2O_4$ doped with Cr^{3+} ions and studied the luminescence properties, as far red luminescence is important for plant growth.[19] Liu *et al.* reported on chromium ion-doped magnesium tantalate having emission in the NIR region.[13] This indicates that the color can be tuned in Cr^{3+}-doped materials by varying the host matrix.

Furthermore, as a host matrix, different oxide hosts have been explored for their utility in lighting and display devices. The zincate-based host matrix possesses good chemical and thermal stability. In this article, the calcium aluminozincate phosphor has been chosen as a host matrix since it possesses excellent luminescent properties when doped with rare earth ions. Therefore, the authors chose the same host matrix and tried to explore the luminescent behavior of the host when doped with transition metal ions.

Furthermore, there are different synthesis techniques to design phosphor materials, including the solid-state reaction method, sol–gel, combustion, hydrothermal, and molten salt. For the synthesis of the Cr^{3+}-doped calcium aluminozincate phosphor, the sol–gel technique is followed as it is a low temperature synthesis technique that provides the facility of

Department of Applied Physics, Delhi Technological University, Shahbad Daulatpur, Bawana Road, New Delhi 110 042, India. E-mail: drsrallam@gmail.com

© 2023 The Author(s). Published by the Royal Society of Chemistry

Open Access Article. Published on 02 June 2023. Downloaded on 6/14/2023 6:39:21 AM.
This article is licensed under a Creative Commons Attribution-NonCommercial 3.0 Unported Licence.

controlling parameters during the reaction process.[21,22] Moreover, the morphology is improved with the low temperature synthesis technique in comparison with the solid-state reaction technique. This results in better luminescent properties of the prepared phosphors.

Hence, in this article, Cr^{3+}-doped calcium aluminozincate phosphors have been developed using the sol–gel technique. The structural and luminescent properties have been examined thoroughly to understand the potential of a rare earth-free phosphor in lighting applications.

2. Experiment and characterizations

$Ca_{3-x}Al_4ZnO_{10}:xCr^{3+}$ (where x = 0.01, 0.02, 0.03, 0.04 & 0.05 mol) phosphors were synthesized *via* sol–gel method. The precursors, including calcium nitrate ($Ca(NO_3)_2\cdot 9H_2O$, 99.9%), zinc nitrate ($Zn(NO_3)_2\cdot 6H_2O$, 99.9%), aluminium nitrate ($Al(NO_3)_3\cdot 6H_2O$, 99.9%) chromium(III) nitrate nonahydrate ($Cr(NO_3)_3\cdot 9H_2O$, 99.9%), and citric acid anhydrous ($C_6H_8O_7\cdot 2H_2O$, 99.5%) were dissolved individually in the de-ionized (DI) water without further purification. At first instance, the nitrates of calcium, zinc and aluminium were added by stirring at 80 °C. Then, a dropwise solution of chromium nitrate in DI water was added, and the solution was allowed to mix by placing it on a magnetic stirrer at 120 °C for 2 h. The solution of citric acid (CA) in DI was added into the above mixture. The ratio of metal nitrates to citric acid was fixed as 1 : 2, and pH = 2 was kept for this reaction to take place successfully to prepare the said phosphor. A volume of 2 ml of polyethylene glycol (PEG) was added dropwise, and the solution was stirred for 10 hours. Brown porous solid flakes were obtained after firing at 500 °C. It was ground and sintered at 1000 °C, and then again ground to carry out further characterizations.

The X-ray Bruker D8 Advance Diffractometer was used to record the XRD patterns of the synthesized phosphor, and it has the Cu source to produce the X-ray (λ = 1.54 Å). A Jasco FP-8300 spectrofluorometer was used to measure the photoluminescence emission and excitation. An Edinburgh FL920 Fluorescence Lifetime Spectrometer was used to record the photoluminescence decay profile. The FT-IR spectrum was recorded by a FT-IR Spectrometer – PerkinElmer Frontier. The temperature-dependent photoluminescence characteristics were investigated by the FLAME-S-XR1-ES model ocean optics spectrometer.

3. Results and discussion

3.1. Phase analysis

As shown in Fig. 1, X-ray diffraction (XRD) patterns of the Cr^{3+}-doped CAZ phosphor at various Cr^{3+} concentrations (0.01, 0.02, 0.03, 0.04, and 0.05 mol) are in accordance with the $Ca_3Al_4ZnO_{10}$ standard card (ICDD card no. 04-009-7304), and the (h k l) planes have been properly indexed. The synthesis of the calcium aluminozincate phosphor is confirmed by the sharp XRD patterns that are free of any extra impurity peaks. This confirms that the prepared phase is pure, and its structure matches with the orthorhombic structure.

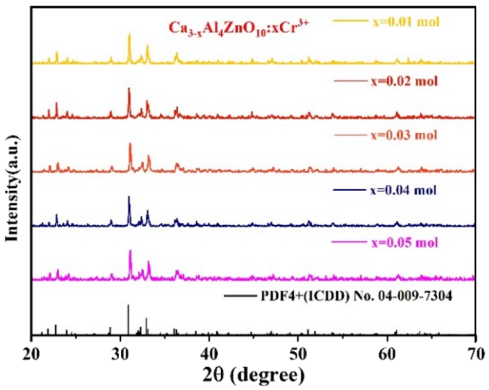

Fig. 1 XRD patterns of the synthesized CAZ samples.

According to the findings, adding Cr^{3+} ions to the calcium aluminozincate phosphor does not significantly alter the host crystal structure.

The average crystallite size of $Ca_{2.97}Al_4ZnO_{10}:0.03Cr^{3+}$ was measured by substituting the related parameters from the recorded XRD data in the Debye–Scherer equation, as reported in the literature.[23] The average crystallite size is estimated as 38 nm.

3.2. Morphology

The morphological image of $Ca_{2.97}Al_4ZnO_{10}:0.03Cr^{3+}$ is conferred in Fig. 2. The synthesized sample has a solid microcrystalline structure, which ascertains the random morphology of the particle along with some agglomeration. The average particle size of the synthesized phosphor is in the range of 1–5 μm, which is suitable for the application in lighting devices.[24]

3.3. FT-IR analysis

The functional group composition study of the synthesized CAZ phosphor was carried out by FT-IR. Fig. 3 represents the FT-IR

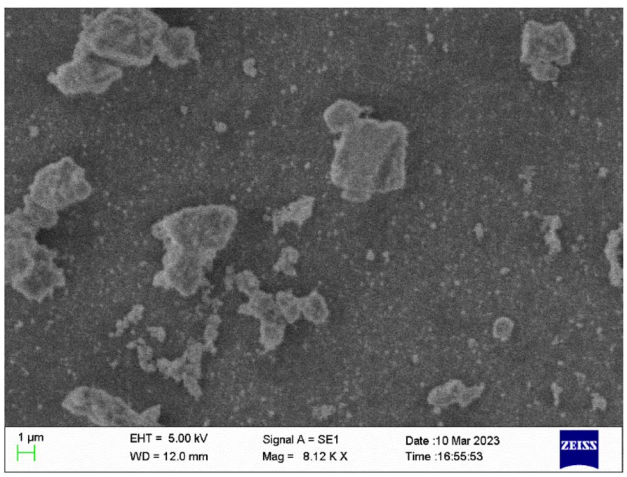

Fig. 2 SEM image of the $Ca_{2.97}Al_4ZnO_{10}:0.03Cr^{3+}$ phosphor.

© 2023 The Author(s). Published by the Royal Society of Chemistry

Open Access Article. Published on 02 June 2023. Downloaded on 6/14/2023 6:39:21 AM.
This article is licensed under a Creative Commons Attribution-NonCommercial 3.0 Unported Licence.

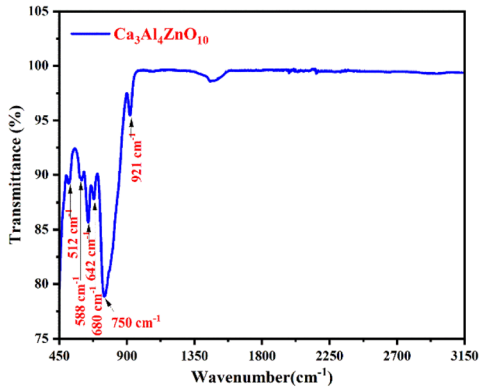

Fig. 3 FT-IR spectrum of the $Ca_{2.97}Al_4ZnO_{10}$:0.03Cr^{3+} phosphor.

spectrum of the $Ca_{2.97}Al_4ZnO_{10}$:0.03Cr^{3+} phosphor in the frequency region of 450 to 3150 cm^{-1}.

The bands in the range of 450–650 cm^{-1} appeared due to the vibration of the bond between the metal and oxygen atoms Al–O and Ca–O.[25] The characteristic bands at 512 and 588 cm^{-1} reveal the vibration of Zn–O in the stretching of the ZnO_4 unit.[26,27] The bands centered at 642, 680 cm^{-1} and 750 cm^{-1} are due to the Al–O bond vibrations in the AlO_4 tetrahedral unit.[25,28,29] The band at 921 cm^{-1} is because of the asymmetric stretch vibrations of the Al_n–OH bond.[30]

3.4. Room temperature luminescence characteristics

The photoluminescence excitation (PLE) spectrum was recorded at an emission wavelength of 688 nm, and is displayed in Fig. 4. The broad excitation peaks appear in the range of 460 to 650 nm and centered at 540 nm due to the spin-allowed transition $^4A_{2g} \rightarrow {}^4T_{2g}$.[19]

The photoluminescence (PL) spectra of the CAZ:$x$$Cr^{3+}$ phosphor were recorded by maintaining its irradiation wavelength at 540 nm for different concentrations of chromium ion, and are shown in Fig. 5. The spectra show numerous distinct peaks that are characteristic of Cr^{3+} ion emission in a strong field with

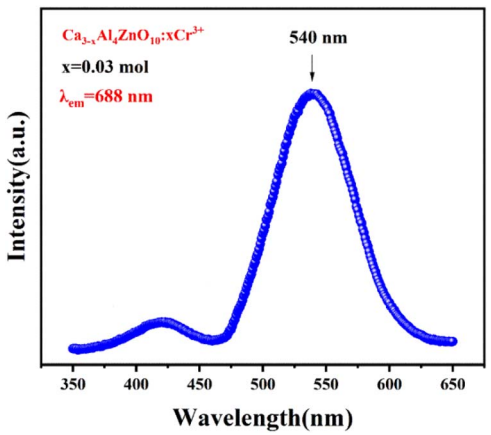

Fig. 4 PLE spectrum of the synthesized sample CAZ:$x$$Cr^{3+}$ (where x = 0.03 mol).

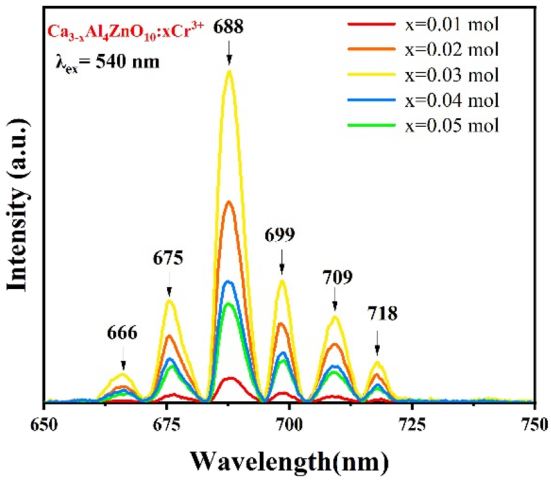

Fig. 5 PL spectra of different Cr^{3+} doping concentrations.

octahedral coordination. The sample with 0.03 mol Cr^{3+} doping shows the highest emission intensity at 688 nm. This is due to the $^2E \rightarrow {}^4A_2$ transition (zero-phonon R-line of Cr^{3+} ions).[19,31] A similar band was observed in $ZnAl_2O_4$ doped with Cr^{3+} ions, as reported by Qiang M. *et al.*[19] However, it is not the case with all of the hosts that they exhibit emission at similar wavelengths. Liu *et al.* reported on $MgTa_2O_6$:Cr^{3+} and observed a broad emission with a peak at 834 nm.[20] This occurs because the valence electrons of the transition metal ions are not shielded with the outer shell. This results in a strong interaction between the ligand field and d electrons of the transition metal ions. Thus, by altering the host, the emission can be tuned in luminescent materials that are being doped with transition metal ions. The additional emission peaks in the present study are positioned at 666 nm, 675 nm, 699 nm, 709 nm, and 718 nm, and include the R-line and the phonon sidebands.[19,31,32]

The side bands are observed due to anti-site defects, which basically arise due to thermal corrosion and anti-stoke displacement.[20] In another reported article by Xiao *et al.*, it has been shown that Cr^{3+} ions occupied multiple sites. Owing to this, there are bands observed at different positions.[17] Thus, it can be anticipated from previously published reports and the work conducted in the present study that the host matrix plays a major role in tuning the emission in Cr^{3+}-doped materials. It is thus possible to tune the emission from red to far infrared (*i.e.*, 650–1400 nm). Moreover, the luminescence intensity increases up to 0.03 mol Cr^{3+} ion doping. After that, it starts to decrease with an increase in doping concentration. This occurs due to concentration quenching. Lai *et al.* reported on a Cr^{3+}-doped $SrGa_4O_7$ host, where the emission was observed at 696 and 770 nm.[18] In general, three interaction processes, exchange interaction, radiation reabsorption, and electric multipolar interaction among activator ions are responsible for non-radiative energy transfer.[33] The exchange interaction can take place at critical distances of up to 5 Å (R_C), which is insufficient for concentration quenching at very low concentration. This cannot be ascribed to concentration quenching because there will be sufficient distance between the two luminous centers.

Open Access Article. Published on 02 June 2023. Downloaded on 6/14/2023 6:39:21 AM.
This article is licensed under a Creative Commons Attribution-NonCommercial 3.0 Unported Licence.

An event of radiation reabsorption takes place only when the excitation and emission spectra are overlapped, which is not seen in the presently studied phosphor. The electric multipole–multipole interaction is majorly affected by the critical distance. The good estimation of non-radiative transfer of energy between the Cr^{3+} ions is provided by the critical distance among Cr^{3+} and Cr^{3+} ions at the critical concentration (X_C). R_C is calculated by the equation, which is mentioned in the literature.[34,35] By using the experimental data, the critical distance is calculated to be 24 Å. The calculated R_C is much greater than 5 Å, which is required for the exchange interaction. As the critical distance is considerably different, it is obvious that the exchange interaction is an unsuitable method for transferring energy in this situation. Instead, multipolar interaction might have taken place in this host.

If the energy transfer takes place by electric multipole interaction, then it can be investigated by Dexter's theory. From Dexter's theory, the emission intensity is given by the following equation:[36]

$$\frac{I}{x} = K\left[(1+\beta(x))^{\frac{Q}{3}}\right]^{-1} \quad (1)$$

where, I is an intensity of the photoluminescence, x is a dopant ion concentration, and K and β are constants for the host lattice. The closest ion interaction type is identified by the Q value, which is equal to 3, 6, 8, and 10 for exchange, dipole–dipole, dipole-quadrupole, and quadrupole–quadrupole interactions, respectively. Simplifying the above equation by taking the log, the simplified equation is given below:

$$\log\frac{I}{x} = P - \frac{Q\log(x)}{3};\ \text{where}(P = \log K - \log\beta) \quad (2)$$

In the above equation, P is not affected by the doping concentration. The value of Q is calculated by plotting the graph between $\log(x)$ and $\log(I/x)$, which is demonstrated in Fig. 6. The as-obtained value of Q from the slope of the graph is 5.52, which is close to 6, specifying that the energy transfer occurred on account of the dipole–dipole interaction.

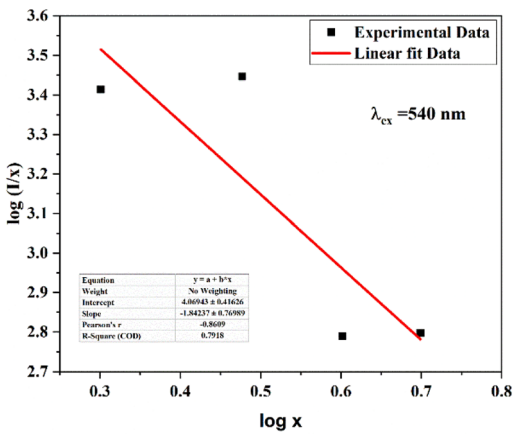

Fig. 6 Plot of $\log(I/x)$ *vs.* $\log(x)$.

The CIE 1931 diagram is a widely used system for obtaining all possible colors by using three primary colors. The CIE coordinate of all synthesized samples is calculated by using the photoluminescence data. The CIE coordinate of the synthesized CAZ:$x$$Cr^{3+}$ is shown in Table 1, and the CIE plot of the chromium-doped CAZ phosphor is shown in Fig. 7. The CIE coordinates fall in the pure red region close to the perimeter of the CIE graph, indicating the deep red emission exhibited by the prepared phosphor. These studies recommend the prospective of utilizing a chromium-doped phosphor in lighting and display devices as a red emitter.

3.5. External quantum yield

The quantum yield (QY) of a luminous material characterizes a radiative transition when combined with the luminescence lifespan, luminescence spectrum, and photostability of the phosphor. The ratio of photons released to photons absorbed by the irradiated sample is known as QY. High quantum yield phosphors are more effective in transforming the absorbed energy into emitted light, which results in brighter and more vibrant colors. For applications where efficiency is crucial, such as in lighting or solar cells, a greater quantum yield also implies that less energy is wasted as heat. The external quantum yield (EQY) of a phosphor, which demonstrates how effectively electrical power is converted to the observed optical power, is a crucial consideration. The EQY of the synthesized phosphor samples were evaluated by using eqn (3), which is given as:

$$\eta = \frac{\int \lambda P(\lambda)\mathrm{d}\lambda}{\int \lambda E(\lambda)\mathrm{d}\lambda} \quad (3)$$

where $E(\lambda)$ and $P(\lambda)$ stand for the excitation and emission spectra's intensity per wavelength, respectively.[37,38] Table 1 lists the quantum yield of the synthesized phosphor material. The efficiency of the synthesized material was shown to rise with an increase in doping up to 0.03 mol, after which it continues to decrease as the luminescence deteriorates at higher concentration due to the quenching mechanism. The EQY (η) of the $Ca_{3-x}Al_4ZnO_{10}$:$x$$Cr^{3+}$ (where x = 0.03 mol) phosphor is calculated as 46.80% under the excitation of 540 nm, which is significantly higher in comparison to previously published studies, such as the $KSrVO_4$ (EQY: 41.64%),[38] Ba_2SrWO_6:Mn^{4+} (EQY: 39.55),[39] $Mg_3Ga_2GeO_8$:Ni^{2+} (EQY: 7.3%)[40] phosphor. This relatively higher quantum yield value signifies the practical application of the phosphor under study.

Table 1 The color coordinates of CIE 1931 diagram and quantum yield

Cr^{3+} doping concentration (mol)	Color coordinates		Quantum yield (η)
	x	y	
0.01	0.7343	0.2556	35.13%
0.02	0.7334	0.2665	38.91%
0.03	0.7336	0.2662	46.80%
0.04	0.7340	0.2659	41.04%
0.05	0.7332	0.2667	32.59%

© 2023 The Author(s). Published by the Royal Society of Chemistry

Open Access Article. Published on 02 June 2023. Downloaded on 6/14/2023 6:39:21 AM.
This article is licensed under a Creative Commons Attribution-NonCommercial 3.0 Unported Licence.

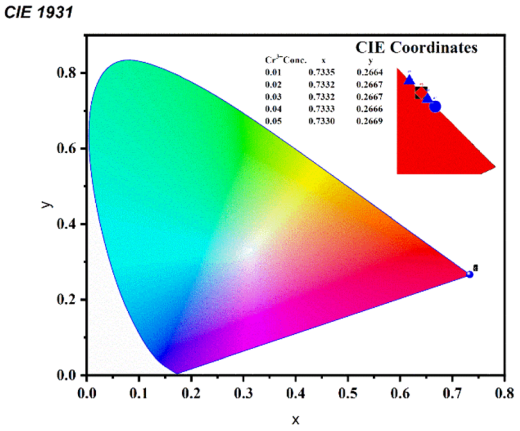

Fig. 7 CIE 1931 plot of the Cr^{3+}-doped CAZ phosphor.

3.6. Decay curve analysis

For additional evaluation of the luminescence behavior of the phosphor, fluorescence lifespan measurements were made. The fluorescence lifespan decay curve of the synthesized phosphor material with different Cr^{3+} ion concentrations is recorded by observing 688 nm emission upon 540 nm excitation. Fig. 8(a–e) manifests the decay curves of the synthesized samples, and the curves are fitted by the following tri-exponential eqn (4):

$$I_t = I_0 + B_1 \exp\left(-\frac{t}{\tau_1}\right) + B_2 \exp\left(-\frac{t}{\tau_2}\right) + B_3 \exp\left(-\frac{t}{\tau_3}\right) \quad (4)$$

For all the samples, where B_1, B_2 and B_3 are fitting parameters, I_t and I_0 are the PL intensities at time t and 0, respectively, and τ_1, τ_2 and τ_3 are the lifetimes corresponding to the fast and followed by two slow decays. The average life τ is calculated by the given formula:[28]

$$\tau = \frac{A_1\tau_1^2 + A_2\tau_2^2 + A_3\tau_3^2}{A_1\tau_1 + A_2\tau_2 + A_3\tau_3} \quad (5)$$

The average lifetime of the synthesized phosphor is calculated to be 12.08, 9.86, 3.06, 2.40, and 0.67 microseconds for 0.01, 0.02, 0.03, 0.04 and 0.05 mol Cr^{3+} ion concentration, respectively. It is observed here that the life time has decreased with the increase in Cr^{3+} ion doping concentration because of the energy transfer among the Cr^{3+} ion at shorter distances. Lifetime with Cr^{3+} ion concentration variation can be seen in Fig. 8(f).

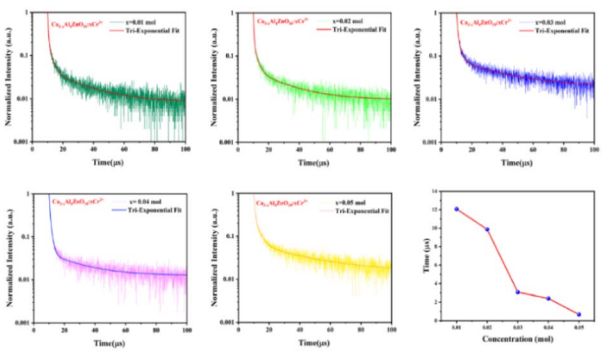

Fig. 8 Decay curves of CAZ:xCr^{3+} for different amount of Cr^{3+} ions in the host and graph of average lifetime *versus* concentration of chromium ions.

3.7. Temperature dependent photoluminescence (TD-PL)

Temperature-dependent PL spectra for the optimized $Ca_{2.97}Al_4ZnO_{10}$:$0.03Cr^{3+}$ phosphor were studied to see the impact of temperature change on the emission profile, and to gain a better understanding of the thermal stability of the aforementioned phosphor. The TD-PL spectra were measured under 540 nm excitation wavelength by alleviating the temperature from 300 to 450 K, as shown in Fig. 9. The emission intensity tends to decrease with a rise in temperature without any change in the emission spectral profile. It was observed from Fig. 9 that the PL intensity dropped by 27.4% at 450 K compared to the intensity at room temperature. The sample also shows a significant emission of 77.31% at 390 K, which is the ambient operating temperature for any practical application. Further analysis of the TD-PL of the $Ca_{2.97}Al_4ZnO_{10}$:$0.03Cr^{3+}$ phosphors to confirm the thermal stability, activation energy (ΔE) was calculated using the Arrhenius eqn (6).

$$I_T = \frac{I_0}{1 + D\exp\left(-\frac{\Delta E}{K_B T}\right)} \quad (6)$$

In this equation, I_0 stands for the emission intensity at room temperature, I_T for the emission intensity at elevated temperature (T), ΔE specifies the activation energy, K_B is the known constant given by Boltzmann, and D is an arbitrary constant. As shown in Fig. 10, the graph between $\ln((I_0/I_T) - 1)$ and $1/K_BT$ is a linear fit to estimate the activation energy (ΔE) value. The activation energy for the $Ca_{2.97}Al_4ZnO_{10}$:$0.03Cr^{3+}$ phosphor was calculated to be 0.309 eV, which is the negative of the slope as obtained from the graph.

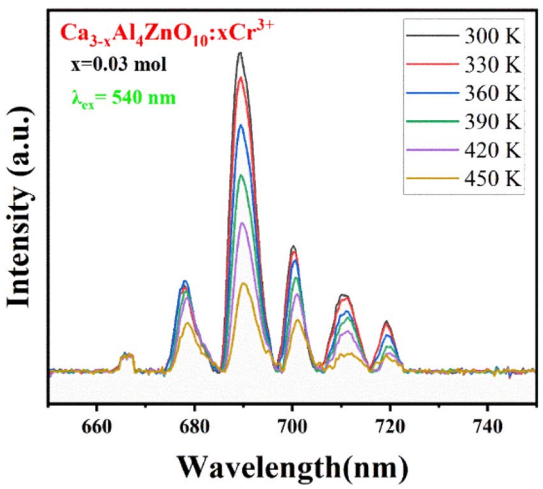

Fig. 9 Temperature-dependent emission spectra (λ_{ex} = 540 nm) of the $Ca_{2.97}Al_4ZnO_{10}$:$0.03Cr^{3+}$ phosphor at the temperature range of 300 K to 450 K.

Open Access Article. Published on 02 June 2023. Downloaded on 6/14/2023 6:39:21 AM.
This article is licensed under a Creative Commons Attribution-NonCommercial 3.0 Unported Licence.

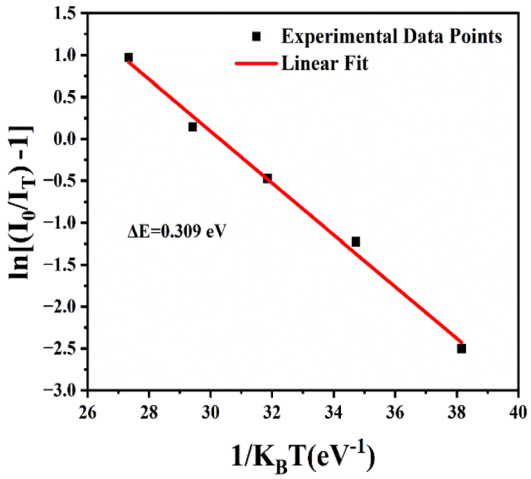

Fig. 10 Computation of the activation energy from the linear fitted plot of $\ln\left[\left(\frac{I_0}{I_T}\right)-1\right]$ and $\frac{1}{K_B T}$.

The activation energy calculated here has a higher value relative to other reported values for Ca_3WO_6:Dy^{3+} (0.105 eV), $CaAl_4O_7$:Mn^{4+} (0.196 eV), $Ca_{1.65}Sr_{0.35}SiO_4$:Ce^{3+} (0.135 eV), $Ca_3Bi(PO_4)_3$:Dy^{3+}(0.223 eV), Na_2CaSiO_4:Sm^{3+} (0.283 eV) and $Ca_9Mg_{1.5}(PO_4)_7$:Eu^{2+} (0.297 eV).[41–45] With a higher activation energy value, it can be concluded that the material has good thermal stability. Since the CAZ phosphor has good thermal stability with a relatively high value of activation energy, it shows potential for lighting and display applications.[44,46]

4. Conclusions

Cr^{3+}-doped calcium aluminozincate phosphors were efficaciously developed by sol–gel technique to study the luminescent behavior of the phosphor. The XRD patterns reveal that the phosphor has been developed in the pure phase with an orthorhombic structure, along with a random morphology of particles, as shown from the SEM image. The prepared phosphors emulate deep red emission by fixing the irradiation wavelength at 540 nm. The optimized amount of chromium ions was observed as 0.03 mol. The CIE coordinates ascertain the red emission exhibited by the prepared phosphors. The recorded decay curves and lifetime evaluation confirm that the energy transfer between the chromium ions occurs as a consequence of dipole–dipole interaction. The luminescent spectra based on temperature variation show that phosphor is thermally stable with a relatively high value of activation energy 0.309 eV. The quantum yield is 46.80% for the optimized sample. The entire study conducted on the prepared Cr^{3+}-doped CAZ phosphor indicates that it is quite appropriate for lighting and display applications.

Author contributions

Sumandeep Kaur: synthesis, data analysis and manuscript writing, Videsh Kumar: data analysis and manuscript writing, A.S. Rao: manuscript correction and supervision.

Conflicts of interest

There are no conflicts to declare.

Acknowledgements

Dr Sumandeep Kaur is grateful to the Council of Scientific and Industrial Research, New Delhi, India for providing financial support in terms of the Research Associate Fellowship (File No. 08/133(0053)/2020-EMR-I).

Notes and references

1 S. Wang, J. Zhu, Y. He, *et al.*, Invisible NIR Spectral Imaging and Laser-Induced Thermal Imaging of Na(Nd/Y)F4@glass with Opposite Effect for Optical Security, *Laser Photonics Rev.*, 2022, **16**(8), 2200039–2200046, DOI: 10.1002/lpor.202200039.

2 E. Rai, R. S. Yadav, D. Kumar, A. K. Singh, V. J. Fulari and S. B. Rai, Effect of Cr^{3+} doping on structural and optical properties of Eu^{3+} doped $LaVO_4$ phosphor, *RSC Adv.*, 2023, **13**(7), 4182–4194, DOI: 10.1039/d2ra06962h.

3 C. Kumari, A. Kumar, S. K. Sharma and J. Manam, Sr_3LiSbO_6:Er^{3+} phosphors for green LEDs and solar cell applications, *Vacuum*, 2023, **207**, 111599, DOI: 10.1016/j.vacuum.2022.111599.

4 W. Xia, H. Cheng, Q. Mao, *et al.*, Improving the luminescence performance of far-red-emitting Sr_2ScSbO_6:Mn^{4+} phosphor with charge compensation and its application in plant growth LEDs, *Ceram. Int.*, 2023, **49**(9PA), 13708–13716, DOI: 10.1016/j.ceramint.2022.12.249.

5 D. Liu, Effects of Cr content and morphology on the luminescence properties of the Cr-doped alpha-Al_2O_3 powders, *Ceram. Int.*, 2013, **39**(5), 4765–4769, DOI: 10.1016/j.ceramint.2012.11.063.

6 Y. R. S. Monika, A. Bahadur and S. B. Rai, Concentration and pump power-mediated color tunability, optical heating and temperature sensing via TCLs of red emission in an Er^{3+}/Yb^{3+}/Li^+ co-doped $ZnGa_2O_4$ phosphor, *RSC Adv.*, 2019, **9**(68), 40092–40108, DOI: 10.1039/c9ra09120c.

7 H. Huang, R. Li, S. Jin, *et al.*, Ytterbium-Doped $CsPbCl_3$ Quantum Cutters for Near-Infrared Light-Emitting Diodes, *ACS Appl. Mater. Interfaces*, 2021, **13**(29), 34561–34571, DOI: 10.1021/acsami.1c09421.

8 J. Zhong, D. Chen, X. Chen, *et al.*, Efficient rare-earth free red-emitting Ca_2YSbO_6:Mn^{4+}, M(M = Li^+, Na^+, K^+, Mg^{2+}) phosphors for white light-emitting diodes, *Dalton Trans.*, 2018, **47**(18), 6528–6537, DOI: 10.1039/c8dt00992a.

9 S. Jin, R. Li, H. Huang, *et al.*, Compact ultrabroadband light-emitting diodes based on lanthanide-doped lead-free double perovskites, *Light: Sci. Appl.*, 2022, **11**(1), 1–21, DOI: 10.1038/s41377-022-00739-2.

10 Z. Zhou, N. Zhou, M. Xia, M. Yokoyama and H. T. Hintzen, Research progress and application prospects of transition metal Mn4+-activated luminescent materials, *J. Mater. Chem. C*, 2016, **4**(39), 9143–9161, DOI: 10.1039/c6tc02496c.

© 2023 The Author(s). Published by the Royal Society of Chemistry

Open Access Article. Published on 02 June 2023. Downloaded on 6/14/2023 6:39:21 AM. This article is licensed under a Creative Commons Attribution-NonCommercial 3.0 Unported Licence.

11 J. Jiang, T. Xu, J. Lu, L. Sun and Z. Ni, Review Article, *Defect Engineering in 2D Materials : Precise Manipulation and Improved Functionalities*, 2019, 2019, DOI: 10.34133/2019/4641739.

12 C. S. Kamal, T. K. Visweswara Rao, T. Samuel, *et al.*, Blue to magenta tunable luminescence from LaGaO3: Bi3+, Cr3+ doped phosphors for field emission display applications, *RSC Adv.*, 2017, **7**(71), 44915–44922, DOI: 10.1039/c7ra08864g.

13 G. Liu, M. S. Molokeev, B. Lei and Z. Xia, Two-site Cr3+occupation in the MgTa2O6:Cr3+phosphor toward broad-band near-infrared emission for vessel visualization, *J. Mater. Chem. C*, 2020, **8**(27), 9322–9328, DOI: 10.1039/d0tc01951h.

14 L. Wang, Z. Dai, R. Zhou, B. Qu and X. C. Zeng, Understanding the quenching nature of Mn^{4+} in wide band gap inorganic compounds: design principles for Mn^{4+} phosphors with higher efficiency, *Phys. Chem. Chem. Phys.*, 2018, **20**(25), 16992–16999, DOI: 10.1039/c8cp02569j.

15 J. Orive, R. Balda, J. Fernández, L. Lezama and M. I. Arriortua, Low temperature red luminescence of a fluorinated Mn-doped zinc selenite, *Dalton Trans.*, 2013, **42**(34), 12481–12494, DOI: 10.1039/c3dt51224j.

16 R. Boonsin, G. Chadeyron, J. P. Roblin, D. Boyer and R. Mahiou, Development of rare-earth-free phosphors for eco-energy lighting based LEDs, *J. Mater. Chem. C*, 2015, **3**(37), 9580–9587, DOI: 10.1039/c5tc01516b.

17 F. Xiao, C. Xie, S. Xie, R. Yi, H. Yuan and H. Zhou, Multi-site Cr3+occupation-related broadband NIR luminescence in Cr^{3+}-doped $Li_3Mg_2NbO_6$, *CrystEngComm*, 2021, **23**(33), 5585–5594, DOI: 10.1039/d1ce00746g.

18 J. Lai, J. Qiu, Q. Wang, *et al.*, Disentangling site occupancy, cation regulation, and oxidation state regulation of the broadband near infrared emission in a chromium-doped $SrGa_4O_7$ phosphor, *Inorg. Chem. Front.*, 2020, **7**(12), 2313–2321, DOI: 10.1039/d0qi00332h.

19 M. Qiang, X. Yin, H. Lin, *et al.*, $ZnAl_2O_4$:Cr^{3+} translucent ceramic phosphor with thermally stable far-red luminescence, *Opt. Mater.*, 2022, **133**, 112887, DOI: 10.1016/j.optmat.2022.112887.

20 J. Zhong, L. Zeng, W. Zhao and J. Brgoch, Producing Tunable Broadband Near-Infrared Emission through Co-Substitution in $(Ga_{1-x}Mg_x)(Ga_{1-x}Ge_x)O_3$:$Cr^{3+}$, *ACS Appl. Mater. Interfaces*, 2022, 10–17, DOI: 10.1021/acsami.2c17902.

21 M. I. Miranda-López, F. F. Contreras-Torres, D. Cavazos-Cavazos, *et al.*, Crystal evolution of nano-sized $CoCr_2O_4$ synthesized by a modified sol–gel method, *J. Phys. Chem. Solids*, 2023, **178**, 111315, DOI: 10.1016/j.jpcs.2023.111315.

22 P. M. Kakade, A. R. Kachere, P. D. Sahare, *et al.*, Structural, compositional and luminescence studies of Y2O3:Eu3+ nanophosphor synthesized by sol-gel method, *J. Alloys Compd.*, 2022, **928**, 167106, DOI: 10.1016/j.jallcom.2022.167106.

23 S. Kaur, A. S. Rao, M. Jayasimhadri, B. Sivaiah and D. Haranath, Synthesis optimization, photoluminescence and thermoluminescence studies of Eu3+ doped calcium aluminozincate phosphor, *J. Alloys Compd.*, 2019, **802**, 129–138, DOI: 10.1016/j.jallcom.2019.06.169.

24 Y. Li, Z. Zhao, Z. Song, R. Wan, J. QIu, Z. Yang, Z. Yin, X. Liu, Q. Liu and Y. Zhou, Far-Red-Emitting BiOCl Eu3 Phosphor with Excellent Broadband.pdf, *J. Am. Ceram. Soc.*, 2015, **98**(7), 2170–2176, DOI: 10.1111/jace.13589.

25 J. Suresh Kumar, K. Pavani, A. Mohan Babu, N. Kumar Giri, S. B. Rai and L. R. Moorthy, Fluorescence characteristics of Dy^{3+} ions in calcium fluoroborate glasses, *J. Lumin.*, 2010, **130**(10), 1916–1923, DOI: 10.1016/j.jlumin.2010.05.006.

26 G. P. Singh, S. Kaur, P. Kaur and D. P. Singh, Modification in structural and optical properties of ZnO, CeO_2 doped $Al_2O_3PbOB_2O_3$ glasses, *Phys. B*, 2012, **407**(8), 1250–1255, DOI: 10.1016/j.physb.2012.01.114.

27 R. P. S. Chakradhar, B. M. Nagabhushana, G. T. Chandrappa, K. P. Ramesh and J. L. Rao, Solution combustion derived nanocrystalline Zn2SiO 4:Mn phosphors: A spectroscopic view, *J. Chem. Phys.*, 2004, **121**(20), 10250–10259, DOI: 10.1063/1.1808420.

28 S. Kaur, A. S. Rao and M. Jayasimhadri, Spectroscopic and photoluminescence characteristics of Sm3+ doped calcium aluminozincate phosphor for applications in w-LED, *Ceram. Int.*, 2017, **43**(10), 7401–7407, DOI: 10.1016/j.ceramint.2017.02.129.

29 P. Colomban, Structure of oxide gels and glasses by infrared and raman scattering – Part 1 Alumina, *J. Mater. Sci.*, 1989, **24**(8), 3002–3010, DOI: 10.1007/BF02385660.

30 E. I. Firsov and P. A. Shafranovsky, IR reflection-absorption study of O2 and H2O interaction with evaporated aluminum films, *Surf. Sci.*, 1991, **244**(1–2), 3–5, DOI: 10.1016/0039-6028(91)90163-M.

31 N. T. Huyen, M. T. Tran, N. Van Quang, *et al.*, Far-red-emitting Cr^{3+}-doped $CaAl_{12}O_{19}$ phosphors with excellent color purity and good quantum efficiency for plant growth LEDs, *Opt. Mater.*, 2022, **133**, 113002, DOI: 10.1016/j.optmat.2022.113002.

32 A. Bessière, S. Jacquart, K. Priolkar, A. Lecointre, B. Viana and D. Gourier, ZnGa_2O_4:Cr^3+: a new red long-lasting phosphor with high brightness, *Opt. Express*, 2011, **19**(11), 10131, DOI: 10.1364/oe.19.010131.

33 D. L. Dexter, *A Theory of Sensitized Luminescence in Solids Articles you may be interested in A Theory of Sensitized Luminescence in Solids*, 2004, 1953, p. 836, DOI: 10.1063/1.1699044.

34 Maheshwary, B. P. Singh, J. Singh and R. A. Singh, Luminescence properties of Eu3+-activated SrWO4 nanophosphors-concentration and annealing effect, *RSC Adv.*, 2014, **4**(62), 32605–32621, DOI: 10.1039/c4ra05903d.

35 Z. Ci, Q. Sun, S. Qin, *et al.*, Warm white light generation from a single phase Dy^{3+} doped Mg2Al4Si5O18 phosphor for white UV-LEDs, *Phys. Chem. Chem. Phys.*, 2014, **16**(23), 11597–11602, DOI: 10.1039/c4cp00357h.

36 S. Kaur, M. Jayasimhadri and A. S. Rao, A novel red emitting Eu3+doped calcium aluminozincate phosphor for applications in w-LEDs, *J. Alloys Compd.*, 2017, **697**, 367–373, DOI: 10.1016/j.jallcom.2016.12.150.

Open Access Article. Published on 02 June 2023. Downloaded on 6/14/2023 6:39:21 AM.
This article is licensed under a Creative Commons Attribution-NonCommercial 3.0 Unported Licence.

37 W. Li, R. J. Xie, T. Zhou, L. Liu and Y. Zhu, Synthesis of the phase pure $Ba_3Si_6O_{12}N_2$:Eu^{2+} green phosphor and its application in high color rendition white LEDs, *Dalton Trans.*, 2014, **43**(16), 6132–6138, DOI: **10.1039/c3dt53603c**.

38 P. Sharma, P. Singh and Kamni, Study of synthesis mechanism, structural, optical and luminescent properties of bluish-violet rare earth doped KSrVO4: Nd3+ nano powders, *Mater. Sci. Eng. B: Solid-State Mater. Adv. Technol.*, 2022, **276**, 115564, DOI: **10.1016/j.mseb.2021.115564**.

39 Y. Zhang, C. Zhou, J. Li, *et al.*, Realization of highly efficient Ba_2SrWO_6:Mn^{4+} phosphor via La addition strategy and application for plant cultivation LED, *J. Alloys Compd.*, 2023, **937**, 168418, DOI: **10.1016/j.jallcom.2022.168418**.

40 C. Wang, J. Lin, X. Zhang, *et al.*, Efficient ultra-broadband NIR-II emission achieved by multi-site occupancy in Mg_3Ga_2GeO8: Ni^{2+} phosphor, *J. Alloys Compd.*, 2023, **942**, 168893, DOI: **10.1016/j.jallcom.2023.168893**.

41 D. Xu, Z. Yang, J. Sun, X. Gao and J. Du, Synthesis and luminescence properties of double-perovskite white emitting phosphor Ca_3WO_6:Dy^{3+}, *J. Mater. Sci.: Mater. Electron.*, 2016, **27**(8), 8370–8377, DOI: **10.1007/s10854-016-4848-z**.

42 K. Li, M. Shang, H. Lian and J. Lin, Photoluminescence Properties of Efficient Blue-Emitting Phosphor α-$Ca_{1.65}Sr_{0.35}SiO_4$:Ce^{3+}: Color Tuning via the Substitutions of Si by Al/Ga/B, *Inorg. Chem.*, 2015, **54**(16), 7992–8002, DOI: **10.1021/acs.inorgchem.5b01197**.

43 P. Li, M. Peng, X. Yin, *et al.*, Temperature dependent red luminescence from a distorted Mn^4+ site in CaAl_4O_7:Mn^4+, *Opt. Express*, 2013, **21**(16), 18943, DOI: **10.1364/oe.21.018943**.

44 H. Kaur, M. Jayasimhadri, M. K. Sahu, P. K. Rao and N. S. Reddy, Synthesis of orange emitting Sm^{3+} doped sodium calcium silicate phosphor by sol-gel method for photonic device applications, *Ceram. Int.*, 2020, **46**(16), 26434–26439, DOI: **10.1016/j.ceramint.2020.04.224**.

45 R. Mi, Y. Liu, L. Mei, *et al.*, Multi-site occupancies and dependent photoluminescence of $Ca_9Mg_{1.5}(PO_4)_7$:Eu^{2+} phosphors: A bifunctional platform for optical thermometer and plant growth lighting, *J. Rare Earths*, 2022, **5**, DOI: **10.1016/j.jre.2022.06.009**.

46 V. Singh, S. Kaur and M. Jayasimhadri, Luminescence properties of orange emitting $CaAl_4O_7$:Sm^{3+} phosphor for solid state lighting applications, *Solid State Sci.*, 2020, **101**, 106049–106054, DOI: **10.1016/j.solidstatesciences.2019.106049**.

© 2023 The Author(s). Published by the Royal Society of Chemistry

Design and Analysis of Vienna Rectifier considering System Parasitic for off-Board EV Charging

Kushank Singh
Department of Electrical Engineering
Delhi Technological University
Delhi, India
singhkushank87@gmail.com

Vanjari Venkata Ramana
Department of Electrical Engineering
Delhi Technological University
Delhi, India
venkat.vr90@gmail.com

2023 International Conference on Power, Instrumentation, Control and Computing (PICC) | 979-8-3503-3446-3/23/$31.00 ©2023 IEEE | DOI: 10.1109/PICC57976.2023.10142796

***Abstract*— The need for higher power ratings and efficient AC-DC conversion led to opting of Vienna Rectifier for off-board electric vehicle (EV) charging applications. In this paper, a complete analysis of three phase Vienna Rectifier considering the effect of parasitic in the system for off-board EV charging application is discussed. To improve the dynamic response a modified dual loop control using d-axis and q-axis current controller including the effect of system parasitic in control loops is proposed. The proposed algorithm is compared with different control algorithms viz., dual loop control using hysteresis current controller and dual loop control using d-axis and q-axis current controller with SVPWM. A comparative performance analysis is discussed in terms of dynamic response during system disturbances like load variation, reference DC bus voltage variation and grid side variations. A 50 kW Vienna Rectifier operating at a switching frequency of 200 kHz is used for performance evaluation of all three control algorithms and is validated using MATLAB-Simulink.**

Keywords—Vienna Rectifier, hysteresis control, SVPWM control, system parasitic, dynamic response, settling time (t_s), Total Harmonic Distortion (THD), FFT analysis.

I. INTRODUCTION

The growing future of EVs needs more reliable and efficient power electronics systems [1]. Advancements in power electronics converters involve a complex control algorithm. The EV charging system has a great involvement of the AC grid. A battery can be charged using a charging station but its impact on the AC grid has to be analyzed [2]. There are many power factor correction methods that have been adopted in literature which include advancement in PFC boost using wide band gap devices in which we can operate at high switching frequency which indirectly reduces the size of the system [3]. For off-board EV charging applications a three-phase power factor correction method needs to be implemented to improve the injected grid current. One of these topologies includes Vienna Rectifier with power factor correction.

In [4] balancing of the output capacitor voltages in Vienna Rectifier using modified Discontinuous PWM to reduce the error between the bus capacitor voltages and to operate at high frequency is proposed. The authors in [5] proposed a hysteresis current control which reduces the computation complexity and is easy to implement. To reduce the THD of grid current a lot of research involves Space Vector PWM control [6]- [7]. In [8], the authors also included the system parasitic in Vienna Rectifier but the effect of parasitic is not included in the controlling loops.

In this paper, a 50 kW AC-DC Vienna Rectifier is designed using the proposed modified q-axis and d-axis current controller by including the effect of parasitic in the controlling loops. Small signal analysis was performed to calculate the mathematical equations required for the controlling loops. The other two control algorithms are dual loop control using a hysteresis controller and dual loop control using d-axis and q-axis control using space vector pulse width modulation (SVPWM). All the control algorithms are compared for different dynamic variations in the system i.e., load variations, reference DC voltage variation, grid voltage variation, and grid frequency variation and validated using MATLAB-Simulink.

Rest of the paper is organized as follows: section II contains the circuit description of Vienna Rectifier, section III describes the design and control of Vienna Rectifier, results and performance evaluation are discussed in section IV, and concluding remarks are made in Section V.

II. CIRCUIT DESCRIPTION

Vienna Rectifier is a three-level AC-DC converter that maintains a desired DC voltage at the output. It also features input power factor correction and eliminates harmonics which leads to a reduction in Total Harmonic Distortion (THD) [9]. The circuit includes three input filter inductances, one for each phase, which helps out in the reduction of input current ripples and also performs the function of boosting. The second stage includes the diode bridge rectifier containing six power diodes, two diodes for each phase. The additional elements in the Vienna Rectifier are the three bi-directional switches Q_a, Q_b and Q_c in each phases due which it is called as multilevel converter. The last stage is the DC bus capacitors which helps to maintain the required DC bus voltage and also reduce the ripples in the output voltage.

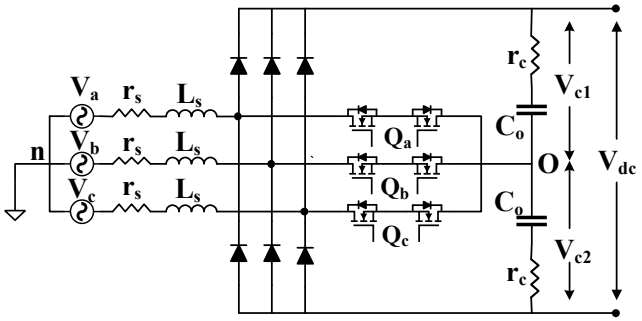

Fig. 1. Three phase Vienna Rectifier circuit diagram including parasitic

979-8-3503-3446-3/23/$31.00 ©2023 IEEE

Authorized licensed use limited to: DELHI TECHNICAL UNIV. Downloaded on June 14,2023 at 05:11:42 UTC from IEEE Xplore. Restrictions apply.

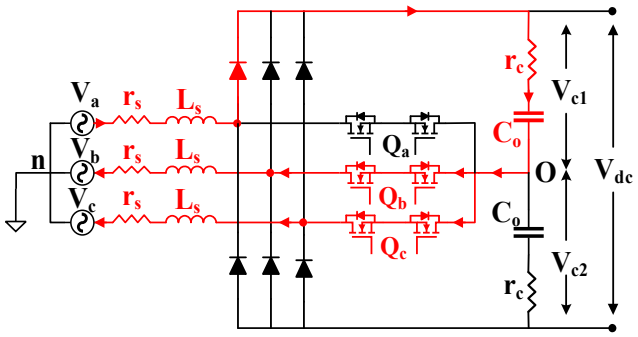

Fig. 2. Vienna Rectifier operation for switching state 011 in sector 1

Vienna Rectifier considering parasitic is shown in Fig. 1. The circuit operation for state 011 in sector 1 which means the positive 'phase a' current and negative 'phase b', 'phase c' current as shown in Fig. 2. During 011 state, the bidirectional switches Q_b and Q_c are conducting, and capacitor mid-point current is equal to 'phase a' current in opposite direction. Similarly, other switching states for different sectors can be analyzed as discussed in [9] .

III. Design and Control of Vienna Rectifier

A. Design Parameters

The system parameters for the Vienna Rectifier can be calculated using [10]. The input filter inductance can be calculated using (1).

$$L_s = \frac{V_{dc}/_2}{4*f_{sw}*\Delta i_{ppmax}} \quad (1)$$

Where, V_{dc} is the output DC bus voltage of Vienna Rectifier, f_{sw} is the operating switching frequency of Vienna Rectifier and Δi_{ppmax} is the maximum ripple in the current through filter inductor. The filter inductance value is inversely proportional to the switching frequency. For the system analysis, f_{sw} =200 kHz is opted for off-board EV charging application due to which the size of the inductor gets reduced and the THD can be minimized using control loops.

The output capacitance value is calculated using (2)

$$C_o = \left(\frac{1}{3}\right)\frac{P_{ac}}{4*f_s*(V_{dc}^2-(V_{dc}-\Delta V_{dc})^2)} \quad (2)$$

Where P_{ac} is the power ratings of the system, f_s is grid frequency, ΔV_{dc} is the bus voltage ripple and V_{dc} is the DC bus voltage. The design specifications considered in this work are tabulated in TABLE I.

TABLE I. Design Specifications for Vienna Rectifier

Parameters	Value
L-L rms grid voltage (V_{abc}), grid frequency (f_s)	400 V, 50 Hz
Output DC bus voltage (V_{dc})	700V
Power rating (P_{ac})	50 kW
Output current (I_o)	71.4285 A
Switching frequency (f_{sw})	200 kHz
Bus capacitor (C_o), ESR (r_c)	4300 uF, 3.8 mΩ
Input filter inductance (L_s), source resistance (r_s)	41 uH, 0.1 Ω
Input current THD	< 2%

B. Dual Loop Control using Hysteresis Current Controller

In this control strategy, there involves different controlling loops, an outer control loop for DC bus voltage uses a PI controller to provide reference signals. The generated reference signals are provided to the inner current control loops and hysteresis controllers which are used instead of PI controller. Three-phase PLL is designed to provide clocking frequency theta/ωt for abc/dq0 and dq0/abc transformations. The three-phase voltages are transformed into alpha-beta and thereafter to d-q transform to extract three phase reference voltages, V_a*,V_b* and V_c*. Finally the output of hysteresis controller for the inner control loops is compared with V_a*, V_b* and V_c* respectively. Switching pulses for controlled bidirectional switches are obtained and Fig. 3 depicts control block diagram for this control strategy [5].

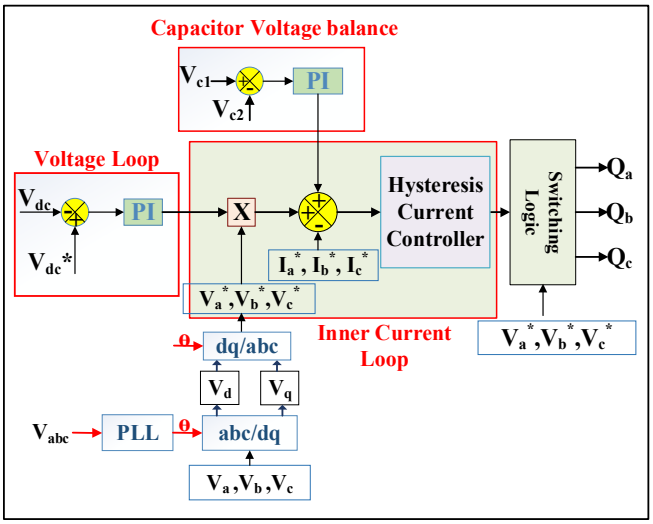

Fig. 3. Block diagram of dual loop control using hysteresis current control scheme

C. Dual Loop Control using d-axis and q-axis Current Controller with SVPWM

The dual loop control strategy using hysteresis controller is able to provide power factor which tends to unity and able to achieve the THD under EV standards but it is not able to mitigate the 1% variations in grid frequency. So, a dual loop control using d-axis and q-axis current control strategy is adopted for further analysis of Vienna Rectifier [6] . In this strategy one loop will be the inner control loop which includes the d-axis current, I_d and q-axis current, I_q control. Second loop is the outer voltage control loop where the output voltage is compared with the DC bus reference voltage and the voltage error is provided to a PI controller and output of this PI controller is reference d-axis current, I_{dref} and compared with the I_d and the error is provided to a PI Controller and generated output is summed with the expression, $V_d+2\pi f_s L_s I_q$ using (6) to generate reference d-axis voltage V_{dref}. Similarly for q-axis controller, I_q is compared with 0 to reduce or eliminate reactive component. The error is provided to the PI controller and the generated output is differenced from an expression, $2\pi f_s L_s I_d$ using (3) to generate reference q-axis voltage V_{qref}. Next step is to convert V_{dref}, V_{qref} and 0 to three phase reference voltage, V_{abc}* using dq0 to abc transformations. Clarke and Park transformation are utilized to transform the three phase grid voltages and current to alpha-beta and then to d-q respectively. Three-phase PLL is used to generate theta/ωt for the clarke and park transformations. I_d and I_q are transformed to three phase reference current, I_{abc}* using dq0 to abc transform. In Vienna Rectifier, the main concern is the capacitor voltage balancing. So, here a proportional controller is incorporated to ensure that the voltage across the capacitors remains balanced under various dynamic changes in the system, to ensure the desired output bus voltage. Fig. 4 depicts block diagram for this control strategy [6]. The final step

Authorized licensed use limited to: DELHI TECHNICAL UNIV. Downloaded on June 14,2023 at 05:11:42 UTC from IEEE Xplore. Restrictions apply.

includes generation of pulses for the three bi-directional switches using SVPWM. The input Control parameters to the SVPWM pulse generator are V_{abc}*, I_{abc}* and controller output for the capacitor voltage balancing.

Vienna Rectifier control using SVPWM can be summarized as in [11], first step is the sector identification on the basis of current direction through each phases. For multilevel Vienna Rectifier it is different from conventional converters as in this case, the current polarity is taken into account. Second step is to normalize the angle calculated from sector identification for simplification. Third step is the calculation of sub-vectors and calculations of dwell time. Next step is to calculate dwell times in case of over modulation and a saturation is used to limit the output such that the magnitude of sum of dwell times should not exceed the switching time. Next step is the capacitor voltage balancing where the redundant switching states are determined which generate the opposite but similar voltage vectors, this definitely have to be considered for the pulse generation. The pulses are generated by calculating on and off timings w.r.t. the bidirectional switches and comparing it with reference values and finally PWM signals are generated. Fig. 5 shows Vienna Rectifier space vector diagram of all existing voltage vectors.

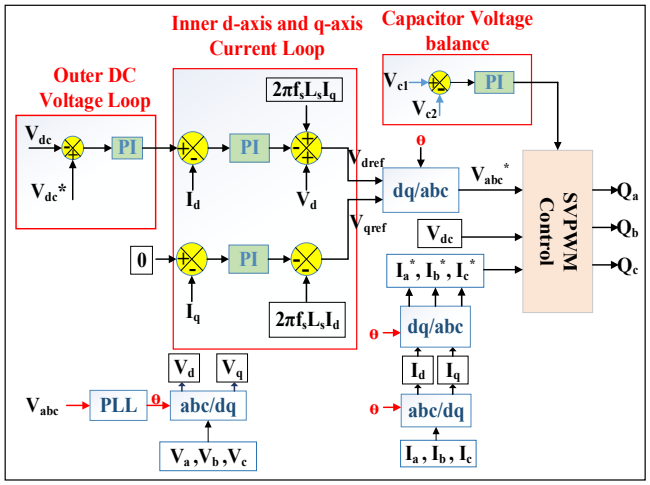

Fig. 4. Block diagram of dual loop control using d-axis and q-axis current control strategy with SVPWM

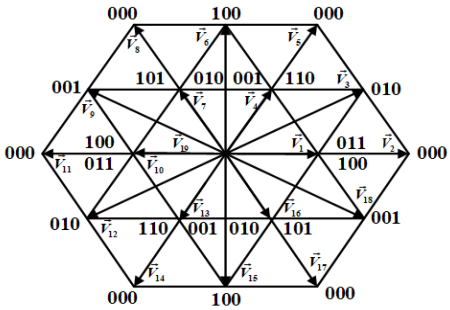

Fig. 5. Diagram of space vectors for Vienna Rectifier

The control loops are designed using following calculated equations,

$$V_{q_{ref}} = \begin{Bmatrix} -\left(K_{p_{i_q}}(0 - I_q) + K_{i_{i_q}} \int (0 - I_q) dt\right) \\ -2\pi f_s L_s I_d \end{Bmatrix} \quad (3)$$

$$I_{d_{ref}} = K_{p_{v_{dc}}}(V_{dc}^* - V_{dc}) + K_{i_{v_{dc}}} \int (V_{dc}^* - V_{dc}) dt \quad (4)$$

$$\Delta V_c = K_{p_{v_c}}(V_{c_1} - V_{c_2}) + K_{i_{v_c}} \int (V_{c_1} - V_{c_2}) dt \quad (5)$$

$$V_{d_{ref}} = \begin{Bmatrix} K_{p_{i_d}}\left(I_{d_{ref}} - I_d\right) + \\ K_{i_{i_d}} \int \left(I_{d_{ref}} - I_d\right) dt \\ +V_d + 2\pi f_s L_s I_q \end{Bmatrix} \quad (6)$$

$$V_{dc} = V_{c_1} + V_{c_2} \quad (7)$$

Where V_{qref}, V_{dref} and I_{qref}, I_{dref} are the reference voltages and currents for q-axis and d-axis respectively. V_{dc}* is the reference output voltage. V_{c1} and V_{c2} are voltages across output bus capacitors. In (3)-(7) the different parameters K_p and K_i are PI controller gains for different loops.

D. *Proposed Modified Dual Loop Control using d-axis and q-axis Current Controller with SVPWM*

In this proposed control strategy, a modification in the controlling loops is introduced where the effect of system parasitic i.e. source resistance 'r_s' in the inner current control loops and ESR of bus capacitance 'r_c' in the capacitor voltage balance loop. The small signal analysis of the proposed modified control can be analyzed and modified using [12] and control loops are designed using (8)-(13). Fig. 6 depicts the block diagram of the proposed modified control strategy.

$$V_{c_1} = V_{c_2} = \frac{V_{dc}}{2} \quad (8)$$

$$\Delta V_c = V_{c_1} - V_{c_2} \quad (9)$$

$$\frac{di_d}{dt} = \frac{1}{L_s}\left(V_d + 2\pi f_s L_s I_q + r_s I_q - \frac{V_{dc}}{2} d_d'\right) \quad (10)$$

$$\frac{di_q}{dt} = \frac{1}{L_s}\left(V_q - 2\pi f_s L_s I_d - r_s I_d - \frac{V_{dc}}{2} d_q'\right) \quad (11)$$

$$\frac{dV_{dc}}{dt} = \frac{1}{C_o}\begin{Bmatrix} \frac{3}{2}\left(d_d' I_d + d_q' I_q\right) - \frac{V_{dc}}{2r_c} - \frac{2}{\pi}\frac{\Delta V_c}{V_{dc}} d_o' I_d \\ -I_o d_q' \end{Bmatrix} \quad (12)$$

$$\frac{d\Delta V_c}{dt} = \frac{1}{C_o}\begin{Bmatrix} -\frac{3}{2}\frac{\Delta V_c}{V_{dc}}\left(d_d' I_d + d_q' I_q\right) - \frac{V_{dc}}{2r_c} \\ -\frac{2}{\pi} d_o' I_d \end{Bmatrix} \quad (13)$$

Where ΔV_c is the mismatch between capacitor voltages and d_d', d_q' and d_0' are the duty ratio for dq0 reference frame.

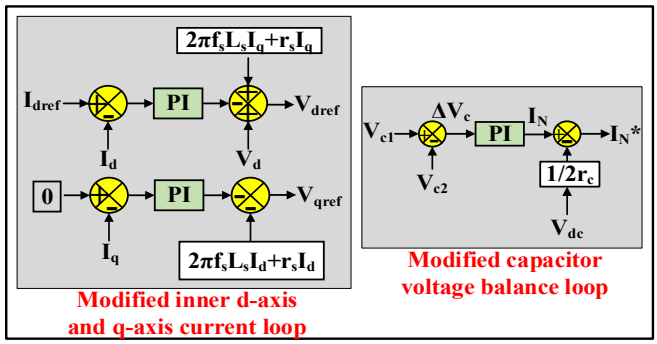

Fig. 6. Block diagram of proposed modified dual loop control using d-axis and q-axis current control strategy

E. *Conduction Power Losses in the System*

The conduction loss in source resistance is,

$$P_{r_s} = r_s * I_{S_{rms}}^2 \quad (14)$$

The conduction loss in ESR of bus capacitance is,

$$P_c = P_{c1} = P_{c2} = r_c * I_{C_{rms}}^2 \quad (15)$$

The conduction loss in bidirectional switch is,

$$P_M = V_{SW_{avg}} * I_{SW_{avg}} = R_{DS(on)} * I_{SW_{rms}}^2 \quad (16)$$

The conduction loss in power diodes is,

Authorized licensed use limited to: DELHI TECHNICAL UNIV. Downloaded on June 14,2023 at 05:11:42 UTC from IEEE Xplore. Restrictions apply.

$$P_D = V_{D_{avg}} * I_{D_{avg}} + r_D * I_{D_{rms}}^2 \quad (17)$$

Where, I_{SWrms} and V_{SWavg} is the rms current and average voltage across bidirectional switch, I_{Crms} is the rms current through bus capacitor, I_{Srms} is the input rms current. V_{Davg} and I_{Drms} are the average diode voltage and rms current respectively. $R_{DS(on)}$ and r_D are the on resistance of switch and diode respectively. The voltage and current across bidirectional switch can be calculated using Fig. 9(f). The total conduction losses can be calculated using (14)-(17). Conduction losses for a complete sector 1 is evaluated in TABLE II.

TABLE II. CONDUCTION LOSSES FOR ALL SWITCHING STATES OF SECTOR 1

Switching States	Conduction Loss
000	$3P_{r_s} + 3P_D + 2P_c$
100	$3P_{r_s} + 2P_D + P_M + P_c$
001	$3P_{r_s} + 2P_D + P_M + 2P_c$
101	$3P_{r_s} + P_D + 2P_M + P_c$
010	$3P_{r_s} + 2P_D + P_M + 2P_c$
110	$3P_{r_s} + P_D + 2P_M + P_c$
011	$3P_{r_s} + P_D + 2P_M + P_c$
111	$3P_{r_s} + 3P_M$

IV. RESULTS AND PERFORMANCE EVALUATION

A 50 kW Vienna Rectifier considering the system parasitic has been analyzed for off-board EV charging application at the switching frequency of 200 kHz. The study has been performed for the three control algorithms, using control 1 i.e. dual loop control using hysteresis current controller, control 2 i.e. Dual loop I_d and I_q control using SVPWM and control 3 (proposed model) i.e. modified dual loop I_d and I_q control. Performance of all controlling strategies under various dynamic changes in the system has been compared in TABLE III. The complete analysis has been verified through MATLAB-Simulink. The DC bus voltage response during load variations, grid voltage variations, reference DC bus voltage variation and FFT analysis during grid frequency variation for control 1, control 2 and control 3 is depicted in Fig. 7, Fig. 8 and Fig. 9 respectively.

A. Load Variation

The analysis was performed during the load current variations and Fig. 7(a), 8(a), 9(a) clearly depicts the load current variation at t= 0.3s from 100% to 50% as in for control 1, 2 and 3 respectively, which indirectly is the effect of load perturbation in the system. At t=0.3s, the load current was suddenly reduced to 50% and the effect of this load variation was analyzed on the DC bus voltage. It was observed from Fig. 7(b) that for hysteresis control algorithm, at t= 0.3s the DC bus voltage was able to reach steady state of 700V but the dynamic response was slightly sluggish with some oscillations in transient state and having settling time, t_s= 60ms. When the system was analyzed for dual loop SVPWM control algorithm, it can be observed from Fig. 8(b) that at t=0.3s the dynamic response was improved and oscillations during transient state were reduced significantly and settling time was, t_s= 50ms. It can be depicted from Fig. 9(b) that the proposed modified dual control loops for SVPWM algorithm which also includes the effects of system parasitic in the controlling loops shows an improved dynamic response with settling time, t_s=20ms. Fig. 7(c), 8(c), 9(c) shows that capacitor voltages are balanced after load variations. For all the control algorithms it was observed that THD was less than 5% and achieving near to unity pf.

B. Reference DC Voltage Variation

Further analysis includes the flexibility in the reference DC bus Voltage variations, V_{dcref} = 600V. From Fig. 7(d), 8(d), 9(d), it can be observed that all the controlling algorithms were able to adapt the provided reference DC bus voltage of 600 V at t= 0.3s. Fig. 7(d), 8(d), 9(d), clearly depicts that dynamic response varies among different control strategies and it resembles the dynamic response achieved after load variation analysis and settling time was t_s=40ms, 50ms, 30ms for control 1, 2 and 3 respectively.

C. Grid Voltage Variation

The results clearly depict that all the control algorithms are able to maintain a constant DC bus voltage when the grid voltage varies by 5% i.e., V_{abc} = 420 V at t=0.15s. From Fig. 7(e) it can be observed that the grid voltage varies from 400 V to 420 V and Fig. 7(f) and Fig. 8(e) clearly depicts that the system maintains constant bus voltage for control 1 and control 2 respectively. Control 3 behaves similarly as control 2.

D. Grid Frequency Variation

From Fig. 7(g) it can be observed that control 1 algorithm is unable to mitigate the grid frequency variations of 1% i.e., f_s = 50.5 Hz. After the FFT analysis it was observed that THD for f_s = 50.5 Hz was 8.29%, which is not acceptable according to EV standards in India and affects the performance of the system. In the comparative analysis, from Fig. 8(f) an observation can be made that control 2 algorithm is able to mitigate the variations in the grid frequency and FFT analysis at 50.5 Hz depicts the THD as 1.96%. From Fig. 9(e) an observation can be made that proposed control 3 algorithm is also able to mitigate the variations in grid frequency and provided with the THD of less than 5% and FFT analysis at 50.5 Hz depicts the THD as 1.83%.

In off-board EV charging application, the required operation of AC/DC converter is to ensure a desired DC bus voltage at disturbances either from grid side or the load side. So, this analysis can also be useful for other applications.

TABLE III. COMPARISON OF DIFFERENT CONTROL ALGORITHMS DUE TO DYNAMIC VARIATIONS IN THE SYSTEM

Control Strategy	Dynamic Variations in the system			
	Grid frequency adaptive	*Grid Voltage adaptive*	*Load variation (t_s)*	*Reference DC voltage variation (t_s)*
Control 1	No	Yes	60ms	40ms
Control 2	Yes	Yes	50ms	50ms
Control 3 (proposed model)	Yes	Yes	20ms	30ms

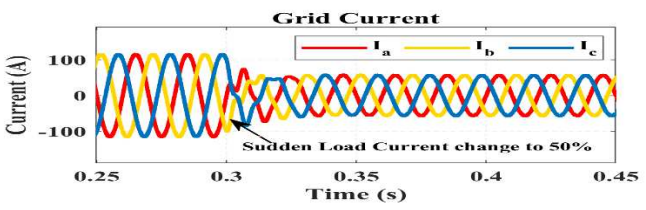

(a)

Authorized licensed use limited to: DELHI TECHNICAL UNIV. Downloaded on June 14,2023 at 05:11:42 UTC from IEEE Xplore. Restrictions apply.

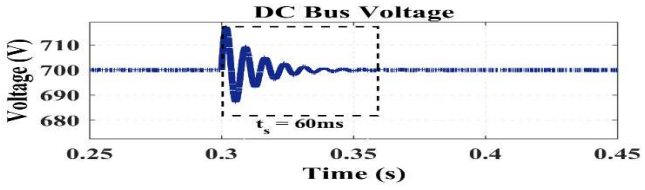

(b)

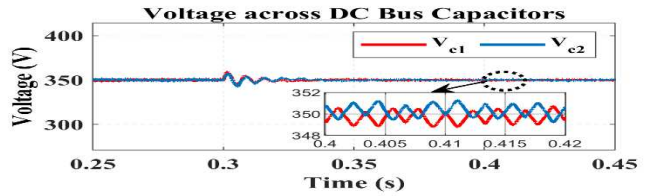

(c)

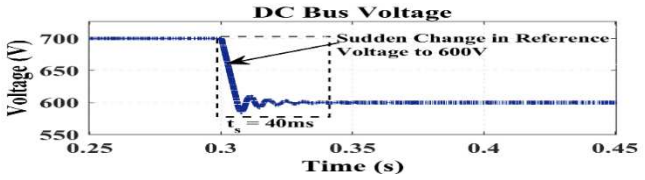

(d)

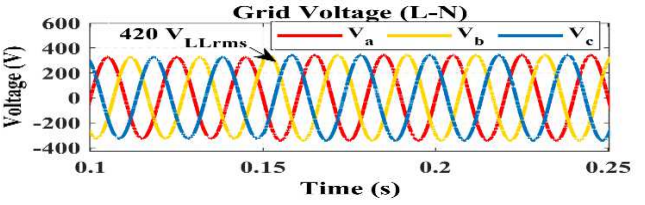

(e)

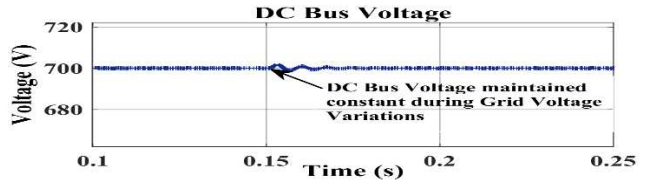

(f)

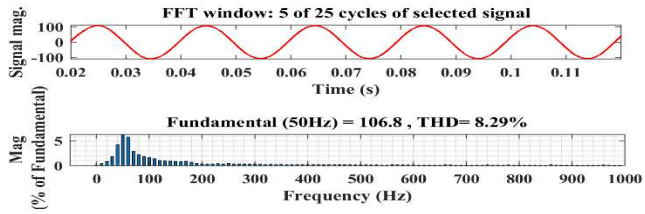

(g)

Fig. 7. Simulation results for dual loop control using hysteresis current control strategy (a) Grid current during load variations (b) DC bus voltage adaption to load variations (c) DC bus capacitor voltage (d) System adaption to reference DC voltage variation (e) Grid voltage variation (f) System adaption to grid voltage variation (g) System non-adaption to grid frequency variation at 50.5 Hz

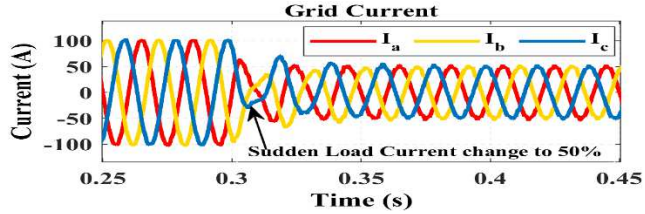

(a)

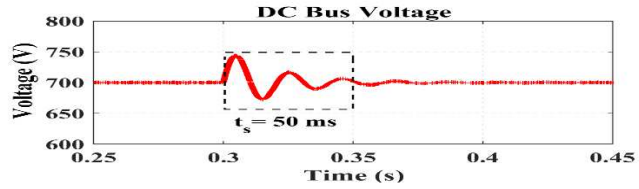

(b)

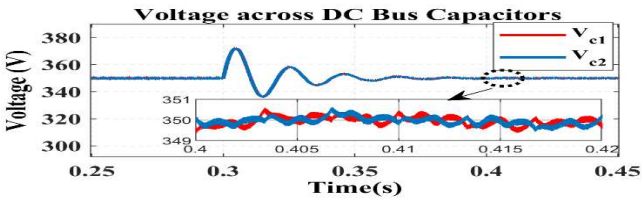

(c)

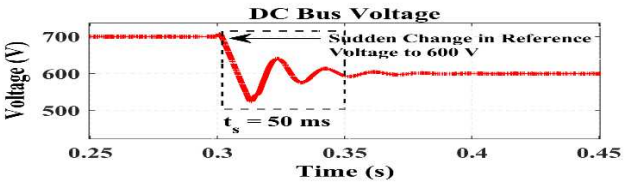

(d)

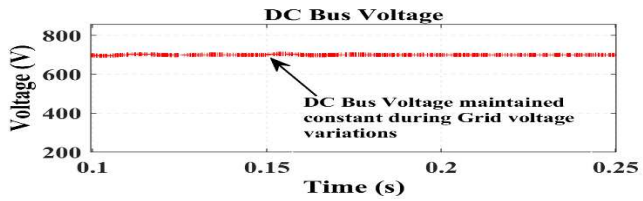

(e)

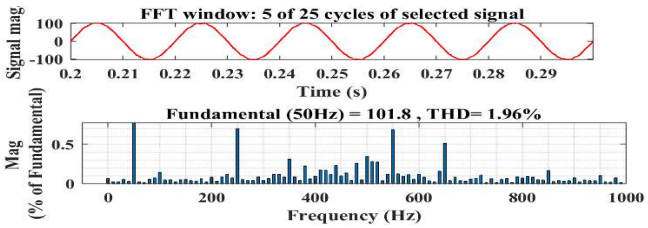

(f)

Fig. 8. Simulation results for dual loop control using d-axis and q-axis current control strategy with SVPWM (a) Grid current during load variations (b) DC bus voltage adaption to load variations (c) DC bus capacitor voltage (d) System adaption to reference DC voltage variation (e) System adaption to grid voltage variation as in Fig 7(e) (f) System adaption to grid frequency variation at 50.5 Hz

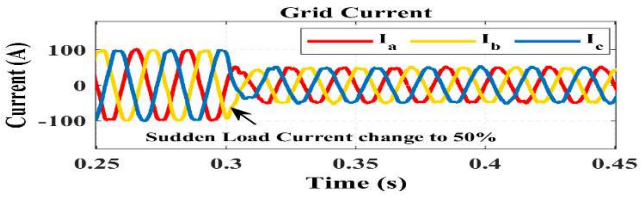

(a)

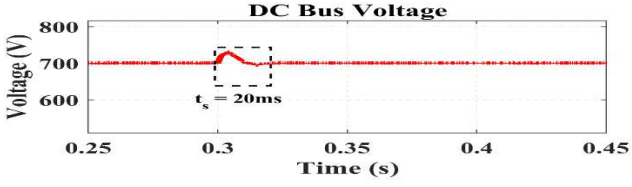

(b)

Authorized licensed use limited to: DELHI TECHNICAL UNIV. Downloaded on June 14,2023 at 05:11:42 UTC from IEEE Xplore. Restrictions apply.

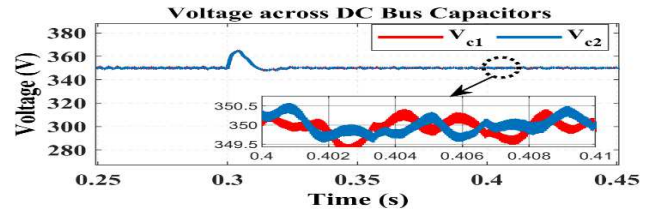

(c)

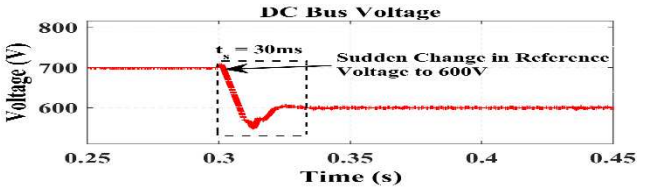

(d)

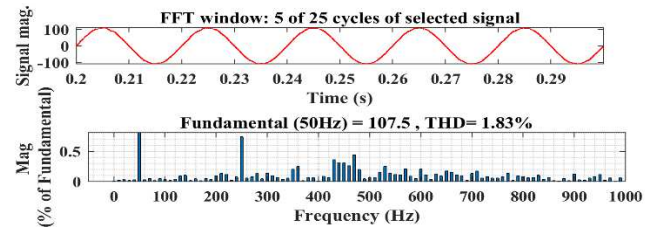

(e)

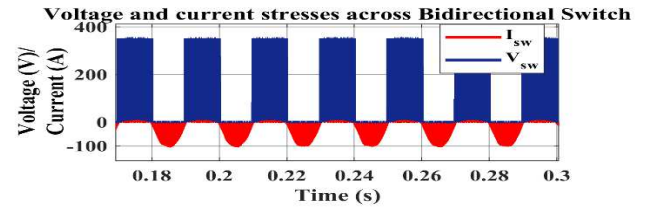

(f)

Fig. 9. Simulation results of proposed modified dual loop control using d-axis and q-axis current control strategy with SVPWM (a) Grid current during load variations (b) DC bus voltage adaption to load variations (c) DC bus capacitor voltage (d) system adaption to reference DC voltage variation (e) System adaption to grid frequency variation at 50.5 Hz (f) Voltage and current stresses across bidirectional switch

V. CONCLUSION

In this paper, a 50 kW Vienna Rectifier considering system parasitic is analyzed using three control algorithms: dual loop using hysteresis current control, dual loop using q-axis and d-axis current control using SVPWM and modified dual loop using q-axis and d-axis current control using SVPWM. The control algorithms are implemented in MATLAB-Simulink. The dual loop hysteresis current control algorithm was adaptive to the grid voltage variations but not adaptive to the grid frequency variations and is able to mitigate the sudden load variations and reference DC Bus voltage variation but with a sluggish dynamic response with oscillations in transient state. The dual loop control using d-axis and q-axis current control algorithm using SVPWM was adaptive to both grid voltage and grid frequency variations including sudden load variations and reference DC Bus voltage variation but with an improved dynamic response with minimal oscillations in transient state. The proposed modified dual loop control using d-axis and q-axis current control algorithm using SVPWM was able to improve the dynamic response by reducing the settling time and eliminating the oscillations in transient state. So, this is the preferred control algorithm compared to other two. To support the proposed modified control, small signal analysis was performed. All the control algorithms were able to achieve near to unity p.f. with varied performance. In this paper, the adopted power ratings are high due to its application, so conduction losses are also analyzed for a complete sector. The system designed is efficiently mitigating the load variations and grid side variations which suits its application in emerging EV charging topologies.

ACKNOWLEDGMENT

The authors would thank the Centre of Excellence for Electric Vehicles and Related Technologies, Delhi Technological University for providing necessary facilities for performing our research work.

REFERENCES

[1] S. Pareek, A. Sujil, S. Ratra and R. Kumar, "Electric Vehicle Charging Station Challenges and Opportunities: A Future Perspective," in *2020 International Conference on Emerging Trends in Communication, Control and Computing (ICONC3)*, Lakshmangarh, India, 2020.

[2] L. Wang, Z. Qin, T. Slangen, P. Bauer and T.V. Wijk, "Grid Impact of Electric Vehicle Fast Charging Stations: Trends, Standards, Issues and Mitigation Measures - An Overview," *IEEE Open Journal of Power Electronics,* vol. 2, pp. 56-74, 2021.

[3] J. Wu, Y. Qi, . F. Muhammad and X. Wu, "A unified switch loss model and design consideration for multilevel boost PFC with GaN devices," *CPSS Transactions on Power Electronics and Applications,* vol. 6, no. 4, pp. 349-358, Dec. 2021.

[4] R. K. Lenka, A. K. Panda, A. R. Dash, L. Senapati and N. Tiwary, "A Unified Control of Grid-Interactive Off-Board EV Battery Charger with Improved Power Quality," *IEEE Transactions on Transportation Electrification,* 2022.

[5] L. Dalessandro, U. Drofenik, S. D. Round and J. W. Kolar, "A novel hysteresis current control for three-phase three-level PWM rectifiers," in *Twentieth Annual IEEE Applied Power Electronics Conference and Exposition, 2005. APEC 2005*, Austin, TX, USA, 2005.

[6] H. Cheng and J. Huang, "Research on SVPWM Control Strategy of Three Phase VIENNA Rectifier," in *2018 5th International Conference on Systems and Informatics (ICSAI)*, Nanjing, China, 2018.

[7] Y. Wang, Y. Li, X. Guo and S. Huang, "Hybrid Space Vector PWM Strategy for Three-Phase VIENNA Rectifiers," *Sensors,* vol. 22, no. 17, p. 6607, Sep. 2022.

[8] L. Beghou, "Generalized Approach for Small Signal Modelling & Loss Analysis in 3-Phase PFC Vienna Rectifiers," in *IECON 2022 – 48th Annual Conference of the IEEE Industrial Electronics Society*, Brussels, Belgium, 2022.

[9] J. W. Kolar, U. Drofenik and F. C. Zach, "VIENNA rectifier II-a novel single-stage high-frequency isolated three-phase PWM rectifier system," *IEEE Transactions on Industrial Electronics,* vol. 46, no. 4, pp. 674-691, Aug. 1999.

[10] Texas Instruments, "Vienna Rectifier-Based, Three-Phase Power Factor Correction (PFC) Reference Design Using C2000™ MCU," 2016-2017.

[11] A. Sunbul and V. K. Sood, "Simplified SVPWM Method for the Vienna Rectifier," in *2019 20th Workshop on Control and Modeling for Power Electronics (COMPEL)*, Toronto, ON, Canada, 2019.

[12] N. B. Hadj-Youssef, K. Al-Haddad, H. Y. Kanaan and F. Fnaiech, "Small-signal perturbation technique used for DSP-based identification of a three-phase three-level boost-type Vienna rectifier," *IET Electric Power Applications,* vol. 1, no. 2, p. 199 – 208, 2007.

Authorized licensed use limited to: DELHI TECHNICAL UNIV. Downloaded on June 14,2023 at 05:11:42 UTC from IEEE Xplore. Restrictions apply.

Design and Control of Fault-Tolerant Interleaved Buck Converter for Battery Charging Applications

1st Abhishek Chawla
CoE for Electric Vehicle and Related Technologies
Department of Electrical Engineering
Delhi Technological University
Delhi, India
abhishekchawla15@gmail.com

2nd Mayank Kumar (*SM IEEE*)
CoE for Electric Vehicle and Related Technologies
Department of Electrical Engineering
Delhi Technological University
Delhi, India
mayankkumar@dtu.ac.in

2023 International Conference on Power, Instrumentation, Control and Computing (PICC) | 979-8-3503-3446-3/23/$31.00 ©2023 IEEE | DOI: 10.1109/PICC57976.2023.10142844

***Abstract*— DC-DC converters are one of the most important and challenging subsystems in charging systems. The reliability of the system has always been an issue because of the failures of the semiconductor switches. The paper presents the design of a 1kW fault-tolerant interleaved buck converter for battery charging applications. It also proposes an algorithm for detection of fault in any of the switches and uses a redundant leg-based topology so that the converter functions like the prior fault condition. The algorithm makes use of the digitally implemented circuit and hence does-not affect the cost of the system much. A modified PI control which works along with fault detection and control scheme is implemented to charge the battery in constant current mode which do not let current and voltage ripples increase after the fault. Also, it distributes the current equally to avoid stress over a particular branch. The modified control alters the faulty phase with the redundant phase after the occurrence of the fault with the help of fault detection system. The fault-tolerant capability ensures the continuous operation of the converter even after a fault and made it suitable for electric vehicle battery charging applications**.

***Keywords*— Electric vehicle, fault-tolerant converter, interleaved buck converter, redundant leg configuration.**

I. INTRODUCTION

As the population on the earth is rising rapidly, the energy consumption of the world is also rising exponentially. At present, conventional resources are used to meet the demand of the world out of which fossil fuels provide 70%-80% of the primary energy required by the world. It not only results in severe consequences like the prolongation of the rise in atmospheric carbon dioxide and the onset of global warming but is disastrous to both the environment and people. Therefore, with this increasing rate of consumption of energy, the nature is affected badly. At this rate, the earth will run out of all the resources very early. Therefore, a paradigm shift is required, and different technologies should be looked upon to compensate the energy demand and not affect the nature. Renewable energy systems (RESs) especially photovoltaic systems and electric vehicles (EVs) work towards meeting the energy needs and development of clean and green transportation system for tomorrow but both these applications required battery to store the energy. Also, the ratings of the battery and the dc link voltage of renewable energy systems are not always same and required a power conversion stage. This is where DC-DC converters finds its application in contributing towards a healthy, clean, and greener tomorrow.

The DC-DC converters are used to either step-up the voltage or to step-down input voltage as well as to regulate the dc link voltage. The power electronics converters are the main building block of a typical charging system. The type of converter depends of input power supply and the converters with least switches are typically preferred for charging purposes as the efficiency of the system should be high and system must be lossless to charge effectively. RESs such as solar PV systems serve as the dc power source and also in case of EVs grid act as the dc power source.

DC-DC Interleaved Converters finds its applications in charging of the battery as they provide the following advantages over normal converter [1]- [2] such as high power, high output current, greater efficiency over normal converters, reduction in ripple voltage, reduced component size and reduced output current ripple. With all such advantages, these converters can be used in the EV charging.

EV charging is possible at three different power levels generally known as level 1, level 2, and level 3 charging. In first level of charging, the vehicle is connected to the AC grid (110V) for approx. 8 hours to 12 hours. It can serve power up to 1.9 kW as it requires a AC to DC conversion stage. Also, these are on-board chargers i.e., these are fitted inside the vehicles only. In the second level of charging, the vehicle remains connected to AC grid (220V) for approximately 4 hours to 6 hours, during charging time, the batteries receive a power of up to 19.2 kW. In level 3 charging, the charger is installed externally and has a maximum power level of 90 kW. The third level is recognized as dc fast charging. The car's battery gets charged up to 80% of its rated capacity by the DC source in 30 minutes at the rate higher than 1C [3], where 1C represents charge rate of the battery. Also, because of the current interleaving, the size of the components reduced and hence they can be implemented small in size and does not require large space along with heat sink to dissipate the power losses in the switches.

Although these converters provide so many advantages, but a single fault can severely affect the performance of the system and in worst case can even shut down the converter. These faults can be caused by defects that the system develops because of both internal and external factors. Short circuits and open circuits faults in the system are the main reliability issues of the converter, and they appear may be because of internal or/and external defects. The faults are typically caused by issues with grounding, or a fast rise in system temperature. Therefore, fault analysis is a crucial design consideration. It gives us thorough information on the damages that different types of defects can do, as well as these faults shows the seriousness of the type of faults

979-8-3503-3446-3/23/$31.00 ©2023 IEEE

Authorized licensed use limited to: DELHI TECHNICAL UNIV. Downloaded on June 14,2023 at 05:03:15 UTC from IEEE Xplore. Restrictions apply.

appeared. It provides us with precise details regarding the highest withstand capacity of each converter component. It greatly aids in the design of the converters within their safe working ranges. In the proposed research, the converter uses a redundant leg-based topology that deals with switch fault and makes it more reliable for battery charging operation. A brief summary of the various fault tolerant control techniques used in dc-dc converters is provided in [4]. It changes the current gain of inner loop and voltage gain of outer loop once the fault is detected. In [5], the fault detection and tolerant control scheme affected by the sensor faults (noise abnormality, gain deviation and open circuit) are discussed. It detects the fault by comparing the threshold value with the residual estimation function which works on residual signal. A reconfiguration approach is followed to implement the tolerant scheme. [6] uses a nominal controller before the prior fault condition and a robust controller after the occurrence of the fault. In [7] experimentally verifies the multi-mode fault tolerant capability of stacked interleaved buck converter which constitutes of main branch having *n* phases and an auxiliary bidirectional buck/boost branch with a series capacitor. In [8] a 250W prototype, hexapod walker with an electrical efficiency of 70% - 90% is built which constitutes of 8 independent legs. As fault occur in any of the legs or in multiple legs, the converter keeps working through remaining legs until a peak current of 6A is reached in independent leg. The uninterrupted power supply and equitable sharing of current between healthy legs (before fault) and between healthy leg and auxiliary leg (after fault) are guaranteed by the suggested fault detection and tolerant control approach integrated with modified PI control [9].

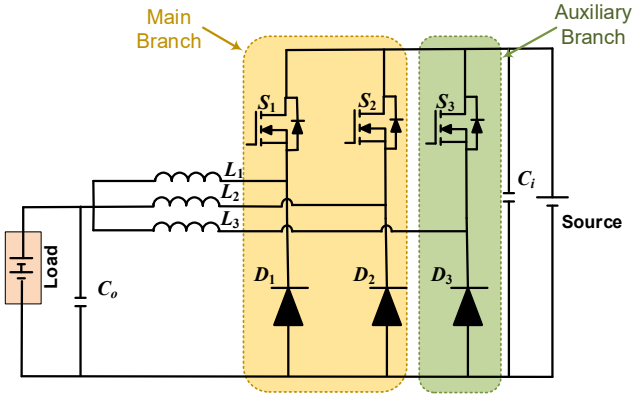

Fig. 1. Redundant leg based interleaved buck converter (IBC).

II. Design and Operation of Interleaved Buck Converter

A switch mode DC- DC power converter known as a "buck converter" transforms the output voltage to lower level than the input voltage. A buck converter is often referred to as a step-down converter. The step-down converter is similar to step down transformers in which the input voltage is stepped down to a level below the input voltage. The proposed redundant leg topology based interleaved buck converter is shown in Fig. 1. It consists of main branch (2-phase interleaved buck converter) and one auxiliary branch. A parallel group of converters called interleaved converters each have their own power MOSFETs and inductors. A phase is the collective name for these parts. These phases share input and output capacitors and are connected in parallel [1]. Individual phases are active at regular intervals during steady-state operation, and the space interval is provided by ø as follows:

$$\phi = \frac{360°}{n} \tag{1}$$

where *n* represents the total number of phases.

Generally, the converter operates in one of the two conduction modes as follows:

i. Continuous current conduction mode (CCM)
ii. Discontinuous current conduction mode (DCM)

As the name suggests, in continuous current conduction mode the current through the inductor never falls back to zero whereas in discontinuous current conduction mode the current through the inductor falls to zero. The reverse current that flows during the rectifying diode's reverse recovery period causes losses in CCM. In low-voltage switching DC-DC conversion, the rectifying diode's reverse voltage and current are both low, hence CCM is often used with output ripple voltage and harmonics reduction as the top priority. The inductance of the inductor used in CCM is greater than that of DCM thereby increasing the size along with the cost. Also, the switching losses in CCM are higher than that of in DCM thereby affecting the efficiency of converter but the allowable power of the switching device is low when compared to that in DCM thereby reducing the size and overall cost [10].

The boundary condition between CCM and DCM is given as follows:

$$i_{L\min} = 0 \tag{2}$$

$$L_{\min} = \frac{(1-D)R}{2f_{sw}} \tag{3}$$

where,

$i_{L\min}$ = minimum inductor current,
L_{min} = critical value of inductance below which it operates in DCM,
D = duty cycle,
R = resistance for fixed value of resistive loads,
f_{sw} = switching frequency.

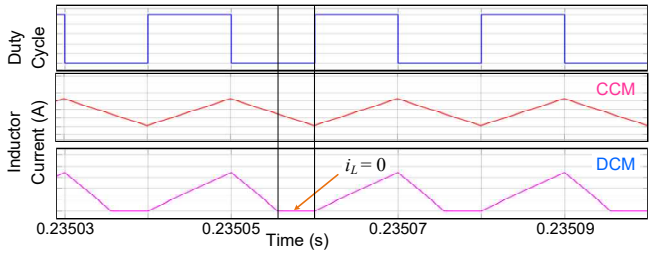

Fig. 2. Operation of continuous and discontinuous conduction mode.

The condition is only valid for a constant load having a fixed switching frequency and duty cycle. In this proposed research, the converter is made to operate in CCM. Fig. 2 shows the difference between CCM and DCM. To simplify the calculations, it is assumed that $L_1 = L_2$ and duty ratio of the first switch is equal to duty ratio of the switch from second leg, where the inductance value of different phase legs are

Authorized licensed use limited to: DELHI TECHNICAL UNIV. Downloaded on June 14,2023 at 05:03:15 UTC from IEEE Xplore. Restrictions apply.

denoted as L_1, L_2. The value of inductance can be calculated as follows:

$$L = \frac{V_{out}(1-D)}{I_{PP} \times f_{sw}} \tag{4}$$

where,

V_{out} = output nominal voltage,

I_{PP} = per phase peak to peak current.

The output current ripple of the converter under steady state condition can be calculated as given in [7]

$$I_{out} = \sum_{i=1}^{n} i_{Li} \tag{5}$$

$$\Delta I_{out} = \frac{V_{in}}{L \times f_{sw}} \left(1 - \frac{m}{nD}\right)(1 + m - nD) \tag{6}$$

where,

V_{in} = input voltage;

m = floor value of nD.

The values of the input capacitance and output capacitance can be calculated as follows [1]:

$$C_{out} = \frac{I_{pp}}{8 \times f_{sw} \times \Delta V_{out}} \tag{7}$$

$$C_{in} = \frac{I_{phaseMAX} \times D \times n(1-D)}{f_{sw} \times \Delta V_{in}} \tag{8}$$

where,

ΔV_{out} = peak to peak output ripple voltage,

ΔV_{in} = peak to peak input ripple voltage.

The voltage and current stress across the switch are given as follows:

$$V_{sw(\max)} = V_{in} \tag{9}$$

$$I_{sw(\max)} = i_{L(\max)} \tag{10}$$

A. Operation under Normal Condition

It is expected that all of the modules are the same under usual circumstances. The primary converter is controlled by a current closed-loop system to ensure equal sharing of current among the phases. Peak-current mode control is used by [11] to charge the battery. The various advantages of peak-current mode control over duty-ratio controller are also covered, including improved line noise rejection, design flexibility and automated overload protection.

A 2:1 mux is used before comparing the phase's inductor current with the reference current. The mux is controlled using a signal which gets active only in case of fault in the respective leg. The mux selects the inductor current between the respective leg or auxiliary leg. Fig. 3 shows the difference between the conventional PI controller used in [4] and modified PI control being implemented. Also, the converters used in [4], [8] doesn't utilize the maximum capability of the phases in order to make the converter fault tolerant and not affect the power ratings after the fault. For a system of 1kW rating, the maximum power that can be transferred from each leg is 333.33W and not 500W under balanced phase current condition, thereby utilizing only 66.67% of that respective leg to make it fault tolerant. Also, it implies the use of three PI controller whereas modified control uses only two PI. Using modified PI control, the ripples in the inductor current does not rise after fault and therefore do not deteriorate the battery health. The implementation of this current sharing scheme with the help of fault detection scheme is shown in Fig. 4 which regulates the current in different phases and generates the duty cycle for the respective phase.

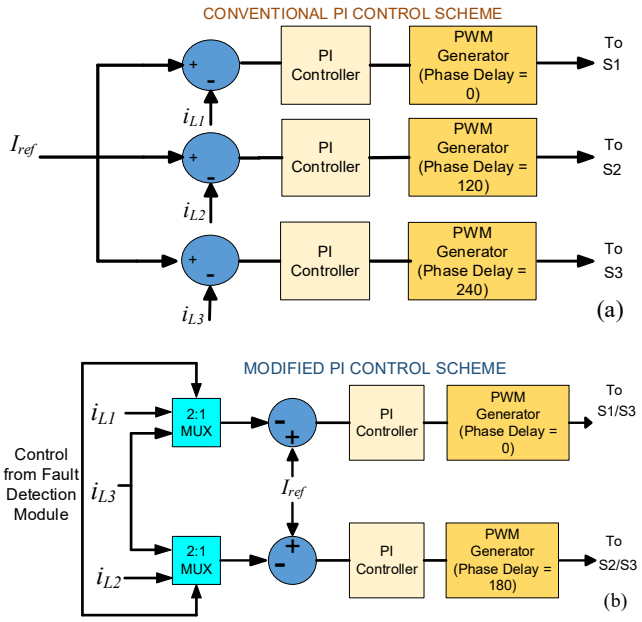

Fig. 3. Block diagram of (a) Conventional PI control (b) Modified PI control.

B. Operation under Faulty Condition

Switch fault is one of the factors that contribute to dc-dc power converter failure. Switch faults can typically be divided into following categories: open circuit fault and short circuit faults [12]- [13]. The suggested system addresses the converter's open circuit issue.

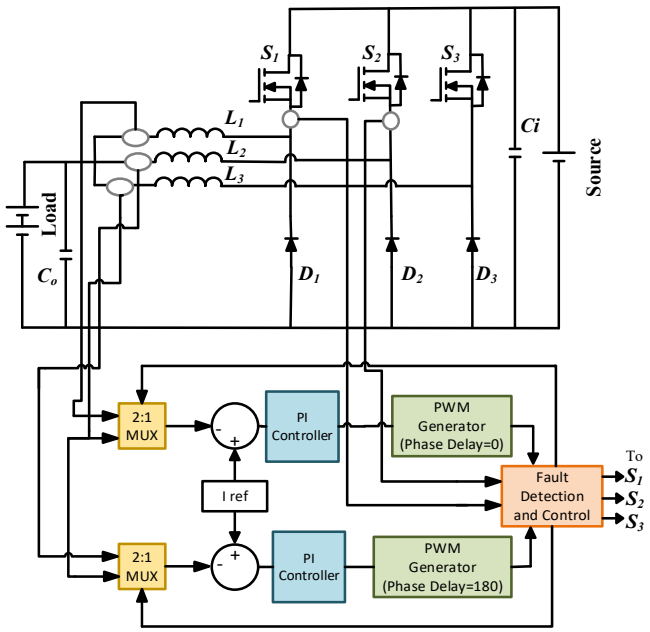

Fig. 4. Fault detection and tolerant control scheme for two-phase IBC with redundant leg.

Authorized licensed use limited to: DELHI TECHNICAL UNIV. Downloaded on June 14,2023 at 05:03:15 UTC from IEEE Xplore. Restrictions apply.

Considering the case when the fault occurs in the system, the fault tolerant algorithm 'high' the fault signal of the respective leg and the inductor current of that leg is replaced with the auxiliary leg. Also, the controller stops sending pulses to the respective leg. e.g. if initially leg 1 and leg 2 are operating and a fault occurs in leg 1, the controller will stop sending the pulses to that leg, instead these same pulses are being fed to the leg 3. Along with the current control technique, the converter keeps working on the same power level rather than a decrease in the power ratings, making it look there's no fault in the system.

III. Fault Tolerant Converter Design

A. Proposed Fault Tolerant Control

The first step in making a converter fault-tolerant is identification of the fault. The second step being isolation of the faulty phase and redundant control to be applied so as not to impede the converter's power ratings. Here, both the cases are considered when there's fault in phase-1 and in phase-2.

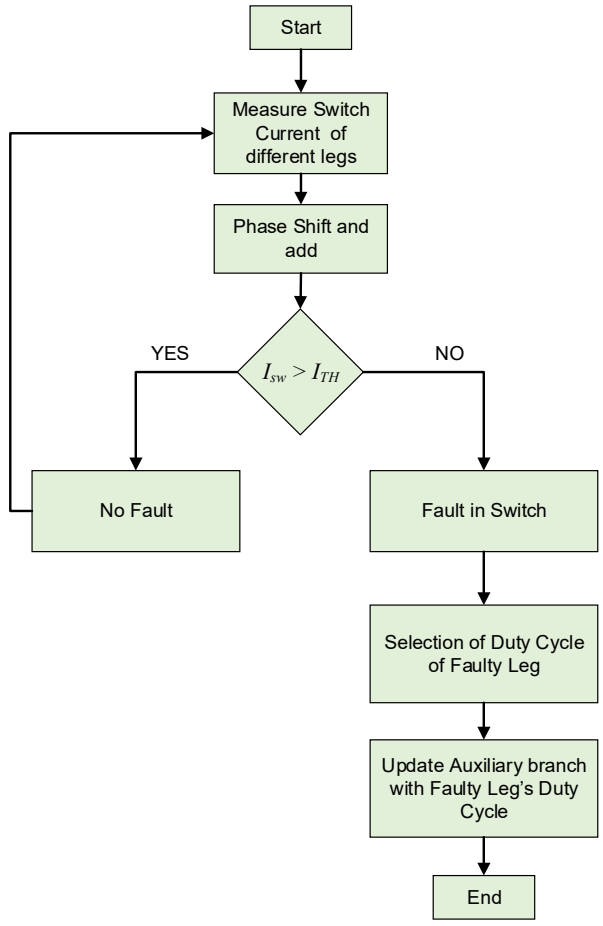

Fig. 5. Flow chart of fault tolerant control scheme.

Fig. 5 shows the proposed flow chart of fault tolerant control scheme for IBC. Consider the scenario in which phase 1 experiences an open-circuit fault. The phase current is detected and sent through the ADC. These are then passed through a phase shifter, followed by addition and passage through a magnitude comparator. This procedure is repeated for two distinct legs. In the event of an open circuit fault (phase current less than threshold current) the magnitude of the respective leg becomes zero as soon as the fault occurs. To break the connection in the occurrence of a short circuit problem, a fuse is fitted. The short circuit fault is treated as an open circuit fault. These signals are passed through an OR gate, which produces output 1 if any of the legs fail. In addition, these two signals control the mux between the PI controller to select the respective leg current or the auxiliary leg current. The output of the OR gate is the control signal of the final multiplexer, which transmits the faulted leg's duty cycle to the redundant leg. Similarly, the entire procedure can be followed in case of fault in 2nd phase. The phase shift operation followed by summing of current varies with the duty cycle of the converter. In this paper, a duty cycle larger than 50 is taken into account.

The effect on varying the threshold value of current I_{TH} can be seen on the fault detection time. The higher the value of threshold current the lower is the fault detection time however, higher values of threshold current can lead to false triggering of the detection system. Therefore, a balance should be made in between the threshold value of the current and the time for detecting the fault and taking appropriate actions. In the following study, gains are adjusted such that the balance between the both is maintained.

B. Current Sharing Scheme

To have a constant current to charge the battery, a proportional and integral (PI) controller is used that determines equal sharing of current among all the healthy phases. An ideal controller must have zero settling time, steady state error, and low peak overshoot. Fig. 6 shows the representation of the PI controller. The control signal U can be written as follows:

$$U = K_p + K_i \int \Delta dt \tag{11}$$

Where,
K_p = controller's proportional gain,
K_i = controller's integral gain,
e = the error or deviation of actual measured value (MV) from the reference value (RV).

$$e = RV - MV \tag{12}$$

The transfer function of PI controller is given by:

$$C(s) = K_p + \frac{K_i}{S} \tag{13}$$

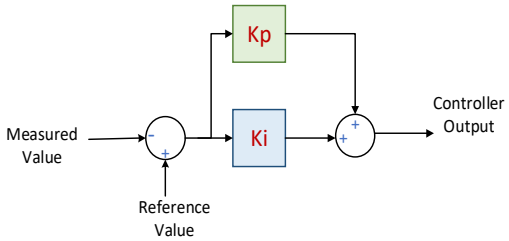

Fig. 6. Block diagram of PI controller.

The following advantages are served by the PI controller: Proportional (P) action boosts loop gain and reduces system sensitivity to changes in system parameters; the steady-state error is eliminated or reduced by the integral (I) action; the integral time can be altered to change the "I" action; both the integral and proportional components of the control action are impacted by changes in the value of K_p [14]- [15].

Authorized licensed use limited to: DELHI TECHNICAL UNIV. Downloaded on June 14,2023 at 05:03:15 UTC from IEEE Xplore. Restrictions apply.

A slight modification is done in closed loop PI controller as 2:1 multiplexer (MUX) is used before that selects either the inductor current of the main branch or the auxiliary branch in case of occurrence of fault in the system. The fault detection technique determines the control signal given to the MUX. The MUX shifts to the auxiliary leg's inductor current as soon as the defect is discovered, maintaining equal current distribution among the phases while not impacting the converter's constant current output. The modified closed loop control is shown in Fig. 3.

IV. Simulation Results

MATLAB software is used to model the suggested fault-tolerant control method in 1kW interleaved buck converter with redundant leg. The parameters used in simulating the system are enumerated in Table I. Fig. 7 shows the inductor current for the different phases with $D > 0.5$. Also, equal current sharing between phases is achieved with the help of PI controller. Fig. 8 shows an open-circuit fault is modelled in second phase of the main branch at $t = 0.3$ sec.

TABLE I: System Parameters

Parameters	Value
Power Ratings	1kW
Switching Frequency	50 kHz
Inductance Per Phase	304 µH
Output Capacitance	100 µF
Input Capacitance	80 µF
Input Voltage	88-104 V
Battery Nominal Voltage	48 V
Battery Ah ratings	100Ahr
Controller's Proportional Gain (Kp)	0.05
Controller's Integral Gain (Ki)	20

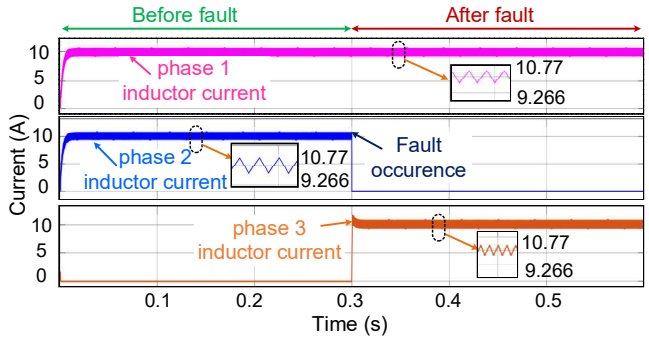

Fig. 7. Inductor current waveforms of different phases under healthy condition and after fault.

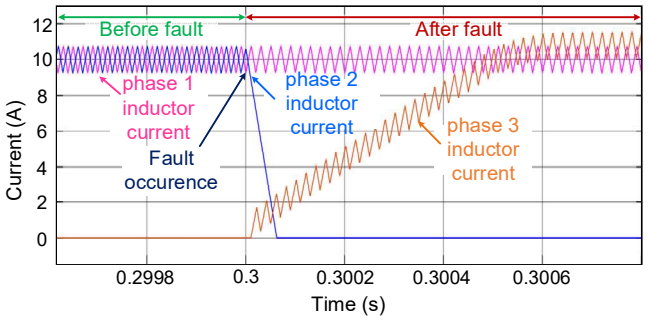

Fig. 8. Effect of fault on different phases of IBC.

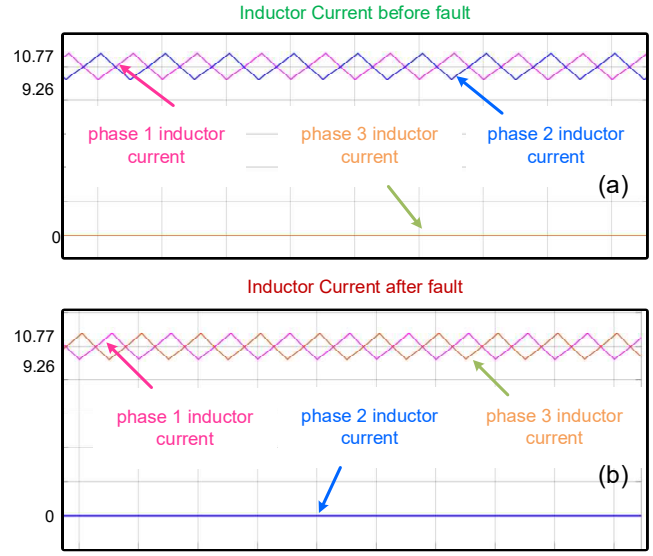

Fig 9. (a)Inductor current before fault (b) Inductor current after fault.

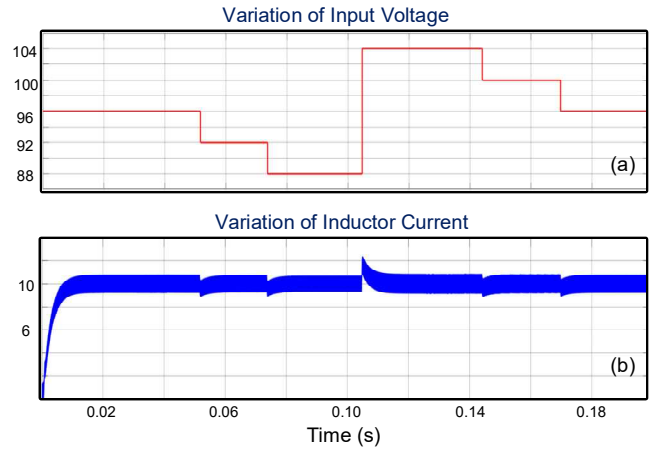

Fig. 10. (a) Variation in input voltage (b)Variation of phase inductor current corresponding to input voltage.

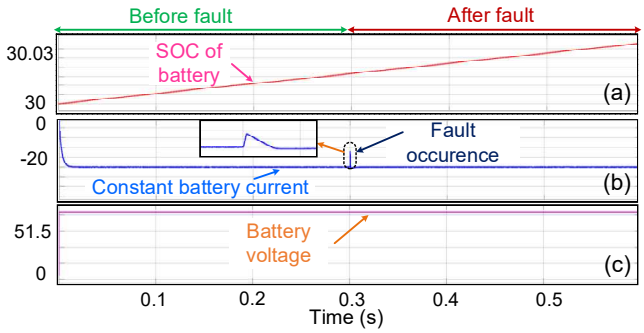

Fig. 11. (a) SoC of battery, (b) Battery current, (c) Battery voltage.

As soon as the fault occurs in the phase, the current through it becomes zero while the redundant leg starts conducting within some microseconds. The tolerant control is activated in less than one cycle i.e., less than 20µs. Also, it does not impact the current in phase 1 of the system as the current doesn't shoot up and it is maintained constant. Fig. 9 ensures that the inductor currents are out of phase with each other even before fault and after fault, thereby ensuring the minimum ripple in the output current along with output voltage for longer life of the battery which is attained with the help of modified PI control. As the switch experiences an open circuit fault, the redundant leg module activates within

Authorized licensed use limited to: DELHI TECHNICAL UNIV. Downloaded on June 14,2023 at 05:03:15 UTC from IEEE Xplore. Restrictions apply.

one switching cycle and shares equal current among two different phases using modified PI controller. The mux helps in selecting in between the main branch and auxiliary branch which is controlled by the fault detection signal of the particular phase. The effectiveness of the PI control is shown in Fig. 10 as it can be seen that the inductor current is maintained constant even after varying the input voltage. Input voltage is varied from extreme low (88V) to extreme high (104V) as per the design specifications. At extreme change in input voltage, from 88V to 104V an overshoot is observed in inductor current, but it settles within small time, thereby making it suitable for battery charging applications. It shares equal current among phases, and it also ensures lower stress over a particular branch. Detection of fault and activation of auxiliary branch is done within microseconds, less than one switching cycle, whereas in [4], [7], it takes milliseconds to activate the redundant control. Fig. 11 shows that the battery is charged with a constant current of 20A. Even after a fault has occurred in the system, the current is maintained constant with a dip in battery's current for just few microseconds. The battery has the amp-hour capacity of 100 Ahr therefore it takes approx. 5 hours to charge completely.

V. Conclusion

This study focused on interleaved buck converter phase current control as well as fault detection and tolerant control. It combines closed loop PI control and tolerant control to deliver constant current for battery charging applications. Each phase of the PI controller shares an exact equal amount of current with the other phase, and it was calibrated to prevent steep overshoots and undershoots. When deciding on the primary branch current and the auxiliary branch current the modified controller uses intelligence in selecting. The size as well as the ripples in the output voltage and output current are reduced by interleaving. The findings demonstrate that a digitally constructed circuit may detect a malfunction within a small time period and take immediate corrective action. Because of such advantages, the converter can be applied to Level 1 EV chargers or can be used other level of charging too. Also, it can be implemented in two stage battery charging from Photovoltaic systems. Moreover, the results can also be applied to other non-isolated interleaved converters.

Acknowledgment

This research supported by the Science and Engineering Research Board (SERB), Department of Science & Technology, Government of India,. under the SERB sanction order number SRG/2021/001640.

References

[1] Texas Instruments, "Multiphase Buck Design From Start to Finish (Part 1), Application Report SLVA882," Texas Instruments, 2017.

[2] . K. Murugappan , . R. Seyezhai, G. S. Kishor, N. Kaashyap and J. J. Ranjit, "Simulation and Analysis of Interleaved Buck DC-DC Converter for EV Charging," in *Advances in Smart Grid Technology*, vol. I , Singapore, Springer, 2020, pp. 369-380.

[3] G. Balen, A. R. Reis, H. Pinheiro and L. Schuch, "Modeling and control of interleaved buck converter for electric vehicle fast chargers," in *2017 Brazilian Power Electronics Conference (COBEP)*, Juiz de Fora, Brazil, 2017.

[4] E. Pazouki, J. A. De Abreu-Garcia and Y. Sozer, "Fault tolerant control method for interleaved DC-DC converters under open and short circuit switch faults," in *2017 IEEE Energy Conversion Congress and Exposition (ECCE)*, Cincinnati, OH, USA, 2017.

[5] J. Li, K. Pan, Q. Su and X. Q. Zhao, "Sensor fault detection and fault-tolerant control for buck converter via affine switched systems," *IEEE Access,* vol. 7, pp. 47124-47134, 2019.

[6] T. Azib, M. Bendali , C. Larouci and K. Hemsas, "Fault tolerant control of interleaved buck converter for automotive application.," *International Review of Electrical Engineering (IREE),* vol. 10, no. 3, pp. 336-343, 2015.

[7] X. Guo , S. Zhang, Z. Liu, L. Sun, Z. Lu, C. Hua and J. Guerrero, "A new multi-mode fault-tolerant operation control strategy of multiphase stacked interleaved Buck converter for green hydrogen production," *International Journal of Hydrogen Energy,* vol. 47, no. 71, pp. 30359-30370, 2022.

[8] Y. Verbelen, A. Banos and Scott, "Fault Tolerant Synchronous Multi-Channel Buck Converter for Nuclear Inspection Instruments," in *25th International Symposium on Design and Diagnostics of Electronic Circuits and Systems (DDECS)*, 2022.

[9] . M. Haque and M. Razzak, "A buck converter-based battery charging controller for electric vehicles using modified PI control system.," in *IEEE International IOT, Electronics and Mechatronics Conference (IEMTRONICS)*, Toronto, Canada, 2021.

[10] "TechWeb," Rohm Semiconductor, 7 September 2017. [Online]. Available: https://techweb.rohm.com/knowledge/acdc/acdc_pwm/acdc_pwm04/3551. [Accessed 29 January 2023].

[11] A. Nugroho, E. Rijanto and . R. , "Buck Converter Control for Lead Acid Battery Charger using Peak Current Mode," *International Journal of Power Electronics and Drive Systems,* vol. 8, no. 2, pp. 686-694, 2017.

[12] M. Kumar, "Time-Domain Characterization and Detection of Open-Circuit Faults for the H-Bridge Power Cell.," *IEEE Transactions on Power Electronics,* vol. 37, no. 2, pp. 2152-2164, 2021.

[13] M. Kumar, "Open circuit fault detection and switch identification for LS-PWM H-bridge inverter," *IEEE Transactions on Circuits and Systems II: Express Briefs,* vol. 68, no. 4, pp. 1363-1367., 2020.

[14] M. Saoudi, A. El-Sayed and M. , "Design and implementation of closed-loop control system for buck converter using different techniques," *IEEE Aerospace and Electronic Systems Magazine,* vol. 32, no. 3, pp. 30-39, 2017.

[15] M. A. Shrud, A. Kharaz, A. S. Ashur, M. Shater and I. Benyoussef, "A study of modeling and simulation for interleaved buck converter," in *1st Power Electronic & Drive Systems & Technologies Conference (PEDSTC)*, Tehran, Iran, 2010.

Authorized licensed use limited to: DELHI TECHNICAL UNIV. Downloaded on June 14,2023 at 05:03:15 UTC from IEEE Xplore. Restrictions apply.

Design and Power Flow Control in Standalone PV System with Reduced Battery Current Ripple

Md. Modassir Masoom
Electrical Engineering Department
Delhi Technological University
Delhi, India
mdmodassirmasoom_2k20phdee505@dtu.ac.in

Narendra Kumar
Electrical Engineering Department
Delhi Technological University
Delhi, India
narendrakumar@dtu.ac.in

Mayank Kumar (*SM IEEE*)
CoE for EVRT,
Electrical Engineering Department
Delhi Technological University
Delhi, India
mayankkumar@dtu.ac.in

***Abstract*: To improve solar photovoltaic (PV) panel efficiency, maximum power point tracking (MPPT) algorithm is needed, which could help to extract the optimal power from solar PV systems. The adaptive backstepping controlling approach is presented in this paper for tracking maximum power points in PV systems. The controller is based on the Lyapunov stability theory and connects the selection of an appropriate Lyapunov function with the design of feedback control action. The reference voltages which are generated for the controller are generated through the maximum power voltage (MPV) searching algorithm. The battery energy storage system (BESS) is linked to a bidirectional converter, which governs both the DC bus voltage and the power flow from the BESS. The operation of the DC microgrid is addressed under varying irradiance changes. Further, the impact of ripple current on the battery heating and its performance are discussed. MATLAB/Simulink software is used to simulate and validate the effectiveness of a BESS-enabled isolated solar PV-based system.**

Keywords – Backstepping mode controller, battery charging, Lyapunov theory, MPPT, PI controller.

I. Introduction

Alternative and ecologically acceptable energy sources are required because of the growing global warming caused by the widespread usage of fossil fuel reserves. Although solar energy is thought to be the most suitable alternative energy source, it has some drawbacks, such as low efficiency. In today's scenario, the demand for energy is constantly increasing, with non-renewable energy resources providing a significant substantial part of the supply. As fossil fuel reserves deplete much faster, the need for generating energy from renewable energy resources expands, and a huge proportion of energy is engendered over the use of countless renewable energy resources. The development of renewable energy systems such as wind systems, PV systems, fuel energy systems, and so on is accelerating. As a result, distributed generation systems are gaining popularity and becoming popular topic of research [1]. By connecting distributed power sources directly to low- or medium-voltage distributed networks, microgrids have become the optimal solution for connecting consumers energy demand or by interfacing power converters.

The efficiency of photovoltaic arrays, which convert solar energy into electrical energy is exceptionally low, and temperature and insolation both have an impact on how well they operate. Therefore, in order to maximize the use of photovoltaic systems, it is important to extract the peak power from the PV array. According to ref. [2], the incremental conductance MPP tracking algorithm for photovoltaic modules outperforms the perturb and observe (P&O) algorithm in terms of response and tracking efficiency.

However, it has been observed in published works that when climatic conditions change, the tracking of MPP is not properly achieved in plots of PV output voltage. In continuation of the literature work, ref.[3], [4] describes a comparison of the ANN-based MPP tracking algorithm and hill-climbing methods. The output voltage and current of the PV array have a logarithmic relationship. PV system analysis necessitates the solution of nonlinear differential equations, and frequency domain transformation is inapplicable. So arduous efforts must be made to advance fitting tools for solving system equations. To encounter the control objectives and design specifications, a nonlinear controller based on Lyapunov stability can be used. Stability analysis for nonlinear systems can be accomplished using Lyapunov stability theory without actually solving the nonlinear differential equations.

Microgrids are replica power systems that use distributed generation (DG) units (such as solar cells or wind turbines). They are classified as AC or DC microgrids [5]–[7]. DC microgrids have much higher end-to-end reliability for DC loads than AC microgrids.

Fig. 1 shows a DC link connecting renewable energy sources to the utility grid. When many distributed generation sources are connected individually, it causes many problems, such as voltage fluctuation and protection circuit problems, so a DC link is preferred for connection to the utility grid. Typically, a substantial number of battery energy storage units are required to maintain the reliability of a DC link (microgrid). The upkeep of continual voltage on the DC bus is critical because it is the feature that determines system performance. Variation in bus voltage is caused by variations in input power from sources such as solar cells. The bus voltage varies in response to changes in solar irradiance or changes in load.

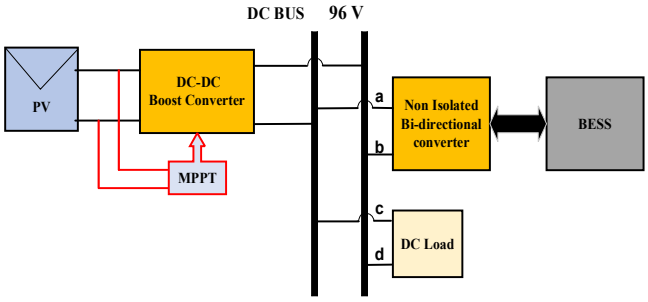

Fig. 1 Block diagram of the proposed standalone PV system.

As a result, bus voltage control and monitoring are obligatory to deliver rated voltage levels at the load end. The use of a bidirectional dc-dc converter (BDC) allows for the charging and discharging of battery energy storage units as needed for energy flow in the system.

Battery energy storage systems (BESS) are used in solar PV system-based microgrids to store excess energy generated by the solar panel during periods of high sunstroke. This stored energy is implemented at night or in poor weather

2023 International Conference on Power, Instrumentation, Control and Computing (PICC) | 979-8-3503-3446-3/23/$31.00 ©2023 IEEE | DOI: 10.1109/PICC57976.2023.10142520

979-8-3503-3446-3/23/$31.00 ©2023 IEEE

Authorized licensed use limited to: DELHI TECHNICAL UNIV. Downloaded on June 14,2023 at 05:08:47 UTC from IEEE Xplore. Restrictions apply.

conditions. The primary goal of installing a BESS in a sustainable power microgrid is to increase the microgrid's self-consumption and self-sufficiency [8], [9], [10]. But before choosing a specific BESS configuration for the necessary microgrid system, it is vital to size the battery parameters.

Investigating and analyzing isolated DC microgrid operation for a fixed DC load is the primary objective of this work with the consideration of battery heating caused by sudden changes in irradiance and temperature conditions. Power flow analysis was performed to determine system power losses, and DC bus voltage regulation and control techniques to achieve optimal efficiency are discussed. To achieve the optimal battery performance, battery parameters have been examined. The capacity, performance, and lifespan of the battery are all enhanced with the appropriate battery sizing. The results were validated using MATLAB/Simulink simulation software.

II. PV Module Specifications

It consists of two series connected modules per string and two parallel strings of Sunrise Solartech SR-P672275 (275.31 watts) module. The characteristics curve at different irradiance and temperatures is shown below in Fig. 2.

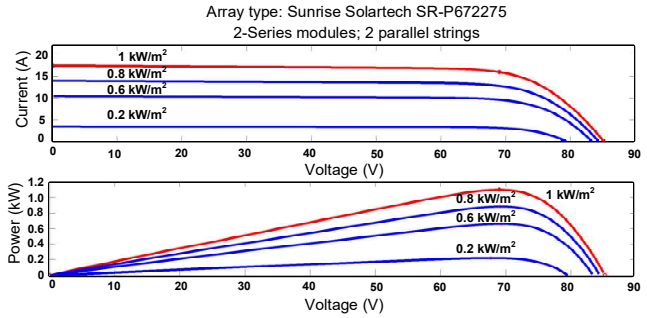

Fig. 2 I-V and P-V characteristics of Sunrise Solartech SR-P672275

The PV module's performance is influenced by fluctuations in insolation and temperature. When a PV panel is confronted to more illumination, it emits more photocurrent and, as a consequence, a larger open circuit voltage. Maximum power is extracted from a photovoltaic (PV) system at a constant temperature when it is introduced to peak insolation (1kW/m^2).

If the irradiance diminishes, the maximal point transition to a reduced value. However, the maximum peak power (MPP) goes higher if this is followed by a temperature drop. Sunrise Solartech SR-P672275 is the solar PV module under concern for the isolated DC microgrid system. Table I shows the datasheet for said Sunrise Solartech SR-P672275 PV module at STC.

TABLE I. PV Module and Converter Parameters

Parameters	***Value***	***Parameters***	***Value***
C_{PV}	2000 µF	Max. Power (MP)	275.31 *W*
L	3 mH	Cells per Module (n_s)	72
C_o	3200 µF	V_{OC}	42.61 *V*
R	20 Ω	I_{SC}	5.96 *A*
Switching frequency	10 kHz	V_{mp}	34.5 *V*
Diode voltage drop	0.82 V	I_{mp}	7.98 A
Ideality factor (A)	0.95512	K_i	0.61 ℃

III. Design of Backstepping MPPT Controller

Backstepping control is achieved by establishing the reliable control law based on the Lyapunov function. Fig. 3 shows a block diagram depiction of the controller used in the PV system. Lyapunov's stability statement must be satisfied for the control algorithm to exist, i.e., the function's first derivative must be negative [11].

$$\dot{V} \leq 0 \tag{1}$$

The following steps are required during the controller design:

i. Obtain the reference voltage from the maximum power voltage (MPV) searching algorithm and define the first voltage-related tracking error. Choosing an appropriate Lyapunov function based on the error dynamics.

ii. Checking for the Lyapunov function's first derivate; if negative, continue; otherwise, update the Lyapunov function.

iii. Defining a stabilization function and citing its value for the next tracking error convergence.

iv. Establishing the final control law based on the Lyapunov function in order to drive the system to asymptotic stability.

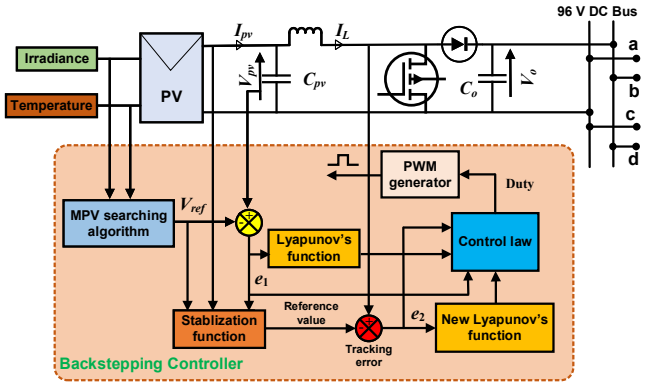

Fig. 3 Proposed standalone PV system with backstepping controller.

A. MPV Searching Algorithm

Based on the linear function between the open circuit voltage and the reference voltage (V_{pv}*), the operating point of the system after MPP can be ascertained under varying irradiance and temperature conditions[12]. The equation is as follows:

$$V_{pv}^{*} = K_v V_{oc} \tag{2}$$

where, V_{oc} = open circuit voltage, and
K_v = constant voltage proportionality.

Depending on the PV Module construction and material, the value of K_v typically lies between 0.73 and 0.83.

The PV generator is made up of series cells (n_s) and parallel panels (n_p). The underlying model of an elementary cell is depicted in Fig 4.

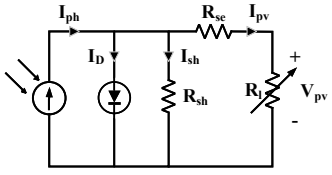

Fig. 4. Single diode model of elementary cell

Authorized licensed use limited to: DELHI TECHNICAL UNIV. Downloaded on June 14,2023 at 05:08:47 UTC from IEEE Xplore. Restrictions apply.

$$I_{pv} = n_s I_{ph} - n_p I_o \left[\exp\left(\frac{q}{nk_bT} \left(\frac{V_{pv} + I_{pv} R_{se}}{n_s} \right) \right) - 1 \right] - \frac{n_s V_{pv} + n_p I_{pv} R_{se}}{R_{sh}} \quad (3)$$

Further derivation of equation (3) for short-circuit current I_{sc} at $R_l = 0$ is possible. Equation (4), in which S/S_{ref} is the per unit change in the received insolation, can be used to express the value of I_{pv}. I_{sc} is the short circuit current, K_i is the short circuit coefficient of temperature, T_{ref} reference temperature.

$$I_{ph} = \frac{S}{S_{ref}} \left\{ I_{sc} + K_i \left(T - T_{ref} \right) \right\} \quad (4)$$

On flouting the shunt current under open circuit scenarios i.e V_{oc} at $R_l = \infty$, the PV current is written as:

$$I_{pv} = n_s I_{ph} - n_p I_o \left[\exp\left(\frac{q}{nk_bT} \left(\frac{V_{pv} + I_{pv} R_{se}}{n_s} \right) \right) - 1 \right] \quad (5)$$

Open circuit voltage can be expressed as follows:

$$I_{ph} = I_{oref} \left\{ \exp\left(\frac{V_{oc}}{n_S V_t} \right) - 1 \right\}$$
$$V_{oc} = n_s V_t \ln\left(\frac{I_{ph} + I_{oref}}{I_{oref}} \right) \quad (6)$$

Where, I_{oref} is the inverse saturation current at T_{ref}.

$V_t = \frac{AK_bT}{q}$ = temperature equivalent voltage.

$$I_o = I_{\text{oref}} \left(\frac{T}{T_{ref}} \right)^3 \exp\left\{ \frac{qE_g}{n_s AK_b} \left(\frac{1}{T_{ref}} - \frac{1}{T} \right) \right\} \quad (7)$$

where, K_b is Boltzmann constant, I_o is reverse saturation current at temperature T, E_g is band gap.

The proposed controller's performance is validated using PV array characteristic curves for each irradiance level. The MPV searching algorithm generates (Vpv*) for the varying irradiance levels. And the Vpv* is tracked by the backstepping controller. Fig. 5 shows the tracking of Vpv* Vs Vpv voltage.

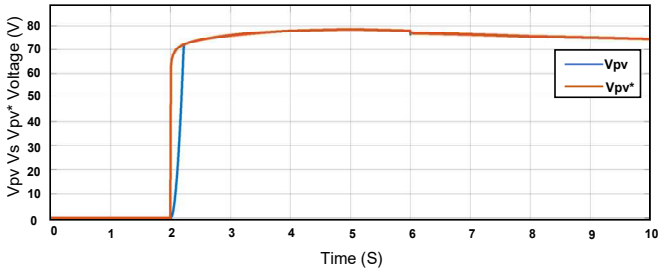

Fig. 5 Tracking of reference voltage (Vpv*) with respect to actual voltage (Vpv)

B. STABILIZATION FUNCTION BUILDUP

System dynamics can be expressed as

$$\frac{dI_L}{dt} = \frac{V_{PV}}{L} - (1-D)\frac{V_0}{L} \quad (8)$$

$$\frac{dV_0}{dt} = \frac{I_L}{C_0}(1-D) - \frac{V_0}{C_0 R} \quad (9)$$

$$\frac{dV_{pv}}{dt} = \frac{1}{Cpv}\left(I_{pv} - I_L \right) \quad (10)$$

The tracking error can be articulated as

$$e_1 = V_{pv} - V_{pv}^* \quad (11)$$

Taking the first derivate of the tracking error

$$\dot{e}_1 = \dot{V}_{pv} - \dot{V}_{pv}^* = \frac{1}{C_{pv}}\left(I_{pv} - I_L \right) - \dot{V}_{pv}^* \quad (12)$$

Selecting the Lyapunov function as

$$V_1 = \frac{1}{2} e_1^2 \quad (13)$$

Taking the first derivate of the function

$$\dot{V}_1 = e_1 \dot{e}_1 = e_1 * \left(\frac{1}{C_{pv}}\left(I_{pv} - I_L \right) - \dot{V}_{pv}^* \right) \quad (14)$$

For the existence of the controller, we know that first derivate of the Lyapunov function should be negative, so choosing $\dot{e}_1 = -d_1 e_1$ and this would make

$$\dot{V}_1 = -d_1 e_1^2 \leq 0 \quad (15)$$

Where d_1 is a positive constant that can be regarded as a design parameter of the controller,
now,

$$\dot{V}_{pv} = \frac{dV_{pv}}{dt} = \frac{1}{C_{pv}}\left(I_{pv} - I_L \right) \quad (16)$$

$$C_{pv} \dot{V}_{pv} = I_{pv} - I_L$$

$$I_L = I_{pv} - C_{pv} \dot{V}_{pv}$$

$$I_L = I_{pv} - C_{pv}\left(\dot{e}_1 + \dot{V}_{pv}^* \right)$$

$$= I_{pv} + C_{pv}\left(d_1 e_1 - \dot{V}_{pv}^* \right)$$

This will be regarded as the stabilization function α, so

$$\alpha = I_{pv} + C_{pv}\left(d_1 e_1 - \dot{V}_{pv}^* \right) \quad (17)$$

The function value will be used as a reference value for the next tracking error convergence, which is defined as

Authorized licensed use limited to: DELHI TECHNICAL UNIV. Downloaded on June 14,2023 at 05:08:47 UTC from IEEE Xplore. Restrictions apply.

$$e_2 = I_L - \alpha \tag{18}$$

Taking the first derivate of the new tracking error

$$\dot{e}_2 = \dot{I}_L - \dot{\alpha} \tag{19}$$

$$\dot{e}_2 = \frac{V_{pv}}{L} - (1-D)\frac{V_o}{L} - \dot{\alpha}$$

Choosing the new Lyapunov function as

$$V_2 = V_1 + \frac{1}{2}e_2^2 \tag{20}$$

Taking the first derivate of the new Lyapunov function

$$\dot{V}_2 = \dot{V}_1 + e_2\dot{e}_2$$

$$\dot{V}_2 = e_1\dot{e}_1 + e_2\dot{e}_2$$

$$\dot{V}_2 = e_1\left(-\frac{e_2}{C_{pv}} - d_1e_1\right) + e_2\left(\frac{V_{pv}}{L} - (1-D)\frac{V_o}{D} - \dot{\alpha}\right)$$

After rearranging we get

$$\dot{V}_2 = -d_1e_1^2 + e_2\left(-\frac{1}{C_{pv}}e_1 + \frac{V_{pv}}{L} - (1-D)\frac{V_o}{L} - \dot{\alpha}\right) \tag{21}$$

Now for the existence of the controller the condition $\dot{V}_2 \leq 0$ should be satisfied, so let

$$\left(-\frac{1}{C_{pv}}e_1 + \frac{V_{pv}}{L} - (1-D)\frac{V_o}{L} - \dot{\alpha}\right) = -d_2e_2 \tag{22}$$

Where $d_2 > 0$, is a positive constant that can be regarded as a design parameter. This makes,

$$\dot{V}_2 = -d_1e_1^2 - d_2e_2^2 \leq 0 \tag{23}$$

C. Control Law Buildup

We know that from the new Lyapunov's function

$$\left(-\frac{1}{C_{pv}}e_1 + \frac{V_{pv}}{L} - (1-D)\frac{V_o}{L} - \dot{\alpha}\right) = -d_2e_2$$

Rearranging the above equation and obtaining the duty cycle expression as

$$D = 1 - \frac{1}{v_o}\left[V_{pv} - L\dot{\alpha} - L\left(\frac{1}{C_{PV}}e_1 - d_2e_2\right)\right] \tag{24}$$

This is the required control law, i.e., updating the duty cycle ratio according to the Lyapunov function to attain tracking error convergence to zero and system asymptotic stability. This duty cycle is then fed into a PWM generator, which generates PWM pulses for MOSFETs.

IV. Controller Design for the Bidirectional Converter and BESS

In the second stage of charging a battery pack, the quantities to be controlled are current (I_{bat}) and DC-link voltage (V_{DC}). Two PI regulators are used to design this control. The DC link voltage in the outer loop is equated with the desired reference value and regulated by the PI controller[13], [14]. This PI controller generates a battery current reference, which is enforced in the inner control loop. The PWM technique is now utilized by this integral control controller to generate the duty cycle and pulses.

$$i_{bat}^* = \left(K_{p1} + \frac{K_{i1}}{S}\right) * \left(V_{DV}^* - V_{DV}\right) \tag{25}$$

$$d_{DC-DC} = \left(K_{p2} + \frac{K_{i2}}{S}\right) * \left(i_{bat}^* - i_{bat}\right) \tag{26}$$

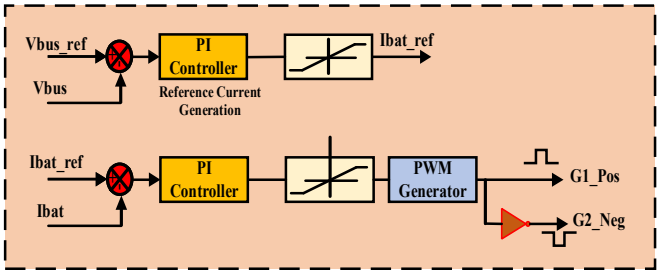

Fig. 6 DC-DC Bidirectional converter controller

TABLE II. BI-DIRECTIONAL CONVERTER PARAMETER SPECIFICATION

Parameters	***Value***
V_{DC} (Bus Voltage)	96 V
C (PV side) / (Grid side)	1200 μF / 18 μF
L	3 mH
Switching Frequency	10 KHz

V. Battery Sizing for Proposed System

Here the isolated DC microgrid is designed for charging Hero electric photon LP series bike and we have considered the BESS specification for the same given in Table III. The load which we have considered is purely a fixed DC load of 500 watts. The main moto to consider these specifications is the nominal voltage of the lithium-ion battery for the said bike is high as compared to the other. Hence, the size of the inductor reduces which will also reduce the ripple currents in both the input and output of the circuits. Substantially, reducing the I^2R losses.

TABLE III. BATTERY PARAMETER SPECIFICATION

Parameters	***Value***
Battery Voltage	72V
Battery Capacity	30Ah
Full Charge	5 Hrs.

C-rate of the battery = $\frac{30Ah}{6A} = 5 = C/5$

This implies the battery can supply 6 A of continuous current for 5 hours.

Authorized licensed use limited to: DELHI TECHNICAL UNIV. Downloaded on June 14,2023 at 05:08:47 UTC from IEEE Xplore. Restrictions apply.

VI. Results and Discussion

The estimated solar insolation characteristics obtained on an average summer day have been plotted in Fig. (7). Beneath the simulation time of 10 seconds, the graph illustrates the fluctuation in solar insolation throughout the day, i.e., low insolation in the evening and early in the morning and increasing signal strength at midday. During times of no irradiance and low solar intensity, the battery meets the overall load demand. As a result, battery power is optimistic. The battery power supply (charges) during the day using excess capacity generated by the solar panels. Fig. (8) displays the peculiarities of the DC bus voltage. For continually fluctuating irradiance conditions, the DC microgrid maintains a constant bus voltage of 96 V with slight oscillations at critical locations. From the Fig. (8) it clearly shows that when irradiance changes at time 2 seconds there is only 0.02 volts of ripple and at time 6 seconds when irradiance changes abruptly from 700 w/m^2 to 500 W/m^2 then also the ripple voltage upholds at 0.02 volts only.

Hence, the DC bus voltage has been kept beneath the negligible range, exhibiting the efficacy of the bidirectional DC-DC converter's control strategy. In Fig. (9) the plot of battery voltage is given and in Fig. (10) the plot of the battery current variations is given which shows the charging and discharging characteristics of the battery. In the first 2 seconds battery is discharging because irradiance is zero hence, the power is supplied by the battery to the load and during high insolation hours i.e., from 2 to 6 seconds battery is charging as well as power is supplied to the load by the solar panel. From the battery current plot, it can be seen that the battery ripple current is only 0.04 A which validates the efficacy of the system[15].

The proposed technique makes it possible for the battery pack current to closely monitor the reference battery current. Fig. (11) presents the BESS state of charge graph. When the PV array emits excess power during period of low power demand, the battery charges. Discharge occurs when there is low insolation in a given area or when the resulting solar power output is less than the peak load.

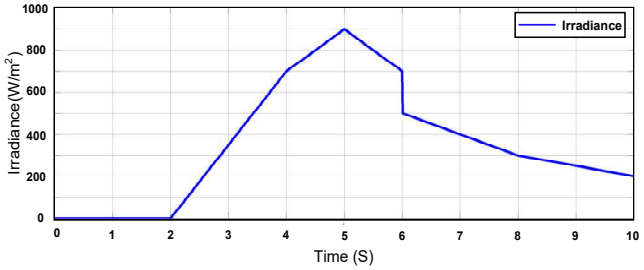

Fig. 7 Irradiance curve

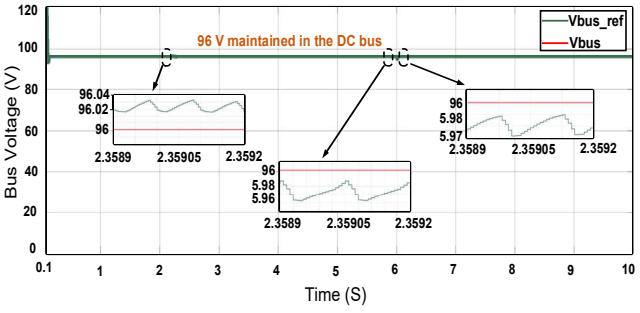

Fig. 8 Simulation result of bus voltage

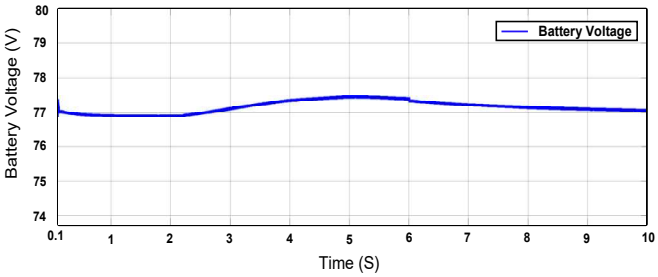

Fig. 9 Simulation result of battery voltage

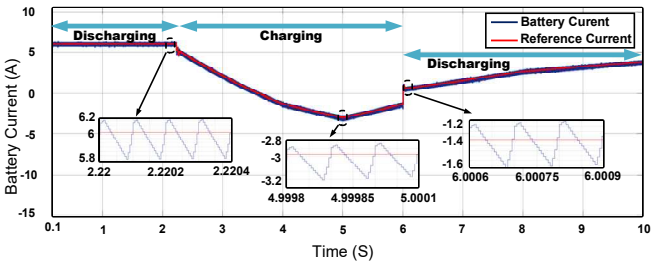

Fig. 10 Simulation result of battery current

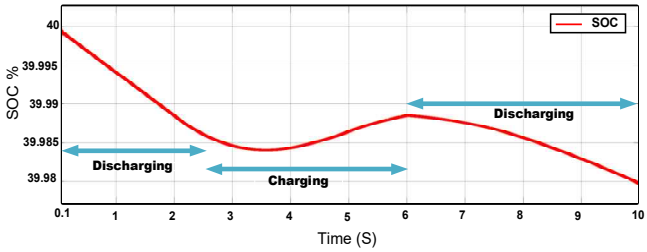

Fig. 11 State of charge of battery

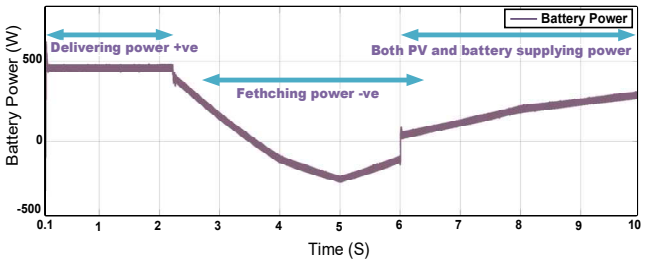

Fig. 12 Simulation result of battery power

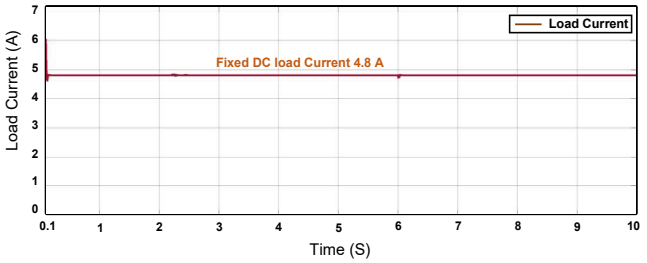

Fig. 13 Simulation result of load current

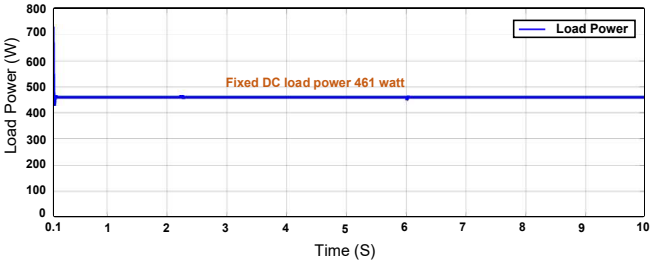

Fig. 14 Simulation result of load power

In Fig. (12) the characteristics of battery power is presented, during low insolation battery is supplying power to the load hence, it is positive and during high insolation

Authorized licensed use limited to: DELHI TECHNICAL UNIV. Downloaded on June 14,2023 at 05:08:47 UTC from IEEE Xplore. Restrictions apply.

battery is fetching power hence, it is negative. And during evening battery power is continuously decreasing as it is tracking irradiance, as the irradiance decreases the battery power starts transition from fetching to supplying power to load and hence, maintains the constant power to the load as shown in Fig. (14). Although there are lots of fluctuations in solar insolation but our converter, controller design maintains the constant power to the load with minimal power losses. Hence, it validates the efficacy of the system.

VII. Conclusion

A nonlinear adaptive backstepping controller is designed to track optimum solar power in a PV system, whereas a PI controller is designed for BESS to sustain overall power stability within a DC microgrid. Closed loop functions are employed to assess overall system stability in MATLAB/Simulink. The main consideration in this paper is to keep the DC bus voltage beneath the marginal range with reduced voltage ripple and with reduced battery current ripple so, that the I^2R loss minimises towards the battery side, as it can be seen from the Fig. (8,10) that DC bus ripple voltage is only 0.02 V and battery current ripple is only 0.04 A which validates the efficacy of the system.

Acknowledgment

This research supported by the Science and Engineering Research Board (SERB), Department of Science & Technology, Government of India,. under the SERB sanction order number SRG/2021/001640.

References

[1] T. K. Roy, M. A. Mahmud, A. M. T. Oo, M. E. Haque, K. M. Muttaqi, and N. Mendis, "Nonlinear adaptive backstepping controller design for controlling bidirectional power flow of BESSs in DC microgrids," *IEEE Ind. Appl. Soc. 52nd Annu. Meet. IAS 2016*, pp. 1–8, 2016, doi: 10.1109/IAS.2016.7731875.

[2] S. B. Kjær, "Evaluation of the hill climbing and the incremental conductance maximum power point trackers for photovoltaic power systems," *IEEE Trans. Energy Convers.*, vol. 27, no. 4, pp. 922–929, 2012, doi: 10.1109/TEC.2012.2218816.

[3] N. Kumar and A. Sharma, "Design and Analysis of Nonlinear Controller for a Standalone Photovoltaic System Using Lyapunov Stability Theory," *J. Sol. Energy Eng.*, vol. 144, no. 1, pp. 1–13, 2022, doi: 10.1115/1.4051584.

[4] A. Sharma and N. Kumar, "Lyapunov Stability Theory based Non Linear Controller Design for a Standalone PV System," *2020 IEEE Int. Conf. Innov. Technol. INOCON 2020*, pp. 1–7, 2020, doi: 10.1109/INOCON50539.2020.9298285.

[5] M. Nasir, H. A. Khan, A. Hussain, L. Mateen, and N. A. Zaffar, "Solar PV-based scalable DC microgrid for rural electrification in developing regions," *IEEE Trans. Sustain. Energy*, vol. 9, no. 1, pp. 390–399, 2018, doi: 10.1109/TSTE.2017.2736160.

[6] S. Kumar Tiwari, B. Singh, and P. K. Goel, "Design and Control of Microgrid Fed by Renewable Energy Generating Sources," *IEEE Trans. Ind. Appl.*, vol. 54, no. 3, pp. 2041–2050, 2018, doi: 10.1109/TIA.2018.2793213.

[7] B. Liu, F. Zhuo, Y. Zhu, and H. Yi, "System Operation and Energy Management of a Renewable Energy-Based DC Micro-Grid for High Penetration Depth Application," *IEEE Trans. Smart Grid*, vol. 6, no. 3, pp. 1147–1155, 2015, doi: 10.1109/TSG.2014.2374163.

[8] M. Kumar, "Solar PV Based DC Microgrid under Partial Shading Condition with Battery-Part 1: Maximum Power Generation," 2018 8th IEEE India International Conference on Power Electronics (IICPE), Jaipur, India, 2018, pp. 1-6, doi: 10.1109/IICPE.2018.8709505.

[9] M. Kumar, "Solar PV Based DC Microgrid under Partial Shading Condition with Battery-Part 2: Energy Management System," *India Int. Conf. Power Electron. IICPE*, vol. 2018-Decem, no. 1, 2018, doi: 10.1109/IICPE.2018.8709437.

[10] R. V. John, R. Gautam, and M. Kumar, "Power Flow Management and BESS Design Consideration for Solar PV fed Isolated DC Microgrid for Residential Applications," *2022 IEEE Delhi Sect. Conf. DELCON 2022*, 2022, doi: 10.1109/DELCON54057.2022.9753360.

[11] Naghmash, H. Armghan, I. Ahmad, A. Armghan, S. Khan, and M. Arsalan, "Backstepping based non-linear control for maximum power point tracking in photovoltaic system," *Sol. Energy*, vol. 159, no. October 2017, pp. 134–141, 2018, doi: 10.1016/j.solener.2017.10.062.

[12] A. Zaidi, K. Dahech, and T. Damak, "Maximum power point tracking of photovoltaic systems based on fast terminal sliding mode controller," *Int. J. Renew. Energy Res.*, vol. 6, no. 4, pp. 1435–1445, 2016.

[13] A. K. Seth and M. Singh, "Control of Two-Stage OFF-Board Electric Vehicle Charger," *ICPEE 2021 - 2021 1st Int. Conf. Power Electron. Energy*, pp. 4–9, 2021, doi: 10.1109/ICPEE50452.2021.9358732.

[14] J. J. Justo, F. Mwasilu, J. Lee, and J. W. Jung, "AC-microgrids versus DC-microgrids with distributed energy resources: A review," *Renew. Sustain. Energy Rev.*, vol. 24, pp. 387–405, 2013, doi: 10.1016/j.rser.2013.03.067.

[15] M. J. Brand, M. H. Hofmann, S. S. Schuster, P. Keil, and A. Jossen, "The Influence of Current Ripples on the Lifetime of Lithium-Ion Batteries," *IEEE Trans. Veh. Technol.*, vol. 67, no. 11, pp. 10438–10445, 2018, doi: 10.1109/TVT.2018.2869982.

Authorized licensed use limited to: DELHI TECHNICAL UNIV. Downloaded on June 14,2023 at 05:08:47 UTC from IEEE Xplore. Restrictions apply.

e-ISSN: 2582-5208
International Research Journal of Modernization in Engineering Technology and Science
(Peer-Reviewed, Open Access, Fully Refereed International Journal)
Volume:05/Issue:05/May-2023 Impact Factor- 7.868 www.irjmets.com

DESIGN AND STRUCTURAL ANALAYSIS OF KNUCKLE JOINT

Manish Kumar[*1], Kartik Bansal[*2], Lalit Mohan Sharma[*3], Neeraj kant[*4]
Pushpendra Singh[*5]

[*1,2,3]Student, Department of Mechanical Engineering, Delhi Technological University, New Delhi, India
[*4]Research Scholar, Department of Mechanical Engineering, Delhi Technological University, New Delhi, India
[*5]Associate Professor, Department of Mechanical Engineering, Delhi Technological University, New Delhi, India
DOI : https://www.doi.org/10.56726/IRJMETS40143

ABSTRACT

A knuckle joint is a mechanical component utilized for joining two rods subjected to tension. It may also permit a small angular misalignment of the rods. The knuckle joint finds application in various scenarios such as connecting tie rods, tension links in bridge structures, cycle chain links, and in the steering system where it connects the steering rod and pinion of the steering gear. In knuckle joint, there are two rods where an eye is formed at the end of one rod and a fork is formed at the end of another rod. The eye fits inside a fork and a pin pass through the fork and the eye. The pin in question is held securely in position through the use of a split pin. The knuckle joint is alternatively referred to as a forked pin joint. There is possibility of accident on failure of knuckle joint. So, proper modelling and analysis is a must to avoid failure. A designer must know forces and stresses that is developed during its operations so that safer design can be modelled. The main aim of the project is to select a proper material and design a knuckle joint under 30KN load and carry out structural analysis in ANSYS Workbench.

Keywords: knuckle joint , Structural analysis ,Solid modelling, Failure Analysis, FEM, ANSYS Workbench

I. INTRODUCTION

A knuckle joint serves the purpose of connecting two rods that are positioned on the same plane, with their axes intersecting or coinciding. Its primary function is to enable limited movement along the pin axis while effectively transmitting forces. This mechanical joint is specifically designed to join two components under loads, allowing for a certain degree of flexibility in movement. Various applications of knuckle joints include roof truss rod joints, roller chain links, and more. The knuckle joint itself comprises five essential components: a knuckle pin, an eye end, a fork end, a collar, and a taper pin. Knuckle joints play a crucial role in various mechanical systems, providing flexibility and allowing rotational movement between two or more components. Knuckle joints hold considerable importance within the realm of mechanical engineering, as they are subject to extensive scrutiny in terms of their design and structural analysis. Engineers and researchers are constantly exploring innovative approaches to optimize the design, improve performance, and ensure the structural integrity of knuckle joints.

Smith, Johnson, and Anderson (2018) conducted a study on the design and analysis of a heavy-duty automotive knuckle joint. They proposed a design approach that considered the joint's load-bearing capacity, fatigue life, and manufacturability. Through the use of finite element analysis (FEA) and experimental validation, they were able to optimize the design parameters of the knuckle joint, leading to improved performance and durability.

Brown, Davis, and Wilson (2016) utilized FEA to investigate the behavior of a knuckle joint under different materials. Their study focused on evaluating the stress distribution, deformation, and fatigue life of the joint using various material options. The findings highlighted the influence of material selection on the joint's strength and performance, providing insights for material optimization in knuckle joint design.

This overview will provide a general understanding of the subject area by presenting the current research and advancements in the design and structural analysis of knuckle joints.

II. METHODOLOGY

SELECTION OF MATERIAL

Knuckle joint is a part which experiences maximum stress. The material selection depends upon the fact that it could withstand the stresses develop in the joint and could deform elastically during its operation. Since knuckle joints are subjected to tensile force, a high tensile strength material is needed. On yield strength basis, stainless steel (Syt=207Mpa, Syc=207Mpa and Sut=586Mpa) is selected for knuckle joint, we have also done our analysis

e-ISSN: 2582-5208
International Research Journal of Modernization in Engineering Technology and Science
(Peer-Reviewed, Open Access, Fully Refereed International Journal)
Volume:05/Issue:05/May-2023 Impact Factor- 7.868 www.irjmets.com

using other material like (STAINLESS STEEL,316,ANNEALED), (STRUCTURAL STEEL,316,Annealed), (Gray Cast Iron,EN GJL 100), (Aluminum Alloy , Wrought,6061,T6) And (Titanium Alloy,Ti-4v,Annealed). For the analysis, we have taken compressive strength equal to tensile strength but in practice the compressive strength is usually higher than tensile strength.

SELECTION OF FACTOR OF SAFETY

The failure of knuckle joint can cause serious accidents. So, a higher FOS=5 is assumed. The FOS of 5 also accounts for stress concentration effects since it is neglected in the stress analysis.

MODES OF FAILURES OF KNUCKLE JOINTS

There are different ways in which a knuckle joint can fail such as:

- Failure of rod end by tension: Excessive tensile stress can cause a rod end to fail by fracturing, thread stripping, or ball separation.
- Failure of rod end by double shear: Excessive double shear forces can cause a rod end to fail.
- Failure of rod end by crushing: Excessive compressive forces can cause a rod end to fail by crushing.
- Failure of forked ends by tension: Excessive tension can lead to the failure of forked ends.
- Failure of forked ends by double shear: Excessive double shear forces can cause forked ends to fail.
- Failure of forked ends by crushing: Excessive compressive forces can cause forked ends to fail by crushing.
- Failure of knuckle pin by tension: Excessive tension can cause a knuckle pin to fail.
- Failure of knuckle pin by double shear: Fracture can occur in a knuckle pin due to excessive double shear forces.
- Failure of knuckle pin by bending: Bending can cause failure in a knuckle pin.

CALCULATIONOFDIMENSIONS:

The yield point and shear point are calculated below

$$\sigma_{xp} = \frac{s_{yt}}{f_{os}} = \frac{207}{5} = 41.4\text{Mpa}$$

$$\sigma_{yc} = \frac{s_{yt}}{f_{os}} = \frac{207}{5} = 41.4\text{Mpa}$$

$$\tau_{sp} = \frac{0.5s_{yt}}{f_{os}} = \frac{0.5 * 207}{5} = 20.7\text{Mpa}$$

Diameter of rods

P=30KN

$$D = \sqrt{\frac{4P}{\pi\sigma_t}}$$

=30.88mm

=32mm (Standard Rod Size Design Data Book)

Enlarged Diameter of Rods

D1=1.1 D=35.2=36mm

Dimensions of a & b

a=0.75*D=24mm

b=1.25*D=40mm

Diameter of Pin

By Shear Consideration

$$d_s = \sqrt{\frac{2P}{\pi\tau}}$$

$d_s = 30.38mm$=32mm

By Bending Consideration

e-ISSN: 2582-5208
International Research Journal of Modernization in Engineering Technology and Science
(Peer-Reviewed, Open Access, Fully Refereed International Journal)
Volume:05/Issue:05/May-2023 Impact Factor- 7.868 www.irjmets.com

$$d_b = \sqrt[3]{\frac{32}{\pi\sigma_b} * \frac{P}{2}[\frac{b}{4} + \frac{a}{3}]}$$

$d_b = 40.50mm = 42mm$

The maximum value of diameter of pin is d=42mm.

Dimension of d_0& d_1

d_0=2*d=42=84mm

d_1=1.5*d=63mm

Checking for tensile, crushing and shear stresses in the eye

$$\sigma_t = \frac{P}{b(d_0 - \mathrm{d})}$$

$$\sigma_t = \frac{30 * 1000}{40 * (84 - 42)}$$

=17.85Mpa<41.4Mpa

$$\sigma_c = \frac{\mathrm{P}}{\mathrm{bd}}$$

$$= \frac{30 * 1000}{40 * 42}$$

=17.85Mpa<41.4Mpa

$$\tau = \frac{P}{b(d_0 - \mathrm{d})}$$

$$= \frac{30 * 1000}{40 * (84 - 42)}$$

=17.85Mpa<20.7Mpa

Checking for tensile, crushing and shear stresses in the fork

$$\sigma_t = \frac{P}{2a(d_0 - \mathrm{d})}$$

$$= \frac{30 * 1000}{2 * 24 * (84 - 42)} = 14.9Mpa$$

$$\sigma_c = \frac{P}{2ad}$$

$$= \frac{30 * 1000}{2 * 24 * 42} = 14.9Mpa < 41.4Mpa$$

$$\tau = \frac{P}{2a(d_0 - \mathrm{d})}$$

$$= \frac{30 * 1000}{2 * 24 * (84 - 42)} = 14.9Mpa < 20.7Mpa$$

Since, tensile, compressive and shear stresses in the fork and eye is less than corresponding permissible stresses, the design is safe.

III. MODELING AND ANALYSIS

The modeling and analysis of a knuckle joint involve examining its structural behavior and performance under various loads and operating conditions. In this paper we have designed knuckle joint under 30KN applied force using solidworks and later done a FEM analysis using Ansys Workbench.

e-ISSN: 2582-5208
International Research Journal of Modernization in Engineering Technology and Science
(Peer-Reviewed, Open Access, Fully Refereed International Journal)
Volume:05/Issue:05/May-2023 Impact Factor- 7.868 www.irjmets.com

CAD MODEL

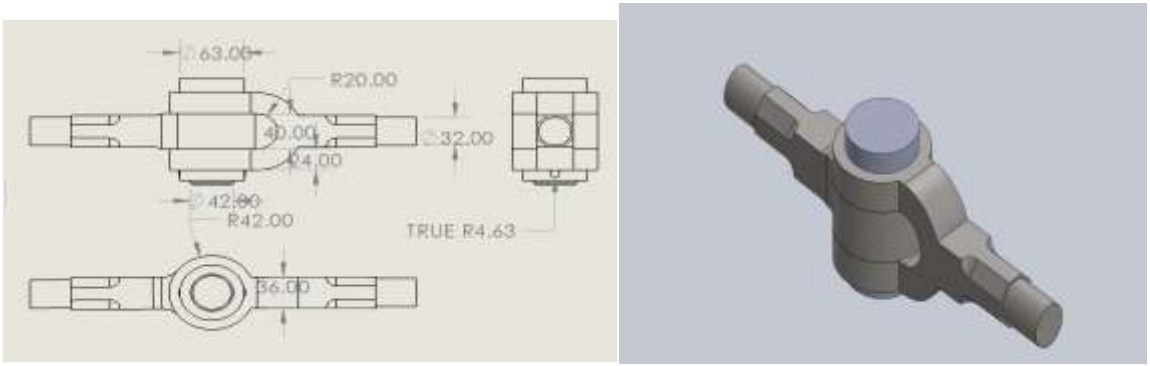

Figure 1: cad model of knuckle joint.

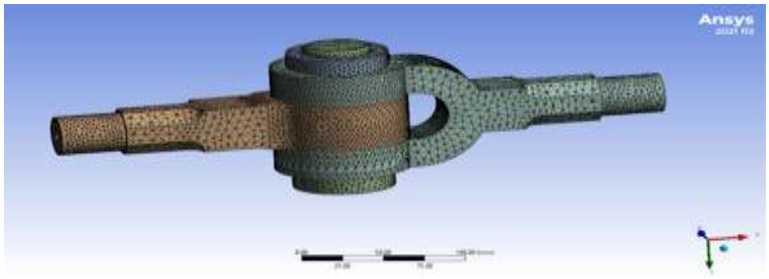

Figure 2: Mesh.

BOUNDARY CONDITIONS

Fixed Support is applied in fork end and Force of P=30KN is applied on one end while the other end was fixed

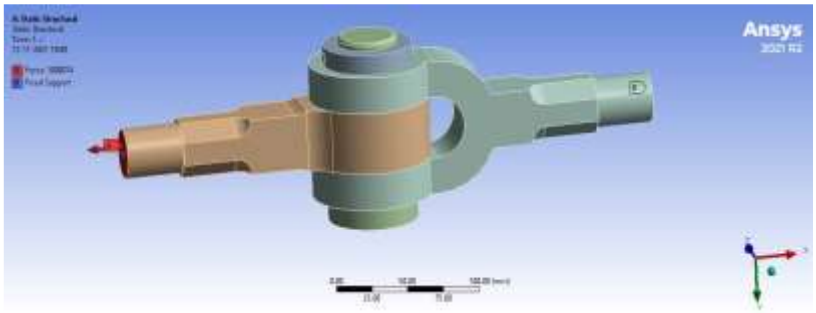

Figure 3: boundary conditions.

IV. RESULTS AND DISCUSSION

Maximum , minimum and average total deformation , equivalent stress, maximum principal stress and maximum shear stress are calculated below

MATERIAL: STAINLESS STEEL,316, ANNEALED(Tensile Yield Strength **(**Syt)=252.1 Mpa, Compressive Yield Strength(Syc)=252.1 MPa, Compressive Ultimate Strength MPa (Sut)=565.1 MPa**)**

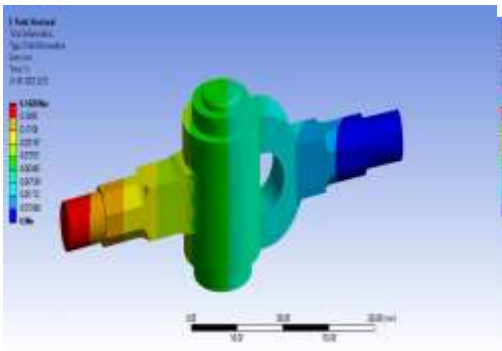

Figure 4: TOTAL DEFORMATION

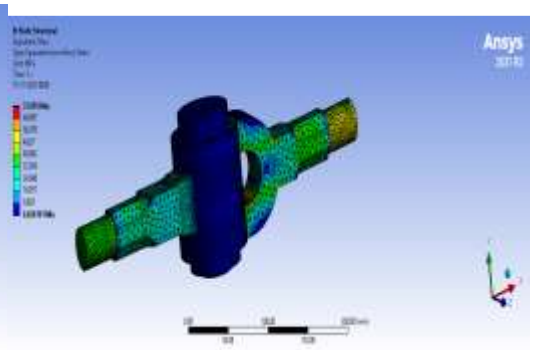

Figure 5: EQUIVALENT STRESS

e-ISSN: 2582-5208
International Research Journal of Modernization in Engineering Technology and Science
(Peer-Reviewed, Open Access, Fully Refereed International Journal)
Volume:05/Issue:05/May-2023 Impact Factor- 7.868 www.irjmets.com

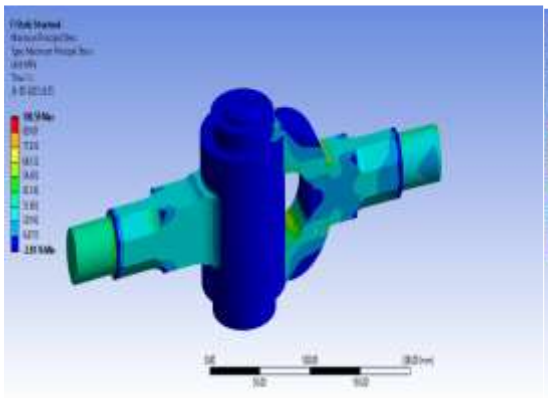

Figure 6: MAXIMUM PRINCIPAL STRESS

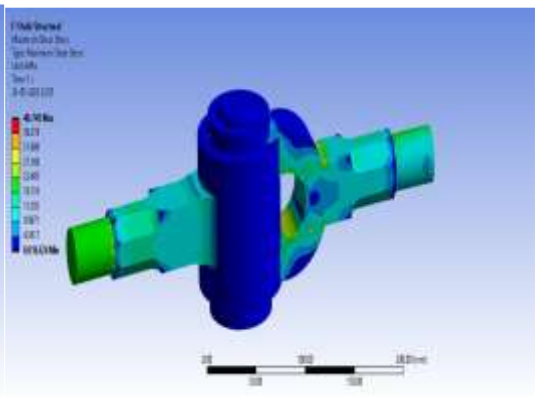

Figure 7: MAXIMUM SHEAR STRESS

ANSYS software has a unique module which can measure the amount of deformation i.e., change in length of the joints. Fig. A typical diagram illustrating the deformation in each component of the knuckle joint is shown. It should be noted that the highest level of deformation is observed at the extremities of the joint, while the least elongation is observed around the pin section. These findings indicate that the greatest elongation occurs at the two ends of the joint is 0.14966mm. Other parameters like equivalent stress, maximum principal stress and maximum shear stress are also found which is 72.095MPa, 103.2MPa and 38.655 MPa respectively which is also mentioned in a tabular form.

s. no.		minimum	maximum	average
1.	TOTAL DEFORMATION	0 mm	0.14928 mm	6.4667e-002 mm
2.	EQUIVALENT STRESS (VON-MISSES)	1.6355e-002 MPa	72.331 MPa	11.625 MPa
3.	IMUM PRINCIPAL STRESS	- 2.8176 MPa	100.59 MPa	11.014 MPa
4.	MAXIMUM SHEAR STRESS	1.6324e-002 MPa	40.745 MPa	6.2155 MPa

Similar results were also found with different materials and the same is depicted in a tabular form and given below:

MATERIAL: STRUCTURAL STEEL,316,annealed(Syt=250MPa, Syc=250MPa, Sut=460MPa)

s. no.		minimum	maximum	average
1.	TOTAL DEFORMATION	0 mm	0.14454 mm	6.5612e-002 mm
2.	EQUIVALENT STRESS (VON-MISSES)	2.0161e-002 MPa	72.095 MPa	11.622 MPa
3.	IMUM PRINCIPAL STRESS	-4.2065 MPa	103.2 MPa	10.747 MPa
4.	MAXIMUM SHEAR STRESS	1.1183e-002 MPa	38.655 MPa	6.0639 MPa

MATERIAL: Titanium Alloy,Ti-4v,annealed (Syt=930MPa, Syc=930MPa, Sut=1070MPa)

s. no.		minimum	maximum	average
1.	TOTAL DEFORMATION	0 mm	0.2871 mm	0.13002 mm
2.	EQUIVALENT STRESS (VON-MISSES)	2.0443e-002 MPa	76.341 MPa	11.942 MPa
3.	IMUM PRINCIPAL STRESS	-4.32 MPa	110.59 MPa	11.042 MPa
4.	MAXIMUM SHEAR STRESS	1.678e-002 MPa	40.659 MPa	6.2479 MPa

e-ISSN: 2582-5208
International Research Journal of Modernization in Engineering Technology and Science
(Peer-Reviewed, Open Access, Fully Refereed International Journal)
Volume:05/Issue:05/May-2023 Impact Factor- 7.868 www.irjmets.com

MATERIAL: Gray Cast Iron,EN GJL 100 (Syt=820MPa,Suc=820MPa, Sut=240MPa)

s. no.		minimum	maximum	average
1.	TOTAL DEFORMATION	0 mm	0.25299 mm	0.11453 mm
2.	EQUIVALENT STRESS (VON-MISSES)	2.1032e-002 MPa	79.251 MPa	11.919 MPa
3.	MAXIMUM PRINCIPAL STRESS	-2.9534 MPa	100.74 MPa	11.017 MPa
4.	MAXIMUM SHEAR STRESS	1.0936e-002 MPa	40.742 MPa	6.2185 MPa

MATERIAL: Aluminum Alloy , wrought,6061,T6 (Syt=280MPa, Syc=280MPa, Sut=310MPa)

s. no.		minimum	maximum	average
1.	TOTAL DEFORMATION	0 mm	0.39047 mm	0.1765 mm
2.	EQUIVALENT STRESS (VON-MISSES)	2.0443e-002 MPa	77.437 MPa	11.932 MPa
3.	IMUM PRINCIPAL STRESS	-3.7375 MPa	103.3 MPa	11.032 MPa
4.	MAXIMUM SHEAR STRESS	1.0509e-002 MPa	40.71 MPa	6.2357 MPa

Final results with all the materials used are given below in a tabular form for better comparison

		STAINLESS STEEL,316 ,ANNEALED	STRUCTURAL STEEL,316,Annealed	Titanium Alloy,Ti-4v,Annealed	Gray Cast Iron,EN GJL 100	Aluminum Alloy , Wrought,6061,T6
1.	TOTAL DEFORMATION(MAX)	0.14928 mm	0.14454 mm	0.2871 mm	0.25299 mm	0.39047mm
2.	EQUIVALENT STRESS (VON-MISSES) (MAX)	72.331 MPa	72.095 MPa	76.341 Mpa	79.251 Mpa	77.437 Mpa
3.	MAXIMUM PRINCIPAL STRESS(MAX)	100.59 MPa	103.2 MPa	110.59 Mpa	100.74 Mpa	103.3 Mpa
4.	MAXIMUM SHEAR STRESS(MAX)	40.75 MPa	38.655 MPa	40.659 Mpa	40.659 Mpa	40.71 Mpa

V. CONCLUSION

The proposed knuckle joint in this study is designed to handle an applied force of 30 KN, with a pin diameter of approximately 42mm. According to the ANSYS FEM analysis, it is determined that a 42mm pin diameter can support a load of 30KN for all materials tested. The maximum operating stress for each material was identified, and the designs were developed accordingly, stainless steel (Syt=207Mpa, Syc=207Mpa and Sut=586Mpa) is selected for knuckle joint, we have also done our analysis using other material like (STAINLESS STEEL,316, ANNEALED), (STRUCTURAL STEEL,316, Annealed), (Gray Cast Iron,EN GJL 100), (Aluminium Alloy , Wrought,6061,T6) And (Titanium Alloy,Ti-4v,Annealed). are all suitable materialsThe findings indicate that the aluminum alloys have a lower weight compared to others. materials but the total deformation in aluminum alloy is slightly higher . The max stress induced in the knuckle joint as tabulated above are much below than the material's tensile and shear stress under a load of 30KN hence, the design is safe. So, any of the materials can be used for the knuckle joint as per the cost, availability and weight requirement. The results show that the aluminum alloys weigh lighter than other materials but the total deformation in aluminum alloy is slightly higher while gray cast iron and stainless steel are the affordable options.

VI. REFERENCES

[1] A Yashodha Rao, B. Krishnajayanth , "Structural Analysis of Knuckle Joint with Different Materials", International Journal & Magazine of Engineering, Technology, Management and Research(ijmetmr), Volume No 5 , Issue: 7,July 2018, ISSN No: 2348-4845

[2] Ms. Nilesha Patil, Mrs. Sayli M.Sable, Mr. Kashinath Munde, "STATIC STRUCTURAL ANALYSIS OF KNUCKLE JOINT", International Conference on Recent Trends In Engineering, Science & Management(ICRTESM), Issue: 9th-10th December 2016, ISBN: 978-93-86171-12-2

[3] Sangamesh B. Herakal, Dr.S.Chakradhar Goud, Ranganath Avadhani "Structural Static Analysis Of Knuckle Joint", International Journal of Engineering Research and General Science Volume 4, Issue 2, March-April, 2016, ISSN 2091-2730

[4] Purushottam Dumbre, Prof A.K.Mishra, V.S.Aher, Swapnil S. Kulkarni, "STRUCTURAL ANALYSIS OF STEERING KNUCKLE FOR WEIGHT REDUCTION", International Journal of Advanced Engineering Research and Studies E-ISSN2249–8974.

[5] Mahesh P. Sharma, Denish S. Mevawala, Harsh Joshi, Devendra A. Patel, "Static analysis of steering knuckle and its shape optimization", IOSR Journal of Mechanical and Civil Engineering (IOSR-JMCE) eISSN: 2278-1684, p-ISSN: 2320-334X.

[6] Shaik.John Bhasha, Hari Sankar Vanka, Modelling and Analysis of Knuckle Joint, International Journal & Magazine of Engineering, Technology, Management and Research, ISSN No: 2348-4845

[7] Sourav Das1, Vishvendra Bartaria, Prashant Pandey, Analysis of Knuckle Joint of 30C8 Steel for Automobile Application, International Journal of Engineering Research & Technology (IJERT),Vol. 3 Issue 1, January – 2014 IJERTIJERT ISSN: 2278-0181

[8] Pankaj Dulani, S. A. K. Jilani, Diameter and Spiral Thickness Optimization of Knuckle Joint Using Neural Network, International Journal of Science and Research (IJSR) ISSN (Online): 2319-7064

[9] AMEYA BHUSARI, ADITYA CHAVAN, SUSHRUT, "FEA &OPTIMISATION OF STEERING KNUCKLE OF ATV", Proceedings of 54th IRF International Conference, 8th May, 2016, India,ISBN: 978-93-86083-10-4

[10] Gondi PrabhuCharan Teja, K.V.P.P.Chandu, Ch. Rama Krishna, K. Yasoda Sreeram, "WEIGHT OPTIMIZATION OF STEERING KNUCKLE JOINT USING FEA", International Research Journal of Engineering and Technology (IRJET) e-ISSN: 2395 - 0056

ResearchGate

See discussions, stats, and author profiles for this publication at: https://www.researchgate.net/publication/371680764

Design Optimisation and Static Analysis of Non-Pneumatic Tyres

Conference Paper · June 2023

CITATIONS
0

READS
29

4 authors, including:

Farzan Shahid
Delhi Technological University
1 PUBLICATION **0** CITATIONS

SEE PROFILE

All content following this page was uploaded by Farzan Shahid on 18 June 2023.

The user has requested enhancement of the downloaded file.

Design Optimisation and Static Analysis of Non-Pneumatic Tyres

Divya Balchandani[1], Shalini Nawariya[1], Farzan Shahid[1], A.K Madan[2]

[1]Student, BTech, Mechanical Engineering, Delhi Technological University
[2]Professor, Department of Mechanical Engineering, Delhi Technological University

---

Abstract -*Transportation is regarded as one of the most important development factors for any country because it maximizes mobility for individuals and moves loads for the industry. Tires play an important role in ensuring end-to-end connectivity. Tires and their structures have evolved to meet the needs and applications of the time. Many changes have been made to solve problems that, if resolved, may improve the performance of tyres. We are attempting to solve the problem of tyre punctures in this paper. The solution is airless tyres, or non-pneumatic tyres (NPT), which do not support the concept of compressed air.*

This paper presents four distinct spoke structures of a Non-Pneumatic Tire model. The structure and material investigation of airless tyres is carried out by contrasting them with pneumatic tyres. A thorough structural analysis of several airless tyres spoke geometries has been done, and these spokes have then been further analyzed for important parameters like total deformation, stress, and strain. Solidworks was used for the 3D modeling of these various designs, while Ansys Software handled the in-depth analysis.

***Key Words*: Non-pneumatic tyre, Honeycomb spokes, Triangular spokes, Curvy spokes, Diamond Spokes, Ansys.**

1. INTRODUCTION

An airless tyre's basic construction is similar to that of a pneumatic tyre. They all have an internal core that contains pressurized air, which is subsequently wrapped with a layer of rubber called a tread that comes in direct contact with the ground. The tread aids in maintaining road traction and guards against sliding and skidding. Because the tread tends to wear down over time, if the tyre has not gone flat, it is normally replaced at this point.

There are three sections to the NPT: a rigid hub, deformable spokes capable of withstanding vertical loads, a strengthened shear band, and a rubber tread that makes contact with the ground. Rolling resistance, Contact pressure, and carrying load capacity of NPT can be changed by modifying NPT materials and dimensions.

1.1REASONS TO PREFER NPT OVER CONVENTIONAL TYRES

The importance of NPT is now understood on a global scale. The most crucial features of

NPT that distinguish it from ordinary tyres are:

1. Because of its shear band, additional suspension, and lower rolling resistance, the NPT tyre aims at performance standards above those made achievable by conventional pneumatic technology.

2. It offers comfortable rides, and a load-carrying capability similar to pneumatics, and because it lacks a cavity for pressurized air, it cannot malfunction due to a loss of air pressure.

3. Its strong lateral rigidity for improved handling without compromising comfort can be achieved, and it may eventually be able to outperform conventional tyres.

4. The conventional tyre is replaced with an NPT tyre, which is lighter than a regular tyre and helps to improve engine economy by lowering the overall weight of the vehicle.

5. Right now, tyre manufacturers must discover a means to recycle the huge pile of bald tyres that is destroying the landscape or come up with a material that is both durable and recyclable. because composite materials are typically used in airless tyres. Because most models' tread lives are longer than that of pneumatic tyres, the rubber does not need to be changed all that frequently.

Table 1: Comparison of NPT with respect to Pneumatic tyres in tabular form.

S.No	Factors considered	Pneumatic tyres	Non Pneumatic tyres
1	Tyre's life	Short life	Comparatively longer life in the case of polymer-made NPT
2	Use of air	Yes	No use of air
3	Problem of Puncture	Yes.	No problem with punctures.

The above factors confirmed the need for validating the NPT tyre performance and the specifications that can lead to better results. Thus, different NPT spoke structures are chosen to determine which structure can withstand the structural ability of pneumatic tyres. As per the currently available literature on NPTs, the static validation of tyre structure is illustrated under a single type of loading scenario only, and the structural validation under different loading conditions is yet to be researched. In this paper, dynamic conditions are not taken into consideration, and the results and inferences are based on static loading analysis. Section II discusses the geometry or 3D modelling of different tyre structures using Solidworks 2020, which contains the CAD of the tyre and will form the physical domain for the static structural analysis. Section III consists of the various inferences and graphical representations obtained after analysis done using Ansys R18.1.

2. CAD MODELLING USING SOLIDWORKS

With the 3D modelling programme Solidworks, four different spoke designs —Honeycomb, Diamond, Triangular, and Curved Spoke Structures—have been developed. The wheel hub, spoke structure and shear band with treads make up the three main parts of these NPT tyre models. To facilitate analysis, a hub-centred axle has been added to the model. This axle serves as the centre from which the vehicle will receive load and power.

CAD Model

SOLIDWORKS 2020 is the design software used for developing the CAD model.

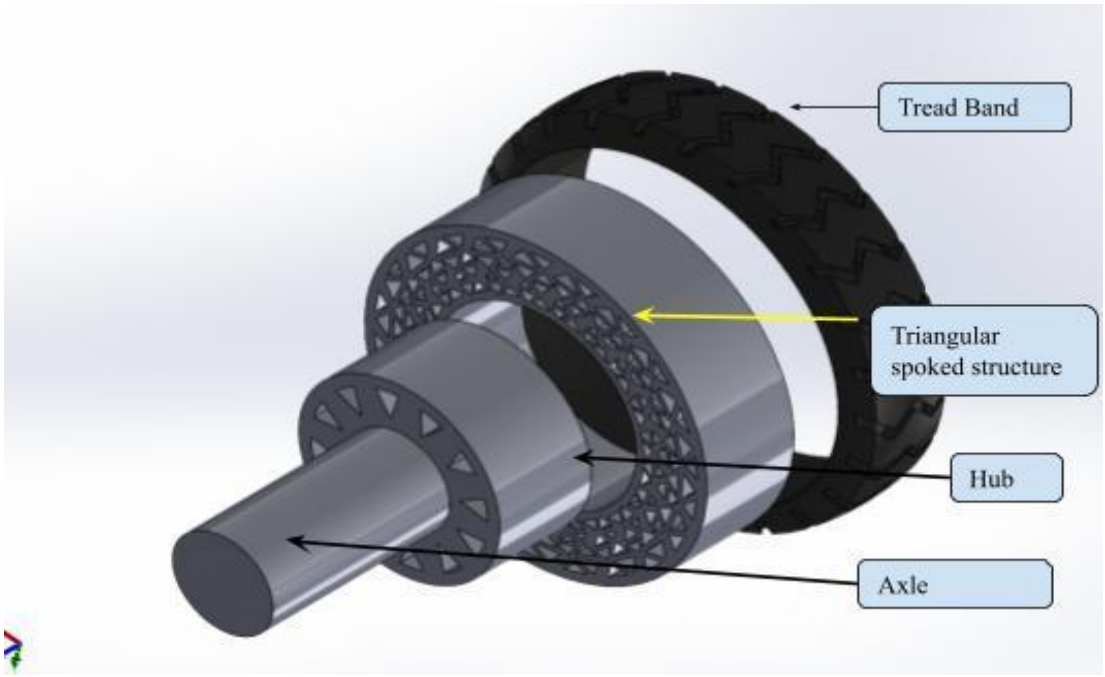

Figure 1: The CAD model of triangular spoked tyre structure representing the division of the structure.

The spoke structures were selected due to their theoretically stable designs.

1. Honeycomb - Due to its evenly balanced angle of 60 degrees in the regular hexagons, this structure is one of the most geometrically stable ones. The fundamental advantage of these structures is their lightweight, which allows them to be utilized for structural protection, thermal isolation, and energy absorption.

2. Diamond - When compared to the preceding constructions, this structure can tolerate heavier loads being applied to the tyre; additionally, because of its sturdy construction and structural design, this structure only experiences a minimal total deformation.

3. Triangular (Equilateral) - Due to the fact that just one force is acting on each of the triangle's sides at once, the triangle as a geometric shape does not bend. The spoke construction is strengthened by this feature, which helps with optimal force and weight distribution.

4. Curved Spokes- The curved spokes can take some of the force of variable torque (rapid speed variations) without breaking. Also, because of the angle of the curve, the wheels have an aerodynamic advantage because less air resistance is created when passing through them.

Following are the figures representing CAD assembly model of : (a) Honeycomb spoke structure (b) Diamond spokes structure (c) Triangular spokes and (d) curvy spokes structures.

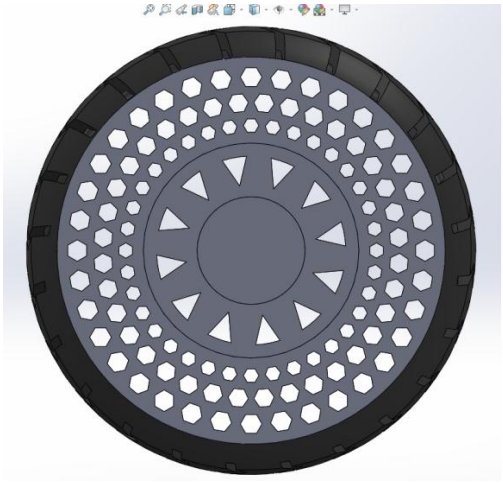

(i) Honeycomb spokes

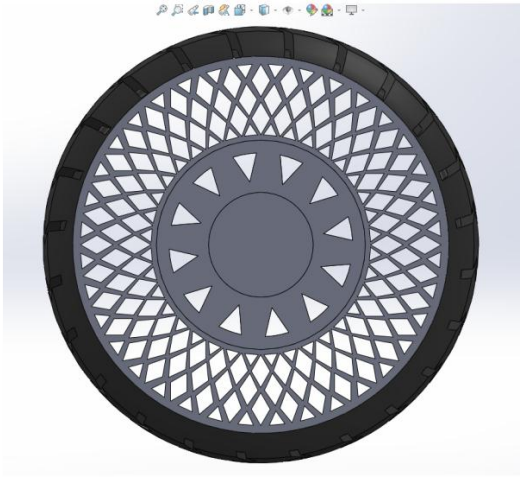

(ii) Diamond spokes

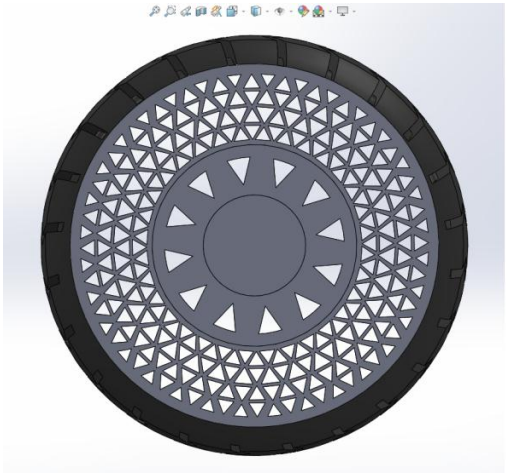

(iii) Triangular spokes

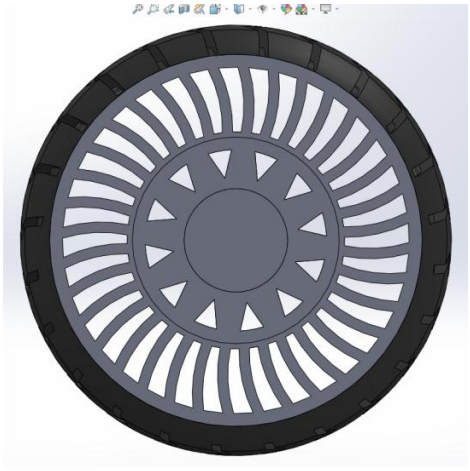

(iv) Curvy spokes

Figure 2: CAD model of different spokes geometry on NPT

MATERIAL PROPERTIES

Aluminium alloy, polyurethane, alloy steel, and nitrile rubber are the materials employed in this analysis for the four distinct tyres with various spoke structures. These materials were chosen primarily due to their vast range of mechanical qualities, including high flexibility, high-temperature resistance, high stiffness and resilience, hyperelasticity, etc. The table below includes the chosen material's properties.

Table 2: Material Properties

PART	**HUB**	**SPOKES**	**OUTER RING**	**SHEAR BAND**
MATERIAL	**UNS A97075**	**POLYURETHANE FOAM**	**AISI 4140**	**NITRILE RUBBER**
Yield Strength (MPa)	503	145	480	1.23
Elastic Modulus (MPa)	75000	35	210000	11.9
Poisson's Ratio	0.33	0.48	0.3	0.48
Density(kg/)	2180	1210	7810	1043
Shear Modulus (MPa)	32000	11.18	80000	4.0203

GEOMETRICAL ASPECTS OF TIRE

1. Wheel size = ϕ 794mm
2. The outer hub diameter is = ϕ 400 mm
3. Inner hub diameter = ϕ 100mm
4. Hub thickness is = 200mm
5. The outer diameter of the wheel is = ϕ 794mm
6. The width of the wheel is = 180mm

3. STATIC STRUCTURAL ANALYSIS

A) Load and Boundary Conditions

Inner and outer band layers combine to form the composite structure of an airless tyre. In airless tyres, steel rings are also employed as reinforcing components. The most common cause of tyre failure is heat accumulation. It's important to determine the mechanical stability of an airless tyre under the applied load in order to improve its design. It is also important to look into the simultaneous development of stress and strain energy distribution. The prediction of metallic elements was validated using the pneumatic tyre data.

Connections

- Contact: Between Axle and Hub - Bonded

  Between the Hub and Spoke structure - Bonded Between the Spoke structure and Shear Band - Bonded
- Vertical Load on a bottommost patch of each wheel = (1800*10)/4 = 4500N
- Fixed Contact = Axle
- Mesh Element Shape - Tetrahedron
- Element Size: 10mm (Fine)

B) Mesh Results

The result obtained after meshing in different spoke structures of the tyre is shown below.

Ansys R18.1 is used for meshing. Here, we used a **Tetrahedron element** for meshing.

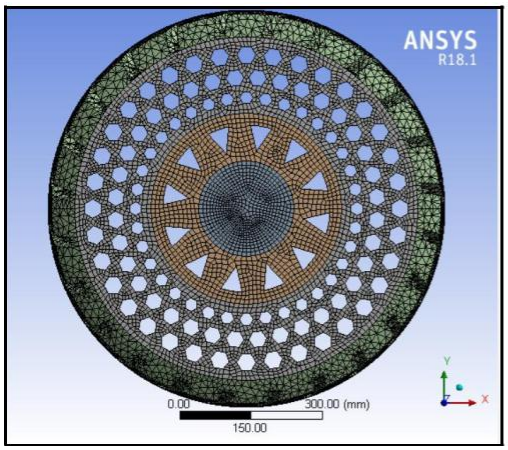

(i)Honeycomb spoke mesh

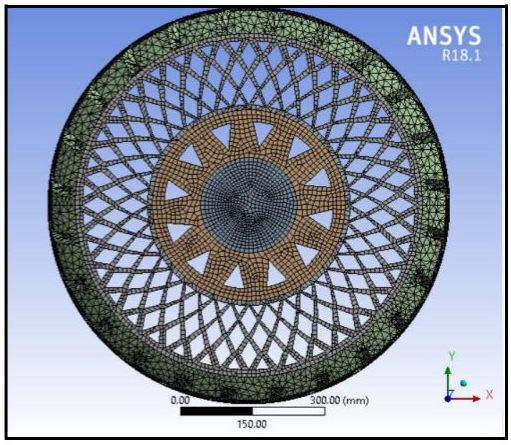

(ii)Diamond spoke mesh

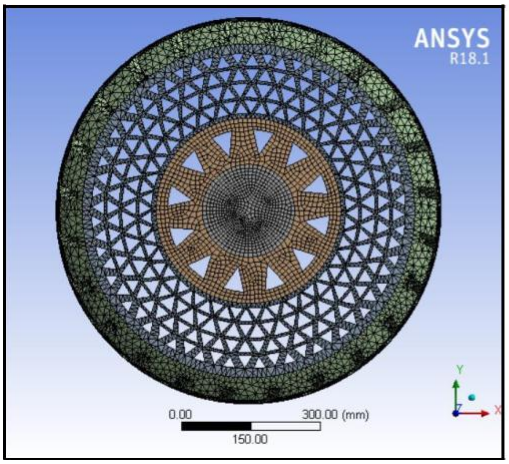

(iii) Triangular spoke mesh

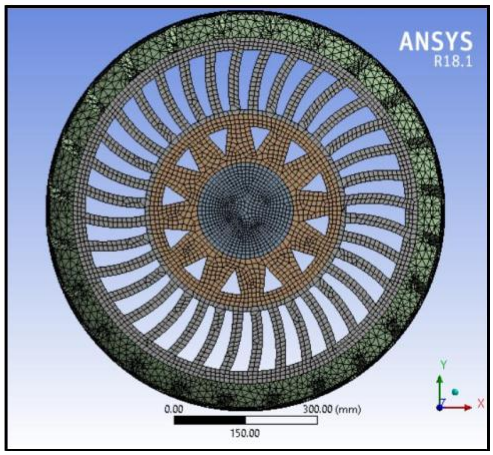

(iv) Curvy spoke mesh

Figure 3: Meshed model of different spokes geometry of NPT

Analysis Results

- The pictorial presentation in the method of contour plots of **Total Deformation**

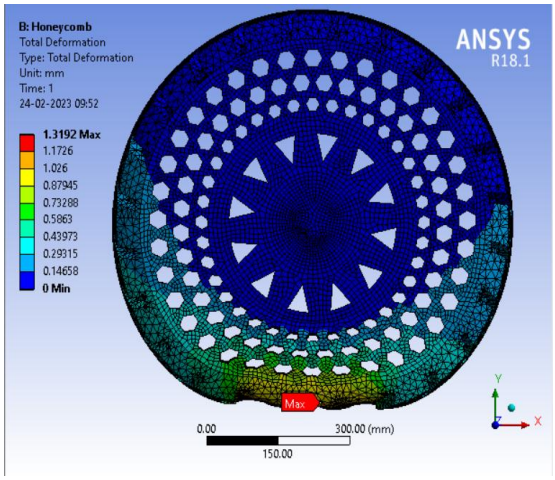

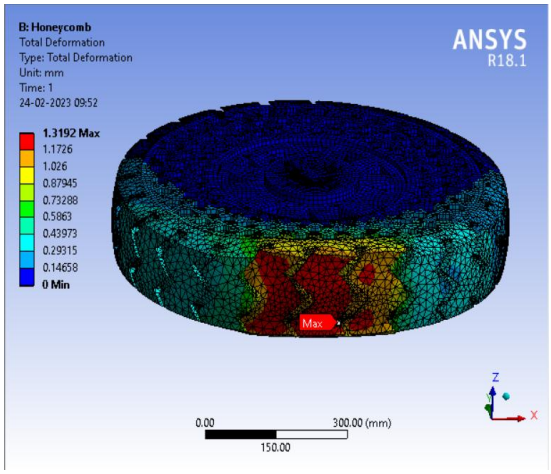

Honeycomb

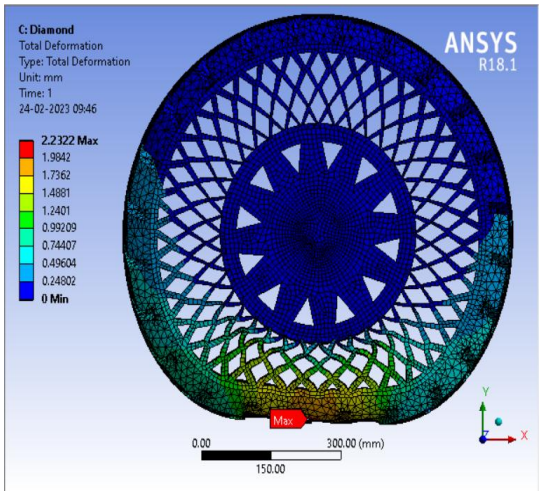

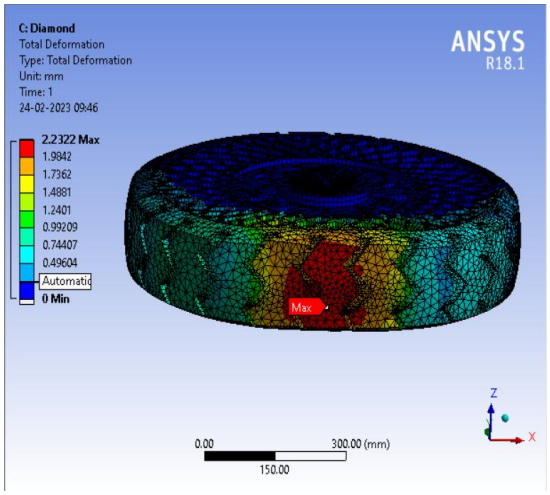

Diamond

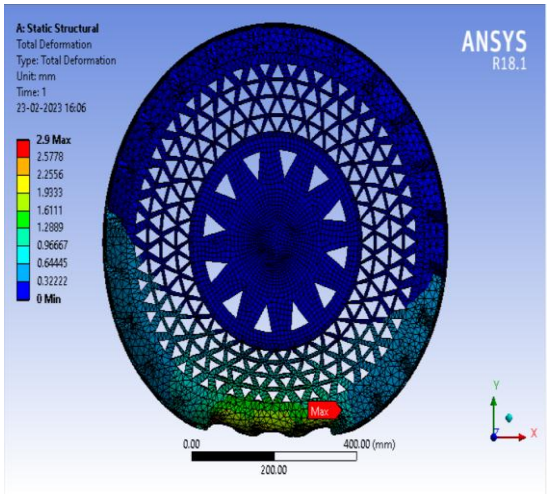

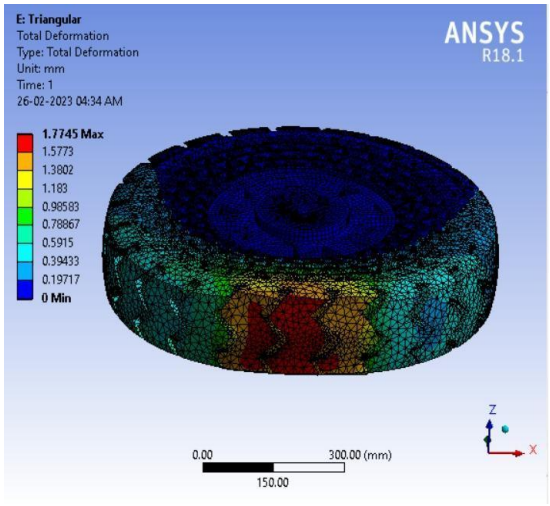

Triangular

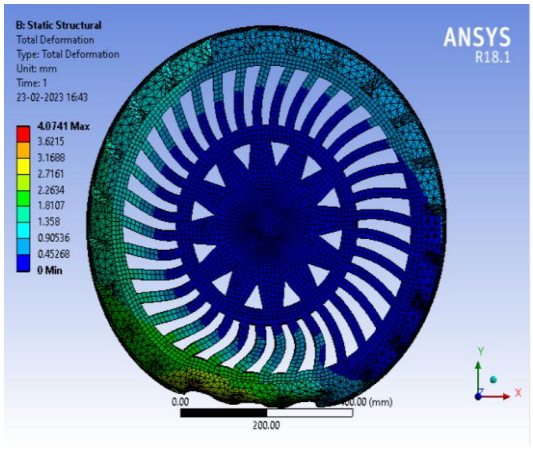

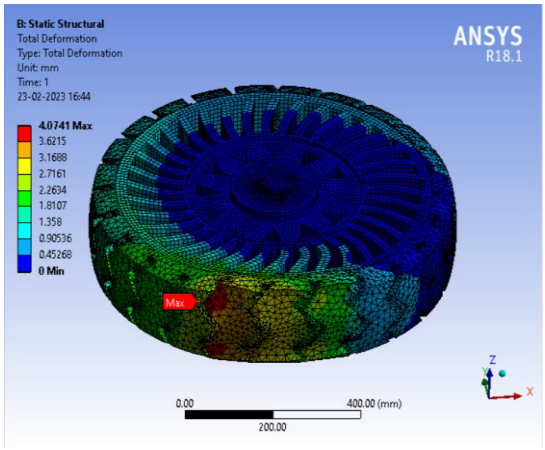

Curvy

Figure 4: Result contour of Total deformation.

- The pictorial presentation in the method of contour plots of Equivalent(Von-Mises) Stress

<table>
<tr><td> 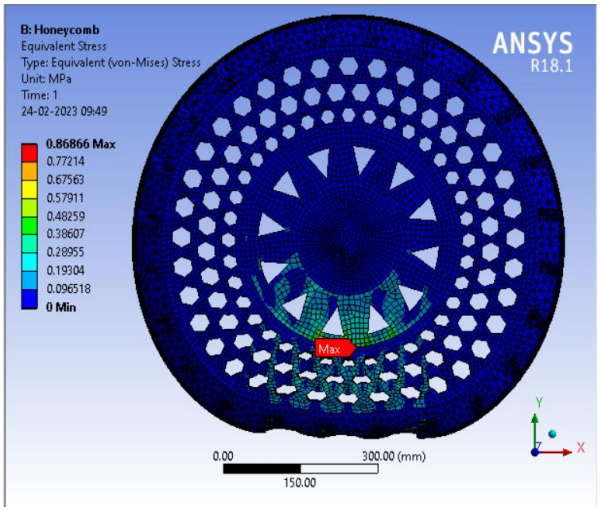
</td><td> 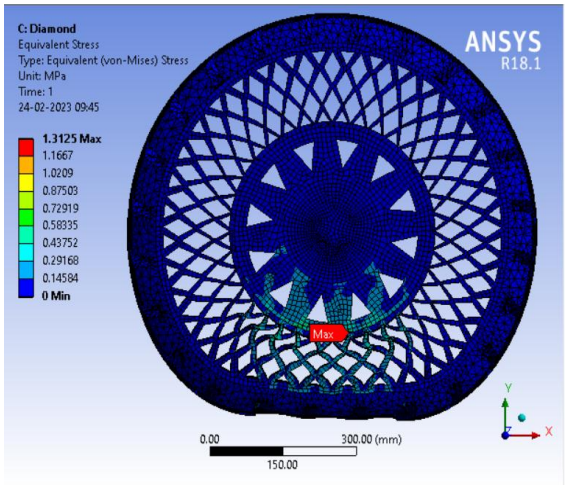
</td></tr>
<tr><td>Honeycomb</td><td>Diamond</td></tr>
<tr><td> 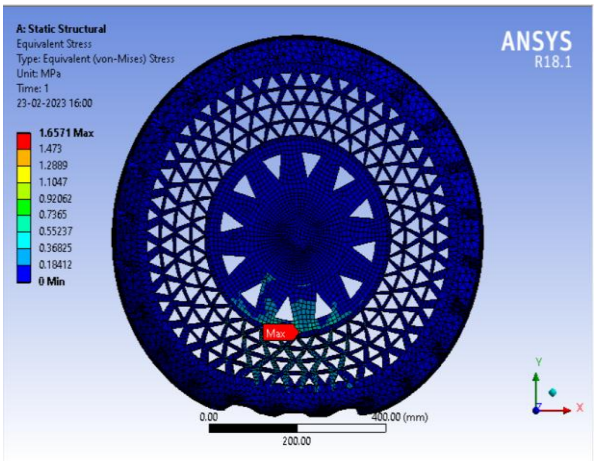
</td><td> 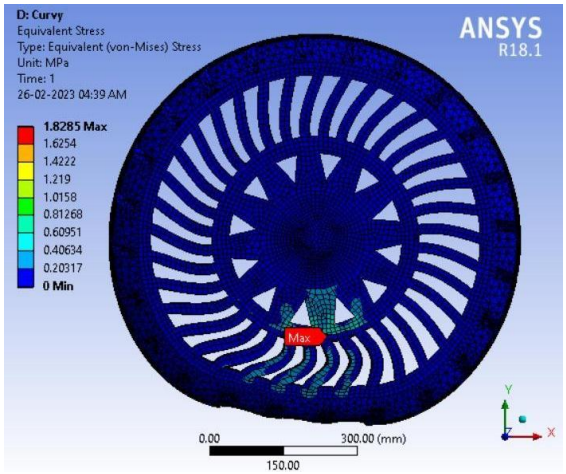
</td></tr>
<tr><td>Triangular</td><td>Curved spokes</td></tr>
</table>

Figure 5: Result contour of Equivalent(Von-Mises) Stress

- The pictorial presentation in the method of contour plots of Maximum Principal Elastic Strain

<table>
<tr><td> 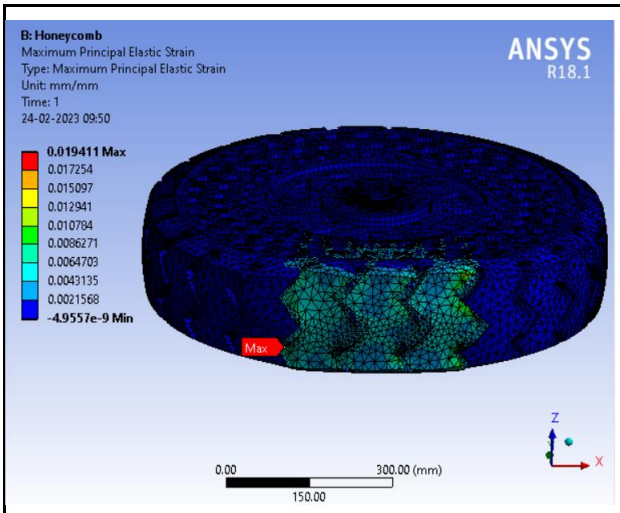
</td><td> 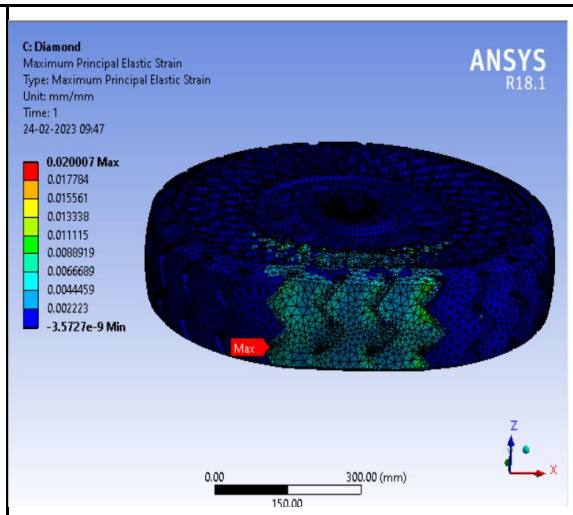
</td></tr>
<tr><td>Honeycomb</td><td>Diamond</td></tr>
<tr><td> 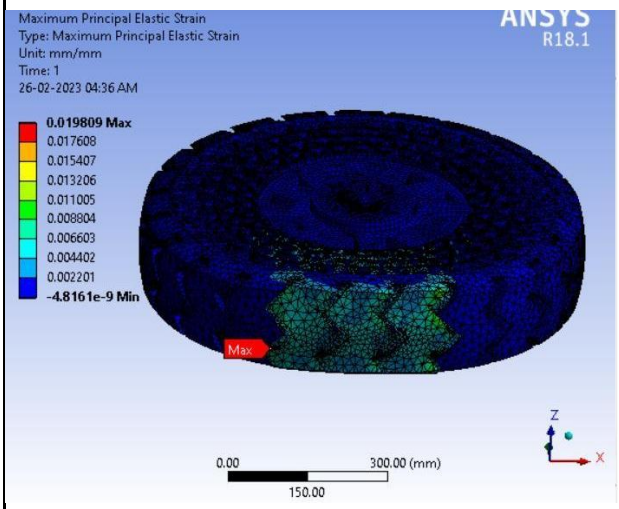
</td><td> 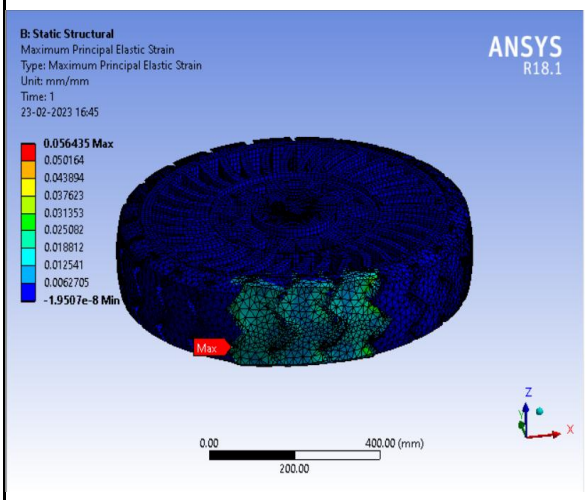
</td></tr>
<tr><td>Triangular</td><td>Curved spokes</td></tr>
</table>

Figure 6: Result contour of Maximum Principal Elastic Strain

- The pictorial presentation in the method of contour plots of Maximum Shear Stress

<table>
<tr><td> 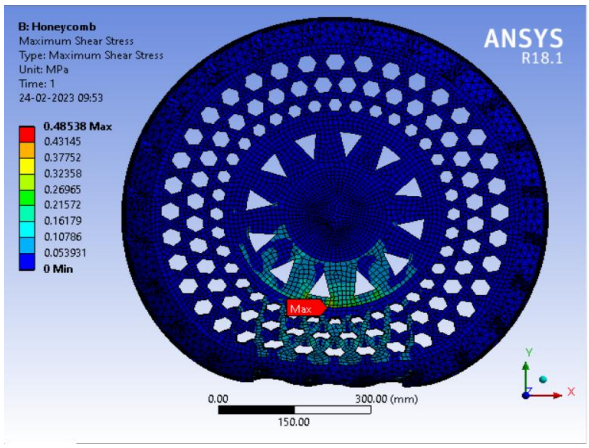
</td><td> 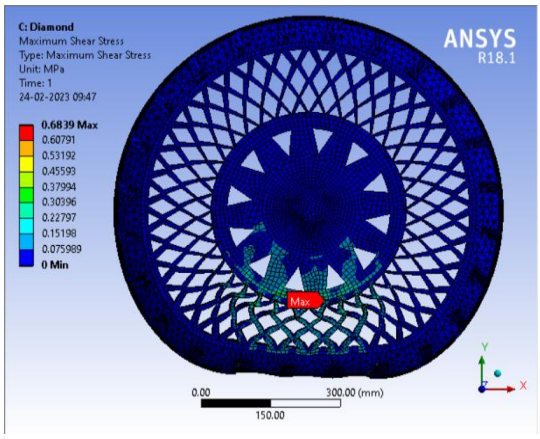
</td></tr>
<tr><td>Honeycomb</td><td>Diamond</td></tr>
<tr><td> 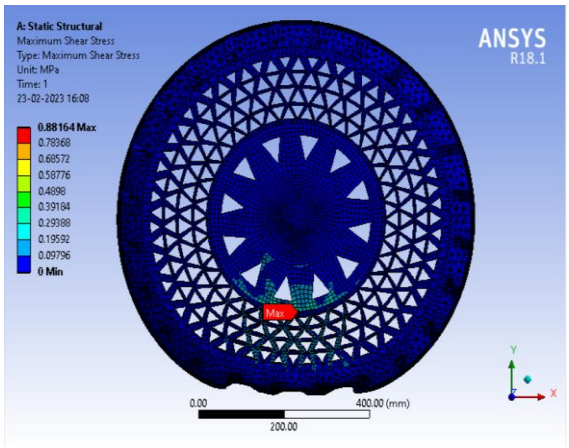
</td><td> 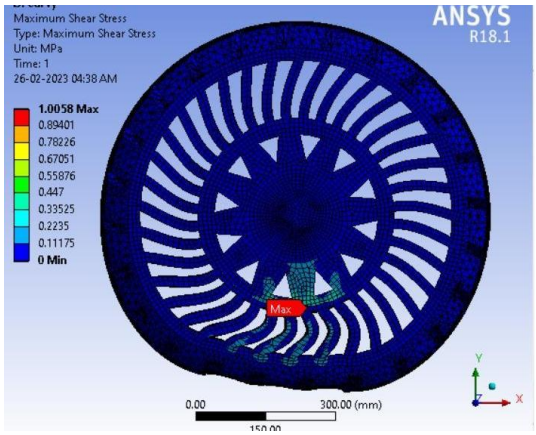
</td></tr>
<tr><td>Triangular</td><td>Curved spokes</td></tr>
</table>

Figure 7: Result contour of Shear Stress

4. RESULTS

The results obtained by comparing the different spoke structures using a mix of materials that were examined are compiled below.

- **Total Deformation**

Table 3: Maximum total deformation values in different spokes structures.

S.No.	Structure	Force Applied (N)	Max Total Deformation (mm)
1.	Honeycomb	4500	1.3192
2.	Diamond	4500	2.2322
3.	Triangular	4500	2.9000
4.	Curved Spokes	4500	4.0741

Graphical Representation: Total deformation (mm) Vs. Tyre Geometry

Inference-

From the above data it's pretty evident that the Honeycomb structure has the least deformation whereas the Curvy structure has the largest deformation. Thus it can be concluded that the Honeycomb structure will give the Highest load-carrying capacity amongst the 4 spoke structures compared and would be suitable for heavier vehicles in contrast to which the Curvy structure would be suitable for lighter vehicles with less load and could provide more cushioning effect.

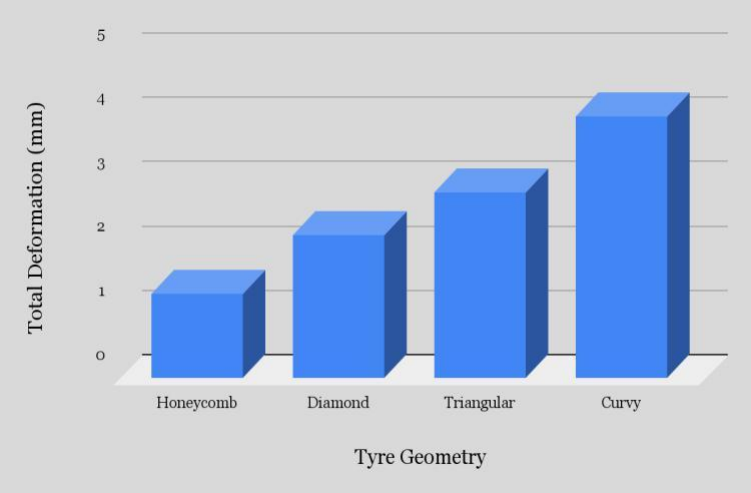

Chart 1: Total deformation (mm) Vs. Tyre Geometry

- **Equivalent(Von- Mises) Stress**

Table 4: Maximum Von-Mises Stress (MPa) values in different spokes structure.

S.No.	Structure	Force Applied(N)	Max Von-Mises Stress (MPa)
1.	Honeycomb	4500	0.86866
2.	Diamond	4500	1.3125
3.	Triangular	4500	1.6571
4.	Curved Spokes	4500	1.7811

Graphical Representation: Von Mises Stress(MPa) Vs. Tyre Geometry

Inference-

From the data collected using the table above , Honeycomb spoke structure came with the least Von mises stress compared to other spokes structure. Thus, this can be said that Honeycomb spoke structure will have the highest Compressive strength. NPT with honeycomb spokes offered minimum stress concentration which is important for Fatigue resistant designs.

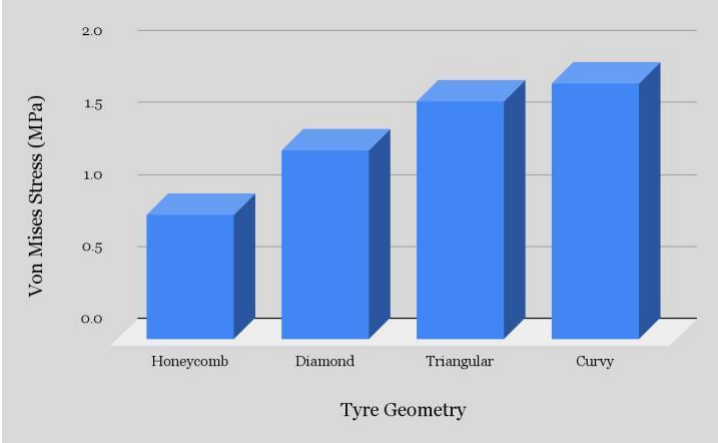

Chart 2: Von Mises Stress (MPa) Vs. Tyre Geometry

- **Maximum Principal Elastic Strain**

Table 5: Maximum Principal elastic Strain values in different spokes structure.

S.No.	Structure	Force Applied(N)	Max Principal Elastic Strain
1.	Honeycomb	4500	0.019411
2.	Diamond	4500	0.020007
3.	Triangular	4500	0.056325
4.	Curved Spokes	4500	0.056435

Graphical Representation: Maximum Principal Elastic strain Vs. Tyre Geometry

Inference-

Here, Honeycomb spokes structure shows the least value of maximum principal elastic strain value while triangular and curvy spokes structure design has similar results. Thus, we can say that Honeycomb structure design in tyres will lead to longer life by reducing the rate of wear and tear.

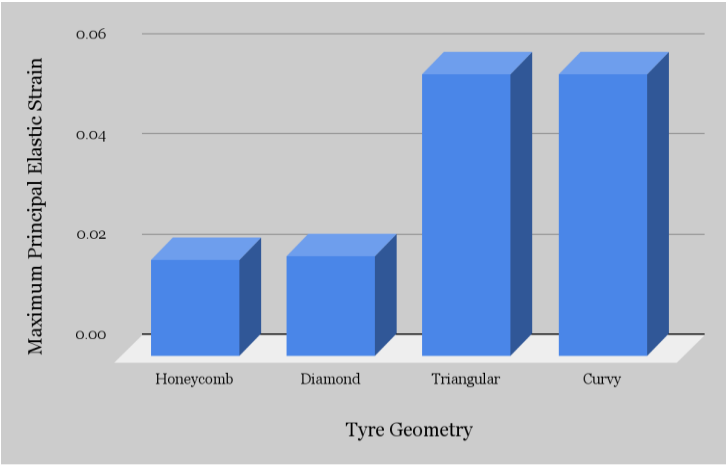

Chart 3: Maximum Principal Elastic strain Vs. Tyre Geometry

- **Maximum Shear Stress**

Table 6: Maximum Shear Stress values in different spokes structure

S.No.	Structure	Force Applied(N)	Max Shear Stress(MPa)
1.	Honeycomb	4500	0.48538
2.	Diamond	4500	0.6839
3.	Triangular	4500	0.88164
4.	Curved Spokes	4500	0.97808

Graphical representation: Maximum Shear Stress (MPa) Vs. Tyre Geometry

Inference-

The maximum shear stress that the tyre can withstand under a load of 4500 N is shown in the above table. For easier comparison and data visualisation, the shear stress of the various spokes in the tyre design are displayed graphically in the right corner.

In this instance as well, the honeycomb spoke structure had the lowest maximum shear stress value when compared to other spoke structures.

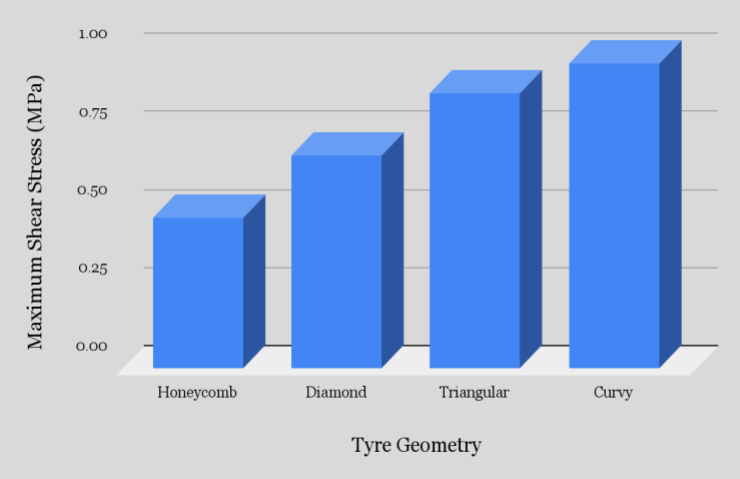

Chart 4: Maximum Shear Stress (MPa) Vs. Tyre Geometry

Consolidated Results

Table below illustrates the compiled results of total deformation, equivalent von-mises stress maximum principal elastic strain, and maximum shear stress for different spoke structures in a non-pneumatic tyre. It also gives a comparative analysis of four different spokes structures used for the same.

Table 7: Consolidated results of static structural analysis.

S.No	Types of analysis	Tyre Structure			
		Honeycomb	Diamond	Triangular	Curvy
1.	Total Deformation (mm)	1.3192	2.2322	2.9000	4.0741
2.	Maximum Elastic Strain	0.019411	0.020007	0.056325	0.056435
3.	Equivalent (Von-mises) Stress (MPa)	0.86866	1.3125	1.6571	1.7811
4.	Shear Stress (MPa)	0.48538	0.6839	0.88164	0.97808

From the result shown in the consolidated table above, we found that the Honeycomb spoke structure model gives better results than the other spoke structures of the tyre model. Similarly in different spokes structure constraints, with mentioned analysis parameters, the Honeycomb spoke structure yields better results. So for the given boundary conditions and applied load, the Honeycomb spoke structure airless tyre is more rigid and durable.

4. CONCLUSION

There are many advantages that Non Pneumatic tyres have in general over Pneumatic tyres. Some of the factors that can be counted includes : Elimination of air Leakage or tyre blow outs, Consistent economy and handling as there is no issue with gas pressure , Its flexibility provides a rise in extent of contact, No maintenance requirement, Elongated tread life,Facilitate utilisation, making a vehicle lot more economical with high lateral strength for higher handling without any loss in comfort, Vehicle remains in restraint even in parking brake, Remains mobile even with a number of the spokes broken or missing , has high Sturdiness & Long Life and Less environmental impact.

- The results obtained from static structural analysis confirms major of the factors stated above and It can be concluded that Honeycomb spokes structure of tyre are more stable structure as they have comparatively higher capability to withstand more load.
- It is found that Honeycomb spokes design constitutes least stress, strains and deformations values in comparison to other designs because the honeycomb structure is more geometrically stable for the same material and symmetrical which can sustain and uniformly distribute large amount of force thereby exhibiting more compressive and shear strength.

As per the analysis done on different spoke structure designs, the honeycomb spokes structure design that has given the results with least deflection is advisable and is concluded to be most suitable for heavier load application purposes.

REFERENCES

[1] R., Sanjeev Kumar & Kumar, K Vetrivel & Ramakrishnan, T. (2021). Design optimization of Airless Tyre - Numerical Approach. IOP Conference Series: Materials Science and Engineering. 1057. 012032. 10.1088/1757-899X/1057/1/012032.

[2] Mathew, Nibin Jacob, Dilip Kumar Sahoo, and E. Mithun Chakravarthy. 2017. "Design and Static Analysis of Airlesstyre to Reduce Deformation." *IOP Conference Series: Materials Science and Engineering* 197 (1): 012042.

[3] Thirumoorthy, Prabhuram & S C, Meenakshi Sundaram & Jegadeeswer, S. & Kannan, V.. (2020). Static analysis of different spoke structures of airless and conventional tyres. IOP Conference Series: Materials Science and Engineering. 923. 012017. 10.1088/1757-899X/923/1/012017.

[4] Mohan, Aravind & Johny, C & Tamilarasu, A & Bhasker, Pradeep & Krishnaiah, Ravi. (2017). Design and Analysis of Non-Pneumatic Tyre. IOP Conference Series: Materials Science and Engineering. 263. 062061. 10.1088/1757-899X/263/6/062061.

[5] Kumar, Nikhil & Mhatre, Pranavee & Pandey, Rinkesh & Pandey, Ashutosh & Ospanova, A.. (2022). Optimization of Non-Pneumatic Tyre. International Journal of Innovative Research in Science Engineering and Technology. 11. 1455-1459. 10.15680/IJIRSET.2022.1104074.

[6] Thirumoorthy, Prabhuram & S C, Meenakshi Sundaram & Jegadeeswer, S. & Kannan, V.. (2020). Static analysis of different spoke structures of airless and conventional tyres. IOP Conference Series: Materials Science and Engineering. 923. 012017. 10.1088/1757-899X/923/1/012017.

[7] Ali, M., Maarij, M. & Hussain, A. Design and structural analysis of non-pneumatic tyres for different structures of polyurethane spokes. *J. Eng. Appl. Sci.* 69, 38 (2022).

[8] Abhishek, Raj, and Anup Kumar. "Non-Pneumatic Tyre design with Honeycomb spoke structure." *IJISET - International Journal of Innovative Science, Engineering & Technology,* vol. 7, no. 6, June 2020, p. 6.

[9] Prabhuram, T., Sundaram, S.M., Jegadeeswer, S. and Kannan, V.S., 2020, September. Static analysis of different spoke structures of airless and conventional tyres. In *IOP Conference Series: Materials Science and Engineering* (Vol. 923, No. 1, p. 012017). IOP Publishing.

[10] Pewekar, M.M. and Gaikwad, S.D., 2018. Strength validation of hexagonal cellular spoked non-pneumatic tyres for automobiles through finite element analysis. *Int J Sci Res Sci Technol*, *4*(5), pp.1044-1055.

[11] Shashavali, S., Reddy, C.R. and Yadiki, G.K., 2016. Design and analysis of four-wheeler airless tyre. *Int J Adv Technol Innov Res*, *8*, pp.4298-4305.

[12] Genovese, A., Garofano, D., Sakhnevych, A., Timpone, F. and Farroni, F., 2021. Static and dynamic analysis of non-pneumatic tyres based on experimental and numerical methods. *Applied Sciences*, *11*(23), p.11232.

[13] Mathew, N.J., Sahoo, D.K. and Chakravarthy, E.M., 2017, May. Design and static analysis of airless tyres to reduce deformation. In *IOP Conference Series: Materials Science and Engineering* (Vol. 197, No. 1, p. 012042). IOP Publishing.

[14] Mohan, A., Johny, C.A., Tamilarasu, A., Bhasker, J.P. and Ravi, K., 2017, November. Design and analysis of non-pneumatic tyres. In *IOP conference series: materials science and engineering* (Vol. 263, No. 6, p. 062061). IOP Publishing.

View publication stats

e-ISSN: 2582-5208
International Research Journal of Modernization in Engineering Technology and Science
(Peer-Reviewed, Open Access, Fully Refereed International Journal)
Volume:05/Issue:05/May-2023 Impact Factor- 7.868 www.irjmets.com

DETERMINING THE OPTIMAL RIDING FREQUENCY FOR AN ALL-TERRAIN VEHICLE (ATV) USING A COMPREHENSIVE MODEL OF A FOUR-WHEELED AUTOMOBILE

Risheek Arora[*1], Rishi Kabra[*2], Rishikesh Dubey[*3], Prof. Atul Kumar Agarwal[*4]

[*1,2,3]UG Student, Mechanical Engineering, Delhi Technological University, Delhi, India.

[*4]Professor, Mechanical Engineering, Delhi Technological University, Delhi, India.

DOI : https://www.doi.org/10.56726/IRJMETS39321

ABSTRACT

The aim of this paper is to determine an appropriate ride frequency for the front and rear suspension of an All-terrain Vehicle (ATV). In order to achieve this objective, a comprehensive car model of the ATV was constructed using the equations of motion. The primary focus was on minimizing the collective impact of the vehicle body's heave, roll, and pitching movements. By employing MATLAB Simulink software, simulations were conducted with various frequency pairs for the front and rear suspensions. Subsequently, the responses obtained from these simulations were analyzed. To facilitate the selection process, the responses were normalized and a weighted average was computed for comparison. Ultimately, the frequency combination yielding the lowest weighted average was chosen as the optimal solution.

Keywords: Ride Quality, Ride Handling, Full Car Model.

I. INTRODUCTION

1.1 OFF - ROAD VEHICLE DESIGN

The design of off-road vehicles faces a significant degree of uncertainty in various factors, leading to a more straightforward approach to design compared to the complex mathematical calculations involved in designing asphalt vehicles. This simplified approach results in a more robust vehicle that can often be repaired after sustaining damage. However, due to the unpredictability of wheel loads in accidents and terrain conditions, some damage may be irreparable. The lack of comprehensive data means that designing the suspension system and other subsystems in an all-terrain vehicle requires an iterative process. Designers estimate a design by approximating various loads and incorporating a factor of safety, the magnitude of which varies depending on personal preferences. The design is then evaluated through simulations and on-road testing, with any flaws noted and used to improve the next iteration of vehicle construction.

1.2 BACKGROUND

This study focuses on a specific type of All-Terrain Vehicle (ATV) called the Baja SAE vehicle. The Baja SAE, also known as a "mini-Baja," is used in collegiate racing competitions organized by the Society of Automotive Engineers in India and the United States of America. These events allow college students to design and build vehicles to compete against each other in specific tasks. A typical Baja SAE vehicle features a steel alloy tube space frame chassis, with a bulkhead called a firewall separating the driver from the engine and drivetrain. The front suspension usually consists of independent suspension, while the rear suspension can be dependent or independent, depending on the designer's preferences and the objectives of the vehicle. Dynamic models derived from mathematical vehicle modeling are crucial for analyzing the behavior and response of a Baja SAE vehicle. These models serve as prototypes that provide insight into the impact of various parameters and constraints. Simulation models allow for the introduction of more variables and the enforcement of various optimization and control algorithms.

1.3 PROBLEM DEFINITION

Despite considerable work being done on suspension models and analysis, research on the subject of ATVs remains limited. There has been no research that studies the correlation between the spring frequencies chosen and it's impact on vehicle parameters like comfort and road handling in simulations with the behavior of real-life ATVs. As a result, designers of off-road vehicles typically follow an extrapolation of the design methodology used for asphalt vehicles. Creating a vehicle dynamics model for an ATV requires basic information such as

e-ISSN: 2582-5208
International Research Journal of Modernization in Engineering Technology and Science
(Peer-Reviewed, Open Access, Fully Refereed International Journal)
Volume:05/Issue:05/May-2023 Impact Factor- 7.868 www.irjmets.com

wheel loads. However, estimating loads and reaction forces on ATV wheels is particularly complex due to the relationship between different terrains, tire materials and construction, tread design, and other surface features. Unlike Pacejka's simplification of slick tires for evaluating cornering and vertical stiffness, a mathematical model for ATV tires requires expensive and complicated equipment. Therefore, simulations based on these assumptions may not accurately reflect the behavior of off-road vehicles in real-life situations.

1.4 OBJECTIVES

Given the challenges mentioned above, it is believed that constructing a sufficiently accurate model for off-road vehicles requires taking into account their unique characteristics and incorporating off-road terrain as the ground input. This report outlines the development of a mathematical model that can analyze how off-road vehicles traverse varying roughness and speeds on different types of terrain. Additionally, it describes a procedure for determining the suspension settings of off-road vehicles, taking into account both the vertical and lateral dynamics of the vehicle. The illustration below depicts a complete car model featuring 7 degrees of freedom (DOF). These include the vertical movement of the four unsprung masses, the motion of the sprung mass, and the pitch and roll movements of the vehicle.

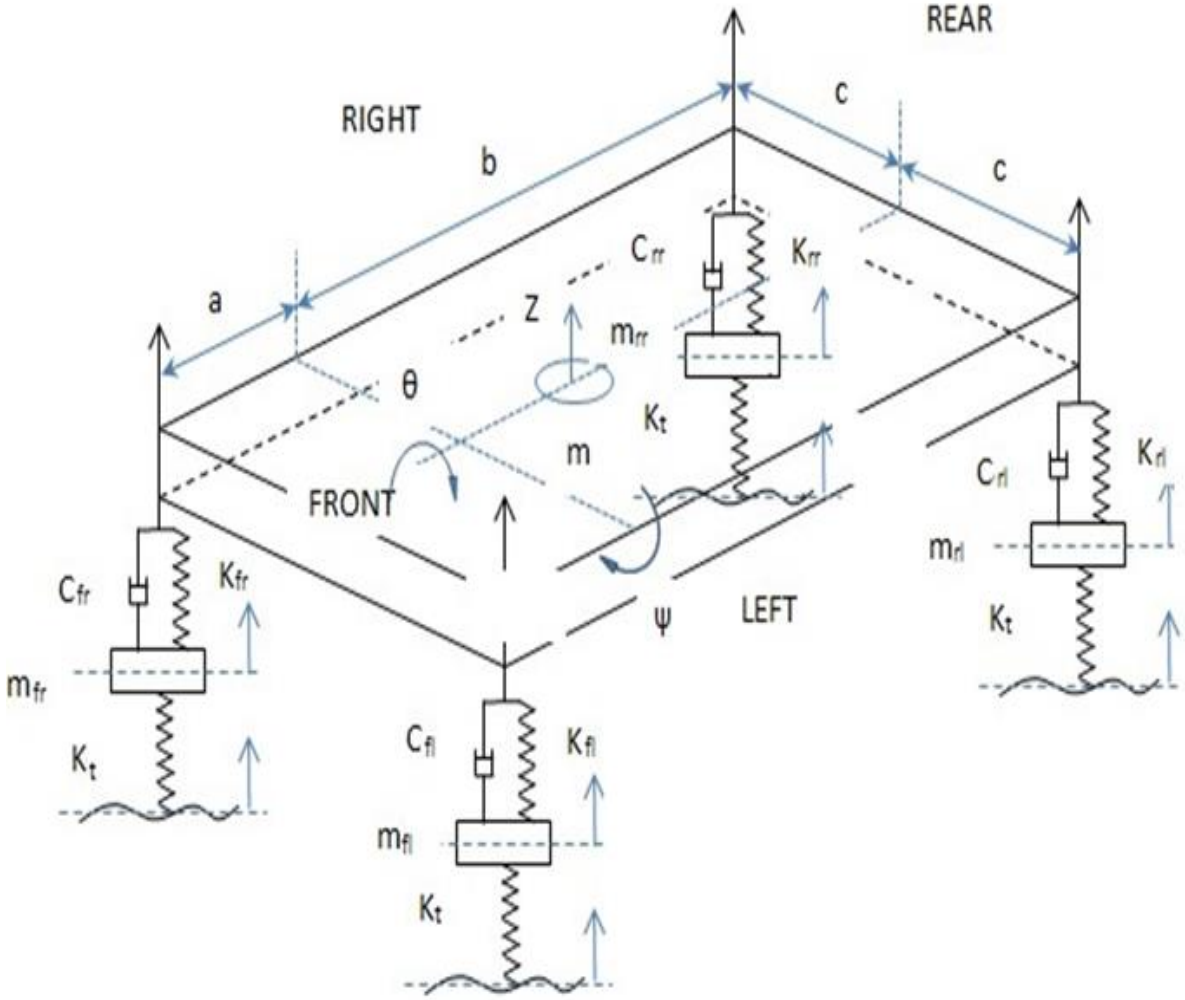

Figure 1: Full Car Model of Car

II. METHODOLOGY

2.1 ASSUMPTIONS

Some Important Assumptions made in this model are:

1) Aerodynamic effects are neglected.
2) The vehicle is assumed to be rigid.
3) Model parameters such as stiffness, damper coefficient are assumed to be invariant with time.

e-ISSN: 2582-5208
International Research Journal of Modernization in Engineering Technology and Science
(Peer-Reviewed, Open Access, Fully Refereed International Journal)
Volume:05/Issue:05/May-2023 Impact Factor- 7.868 www.irjmets.com

Table 1: Parameters of the system

S.no	Parameters	Value	Units
1	m_f	15	kg
2	m_r	15	Kg
3	m_s	160	kg
4	C_s	200	N s/m
5	I_x	50	$Kg*m^2$
6	I_y	60	$Kg*m^2$
7	a	460	mm
8	b	690	mm
9	c	550	mm
10	K_t	55000	N/m

2.2 EQUATIONS

As seen in FIgure 1; 7 Different Equations of Motion govern the interconnected movement of the Full Car Model. Those equations of motion are:

1) Vertical equilibrium of sprung mass: **(1)**

$$m_s\ddot{Z}_{cg} = -(2k_{sf} + 2k_{sr})Z_{cg} - (2C_{sf} + 2C_{sr})\dot{Z}_{cg} + (2aK_{sf} - 2bK_{sr})\phi - (2aC_{sf} - 2bC_{sr})\dot{\phi} + K_{sf}Z_{fl} + C_{sf}\dot{Z}_{fl} + K_{sr}Z_{rl} + K_{sr}Z_{rr} + C_{sr}\dot{Z}_{rr} + k_{sf}Z_{fr} + C_{sf}\dot{Z}_{fr} + C_{sr}\dot{Z}_{rl}$$

2) Pitch equilibrium of sprung mass: **(2)**

$$I_y\ddot{\phi} = (2aK_{sf} - 2bK_{sr})Z_{cg} + (2aC_{sf} - 2bC_{sr})\dot{Z}_{cg} - (2a^2K_{sf} + 2b^2K_{sr})\phi - (2a^2C_{sf} + 2b^2C_{sr})\dot{\phi} - aK_{sf}Z_{fl} - aC_{sf}\dot{Z}_{fl} - aK_{sf}Z_{fr} - aC_{sf}\dot{Z}_{fr} + bK_{sr}Z_{rl} + bC_{sr}\dot{Z}_{rl} + bK_{sr}Z_{rr} + bC_{sr}\dot{Z}_{rr}$$

3) Roll equilibrium of sprung mass: **(3)**

$$I_x = -c^2(2k_{sf} + 2k_{sr}) - c^2(2c_{sf} + 2c_{sr}) + cK_{sf}Z_{fl} - cK_{sf}Z_{fr} - cC_{sf}Z_{fr} + K_{sr}Z_{rl} + cC_{sr}Z_{rl} - cK_{sr}Z_{rr} - cC_{sr}Z_{rr}$$

4) Vertical equilibrium of unsprung mass 1: **(4)**

$$m_f\ddot{Z}_{fl} = k_{sf}(Z_{cg} - Z_{fl} - c + a\phi) - C_{sf}(\dot{Z}_{cg} - \dot{Z}_{fl} - c + a\dot{\phi}) - k_t(Z_{fl} - Z_{r1})$$

5) Vertical equilibrium of unsprung mass 2: **(5)**

$$m_f\ddot{Z}_{fr} = k_{sf}(Z_{cg} - Z_{fr} + c + a\phi) - C_{sf}(\dot{Z}_{cg} - \dot{Z}_{fr} + c + a\dot{\phi}) - k_t(Z_{fr} - Z_{r2})$$

6) Vertical equilibrium of unsprung mass 3: **(6)**

$$m_r\ddot{Z}_{rl} = k_{sr}(Z_{cg} - Z_{rl} - c - b\phi) - C_{sr}(\dot{Z}_{cg} - \dot{Z}_{rl} - c - b\dot{\phi}) - k_t(Z_{rl} - Z_{r3})$$

7) Vertical equilibrium of unsprung mass 4: **(7)**

$$m_r\ddot{Z}_{rr} = k_{sr}(Z_{cg} - Z_{rr} + c - b\phi) - C_{sr}(\dot{Z}_{cg} - \dot{Z}_{rr} + c - b\dot{\phi}) - k_t(Z_{rl} - Z_{r4})$$

III. MODELING AND ANALYSIS

3.1 SIMULINK MODEL

To create a complete car model, a free body diagram was utilized for all five masses, including four unsprung masses and one for the sprung mass. This approach resulted in a system of seven second-order differential

e-ISSN: 2582-5208
International Research Journal of Modernization in Engineering Technology and Science
(Peer-Reviewed, Open Access, Fully Refereed International Journal)
Volume:05/Issue:05/May-2023 Impact Factor- 7.868 www.irjmets.com

equations, with four equations representing the acceleration of the unsprung masses, one equation representing the acceleration of the sprung mass, and one equation each representing Roll and Pitch.

The input for these 7 equations was created using the road profile's disturbance, and a Simulink model was created to solve these differential equations of second order. Assuming the system to be at equilibrium at t=0 we use the initial values to solve for the output variables. Consequently, solving these equations resulted in the output variables as a function of time. To evaluate the model's performance, a frequency range was chosen based on the passenger data available for simulating the model.

$$f_{(rear)} = 1Hz\text{-}2hz \quad (8)$$

$$(f_{(rear)} - 0.5) < f_{(front)} < (f_{(rear)} + 0.5) \quad (9)$$

By applying the above scheme, we obtained a total of 121 frequency combinations for both the front and the rear. These frequency combinations were then utilized to determine the spring stiffness at the front and the rear, which were subsequently used to substitute in the equations.

$$K_{sf} = (4\pi^2 F_{front}^2 m_f)/(MR)^2 \quad (10)$$

$$K_{sr} = (4\pi^2 F_{rear}^2 m_r)/(MR)^2 \quad (11)$$

Substituting the values of Kf and Kr as obtained above, a Simulink model was built for each combination (through looping). The model was subjected to disturbances, and the model's response was analyzed for all combinations. To identify the frequency combination that produces the best results, we select the combination that minimizes:

- Roll (20% weightage)
- Pitch (60% weightage)
- Sprung mass displacement. (20% weightage)

The mean pitching, mean roll, and mean sprung mass displacement were calculated for each combination to obtain the final results. These values were then normalized, and a weighted average was computed to facilitate comparisons. The frequency combination that produced the lowest weighted average for these variables was ultimately chosen.

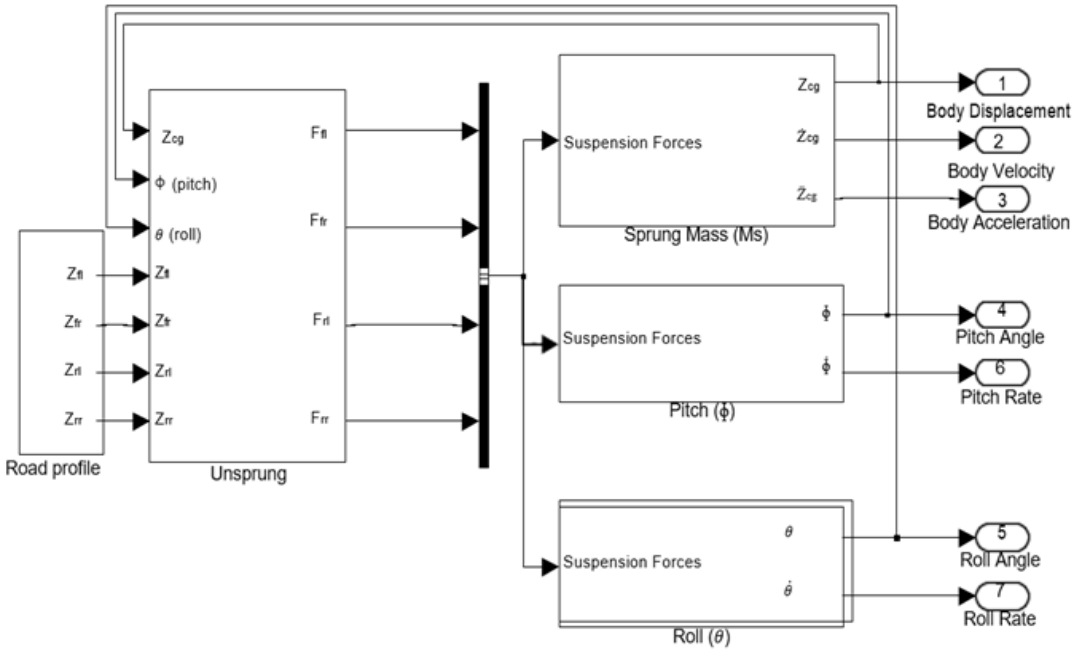

Figure 2: Simulink Block Diagram

3.2 MODEL VALIDATION

It is a convention that the frequency of the rear of a vehicle should be distinct from that of the front to minimize the pitch of the vehicle over bumps. The rear ride frequency is usually higher than the front to ensure that the

e-ISSN: 2582-5208
International Research Journal of Modernization in Engineering Technology and Science
(Peer-Reviewed, Open Access, Fully Refereed International Journal)
Volume:05/Issue:05/May-2023 Impact Factor- 7.868 www.irjmets.com

rear catches up with the front after encountering a bump, resulting in the front and rear moving in sync. Our model's outcomes validate this statement.

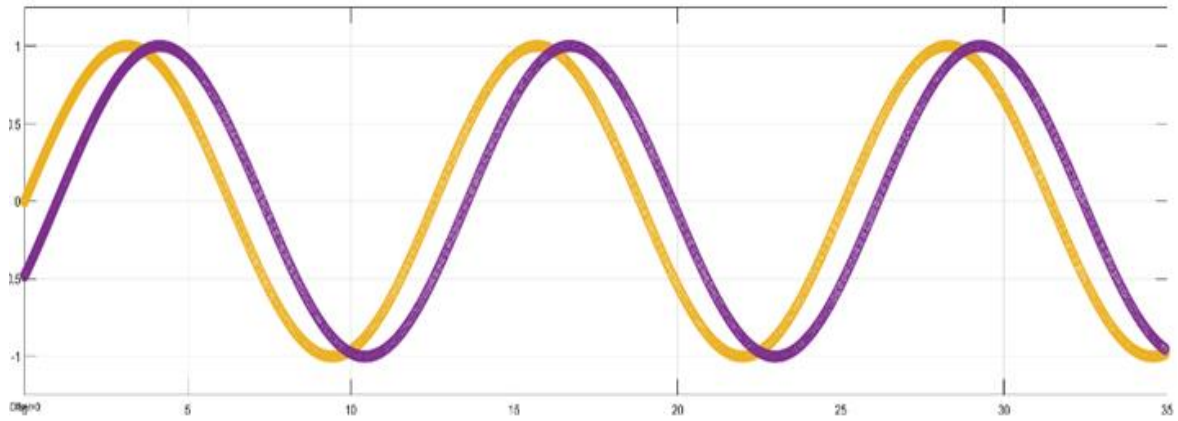

Figure 3: Phase lag at the front and rear of the vehicle when encountering a bump

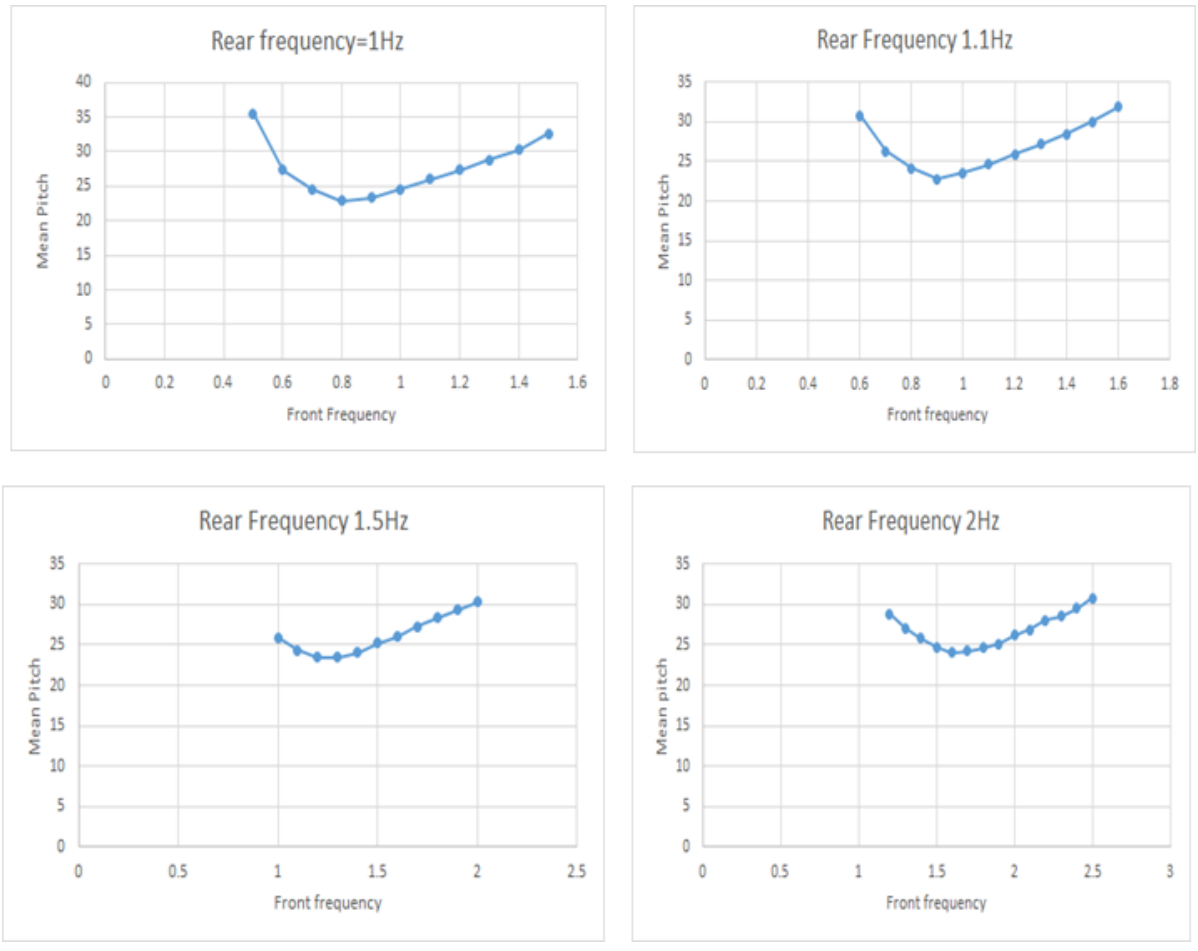

Figure 4: Phase lag at the front and rear of the vehicle when encountering a bump

In the above graphs, the rear ride frequency of the vehicle has been kept constant, and the front ride frequency(x-axis) is varied. By plotting the mean pitch as a function of the front frequency, it was observed that the average pitch angle for the entire ride is minimized when the ride frequency at the front of the vehicle is approximately 20% lower than the rear, as shown in the results. Thus, the conventional assumption can be validated.

IV. RESULTS AND DISCUSSION

As discussed, the purpose of this article is to determine the frequency of an ATV ride using a complete vehicle model. The findings reveal that the simulation outcomes for various parameters conform to the simulation

e-ISSN: 2582-5208
International Research Journal of Modernization in Engineering Technology and Science
(Peer-Reviewed, Open Access, Fully Refereed International Journal)
Volume:05/Issue:05/May-2023 Impact Factor- 7.868 www.irjmets.com

conditions, fluctuating in a periodic manner akin to the sinusoidal disturbance imposed on them. The objective of the study was to determine the best combination of ride frequency for the front and rear of a vehicle. To achieve this, we utilized a weighted average of the mean pitch, mean roll, and mean sprung mass displacement. The provided table showed the frequencies for both the front and rear of the vehicle, as well as their corresponding weighted averages. In our research, we gave the most significant weight to the mean pitch, while we assigned equal weights to both the mean roll and CG displacement.

In order to achieve maximum stability, it is recommended to select the frequency combination with the lowest weighted average. Based on our analysis, the combination of 1Hz as the front frequency and 1.2 Hz as the rear frequency was found to be the optimal choice. Therefore, this combination was selected as the final result. In general, it is observed that combinations with higher frequencies can lead to an increase in the sprung mass displacement, which is generally undesirable. As a result, it is recommended to avoid frequency combinations that are higher in value.

Table 2: Frequency Combinations

Front frequency (Hz)	**Rear frequency (Hz)**	**Weighted Average (60*pitch) +(20*roll) + (20*cg displacement)**
0.8	1	54.387
1	1.2	53.606
1.2	1.5	62.199
1.4	1.7	64.842
1.6	2.0	72.219

V. CONCLUSION

The development and validation of a complete 7-degree-of-freedom model for a full car vehicle using Simulink has been a success. This model accurately captures the vehicle's dynamics by accounting for the motion of the car in three-dimensional space and its pitch, roll, and yaw angles. The simulation results obtained from the model have been verified to comply with established vehicle dynamics principles, which are essential for ensuring the vehicle's optimal performance in real-life scenarios. The model's ability to calculate the optimal ride frequency for different vehicle configurations makes it an invaluable tool for vehicle design and optimization.

However, even though the model has been validated, there is still a need to confirm its results in various real-life scenarios. Alternative modeling techniques such as Genetic Algorithm and Fuzzy Logic can also be used to perform similar simulations, further improving the accuracy and reliability of the results. Incorporating more precise assumptions about the car's chassis and tires in future research work can also increase the accuracy of the model.

Overall, there are several promising areas for future research in this field. The use of advanced modeling techniques and incorporating more accurate assumptions regarding the vehicle's components can significantly enhance the model's reliability and accuracy. These findings can then be applied to design and optimize vehicle performance, resulting in safer and more efficient automobiles.

MATHEMATICAL NOTATIONS

k_{sf}= Stiffness of front spring.

k_{sr} = Stiffness of rear spring.

m_s = sprung mass.

C_{sf} = damping stiffness of front suspension.

C_{sr} = damping stiffness of rear suspension.

K_t = tire stiffness.

Z_{cg} = displacement of cg.

Z_r = displacement of road.

Z_{fr} = displacement of front right wheel.

Z_{fl} = displacement of front left wheel.

Z_{rr} = displacement of rear right wheel.

Z_{rl} = displacement of rear left wheel.

I_x = moment of inertia in roll.

I_y = moment of inertia in pitch.

a = distance between front tyre center and CG in longitudinal direction.

b = distance between rear tyre center and CG in longitudinal direction.

c = distance between tyre Centre and CG in lateral direction.

m_f = Unsprung mass of front right/left wheel.

m_r = Unsprung mass of rear right/left wheel.

MR = motion ratio.

ACKNOWLEDGEMENTS

We would like to place on record our deep sense of gratitude to our mentor and advisor Dr. Atul Kumar Agarwal, Professor, Dept. of Mechanical Engineering, Delhi Technological University, Delhi for his patience, generous guidance, help, useful suggestions, and continuous encouragement throughout the course of present work and for enlightening us with his immense knowledge of the subject. His cooperation and support during the whole research process was one of the main reasons we could complete this thesis with a satisfactory conclusion. We also wish to extend our thanks to the faculty of the Department of Mechanical Engineering and the Head of the Department, Dr. SK Garg, and other colleagues for their insightful comments and constructive suggestions to improve the quality of this project work.

VI. REFERENCES

[1] Hedrick, J.K., Nonlinear control of a Quarter Car active suspension, Proceedings of the American Control Conference, Chicago, June 1992.

[2] Gobbi, M. and Mastinu, G., Analytical description and optimization of the dynamic behaviour of passively suspended road vehicles, Journal of Sound and Vibration, Vol.245, No.3, 2001, pp. 457 – 481.

[3] Lin, Y., and Kortum, W., Identification of system physical parameters for vehicle systems with nonlinear components, International Journal of Vehicle Mechanics and Mobility, Vol.46, No.12, 2007, pp. 354 – 365.

[4] Roberto Spinola Barbosa, Vehicle vibration response subjected to long wave measured pavement roughness, Journal of Mechanical Engineering and Automation, Vol. 2, No.2, 2012, pp. 17 – 24.

[5] Phalke, T. P., and Mitra, A. C., "Analysis of Ride comfort and Road holding of Quarter car model by SIMULINK" Mater. Today. Proc 4(2) 2425-2430 (2017).

[6] W. Can, W. Weirui, "Chaotic Behaviors of Half Car Model Excited by the Road Surface Profile," Information Science and Engineering (ICISE), 2009 1st International Conference pp.3752-3755, Nanjing, China, 18-20 Dec. 2009.

[7] P.S.A. Singh, I.Z.M. Darus, "Enhancement of SUV Roll Dynamics Using Fuzzy Logic Control," Informatics and Computational Intelligence (ICI), 2011 First International Conference, pp. (106-111), Bandung, Indonesia, 12-14 Dec. 2011

[8] Libin Li, and Qiang Li., Vibration analysis based on full multi-body model for the commercial vehicle suspension system, Proceedings of the 6th International Conference on Signal Processing, Robotics and Automation, Greece, February 2007, pp. 203 – 207.

[9] N. P. Puneet , Abhinandan Hegale , Hemantha Kumar and K. V. Gangadharan , Multi objective optimization for quarter car parameters for better ride comfort and road holding. (2021).

[10] Hajkurami, H., Samandari, H., Ziaei-Rad, S., Analysis of chaotic vibration of nonlinear seven degree of freedom full car model, 3rd International Conference on Integrity, Reliability and Failure, Portugal, July 2009.

[11] Ammar Majid Hameed Al-Ghanim, Dr. Ameen Ahmed Nassar "Modeling, Simulation, and Control of Half Car suspension system using MATLAB/SIMULINK". (2018)

[12] Tech Tip: Springs & Dampers by Matt Giaraffa.

[13] Kasi Kamalakkannan, Elayperumal, A., and Satyaprasad Managalaramam., Simulation aspects of a full-car ATV model semi active suspension, Journal of Scientific Research Engineering, Vol.4, 2012, pp.384 – 389.

[14] A PhD dissertation by Fu-Cheng Wang, "Design and Synthesis of Active and Passive Vehicle Suspensions", University of Cambridge, September 2001.

[15] Eng. Ahmad Alenezi, "Active Suspension Control based on a Full-Vehicle Model", IOSR Journal of Electrical and Electronics Engineering (IOSR-JEEE) e-ISSN: 2278-1676, p-ISSN: 2320-3331, Volume 9, Issue 2 Ver. VI (Mar – Apr. 2014), PP 06-18.

[16] J. NireshN, ArchanaG, Raj "Optimisation of Linear Passive Suspension System Using MOPSO and Design of Predictive Tool with Artificial Neural Network.

2023 International Conference on Advancement in Computation & Computer Technologies (InCACCT) | 979-8-3503-9648-5/23/$31.00 ©2023 IEEE | DOI: 10.1109/InCACCT57535.2023.10141709

DIGITAL IMAGE ENCRYPTION USING 256-BIT ADVANCED ENCRYPTION STANDARD ALGORITHM

Jaideep kala
Department of Electronics and Communication
Delhi Technological University
New Delhi, India
jaideepkala_2k21spd04@dtu.ac.in

Jeebananda Panda
Department of Electronics and Communication
Delhi Technological University
New Delhi, India
jpanda@dce.ac.in

Lavi Tanwar
Department of Electronics and Communication
Delhi Technological University
New Delhi, India
lavi.tanwar@dtu.ac.in

***Abstract*— Ensuring secure communication of multi-media messages is crucial for social networking and data sharing platforms. Prevention of data manipulation and theft has led to the development of various encryption techniques, but scope remains for a fast and efficient multi-media encryptor. Advanced Encryption Standard (AES) is mathematically one of the most complex cipher algorithms to crack and has been widely deployed in the banking sector. This paper aims to present a high throughput implementation of 256-bit AES cipher for encrypting digital images and explore its practicality in peer-to-peer communication. Pre-processing of images has been performed to make them suitable for encryption. A detailed study of the encryption results and histogram analysis has been carried out. The proposed algorithm achieved a Peak Signal to Noise Ratio (PSNR) of 61 dB for the decrypted image. Correlation between the input and the decrypted image was found to be 0.994 while the Mean Square Error (MSE) was calculated to be 0.0030.**

Keywords— Advanced Encryption Standard, Decryption, Images, Key, Secure, Simulation.

I. INTRODUCTION

Cyber-attacks and data theft are a major concern for companies worldwide. Securing messages containing digital images and videos for real time communication can be a difficult and computationally expensive task. AES has been widely used for secure storage and transmission of digital information but its application in real time image/video encryption has been limited [1]. Developed in the year 2001 by National Institute of Standards and Technology, AES is a cryptographic algorithm that uses a symmetric public key for undertaking encryption and decryption tasks [2]. It is robust to existing brute force attacks and has been widely used by financial institutions and government agencies to carry out secure transactions and sharing of sensitive information.

AES processes 128-bit packets of data, although it can have a key size of 128,192 or 256 bits [3]. AES-256 is the most secure form of AES encryption and consists of 14 rounds of iterations for manipulating data into an unrecognizable form [4]. Encryption of multimedia messages using existing cipher technologies requires high bandwidth and large latencies are observed in peer-to-peer communication [5]. A high throughput encryption technique coupled with modules for pre, and post processing of images is needed for solving this issue and have a vast application in social networking / message sharing apps. AES can operate in 5 different modes, most common among these are Cipher Block Chaining, Electronic Code Book [6]. ECB is a widely used mode as it does not require an Initialization Vector (IV) for its operations. CBC requires IV which may lead to propagation of error through the encryption stages [7]. The remaining part of this paper is presented as follows. Section II shows the related work carried out in this field and contribution of this paper. Section III discusses the proposed methodology and steps involved in image encryption. Section IV presents the results of encrypted and decrypted images along with their histogram analysis. Section V concludes the work carried out in this paper along with some limitations and future scope.

II. LITERATURE SURVEY

There have been significant efforts in the past aimed at utilizing AES algorithm for encrypting alphanumerical messages, but very limited work has been carried out for multimedia messages. Hajihassani et al. [8] proposed a high throughput AES architecture based on bit slicing, which processed 32 128-bit data stream parallelly to provide an encryption throughput of 1.47 Tbps. This method performs expensive Byte transformations using shifting and swapping of registers. Kim et al. [9] utilized the CTR mode in AES for fast encryption in low-end microcontrollers. This led to a reduced computation of 2 Add Round Key, 2 Shift-Rows, 2 Substitution Bytes, and 1 Mixed Column transformation. Alomari et al. [10] compared different encryption techniques for storage devices for different operating modes. A detailed performance analysis was done to provide guidelines for disk encryption. Le et al. [11] proposed a fast GPU parallel computing design for AES cryptography. This technique accelerates the speed of AES encryption significantly. A novel low latency FPGA based AES architecture was proposed by Zhang et al. [12] in which an efficient key expansion method along with pipelining was used to obtain a throughput of nearly 21.56 Gbps. Custom S-box techniques are implemented for low energy consumption applications for AES designed for battery operated devices [13],[14]. Pipelined AES architectures proposed by Chellappa et al. [15] and Oukili et al. [16] provided high throughput encryption of up to 64-79 Gbps.

ISBN: 979-8-3503-9648-5/23/$31.00 ©2023 IEEE

Authorized licensed use limited to: DELHI TECHNICAL UNIV. Downloaded on June 14,2023 at 05:02:33 UTC from IEEE Xplore. Restrictions apply.

For encryption of images, Zhang et al. [17] performed MATLAB implementation of AES-128 followed by digital image processing to obtain the encrypted and recovered test image. AES in CBC mode was utilized for image encryption [18] and its security performance was tested and compared with existing systems based on chaos. A similar system was proposed by Arab et al. [19] for novel image encryption using chaos sequence and an improvised AES-128. This approach reduces computational time and increases the diffusion ability of the proposed scheme. Singh et al. [20] proposed a dynamic AES developed using key dependent S-box for image encryption. Contributions of this paper:

- This paper intends to incorporate a high throughput image encryption system using 256-bit AES algorithm, while maintaining design simplicity and ease of implementation.
- A detailed study is carried out by analyzing histogram and correlation data for the encrypted and recovered (decrypted) images.

III. Methodology

AES encrypts a stream of input data by performing several substitution and shifting operations in an iterative manner. A 256-bit AES algorithm comprises of 14 rounds of transformation. In the proposed method a 256-bit key is entered by the user (as plain text) along with the input image that needs to be encrypted. The cipher key is symmetric in nature i.e., the same key is utilized for encryption and decryption process [21]. The symmetric key undergoes expansion from 8 words (4 bytes each) to 60 words using the key expansion process. Each iterative round manipulates the input through a series of substitutions and permutations based on Shannon's theory of confusion and diffusion [22]. Each of these rounds consist of four processes, Substitute bytes, Shift rows, Mix Column and Add round keys [23]. Only the last round is different from previous rounds as it does not contain mix-column step. Before the input matrix is passed through the first stage, the key is XORed with the input matrix and then the key expansion process takes place. All operations inside the AES are performed on 128-bit packets of data arranged in a 4×4 matrix with each element of size 1 byte.

A. Key Expansion

The 256-bit cipher key provided by the user is first converted to hexadecimal form and XORed with input message/Image matrix in the pre-round transformation. The 8-word cipher key is then expanded to 60 words as shown in Figure 1.

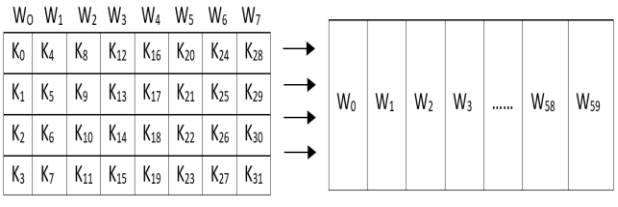

Fig.1. Key Expansion process for 256-bit symmetric key.

Figure 2 shows the process of obtaining the next four words (W_8-W_{11}) from the last 4 words (W_4-W_7) of the original cipher key using the "g" function.

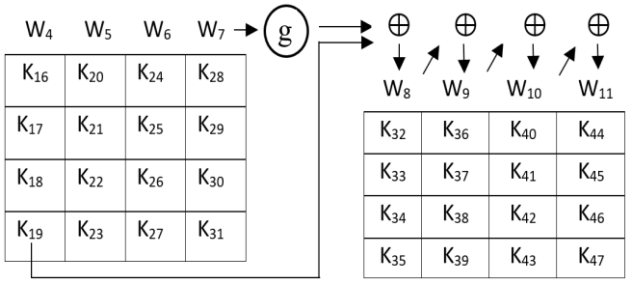

Fig.2. Key expansion operation for obtaining next 4 key words.

Mathematically this expansion can be represented as:

$$W_8 = W_4 \oplus g(W_7) \quad (1)$$

$$W_9 = W_8 \oplus W_5 \quad (2)$$

$$W_{10} = W_9 \oplus W_6 \quad (3)$$

$$W_{11} = W_{10} \oplus W_7 \quad (4)$$

Here $g(W_7)$ is obtained by performing a 3-step process, one-byte circular left-shift of W_7 to get X_1 and then performing a byte substitution operation on each byte of X_1 using Substitution box to get Y_1.

Finally,

$$g(W_7) = Y_1 \oplus R_{CON}[j] \quad (5)$$

Here $R_{CON}[j]$ is the round constant matrix described for each iteration as shown in Figure 3 [24].

R1	R2	R3	R4	R5	R6	R7	R8	R9	R10	R11	R12	R13	R14
01	02	04	08	10	20	40	80	1B	36	6C	D8	200	400
00	00	00	00	00	00	00	00	00	00	00	00	00	00
00	00	00	00	00	00	00	00	00	00	00	00	00	00
00	00	00	00	00	00	00	00	00	00	00	00	00	00

Fig. 3. Round constants R_1-R_{14} for 14 rounds of transformation [24].

B. Substitute Bytes

Substitute bytes is the first operation in each iterative round. The state matrix obtained after pre-round transformation is used as input here and each element of this intermediate matrix is replaced by a new element using the 16×16 LUT S-box shown in Figure 4.[25].

	0	1	2	3	4	5	6	7	8	9	A	B	C	D	E	F
0	77	E5	52	C0	3D	AF	18	8A	E3	71	C6	54	A9	3B	8C	1E
1	5E	CC	7B	E9	14	86	31	A3	CA	58	EF	7D	80	12	A5	37
2	25	B7	00	92	6F	FD	4A	D8	B1	23	94	06	FB	69	DE	4C
3	0C	9E	29	BB	46	D4	63	F1	98	0A	BD	2F	D2	40	F7	65
4	D3	41	F6	64	99	0B	BC	2E	47	D5	62	F0	0D	9F	28	BA
5	FA	68	DF	4D	B0	22	95	07	6E	FC	4B	D9	24	B6	01	93
6	81	13	A4	36	CB	59	EE	7C	15	87	30	A2	5F	CD	7A	E8
7	A8	3A	8D	1F	E2	70	C7	55	3C	AE	19	8B	76	E4	53	C1
8	3E	AC	1B	89	74	E6	51	C3	AA	38	8F	1D	E0	72	C5	57
9	17	85	32	A0	5D	CF	78	EA	83	11	A6	34	C9	5B	EC	7E
A	6C	FE	49	DB	26	B4	03	91	F8	6A	DD	4F	B2	20	97	05
B	45	D7	60	F2	0F	9D	2A	B8	D1	43	F4	66	9B	09	BE	2C
C	9A	08	BF	2D	D0	42	F5	67	0E	9C	2B	B9	44	D6	61	F3
D	B3	21	96	04	F9	6B	DC	4E	27	B5	02	90	6D	FF	48	DA
E	C8	5A	ED	7F	82	10	A7	35	5C	CE	79	EB	16	84	33	A1
F	E1	73	C4	56	AB	39	8E	1C	75	E7	50	C2	3F	AD	1A	88

Fig. 4. Substitution byte transformation using 16x16 S-box [25].

C. Shift Rows

The result obtained from previous step undergoes a left shift as depicted in figure 5. No shifting takes place in the first row of the matrix, a 1-byte circular left shift takes place

Authorized licensed use limited to: DELHI TECHNICAL UNIV. Downloaded on June 14,2023 at 05:02:33 UTC from IEEE Xplore. Restrictions apply.

in the second row, followed by 2 and 3 bytes circular left shift in row 3 and 4 respectively [26]. Figure 5 shows the shifting operation performed on the data.

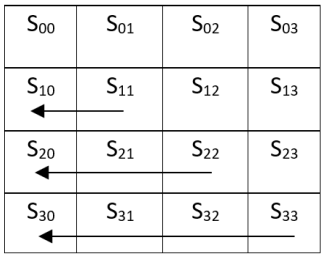

Fig 5. Shift rows operation on 128-bit block size data.

D. Mix Columns and Add Round Keys

In this step, the result obtained from previous step under goes bit by bit multiplication with a constant matrix followed by the XOR operation with extended key. After this operation is complete, the state matrix is passed onto next round and same process repeats with the data [27]. Figure 6 shows the complete flow of data through different rounds in the AES-256 algorithm and the XOR operations in each round.

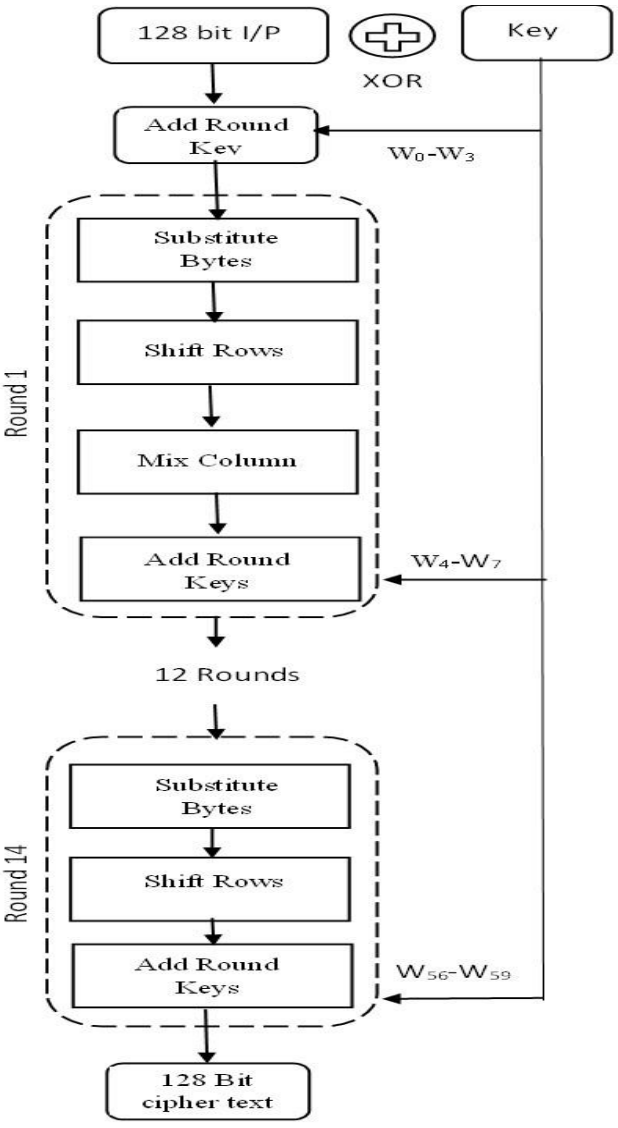

Fig.6. XOR of expanded key with each round of AES.

E. Image encryption using AES-256

Digital image undergoes pre-processing before it is sent for encryption. In this paper a digital color image has been taken under consideration. First the Red, Green, and Blue (RGB) layers are extracted from the image [28]. This image is then converted to grey scale format of size 256×256 pixels. This grey scale image is then broken into 4×4 matrices (128-bits each) with each element of size 1 byte. These matrices are fed to the input of AES-256 algorithm along with the 256-bit cipher key and encrypted 4×4 matrices are obtained at output, which are then stitched together to form the 256×256 encrypted image [29]. Each set of 4×4 matrix undergoes exactly same encryption process. Figure 7 shows the flow chart for RGB image encryption with an image pre-processing component at top of the AES cipher.

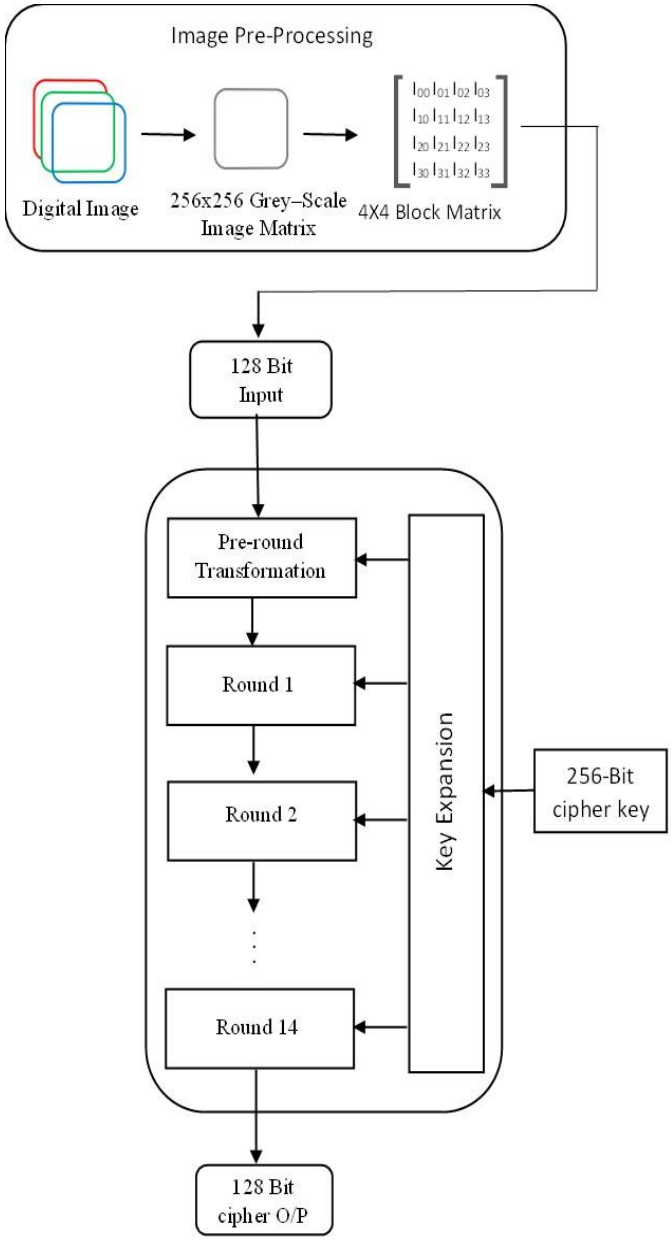

Fig.7. Flow chart for encryption process of RGB Image.

Authorized licensed use limited to: DELHI TECHNICAL UNIV. Downloaded on June 14,2023 at 05:02:33 UTC from IEEE Xplore. Restrictions apply.

IV. RESULTS

The implementation and simulation of AES-256 for digital image encryption has been carried out on MATLAB 2021a. The 256-bit key considered for encryption is "*secure encryption password 10111*" (32 characters in plain text). Cipher key representation in hex format "*736563757265206 56e6372797074696f6e207061737377 6f7264203130313131*". Figure 8 shows the RGB image along with its histogram plot and its gray scale conversion and corresponding histogram plot. The 4×4 image matrices extracted from the gray scale image that is fed into the encryptor is shown in figure 9. The packets of 4×4 encrypted images obtained at the encryptor output are stitched together to form the 256×256 pixels encrypted form of the original gray scale image. Figure 10 shows the 4×4 encrypted image matrix (in Hex).

Figure 11 shows the Encrypted image and its histogram plot along with the recovered image (decrypted) and its corresponding histogram plot. The results exhibited a high PSNR of 61 dB for the decrypted image and the correlation between the input digital image and the decrypted (recovered) image was found to be 0.994. The MSE between the input and the decrypted image was calculated to be 0.0030, indicating very low levels of distortion in the recovered image. This proves that AES-256 is highly suitable for image encryption and is robust to any distortions induced during the encryption processes. Decryption of the encrypted image matrix follows similar approach as the encryption, an inverted S-box is utilized but the flow remains mostly same [30]. Post processing of obtained decrypted matrix is done for stitching of image and conversion to original form.

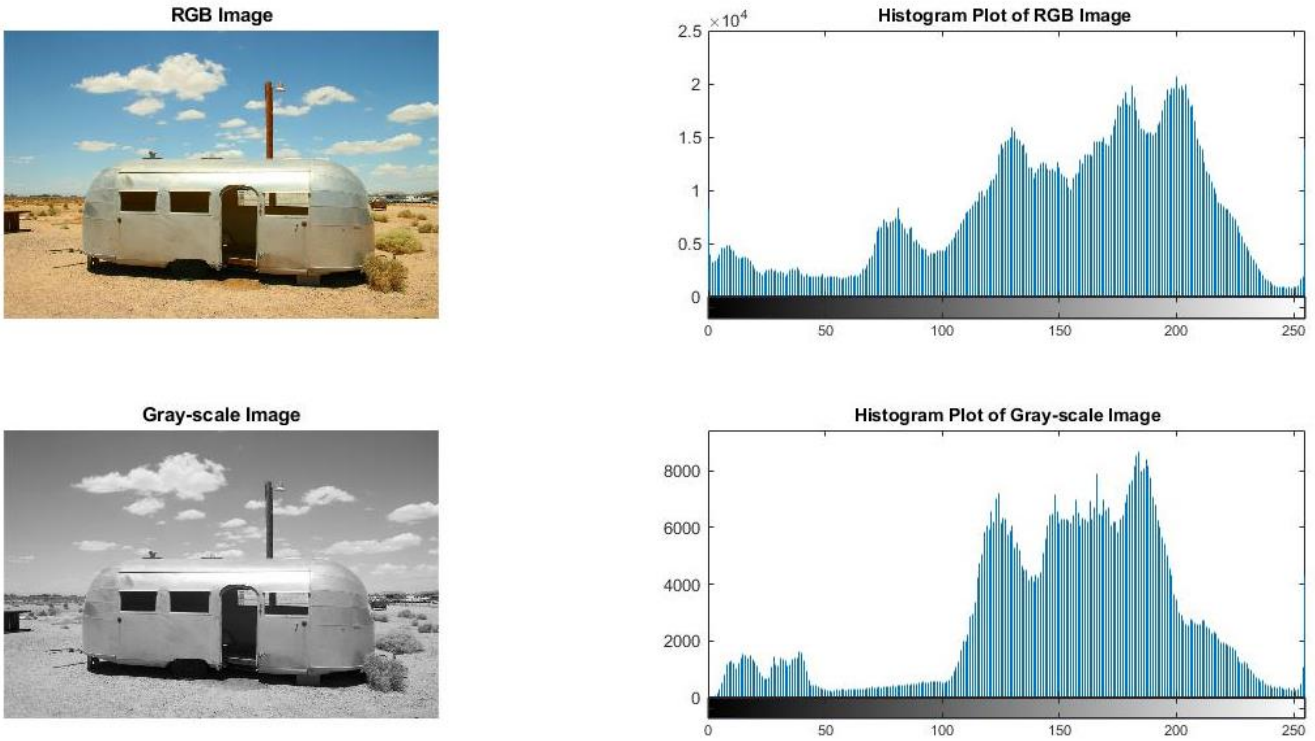

Fig. 8. RGB Image and Gray scale image with their Histogram plots.

Fig. 9. Input image matrix to the AES-256.

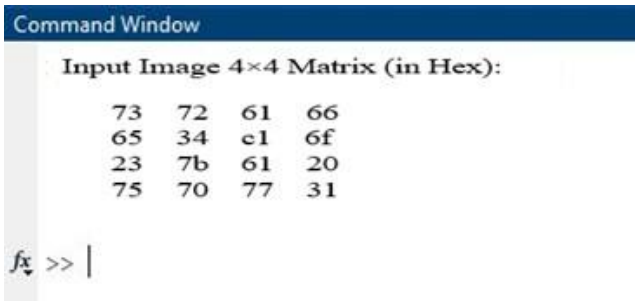

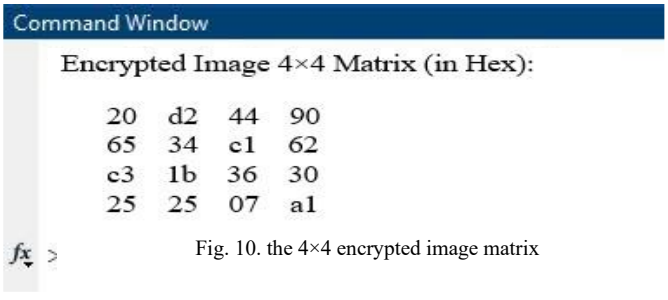

Fig. 10. the 4×4 encrypted image matrix

Authorized licensed use limited to: DELHI TECHNICAL UNIV. Downloaded on June 14,2023 at 05:02:33 UTC from IEEE Xplore. Restrictions apply.

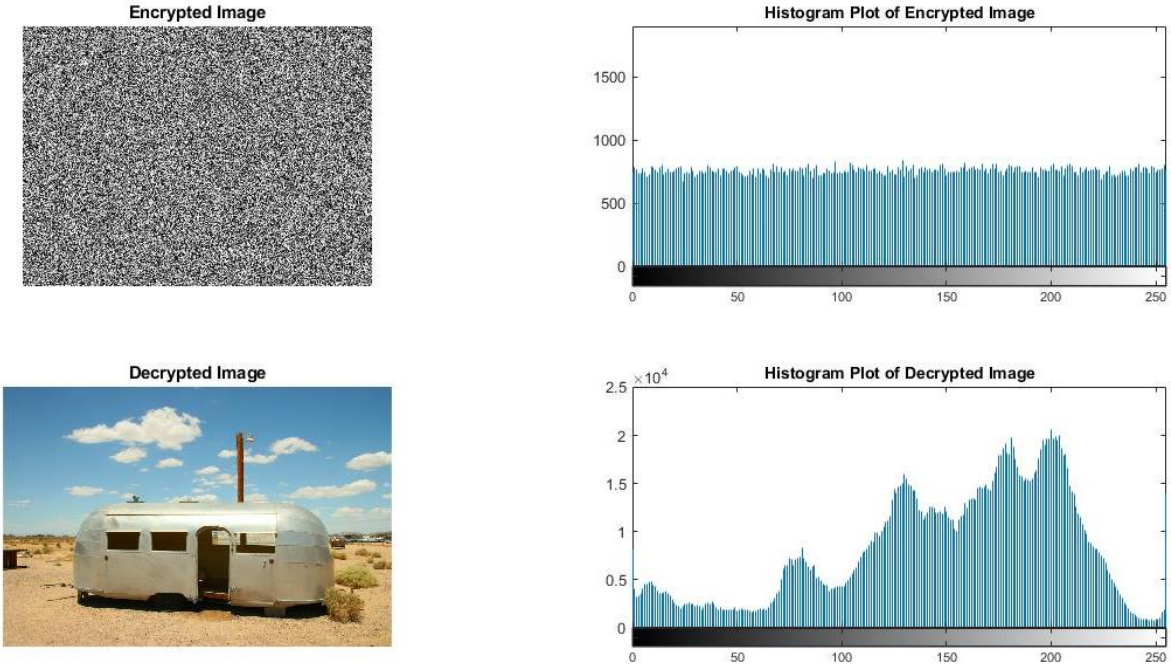

Fig. 11. Encrypted & Decrypted images with their Histogram plots.

V. CONCLUSIONS

This paper proposed an efficient and high throughput 256-bit AES cipher algorithm for encrypting digital image. A user input symmetric cipher key-based encryption process was simulated along with preprocessing of image data. A detailed study of the input image and the encrypted/decrypted images was carried out along with their histogram plots. The results exhibited high PSNR of 61 dB for the decrypted image and the correlation between the input image and the decrypted image was found to be 0.994. The MSE between the two images was calculated to be 0.0030. This architecture proved to be more efficient and easier to implement as compared to other techniques adopted for image encryption and has vast applications in messaging apps and data sharing platforms. The results proved the robustness of the algorithm as very little deviations were observed in the recovered image. AES is a computationally expensive and power-hungry algorithm hence not suitable for encryption of high-resolution images when there are low power constraints. Future improvements on this work include pipelining of AES algorithm for higher throughput and use of a low power multiplier in the mix-column step to reduce the power consumption. AES-256 can be made furthermore secure using a dynamic S-box in the substitution byte step.

REFERENCES

[1] S. H. Kamali, R. Shakerian, M. Hedayati and M. Rahmani, "A new modified version of Advanced Encryption Standard based algorithm for image encryption," 2010 International Conference on Electronics and Information Engineering, Kyoto, Japan, 2010, pp. V1-141-V1-145, doi: 10.1109/ICEIE.2010.5559902.

[2] W. E. Burr, "Selecting the Advanced Encryption Standard," in IEEE Security & Privacy, vol. 1, no. 2, March-April 2003, pp. 43-52, doi: 10.1109/MSECP.2003.1193210.

[3] D. -H. Bui, D. Puschini, S. Bacles-Min, E. Beigné and X. -T. Tran, "AES Datapath Optimization Strategies for Low-Power Low-Energy Multisecurity-Level Internet-of-Things Applications," in IEEE Transactions on Very Large Scale Integration (VLSI) Systems, vol. 25, no. 12, Dec. 2017, pp. 3281-3290, doi: 10.1109/TVLSI.2017.2716386.

[4] P. Hamalainen, T. Alho, M. Hannikainen and T. D. Hamalainen, "Design and Implementation of Low-Area and Low-Power AES Encryption Hardware Core," 9th EUROMICRO Conference on Digital System Design (DSD'06), 2006, pp. 577-583, doi: 10.1109/DSD.2006.40.

[5] A. Das and M. M. Islam, "SecuredTrust: A Dynamic Trust Computation Model for Secured Communication in Multiagent Systems," in IEEE Transactions on Dependable and Secure Computing, vol. 9, no. 2, March-April 2012, pp. 261-274, doi: 10.1109/TDSC.2011.57.

[6] S. Almuhammadi and I. Al-Hejri, "A comparative analysis of AES common modes of operation," 2017 IEEE 30th Canadian Conference on Electrical and Computer Engineering (CCECE), Windsor, ON, Canada, 2017, pp. 1-4, doi: 10.1109/CCECE.2017.7946655.

[7] D. Jayasinghe, R. Ragel, J. A. Ambrose, A. Ignjatovic and S. Parameswaran, "Advanced modes in AES: Are they safe from power analysis based side channel attacks?," 2014 IEEE 32nd International Conference on Computer Design (ICCD), Seoul, Korea (South), 2014, pp. 173-180, doi: 10.1109/ICCD.2014.6974678.

[8] O. Hajihassani, S. K. Monfared, S. H. Khasteh and S. Gorgin, "Fast AES Implementation: A High-Throughput Bitsliced Approach," in IEEE Transactions on Parallel and Distributed Systems, vol. 30, no. 10, 1 Oct. 2019, pp. 2211-2222, doi: 10.1109/TPDS.2019.2911278.

[9] K. Kim, S. Choi, H. Kwon, Z. Liu, and H. Seo, "FACE–LIGHT: Fast AES–CTR Mode Encryption for Low-End Microcontrollers." Lecture Notes in Computer Science, 2020, pp. 102-114, doi: 10.1007/978-3-030-40921-0_6.

[10] M. A. Alomari, K. Samsudin and A. R. Ramli, "A Study on Encryption Algorithms and Modes for Disk Encryption," 2009 International Conference on Signal Processing Systems, Singapore, 2009, pp. 793-797, doi: 10.1109/ICSPS.2009.118.

Authorized licensed use limited to: DELHI TECHNICAL UNIV. Downloaded on June 14,2023 at 05:02:33 UTC from IEEE Xplore. Restrictions apply.

[11] D. Le, J. Chang, X. Gou, A. Zhang and C. Lu, "Parallel AES algorithm for fast Data Encryption on GPU," 2010 2nd International Conference on Computer Engineering and Technology, Chengdu, China, 2010, pp. V6-1-V6-6, doi: 10.1109/ICCET.2010.5486259.

[12] X. Zhang and K. K. Parhi, "High-speed VLSI architectures for the AES algorithm," in IEEE Transactions on Very Large Scale Integration (VLSI) Systems, vol. 12, no. 9, Sept. 2004, pp. 957-967, doi: 10.1109/TVLSI.2004.832943.

[13] C. Duran and E. Roa, "A 10pJ/bit 256b AES-SoC Exploiting Memory Access Acceleration," in IEEE Transactions on Circuits and Systems II: Express Briefs, vol. 69, no. 3, March 2022, pp. 1612-1616, doi: 10.1109/TCSII.2021.3126984.

[14] M. Sumio, and A. Satoh. "An optimized S-Box circuit architecture for low power AES design." In *International Workshop on Cryptographic Hardware and Embedded Systems*, Springer, Berlin, Heidelberg, 2002, pp. 172-186.

[15] S. Chellappa, C. Ramamurthy, V. Vashishtha and L. T. Clark, "Advanced encryption system with dynamic pipeline reconfiguration for minimum energy operation," Sixteenth International Symposium on Quality Electronic Design, 2015, pp. 201-206, doi: 10.1109/ISQED.2015.7085425.

[16] S. Oukili and S. Bri, "High speed efficient advanced encryption standard implementation," 2017 International Symposium on Networks, Computers and Communications (ISNCC), 2017, pp. 1-4, doi: 10.1109/ISNCC.2017.8071975.

[17] Q. Zhang and Q. Ding, "Digital Image Encryption Based on Advanced Encryption Standard (AES)," 2015 Fifth International Conference on Instrumentation and Measurement, Computer, Communication and Control (IMCCC), Qinhuangdao, China, 2015, pp. 1218-1221, doi: 10.1109/IMCCC.2015.261.

[18] Y. Zhang, "Test and Verification of AES Used for Image Encryption." 3D Research, vol. 9, no. 1, 2018, doi: 10.1007/s13319-017-0154-7.

[19] A. Arab, M. J. Rostami, and B. Ghavami, "An image encryption method based on chaos system and AES algorithm." The Journal of Supercomputing, vol. 75, no. 10, 2019, pp. 6663-6682, doi: 10.1007/s11227-019-02878-7.

[20] A. Singh, P. Agarwal and M. Chand, "Image Encryption and Analysis using Dynamic AES," 2019 5th International Conference on Optimization and Applications (ICOA), Kenitra, Morocco, 2019, pp. 1-6, doi: 10.1109/ICOA.2019.8727711.

[21] C. H. Kim, "Improved Differential Fault Analysis on AES Key Schedule," in IEEE Transactions on Information Forensics and Security, vol. 7, no. 1, Feb. 2012, pp. 41-50, doi: 10.1109/TIFS.2011.2161289.

[22] C. E. Shannon, "Communication theory of secrecy systems," in The Bell System Technical Journal, vol. 28, no. 4, Oct. 1949, pp. 656-715, doi: 10.1002/j.1538-7305.1949.tb00928.x.

[23] C. Sivakumar and A. Velmurugan, "High Speed VLSI Design CCMP AES Cipher for WLAN (IEEE 802.11i)," 2007 International Conference on Signal Processing, Communications and Networking, Chennai, India, 2007, pp. 398-403, doi: 10.1109/ICSCN.2007.350770.

[24] N. Su, Y. Zhang and M. Li, "Research on Data Encryption Standard Based on AES Algorithm in Internet of Things Environment," 2019 IEEE 3rd Information Technology, Networking, Electronic and Automation Control Conference (ITNEC), Chengdu, China, 2019, pp. 2071-2075, doi: 10.1109/ITNEC.2019.8729488.

[25] A. Hodjat and I. Verbauwhede, "Area-throughput trade-offs for fully pipelined 30 to 70 Gbits/s AES processors," in IEEE Transactions on Computers, vol. 55, no. 4, April 2006, pp. 366-372, doi: 10.1109/TC.2006.49.

[26] A. Samiah, A. Aziz and N. Ikram, "An Efficient Software Implementation of AES-CCM for IEEE 802.11i Wireless St," 31st Annual International Computer Software and Applications Conference (COMPSAC 2007), Beijing, China, 2007, pp. 689-694, doi: 10.1109/COMPSAC.2007.62.

[27] Hua Li and Z. Friggstad, "An efficient architecture for the AES mix columns operation," 2005 IEEE International Symposium on Circuits and Systems (ISCAS), Kobe, 2005, pp. 4637-4640 Vol. 5, doi: 10.1109/ISCAS.2005.1465666.

[28] H. Wen et al., "Dynamic Selective Network for RGB-D Salient Object Detection," in IEEE Transactions on Image Processing, vol. 30, 2021, pp. 9179-9192, doi: 10.1109/TIP.2021.3123548.

[29] L. Vincent, "Morphological grayscale reconstruction in image analysis: applications and efficient algorithms," in IEEE Transactions on Image Processing, vol. 2, no. 2, April 1993, pp. 176-201, doi: 10.1109/83.217222.

[30] M. Mozaffari-Kermani and A. Reyhani-Masoleh, "A Low-Power High-Performance Concurrent Fault Detection Approach for the Composite Field S-Box and Inverse S-Box," in IEEE Transactions on Computers, vol. 60, no. 9, Sept. 2011, pp. 1327-1340, doi: 10.1109/TC.2011.85.

Authorized licensed use limited to: DELHI TECHNICAL UNIV. Downloaded on June 14,2023 at 05:02:33 UTC from IEEE Xplore. Restrictions apply.

2023 2nd International Conference on Smart Technologies and Systems for Next Generation Computing (ICSTSN) | 979-8-3503-4800-2/23/$31.00 ©2023 IEEE | DOI: 10.1109/ICSTSN57873.2023.10151531

Diospyros kaki's phytochemical mediated inhibition of GBM by targeting PDK-1: An in-silico docking and machine learning model.

Harsh Aahra
Department of Biotechnology
Delhi Technological University
New Delhi, India
aahraharash@gmail.com

Nida E Falak
Department of Biotechnology
Delhi Technological University
New Delhi, India
nidaefalak380@gmail.com

Dr. Asmita Das
Department of Biotechnology
Delhi Technological University
New Delhi, India
asmitadas1710@dce.ac.in

***Abstract*— Glioblastoma Multiforme (GBM), a grade 4 brain tumor, is resistant to standard treatments and exhibits a 100 percent recurrence rate. By obstructing the primary pathways involved in tumour sustenance and progression, GBM can be completely eliminated. Since high levels of p-AKT (Phosphorylated Protein Kinase B) have been detected in recurring GBM, the AKTmTOR pathway has received the most attention in GBM therapies. AKT can be activated by PDK-1 (3-phosphoionsitide-dependent kinase-1) phosphorylation. Targeting and hampering PDK-1 can prevent such activation. Through in-silico analysis, this study seeks to investigate several phytochemicals that have the potential to target PDK-1. The phytochemical profile of *Diospyros kaki* holds immense significance. Carotenoids, tannins, and phenolic compounds impart *Diospyros kaki* excellent anti-oxidant potential making it a promising candidate for anticancer drug compound extraction. After docking 40 selected phytochemicals against PDK-1 protein, the results revealed that Diospyrin and Neodiospyrin show maximum binding energies (-10.6 and -10.4 kcal/mol respectively) comparable to that of the standard inhibitor 2-(5-{[2R)-2-amino-3-phenylpropyloxy}pyridine-3-yl)8,9dimethoxybenzo[c][2,7]naphthyridine-4-amine (ID-8I1) compound(-10.1 kcal/mol). Validating the docking results by machine learning, multiple analyses were carried out to find the drug likeness, bioactivity and bioavailability of the selected phytochemicals so as to imply them as a therapeutic agent against GBM.**

Keywords — ***Glioblastoma, PDK-1, Diospyros kaki, molecular docking, machine learning.***

I. INTRODUCTION

Glioblastoma owes its high chances of recurrence and resistance to therapy to a fraction of GBM cells that become highly active and begin to display characteristics resembling those of multipotent stem cells. These cells are referred to as Glioma Stem Cells (GSCs) [1] [2] Several pathways are involved in imparting tumorigenic potential to GSCs [3]. GBM occurrence and resistant to classical drugs like TMZ (Temozolomide) has been linked to genetic mutated or genetically altered (overexpressed) EGFR (Epidermal Growth Factor Receptor) [4]or increased phosphorylated AKT levels [2]

Studies reveal significantly increased phosphorylation of AKT protein in GBM tumor cells, that makes the P13/AKT/mTor pathway a potential blockade target. Upon receiving the signal from the RTKs (Receptor Tyrosine Kinases), PI3K (Phosphoinositide-3-kinase) converts PIP2(Phosphatidylinositol 4,5-bisphosphate) into PIP3 (phosphatidylinositol (3,4,5)-trisphosphate) which is further converted to AKT, the most significant player in the pathway. Being highly susceptible to mutations, it cannot be used a drug target site. PDK-1 is a regulatory enzyme which provides the phosphate group and hence phosphorylates AKT. This phosphorylated AKT in turn activates the mTORC1 (mammalian target of rapamycin complex 1) pathway and induces tumorigenic properties[5]

Numerous proteins, including PDK-1, PDK-2, or the TORC2 complex of the mTOR, phosphorylate AKT. AKT can be stimulated by PDK-1 phosphorylation alone, but PDK-2 or TORC2 facilitate increased phosphorylation[2] This work intends to target PDK-1 by phytochemicals derived from *Diospyros kaki* since PDK-1 stimulates oncogenesis and tumour sustenance through AKT[6]. Currently, phytochemicals are widely being implied as anticancer drugs due to their vast availability, simple extraction procedures and minimal toxicity[7]. Persimmons (*Diospyros kaki*) belonging to family Ebeneceae, not only excel in taste but also hold great therapeutic value. Being a rich source of polyphenols and antioxidants, their phytochemical configuration suggest that they can be implied as therapeutic agents against cancer cells [8].

40 phytochemicals derived from *Diospyros kaki* were assessed in an in-silico analysis against the PDK-1 protein. The molecular docking between these phytochemicals and PDK-1 was carried out using Autodock Vina [7]. Using compund 8I1 as a standard, the phytochemicals with binding affinities comparable to 8i1 were selected. The in-silico screening was performed in several steps, commencing with molecular docking to anticipate the interactions between phytochemicals and PDK-1, and then Machine Learning to verify and validate the docking results. The drug likeness of the selected phytochemicals was determined using various parameters like Lipinski's rule of five, Bioavailability radars and Bioactivity scores [7] [9], [10].

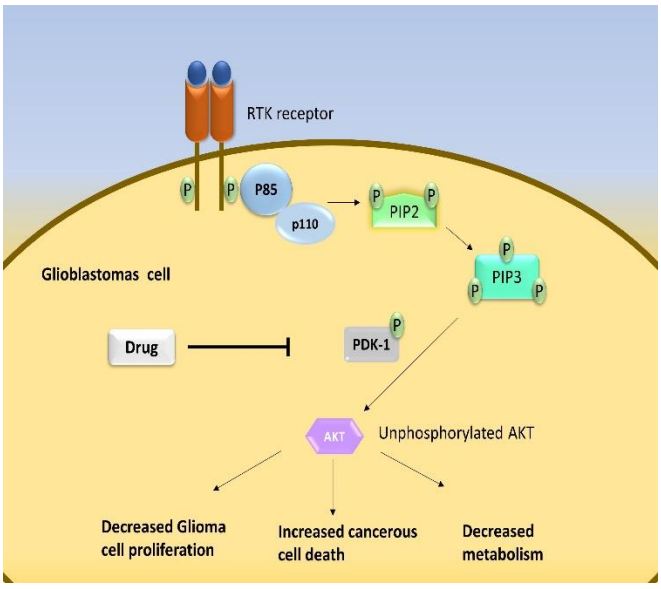

Figure 1: Depicts the phytochemical mediated inhibition of PDK-1 that affects the P13/AKT/mTor pathway in GBM cells resulting in decreased tumorigenic characteristics and eventually death of GBM tumour cells.

Authorized licensed use limited to: DELHI TECHNICAL UNIV. Downloaded on June 28,2023 at 06:27:32 UTC from IEEE Xplore. Restrictions apply.

II. MATERIALS AND METHODOLOGY

HP- Pavilion 11th Gen i5 Core with 16.0 GB and 64-bit operating system was used for the in-silico analysis. The protein structure of Human PDK-1 derived from the protein database[11] (PDB) coupled to 8il was selected as the receptor for docking.

The IMPPAT[12] database's pdb format was used to harvest forty bioactive chemicals from *Diospyros kaki*.

The Auto Dock 1.7.5 docking tool was used to perform molecular docking of actives to PDK-1 prepared structures, Open Babel GUI were used to prepare protein and ligands from pdb format to pdbqt format. Protein-ligand interaction fingerprints were generated using PLIP and the BIOVIA Discovery studio visualizer from the dock poses of actives with PDK-1 that achieved the best docking score. SwissADME[13], admetSAR, Molinspiration, Python, Random-forest classifier were used for further clarification of drug likeness of selected natural compounds.

A. Selection and preparation of ligands/Retrieving phytochemicals and preparation of drug library

Forty bioactive compounds from *Diospyros kaki* were collected from IMPPAT database in pdb format. [12].Using Open Babel GUI, pdbqt formats of the files were obtained.

B. Protein Preparation

The structure of target protein PDK-1 (3-Phosphoinositide-dependent kinase 1) was retrieved from PDB. Along with the target protein structure, the structure of PDK-1 inhibitor 8I1 was also retrieved to be used as a reference. [11]

Using Autodock Vina 1.7.5, Water molecules were removed and polar hydrogens along with Kollman's charges were added and pdbqt format of the protein was retrieved.

Open Babel GUI was used to convert inhibitor 8i1 from pdb format to pdbqt format.

C. Molecular docking

- **Protein-ligand docking using Auto dock Vina**: Autodock Vina 1.5.7 employed a computational docking strategy by setting the x, y, and z centre dimensions to -35.04, -26.046, and -1.741, respectively, and the x, y, and z sizes to 58, 48, and 74, respectively, docking analysis was performed. Number of modes and energy ranges were set to 10 and 4 respectively. All phytochemicals are docked against the target protein by using Auto dock Vina and Perl. The standard inhibitor 8i1 was also docked against target protein.
- **Docking/Interaction analysis**: The downloaded outputs from auto dock were analyzed via PLIP and Discovery studio to identify by which amino acid the ligand binds to the protein. The binding energies of ligands and standard were compared and phytochemicals with high binding energies were selected.

D. Confirmation by Machine Learning

- A machine learning model RandomForest classifier was built by 730 inhibitory compounds of PDK-1, which was obtained from CheMBL database[14] by using python library chembl_webresource_client to train the model on the basis of 307 molecular descriptors of aforementioned 730 inhibitory. Molecular descriptors are the chemical and physical properties of a chemical compound in the form of numeric values. The molecular descriptors of the compound were generated by using python library called Padelpy. These 307 molecular descriptors served as the model's training set. The data was divided into testing and training sets in a ratio of 20:80. Thereafter, the data was fed to the machine learning modelling RandomForestClassifier of python library scikit-learn, which was used to determine the prospective inhibitor of protein PDK1. The cross- validation score of the model came out to be 82.3.
- Phytochemicals Retrieval and Prediction: IMPPAT database was used to retrieve 40 phytochemicals of *Diospyros kaki*. The molecular descriptors of the phytochemicals were generated by python library Padelpy. After that, the trained machine learning model was used to determine the inhibitory phytochemicals.

E. Pharmacokinetic and Drug Likeness Screening of selected Phytochemicals:

Only phytochemicals that can get past the initial round of binding energy range screening are subjected to further analysis based on their drug likeness and pharmacokinetics.

- **Lipinski's RO5 analysis:** The rule of five assesses drug likeness, or the likelihood that a molecule will be active when taken orally. The selected phytochemicals were subjected to Lipinski's RO5 to analyze their oral activity. [15]
- **In-silico bioavailability analysis:** To comprehend the pharmacokinetics of a drug, it's vital to understand its absorption, distribution, metabolism, and excretion. In order to evaluate the bioavailability radars of the phytochemicals, SwissADME and admetSAR [13]were employed. By providing canonical SMILES of phytochemicals as input, these values can be determined
- **Bioactivity score:** To determine the druggability characteristics of ligands like NRL, PI, and EI, GPCR, ICM and KI, bioactivity score is required. The scores can be predicted by providing canonical SMILES of phytochemicals as input to

  Molinspiration**. (**Molinspiration Cheminformatics free web services, https://www.molinspiration.com, Slovensky Grob, Slovakia)

III. RESULTS

A. Docking Analysis

40 phytochemical of plant *Diospyros kaki* is extracted from database IMMPAT, and their Docking analysis reveal that Maximum binding energies were shown by Diospyrin (-10.6 kcal/mol), Neodiosprin (-10.4 kcal/mol), Vitexin (-9.6 kcal/mol), Beta-sitosterol (-8.7 kcal/mol), Flavylium (-8.4 kcal/mol). Further PLIP analysis revealed that Diospyrin, Neodiosprin and vitexin ligands show a good similarity between the interacting amino acids of test ligands and the standard ligand with the target protein PDK-1 (Table 1).

B. Machine learning analyses

In order to predict the inhibitory capability of Diospyros kaki phytochemicals using the ChEMBL database, we had selected the RandomForest classification approach to train the model on structural interaction fingerprints of targets. Ligand Data was further classified as active or inactive on the basis of their IC50 value. Latent knowledge, molecular interactions, and chemical property features were used to create 307 dimensional features for 730 natural chemicals by pedalpy. The generated features and confirmed data on pharmacological indications were used to train the machine learning model. The trained model accurately predicted prospective efficacies with high accuracy (87.3), sensitivity, and specificity when the characteristics of natural substances were used as input. Six phytochemicals with PDK-1 binding potential, namely

Authorized licensed use limited to: DELHI TECHNICAL UNIV. Downloaded on June 28,2023 at 06:27:32 UTC from IEEE Xplore. Restrictions apply.

Neodiospyrin, Diospyrin, Cyanidin, Vitexin, Flavylium, and Beta-sitosterol, were prioritised by the RandomForest models.

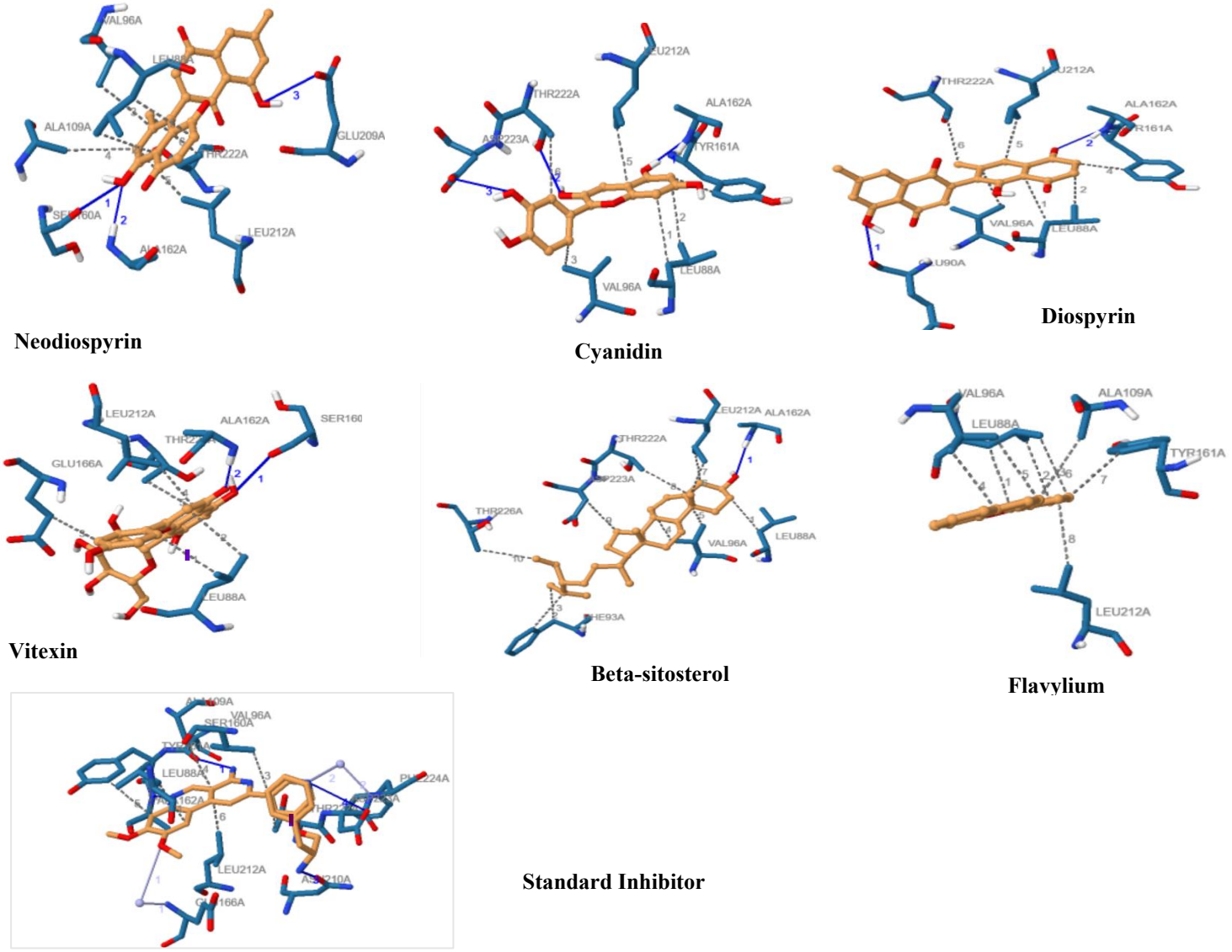

Figure 2: Molecular docking of ligands and target protein (PDK-1) from PLIP.

Table 1: Molecular docking of phytochemicals against target protein (PDK-1) in-silico

Phytochemical	Binding energy(kcal/mol)	Hydrogen bonds	KI	Amino acid participating
Diospyrin	-10.6	1	16.2 nM	ALA 162
Neodiospyrin	-10.4	2	22.8 nM	SER 160, ALA 162
Compound 8i1 (Standard inhibitor)	-10.1	3	37.8 nM	ALA 162, ASN 210, ASP 223
Vitexin	-9.6	2	88.2 nM	SER 160, ALA 162
Beta-sitosterol	-8.7	1	0.404 µM	ALA 162
Flavylium	-8.4	0	0.671 µM	0
Kaempferol	-8.3	2	0.795 µM	ALA 162, ASP 223
Cyanidin	-8.1	3	1.116 µM	ALA 162, THR 222, ASP 223
Plumbagin	-7.7	2	2.196 µM	SER 160, ALA 162

Authorized licensed use limited to: DELHI TECHNICAL UNIV. Downloaded on June 28,2023 at 06:27:32 UTC from IEEE Xplore. Restrictions apply.

Table 2: Lipinski's Rule of Five Analysis (RO5)
Mass<500, H-bond donors<5, Hbond acceptors<10, LogP value<5

Phytochemicals	Mass	Hydrogen bond donor	Hydrogen bond acceptor	LogP value	Molar refractivity	No. of violations
Neodiospyrin	374.35	2	6	3.1 1	101.30	0
Cyanidin	287.25	5	5	2.9 1	76.17	0
Diospyrin	374.35	2	6	3.1 1	101.3	0
Vitexin	432.38	7	10	0.0 9	106.61	1
Flavylium	207.25	0	0	4.3 8	66.06	0
Beta-sitosterol	441.72	1	1	8.0 2	133.23	1

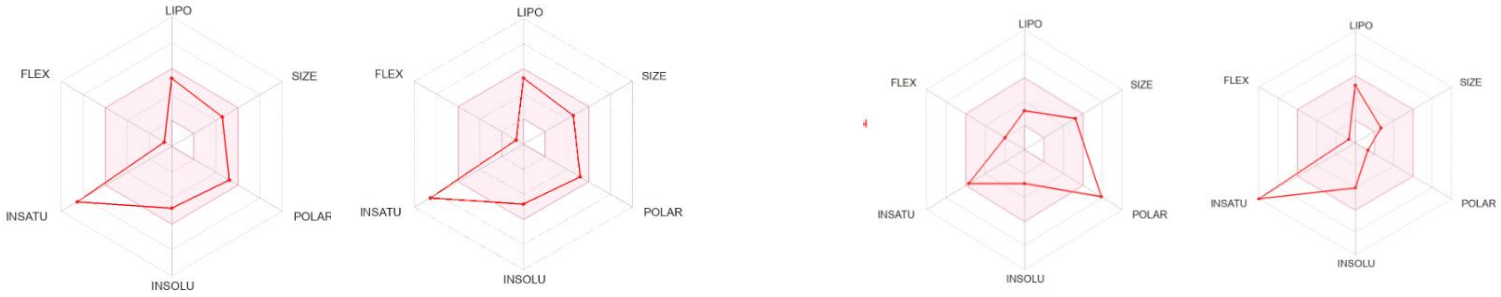

Figure 3: Bioavailability radars of Neodiospyrin, Diospyrin,Vitexin and Flavylium respectively retrieved using swisADME

Table 3: Bioactivity Scores of Phytochemicals retrieved from Molinspiration.
GPCR (G-Protein coupled receptor ligand), PI (Protease Inhibitor), EI (Enzyme Inhibitor), NRL(Nuclear Receptor Ligand), KI (Kinase Inhibitor), ICM (Ion Channel Modulator).

Phytochemical	GPCR	PI	EI	NRL	KI	ICM
Neodiospyrin	-0.10	-0.14	0.23	0.13	0.03	-0.28
Cyanidin	-0.13	-0.30	0.01	0.09	0.02	-0.09
Diospyrin	-0.06	-0.09	0.29	0.09	0.04	-0.18
Vitexin	0.13	0.03	0.46	0.23	0.19	-0.14
Flavylium	-0.61	-0.75	-0.38	-0.65	-0.57	-0.30
Beta-sitosterol	0.14	0.07	0.51	0.73	-0.51	0.04

IV. CONCLUSION

Side effects and toxicity exhibited by synthetic drugs used in cancer has shifted the focus towards non-toxic and easily available phytochemicals, to be used as anti-cancer therapeutic agents. *Diospyros kaki* is renowned for its numerous health benefits and possess many bioactive compounds in its phytochemical profile. This in-silico study aimed at suppressing PDK-1 activity with the aid of bioactive compounds derived from *Diospyros kaki*. Additional parameters like minimal cytotoxicity, maximum bioavailability, bioactivity and BBB (Blood Brain Barrier) permeation were also taken into account to categorize the phytochemicals as potential therapeutic drug. Other proteins involved in the AKT-mTOR pathway can also be inhibited implying the same approach. More research in this field should be encouraged to understand the fundamental molecular mechanisms behind the recurrence and sustenance of GSCs so that the exact proteins involved can precisely be pinpointed.

V. REFERENCES

[1] S. Daniele *et al.*, 'Dual Inhibition of PDK1 and Aurora Kinase A: An Effective Strategy to Induce Differentiation and Apoptosis of Human Glioblastoma Multiforme Stem Cells', *ACS Chem Neurosci*, vol. 8, no. 1, pp. 100–114, Jan. 2017, doi: 10.1021/acschemneuro.6b00251.

[2] E. Majewska, 'AKT/GSK3β Signaling in Glioblastoma', 2044, doi: 10.1007/s11064-016-2044-x/Published.

[3] M. Signore *et al.*, 'Combined PDK1 and CHK1 inhibition is required to kill glioblastoma stem-like cells in vitro and in vivo', *Cell Death Dis*, vol. 5, no. 5, 2014, doi: 10.1038/cddis.2014.188.

Authorized licensed use limited to: DELHI TECHNICAL UNIV. Downloaded on June 28,2023 at 06:27:32 UTC from IEEE Xplore. Restrictions apply.

[4] H. Xu *et al.*, 'Epidermal growth factor receptor in glioblastoma (Review)', *Oncol Lett*, vol. 14, no. 1, pp. 512–516, 2017, doi: 10.3892/ol.2017.6221.

[5] X. Li *et al.*, 'PI3K/Akt/mTOR signaling pathway and targeted therapy for glioblastoma', 2016. [Online]. Available: www.impactjournals.com/oncotarget

[6] H. J. Lin, F. C. Hsieh, H. Song, and J. Lin, 'Elevated phosphorylation and activation of PDK-1/AKT pathway in human breast cancer', *Br J Cancer*, vol. 93, no. 12, pp. 1372–1381, Dec. 2005, doi: 10.1038/sj.bjc.6602862.

[7] L. E. Mendie and S. Hemalatha, 'Molecular Docking of Phytochemicals Targeting GFRs as Therapeutic Sites for Cancer: an In Silico Study', *Appl Biochem Biotechnol*, vol. 194, no. 1, pp. 215–231, Jan. 2022, doi: 10.1007/s12010-021-03791-7.

[8] R. Direito, J. Rocha, B. Sepodes, and M. Eduardo-Figueira, 'From diospyros kaki L. (persimmon) phytochemical profile and health impact to new product perspectives and waste valorization', *Nutrients*, vol. 13, no. 9. MDPI, Sep. 01, 2021. doi: 10.3390/nu13093283.

[9] M. Z. Mumtaz, F. Kausar, M. Hassan, S. Javaid, and A. Malik, 'Anticancer activities of phenolic compounds from Moringa oleifera leaves: in vitro and in silico mechanistic study', *Beni Suef Univ J Basic Appl Sci*, vol. 10, no. 1, Dec. 2021, doi: 10.1186/s43088-021-00101-2.

[10] I. Muthiah, K. Rajendran, and P. Dhanaraj, 'In silico molecular docking and physicochemical property studies on effective phytochemicals targeting GPR116 for breast cancer treatment', *Mol Cell Biochem*, vol. 476, no. 2, pp. 883–896, Feb. 2021, doi: 10.1007/s11010-020-03953-x.

[11] H. M. Berman *et al.*, 'The Protein Data Bank', 2000. [Online]. Available: http://www.rcsb.org/pdb/status.html

[12] K. Mohanraj *et al.*, 'IMPPAT: A curated database of Indian Medicinal Plants, Phytochemistry and Therapeutics', *Sci Rep*, vol. 8, no. 1, Dec. 2018, doi: 10.1038/s41598-018-22631-z.

[13] A. Daina, O. Michielin, and V. Zoete, 'SwissADME: A free web tool to evaluate pharmacokinetics, drug-likeness and medicinal chemistry friendliness of small molecules', *Sci Rep*, vol. 7, Mar. 2017, doi: 10.1038/srep42717.

[14] A. Gaulton *et al.*, 'ChEMBL: A large-scale bioactivity database for drug discovery', *Nucleic Acids Res*, vol. 40, no. D1, Jan. 2012, doi: 10.1093/nar/gkr777.

[15] Benet LZ, Hosey CM, Ursu O, Oprea TI: BDDCS, the Rule of 5 and drugability. Adv Drug Deliv Rev. 2016 Jun 1; 101:89-98. doi: 10.1016/j.addr.2016.05.007. Epub 2016 May 13.

Authorized licensed use limited to: DELHI TECHNICAL UNIV. Downloaded on June 28,2023 at 06:27:32 UTC from IEEE Xplore. Restrictions apply.

Authorized licensed use limited to: DELHI TECHNICAL UNIV. Downloaded on June 28,2023 at 06:27:32 UTC from IEEE Xplore. Restrictions apply.

e-ISSN: 2582-5208
International Research Journal of Modernization in Engineering Technology and Science
(Peer-Reviewed, Open Access, Fully Refereed International Journal)
Volume:05/Issue:05/May-2023 Impact Factor- 7.868 www.irjmets.com

DREAMVERSE: NFT MARKET PLACE

Aditya Kumar*1, Anup Kumar*2, Bindu Verma*3

*1,2Student, Information Technology, Delhi Technological University, Shahbad Daulatpur Village, Rohini, Delhi, India.

*3Professor, Information Technology, Delhi Technological University, Shahbad Daulatpur Village, Rohini, Delhi, India.

DOI : https://www.doi.org/10.56726/IRJMETS39592

ABSTRACT

The market for Non-Fungible Tokens (NFT) has grown significantly during the past few years. The idea behind NFT (Non-Fungible Tokens) is derived from the Ethereum token standard, which seeks to distinguish between Tokens with various indications. These NFTs are the type of digital token that may be used to pinpoint a certain characteristic of a digital asset. These NFTs make advantage of cutting-edge blockchain technology. The Non-Fungible Tokens (NFTs), which are tokens with integrated digital assets and proof of work, are the result of extensive study in the blockchain industry.

Keywords: Blockchain, Ethereum, NFT, Digital Assets, Decentralization, Polygon.

I. INTRODUCTION

NFT stands for Non-Fungible Tokens which means it has a unique property in this vast sea of the internet and cannot be easily replaced by a person. In simpler terms - An NFT is an era that proves who the possession of a digital item is. This virtual item will be a track, a photo, a video, a tweet - or maybe a chunk of virtual land within the video game or virtual global.

Fungible & Non-fungible: An Object is a fungible entity that means if a user has an object of some value and if it can be replaced or interchangeable by another object with a similar value, then it is called fungible. If something is non-fungible this means that it cannot be replaced or exchanged because it will hold some unique constraint which no other object can hold.

Blockchain is an encrypted, decentralized and distributive immutable ledger which is used to record the transaction between two parties, or you can say that it is a distributed database that records any transactions and this database is accessible across several hundreds and thousands of computers which are connected by a blockchain. And the transaction stored on the blockchain can neither be changed nor be owned by any centralized body. Because the blockchain is a distributed ledger, each transaction is stored on more than one computer, ensuring that each transaction proceeds lossless as the blockchain is distributed and can be owned and not fully controlled by one person.

II. LITERATURE REVIEW

Decentralization:

Decentralization is a key concept in blockchain technology and means that there is no central authority or intermediary in managing and verifying transactions In a decentralized system, transactions are verified and documented in a distributed ledger of stakeholders managed by a group of users, not one central authority The use of blockchain technology in the country offers many advantages. For example, it increases the security and transparency of transactions by making it more difficult for the same entity to modify or change the ledger This also eliminates the need for intermediaries, which can lead to lower transaction costs and fast repair time is eliminated.

Why Decentralization matters: Decentralization matters in blockchain technology for several reasons:

1. Security: By distributing the ledger and transactions throughout a network of individuals, in preference to relying on a single central authority, blockchain generation will become more proof against hacking, tampering, and other types of malicious activity.
2. Transparency: Decentralization provides more transparency, as all network participants have access to the same information and can verify the accuracy of the ledger. This makes it easier to detect and prevent

e-ISSN: 2582-5208
International Research Journal of Modernization in Engineering Technology and Science
(Peer-Reviewed, Open Access, Fully Refereed International Journal)
Volume:05/Issue:05/May-2023 Impact Factor- 7.868 www.irjmets.com

fraudulent activities.

Importance of NFTs innovation in today's technology:

Due to the fact that they provide a fresh method of proudly possessing and exchanging exact virtual possessions, non-fungible tokens (NFTs) are a significant innovation in the realm of blockchain technology.

Digital assets like photos, movies, and music were once thought to be fungible, which meant they could be traded and had values that varied entirely based on the content. On the other hand, with NFTs, each virtual asset is unique and has a charge for its unique character that is logged on the blockchain.

There are numerous significant ramifications of this new method of digital asset ownership:

1. Ownership and authenticity: NFTs offer a mechanism to demonstrate a digital asset's ownership and authenticity. This makes it simpler to trace and confirm a digital asset's ownership history.
2. New income sources: Because NFTs allow creators of digital material to offer their work as distinctive, one-of-a-kind objects, they now have access to new revenue sources.
3. Investment opportunities: Because the value of special digital assets might rise over time, NFTs provide a new avenue for investment for investors, collectors, and lovers of fine art.

Ethereum till date:

Ethereum emerges as a blockchain network and unlike Bitcoin provides the ability to create and execute smart contracts, which are often referred to as Dapps (decentralized applications). It provides a full-fledged programming language and can be used for smart contracts. It also provides a platform for hosting other applications to its blockchain network

III. METHODOLOGY

Some of the pre-requisites before proceeding to the implementation:

1. Version 16.14.0 or later of Node.js must be installed on your machine. Installing Node should be done using either "nvm" or "fnm".
2. Installed browser add-on for the Meta mask wallet.

Tech stack used:

1. The framework of web application - Next.js.
2. Solidity Development Environment – HardHat.
3. Storage - IPFS (InterPlanetary File System).
4. An Ethereum Web Client Library called Ethers JS.

IV. DESIGN AND IMPLEMENTATION

NFT-marketplace (DreamVerse):

DreamVerse is an NFT marketplace where users may purchase, sell, and create their own NFT. NFT stands for Non-Fungible Token. The user selected to use Polygon Network PoS blockchain because it is a Layer 2 solution for Ethereum that is quicker, less expensive, and of Indian origin. The Polygon blockchain is based on the same Ethereum EVM, however, Polygon addresses and fixes several of Ethereum's shortcomings. The user used Next.js as our front-end technology because it is a React Js framework that fixes some of React Js' drawbacks. The sole backend technology user has utilised connects the next.Js app to the blockchain using a few packages, and all data reading and writing has been done using a polygon network.

Cryptographic Hash Functions

By employing mathematical procedures known as cryptographic hash capabilities, information or a message is transformed into a fixed-size yield, also known as an overview or hash. Given that these techniques are designed to make it more difficult to reconstruct the original message from the hash, even a tiny alteration to the input message might result in an altogether different hash output.

Hash abilities are comprehensively used in cryptography for different purposes, including:

Message uprightness: Utilizing hash capabilities, you can ensure that a message hasn't changed during transmission. Senders can, for instance, calculate the hash of a message and send it to the recipient with the hash. The sender's hash can then be used by the recipient to examine the message. The beneficiary can have

confidence that the message has not been modified on the way assuming the two hashes are in shape.

Electronic marks: Computerized marks, which are utilized to check a message's genuineness and trustworthiness, can be made utilizing hash capabilities.

Space for passwords: Hash functions are frequently used with well-kept passwords. The secret phrase's hash, not the secret word itself, is saved when a client makes a secret key. when the client signs into the framework, compares the hash of the entered secret word to the saved hash, and so on.

Blockchain: Hash functions are essential in the blockchain era because they are used to create a stable and tamper-proof transaction ledger. Each block in a blockchain consolidates a hash from the previous block, creating a series of hashes that are extremely difficult to alter.

Among the most widely used cryptographic hash functions are MD5, SHA-256, and SHA-three. It's memorable's critical that hash highlights are made to rapidly figure the hash however consume a large chunk of the day to invert the cycle (work out the extraordinary message from the hash).

SHA-256 is an extensively used cryptographic hash capacity that is habitually used to deliver exceptional electronic imprints for NFTs (Non-Fungible Tokens) in blockchain networks.

Hard-Hat:

In the Hardhat development environment, which runs on the Ethereum blockchain, smart contracts are developed and tested. It provides a collection of tools and frameworks that enable it simpler to develop, test, and build smart contracts and communicate with them via a local blockchain community.

Hardhat is planned to be inconceivably versatile and configurable, permitting specialists to accommodate their improvement environment to their care wishes. It helps more than one Ethereum network, including the mainnet, testnets, and local networks, and it works with popular Ethereum development tools like Ganache and Truffle. The limit of Hardhat to complete programmed evaluations for savvy contracts is quite possibly its most significant element. It contains a certain assessing framework that licenses makers to create examinations for their arrangements in Strength, JavaScript, or TypeScript. These tests can be done locally or on a continuous integration (CI) server to make sure that clever contracts are thoroughly tested before they are put into a live network. Despite the fact that Hardhat is generally utilized as an improved climate for making, testing, and sending shrewd agreements on the Ethereum blockchain, it can likewise be utilized to execute records in Robustness (.Sol).

1. To begin, you must ensure that Node.js is installed on your computer.
2. The official Node.js website, https://nodejs.org/en/. You can use the Hub Bundle Chief (npm) to introduce Hardhat after introducing Node.js. To accomplish this, simply type the following command into a terminal or command prompt: hardhat.
3. npm introduce - - save-dev Hardhat and its conditions will be introduced in your venture registry by this.

With Hardhat installed, you can begin developing and testing smart contracts on the Ethereum blockchain. For your examination paper, here are a few additional considerations regarding your use of Hardhat: Setting up a new Hardhat project: Before you can use Hardhat, you must run the npx hardhat command and create a new project directory. Test agreements, tests, and sending scripts will all be incorporated into the fundamental task structure that will result from this.

1. Go to the agreements registry of your recently created project to compose and order Strength code with Hardhat. Solidity code can be written in any text editor or Integrated Development Environment (IDE). The "npx hardhat order" order can be utilized to aggregate the code utilizing the Hardhat compiler after it has been composed.
2. Test the limits of your smart contracts: Thanks to Hardhat's testing framework, you can write tests for your smart contracts in Solidity, JavaScript, or TypeScript. These tests can be run with the npx hardhat test command, which will also generate a report.

3. Utilizing your smart contracts: After your smart contracts have been tested and are ready to go, you can deploy them to the Ethereum network using Hardhat's deployment scripts. Typically written in JavaScript, these materials connect to the Ethereum organization through the Hardhat libraries.

Transactions take place on MainNet:

The Ethereum blockchain network's live, production version is known as the mainnet. It is the network where

e-ISSN: 2582-5208
International Research Journal of Modernization in Engineering Technology and Science
(Peer-Reviewed, Open Access, Fully Refereed International Journal)
Volume:05/Issue:05/May-2023 Impact Factor- 7.868 www.irjmets.com

real transactions take place, where users can interact with smart contracts and decentralized applications (dApps) and buy and sell Ether (ETH) and other cryptocurrencies.

The capacity of the Ethereum mainnet to carry out smart contracts is one of its most significant features. Self-executing contracts, or smart contracts, allow for the automatic processing of transactions without the use of middlemen. These agreements can be used for a number of things, such as supply chain management, the processing of payments, and digital identity verification.

The development and use of decentralised applications, or dApps, is also supported by the Ethereum mainnet. These programmes utilise the decentralised infrastructure of the Ethereum network, which they are built on top of, to offer users a wide range of services and capabilities. Prediction markets, gaming platforms, and decentralised exchanges (DEXs) are a few well-known dApps.

To use Hardhat to deploy your NFT marketplace to the mainnet, follow these basic steps:

Create the Solidity code for your smart contract for the NFT marketplace.

1. To convert your Solidity code into bytecode, make use of Hardhat.
2. Make use of Hardhat's deployment script to push your smart contract to the mainnet.
3. Make use of Hardhat's testing framework to thoroughly test your smart contract.
4. Allow users to buy and sell NFTs using real Ether by launching your NFT marketplace on the mainnet and charging fees for each transaction.

Creation of a Non-Fungible Token market:

The procedure of creating an NFT marketplace is quite similar to that of creating any other marketplace. You'll need to figure out who your target audience is, what functionality they'll need, and how you'll build it.

Step 1: Users create an account on the NFT platform.

Step 2: They select a digital wallet of their choice.

Step 3: A non-fungible token will be made. Users must submit a digital asset to accomplish this.

Step 4: Put your digital products up for sale. Sellers have the option of setting a fixed price or selecting a bid for an auction.

Step 5: Item moderation begins.

Step 6: Once new NFTs have been authorized, they are put on the sales list.

Step 7: The token's owner begins taking bids.

Step 8: When the auction ends, they are notified of the highest bidders.

Step 9: Digital assets and funds are transferred over the NFT marketplace.

There are 4 Pages on the website:

→ Marketplace.

→ Create & sell.

→ My Digital Assets.

→ Creator Dashboard

V. RESULTS AND DISCUSSION

Marketplace:

NFT marketplaces play an important role in the world of NFTs, providing a platform for NFTs transactions to occur and enabling the buying, selling, and trading of unique digital assets.

This is the place where all magic happens, here you can see all the NFTs listed by you and other users across the world. Each NFT has its own name and description, and price here you can pay the price and purchase these NFTs.

e-ISSN: 2582-5208
International Research Journal of Modernization in Engineering Technology and Science
(Peer-Reviewed, Open Access, Fully Refereed International Journal)
Volume:05/Issue:05/May-2023 Impact Factor- 7.868 www.irjmets.com

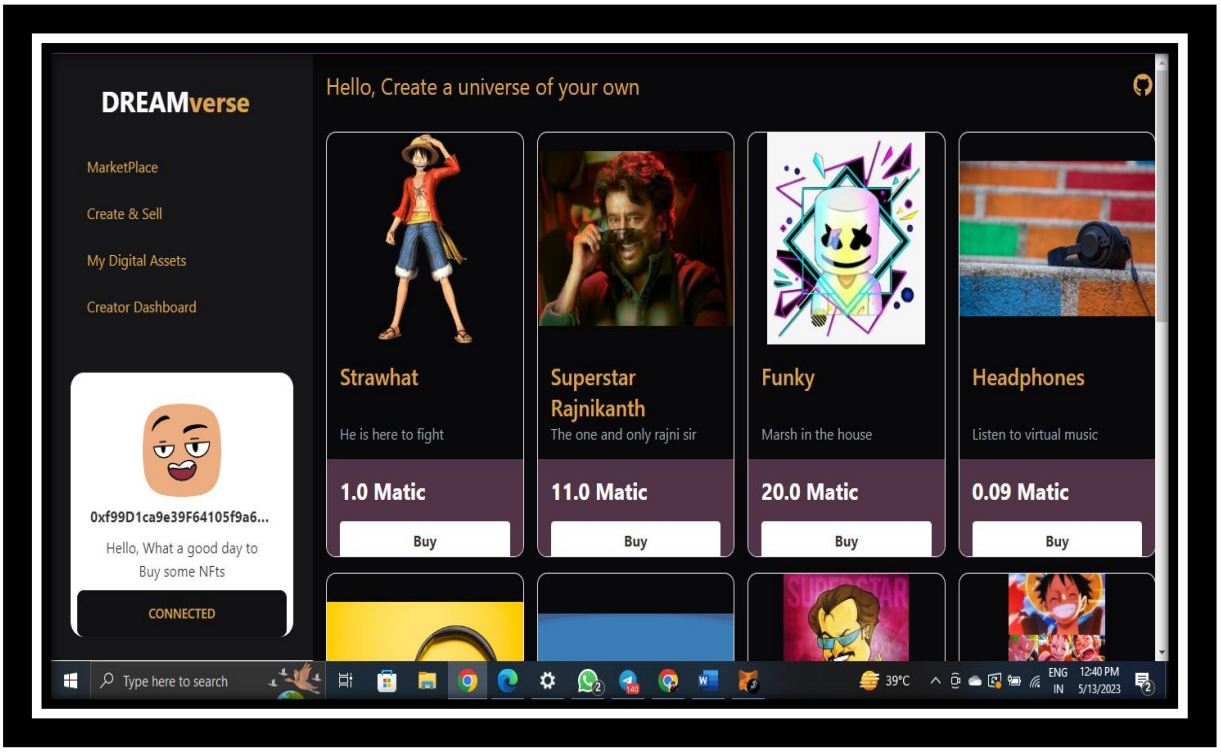

Figure 1: NFTs appearing on the home page

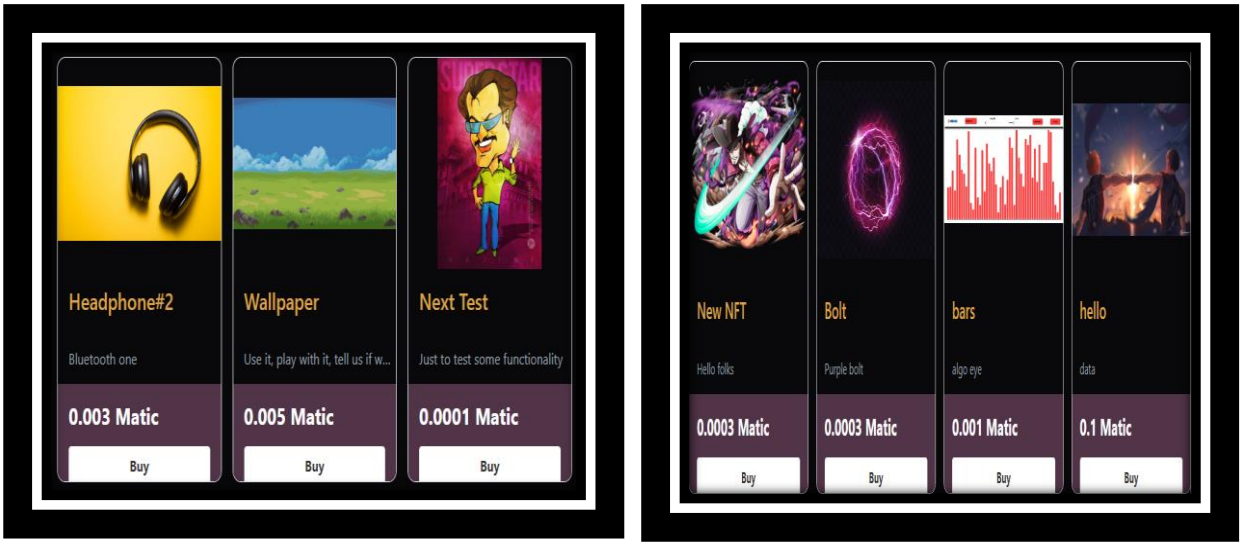

(A) (B)

Figure 2: Buying options of NFTs

Create & Sell:

This is the page where you can create your NFT and list them on Marketplace, Here in the background when you click on create button the Image you choose will get uploaded to IPFS, and all the metadata related to your NFT is also uploaded to IPFS, and the link of the metadata is then connected with your NFTs token ID that is registered on the blockchain

An interface that lets you upload any image you want is displayed when you access the NFT creation page. Subsequent to choosing a picture, tapping on the "make" button sets off an interaction where the picture document is transferred to IPFS, a decentralized record stockpiling framework. The metadata connected with the NFT, like its name, depiction, and different traits, is additionally transferred to IPFS.

e-ISSN: 2582-5208
International Research Journal of Modernization in Engineering Technology and Science
(Peer-Reviewed, Open Access, Fully Refereed International Journal)
Volume:05/Issue:05/May-2023 Impact Factor- 7.868 www.irjmets.com

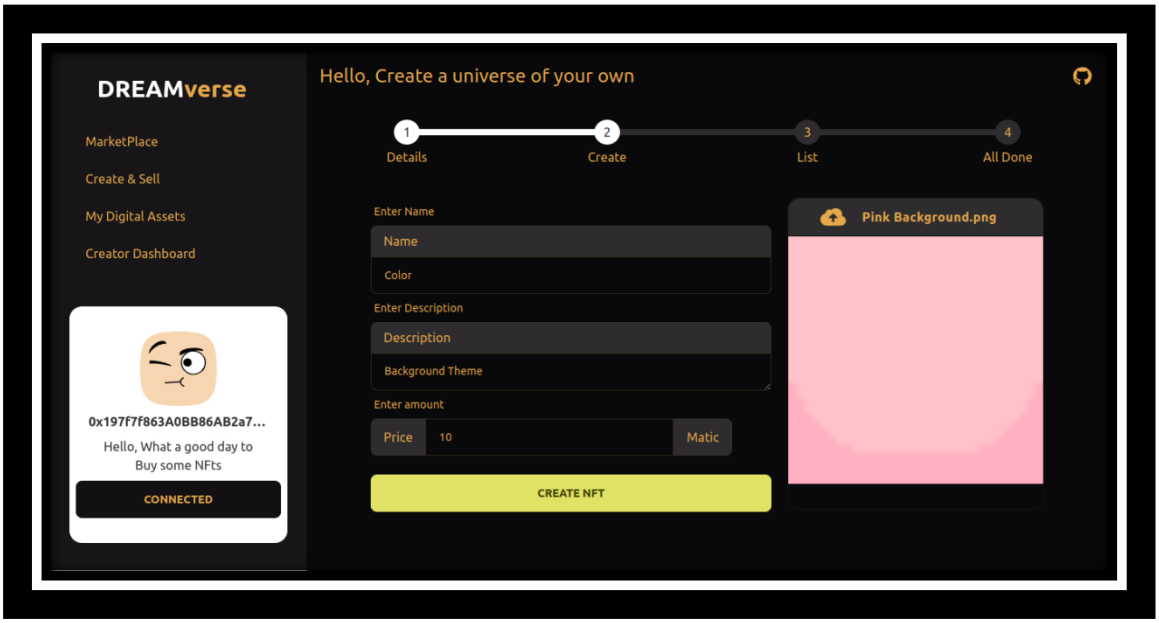

Figure 3: Buying options of NFTs

My Digital Asset:

On this page, you will get all the NFTs you have purchased using DreameVerse Marketplace, here you can also re-list them on the marketplace with new prices, using which you can create profit on your NFTs investment.

This page provides you with an overview of your current NFT holdings by displaying all of the NFTs that you have acquired through DreameVerse Marketplace. In addition, it enables you to relist your NFTs on the market at new prices, allowing you to profit from your investment.

A new price must be set for an NFT before it can be relisted and put back on the market. You profit from the difference between the initial purchase price and the new sale price if another user purchases your NFT at the new price. You can carry out this procedure as many times as you want, allowing you to potentially profit from your NFT holdings.

The DreameVerse Marketplace platform makes it simple for anyone to participate in the NFT market and take advantage of potential profit opportunities by providing a user-friendly interface for relisting NFTs. Because users are able to easily buy and sell NFTs, it also adds liquidity to the market, making it more dynamic and accessible to everyone.

Creator Dashboard:

Here reside all your details about the NFts you created on Dreameverse smart contract, how much you sold and your earnings and will show all the NFTs you ever created and also NFTs owned by you.

This part of the DreameVerse stage provides you with a point-by-point rundown of all the NFTs you've made on the stage and own at the present time. Two examples are the information displayed about the NFT, including the amount you earned from its sale.

The stage tracks commonly your NFTs and their connected data, similar to the image, depiction, and various qualities, allowing you to follow their presentation over an extended time. You can use this information to check for patterns in the NFT market and modify your systems as needed.

DreameVerse Commercial Center, on the other hand, provides a straightforward and unchanging record of your possession and exchange history by providing a comprehensive record of all the NFTs you have created and sold. This information may be beneficial to investors and collectors who wish to verify the authenticity and provenance of an NFT.

A comprehensive record of your NFTs, the data that is associated with them, and the transaction history of those NFTs are just some of the features and information available in this section of the DreameVerse platform. This information can be significant for following the introduction of your NFTs, changing your procedures, and affirming the validity and provenance of NFTs you are excited about.

e-ISSN: 2582-5208
International Research Journal of Modernization in Engineering Technology and Science
(Peer-Reviewed, Open Access, Fully Refereed International Journal)
Volume:05/Issue:05/May-2023 Impact Factor- 7.868 www.irjmets.com

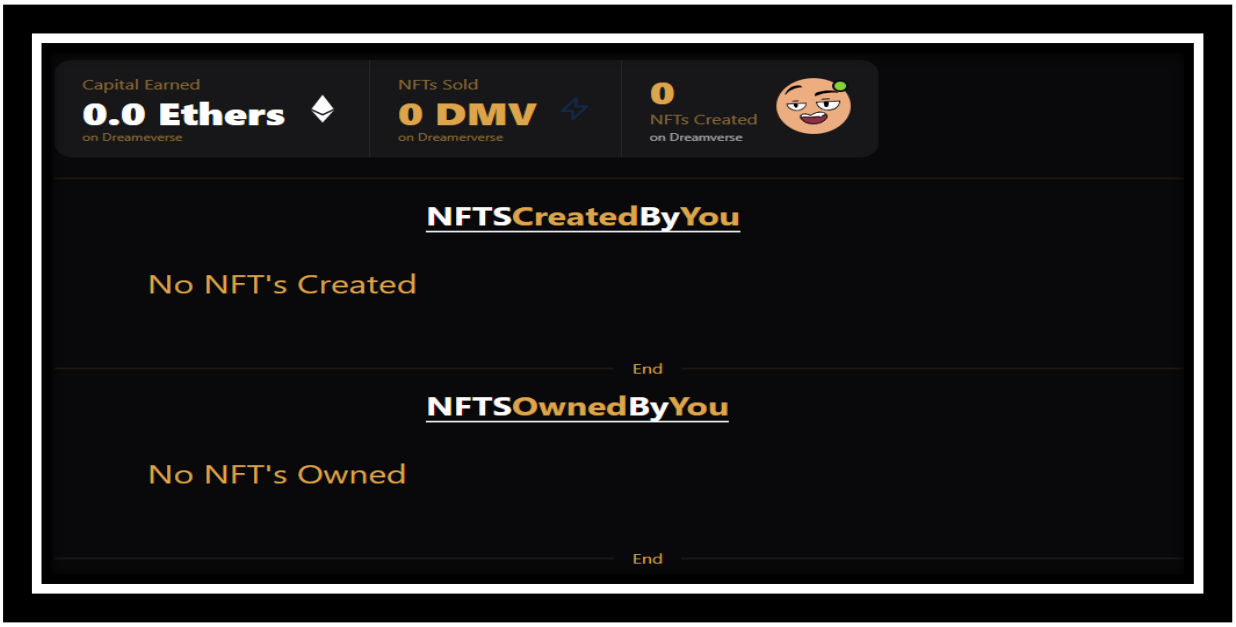

Figure 4: Initial stage of creator's dashboard

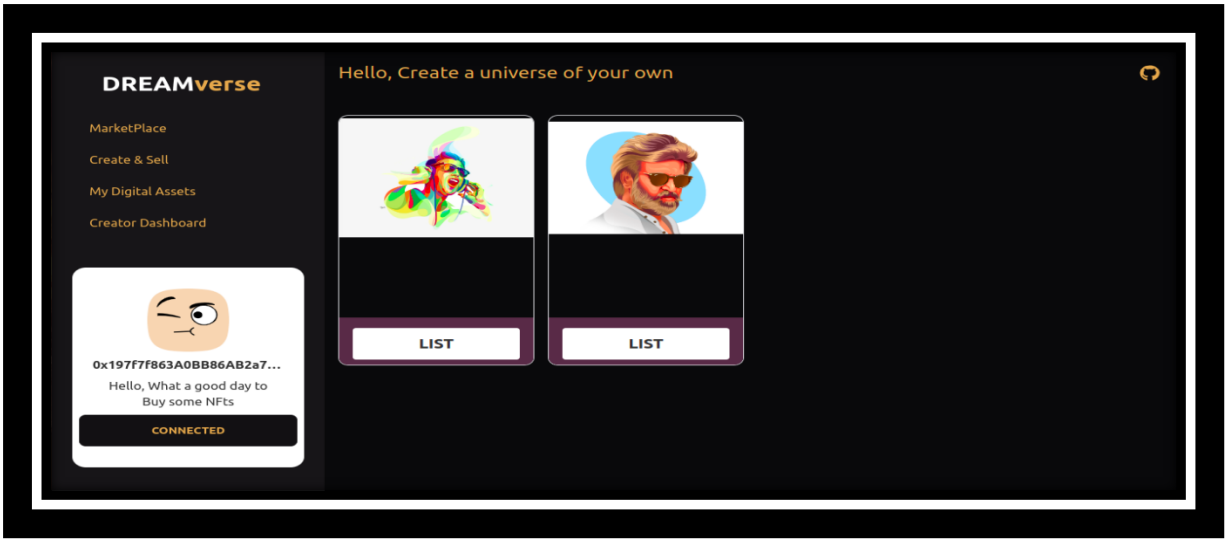

Figure 5: NFT portfolio and transaction details

VI. CONCLUSION

The number of people who go missing around the world keeps rising, and more than half of them are never found, falling victim to various occupations that have negative effects or slavery. A nation with this many people cannot afford to lose its priceless citizens to the betrayal and retribution of criminals. The loss of a sizable number of children, adults, or even the elderly, however, has a substantial impact on the country as a whole and diminishes productivity. In addition, our children and adults who disappear and are never found are either left for begging or have so severe disabilities that they are practically unrecognizably disabled, exactly like in India. This has a significant impact on the future of our country.

Thanks to NFTs and NFT marketplaces, a new ecosystem for digital art, collectables, and other distinctive digital items has emerged. As more makers and artists adopt this technology, the user might expect to see more innovative applications of NFTs as well as an increase in the value of distinctive digital assets. Additionally, as the use of NFT increases, the art world encounters new challenges such as issues with authenticity and ownership that need to be dealt with as the technology develops.

Furthermore, The development of NFT marketplaces has also increased worries about the environmental impacts of blockchain technology, particularly the high energy needs for cryptocurrency mining. As a result, initiatives to create greener and more energy-efficient alternatives, such as Proof of Stake (PoS) consensus

techniques, have grown. Because of NFT marketplaces, the world of digital assets now faces both new opportunities and challenges. As technology and the industry continue to grow, it will be essential to keep a close watch on developments and to respond to any new difficulties in a timely and responsible manner.

ACKNOWLEDGEMENTS

We would like to extend our profound appreciation to everyone who has worked on this research study, both people and institutions. We would like to start by sincerely thanking our supervisor, Dr Bindu Verma, for her guidance, expertise, and unwavering support during this research effort. Their wise counsel, constructive criticism, and steadfast support have had a significant impact on the breadth and quality of our work.

We also like to express our gratitude to Delhi Technological University's teachers and staff for giving us access to its facilities, tools, and resources. Their help and encouragement were essential to the completion of this research.

We are grateful to our classmates and friends for their informative discussions, wise counsel, and moral support during this study effort. Their friendship and intellectual rigor have been crucial to the expansion and development of our thoughts.

We would like to use this opportunity to express our sincere thanks to everyone who has contributed to this research work, regardless of how little or how much. The results and significance of this work have been greatly influenced by your input.

VII. REFERENCES

[1] Hijab e Zainab, Wajiha Rehman, Narmeen Zakaria Bawany, Jaweria Imran, NFTs: Applications and Challenges (Narmeen Bawany, Jinnah University for Women, 2021), pp. 8.

[2] Shiping Chen, Qin Wang, Rujia Li, Qi Wang, Non-Fungible Token (NFT): Overview, Evaluation, Opportunities and Challenges", (Creative Commons Attribution 4.0 International, 2021), pp. 30

[3] Arhum Naseem Khawaj, Ms Syeda Habibah Hussain, Rizvi Writing and Communication, NFT Research Essay, (Arhum Khawaja, Lahore Institute of Management & Science,21 April 2021), pp. 14.

[4] J. McMenamy, I. Macaluso, E. D. Pascale and L. Doyle. Smart con tract slas for dense small-cell-as-aservice. CoRR, abs/1703.04502, 2017.

[5] Saffan Khan, Nishant Agnihotri, DigitalStack: A NFT Marketplace, (International Journal for Creative Research Thoughts, 4 April 2022), ISSN: 2320-2882.

[6] C. Usman W, Non-Fungible Tokens: Blockchains, Scarcity, and Value, (Critical Blockchain Research Initiative (CBRI) Working Papers, 2021), pp. 14.

[7] G. Wood, A secure decentralised generalised transaction ledger, (Ethereum: 2014), pp. 1-32.

[8] W. e. a. Cai, Zehua Wang, Jason B. Ernst, Zhen Hong, Chen Feng, Victor C. M. Leung, Decentralized Applications: The Blockchain-Empowered Software System, (IEEE, 2018), pp. 53019 - 53033.

[9] Stefano Ferretti, Gabriele D'Angelo, On the Ethereum Blockchain Structure: a Complex Networks Theory Perspective, (Gabriele D'Angelo, University of Bologna, 2019), p. 12.

[10] G. D'Angelo, S. Ferretti, and M. Marzolla. A blockchain-based flight data recorder for cloud accountability. In Proc. of the 1st Workshop on Cryptocurrencies and Blockchains for Distributed Systems, Cry- Block'18, pages 93–98, New York, NY, USA, 2018. ACM.

[11] A. Durand, P. Gremaud, and J. Pasquier, Resilient, crowd-sourced LPWAN infrastructure using blockchain. In CRYBLOCK@MobiSys, pages 25–29. ACM, 2018.

[12] R. De Michele, S. Ferretti, and M. Furini. On helping broadcastersto promote tv-shows through hashtags. Multimedia Tools and Appli- cations, Aug 2018.

[13] Z. Gao, L. Xu, G. Turner, B. Patel, N. Diallo, L. Chen, and W. Shi. Blockchain-based identity management with mobile device. In CRY- BLOCK@MobiSys, pages 66–70. ACM, 2018.

[14] J. Herrera-Joancomarti. Research and challenges on bitcoin anonymity. In Proc. of the 9th International Workshop on DataPrivacy Management, volume 8872, 09 2014.

[15] O. Lo´pez-Pintado, M. Dumas, L. Garc´ıa-Ban˜uelos, and I. Weber. Dynamic role binding in blockchainbased collaborative business processes. CoRR, abs/1812.02909, 2018.

Proceedings of the 7th International Conference on Intelligent Computing and Control Systems (ICICCS-2023)
IEEE Xplore Part Number: CFP23K74-ART; ISBN: 979-8-3503-9725-3

2023 7th International Conference on Intelligent Computing and Control Systems (ICICCS) | 979-8-3503-9725-3/23/$31.00 ©2023 IEEE | DOI: 10.1109/ICICCS56967.2023.10142379

Driver's Drowsiness Detection using MobileNet on Web

Shwetanshu Singh Bharti
Department of Computer Science and Engineering
Delhi Technological University, Delhi, India
Delhi, India
ssbharti.22@gmail.com

Rijul Mahajan
Department of Computer Science and Engineering
Delhi Technological University, Delhi, India
Delhi, India
rijul.mahajan01@gmail.com

Sonali Bhoriya
Department of Computer Science and Engineering
Delhi Technological University, Delhi, India
Delhi, India
sonaliibhoriya@gmail.com

Dr. Aruna Bhat
Department of Computer Science and Engineering
Delhi Technological University, Delhi, India
Delhi, India
aruna.bhat@dtu.ac.in

***Abstract*—Drowsiness detection is an important aspect of ensuring safety on the road, at work, and in various other activities where alertness is critical. With the increasing use of mobile devices and the internet, there is a growing need for a drowsiness detector that can be used on web-based platforms. This research paper presents a novel drowsiness detection system that uses MobileNet, a deep convolutional neural network, for real-time detection of drowsiness. The proposed system utilizes facial feature extraction and classification to detect drowsiness and provides an alert in real-time. The experimental results show the effectiveness of the proposed system in detecting drowsiness with high accuracy and low latency. This system can be used as a tool to promote safety in various activities and has potential applications in areas such as transportation, healthcare, and workplace safety.**

Keywords—Face recognition, Convolutional Neural Networks, MobileNet

I. INTRODUCTION

For road accidents globally, driver's drowsiness has been a crucial cause. According to the World Health Organization (WHO), it is estimated that up to 20% of all road accidents are caused by driver fatigue, with around 100,000 fatalities each year. The NHTSA in the United States reports that 1,550 deaths, 71,000 injuries, and $12.5 billion in economic losses each year are caused due to drowsiness of drivers. The European Commission estimates that driver fatigue is a factor in around 10% of all road accidents in Europe, resulting in approximately 40,000 injuries and 1,000 fatalities each year. While specific statistics on accidents caused by driver's drowsiness in India are not available, it is estimated that drowsy driving is responsible for around 20% of all road accidents in the country, according to a report by the Ministry of Road Transport and Highways.

Drowsiness detection systems are essential for ensuring the safety of drivers on the road. The number of accidents caused by driver fatigue has had a considerable increase in the current years. This has led to the development of various technologies aimed at detecting and preventing drowsiness while driving. One such technology is the use of MobileNet, a deep learning model, for drowsiness detection.

MobileNet is a type of convolutional neural network that is designed for efficient computation on mobile devices. It is well-suited for applications that require real-time image processing, making it an ideal choice for drowsiness detection systems. This research paper aims to explore the use of MobileNet for drowsiness detection in a web-based system. The goal is to demonstrate the effectiveness of MobileNet in detecting drowsiness from facial images, and to provide insight into its potential for use in practical drowsiness detection systems.

II. RELATED WORK

The development of systems for detecting driver drowsiness to promote safety on the road has seen a rapid growth of interest in the recent years. Numerous research studies have been conducted to address this problem using various approaches and technologies.

[1] The research paper focuses on using visual analysis of eye state and head pose to monitor driver alertness. The authors proposed a new method for drowsiness detection using a machine learning approach that combines features from eye state and head pose analysis. The eye state analysis was performed using a combination of Haar-like features and AdaBoost algorithm to detect the eye state and eyelid movement, while head pose was analyzed using a particle filter-based algorithm. Maintaining the Integrity of the Specifications.

[2] The authors propose a system that uses both yawning and eye closure as indicators of drowsiness. They used a machine learning algorithm to analyze the data collected from cameras that monitored the driver's face. The results of the study showed that the proposed system had a high accuracy rate in detecting drowsiness compared to traditional methods that only relied on eye closure. This paper highlights the importance of considering multiple factors in detecting drowsiness in drivers and provides a new method that could be used to improve road safety.

[3] proposes a system that uses facial landmarks and analysis of EAR values for mobile-based driver sleepiness detection. EAR (Eye Aspect Ratio) is a measure of the

Authorized licensed use limited to: DELHI TECHNICAL UNIV. Downloaded on June 14,2023 at 05:10:26 UTC from IEEE Xplore. Restrictions apply.

degree of eye closure and is used to infer the drowsiness level of a driver. The proposed system uses facial landmark detection to locate the eyes, nose, and mouth regions of a driver's face, and then calculates the EAR values to determine the driver's sleepiness level. The system was evaluated using a dataset of videos captured from drivers in a real driving environment. The results showed that the proposed system achieved high accuracy in detecting driver sleepiness, with an overall accuracy of 92.6%. The study suggests that the proposed system could be used as a non-intrusive and cost-effective method for driver sleepiness detection in real-world driving situations. [11] The system uses a camera to capture images of the driver's eyes and analyses the eye state using image processing techniques to detect drowsiness. The system then uses machine learning algorithms to classify the driver's level of fatigue based on the eye state features. The proposed method was evaluated using a dataset of 1300 images and achieved an accuracy of 94.23% in detecting drowsiness. The authors conclude that their proposed system has the potential to be an effective tool for preventing drowsy driving accidents.

TABLE I. ACCURACY COMPARISION

Methods	Accuracy
EAR values [3]	92.6
Eye state [11]	94.23
Mobilenet v1	97.45

III. PROPOSED WORK

MobileNet is a type of convolutional neural network (CNN) that is designed to be computationally efficient and therefore suitable for mobile devices with limited processing power. It is commonly used in image recognition tasks, such as object detection and facial feature detection. It was first introduced in 2017 by researchers at Google and has since become a widely used architecture in computer vision applications.

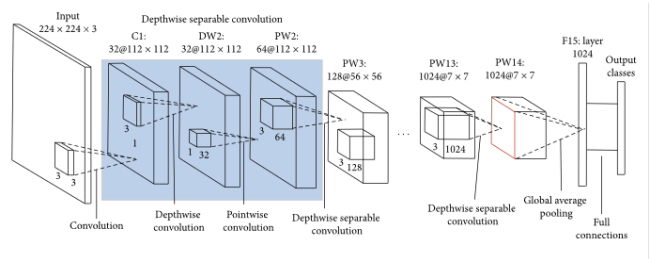

Fig. 1. The architecture of MobileNet

A. Architecture of MobileNet

The main innovation of MobileNet v1 is the use of depthwise separable convolutions. Traditional convolutional neural networks (CNNs) apply a filter to the entire input volume at each layer, which can be computationally expensive. In contrast, depthwise separable convolutions are composed of two smaller convolutions: a single filter is applied in a depthwise convolution to every single input channel separately, and a pointwise convolution that applies a 1x1 filter to the output of the depthwise convolution. This lowers the amount of computational power needed to process the input, while maintaining high accuracy. It involves a number of convolutional layers, including a pooling layer of a global average and a completely connected layer. The convolutional layers are organized into blocks, each consisting of a depthwise convolution and a pointwise convolution. The number of filters in each depthwise convolution is determined by a multiplier, which controls the overall complexity of the network. For example, a multiplier of 1 reduces the number of filters in each convolutional layer by a factor of 8, while a multiplier of 0.5 reduces the number of filters by a factor of 16. It also includes shortcut connections, which allow information to bypass some of the convolutional layers. These connections improve the flow of gradients during training, leading to faster convergence and better accuracy. In addition, it uses batch normalization and ReLU activation functions to improve the stability and performance of the network. The role of the ReLU activation function is to introduce non-linearity to the network, allowing it to learn complex patterns and make better predictions. The main advantage of using the ReLU activation function is its ability to help prevent the vanishing gradient problem that can occur with other activation functions such as the sigmoid and tanh functions. The vanishing gradient problem occurs when the gradients become very small during backpropagation, which can make it difficult to train the network effectively.

MobileNet v1 has been shown to achieve state-of-the-art performance on a range of computer vision tasks, including image classification, object detection, and semantic segmentation. It requires fewer computations and memory resources than other architectures, making it well-suited for mobile and embedded devices. In addition, the modular design of MobileNet v1 makes it easy to adapt to different input sizes and tasks, making it a flexible architecture for a wide range of applications.

B. Working of MobileNet

- It employs a depthwise separable convolution process with two layers: a depthwise convolution and a pointwise convolution. Depthwise convolution aims to assign filter to every input signal individually, whereas pointwise convolution generates the final outcome by applying a 1x1 filter to the depthwise convolution output.
- It employs a bottleneck architecture, where the number of parameters channels is reduced just before depthwise convolution, and the result is expanded restored to the initial amount of feeds afterwards the pointwise convolution. This serves to minimise the model's parameter count and computational efficiency.
- It introduces a hyperparameter called the width multiplier, which controls the count of filters used in all the layers. By reducing the count of the filters, the model becomes more computationally efficient, but also less accurate.
- It also uses a smaller input image size than traditional CNNs. By reducing the input image size, the model requires fewer computations to process each image, which is especially important for mobile and embedded devices with limited computational resources.

Authorized licensed use limited to: DELHI TECHNICAL UNIV. Downloaded on June 14,2023 at 05:10:26 UTC from IEEE Xplore. Restrictions apply.

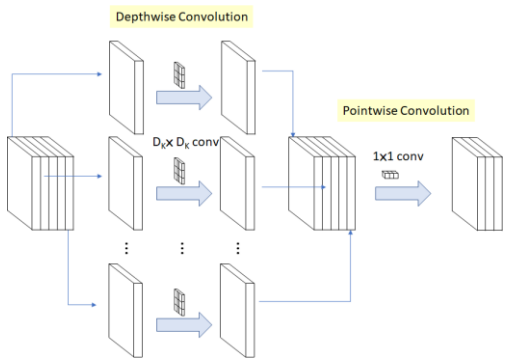

Fig. 2. Depthwise and pointwise convolution

C. *Detection of facial features using MobileNet*

In the case of facial feature detection, MobileNet would be trained on a dataset of labeled pictures of faces that includes information about the locations of various facial features, such as eyes, nose, and mouth.

During the training process, MobileNet learns to gather features from the input images that are relevant for the task at hand. Typically, this process involves passing the input image through a series of convolutional layers, which apply a set of filters to the image and produce a set of feature maps. Each filter is designed to detect a specific feature, such as an edge or a corner, and produces a response map that highlights the regions of the input image where that feature is present. These features can be thought of as patterns or characteristics that are useful for identifying the presence and location of facial features in an image. Once MobileNet has been trained, it can be used to detect facial features in new images. This is done by passing the image through the network and using its learned features to identify the locations of facial features. The output of the network will typically include a set of coordinates that correspond to the location of each detected facial feature in the image. These coordinates can then be used to draw bounding boxes or landmarks on the image, indicating the location of each feature. One of the main advantages of using MobileNet v1 for facial feature detection is its small size and low computational requirements. This allows it to be deployed on mobile devices with limited resources such as smartphones and tablets. Additionally, the use of depthwise separable convolutional layers allows for faster inference times, which is essential for real-time applications such as video conferencing and augmented reality.

In conclusion, facial feature detection using MobileNet v1 is a powerful and efficient technique that has a wide range of applications in mobile and embedded devices. Its small size, low computational requirements, and fast inference times make it an ideal choice for real-time facial analysis and recognition tasks.

D. *Using TensorFlow.js to integrate on the internet*

TensorFlow.js is a JavaScript library that allows you to run machine learning models in the browser or Node.js. One of the features of TensorFlow.js is the ability to load pre-trained models such as MobileNet v1, using the tf.loadLayersModel() function. When tf.loadLayersModel() is used to load a pre-trained model, TensorFlow.js first downloads the model files from the specified URL, which in this case is the Google Cloud Storage API.

The model files are typically stored as a collection of JSON files and binary weights files. Once the model files have been downloaded, TensorFlow.js uses them to construct a TensorFlow.js model object that can be used to make predictions. The process of constructing the model object involves parsing the JSON files to create the model architecture, and loading the weights from the binary files. Overall, the process of loading MobileNet v1 in TensorFlow.js involves downloading the model files from Google Cloud Storage, and constructing a TensorFlow.js model object from those files. Once the model object is created, it can be used to make predictions on new images.

IV. RESULT

The results show that using this method, a real-time update about the state of the driver can be delivered. The model can be self-trained to send alerts about the driver being potentially sleepy or already being asleep “Fig. 4, 5”, respectively.

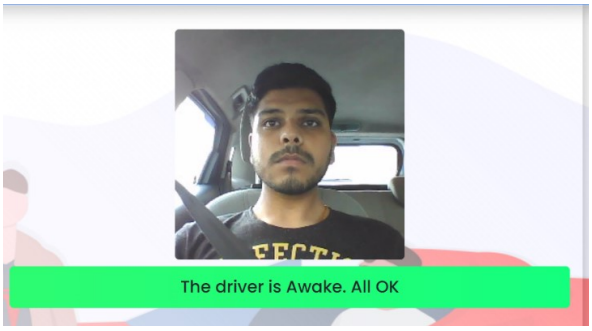

Fig 3. Predicting that the driver is awake

The “Fig. 3” depicts the driver as awake, indicating the successful application of the model built using Mobilenet v1 architecture. The model was trained to recognize patterns in the driver's behavior and provide real-time alerts if the driver shows signs of drowsiness or fatigue. The model was trained just before the use by the user itself, ensuring personalized training for each user.

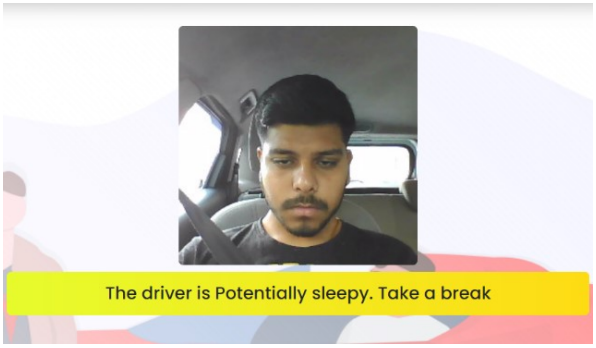

Fig 4. Alerting the driver about potential sleepiness

The “Fig. 4” shows the driver being identified as potentially sleepy. The model was trained to analyze various facial features, such as eye movement and head posture, to detect signs of drowsiness accurately. This detection system would provide an alert to the driver and prompt to take a break and rest before continuing their journey.

Authorized licensed use limited to: DELHI TECHNICAL UNIV. Downloaded on June 14,2023 at 05:10:26 UTC from IEEE Xplore. Restrictions apply.

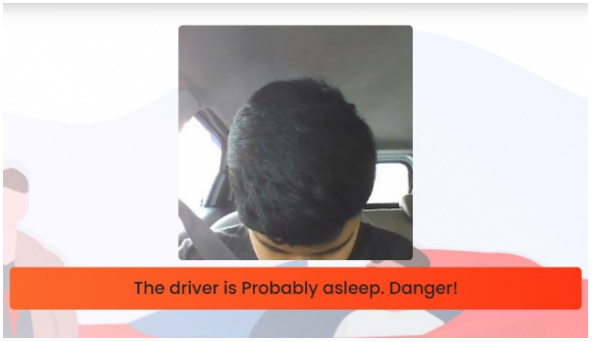

Fig 5. Sending an alert that the driver is asleep

The "Fig. 5" displays the driver identified as asleep, which is a critical alert that ensures the safety of the driver and passengers. This innovative approach would undoubtedly play a significant role in reducing accidents and fatalities on the roads.

The accuracy measures the percentage of correctly classified images out of the total number of images in the test dataset. The proposed model achieved an accuracy of 97.45%, which is a promising result for this task. The loss, on the other hand, indicates the degree of error in the model's predictions. The model achieved a relatively low loss of 0.18, indicating that it was able to make accurate predictions while minimizing errors. These results demonstrate the effectiveness of the proposed model for image classification and suggest its potential for further development and deployment in real-world applications.

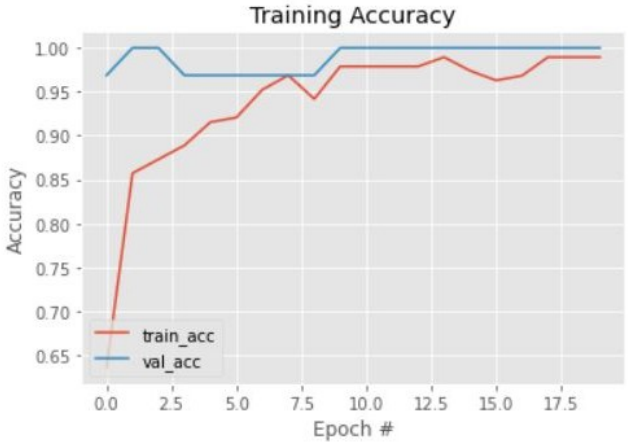

Fig 6. Training and validation accuracy curves

The graph shows two curves, one for accuracy and one for validation accuracy, plotted against the number of epochs. The proportion of accurate predictions generated by the model on the training sample is referred to as accuracy, whereas validation accuracy is the percentage of right predictions made on a different validation data that is not included for learning.

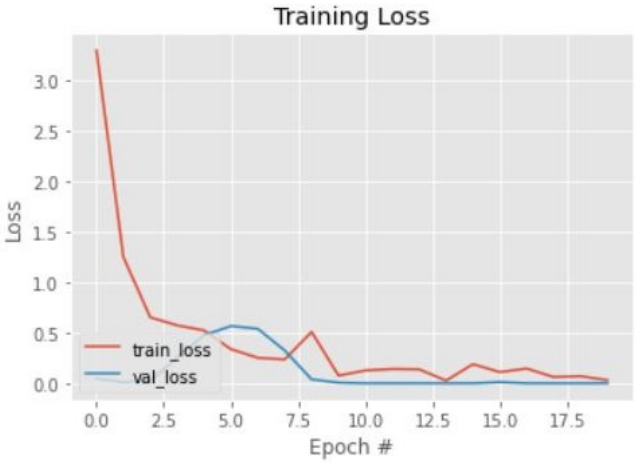

Fig 7. Training and validation loss curves

The graph displays two curves, one for loss and one for validation loss, plotted against the number of epochs. Loss refers to the amount of error between the predicted output and the actual output on the training set, while validation loss represents the amount of error on the separate validation set.

The model trained using MobileNet v1 is capable of detecting whether the driver is awake, drowsy, or has slept. The model is designed to be trained by individual users, which suggests that it can be personalized and customized according to the specific needs and characteristics of each driver.

The research findings show that the offered approach is efficient for driver drowsiness detection, which could ultimately help reduce the number of accidents caused by drowsy driving. By using the trained model, drivers can be alerted whenever signs of drowsiness or falling asleep are displayed, which could potentially prevent accidents caused by driver fatigue. However, it is important to note that the accuracy and effectiveness of the model may vary depending on factors such as the quality of training data, the conditions of use, and the individual characteristics of the driver.

Overall, the use of deep learning models such as the one presented in these pictures can be a promising approach for improving driver safety and preventing accidents caused by driver fatigue.

V. CONCLUSION

In conclusion, this research paper presents a novel approach to drowsiness detection using the MobileNet V1 architecture integrated on a web platform. The proposed model achieved an accuracy of 97.45 percent and a loss of 0.18, indicating its effectiveness in detecting drowsiness accurately. The integration of the model on a web platform provides an accessible and convenient way to detect drowsiness in real-time, which can improve road safety and prevent accidents caused by drowsy driving. The proposed approach can be further improved by integrating it with other systems, such as in-car alert systems, to provide a comprehensive solution for drowsiness detection and prevention. The results of this study demonstrate the potential of deep learning models for drowsiness detection and the significance of integrating such models on web platforms for wider accessibility and usability.

Authorized licensed use limited to: DELHI TECHNICAL UNIV. Downloaded on June 14,2023 at 05:10:26 UTC from IEEE Xplore. Restrictions apply.

ACKNOWLEDGEMENT

This work was carried out as part of" Main project" during eighth semester B Tech Computer Science and Engineering in partial fulfillment of the requirement for the award of Bachelor of Technology Degree in Computer Science and Engineering under Delhi Technological University.

REFERENCES

[1] R. O. Mbouna, S. G. Kong and M.-G. Chun, "Visual analysis of eye state and head pose for driver alertness monitoring", IEEE Trans. Intell. Transp. Syst., vol. 14, no. 3, pp. 1462- 1469, Sep. 2013.

[2] M. Omidyeganeh, A. Javadtalab and S. Shirmohammadi, "Intelligent driver drowsiness detection through fusion of yawning and eye closure", Proc. IEEE Int. Conf. Virtual Environ. Hum.-Comput. Interfaces Meas. Syst., pp. 1-6, Sep. 2011.

[3] C. Huda, H. Tolle, and F. Utaminingrum, "Mobile-Based Driver Sleepiness Detection Using Facial Landmarks and Analysis of EAR Values", Int. J. Interact. Mob. Technol., vol. 14, no. 14, pp. pp. 16–30, Aug. 2020.

[4] P. Viola and M. Jones, "Rapid object detection using a boosted cascade of simple features," Proceedings of the 2001 IEEE Computer Society Conference on Computer Vision and Pattern Recognition. CVPR 2001, Kauai, HI, USA, 2001, pp. I-I, doi: 10.1109/CVPR.2001.990517.

[5] N. Dalal and B. Triggs, "Histograms of oriented gradients for human detection," 2005 IEEE Computer Society Conference on Computer Vision and Pattern Recognition (CVPR'05), San Diego, CA, USA, 2005, pp. 886-893 vol. 1, doi: 10.1109/CVPR.2005.177.

[6] H. A. Rowley, S. Baluja and T. Kanade, "Neural network-based face detection," in IEEE Transactions on Pattern Analysis and Machine Intelligence, vol. 20, no. 1, pp. 23-38, Jan. 1998, doi: 10.1109/34.655647.

[7] G. Huang, Z. Liu, L. Van Der Maaten and K. Q. Weinberger, "Densely Connected Convolutional Networks," 2017 IEEE Conference on Computer Vision and Pattern Recognition (CVPR), Honolulu, HI, USA, 2017, pp. 2261-2269, doi: 10.1109/CVPR.2017.243.

[8] M. Sandler, A. Howard, M. Zhu, A. Zhmoginov and L. -C. Chen, "MobileNetV2: Inverted Residuals and Linear Bottlenecks," 2018 IEEE/CVF Conference on Computer Vision and Pattern Recognition, Salt Lake City, UT, USA, 2018, pp. 4510-4520, doi: 10.1109/CVPR.2018.00474.

[9] K. He, X. Zhang, S. Ren and J. Sun, "Deep Residual Learning for Image Recognition," 2016 IEEE Conference on Computer Vision and Pattern Recognition (CVPR), Las Vegas, NV, USA, 2016, pp. 770-778, doi: 10.1109/CVPR.2016.90.

[10] J. Dai et al., "Deformable Convolutional Networks," 2017 IEEE International Conference on Computer Vision (ICCV), Venice, Italy, 2017, pp. 764-773, doi: 10.1109/ICCV.2017.89.

[11] M. Öztürk , A. Küçükmanisa and O. Urhan , "Drowsiness Detection System Based on Machine Learning Using Eye State", Balkan Journal of Electrical and Computer Engineering, vol. 10, no. 3, pp. 258-263, Jul. 2022, doi:10.17694/bajece.1028110.

[12] Z. Cai and N. Vasconcelos, "Cascade R-CNN: Delving Into High Quality Object Detection," 2018 IEEE/CVF Conference on Computer Vision and Pattern Recognition, Salt Lake City, UT, USA, 2018, pp. 6154-6162, doi: 10.1109/CVPR.2018.00644.

[13] Hwang B, Lee S, Lee S. HISFCOS: Half-Inverted Stage Block for Efficient Object Detection Based on Deep Learning. J Imaging. 2022 Apr 17;8(4):117. doi: 10.3390/jimaging8040117. PMID: 35448244; PMCID: PMC9026111.

[14] Tan, M. and Le, Q.V. (2019) EfficientNet: Rethinking Model Scaling for Convolutional Neural Networks. Proceedings of the 36th International Conference on Machine Learning, ICML 2019, Long Beach, 9-15 June 2019, 6105-6114. http://proceedings.mlr.press/v97/tan19a.html

[15] R. Ranjan, S. Sankaranarayanan, C. D. Castillo and R. Chellappa, "An All-In-One Convolutional Neural Network for Face Analysis," 2017 12th IEEE International Conference on Automatic Face & Gesture Recognition (FG 2017), Washington, DC, USA, 2017, pp. 17-24, doi: 10.1109/FG.2017.137.

[16] Howard, A. G., Zhu, M., Chen, B., Kalenichenko, D., Wang, W., Weyand, T., ... & Adam, H. (2017). Mobilenets: Efficient convolutional neural networks for mobile vision applications. arXiv preprint arXiv:1704.04861.

Authorized licensed use limited to: DELHI TECHNICAL UNIV. Downloaded on June 14,2023 at 05:10:26 UTC from IEEE Xplore. Restrictions apply.

Proceedings of the Second International Conference on Applied Artificial Intelligence and Computing (ICAAIC 2023)
IEEE Xplore Part Number: CFP23BC3-ART; ISBN: 978-1-6654-5630-2

Early Detection of Alzheimer's Disease: The Importance of Speech Analysis

Kritesh Rauniyar
Dept. of Computer Science Engineering
Delhi Technological University
New Delhi, India
rauniyark11@gmail.com

Shuvam Thakur
Dept. of Computer Science Engineering
Delhi Technological University
New Delhi, India
shuvamthakur@outlook.com

Aayush Nevatia
Dept. of Computer Science Engineering
Delhi Technological University
New Delhi, India
aayushnevatia7@gmail.com

Prashant Giridhar Shambharkar
Dept. of Computer Science Engineering
Delhi Technological University
New Delhi, India
prashant.shambharkar@dtu.ac.in

2023 2nd International Conference on Applied Artificial Intelligence and Computing (ICAAIC) | 978-1-6654-5630-2/23/$31.00 ©2023 IEEE | DOI: 10.1109/ICAAIC56838.2023.10140703

***Abstract*—Almost 50 million individuals throughout the world suffer from Alzheimer's disease (AD), a disease of the nervous system. There are no licensed medications on the market right now that can treat AD or halt its development. There are, however, treatments available that can help mediate AD in earlier stages. This demonstrates the necessity of early diagnosis. One of the notable symptoms of Alzheimer's can be in the patient's cognitive abilities. In daily chores, there is an indication of a diminished capacity for interpreting or producing speech. As a result, natural language processing can be a useful method for analyzing patient speech. Due to the rapid advancements in the field of computer science, we can use NLP to process these speech extracts from AD patients. NLP has a great deal of potential to help individuals who are suffering from mental illnesses receive better care. The study employs various Machine Learning models with ensemble learners and Deep Learning models for a comparative analysis to set a proper baseline for further research and advancements in the detection of Alzheimer's disease.**

***Index Terms*—NLP, Machine Learning, Deep Learning, Alzheimer's Disease, Speech Analysis**

I. Introduction

Alzheimer's disease (AD) is a neurological ailment that steadily impairs mental and physical abilities, finally, the capacity to perform simple tasks. AD accounts for 65-85% of all the cases. The possibility for clinical care to totally treat or even halt the course of it is made even more dangerous by the disease. There are various treatment options for the milder stage of the illness to alleviate symptoms quickly and enhance life quality. Early detection is essential for the management and treatment of AD as disease progression results in significant cognitive impairment and irreparable brain damage. This has motivated scientists to look into novel approaches to detect AD. One of the primary symptoms of AD patients is changes in speech. As the patient's brain deteriorates, so does their ability to process words. Deciphering the human language requires powerful tools like NLP [11]. These symptoms are caused by neurodegeneration in particular brain regions, most notably the hetero modal association and paralimbic areas. The first neurons to become destroyed are those in areas of the brain that control language, thought, and memory. The number of damaged neurons and impacted brain regions increases with time. According to the 2018 World Alzheimer Report, there will be more than 150 million Alzheimer's disease (AD) sufferers worldwide by 2050. By 2030, it is anticipated that the cost of treating AD will reach US $2 trillion. Dementia affects 1 in 3 elderly people who pass away. Moreover, other tests are carried out, including EEGs, blood tests, and genotyping. The third ventricle has expanded and there is cerebral atrophy, according to a brain CT. Artificial Intelligence has played a vital role in the improvement of health science [12]. While non-specific, it is indicative of AD. It is essential to have a computer-aided approach for the early detection of AD since it is expected that the medical expenses for patients with Alzheimer's disease would increase steadily.

The "sandwich generation" of carers, who look after a patient with the condition as well as a child or grandchild, makes up almost one-fourth of those who care for people with Alzheimer's and dementia. In the proposed investigation, a number of classifiers have been suggested to function for the English language's early detection of Alzheimer's disease. Classical ML techniques are used for the classification task in various sectors [2]. The interpretation and analysis of the patient's speech can thus benefit greatly from the use of natural language processing. The oral narratives of the research subjects can be analyzed using NLP to identify AD thanks to quick advances in computing technology. For mental diseases like depression, NLP's potential is being investigated. The project seeks to establish a baseline for future research on applying this technique in the Nepalese language for the early detection of AD. Also, a fresh dataset of English-language transcripts from AD patients and controls is being used in the research. This paper's main contributions are an amalgamation

Authorized licensed use limited to: DELHI TECHNICAL UNIV. Downloaded on June 14,2023 at 05:04:45 UTC from IEEE Xplore. Restrictions apply.

of a lot of research in the NLP field and classification based on processed speech transcripts. These purposes can be summarized as:

- Proper Natural Language Processing for the Speech transcripts
- Machine Learning models with Ensemble Learners for the base classification performance measures
- Pre-trained and Deep Learning models for advanced performance measures

II. Related Works

Recent years have seen a plethora of studies being conducted on the subject of early AD diagnosis utilizing the individuals' own speech. Using data from the Oxford Project to Study Memory and Aging (OPTIMA) project, features were identified that were useful for diagnosing dementia from speech [1]. It was discovered that language was gradually hampered as the disease advanced and recommended classifying patients using semantic, lexical content, and syntactic complexity criteria.

Transcripts were used to categorize individuals with MCI and AD. The study emphasized the significance of speech-based and morphological factors. Support Vector Machines (SVM) delivered up to 75% accuracy using just statistically relevant parameters. Some earlier works also made use of machine learning models. Hand-crafted features are necessary for ML approaches. As a result of the researchers' varying levels of experience in AD diagnosis, these hand-crafted traits vary greatly. Also, given how quickly language and culture may change, hand-picked elements are out of date very fast [13]. Syntactic, lexical, and n-gram-based characteristics were used by Orimaye et al. to develop the diagnostic model. As compared to models that just employed lexical and syntactic variables, n-gram models performed better. By using the Leave Pair Out Cross Validation technique, the model produced an Area Under Curve value of 0.92 by using top 1000 n-gram attributes. [3].

Long Short-Term Memory (LSTM) cells were employed to improve the statistical approach used in n-gram language models [4]. The accuracy of the model was calculated by calculating how complex it is, and it was found to be 0.85.

Turkish-speaking microphones were used to capture 10 minutes of telephone conversations [5]. The learning algorithms were employed, and the sentences were manually translated. The models were developed using conversational recorded transcripts of some numbers of AD sufferers and a certain number of healthy people. They included POS-based elements, complexity features such as phonemes per word, etc., as well as confusion, hesitation, and unintelligible word rate. They also employed decision trees, LDA, and support vector machines (SVM). The researchers achieved up to 90% accuracy using the LOOCV technique. It is clear that several efforts have been made to create models in various languages.

A brand-new feature group termed spatial neglect features based on the information units was suggested. In order to quantify spatial neglect, they divided the image vertically into two halves and calculated characteristics such as the number of times every information item was mentioned in each zone. With the use of their novel feature group combined with acoustic, linguistic, demographic (age) attributes, and information unit, they were able to reach an accuracy of 84.4% [6].

For the automated identification of AD, an attention-based hybrid network was presented [7]. The classification accuracy of the hybrid model was 97.4%. According to the article, by adding attention processes, the network was able to underline the key characteristics of the subjects. The English language has seen a lot of studies, and some of the trials have produced state-of-the-art models. The English language's linguistic subunits that influence how CN, MCI, and AD are classified have been thoroughly studied. According to WHO, 58% of all dementia patients originate from low- and middle-income nations, which account for the majority of dementia cases globally.

III. Methodology

The below diagram is the proposed methodology employed in this paper. Starting with the data collection of data. The data is preprocessed and its unique features are extracted for the models to understand their classification. After training the classifiers, the performance of the models is evaluated and the comparisons are made to determine the best-performing model for the required problem statement ie. classification of AD and CN patients using speech transcripts. Figure 1 shows the methodology flowchart.

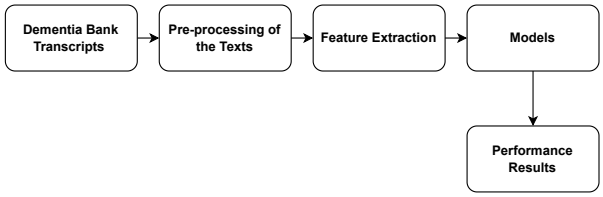

Fig. 1. Flowchart of methodology

A. Data Collection

The Pitt Corpus from DementiaBank is used in this research. Among the best collections of audio interview recordings and transcripts of participants in Becker's study at the University of Pittsburgh School of Medicine is the DementiaBank. The Dementia Bank's Corpus is audio files and text transcripts that are the recordings of the subjects that participated in the study, where said subjects were to describe a kitchen scene with children stealing cookies, where the brother who is performing the actual theft is on an unsteady stool, and mother is washing or drying the dishes as the sink overflows from the tap water. The CHAT protocol performed manual transcription of the recordings.

B. Data Preprocessing

Data preprocessing was done on the dataset to make the data noise free. Filter words and unnecessary information were removed from the data as they would not add to the lexical meaning of the sentence. Punctuation marks (commas, semicolons,

Authorized licensed use limited to: DELHI TECHNICAL UNIV. Downloaded on June 14,2023 at 05:04:45 UTC from IEEE Xplore. Restrictions apply.

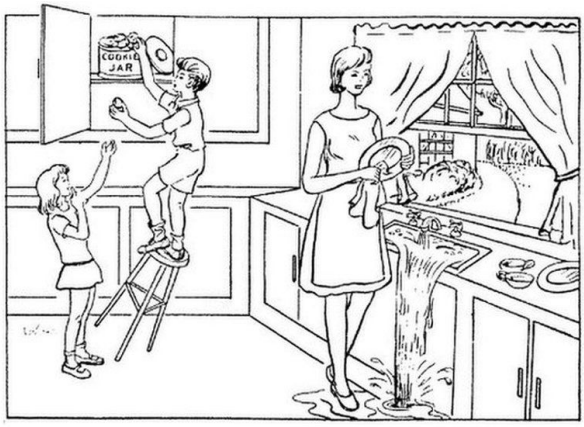

Fig. 2. Image of cookie theft [14]

apostrophes, etc.) were removed along with contractions (ain't, won't, etc.) were elongated to their original words (are not, will not, etc.). Case sensitivity was adjusted. Stopwords such as 'and' and 'but' were also removed. The filter words and stop words were removed with the help of the Natural Language Toolkit (NLTK). The array of words generated was compared to the text and removed. NLTK was also used to tokenize the text. Eventually, the text was converted into a format ready for training and feature extraction.

Fig. 3. Wordcloud for the words in dataset

C. Vectorization and Word embeddings

The study makes use of vectorization techniques and word embeddings as features. Countvectorizer and Term Frequency Inverse Document Frequency (TF-IDF) [9] were the chosen techniques for vectorization. For Word Embeddings, both Word2Vec [15] and fastText [10] is used.

CV builds a lexicon of known words from the test dataset and encodes the new documents using the vocabulary. CV tokenizes and creates a respective vector representation of each word that is used to train the machine-learning model. TF-IDF represents the importance of words in reference to the document by counting the number of occurrences. It will punish the words that appear more often, thus giving more weight to the relevant words.

Word embeddings work by assigning real-valued vectors to words. They work with the base as if features have similar meanings, we can exploit these features having similarities [8]. The two-word embeddings, Word2Vec and fastText that have been employed in the study are both of which are pre-trained and domain-specific. Count Vectorization is the process of converting text to numerical data. Sentences are transformed into sparse matrices. The Science Kit (SciKit) libraries Count Vectorizer module was used mainly for the vectorization procedure, the result of which was converted to arrays. TF-IDF was implemented using the SciKit library. It was used to calculate the relevance of words in the text. The significance of the words grows exponentially with the frequency of appearances in the text. For words embeddings, Word2Vec uses Common Bag of Words(CBOW) and Skip gram to create word embeddings. FastText is an open-source library that allows users to learn word representation and text classification.

Word	TF-IDF value
cookie	0.389
water	0.275
dish	0.272
stool	0.238
sink	0.232
little	0.222
boy	0.222
mother	0.220
jar	0.219
girl	0.202

TABLE I
MOST FREQUENTLY OCCURRING WORD IN THE DATASET

D. Classifiers

The paper makes use of machine learning models and deep learning models with ensemble learners to classify the transcripts with greater accuracy for comparison. Machine learning models were mainly used as a baseline to evaluate the performance of the algorithms used. Decision Tree(DT), Support Vector Machines(SVM), Naive Bayes(NB), and ensemble learning models like Random Forest(RF), AdaBoost(ADB), and XGBoost(XGB) were implemented as the machine learning models (Table: II, Table: V).

As for Deep Learning models, Convolutional Neural Network(CNN), BiDirectional Long-Short Term Memory(BiLSTM), a combination of CNN and BiLSTM, and different architectures for CNN like Kim's CNN architecture were employed. Deep Learning models provide better classification accuracy dealing with subtle linguistic components. Hyperparameters were fine-tuned to suit our project and provide good efficacy, such as epochs being set between 20 and 50. The experiment makes use of Adam as an optimizer in all cases (Table: IV).

Authorized licensed use limited to: DELHI TECHNICAL UNIV. Downloaded on June 14,2023 at 05:04:45 UTC from IEEE Xplore. Restrictions apply.

Google's BERT was also deployed, as well as different approaches of BERT architecture such as ALBERT, and ROBERTA were also used for comparison (Table: III).

E. Performance Measures

For performance measures, the study makes use of general performance evaluation calculations such as Accuracy and F1 scores. Macro mean averaged errors (MMAE) are also calculated for the test and predicted results.

IV. Experimental Results

The machine learning model results that are to be baselines with TF-IDF and CV are presented in Table II. We can see that XGB performs best with TF-IDF as the vectorizer (accuracy: 0.81, MMAE score:0.19, F1 Macro-score: 0.81), while RF performs best with CV(accuracy: 0.83, MMAE score:0.17, F1 Macro-score: 0.82). The ML models perform similarly to each other with only slight improvement in some models.

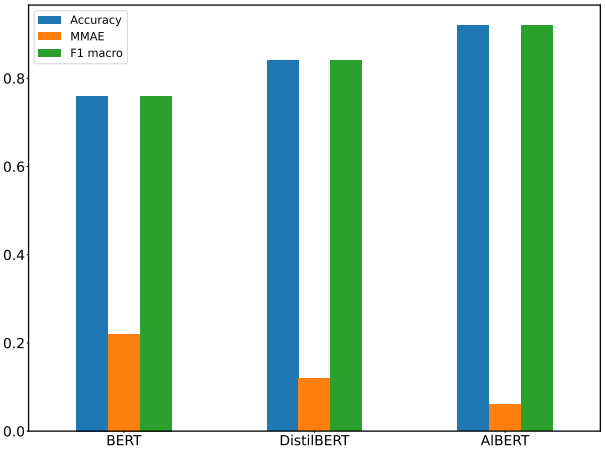

Fig. 4. Result of large pre-trained models

Among the DL models shown in Table IV and V, CNN+BiLSTM performs better than the other DL models as well as the ML models with Word2Vec as word embeddings. DL models were trained using the same preprocessing on the text and with the same extracted text features. The epochs and learning rate along with other hyperparameters were tuned using hit and trail to achieve the best possible performance scores. CNN + BiLSTM with 4 convolutional layers and 2 LSTM layers performed the best. The inclusion of maxpool layer in the BiLSTM model with the convolutional layer added to the performance of the combined model. The DL models performed better using Word2Vec as word embeddings than fastText in all measures. We can see from Table III that the best-performing model is the AlBERT model with an accuracy of 0.92, an MMAE of 0.06, and an F1-macro score of 0.92. It outperforms all the models implemented in the study. The pre-trained models performed well and scored well in all measures. The deep learning models have different architectures. CNN + BiLSTM with 4 convolutional layers and 2 LSTM layers performed the best. The inclusion of maxpool layer in the BiLSTM model with the convolutional layer added to the performance of the combined model. Figure 4, 5 and 6 show the result of baseline models.

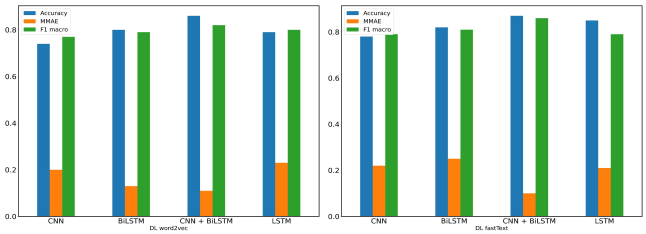

Fig. 5. Result of DL models

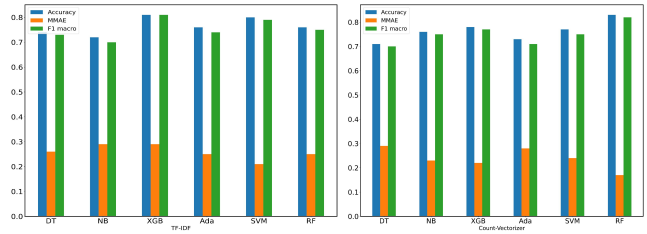

Fig. 6. Result of ML models

V. Conclusion

Early Alzheimer's Disease detection is a very important process for the world considering the aging population and much research has been done in this field. This study, however, focused on compiling the available resources to perform a collective analysis of the best performers in the field. This study can be used as a baseline for any further research in detection as it employs concrete NLP techniques for the processing data and performs a comparative analysis of many models that can be used in predictive analysis. The study is a cheap and effective way of prognosis, albeit the efficacy can only be a small indicator of the diagnosis. Further improvements in the NLP and ML domains can make great advancements in detection. Improvements in word embeddings and vectorization techniques can also improve the performance of the models used in the study. More data can also make drastic improvements in the study. Amongst research constraints, the lack of diverse and valuable data was encountered. The data used in the research was not high quality or quantity with not a lot of ambiguity in the text and not much features. The lack of processing power in normal day to day computers as well as lack of trustworthy text processing, tokenization, and vectorization libraries that perform well with all types of textual data also hindered the research process. However, more diverse and valuable data was the biggest research constraint faced. This research can be a great motivation and baseline for future work in the field of the detection of Alzheimer's disease using speech.

Authorized licensed use limited to: DELHI TECHNICAL UNIV. Downloaded on June 14,2023 at 05:04:45 UTC from IEEE Xplore. Restrictions apply.

Classifier	TF-IDF			Count Vectorizer (CV)		
	Acc↑	MMAE↓	$F1_{macro}$↑	Acc↑	MMAE↓	$F1_{macro}$↑
Decision Trees	0.74	0.26	0.73	0.71	0.29	0.70
Naive Bayes	0.72	0.29	0.70	0.76	0.23	0.75
XGBoost	0.81	0.19	0.81	0.78	0.22	0.77
AdaBoost	0.76	0.25	0.74	0.73	0.28	0.71
SVM	0.80	0.21	0.79	0.77	0.24	0.75
Random Forest	0.76	0.25	0.75	0.83	0.17	0.82

TABLE II
RESULTS WITH DIFFERENT ML ALGORITHMS

Classifier	Acc↑	MMAE↓	$F1_{macro}$↑	Batch Size	Epochs	Learning Rate	Parameters
BERT	0.76	0.22	0.76	16	5	2×10^{-5}	66M
DistilBERT	0.84	0.12	0.84	16	6	2×10^{-5}	66.9M
AlBERT	0.92	0.06	0.92	16	6	2×10^{-5}	11.6M

TABLE III
DETAILS OF FEW LARGE PRE-TRAINED MODELS

Classifier	Word2Vec			fastText		
	Acc↑	MMAE↓	$F1_{macro}$↑	Acc↑	MMAE↓	$F1_{macro}$↑
CNN	0.74	0.20	0.77	0.78	0.22	0.79
BiLSTM	0.80	0.13	0.79	0.82	0.25	0.81
CNN + BiLSTM	0.86	0.11	0.82	0.87	0.10	0.86
LSTM	0.79	0.23	0.80	0.85	0.21	0.79

TABLE IV
RESULTS OF DEEP-LEARNING ALGORITHMS

Classifier	Count of CNN layer	Count of LSTM layer	Count of Maxpool layer	Droupout	Count of dense layer
CNN	4	-	2	-	1
BiLSTM	-	4	-	0.6,0.2	2
CNN + BiLSTM	4	2	2	-	3
LSTM	-	4	-	0.5,0.2	2

TABLE V
PARAMETERS OF DL

REFERENCES

[1] Ahmed, Samrah, et al. "Semantic processing in a connected speech at a uniformly early stage of autopsy-confirmed Alzheimer's disease." Neuropsychology 27.1 (2013): 79.

[2] Rauniyar, Kritesh, Javed Ahmad Khan, and A. Monika. "Review of Different Machine Learning Techniques for Stock Market Prediction." Inventive Systems and Control: Proceedings of ICISC 2021. Springer Singapore, 2021.

[3] Orimaye, Sylvester O., et al. "Predicting probable Alzheimer's disease using linguistic deficits and biomarkers." BMC bioinformatics 18.1 (2017): 1-13.

[4] Fritsch, Julian, Sebastian Wankerl, and Elmar Nöth. "Automatic diagnosis of Alzheimer's disease using neural network language models." ICASSP 2019-2019 IEEE International Conference on Acoustics, Speech and Signal Processing (ICASSP). IEEE, 2019.

[5] Khodabakhsh, Ali, Serhan Kuşxuoğlu, and Cenk Demiroğlu. "Natural language features for detection of Alzheimer's disease in conversational speech." IEEE-EMBS International Conference on Biomedical and Health Informatics (BHI). IEEE, 2014.

[6] Masrani, Vaden. Detecting dementia from written and spoken language. Diss. University of British Columbia, 2018.

[7] Chen, Jun, Ji Zhu, and Jieping Ye. "An Attention-Based Hybrid Network for Automatic Detection of Alzheimer's Disease from Narrative Speech." INTERSPEECH. 2019.

[8] Naseem, Usman, and Katarzyna Musial. "Dice: Deep intelligent contextual embedding for twitter sentiment analysis." 2019 International conference on document analysis and recognition (ICDAR). IEEE, 2019.

[9] Singh, Pramod. Machine Learning with PySpark: With Natural Language Processing and Recommender Systems. Apress, 2018.

[10] Bengio, Yoshua, Réjean Ducharme, and Pascal Vincent. "A neural probabilistic language model." Advances in neural information processing systems 13 (2000).

[11] Thapa, Surendrabikram, et al. "Detecting Alzheimer's disease by exploiting linguistic information from Nepali transcript." Neural Information Processing: 27th International Conference, ICONIP 2020, Bangkok, Thailand, November 18–22, 2020, Proceedings, Part IV 27. Springer International Publishing, 2020.

[12] Rauniyar, Kritesh, and Javed Ahmad Khan. "Application of IoT and AI in the Development of Smart Cities." Smart Cities. CRC Press, 2022. 181-196.

[13] Vincze, Veronika, et al. "Detecting mild cognitive impairment by exploiting linguistic information from transcripts." Proceedings of the 54th Annual Meeting of the Association for Computational Linguistics (Volume 2: Short Papers). 2016.

[14] Cummings, Louise. "Describing the cookie theft picture: Sources of breakdown in Alzheimer's dementia." Pragmatics and Society 10.2 (2019): 153-176.

[15] Mikolov, Tomas, et al. "Distributed representations of words and phrases and their compositionality." Advances in neural information processing systems 26 (2013).

Authorized licensed use limited to: DELHI TECHNICAL UNIV. Downloaded on June 14,2023 at 05:04:45 UTC from IEEE Xplore. Restrictions apply.

2023 International Conference on Advancement in Computation & Computer Technologies (InCACCT) | 979-8-3503-9648-5/23/$31.00 ©2023 IEEE | DOI: 10.1109/InCACCT57535.2023.10141761

Effectiveness of Vision Transformers in Human Activity Recognition from Videos

Rahul Kumar
Department of Computer Science & Engineering
Delhi Technological University
Delhi, India
rahuldtucs@gmail.com

Shailender Kumar
Department of Computer Science & Engineering
Delhi Technological University
Delhi, India
shailenderkumar@dce.ac.in

***Abstract*— Human Action Recognition (HAR) has got the attention of computer vision domain researchers due to its wide variety of applications like surveillance, behavior detection, sports action monitoring, and elderly monitoring. Due to the huge amount of data, the Deep Learning-based method is widely used in HAR compared to the Machine Learning-based approach. This study explored the various Deep Learning and pre-trained Deep Learning models in HAR. In the pre-trained model, we do not require to train the model from scratch, which is already trained on huge data. This study explored the recent pre-trained Deep Learning model to classify action accurately. This study helps the researcher to evaluate the benefit of the latest Vision Transformer model in the domain of HAR.UCF 50 action dataset is used in this study to examine the effectiveness of the Vision Transformer model in HAR. On UCF 50 action dataset, we have achieved 94.70 % accuracy using the Vision Transformer model variant.**

Keywords—Transformer; Deep Learning; Human Action Recognition; Machine Learning

I. INTRODUCTION

HAR is an active hot research area due to its broad variety of applications, such as video retrieval, security, behavior monitoring, patient activity, elderly monitoring and defense. HAR has several steps: data pre-processing, feature extraction (pose-based, shape-based), learning algorithm and action classification. Real-time Action Recognition (AR) is a hot research domain in HAR for security reasons. In real-time, first, we have to train the model on less available data; after that, data increase rapidly and requires lots of computation. Machine Learning (ML) based classification method used by the researcher earlier to recognize the action. Due to a large amount of data ML-based method does not perform better. Due to the less effectiveness of the ML-based method on huge data, the researcher used Deep Learning (DL) methods to identify action from the video sequences. DL-based methods require more computation power to train the model on huge data. Convolution-Neural-Network (CONET) plays a crucial role in computer vision to identify images and patterns. Other deep learning models like Long Short-Term Memory (LSTM), Recurrent Neural Networks (RNN), and Generative Adversarial Networks (GAN) are used by the researcher's community and are constantly improved. The DL-based approach performs better as compared to traditional ML-based methods. HAR can be classified into 4 action levels[1]: Gesture, Interaction, Group Activity and Action.

HAR still faces issues with action classification due to the view-invariant, low resolution and variable length sequences in datasets. Several ML-based algorithms have been introduced, but each has some limitations. Some methods work well on a specific dataset, short-length videos, single view and unrealistic conditions. The well-suited HAR model can handle challenges and perform better in each circumstance. The DL methods can handle a large amount of data compared to ML methods because they need to perform better when data is large. Researchers are constantly improving methods to recognize action accurately. Some multimodal approaches are also introduced to learn specific actions. In the multimodal approach, we fed various modalities to the model, for example, RGB, Depth data, and Skelton data. Fusion techniques (early fusion, slow fusion, late fusion) are used in a multimodal approach to combine features we received from various modalities. Common steps in the HAR process are Data Pre-Processing, Object Segmentation, Feature Extraction, Training of data and classification. The DL-based method uses an automated feature extraction method and the ML-based approach uses a handcrafted feature approach (pose-based, shape based). The HAR process is depicted in Fig. 1.

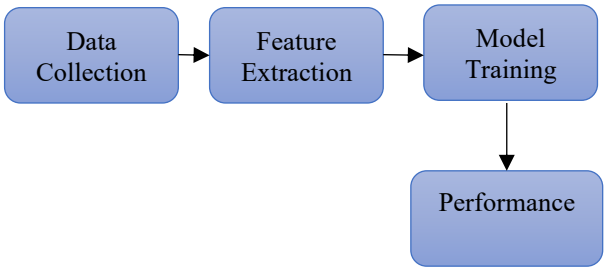

Fig. 1 HAR Complete Process.

DL method succeeded in image classification, object detection and recognizing the action. Deep Learning provides various architectures like CONET employs the best feature extraction approach compared to the handcrafted feature extraction method[2]. Many frameworks depend on CONET to solve the HAR issue. Recurrent Neural Network (RNN) is another framework of DL, whereas Links among nodes create a directed graph along a time sequence, enabling dynamic activity[3]. The main offering of this study is to classify action with the help of the latest Vision Transformer model and compare it with state-of-the-art methods.

This article is structured as follows: Section 2 describes the relevant research in AR. The techniques and data used to assess

ISBN: 979-8-3503-9648-5/23/$31.00 ©2023 IEEE

Authorized licensed use limited to: DELHI TECHNICAL UNIV. Downloaded on June 14,2023 at 05:09:18 UTC from IEEE Xplore. Restrictions apply.

model performance are described in Section 3. Section 4 addresses the outcome and its comparison to recent approaches.

II. Related work

Deep architecture CONET for feature extraction and sequential pattern learning by LSTM architecture in [4]. Automated Learning of features suggested by ji et al. [5]. They used 3-D CONET for HAR. But this model is unsuitable for variable-length clips because of inflexible architecture frames and optical flow input base dual stream model suggested by Simoyan et al.[6] and input fed into the pre-trained DL model. CONET is employed for FE and classification of action of KTH 1 or KTH 2 dataset in and named two-step approach[7]. Ijjina and Mohan developed a deep hybrid model by mixing homogeneous CONETs, which obtained 99.68% accuracy on the UCF 50 dataset [8] Liang et al.[9] studied a highly unsupervised learning model for human segmentation jobs. The video-context-driven human mask inference and CONET-based segmentation network learning iterated until mutual improvement was no longer possible. PASCAL VOC 2012 passed exhaustive testing with an accuracy of 81.8%.

Safaei M et al. [10] suggested an advanced CONET-based technique for forecasting future action and recognizing the form and position of the image's prominent components. They trained a single framework for every move in a one-versus-all approach and obtained a 76.1% accuracy. In [11] capture, pose-based characteristics from the 3D CONET network are capable of 3D posture, 2D appearance, and motion flow unification. The extraction of joint color features for the 3D CONET will result in considerable complexity; consequently, a 15-channel heatmap is generated, and convolution is conducted in each map. Feichtenhofer et al.[12] present a two-stream convolution system for combining dual temporal and spatial streams, in which RGB info (spatial) and optical flow (motion) are modeled simultaneously and estimates are aggregated in the final layers. Due to optical flow, this network cannot capture long-term motion; another drawback of the spatial CONET stream is that its performance depends on a randomly selected image from the input video. Due to background muddle and viewpoint shifts, complications develop.

Shi et al.[13] offer another two-stream network to improve the performance of skeletal joints-based HAR. The Adaptive Graph Convolutional Network (AGCN) network processes a two-stream containing joint and bone information. The network is made up of a stack of these fundamental components. The soft-max layer has been added to the final result. Ullah et al.[14] use real-time video from a non-stationary camera to perform HAR on the system. CONET, a deep learning approach, automatically extracts frame-level characteristics. Jian et al. describe a method for extracting ROI using a Fully Convolutional Network (FCN)[15]. CONET is utilized to determine each frame's posture probability. Key-frame extraction is carried out using the nearby probability difference of frames. The variation-aware key-frame extraction method considers the frame with the greatest probability of a key pose, as assessed by CONET. If many frames give the same key pose probability value, the Central frame is selected. [16] A DL-based solution for temporal 3D poses identification challenges using a CONET and an LSTM recurrent network. They begin by training the CONET and then tweak the combination (CONET+ LSTM). CONET extracts the relevant information, which the LSTM subsequently uses to classify the target action classes. This sort of innovative training strategy outperforms single-stage training. On small-sized data, the results outperform several state-of-the-art approaches. [17] devised a one-of-a-kind HAR model with three primary stages: pre-processing, background removal, and classification. Their technique greatly enhances the results for five action classes extracted from the INRIA and KTH datasets: running, walking, leaping, standing, and sitting. To capture local Spatio-temporal information, [18] presented a multi-resolution CONET architecture for feature connectivity in the time domain. Such a method is being tested on a current "YouTube 1 million videos dataset" with 487 action sequences of classes. The authors mentioned that the foveated design of CONET sped up training complexity. They raised their action categorization rate for big datasets to 63.9%, but their recognition rate for UCF101 is still 63.3%, which is insufficient for such a critical job as action recognition.

Bilen et al. [19]examine the feature maps of a pre-trained model for dynamic image video representation. At the tuning step, they introduced a rank pooling operator and an approximation rank pooling layer, which combine the mappings of all frames into a single dynamic picture representing the whole movie. Deep learning-based algorithms may dependably uncover hidden patterns in visual data due to their extensive feature representation pipeline. On the other hand, it requires a vast quantity of data for training and a high degree of computer processing power. Wu et al. [20] introduced a deep learning-based MPCA-Net technique for classifying human actions. Tensor interaction is used in this strategy to improve the recognition rate. It comprises three layers: projection dictionaries, a projection encoder layer, and a pooling layer. The suggested method is examined on UCF11, different medical imaging datasets, and UCF sports action datasets to establish its effectiveness. Majd et al.[21] suggested a correlational convolutional LSTM (C^2 LSTM) for handling spatial and movement knowledge of surveillance video data. Conv-LSTM is a connectivity combination model for violence detection proposed in [22]. This design employed the CONET network as the fed into the LSTM network for feature analysis and action categorization. Jaouedi et al. proposed a unique method for motion tracking through human monitoring and spatial feature gathering from video sequences. Two techniques were used to build a robust feature vector for classification: Gaussian mixture model (GMM) and Kalman filter (KF) algorithms to detect and extract moving persons, and Gated Recurrent Neural Networks to gather data in each frame and predict human activity. They tested their technique using datasets from UCF Sports, UCF101, and KTH, achieving 89.01%, 89.30%, and 96.30%, respectively.[23]

III. Proposed approach

Deep Learning-based methods play a crucial role in action recognition with their model CONET, LSTM, GAN and Autoencoder and achieve better results than ML-based methods. DL-based methods are capable of dealing with huge amounts of data. But training from scratch for each model is very complex, so various Transfer Learning based methods suggested pre-trained on the huge amount of data. In this study, we evaluated Vision Transformer (VT) for action recognition in video sequences. **Fig. *2*** represents how VT works on frame sequences to detect a class of corresponding frames.

Authorized licensed use limited to: DELHI TECHNICAL UNIV. Downloaded on June 14,2023 at 05:09:18 UTC from IEEE Xplore. Restrictions apply.

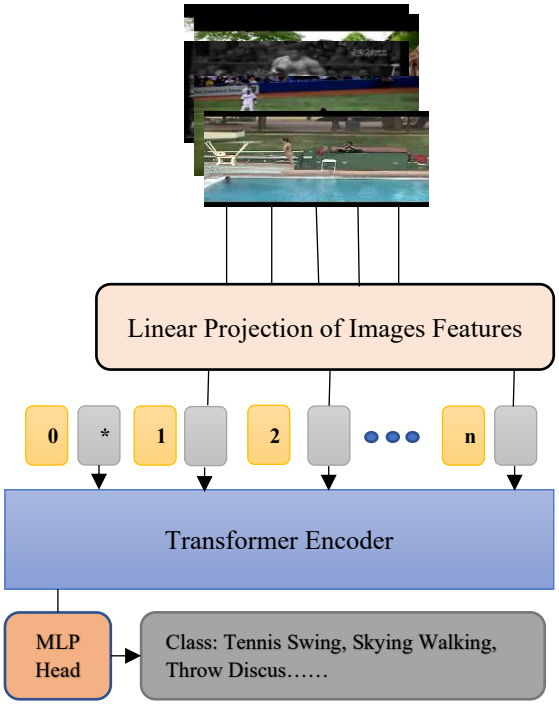

Fig. 2 Action Transformer architecture to recognize action class.

A. Transformer

A 1D sequence of token embeddings is fed into the standard Transformer. In the Transformer, to manage 2-D images reshaping required images $x \epsilon \mathbb{R}^{H \times W \times C}$ into an order of flattened two-dimensional spots $x_p \epsilon \mathbb{R}^{N \times P^2 \times C}$, images resolution is represented by (H, W), count of the channel with the help of C, Each image's resolution shows from (P, P) and the total number of patches represented by $N = HW/P^2$, which also acts as the essential input order span for the Transformer. Because the Transformer uses a constant latent vector size D throughout its stages, they use a trainable linear projection to straighten the areas and transfer to D dimensions. The VT's first layer sequentially reflects the smoothed regions into a shorter realm[24]. The characteristics resemble appropriate basis functions for a low-dimensional representation of the fine structure contained inside each patch. After the projection, the patch representations are then improved with a learned position embedding.

In location embedding resemblance, the model learns to express distance inside the visual, i.e., closer patches have more similar position embeddings. The row-column structure is also obvious; deep characteristics are identical within the same row/column. Because of self-attention, VT can acquire data during the whole visual, even at the lowest levels[24].

B. Dataset

UCF 50 action dataset was used to evaluate the performance of the VT model. This dataset was presented by Reddy et al.[25] in 2012. Action videos are gathered from online sources such as YouTube and have a realistic environment. This dataset has 50 distinct action classes, such as playing tabla, baseball pitch, yo-yo, walking with the dog, and throwing discus. The dataset contains about 100 short videos on every class, with a broad span of camera motion, object look and posture, object scale, perspective, cluttered backdrop, illumination conditions, and so forth. **Fig. *3*** depicts the action sequences from UCF 50 dataset

Fig. 3 Action sequence taken from UCF 50 dataset.

IV. Results & Discussion

Transfer learning is a weight initialization approach where the neural network is not learned using stochastic weights and biases but rather with pre-learned weights and biases from the ImageNet dataset. The network is then permitted to learn and upgrade its parameters on the training data, the HAR vision datasets. In this approach, it just becomes fine-tuned for such a current categorization goal. We used the VT model to classify each action of the UCF50 dataset and compared these with state-of-the-art methods. VT variants are pre-trained deep learning models trained on large-scale dataset ImageNet[26].

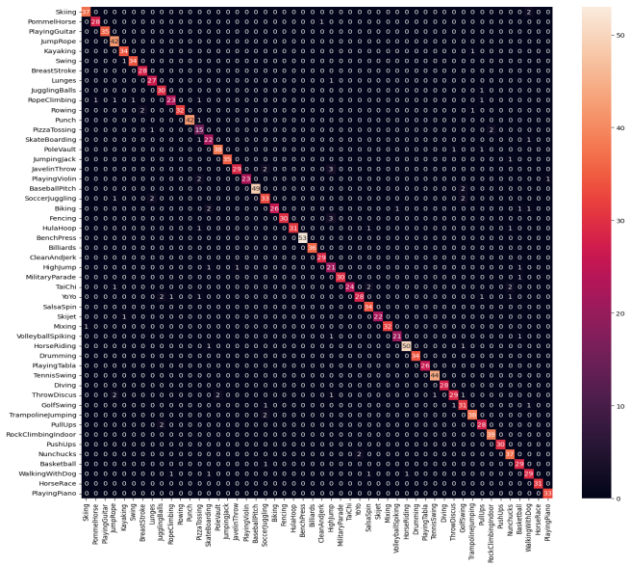

Fig. 4 Confusion Matrix for UCF 50 action dataset classification using VT_B_16 model.

Authorized licensed use limited to: DELHI TECHNICAL UNIV. Downloaded on June 14,2023 at 05:09:18 UTC from IEEE Xplore. Restrictions apply.

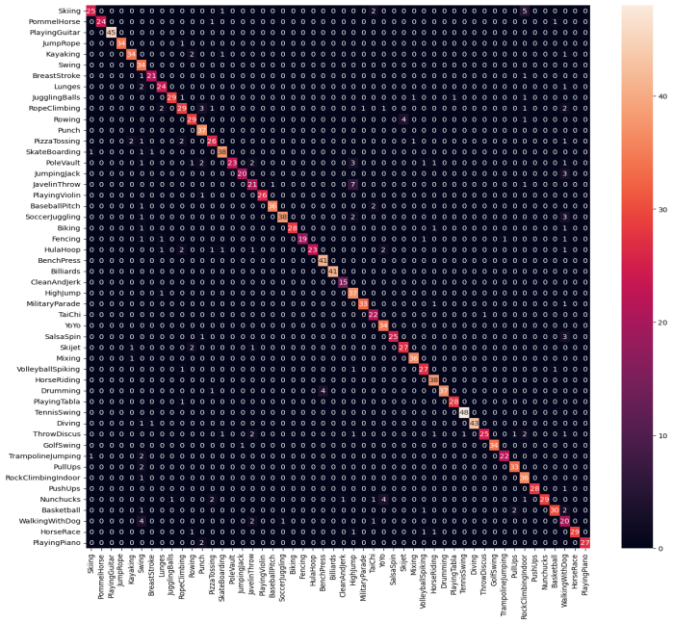

Fig. 5 Classification of action sequence of UCF 50 dataset with VT_l_16 model.

These models can classify each action accurately and do not need to train the model from scratch. This study has compared the accuracy of the various variants of VT on the UCF 50 dataset. This study has extracted sequences of images of each action category and trained them with the help of these frames. VT performs better as compared to the various Transfer Learning and DL models. Fig. 4 & Fig. 5 represent the confusion matrix for UCF 50 dataset. We have compared different variant performances of the VT model in Table 1 and plotted a comparison graph in Fig. 6.

Table 1: Comparison of performance between Vision Transformer variants

Model Name	Accuracy	Precision	Recall	F1-Score
Vision Transformer(vit_b-16)	94.70	94.36	94.17	94.11
Vision Transformer(vit_l_16)	89	91.07	89.47	89.69

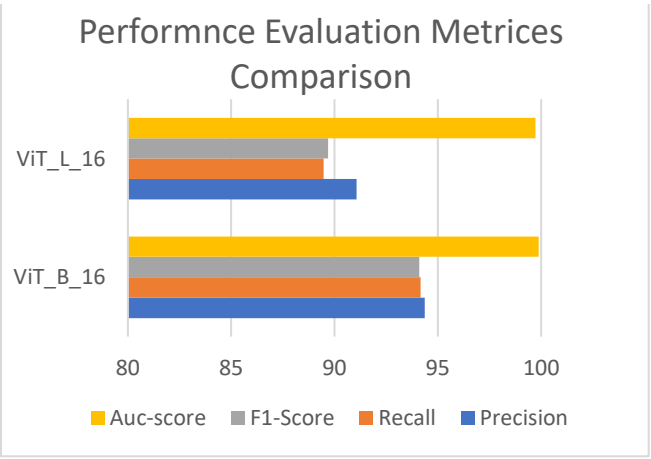

Fig. 6 Comparison Graph of Evaluation Metrics

In this study, UCF 50 action dataset has been employed to examine the effectiveness of the VT model in terms of accuracy, precision and recall. VT models are pre-trained models and can classify each action effectively. We implemented VT models on GPU to evaluate the effectiveness of these models in HAR. This study has used two variants of VT (VT_b_16 & VT_l_16), which means base or large model. They contain 16 X 16 input sizes. The base model has 12 layers with 32 M params and the large model has 24 layers with 307 M params. **Table *2*** compares these models with other state-of-the-art methods in terms of accuracy.

Table 2: Evaluation on the UCF 50 dataset against state-of-the-art methodologies.

Reference Model	**Accuracy (in %)**
Action Bank [27].	76.4
Multi-Channel Descriptor [28]	83.3
Global-Spatio Temporal Feature[29]	70.1
Wang et al[30]	91.7
Vision Transformer (VT_b_16)[24]	**94.70**
Vision Transformer (VT_l_16) [24]	89.00

V. CONCLUSION

This article has explored the VT model in the domain of HAR.VT models are capable of classifying action effectively because of their deep architecture. Using the UCF 50 dataset, we compared the effectiveness of these models to that of state-of-the-art methods. This study compared various evaluation metrics of the model (f1-score, precision, recal,l etc.) to look at effectiveness. The VT model outperforms other suggested methods on the UCF 50 action dataset, with an accuracy of 94.70%. In the future, more complex and Multiview datasets can be tested. These models can be used to classify online action and complex action identification. Numerous variants of Transformer suggested with fewer parameters, requiring less time and computing power. These models are also used in surveillance data for quick response.

VI. REFERENCES

[1] S. Vishwakarma and A. Agrawal, "A survey on activity recognition and behavior understanding in video surveillance," in *Visual Computer*, Oct. 2013, vol. 29, no. 10, pp. 983–1009. doi: 10.1007/s00371-012-0752-6.

[2] A. Krizhevsky, I. Sutskever, and G. E. Hinton, "ImageNet Classification with Deep Convolutional Neural Networks." [Online]. Available: http://code.google.com/p/cuda-convnet/

[3] A. Graves, A. Mohamed, and G. Hinton, "Speech Recognition with Deep Recurrent Neural Networks," Mar. 2013, [Online]. Available: http://arxiv.org/abs/1303.5778

[4] A. Ullah, J. Ahmad, K. Muhammad, M. Sajjad, and S. W. Baik, "Action Recognition in Video Sequences using Deep Bi-Directional LSTM with CNN Features," *IEEE Access*, vol. 6, pp. 1155–1166, Nov. 2017, doi: 10.1109/ACCESS.2017.2778011.

[5] S. Ji, W. Xu, M. Yang, and K. Yu, "3D Convolutional Neural Networks for Human Action Recognition." [Online]. Available: http://www-nlpir.nist.gov/projects/trecvid/

[6] K. Simonyan and A. Zisserman, "Two-Stream Convolutional Networks for Action Recognition in Videos."

[7] M. Baccouche, F. Mamalet, C. Wolf, C. Garcia, and A. Baskurt, "Sequential Deep Learning for Human Action Recognition."

[8] E. P. Ijjina and C. Krishna Mohan, "Hybrid deep neural network model for human action recognition," *Applied Soft Computing*

Authorized licensed use limited to: DELHI TECHNICAL UNIV. Downloaded on June 14,2023 at 05:09:18 UTC from IEEE Xplore. Restrictions apply.

Journal, vol. 46, pp. 936–952, Sep. 2016, doi: 10.1016/j.asoc.2015.08.025.

[9] X. Liang *et al.*, "Learning to Segment Human by Watching YouTube," *IEEE Trans Pattern Anal Mach Intell*, vol. 39, no. 7, pp. 1462–1468, Jul. 2017, doi: 10.1109/TPAMI.2016.2598340.

[10] M. Safaei and H. Foroosh, "Single Image Action Recognition by Predicting Space-Time Saliency," May 2017, [Online]. Available: http://arxiv.org/abs/1705.04641

[11] Y. Huang, S.-H. Lai, and S.-H. Tai, "Human Action Recognition Based on Temporal Pose CNN and Multi-Dimensional Fusion."

[12] C. Feichtenhofer, A. Pinz, and A. Zisserman, "Convolutional Two-Stream Network Fusion for Video Action Recognition," in *Proceedings of the IEEE Computer Society Conference on Computer Vision and Pattern Recognition*, Dec. 2016, vol. 2016-December, pp. 1933–1941. doi: 10.1109/CVPR.2016.213.

[13] L. Shi, Y. Zhang, J. Cheng, and H. Lu, "Two-Stream Adaptive Graph Convolutional Networks for Skeleton-Based Action Recognition." [Online]. Available: https://github.com/lshiwjx/2s-AGCN

[14] A. Ullah, K. Muhammad, I. U. Haq, and S. W. Baik, "Action recognition using optimized deep autoencoder and CNN for surveillance data streams of non-stationary environments," *Future Generation Computer Systems*, vol. 96, pp. 386–397, Jul. 2019, doi: 10.1016/j.future.2019.01.029.

[15] J. Dai, Y. Li, K. He, and J. Sun, "R-FCN: Object Detection via Region-based Fully Convolutional Networks." [Online]. Available: https://github.com/daijifeng001/r-fcn.

[16] J. C. Núñez, R. Cabido, J. J. Pantrigo, A. S. Montemayor, and J. F. Vélez, "Convolutional Neural Networks and Long Short-Term Memory for skeleton-based human activity and hand gesture recognition," *Pattern Recognit*, vol. 76, pp. 80–94, Apr. 2018, doi: 10.1016/j.patcog.2017.10.033.

[17] G. Sulong and A. Mohammedali, "RECOGNITION OF HUMAN ACTIVITIES FROM STILL IMAGE USING NOVEL CLASSIFIER 1," *J Theor Appl Inf Technol*, vol. 10, no. 1, 2015, [Online]. Available: www.jatit.org

[18] A. Karpathy, G. Toderici, S. Shetty, T. Leung, R. Sukthankar, and L. Fei-Fei, "Large-scale Video Classification with Convolutional Neural Networks." [Online]. Available: http://cs.stanford.edu/people/karpathy/deepvideo

[19] H. Bilen, B. Fernando, E. Gavves, A. Vedaldi, and S. Gould, "Dynamic Image Networks for Action Recognition."

[20] J. Wu, S. Qiu, R. Zeng, Y. Kong, L. Senhadji, and H. Shu, "Multilinear Principal Component Analysis Network for Tensor Object Classification," *IEEE Access*, vol. 5, pp. 3322–3331, 2017, doi: 10.1109/ACCESS.2017.2675478.

[21] M. Majd and R. Safabakhsh, "Correlational Convolutional LSTM for human action recognition," *Neurocomputing*, vol. 396, pp. 224–229, Jul. 2020, doi: 10.1016/j.neucom.2018.10.095.

[22] IEEE Signal Processing Society, IEEE Computer Society, and Institute of Electrical and Electronics Engineers, *2017 14th IEEE International Conference on Advanced Video and Signal Based Surveillance (AVSS) : Aug. 29 2017-Sept. 1 2017.*

[23] N. Jaouedi, N. Boujnah, and M. S. Bouhlel, "A new hybrid deep learning model for human action recognition," *Journal of King Saud University - Computer and Information Sciences*, vol. 32, no. 4, pp. 447–453, May 2020, doi: 10.1016/j.jksuci.2019.09.004.

[24] A. Dosovitskiy *et al.*, "An Image is Worth 16x16 Words: Transformers for Image Recognition at Scale," Oct. 2020, [Online]. Available: http://arxiv.org/abs/2010.11929

[25] K. K. Reddy and M. Shah, "Recognizing 50 Human Action Categories of Web Videos."

[26] O. Russakovsky *et al.*, "ImageNet Large Scale Visual Recognition Challenge," *Int J Comput Vis*, vol. 115, no. 3, pp. 211–252, Dec. 2015, doi: 10.1007/s11263-015-0816-y.

[27] S. Sadanand and J. J. Corso, "Action bank: A high-level representation of activity in video," in *Proceedings of the IEEE Computer Society Conference on Computer Vision and Pattern Recognition*, 2012, pp. 1234–1241. doi: 10.1109/CVPR.2012.6247806.

[28] F. Shi, E. Petriu, and R. Laganiere, "Sampling strategies for real-time action recognition," in *Proceedings of the IEEE Computer Society Conference on Computer Vision and Pattern Recognition*, 2013, pp. 2595–2602. doi: 10.1109/CVPR.2013.335.

[29] G. Somasundaram, A. Cherian, V. Morellas, and N. Papanikolopoulos, "Action Recognition Using Global Spatio-Temporal Features Derived from Sparse Representations."

[30] H. Wang, D. Oneata, J. Verbeek, and C. Schmid, "A Robust and Efficient Video Representation for Action Recognition," *Int J Comput Vis*, vol. 119, no. 3, pp. 219–238, Sep. 2016, doi: 10.1007/s11263-015-0846-5.

Authorized licensed use limited to: DELHI TECHNICAL UNIV. Downloaded on June 14,2023 at 05:09:18 UTC from IEEE Xplore. Restrictions apply.

arXiv:2306.03999v1 [gr-qc] 6 Jun 2023

Exploring the Observational Signatures of $f(R, G, \mathcal{T})$ Gravity in FRW Universe

Himanshu Chaudhary,[1,2,*] Amine Bouali,[3,†] Niyaz Uddin Molla,[4,‡] Ujjal Debnath,[4,§] and G.Mustafa[5,¶]

[1]*Department of Applied Mathematics, Delhi Technological University, Delhi-110042, India,*
[2]*Department of Mathematics, Shyamlal College, University of Delhi, Delhi-110032, India.*
[3]*Laboratory of Physics of Matter and Radiation, Mohammed I University, BP 717, Oujda, Morocco,*
[4]*Department of Mathematics, Indian Institute of Engineering Science and Technology, Shibpur, Howrah-711 103, India.*
[5]*Department of Physics, Zhejiang Normal University, Jinhua 321004, Peoples Republic of China,*

The paper is devoted to study the observational signatures of $f(R, G, \mathcal{T})$ Gravity in FRW Universe. In this research article, we present a new cosmological model formulated within the $f(R, G, \mathcal{T})$ framework. To constrain the model parameters, we employ the Markov Chain Monte Carlo (MCMC) technique, which enables us to explore the parameter space effectively, and used the 36 points of Cosmic Chronometers and 1701 points from Pantheon Plus data. We compare our proposed $f(R, G, \mathcal{T})$ model with the widely accepted ΛCDM model, considering different cosmological parameters, including Deceleration, Snap, and Jerk. By evaluating these parameters, we gain valuable insights into the dynamics and evolution of the universe within the context of our new model. Moreover, various diagnostic tests have been conducted, such as Statefinder and Om Diagnostic, to further investigate the behavior and consistency of our $f(R, G, \mathcal{T})$ model. These tests offer deeper insights into the properties of our model and its compatibility with observational data. We subject our model to statistical analysis using Information Criteria, which serves as a rigorous quantitative assessment of the model's goodness of fit to the data. This analysis aids in determining the level of agreement between our $f(R, G, \mathcal{T})$ model and the observational data, thus establishing the viability and reliability of our proposed cosmological framework. Our findings highlight the potential of the $f(R, G, \mathcal{T})$ framework in understanding the fundamental aspects of the universe's evolution and dynamics. The comparative analysis with ΛCDM, as well as the comprehensive diagnostic tests performed, demonstrate the efficacy and validity of our model in explaining the observed cosmological phenomena. These results contribute to the ongoing pursuit of accurate and comprehensive models that can provide a deeper understanding of the nature of our universe.

CONTENTS

I. Introduction 2

II. Basic Equations in $f(R, G, \mathcal{T})$ Gravity 3

III. Cosmological tests of the $f(R, G, \mathcal{T})$ dark energy model 5
A. Methodology 5
B. Data description 5
1. Cosmic chronometers Dataset 5
2. Pantheon + Dataset 6

IV. Observational, and theoretical comparisons of the Hubble functions 8
A. Comparison with the Cosmic chronometers dataSet. 8
B. Comparison with the Relative difference between $f(R, G, \mathcal{T})$ dark energy model and ΛCDM 8
C. Comparison with the Pantheon + dataSet 8

V. Cosmographic analysis 9
A. The deceleration parameter 9
B. The jerk parameter 9
C. The snap parameter 10

VI. Statefinder Diagnostic 11

VII. Om Diagnostic 11

VIII. Information Criteria 12

IX. Results 12

X. Discussions and Concluding Remarks 15

References 16

* himanshuch1729@gmail.com
† a1.bouali@ump.ac.ma
‡ niyazuddin182@gmail.com
§ ujjaldebnath@gmail.com
¶ gmustafa3828@gmail.com

I. INTRODUCTION

Recent astronomical observations have strongly suggested that our universe is undergoing an accelerated expansion [1–4] and some unknown matter causes of this acceleration called Dark energy (DE) which is basically the negative pressure and positive energy density form of matter satisfying $\rho + 3P < 0$ [5, 6]. This DE is one of the most interesting and important discovery of the mysterious energy in modern cosmology, which was first investigated in type Ia Supernovae (SNe Ia)[10–12] and afterwards others numerous investigations were done with further astronomical data [13–17][].It has also been investigated from the different point of view such as observational Hubble parameter data,power spectra, cosmic microwave background radiation(CMBR) and large-scale structure of the new version of the universe [18–22]. It has been suggested that the new version of the universe is made of about 74% DE , 4% ordinary matter and about 22% dark matter.The most simplest form of DE is known as cosmological constant [23, 24], also called the Λ cold-dark-matter (ΛCDM) model, which has been successfully employed to describing the various aspects of the observed universe. For a long time, researchers on the universe mainly motivated by theories.However, huge progresses on observational/ experimental explorations of accelerated expansion of the universe have been witnessed in the last few years. Now a days , the modern researchers have a great challenging task to know the nature/properties of the new version of the universe in details. In the investigation of the accelerated expansion of the universe, several cosmological model have been explored mainly in two different ways. One of them is modified theories of gravity as a classical modification of Einstein theory of gravity and other approaches is the existence of mysterious energy so-called DE. It is worth suggesting that the new version of the universe is while accelerating , the value of EoS parameter (ratio between pressure and its energy density) is less than $< -\frac{1}{3}$ and also by the observational point of view , the value of the EoS parameter is very close to -1. For this purpose, several works have been studied by some authors to describe the DE on several topics such as quintessence[25–28], quintom [29–31], cosmological constant [32–35] ,phantom [36–41] ,tachyon [42, 43], modified gravity [44–51], teleparallel gravity [52, 53], Chaplygin gas models [54–60],holography [61–67], new agegraphics [68–71], bouncing theory [72–74] and braneworld models [75, 76].

An enormous relativistic astrophysicist have been proposed the various modified gravity theories which are obtained via changing the ricci scalar R in standard Einstein-Hilbert(EH) action. The standard EH action is changed by the different function of ricci scalar (i.e. f(R) gravity)[77, 78]or Gauss-Bonnet (GB) invarient G (i.e.f(G) gravity)[79, 80]. The formulation of this modifications could be applied as an important role to investigating the cases of cosmic rapid expansion [81–94]. Without considering any other dark components ,these modification could also be described the early-time inflation as well as late time acceleration and these cosmological model could also be consistent with the solar system constraint[95]. Modified gravity theories refer to the alternative theories of gravity that differ from Einstein's general theory of relativity (GR) by modifying the fundamental gravitational action. In particular, $f(R)$ gravity, where R is the Ricci scalar, is a popular modified gravity theory that has received significant attention in recent years due to its ability to explain the current cosmic acceleration without invoking dark energy. However, $f(R)$ gravity alone cannot explain all of the observed phenomena in astrophysics and cosmology. A class of generalized $f(R)$ modified theories of gravity was derived by Bertolami et. al [96] by considering an explicit coupling between of an arbitrary function of the ricci scalar curvature R and the matter Lagrangian density $\mathcal{L}_m$. In the description of early-time and late-time accelerated universe, Norjiri et al. [97] investigated the non-minimal coupling of f(R) and f(G) gravity of theories with the Lagrangian density of matter $\mathcal{L}_m$ and shown that the unified description of the inflationary era with the present cosmic accelerated expansion. As an alternative to DE, to study the various cosmic issues, an systemetic method has discussed by the f(G) gravity [98] and it is extremely useful to study the restricted period of the future discontinuties and the pace of cosmos over the long period time [99, 100][37][38]. Harko et al [101] introduced another important extension of general theory relativity such as f(R,T) and f(R,T^{ϕ}) where the gravitational Lagrangian is the function of ricci scalar R and trace of stress energy tensor T where as T^{ϕ} for the scalar field stress energy tensor. Several important implication in f(R,T) gravity theory have been extremely discussed in some Litaratures [102–107].Later, Researchers have introduced the another type of modified gravity such as f(R,G) gravity [108].Several cosmological implication including the energy conditions,future finite-time singularities have been discussed in several literatures [109–116]. In [117], Sharif and Ikram proposed another kind of extension of modified theory of gravity like f(G,T) gravity theory. They reconstructed the f(G,T) gravity theory through the power-law, de-sitter expansion of the universe. They also studied the stability of some reconstructed cosmological model with liner perturbations in f(G,T) Shamir and Ahmed [118] investigated the f(G,T) gravity using the Noether symmetry of some cosmological viable.

In the ref. [119], the author proposed the modification of above modified gravity like $f(R, G, \mathcal{T})$ gravity. $f(R, G, \mathcal{T})$ gravity is a more general modification of gravity, where G and $\mathcal{T}$ are the Gauss-Bonnet invariant and the trace of the energy-momentum tensor, respectively. It has been found the forms of the function $f(R, G, \mathcal{T})$ by the three types of standard expansion models such

as de Sitter, power-law and future singularity models. This theory is considered more promising because it can address not only the cosmic acceleration but also several other problems in the field of astrophysics and cosmology. One of the most significant implications of $f(R,G,\mathcal{T})$ gravity is its ability to explain the current cosmic acceleration without introducing dark energy. Recent observational studies have confirmed that the expansion rate of the universe is increasing, but the cause of this acceleration is not yet fully understood. In standard cosmology, dark energy is invoked to explain this phenomenon. However, $f(R,G,\mathcal{T})$ gravity provides a viable alternative explanation without introducing any new unknown physical entity. Moreover, $f(R,G,\mathcal{T})$ gravity can also address some of the shortcomings of the $f(R)$ gravity. For example, $f(R)$ gravity is known to produce some inconsistencies when tested against observations of gravitational waves. However, $f(R,G,\mathcal{T})$ gravity is free from these inconsistencies, making it a more attractive theory. In addition to explaining the cosmic acceleration, $f(R,G,\mathcal{T})$ gravity can also address the issue of dark matter and the formation of large-scale structures in the universe. Recent studies have shown that $f(R,G,\mathcal{T})$ gravity can explain the observed rotation curves of galaxies without the need for dark matter. Furthermore, it can also reproduce the observed cosmic microwave background radiation and large-scale structure formation. While $f(R,G,\mathcal{T})$ gravity is still a relatively new and untested theory, it has shown great potential in addressing some of the most significant problems in the field of astrophysics and cosmology. Its ability to unify modified gravity theories and address several issues makes it an important area of research. Subsequently, some authors [120–123] have studied the wormhole and compact star models in the framework of $f(R,G,\mathcal{T})$ gravity.

In the present work, we consider the newly proposed $f(R,G,\mathcal{T})$ gravity model in FRW universe. In section 2, we assume the universe is filled with radiation and dark matter in the framework of $f(R,G,\mathcal{T})$ gravity. We are not taking any external dark energy where the effect of this modification of gravity can be treated as alternative to dark energy. Then we assume a power-law form of the function $f(R,G,\mathcal{T})$ and then form a differential equation of the Hubble parameter $H(z)$. In section 3, we constrain the parameters of the $f(R,G,\mathcal{T})$ gravity model by MCMC method and then obtain the viability of the model. Finally, results are presented in section 5.

II. BASIC EQUATIONS IN $f(R,G,\mathcal{T})$ GRAVITY

In this section, we review the $f(R,G,\mathcal{T})$ gravity theory in details. The HE action for $f(R,G,\mathcal{T})$ gravity theory is defined in the form [119]

$$S=\frac{1}{2}\int f(R,G,\mathcal{T})\sqrt{-g}\;d^4x+\int L_m\sqrt{-g}\;d^4x \quad (1)$$

where $f(R,G,\mathcal{T})$ denotes the arbitrary function of R, G and $\mathcal{T}$ where L_m denotes the matter Lagrangian, $g=|g_{\mu\nu}|$ ($g_{\mu\nu}$ is the metric tensor) (choosing $8\pi G_N=c=1$, G_N is the Newtonian constant). The Ricci scalar R , Gauss-Bonnet invariant G and the trace of stress energy tensor $\mathcal{T}$ are defined as follows:

$$R=g^{\mu\nu}R_{\mu\nu},\; G=R^2-4R_{\mu\nu}R^{\mu\nu}+R_{\mu\nu\xi\eta}R^{\mu\nu\xi\eta},\; \mathcal{T}=g^{\mu\nu}gT_{\mu\nu} \quad (2)$$

The desired field equations of $f(R,G,\mathcal{T})$ gravity theory are obtained by the variation of action (1) as follows

$$(R_{\mu\nu}+g_{\mu\nu}\nabla^2-\nabla_\mu\nabla_\nu)f_R-\frac{1}{2}\,fg_{\mu\nu}$$

$$+(2RR_{\mu\nu}-4R^{\xi}_{\mu}R_{\xi\nu}-4R_{\mu\xi\nu\eta}R^{\xi\eta}+2R^{\xi\eta\lambda}_{\mu}R_{\nu\xi\eta\lambda})f_G$$

$$+(2Rg_{\mu\nu}\nabla^2-2R\nabla_\mu\nabla_\nu-4g_{\mu\nu}R^{\xi\eta}\nabla_\xi\nabla_\eta$$

$$-4R_{\mu\nu}\nabla^2+4R^{\xi}_{\mu}\nabla_\nu\nabla_\xi+4R^{\xi}_{\nu}\nabla_\mu\nabla_\xi+4R_{\mu\xi\nu\eta}\nabla^\xi\nabla^\eta)f_G$$

$$=T_{\mu\nu}-(T_{\mu\nu}+\Theta_{\mu\nu})f_{\mathcal{T}} \quad (3)$$

where $f_R=\frac{\partial f}{\partial R}$, $f_G=\frac{\partial f}{\partial G}$, $f_{\mathcal{T}}=\frac{\partial f}{\partial \mathcal{T}}$, $\nabla^2=\nabla_\mu\nabla^\mu$ is the D'Alembert operator, $T_{\mu\nu}$ is the energy-momentum tensor and $\mathcal{T}$ is its trace. The energy momentum tensor for an ideal fluid is represented as

$$T_{\mu\nu}=(\rho+p)u_\mu u_\nu+pg_{\mu\nu} \quad (4)$$

where the symbol ρ and p denote the energy density and pressure of the ideal fluid respectively . The four velocity of the fluid's u_μ satisfies $u_\mu u^\mu=-1$ and $u^\mu\nabla_\nu u_\mu=0$. Also $\Theta_{\mu\nu}=-2T_{\mu\nu}+pg_{\mu\nu}$. The line element of the flat Friedmann-Robertson-Walker (FRW) model of the universe assumed as

$$ds^2=-dt^2+a^2(t)\left[dr^2+r^2(d\theta^2+sin^2\theta d\phi^2)\right] \quad (5)$$

where $a(t)$ is the scale factor. From equation (2), we can obtain

$$R=6(\dot{H}+2H^2),\quad G=24H^2(\dot{H}+H^2) \quad (6)$$

Here $H=\dot{a}/a$ denotes the Hubble parameter where *dot* denotes the derivative w.r.t. cosmic time t.Using the above metric (5) , we get the trace of $T_{\mu\nu}$ is $\mathcal{T}=3p-\rho$. Now, the basic conservation equation $\nabla^\mu T_{\mu\nu}=0$ for an ideal fluid gives

$$\dot{\rho}+3H(\rho+p)=0 \quad (7)$$

with the help of the equation (3), the field equations for $f(R,G,\mathcal{T})$ gravity are obtained as follows

$$3H^2 = \frac{1}{f_R}\Bigg[\rho + (\rho+p)f_{\mathcal{T}} + \frac{1}{2}(Rf_R - f) - 3H\dot{f}_R + 12H^2(\dot{H}+H^2)f_G - 12H^3\dot{f}_G\Bigg] \tag{8}$$

and

$$(2\dot{H}+3H^2) = -\frac{1}{f_R}\Bigg[p - \frac{1}{2}(Rf_R - f) + 2H\dot{f}R + \ddot{f}R - 12H^2 (\dot{H}+H^2)f_G + 8H(\dot{H}+H^2)\dot{f}G \tag{9}$$

$$+ 4H^2\ddot{f}G\Bigg] \tag{10}$$

In the standard Einstein's field equations, the above two field equations can be written as

$$3H^2 = \rho_{eff} \;\; and \;\; (2\dot{H}+3H^2) = -p_{eff} \tag{11}$$

where

$$\rho_{eff} = \frac{1}{f_R}\Bigg[\rho + (\rho+p)f_{\mathcal{T}} + \frac{1}{2}(Rf_R - f) - 3H\dot{f}_R + 12H^2(\dot{H}+H^2)f_G - 12H^3\dot{f}_G\Bigg] \tag{12}$$

and

$$p_{eff} = \frac{1}{f_R}\Bigg[p - \frac{1}{2}(Rf_R - f) + 2H\dot{f}R + \ddot{f}R - 12H^2 (\dot{H}+H^2)f_G + 8H(\dot{H}+H^2)\dot{f}G + 4H^2\ddot{f}G\Bigg] \tag{13}$$

We assume that the fluid components of the universe are composed of radiation, pressureless dark matter, and dark energy where dark energy can be produced by modified gravity. So $\rho = \rho_r + \rho_m$ and $p = p_r + p_m$ with $p_m = 0$. The energy density for radiation and dark matter are respectively $\rho_r = 3H_0^2\Omega_{r0}(1+z)^4$ and $\rho_m = 3H_0^2\Omega_{m0}(1+z)^3$, where $\Omega_{r0} = \frac{\rho_{r0}}{3H_0^2}$ and $\Omega_{m0} = \frac{\rho_{m0}}{3H_0^2}$ are the dimensionless density parameters, H_0 is the present value of the Hubble parameter and z is the redshift.

Now we assume a power-law form of $f(R,G,\mathcal{T})$ as in the form

$$f(R,G,\mathcal{T}) = \alpha_1 R^{\beta_1} + \alpha_2 G^{\beta_2} + \alpha_3(-\mathcal{T})^{\beta_3} \tag{14}$$

where α_i and β_i $(i = 1,2,3)$ are constants. So from equation (8), we obtain the differential equation of the Hubble parameter $H(z)$:

$$\begin{aligned}
&24^{\beta_2}\alpha_2(1-\beta_2)\left(H^3\left(H-(1+z)H'\right)\right)^{\beta_2} \\
&+6^{\beta_1}\alpha_1\beta_1 H^2\left(H\left(2H-(1+z)H'\right)\right)^{\beta_1-1} + 6^{\beta_1}\alpha_1(1-\beta_1)\left(H\left(2H-(1+z)H'\right)\right)^{\beta_1} \\
&+6^{\beta_1}(1+z)\alpha_1\beta_1\left(\beta_1-1\right)H^3\left(H\left(2H-(1+z)H'\right)\right)^{\beta_1-2}\left((1+z)H'^2 - H\left(3H'-(1+z)H''\right)\right) \\
&+24^{\beta_2}(1+z)\alpha_2\beta_2\left(\beta_2-1\right)H^{3\beta_2}\left(H-(1+z)H'\right)^{\beta_2-2}\left(3(1+z)H'^2 + H\left(-3H'+(1+z)H''\right)\right) \\
&= -2\alpha_3 H_0^2\left(3H_0^2\Omega_{m0}(1+z)^3\right)^{\beta_3-1}\left[3(\beta_3-0.5)\Omega_{m0}(1+z)^3 + 4\beta_3\Omega_{r0}(1+z)^4\right] \\
&+6H_0^2\left[\Omega_{m0}(1+z)^3 + \Omega_{r0}(1+z)^4\right]
\end{aligned} \tag{15}$$

where $H' = dH/dz$ and $H'' = d^2H/dz^2$.

III. COSMOLOGICAL TESTS OF THE $f(R,G,\mathcal{T})$ DARK ENERGY MODEL

In this section, we conduct a comprehensive comparison between the predictions of the $f(R,G,\mathcal{T})$ dark energy model and observational data to obtain constraints on the model's free parameters. Our analysis employs two observational datasets, namely the Cosmic chronometers data and the Pantheon + dataset, which consists of 36 and 1701 data points, respectively. The nine free parameters of the $f(R,G,\mathcal{T})$ dark energy model, namely $(H_0, \Omega_{\rm m0}, \Omega_{\rm r0}, \beta_1, \beta_2, \beta_3, \alpha_1, \alpha_2, \alpha_3)$, along with the present-day value of the Hubble function H_0, are constrained using the standard Bayesian technique, likelihood function approach, and Markov Chain Monte Carlo (MCMC) method. Once the best-fit values of the model parameters are obtained, we examine the model's cosmographic behavior by analyzing the evolution of the deceleration, jerk, and snap parameters, and compare the model predictions with those of the standard ΛCDM cosmological model.

A. Methodology

Markov Chain Monte Carlo (MCMC) is a widely used statistical technique in cosmology for exploring the parameter space of complex models and generating probability distributions for cosmological parameters [128]. MCMC is particularly useful when there is a large parameter space and the likelihood function is non-Gaussian or non-linear [129]. The basic idea behind MCMC is to create a Markov chain that samples the parameter space of a model according to a probability distribution. The chain consists of a sequence of parameter values, where each value is generated from the previous value using a set of transition rules that depend on a proposal distribution [130]. The proposal distribution suggests a new parameter value that may or may not be accepted based on its posterior probability given the data and the prior probability distribution [130]. To ensure that the Markov chain converges to the true posterior distribution, several methods are used, including adjusting the proposal distribution to optimize the acceptance rate, tuning the length of the chain to obtain independent samples, and assessing the convergence of the chain using diagnostic tests [129, 130]. Once the chain has converged, the posterior distribution for the parameters can be estimated by computing the frequency of the parameter values in the chain [130]. The posterior distribution can then be used to estimate the best-fit values and uncertainties for the cosmological parameters and to make predictions for observables such as the cosmic microwave background radiation and the large-scale structure of the universe [128, 129]. MCMC is a powerful tool for analyzing cosmological data and has been used in a wide range of cosmological studies, including measurements of the cosmic microwave background, large-scale structure, and dark energy [128, 129]. The technique is computationally intensive, but with the increasing power of modern computing, it has become an essential tool for cosmologists in understanding the nature and evolution of the universe [128, 129].

B. Data description

1. *Cosmic chronometers Dataset*

Cosmic chronometers are a class of astronomical objects that provide valuable data for measuring the expansion history of the universe. These objects are typically old, quiescent galaxies that have stopped forming stars and are identified by their spectra and colors [131]. The data used in cosmic chronometry is based on measurements of the ages of these galaxies at different redshifts. Elliptical galaxies are the most commonly used cosmic chronometers since they have relatively simple stellar populations and are thought to have formed early in the history of the universe [133]. The ages of stars in these galaxies can be determined from their spectra, which provide information on the chemical composition and internal processes that have occurred within them [134]. Other potential cosmic chronometers include white dwarfs, globular clusters, and the oldest stars in the Milky Way. However, these objects are more challenging to observe and analyze than elliptical galaxies [135], and their use as cosmic chronometers is still an area of ongoing research. To collect cosmic chronometry data, astronomers use large telescopes and spectrographs to measure the spectra and colors of these galaxies with high precision [132]. Sophisticated statistical techniques are then employed to determine the ages of the galaxies and the expansion history of the universe [136]. Ccosmic chronometry provides an essential tool for studying the universe's expansion history and testing cosmological models [131]. The data obtained from cosmic chronometers is crucial to our understanding of the universe and the fundamental laws of physics that govern it.

In our analysis, we incorporated Hubble expansion rate data to obtain tighter constraints on our dark energy (DE) models. The CC dataset can be derived through different methods. One approach is based on the clustering of galaxies and quasars, where the Baryon Acoustic Oscillations (BAO) in the radial direction are measured [124, 125]. Another method is the differential age method, which expresses the Hubble parameter as

$$H(z) = -\frac{1}{1+z}\frac{dz}{dt}, \tag{16}$$

where $\frac{dz}{dt}$ can be inferred from $\frac{\Delta z}{\Delta t}$. Here, Δz and

Δt represent the redshift difference and the age difference between two passively evolving galaxies, respectively [126, 127]. For our analysis, we utilized a compilation of 36 data points of the CC dataset, with each data point accompanied by its corresponding reference. While the CC data points are considered uncorrelated, we can define the $\chi^2_{H(z)}$ function as

$$\chi^2_{CC} = \sum_{i=1}^{36} \left[\frac{H_{\rm obs,i} - H(z_i)}{\sigma_{H,i}} \right]^2, \tag{17}$$

where $H_{\rm obs,i}$ represents the observed value of the Hubble parameter for each redshift z_i (references), and $H(z)$ denotes the theoretical prediction of the Hubble parameter. By evaluating the χ^2_{CC} function, we can quantify the level of agreement between the observed Hubble parameter values and the predictions of our DE models. This analysis allows us to assess the fit quality and obtain valuable constraints on the parameters of the models.

2. *Pantheon + Dataset*

The updated Pantheon + dataset represents a significant advancement in our understanding of the universe's expansion history. This compilation incorporates a comprehensive collection of 1701 data points, providing a wealth of information for cosmological investigations. These data points cover a wide range of redshifts, from $0.001 < z < 2.3$ allowing researchers to probe the expansion dynamics over a significant cosmic timeline. The Pantheon + dataset builds upon previous SNIa compilations and includes the latest observations of Type Ia supernovae. These supernovae have been instrumental in unveiling the accelerating expansion of the universe. As highly luminous astrophysical objects, SNIa serves as valuable standard candles for measuring relative distances based on their apparent and absolute magnitudes.

Type Ia supernovae (SNIa) have played a significant role in our understanding of the accelerating expansion of the universe. These astrophysical objects have proven to be valuable tools for studying the nature of the component responsible for this cosmic acceleration. Several compilations of SNIa data have been released in recent years, such as Union [140], Union2 [139], Union2.1 [141], Joint Light-curve Analysis (JLA) [142], Pantheon [143], and the more recent Pantheon+ [137]. The Pantheon+ dataset, which contains 1701 SNIa spanning a redshift range of $0.001 < z < 2.3$, provides a valuable resource for cosmological investigations. SNIa are exceptionally luminous objects and are often considered as standard candles for measuring relative distances in the universe using the distance modulus. The chi-square values associated with the Pantheon+ dataset are calculated as follows:

$$\chi^2_{\rm Pantheon+} = \vec{D}^T \cdot \mathbf{C}^{-1}_{\rm Pantheon+} \cdot \vec{D}, \tag{18}$$

where $\mathbf{C}_{\rm Pantheon+}$ represents the covariance matrix provided with the Pantheon+ data, encompassing both statistical and systematic uncertainties. In Equation (18), $\vec{D} = m_{Bi} - M - \mu_{\rm model}$, with m_{Bi} and M denoting the apparent and absolute magnitudes, respectively. The term $\mu_{\rm model}$ represents the predicted distance modulus based on a chosen cosmological model, given by

$$\mu_{\rm model}(z_i) = 5\log_{10}\left(\frac{D_L(z_i)}{\frac{H_0}{c}\,\mathrm{Mpc}} \right) + 25, \tag{19}$$

where H_0 is the present value of the Hubble rate, and $D_L(z)$ denotes the luminosity distance. For a flat, homogeneous, and isotropic FLRW universe, $D_L(z)$ is given by

$$D_L(z) = (1+z)H_0 \int_0^z \frac{dz'}{H(z')}. \tag{20}$$

Unlike the Pantheon dataset, the degeneracy between the absolute magnitude M and H_0 is broken in Pantheon+. This is achieved by rewriting the vector $\vec{D}$ in Equation (18) in terms of the distance moduli of SNIa in Cepheid hosts. This allows for an independent constraint on M, resulting in the following expression:

$$\vec{D}'_i = \begin{cases} m_{Bi} - M - \mu_i^{\rm Ceph} & i \in \text{ Cepheid hosts} \\ m_{Bi} - M - \mu_{\rm model}\ (z_i) & \text{otherwise}\ , \end{cases} \tag{21}$$

where $\mu_i^{\rm Ceph}$ represents the distance modulus corresponding to the Cepheid host of the $i^{\rm th}$ SNIa, measured independently using Cepheid calibrators. Thus, Equation (18) can be rewritten as:

$$\chi^2_{\rm SN} = \vec{D}'^T \cdot \mathbf{C}^{-1}_{\rm Pantheon+} \cdot \vec{D}'. \tag{22}$$

In order to combine the SNIa data with other cosmological probes, the total chi-square value, $\chi^2_{\rm tot}$, is obtained by adding the contributions from the cosmic chronometers (CC) and the other cosmological datasets (Pantheon +).

$$\chi^2_{Tot} = \chi^2_{CC} + \chi^2_{Pantheon+}. \tag{23}$$

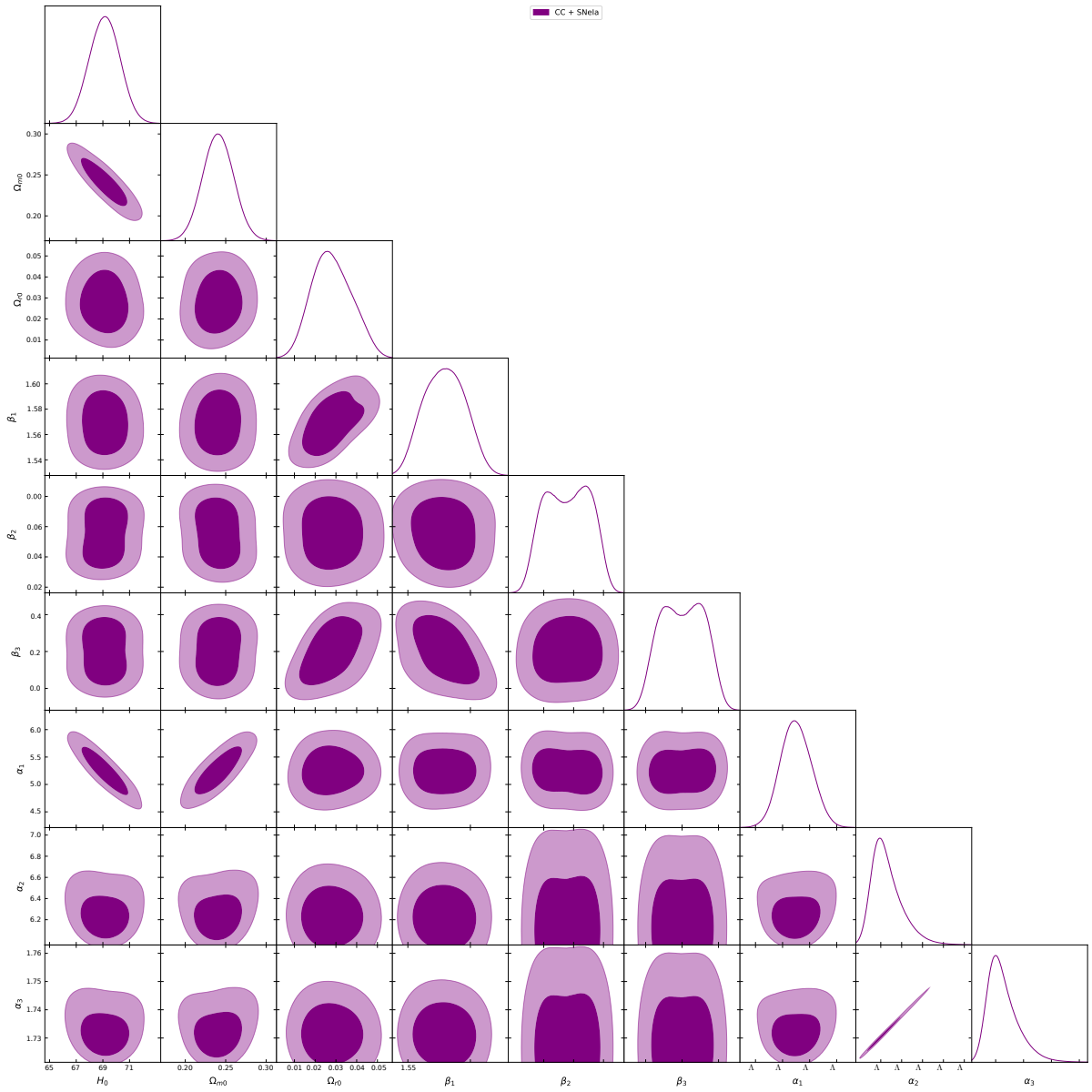

FIG. 1. The contour plot of free parameter space $(H_0, \Omega_{\rm m0}, \Omega_{\rm r0}, \beta_1, \beta_2, \beta_3, \alpha_1, \alpha_2, \alpha_3)$ for our model I with $1-\sigma$ and $2-\sigma$ errors obtained from the datasets.

MCMC Results of $f(R, G, \mathcal{T})$ Model			
Model	Parameters	Prior	Best fit Value
ΛCDM Model	H_0	[50.,100.]	$69.854848^{+1.259100}_{-1.259100}$
Model	H_0	[50.,100.]	$69.131041^{+0.139490}_{-0.139490}$
	$\Omega_{\rm m0}$	[0.,1.]	$0.240739^{+0.018284}_{-0.018284}$
	$\Omega_{\rm r0}$	[0.,1]	$0.028080^{+0.009746}_{-0.009746}$
	β_1	[1.,2.]	$1.570660^{+0.018798}_{-0.018798}$
	β_2	[0.,0.1]	$0.024082^{+0.017751}_{-0.017751}$
	β_3	[0.,1]	$0.232398^{+0.004917}_{-0.004917}$
	α_1	[5.,6.]	$5.496010^{+2.820425}_{-2.820425}$
	α_2	[6.,6.5]	$6.250227^{+1.312755}_{-1.312755}$
	α_3	[1.,2.]	$1.732398^{+0.004917}_{-0.004917}$

TABLE I. Summary of the MCMC results using dataset.

IV. OBSERVATIONAL, AND THEORETICAL COMPARISONS OF THE HUBBLE FUNCTIONS

A. Comparison with the Cosmic chronometers dataSet.

The Hubble function is a crucial parameter in cosmology, as it relates the universe's expansion rate to its present age and the distribution of matter and energy within it. The ΛCDM model is the most widely accepted cosmological model, describing the universe as composed of dark matter, dark energy, and ordinary matter. In this study, we perform curve fitting of the Hubble function using the ΛCDM model, $f(R,G,\mathcal{T})$ dark energy model, and 36 points of Cosmic Chronometers (CC) by using the best-fit values of both the model parameters obtained by minimizing the χ^2 function.

Our results demonstrate that the ΛCDM model provides an excellent fit to the CC data, and $f(R,G,\mathcal{T})$ dark energy model. The comparison findings are shown in Figure 2.

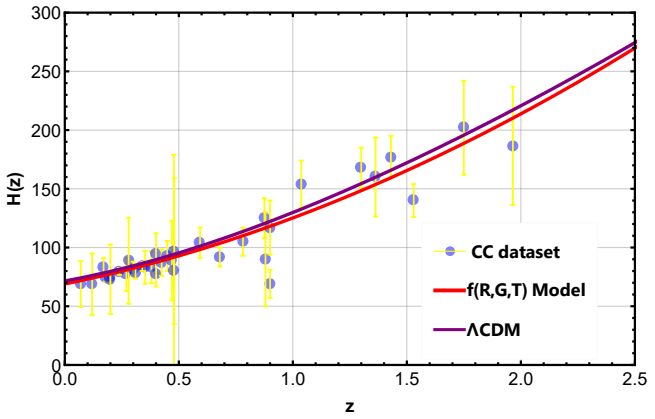

FIG. 2. The figure shows the theoretical curve of the Hubble function $H(z)$ corresponding to the studied (red curve) and ΛCDM (black dashed curve) models against the 36 measurements of CC measurements shown in blue dots with their corresponding error bars in the yellow line. For ΛCDM the parameters were fixed at $\Omega_m = 0.301 \pm 0.012$ and $\Omega_\Lambda = 0.699 \pm 0.012$.

B. Comparison with the Relative difference between $f(R,G,\mathcal{T})$ dark energy model and ΛCDM

In this subsection, we aim to study the difference between the $f(R,G,\mathcal{T})$ dark energy model and the ΛCDM model as a function of redshift, by comparing their predicted values for the Hubble parameter against Cosmic Chronometers (CC) measurements. We then analyze how this difference varies with redshift.

Our findings indicate that there is a negligible difference between the $f(R,G,\mathcal{T})$ dark energy model and the ΛCDM model at low redshifts but slightly increases at higher redshifts, However, we acknowledge that the uncertainties in the CC measurements also increase with redshift, so caution must be taken when interpreting these results. Overall, our investigation provides significant insights into the limitations of the ΛCDM model and the potential of $f(R,G,\mathcal{T})$ dark energy model to better explain the behavior of the universe at higher redshifts. The comparison findings are shown in Figure 3.

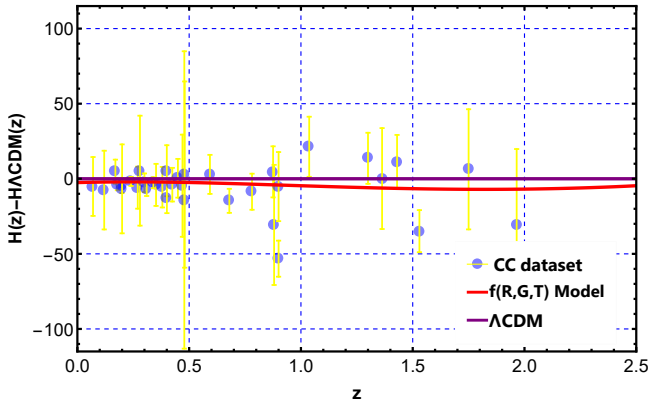

FIG. 3. The variation of the difference between $f(R,G,T)$ Model corresponding to the studied (red curve) and ΛCDM (purple line) as a function of the redshift z against the CC measurements shown in blue dots with their corresponding error bars in the yellow line. For ΛCDM the parameters were fixed at $\Omega_m = 0.301 \pm 0.012$ and $\Omega_\Lambda = 0.699 \pm 0.012$.

C. Comparison with the Pantheon + dataSet

The distance modulus function has been fitted with the ΛCDM model and $f(R,G,\mathcal{T})$ dark energy model using the Pantheon Plus dataset. The Pantheon Plus dataset comprises 1701 SNe Ia data points in the redshift range $0.01 < z < 2.3$. The fitting process involves minimizing the χ^2 function, which measures the deviation of the theoretical model from the observed data. The theoretical model involves the distance modulus function, which is related to the luminosity distance $d_L(z)$ as $\mu(z) = 5\log_{10}\left[\frac{d_L(z)}{Mpc}\right] + 25$, where Mpc is the unit of distance. The luminosity distance $d_L(z)$ is defined as $d_L(z) = (1+z)\int_0^z \frac{c}{H(z)}dz'$, where c is the speed of light and $H(z)$ is the Hubble parameter.

Our results demonstrate that the ΛCDM model provides an excellent fit to the Pantheon Plus dataset, and $f(R,G,\mathcal{T})$ dark energy model. The comparison findings are shown in Figure 4.

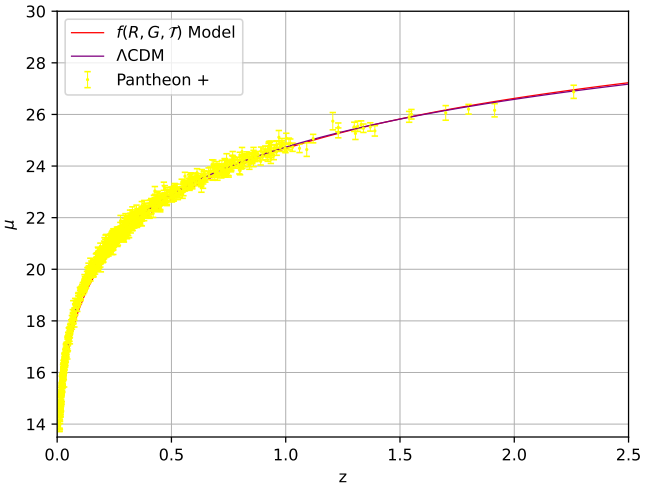

FIG. 4. The figure shows the theoretical curve of the distance modulus $\mu(z)$ corresponding to the studied (red curve) and ΛCDM (black dashed curve) models against the Supernovae type Ia dataset shown in blue with their corresponding error bars. For ΛCDM the parameters were fixed at $\Omega_{m0} = 0.3$ and $\Omega_\Lambda = 0.7$.

V. COSMOGRAPHIC ANALYSIS

Cosmography parameters are a set of cosmological parameters that describe the expansion history of the universe in a model-independent way. These parameters are derived solely from the measurement of the cosmic expansion rate, also known as the Hubble parameter, and its derivatives with respect to redshift. The most commonly used cosmography parameters are the Hubble constant (H_0), the deceleration parameter (q_0), and the jerk parameter (j_0) [144, 145]. H_0 represents the current expansion rate of the universe, while q_0 and j_0 describe the acceleration and jerk of the expansion, respectively. Cosmography parameters have several advantages over other cosmological parameters, such as those derived from cosmic microwave background radiation or the large-scale structure of the universe. They are model-independent, meaning that they do not rely on any assumptions about the underlying cosmological model. This makes them useful for testing the validity of different cosmological models and for constraining the properties of dark energy, which is responsible for the acceleration of the expansion [146]. Cosmography parameters are relatively easy to measure from observational data. The Hubble constant can be determined from observations of Type Ia supernovae, gravitational lensing, and other methods, while the higher-order cosmography parameters can be estimated from measurements of the Hubble parameter at different redshifts [144, 145]. Cosmography parameters can be used to test the validity of the cosmological principle, which states that the universe is homogeneous and isotropic on large scales. Deviations from the cosmography predictions could indicate the presence of large-scale structures or other departures from the standard cosmological model [147]. Cosmography parameters provide a powerful tool for measuring the expansion history of the universe and testing cosmological models in a model-independent way. The ease of measurement and their ability to test the cosmological principle make them an important component of modern cosmology research.

A. The deceleration parameter

The deceleration parameter is a crucial cosmological parameter that characterizes the expansion rate of the universe. It is defined as the ratio of the deceleration of the universe's expansion to the present expansion rate. A positive deceleration parameter implies that the expansion of the universe is slowing down, while a negative deceleration parameter indicates that the expansion of the universe is accelerating. In other words, the deceleration parameter is a measure of the transition between the decelerated and accelerated phases of the universe's expansion. Mathematically, one can define it as

$$q = -\frac{a\ddot{a}}{\dot{a}^2}. \tag{24}$$

Observational analysis plays a critical role in determining the range of values for the deceleration parameter. For instance, the apparent brightness and redshift for supernovae in distant galaxies can be used to estimate the deceleration parameter [1, 2]. Recent observations strongly support models that predict an accelerating universe. However, obtaining an accurate value for the deceleration parameter remains a challenging task. It is essential to note that the Hubble parameter's behavior is determined by the sign of the deceleration parameter. If the deceleration parameter is positive, the Hubble parameter decreases with time, and if it is negative, the Hubble parameter increases with time. Therefore, the deceleration parameter provides valuable insights into the dynamics of the universe's expansion. It is crucial to explore the ranges of possible values for the deceleration parameter through observational analyses and to obtain accurate estimates to gain a better understanding of the universe's evolution.

B. The jerk parameter

The jerk parameter is a cosmological parameter that generalizes the expansion rate of the universe beyond the usual parameters of $a(t)$ and q. It arises from the fourth term in a Taylor series of the scale factor around a given time t_0 [148]:

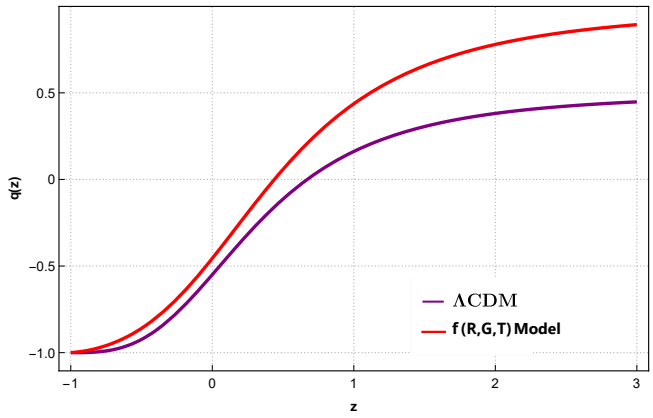

FIG. 5. Evolution of the deceleration parameter as a function of the redshift z

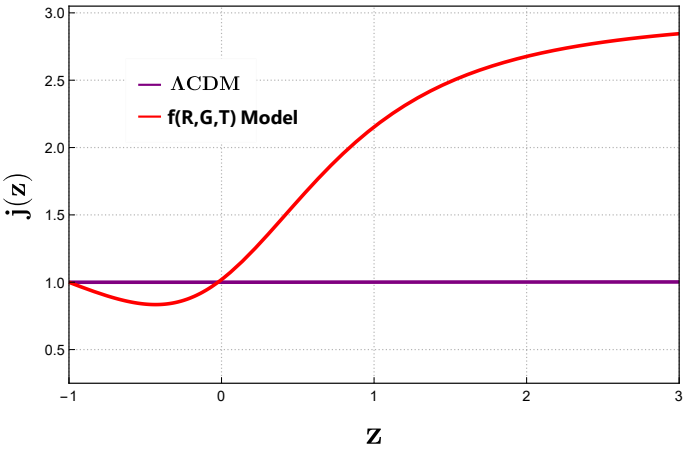

FIG. 6. Evolution of the jerk parameter as a function of the redshift z

$$\frac{a(t)}{a_0} = 1 + H_0(t-t_0) - \frac{1}{2}q_0H_0^2(t-t_0)^2 + \frac{1}{6}j_0H_0^3(t-t_0)^3 + O\left[(t-t_0)^4\right]. \tag{25}$$

The jerk parameter, denoted as j, is defined as the third derivative of the scale factor with respect to cosmic time [144]:

$$j = \frac{1}{a}\frac{d^3a}{d\tau^3}\left[\frac{1}{a}\frac{da}{d\tau}\right]^{-3} = q(2q+1) + (1+z)\frac{dq}{dz}. \tag{26}$$

The jerk parameter plays a significant role in the search for a suitable candidate for the physical interpretation of cosmic dynamics in the presence of various dark energy proposals [144]. The value of the jerk parameter can provide insight into the transitions between different eras of accelerated expansion. A specific value of the jerk parameter can establish a correspondence between dark energy proposals and standard universe models, facilitating the search for a favorable candidate for cosmic dynamics. For example, in the flat ΛCDM model, the jerk parameter has a value of $j = 1$ [144]. The jerk parameter is a useful tool in understanding the dynamics of the universe and in distinguishing between different dark energy proposals. Its value can help us better comprehend the various eras of accelerated expansion and identify a suitable model for cosmic dynamics.

C. The snap parameter

The Snap parameter, or the jounce parameter, is a higher-order time derivative of the expansion factor of the universe. It is the fifth term in the Taylor series expansion of the scale factor around the present time a_0,

$$\frac{a(t)}{a_0} = 1 + H_0(t-t_0) - \frac{1}{2}q_0H_0^2(t-t_0)^2 + \frac{1}{6}j_0H_0^3(t-t_0)^3 + \frac{1}{24}s_0H_0^4(t-t_0)^4 + O\left[(t-t_0)^5\right]. \tag{27}$$

and it characterizes the deviation of the universe's expansion from the ΛCDM model. The snap parameter is defined as the fourth derivative of the scale factor with respect to cosmic time,

$$s = \frac{1}{a}\frac{d^4a}{d\tau^4}\left[\frac{1}{a}\frac{da}{d\tau}\right]^{-4} = \frac{j-1}{3\left(q-\frac{1}{2}\right)}, \tag{28}$$

normalized by a certain combination of the scale factor and its time derivatives. The snap parameter plays a crucial role in characterizing the dynamics of the universe [149]. Specifically, it helps to identify the degree of deviation from the standard ΛCDM model, which assumes a cosmological constant as the source of dark energy. The snap parameter is related to the cosmic jerk parameter, and their relative behavior provides insights into the transitions between different eras of the universe's accelerated expansion. In particular, the divergence of the snap parameter with respect to the deceleration parameter determines how the universe's evolution deviates from the ΛCDM dynamics. Therefore, the snap parameter is a valuable tool for studying the nature of dark energy and its role in the evolution of the universe.

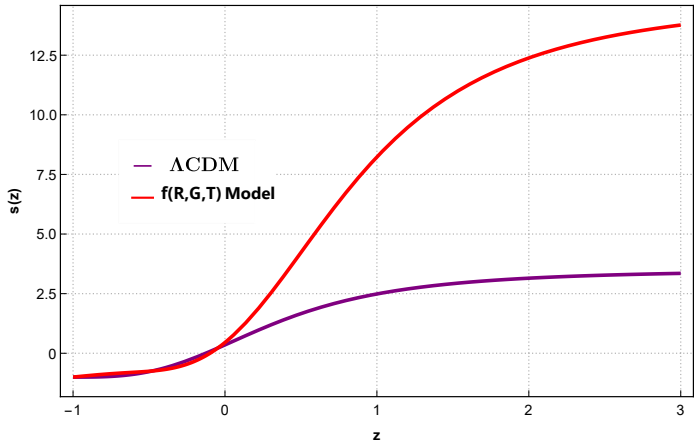

FIG. 7. Evolution of the snap parameter as a function of the redshift z

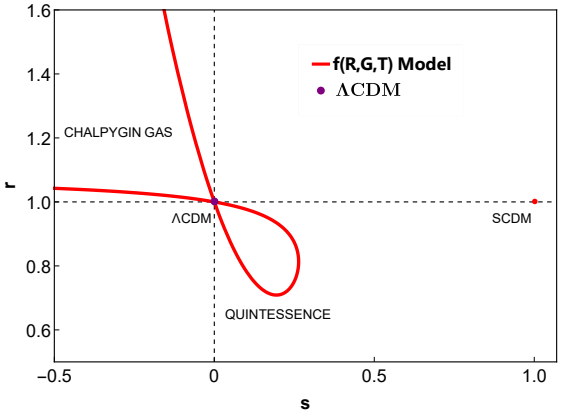

FIG. 8. Behavior of $\{s, r\}$ profile.

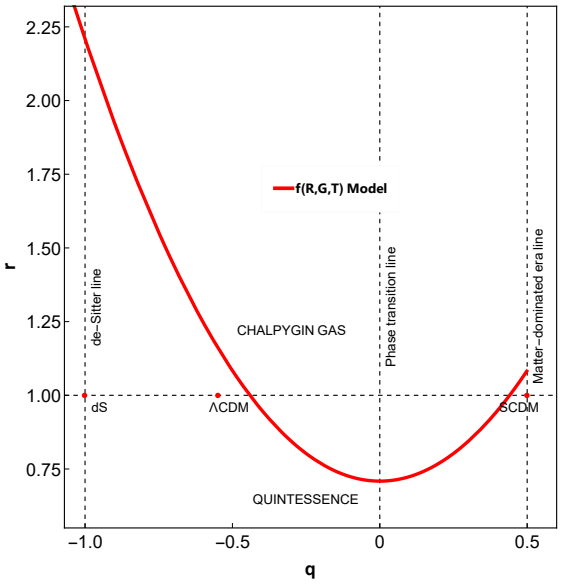

FIG. 9. Behavior of $\{q, r\}$ profile.

VI. STATEFINDER DIAGNOSTIC

The Statefinder diagnostics is a powerful tool used to study different models of dark energy (DE) and understand their characteristics based on higher-order derivatives of the scale factor. It provides a dimensionless pair of parameters, $\{r, s\}$, which can be used to analyze the cosmic properties of DE independent of specific models. The calculations for r and s involve expressions that involve the third derivative of the scale factor ($\dddot{a}$), the Hubble parameter (H), and the deceleration parameter (q) [148]. The parameter s is a linear combination of r and q, enabling further insights into the DE behavior:

$$r = \frac{\dddot{a}}{aH^3}, \quad s = \frac{r-1}{3\left(q-\frac{1}{2}\right)}. \tag{29}$$

Certain pairs of r and s have been associated with standard models of DE. For example, $\{r, s\} = \{1, 0\}$ corresponds to the ΛCDM model, while $\{r, s\} = \{1, 1\}$ corresponds to the standard cold dark matter model (SCDM) in the Friedmann-Lematre-Robertson-Walker (FLRW) universe. The range $(-\infty, \infty)$ represents the Einstein static universe. By examining the $r - s$ plane, it is possible to identify quintessence-like and phantom-like models of DE, characterized by positive and negative values of s, respectively. Deviations from the standard range $\{r, s\} = \{1, 0\}$ can indicate an evolutionary process from phantom-like to quintessence-like behavior [144].The Statefinder diagnostics provide a comprehensive framework to explore and analyze various DE models. By employing the $\{r, s\}$ parameter pair, independent of specific DE models, one can gain insights into the cosmic behavior of DE. This diagnostic tool aids in understanding the transition between different DE phases, distinguishing between quintessence-like and phantom-like behavior, and identifying the standard DE models within the $r - s$ plane.

VII. Om DIAGNOSTIC

In cosmology, a geometrical formalism is employed in which the Hubble parameter serves as a null test for the ΛCDM model [150]. Additionally, the Om diagnostic parameter is used to effectively differentiate various dark energy (DE) models from the ΛCDM model by observing the slope variation of $Om(z)$ [151]. A quintessence or phantom model can be identified through a positive or negative slope of the diagnostic parameter, respectively. Furthermore, a constant slope with respect to redshift depicts a DE model corresponding to the cosmological constant. For a flat universe, the diagnostic parameter $Om(z)$ is defined as:

$$Om(z) = \frac{\left(\frac{H(z)}{H_0}\right)^2 - 1}{(1+z)^3 - 1}. \tag{30}$$

This diagnostic parameter involves only the first-order temporal derivative, as compared to the statefinder diag-

nosis [152], which is discussed in [151]. Additionally, it is applicable to Galileon models [153, 154], as described in [155]. Overall, the Om diagnostic parameter is a useful tool for studying the properties of dark energy models and distinguishing them from the cosmological constant model.

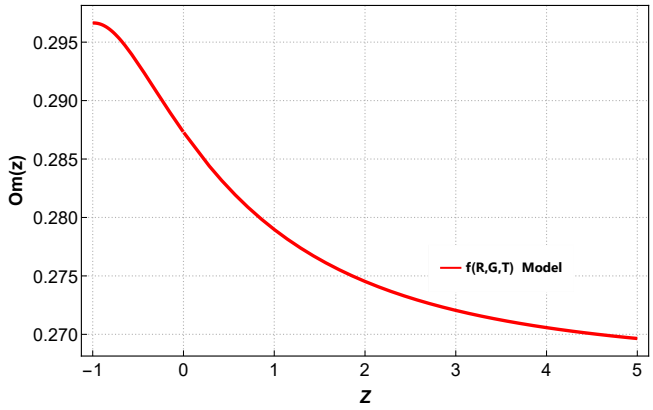

FIG. 10. Evolution of $Om(z)$ profile

VIII. INFORMATION CRITERIA

In cosmology, the $\chi^2_{\rm min}$, $\chi^2_{\rm red}$, Akaike Information Criterion (AIC), and ΔAIC are commonly used statistical measures to assess the goodness of fit and compare different cosmological models based on observational data [156, 157]. The $\chi^2_{\rm min}$ is defined as the minimum value of the χ^2 statistic, which quantifies the difference between the observed data and the theoretical predictions of a model. It is calculated as the sum of the squared differences between the observed data points and the corresponding model predictions, divided by the measurement uncertainties:

$$\chi^2_{\rm min} = \sum \frac{(O_i - E_i)^2}{\sigma_i^2}, \tag{31}$$

where O_i and E_i represent the observed and expected values, respectively, and σ_i is the corresponding measurement uncertainty. The $\chi^2_{\rm red}$ is the reduced chi-square statistic, obtained by dividing the $\chi^2_{\rm min}$ by the number of degrees of freedom (NDF). The NDF is equal to the total number of data points minus the number of free parameters in the model:

$$\chi^2_{\rm red} = \frac{\chi^2_{\rm min}}{\rm NDF}. \tag{32}$$

The $\chi^2_{\rm red}$ provides a normalized measure of the goodness of fit per degree of freedom, allowing for comparisons between models with different numbers of free parameters. The AIC is a statistical criterion that takes into account both the goodness of fit and the complexity of a model. It is calculated as:

$$\text{AIC} = 2k - 2\ln(\mathcal{L}), \tag{33}$$

where k is the number of free parameters in the model and $\mathcal{L}$ is the maximum likelihood of the model. The AIC penalizes models with more parameters, favoring simpler models that provide a good fit to the data. The ΔAIC is the difference in AIC values between the two models. It is calculated as:

$$\Delta\text{AIC} = \text{AIC}_i - \text{AIC}_{\rm min}, \tag{34}$$

where AIC_i and $\text{AIC}_{\rm min}$ are the AIC values of the ith model and the model with the minimum AIC value, respectively. The ΔAIC provides a measure of the relative support for different models, with lower values indicating better model fit and higher likelihood. In cosmology, these statistical measures are widely used to compare different models, such as different parameterizations of the cosmological parameters or different dark energy models, based on observational data. By calculating the $\chi^2_{\rm min}$, $\chi^2_{\rm red}$, AIC, and ΔAIC, researchers can quantify the goodness of fit and identify the most favored models given the data. The $\chi^2_{\rm min}$, $\chi^2_{\rm red}$, AIC, and ΔAIC are important statistical measures in cosmology for assessing the goodness of fit and comparing different models. They provide quantitative tools to evaluate the agreement between theoretical predictions and observational data and aid in the selection of the most suitable models for describing the universe's behavior.

Model	$\chi^{2\ min}_{\rm tot}$	$\chi^2_{\rm red}$	AIC	ΔAIC
ΛCDM Model	1778.74	0.93474	1783.39	0
$f(R,G,\mathcal{T})$ Model	1765.2268	0.9285	1784.77	-1.37941

TABLE II. Summary of $\chi^{2\ min}_{\rm tot}$, $\chi^2_{\rm red}$, AIC_c and ΔAIC_c for ΛCDM and $f(R,G,\mathcal{T})$ model

IX. RESULTS

a. deceleration parameter The fig 5 represents the behavior of the deceleration parameter (q) for the $f(R,G,\mathcal{T})$ model and the ΛCDM model at different epochs and the phase transition redshift. At high redshifts ($z \to \infty$), the $f(R,G,\mathcal{T})$ model has a deceleration parameter value of 0.824, suggesting a decelerating expansion of the universe. On the other hand, the ΛCDM model exhibits a slightly lower deceleration

parameter value of 0.451, indicating a comparatively slower deceleration. As we move towards the present epoch ($z \to 0$), both models show a transition towards a negative deceleration parameter. The $f(R, G, \mathcal{T})$ model has a deceleration parameter value of -0.494, indicating a transition to an accelerating phase. Similarly, the ΛCDM model exhibits a slightly lower value of -0.555, also signifying a transition towards acceleration. At the cosmological constant limit ($z \to -1$), both models converge to a deceleration parameter value of -1, indicating a transition to a de Sitter phase where the expansion is accelerating at an ever-increasing rate. Lastly, the figure provides the phase transition redshift (z_{tr}) at which the deceleration parameter for each model reaches zero ($q = 0$). For the $f(R, G, \mathcal{T})$ model, the transition occurs at $z_{tr} = 0.4253$, while for the ΛCDM model, the transition occurs at a slightly higher redshift of $z_{tr} = 0.659$. Overall, the figure demonstrates the different behaviors of the deceleration parameter between the $f(R, G, \mathcal{T})$ model and the ΛCDM model at various epochs and the phase transition redshift. It illustrates how the expansion of the universe transitions from a decelerating phase to an accelerating phase, with the $f(R, G, \mathcal{T})$ model showing slightly different values compared to the ΛCDM model at each epoch.

b. jerk parameter The fig 6 presents the behavior of the jerk parameter (j) for the $f(R, G, \mathcal{T})$ model and the ΛCDM model at different epochs and the cosmological constant limit ($z \to -1$). At high redshifts ($z \to \infty$), The $f(R, G, \mathcal{T})$ model exhibits a value of 2.7345 for the jerk parameter (j). On the other hand, the ΛCDM model maintains a jerk parameter value of 1 at this epoch. This distinction suggests that at very high redshifts, the $f(R, G, \mathcal{T})$ model differs from the ΛCDM model in terms of the rate of change of acceleration. The $f(R, G, \mathcal{T})$ model exhibits a higher value for the jerk parameter, indicating a potentially different dynamic behavior compared to the constant rate of change of acceleration observed in the ΛCDM model. As we approach the present epoch ($z \to 0$), the $f(R, G, \mathcal{T})$ model exhibits a jerk parameter value of 1, suggesting a constant acceleration similar to the ΛCDM model. At the cosmological constant limit ($z \to -1$), both models have a jerk parameter value of 1. This implies that the acceleration remains constant in both models at this limit. The fig 6 provides a comparative analysis of the jerk parameter for the $f(R, G, \mathcal{T})$ model and the ΛCDM model at different epochs and the phase transition redshift. At high redshifts, the $f(R, G, \mathcal{T})$ model shows a higher rate of change of acceleration compared to the ΛCDM model. However, as we approach the present epoch and the cosmological constant limit, both models converge to the same rate of change of acceleration.

c. snap parameter The fig 7 presents the behavior of the snap parameter (s) for the $f(R, G, \mathcal{T})$ model and the ΛCDM model at different epochs and the cosmological constant limit ($z \to -1$). At high redshifts ($z \to \infty$), the snap parameter for the $f(R, G, \mathcal{T})$ Model is 13.353, while for the ΛCDM model, it is 2.634. This indicates a significant deviation in the curvature and evolution of the two models during the early stages of the universe. The $f(R, G, \mathcal{T})$ Model exhibits a higher snap parameter, suggesting a more pronounced curvature and evolution compared to the ΛCDM model. As we approach the present epoch ($z \to 0$), the snap parameter for both models decreases. For the $f(R, G, \mathcal{T})$ model, it becomes 0.1685, while for the ΛCDM model, it is 0.1674. This implies that both models converge to a similar behavior in terms of curvature and evolution at the current epoch. At the cosmological constant limit ($z \to -1$), both models have a snap parameter of -1. This indicates a transition to an accelerated expansion phase, where the universe's curvature and evolution are primarily governed by the cosmological constant. The fig 7 provides a comparative analysis of the snap parameter for the $f(R, G, \mathcal{T})$ model and the ΛCDM model at different epochs and the cosmological constant limit. It reveals that the two models exhibit different behaviors in terms of curvature and evolution at high redshifts, with the $f(R, G, \mathcal{T})$ model showing a more pronounced curvature. However, as we approach the present epoch, both models converge to a similar behavior. At the cosmological constant limit, both models exhibit an accelerated expansion phase.

d. The $\{s, r\}$ Parameter fig 8 provides a comprehensive description of the behavior and evolution of a cosmological model. In the case of the given model, the Statefinder parameters r and s are used to characterize the nature of dark energy and its transition between different phases. At early times, the $f(R, G, \mathcal{T})$ model is found to have values of $r > 1$ and $s < 0$. These values indicate that the model resembles a Chaplygin gas-type dark energy model. The Chaplygin gas is a theoretical construct that can describe the behavior of dark energy, characterized by an equation of state that deviates from the standard cosmological constant. As the universe evolves, the $f(R, G, \mathcal{T})$ model transitions to values between $r < 1$ and $s > 0$, indicating a quintessence domain. Quintessence refers to a form of dark energy that possesses a dynamic nature, often associated with a slowly evolving scalar field. The quintessence domain represents a phase in which the dark energy density remains relatively constant over time. During this evolution, the $f(R, G, \mathcal{T})$ model crosses an intermediate fixed point, represented by the ΛCDM point $\{1, 0\}$. The ΛCDM model is the standard cosmological model that includes a cosmological constant (Λ) and cold dark matter (CDM). Crossing this fixed point suggests a transition from one phase to another, from a Chaplygin

gas-like behavior to a quintessence-like behavior. Finally, at late times, the $f(R, G, \mathcal{T})$ model returns to the Chaplygin gas domain by passing an interim fixed ΛCDM point. This indicates a transition back to a Chaplygin gas-type dark energy behavior. The specific details and dynamics of this late-time behavior would depend on the specific mathematical form and parameters of the model. Overall, the described model exhibits a rich cosmological evolution, transitioning between different phases of dark energy behavior. It begins as a Chaplygin gas-type model, evolves through a quintessence domain while crossing an intermediate ΛCDM fixed point, and eventually returns to the Chaplygin gas-type behavior at late times. This dynamic behavior provides insights into the nature and characteristics of dark energy and its role in the overall evolution of the universe.

e. The $\{q, r\}$ Parameter In the case of the $f(R, G, \mathcal{T})$ energy model, the diagnostics reveal interesting behavior throughout different cosmic epochs. Fig 9 provides further insights into the model's evolution. At early times, the model exhibits values in the range $q < 0$ and $r < 1$ corresponds to the quintessence domain. As the model evolves, it transitions to values where $r > 1$ and $q < 0$. This region indicates the presence of the Chaplygin gas domain. The transition from the quintessence domain to the Chaplygin gas domain signifies a change in the dominant energy component of the universe, potentially leading to different cosmological behaviors. Finally, at late times, the $f(R, G, \mathcal{T})$ model departs from the de Sitter point, represented by $\{-1, 1\}$. The de Sitter point corresponds to a universe dominated by dark energy, resulting in accelerated expansion and a constant equation of state parameters. Departure from this point indicates deviations from a pure de Sitter universe, potentially due to the influence of additional cosmological components or modified gravity. Overall, the Statefinder diagnostics of the $f(R, G, \mathcal{T})$ energy model reveal a rich cosmological evolution. The model transitions from a quintessence domain to a Chaplygin gas domain, indicating changes in the dominant energy component. Departure from the de Sitter point at late times suggests the presence of additional effects or modifications to the standard cosmological model. These findings provide valuable insights into the behavior and characteristics of the $f(R, G, \mathcal{T})$ model throughout different cosmic epochs.

f. Om Diagnostic The OM Diagnostic is a cosmological quantity that helps characterize the behavior of the matter density in the universe. The Fig 10 provided presents the values of the OM Diagnostic for $f(R, G, \mathcal{T})$ model at different epochs represented by the redshift z. At $z \to \infty$, which corresponds to the early universe or the farthest observable regions, the OM Diagnostic for $f(R, G, \mathcal{T})$ is recorded as 0.270. This value indicates the matter density contribution to the overall energy density of the universe at very high redshifts. As we approach the present time, represented by $z \to 0$, the OM Diagnostic for $f(R, G, \mathcal{T})$ model increases to 0.2855. This suggests that matter density plays a slightly more significant role in the total energy density of the universe as compared to the early universe. Finally, at the phase transition redshift $z \to -1$, which signifies the late-time universe, the OM Diagnostic reaches a value of 0.2952. This indicates that matter density continues to have a non-negligible contribution to the total energy density of the universe, even in the late stages of cosmic evolution. Overall, the values of the OM Diagnostic for $f(R, G, \mathcal{T})$ model suggest that matter density remains an important component of the energy content of the universe throughout its history, from the early universe to the present and even in the late-time universe.

g. Information Criteria In our analysis one could see in table II, we have obtained a ΔAIC value of -1.37941 for our model, while the ΛCDM model has a ΔAIC value of 0. This indicates that our model performs slightly better than the ΛCDM model in terms of goodness of fit and model selection. A negative ΔAIC value suggests that our model provides a better fit to the data compared to the ΛCDM model. The lower the ΔAIC value, the stronger the evidence in favor of our model relative to the ΛCDM model. In our case, the negative value indicates that our model is preferred over the ΛCDM model. The ΔAIC value quantifies the relative support for different models based on their AIC values. A smaller ΔAIC implies a more significant improvement in model fit, indicating that our model captures the observed data more accurately or has a better balance between the goodness of fit and model complexity compared to the ΛCDM model. However, it is important to note that the interpretation of the ΔAIC value should be done in conjunction with other statistical considerations and domain knowledge. While our model may have a slightly better fit than the ΛCDM model based on the AIC analysis, it is necessary to thoroughly assess the robustness and consistency of our model with other observational data and theoretical expectations in cosmology. Further investigations and analyses are required to gain a deeper understanding of the implications and implications of our model compared to the well-established ΛCDM model. The examination of additional statistical measures, model diagnostics, and physical interpretations can provide a more comprehensive evaluation of the strengths and weaknesses of our model in relation to the ΛCDM framework. Overall, the negative ΔAIC value suggests that our model offers some advantages over the ΛCDM model in terms of goodness of fit, but further investigations and analyses are necessary to fully understand its implications and to validate its consistency with other cosmological observations and theories.

X. DISCUSSIONS AND CONCLUDING REMARKS

In this study, we have investigated the behavior and evolution of the $f(R, G, \mathcal{T})$ model. By analyzing various cosmological parameters and diagnostics, we have gained insights into the characteristics and dynamics of this model compared to the well-established ΛCDM model. Our analysis of the deceleration parameter (q) reveals that the $f(R, G, \mathcal{T})$ model exhibits a transition from a decelerating phase to an accelerating phase. The analysis of jerk parameter (j) demonstrates that the $f(R, G, \mathcal{T})$ model exhibits a higher rate of change of acceleration at high redshifts compared to the ΛCDM model. However, as we approach the present epoch and the cosmological constant limit, both models converge to a constant rate of change of acceleration. The analysis of snap parameter (s) reveals that the $f(R, G, \mathcal{T})$ model exhibits a more pronounced curvature and evolution at high redshifts compared to the ΛCDM model. However, as we approach the present epoch, both models converge to a similar behavior, indicating a transition to an accelerated expansion phase. The analysis of Statefinder parameters provides valuable insights into the nature of dark energy and its transition between different phases in the $f(R, G, \mathcal{T})$ model. The model exhibits transitions from a Chaplygin gas-like behavior to a quintessence-like behavior, crossing an intermediate ΛCDM fixed point. This rich cosmological evolution highlights the dynamic nature of dark energy in the $f(R, G, \mathcal{T})$ model. The analysis of OM diagnostic indicates that matter density remains an important component of the energy content of the universe throughout its history, including the early universe, the present epoch, and even the late-time universe. Furthermore, the comparison of information criteria suggests that the $f(R, G, \mathcal{T})$ model performs slightly better than the ΛCDM model in terms of goodness of fit and model selection.

In conclusion, the $f(R, G, \mathcal{T})$ model exhibits interesting and distinct features compared to the well-established ΛCDM model. Its dynamics, including the transition from a decelerating phase to an accelerating phase. While further investigations and analyses are necessary to validate the model's consistency with other observational data and theoretical expectations, the obtained results in this study suggest that the $f(R, G, \mathcal{T})$ model has the potential to revolutionize the field of cosmology. Its ability to capture and explain various cosmological phenomena opens up new avenues for exploring the fundamental principles governing the evolution and behavior of our universe. The $f(R, G, \mathcal{T})$ model, with its unique characteristics and dynamics, offers a promising framework for advancing our understanding of the universe. Future studies could focus on further constraining the model parameters using a broader range of observational data, such as measurements of cosmic microwave background radiation, large-scale structure formation, and gravitational wave events. Additionally, it would be valuable to investigate the implications of the $f(R, G, \mathcal{T})$ model for other cosmological phenomena, such as the formation and evolution of galaxies, and the behavior of dark matter. Furthermore, exploring the theoretical foundations of the $f(R, G, \mathcal{T})$ model could provide deeper insights into the underlying physics that drives the modifications to general relativity and the interplay between matter density, curvature, and dark energy. This could involve investigating the model in the context of quantum gravity theories, studying its implications for particle physics, and exploring its connections to other modified gravity theories. Moreover, it would be valuable to investigate the $f(R, G, \mathcal{T})$ model in the context of other astrophysical and cosmological observations, such as the study of gravitational lensing, the cosmic microwave background polarization, and the behavior of cosmic voids. These investigations could provide additional constraints and tests for the model, helping to determine its viability and consistency with a wide range of observational data. In conclusion, the $f(R, G, \mathcal{T})$ model represents a promising avenue for advancing our understanding of the universe. By further investigating its behavior, constraining its parameters, and exploring its implications for various astrophysical and cosmological phenomena, we can deepen our understanding of the fundamental principles that govern our universe and potentially uncover new insights into its evolution and dynamics. The findings in our analysis indicate that $f(R, G, \mathcal{T})$ gravity model may be served as a good candidate for gravitational modifications.

Acknowledgement: NUM is thankful to CSIR, Govt. of India for providing Senior Research Fellowship (No. 08/003(0141))/2020-EMR-I).

[1] A.G. Riess et al., Astron. J. 116, 1009 (1998).
[2] S. Perlmutter et al., Astrophys. J. 517, 565 (1999).
[3] D. N. Spergel et al., Astrophys. J. Suppl. Ser. 148, 175 (2003).
[4] D. N. Spergel et al., Astrophys. J. Suppl. 170, 377 (2007).
[5] S. Briddle et al., Science 299, 1532 (2003).
[6] E. J. Copland, M. Sami and S. Tsujukawa, Int. J. Mod. Phys. D 15, 1753 (2006).
[7] D. Pietrobon, A. Balbi, and D. Marinucci, Physical Review D, 74,4,043524 (2006).
[8] T. Giannantonio, R. G Crittenden, R. C Nichol, R. Scranton, G. T Richards, A. D Myers, R. J Brunner, A. G Gray, A.J Connolly, and D. P Schneider, Physical Review D, 74,6,063520 (2006).
[9] A. G Riess, L.-G. Strolger, Stefano Casertano, Henry C Ferguson, Bahram Mobasher, Ben Gold, Peter J Challis, Alexei V Filippenko, Saurabh Jha, Weidong Li, et al, The Astrophysical Journal, 659(1),98, (2007).
[10] S.Perlmutter, et al., Astrophys. J. 483, 565 (1997).
[11] S.Perlmutter, et al., Nature 391, 51 (1998).
[12] S. Perlmutter, et al.: Astrophys. J. 517, 565 (1999).
[13] C.Fedeli,L. Moscardini,M. Bartelmann, , Astron. Astrophys. 500, 667 (2009).
[14] A.G. Riess, et al., Astron. J. 607, 665 (2004).
[15] R.R.Caldwell, Doran, M.: Phys. Rev. D 69, 103517 (2004).
[16] S.F.Daniel, R.R.Caldwell, A. Cooray, A.Melchiorri, Phys. Rev. D 77, 103513 (2008).
[17] Z.-Y.Huang, B.Wang, E. Abdalla, R.-K.Sul, J. Cosmol. Astropart. Phys. 05, 013 (2006).
[18] A.G. Riess et al., Astrophys. J. 560, 49 (2001).
[19] S. Perlmutter, M.S. Turner, M. White, Phys. Rev. Lett. 83, 670 (1999).
[20] C.L. Bennett et al., Astropyhs. J. Suppl. Ser. 148, 1 (2003)
[21] G. Hinshaw et al., Astropyhs. J. Suppl. Ser. 148, 135 (2003).
[22] D.J. Eisenstein et al., Astrophys. J. 633, 560 (2005).
[23] T. Padmanabhan, Phys. Rep. 380, 235 (2003).
[24] V. Sahni and A. A. Starobinsky, Int. J. Mod. Phys. D 9, 373 (2000).
[25] R. A. Battye and F. Pace, Physical Review D 94, no. 6 , 063513 (2016).
[26] M. Li, T. Qiu, Y. Cai and X. Zhang, J. Cos. Astroparticle Phys. , no. 04 , 003(2012).
[27] M. Khurshudyan, E. Chubaryan and B. Pourhassan, Int. J. Theo. Phys. 53, no. 7 ,2370-2378(2014).
[28] M. Khurshudyan, B. Pourhassan, R.Myrzakulov and S. Chattopadhyay, Astrophysics and Space Science 356, no. 2 , 383-391(2015).
[29] Z. K. Guo, Y. S. Piao, X. Zhang and Y. Z. Zhang, Physics Letters B 608, no. 3-4 , 177-182(2005).
[30] M. R. Setare, J. Sadeghi, and A. R. Amani, International Journal of Modern Physics D, 18, no. 08 (2009): 1291-1301.
[31] A. R. Amani, International Journal of Theoretical Physics, 50,10,3078 (2011).
[32] S. Weinberg, Reviews of modern physics 61, no. 1 , 1(1989).
[33] R. R. Caldwell, Physics Letters B, 545(1),23 (2002).
[34] J. Sadeghi, and A. R. Amani, International Journal of Theoretical Physics, 48,1,14(2009).
[35] M. R. Setare, J. Sadeghi, and A. R. Amani, Physics Letters B, 673,4,241 (2009).
[36] J. Sadeghi, M. Khurshudyan, A. Movsisyan and H. Farahani, Journal of Cosmology and Astroparticle Physics 2013, no. 12, 031 (2013).
[37] J. Sadeghi, M. Khurshudyan and H. Farahani, International Journal of Modern Physics D 1650108 (2014).
[38] B. Pourhassan and J. Naji, International Journal of Modern Physics D , 1750012(2014).
[39] M. Khurshudyan and B. Pourhassan, International Journal of Theoretical Physics 54, no. 9 ,3251-3267(2015).
[40] J. Sadeghi and H. Farahani, Modern Physics Letters A 30, no. 01 , 1550008(2015).
[41] M. Khurshudyan, A. Pasqua, J. Sadeghi and H. Farahani, Chinese Physics Letters 32, no. 10 109501(2015).
[42] L. Iorio, M. L. Ruggiero, N. Radicella and E. N. Saridakis, Physics of the Dark Universe 13 , 111-120 (2016).
[43] V. Faraoni, Physics of the Dark Universe 11 , 11-15(2016).
[44] M. Khurshudyan, B. Pourhassan and A. Pasqua, Canadian Journal of Physics 93, no. 4, 449-455 (2014).
[45] J. Sadeghi, B. Pourhassan, A. S. Kubeka and M. Rostami, Int. J. Mod. Phys. D 25, no. 07 1650077(2016).
[46] J. Sadeghi and H. Farahani, Physics Letters B 751 , 89-95(2015).
[47] H. Wei, Communications in Theoretical Physics, 52(4),743 (2009).
[48] A. R. Amani, J. Sadeghi, H. Farajollahi, and M. Pourali, Canadian Journal of Physics, 90(1),61, (2011).
[49] M. Li, Physics Letters B 603, no. 1 , 1-5(2004).
[50] S. Del Campo, J. C. Fabris, R. Herrera and W. Zimdahl, Physical Review D 83, no. 12 , 123006(2011).
[51] Y. Hu, M. Li, N. Li and Z. Zhang, J. Cos. Astroparticle Phys. 2015, no. 08 , 012 (2015).
[52] V. Sahni, and Y. Shtanov, Journal of Cosmology and Astroparticle Physics, 11,014(2003).
[53] A. Pourbagher and A. Amani, Modern Physics Letters A,35 ,20, 2050166(2020) . DOI: 10.1142/S0217732320501667.
[54] A. R. Amani, C.Escamilla-Rivera, and H. R. Faghani, Phys. Rev. D 88,124008 (2013).
[55] A. R. Amani, and B. Pourhassan, Int. J. Geo. Meth. Mod. Phys., 11(08),1450065, 2014.
[56] J. Naji, B. Pourhassan, and A. R. Amani, Int. J. Mod. Phys. D, 23, no. 02 , 1450020 (2014).
[57] M. Khurshudyan, J. Sadeghi, M. Hakobyan, H. Farahani and R. Myrzakulov, The European Physical Journal Plus 129, no. 6 , 119 (2014).
[58] A. R. Amani and B. Pourhassan, Int. J. Theo. Phys. 52, no. 4 , 1309-1313(2013).
[59] B. Pourhassan and E. O. Kahya, Results in Physics 4 ,101 (2014).
[60] B. Pourhassan, Canadian Journal of Physics 94, no. 7 , 659-670(2016).
[61] V. Fayaz, H. Hossienkhani, A. Pasqua, M. Amirabadi, and M. Ganji, The European Physical Journal Plus 130, no. 2 , 1-12(2015).
[62] H. Saadat, International Journal of Theoretical Physics

52, no. 3 , 1027-1032 (2013).
[63] J. Morais, M. Bouhmadi-Lopez, K. Sravan Kumar, J. Marto and Y. Tavakoli, Physics of the Dark Universe 15 , 7-30 (2017).
[64] M. Khurshudyan, B. Pourhassan and E. O. Kahya, Int. J. Geo. Meth. Mod. Phys., 11(06), 1450061, (2014).
[65] M. Khurshudyan, J. Sadeghi, M. Hakobyan, H. Farahani and R. Myrzakulov, The European Physical Journal Plus 129, no. 6 , 119 (2014).
[66] Y. Zhang, Physics of the Dark Universe 15 , 82(2017).
[67] M. B.-Lopez, J. Morais and A. Zhuk, Physics of the Dark Universe 14 , 11-20 (2016).
[68] M. Khurshudyan, J. Sadeghi, A. Pasqua, S. Chattopadhyay, R. Myrzakulov and H. Farahani, International Journal of Theoretical Physics 54, no. 3 , 749-760(2015).
[69] J. Sadeghi, M. Khurshudyan, M. Hakobyan and H. Farahani, International Journal of Theoretical Physics 53, no. 7 ,2246-2260(2014) .
[70] J. Sadeghi, B. Pourhassan and Z. Abbaspour Moghaddam, International Journal of Theoretical Physics 53, no. 1 , 125-135(2014).
[71] J. Sadeghi, F. Milani, and A. R. Amani, Modern Physics Letters A 24, no. 29 , 2363-2376 (2009).
[72] J. Sadeghi, M. R. Setare, A. R. Amani, and S. M. Noorbakhsh, Physics Letters B 685, no. 4 229-234 (2010).
[73] A. R. Amani, International Journal of Modern Physics D 25, no. 06 , 1650071(2016).
[74] T. Singh, R. Chaubey and A. Singh, Canadian Journal of Physics 94, no. 7 , 623-627(2016).
[75] M. R. Setare, J. Sadeghi, and A. R. Amani, Physics Letters B, 660,4,299, (2008).
[76] G. P. de Brito, J. M. Hoff da Silva, P. Michel LT da Silva, and A. de Souza Dutra, International Journal of Modern Physics D, 24, no. 11 , 1550089(2015).
[77] K. Bamba, S. Nojiri and S. D. Odintsov, J. Cosmol. Astropart. Phys. 0810, 045 (2008).
[78] S. Capozziello and M. Francaviglia, Gen. Relativ. Gravit. 40, 357 (2008).
[79] M. Sami, A. Toporensky, P. V. Tretjakov and S. Tsujikawa, Phys. Lett. B 619, 193 (2005).
[80] S. Nojiri and S. D. Odintsov, Phys. Lett. B 631, 1 (2005).
[81] A. Joyce, B. Jain, J. Khoury, and M.Trodden.,Phys.Rept. 568 , 1-98 (2015).
[82] S. Capozziello and M. De Laurentis, Physics Reports, Phys.Rept. 509 , 167-321(2011).
[83] K. Bamba, S. Capozziello, S. Nojiri, and S.D Odintsov,Astrophys.Space Sci. 342 , 155-22(2012).
[84] K. Koyama, Reports on Progress in Physics, 79,4,,046902 (2016).
[85] De la Cruz-Dombriz, Diego Sáez-Gómez, et al., Entropy, 14(9), 1717-1770 (2012).
[86] K. Bamba, SI Nojiri, and Sergei D Odintsov, arXiv preprint arXiv:1302.4831 (2013).
[87] K. Bamba and S. D Odintsov, arXiv preprint arXiv:1402.7114 (2014).
[88] Z. Yousaf, K. Bamba, et al., Physical Review D, 93(6):064059 (2016).
[89] Z. Yousaf, K. Bamba, and M Z.-u.-H. Bhatti. , Physical Review D, 93(12):124048 (2016).
[90] S.I. Nojiri and S.D. Odintsov. econf c0602061, 06 (2006). Int. J. Geom. Meth. Mod. Phys, 4(115):16, (2007).
[91] SI Nojiri and Sergei D Odintsov, arXiv preprint arXiv:0801.4843 (2008).
[92] S.I. Nojiri and S. D Odintsov. arXiv preprint arXiv:0807.0685 (2008).
[93] S.H. Hendi, B. Eslam Panah, and C. Corda. , Canadian Journal of Physics, 92(1):76¬81, (2014).
[94] S. Capozziello, M. De Laurentis, I De Martino, M Formisano, and SD Odintsov, Physical Review D, 85,4,,044022, (2012).
[95] 25. A. De Felice and S. Tsujikawa, Phys. Rev. D 80, 063516 (2009).
[96] 26. O. Bertolami, C. G. Boehmer, T. Harko and F. S. N. Lobo, Phys. Rev. D 75, 104016 (2007).
[97] 27. S. Nojiri, S. D. Odintsov and P. V. Tretyakov, Prog. Theor. Phys. Suppl. 172, 81 (2008).
[98] S. Nojiri and S. D Odintsov., Phys.Rept. 505, 59-144 (2011).
[99] S. Nojiri, S. D Odintsov, and P. V Tretyakov, Progress of Theoretical Physics Supplement, 172,81-89, 2008.
[100] K. Bamba, S. D Odintsov, L. Sebastiani, and S. Zerbini, The European Physical Journal C, 67,1,295-310, 2010.
[101] T. Harko, F. S. N. Lobo, S. Nojiri and S. D. Odintsov, Phys. Rev. D 84, 024020 (2011).
[102] M. Jamil, D. Momeni and M. Raza, Eur. Phys. J. C 72, 1999 (2012).
[103] M. J. S. Houndjo, C. E. M. Batista, J. P. Campos and O. F. Piattella, Can. J. Phys. 91, 548 (2013).
[104] M. Sharif and M. Zubair, J. Cosmol. Astropart. Phys. 1203, 028 (2012).
[105] F. G. Alvarenga, M. J. S. Houndjo, A. V. Monwanou and J. B. C. Orou, J. Mod. Phys. 4, 130 (2013).
[106] R. Myrzakulov, Eur. Phys. J. C 72, 2203 (2012).
[107] S. Chakraborty, Gen. Relativ. Gravit. 45, 2039 (2013).
[108] K. Bamba, S. D. Odintsov, L. Sebastiani and S. Zerbini, Eur. Phys. J. C 67, 295 (2010).
[109] A. De Felice, J.-M. Gerard and T. Suyama, Phys. Rev. D 82, 063526 (2010).
[110] A. De Felice and T. Tanaka, Prog. Theor. Phys. 124, 503 (2010).
[111] A. De Felice and T. Suyama, Prog. Theor. Phys. 125, 603 (2011).
[112] A. De Felice, T. Suyama and T. Tanaka, Phys. Rev. D 83, 104035 (2011).
[113] A. de la Cruz-Dombriz and D. Saez-Gomez, Class. Quantum Grav. 29, 245014 (2012).
[114] A. N. Makarenko, V. V. Obukhov and I. V. Kirnos, Astrophys. Space Sci. 343, 481 (2013).
[115] K. Atazadeh and F. Darabi, Gen. Relativ. Gravit. 46, 1664 (2014).
[116] E. Elizalde, S. D. Odintsov, V. K. Oikonomou and T. Paul, Nucl. Phys. B 954, 114984 (2020).
[117] M. Sharif and A. Ikram, Phys. Dark Univ. 17, 1 (2017).
[118] M. F. Shamir and M. Ahmad, Eur. Phys. J. C 77, 55 (2017).
[119] U. Debnath, Int. J. Mod. Phys. A, 35, 2050203 (2020).
[120] M. Ilyas, Int. J. Mod. Phys. A 36, 2150165 (2021).
[121] M. Ilyas, A. R. Athar and Asma Bibi, arXiv:2205.14155 [gr-qc].
[122] M. Ilyas, A. Ahmad and M. Wasif, arXiv:2206.05114 [gr-qc].
[123] M. Ilyas, A. R. Athar and N. Ghafoor, arXiv:2207.02141 [gr-qc].
[124] D. J. Eisenstein, et al. , The Astrophysical Journal, 633,2, 560-574 (2005).
[125] W. J. Percival, et al. , Monthly Notices of the Royal Astronomical Society, 401(4), 2148-2168 (2010).

[126] R. Jimenez, et al. , The Astrophysical Journal, 593(2), 622-629 (2003).

[127] J.Simon, et al., Physical Review D, 71(12), 123001 (2005).

[128] A. Lewis, A., & S. Bridle,Physical Review D, 66,10, 103511 (2002).

[129] S. Brooks, & A.Gelman, Journal of Computational and Graphical Statistics, 7(4), 434-455 (1998).

[130] W. R. Gilks, S.Richardson, & D. J. Spiegelhalter, Markov Chain Monte Carlo in Practice. Chapman and Hall/CRC (1996).

[131] M. Moresco, Monthly Notices of the Royal Astronomical Society, 463(1), L6-L10 (2016).

[132] M.Moresco, Journal of Cosmology and Astroparticle Physics, 08, 006 (2012).

[133] R.Jimenez, & A. Loeb, The Astrophysical Journal, 573(1), 37-42(2003).

[134] D. Thomas, C.Maraston, R.Bender, & C.Mendes de Oliveira, The Astrophysical Journal Letters, 717(2), L77-L81 (2010).

[135] R.Jimenez, & A. Loeb, arXiv preprint arXiv:1901.07155 (2019).

[136] D.Stern, R.Jimenez, L.Verde, M.Kamionkowski, &S. A. Stanford, Journal of Cosmology and Astroparticle Physics, 02, 008 (2010).

[137] D. Scolnic, D. Brout, A. Carr, A. G. Riess, T. M. Davis, A. Dwomoh, D. O. Jones, N. Ali, P. Charvu and R. Chen, *et al.* , Astrophys. J. 938, no.2, 113(2022) . [arXiv:2112.03863 [astro-ph.CO]].

[138] V. Sahni, T. D. Saini, A. A. Starobinsky and U. Alam, , JETP Lett. 77, 201-206 (2003) [arXiv:astro-ph/0201498 [astro-ph]].

[139] R. Amanullah, C. Lidman, D. Rubin, G. Aldering, P. Astier, K. Barbary, M. S. Burns, A. Conley, K. S. Dawson and S. E. Deustua, *et al.*, Astrophys. J. 716, 712-738(2010). [arXiv:1004.1711 [astro-ph.CO]].

[140] M. Kowalski *et al.* , Astrophys. J. 686, 749-778(2008). [arXiv:0804.4142 [astro-ph]].

[141] N. Suzuki *et al.* ,Astrophys. J. 746, 85(2012).[arXiv:1105.3470 [astro-ph.CO]].

[142] M. Betoule *et al.* , Astron. Astrophys. 568, A22(2014). [arXiv:1401.4064 [astro-ph.CO]].

[143] D. M. Scolnic *et al.* , Astrophys. J. 859, no.2, 101(2018). [arXiv:1710.00845 [astro-ph.CO]].

[144] M. Visser, General Relativity and Gravitation, 37,9, 1541-1548 (2004).

[145] A.Shafieloo, V.Sahni, & A. A. Starobinsky, Journal of Cosmology and Astroparticle Physics, 04, 026, (2012).

[146] R.Lazkoz, S.Nesseris, & L. Perivolaropoulos, Journal of Cosmology and Astroparticle Physics, 07, 010 (2005).

[147] A. Gómez-Valent, & J.Solà, Frontiers in Physics, 6, 140 (2018).

[148] V. Sahni,T. D. Saini, A. A.Starobinsky, & U.Alam, Journal of Experimental and Theoretical Physics Letters, 77,5, 201-206 (2002).

[149] S.Capozziello,S. Nojiri,S. D. Odintsov, & A. Troisi, Physics Letters B, 639(2-3), 135-143 (2003).

[150] V.Sahni, &A. Starobinsky, International Journal of Modern Physics D, 15(14), 2105-2132 (2006).

[151] V. Sahni, A. Shafieloo & A. A. Starobinsky , Physical Review D, 78(10), 103502 (2008).

[152] V.Sahni, & Y.Shtanov, Braneworld models of dark energy. Journal of Cosmology and Astroparticle Physics, JCAP 11 , 014(2003) .

[153] N. Chow, J. Khoury, & P. J. ,Steinhardt, Physical Review D, 80(4), 043516 (2009).

[154] S. A. Appleby, & E. V.Linder, Journal of Cosmology and Astroparticle Physics, 2009(05), 012 (2009).

[155] V.Sahni, A. Shafieloo, & A.Starobinsky, Astrophysical Journal Letters, 793(2), L40 (2014).

[156] A. R. Liddle , arXiv preprint arXiv:0708.3770 (2007).

[157] M. Szydlarski, & O. Doré,Physics Reports, 735, 1-61 (2018).

Molecular Biotechnology
https://doi.org/10.1007/s12033-023-00783-2

REVIEW

Exploring the Potential Therapeutic Approach Using Ginsenosides for the Management of Neurodegenerative Disorders

Manju[1] · **Navneeta Bharadvaja**[1]

Received: 22 February 2023 / Accepted: 31 May 2023
© The Author(s), under exclusive licence to Springer Science+Business Media, LLC, part of Springer Nature 2023

Abstract

There is a need for an efficient and long-lasting treatment due to the population's increasing prevalence of neurodegenerative disorders. In an effort to generate fresh ideas and create novel therapeutic medications, scientists have recently started to investigate the biological functions of compounds derived from plants and herbs. Ginseng, famous Chinese herbal medicine, has therapeutic value by virtue of its compounds ginsenosides or panaxosides, which are triterpene saponins and steroid glycosides. Research revealed positive impacts on ameliorating various disease conditions and found it as a possible drug candidate. Several neuroprotection mechanisms followed by this compound are inhibition of cell apoptosis, oxidative stress, inflammatory, and tumor activity. It has been demonstrated that controlling these mechanisms enhances cognitive performance and safeguards the brain against neurodegenerative disorders. The main objective of this review is to give a description of the most recent studies on ginsenoside's possible therapeutic application in the treatment of neurodegenerative diseases. Using organic compounds like ginseng and its various components may create new avenues for innovative treatment approaches development for neurological diseases. However, further research is necessary to confirm the stability and effectiveness of ginsenosides for neurodegenerative disease.

Graphical Abstract

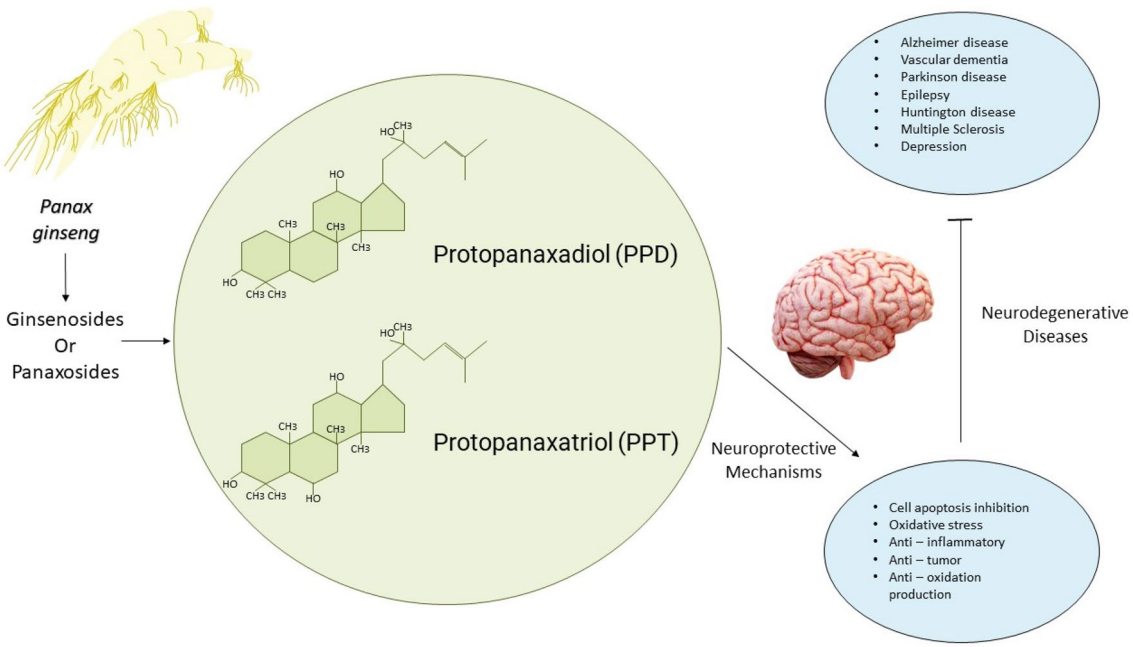

Keywords Ginseng · Ginsenosides · Natural product · Protopanaxadiol · Protopanaxatriol · Neurodegenerative diseases

Extended author information available on the last page of the article

Published online: 18 June 2023

Introduction

The perennial plant *Panax ginseng* C.A. Meyer (*P. ginseng*), often known as Asian or Korean ginseng, is a member of the Araliaceae family and has a long history of use in traditional medicine. It is native to eastern Asia and North America, especially China and Korea, where it has been used in medicine traditionally to cure a number of diseases. The plant is typically found in hilly areas and grows well in shady areas of deciduous forests. It is a slow-growing plant that normally takes 4–6 years to reach maturity, and therapeutic benefits are mostly derived from its roots [1]. Ginsenosides, which are present in the roots provide several health advantages, including better cognitive function, decreased inflammation, and increased antioxidant activity. *Panax ginseng* is frequently used as an adaptogen, which means it can enhance general health and wellness by assisting the body in adjusting to stress [2]. In traditional Chinese medicine, the roots of *P. ginseng* and *P. quinquefolius L.* also known as Oriental ginseng and American ginseng respectively, are the most valuable medicinal herbs [3]. American ginseng, as represented by its name, is a species native to North America and is largely produced in the United States and Canada, whereas Oriental ginseng is indigenous to China, Korea, and Russia. The steam-produced red version of Oriental ginseng is "warm" and is known to restore "vital energy," but American ginseng is "cool" and is mostly used to lessen "internal heat" as well as promote the release of body fluids [4]. Additionally, due to their therapeutic abilities, they are frequently utilized in cultural acts and ceremonies [5].

Ginseng's medicinal properties are partly due to its active ingredients, which include polysaccharides, amino acids, terpenoids, fatty acids, volatile oils, alcohols, and ginsenosides. According to recent studies, ginsenosides which are the main bioactive compounds present in the roots of ginseng may have therapeutic potential to cure neurodegenerative disorders (NDDs). The term "neurodegenerative diseases" refers to a group of disorders that damage the nervous system and cause neurons to gradually lose their functionality and eventually die [6]. Neurodegenerative disorders presently have no known cure, and therapies often concentrate on symptom management and reducing the disease's progression. A number of studies reported ginsenosides to have neuroprotective effects by reducing inflammation and oxidative stress that contribute to the onset and progression of NDDs. Ginsenosides have been demonstrated to lessen oxidative stress by boosting antioxidant enzyme activity and by scavenging free radicals [7]. Furthermore, it has been demonstrated that ginsenosides can be helpful in controlling depression and anxiety, both of which are frequently linked to neurodegenerative disorders. This review gives an insight into different mechanisms through which distinct ginsenosides are useful in mitigating above mentioned neurological disorders along with some basic knowledge of common ginsenoside compounds found in nature. The review covers the precise processes through which ginsenosides have therapeutic benefits, such as regulating neurotransmitter activity, lowering inflammation and oxidative stress, and enhancing neuronal survival. It also goes through how various ginsenosides might be used to treat various neurological conditions. By combining the current preclinical and clinical information, this study aims to investigate ginsenosides' potential therapeutic role in the treatment of NDDs.

Ginseng

Ginsengs are regarded as versatile herbs with the ability to heal a variety of ailments and were among the most valuable herbs in ancient China, Japan, and Korea. Ginseng has been found in the hilly areas of Manchuria in China and was utilized by the Chinese Emperors [8]. Herbs and medicinal plants were used in ancient times to cure a wide variety of illnesses and had a key role in enriching human health. According to a study, ginseng has a high amount of anti-inflammatory and antioxidant substances [9], that can be exploited to cure NDDs. Nutritionally, one teaspoon of ginseng (2gm) provides 0 gm fat, 1.6 gm calories, 8.3 mg potassium, 0 gm protein, 0.3 mg sodium, 0.2% daily value (DV) Vitamin C, 0.4 gm carbohydrates, and 0.1% DV Iron [10]. There are various phytochemicals that are present in ginseng which are shown in Fig. 1.

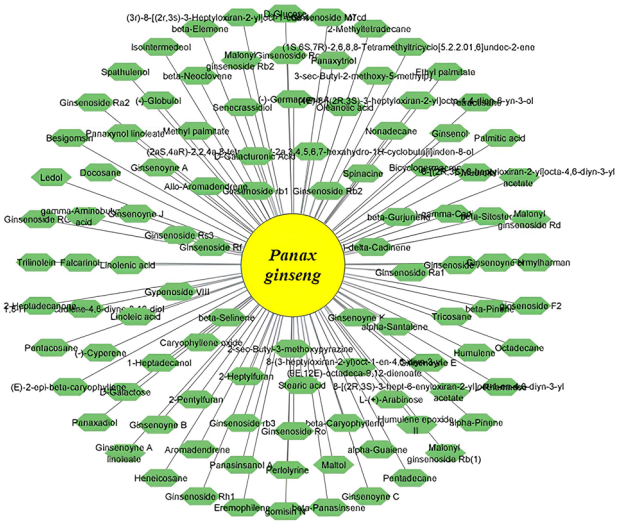

Fig. 1 Different phytochemicals that are present in the ginseng root

There are now over 40 countries where Asian ginseng is cultivated commercially [11]. About 110 chemical compounds and their metabolites are derived from ginseng plants using sophisticated analytical methods. These substances have various biological capabilities that can help with the treatment of a variety of illnesses, and they have been divided into several categories depending on their structural characteristics [12]. Due to its numerous medicinal and pharmacological applications, ginseng is one of the high demanded herbs in the Chinese market [13].

Ginsenosides

The core bioactive constituents of ginseng are ginsenosides or panaxosides, which are steroid glycosides and triterpene saponins, and are obtained from the ginseng's roots, stems, leaves, and fruits [14]. Ginseng root contains 2–3% ginsenosides [15]. Based on the age of the plant, the growing environment, and the extraction process, the approximate composition of ginsenosides in ginseng extract can vary. Ginsenosides can be written as 'Rx'. In 'Rx', Root is denoted by the symbol R, and chromatographic polarity is denoted by the letter x. Around 30 different kinds of ginsenosides have been discovered, each having a distinct chemical composition and potential therapeutic benefits. Rb1, Rg1, Re, Rc, Rd, and Rf are some of the ginsenosides that have undergone the most research [16]. Each species of ginseng has its unique characteristics and traditional uses along with their respective ginsenosides compositions are mentioned in Table 1.

Many biological activities of these ginsenosides, like neuroprotective, immunomodulatory, antioxidant, and anti-inflammatory effects. In addition to these active ingredients, ginseng extract also has flavonoids, polysaccharides, and polyacetylenes, which contribute to its therapeutic effects [21]. Ginsenosides are commonly extracted from ginseng using very sensitive techniques like HPLC and GC, which provide significant information on the composition and quality of ginsenoside extracts**.** HPLC is particularly useful for isolating and quantifying individual ginsenosides, whereas GC is typically used to examine volatile components and determine the chemical structure of ginsenosides. It can strengthen the body's defenses and delay aging. There are several therapeutic applications for ginsenosides in the management of NDDs. Ginsenosides have been demonstrated to enhance cognitive performance and decrease amyloid-β deposition in Alzheimer's disease (AD) [22]. Moreover, they have anti-inflammatory properties and can guard neurons against oxidative stress. Acetylcholine is one of the neurotransmitters whose activity is modulated by ginsenosides in

Table 1 Different Species of Ginseng, representative saponins, and their therapeutic uses

Species	Common Name	Geographical location	Representative saponins	Traditional uses	References
P. ginseng C.A. Meyer	Asian ginseng	China, Korea, Russia	Rd, Rb1, Rb2, Rc, Re, Rg1, Rf	Revitalizing tonic to improve physical and mental performance, reduce fatigue	[17]
P. quinquefolius	American ginseng	Southern Canada and the USA	Rb1, Re, Rg1, Rc, Rd	Reducing stress, improving digestion, and enhancing overall wellbeing	[17]
P. japonicas	Japanese Ginseng	Japan	Ro, Rb1, Re, Rd	Improving cognitive function, reducing stress and fatigue	[17]
P. pseudoginseng	Notoginseng	China, Japan, and korea	Rb1, Re, Rg1, Rg2, Rd, Ro	Stopping the bleeding, reducing swelling, and promoting blood circulation	[17]
P. notoginseng	Sanqi or Tianqi ginseng	China	Rg1, Rb1, Rd, Re, Rc	Reducing swelling and promoting blood circulation	[18]
P. vietnamensis	Vietnamese ginseng	Vietnam	Rb1, Rb2, Rd, Rg, Re	Boosting energy, improving vitality, and reducing fatigue	[19]
Withania somnifera	Indian ginseng or ashwagandha	India, the middle east, and some parts of Africa	Rh1, Rg3	Used in Ayurvedic medicine to improve vitality, reduce stress and boost the immune system	[20]

This table contains information about a variety of ginseng species, such as their common names, geographical locations, and representative ginsenosides. The purpose of the data in this table is to provide a comprehensive overview of the many ginseng species

the brain [23]. Ginsenosides have demonstrated neuroprotective effects on dopaminergic neurons and reduced inflammatory effects on the brain, both of which are crucial contributors to the development of Parkinson's disease (PD). It can postpone the initiation and onset of Huntington's disease (HD) by defending the neurons from oxidative stress and reducing inflammation [24]. In animal models of multiple sclerosis, ginsenosides have been demonstrated to lessen inflammation and enhance neurological function [25]. They could also aid in preventing the disease from damaging neurons.

Chemical Structure of Ginsenoside

The ginsenosides are grouped into two categories on the basis of the position and sugar moieties like arabinose, glucose, rhamnose, and xylose [26]. Protopanaxadiol (PPD)—Rb1, Rd, Rh2, Rb2, & Rg3 and protopanaxatriol (PPT)—Rg1, Rg2, Rh1 & Re are two distinct forms of triterpene saponins that are found in ginseng plants [27] and the illustration of their chemical structure as shown in Fig. 2 which described the constituents of ginsenosides like Rh1, Rh2 and others that are commonly found in ginseng with their side chain modifications.

The two groups have significant variances while bearing a comparable chemical structure. The arrangement and number of hydroxyl groups in PPD and PPT are two of their main variations. In contrast to PPT, which contains two hydroxyl groups at positions 6th and 20th, PPD has three hydroxyl groups at positions 3rd and 20th [28]. These variations in hydroxyl group position may have an impact on the biological activity of these compounds and lead to various physiological outcomes. Furthermore, PPD is metabolized by the liver into compound K (CK), which offers several therapeutic advantages that have been shown, like anti-diabetic, anti-cancer, and anti-inflammation. On the other hand, PPT is metabolized into PPD-type saponins instead of CK, which have neuroprotective and anti-inflammatory properties [29]. While ginseng having PPT is well recognized for its relaxing and stress-relieving characteristics, ginseng containing PPD is frequently utilized for its immune-boosting and stimulating qualities. It is crucial to comprehend the variations between PPD and PPT to choose which molecule is most suited for treating certain illnesses.

Protopanaxadiol

Protopanaxadiol (PPD) constitutes the ginsenosides Rb1, Rb2, Rg3, Rd, and Rh2. PPD has been investigated for its possible neuroprotective effects and for its potential to arrest or delay the advancement of NDDs including AD and PD [15]. According to studies, PPD can protect neurons against inflammation and oxidative stress, two factors that are thought to have a role in the development of NDDs. Moreover, it has been demonstrated in animal model experiments to improve memory and cognitive performance [30]. PPD has been demonstrated to increase the production of

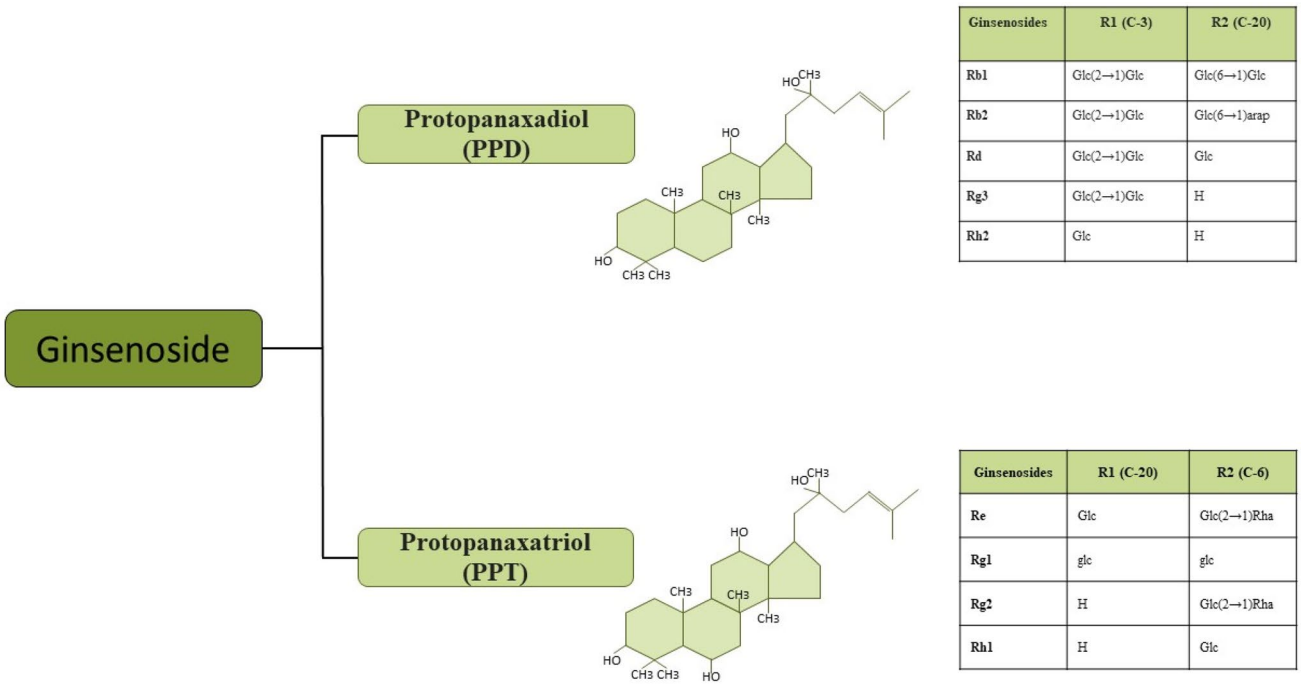

Ginsenosides	R1 (C-3)	R2 (C-20)
Rb1	Glc(2→1)Glc	Glc(6→1)Glc
Rb2	Glc(2→1)Glc	Glc(6→1)arap
Rd	Glc(2→1)Glc	Glc
Rg3	Glc(2→1)Glc	H
Rh2	Glc	H

Ginsenosides	R1 (C-20)	R2 (C-6)
Re	Glc	Glc(2→1)Rha
Rg1	glc	glc
Rg2	H	Glc(2→1)Rha
Rh1	H	Glc

Fig. 2 Chemical structure of protopanaxadiol (PPD) and Protopanaxatriol (PPT)- type ginsenosides and their side chain modifications

brain-derived neurotrophic factor (BDNF), a protein necessary for the survival and growth of neurons. [31].

Ginsenoside-Rb1 Ginsenoside-Rb1 (Rb1) is one of the most prevalent and extensively researched ginsenosides in ginseng and is widely known for its numerous health advantages. Rb1 has a number of potential advantages, including the capacity to raise immunity, lessen inflammation, enhance cognitive function, and lower blood sugar and cholesterol levels. Rb1 contributes anti-stress and favorable effects on the central nervous system (CNS) [32], and exhibits anti-allergenic, anti-cancerous, immuno-modulatory, anti-hypersensitive, anti-allergenic, anti-atherosclerotic, and anti-diabetic properties.

Rb1 appears to have anti-inflammatory properties since it decreases the synthesis of tumor necrosis factor-alpha (TNF-α) in lipopolysaccharide (LPS)-induced macrophages [33]. Furthermore, the nuclear factor kappa B (NF-κB) pathway, which is well-recognized for controlling inflammation, is suppressed by Rb1 [34]. Additionally, NF-κB, inhibitory κB kinase alpha (IKK-α), and mitogen-activated protein kinases (MAPKs) are known to be inhibited by IL-1 receptor-associated kinases (IRAK)-1, which is also known to limit its activity, and is strongly inhibited by Rb1. Rb1 was shown to decrease IRAK activation-mediated inflammatory responses in a 2,4,6-trinitrobenzene sulfuric acid-induced animal model [34]. Figure 3 illustrates the pharmacological effects of Rb1 in which its positive benefits have been observed due to its anti-inflammatory, antioxidative, and anti-apoptotic properties. These effects may govern several roles such as preventing TNF-α from binding to cell surface receptors, and inhibiting the NF-κB and c-Jun N-terminal kinases (JNK) signaling pathways from activating and preventing biomolecules from oxidative damage by scavenging reactive oxygen species (ROS).

Ginsenoside-Rb2 The root of the ginseng plant contains a naturally occurring substance called ginsenoside-Rb2 (Rb2). Rb2 may provide a variety of health advantages, including anti-inflammatory, anti-cancer, and neuroprotective effects. Additionally, it has been observed to have an advantageous impact on memory and cognitive function. Rb2 significantly reduces TNF-α production in cellular studies that have been activated by LPS, providing neuroprotection [34]. Rb2 inhibits IkBα activation, indicating that Rb2-mediated NF-κB inhibition, which is indeed responsible for TNF-α generation in microglia [34].

Ginsenoside-Rd The intriguing substance ginsenoside-Rd (Rd) has a number of potential health advantages. It has been shown that Rd possesses neuroprotective effects, which may aid in guarding against brain deterioration and

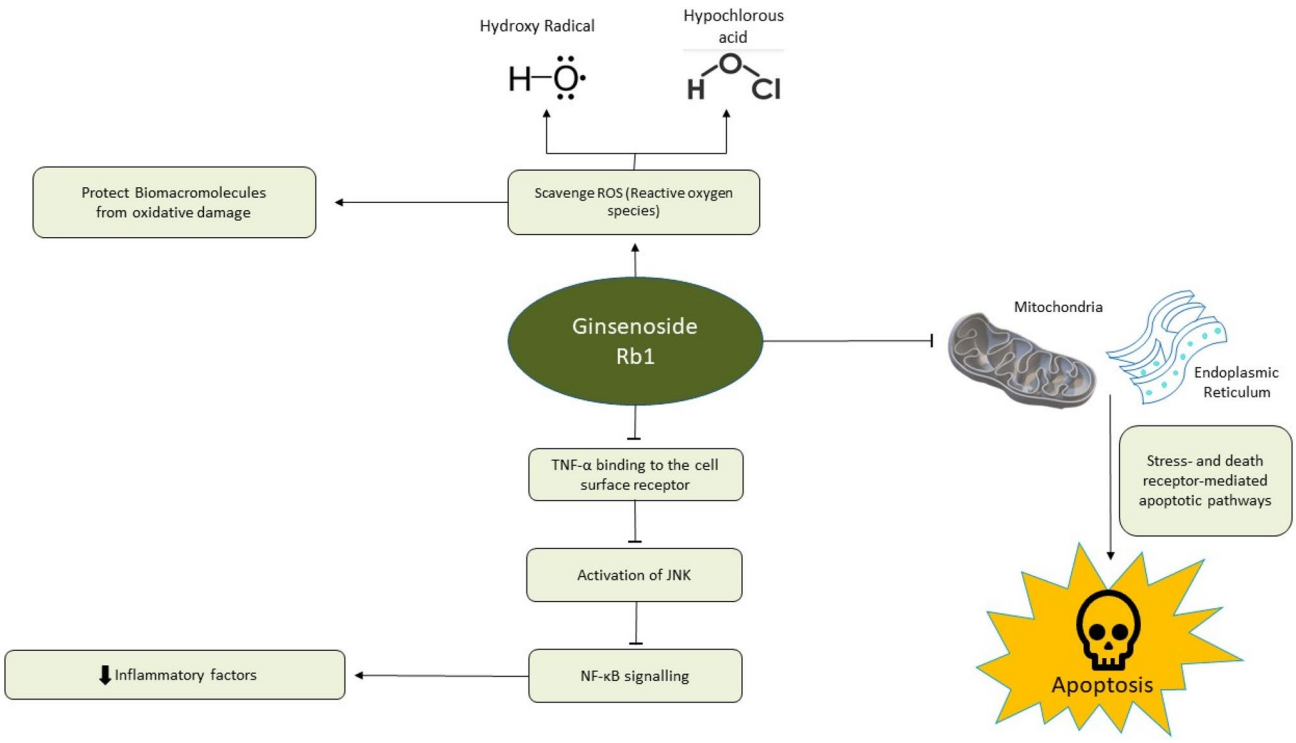

Fig. 3 Mode of action of ginsenoside Rb1 where Ginsenoside Rb1 has anti-apoptotic, antioxidant, and anti-inflammatory effects. ER stands for endoplasmic reticulum

injury. Rd reduces the activation of LPS-induced TNF-α and NF-κB production [35]. In an acute localized cerebral ischemia murine model, Rd regulates the initial antioxidative mechanism and a late anti-inflammatory mechanism, demonstrating neuroprotective advantages. Rd also inhibits initial protein and DNA cumulation, hydroxyl radical generation, as well as lipid peroxidation [36]. It reduces episodes of inflammation in the later phases of ischemia by blocking the synthesis of inducible cyclooxygenase-2 (COX-2) and nitric oxide synthase (iNOS). The anti-inflammatory action decreases NO (nitric oxide), Prostaglandin E2 (PGE2), and NF-κB action.

Ginsenoside-Rg3 Ginsenosides Rg3 (Rg3), which may cross the blood–brain barrier, may be helpful in treating Alzheimer's disease and enhancing cognitive performance in Alzheimer's patients [37]. Rg3 decreases reactive neurotoxicity and microglial activation [38], thus having negative effects on neurodegenerative disorders. The CNS's primary inflammatory response cells are phagocytic in nature, called microglia. By their pathophysiological role, they contribute to both potentially beneficial phagocytic and neurotoxic activities. Rg3 dramatically reduces the activation of NF-κB induced by Aβ-42, accompanied by the prevalence of TNF-α in microglia [39]. TNF-α treated neuronal cells demonstrated a greater survival rate after being pretreated with Rg3 [34].

Ginsenoside-Rh2 Ginsenoside-Rh2 (Rh2) inhibits the activity of α-synuclein protein and hence reducing the symptoms of neurodegenerative disease. Rh2 has anti-inflammatory impacts on astrocytes as well as microglia. By the regulation of protein kinase A (PKA)/AP-1 signaling pathways, it can inhibit LPS/IFN-γ-induced NO generation, TNF-α, COX-2, IL-1β and iNOS production and expression within mouse microglial cells [34]. In astroglial cells, Rh2 suppresses JNK/AP-1 and NF-κB pathways. Additionally, Rh2 has a cell-specific impact on the NF-κB signaling pathway [40] and MAPK phosphorylation. When both the signaling pathway (p38 MAPK and NF-κB) are taken together it may be beneficial in the treatment of inflammatory airway illnesses like asthma. Rh2 has now been developed into sulfated derivatives such as Rh2-B1 and Rh2-B2 due to its poor oral bioavailability and water solubility. These Rh2 compounds inhibit the actions of JNK, p38 MAPK, and NF-Kb [40] with the synthesis of LPS-induced TNF-α, IL-6, and IL-1β.

Protopanaxatriol

Protopanaxatriol (PPT) is a member of the dammarane-type triterpenoid saponin family and has been found to have various pharmacological effects [41], which govern neuroprotective properties. Research has demonstrated that PPT and other ginsenosides can improve mood, physical performance, and cognitive function [42]. PPT has been demonstrated to enhance cognitive performance, lessen neuronal damage, and raise levels of essential neuroprotective molecules in the NDD models [43]. If these impacts apply to people, then to discover the most effective PPT dosage and duration for neurodegenerative illnesses, more study is required.

Ginsenoside-Re Ginsenoside Re (Re) exhibited neuroprotection in an in vitro AD model made up of cytotoxicity brought on by Aβ25-35 [36]. Re has an anti-inflammatory property because it prevents LPS and Toll-like receptor 4 (TLR4) from interacting with macrophages. Re inhibits the phosphorylation and degradation of IRAK-1 caused by LPS as well as IKK-α-phosphorylation, NF-κB stimulation, & production of cytokine, e.g., TNF-α and IL-1β that cause inflammation. Inflammation brought on by LPS has been connected to neurological conditions such as PD, AD, and multiple sclerosis (MS). LPS is known to promote microglial cells in the CNS by decreasing iNOS and COX2 mediators and Re guards against inflammation in the nervous system in the CNS by inhibiting p38 MAPK signaling.

Ginsenoside-Rg1 Ginsenoside-Rg1 (Rg1) regulates microglial activation, which is significant in NDDs [44]. In cellular studies, Rg1 inhibits ERK1/2, NF-κB/p65, and Akt activation [45]. Rg1 defends neurons by preventing neuronal apoptosis and reducing the production and free radical scavenging in the brain [45]. In microglial cells, Rg1 lowers the concentrations of TNF-α, IL-1β, COX-2, iNOS, and NF-κB that have been activated by LPS [34]. Rg1's anti-inflammatory effects were seen in macrophages. Rg1 reduces IL-6 transcripts and protein LPS-induced cells as well as mouse macrophages by inhibiting the NF-κB pathway. Rg1 has a pivotal role in inflammation brought on by macrophages with several mechanisms of action via altering NF-κB or Akt/mTOR signaling pathways. In the studied animal models, Rg1 dramatically reduces the signs and symptoms of colitis brought on by TNBS and alcoholic hepatitis by not allowing the NF-κB signaling pathway to activate [46].

Ginsenoside-Rg2 A previous study has shown that ginsenoside-Rg2 (Rg2) has been illustrated to protect cells from injury caused by glutamate [37]. Rg2 reduces cell survival, elevated internalized Ca^{2+} concentration, insufficient MDA and NO generation, as well as elevated quantities of caspase-3, calpain II, and Aβ1-40 protein translation, are all signs that Rg2 prevents neurotoxicity in glutamate-induced PC12 cells [37]. In the murine models of dementia, Rg2 has also been found to defend against memory loss by way of inhibiting apoptosis [47].

Ginsenoside-Rh1 Ginsenoside-Rh1 (Rh1) has anti-inflammatory activities that block the iNOS and COX-2 formation [48]. In particular, microglial cells offer compelling evidence for the molecular pathway underlying the suppression of iNOS by Rh1. Rh1 blocks IFN-gamma-induced neuroinflammation [49] and iNOS production in microglial cells by blocking Janus kinase (JAK)/STAT and ERK signaling, as well as its downstream transcriptional regulators such as STAT1, NF-κB, and IRF-1. Ginsenoside Rh1 lowers IgE and IL-6 levels in the blood [50], which has a significant influence on cell infiltration related to inflammation and mast cell granulation [34]. The Rh1 also lowers ear hypertrophy and atopic dermatitis indications, indicating that it can be used to treat atopic dermatitis by acting as an anti-inflammatory drug and preventing iNOS expression and neuroinflammation.

Mechanism of Therapeutic Action of Ginsenoside in Neurodegenerative Diseases

According to predictions, NDDs are expected to be the largest public health problem and a prominent reason for death in the twenty-first century. Various ginsenosides have different roles in neuroprotection from NDDs (Fig. 4) such as reducing cell death, lessening oxidative stress, and controlling inflammation to have neuroprotective benefits. These pathways support the maintenance of neuronal integrity and function, which eventually enhances cognitive function and stops or delays the advancement of NDD. Furthermore, it has been shown that ginsenosides have immunomodulatory and anti-inflammatory properties, which may aid in reducing neuroinflammation and halting neuronal damage in NDDs.

Ginseng contains certain neuroprotective features that may be utilized to treat and alleviate brain damage as well as pathologically related illnesses, in particular, AD, PD, HD, Epilepsy, and MS. There exist two distinct patterns of neurodegenerative illness: chronic neurodegenerative disease and acute neurodegenerative disease. Alzheimer's is an example of a chronic neurodegenerative illness, whereas cerebral ischemia–reperfusion injury is an example of an acute neurodegenerative disease. Common mechanisms in the majority of NDDs have been identified and shown in Table 2, including protease resistance misfolding, elevated oxidative stress, chronic neuroinflammation, and aggregation of proteins, rendering them non-functional.

Dementia

Declining cognitive functions such as thinking, memorizing, and interpreting are the hallmark of dementia. The primary factor in all dementia etiology is aging. Dementia can occur from several conditions and diseases. As the world's population ages, dementia prevalence is expected to increase roughly double every twenty years, with 66 million dementia cases estimated in 2030 and 115 million in 2050 [51]**.** Neurodegenerative illnesses result in gradual and permanent loss of neurons and brain function. The two most common types of dementia are Alzheimer's disease and vascular dementia.

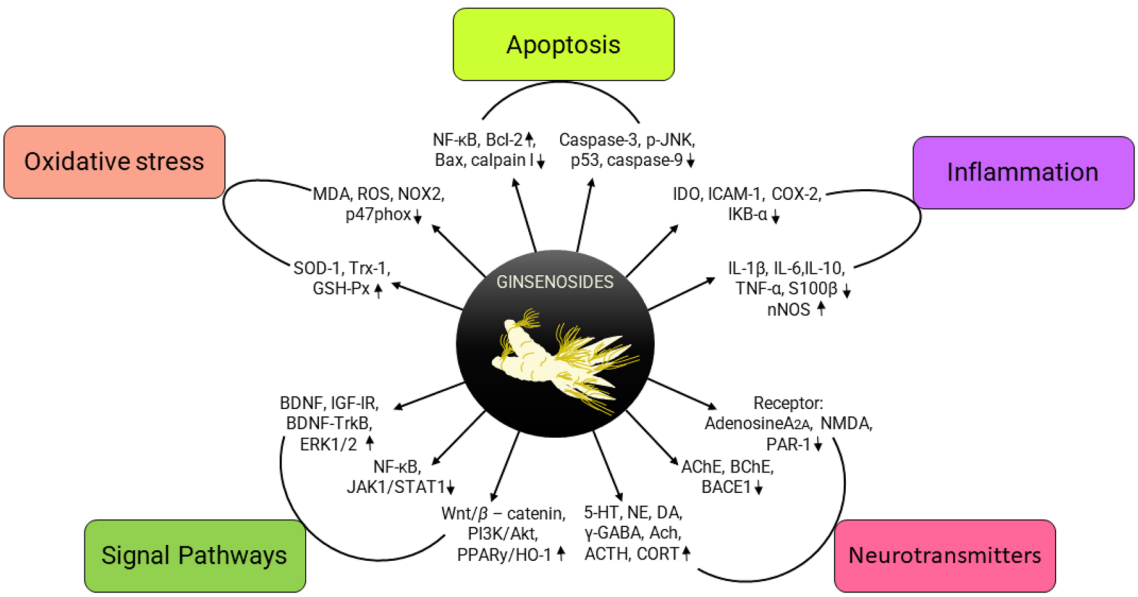

Fig. 4 Neuroprotective mechanisms of ginsenosides

Table 2 Therapeutic effects of ginsenosides on NDDs

Disease	Models	Signaling pathways	Effects of ginsenosides on disease	References
Alzheimer Disease	SAMP8 mice	Rg1 & Rb1	Reduction of Aβ levels, Improved hippocampus histopathology, and cognitive performance Increased levels of acetylcholine and dopamine	[97]
Vascular dementia	BCAS model mice	Rg1	Repair hippocampus neuronal damage	[98]
Parkinson's disease	MPTP mice model LPS model	Rb1	Guards against neurotoxicity in DA neurons Toxicity of α-synuclein	[32]
Huntington's disease	R6/2 mouse	Rg3, Rf & Rg1	Reduce mitochondrial dysfunction and cellular death in HD neuronal cells Reduction in p53, Bax, and cleaved caspase-3	[99]
Epilepsy	Adult male Sprague–Dawley rats	Rb1 & Rb2	Improves memory impairment Decreases intracellular Ca^{2+} level	[100]
Multiple sclerosis	EAE (experimental autoimmune encephalomyelitis)	Rd	Decreased BBB's permeability Modulation of the Treg/Th17 imbalance An elevation of the inhibitory cytokines TGF-β and IL-10 Downregulation of IL-17 and IL-6	[91]

Inhibiting cell apoptosis, lowering oxidative stress, controlling inflammation, and enhancing memory and cognitive function are some of the therapeutic benefits listed in the table

Alzheimer's Disease (AD)

AD is the most prevalent form of dementia which results in a degenerative neurological condition, loss of memory, as well as deterioration concerning cognitive and thinking capability and communication, which prove fatal in the later stages. After cardiovascular disease and cancer, AD ranks third in terms of mortality [52]. The pathophysiology of AD is multifaceted, but it is primarily characterized by the amyloid cascade brought on by oxidative stress, accumulation of the protein β-amyloid (Aβ), hyperphosphorylation of tau, and neuronal cholinergic degeneration brain inflammation, accompanied by destabilization of the gut flora. The development of AD may also be influenced by elements including calcium abnormalities, insulin signal transduction problems, and ApoE4 alleles [53]. Ginsenoside Rg1 especially was discovered to possess the biggest impact on memory retention and acquisition in AD models, even though ginsenosides exhibit anti-AD action. In animal studies of cognitive impairment, Rg1 decreased pathology related to AD, regulated synaptic spaces, and prevented inflammation as well as oxidative damage [54], shown in Fig. 5 (a).

Numerous studies have demonstrated that Rg1 enhances learning and spatial memory in animal models of AD. According to research, via inhibiting the amyloid precursor protein (APP) formation and controlling alpha(α-), beta(β-), and gamma (γ-) secretase activities, Rg1 has a curative impact on AD, and reducing the creation and promoting the destruction of Aβ to improve Aβ pathology. According to Chen et al.'s study, Rg1 may reduce the generation of Aβ1-42 in both in vitro—CHO-2B7 cells and in vivo—Tg2576 mice [55]. Additionally, research has shown that Rg1 can lessen Aβ by modulating APP concentrations and its main metabolic pathways, shown in Fig. 5 (a). First, Rg1 reduces APP expression to block the source of Aβ production. In murine experiments, the scientists discovered that Rg1 decreased the amounts of Aβ1-42 and cerebrospinal fluids (CTFs) via lowering the transcription of APP mRNA [56]. Second, Rg1 controls α-secretase, which regulates the metabolic pathway of APP that is not amyloidogenic. By increasing α-secretase mRNA levels, Rg1 could reduce Aβ1-40 and APP production in the hippocampi, as well as in A25-35 and dexamethasone-induced rat models of AD [52]. Thirdly, Rg1 regulates the activity of the enzyme β-secretase, which in turn regulates the APP's amyloidogenic metabolism [52]. The findings of research conducted in vitro and in vivo indicate that Rg1 may control β -secretase activity, reduce β -site APP cleaving enzyme-1 (BACE1) levels, and limit β -secretase transcript levels in the hippocampus of AD-rats [57]**.** Studies demonstrate that Rg1 prevents tau hyper-phosphorylation both in vitro and in vivo, protecting against AD. By controlling synaptic activity, Rg1 is believed to have a medicinal impact in reducing AD symptoms. Rg1 reversed the reduction of axons and the expression of acetyltransferase, a crucial enzyme in the production of ACh, in cortical neurons induced by Aβ25-35 and greatly enhanced the quantity of ACh in the hippocampi of AD-rats [58].

By controlling BDNF production and associated processes, Rg1 also enhanced synaptic activity and cognitive impairment. By regulating the mitochondrial apoptotic cascade and associated pathways, Rg1 also reduced neuronal death in AD mice. Rg1 may prevent the death of nerve cells in the cerebral cortex and hippocampus [59]. These outcomes imply that Rg1 controls mitochondrial activity

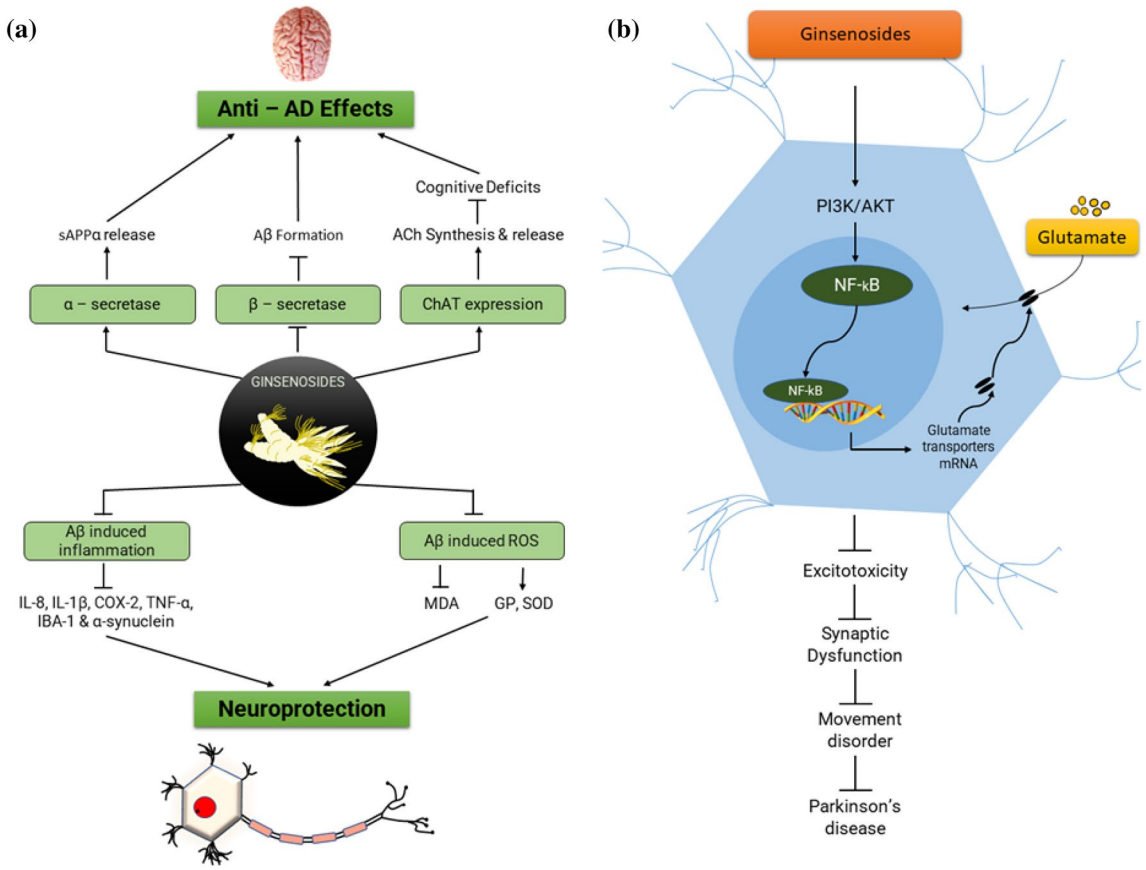

Fig. 5 Ginsenoside's action on neurodegenerative diseases **a** Neuroprotective mechanism of Alzheimer's disease **b** Neuroprotective mechanism of Parkinson's disease

under oxidative stress brought on by Aβ. Numerous signaling pathways are involved in Rg1's anti-apoptotic action. Increased p-AKT/AKT levels, higher GSK-3β protein production, and p38MAPK signaling pathway are all effects of the FGF2-AKT signaling pathway. Through the GR-ERK pathway, Rg1 inhibited the apoptosis that A25-35 caused. Rg1's protective effects against Aβ25-35-induced cell damage may include GR-ERK-dependent regulation of a special hypoxia-inducible factor (HIF-1)/RNS pathway. Rg1 inhibits HIF-1 activation and reduces ROS levels in the brains of model mice, particularly malondialdehyde and 8-hydroxydeoxyguanosine [57]**.**

Rg1 prevents the production of cytokines that induce inflammation, in living mice as well as in vitro and iNOS in senescence-accelerated mice P8 (SAMP8) mice through lowering astrocyte stimulation [52]. Dexamethasone-induced neuronal death, as well as learning and memory deficits, were reduced by Rg1. It can substantially reduce the production of NLRP1, ASC, caspase-1and caspase-5in the brains of mice compared to the control group. Ginsenoside Rg1 has comparable effects on NLRP1 in vitro research. In HT22 cells, where IL-1β, NLRP1, and caspase-1 were originally stimulated by LPS, Rg1 reduced their levels [60]. This suggested that it could reduce the signs and symptoms of AD by obstructing the NLRP1 inflammation process. PC12 cells that had been exposed to hydrogen peroxide and HT22 cells that had been exposed to LPS, Rg1 reduced NF-κB/p65 phosphorylation and NF-κB expression [60]. Rg1's wide array of pharmacological effects on AD is mostly due to its control over the PKC, p21WAF1/CIP1, PKA/CREB, MAPK, FGF2/AKT, PI3K/AKT, CDK5, BNDF/TrkB, GSK-3β, NF-κB, TLR3, TLR4, and NLRP1 signaling pathways.

By regulating the concentrations of PP2A and p-GSK3β in the cortex and hippocampal regions, Rb1 prevented tau hyperphosphorylation and restored memory impairment brought on by aluminum exposure [61]. Rg1 improved the acquisition deficit in the MWM test better than Rb1. Additionally, Rg1 has a greater ability than Rb1 to inhibit acetylcholinesterase (AChE) activity.

For the very first time, the delayed recall test used in this piece of work showed that non-spatial memory deficits in SAMP8 mice were more successfully treated by Rb1 than by Rg1. The SAMP8 mice entered the dark room significantly

more quickly than the SAMR1 animals did [62]. When compared to SAMP8 mice, Rb1 dramatically decreased the production of TNF-α but Rg1 did not. Rb1 may enhance memory and cognitive abilities in the Aβ1-40 induced AD rat model by increasing levels of the anti-apoptosis mediator and decreasing levels of the pro-apoptosis regulator [63]. Moreover, Rb1 demonstrated that it can modulate inflammation by preventing ASC and caspase-1 in the brain by greatly reducing the expression of these two proteins, caspase-1 and ASC.

Vascular Dementia (VD)

This type of dementia is the second most common after AD. Vascular dementia is observed in the brain brought by blood vessel damage, leading to cognitive impairment. Memory impairment, behavioral changes, and psychological issues like anxiety and depression are the common symptoms of VD [64]. Brain regions including the cortex and hippocampus have certain abnormal alterations.

Rg1 can reduce cognitive impairment and neuronal destruction in VD rats. Ginsenoside compound K (CK) is the primary metabolic product generated from ginsenoside Rb1, Rb, and Rc [65] which has high bioavailability and pharmacological actions including those with anti-inflammatory, antioxidant, anti-cancer, anti-aging, and antimutagenic properties [66]. Another research indicated the role of Rg1 in curing VD by suppressing neuronal cell death and improving neuronic damage in bilateral common carotid artery stenosis.

C-K protects against VD brought on by chronic cerebral hypoperfusion (CCH). Enough proof is now there that poor insulin signaling within the brain accelerates dementia development and declines cognitive function. The PI3K/Akt mechanism that is essential for promoting neuronal development, neuron survival, memory, and learning is primarily impacted by brain insulin resistance [67]. Phosphorylated Akt prevents GSK-3β from producing Aβ1-42 by enhancing the phosphorylation of Ser9 of GSK-3β, which is produced by γ-secretase at the APP proteolysis. On the other hand, downregulation of the PI3K/Akt pathway lowers the activity of enzymes that break down insulin, necessary for the breakdown of Aβ1-42. The synthesis and clearance of Aβ1-42 are both significantly influenced by the insulin signal pathway [68]. When Aβ1-42 is administered, the PI3K/Akt pathway is directly disrupted, which may result in the deactivation of IDE and pSer9-GSK-3β. Aβ1-42 levels rise as a result of the disrupted PI3K/Akt signaling, both of the steps occurring cyclically. As a result, activation of PI3K/Akt signaling breaks up this cycle and prevents the synthesis of Aβ1-42. Previously conducted research demonstrated that C-K might enhance the brain's PI3K/Akt signaling pathway [68]. Intriguingly, rats with VD who received C-K therapy had higher amounts of IDE, pSer9-GSK-3, and pSer473-Akt in their hippocampi.

Parkinson's Disease (PD)

Parkinson's disease (PD) is a type of neurologically damaging ailment that typically manifests in later years of life with bradykinesia and a minimum of one symptom like rigidity or resting tremors. Gradually progressing symptoms of compromised emotional, olfactory, and cognitive capabilities are usually seen in patients of PD, in addition to motor difficulties [69]. The alpha-synuclein (SNCA) gene produces a tiny protein called α-synuclein, which shows an increased level of expression in the presynaptic terminals present at the CNS. One of the most common neurobiology-associated characteristics is the aberrant buildup of α-synuclein protein in the forms of Lewy neurites and Lewy bodies. There are several pathogenic pathways for Parkinson's disease, and one of these is inflammation, namely the fast activation of microglia. According to research [70], Rg1 is now known to have an anti-inflammatory function as well as antiapoptotic, and antioxidant in PD.

Anti-inflammatory cytokines and neurotrophin were dramatically elevated whereas a substantial decrease in pro-inflammatory cytokines such as IL-6, TNF-α, and IL-1β. Ginsenoside-Rg1 was discovered to dramatically block NF-κB nuclear translocation, which shifted microglia away from the M1 phenotype and toward the M2. Rg1 protects the neurodegeneration brought on by LPS by boosting the production of neurotrophins and anti-inflammatory cytokines while decreasing the release of proinflammatory cytokines and glial activation [71]. Even if the deeper causes of PD are fully clear, at least one indication is that disruption in the Wnt/β-catenin signaling route is a significant factor. Evidence has shown that abnormalities significantly impact nigrostriatal dopaminergic neurons' pathology in PD models in the Wnt/β-catenin pathway [72]. Dickkopf-1 (Dkk1), an extrinsic protein that interacts with LRP5/6 and produces toxicity in PC12 cells in addition to the neurodegenerative problem, may interfere with the canonical Wnt signaling pathway.

In DA neurons, PC12 cells, and SH-SY5Y cells, Rb1 can protect against the harmful consequences of 1-methyl-4-phenyl pyridinium-iodide (MPP +) or 6-OHDA [32]. Additionally, Rb1 may break apart produced fibrils, block the polymerization of α-synuclein in vitro, and reduce fibrillation & toxicity of α-synuclein [73]. Rb1's underlying mechanism for treating PD in the MPTP model. By controlling the production of glutamate transporters and altering the glutamatergic transmission routes in the nigrostriatum and corticonigrum, Rb1 improves motor impairments, as shown in Fig. 5 (b). In PD, ginsenosides have been shown to have neuroprotective effects by inhibiting the PI3/AKT pathway

which results in the reduction of oxidative stress, modulating inflammation, and regulating the dopaminergic system.

Iron metabolism disturbance is another factor in the emergence of PD. A type of non-apoptotic cell death known as ferroptosis that depends on iron via an extrinsic (transporter-dependent) and/or an intrinsic (enzyme-regulated) pathway [74]. A redox disequilibrium between oxidants and antioxidants, fueled by aberrant production and control of redox-active enzymes, is what leads to ferroptosis. These enzymes catalyze several processes that result in fatty acid oxidation products, including lipid-based ROS [75]. Hence, ferroptosis may have several causes, including lipid peroxidation. The crucial function of excessive lipid oxidation is in illness and cell death. The neuroprotective role of Rg1 has been demonstrated in the chronic murine PD model created by MPTP/Pro. By preventing the production of ROS, reducing the damage to DNA, and preventing the formation of lipid peroxide in the striatum, it may have a particularly substantial effect on oxidative stress. Regulating oligodendrocytes, also had an impact on iron dyshomeostasis [76].

Rg1 may cause the Wnt pathway to become active to mediate its neuroprotective benefits against MPTP/MPP + damage. The findings suggested that Rg1's effects on PD models are mediated via the Wnt pathway [72]. Additionally, Rg1 can control microglia polarisation dynamics, which is accompanied by NF-κB nuclear translocation, which was directly linked to its anti-neuroinflammatory activities. By controlling the oligodendrocytes during the PD formation phase, Rg1 might restore the iron balance in the brain.

Epilepsy

Seizures are brought on by the neurological condition known as epilepsy, which damages the brain. Seizures are aberrant electrical discharges in the brain that can cause convulsions, loss of consciousness, and altered sensory perception [77]. It is marked by repeated seizures owing to an unbalance in brain excitation and inhibition. Epilepsy can be caused by several complicated factors, including febrile seizures, birth injuries, head injuries, strokes, brain tumors, certain infections, and heredity [78]. ROS and autophagy have a role in the formation of epilepsy along with other factors, but the pathophysiological mechanism is yet to be understood. The most important neurotransmitter systems to target for the treatment of epilepsy are glutamatergic and GABAergic neurotransmission [66]. Having no treatment for epilepsy creates an opportunity for scientists.

To establish the efficacy of ginsenosides in epilepsy, some researchers tested Rb1 in an epileptic rat model where they induced the condition ‘in vivo by pentylenetetrazol (PTZ), which is a GABA receptor antagonist, and in vitro by culturing hippocampal neurons in Mg2 + free medium. When Rb1 impacts epilepsy, they discovered that the nuclear factor erythroid 2-related factor (Nrf2/ARE) pathway is activated [79]. The ARE has characteristics that distinguish it as a unique oxidative stress responder, and in combination with Nrf2, a transcription factor (TF), it regulates an internal cytoprotective system. Nrf2, upon triggering, moves into the nucleus and forms heterodimers with another TF such as c-Jun [79]. This heterodimer attaches to the ARE and triggers the production of antioxidants. They have also found that Rb1 has the potential to decrease seizure duration with an enhancement in seizure latency among PTZ-induced models [79].

Previous studies established the role of ginsenoside compound K (GCK) similar to that of Rb1 and another group hypothesized that GCK could reduce seizures by rising GABA levels as it was observed that it is a crucial inhibitory neurotransmitter in the brain [80], is diminished after a seizure. GABA shortage causes neuronal hyperexcitability, which contributes to seizure incidence. They used the lithium-pilocarpine model of epilepsy and administered GCK so that the GCK's antiepileptic impact was examined, and it was shown that increasing the latent period of GCK before the onset of Status epilepticus (SE) [66] and decreasing the seizure intensity had a positive correlation. GABA, a prominent inhibitory neurotransmitter has been identified to be present in the brain before a seizure. These results imply that GCK could prevent SE or even partial seizures [66].

Huntington’s Disease (HD)

Huntington’s Disease is an NDD that is incurable and autosomal dominant that develops gradually and it is brought on by an increase in CAG nucleotides in the CNS's mutant huntingtin (mHtt) gene [81]. The primary mechanism, as shown in the HD brain, is the buildup of polyglutamine in the cortex and striatum using R6/2 mouse brain stem cells in primary culture as HD models, the effects of ginsenosides on mHtt aggregation and mitochondria-related apoptotic markers can be examined. CAG nucleotides have 115–150 repetitions in exon 1 of the human mHtt gene on the R6/2 mouse chromosome [82]. In the R6/2 mouse model, body weight and motor performance declined fast, as did polyglutamine accumulation in the cortex and striatum. R6/2-derived neural stem cells exhibit ginsenoside Rf and Rg3 can lead to the decrement of mHtt agglomeration [83]. Additionally, chemicals linked to sick neuronal cells' death and mitochondrial malfunction were controlled. Mitochondrial dysfunction, synaptic inefficiency, Oxidative stress, striatal cell death, and anomalies in metabolism are among the results of the harm caused by mHtt protein [84]. The production of PGC-1alpha, a critical regulator of mitochondrial biosynthesis and respiration, is regulated by the cAMP response element binding (CREB) protein's phosphorylation. Motor

dysfunction, striatal atrophy, and mitochondrial failure—all important signs of HD—were seen in PGC-1 knockout animals. Given that PGC-1 restoration improves mitochondrial function and subsequently HD, then it seems that the CREB-PGC-1 pathway is mistargeted and may provide HD treatment options. It has been shown that Rg3 and Rf enhance PGC-1 and phosphorylated CREB levels while decreasing mitochondrial apoptotic factors. Thus, positive benefits of ginseng on HD may be generated by the bioactive components ginsenoside Rg3 and Rf [85]. This demonstrates that ginsenosides can reduce mHtt agglomeration and mitochondrial impairment, two critical factors for the development of HD. Hence, reducing the death of neurons. In HD neuronal cells, ginsenosides Rg3 and Rf may lessen mitochondrial dysfunction and cellular death, potentially by reducing mHtt aggregation [85].

A naturally occurring neurotoxin synthesized by the plant Indigofera is 3-nitro propionic acid (3-NP), which is infused to produce HD in a rat model [86]. As a result of 3-NP's inhibition of subdural hematoma (SDH) function in striatal cells, the striatum experiences neuronal loss and mitochondrial dysfunction with the rupture of the BBB, which causes an excessive leakage of too many peripheral proinflammatory cells and microglia. 3-NP induces the MAP Kinase and NF-κB pathways in microglia [45]. Through lowering striatal microglial activation, cell loss, and cytokine production, Rg1 not only lessens the effects of 3-NP on the BBB and mitochondrial malfunction but also aids in saving the striatal neurons. Rg1 blocks the activation of proteins linked to the MAPK and NF-κB pathways, preventing the death of striatal neurons.

Multiple Sclerosis (MS)

This involves an immune response towards myelin sheath, which was intended for protection and efficient signal transmission, causing inflammation in the CNS and making MS an autoimmune inflammatory condition. Sclerosis is the result of the myelin sheath disappearing or being degraded in several areas, which are known as plaques or lesions, so MS can be defined as “scar tissue in multiple locations".

Upon stimulation of the transcriptional factor Foxp3, Multiple sclerosis (MS) leads to the decrease in the expansion of auto-reactive T-lymphocytes producing IFN-γ, IL-17, and IL-1β, with an increase in the creation of immunosuppressive regulatory T cells (Tregs) [87]. A typical in vivo MS model used to investigate its behavioral symptoms, immunologic events, and histopathological characteristics is experimental autoimmune encephalomyelitis (EAE) [88]. One of the key components of both MS and EAE's pathophysiology is BBB failure, and in both conditions, the stimulation of auto-aggressive immune cells, CD4 + T cells, may cross the BB barrier and may cause inflammation and injury of neurons as well as degradation of myelin sheath itself [83]. MS and EAE pathophysiology are significantly influenced by the malfunctioning of the Treg cell population and the excessive autoimmune reactions of the Th17 cell population. Agents that can preserve BBB integrity might thus be used to treat MS.

A promising neuroprotective agent is ginsenoside Rd. By reversing the oxidation/reduction equilibrium, lowering the inflammation and cell mortality in the murine model's spinal tissue can reduce the damage to the BBB caused by cerebral ischemia and spinal injury as well as secondary harm caused by the spinal cord [89].

NADPH oxidases create ROS, which is crucial in several processes underpinning the pathology of MS and EAE. According to López et al., the primary mechanism through which ginsenosides have a neuroprotective effect on astrocytes is by activating antioxidant enzymes. Interestingly, in an Adriamycin-induced cardiotoxicity model, by stimulating the Nrf2-ARE pathway, ginsenoside-Rg3 can lessen endothelial dysfunction brought on by oxidative stress [90].

Due to its advantages of having anti-inflammatory and antioxidant properties, in the chronic EAE model, Rg3-enriched Rg3-KRGE was tried to enhance BBB integrity. and reported positive results. Researchers discovered that Rg3-KRGE prevents BBB breakdown by upregulating tight junctional molecules and downregulating PECAM-1, fibronectin, and MMP9. By affecting mRNA expression, Rg3-KRGE also has an impact on the degree of inflammatory cytokine production [83]. Cytokines which cut down inflammation (TGFB and IL-10) are increased, while the effects of Rd on IL-6 and IL-17, two proinflammatory cytokines, are reduced [91]. The NOX2/4 gene expression, which is in charge of elevated oxidative stress, was also lessened in the spinal cords of EAE animals given Rg3-KRGE [83].

Depression

Depression is among the most common neuropsychiatric conditions, distinguished by low mood, uncertainty, hopelessness, and sometimes thoughts of suicide [92]**.** Pro-inflammatory chemicals such as TNF-α, ROS, IL-1, and IL-6 were present in excessive amounts in those with severe mental disorders. Gap junctions are responsible for communication between adjacent cells, which have two hemichannels or connexons, each having six connexins [93]. The predominant isoform of the connexin group produced in astrocytes is Connexin43 (Cx43)—gap junction**,** it is believed to be a novel goal to treat depression**.** Research has shown that Rg1's antidepressant effects can improve the performance of the Cx43-gap junction [93] and possible Rg1 targets for the treatment of depression include Cx43. Depression could be triggered by Cx43 changes brought on

by gap junctional dysfunction brought on by corticosterone (CORT) in astrocytes [94]. CORT decreases levels of Cx43 via downregulating Cx43 transcripts and speeding up Cx43 destruction, which may be mediated through ubiquitination and autophagy mechanisms. Rg1 might preclude Cx43 transcripts and decrease Cx43 destruction to raise Cx43 proteins, this could be due to Rg1's impacts on the above-mentioned Cx43 destruction pathways [95]. One of the pathogenic mechanisms is inflammation for depression among others and according to one research, Rg1 may reduce neuroinflammation by inhibiting Cx43 ubiquitination to lessen depression [96]. Several pathways may be employed to prevent brain inflammation in addition to this one, ginsenoside Rg1, for example, caused a reduction in NF-κB and MAPK pathways within the brain cortex as well as the hippocampus to lessen the inflammatory response brought on by LPS. Behavioral reactions to chronic unpredictable mild stress (CUMS) in mice receiving ginsenoside-Rg1 pretreatment, a model for evaluating the efficacy of antidepressants, were prevented, indicating that ginsenoside-Rg1 treatment exerts antidepressant-like impacts [96]. Ginsenoside Rg1 can boost the antioxidants in the hippocampal region, which can enhance cognitive function. These findings showed that Rg1 seems to be a natural molecule with several targets that may influence several routes, with comprehensive identification of the neuronal processes being particularly interesting. In conclusion, Rg1 has the following effects: 1) reduction of pro-inflammatory cytokine production and glial activation; 2) improvement of structural modifications to neurons by minimizing impairments in spines and synapses; and 3) reduction of pro-apoptotic cytokine levels at certain localized regions of neurons.

Conclusion

Ginseng's main active component is ginsenosides, which have several effects connected to stress and have apoptotic, antioxidant, and anti-inflammatory characteristics. Several ginsenosides that possess protective effects have been identified and described in this study with their mechanisms of action and roles in neurological disorders. Ginsenosides' molecular mechanisms include free radical scavenging, inflammation suppression, and excitotoxicity prevention. Ginsenosides could prove really useful medications for treating NDDs, according to the expanding body of research on the neuroprotective properties of these herbs. Based on their mode of action, ginsenosides are believed to modulate inflammatory responses predominantly by regulation of the NF-κB signaling pathway. Clinical evaluation and confirmation of preclinical findings in patients with a specific neurological condition are lacking.

Future advancements in the treatment of neurodegenerative illnesses may be made possible by the prospective therapeutic use of ginsenosides. It is possible to create oral supplements that improve the convenience of administration while also increasing the rate of absorption. In a combinatorial strategy, ginsenosides can be taken alongside other medications to increase their effectiveness and minimize their negative effects. Ginsenosides may work better when combined with other therapeutic approaches. These compounds are a desirable choice for individuals looking for alternative therapies due to their natural nature. To create novel medications or therapies, scientists might concentrate on examining the efficacy and durability of ginsenosides as a potential therapy for neurodegenerative diseases. Future studies may also be crucial in determining the best ginsenoside dose and route of delivery. Overall, the prospective therapeutic application of ginsenosides presents a promising route for the creation of efficient and durable medicines for neurodegenerative diseases, giving patients and their families hope.

In conclusion, ginsenosides and their metabolites/derivatives are strong candidates that can be utilized as active agents in the future treatment and control of brain illnesses, as demonstrated by several investigations on ginsenosides. Additionally, scientists should continue to study and provide evidence for their neuroprotective benefits and methods of action. Moreover, variances in people might happen as a result of ginsenoside therapy. Consequently, more research in randomized clinical trials is strongly advised to produce more trustworthy data on the effectiveness and adverse effects of ginsenoside.

Acknowledgements We appreciate all of the help and advice we have received from the Delhi Technological University in Delhi, India.

Author Contributions Each author has contributed equally. The final document has been read by all writers.

Funding The authors affirm that they did not accept any money, grants, or other assistance for the creation of this manuscript.

Data Availability The authors confirm that the data supporting the findings of this study are available within the article.

Declarations

Conflict of interest The authors affirm that they have no competing interests with this work. There are no material financial or non-financial interests of the authors to report.

Research Involving Human Participants and/or Animals No.

Informed Consent Yes, we are aware of every detail of our involvement.

References

1. Walia, S., Kumar, P., Kumar, D., & Kumar, R. (2023). A preliminary study on suitability of growing ginseng (Panax ginseng Meyer) in western Himalayan region. *Plant, Soil and Environment, 69*(2), 71–80. https://doi.org/10.17221/288/2022-PSE
2. Amir, M., Vohra, M., Raj, R. G., Osoro, I., & Sharma, A. (2023). Adaptogenic herbs: A natural way to improve athletic performance. *Health Sciences Review*. https://doi.org/10.1016/j.hsr.2023.100092
3. Balusamy, S. R., et al. (2023). A comprehensive and systemic review of ginseng-based nanomaterials: Synthesis, targeted delivery, and biomedical applications. *Medicinal Research Reviews*. https://doi.org/10.1002/med.21953
4. C.-Z. Wang, S. Anderson, W. DU, T.-C. He, and C.-S. Yuan, (2016) "Red ginseng and cancer treatment.," *Chin J Nat Med*, vol. 14, no. 1, pp. 7–16
5. Zhang, H., et al. (2020). Characteristics of panax ginseng cultivars in Korea and China. *Molecules*. https://doi.org/10.3390/molecules25112635
6. Sahiner, M., Yilmaz, A. S., Gungor, B., & Sahiner, N. (2023). A review on phyto-therapeutic approaches in alzheimer's disease. *J Funct Biomater, 14*(1), 50. https://doi.org/10.3390/jfb14010050
7. Babazadeh, A., Vahed, F. M., Liu, Q., Siddiqui, S. A., Kharazmi, M. S., & Jafari, S. M. (2023). Natural bioactive molecules as neuromedicines for the treatment/prevention of neurodegenerative diseases. *ACS Omega, 8*(4), 3667–3683. https://doi.org/10.1021/acsomega.2c06098
8. Sun, X.-F., & Pradeep Singh, S. (2023). Network pharmacology integrated molecular docking demonstrates the therapeutic mode of Panax ginseng against ovarian cancer. *Tropical Journal of Pharmaceutical Research, 22*(3), 589–596. https://doi.org/10.4314/tjpr.v22i3.16
9. Baik, I.-H., Kim, K.-H., & Lee, K.-A. (2021). Antioxidant, anti-inflammatory and antithrombotic effects of ginsenoside compound K enriched extract derived from ginseng sprouts. *Molecules, 26*(13), 4102. https://doi.org/10.3390/molecules26134102
10. "Calories in Ginseng." https://www.nutritionix.com/food/ginseng (accessed Apr. 07, 2023).
11. Guo, M., Shao, S., Wang, D., Zhao, D., & Wang, M. (2021). Recent progress in polysaccharides from *Panax ginseng* C. A. Meyer. *Food & Function, 12*(2), 494–518. https://doi.org/10.1039/D0FO01896A
12. Lee, J., et al. (2017). Mass spectrometry based profiling and imaging of various ginsenosides from panax ginseng roots at different ages. *International Journal of Molecular Sciences*. https://doi.org/10.3390/IJMS18061114
13. Lee, I.-S., Kang, K. S., & Kim, S.-Y. (2019). Panax ginseng pharmacopuncture: current status of the research and future challenges. *Biomolecules, 10*(1), 33. https://doi.org/10.3390/biom10010033
14. Karmazyn, M., & Gan, X. T. (2021). Chemical components of ginseng, their biotransformation products and their potential as treatment of hypertension. *Molecular and Cellular Biochemistry, 476*(1), 333–347. https://doi.org/10.1007/s11010-020-03910-8
15. S. Khan, A. Tosun, and Y. S. Kim, "Ginsenosides as Food Supplements and Their Potential Role in Immunological and Neurodegenerative Disorders," in *Bioactive Nutraceuticals and Dietary Supplements in Neurological and Brain Disease*, Elsevier, 2015, pp. 303–309. doi: https://doi.org/10.1016/B978-0-12-411462-3.00031-X.
16. Lee, D. G., Lee, J. S., Kim, K.-T., Kim, H. Y., & Lee, S. (2019). Analysis of major ginsenosides in various ginseng samples. *Journal of Applied Biological Chemistry, 62*(1), 87–91. https://doi.org/10.3839/jabc.2019.013
17. Chen, W., Balan, P., & Popovich, D. G. (2020). Comparison of ginsenoside components of various tissues of new zealand forest-grown asian ginseng (Panax ginseng) and american ginseng (panax quinquefolium l.). *Biomolecules*. https://doi.org/10.3390/biom10030372
18. Jia, X. H., et al. (2013). Comparative studies of saponins in 1–3-year-old main roots, fibrous roots, and rhizomes of Panax notoginseng, and identification of different parts and growth-year samples. *Journal of Natural Medicines, 67*(2), 339–349. https://doi.org/10.1007/s11418-012-0691-6
19. T. Hong Van Le *et al.*, "Ginseng Saponins in Different Parts of Panax vietnamensis," 2015.
20. P. Mikulska *et al.*, "Ashwagandha (Withania somnifera)—Current research on the health-promoting activities: a narrative review," *Pharmaceutics 2023,* vol. 15, no. 4, p. 1057, 2023, doi: https://doi.org/10.3390/PHARMACEUTICS15041057.
21. Mohsin, M. M., Hanif, M. A., Ayub, M. A., & Dharmadasa, R. M. (2022). *Ginseng* (pp. 331–340). Amsterdam: Medicinal Plants of South Asia Novel Sources for Drug Discovery. Elsevier.
22. Lee, J.-H., Ahn, N.-H., Choi, S.-B., Kwon, Y., & Yang, S.-H. (2021). Natural products targeting amyloid beta in Alzheimer's Disease. *International Journal of Molecular Sciences, 22*(5), 2341. https://doi.org/10.3390/ijms22052341
23. Abduljawad, A. A., et al. (2022). Alzheimer's disease as a major public health concern: role of dietary saponins in mitigating neurodegenerative disorders and their underlying mechanisms. *Molecules, 27*(20), 6804. https://doi.org/10.3390/molecules27206804
24. P. T. Lum, M. Sekar, S. H. Gan, S. R. Bonam, and Mohd. F. Shaikh, "Protective effect of natural products against huntington's disease an overview of scientific evidence and understanding their mechanism of action," *ACS Chem Neuroscience*, 2021, doi: https://doi.org/10.1021/acschemneuro.0c00824.
25. Zha, Z., Liu, S., Liu, Y., Li, C., & Wang, L. (2022). Potential utility of natural products against oxidative stress in animal models of multiple sclerosis. *Antioxidants, 11*(8), 1495. https://doi.org/10.3390/antiox11081495
26. He, et al. (2019). Recent advances in biotransformation of saponins. *Molecules, 24*(13), 2365. https://doi.org/10.3390/molecules24132365
27. Hou, M., Wang, R., Zhao, S., & Wang, Z. (2021). Ginsenosides in Panax genus and their biosynthesis. *Acta Pharm Sin B, 11*(7), 1813–1834. https://doi.org/10.1016/j.apsb.2020.12.017
28. W. Chen, P. Balan, and D. G. Popovich, "Comparison of the ginsenoside composition of Asian ginseng (Panax ginseng) and American ginseng (Panax quinquefolius L.) and their transformation pathways," 2019, pp. 161–195. doi: https://doi.org/10.1016/B978-0-12-817901-7.00006-X.
29. Sun, Y., et al. (2020). Synthesis and structure-activity relationship of pyxinol derivatives as novel anti-inflammatory agents. *ACS Medicinal Chemistry Letters, 11*(4), 457–463. https://doi.org/10.1021/acsmedchemlett.9b00562
30. Lu, C., et al. (2018). The protective effect of 20(S)-protopanaxadiol (PPD) against chronic sleep deprivation (CSD)-induced memory impairments in mice. *Brain Research Bulletin, 137*, 249–256. https://doi.org/10.1016/j.brainresbull.2017.12.012
31. Zarneshan, S. N., Fakhri, S., & Khan, H. (2022). Targeting Akt/CREB/BDNF signaling pathway by ginsenosides in neurodegenerative diseases: A mechanistic approach. *Pharmacological Research*. https://doi.org/10.1016/j.phrs.2022.106099
32. Ahmed, T., et al. (2016). Ginsenoside Rb1 as a neuroprotective agent: A review. *Brain Research Bulletin, 125*, 30–43. https://doi.org/10.1016/j.brainresbull.2016.04.002

33. Gao, H., et al. (2020). Ginsenoside Rb1 exerts anti-inflammatory effects in vitro and in vivo by modulating toll-like receptor 4 dimerization and NF-kB/MAPKs signaling pathways. *Phytomedicine*. https://doi.org/10.1016/j.phymed.2020.153197
34. Kim, J. H., Yi, Y.-S., Kim, M.-Y., & Cho, J. Y. (2017). Role of ginsenosides, the main active components of Panax ginseng, in inflammatory responses and diseases. *Journal of Ginseng Research, 41*(4), 435–443. https://doi.org/10.1016/j.jgr.2016.08.004
35. Qu, B., Cao, T., Wang, M., Wang, S., Li, W., & Li, H. (2022). Ginsenosides Rd monomer inhibits proinflammatory cytokines production and alleviates DSS-colitis by NF-κB and P38MAPK pathways in mice. *Immunopharmacology and Immunotoxicology, 44*(1), 110–118. https://doi.org/10.1080/08923973.2021.2012482
36. Moratilla-Rivera, I., Sánchez, M., Valdés-González, J. A., & Gómez-Serranillos, M. P. (2023). Natural products as modulators of Nrf2 signaling pathway in neuroprotection. *International Journal of Molecular Sciences, 24*(4), 3748. https://doi.org/10.3390/IJMS24043748
37. Y.-J. Ji, "Heat Treatment Enhances the Neuroprotective Effects of Crude Ginseng Saponin by Increasing Minor Ginsenosides," 2023, doi: https://doi.org/10.21203/rs.3.rs-2532316/v1.
38. Hou, J., Xue, J., Wang, Z., & Li, W. (2018). Ginsenoside Rg3 and Rh2 protect trimethyltin-induced neurotoxicity via prevention on neuronal apoptosis and neuroinflammation. *Phytotherapy Research, 32*(12), 2531–2540. https://doi.org/10.1002/ptr.6193
39. Wang, Z., Zhang, Z., Liu, J., Guo, M., & Li, H. (2023). Panax Ginseng in the treatment of Alzheimer's disease and vascular dementia. *Journal of Ginseng Research*. https://doi.org/10.1016/j.jgr.2023.03.001
40. Xu, C., et al. (2022). Effects of G-Rh2 on mast cell-mediated anaphylaxis via AKT-Nrf2/NF-κB and MAPK-Nrf2/NF-κB pathways. *Journal of Ginseng Research, 46*(4), 550–560. https://doi.org/10.1016/j.jgr.2021.10.001
41. "The Power of Natural Chinese Medicine, Ginger and Ginseng Root in an Organic Life", doi: https://doi.org/10.5829/idosi.mejsr.2019.64.71.
42. B. de Oliveira Zanuso, A. R. de Oliveira dos Santos, V. F. B. Miola, L. M. Guissoni Campos, C. S. G. Spilla, and S. M. Barbalho, "Panax ginseng and aging related disorders: A systematic review," *Experimental Gerontology*, 2022, doi: https://doi.org/10.1016/j.exger.2022.111731.
43. Wang, Z.-Y., et al. (2021). Traditional Chinese medicine compounds regulate autophagy for treating neurodegenerative disease: A mechanism review. *Biomedicine & Pharmacotherapy*. https://doi.org/10.1016/j.biopha.2020.110968
44. Lee, J.-W., et al. (2021). The Role of Microglia in the Development of Neurodegenerative Diseases. *Biomedicines, 9*(10), 1449. https://doi.org/10.3390/biomedicines9101449
45. Liu, S., et al. (2018). Intravenous immunoglobulin ameliorates motor and cognitive deficits and neuropathology in R6/2 mouse model of Huntington's disease by decreasing mutant huntingtin protein level and normalizing NF-κB signaling pathway. *Brain Research, 1697*, 21–33. https://doi.org/10.1016/j.brainres.2018.06.009
46. Lee, S.-Y., Jeong, J.-J., Eun, S.-H., & Kim, D.-H. (2015). Anti-inflammatory effects of ginsenoside Rg1 and its metabolites ginsenoside Rh1 and 20(S)-protopanaxatriol in mice with TNBS-induced colitis. *European Journal of Pharmacology, 762*, 333–343. https://doi.org/10.1016/j.ejphar.2015.06.011
47. Cui, J., Shan, R., Cao, Y., Zhou, Y., Liu, C., & Fan, Y. (2021). Protective effects of ginsenoside Rg2 against memory impairment and neuronal death induced by Aβ25-35 in rats. *Journal of Ethnopharmacology*. https://doi.org/10.1016/J.JEP.2020.113466
48. Lu, Q., Li, R., Yang, Y., Zhang, Y., Zhao, Q., & Li, J. (2022). Ingredients with anti-inflammatory effect from medicine food homology plants. *Food Chemistry*. https://doi.org/10.1016/J.FOODCHEM.2021.130610
49. Kim, M., Mok, H., Yeo, W.-S., Ahn, J.-H., & Choi, Y. K. (2021). Role of ginseng in the neurovascular unit of neuroinflammatory diseases focused on the blood-brain barrier. *Journal of Ginseng Research, 45*(5), 599–609. https://doi.org/10.1016/j.jgr.2021.02.003
50. Tam, D. N. H., et al. (2018). Ginsenoside Rh1: A systematic review of its pharmacological properties. *Planta Medica, 84*(3), 139–152. https://doi.org/10.1055/S-0043-124087/ID/RB0467-2
51. "2017 Alzheimer's disease facts and figures," *Alzheimer's & Dementia*, vol. 13, no. 4, pp. 325–373, 2017, doi: https://doi.org/10.1016/j.jalz.2017.02.001.
52. Wu, J., et al. (2022). New insights into the role and mechanisms of ginsenoside Rg1 in the management of Alzheimer's disease. *Biomedicine & Pharmacotherapy*. https://doi.org/10.1016/j.biopha.2022.113207
53. Abeysinghe, A. A. D. T., Deshapriya, R. D. U. S., & Udawatte, C. (2020). Alzheimer's disease; a review of the pathophysiological basis and therapeutic interventions. *Life Sciences*. https://doi.org/10.1016/j.lfs.2020.117996
54. Liang, H.-Y., et al. (2021). Preclinical systematic review of ginsenoside Rg1 for cognitive impairment in Alzheimer's disease. *Aging, 13*(5), 7549–7569. https://doi.org/10.18632/aging.202619
55. Chen, F., Eckman, E. A., Eckman, C. B., Chen, F., Eckman, E. A., & Eckman, C. B. (2006). Reductions in levels of the Alzheimer's amyloid β peptide after oral administration of ginsenosides. *The FASEB Journal, 20*(8), 1269–1271. https://doi.org/10.1096/fj.05-5530fje
56. Bhat, B. A., et al. (2022). Natural therapeutics in aid of treating alzheimer's disease: a green gateway toward ending quest for treating neurological disorders. *Frontiers in Neuroscience*. https://doi.org/10.3389/fnins.2022.884345
57. Zhang, H., et al. (2021). Ginsenoside Rg1 alleviates Aβ deposition by inhibiting NADPH oxidase 2 activation in APP/PS1 mice. *Journal of Ginseng Research, 45*(6), 665–675. https://doi.org/10.1016/j.jgr.2021.03.003
58. Liu, Y., Gao, Y., Li, K.-X., & Xue, W. (2019). Pharmacokinetics and acetylcholine releasing effects of ginsenoside Rg1 in hippocampus of beta-amyloid model rats. *Journal of Asian Natural Products Research, 21*(8), 772–781. https://doi.org/10.1080/10286020.2018.1540596
59. Guo, Y., et al. (2021). Ginsenoside Rg1 improves cognitive capability and affects the microbiota of large intestine of tree shrew model for Alzheimer's disease. *Molecular Medicine Reports, 23*(4), 291. https://doi.org/10.3892/mmr.2021.11931
60. Zhang, Y., et al. (2021). Ginsenoside Rg1 alleviates lipopolysaccharide-induced neuronal damage by inhibiting NLRP1 inflammasomes in HT22 cells. *Experimental and Therapeutic Medicine*. https://doi.org/10.3892/etm.2021.10214
61. Feng, H., Xue, M., Deng, H., Cheng, S., Hu, Y., & Zhou, C. (2022). Ginsenoside and its therapeutic potential for cognitive impairment. *Biomolecules, 12*(9), 1310. https://doi.org/10.3390/biom12091310
62. Pačesová, A., et al. (2022). Age-related metabolic and neurodegenerative changes in SAMP8 mice. *Aging, 14*(18), 7300–7327. https://doi.org/10.18632/aging.204284
63. Wang, Y., et al. (2018). Ginsenoside Rb1 inhibit apoptosis in rat model of Alzheimer's disease induced by Aβ1-40. *Am J Transl Res, 10*(3), 796–805.
64. van der Flier, W. M., et al. (2018). Vascular cognitive impairment. *Nature Reviews. Disease Primers*. https://doi.org/10.1038/nrdp.2018.3
65. Dinh, Q. N., Vinh, A., Arumugam, T. V., Drummond, G. R., & Sobey, C. G. (2021). G protein-coupled estrogen receptor 1: a novel target to treat cardiovascular disease in a sex-specific

manner? *British Jounal of Pharmacology, 178*(19), 3849–3863. https://doi.org/10.1111/bph.15521
66. Zeng, X., et al. (2018). The effects of ginsenoside compound K against epilepsy by enhancing the γ-aminobutyric acid signaling pathway. *Frontiers in Pharmacology*. https://doi.org/10.3389/fphar.2018.01020
67. Liu, H., Deng, H., Zhao, Y., Li, C., & Liang, Y. (2018). LncRNA XIST/miR-34a axis modulates the cell proliferation and tumor growth of thyroid cancer through MET-PI3K-AKT signaling. *Journal of Experimental & Clinical Cancer Research, 37*(1), 279. https://doi.org/10.1186/s13046-018-0950-9
68. Zong, W., et al. (2019). Ginsenoside compound K attenuates cognitive deficits in vascular dementia rats by reducing the Aβ deposition. *Journal of Pharmacological Sciences, 139*(3), 223–230. https://doi.org/10.1016/j.jphs.2019.01.013
69. Emamzadeh, F. N., & Surguchov, A. (2018). Parkinson's disease: biomarkers, treatment, and risk factors. *Frontiers in Neuroscience*. https://doi.org/10.3389/fnins.2018.00612
70. Zhang, Y., et al. (2017). Ginsenoside Rg1 protects against neuronal degeneration induced by chronic dexamethasone treatment by inhibiting NLRP-1 inflammasomes in mice. *International Journal of Molecular Medicine, 40*(4), 1134–1142. https://doi.org/10.3892/ijmm.2017.3092
71. Li, X., et al. (2022). Ginsenoside Rg1 alleviates learning and memory impairments and Aβ disposition through inhibiting NLRP1 inflammasome and autophagy dysfunction in APP/PS1 mice. *Molecular Medicine Reports, 27*(1), 6. https://doi.org/10.3892/mmr.2022.12893
72. Marchetti, B. (2018). Wnt/β-catenin signaling pathway governs a full program for dopaminergic neuron survival, neurorescue and regeneration in the MPTP Mouse Model of Parkinson's Disease. *International Journal of Molecular Sciences, 19*(12), 3743. https://doi.org/10.3390/ijms19123743
73. Ardah, M. T., et al. (2015). Ginsenoside Rb1 inhibits fibrillation and toxicity of alpha-synuclein and disaggregates preformed fibrils. *Neurobiology of Diseases, 74*, 89–101. https://doi.org/10.1016/j.nbd.2014.11.007
74. Tang, D., Chen, X., Kang, R., & Kroemer, G. (2021). Ferroptosis: Molecular mechanisms and health implications. *Cell Research*. https://doi.org/10.1038/s41422-020-00441-1
75. Hirschhorn, T., & Stockwell, B. R. (2019). The development of the concept of ferroptosis. *Free Radical Biology & Medicine, 133*, 130–143. https://doi.org/10.1016/j.freeradbiomed.2018.09.043
76. Chen, Y., Li, Y.-Y., Wang, S., Zhou, T., Chen, N., & Yuan, Y. (2022). Ginsenoside Rg1 plays a neuroprotective role in regulating the iron-regulated proteins and against lipid peroxidation in oligodendrocytes. *Neurochemical Research, 47*(6), 1721–1735. https://doi.org/10.1007/s11064-022-03564-6
77. Hauser, R. M., Henshall, D. C., & Lubin, F. D. (2018). The epigenetics of epilepsy and its progression. *The Neuroscientist, 24*(2), 186–200. https://doi.org/10.1177/1073858417705840
78. Singh, A., & Trevick, S. (2016). The Epidemiology of Global Epilepsy. *Neurologic Clinics, 34*(4), 837–847. https://doi.org/10.1016/j.ncl.2016.06.015
79. Shi, Y., Miao, W., Teng, J., & Zhang, L. (2018). Ginsenoside Rb1 protects the brain from damage induced by epileptic seizure via Nrf2/ARE signaling. *Cellular Physiology and Biochemistry, 45*(1), 212–225. https://doi.org/10.1159/000486768
80. Hinton, T., & Johnston, G. A. R. (2018). "GABA, The Major Inhibitory Neurotransmitter in the Brain", in *Reference Module in Biomedical Sciences*. *Elsevier*. https://doi.org/10.1016/B978-0-12-801238-3.96594-2
81. Walter, C., et al. (2016). Activation of AMPK-induced autophagy ameliorates Huntington disease pathology in vitro. *Neuropharmacology, 108*, 24–38. https://doi.org/10.1016/j.neuropharm.2016.04.041
82. Rué, L., et al. (2016). Targeting CAG repeat RNAs reduces Huntington's disease phenotype independently of huntingtin levels. *Journal of Clinical Investigation, 126*(11), 4319–4330. https://doi.org/10.1172/JCI83185
83. Lee, M. J., et al. (2021). Rg3-enriched Korean Red Ginseng extract inhibits blood-brain barrier disruption in an animal model of multiple sclerosis by modulating expression of NADPH oxidase 2 and 4. *Journal of Ginseng Research, 45*(3), 433–441. https://doi.org/10.1016/j.jgr.2020.09.001
84. Jang, M., & Cho, I.-H. (2016). Sulforaphane ameliorates 3-nitropropionic acid-induced striatal toxicity by activating the Keap1-Nrf2-ARE pathway and inhibiting the MAPKs and NF-κB pathways. *Molecular Neurobiology, 53*(4), 2619–2635. https://doi.org/10.1007/s12035-015-9230-2
85. Lee, M., Ban, J.-J., Won, B. H., Im, W., & Kim, M. (2021). Therapeutic potential of ginsenoside Rg3 and Rf for Huntington's disease. *In Vitro Cellular and Developmental Biology. Animal, 57*(6), 641–648. https://doi.org/10.1007/s11626-021-00595-1
86. X. Yang, S. Feng Chu, Z. zhen Wang, F. fang Li, Y. he Yuan, and N. hong Chen, "Ginsenoside Rg1 exerts neuroprotective effects in 3-nitropronpionic acid-induced mouse model of Huntington's disease via suppressing MAPKs and NF-κB pathways in the striatum," *Acta Pharmacol Sin*, vol. 42, no. 9, pp. 1409–1421, 2021, doi: https://doi.org/10.1038/s41401-020-00558-4.
87. Danikowski, K. M., Jayaraman, S., & Prabhakar, B. S. (2017). Regulatory T cells in multiple sclerosis and myasthenia gravis. *Journal of Neuroinflammation, 14*(1), 117. https://doi.org/10.1186/s12974-017-0892-8
88. Burrows, D. J., et al. (2019). Animal models of multiple sclerosis: From rodents to zebrafish. *Multiple Sclerosis Journal*. https://doi.org/10.1177/1352458518805246
89. Zhang, X., Liu, X., Hu, G., Zhang, G., Zhao, G., & Shi, M. (2020). Ginsenoside Rd attenuates blood-brain barrier damage by suppressing proteasome-mediated signaling after transient forebrain ischemia. *NeuroReport, 31*(6), 466–472. https://doi.org/10.1097/WNR.0000000000001426
90. Wang, X., et al. (2015). Ginsenoside Rg3 antagonizes adriamycin-induced cardiotoxicity by improving endothelial dysfunction from oxidative stress via upregulating the Nrf2-ARE pathway through the activation of akt. *Phytomedicine, 22*(10), 875–884. https://doi.org/10.1016/j.phymed.2015.06.010
91. Jin, B., Zhang, C., Geng, Y., & Liu, M. (2020). Therapeutic effect of ginsenoside rd on experimental autoimmune encephalomyelitis model mice: regulation of inflammation and Treg/Th17 cell balance. *Mediators of Inflammation, 2020*, 1–12. https://doi.org/10.1155/2020/8827527
92. Wang, H. Q., Wang, Z. Z., & Chen, N. H. (2021). The receptor hypothesis and the pathogenesis of depression: Genetic bases and biological correlates. *Pharmacological Research*. https://doi.org/10.1016/j.phrs.2021.105542
93. Lou, Y.-X., et al. (2020). The protective effect of ginsenoside Rg1 on depression may benefit from the gap junction function in hippocampal astrocytes. *European Journal of Pharmacology*. https://doi.org/10.1016/j.ejphar.2020.173309
94. Huang, D., Li, C., Zhang, W., Qin, J., Jiang, W., & Hu, C. (2019). Dysfunction of astrocytic connexins 30 and 43 in the medial prefrontal cortex and hippocampus mediates depressive-like behaviours. *Behavioural Brain Research*. https://doi.org/10.1016/j.bbr.2019.111950
95. Wang, H.-Q., et al. (2021). Novel antidepressant mechanism of ginsenoside Rg1: Regulating biosynthesis and degradation of connexin43. *Journal of Ethnopharmacology*. https://doi.org/10.1016/j.jep.2021.114212

96. Wang, H., et al. (2021). Ginsenoside Rg1 ameliorates neuroinflammation via suppression of Connexin43 ubiquitination to attenuate depression. *Frontiers in Pharmacology*. https://doi.org/10.3389/fphar.2021.709019
97. Ghaeminia, M., Rajkumar, R., Koh, H.-L., Dawe, G. S., & Tan, C. H. (2018). Ginsenoside Rg1 modulates medial prefrontal cortical firing and suppresses the hippocampo-medial prefrontal cortical long-term potentiation. *Journal of Ginseng Research, 42*(3), 298–303. https://doi.org/10.1016/j.jgr.2017.03.010
98. Ou, L., Lin, S., Song, B., Liu, J., Lai, R., & Shao, L. (2017). The mechanisms of graphene-based materials-induced programmed cell death: A review of apoptosis, autophagy, and programmed necrosis. *International Journal of Nanomedicine, 12*, 6633–6646. https://doi.org/10.2147/IJN.S140526
99. Bates, G. P., et al. (2015). Huntington disease. *Nature Reviews Disease Primers*. https://doi.org/10.1038/nrdp.2015.5
100. Seo, J. Y., Ju, S. H., Oh, J., Lee, S. K., & Kim, J. S. (2016). Neuroprotective and cognition-enhancing effects of compound k isolated from red ginseng. *Journal of Agriculture and Food Chemistry, 64*(14), 2855–2864. https://doi.org/10.1021/acs.jafc.5b05789

Publisher's Note Springer Nature remains neutral with regard to jurisdictional claims in published maps and institutional affiliations.

Springer Nature or its licensor (e.g. a society or other partner) holds exclusive rights to this article under a publishing agreement with the author(s) or other rightsholder(s); author self-archiving of the accepted manuscript version of this article is solely governed by the terms of such publishing agreement and applicable law.

Authors and Affiliations

Manju[1] · Navneeta Bharadvaja[1]

✉ Navneeta Bharadvaja
navneetab@dce.ac.in

Manju
manjudahiya2001@gmail.com

[1] Department of Biotechnology, Delhi Technological University, Main Bawana Road, Delhi 110042, India

2023 2nd International Conference on Smart Technologies and Systems for Next Generation Computing (ICSTSN) | 979-8-3503-4800-2/23/$31.00 ©2023 IEEE | DOI: 10.1109/ICSTSN57873.2023.10151586

Fate of Jeratinine E as a potential compound to target NNMT protein in countering Parkinson's disease

Kumud Kaul
Molecular Neuroscience and Functional Genomics Laboratory,
Dept. of Biotechnology
Delhi Technological University
Delhi – 110042, India
kaulkumud@Gmail.com

Pravir Kumar
Molecular Neuroscience and Functional Genomics Laboratory,
Dept. of Biotechnology
Delhi Technological University
Delhi – 110042, India
pravirkumar@dtu.ac.in

***Abstract*— Parkinson's disease (PD), the second-most common neurological condition, is expected to increase in prevalence during the following 30 years. Parkinson's disease diagnosis is still challenging, and research is ongoing to define the condition's early stages. Parkinson's disease might be an autointoxication-related illness. A requirement for neurotoxicity in the human brain is the enzyme nicotinamide N-methyltransferase (NNMT), as charged compounds cannot cross the blood-brain barrier. Additionally, the parkinsonian brain exhibits it in elevated concentration. A significant shift in perspective on primary and secondary prevention. The GEO dataset makes medical records and gene expression data on persons with PD accessible in order to anticipate patient mortality and, ultimately, establish PD biomarkers. We performed analysis through functional enrichment and protein-protein interaction (PPI). The GDC information gateway was utilized in this research to evaluate connected genes with clinical information to identify the most important PD genes. We found differential expression genes to separate the genes with varying levels of expression between the mutant and normal groups (DEGs). Additionally, we evaluated their importance in PD using the GDC Data site. Jeratinine E, an alkaloid, might be considered as a treatment option. Molecular docking study was carried out to have a better knowledge of the chemical reactions between the compounds that are bioactive and the NNMT protein. The molecular docking research indicates that Jeratinine E has a greater selectivity for NNMT. The ADMET analysis also highlighted the ability for additional study of jeratinine E.**

Keywords*— *Parkinson's, Datasets, Differential expression genes, Biomarkers, NNMT protein, Jeratinine E

I. Introduction

Parkinson's disease (PD), the second most common neurodegenerative condition and movement disability, affecting 1% of adults over 60.[1].According to medical terminology, Parkinson's disease is classified as a neurodegenerative ailment that affects both motor and nonmotor brain circuits. It causes progressive movement problems.[2]. The number of people with PD will significantly rise over the following 25 years. [3]. PD is a known heterogeneous disorder with an innately complex clinical presentation, a fast rate of disease progression, and a high risk of consequences [4].The -synuclein component of Lewy bodies is misfolded and show in several patient systems, and the premature selective death of dopamine neurons are the two key pathologic characteristics of Parkinson disease. According to pathologic study, neurons age over a long length of time in phases, with each damaged area corresponding to a certain symptomatology of Parkinson disease. When motor symptoms first manifest, a pathologic examination of the substantia nigra indicates a 30–70% cell loss [2].Concisely, the substantia nigra's pigmented neurons slowly die, which causes the striatum's dopamine levels to drop, which in turn causes the disease[5]. By the time of death, this area of the brain has lost 50–70% of its neurons, compared to the same region in people who are not affected.[1]. PD has the features of asymmetric development of bradykinesia, stiffness, and resting tremor[6]. Similar associations have been seen between more harmful forms of PD and gait problems, postural instability, and motor dysfunction in both dopaminergic and non-dopaminergic brain areas, as well as more drastic modifications [7]. Around 40% of the diversity in PD risk is explained by as-yet undiscovered PD susceptibility genes[8]. PD's etiology has been linked to oxidative stress, but the exact reason is still unknown. Due to their functions in reductive processes and energetics, pyridine nucleotides are crucial under oxidative stress[10]. The CpG site cg10917602 predicts Parkinson's disease risk, indicating to a potential causal function for methylation at this locus. [11].

Nicotinamide is methylated by Nicotinamide N-methyltransferase (NNMT) to generate,1-methylnicotinamide, using S-adenosylmethionine as a cofactor[12]. NNMT's neuronal mechanisms of action are still unknown, despite epidemiological data suggesting it is a risk factor for neurodegenerative illnesses like Parkinson's disease (PD) and schizophrenia. [13].The structure of nicotinamide includes a pyridine ring, and it can be metabolized through processes related to those of natural neurotoxins. It has been proposed that azahetero cyclic amines' excessive N-methylation capacity prior to onset cn cause Parkinson's disease [14]. Given that the byproducts of NNMT's N-methylation of pyridines are related to another well-known dopaminergic neurotoxin, methylphenyl pyridinium ion, it is possible that NNMT activity in the brain contributes in genesis of Parkinson disease (PD)[15].It has been suggested that Parkinson's disease may be influenced by the enzyme nicotinamide-N-methyltransferase (NNMT), which is present in all human tissues, including the nervous system and is a key factor in NAD+/NADH metabolism. NAD+, which is often converted to NADH throughout these processes, is a crucial coenzyme for fuel oxidation and the interconversion of a wide variety of metabolites. [13].
NNMT is a crucial link between cellular metabolism and epigenetic gene regulation, according to mounting evidence,

Authorized licensed use limited to: DELHI TECHNICAL UNIV. Downloaded on June 28,2023 at 06:27:58 UTC from IEEE Xplore. Restrictions apply.

and it is implicated in a number of illnesses. The human brain's various brain areas express NNMT, a protein that is exclusively neuronal, at different levels. It has recently been shown that NNMT is a requirement for neurotoxicity in the human brain because charged chemicals cannot traverse the blood-brain barrier. It is also more obvious in the parkinsonian brain. With increasing enzymatic activity, N-methyl nicotinamide, an MPP+ analogue, would rise while intraneuronal nicotinamide, a neuroprotectant at various levels, would fall. We shall therefore focus on NNMT gene with its role in PD in order to analyze and correct the same.

II. Method and Material

A. Data Set Collection

The microarray gene expression datasets used in this study were obtained from the National Center for Biotechnology Information's NCBI-GEO database (https://www.ncbi.nlm.nih.gov/gds). We examined the gene expression in 20 individuals with Parkinson's disease of varied severity and 9–10 healthy controls with regard to these results. After then, the 32 patients' levels of gene expression were compared. The findings showed a significant regulatory response with many genes that were highly correlated with PD indicators. There was a relationship between genes in both the controls and the Parkinson's disease patients in the early stages. DEGs with log > 1.2 and P 0.05 were considered.

B. Functional Enrichment Analysis of DEGs

Using the EnrichR pathway and GO analysis tool, all of the DEGs that were shared by the microarray PD datasets were examined. (https://maayanlab.cloud/Enrichr/) is the online gene set enrichment analysis (GSEA). P 0.05 was chosen as the cutoff in this investigation for a biological procedure (BP) Gene Ontology, or GO, tagging source. At a maximum p-value of 0.05, the study of pathway KEGG enrichment was deemed significant.

C. Protein-Protein Interactions (PPI) Network Analysis

The relevant DEGs were connected by a network of Protein Protein Interactions using the web visualization tool STRING. In a database known as the Protein Protein Interactions Network, structural and functional characteristics of proteins are related. Using the online visualization tool STRING (https://string-db.org), the associations between the relevant DEGs were displayed. Correlations between proteins' structural and functional properties can be found in the Protein Protein Interactions Network database.

D. Data Collection for Molecular Docking

An online initiative named COCONUT (Collection of Open Natural Products) (https://coconut.naturalproducts.net/) is used to store, locate, and analyse natural products. 40 naturally occurring chemicals with alkaloidal qualities and the widely recognised organic compound F0P was taken as reference when looking for natural remedies for PD. We obtained these compounds' SDF structures from PubChem portal. Jerantinine E was prepared to execute docking using Discovery Studio. 32 compounds were converted into mol2 form by Discovery Studio. Once the binding agents and proteins were prepared, docking was carried out via Webina.

E. ADMET Analysis using SwissADME

We were able to forecast ADME parameters for drug discovery using SwissADME, an online programme (http://www.swissadme.ch/). The SwissADME tools are employed to evaluate the simulated physical and chemical properties of all binding agents, comprising bioavailability score, Lipinski parameters, solubility, lipophilicity, pharmacodynamics and kinetics metrics. The Canonical SMILES were collected from PubChem.

III. Results

A. Differentially Expressed Genes' (DEGs) Identification

The selected microarray dataset was compared to healthy samples and PD cases. There have been found to be 32 genes. datasets were examined.

B. Functional Enrichment Analysis

In order to demonstrate the molecular processes and functionalities related to PD, the biological procedure (BP) GO and KEGG pathway fundamental enrichment investigation used 32 DEGs. The TABLE I. and TABLE II. display KEGG and GO pathways respectively that are related to Parkinsons and the central nervous system.

C. Analysis of the Protein Protein Interactions network

The selected microarray dataset was investigated by comparing normal samples with PD cases. The genes were identified.

D. Molecular Docking Result

The relationship of NNMT protein with organic compounds was examined using Webina. Jeratinine E, among the 40 natural chemicals docked, had the most negative affinity for binding to the protein. as shown in Fig. 2.

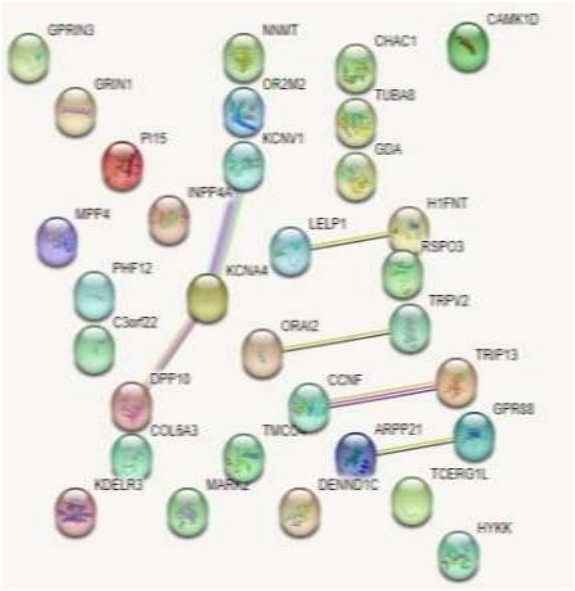

Fig. 2. PPI network showing 32 genes

Authorized licensed use limited to: DELHI TECHNICAL UNIV. Downloaded on June 28,2023 at 06:27:58 UTC from IEEE Xplore. Restrictions apply.

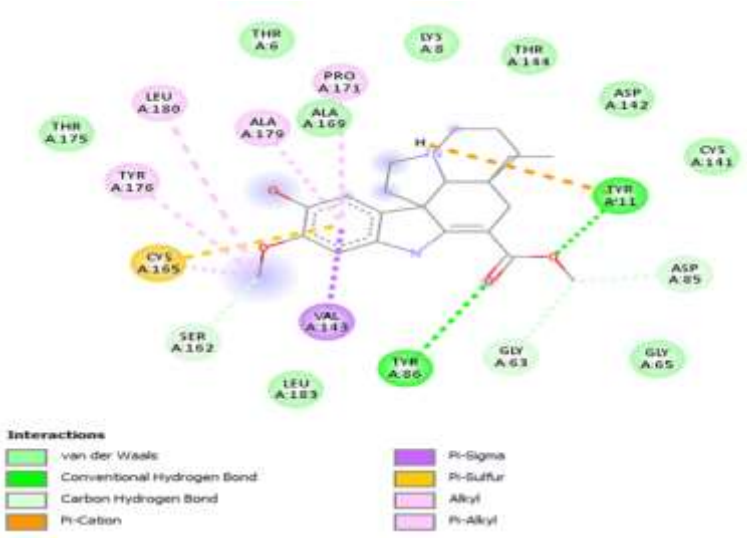

Fig. 3. Docking result of Jeratinine E with NNMT derivative.

TABLE I. KEGG PATHWAY HUMAN

Term	Overlap	P-value	Adjusted P-value	Odds Ratio	Combined Score	Genes
Calcium signaling pathway	3/240	0.006547666903	0.2911169792	8.612396333	43.3086966	CAMK1D;ORAI2;GRIN1
Tight junction	2/169	0.02982692652	0.2911169792	7.904590818	27.76363991	MPP4; TUBA8
Nicotinate and nicotinamide metabolism	1/35	0.05454814878	0.2911169792	18.91271347	55.01087073	NNMT
Nicotine addiction	1/40	0.06210151106	0.2911169792	16.48387097	45.80842946	GRIN1
Prion disease	2/273	0.07044757029	0.2911169792	4.845510455	12.85458942	GRIN1; TUBA8
Cocaine addiction	1/49	0.07555050634	0.2911169792	13.38709677	34.57825366	GRIN1
Vibrio cholerae infection	1/50	0.07703325543	0.2911169792	13.11323239	33.61600808	KDELR3
Huntington disease	2/306	0.08574379907	0.2911169792	4.312280702	10.5926497	GRIN1;TUBA8
Glutathione metabolism	1/57	0.08734818103	0.2911169792	11.47004608	27.96228702	CHAC1
Lysine degradation	1/63	0.0961005865	0.2911169792	10.35691988	24.25963339	HYKK
Cortisol synthesis and secretion	1/65	0.09899994384	0.2911169792	10.03225806	23.20096112	KCNA4

TABLE II. GO BIOLOGICAL FUNCTION

Term	Overlap	P-value	Adjusted P-value	Odds Ratio	Combine Score	Genes
Voltage Gated Potassium Channels R-HSA-1296072	2/43	0.002149649714	0.2107872633	32.40162602	199.0253798	KCNV1;KCNA4
RUNX1 Regulates Transcription Of Genes Involved In WNT Signaling R-HSA-8939256	1/6	0.009562772251	0.2107872633	128.7935484	598.8742369	RSPO3
Potassium Channels R-HSA-1296071	2/102	0.01156369378	0.2107872633	13.24533333	59.0726626	KCNV1;KCNA4
Phase II - Conjugation Of Compounds R-HSA-156580	2/107	0.01266811495	0.2107872633	12.61142857	55.09513279	NNMT;CHAC1
Metabolism Of Ingested SeMet, Sec, MeSec Into H2Se R-HSA-2408508	1/8	0.01273064621	0.2107872633	91.98617512	401.4040374	NNMT
Lysine Catabolism R-HSA-71064	1/12	0.01903697989	0.2107872633	58.52492669	231.8389989	HYKK
Glutathione Synthesis And Recycling R-HSA-174403	1/12	0.01903697989	0.2107872633	58.52492669	231.8389989	CHAC1
Synthesis Of IP2, IP, And Ins In Cytosol R-HSA-1855183	1/14	0.02217549735	0.2107872633	49.51612903	188.5954142	INPP4A
Methylation R-HSA-156581	1/14	0.02217549735	0.2107872633	49.51612903	188.5954142	NNMT
Response Of EIF2AK1 (HRI) To Heme Deficiency R-HSA-9648895	1/15	0.02374110642	0.2107872633	45.97695853	171.9789874	CHAC1
Elevation Of Cytosolic Ca2+ Levels R-HSA-139853	1/15	0.02374110642	0.2107872633	45.97695853	171.9789874	ORAI2

Authorized licensed use limited to: DELHI TECHNICAL UNIV. Downloaded on June 28,2023 at 06:27:58 UTC from IEEE Xplore. Restrictions apply.

E. ADMET Analysis

Using SwissADME for ADMET analysis, it was discovered that Jeratinine E has a high capacity for GI absorption and is BBB permeant. One of the most widely utilized criteria for assessing a small molecule's drug-likeness is the Lipinski rule. Jeratinine E meets the drug-likeness requirements of the Lipinski rule for bioavailable medicines with a bioavailability score of 0.55 and 0 infractions. Refer to TABLE III. for detailed analysis.

TABLE III. MOLECULAR DOCKING /ADMET ANALYSIS RESULT

Compound	GI absorption	Lipinski	BBB permeant	Log Kp (skin permeation)	Num. H-bond acceptors	Num. H-bond donors	Molar Refractivity	Molecular weight	Affinity(kcal/mol)
3-O-Acetylnarcissidine	High	Yes; 0 violation	No	-8.49 cm/s	7	1	100.95	375.42 g/mol	-7.6
5Hydroxyacridine2methanol	High	Yes; 0 violation	Yes	-6.28 cm/s	3	2	67.4	225.24 g/mol	-8.6
6hydroxymetatacarbolineF	Low	Yes; 1 violation: NorO>10	No	-7.64 cm/s	8	5	134.9	496.51 g/mol	-8.7
7Methylxanthosine5monophosphate	Low	No; 2 violations: NorO>10, NHorOH>5	No	-11.18 cm/s	9	6	87.64	380.25 g/mol	-8.8
Asperindole D	High	Yes; 1 violation: MW>500	No	-7.56 cm/s	8	2	153.62	577.66 g/mol	-8
Jerantinine E	High	Yes; 0 violation	Yes	-6.44 cm/s	5	2	113.44	384.47 g/mol	-10
Atranone	High	Yes; 0 violation	No	-7.62 cm/s	7	2	114.07	432.51 g/mol	-7.9
Bohemamine G	High	Yes; 0 violation	Yes	-6.25 cm/s	2	1	79.09	262.35 g/mol	-8.1
Brevianamide Q	High	Yes; 0 violation	No	-6.50 cm/s	3	3	111.73	365.43 g/mol	-8.5

IV. Discussion

We conducted GO biological process and KEGG pathway studies to determine the molecular role of the typical DEGs. Using the identified overlapped DEGs, a schematic analysis of the PPI network was performed to evaluate probable protein interactions. Recent advances in the use of natural compounds as pharmaceuticals to expedite the drug development process include in silico techniques like molecular docking. With the help of this technique, we were able to predict that Jeratinine E would act as a potent NNMT gene inhibitor in Parkinson's. It has shown potential advantages as a superior inhibitor and has a binding energy of -10 in comparison to other chemicals. Moreover, it has good drug-like properties and is BBB permeable, according to research.

V. Conclusion & Future Scope

In this work, 32 distinct microarrays were used to examine the gene expression in nine healthy controls and 20 patients with varying degrees of severity. The NNMT gene was found to be one of 32 associated with the aetiology of Parkinson's disease. For controlled autophagy, NNMT might be a trustworthy prognostic marker. Jeratinine E may be a potent treatment for Parkinson's disease, based on the results of molecular docking study combining NNMT genes and 40 naturally substances. The results of the ADMET analysis of Jeratinine E show that it is more drug-like, follows the Lipinski rule, and has BBB permeation. The real wet-lab work will help in determining whether to target the Jeratinine E molecule.

References

[1] J. Zhou, J. Li, A. B. Papaneri, N. P. Kobzar, and G. Cui, "Dopamine Neuron Challenge Test for early detection of Parkinson's disease," *NPJ Parkinson's Dis*, vol. 7, no. 1, p. 116, Dec. 2021, doi: 10.1038/s41531-021-00261-z.

[2] P. Rizek, N. Kumar, and M. S. Jog, "An update on the diagnosis and treatment of Parkinson disease," *Can Med Assoc J*, vol. 188, no. 16, pp. 1157–1165, Nov. 2016, doi: 10.1503/cmaj.151179.

[3] E. R. Dorsey *et al.*, "Projected number of people with Parkinson disease in the most populous nations, 2005 through 2030," *Neurology*, vol. 68, no. 5, pp. 384–386, Jan. 2007, doi: 10.1212/01.wnl.0000247740.47667.03.

[4] M. Lawton *et al.*, "Developing and validating Parkinson's disease subtypes and their motor and cognitive progression," *J Neurol Neurosurg Psychiatry*, vol. 89, no. 12, pp. 1279–1287, Dec. 2018, doi: 10.1136/jnnp-2018-318337.

[5] R. B. Parsons, S. W. Smith, R. H. Waring, A. C. Williams, and D. B. Ramsden, "High expression of nicotinamide N-methyltransferase in patients with idiopathic Parkinson's disease," *Neurosci Lett*, vol. 342, no. 1–2, pp. 13–16, May 2003, doi: 10.1016/S0304-3940(03)00218-0.

[6] K. R. Chaudhuri *et al.*, "The metric properties of a novel non-motor symptoms scale for Parkinson's disease: Results from an

Authorized licensed use limited to: DELHI TECHNICAL UNIV. Downloaded on June 28,2023 at 06:27:58 UTC from IEEE Xplore. Restrictions apply.

international pilot study," *Movement Disorders*, vol. 22, no. 13, pp. 1901–1911, Oct. 2007, doi: 10.1002/mds.21596.

[7] M. C. Gonzalez, I. Dalen, J. Maple-Grødem, O.-B. Tysnes, and G. Alves, "Parkinson's disease clinical milestones and mortality," *NPJ Parkinsons Dis*, vol. 8, no. 1, p. 58, May 2022, doi: 10.1038/s41531-022-00320-z.

[8] T. H. Hamza and H. Payami, "The heritability of risk and age at onset of Parkinson's disease after accounting for known genetic risk factors," *J Hum Genet*, vol. 55, no. 4, pp. 241–243, Apr. 2010, doi: 10.1038/jhg.2010.13.

[9] Y. Bi *et al.*, "Neuroprotective effects of alkaloids from *Piper longum* in a MPTP-induced mouse model of Parkinson's disease," *Pharm Biol*, vol. 53, no. 10, pp. 1516–1524, Oct. 2015, doi: 10.3109/13880209.2014.991835.

[10] L. K. Klaidman, S. K. Mukherjee, and J. D. Adams, "Oxidative changes in brain pyridine nucleotides and neuroprotection using nicotinamide," *Biochimica et Biophysica Acta (BBA) - General Subjects*, vol. 1525, no. 1–2, pp. 136–148, Feb. 2001, doi: 10.1016/S0304-4165(00)00181-1.

[11] K. Rawlik, A. Rowlatt, and A. Tenesa, "Imputation of DNA Methylation Levels in the Brain Implicates a Risk Factor for Parkinson's Disease," *Genetics*, vol. 204, no. 2, pp. 771–781, Oct. 2016, doi: 10.1534/genetics.115.185967.

[12] M. J. van Haren *et al.*, "The kinetic analysis of the N-methylation of 4-phenylpyridine by nicotinamide N-methyltransferase: Evidence for a novel mechanism of substrate inhibition," *International Journal of Biochemistry and Cell Biology*, vol. 98, pp. 127–136, May 2018, doi: 10.1016/j.biocel.2018.03.010.

[13] K. Schmeisser and J. A. Parker, "Nicotinamide-N-methyltransferase controls behavior, neurodegeneration and lifespan by regulating neuronal autophagy," *PLoS Genet*, vol. 14, no. 9, p. e1007561, Sep. 2018, doi: 10.1371/journal.pgen.1007561.

[14] K. Aoyama *et al.*, "Nicotinamide-N-methyltransferase is higher in the lumbar cerebrospinal fluid of patients with Parkinson's disease," *Neurosci Lett*, vol. 298, no. 1, pp. 78–80, Jan. 2001, doi: 10.1016/S0304-3940(00)01723-7.

[15] R. B. Parsons, M.-L. Smith, A. C. Williams, R. H. Waring, and D. B. Ramsden, "Expression of Nicotinamide N-Methyltransferase (E.C. 2.1.1.1) in the Parkinsonian Brain," *J Neuropathol Exp Neurol*, vol. 61, no. 2, pp. 111–124, Feb. 2002, doi: 10.1093/jnen/61.2.111.

Authorized licensed use limited to: DELHI TECHNICAL UNIV. Downloaded on June 28,2023 at 06:27:58 UTC from IEEE Xplore. Restrictions apply.

Multimedia Tools and Applications
https://doi.org/10.1007/s11042-023-15908-7

FRN: Fusion and recalibration network for low-light image enhancement

Kavinder Singh[1] · Ashutosh Pandey[1] · Akshat Agarwal[1] · Mohit Kumar Agarwal[1] · Aditya Shankar[1] · Anil Singh Parihar[1]

Received: 13 December 2022 / Revised: 28 April 2023 / Accepted: 22 May 2023
© The Author(s), under exclusive licence to Springer Science+Business Media, LLC, part of Springer Nature 2023

Abstract
This paper proposes a Fusion and Recalibration Network (FRN) for low-light image enhancement. Firstly, The proposed method generates multi-exposure images from a single image to enhance low-light images. The proposed Feature Extraction Module (FEM) extracts multi-level features from an image. The proposed method uses Feature Augmentation Module (FAM), a U-net-like structure, to encode the multi-level features and assist in the reconstruction. The proposed Feature Fusion and Re-calibration Module (FFRM) re-calibrates and merges the features to provide an enhanced output image. The advantage of dynamically selecting features from extremely bright regions of the artificially darkened images and darker regions of the artificially brightened image results in a balanced output image. The proposed model was evaluated on various datasets and significantly outperformed most state-of-the-art techniques. Additionally, the experimental assessment shows that the proposed FRN model outperforms other quantitative and qualitative assessment approaches.

Keywords Low-light (LOL) image enhancement (LLIE) · Deep learning-based network · Multi-exposure fusion · Multi-level feature extraction · Convolutional neural networks

1 Introduction

Social media and other content-sharing platforms are gaining popularity in modern society resulting in more and more people partaking in digital photography. Moreover, various applications of machine learning and computer vision like driver-assistance [39], human-action [10, 59], facial recognition [4, 5, 9, 56], object detection [26, 58], generative models [6, 7, 22, 52, 53], and many others [14, 15, 20, 35, 40] require high-quality images for optimal performance. However, only a few capturing these images are skilled professional photographers, and the lighting conditions are frequently sub-optimal. Images captured in low-light conditions suffer from low visibility, lack of details, and noise affecting the overall quality

✉ Anil Singh Parihar
parihar.anil@gmail.com

[1] Machine Learning Research Laboratory, Department of Computer Science and Engineering, Delhi Technological University, Delhi, India

of the image and its utility in vision-based applications. If the image resolution also needs improvement along with the lightness, one may use super-resolution methods [3, 48, 51] as a pre-processing step. In contrast, various alternate solutions (like using flash, boosting the ISO, or shooting long-exposure photographs) may assist in minimizing the problem at hand. Such solutions also create other issues, such as color inconsistency, noise, and fuzzy images. We require an effective method for low-light image enhancement because photographing in lousy lighting is inevitable.

Many conventional techniques [42, 43, 50] exist to reduce the degradation in images captured under sub-optimal lighting conditions and enhance the aesthetic qualities. Histogram Equalization (HE) [11] is a simple yet efficient method that keeps track of the frequency of the pixel values. However, HE-based approaches focus on contrast enhancement instead of actual illumination causes, resulting in over, and under-enhancement. Retinex-based methods [24, 44, 45, 55, 65] performed better in enhancing low-light images. Retinex-based models assume an image is a combination of two components: illumination and reflectance. Reflectance is a characteristic attribute of the scene, containing detail and color information of the original image, which does not differ with different lighting conditions. The illumination map represents the intensity value and distribution of light in the original image. Therefore, the illumination map for a low-light image can be enhanced to get its corresponding enhanced image. The early Retinex decomposition assumes the illumination component to be piece-wisely smooth. However, the over-smoothed illumination component results in a large amount of structure and texture information getting into the reflectance component, which further causes the image to sharpen within the brightness enhancement procedure.

Another recent method that has produced impressive results is deep-learning-based methods that use Convolutional Neural Networks (CNN). Deep learning approaches utilize multiple layers of processing to extract high-level information from the input data progressively. Compared to the approaches mentioned earlier, deep learning-based methods benefit from a vast computational capacity and larger datasets for training. Hence, the methods can produce better details and edges in such images. Some approaches for CNN-based techniques include Generative Adversarial Networks, or GANs [16], which learn by mapping the distance between the ground-truth and low-light images. The generator uses the low-light input image to estimate the enhanced image, which the discriminator then tries to differentiate from the dataset for the corresponding input. Nevertheless, models utilizing this method are difficult to train as problems like the non-convergence of the training model or the diminished gradient of the generator leading to minimal learning of the model are common training issues.

Although considerable progress has been made in low-light image enhancement using CNN, further research is required to explore and study new structures and techniques that may provide better results. This paper proposes a novel CNN structure (i.e., the Fusion and Recalibration Network) capable of enhancing low-light images. The proposed model utilizes synthetically generated multi-exposure images to extract multi-level features, which are later enhanced and combined to form the final image. The fundamental idea is to extract multi-level features containing high-level and low-level details using artificially generated multi-exposure images. The extracted features are recalibrated and combined to generate an enhanced low-light image. These dynamically extracted features allow us to extract greater details from the darker regions of the image while preserving the details in the bright regions of the image. The proposed network architecture is divided into four components, namely, the multi-exposure image generator, the Feature Extraction Module (FEM), the Feature Augmentation Module (FAM), and the Feature Fusion and Recalibration Module (FFRM). The multi-exposure image generator synthetically generates images with different exposures

using a single input low-light image. The output multi-exposure images are then passed onto the FEM to extract various low and high-level features from the images. These extracted features are then enhanced by the FAM and combined with the FFRM to generate the final enhanced low-light image.

In summary, the contributions made in the paper are as follows:

- We propose a novel Fusion and Recalibration Network (FRN) that utilizes features extracted from multiple generated images with different exposures to dynamically enhance local regions in the low-light images.
- We propose Feature Fusion and Recalibration Module (FFRM) to combine multiple local features from generated images for low-light image enhancement. FFRM combines the multi-level extracted features from multi-exposure images to generate the enhanced output.
- We propose asymmetrical illumination loss for multiple generated images prioritizing structural detail retention and enhancement of darker regions from multiple images. It allows the enhancement of darker regions while avoiding over-enhancement in the brighter regions of the input image.

The subsequent sections are organized as follows: Section II briefly discusses the various existing techniques. Section III describes the generation of multi-exposure images and the proposed FRN model. Section IV shows experimental results, and Section V concludes the paper.

2 Related works

Retinex-based approaches [24, 45, 65] are the most relevant among the conventional low light enhancement techniques. Retinex-based methods generally enhance illumination after estimation to enhance the lightness in a low-light image. A common drawback of the retinex approach is that it is generally prone to unrealistic or over-enhanced outputs. Li *et al.* [29] presented a model that incorporated the noise with the classic retinex model, as intensive noise is inevitable in low-light images. Subsequently, Guo *et al.* [17] proposed LIME that includes BM3D [12] in post-processing to remove the noise present in the reflectance component. Hao *et al.* [19] proposed semi-decoupled decomposition (LLSDM), which introduced the noise term with the reflectance component only. LLSDM proposes a modified retinex model with a new two-stage model for the estimation of illumination and reflectance. Ren *et al.* [47] proposed a low-rank regularized retinex model LR3M, which uses a low-rank minimization before decomposition to reduce noise output image. LR3M aimed to deal with the noise within the process of enhancement.

Deep Learning techniques [23, 54, 63] have lately emerged as reliable and robust for exposure enhancement with better detail preservation. Wei *et al.* [63] introduce the Retinex-Net, which demonstrates the use of CNNs (Convolutional Neural Networks) to decompose the image and then uses traditional approaches for the enhancement of the image. The work also introduces the LOL dataset (Low-Light) for low-light enhancement applications. Jiang *et al.* [23] aim to resolve the dependence of deep learning approaches on paired datasets by introducing an effective unsupervised GAN (Generative Adversarial Network) that generates an unpaired mapping between the expected and low light image spaces eliminating the requirement of synthetic paired datasets. Ren *et al.* [46] utilize a hybrid neural network to develop enhanced images with higher visual qualities preserving edge details and content details using an edge-stream network using RNNs and a content-stream network. Wang *et*

al. [61] introduce a residual learning model and a new LBP structure with lightning and darkening operations to learn the residual low-light enhancement effectively. In LLFLOW, Wang *et al.* [62] introduce a normalizing flow model that learns the local and global image properties via modeling the Gaussian distributions over usually exposed images. The noise being a prominent degradation in real-world images, Zhen *et al.* [66] introduce an adaptive UTVnet that learns the balancing parameters from the low light images in modeling to quite effectively estimate and remove noise while recovering finer details within the image. DeepLFP [38] enhances the image by regressing the local parameters of localized filters.

Multiple-Scale Exposure Fusion (MEF) is one of the most widely adopted methodologies to produce images with a High Dynamic Range (HDR) [41]. MEF employs the fusion of multiple LDR images with varying exposures, resulting in an image covering the entire combined dynamic range of the LDR images. Ma et al. [34] introduce a novel fusion technique patch decomposition, that generates noise-free weight maps and high-quality fused images. Li et al. [29] produce high-quality images with delicate details using weighted guided image filters (WGIF) to smooth the weight maps. Li et al. [31] propose an algorithm that enhances the local contrast and details of the output image using an adaptive HE algorithm based on a modified pyramid transform. [57] propose a weight map extraction technique based on watershed masking and liner embedding. Gupta et al. [18] uses a genetic algorithm that utilizes pseudo-multi-exposure images originating from a solo image generated by IMF to learn the relationship between the multi-exposure images and fuses the images to produce an HDR-like image. Xu et al. [64] introduce an innovative MEF strategy using tensor single value decomposition and tensor product. The luminance and chrominance channels decomposed from the image are processed and fused to enhance the image.

We aim to harness the capacity of MEF to produce HDR-like images and combine it with the capability of the deep learning-based approach and build a technique that combines the strengths of both these techniques.

3 The proposed approach

The section describes the proposed method in detail. The human-vision system adapts to different light conditions and processes them accordingly. However, computer vision sensors are unable to adapt to different light conditions automatically. The proposed approach (FRN) attempted to deal with different lighting conditions by varying the exposure level. The proposed FRN extracts multi-level features from multi-exposure images. The extracted features are augmented and fused to generate the final enhanced image. The proposed FRN contains four modules: multi-exposure image generator, feature extraction, feature augmentation, and feature fusion.

The motivation behind the proposed approach is that features extracted from brighter-regions of the dark-images will have more details. While in the bright-images (overexposed images), the feature extracted from the darker-regions will have more details. Thus, we have generated multiple instances of an image with different exposures. Multiple instances (multi-exposure) of the same image are used to extract features to obtain an enhanced image.

3.1 Network architecture

Figure 1 shows the architecture of the proposed FRN model. The proposed FRN consists of four components: Multi-Exposure Image Generation, Feature Extraction, Feature Aug-

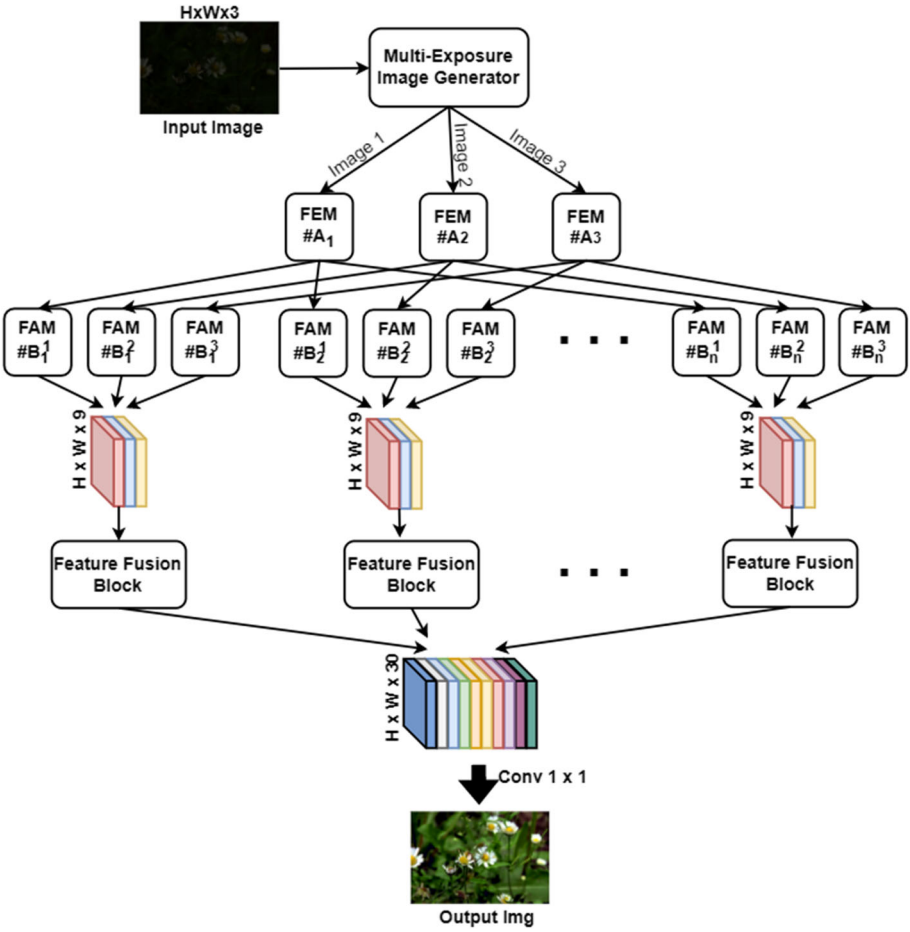

Fig. 1 The proposed network with the Multi-Exposure Image Generator, Feature Extraction Module(FEM), Feature Augmentation Module(FAM), and Feature Fusion Block(FFB)

mentation, and Feature Fusion and Recalibration. Multi-exposure image generation module generates images with different exposure levels. The feature extraction and augmentation module uses multi-exposed images. After feature extraction, the proposed FRN performs a feature fusion of augmented features. At last, it performs finally combines all the fused results to generate the final output.

3.1.1 Multi-exposure image generation

The proposed FRN model generates multiple instances of an input image with varying exposures. While generating multi-exposure images, the proposed model scales the pixel values non-linearly to generate images with distinct exposures from an input. These multiple instances (of the input image) are used for feature extraction. The extracted features are then used for fusion to generate an enhanced image. The proposed model is able to capture a wider

range of light conditions which helps in generating an enhanced image with better details and dynamic range.

The input image ($I_{low} \in \mathbb{R}^{H \times W \times 3}$) and a set of amplification factors ($k_1, k_2, ..., k_N$) are given for generating multi-exposure instances. To generate n multi-exposure instances, we scale the input image non-linearly. The multi-exposure images ($I = I_1, I_2, ..., I_N$) with non-linear scaling can be expressed as:

$$I_i = min(I_{low}^{k_i}, 1) \tag{1}$$

where $min(x, 1)$ performs pixel-wise clipping of the image.

3.1.2 Feature extraction

We first need to extract the low and high-level features from the input multi-exposure images to perform the low-light image enhancement described previously. CNN has inherent multi-scale feature representations, we use a hierarchical CNN structure to extract shallow layer features (like edges and textures) and deep layer features that yield global components (like shape and shading details). The global details help determine the illumination conditions. In contrast, local features benefit detail preservation in the final output image. Hence, the local and global features are essential for low-light image enhancement.

We propose the Feature Extraction Module (FEM), which comprises multiple single-stream convolutional sub-networks with ten convolution layers, each of which consists of 3 x 3 size kernels with a stride of 1 and activation function ReLU with no pooling operation as shown in Figure 2. The FEM can be expressed as:

$$\mathcal{F}_1^i = Conv(I_i) \tag{2}$$

$$\mathcal{F}_k^i = Conv(\mathcal{F}_{(k-1)}^i) \tag{3}$$

where I_i denotes the i^{th} multi-exposure instance, and $\mathcal{F}_k^i$ denotes the k^{th} feature map of i^{th} multi-exposure instance. The previously generated multi-exposure images are provided to the FEM to draw out the local and global features, which are passed to the FAM (feature augmentation module) as input.

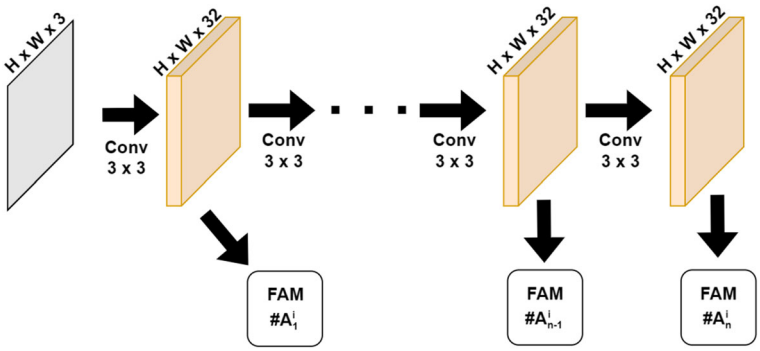

Fig. 2 Feature Extraction Module (FEM) Architecture

3.1.3 Feature augmentation

Features extracted from the input images must be processed accordingly to generate the enhanced low-light image. Therefore, we use a U-net to decompose the input features into a generalized representation during encoding and enhance the illumination of the features during decoding. Further, skip connections are added to the U-net to assist in reconstructing and preserving image details during the decoding process. FAM provides the desired effect of maintaining textural and edge details according to the input features. Figure 3 represents the architecture of FAM. The input given to FAM is the output from a FEM layer. The processing and downsampling of FAM can be expressed as:

$$DB_k(1) = Conv(\mathcal{F}_k^1 \odot \mathcal{F}_k^2 \odot \mathcal{F}_k^3) \tag{4}$$

$$DB_k(l) = Conv(maxPool(DB_k(l-1))) \tag{5}$$

where $DB_k(l)$ denotes the features (while downsampling) of k^{th} block at l^{th} level in U-Net, and maxPool is two-dimensional operation. The Upscaling and processing of features in FAM are expressed as:

$$UB_k(l) = DB_k(l) + Conv(DeConv(UB_k(l+1))) \tag{6}$$

where $UB_k(l)$ denotes the features (while upsampling) of k^{th} block at l^{th} level in U-Net, and DeConv denotes deconvolution operation.

3.1.4 Feature fusion and recalibration

The purpose of extracting and enhancing the features individually from different multi-exposure images is to obtain a collection of features that can be combined appropriately to generate a well-balanced and enhanced low-light image. The agenda behind the operation is to utilize the information extracted in a complementary fashion, where the features extracted from the artificially darkened images can supplement the features extracted from

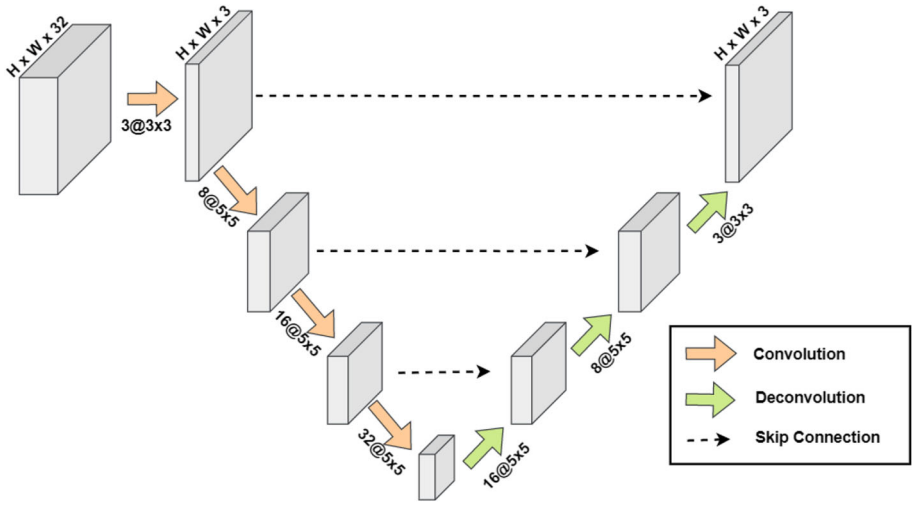

Fig. 3 Feature Augmentation Module (FAM) Architecture used to enhance features extracted

the artificially brightened image. We need a system capable of identifying and learning the interdependencies between the different features to perform such a dynamic fusion operation (Fig. 4).

We propose the Feature Fusion Block (FFB) that utilizes a modified Squeeze-and-Excitation (SE) [21] network. This improves the characterization capacity of the model by identifying the correlation between different features. Here, we utilize a modified SE block to perform concurrent spatial and channel-wise calibration on the input feature map. The operation combines the Spatial Squeeze and Channel Excitation Block(cSE) and the Channel Squeeze and Spatial Excitation Block (sSE). The concurrent spatial and channel Squeeze and Excitation block (scSE) is as follows:

$$\hat{U}_{scSE} = \hat{U}_{cSE} + \hat{U}_{sSE} \tag{7}$$

where $\hat{U}_{scSE}$ represents the output from the Concurrent Spatial and Channel Squeeze and Excitation Block, $\hat{U}_{cSE}$ represents the output from the Spatial Squeeze and Channel Excitation Block, and $\hat{U}_{sSE}$ represents the output from the Channel Squeeze and Spatial Excitation Block.

$$\hat{U}_{cSE} = [\sigma(\hat{z_1})u_1, \sigma(\hat{z_2})u_2, ..., \sigma(\hat{z_C})u_C] \tag{8}$$

where U represents the input features, $u_i \in \mathbb{R}^{H \times W}$ maps to the combination of channels, $\hat{z_k} = \frac{1}{H \times W} \sum_i^H \sum_j^W u_k(i, j)$ denotes a global average pooling layer, $\sigma(\hat{z_k})$ denotes the sigmoid activation.

$$\hat{U}_{sSE} = [\phi(q_{1,1})u^{1,1}, .., \phi(q_{i,j})u^{i,j}, .., \phi(q_{H,W})u^{H,W}] \tag{9}$$

where U represents the input features, $u^{i,j} \in \mathbb{R}^{1 \times 1 \times C}$ maps to the spatial coordinates i, j with $i \in \{1, 2, ..., H\}$ and $j \in \{1, 2, ..., W\}$, $q_{i,j}$ is the combined linear rendition of C channels in a spatial location (i, j), and $\phi(q_{i,j})$ is the re-scale operation to [0, 1].

The significant advantage of using the Feature Fusion and Recalibration block is the ability of the network to carry out feature re-calibration using the channel and spatial information before performing feature fusion. This allows the network to dynamically utilize channel details to re-calibrate the features while using the overall feature illumination to perform spatial re-calibration. Therefore, the large number of features obtained from the Feature Extraction Module coupled with the Feature Augmentation Module can be appropriately

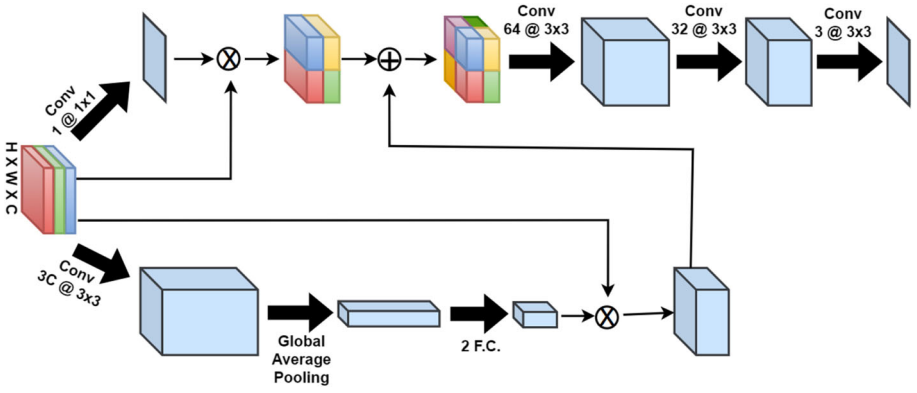

Fig. 4 Feature Fusion and Recalibration (FFRM) block used to recombine multi-exposure features dynamically

re-calibrated before being combined with learning more meaningful features and generating better enhancement.

3.2 Loss functions

To refine the performance of the proposed technique and improve the qualitative and quantitative quality of the images generated, standard loss functions like MSE and MAE [8, 32] prove to be inefficient. Therefore, we propose a novel loss function that considers the various requirements of our model by considering structural information, contextual information, and illumination differences in the image. The proposed loss is as follows:

$$Loss = L_{Str} + L_{Per} + L_{Ill} \tag{10}$$

where L_{Str} denotes Structural Loss, L_{Per} denotes Perception Loss, and L_{Ill} denotes Asymmetric Illumination Loss.

3.2.1 Structural loss

Structural loss is responsible for strengthening the visual standard of the output image and reinforcing the structural information stored in the image. Since low-light images suffer from various visual and structural distortions like blur effects, haloing, and noise, which cannot be handled appropriately by regular MSE and MAE losses [8, 32], we use the structural loss to compute the visual differences among the output enhanced image and the ground truth image to guide the learning process better. For this purpose, we use the popular quantitative image quality evaluation technique, SSIM [60], to form the basis of our structural loss. We also include MAE loss into the structural loss to complement SSIM since it better enforces information retention during training. SSIM for a pixel p is as follows:

$$L_{SSIM} = -\frac{1}{N} \sum_{p \in img} \frac{2\mu_x \mu_y + C_1}{\mu_x^2 + \mu_y^2 + C_1} \cdot \frac{2\sigma_{xy} + C_2}{\sigma_x^2 + \sigma_y^2 + C_2} \tag{11}$$

where x and y represent two windows of size $N \times N$ under comparison, μ_x and μ_y are pixel value averages, σ_x and σ_y are variances, σ_{xy} is co-variance, and C_1 and C_2 are constants. The value of SSIM is in the range of (-1, 1]. $L_{Str} = L_{SSIM} + L_{MAE}$ gives the final structural loss.

3.2.2 Perception loss

While loss metrics like SSIM and MAE focus on low-level information, we also need to devise a metric that can strengthen the image's perceptual quality by utilizing higher-level information. A similar strategy was proposed in SRGAN [27] to guide the network's training. The VGG-19 Network [49] is used as the context extractor as it has proven to be a well-structured, well-behaved, and versatile network for various tasks. perceptual loss compares the feature maps of the same layer in the VGG network for both the output and ground-truth images. The perception loss is computed using the output from the ReLU activation layers in the pre-trained VGG-19 network. Additionally, to compute the difference in context

representations among the output and ground truth images, we compute the summation of the absolute differences as follows:

$$L_{Per} = \frac{1}{W_{i,j} H_{i,j} C_{i,j}} \sum_{x=1}^{W_{i,j}} \sum_{y=1}^{H_{i,j}} \sum_{z=1}^{C_{i,j}} \left\| \phi_{i,j}(E)_{x,y,z} - \phi_{i,j}(G)_{x,y,z} \right\| \tag{12}$$

where E and G represent the enhanced and ground truth images respectively, $W_{i,j}$, $H_{i,j}$, and $C_{i,j}$ describe the proportions of the feature maps. Additionally, $\phi_{i,j}$ describes the feature map for the j^{th} convolutions layer within the i^{th} block of the VGG-19 Network. The $C_{i,j}$ component of the ground-truth and output image helps in assessing the difference in the visual features at that particular location in the image.

3.2.3 Asymmetric illumination loss

Low-Light Image enhancement needs to extract greater detail from darker image sections than brighter sections. We propose the asymmetric illumination loss function for multi-exposure images, which employs a simple strategy to separate the various regions of the image according to their illumination and find the weighted sum of losses for the different image regions. Various techniques have emerged in the past to separate the darker and brighter regions of the images. However, preliminary experiments show that selecting the 40% darkest pixels in the image gives the best results for the proposed technique. The proposed asymmetric illumination loss function is defined as follows:

$$\begin{aligned} L_{Ill} = & w_D \cdot \frac{1}{m_D n_D} \sum_{i=1}^{n_D} \sum_{j=1}^{m_D} (\left\| E_D(i,j) - G_D(i,j) \right\|) + \\ & w_B \cdot \frac{1}{m_B n_B} \sum_{i=1}^{n_B} \sum_{j=1}^{m_B} (\left\| E_B(i,j) - G_B(i,j) \right\|) \end{aligned} \tag{13}$$

where E_D and G_D are the dark regions of the enhanced low-light and ground truth images, while E_B and G_B represent the rest of the image. From experimentation, we suggest $w_D = 4$ and $w_B = 1$.

4 Experimentation

4.1 Implementation and training details

The network is implemented using the Keras Functional API, while the loss functions are defined using built-in TensorFlow functions. The overall network is then trained on the input training dataset using the mini-batch gradient descent algorithm and the Adam optimizer to guide the training. The mini-batch gradient descent algorithm was used due to the memory restrictions of the system used for training. In contrast, the Adam optimizer was used due to its superior performance on image reconstruction and classification operations. The proposed method is trained for hundred epochs with a batch size of six images. In addition, the proposed method considers multiple augmentation methods like rotation, scaling, transpose, and crop. The learning rate for the training is taken as 0.001 with a decay of 0.99. We trained the proposed method with the above-mentioned parameters on the LOL dataset [63]. We use the Google Colaboratory platform for training and testing.

4.2 Dataset

The proposed FRN is trained on the LOL dataset [63] that contains pairs of low-light and ground truth images. The training of FRN uses a combination of 485 image pairs from the LOL dataset [63] and 76 images from the VDS dataset [28]. The LOL dataset mainly consisted of images in indoor lighting conditions. In the LOL dataset, the images are captured by varying the ISO of the camera to capture low-light images in a normal light environment. In contrast, the VDS dataset incorporated handpicked HDR pair of ground truth images and low-light images with exposure set to -3e. We use all these images in their original resolution and aspect ratio. We set the amplification factor as 0.5 for the artificially brightened images and 2.0 for the artificially darkened images for training. The lower amplification factor (0.5) focuses on sufficient light of the scene. The higher amplification (2.0) focuses to capture a wider dynamic range and contrast. The input image along with the multiple instances helps in maintaining the trade-off.

4.3 Ablation study

To compute the loss function, we have taken structural information, context information, and regional differences into consideration. We assessed the effect of different loss functions by taking multiple combinations of these three factors. The graphs for the SSIM scores and PSNR scores are shown in Figs. 5 and 6. Using structural loss, regional loss or a combination of structural and context loss yields a similar SSIM score. The loss we achieved by combining structural, context, and regional loss yields the best SSIM score(0.832). Similarly, the PSNR scores when structural loss, regional loss, or a combination of structural and context loss is

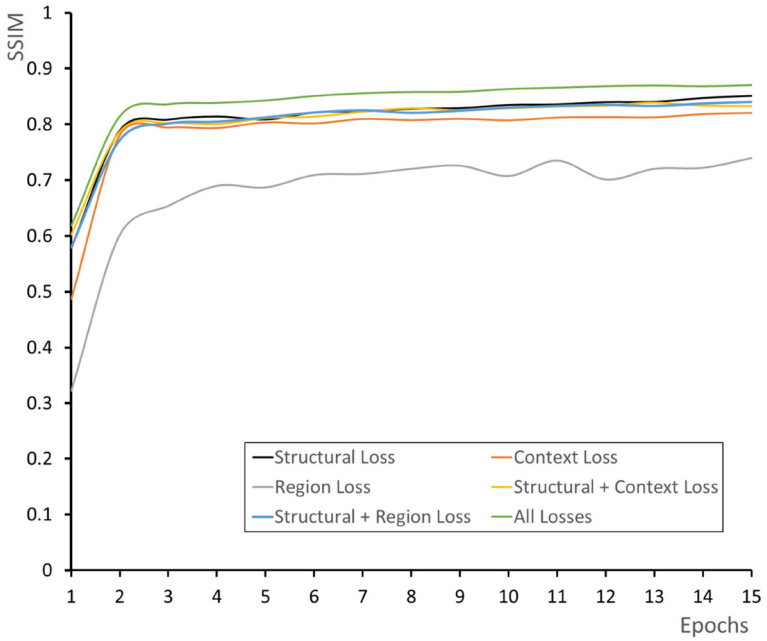

Fig. 5 Comparison of performance of different loss functions using SSIM

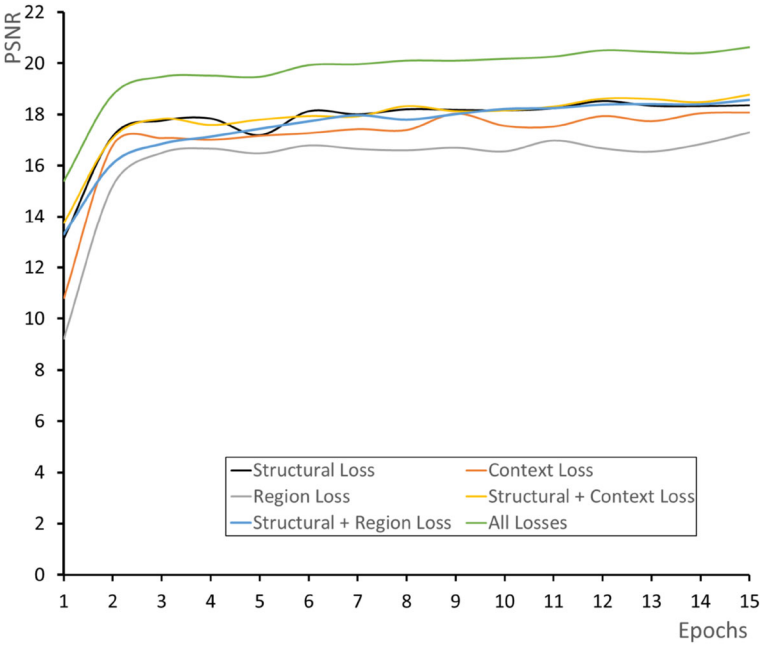

Fig. 6 Comparison of performance of different loss functions using PSNR

considered as the loss function lies in the range from 16.534dB to 18.744dB. The PSNR value for the loss function used in FRN consisting of a combination of all three factors exceeds the other with a great range(2.859dB=21.602dB-18.744dB). It testifies that using a combination of structural, context, and regional loss can improve the performance of FRN.

Additionally, the performance of the novel FFRM block during the testing improves the model's performance significantly. To test the contribution of the FFRM block to the overall network, we replaced the respective FFRM blocks with a simple layer-wise addition operation and kept the rest of the network the same. This yielded significantly degraded results with the SSIM score(0.783) and PSNR score(18.132dB). This testifies that the dynamic calibrations performed by the FFRM block have a tangible effect on the results produced by the model.

We tested the model with various input strategies to obtain the best performance for the lowest computational complexity. When we feed five images(2 artificially darkened, two artificially brightened, and one low light image) into FRN, the performance is on a similar scale to when we feed three images(1 artificially darkened, one artificially brightened, and one low light image) but the complexity increases by a great extent. Hence, we fixed the number of images as three in FRN to achieve the best result with the minimum complexity.

4.4 Quantitative analysis

In this section, we compare the results of the FRN with other currently available methods. We have used the codes and parameters that were publicly available from the authors for LIME [17], MBLLEN[33], Structure Revealing (SRIE) [30], DLN [61], LLFLOW [62], and EnlightenGAN [23]. As there are no such objective quantitative measurement metrics to analyze the low light enhancement, we utilize the Peak Signal-to-Noise Ratio (PSNR)

and Structural Similarity (SSIM) [60] as our evaluation metrics on the assumption that the enhanced images must be as similar to the ground truth images as possible. The higher value of SSIM and PSNR shows better enhancement. We also used the Naturalness Image Quality Evaluator (NIQE) [36], and BRISQUE [37], which are no-reference image quality scores. The lower value of NIQE and BRISQUE shows better enhancement. Various other quantitative measures are available for different tasks, like saliency feature based [1, 2] measures are used to analyze the structure in the domains that deal with the change of texture in images (i.e., image inpainting). Such measures of other domains are less useful in analyzing low-light image enhancement.

Table 1 shows the comparison of mean values of the proposed method with LIME [17], MBLLEN[33], Structure Revealing (SRIE) [30], DLN [61], LLFLOW [62], and Enlighten-GAN [23] on distinct quantitative measures. Table 1 shows that the FRN outperforms all the other techniques, exceeding the best among the other approaches on the average scores over the testing dataset. These scores help display the superior performance of the proposed method for low-light image enhancement. In comparison to existing methods, the proposed method's SSIM value demonstrates the enhanced image's higher quality of structural details. As a result, the quantitative measurements confirm that the proposed FRN is better than the existing methods. The best outcomes are highlighted in bold.

4.5 Qualitative analysis

Figure 7 shows the results of the various methods mentioned above, along with the input and the ground truth images from the LOL testing dataset [63]. Figure 7(b) shows the results of LIME. It can be observed that LIME consistently produced the image with the most saturation within the samples. However, the results of LIME contain more distortion and artifacts. The results of MBLLEN provide limited enhancement, as shown in figure 7(c). The results of DLN are shown in figure 7(d), which contains lesser details in the enhanced image. Figure 7(e) shows the results of EnlightenGan. EnlightenGAN generates output with limited lightness enhancement, resulting in darker outputs. The results of LLFLOW in figure 7(f) provide proper lightness in the enhanced image; however, LLFLOW generates images with lesser details and noise. Figure 7(g) shows the results of the proposed FRN. Our proposed model learned to enhance the darker areas with greater detail and low artifacts while avoiding overexposure of the highlights, producing images closest to the ground truth with much greater detail and minimal noise levels compared to the other models.

Figure 8 displays a visual representation of the performance of the FRN network on low-light images picked from various datasets [13, 25]. The proposed network shows satisfactory

Table 1 Quantitative results (SSIM, PSNR, NIQE, BRISQUE) of state-of-the-art methods and proposed method

	SSIM	PSNR	NIQE	BRISQUE
LIME	0.425	16.520	9.133	23.56
MBLLEN	0.718	15.433	4.009	22.84
SRIE	0.669	13.876	3.952	26.11
DLN	0.696	19.255	6.325	23.24
EnlightenGAN	0.622	16.973	4.815	24.49
LLFlow	0.830	19.341	4.063	25.21
OURS	**0.832**	**21.602**	**3.495**	**22.36**

Fig. 7 Visual comparison of various algorithms on LOL dataset[63]

results in datasets other than the training dataset with an average SSIM of **0.702** and an average PSNR of **18.260** with a visually pleasing enhanced output. These results prove the model's reliability in varying cases of low-light image enhancement.

Fig. 8 Visual Examples of enhancement performed by FRN Network on untrained low light images

4.6 Subjective analysis

We performed subjective analysis between ground truth and the enhanced image. We have requested 25 participants to evaluate the enhancement from various methods. The participants voted between zero to ten, where ten means better enhancement and one means poor enhancement. The results were shown blindly to the participants for their opinion. Table 2 shows the average scores from all participants. It can be observed from Table 2 that the proposed method achieves a better mean score for the subjective analysis.

5 Conclusion

This paper introduced the Fusion Recalibration Network (FRN) for low-light image enhancement. Unlike existing techniques that only utilize a single input image for low-light image enhancement, the proposed method utilizes multiple images with varying exposure levels to perform the low-light image enhancement task. We have evaluated our model's performance using quantitative and qualitative assessments. Consequently, our model has shown significant performance gains compared to other state-of-the-art techniques. Moreover, the proposed approach has also shown improved performance over existing methods for images captured in high-dynamic range conditions.

Table 2 Subjective analysis for various algorithms

LIME	MBLLEN	SRIE	DLN	EnlightenGAN	LLFLOW	OURS
7.40	7.96	7.04	8.10	6.96	7.82	8.32

In further works, we will continue to improve the model's performance by exploring more effective and efficient CNN structures. Other advanced deep learning techniques like GANs based on perception reconstruction may yield better results. The use of GANs may not be limited to the model but may also be used to generate a more cohesive dataset that can better train the model to perform the task of low-light image enhancement.

Acknowledgements Akshat Agarwal, Mohit Kumar Agarwal, and Aditya Shankar worked on the implementation and analysis. Akshat Agarwal and Ashutosh Pandey worked on exploration and the initial draft of the paper writing. Kavinder Singh and Anil Singh Parihar finalized the problem, guided implementation, revised the rough draft of the paper, and took care of the revision

Data Availability Data sharing not applicable to this article as no datasets were generated during the current study

Declarations

Conflicts of interest The author has no conflicts of interest to declare that are relevant to the content of this article

References

1. Amirkhani D, Bastanfard A (2021) An objective method to evaluate exemplar-based inpainted images quality using jaccard index. Multimedia Tools Appl 80(17):26199–26212
2. Amirkhani D, Bastanfard A (2019) Inpainted image quality evaluation based on saliency map features. In 2019 5th Iranian Conference on Signal Processing and Intelligent Systems (ICSPIS), pp 1–6
3. Bastanfard A, Amirkhani D, Mohammadi M (2022) Toward image superresolution based on local regression and nonlocal means. Multimedia Tools Appl 81(16):23473–23492
4. Bellamkonda S, Gopalan N (2020) An enhanced facial expression recognition model using local feature fusion of gabor wavelets and local directionality patterns. Intell J Ambient Comput Intell (IJACI) 11(1):48–70
5. Bellamkonda S, Gopalan N, Mala C, Settipalli L (2022) Facial expression recognition on partially occluded faces using component based ensemble stacked cnn. Cogn Neurodyn pp 1–24
6. Bhat N, Saggu N, Pragati, Kumar S (2020) Generating visible spectrum images from thermal infrared using conditional generative adversarial networks. In 2020 5th International Conference on Communication and Electronics Systems (ICCES), pp 1390–1394
7. Bhowmik A, Kumar S, Bhat N (2021) Evolution of automatic visual description techniques-a methodological survey. Multimedia Tools Appl 80(18):28015–28059
8. Cai J, Gu S, Zhang L (2018) Learning a deep single image contrast enhancer from multi-exposure images. IEEE Trans Image Process 27(4):2049–2062
9. Chakraborty S, Singh SK, Chakraborty P (2018) Correction to: Local directional gradient pattern: a local descriptor for face recognition. Multimedia Tools Appl 77(15):20269–20269
10. Chakraborty S, Mondal R, Singh PK, Sarkar R, Bhattacharjee D (2021) Transfer learning with fine tuning for human action recognition from still images. Multimedia Tools Appl 80(13):20547–20578
11. Cheng HD, Shi X (2004) A simple and effective histogram equalization approach to image enhancement. Digital signal Process 14(2):158–170
12. Dabov K, Foi A, Egiazarian K (2007) Video denoising by sparse 3d transform-domain collaborative filtering. In 2007 15th European Signal Processing Conference, IEEE, pp 145–149
13. Dang-Nguyen DT, Pasquini C, Conotter V, Boato G (2015) Raise: A raw images dataset for digital image forensics. In Proceedings of the 6th ACM multimedia systems conference, pp 219–224
14. Dehshibi MM, Bastanfard A (2010) Portability: A new challenge on designing family image database. In: IPCV, pp 270–276
15. Dehshibi MM, Bastanfard A, Kelishami AA (2010) Lpt: Eye features localizer in an n-dimensional image space. In IPCV, Citeseer, pp 347–352
16. Goodfellow I, Pouget-Abadie J, Mirza M, Xu B, Warde-Farley D, Ozair S, Courville A, Bengio Y (2014) Generative adversarial nets. Adv Neural Inform Process Syst 27

17. Guo X, Li Y, Ling H (2016) Lime: Low-light image enhancement via illumination map estimation. IEEE Trans Image Process 26(2):982–993
18. Gupta SS, Hossain S, Kim KD (2021) Hdr-like image from pseudoexposure image fusion: A genetic algorithm approach. IEEE Trans Consumer Electronics 67(2):119–128
19. Hao S, Han X, Guo Y, Xu X, Wang M (2020) Low-light image enhancement with semi-decoupled decomposition. IEEE Trans Multimedia 22(12):3025–3038
20. Hebbache L, Amirkhani D, Allili MS, Hammouche N, Lapointe JF (2023) Leveraging saliency in single-stage multi-label concrete defect detection using unmanned aerial vehicle imagery. Remote Sensing 15(5):1218
21. Hu J, Shen L, Sun G (2018) Squeeze-and-excitation networks. In IEEE conference on computer vision and pattern recognition, pp 7132–7141
22. Jain G, Chopra S, Chopra S, Parihar AS (2022) Attention-net: An ensemble sketch recognition approach using vector images. IEEE Trans Cogn Dev Syst 14(1):136–145. https://doi.org/10.1109/TCDS.2020.3023055
23. Jiang Y, Gong X, Liu D, Cheng Y, Fang C, Shen X, Yang J, Zhou P, Wang Z (2021) Enlightengan: Deep light enhancement without paired supervision. IEEE Trans Image Process 30:2340–2349
24. Jobson DJ, Rahman Zu, Woodell GA (1997) A multiscale retinex for bridging the gap between color images and the human observation of scenes. IEEE Trans Image Process 6(7):965–976
25. Kalantari NK, Ramamoorthi R et al (2017) Deep high dynamic range imaging of dynamic scenes. ACM Trans Graph 36(4):144–1
26. Kaur J, Singh W (2022) Tools, techniques, datasets and application areas for object detection in an image: a review. Multimedia Tools Appl pp 1–55
27. Ledig C, Theis L, Huszár F, Caballero J, Cunningham A, Acosta A, Aitken A, Tejani A, Totz J, Wang Z, et al. (2017) Photo-realistic single image super-resolution using a generative adversarial network. In IEEE conference on computer vision and pattern recognition, pp 4681–4690
28. Lee S, An GH, Kang SJ (2018) Deep chain hdri: Reconstructing a high dynamic range image from a single low dynamic range image. IEEE Access 6:49913–49924
29. Li Z, Wei Z, Wen C, Zheng J (2017) Detail-enhanced multi-scale exposure fusion. IEEE Trans Image Process 26(3):1243–1252
30. Li M, Liu J, Yang W, Sun X, Guo Z (2018) Structure-revealing low-light image enhancement via robust retinex model. IEEE Trans Image Process 27(6):2828–2841
31. Li H, Ma K, Yong H, Zhang L (2020) Fast multi-scale structural patch decomposition for multi-exposure image fusion. IEEE Trans Image Process 29:5805–5816
32. Lore KG, Akintayo A, Sarkar S (2017) Llnet: A deep autoencoder approach to natural low-light image enhancement. Pattern Recogn 61:650–662
33. Lv F, Lu F, Wu J, Lim C (2018) Mbllen: Low-light image/video enhancement using cnns. In BMVC 220:4
34. Ma K, Li H, Yong H, Wang Z, Meng D, Zhang L (2017) Robust multiexposure image fusion: a structural patch decomposition approach. IEEE Trans Image Process 26(5):2519–2532
35. MirMashhouri A, Bastanfard A, Amirkhani D (2022) Collecting a database for emotional responses to simple and patterned two-color images. Multimedia Tools Appl 81(13):18935–18953
36. Mittal A, Soundararajan R, Bovik AC (2012) Making a “completely blind" image quality analyzer. IEEE Signal Process Lett 20(3):20–212
37. Mittal A, Moorthy AK, Bovik AC (2011) Blind/referenceless image spatial quality evaluator. In: 2011 conference record of the forty fifth asilomar conference on signals, systems and computers (ASILOMAR), IEEE, pp 723–727
38. Moran S, Marza P, McDonagh S, Parisot S, Slabaugh G (2020) Deeplpf: Deep local parametric filters for image enhancement. In IEEE conference on computer vision and pattern recognition, pp 12826–12835
39. Pandey NN, Muppalaneni NB (2022) A survey on visual and non-visual features in driver’s drowsiness detection. Multimedia Tools Appl pp 1–41
40. Parihar AS, Singh K, Ganotra A, Yadav A, Devashish (2022) Contrast aware image dehazing using generative adversarial network. In 2022 2nd international conference on intelligent technologies (CONIT), pp 1–6. https://doi.org/10.1109/CONIT55038.2022.9847710
41. Parihar AS, Singh K, Rohilla H, Asnani G, Kour H (2020) A comprehensive analysis of fusion-based image enhancement techniques. In 2020 4th international conference on intelligent computing and control systems (ICICCS), pp 823–828. https://doi.org/10.1109/ICICCS48265.2020.9120999
42. Parihar AS, Varshney D, Pandya K, Aggarwal A (2021) A comprehensive survey on video frame interpolation techniques. Visl Comput pp 1–25
43. Parihar AS, Verma OP (2016) Contrast enhancement using entropy-based dynamic sub-histogram equalisation. IET Image Process 10(11):799–808

44. Parihar AS, Singh K, Rohilla H, Asnani G (2021) Fusion-based simultaneous estimation of reflectance and illumination for low-light image enhancement. IET Image Process 15(7):1410–1423
45. Park S, Yu S, Moon B, Ko S, Paik J (2017) Low-light image enhancement using variational optimization-based retinex model. IEEE Trans Consum Electron 63(2):178–184
46. Ren W, Liu S, Ma L, Xu Q, Xu X, Cao X, Du J, Yang MH (2019) Lowlight image enhancement via a deep hybrid network. IEEE Trans Image Process 28(9):4364–4375
47. Ren X, Yang W, Cheng WH, Liu J (2020) Lr3m: Robust low-light enhancement via low-rank regularized retinex model. IEEE Trans Image Process 29:5862–5876
48. Rohith G, Kumar LS (2021) Paradigm shifts in super-resolution techniques for remote sensing applications. The Visual Computer 37(7):1965–2008
49. Simonyan K, Zisserman A (2014) Very deep convolutional networks for large-scale image recognition. arXiv preprint arXiv:1409.1556
50. Singh K, Parihar AS (2021) Variational optimization based single image dehazing. J Visual Commun Image Represent 79:103241
51. Singh N, Rathore SS, Kumar S (2022) Towards a super-resolution based approach for improved face recognition in low resolution environment. Multimedia Tools Appl 81(27):38887–38919
52. Singh K, Khare V, Agarwal V, Sourabh (2022) Weakly supervised image dehazing using generative adversarial networks. In 2022 4th international conference on advances in computing, communication control and networking (ICAC3N), pp 870–875. https://doi.org/10.1109/ICAC3N56670.2022.10074393
53. Singh K, Khare V, Agarwal V, Sourabh S (2022) A review on gan based image dehazing. In 2022 6th International conference on Intelligent Computing and Control Systems (ICICCS), pp 1565–1571. https://doi.org/10.1109/ICICCS53718.2022.9788377
54. Singh K, Parihar AS (2023) Dse-net: Deep simultaneous estimation network for low-light image enhancement. J Visual Commun Image Represent p 103780
55. Singh K, Parihar AS (2023) Illumination estimation for nature preserving low-light image enhancement. The Visual Computer pp 1–16
56. Sivaiah B, Gopalan N, Mala C, Lavanya S (2022) Fl-capsnet: facial localization augmented capsule network for human emotion recognition. Signal, Image Video Process pp 1–9
57. Ulucan O, Karakaya D, Turkan M (2021) Multi-exposure image fusion based on linear embeddings and watershed masking. Signal Process 178:107791
58. Vaidwan H, Seth N, Parihar AS, Singh K (2021) A study on transformerbased object detection. In 2021 international conference on intelligent technologies (CONIT), pp 1–6. https://doi.org/10.1109/CONIT51480.2021.9498550
59. Vishwakarma DK, Dhiman C (2019) A unified model for human activity recognition using spatial distribution of gradients and difference of gaussian kernel. Vis Comput 35(11):1595–1613
60. Wang Z, Bovik AC, Sheikh HR, Simoncelli EP (2004) Image quality assessment: from error visibility to structural similarity. IEEE Trans Image Process 13(4):600–612
61. Wang LW, Liu ZS, Siu WC, Lun DP (2020) Lightening network for low-light image enhancement. IEEE Trans Image Process 29:7984–7996
62. Wang Y, Wan R, Yang W, Li H, Chau LP, Kot AC (2021) Low-light image enhancement with normalizing flow. arXiv preprint arXiv:2109.05923
63. Wei C, Wang W, Yang W, Liu J (2018) Deep retinex decomposition for low-light enhancement. arXiv preprint arXiv:1808.04560
64. Xu H, Jiang G, Yu M, Zhu Z, Bai Y, Song Y, Sun H (2021) Tensor product and tensor-singular value decomposition based multi-exposure fusion of images. IEEE Trans Multimedia
65. Zhang Q, Nie Y, Zhu L, Xiao C, Zheng WS (2020) Enhancing underexposed photos using perceptually bidirectional similarity. IEEE Trans Multimedia 23:189–202
66. Zheng C, Shi D, Shi W (2021) Adaptive unfolding total variation network for low-light image enhancement. In Proceedings of the IEEE/CVF international conference on computer vision, pp 4439–4448

Publisher's Note Springer Nature remains neutral with regard to jurisdictional claims in published maps and institutional affiliations.

Springer Nature or its licensor (e.g. a society or other partner) holds exclusive rights to this article under a publishing agreement with the author(s) or other rightsholder(s); author self-archiving of the accepted manuscript version of this article is solely governed by the terms of such publishing agreement and applicable law.

This article has been accepted for publication in IEEE Transactions on Cognitive and Developmental Systems. This is the author's version which has not been fully edited and content may change prior to final publication. Citation information: DOI 10.1109/TCDS.2023.3281877

Graph theory-based EEG source connectivity for assessing biomechanical performance in transfemoral amputees with vibrotactile feedback.

Saurabh Kumar, Aayushi Khajuria, and Deepak Joshi*, *Member, IEEE*

***Abstract*—** Recent research has shown that the complex and dynamic behaviour of isolated regions is necessary for the proper functioning of the human brain. To this end, network neuroscience evaluates the neural channels that respond to diverse motor tasks and assesses the brain's functionality. However, the utilization of network neuroscience has not been done to map out the cortical sources in lower limb amputee's postural control. Our earlier research shows that transfemoral amputees' fronto-central region and secondary somatosensory cortex have substantial functional connections while they are balancing with vibrotactile feedback. In this work, we advanced to investigate the cortical sources of transfemoral amputee's postural stability improvement with vibrotactile feedback. The results highlight the predominance of cortical sources in frontal and parietal lobe in alpha frequency band. The observation shows the connectivity of left superiorparietal, lateralorbitofrontal and right rostranteriorcingulate, supramarginal, and inferiorparietal sources. Moreover, the node strength of these cortical sources significantly changes ($p<0.05$, *ANOVA*) with the effect of feedback and visual input. In future, it could be interesting to develop some neural feedback techniques intended to improve the postural performance of lower limb amputees by making these cortical sources more adaptable via local stimulation techniques.

***Index Terms*—**Brain network, Source connectivity, balance, EEG, lower-limb amputees, postural performance, vibrotactile feedback.

I. Introduction

HUMAN postural control is a complicated feedback mechanism that uses a wide range of sensory data to keep the body in a steady upright position [1]. New research has revealed that the brain cortex is crucial to how this information is processed [2]. The sensory areas such as visual, auditory, somatosensory, and gustatory receive inputs from the thalamus and process information related to the senses. The motor areas such as the primary and secondary motor cortex regulate voluntary movements [3]. However, after lower limb amputation, achieving postural stability is extremely difficult due to the absence of sensory information from the severed leg. Lower limb amputees have been proven to have poor postural stability when compared to able-bodied individuals [4-8]. With amputation, the feedback from the sensory receptors in the amputated limb is completely lost. This restricts the brain from information processing and decision-making. Furthermore, spinal reflexes were shown to shift more control towards the brain after amputation [9]. Therefore, an important research question arises - how the brain strategies the functional connectivity for the loss of sensory input from a missing limb. Based on the pattern of afferent nerve impulses, the representation of diverse body parts in the cortex is continually changing. Neighboring cortical areas of the sensory cortex will fill the silent spaces if a cortical area loses its input, such as after an amputation [10]. This is called cortical reorganizations or neuroplasticity. These neuroplastic changes take a long time to significantly rewire the brain. For, example, after years of amputation and prolonged use of prosthesis, neuroplasticity outcomes seem to be modulated provided that the prosthesis is able to restore sensory inputs.

Therefore, lower limb amputees generally undergo rehabilitation protocols to improve their postural stability [11]. However, due to the limited availability of physical therapists, access to clinical facilities, and cost issues often prohibit their participation in these regimens [12]. Hence, utilizing biofeedback technology in rehabilitation is the current area of interest. Vibrotactile feedback, one of these, has demonstrated effective results in terms of improving balance in lower limb amputees [13-16]. In our latest work [17], we demonstrated that the increased limit of stability (LOS) with vibrotactile feedback in transfemoral amputees was due to strong theta and gamma oscillations in the brain. The sensory information from vibrotactile feedback is processed by the secondary somatosensory cortex (S2) contralateral to the severed side by drastically lowering theta spectral power. In order to enhance LOS, the fronto-central region greatly increased the gamma spectral power. Along with this, due to the strong functional connectivity between S2 and the fronto-central region, while perceiving vibrotactile feedback, the LOS was shown to

Saurabh Kumar is with the Center for Biomedical Engineering, Indian Institute of Technology Delhi (e-mail: kr.saurabh@outlook.com).

Aayushi Khajuria is with the Department of Nuclear Magnetic Resonance (NMR), All India Institute of Medical Sciences (AIIMS), New Delhi. (e-mail: aayushikhajuria@gmail.com).

(Saurabh Kumar and Aayushi Khajuria shares the equal authorship)

Deepak Joshi is with the Center for Biomedical Engineering, Indian Institute of Technology Delhi and with Department of Biomedical Engineering, All India Institute of Medical Sciences (AIIMS), New Delhi (e-mail: joshid@cbme.iitd.ac.in).

Authorized licensed use limited to: DELHI TECHNICAL UNIV. Downloaded on June 14,2023 at 05:38:30 UTC from IEEE Xplore. Restrictions apply.
© 2023 IEEE. Personal use is permitted, but republication/redistribution requires IEEE permission. See https://www.ieee.org/publications/rights/index.html for more information.

This article has been accepted for publication in IEEE Transactions on Cognitive and Developmental Systems. This is the author's version which has not been fully edited and content may change prior to final publication. Citation information: DOI 10.1109/TCDS.2023.3281877

improve [17]. However, functional connectivity limits revealing the exact source locations/nodes in the cortical region which are connected during the balancing task with vibrotactile feedback. In addition to this, through functional connectivity measures, the extent to which different nodes interact with each other cannot be revealed.

To this end, network neuroscience comes into play. It is a relatively recent area of research that evaluates brain functions using graph theory methods. Additionally, it offers a strong set of tools for quantifying and researching the complex relationships that control all aspects of brain activity. In order to map, record, analyze, and model the components and interconnections of neurobiological systems, network neuroscience looks for innovative methods [18]. Understanding the finely bound functioning of the brain depends critically on the knowledge it offers regarding the integration and collaboration of interconnections among cortical areas. Thus, it overcomes the constrained notion of "functional localization," in which each isolated zone tends to a certain function [19]. In network neuroscience, the brain's incredibly intricate architecture is abstracted into a graph where nodes signify areas of the brain and edges signify connections between those nodes. Electroencephalography (EEG), one of the neuroimaging methods that can offer pertinent details on the dynamics of the functional network, has made significant advancements in recent years [20]. The study of functional brain networks at the cortical source level using EEG has gained a lot of attention lately [21]. In order to identify the cortical sources that become active during balance tasks and postural movements, high-density EEG data can be analyzed using independent component analysis (ICA) [22-23]. Recent technology developments allow researchers to directly analyze cortical dynamics at the level of cortical sources [24-25].

In connection to prior evidence postural control is intricately linked to anatomical and functional brain properties [26], it is of utmost interest to understand the organization of cortical networks in transfemoral amputees. A recent study in this domain investigated the connectivity of cortical sources during a postural control task in healthy individuals. Here the participant's quiet stance was disrupted by mechanical skeletal muscle vibrations [19]. The results highlight the predominance of frontal lobe connections during eyes open session and the strengthening of temporo-parietal network connections in the absence of vision. Another study investigated the effect of whole-body vibratory stimulation on postural control strategies employed to maintain an upright posture of healthy participants [27]. They observed that cortical activity is necessary to modulate the muscle activations via the formation of new synergies. Taking these studies as a base, in the present work, cortical connections' complexity, which controls the process of better functional results in amputees with vibrotactile feedback was explored. Using graph theory-based source connectivity, the current strategy aims to identify cortical sources in transfemoral amputees that were engaged while performing a balance task with vibrotactile feedback.

Specifically, the contributions of the present study are summarized as:

1. The present approach attempts to locate the cortical sources in transfemoral amputees during the balance task with vibrotactile feedback.
2. To investigate whether the strength of these cortical sources depend upon the availability of vision and feedback or not.
3. To confirm whether the spotted cortical sources are within the region of interests (Secondary somatosensory area and frontal region).

We hypothesize that, those cortical sources whose strength value depends upon the availability of feedback and vision during the balance task, must be spotted within the region of interests. Therefore, the goal of this study was to determine whether the network-based analysis could aid in the creation of neurofeedback techniques that were focused on identified nodes (brain areas) of the cortical network and help to improve the postural performance in transfemoral amputees.

Non-invasive scalp EEG was preferred because it is now recognized as a potent method for capturing the brain activity with the distinct benefit of assessing neuronal processes as they occur. EEG devices with exact information about the head anatomy and powerful source localization algorithms are now available, transforming the EEG into a real neuroimaging modality.

II. Materials and Methods

A. Participants

Following permission by the Institute Ethics Committee, All India Institute of Medical Science (AIIMS), New Delhi (Ref: IEC-222/04.05.2018), data were collected at IIT Delhi's Neuromechanics Research Lab. Six trauma patients with transfemoral amputation (age = 27.33 $\pm$ 6.08 years, height = 171 $\pm$ 8.07 cm, weight = 66 $\pm$ 6.13 kg) being able to walk while wearing a prosthesis, who had no musculoskeletal, neurological, cardiovascular, or vestibular issues were chosen for the study. All the participants were amputated from the right leg and were using the prosthesis having SACH (solid ankle cushioned heel) prosthetic foot. The inclusion criteria also incorporates that the time of amputation for all the participants should be more than a year to allow for proper prosthetic adaptation. All the participants used mechanical single axis weight activated knee joint in the prosthesis with total contact socket and total elastic suspension (TES) belt. Table 1 lists the demographics of all the participants.

B. Instrumentation

The cortical activity was wirelessly recorded at 1000 Hz using a 64-channel Ag/AgCl active electrode Electroencephalography (EEG) setup with an actiCHamp amplifier from Brain Products, GmbH, Germany. The worldwide 10:10 electrode placement technique was used to put each electrode on the scalp. A conductive EEG gel was applied beneath each electrode to maintain the resistance under 20 kΩ in order to produce a high signal-to-noise ratio. EEG data were referenced to channel Fz online.

The vibrotactile feedback system was linked to the front (quadriceps muscles) and back (hamstrings muscles) surfaces of the amputee's socket at 2/3rd of the length of the stump from the greater trochanter (Fig. 1a). It consisted of two tactors

Authorized licensed use limited to: DELHI TECHNICAL UNIV. Downloaded on June 14,2023 at 05:38:30 UTC from IEEE Xplore. Restrictions apply.
© 2023 IEEE. Personal use is permitted, but republication/redistribution requires IEEE permission. See https://www.ieee.org/publications/rights/index.html for more information.

This article has been accepted for publication in IEEE Transactions on Cognitive and Developmental Systems. This is the author's version which has not been fully edited and content may change prior to final publication. Citation information: DOI 10.1109/TCDS.2023.3281877

(Vibration Motor 310-113 from Precision Microdrives Ltd, at London, U.K.). Each tactor had the dimensions of a coin: 10 mm in diameter, 3.4 mm in length, and 1.2 g in weight. For vibrotactile feedback, the center of pressure (CoP) measurement insoles' vertical length was divided into three zones: the posterior (20%), mid (30%), and anterior (50%) zones (Fig. 1b). Because it mimics CoP when one is standing normally, CoP in the mid-zone was termed the non-vibratory area. Whenever the CoP value is outside the mid zone and exceeds the threshold value, the associated tactor begins to vibrate. For example, when *CoP > 50%* of insole length (anterior zone), the anterior tactor will vibrate. When *CoP < 20%* of insole length (posterior zone), the posterior tactor will vibrate. The resistance of the force-sensitive resistors was recorded by an Arduino microcontroller (MEGA 2560 R3: ATmega2560, 16 MHz, Arduino LLC, Boston, MA), which also calculated the CoP and continuously mapped the CoP to identify the feedback from vibrating tactors. The instrumentation for vibrotactile feedback along with center of pressure (CoP) measurement insoles used for the data collection can be found all over at Khajuria A et al. 2022 [17].

TABLE I
DEMOGRAPHIC DETAILS OF THE PARTICIPANTS

Subject	Height (cm)	Weight (kg)	Age (years)	Duration of Prosthetic Usage (years)	Stump length (%)
A1	164	58	28	10	91.1
A2	180	75	27	9	87.8
A3	182	70	21	10	80.5
A4	166	67	35	20	93.9
A5	164	61	20	2	86.2
A6	170	65	33	2	92.4
(mean ± SD)	171±8.07	66±6.13	27.33±6.08	8.83±6.64	88.65±4.91

C. Experimental protocols

Before beginning the experiment, all participants were given a description of the balance task. To begin with, it was instructed that the participants stand normally (having an equivalent stance width to their inter-ASIS distance [28]), then to lean as far forward as they could before returning to a normal upright stance. Similar to that, they were instructed to lean backward (posterior), taking care not to flex their hip joints or lift their heels or toes (Fig. 1c). They were then outfitted with the wireless EEG equipment, CoP measurement insoles, and feedback circuitry. EEG data was gathered in two sessions, one with and one without vibrotactile input. In each session, the data was collected in two conditions: open eyes (OE) and closed eyes (CE). In order to balance participant fatigue with the need for enough data for statistical analysis, all the participants completed four balance task trials in each condition during each session. Prior to the experimental trials, there was no opportunity for practice, so each participant's naive response was recorded. A lapse of about 20 seconds separated various trials. Five minutes rest were given in between the two sessions. Oral instructions to adjust the balancing posture were delivered to each participant by the researcher at the precise time interval (utilizing a stopwatch built into the EEG recorder) during recording.

III. DATA ANALYSIS

A. Pre-processing

Matlab2022a and EEGLAB were used for offline analysis of the acquired EEG data. Raw data sampled at 1000Hz was firstly down-sampled to 100 Hz. After that, a 4th order Butterworth high pass filter at 0.1Hz was used to obtain the desired frequency components. In order to remove the line noise, an additional notch filter at 50Hz was used. The artifactual regions in the EEG data were found and reconstructed using artefact subspace reconstruction (ASR) [29]. The bilateral mastoid reference was then used to re-reference the data. To disentangle otherwise mixed brain signals and to remove the remaining artifacts, the data was then subjected to independent component analysis (ICA) utilizing an adaptive mixture (AMICA) [30].

B. EEG source connectivity

The functional brain dynamics were reconstructed using BRAINSTORM software and the EEG source connectivity approach [31-32]. To reconstruct the cortical sources, this method calls for the solution of an inverse problem and to solve this problem, Weighted Minimum Norm Estimate (wMNE) algorithm [33-34] was used. The Brain, Skull, and Scalp Boundary element model (BEM) was used to construct the inverse problem domain. The head modelling was done using standard head model template provided by BrainStorm. A graph

Authorized licensed use limited to: DELHI TECHNICAL UNIV. Downloaded on June 14,2023 at 05:38:30 UTC from IEEE Xplore. Restrictions apply.
© 2023 IEEE. Personal use is permitted, but republication/redistribution requires IEEE permission. See https://www.ieee.org/publications/rights/index.html for more information.

This article has been accepted for publication in IEEE Transactions on Cognitive and Developmental Systems. This is the author's version which has not been fully edited and content may change prior to final publication. Citation information: DOI 10.1109/TCDS.2023.3281877

with nodes representing the various cortical areas was used to depict the brain for network analysis purposes. Using the Desikan-Kiliany anatomical atlas, 68 nodes were identified in the cortex [35]. A measure of statistical coupling in between regional time-series at the cortex-level was produced after the Functional Connectivity (FC) based on the Phase Locking Value (PLV) was computed. There has been significant discussion on the benefits and drawbacks of various connection measures in the literature [36], and earlier research on simulated data revealed that the combination of wMNE and PLV had the highest accuracy in terms of resemblance with the reference network [37]. The measure of the 68 nodes' functional connectivity values was calculated in three frequency bands: Alpha (α, [8-13] Hz); Beta (β, [13-30] Hz); and Gamma (γ, [30-45] Hz).

The overall properties of the brain network during the balance task were examined using network analysis. Using a proportionate threshold (such as top 10%) for group comparisons assures that each group's networks have the same number of nodes, or network size, and edges, or global degree. A range of proportional thresholds have been reported in the literature, from 5 to 40% [38, 39]. The connection matrices were also thresholded by retaining the nodes with the highest strength values (top 1%) [40]. Another study used three proportionate thresholds: 5%, 15% and 30% and found high agreement among the obtained results [41]. Therefore, the previous research is unclear about which threshold should be used. In an attempt to show that results are sensitive to the choice of thresholds, a study examined the stability of network metrics across thresholds in a sizable dataset of functional connectivity in the resting state [39]. They found that network measures were dependent upon the choice of thresholds. Therefore, to ensure that the obtained results are not sensitive to threshold value, we performed our analysis across three proportionate thresholds: 10%, 20% and 30%. Properties of cortical regions was characterized by

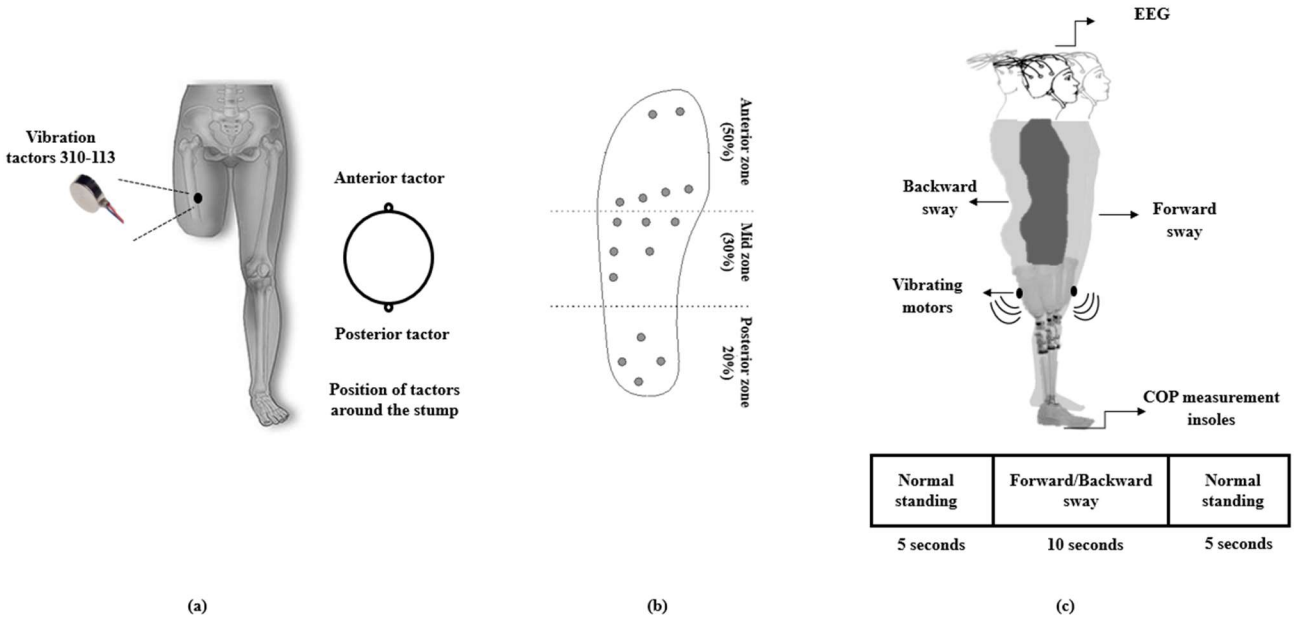

Fig. 1. Representation of experimental procedure. (a) Position of tactors around the stump; (b) division of CoP measurement insole for vibratory feedback; (c) Representative amputee participant performing the balancing task.

evaluating the properties of individual network nodes and mapping their significance in network changes under various experimental settings. By concentrating on inter-regional links, Network-Based Statistics provides a global picture of the network reconfiguration under various conditions [42]. The degree of a node and node's strength were two network measures. Degree reflects the number of connections associated to that specific node i.e., total number of edges connected to a node. Strength is the total of the edges' weights that are connected to the node. Suppose N is the set of all nodes in the network, and 'n' is the number of nodes. (i, j) is a link between nodes i and j, (i, j ∈ N). a_{ij} is the connection status between i and j.

Degree of a node i,

$$k_i = \Sigma_{i,j \in N} a_{ij}. \quad (1)$$

Links (i, j) are associated with connection weights w_{ij}. We assume that weights are normalized, such that $0 \leq w_{ij} \leq 1$ for all i and j. Strength of a node i,

$$s_i = \sum_{j=1}^{N} a_{ij} w_{ij}. \quad (2)$$

C. *Statistical analysis*

The statistical difference between conditions (feedback vs without feedback) was performed at the level of each region (a node-wise analysis). Thus, the results are a set of brain regions that show significant differences between the conditions. The interaction effect of visual input to feedback conditions was also statistically assessed. Due to low sample size, no assumption of normality was made, and therefore Quade's rank analysis of covariance (RANCOVA) was utilized as a nonparametric test. Briefly, at first, the strength (node-wise with various thresholds) was ranked separately, ignoring the

Authorized licensed use limited to: DELHI TECHNICAL UNIV. Downloaded on June 14,2023 at 05:38:30 UTC from IEEE Xplore. Restrictions apply.
© 2023 IEEE. Personal use is permitted, but republication/redistribution requires IEEE permission. See https://www.ieee.org/publications/rights/index.html for more information.

This article has been accepted for publication in IEEE Transactions on Cognitive and Developmental Systems. This is the author's version which has not been fully edited and content may change prior to final publication. Citation information: DOI 10.1109/TCDS.2023.3281877

visual inputs (eye open or eye closed). Then a regression was run of the with feedback ranks on the without feedback ranks, again ignoring the visual inputs, and the residuals were computed. An ANOVA on such residuals was conducted for the effect of visual input (i.e., Vision X Feedback interaction). All the statistical analysis was conducted on IBM SPSS version 1.0.0.1406. The level of significance was set to 0.05.

IV. Results

The following results illustrates the outcome of the source connectivity analysis in alpha frequency band(α, [8-13] Hz). The data for other frequency bands were not displayed because none of the nodes demonstrated statistical significance [43, 44]. Various nodes that were connected during balancing with vibrotactile feedback are shown in figure 2. These nodes were mainly located in the frontal, central and parietal regions of the brain.

A. Nodewise analysis

Nodewise analysis investigates global characteristics of brain network during the execution of the balance task. The nodewise analysis revealed that the strength of some specific nodes depends upon the availability of vision and feedback during the balance task (figure 3). Our results were threshold dependent as for 10% threshold, we found left lateralorbitofrontal ($p=0.033$) and left parstriangularis ($p=0.033$) in the frontal region of the brain. For 20% threshold, left lateralorbitofrontal ($p=0.045$) in the frontal region, left fusiform ($p=0.018$) in the temporal region, left inferiorparietal ($p=0.012$) and right superiorparietal ($p=0.034$) in the parietal region, and right lateraloccipital ($p=0.008$) in the occipital region were found. For 30% threshold, right rostralanteriorcingulate ($p=0.009$) in the frontal region, left entorhinal ($p=0.025$) in the temporal region, right supramarginal ($p=0.009$) and Right inferiorparietal ($p=0.042$) in the parietal region were found as shown in Table II. The interaction effect of vision and feedback for each of the highlighted node is shown in figure 4.

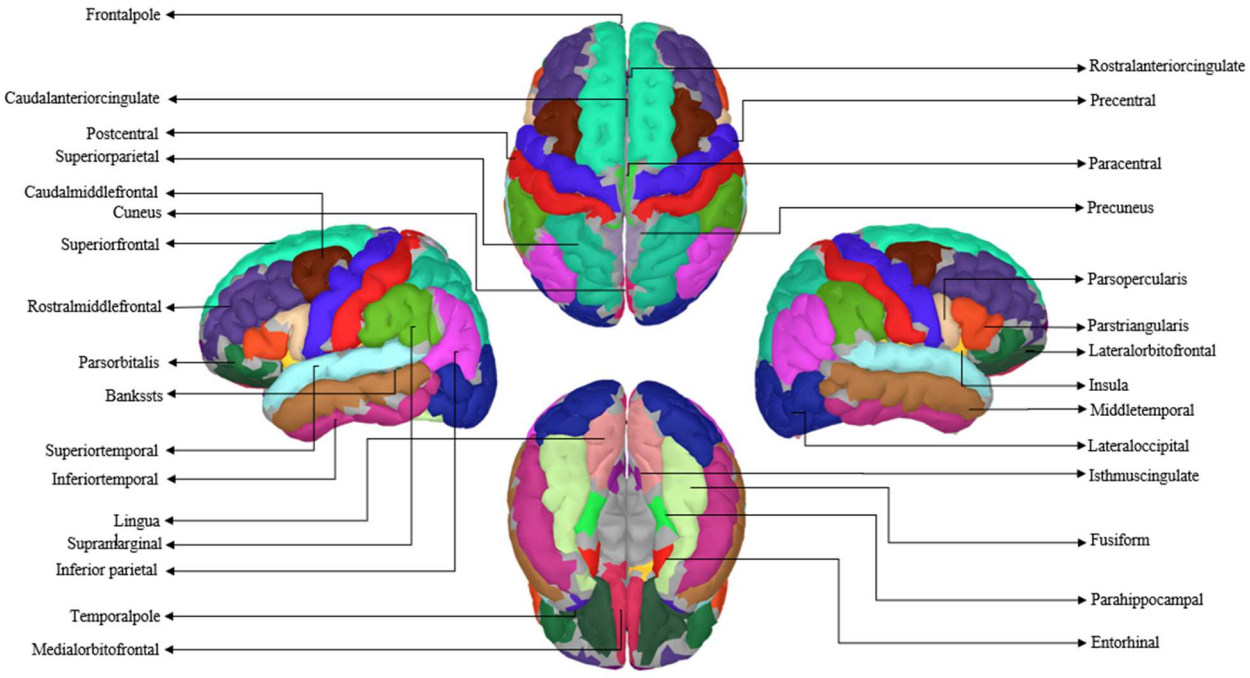

Fig 2. The brain is shown from the top, bottom as well as in the medial and lateral view of each hemisphere. The anatomical representation displays the nodes of the network as the corresponding 68 cortical regions that were Connected during balancing with vibrotactile feedback, parcellated according to the Desikan-Killiany atlas.

Authorized licensed use limited to: DELHI TECHNICAL UNIV. Downloaded on June 14,2023 at 05:38:30 UTC from IEEE Xplore. Restrictions apply.
© 2023 IEEE. Personal use is permitted, but republication/redistribution requires IEEE permission. See https://www.ieee.org/publications/rights/index.html for more information.

This article has been accepted for publication in IEEE Transactions on Cognitive and Developmental Systems. This is the author's version which has not been fully edited and content may change prior to final publication. Citation information: DOI 10.1109/TCDS.2023.3281877

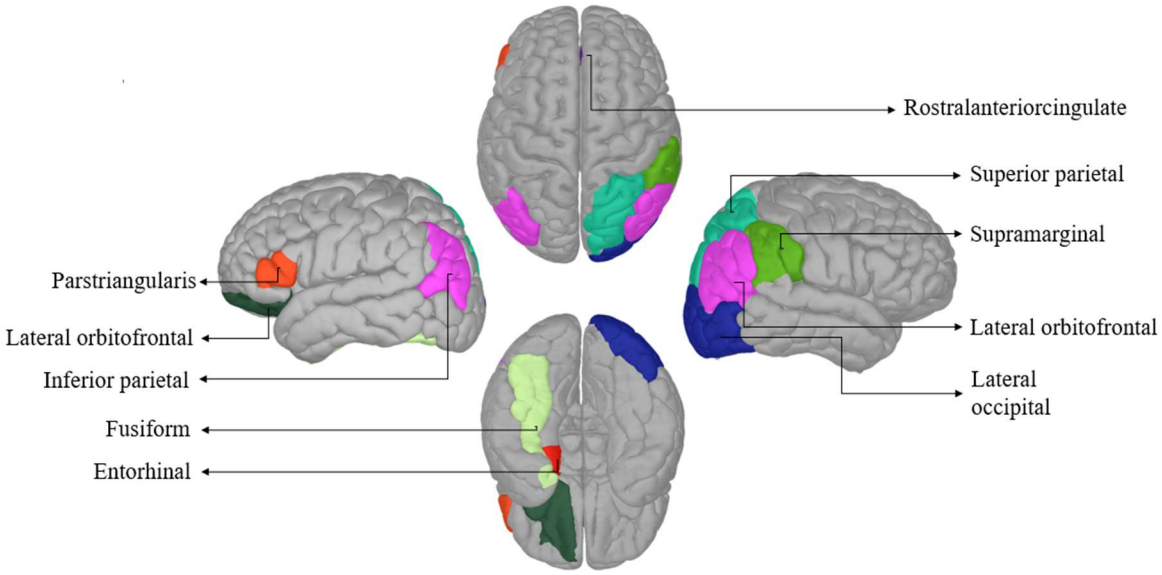

Fig 3. **Nodewise analysis.** Top, bottom as well as in the medial and lateral view of each hemisphere of the brain showing Connected nodes whose strength value depends upon the availability of vision and feedback during the balance task.

TABLE II

LIST OF CORTICAL SOURCES WHOSE STRENGTH VALUE SIGNIFICANTLY DEPENDS UPON THE AVAILABILITY OF VISION AND FEEDBACK DURING THE BALANCE TASK. (AVERAGE NODE STRENGTH ± SD)

Region	Nodes (10% Threshold)	Nodes (20% Threshold)	Nodes (30% Threshold)	Eyes open		Eyes closed		p-value
				Without f/b	With f/b	Without f/b	With f/b	
Frontal	Left lateralorbitofrontal			1.92±1.05	2.38±0.95	0.67±1.04	0.46±0.77	0.033
	Left parstriangularis			3.30±1.02	3.75±0.93	5.65±3.32	4.91±1.78	0.033
		Left lateralorbitofronta l		3.50±0.56	3.63±0.59	2.74±2.78	2.67±0.58	0.045
			Right rostralanteriorcingul ate	13.79±1.34	14.10±1.98	19.50±8.69	21.30±5.20	0.009
Temporal		Left fusiform		4.31±2.42	3.91±2.13	2.45±2.12	2.71±2.28	0.018
			Left entorhinal	12.05±3.81	10.90±2.16	11.31±2.88	13.06±4.22	0.025
Parietal		Left inferiorparietal		10.08±5.16	7.91±5.09	10.42±6.31	11.28±6.33	0.012
		Left superiorparietal		3.52±2.58	3.92±2.02	5.74±6.48	6.71±6.55	0.034
			Right supramarginal	13.04±1.69	13.52±1.93	18.72±8.44	20.03±5.40	0.009
			Right inferiorparietal	15.19±1.17	15.74±2.05	27.35±10.40	26.93±8.39	0.042
Occipital		Right lateraloccipital		6.11±1.93	5.30±1.84	9.12±4.28	7.84±1.74	0.008

Authorized licensed use limited to: DELHI TECHNICAL UNIV. Downloaded on June 14,2023 at 05:38:30 UTC from IEEE Xplore. Restrictions apply.
© 2023 IEEE. Personal use is permitted, but republication/redistribution requires IEEE permission. See https://www.ieee.org/publications/rights/index.html for more information.

This article has been accepted for publication in IEEE Transactions on Cognitive and Developmental Systems. This is the author's version which has not been fully edited and content may change prior to final publication. Citation information: DOI 10.1109/TCDS.2023.3281877

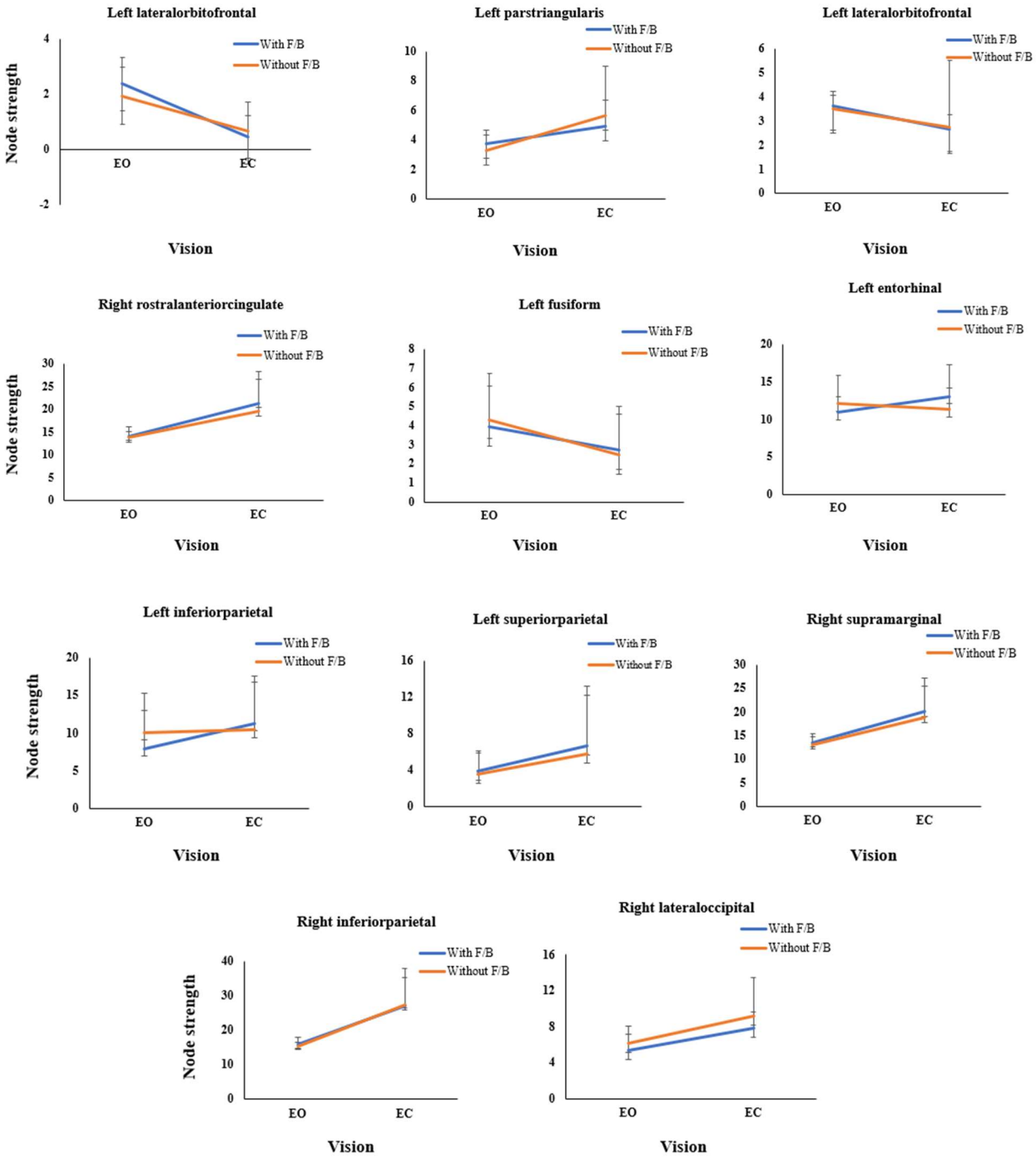

Fig. 4. Interaction effect of feedback and vision for each connected node during the balance task. Statistical significance ($p<0.05$, *ANOVA*)

B. Edgewise analysis

Changes in connectivity values were used to evaluate the network setup in the alpha band during balancing with feedback in OE and CE circumstances. It shows the involvement of 2193 edges of the network, all of which demonstrated greater connection during balancing with feedback. Out of these 10% of the strongest connections are in between 480 edges, 20% of the strongest connections are in between 528 edges, and 30% of the strongest connections are in between 637 edges shown in figure 5. The resulting network exhibits connections across and within hemispheres and is spatially concentrated in the frontal, central and parietal regions of the brain. The significant connections involved mainly the frontal (superior and middle) and parietal (superior and inferior) brain regions. Network configuration during balancing with feedback reflects the predominance of the left hemisphere and might indicates the involvement of the prosthetic leg in maintaining balance. Table 3 shows the degree (average ± SD) of each node whose strength value depends upon the availability of vision and feedback during the balance task.

Authorized licensed use limited to: DELHI TECHNICAL UNIV. Downloaded on June 14,2023 at 05:38:30 UTC from IEEE Xplore. Restrictions apply.
© 2023 IEEE. Personal use is permitted, but republication/redistribution requires IEEE permission. See https://www.ieee.org/publications/rights/index.html for more information.

This article has been accepted for publication in IEEE Transactions on Cognitive and Developmental Systems. This is the author's version which has not been fully edited and content may change prior to final publication. Citation information: DOI 10.1109/TCDS.2023.3281877

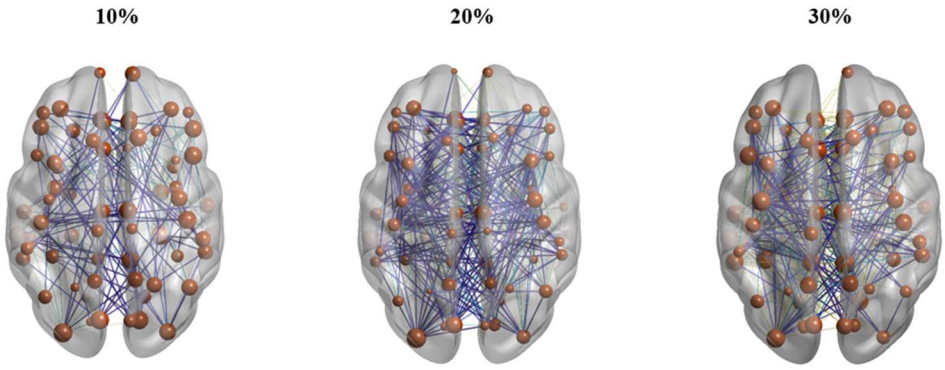

Fig 5. Edgewise analysis. Cortical areas are represented as network nodes (for 10%, 20% and, 30% threshold), whereas edges represent connections between nodes.

TABLE III
LIST OF HIGHLIGHTED CORTICAL SOURCES WITH THEIR DEGREE.
(AVERAGE NODE DEGREE ± SD)

Region	Nodes (10% Threshold)	Nodes (20% Threshold)	Nodes (30% Threshold)	Eyes open		Eyes closed	
				Without f/b	With f/b	Without f/b	With f/b
Frontal	Left lateralorbitofrontal			10±4.88	9±2.36	11±10.65	10±8.97
	Left parstriangularis			12±1.09	12±3.18	7±5.13	5±3.37
		Left lateralorbitofrontal		22±7.74	21±4.83	23±9	22±8.45
			Right rostralanteriorcingulate	33±3.93	33±3.20	41±13.10	43±8.98
Temporal		Left fusiform		17±6.41	15±6.88	7±5.78	8±6.94
			Left entorhinal	32±4.35	33±7.13	46±11.99	44±13.25
Parietal		Left inferiorparietal		23±3.74	23±4.63	32±2.78	31±5.85
		Left superiorparietal		21±5.64	21±5.05	28±5.39	24±6.22
			Right supramarginal	32±3.44	34±3.09	40±12.69	43±9.72
			Right inferiorparietal	40±2.82	38±1.86	47±10.98	46±11.58
Occipital		Right lateraloccipital		20±4.19	20±2.78	18±5.16	17±5.03

V. DISCUSSION

Most of the previous studies relied on scalp-level approach, which has limitations in terms of changes brought about by the volume conduction effect [45]. Rarely has the literature employed EEG source connectivity to describe functional networks involved in the postural control of lower limb amputees. The following sub-sections discusses the various outcomes of the study.

A. Effect of threshold

To use binary graphs derived from functional connectivity data, thresholding is a required step. The thresholding procedure's basic idea (removing the weak edges) implies that finding a stable experimental effect is only feasible in the absence of spurious connections (at high thresholds). In this work, we applied three different proportionate thresholds i.e., 10%, 20% and 30% to the data. Distinct nodes were discovered (shown in table 2) whose strength values significantly varies with vision and feedback at various thresholds. Since there is currently no "ground truth" method for determining the ideal

Authorized licensed use limited to: DELHI TECHNICAL UNIV. Downloaded on June 14,2023 at 05:38:30 UTC from IEEE Xplore. Restrictions apply.
© 2023 IEEE. Personal use is permitted, but republication/redistribution requires IEEE permission. See https://www.ieee.org/publications/rights/index.html for more information.

This article has been accepted for publication in IEEE Transactions on Cognitive and Developmental Systems. This is the author's version which has not been fully edited and content may change prior to final publication. Citation information: DOI 10.1109/TCDS.2023.3281877

threshold value, this poses one of the biggest challenges in the functional connectivity thresholding issue. Therefore, the nodes estimated at different thresholds might lead to different conclusions. Recent studies have reported findings across a range of thresholds [39, 46, 47]. A data-driven approach proposed to choose an arbitrary threshold so as to consider the strong connections within the brain [48]. However, numerous studies have demonstrated that weak connections can be crucial when examining the relationships between network characteristics [49]. Proportional thresholds do not account for absolute differences in correlation values in the network, therefore, information about overall group differences may be lost. Proportional thresholding also led to substantial distortions in the graph structure across thresholds [47]. This might be reason for the variation of resulted nodes with the threshold value in the present study. Therefore, rather than relying on a single threshold value, using multiple threshold values can help to identify connections that are consistently significant across a range of thresholds. This can also provide a more robust and reliable analysis.

B. *Effect of vibrotactile feedback*

Utilizing 68 regional time-series derived from reconstructed cortical sources, the properties of the cortical network structure in the two experimental sessions of the balance task, with and without feedback, were examined. Examining the outcomes of the nodewise analysis, where we analyzed the node strengths, display clear differences in node strengths in frontal, temporal parietal, and occipital regions. Increase in the strength of nodes in the frontal region during balancing with feedback was shown in lateralorbitofrontal node which acts as a center for sensory integration [50]. The rostralanteriorcingulate of the frontal region controls high level functions such as attention allocation and error detection also exhibit a notable rise in node strength with feedback. Parstriangularis on the inferior frontal gyrus is involved during the modulation of timing during the tasks. This suggests that the activation of the frontal region for LOS improvement has its sources in lateralorbitofrontal, parstriangularis and rostralanteriorcingulate. Balancing with feedback also shows the significant increase in node strength in the temporal region including fusiform and entorhinal sources. Fusiform is involved in the processing of object recognition and identification of external stimuli. On the other hand, entorhinal is involved in the processing of sensory information and formation and retrieval of memories. In the parietal lobe of the brain, superiorparietal and inferioparietal node which are known to be involved with sensorimotor integration has shown significant increase in node strength. Along with this, supramarginal also shows a significant increase in the node strength with vibrotactile feedback. The supramarginal gyrus is involved in sensory integration and perception, particularly in the sense of touch and proprioception. These sources might have triggered the secondary somatosensory cortex of amputees to perceive the sensory information from vibrotactile stimuli. Therefore, with vibrotactile feedback, the perceived vibratory information has its cortical sources in superiorparietal, inferioparietal and supramarginal node. These, nodes were responsible for triggering the brain region S2 and then frontal region to improve the LOS with vibrotactile feedback.

C. *Effect of visual input*

In our previous study [17], we evaluated the functional connectivity between secondary somatosensory cortex S2 (contralateral to prosthetic leg) and fronto-central region of amputees in eyes closed condition. The primary reason of closing the eyes was that in both static and dynamic balancing situations, the amputee depends on the visual information to complete daily chores [51]. In the present study, we repeated the data collection with eyes open condition, in order to explore the dependence of connected nodes with feedback on vision. Prior studies have demonstrated the frontal lobe's function in the distribution of attentional resources during motor performance [52]. Our finding suggests that balancing with feedback engage the frontal lobe which is the primary location of the attention-related network in the α band and is primarily driven by visual input from occipital region. The OE state is distinguished by the significant decrease in the node strength in the frontal, parietal and occipital sources. The Frontal Eye Field, in particular, is associated with visual field perception, awareness, and the sustaining of attention to peripheral areas [53]. The CE condition showed the significant increase in the node strength in various nodes as shown in table 2. During vibrotactile feedback with visual input (OE) shows decreased node strength in the rostralanteriorcingulate, inferioparietal, superiorparietal, supramarginal and lateraloccipital nodes. These nodes are related to decision making [54], processing of sensory input, motor control and voluntary movements and therefore play a crucial role in identifying unstable posture and developing a remedial approach after that [55]. Observing the nodewise examination for CE condition, it becomes obvious that the frontal and parietal zones are dominant independent of the feedback. The brain relies on the integration of vestibular data from the inner ear's sensors to correctly identify the perceived motion and correct errors in the visual signal. This might have connected the nodes in the temporal region (fusiform and entorhinal). Overall, these results describe the cortical network's alpha band activity and how it establishes itself in conjunction with vision's effects in response to a balancing task in the presence or absence of vibrotactile input.

D. *Location of cortical sources*

The majority of earlier research emphasizes cortical activation using spectral and power-based analysis. In our previous work [17], similar methodology was proposed involving functional connectivity which depend on the phase locking value (PLV) between S2 and fronto-central region. In contrast to their magnitude, the cortical signals' phase synchronization is the main focus of this study. In the present work, we were interested to find out the sources of connectivity. In particular, we were interested to find out whether the sources of connectivity (nodes) located in the previously highlighted regions (S2 and fronto-central) or not. The results of the present study confirm that, with vibrotactile feedback, the majority of connected nodes were present frontal and parietal regions of the cortex and their strength value depends upon the availability of vision and vibrotactile feedback. Left parietal (leftsuperiorparietal) with degree 21 and significant increase in node strength with feedback was found in the superior and medial to the intraparietal sulcus (IPS). Its principal functions are related to

Authorized licensed use limited to: DELHI TECHNICAL UNIV. Downloaded on June 14,2023 at 05:38:30 UTC from IEEE Xplore. Restrictions apply.
© 2023 IEEE. Personal use is permitted, but republication/redistribution requires IEEE permission. See https://www.ieee.org/publications/rights/index.html for more information.

This article has been accepted for publication in IEEE Transactions on Cognitive and Developmental Systems. This is the author's version which has not been fully edited and content may change prior to final publication. Citation information: DOI 10.1109/TCDS.2023.3281877

perceptual-motor coordination, perception, and visual attention. In the frontal cortex (rostralanteriorcingulate) with degree 34 and significant increase in node strength with feedback was found. It has been implicated in various functions, including error detection, conflict monitoring, decision-making, and emotion regulation. This observation suggests the early signs of LOS improvement in desired cortical sources (superiorparietal and rostralanteriorcingulate) in the parietal (S2 contralateral to prosthetic leg) and frontal region which were connected while performing the balance task with vibrotactile feedback.

VI. CONCLUSION

The methods of network neuroscience make it possible to locate and understand the connections between the cortical areas that are primarily responsible for the high-level coordination of the balance task. The findings show changes in the cortical networks' characteristics in terms of both their individual areas and overall organization during the execution of a balance task with and without feedback under open- and closed-eye experimental settings. Statistical significance supports variations in individual node strength with vision and feedback. The results confirm that, cortical sources in the parietal and frontal region were connected while performing the balance task with vibrotactile feedback. Overall, it is consistent with their participation in highly integrative tasks marked by complex linkages of visual, vestibular, and proprioceptive processes that great flexibility arises in the described frontal, temporal, and parietal regions. It will be fascinating to see how well the flexibility index of these locations correlates with a well-established assessment of postural performance in transfemoral amputees while they balance with vibrotactile feedback in the future.

Funding Information This work was supported by the Department of Science and Technology (DST), Government of India through the INSPIRE faculty fellowship [DST/INSPIRE/04/2022/000259].

Conflicts of Interest The authors declare no conflict of interest.

Acknowledgment We warmly thank all the volunteers who participated in the study and willingly gave us several hours of their time. We would like to thank the Department of Science and Technology (DST) for funding this research work.

Author's Contributions Conceptualization, Supervision, Review, and Suggestions: **Deepak Joshi**; Funding acquisition, Subject recruitment, Data collection, Writing-original draft preparation, final editing: **Aayushi Khajuria;** and processing, Analysis, Software: **Saurabh Kumar**.

Data availability All data are available by the corresponding author upon request.

REFERENCES

[1] Nashner LM, McCollum G, The organization of human postural movements: a formal basis and experimental synthesis, Behav and Brain Sci. 1985; 8: 135–172.

[2] Fornito A, Zalesky A, and Bullmore E. T, Fundamentals of Brain Network Analysis. Elsevier Inc., 2016.

[3] Thought Co. What Does the Brain's Cerebral Cortex Do? Available from: https://www.thoughtco.com/anatomy-of-the-brain-cerebral-cortex-373217

[4] Isakov E, Mizrahi J, Ring H, Susak Z, Hakim N. Standing sway and weight-bearing distribution in people with below-knee amputations. Archives of Physical Medicine and Rehabilitation 1992; 73:174–178.

[5] Isakov E, Mizrahi J, Susak Z, Ona I, Hakim N. Influence of prosthesis alignment on the standing balance of below-knee amputees. Clinical Biomechanics 1994; 9:258–62.

[6] Buckley JG, O'Driscoll D, Bennett SJ. Postural sway and active balance performance in highly active lower-limb amputees. American Journal of Physical Medicine and Rehabilitation 2002; 81:113.

[7] Vrieling A, Van Keeken H, Schoppen T, Otten E, Hof A, Halbertsma J, Postema K. Balance control on a moving platform in unilateral lower limb amputees. Gait and Posture 2008; 28:222–8.

[8] Vanicek N, Strike S, McNaughton L, Polman R. Postural responses to dynamic perturbations in amputee fallers versus non-fallers: a comparative study with able-bodied subjects. Archives of Physical Medicine and Rehabilitation 2009; 90:1018–25.

[9] William C. Miller et al., The influence of falling fear of falling and balance confidence on prosthetic mobility and social activity among individuals with a lower extremity amputation, Archives of physical medicine and rehabilitation 2001; 82: 1238-1244.

[10] Karl A, Birbaumer N, Lutzenberger W, Cohen LG, and Flor H. Reorganization of motor and somatosensory cortex in upper extremity amputees with phantom limb pain. The Journal of Neuroscience: The Official Journal of the Society for Neuroscience, 2001.

[11] Barnett CT, Vanicek N, Polman RCJ, Postural responses during volitional and perturbed dynamic balance tasks in new lower-limb amputees: a longitudinal study, Gait Posture. 2013; 37: 319–325.

[12] Dulmen SV, Sluijs E, Dijk LV, Ridder DD, Heerdink R, and Bensing J, Patient adherence to medical treatment: A meta-review. BMC Health Serv. Res. 2007; 7.

[13] Crea S, Cipriani C, Donati M, Carrozza M C, and Vitiello N, Providing time-discrete gait information by wearable feedback apparatus for lower-limb amputees: usability and functional validation. IEEE Trans Neural Syst Rehabil Eng 2015; 23: 250–257.

[14] Vimal AK, Godiyal AK, Singh U, Bhasin S, Joshi D, Transfemoral amputee's limit of stability and sway analysis during weight shifting exercise with a vibrotactile feedback system. Somatosensory and Motor Research 2019; 36: 31-41.

[15] Rusaw D, Hagberg K, Nolan L, Ramstrand N. Can vibratory feedback be used to improve postural stability in persons with transtibial limb loss? J. Rehabil. Res. Dev. 2012; 49: 1239-1254.

[16] Aayushi Khajuria, Deepak Joshi, Effects of vibrotactile feedback on postural sway in trans-femoral amputees: A wavelet analysis. J Biomech.2021; 115:110145. https://doi.org/10.1016/j.jbiomech.2020.110145.

[17] Aayushi Khajuria, Deepak Joshi, EEG-explained cortical correlates of transfemoral amputees during balancing with vibrotactile feedback: A pilot study, Medical Engineering & Physics, 2022; 101: 1350-4533, https://doi.org/10.1016/j. medengphy.2022.103772.

[18] Bassett D. and Sporns O. Network Neuroscience. Nature Neuroscience 2017; 20: 353-364. https://doi.org/10.1038/nn.4502.

[19] Barollo F, Hassan M, Petersen H, Rigoni I, Ramon C. et al., Cortical Pathways During Postural Control: New Insights from Functional EEG Source Connectivity, IEEE Transactions on Neural Systems and Rehabilitation Engineering 2022; 30: 72-84. https://doi.org/10.1109/TNSRE.2022.3140888.

[20] Kennett R. Modern electroencephalography. J Neurol. 2012; 259(4):783-9. https://doi.org/10.1007/s00415-012-6425-6.

[21] Hassan M, Dufor O, Merlet I, Berrou C, Wendling F. EEG source connectivity analysis: from dense array recordings to brain networks. PLoS One. 2014; 9(8): e105041. 10.1371/journal.pone.0105041.

[22] Gwin JT, Gramann K, Makeig S, Ferris DP. Electrocortical activity is coupled to gait cycle phase during treadmill walking. Neuroimage 2011; 54: 1289–1296.

[23] Wagner J, Solis-Escalante T, Grieshofer P, Neuper C, Muller-Putz G, Scherer R. Level of participation in robotic-assisted treadmill walking modulates midline sensorimotor EEG rhythms in able-bodied subjects. Neuroimage 2012; 63: 1203–1211.

[24] Gramann K, Gwin JT, Ferris DP, Oie K, Jung TP, Lin CT, Liao LD, Makeig S. Cognition in action: imaging brain/body dynamics in mobile humans. Rev Neurosci 2011; 22: 593–608.

Authorized licensed use limited to: DELHI TECHNICAL UNIV. Downloaded on June 14,2023 at 05:38:30 UTC from IEEE Xplore. Restrictions apply.
© 2023 IEEE. Personal use is permitted, but republication/redistribution requires IEEE permission. See https://www.ieee.org/publications/rights/index.html for more information.

This article has been accepted for publication in IEEE Transactions on Cognitive and Developmental Systems. This is the author's version which has not been fully edited and content may change prior to final publication. Citation information: DOI 10.1109/TCDS.2023.3281877

[25] Makeig S, Jung TP, Bell AJ, Ghahremani D, Sejnowski TJ. Blind separation of auditory event-related brain responses into independent components. Proc Natl Acad Sci USA 1997; 94: 10979–10984.

[26] Sullivan EV, Rose J, Rohlfing T, and Pfefferbaum A, Postural sway reduction in aging men and women: Relation to the brain structure, cognitive status, and stabilizing factors, Neurobiological Aging 2009; 30 (5): 793–807.

[27] Rigoni I, Degano G, Hassan M. *et al.* Sensorimotor recalibration of postural control strategies occurs after whole body vibration. Scientific Reports 2023; 13: 522. https://doi.org/10.1038/s41598-022-27117-7

[28] Winter DA, Patla AE, Prince F, Ishac M, Gielo-Perczak K. Stiffness control of balance in quiet standing. J Neurophysiology 1998; 80:1211–21.

[29] Chang C, Hsu S, Pion-Tonachini L, Jung T. Evaluation of artifact subspace reconstruction for automatic artifact components removal in multi-channel EEG recordings. IEEE Trans Biomed Eng 2020; 67:1114–21. https://doi.org/10.1109/ TBME.2019.2930186.

[30] Palmer JA, Kreutz-Delgado K, Makeig S, AMICA: an adaptive mixture of independent component analyzers with shared components 2011.

[31] Tadel F, Baillet S, Mosher JC, Pantazis D, Leahy RM. Brainstorm: a user-friendly application for MEG/EEG analysis. Comput Intell Neurosci. 2011; 2011:879716. https://doi.org/10.1155/2011/879716.

[32] Hassan M and Wendling F, Electroencephalography Source Connectivity: Aiming for High Resolution of Brain Networks in Time and Space, IEEE Signal Processing Magazine 2018;35: 81-96. https://doi.org/10.1109 /MSP.2017.2777518.

[33] Grech, R, Cassar, T, Muscat, J. *et al.* Review on solving the inverse problem in EEG source analysis. J NeuroEngineering Rehabilitation 2008; 5, 25. https://doi.org/10.1186/1743-0003-5-25

[34] Hincapié AS, Kujala J, Mattout J, Daligault S, Delpuech C, Mery D, Cosmelli D, Jerbi K. MEG Connectivity and Power Detections with Minimum Norm Estimates Require Different Regularization Parameters. Comput Intell Neurosci. 2016; 2016: 3979547. https://doi.org/10.1155/ 2016/3979547.

[35] Desikan RS, Ségonne F, Fischl B, Quinn BT, Dickerson BC, Blacker D, Buckner RL, Dale AM, Maguire RP, Hyman BT, Albert MS, Killiany RJ. An automated labeling system for subdividing the human cerebral cortex on MRI scans into gyral based regions of interest. Neuroimage. 2006; 31(3): 968-80. https://doi.org/10.1016/j.neuroimage.

[36] Wendling F, Chauvel P, Biraben A, Bartolomei F. From intracerebral EEG signals to brain connectivity: identification of epileptogenic networks in partial epilepsy. Front Syst Neurosci. 2010; 4:154. https://doi.org/10.3389/fnsys.2010.00154.

[37] Hassan M, Merlet I, Mheich A, Kabbara A, Biraben A, Nica A, Wendling F. Identification of Interictal Epileptic Networks from Dense-EEG. Brain Topogr. 2017; 30:60-76. https://doi.org/10.1007/s10548-016-0517-z.

[38] Fornito A, Zalesky A, Bullmore ET. Network scaling effects in graph analytic studies of human resting-state FMRI data. Front Syst Neurosci. 2010 Jun 17; 4:22. https://doi.org/10.3389/fnsys.2010.00022.

[39] Garrison KA, Scheinost D, Finn ES, Shen X, Constable RT. The (in)stability of functional brain network measures across thresholds. Neuroimage. 2015 Sep; 118: 651-61. https://doi.org/10.1016/j. neuroimage.2015.05.046.

[40] Hassan M, Merlet I, Mheich A, Kabbara A, Biraben A, Nica A, Wendling F. Identification of Interictal Epileptic Networks from Dense-EEG. Brain Topogr. 2017 Jan;30(1):60-76. doi: 10.1007/s10548-016-0517-z.

[41] Kabbara A, Paban V, Hassan M. The dynamic modular fingerprints of the human brain at rest. Neuroimage. 2021 Feb 15; 227:117674. https://doi.org/10.1016/j.neuroimage.2020.117674

[42] Zalesky A, Fornito A, Bullmore ET. Network-based statistic: identifying differences in brain networks. Neuroimage. 2010 Dec; 53(4):1197-207. doi: 10.1016/j.neuroimage.2010.06.041.

[43] Mierau A, Pester B, Hülsdünker T, Schiecke K, Strüder HK, Witte H. Cortical Correlates of Human Balance Control. Brain Topogr. 2017 Jul;30(4):434-446. doi: 10.1007/s10548-017-0567-x.

[44] Peterson SM, Ferris DP. Group-level cortical and muscular connectivity during perturbations to walking and standing balance. Neuroimage. 2019 Sep; 198:93-103. doi: 10.1016/j.neuroimage.2019.05.038.

[45] Schoffelen JM, Gross J. Source connectivity analysis with MEG and EEG. Hum Brain Mapp. 2009 Jun;30(6):1857-65. doi: 10.1002/hbm.20745.

[46] Buchanan CR, Bastin ME, Ritchie SJ, Liewald DC, Madole JW, Tucker-Drob EM, Deary IJ, Cox SR. The effect of network thresholding and weighting on structural brain networks in the UK Biobank. Neuroimage. 2020 May 1; 211:116443. doi: 10.1016/j.neuroimage.2019.116443.

[47] Adamovich T, Zakharov I, Tabueva A, Malykh S. The thresholding problem and variability in the EEG graph network parameters. Sci Rep. 2022 Nov 4;12(1):18659. doi: 10.1038/s41598-022-22079-2.

[48] Dimitriadis SI, Salis C, Tarnanas I, Linden DE. Topological Filtering of Dynamic Functional Brain Networks Unfolds Informative Chronnectomics: A Novel Data-Driven Thresholding Scheme Based on Orthogonal Minimal Spanning Trees (OMSTs). Front Neuroinform. 2017 Apr 26; 11:28. doi: 10.3389/fninf.2017.00028.

[49] Santarnecchi E, Galli G, Polizzotto NR, Rossi A, Rossi S. Efficiency of weak brain connections support general cognitive functioning. Hum Brain Mapp. 2014 Sep;35(9):4566-82. doi: 10.1002/hbm.22495.

[50] Kringelbach ML. The human orbitofrontal cortex: linking reward to hedonic experience. Nat Rev Neurosci. 2005 Sep;6(9):691-702. doi: 10.1038/nrn1747.

[51] Barnett CT, Vanicek N, Polman RCJ, Postural responses during volitional and perturbed dynamic balance tasks in new lower limb amputees: a longitudinal study, Gait Posture, 2013; 37: 319–325.

[52] Fujita H, Kasubuchi K, Wakata S, Hiyamizu M, Morioka S. Role of the Frontal Cortex in Standing Postural Sway Tasks While Dual-Tasking: A Functional Near-Infrared Spectroscopy Study Examining Working Memory Capacity. Biomed Res Int. 2016; 2016:7053867. doi: 10.1155/2016/7053867.

[53] Schall JD, Frontal Eye Fields, in Encyclopedia of Neuroscience, Springer Berlin Heidelberg 2008, 1635–1638.

[54] Lavin C, Melis C, Mikulan E, Gelormini C, Huepe D, Ibañez A. The anterior cingulate cortex: an integrative hub for human socially driven interactions. Front Neurosci. 2013; 7: 64. doi: 10.3389/fnins.2013.00064.

[55] Slobounov S, Cao C, Jaiswal N, Newell KM. Neural basis of postural instability identified by VTC and EEG. Exp Brain Res. 2009 Oct;199(1):1-16. doi: 10.1007/s00221-009-1956-5.

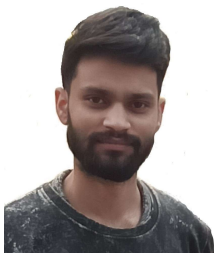

Saurabh Kumar is a PhD scholar in the Centre for Biomedical Engineering, Indian Institute of technology Delhi (IIT Delhi). He completed his post-graduation in Signal Processing and Digital Design from Delhi Technological University, New Delhi, during which he learned to analyze EEG signals during motor imagery. He is studying the mechanics of human, neural control, and physiology to understand how nervous systems control our movements. He is also interested in technologies that use neural activity readings to control external devices.

Aayushi Khajuria is a DST Inspire Faculty at the Department of NMR, All India Institute of Medical Sciences (AIIMS), New Delhi. She received her Ph.D. in Biomedical Engineering from Indian Institute of Technology Delhi (IIT Delhi). Her research interests explore the understanding biomechanics, neuromechanics and biofeedback for the rehabilitation of lower limb amputees and Parkinson's patients. She is actively engaged in the projects related to experimental and signal processing techniques to understand the human cortical activity with Electroencephalography (EEG).

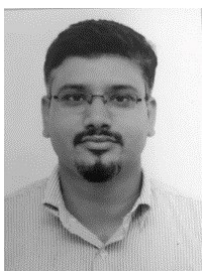

Deepak Joshi is a faculty at Biomedical Engineering at IIT Delhi and All India Institute of Medical Sciences Delhi. He received his PhD in biomedical engineering from Indian Institute of Technology (IIT) Delhi. He has been working in the area of neuroprosthetics and neurorehabilitation for last nearly fourteen years. Before joining IIT Delhi, he worked at various places including National University of Singapore, Newcastle University UK, and University of Oregon, USA. Dr. Joshi's current research work combines experimental and computational techniques to understand the neural correlates during balancing and seamless transitions during walking.

Authorized licensed use limited to: DELHI TECHNICAL UNIV. Downloaded on June 14,2023 at 05:38:30 UTC from IEEE Xplore. Restrictions apply.
© 2023 IEEE. Personal use is permitted, but republication/redistribution requires IEEE permission. See https://www.ieee.org/publications/rights/index.html for more information.

AIP Conference Proceedings

RESEARCH ARTICLE | JUNE 22 2023

Ground improvement technique by soil nailing: A theoretical analysis FREE

Prashant C. Ramteke ✉; Anil Kumar Sahu

Check for updates

AIP Conference Proceedings 2810, 050001 (2023)
https://doi.org/10.1063/5.0146861

View Online Export Citation CrossMark

28 June 2023 04:23:34

AIP Advances
Why Publish With Us?
25 DAYS average time to 1st decision
740+ DOWNLOADS average per article
INCLUSIVE scope
Learn More
AIP Publishing

AIP Publishing

Ground Improvement Technique by Soil Nailing: A Theoretical Analysis

Prashant C. Ramteke [1, 2, a)] and Anil Kumar Sahu [1]

[1] *Civil Engineering Department, Delhi Technological University Delhi, New Delhi – 110042, India*
[2] *Civil Engineering, G. B. Pant, DSEU Okhla-III campus, New Delhi-110020, India*

[a)] Corresponding author: prashant_2k16phdce12@dtu.ac.in

Abstract: Soil nailing is a versatile construction technique used in stabilizing natural as well as man-made earth slopes. In Europe, this technique was initially developed and probable in various provinces. Now, this technique is widely used worldwide and used in India also. The process of soil nailing is simply embracing reinforcement for passively strengthening soil slopes. The soil nailing is mostly incumbent on the method of construction as well as the type and nature of soil or rock. The nail bending, dilation, soil moisture, overburden pressure, grout pressure, and nail roughness also affect the soil nail resistance. This paper aims to explore some important ideas or state of the art on ground improvement techniques, such as nailed soil slope and systematic techniques prolonged by a broad investigation of the method of slope stability.

28 June 2023 04:23:34

INTRODUCTION

Soil nailing is used in the construction of highways, railways, dams, etc. for the embankment. When embankments are constructed on stable ground with good geotechnical characteristics, there will not be difficulties due to the compressibility and shear strength of the soil. If they are built on unreliable ground, this may be contradictory. Due to the unapproachability of appropriate land for construction, many projects are forced to be accepted on soft lands. Over the past few decades, construction on the lenient ground has amplified due to more demand for construction and the non-availability of suitable land because of the fast growth of the world population and the need for infrastructure development. Generally, geotechnical engineers are facing many difficulties while constructing and designing embankments or slopes over unreliable/unstable ground. Because soft soils have (a) low bearing capacity (b) excessive settlements, (c) high compressibility, and (d) insufficient shear strength, etc. These embankments will undergo large deformations and lateral movements, which are likely to cause the failure of the embankment and structure. Hence, the soft ground has to be improved before using it for project work to prevent these incidents. Various techniques have been used for ground improvement like vertical drains, preloading, stepped construction, excavating the existing soft soil and replacing it with suitable materials, grout injection, reinforcing the embankment with geo-grids, or providing additional supports by adding column supports [22]. Ground improvement technique has role play in (i) increase in bearing capacity of soil, (ii) increase in shear strength of soil, (iii) increase in density of soil strata (iv) provide lateral stability (v) decrease imposed loads, (vi) increase in liquefaction resistance, (vii) control deformations, (viii) control settlement, (x) accelerated consolidation, and (x) fill voids [42, 43].

CONVENTIONAL GROUND IMPROVEMENT TECHNIQUES

Mitchell [22]; Terashi and Juran [29] has explained various ground improvement techniques as under:

Reinforcement. The main function of reinforcement is to provide lateral stability and improve engineering characteristics. The methods of reinforcement are: (a) Mechanically stabilized earth (b) Fiber reinforcement (c) Soil nailing/anchoring (d) Column supported embankments (e) Micro piles (f) Geosynthetic reinforced embankments (g) Columns: (i) Stone and lime columns (ii) Jet grouting (iii) Aggregate piers (iv) Geotextile encased columns (v)

International Conference on Smart Materials and Structures, ICSMS-2022
AIP Conf. Proc. 2810, 050001-1–050001-12; https://doi.org/10.1063/5.0146861
Published by AIP Publishing. 978-0-7354-4562-8/$30.00

Sand compaction piles (vi) Dowelling etc. enlightened in their research/study by Azzam [45]; Cruyssen and Van Der [47]; Mishra [4]; Mitchell [22].

Densification. It increases bearing capacity, density, strength of cohesive soils, frictional strength, decreases compressibility, liquefaction resistance, etc. The methods of densification are: (a) Dynamic compaction (b) Compaction grouting (c) Vibroflotation (d) Vibrocompaction (e) Blasting compaction (e) Surface compaction [4, 22,43]

Consolidation. The rate of consolidation is accelerated, increased strength, and reduced settlement of soil strata. The methods of consolidation are: (a) Preloading with vertical drains (b) Preloading without drains (c) Electro-osmosis (d) Vacuum consolidation. [4, 22, 43].

Chemical Treatment. It increases density, fills voids, forms seepage cut-offs, and increases compressive as well as tensile strength, etc. Methods of chemical treatment are: (a) Lime columns (b) Compaction grouting (c) Jet grouting (d) Deep soil mixing (wet & Dry) (e) Bulk filling (f) Fracture grouting (g) Permeation grouting. [22, 43]

Load Reduction. The main function of load reduction is reduced settlement and increased slope stability. In this category, the load is reduced on foundation soils. Methods of load reduction are: (a) Geofoam (b) Foamed concrete and (c) lightweight fills etc. [43]

Biotechnical stabilization. The function of biotechnical stabilization is to increase strength and reinforce the soil strata. Methods are (a) Microbial methods and (b) Vegetation in slopes as reinforcement [4, 43]

Thermal stabilization. This technique is applied to the enhancement of shear strength and provide cut-offs. Thermal stabilization methods are: (a) Ground heating and verification (b) Ground freezing [22, 43].

SOIL NAILING APPLICATIONS

For excavation utilities, soil nailing of slopes is more suitable [9]. In the past, for repair and stabilization, soil nails have been used for existing bridge abutments, highway cuts, realignment of existing retaining structures, tunnel portals, etc. Soil nailing is used for various purposes. Which are brief in forthcoming heads [14].

Roadway or Highway cut excavations

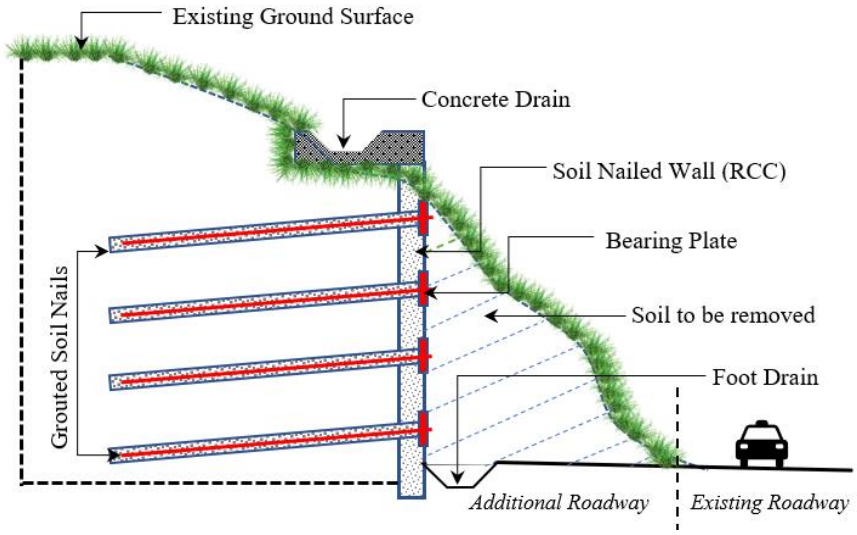

Figure 1. Roadway cut supported with soil nails.

Due to limited excavation and proper right-of-way (ROW), the application of soil nailing is more appealing in roadway cuts. Along the transportation corridor, these factors help in the reduction of environmental impacts.

28 June 2023 04:23:34

During the construction phase, the traffic effect can be minimized by using small equipment in the installation of soil nails. The realities of surplus controls through additional roadway are shown in Fig 1.

Road widening (Under Existing Bridge)

For underpass widening, nail walls are most beneficial. Under a bridge abutment, the installation cost of soil nail wall is more beneficial comparative to other methods. The equipment required for installation and positioning of soil nails is very small and hence may not need to disturb traffic flow while widening the underpass. Underpass can be made functional within a limited time, at a low cost.

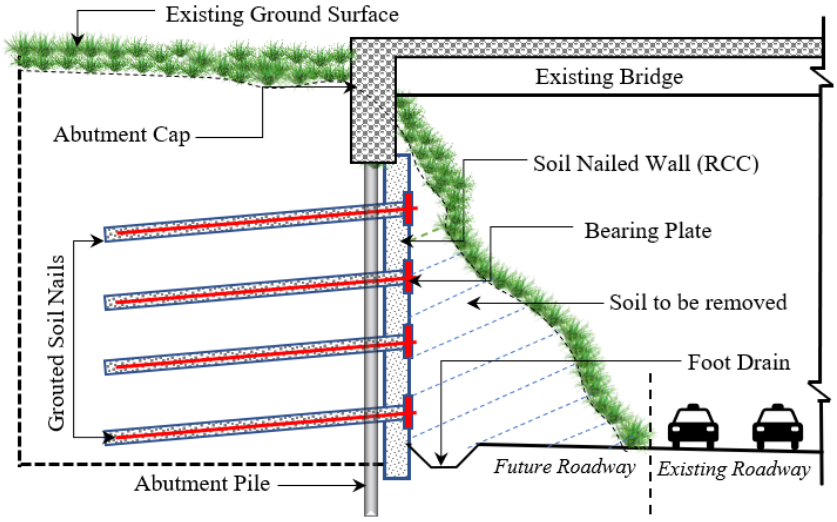

Figure 2. Road widening under existing bridge.

The necessity of Soil nailing is prudently planned and well designed for the length, inclination, location, etc. The nails do not intervene in existing bridge girders and the block foundation. The upper nails should be located in a space between the bridge girders. These nails are placed parallel to the bridge girder. In the revised arrangement of vertical micro-piles and soil nails have also been used. Micro-piles support the modified abutments and prevent their settlements (Fig. 2). In these applications, the combinatorial use of micro piles and nails are very attractive. The main advantage of soil nailing in this application is to speed up construction. During the widening or construction of the underpass, the bridge remains open for traffic movement.

Figure 3. Tunnel portals Stabilization

28 June 2023 04:23:34

Tunnel portals

The portal of the tunnel can also be stabilized by using soil nails. The principle used in the road cuts is very much applicable to soil nails in tunnel portions with due care and consideration in the design and its construction (Fig. 3). In tunnel portals, the following consideration should be taken into account while using soil nailing: (1) Shotcrete facing provided above the tunnel for vertical stability. (2) The possible transmission of soil wedge load transfer to the tunnel structure at the entrance. (3) The interaction amongst soil nails near the portal (4) Tunnel lining and initial shotcrete support need to be thoroughly calculated. The arrangement of soil nails may differ from traditional use in roadway applications. Nails should be fixed with a suitable lateral slope and a vertical direction to avoid interference with tunnel support constituents.

Existing retaining structures, repair, and reconstruction

Nails are used to reinforce the soil structure that is to maintain the stability of the structure [21]. Such as, Mechanically Stabilized Earth (MSE) walls may show exorbitant distortion due to weak construction and underprivileged design or both. The soil nail can be placed in front of the MSE wall when it is stable and resists load while drilling. When the MSE wall continues to deform, it transfers the load on the nails and backfill of the wall. There will be the requirement of special concern in these cases to transfer the load to the stable soil located at the back of the MSE-reinforced segment of soil. The stability of the existing MSE wall should not be damaged by the drilling and grouting process. The arrangement of existing road widening is shown in Fig 4. For support stabilizing the MSE and masonry walls selection of a suitable bearing plate is very important in soil nailing. Without damage to the stable facing the bearing plate sustains the load completely [5]. In most cases, going through the load considered on the bearing plate shall govern the design [23].

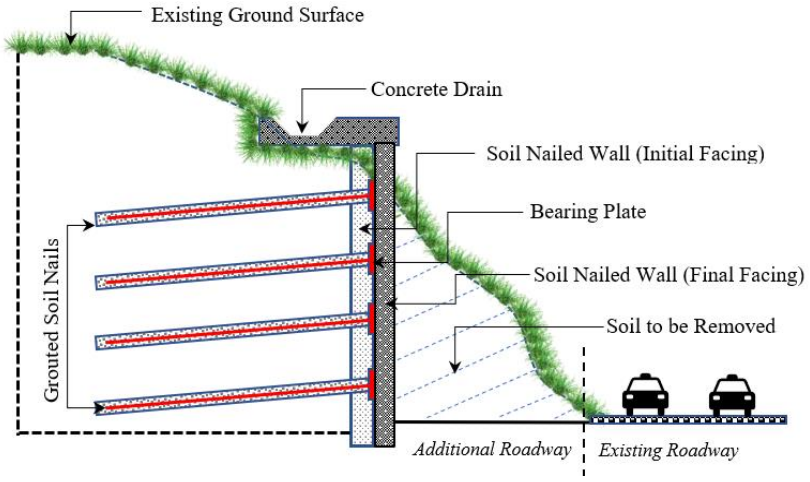

Figure 4. Typical cross-section of a soil nail wall.

Hybrid soil nail wall systems

Soil nail walls are often used with alternative techniques like MSE walls and ground anchor walls to exploit both techniques. This example may arise with the values related to the various earth-retaining systems having area units too high and fancy wall layout. Wood et al. [41], suggested combining soil nail wall and MSE wall gives a much more economical design than used in the entire elevation of MSE walls. A hybrid soil nail and MSE wall are shown in Fig 5. The other example of a hybrid nail wall is the juxtaposition of ground nails with soil nails. This is applicable where utilities or alternative underground barriers exist. This application isn't able to keep soil nails within the upper section. In this situation, the wall face is often designed to behave as a cantilever. One or two rows of soil anchors are provided for lateral restriction on the cantilever. Nails are used at the bottom rows. Soil nails generally do not seem to be suitable to behave properly instability on deep-rooted slip surfaces. Ground anchors are often introduced with soil nails wherever the deep roots of the proposed roadway cuts have the potential for

28 June 2023 04:23:34

instability. Soil nail walls can also be used as support to the topmost gradient for layer walls and provide global stability.

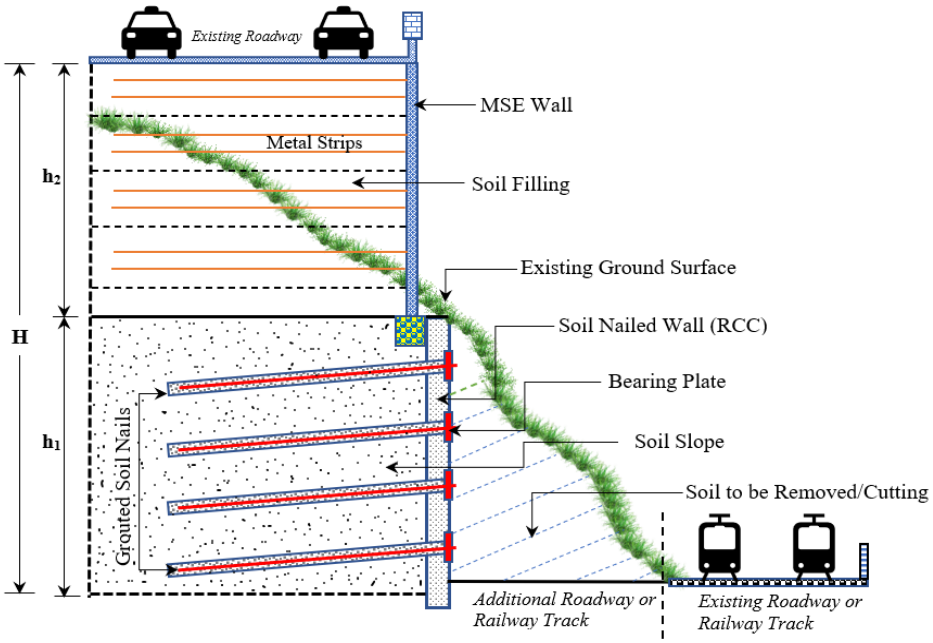

Figure 5. Hybrid soil nail/MSE wall.

SMSE (Shored Mechanically Stabilized Earth) walls

To widen low-traffic volume roads from place to place in steep terrain, the soil nail walls are progressively used with MSE walls in the coalition. To execute the construction of the MSE wall in the flat ground, the reinforcement of the soil needs excavation to install a flat bench. Below the toe of the wall, the stability of the slope increases with the specified embedment depth. For the MSE wall, excavation becomes unfeasible if the slope is very steep, especially in circumstances wherever transportation should be maintained throughout widening [26]. To stabilize the initial slope (or back-cut) ceramics are often used as shoring. Traditional MSE wall construction in front of the soil nail wall is shown in Fig 6. Soil nails will expressively extenuate protracted lateral pressure on the MSE wall. The soil nail wall is considered to be a permanent wall. This arrangement is said to be an SMSE wall. It's modernized in the FHWA report in the L.R.F.D. platform [36].

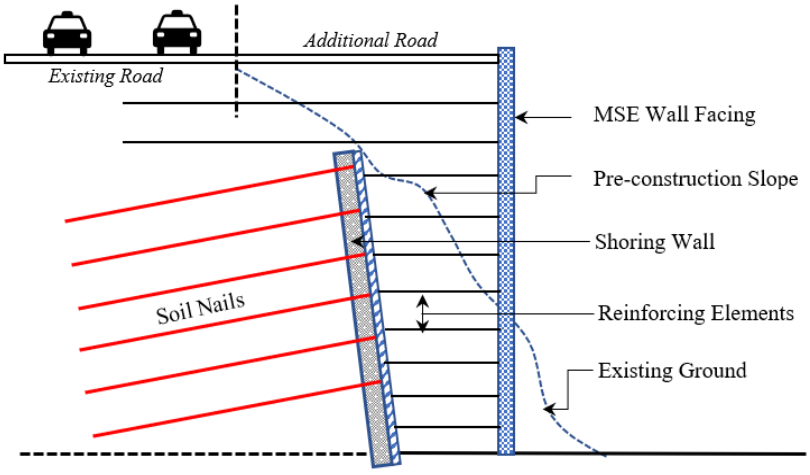

Figure 6. SMSE wall for steep terrain.

28 June 2023 04:23:34

LITERATURE REVIEW

A literature study has been carried out from various sources like scholarly articles, national as well as international technical journals, and other sources which are relevant to the particular issue and areas of research in slope stabilization and soil nailing. This literature study endues statements, delicate evaluation, description, and summary of the works so far done concerning the research problem being investigated. Soil nailing is commonly used for steep slopes. This approach also represents environmental and economic benefits due to its distinctiveness to assent the growth of vegetation (i.e. green walls). Generally, soil nails are composed of steel bars grouted with cement [20]. The grout protects the steel bars from corrosion and increases the life and efficiency of nail bars [12]. Sometimes at the face of construction, a soil-nailed wall with nailhead plates is provided. Soil nailing is effective, economical, and easy to construct method as compared to other conventional methods [16, 46].

Literature review based on numerical Methods (FEM and FDM)

Either softwares are commercial packages or self-developed packages and used in design of the nailing system. The design of soil-nailed retaining structures is currently based on different methods of FEM analysis. A brief review of the work carried out by various researchers' is tabulated below:

Table 1. Literature Review on methods of FEM analysis used

S.N.	Method used	Researchers	Brief of research Work
(A)	**Finite Element Method (FEM)**		
1.	2D FEM	Ann et al. (2004)	The evaluation of FEM with field data results displayed Mohr-Coulomb failure criteria.[40]
2.	2D and 3D	Olia and Liu (2011)	Numerical behaviour of soil nail wall during different stages of construction. [1]
3.	FEM	Sawicki et al.(1988)	Studied and Compared experimental and numerical data to obtain stresses in nails. [3]
4.	3D FEM	Zhang Mingju et al. (1999)	A parametric study of ground movement analysis of soil nailing construction by FEM.[30]
5.	3D FEM using ABAQUS	Ng and Lee (2002)	A parametric study of the use of soil nails for stabilizing tunnel face. [6]
6.	2D FEM using PLAXIS	Singh and Babu (2010)	Studied the nail wall performance by using different soil models. [44]
7	2D FEM using PLAXIS	Azzam and Shobhey (2019)	By using different sand slope models, the failure pattern of the sandy slope with and without soil nailing under seismic loading has been found. [45]
8.	FEM using 2D PLAXIS	Sharma et al. (2018)	Examined a comparative study between a factor of safety of conventional soil nail and helical soil nail. [31]
9.	SLOPE/W & 2D PLAXIS	Rawat and Gupta (2016)	Compared result /outcomes of PLAXIS 2D (finite element based) and SLOPE/W (Limit equilibrium based) for reinforced soil slope. [39]
10	FEM using 2D PLAXIS	Potgieter and Jacobsz (2019)	Compared the factors of safety in lateral support design, from limit equilibrium and finite element analysis. [25]
(B)	**Finite Difference Method (FDM)**		
11.	FDM using FLAC	Babu and Murthy (2002)	Investigated the effect of construction factors on soil nailed wall behaviour. [15]
12.	FDM using FLAC	Cheuk et al. (2005)	Investigated the soil nailed walls behaviour in loose fill slopes. [8]
13.	FDM using FLAC	Wei and Cheng (2010)	Made comparison between SRM and LEM for analysis of soil-nailed walls.[46]

28 June 2023 04:23:34

Literature review based on physical modelling

Many researchers, such as Hayashi et al. [38], Jewell and Wroth [32], Jewell [35], Marchal [24], Palmeira and Milligan [10], etc, has demonstrated various laboratory experiment to investigate the effect on strengthening of soil due to the leaning of nails.

Hayashi et al. [38], conducted a shear test on sand samples with polymer grids or bronze bars as reinforcement on a specially designed versatile shear testing apparatus. The shear box is designed to accommodate 20 elements made from aluminum. To reduce the friction between elements, flat bearings are used with four guided pins and rods to restrain each element. The shear box is devised to induce uniform shear deformation. A specimen of size 200 x 200 x 200 mm is used and a 0.3 mm thick latex rubber membrane is used for enveloping the specimen. This shear test is conducted in several patterns of strain conditions [38]. During the testing process to measure the stress changes in the reinforcement, the strain gauges were installed. Orientation of reinforcement between 20^0 and -20^0 resulted in changes in the soil shear strength. The finding of the test confirmed that particular orientation of the reinforcement has resulted in enhanced soil shear strength [38, 48]

Jewell and Wroth [32], suggested that the shear strength of the soil is upgraded through the tensile force in two ways: (1) decreasing the driving shear force and (2) Increasing the normal stress. The collective reinforcement force and shear strength of soil both are directly dependent on each other.

Jewell [35] carried out a study on grid reinforcement and tests on reinforced sand samples with bars in series on direct shear box tests and examined the basic behavior of reinforced soils. An important investigation of his work is, the reinforced soil shear strength is incumbent on the bending reinforcement. Jewell's research juxtaposes the stress patterns. In this stress pattern, the researcher has compared the results of soil tests between reinforced and unreinforced samples. The reinforcement in sand causes soil stress improvement. Near the reinforcement, the soil strains are smaller and failure avoids the formation of the shear plane. Friction between the reinforcement and the soil develops the tensile force. Soil starts to gain increase in the shear strength when tensile stress increase in the direction of reinforcement. In the direction of a narrower pressure increase, the shear strength of the reinforced soil decreases. This suggests that the reinforcement should be placed in the direction of main tensile reinforcement for optimizing the enhancement of strength of the soil. The strength improvement is reduced after the reinforcement diverges from its optimal orientation [38, 48].

Marchal [24] reported the behavior of reinforced soil with nails through his laboratory study. For the laboratory test, he has used a device i.e. circular shear box of 500 mm height and 600 mm diameter. The reinforcement was used as hardened steel bars with a 50 mm width and 8.8 mm thickness and a thickness of 2 mm flat bars with flexible aluminium alloy and width varying from 10 to 20 mm. To measure bending moments and stresses, nails were fitted with tension gauges. In this study, they have installed nails on different inclinations [48]. Marchal [24] identified shear resistance for reinforced soils; it indicated the presence of a peak, for larger shear strains which was a decrease in the constant value. For different reinforcement orientations, the shear resistance ratio was measured for reinforced soils (τ') to unreinforced soils (τ). Researcher optimized the function of the orientation of nails for (a) Flexible reinforcement and (b) Rigid reinforcement. Compressive force or tensile force were primarily mobilized after reinforcements were progressively subordinated to shear forces, similar to both flexible and rigid reinforcements. After soil shear displacement the P_S ratio curves moved towards a constant minimum value of 60 to 70 mm for flexible and 20 mm for rigid reinforcements. Results of the study suggest that reinforcement orientation plays a vital role in overall soil shear strength improvement. The research also suggested the presence of an optimal reinforcement orientation in the context of soil strengthening. Jewell and Jewell et al. [33, 34, 32, 35] also confirmed these findings.

Palmeira and Milligan [10], stated the results of experiments conducted on sand samples by direct shear tests. Sheet reinforcements and a variety of grids were used for reinforcing sand samples. For the experiments 1.0 m x 1.0 m x 1.0 m size direct shear device was used. In the reinforced and unreinforced samples the major strains occur at peak stress ratio. In unreinforced sand samples, the principal tensile stress is inclined at 30° with the vertical direction. A larger proportion of the soil was stretched, which then remained unchanged due to the presence of inclined reinforcements. Dominant tensile stress orientation was away from the reinforcement and in the central area, stagnant parallel to the reinforcement surface. In the path of principal tensile strains, a layer of reinforcement was aligned. In shear strength, strains lead to enlargement of a reinforced specimen. In the flank of the principal

28 June 2023 04:23:34

tensile stresses, the reinforcement is installed. The horizontal component-part of the reinforced tensile stress intercepted the shear stress evolution. Under the same operational condition of reinforcement, the layer aligned in the direction of principal tensile strain a reinforced sample increases the shear strength as compared to unreinforced soil sample [17]. In the central region of the sample, the reduction in shear strain was caused due to the presence of the reinforcement layer. Wherever the reinforcement layer is placed in the direction of minor principal tensile strain, more shear strain develops because of the contribution from the horizontal components of reinforcement force [17].

Studies involving Soil Nail Bending Stiffness Effect

Direct shear tests were conducted by Marchal [24] on soil nails and described how the shear forces were developed in the reinforcement. Experimental results revealed development in the reinforcement and the deviations amongst the axial tension and the shear force (T/Ps). For flexible and rigid reinforcements, compressive or tensile forces were mobilized first. Shear displacements of the soil are (1) for rigid reinforcement - 20 mm. and (2) for flexible reinforcement- 60 mm to 70 mm.

Davies and Masourier [27], presented the results on the large-scale shear box which was made by steel plates. Observations were made using 25 mm diameter and 2.8 m long aluminium nails for testing on 3000 mm x 1500mm x 1500mm shear box. Researchers observed that when the shear load was applied on the specimen then tensile forces developed in nails. The tensile forces reached a rapid peak after 30mm shear displacement, after that with shear displacement it remained constant. The nail withdrawal capacity was controlled by the tensile force. The shear force was not carried by the nails until the occurrence of 20 mm displacement, thereafter the shear force enhanced continuously. The possible maximum shear force was limited at the nail at plastic moment.

Tan et al. [37], stratified a failure mode series used to describe the lateral action behavior of soil nails. They included: nail yield failure, soil yield failure, and simultaneous yield of both the failures. These are reliant on soil strength and nail, horizontal movement, as well as comparative stiffness. Due to the extent deformation, axial and shear forces developed in the nail. Horizontal resistance of soil wedge taken into account for failure modes [2, 37].

Smith and Su [18], examined soil nailed walls with 3D finite element analysis and concluded that during construction nails developed shear resistance and little bending under service loads. Due to surplus load close to the collapse of the wall the bending moment and shear stress were mobilized [2].

Plumelle et al. [7], examined test results on 7 m height instrumented soil nailed wall. The nailed soil mass saturated progressively and was made to fail. The first mechanism mobilized is tensile force and during excavation, it gradually developed. Additional safety factor was considered in design due to failure on account of large deformations as well as mobilization of bending stiffness.

THE MERITS AND DEMERITS OF SOIL NAILING

During this brief cardinal study, it is observed that soil nailing is the more appropriate method for earthen embankment as well as in rocks also. Some advantages are found during this study are pointed out below:

Advantages of Soil Nailing

1. For short as well as long duration, soil nailing is a more cost-effective method of stabilization of proposed flat as well as steep existing slopes.
2. There is no need to install any structural element at the nethermost of excavation in soil nailed walls.
3. Soil nailing is a more suitable method for many types of soil strata except pebbles.
4. This technique is more suitable in intensive traffic areas because construction/installation of soil nailing requires small equipments as compared to other methods causing minimal obstruction to traffic.
5. During earthquakes, the soil nailed structure performs better due to its elastic properties.
6. A small diameter drilled hole is required for nail installation in case underground obstructions are encountered to solve it instantly.
7. Soil nailed structure is flexible and hence this technique is more suitable under heavy traffic.
8. The requirement of construction material is very less as compared to other methods.

28 June 2023 04:23:34

Disadvantages of Soil Nailing

Soil nailing is a more economical & hard-core stabilization technique but it has a few demerits also, as stated below:

1. Placing the nail in centralized alignment is difficult.
2. Nails are made of steel and hence corrode rapidly. For preventing the nails from corrosion special types of coating around the nails are essential. (i.e. cement paste grout coating, epoxy grout coating, etc.)
3. Highly skilled, experienced, and technical personnel are required for the installation of nails and centralizing the nails in the hole during construction.
4. The special arrangement at the facing side is essential in the form of a bearing plate.
5. Due to the surcharge load, soil pressure acts on the exposed face of an embankment and nailed wall on account of this chances of the embedded plate failure are more. Hence the distinct design of embedded plate becomes mandatory.
6. Due to inadequate grout fill, grout block of nail and grout tends to pull out of the embankment.
7. Routine inspection is required to check the facing, connection between the outer face wall, and a bearing plate fixed with studs and bolts.

IMPORTANT SUGGESTIONS BASED ON COMPREHENSIVE STUDY

From the literature summary, it is suggested that:

1. Nails reinforced in soil slopes provide higher strength and improve the stability of natural as well as manmade slope structures. Hence soil nailing is more suitable in hilly areas where steep slopes are found and landslides may occur.
2. The shear strength of soil mass improves by reinforcing hence providing more resistance to the failures.
3. The soil nailing structure is more flexible and restricts the tension cracks in the slope. Hence soil nailing structures are more suitable in earthquake-prone zones.
4. The amalgamation of deformation in slope and pull-out failure are accepted nail failures.
5. During the loading condition of the slope, the deflections in nails increase at different places with different distributions.
6. In slope failure or slip surface, deformations are estimated according to the localization area. The deformation of the slope is reduced by soil nailing and delays the deformation.
7. Stability of slope may improve by increasing the nail length behind the slip surface or failure surface.

FUTURE SCOPE OF SOIL NAILING

1. It can be used for amelioration in the excavations, embankment, retaining walls, and stability of slopes.
2. It can be useful to stabilize soil mass or steep slopes in a hilly area where landslides occur.
3. Explore possibilities for use of soil nails in river banks, tunnels, caves, etc.
4. To study system behavior that may be affected by various loading conditions.
5. To prepare guidelines for on-site investigation, soil-nailed design system, distinguished testing, and landscape treatment using soil nails.
6. To compare guidelines for construction, supervision, and control of sloped engineering works with other methods.

PURPOSE OF THEORETICAL ANALYSIS

The main aim of this study is to endorse a standard of good practice for the construction, monitoring, maintenance, and design of soil-nailed systems worldwide. The indication of this literature survey is to convey different parameters of soil nailed systems to professionally qualified engineers and young researchers/learners. This study can help various practicing engineers and researchers who are knowledgeable with the applicable geotechnical engineering principles/moralities and procedures keeping pace of development of transport infrastructure including highways, railways, tunnelling, tunnel portal, etc.

28 June 2023 04:23:34

CONCLUSION

Several available improvement techniques can be used to increase capacity, increase shear strength and replacement of saturated medium soils such as soil preloading with condensate drains, adding stone columns, stabilizers with additives, and thermal methods. Unfortunately, there is limited research that considers all governing factors such as soil bearing capacity, cost of foundation work, simple execution, etc. This paper concluded that there is an essential requirement to study the technique of removal and replacement to improve soil behaviors, keeping in view the geotechnical requirements corresponding to the maximum replacement layer thickness and minimum total cost of foundation work, cost to obtain the most suitable material. It can be concluded from this study that, ground improvement technique such as soil nailing is cost-effective and feasible for soils. Soils have to be remedied and made suitable for construction because soils are weak in strength. Nowadays various technologies are used and tested for the projects of excavation, tunnelling, railways, runways, highways, dams, ports, slope stabilization, industrial structures, etc. For various types of soils such as silt, clay, loose sand, and weak rocks etc. soil nailing method is more effective and hence it has been used worldwide. For ground improvement techniques following points should be kept in mind while designing: Type of soil, Nature of soil, Intensity of loading, and Intensive performance. Before selecting any technique of ground improvement it is important to evaluate (1) available equipment, (2) soil improvement expectation (3) particular method cost, etc. these factors are useful for deciding the selection of the most appropriate method. This theoretical analysis indicated that soil nailing is more effective in imparting stability to the soil, when nails are installed early and cost-effective.

ACKNOWLEDGMENTS

The work presented in this article is supported by Delhi Technological University, Civil Engineering Department, and G. B. Pant, Delhi Skill and Entrepreneurship University, Okhla-III, Campus, New Delhi.

REFERENCES

1. A. Olia and J. Liu, Numerical investigation of soil nail wall during construction. Pan-Am CGS, 2011 Geotechnical Conference, GEO (2011), pp. 8-20.
2. A. S. Stipho, Model Test of Reinforced Earth Retaining Wall, Proceeding Second International Conference Case Histories in Geotechnical Engineering St. Louis, 1-5 June 1988, Paper No. (6.76).
3. A. Sawicki, D. Lesniewska, M. Kulczykowski, Measured and Predicted Stresses and Bearing Capacity of a Full-Scale Slope Reinforced with Nails. Soils and Foundation, Vol. 28(4), 47-56 (1988).
4. B. Mishra, A Study on Ground Improvement Techniques and Its Applications. International Journal Innovative Research in Science Engineering and Technology, 5(1), 72–86 (2016.).
5. B. V. S. Viswanadham and V. Rotte, Effect of facing type on the behaviour of soil- nailed slopes: centrifuge and numerical study. Discov. Publication. 46, 214-223 (October 2015).
6. C. Ng and Lee, A Three-Dimensional Parametric Study of the Use of Soil Nails for Stabilising Tunnel Faces. Computers and Geotechnics. 29(8), 673-697 (2002).
7. C. Plumelle and F. Schlosser, A French National Research Project on Soil Nailing: Clouterre. In: Proceedings of a conference on design and performance of earth retaining structures, Ithaca, USA, (Geotechnical Special Publication No. 18-21 June 1990) (25), 660-675.
8. C. Y. Cheuk, C. W. Ng and H. W. Sun, Numerical Experiments of Soil Nails in Loose Fill Slopes Subjected to Rainfall Infiltration Effects. Computers and Geotechnics; 32(4), 290-303 (2005).
9. D. Bruce, In-situ earth reinforcing by soil nailing. Science Business Media Dordrecht (2), 340–1(1993).
10. E. M. Palmeira, and G. W. E. Milligan, Large Scale Direct Shear Tests on Reinforced Soil. Soils and Foundations, March 1989, Vol. 29(1), 18-30.
11. Fan, Chia-Cheng and Luo Jiun-Hung, Numerical Study on the Optimum Layout of Soil ailed Slopes. Computers and Geotechnics 35(4), 585-599 (2007).
12. FHWA (1993a) FHWA International Scanning Tour for Geo-technology, Soil Nailing Summary Report, Report No. FHWA-PL-93-020, Washington, DC, (September-October 1992).
13. FHWA (1993b) French National Research Project Clouterre, 1991-Recommendations Clouterre 1991, (English Translation) Soil Nailing Recommendations, Report No. FHWA-SA-93-026, Washington, D. C. (1991).

28 June 2023 04:23:34

14. FHWA 1998 Manual for design and construction monitoring of soil nails walls. Federal Highway Publication No. SA-96-069R, U.S. Department of Transportation, Federal Highway Administration, Washington, D. C. (1998).
15. G. Babu, B. R.Murthy and A. Srinivas, Analysis of Construction Factors Influencing the Behaviour of Soil-Nailed Earth Retaining Walls; Ground Improvement, 6(3), 137-143 (2002).
16. G. Gassler and G. Gudehus, Soil Nailing - Some Aspects of a New Technique. International Society of Soil Mechanics and Geotech Engineering. 12(20) 665–670.
17. G. Milligan and T. Kouji, .The Pull-Out Resistance of Model Soil Nails. Soils Found Japanese Geotech Society. 38(2), 179–190 (1998).
18. I. M. Smith and N. Su, Three-dimensional FE Analysis of a Nailed Wall Curved in Plan. International Journal for Numerical and Analytical Methods in Geomechanics. 21, 583-597 (1997).
19. J. A. Porterfield, D. M. Cotton and R. J. Byrne, Soil Nailing Field Inspectors Manual, Project Demonstration 103, Publication No. FHWA-SA-93-068, Federal Highway Administration, Washington, D.C. (1994)
20. J. A. R. Ortigao and E. M. Palmeira, Soil nailing. Handbook of Slope Stabilisation. Verlag Berlin Heidelb. 2004: Chapter 13.
21. J. A. Rodríguez and N. Freitag, Design of reinforced slopes and embankments. Proceeding State of the art. International Society of Soil Mechanics and Geotech Engineering (2009).
22. J. K. Mitchell, "Soil Improvement: State-of-the-Art," 10 International Conference on Soil Mechanics and Foundation Engineering, Stockholm, Sweden; June 1981, Vol. (4), pp.509-565.
23. J. L. Bariaud and Y. Lim, Soil Nailed Wall under Pilled Bridge Abutment: Simulation and Guidelines. Journal of Geotechnical and Geo-environmental Engineering, ASCE; 123(11), 1043-1050 (1997).
24. J. Marchal, Soil Nail-Experimental Laboratory Study of Soil Nail Interaction. Transport and Road Research Laboratory, Department of Transport No. 239 (1986).
25. J. Potgieter and S. W. Jacobsz, Comparing the factors of safety from finite element and limit equilibrium analyses in lateral support design. Technical Paper Journal, South African Institute Civil Engineering. 2019, 61(4), 29-41.
26. K. Morrison, F. Harrison and S. Anderson, Evolution of Mechanically Stabilized Earth Wall Design to Incorporate Permanent Shoring, GEO-Volution, Denver, CO, 2006, pp.149-157.
27. M. C. R. Davies and J. W. Le Masurier, Soil/Nail Interaction Mechanism from Large Direct Shear Tests. Proceedings of the Third International Conference on Ground Improvement Geo-Systems, London: 493-499 (1997).
28. M. F. Stocker, G. W. Korber and G. Gassler, Soil nailing. C.R. Col. Int. Reinforced des. Sols. Paris, 469-474 (1979).
29. M. Terashi, and I. Juran, Ground Improvement- State of the Art. GeoEng-2000, Melbourne, Australia, Invited Papers, Technomic Publishing Company, Inc., Lancaster. 19-24 November 2000, (1), 461-519.
30. M. Zhang, S. Erxiang and C. Zhaoyuan, Ground movement analysis of soil nailing construction by three-dimensional (3-D) finite element modelling (FEM), Computer and Geotechnics, 25, 191-204 (December 1999).
31. P. Sharma, S. Rawat and A. K. Gupta, Comparative Study between Factor of Safety of a Slope using Conventional Soil Nail and Helical Soil Nail. 3rd Himachal Pradesh Science Congress, India, 2018, pp. 1-9.
32. R. A. Jewell and C. P. Wroth, Direct shear tests on reinforced sand. Géo-technique, 37(1), 53-68 (1987).
33. R. A. Jewell and M. J. Pedley, Analysis for Soil Reinforcement with Bending Stiffness. Journal of Geotechnical Engineering, ASCE, 118(10), 1505-1528 (1992).
34. R. A. Jewell and M. J. Pedley, Soil nailing design: the role of bending stiffness. Ground Engineering; 30-36 (March 1990).
35. R. A. Jewell, Some effects of reinforcement on the mechanical behaviour of soils. PhD thesis, University of Cambridge, 1980.
36. R. R. Berg, A. Carlos, Lazarte, R. Helen, E. Jesús, Gómez, Andrew Baxter and Allen Cadden. Soil Nail Walls-Reference Manual, Geotechnical Engineering Circular No. 7, Report No. FHWA-NHI-14-007, National Highway Institute, Washington, DC; (February 2015).
37. S. A. Tan, S. Q. Luo and K. Y. Yong, Simplified models for soil-nail lateral interaction. Ground Improvement, Thomas Telford, October 2000, 4, 141-152.
38. S. Hayashi, H. Ochiai, A. Yoshimoto, K. Sato and T. Kitamura, Functions and Effects of Reinforcing Materials in Earth Reinforcement. (Proceedings of International Geotechnical Symposium on Theory and Practice of Earth Reinforcement, Fukuoka; 5 -7 October 1988), pp.99-104.

28 June 2023 04:23:34

39. S. Rawat and A. K. Gupta, Analysis of a Nailed Soil Slope Using Limit Equilibrium and Finite Element Methods. International Journal of Geosynthetics and Ground Engineering. December-2016; 2(34),1–23.
40. T. Ann, W. Cheang, O. P. Hai and D. Tan, Finite element analysis of soil nailed slope-some recent experience; Proceedings of the third Asian Regional Conference on Geosynthetics, Seoul, Korea, pp.183-192 (2004).
41. T. Wood, P. Jayawickrama, and W. Lawson, Instrumentation and Monitoring of an MSE/Soil Nail Hybrid Retaining Wall, Contemporary Topics in Ground Modification, Problem Soils and Geo-Support, GSP No. 187, Reston, VA, 177-184 (2009).
42. V. Elias, J. Welsh, J. Warren, R. Lukas, J. G. Collin and R. R. Berg, Ground Improvement Methods. FHWA NHI-06-019 (Vol. 1) and FHWA NHI-06-020 (Vol. 2), 1056, (2006).
43. V. R. Schaefer, J. K. Mitchell, R. R. Berg, G. M. Filz and S. C. Douglas, Ground Improvement in the 21st Century: A Comprehensive Web-Based Information System. Conference May 2012, pp.1–22.
44. V. Singh and G. Babu, 2D Numerical Simulation of Soil Nail Walls. Geotechnical and Geological Engineering. 28(4), 299-309 (2010).
45. W. Azzam and Sobhey, Utilization of Soil Nailing Technique to Improve Sand Slopes under Seismic Loading. (International Conference Advance Structures Geotech Engineering, Hurghada, Egypt. April 2019), pp.1– 10.
46. W. B. Wei and Y. M. Cheng, Soil Nailed Slope by Strength Reduction and Limit equilibrium Methods. Computers and Geotechnics. 37(5), 602-618 (2010).
47. W. V. Cruyssen, and J. M. Van Der, Soil improvement experiences in Belgium: part I. Overview and dynamic compaction. Ground Improvement. (1), 147–155 (1997).
48. Y. K. Shiu and G. W. K. Chang, Effects of Inclination, Length Pattern and Bending Stiffness of Soil Nails on Behaviour of Nailed Structures, Government of The Hong Kong GEO Special Project Report No. SPR- 6, (2005).

28 June 2023 04:23:34

Proceedings of the Second International Conference on Applied Artificial Intelligence and Computing (ICAAIC 2023)
IEEE Xplore Part Number: CFP23BC3-ART; ISBN: 978-1-6654-5630-2

Hate Speech Detection using Multimodal Meme Analysis

Aruna Bhat
Computer Engineering
Delhi Technological University
Delhi,India
aruna.bhat@dtu.ac.in

Vaibhav Vashisht
Computer Engineering
Delhi Technological University
Delhi,India
vvashisht2000@gmail.com

Vaibhav Raj Sahni
Computer Engineering
Delhi Technological University
Delhi,India
vaibhavsahniji@gmail.com

Sumit Meena
Computer Engineering
Delhi Technological University
Delhi,India
sumitmeena2902@gmail.com

***Abstract*— Hateful memes, which often contain offensive language and derogatory images, have become increasingly prevalent on social media platforms, posing a significant challenge to content moderation efforts. To address this issue, the proposed approach explores the detection of hateful memes through a multimodal analysis that utilizes both visual and textual modalities. A novel lightweight architecture is proposed which involves generating object tags and image captions and utilising them to combine the visual and textual cues. In the final classification phase, various classification models, such as Support Vector Classifier and Gradient Boosted Decision Trees, are trained. This layer combines the results of concurrent processing branches (textual and visual) to provide predictions for the sample.**

Keywords*— BERT, Hate speech ,Logistic Regression, Multimodal Analysis, ResNet, Support Vector Classifier, Gradient Boosted Decision Tree, Unimodal Analysis

I. INTRODUCTION

Social media platforms today have a significant impact on how individuals live their daily lives. Despite its many advantages, it also has the power to influence religious and public opinion around the globe. It can be used to directly or indirectly insult people on the basis of their race, caste, religion, culture, country, sex, gender identity, and illness or handicap[1]. Online hate speech can lead to polarization of society and hate crimes. Since it is extremely challenging for an individual to keep track of the origin and dissemination of such destructive actions on huge platforms like Twitter, Instagram and Facebook, the task of effectively finding hate speech lies in the hands of the machine learning professionals and the people researching actively in the artificial intelligence domain. Social media is constantly coming up with new memes, making it impossible to manually weed out the offensive ones. As a result, this task essentially requires an automated solution.

Without even utilizing multimodal comprehension and reasoning, baseline models trained on the language domain can excel in tasks like VQA and multimodal machine translation [2]. On the other hand, the Hateful Memes Dataset of Facebook is created in a way that only models that can acquire a good multi-modal understanding of the data will succeed, rendering uni-modal models that simply exploit the language or vision domain independently ineffective.

Let's take the phrase "dishwasher for sale, missing parts" as an example. When coupled with the equally innocent image of a girl missing a hand, this harmless sentence turns into a nasty tone (Fig. 1). The detection of hate speech on online social media platforms is a significant real-world issue, therefore this task set is a great first step in making it easier to construct reliable multi-modal models.

The majority of previous work baselines attempt to resolve this issue by aligning the two modalities, but they struggle since they are ineffective in combining the textual and visual inputs. In order to investigate the two modalities and comprehend the context and interaction between them, the aim is to study those using pre-trained models of image captioning and object detection in the present research. The textual part of hate speech is frequently given more attention in several baselines. By obtaining a deeper comprehension of the image through captioning and object tag detection, an attempt is being made to harmonize the two modalities' representations here.

2023 2nd International Conference on Applied Artificial Intelligence and Computing (ICAAIC) | 978-1-6654-5630-2/23/$31.00 ©2023 IEEE | DOI: 10.1109/ICAAIC56838.2023.10140393

Authorized licensed use limited to: DELHI TECHNICAL UNIV. Downloaded on June 14,2023 at 05:09:49 UTC from IEEE Xplore. Restrictions apply.

Fig. 1. Hateful meme detection as a multimodal analysis

II. Related Works

Hate speech detection is an important tool for promoting online safety, protecting vulnerable groups, and combating hate speech and discrimination in society. Hate speech detection is a challenging task because hate speech can be expressed in many different ways, including through coded language and sarcasm. The authors of [3] have proposed detailed process of improving LSTM used for hate speech detection using knowledge distillation. Hate speech detection typically involves the use of natural language processing (NLP) techniques, such as sentiment analysis to analyze text data and identify patterns that indicate hate speech. In [4], the authors have proposed a multimodal sentiment analysis technique using Bert embedding and Resnet-50. Machine learning researchers are increasingly interested in multimodal analysis. It offers superior outcomes and context inference in addition to being a good substitute for unimodal analysis.

Multimodal hate speech detection is an emerging research area that involves analyzing multiple modes of communication, such as text, images, and videos, to identify hate speech content. Multimodal hate speech detection aims to overcome the limitations of text-based hate speech detection by analyzing the additional context provided by visual and audio elements. Due to unimodal models' subpar performance on tasks requiring multiple modalities, the use of multimodal techniques to learn the representation and links between text and images have increased. In such methods, vision and language models to interpret the links and interaction between the different modalities and achieve good results. State of the art multimodal techniques aim to process the different modalities by employing an early-fusion or a late-fusion approach. Prior to the final classification layer, late-fusion techniques typically use unimodal approaches to separately process the two different data modalities and then merge their characteristics (for example by concatenation). On the other hand, early fusion techniques like VisualBERT [5] use increasingly complex architectures to handle text and images concurrently in their architecture.

MMHS150K dataset was put forward by the authors of [6].The dataset consists of tweets having text as well as images which can be used for hatefulness detection. The authors compared three multimodal architectures – Textual Kernels Model (TKM), Feature Concatenation Model (FCM) and Spatial Concatenation Model (SCM) for the multimodal task. Yang et al in [7] proposed that augmenting images features along with text can increase accuracy in hate speech detection. The authors used a pre-trained ResNet model to form image embeddings. Concatenating the text and image vectors is the easiest technique to include text with image elements. For the final hate speech categorization, dropout, MLP, and softmax operations are performed on the concatenated vector.

The authors in [8] introduced a multimodal dataset for hateful meme classification- the hateful meme challenge. The authors also provided baseline models for unimodal and multimodal approaches. Aggarwal et al. [9] worked on the hateful meme challenge dataset and employed a pre-trained ResNet-152 model to extract image features while the text features were extracted by passing the textual data through Facebook's FastText encoder [10], and then performed simple concatenation to combine both the feature vectors. A fully connected neural network was fine tuned for the final classification. The authors of [11] propose detection of hateful memes by utilizing a Transformer-based Vision-Language Pre-Training Model (VL-PTM) named OSCAR+ to perform cross-modal learning. To achieve this, the authors use visual features, object tags, and text features of memes generated by the object detection model called Visual features in Vision-Language (VinVl) and the optical character recognition (OCR) technology, which are combined into a triplet and fed into the VL-PTM. The authors in [12] have proposed the use of object tags extracted using Xception and ResNet-50 and concatenate them to the Bert embedding to identify hate speech in memes. The dataset used is the hateful memes dataset [8].

TABLE I. Related Works

Paper	Dataset	Accuracy	AUROC
[6]	MMHS150K	68.32	0.73
[7]	Collected visual and textual data from social media	-	0.83
[8]	Hateful meme challenge	62.2	0.71
[9]	Hateful meme challenge	64	-
[11]	Hateful meme challenge	67	0.76
[12]	Hateful meme challenge	71.08	0.71

III. EXPERIMENTAL DESIGN

A. Dataset

The authors of [8] created the hateful meme dataset, with 37% of the samples being hateful and the other 63% of the samples being non-hateful. The Dataset with a total of 12,140 samples, turns out to be a challenging one. These memes contain text and image confounders, which modify the hateful meme's language or picture to make it appear less hateful. As

Authorized licensed use limited to: DELHI TECHNICAL UNIV. Downloaded on June 14,2023 at 05:09:49 UTC from IEEE Xplore. Restrictions apply.

a result, models must use both modalities to be effective. Analysis of the dataset revealed that most hate attacks against minorities include playing on preconceptions and going beyond them to indicate threats or aggression. The Fig 2. show the distribution of different type of memes in the dataset.

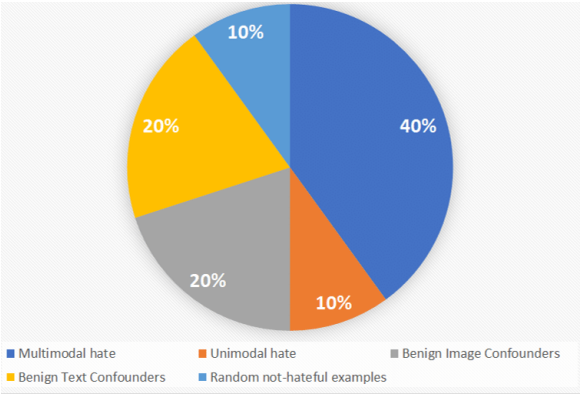

Fig. 2. Different types of memes in the dataset[8]

B. Baseline Model

The VisualBERT model [5] is the baseline multimodal strategy for the Facebook hateful meme challenge. VisualBERT is a straightforward and adaptable framework for simulating a wide variety of vision and language-related tasks. In VisualBERT, regions in a related input picture and textual elements are implicitly aligned with self-attention using a stack of Transformer layers.

C. Proposed Model

In the concerned dataset, a lot of memes actually turn out to be non-hateful, when only text or only image is present. But the combination of the image and text creates an offensive and hateful meme. Previous works struggle to correctly classify and identify these hateful memes. Hence, we propose a novel lightweight architecture to combine the two modalities by using object tags and image captioning information from the meme image by passing them through pre-trained models and merging them with the textual features of the meme caption. We finally pass these integrated feature though various classification models to improve the accuracy and AUROC score.

Object Tags

The proposed method suggests the use of object tags extracted from the images for hateful meme classification to help solve this issue of combining the modalities. We used the Detectron [18] network of mmf framework trained on Visual Genome [17] on every image to extract region-based image features (object tags). Detectron is a cutting-edge object detection model based on mask RCNN. The meme caption were fed to a language model (BERT) to create the text embeddings. BERT is a deep neural network architecture that is designed to generate contextualized word embeddings by taking into account the surrounding text. It uses a bi-directional transformer architecture, which means it can take into account both the preceding and following words in a sentence while generating embeddings. Parallelly, the images were passed through the image model (ResNET network) to get the image features. And as mentioned before, the images were also passed through the detectron model to achieve the object tags of the images and the object tags were then converted to text embeddings using BERT. The three outputs were concatenated (meme caption features, image features, object tag features) to get a 1-D feature representation and the obtained features were fitted using machine learning models(SVC,LR, GBDT) tuned for hateful meme classification. Fig. 4 shows the architecture of this framework.

Image Captions

In the second experimental approach, an attention based image captioning model was trained as proposed by [13]. The architecture uses a CNN model as encoder and LSTM model as the decoder to produce the image captions. The model is trained on the msCOCO dataset. The meme caption were passed through a language model (BERT) to create the text embeddings. Parallelly, the images were fed into the image model (ResNET network) to get the image features. Finally, the image captions produced by the image captioning model were passed through BERT. The three outputs were concatenated (meme caption features, image features, object tag features) to get a 1 D feature representation and these features were fitted on machine learning models (SVC,LR, GBDT) for hateful meme classification. The architecture is shown in Fig. 5.

Object Tags/Image Captions and LR

Logistic regression is a statistical machine learning algorithm used for binary classification problems, where the output variable is binary, i.e., it can take one of two possible values, such as true/false or yes/no. In logistic regression, the output is a logistic or sigmoid function of the input features. The logistic function maps any input value to a value between 0 and 1, which can be interpreted as a probability score. To process textual and visual data, the BERT and Resnet Models are used, respectively, and the resulting output features are fed into a logistic regression model.

Object Tags/Image Captions and CSV

SVM stands for Support Vector Machine, which is a type of machine learning algorithm used for classification and regression analysis. In classification, the SVM algorithm attempts to find a hyperplane in a high-dimensional space that separates the input data into different classes. The hyperplane is chosen such that it maximizes the distance between the closest data points from each class, which are called support vectors. The BERT and Resnet Models are utilized for handling textual and visual data, correspondingly. The outcome features obtained from these models are then fed into a SVM model to predict the hatefulness.

Object Tags/Image Captions and GBDT

Gradient Boosted Decision Tree is a machine learning algorithm that combines the power of decision trees and gradient boosting. The algorithm works by iteratively adding decision trees to the model, with each new tree attempting to correct the errors made by the previous trees. In each iteration, the gradient of the loss function is computed with respect to the output of the previous model, and the new decision tree is trained to minimize this gradient. The final prediction is obtained by aggregating the predictions of all the individual decision trees. The BERT and ResNet models are employed to process text and visual data, respectively. The features generated from the aforementioned models are fed into a gradient boosted decision tree model in order to make predictions regarding the degree of hateful content.

Authorized licensed use limited to: DELHI TECHNICAL UNIV. Downloaded on June 14,2023 at 05:09:49 UTC from IEEE Xplore. Restrictions apply.

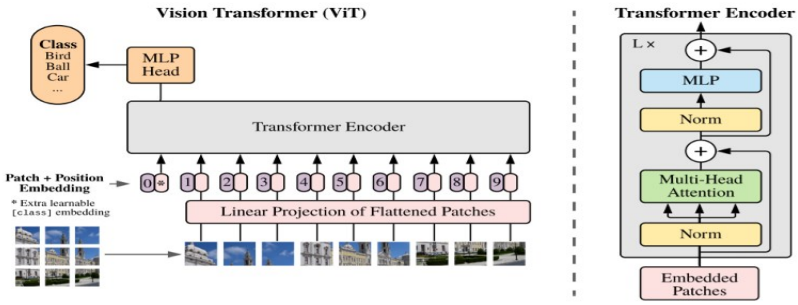

Fig. 3. VisualBert Architecture [5]

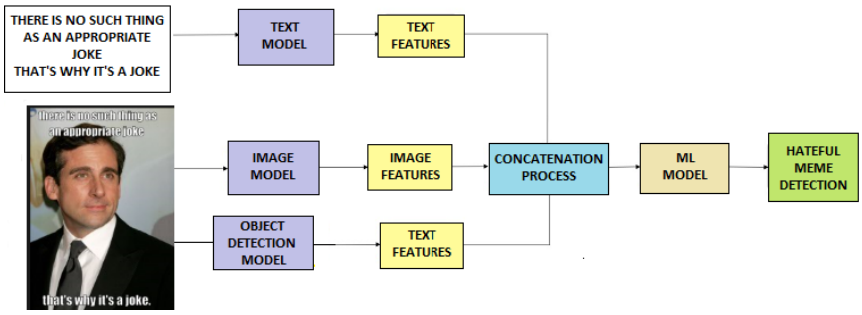

Fig. 4. Our Model architecture using object tags

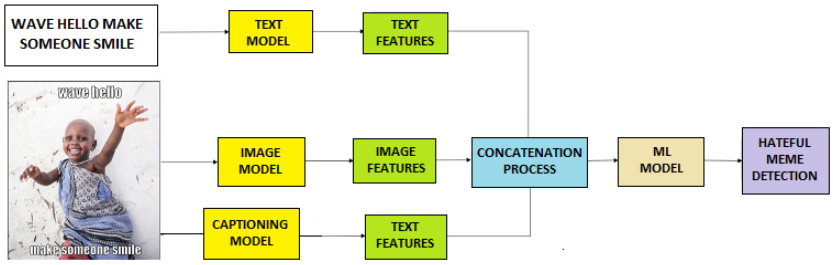

Fig. 5. Our Model architecture using image captions

IV. Result And Analysis

A. Evaluation Metrics

As specified in the original hateful meme paper, AUROC score and classification accuracy is used as the evaluation metric. A graph of True Positive Rate (TPR) vs. False Positive Rate(FPR) is known as the Receiver Operating Characteristics Curve. As the decision threshold is changed, it evaluates how well the binary classifier can distinguish between the classes [15]. TPR represents the proportion of actual positive cases that are correctly classified as positive by the model. It is also known as sensitivity and is calculated as,

$$TPR = TP/P \quad (1)$$

where TP is the number of true positives and P is the total number of positive cases.

FPR represents the proportion of actual negative cases that are incorrectly classified as positive by the model. It is calculated as,

$$FPR = FP/N \quad (2)$$

where FP is the number of false positives and N is the total number of negative cases

The top left corner of the plot, which has a TPR of 1, and an FPR of 0, is the optimal location for a perfect classifier, with an area under the curve of 1. In order to increase TPR and reduce FPR, each classifier should aim for a greater area under the curve. AUROC score can be calculated using the following formula,

$$AUROC = \int_{x=0}^{1} TPR\left(FPR^{-1}(x)\right)dx \quad (3)$$

We also use the classification accuracy which is the ratio of total correctly predicted samples and the total number of samples in the test set,

Authorized licensed use limited to: DELHI TECHNICAL UNIV. Downloaded on June 14,2023 at 05:09:49 UTC from IEEE Xplore. Restrictions apply.

$$Accuracy = \frac{Number\ Of\ Images\ Correctly\ Classified}{Total\ Number\ Of\ Images} \quad (4)$$

B. Discussion Of Results

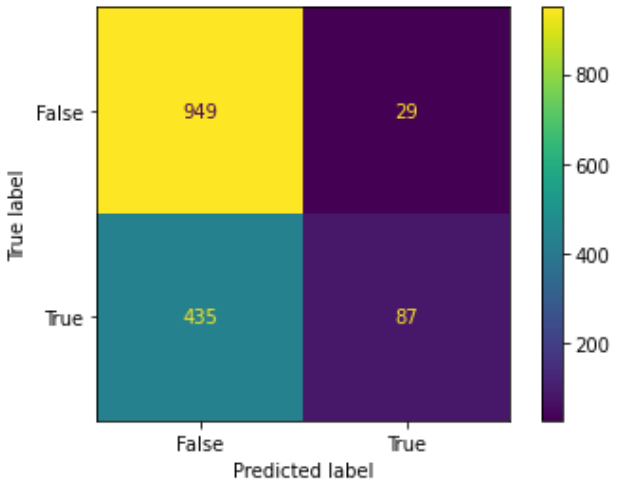

Fig. 6. Confusion Matrix for image captions + LR model

The results indicate that the proposed models outperformed the unimodal text-based approaches [7]. Humans can achieve an accuracy of 84.70 and AUROC score of 0.82 for this task of hatefulness detection in memes [14]. The result of our models is comparable to this score. Our Multimodal models achieve better results than the baseline models proposed in [b7]. The text modality for hate speech is typically given more attention in the multi-modal baselines. By bringing in the picture modality, identifying its object tags or real caption, and simultaneously transmitting the image representation for the concatenation phase, our methods seek to uncover a deeper link between the text modality and the image modality. This will aid in focusing on both modalities, which may assist to define a more accurate representation for the problem statement.

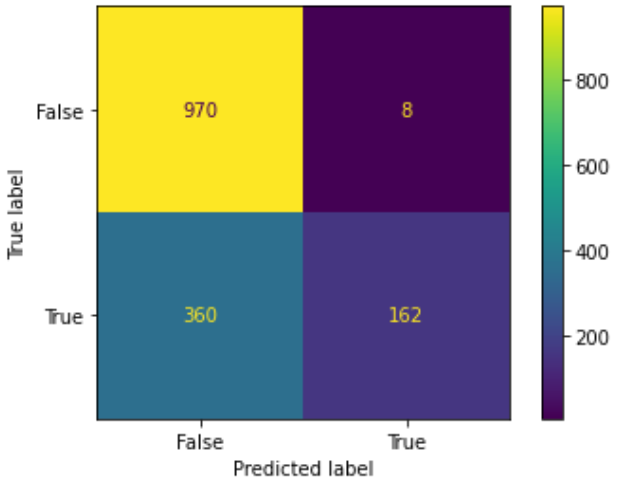

Fig. 7. Confusion Matrix for image captions + SVC

For creating text embedding, we have used the Bert model, and for processing images, we have used the ResNet model. The ResNet model aids in eliminating the vanishing gradient issues resulting due to very small network gradients, preventing the network weights from changing values when neural networks are being trained. In our first model, by using object tags, we integrate the modalities of text and image. We have used the Detectron tagger, which can provide detailed descriptions of items, to tag objects present in the image part of the meme. Our object tag model is able to outperform both the unimodal approach and the multimodal baseline models. In our second model we use a visual attention-based captioning model trained on visual genome dataset to learn the relations between objects present in image part of the meme. The image caption models are also able to perform better than the unimodal and the baseline multimodal models as well as than our object tag models.

The image captioning performs better than the object tag approach as it finds a deeper insight of the image through captioning, and strikes a balance in the relationship between the two modalities.

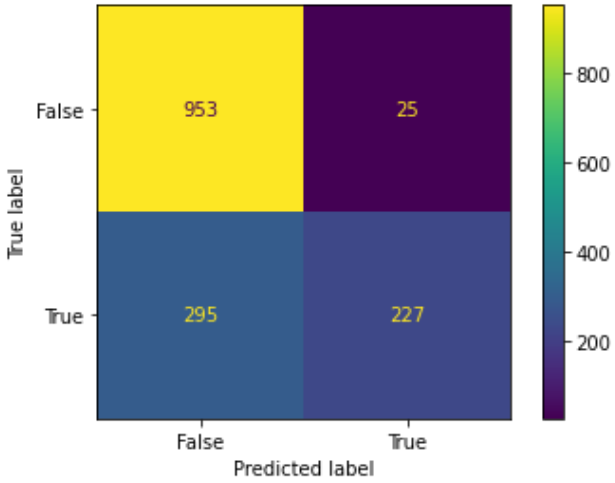

Fig. 8. Confusion Matrix for image captions + GBDT

The object tag/Image caption + SVC achieves better results than the LR model as SVC is able to deal with the non-linearity of the data by using the rbf kernel. The Object tag/Image caption + Gradient boosting trees models perform better than SVC and LR because we train the former sequentially, one tree at a time, each to correct the errors of the previous ones and hence they're capable of capturing complex patterns in the data.

TABLE II. RESULTS

MODEL	ACCURACY	AUROC
Unimodal Text Model	**59**	**0.64**
VisualBert	**62.2**	**0.71**
Object Tag (with LR)	**68.7**	**0.65**
Object Tag (with SVC)	**74**	**0.67**
Object Tag (with GBDT)	**71.7**	**0.72**
Image Captions (with LR)	**69**	**0.68**
Image Captions (with SVM)	**75.4**	**0.76**
Image Captions (with GBDT)	**77.6**	**0.74**

Authorized licensed use limited to: DELHI TECHNICAL UNIV. Downloaded on June 14,2023 at 05:09:49 UTC from IEEE Xplore. Restrictions apply.

V. Conclusion And Future Work

Today's social media platforms frequently contain memes. They are very important in the dissemination of ideas. Therefore, it's important to keep an eye on the memes shared on these social networking sites. We have evaluated multimodal techniques utilizing object tags and image captioning methods to link the relationship between the two modalities and classify the memes as hateful or not. Our model achieved accuracy and AUROC scores better than the unimodal and multimodal baseline models. Due to the large size of data available and large and complex model architectures, hardware resources (GPU) are needed to gain optimum results.

For future work, we can use other features of the images along with image captions and object tags in our models, and use other pre-trained architectures for the image and text analysis to further increase our accuracy and AUROC scores. Also, we can combine other meme datasets to train our models so that they can get generic models that can be used to detect hateful memes.

References

[1] Kumar, Raju & Bhat, Aruna. (2022). A study of machine learning-based models for detection, control, and mitigation of cyberbullying in online social media. International Journal of Information Security. 21. 1-23. 10.1007/s10207-022-00600-y.J . Clerk Maxwell, A Treatise on Electricity and Magnetism, 3rd ed., vol. 2. Oxford: Clarendon, 1892, pp.68–73.

[2] Devlin, J., Gupta, S., Girshick, R., Mitchell, M., and Zitnick, C. L. Exploring nearest neighbor approaches for image captioning. arXiv preprint arXiv:1505.04467, 2015

[3] Isaac, A., Bhat, A. (2022). A Conceptual Enhancement of LSTM Using Knowledge Distillation for Hate Speech Detection. In: Zhang, YD., Senjyu, T., So-In, C., Joshi, A. (eds) Smart Trends in Computing and Communications. Lecture Notes in Networks and Systems, vol 286. Springer, Singapore. https://doi.org/10.1007/978-981-16-4016-2_53

[4] A. Bhat, R. Mahar, R. Punia and R. Srivastava, "Exploring Multimodal Sentiment Analysis through Cartesian Product approach using BERT Embeddings and ResNet-50 encodings and comparing performance with pre-existing models," 2022 3rd International Conference for Emerging Technology (INCET), Belgaum, India, 2022, pp. 1-6, doi: 10.1109/INCET54531.2022.9825245.

[5] Li, L. H., Yatskar, M., Yin, D., Hsieh, C. J., & Chang, K. W. (2019). Visualbert: A simple and performance baseline for vision and language. arXiv preprint arXiv:1908.03557.

[6] Gomez, R., Gibert, J., Gomez, L., & Karatzas, D. (2020). Exploring hate speech detection in multimodal publications. In Proceedings of the IEEE/CVF winter conference on applications of computer vision (pp. 1470-1478).

[7] Yang, F., Peng, X., Ghosh, G., Shilon, R., Ma, H., Moore, E., and Predovic, G.Exploring deep multimodal fusion of text and photo for hate speech classification. In Proceedings of the Third Workshop on Abusive Language Online, pp. 11–18, Florence, Italy, August 2019. Association for Computational Linguistics. doi: 10.18653/ v1/W19-3502

[8] Kiela, D., Firooz, H., Mohan, A., Goswami, V., Singh, A., Fitzpatrick, C. A., & Parikh, D. (2021, August). The Hateful Memes Challenge: Competition Report. In NeurIPS 2020 Competition and Demonstration Track (pp. 344-360). PMLR.

[9] Aggarwal, Apeksha & Sharma, Vibhav & Trivedi, Anshul & Yadav, Mayank & Agrawal, Chirag & Singh, Dilbag & Mishra, Vipul & Gritli, Hassène. (2021). Two-Way Feature Extraction Using Sequential and Multimodal Approach for Hateful Meme Classification. Complexity. 2021. 1-7. 10.1155/2021/5510253.3.

[10] Piotr Bojanowski, Edouard Grave, Armand Joulin and Tomas Mikolov. (2017).Enriching word vectors with subword information. Transactions of the association for computational linguistics, 5, 135-146.

[11] Chen, Y. and Pan, F., 2022. Multimodal detection of hateful memes by applying a vision-language pre-training model. Plos one, 17(9), p.e0274300.

[12] A. Bhat, V. Varshney, V. Bajlotra and V. Gupta, "Detection of hatefulness in Memes using unimodal and multimodal techniques," 2022 6th International Conference on Intelligent Computing and Control Systems (ICICCS), Madurai, India, 2022, pp. 65-73, doi: 10.1109/ICICCS53718.2022.9788376.

[13] Xu, K., Ba, J., Kiros, R., Cho, K., Courville, A., Salakhudinov, R., & Bengio, Y. (2015, June). Show, attend and tell: Neural image caption generation with visual attention. In International conference on machine learning (pp. 2048-2057). PMLR.

[14] Deshpande, T., & Mani, N. (2021, October). An Interpretable Approach to Hateful Meme Detection. In Proceedings of the 2021 International Conference on Multimodal Interaction (pp. 723-727).

[15] Bradley, A. P. The use of the area under the roc curve in the evaluation of machine learning algorithms. Pattern Recognition, 30(7):1145–1159, 1997. doi: 10.1016/S0031-3203(96)00142-2.

[16] He, Kaiming, Xiangyu Zhang, Shaoqing Ren, and Jian Sun. "Deep residual learning for image recognition." In Proceedings of the IEEE conference on computer vision and pattern recognition, pp. 770-778. 2016.

[17] Krishna, R., Zhu, Y., Groth, O., Johnson, J., Hata, K., Kravitz, J., & Fei-Fei, L. (2017). Visual genome: Connecting language and vision using crowdsourced dense image annotations. International journal of computer vision, 123, 32-73.

[18] R. Girshick, I. Radosavovic, G. Gkioxari, P. Dollár, and K. He, 'Detectron', 2018. [Online]. Available: https://github.com/facebookresearch/detectron.

Authorized licensed use limited to: DELHI TECHNICAL UNIV. Downloaded on June 14,2023 at 05:09:49 UTC from IEEE Xplore. Restrictions apply.

arXiv:2306.11215v1 [math.CV] 20 Jun 2023

HIGHER ORDER DIFFERENTIAL SUBORDINATION FOR $\mathcal{S}_e^*$

NEHA VERMA AND S. SIVAPRASAD KUMAR

Abstract. This paper presents several results concerning second and third-order differential subordination for the class $\mathcal{S}_e^* := \{f \in \mathcal{A} : zf'(z)/f(z) \prec e^z\}$, which represents the class of starlike functions associated with exponential function.

1. Introduction

Suppose $\mathcal{H} = \mathcal{H}(\mathbb{D})$ be the class of analytic functions in $\mathbb{D} := \{z \in \mathbb{C} : |z| < 1\}$. For any positive integer n and $a \in \mathbb{C}$, define

$$\mathcal{H}[a, n] := \{f \in \mathcal{H} : f(z) = a + a_n z^n + a_{n+1} z^{n+1} + a_{n+2} z^{n+2} + \cdots\}.$$

Let $\mathcal{A}$ be the class of normalized analytic functions defined as

$$\mathcal{A} = \{f \in \mathcal{H} : f(z) = z + a_2 z^2 + a_3 z^3 + \cdots\}$$

and $\mathcal{S} \subset \mathcal{A}$ contains univalent functions. Any function $f \in \mathcal{S}$ is called starlike if and only if $\mathrm{Re}(zf'(z)/f(z)) > 0$ and the class consisting of all such functions is denoted by $\mathcal{S}^*$. Let h and g are in the class $\mathcal{A}$, we say that h is subordinate to g (denoted by $h \prec g$), if there exists a Schwarz function w with $w(0) = 0$ and $|w(z)| \leq |z|$ such that $h(z) = g(w(z))$. Moreover, if g is univalent, then $h \prec g$ if and only if $h(0) = g(0)$ and $h(\mathbb{D}) \subseteq g(\mathbb{D})$. A significant development in the direction of differential subordination was made with the appearance of Miller and Mocanu's monograph, "Differential Subordination and Univalent Functions," in 1981. It is a compendium of its time and this book initiated a significant revolution among researchers. In 1992, Ma and Minda [12] unified various subclasses of $\mathcal{S}^*$ by introducing the following class $\mathcal{S}^*(\varphi)$ through subordination:

$$\mathcal{S}^*(\varphi) = \left\{f \in \mathcal{A} : \frac{zf'(z)}{f(z)} \prec \varphi(z)\right\}, \tag{1.1}$$

with φ as an analytic univalent function so that $\mathrm{Re}\,\varphi(z) > 0$, $\varphi(\mathbb{D})$ is symmetric about the real axis and starlike with respect to $\varphi(0) = 1$ with $\varphi'(0) > 0$. Through the process of specializing the function φ in (1.1), researchers have obtained several significant subclasses of $\mathcal{S}^*$. Some of these subclasses are mentioned below for ready reference.

Class	Author(s)	Reference
$\mathcal{S}^*[C, D] := \mathcal{S}^*((1 + Cz)/(1 + Dz))$	Janowski	[7]
$\mathcal{S}_\rho^* := \mathcal{S}^*(1 + \sinh^{-1}(z))$	Arora and Kumar	[2]
$\mathcal{S}_S^* := \mathcal{S}^*(1 + \sin z)$	Cho et al.	[4]
$\mathcal{S}_{SG}^* := \mathcal{S}^*(2/(1 + e^{-z}))$	Goel and Kumar	[5]
$\mathcal{S}_\varrho^* := \mathcal{S}^*(1 + ze^z)$	Kumar and Kamaljeet	[10]
$\mathcal{S}_q^* := \mathcal{S}^*(z + \sqrt{1 + z^2})$	Raina and Sokół	[18]
$\mathcal{S}_L^* := \mathcal{S}^*(\sqrt{1 + z})$	Sokół and Stankiewicz	[19]

2010 *Mathematics Subject Classification.* 30C45, 30C80.

Key words and phrases. Differential Subordination, Exponential, Starlike.

Similarly, Mendiratta et al. [14] introduced and studied the class $\mathcal{S}_e^* := \mathcal{S}^*(e^z)$. Geometrically, we say a function $f \in \mathcal{S}_e^*$ if and only if $zf'(z)/f(z) \in \Delta_e := \{\delta \in \mathbb{C} : |\log \delta| < 1\}$. In this investigation, they obtained the conditions on β parameter so that $p(z) \prec e^z$ when $1 + \beta zp'(z)/p(z) \prec h(z)$ by choosing $h(z) = (1 + Cz)/(1 + Dz)$, $\sqrt{1+z}$ and e^z. Further, Kumar and Ravichandran [11] extended their results and obtained sharp bounds on β so that $p(z) \prec e^z$ when $1 + \beta zp'(z)/p^j(z) \prec h(z)$ for $j = 0, 2$ and $h(z) = (1 + Cz)/(1 + Dz)$ and $\sqrt{1+z}$. Later on, Naz et al. [17] derived a wide range of first-order subordination implications for the exponential function and generalized the results of [14]. Madaan et al. [13] conducted an investigation for the class of admissible functions associated with the lemniscate of Bernoulli for several implications of first and second order differential subordination. Similarly, Goel and Kumar [5] derived results focusing on first-order subordination results considering the class $\mathcal{S}_{SG}^*$. To explore the latest developments in this theory, one can refer to [3,8,9,16]. Motivated by the above work, in this article, we focus on establishing certain second and higher-order subordination implications related to the exponential function. Now, we state some basic definitions and notations required for differential subordination.

Definition 1.1. [1] Let $\xi(r, s, t, u; z) : \mathbb{C}^4 \times \mathbb{D} \to \mathbb{C}$ and $h(z)$ be a univalent function in $\mathbb{D}$, if p is an analytic function in $\mathbb{D}$ satisfying the third-order differential subordination

$$\xi(p(z), zp'(z), z^2p''(z), z^3p'''(z); z) \prec h(z) \tag{1.2}$$

then p is called the solution of the differential subordination. The univalent function q is said to be a dominant of the solutions of the differential subordination if $p \prec q$ for all p satisfying (1.2). A dominant $\bar{q}$ that satisfies $\bar{q} \prec q$ for all dominants q of (1.2) is said to be the best dominant of (1.2), which is unique upto the rotation.

Furthermore, let Q denote the set of analytic and univalent functions $q \in \overline{\mathbb{D}} \setminus \mathbb{E}(q)$, where

$$\mathbb{E}(q) = \{\zeta \in \partial\mathbb{D} : \lim_{z\to\zeta} q(z) = \infty\}$$

such that $q'(\zeta) \neq 0$ for $\zeta \in \partial\mathbb{D} \setminus \mathbb{E}(q)$. The subclass of Q for which $q(0) = a$ is denoted by $Q(a)$.

Lemma 1.2. *[1] Let $z_0 \in \mathbb{D}$ and $r_0 = |z_0|$. Let $f(z) = a_nz^n + a_{n+1}z^{n+1} + \cdots$ be continuous on $\overline{\mathbb{D}}_{r_0}$ and analytic on $\mathbb{D} \cup \{z_0\}$ with $f(z) \neq 0$ and $n \geq 2$. If $|f(z_0)| = \max\{|f(z)| : z \in \overline{\mathbb{D}}_{r_0}\}$ and $|f'(z_0)| = \max\{|f'(z)| : z \in \overline{\mathbb{D}}_{r_0}\}$, then there exist real constants m, k and l such that*

$$\frac{z_0f'(z_0)}{f(z_0)} = m, \quad 1 + \frac{z_0f''(z_0)}{f'(z_0)} = k \quad \text{and} \quad 2 + \operatorname{Re}\left(\frac{z_0f'''(z_0)}{f''(z_0)}\right) = l$$

where $l \geq k \geq m \geq n \geq 2$.

2. Preliminaries

In 2020, Kumar and Goel [9] made modifications to the results established by Antonino and Miller [1], ensuring that the Ma-Minda functions meet the requirements for third-order differential subordination. The revised results are presented below in the form of a definition and theorem, which are needed to achieve our main results for the class $\mathcal{S}_e^*$.

Definition 2.1. [9] Let Ω be a set in $\mathbb{C}$, $q \in Q$ and $k \geq m \geq n \geq 2$. The class of admissible operators $\xi_n[\Omega, q]$ consists of those $\xi : \mathbb{C}^4 \times \mathbb{D} \to \mathbb{C}$ that satisfy the admissibility condition

$$\xi(r, s, t, u; z) \notin \Omega \quad \text{whenever} \quad z \in \mathbb{D}, \quad r = q(\zeta), \quad s = m\zeta q'(\zeta),$$

$$\operatorname{Re}\left(1 + \frac{t}{s}\right) \geq m\left(1 + \operatorname{Re}\frac{\zeta q''(\zeta)}{q'(\zeta)}\right)$$

and

$$\operatorname{Re}\frac{u}{s} \geq m^2 \operatorname{Re}\frac{\zeta^2 q'''(\zeta)}{q'(\zeta} + 3m(k-1)\operatorname{Re}\frac{\zeta q''(\zeta)}{q'(\zeta)}$$

for $\zeta \in \partial\mathbb{D} \setminus \mathbb{E}(q)$.

Theorem 2.2. *[9] Let $p \in \mathcal{H}[a,n]$ with $m \geq n \geq 2$, and let $q \in Q(a)$ such that it satisfies*

$$\left|\frac{zp'(z)}{q'(\zeta)}\right| \leq m, \tag{2.1}$$

for $z \in \mathbb{D}$ and $\zeta \in \partial\mathbb{D} \setminus \mathbb{E}(q)$. If Ω is a set in $\mathbb{C}$, $\xi \in \Psi_n[\Omega, a]$ and

$$\xi(p(z), zp'(z), z^2p''(z), z^3p'''(z); z) \subset \Omega,$$

then $p \prec q$.

Here, we provide two lemmas which are necessary for the proof of results in the coming sections.

Lemma 2.3. *[9, Lemma 4, Pg No. 192] For any complex number z, we have*

$$|\log(1+z)| \geq 1 \quad \text{if and only if} \quad |z| \geq e-1.$$

Lemma 2.4. *[5] Let $r_0 \approx 0.546302$ be the positive root of the equation $r^2 + 2\cot(1)r - 1 = 0$. Then*

$$\left|\log\left(\frac{1+z}{1-z}\right)\right| \geq 1 \quad \text{on} \quad |z| = R \quad \text{if and only if} \quad R \geq r_0.$$

3. The admissibility conditions

This section examines the function $q(z) := e^z$ and define the admissibility class $\Psi[\Omega, q]$, where $\Omega \subset \mathbb{C}$. We know that q is analytic and univalent on $\overline{\mathbb{D}}$ with $q(0) = 1$ and it maps $\mathbb{D}$ onto the domain Δ_e. Since $\mathbb{E}(q)$ is empty for $\zeta \in \partial\mathbb{D} \setminus \mathbb{E}(q)$ if and only if $\zeta = e^{i\theta}$ ($\theta \in [0, 2\pi]$). Now, consider

$$|q'(\zeta)| = e^{\cos\theta} =: b(\theta) \tag{3.1}$$

has a minimum value of e^{-1}. It is evident that $\min|q'(\zeta)| > 0$, which implies that $q \in Q(1)$, and consequently, the admissibility class $\Psi[\Omega, q]$ is well-defined. While considering $|\zeta| = 1$, we observe that $q(\zeta) \in q(\partial\mathbb{D}) = \partial\Delta_e = \{\delta \in \mathbb{C} : |\log\delta| = 1\}$. Consequently, we have $|\log q(\zeta)| = 1$ and $\log(q(\zeta)) = e^{i\theta}$ ($\theta \in [0, 2\pi]$), implies that $q(\zeta) = e^{\zeta}$. Moreover, $\zeta q'(\zeta) = e^{i\theta}e^{e^{i\theta}}$ and

$$\frac{\zeta q''(\zeta)}{q'(\zeta)} = e^{i\theta}. \tag{3.2}$$

By comparing the real parts on both sides of (3.2), we obtain

$$\operatorname{Re}\left(\frac{\zeta q''(\zeta)}{q'(\zeta)}\right) = \cos\theta =: l(\theta). \tag{3.3}$$

The function $l(\theta)$ defined in (3.3) achieves its minimum value at $\theta = \pi$, given by $l(\pi) \approx -1$. Moreover, the class $\Psi[\Omega, e^z]$ is precisely defined as the class of all functions $\xi : \mathbb{C}^3 \times \mathbb{D} \to \mathbb{C}$ that satisfy the following conditions:

$$\xi(r, s, t; z) \notin \Omega,$$

whenever

$$r = q(\zeta) = e^{e^{i\theta}}; \quad s = m\zeta q'(\zeta) = me^{i\theta}e^{e^{i\theta}}; \quad \operatorname{Re}\left(1 + \frac{t}{s}\right) \geq m(1 + l(\theta)), \tag{3.4}$$

where $z \in \mathbb{D}$, $\theta \in [0, 2\pi]$ and $m \geq 1$. If $\xi : \mathbb{C}^2 \times \mathbb{D} \to \mathbb{C}$, then the admissibility condition (3.4) becomes

$$\xi(e^{e^{i\theta}}, me^{i\theta}e^{e^{i\theta}}; z) \notin \Omega \quad (z \in \mathbb{D}, \theta \in [0, 2\pi], m \geq 1).$$

Taking $q(z) = e^z$, we deduce the following theorem as a special case of Miller and Mocanu [15, Theorem 2.3b], which is necessary to prove our main results.

Theorem 3.1. *Let $\xi \in \Psi[\Omega, e^z]$. If $p \in \mathcal{H}[1, n]$ satisfies*

$$\xi(p(z), zp'(z), z^2p''(z); z) \in \Omega$$

then $p(z) \prec e^z$.

Further, let $q(z) = e^z$, we have

$$\zeta^2 \frac{q'''(z)}{q'(\zeta)} = e^{2i\theta}.$$

On comparing the real parts of both the sides, we get

$$\operatorname{Re}\left(\zeta^2 \frac{q'''(z)}{q'(\zeta)}\right) = \cos 2\theta =: h(\theta).$$

The minimum value of $h(\theta)$ is -1, which is attained at $\theta = \pi/2$. Thus, if $\xi : \mathbb{C}^4 \times \mathbb{D} \to \mathbb{C}$ then $\xi \in \Psi[\Omega, e^z]$, provided ξ satisfies the following conditions:

$$\xi(r, s, t, u; z) \notin \Omega \quad \text{whenever} \quad r = q(\zeta) = e^{e^{i\theta}}, \quad s = m\zeta q'(\zeta) = me^{i\theta}e^{e^{i\theta}},$$

$$\operatorname{Re}\left(1 + \frac{t}{s}\right) \geq m(1 + l(\theta)) \quad \text{and} \quad \operatorname{Re}\frac{u}{s} \geq m^2h(\theta) + 3m(k-1)l(\theta),$$

for $z \in \mathbb{D}$, $\theta \in [0, 2\pi]$ and $k \geq m \geq 2$. Given the above conditions, we deduce a special case of Theorem 2.2, which will be implemented in the last section of this article.

Lemma 3.2. *Let $p \in \mathcal{H}[1, n]$ with $m \geq n \geq 2$ such that for $z \in \mathbb{D}$ and $\zeta \in \partial\mathbb{D}$, it satisfies*

$$|zp'(z)e^{\zeta}| \leq m.$$

If Ω is a set in $\mathbb{C}$ and $\xi \in \Psi[\Omega, e^z]$, then

$$\xi(p(z), zp'(z), z^2p''(z), z^3p'''(z); z) \subset \Omega \implies p(z) \prec e^z.$$

4. Second order differential subordination

In this section, we discuss the implications of the following second order differential subordination

$$1 + \alpha_1 zp'(z) + \alpha_2 z^2 p''(z) \prec h(z) \implies p(z) \prec e^z. \tag{4.1}$$

For different choices of $h(z)$, we derive conditions on the constants α_1 and α_2 to ensure that (4.1) holds.

If we take $h(z) = (1 + Cz)/(1 + Dz)$ and $\sqrt{1+z}$, we have the following results.

Theorem 4.1. *Suppose α_1, $\alpha_2 > 0$ and $(\alpha_1 - \alpha_2)(1 - D^2) \geq e(C - D)(1 + |D|)$, where $-1 < D < C \leq 1$. Consider the analytic function p in $\mathbb{D}$ such that $p(0) = 1$ and*

$$1 + \alpha_1 zp'(z) + \alpha_2 z^2 p''(z) \prec \frac{1 + Cz}{1 + Dz}$$

implies $p(z) \prec e^z$.

Proof. Suppose $h(z) = (1 + Cz)/(1 + Dz)$ for $z \in \mathbb{D}$ and

$$\Omega = h(\mathbb{D}) = \left\{\delta \in \mathbb{C} : \left|\delta - \frac{1 - CD}{1 - D^2}\right| < \frac{C - D}{1 - D^2}\right\}.$$

We define $\xi : \mathbb{C}^3 \times \mathbb{D} \to \mathbb{C}$ as $\xi(\eta_1, \eta_2, \eta_3; z) = 1 + \alpha_1\eta_2 + \alpha_2\eta_3$. It is clear that $\xi \in \Psi[\Omega, \Delta_e]$ if $\xi(r, s, t; z) \notin \Omega$ for $z \in \mathbb{D}$. Consider

$$\begin{aligned}\left|\xi(r,s,t;z) - \frac{1-CD}{1-D^2}\right| &= \left|1 + \alpha_1 s + \alpha_2 t - \frac{1-CD}{1-D^2}\right| \\ &\geq |\alpha_1 s + \alpha_2 t| - \frac{|D|(C-D)}{1-D^2} \\ &\geq |\alpha_1 s| \operatorname{Re}\left(1 + \frac{\alpha_2}{\alpha_1}\frac{t}{s}\right) - \frac{|D|(C-D)}{1-D^2} \\ &\geq m\alpha_1 b(\theta) \operatorname{Re}\left(1 + \frac{\alpha_2}{\alpha_1}(ml(\theta) + m - 1)\right) - \frac{|D|(C-D)}{1-D^2}.\end{aligned}$$

Here $b(\theta)$ and $l(\theta)$ are given in (3.1) and (3.3). As $m \geq 1$, therefore

$$\begin{aligned}\left|\xi(r,s,t;z) - \frac{1-CD}{1-D^2}\right| &\geq \alpha_1 b(\theta) \operatorname{Re}\left(1 + \frac{\alpha_2}{\alpha_1} l(\theta)\right) - \frac{|D|(C-D)}{1-D^2} \\ &\geq \frac{1}{e}\Big(\alpha_1 - \alpha_2\Big) - \frac{|D|(C-D)}{1-D^2} \\ &\geq \frac{C-D}{1-D^2}.\end{aligned}$$

Thus, $\xi \in \Psi[\Omega, \Delta_e]$. Furthermore, $p(z) \prec e^z$ through Theorem 3.1. ∎

If we consider $p(z) = zf'(z)/f(z)$ in above theorem, we get the following result:

Corollary 4.2. *Suppose α_1, $\alpha_2 > 0$ and $f \in \mathcal{A}$. Let*

$$Y_f(z) := 1 + \alpha_1(A_2 - A_1^2 + A_1) + \alpha_2(A_3 + 2A_2 + 2A_1^3 - 2A_1^2 - 3A_1A_2). \tag{4.2}$$

where $A_1 := zf'(z)/f(z)$, $A_2 := z^2f''(z)/f(z)$ and $A_3 := z^3f'''(z)/f(z)$. Then, $f(z) \in \mathcal{S}_e^*$ if $Y_f(z) \prec (1+Cz)/(1+Dz)$ and $(\alpha_1 - \alpha_2)(1-D^2) \geq e(C-D)(1+|D|)$ whenever $-1 < D < C \leq 1$.

Theorem 4.3. *Suppose α_1, $\alpha_2 > 0$ and ${\alpha_1}^2 - 2\alpha_1\alpha_2 + {\alpha_2}^2 - 2e\alpha_1 + 2e\alpha_2 \geq e^2$. Consider the analytic function p in $\mathbb{D}$ such that $p(0) = 1$ and*

$$1 + \alpha_1 zp'(z) + \alpha_2 z^2 p''(z) \prec \sqrt{1+z}$$

implies $p(z) \prec e^z$.

Proof. Suppose $h(z) = \sqrt{1+z}$ for $z \in \mathbb{D}$ and $\Omega = h(\mathbb{D}) = \{\delta \in \mathbb{C} : |\delta^2 - 1| < 1\}$. Let us define $\xi : \mathbb{C}^3 \times \mathbb{D} \to \mathbb{C}$ as $\xi(\eta_1, \eta_2, \eta_3; z) = 1 + \alpha_1\eta_2 + \alpha_2\eta_3$. It is clear that $\xi \in \Psi[\Omega, \Delta_e]$ if $\xi(r, s, t, ; z) \notin \Omega$ for $z \in \mathbb{D}$. Note that

$$\begin{aligned}|(\xi(r,s,t;z))^2 - 1| &= |(1 + \alpha_1 s + \alpha_2 t)^2 - 1| \\ &\geq |\alpha_1 s + \alpha_2 t|(|\alpha_1 s + \alpha_2 t| - 2) \\ &\geq |\alpha_1 s| \operatorname{Re}\left(1 + \frac{\alpha_2}{\alpha_1}\frac{t}{s}\right)\left(|\alpha_1 s| \operatorname{Re}\left(1 + \frac{\alpha_2}{\alpha_1}\frac{t}{s}\right) - 2\right)\end{aligned}$$

Using the fact that $m \geq 1$ and analogous to Theorem 4.1, we have

$$\begin{aligned}|(\xi(r,s,t;z))^2 - 1| &\geq \frac{1}{e}\Big(\alpha_1 - \alpha_2\Big)\left(\frac{1}{e}\Big(\alpha_1 - \alpha_2\Big) - 2\right) \\ &= \frac{{\alpha_1}^2 - 2\alpha_1\alpha_2 + {\alpha_2}^2 - 2e\alpha_1 + 2e\alpha_2}{e^2} \\ &\geq 1.\end{aligned}$$

Therefore, $\xi \in \Psi[\Omega, \Delta_e]$ and thus $p(z) \prec e^z$ as a consequence of Theorem 3.1. ∎

Corollary 4.4. *By considering $p(z) = zf'(z)/f(z)$ in above theorem and through (4.2), we deduce that $f(z) \in \mathcal{S}_e^*$ if $Y_f(z) \prec \sqrt{1+z}$ and $\alpha_1{}^2 - 2\alpha_1\alpha_2 + \alpha_2{}^2 - 2e\alpha_1 + 2e\alpha_2 \geq e^2$.*

Next, we consider $h(z) = 2/(1+e^{-z})$ and $z + \sqrt{1+z^2}$ in the coming results.

Theorem 4.5. *Suppose α_1, $\alpha_2 > 0$ and $\alpha_1 - \alpha_2 \geq er_0$, where $r_0 \approx 0.546302$ is the positive root of the equation $r^2 + 2\cot(1)r - 1 = 0$. Consider the analytic function p in $\mathbb{D}$ such that $p(0) = 1$ and*

$$1 + \alpha_1 zp'(z) + \alpha_2 z^2 p''(z) \prec \frac{2}{1+e^{-z}}$$

implies $p(z) \prec e^z$.

Proof. Suppose $h(z) = 2/(1+e^{-z})$ and $\Omega = h(\mathbb{D}) = \{\delta \in \mathbb{C} : |\log(\delta/(2-\delta))| < 1\}$. Define $\xi : \mathbb{C}^3 \times \mathbb{D} \to \mathbb{C}$ as $\xi(\eta_1, \eta_2, \eta_3; z) = 1 + \alpha_1\eta_2 + \alpha_2\eta_3$. We know that $\xi \in \Psi[\Omega, \Delta_e]$ only when $\xi(r, s, t; z) \notin \Omega$. First we consider,

$$\begin{aligned} |\alpha_1 s + \alpha_2 t| &= \alpha_1 |s| \left| 1 + \frac{\alpha_2}{\alpha_1}\frac{t}{s} \right| \\ &\geq \alpha_1 |s| \operatorname{Re}\left(1 + \frac{\alpha_2}{\alpha_1}\frac{t}{s}\right) \\ &\geq m\alpha_1 b(\theta)\left(1 + \frac{\alpha_2}{\alpha_1}(ml(\theta) + m - 1)\right). \end{aligned}$$

As $m \geq 1$, we obtain

$$\begin{aligned} |\alpha_1 s + \alpha_2 t| &\geq b(\theta)(\alpha_1 + \alpha_2 l(\theta)) \\ &\geq \frac{1}{e}(\alpha_1 - \alpha_2) \\ &\geq r_0. \end{aligned} \tag{4.3}$$

Now, we consider

$$\left| \log\left(\frac{\xi(r, s, t; z)}{2 - \xi(r, s, t; z)}\right) \right| = \left| \log\left(\frac{1 + \alpha_1 s + \alpha_2 t}{1 - (\alpha_1 s + \alpha_2 t)}\right) \right|.$$

Through Lemma 2.4 and (4.3), we have

$$\left| \log\left(\frac{1 + \alpha_1 s + \alpha_2 t}{1 - (\alpha_1 s + \alpha_2 t)}\right) \right| \geq 1,$$

which implies that $\xi \in \Psi[\Omega, \Delta_e]$. Therefore, $p(z) \prec e^z$ using Theorem 3.1. ∎

Theorem 4.6. *Suppose α_1, $\alpha_2 > 0$ and $\alpha_1 - \alpha_2 \geq \sqrt{2}e$. Let p be an analytic function in $\mathbb{D}$ such that $p(0) = 1$ and*

$$1 + \alpha_1 zp'(z) + \alpha_2 z^2 p''(z) \prec z + \sqrt{1+z^2}$$

implies $p(z) \prec e^z$.

Proof. Suppose $h(z) = z + \sqrt{1+z^2}$ for $z \in \mathbb{D}$ and $\Omega = \{\delta \in \mathbb{C} : |\delta^2 - 1| < 2|\delta|\}$. We define $\xi : \mathbb{C}^3 \times \mathbb{D} \to \mathbb{C}$ as $\xi(\eta_1, \eta_2, \eta_3; z) = 1 + \alpha_1\eta_2 + \alpha_2\eta_3$. For $\xi \in \Psi[\Omega, \Delta_e]$, we must have $\xi(r, s, t; z) \notin \Omega$. From the graph of $z + \sqrt{1+z^2}$ (see Fig. 1), we note that Ω is constructed by the circles

$$C_1 : |z - 1| = \sqrt{2} \quad \text{and} \quad C_2 : |z + 1| = \sqrt{2}.$$

It is obvious that Ω contains the disk enclosed by C_1 and excludes the portion of the disk enclosed by $C_2 \cap C_1$. We have

$$|\xi(r, s, t; z) - 1| = |\alpha_1 s + \alpha_2 t|.$$

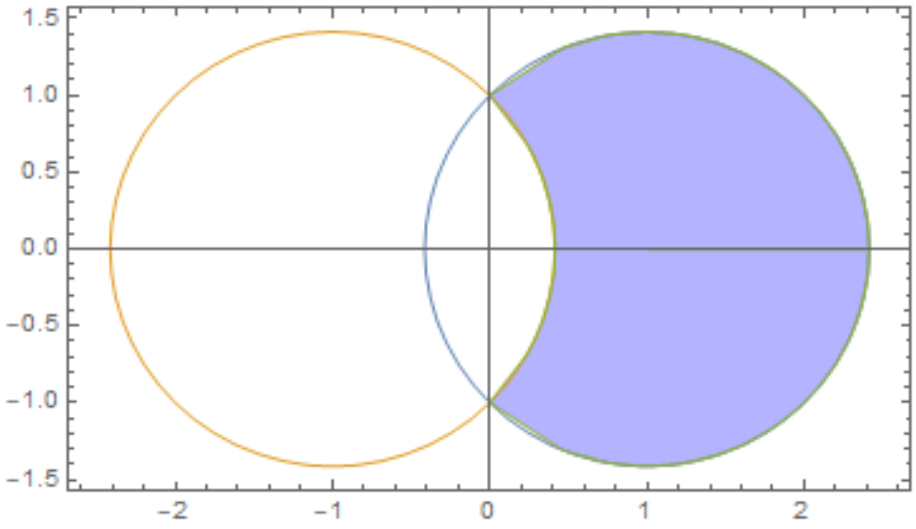

FIGURE 1. Graph of two circles, namely C_1 (blue boundary) and C_2 (orange boundary). While the shaded region (solid purple) represents $z + \sqrt{1+z^2}$.

Analogous to Theorem 4.5, we have

$$\begin{aligned} |\alpha_1 s + \alpha_2 t| &\geq b(\theta)(\alpha_1 + \alpha_2 l(\theta)) \\ &\geq \frac{1}{e}(\alpha_1 - \alpha_2) \\ &\geq \sqrt{2}. \end{aligned}$$

The fact that $\xi(r,s,t;z) \notin C_1$ suffices us to deduce that $\xi(r,s,t;z) \notin \Omega$. Consequently, $\xi \in \Psi[\Omega, \Delta_e]$ and thus $p(z) \prec e^z$ by using Theorem 3.1. ∎

Now, if we choose $h(z)$ to be $1 + \sin z$ and $1 + ze^z$, we derive the conditions on α_1 and α_2 as follows:

Theorem 4.7. *Suppose $\alpha_1,\ \alpha_2 > 0$ and $\alpha_1 - \alpha_2 \geq e \sinh 1$. Let p be an analytic function in $\mathbb{D}$ such that $p(0) = 1$ and*

$$1 + \alpha_1 z p'(z) + \alpha_2 z^2 p''(z) \prec 1 + \sin z$$

implies $p(z) \prec e^z$.

Proof. Suppose $h(z) = 1 + \sin z$ for $z \in \mathbb{D}$ and $\Omega = \{\delta \in \mathbb{C} : |\arcsin(\delta - 1)| < 1\}$. Define $\xi : \mathbb{C}^3 \times \mathbb{D} \to \mathbb{C}$ as $\xi(\eta_1, \eta_2, \eta_3; z) = 1 + \alpha_1\eta_2 + \alpha_2\eta_3$. For $\xi \in \Psi[\Omega, \Delta_e]$, we must have $\xi(r,s,t;z) \notin \Omega$. Through [4, Lemma 3.3], we note that the smallest disk containing Ω is $\{\delta \in \mathbb{C} : |\delta - 1| < \sinh 1\}$. So,

$$|\xi(r,s,t;z) - 1| = |\alpha_1 s + \alpha_2 t|.$$

Analogous to Theorem 4.5, we have

$$\begin{aligned} |\alpha_1 s + \alpha_2 t| &\geq b(\theta)(\alpha_1 + \alpha_2 l(\theta)) \\ &\geq \frac{1}{e}(\alpha_1 - \alpha_2) \\ &\geq \sinh 1. \end{aligned}$$

Clearly, $\xi(r,s,t;z) \notin \{w : |w - 1| < \sinh 1\}$ which is enough to conclude that $\xi(r,s,t;z) \notin \Omega$. Therefore, $\xi \in \Psi[\Omega, \Delta_e]$ and thus $p(z) \prec e^z$ through Theorem 3.1. ∎

Theorem 4.8. *Suppose α_1, $\alpha_2 > 0$ and $\alpha_1 - \alpha_2 \geq e^2$. Consider the analytic function p in $\mathbb{D}$ such that $p(0) = 1$ and*

$$1 + \alpha_1 z p'(z) + \alpha_2 z^2 p''(z) \prec 1 + ze^z$$

implies $p(z) \prec e^z$.

Proof. Suppose $h(z) = 1 + ze^z$ for $z \in \mathbb{D}$ and $\Omega = h(\mathbb{D})$. Let us define $\xi : \mathbb{C}^3 \times \mathbb{D} \to \mathbb{C}$ as $\xi(\eta_1, \eta_2, \eta_3; z) = 1 + \alpha_1\eta_2 + \alpha_2\eta_3$. For $\xi \in \Psi[\Omega, \Delta_e]$, we need to have $\xi(r, s, t; z) \notin \Omega$. Through [10, Lemma 3.3], we observe that the smallest disk containing Ω is $\{\delta \in \mathbb{C} : |\delta - 1| < e\}$. Thus

$$|\xi(r, s, t; z) - 1| = |\alpha_1 s + \alpha_2 t|.$$

Analogous to Theorem 4.5, we have

$$\begin{aligned} |\alpha_1 s + \alpha_2 t| &\geq b(\theta)(\alpha_1 + \alpha_2 l(\theta)) \\ &\geq \frac{1}{e}(\alpha_1 - \alpha_2) \\ &\geq e. \end{aligned}$$

Clearly, $\xi(r, s, t; z) \notin \{\delta \in \mathbb{C} : |\delta - 1| < e\}$ which suffices us to conclude that $\xi(r, s, t; z) \notin \Omega$. Therefore, $\xi \in \Psi[\Omega, \Delta_e]$ and thus $p(z) \prec e^z$ by using Theorem 3.1. ∎

Now, we conclude this section by choosing $h(z)$ to be $1 + \sinh^{-1} z$ and e^z itself, followed by its subsequent corollary.

Theorem 4.9. *Suppose α_1, $\alpha_2 > 0$ and $2(\alpha_1 - \alpha_2) \geq \pi e$. Consider the analytic function p in $\mathbb{D}$ such that $p(0) = 1$ and*

$$1 + \alpha_1 z p'(z) + \alpha_2 z^2 p''(z) \prec 1 + \sinh^{-1} z$$

implies $p(z) \prec e^z$.

Proof. Suppose $h(z) = 1 + \sinh^{-1} z$ for $z \in \mathbb{D}$ and $\Omega = h(\mathbb{D}) = \{\delta \in \mathbb{C} : |\sinh(\delta - 1)| < 1\}$. We define $\xi : \mathbb{C}^3 \times \mathbb{D} \to \mathbb{C}$ as $\xi(\eta_1, \eta_2, \eta_3; z) = 1 + \alpha_1\eta_2 + \alpha_2\eta_3$. For $\xi \in \Psi[\Omega, \Delta_e]$, we must have $\xi(r, s, t; z) \notin \Omega$. Through [2, Remark 2.7], we note that the disk $\{\delta \in \mathbb{C} : |\delta - 1| < \pi/2\}$ is the smallest disk containing Ω. So,

$$|\xi(r, s, t; z) - 1| = |\alpha_1 s + \alpha_2 t|.$$

Analogous to Theorem 4.5, we have

$$\begin{aligned} |\alpha_1 s + \alpha_2 t| &\geq b(\theta)(\alpha_1 + \alpha_2 l(\theta)) \\ &\geq \frac{1}{e}(\alpha_1 - \alpha_2) \\ &\geq \frac{\pi}{2}. \end{aligned}$$

Clearly, $\xi(r, s, t; z)$ does not belong to the disk $\{\delta \in \mathbb{C} : |\delta - 1| < \pi/2\}$ which suffices us to conclude that $\xi(r, s, t; z) \notin \Omega$. Therefore, $\xi \in \Psi[\Omega, \Delta_e]$ and thus $p(z) \prec e^z$ by using Theorem 3.1. ∎

Theorem 4.10. *Suppose α_1, $\alpha_2 > 0$ and $\alpha_1 - \alpha_2 \geq e(e - 1)$. Consider the analytic function p in $\mathbb{D}$ such that $p(0) = 1$ and*

$$1 + \alpha_1 z p'(z) + \alpha_2 z^2 p''(z) \prec e^z$$

implies $p(z) \prec e^z$.

Proof. Suppose $h(z) = e^z$ for $z \in \mathbb{D}$ and $\Omega = \Delta_e$. Define $\xi : \mathbb{C}^3 \times \mathbb{D} \to \mathbb{C}$ as $\xi(\eta_1, \eta_2, \eta_3; z) = 1 + \alpha_1\eta_2 + \alpha_2\eta_3$. For $\xi \in \Psi[\Delta_e, \Delta_e]$, we must have $\xi(r, s, t; z) \notin \Delta_e$. So,

$$|\xi(r, s, t; z) - 1| = |\alpha_1 s + \alpha_2 t|.$$

Analogous to Theorem 4.5, we have

$$\begin{aligned}|\alpha_1 s + \alpha_2 t| &\geq b(\theta)(\alpha_1 + \alpha_2 l(\theta)) \\ &\geq \frac{1}{e}(\alpha_1 - \alpha_2) \\ &\geq e - 1. \end{aligned} \tag{4.4}$$

Further, we have

$$|\log(\xi(r, s, t; z)| = |\log(1 + \alpha_1 s + \alpha_2 t)|.$$

Through Lemma 2.3 and (4.4), we have

$$|\log(1 + \alpha_1 s + \alpha_2 t)| \geq 1,$$

which implies that $\xi(r, s, t; z) \notin \Delta_e$. Therefore, $\xi \in \Psi[\Delta_e, \Delta_e]$ and thus $p(z) \prec e^z$ through Theorem 3.1. ∎

Theorems 4.5-4.10 yield the following conclusion if $p(z) = zf'(z)/f(z)$ is considered as in (4.2).

Corollary 4.11. *Suppose α_1, $\alpha_2 > 0$ and $f \in \mathcal{A}$. Then, $f \in \mathcal{S}_e^*$ if any of these conditions hold:*

(*i*) $Y_f(z) \prec 2/(1 + e^{-z})$ *and* $\alpha_1 - \alpha_2 \geq er_0$, *where* $r_0 \approx 0.546302$ *is the positive root of the equation* $r^2 + 2\cot(1)r - 1 = 0$.

(*ii*) $Y_f(z) \prec z + \sqrt{1 + z^2}$ *and* $\alpha_1 - \alpha_2 \geq \sqrt{2}e$.

(*iii*) $Y_f(z) \prec 1 + \sin z$ *and* $\alpha_1 - \alpha_2 \geq e \sinh 1$.

(*iv*) $Y_f(z) \prec 1 + ze^z$ *and* $\alpha_1 - \alpha_2 \geq e^2$.

(*v*) $Y_f(z) \prec 1 + \sinh^{-1} z$ *and* $2(\alpha_1 - \alpha_2) \geq \pi e$.

(*vi*) $Y_f(z) \prec e^z$ *and* $\alpha_1 - \alpha_2 \geq e(e - 1)$.

5. Third order differential subordination

The objective of this section is to determine the sufficient conditions on α_1, α_2 and $\alpha_3 \in \mathbb{R}^+$ involving the constants m and k (defined in Lemma 1.2 when $f(z) = \log(p(z))$, to satisfy the third order differential subordination implication, given by

$$1 + \alpha_1 zp'(z) + \alpha_2 z^2 p''(z) + \alpha_3 z^3 p'''(z) \prec h(z) \implies p(z) \prec e^z.$$

We obtain the following results upon considering $h(z) = (1 + Cz)/(1 + Dz)$ and $\sqrt{1 + z}$.

Theorem 5.1. *Suppose α_1, α_2, $\alpha_3 > 0$ and $(\alpha_1 - \alpha_2 - m^2\alpha_3 - 3m(k - 1)\alpha_3)(1 - D^2) \geq e(1 + |D|)(C - D)$ where $-1 < D < C \leq 1$. Consider the analytic function p in $\mathbb{D}$ such that $p(0) = 1$ and*

$$1 + \alpha_1 zp'(z) + \alpha_2 z^2 p''(z) + \alpha_3 z^3 p'''(z) \prec \frac{1 + Cz}{1 + Dz}$$

implies $p(z) \prec e^z$.

Proof. Suppose $h(z) = (1 + Cz)/(1 + Dz)$ for $z \in \mathbb{D}$ and

$$\Omega = \left\{\delta \in \mathbb{C} : \left|\delta - \frac{1 - CD}{1 - D^2}\right| < \frac{C - D}{1 - D^2}\right\}.$$

Define $\xi : \mathbb{C}^4 \times \mathbb{D} \to \mathbb{C}$ as $\xi(\eta_1, \eta_2, \eta_3, \eta_4; z) = 1 + \alpha_1\eta_2 + \alpha_2\eta_3 + \alpha_3\eta_4$. For $\xi \in \Psi[\Omega, \Delta_e]$, it is needed that $\xi(r, s, t, u; z) \notin \Omega$ for $z \in \mathbb{D}$. Consider

$$\begin{aligned}\left|\xi(r,s,t,u;z) - \frac{1-CD}{1-D^2}\right| &= \left|1 + \alpha_1 s + \alpha_2 t + \alpha_3 u - \frac{1-CD}{1-D^2}\right| \\ &\geq |\alpha_1 s + \alpha_2 t + \alpha_3 u| - \frac{|D|(C-D)}{1-D^2} \\ &\geq |\alpha_1 s| \operatorname{Re}\left(1 + \frac{\alpha_2}{\alpha_1}\frac{t}{s} + \frac{\alpha_3}{\alpha_1}\frac{u}{s}\right) - \frac{|D|(C-D)}{1-D^2} \\ &\geq m\alpha_1 b(\theta)\left(1 + \frac{\alpha_2}{\alpha_1}(ml(\theta) + m - 1) + \frac{\alpha_3}{\alpha_1}(m^2 h(\theta) + 3m(k-1)l(\theta))\right) \\ &\quad - \frac{|D|(C-D)}{1-D^2}.\end{aligned}$$

As $m \geq 1$ and $\operatorname{Re}(1 + l(\theta)) > 0$, we get

$$\begin{aligned}\left|\xi(r,s,t,u;z) - \frac{1-CD}{1-D^2}\right| &\geq \alpha_1 b(\theta)\left(1 + \frac{\alpha_2}{\alpha_1}l(\theta) + \frac{\alpha_3}{\alpha_1}(m^2 h(\theta) + 3m(k-1)l(\theta))\right) - \frac{|D|(C-D)}{1-D^2} \\ &\geq \frac{1}{e}\left(\alpha_1 - \alpha_2 - \alpha_3(m^2 + 3m(k-1))\right) - \frac{|D|(C-D)}{1-D^2} \\ &\geq \frac{C-D}{1-D^2}.\end{aligned}$$

From the above calculations, we conclude that $\xi \in \Psi[\Omega, \Delta_e]$ and hence $p(z) \prec e^z$ through Lemma 3.2. ∎

Corollary 5.2. *Suppose α_1, α_2, $\alpha_3 > 0$ and $f \in \mathcal{A}$. Let*

$$\begin{aligned}\chi_f(z) := 1 &+ \alpha_1 A_1 + (\alpha_1 + 2\alpha_2)(A_2 - A_1^2) + (\alpha_2 + 3\alpha_3)(2A_1^3 - 3A_1A_2 + 3A_3) \\ &+ \alpha_3(A_4 - 3A_2^2 - (6A_1)^4 - 4A_1A_3 + 12A_1^2A_2),\end{aligned} \tag{5.1}$$

where A_1, A_2, A_3 are same as defined in Corollary 4.2 and $A_4 := z^4 f''''(z)/f(z)$. Then, $f(z) \in \mathcal{S}_e^*$ if $\chi_f(z) \prec (1 + Cz)/(1 + Dz)$ and $(\alpha_1 - \alpha_2 - m^2\alpha_3 - 3m\alpha_3(k-1))(1 - D^2) \geq e(1 + |D|)(C - D)$ whenever $-1 < D < C \leq 1$.

Theorem 5.3. *Suppose α_1, α_2 and α_3 be positive real numbers and $(\alpha_1 - \alpha_2 - m^2\alpha_3 - 3m(k-1)\alpha_3)(\alpha_1 - \alpha_2 - m^2\alpha_3 - 3m(k-1)\alpha_3 - 2e) \geq e^2$. Consider the analytic function p in $\mathbb{D}$ such that $p(0) = 1$ and*

$$1 + \alpha_1 z p'(z) + \alpha_2 z^2 p''(z) + \alpha_3 z^3 p'''(z) \prec \sqrt{1+z}$$

implies $p(z) \prec e^z$.

Proof. Suppose $h(z) = \sqrt{1+z}$ and $\Omega = h(\mathbb{D}) = \{\delta \in \mathbb{C} : |\delta^2 - 1| < 1\}$. Consider $\xi : \mathbb{C}^4 \times \mathbb{D} \to \mathbb{C}$ defined as $\xi(\eta_1, \eta_2, \eta_3, \eta_4; z) = 1 + \alpha_1\eta_2 + \alpha_2\eta_3 + \alpha_3\eta_4$. We know that $\xi \in \Psi[\Omega, \Delta_e]$ if $\xi(r, s, t, u; z) \notin \Omega$ for $z \in \mathbb{D}$. Consider

$$\begin{aligned}|(\xi(r,s,t,u;z))^2 - 1| &= |(1 + \alpha_1 s + \alpha_2 t + \alpha_3 u)^2 - 1| \\ &\geq |\alpha_1 s + \alpha_2 t + \alpha_3 u|(|\alpha_1 s + \alpha_2 t + \alpha_3 u| - 2) \\ &\geq |\alpha_1 s| \operatorname{Re}\left(1 + \frac{\alpha_2}{\alpha_1}\frac{t}{s} + \frac{\alpha_3}{\alpha_1}\frac{u}{s}\right)\left(|\alpha_1 s| \operatorname{Re}\left(1 + \frac{\alpha_2}{\alpha_1}\frac{t}{s} + \frac{\alpha_3}{\alpha_1}\frac{u}{s}\right) - 2\right).\end{aligned}$$

Analogous to the proof of Theorem 5.1 and the fact that $m \geq 1$, we obtain

$$\begin{aligned}|(\xi(r,s,t,u;z))^2 - 1| &\geq \alpha_1 b(\theta)\bigg(1 + \frac{\alpha_2}{\alpha_1}l(\theta) + \frac{\alpha_3}{\alpha_1}(m^2h(\theta) + 3m(k-1)l(\theta))\bigg)\bigg\{\alpha_1 b(\theta)\bigg(1 + \frac{\alpha_2}{\alpha_1}l(\theta)\\ &\quad + \frac{\alpha_3}{\alpha_1}(m^2h(\theta) + 3m(k-1)l(\theta))\bigg) - 2\bigg\}\\ &\geq \frac{1}{e^2}\bigg(\alpha_1 - \alpha_2 - \alpha_3(m^2 + 3m(k-1))\bigg)\bigg(\alpha_1 - \alpha_2 - \alpha_3(m^2 + 3m(k-1)) - 2e\bigg)\\ &\geq 1.\end{aligned}$$

This implies that $\xi \in \Psi[\Omega, \Delta_e]$. Thus, $p(z) \prec e^z$ as a consequence of Lemma 3.2. ∎

Corollary 5.4. *By considering $p(z) = zf'(z)/f(z)$ in above theorem and through (5.1), we deduce that $f(z) \in \mathcal{S}_e^*$ if $\chi_f(z) \prec \sqrt{1+z}$ and $(\alpha_1 - \alpha_2 - m^2\alpha_3 - 3m\alpha_3(k-1))(\alpha_1 - \alpha_2 - m^2\alpha_3 - 3m(k-1)\alpha_3 - 2e) \geq e^2$.*

The next two results deal with the case when $h(z) = 2/(1+e^{-z})$ and $z + \sqrt{1+z^2}$.

Theorem 5.5. *Suppose α_1, α_2, $\alpha_3 > 0$ and $\alpha_1 - \alpha_2 - m^2\alpha_3 - 3m(k-1)\alpha_3 \geq er_0$, where $r_0 \approx 0.546302$ is the positive root of the equation $r^2 + 2\cot(1)r - 1 = 0$. Consider the analytic function p in $\mathbb{D}$ such that $p(0) = 1$ and*

$$1 + \alpha_1 zp'(z) + \alpha_2 z^2 p''(z) + \alpha_3 z^3 p'''(z) \prec \frac{2}{1+e^{-z}}$$

implies $p(z) \prec e^z$.

Proof. Suppose $h(z) = 2/(1+e^{-z})$ and $\Omega = \{\delta \in \mathbb{C} : |\log(\delta/(2-\delta))| < 1\}$. Define $\xi : \mathbb{C}^4 \times \mathbb{D} \to \mathbb{C}$ as $\xi(\eta_1, \eta_2, \eta_3, \eta_4; z) = 1 + \alpha_1\eta_2 + \alpha_2\eta_3 + \alpha_3\eta_4$. For $\xi \in \Psi[\Omega, \Delta_e]$, it is required that $\xi(r,s,t,u;z) \notin \Omega$. Consider

$$\begin{aligned}|\alpha_1 s + \alpha_2 t + \alpha_3 u| &= \alpha_1|s|\left|1 + \frac{\alpha_2}{\alpha_1}\frac{t}{s} + \frac{\alpha_3}{\alpha_1}\frac{u}{s}\right|\\ &\geq \alpha_1|s|\,\mathrm{Re}\left(1 + \frac{\alpha_2}{\alpha_1}\frac{t}{s} + \frac{\alpha_3}{\alpha_1}\frac{u}{s}\right)\\ &\geq m\alpha_1 b(\theta)\bigg(1 + \frac{\alpha_2}{\alpha_1}(ml(\theta) + m - 1) + \frac{\alpha_3}{\alpha_1}(m^2h(\theta) + 3m(k-1)l(\theta))\bigg).\end{aligned}$$

As $m \geq 1$ and $\mathrm{Re}(1 + l(\theta)) > 0$, we have

$$\begin{aligned}|\alpha_1 s + \alpha_2 t + \alpha_3 u| &\geq b(\theta)\bigg(\alpha_1 + \alpha_2 l(\theta) + \alpha_3(m^2h(\theta) + 3m(k-1)l(\theta))\bigg)\\ &\geq \frac{1}{e}(\alpha_1 - \alpha_2 - m^2\alpha_3 - 3m(k-1)\alpha_3)\\ &\geq r_0. \qquad (5.2)\end{aligned}$$

Next, we consider

$$\left|\log\left(\frac{\xi(r,s,t,u;z)}{2 - \xi(r,s,t,u;z)}\right)\right| = \left|\log\left(\frac{1 + \alpha_1 s + \alpha_2 t + \alpha_3 u}{1 - (\alpha_1 s + \alpha_2 t + \alpha_3 u)}\right)\right|.$$

Through Lemma 2.4 and (5.2), we have

$$\left|\log\left(\frac{1 + \alpha_1 s + \alpha_2 t + \alpha_3 u}{1 - (\alpha_1 s + \alpha_2 t + \alpha_3 u)}\right)\right| \geq 1.$$

Therefore, $\xi \in \Psi[\Omega, \Delta_e]$ and $p(z) \prec e^z$ as a consequence of Lemma 3.2. ∎

Theorem 5.6. *Suppose α_1, α_2, $\alpha_3 > 0$ and $\alpha_1 - \alpha_2 - m^2\alpha_3 - 3m(k-1)\alpha_3 \geq \sqrt{2}e$. Consider the analytic function p in $\mathbb{D}$ such that $p(0) = 1$ and*

$$1 + \alpha_1 z p'(z) + \alpha_2 z^2 p''(z) + \alpha_3 z^3 p'''(z) \prec z + \sqrt{1+z^2}$$

implies $p(z) \prec e^z$.

Proof. Suppose $h(z) = z + \sqrt{1+z^2}$ for $z \in \mathbb{D}$ and $\Omega = \{\delta \in \mathbb{C} : |\delta^2 - 1| < 2|\delta|\}$. Define $\xi : \mathbb{C}^4 \times \mathbb{D} \to \mathbb{C}$ as $\xi(\eta_1, \eta_2, \eta_3, \eta_4; z) = 1 + \alpha_1\eta_2 + \alpha_2\eta_3 + \alpha_3\eta_4$. For $\xi \in \Psi[\Omega, \Delta_e]$, we must have $\xi(r, s, t, u; z) \notin \Omega$. From the graph of $z + \sqrt{1+z^2}$ (see Fig. 1), we note that Ω is constructed by two circles

$$C_1 : |z - 1| = \sqrt{2} \quad \text{and} \quad C_2 : |z + 1| = \sqrt{2}.$$

It is obvious that Ω contains the disk enclosed by C_1 and excludes the portion of the disk enclosed by $C_2 \cap C_1$. We have

$$|\xi(r, s, t, u; z) - 1| = |\alpha_1 s + \alpha_2 t + \alpha_3 u|.$$

Analogous to Theorem 5.5, we have

$$\begin{aligned} |\alpha_1 s + \alpha_2 t + \alpha_3 u| &\geq b(\theta)\Big(\alpha_1 + \alpha_2 l(\theta) + \alpha_3(m^2 h(\theta) + 3m(k-1)l(\theta))\Big) \\ &\geq \frac{1}{e}(\alpha_1 - \alpha_2 - m^2\alpha_3 - 3m(k-1)\alpha_3) \\ &\geq \sqrt{2}. \end{aligned}$$

Thus, we can say that $\xi(r, s, t, u; z)$ does not belong to the circle C_1 which suffices us to deduce that $\xi(r, s, t, u; z) \notin \Omega$. Therefore, $\xi \in \Psi[\Omega, \Delta_e]$ and thus $p(z) \prec e^z$ by using Lemma 3.2. ∎

If we take $h(z)$ to be $1 + \sin z$ and $1 + ze^z$, the results are as follow:

Theorem 5.7. *Suppose α_1, α_2, $\alpha_3 > 0$ and $\alpha_1 - \alpha_2 - m^2\alpha_3 - 3m(k-1)\alpha_3 \geq e \sinh 1$. Consider the analytic function p in $\mathbb{D}$ such that $p(0) = 1$ and*

$$1 + \alpha_1 z p'(z) + \alpha_2 z^2 p''(z) + \alpha_3 z^3 p'''(z) \prec 1 + \sin z$$

implies $p(z) \prec e^z$.

Proof. Suppose $h(z) = 1 + \sin z$ and $\Omega = \{\delta \in \mathbb{C} : |\arcsin(\delta - 1)| < 1\}$. Let us define $\xi : \mathbb{C}^4 \times \mathbb{D} \to \mathbb{C}$ as $\xi(\eta_1, \eta_2, \eta_3, \eta_4; z) = 1 + \alpha_1\eta_2 + \alpha_2\eta_3 + \alpha_3\eta_4$. For $\xi \in \Psi[\Omega, \Delta_e]$, it is required that $\xi(r, s, t, u; z) \notin \Omega$. Through [4, Lemma 3.3], we note that the smallest disk containing Ω is $\{\delta : |\delta - 1| < \sinh 1\}$. So,

$$|\xi(r, s, t, u; z) - 1| = |\alpha_1 s + \alpha_2 t + \alpha_3 u|.$$

Analogous to the proof of Theorem 5.5, we have

$$\begin{aligned} |\alpha_1 s + \alpha_2 t + \alpha_3 u| &\geq b(\theta)\Big(\alpha_1 + \alpha_2 l(\theta) + \alpha_3(m^2 h(\theta) + 3m(k-1)l(\theta))\Big) \\ &\geq \frac{1}{e}(\alpha_1 - \alpha_2 - m^2\alpha_3 - 3m(k-1)\alpha_3) \\ &\geq \sinh 1. \end{aligned}$$

Clearly, $\xi(r, s, t, u; z)$ does not belong to the disk $\{\delta : |\delta - 1| < \sinh 1\}$ indicates that $\xi(r, s, t, u; z) \notin \Omega$. Therefore, $\xi \in \Psi[\Omega, \Delta_e]$ and thus $p(z) \prec e^z$ by employing Lemma 3.2. ∎

Theorem 5.8. *Suppose α_1, α_2, $\alpha_3 > 0$ and $\alpha_1 - \alpha_2 - m^2\alpha_3 - 3m(k-1)\alpha_3 \geq e^2$. Consider the analytic function p in $\mathbb{D}$ such that $p(0) = 1$ and*

$$1 + \alpha_1 z p'(z) + \alpha_2 z^2 p''(z) + \alpha_3 z^3 p'''(z) \prec 1 + ze^z$$

implies $p(z) \prec e^z$.

Proof. Suppose $h(z) = 1 + ze^z$ and $\Omega = h(\mathbb{D})$. We define $\xi : \mathbb{C}^4 \times \mathbb{D} \to \mathbb{C}$ as $\xi(\eta_1, \eta_2, \eta_3, \eta_4; z) = 1 + \alpha_1\eta_2 + \alpha_2\eta_3 + \alpha_3\eta_4$. For $\xi \in \Psi[\Omega, \Delta_e]$, we need to have that $\xi(r, s, t, u; z) \notin \Omega$. Through [10, Lemma 3.3], we note that the smallest disk containing Ω is $\{\delta \in \mathbb{C} : |\delta - 1| < e\}$. Also,

$$|\xi(r, s, t, u; z) - 1| = |\alpha_1 s + \alpha_2 t + \alpha_3 u|.$$

Analogous to the proof of Theorem 5.5, we have

$$\begin{aligned} |\alpha_1 s + \alpha_2 t + \alpha_3 u| &\geq b(\theta)\bigg(\alpha_1 + \alpha_2 l(\theta) + \alpha_3(m^2 h(\theta) + 3m(k-1)l(\theta))\bigg) \\ &\geq \frac{1}{e}(\alpha_1 - \alpha_2 - m^2\alpha_3 - 3m(k-1)\alpha_3) \\ &\geq e. \end{aligned}$$

Clearly, $\xi(r, s, t, u; z)$ does not belong to the disk $\{\delta \in \mathbb{C} : |\delta - 1| < e\}$, is enough to conclude that $\xi(r, s, t, u; z) \notin \Omega$. Therefore, $\xi \in \Psi[\Omega, \Delta_e]$ and thus $p(z) \prec e^z$ by using Lemma 3.2. ∎

We complete this section by considering $h(z) = 1 + \sinh^{-1} z$ and e^z itself which are followed by a resulting corollary.

Theorem 5.9. *Suppose α_1, α_2, $\alpha_3 > 0$ and $2(\alpha_1 - \alpha_2 - m^2\alpha_3 - 3m(k-1)\alpha_3) \geq \pi e$. Consider the analytic function p in $\mathbb{D}$ such that $p(0) = 1$ and*

$$1 + \alpha_1 z p'(z) + \alpha_2 z^2 p''(z) + \alpha_3 z^3 p'''(z) \prec 1 + \sinh^{-1} z$$

implies $p(z) \prec e^z$.

Proof. Suppose $h(z) = 1 + \sinh^{-1} z$ and $\Omega = \{\delta \in \mathbb{C} : |\sinh(\delta - 1)| < 1\}$. Define $\xi : \mathbb{C}^4 \times \mathbb{D} \to \mathbb{C}$ as $\xi(\eta_1, \eta_2, \eta_3, \eta_4; z) = 1 + \alpha_1\eta_2 + \alpha_2\eta_3 + \alpha_3\eta_4$. For $\xi \in \Psi[\Omega, \Delta_e]$, it is required that $\xi(r, s, t, u; z) \notin \Omega$. Through [2, Remark 2.7], we note that the smallest disk containing Ω is $\{\delta \in \mathbb{C} : |\delta - 1| < \pi/2\}$. So,

$$|\xi(r, s, t, u; z) - 1| = |\alpha_1 s + \alpha_2 t + \alpha_3 u|.$$

Analogous to Theorem 5.5, we have

$$\begin{aligned} |\alpha_1 s + \alpha_2 t + \alpha_3 u| &\geq b(\theta)\bigg(\alpha_1 + \alpha_2 l(\theta) + \alpha_3(m^2 h(\theta) + 3m(k-1)l(\theta))\bigg) \\ &\geq \frac{1}{e}(\alpha_1 - \alpha_2 - m^2\alpha_3 - 3m(k-1)\alpha_3) \\ &\geq \frac{\pi}{2}. \end{aligned}$$

Clearly, $\xi(r, s, t, u; z) \notin \{\delta \in \mathbb{C} : |\delta - 1| < \pi/2\}$ which suffices to prove that $\xi(r, s, t, u; z) \notin \Omega$. Therefore, $\xi \in \Psi[\Omega, \Delta_e]$ and thus $p(z) \prec e^z$ by Lemma 3.2. ∎

Theorem 5.10. *Suppose α_1, α_2, $\alpha_3 > 0$ and $\alpha_1 - \alpha_2 - m^2\alpha_3 - 3m(k-1)\alpha_3 \geq e(e-1)$. Consider the analytic function p in $\mathbb{D}$ such that $p(0) = 1$ and*

$$1 + \alpha_1 z p'(z) + \alpha_2 z^2 p''(z) + \alpha_3 z^3 p'''(z) \prec e^z$$

implies $p(z) \prec e^z$.

Proof. Suppose $h(z) = e^z$ and $\Omega = \Delta_e$. We define $\xi : \mathbb{C}^4 \times \mathbb{D} \to \mathbb{C}$ as $\xi(\eta_1, \eta_2, \eta_3, \eta_4; z) = 1 + \alpha_1\eta_2 + \alpha_2\eta_3 + \alpha_3\eta_4$. For $\xi \in \Psi[\Delta_e, \Delta_e]$, it is necessary to have $\xi(r, s, t, u; z) \notin \Delta_e$. So,

$$|\xi(r, s, t, u; z) - 1| = |\alpha_1 s + \alpha_2 t + \alpha_3 u|.$$

Analogous to Theorem 5.5, we get

$$\begin{aligned}|\alpha_1 s+\alpha_2 t+\alpha_3 u| &\geq b(\theta)\bigg(\alpha_1+\alpha_2 l(\theta)+\alpha_3(m^2h(\theta)+3m(k-1)l(\theta))\bigg)\\ &\geq \frac{1}{e}(\alpha_1-\alpha_2-m^2\alpha_3-3m(k-1)\alpha_3)\\ &\geq e-1. \end{aligned} \tag{5.3}$$

Next, we consider

$$|\log(\xi(r,s,t,u;z)|=|\log(1+\alpha_1 s+\alpha_2 t+\alpha_3 u)|.$$

Through Lemma 2.3 and (5.3), we have

$$|\log(1+\alpha_1 s+\alpha_2 t+\alpha_3 u)|\geq 1,$$

which implies that $\xi(r,s,t,u;z)\notin\Delta_e$. Therefore, $\xi\in\Psi[\Delta_e,\Delta_e]$ and thus $p(z)\prec e^z$. ∎

Theorems 5.5-5.10 yield the following conclusion if $p(z)=zf'(z)/f(z)$ is considered as in (5.1).

Corollary 5.11. *Suppose α_1, α_2 and α_3 be positive real numbers with $f\in\mathcal{A}$. Then, $f(z)\in\mathcal{S}_e^*$ if any of these conditions hold:*

(*i*) $\chi_f(z)\prec 2/(1+e^{-z})$ *and* $\alpha_1-\alpha_2-m^2\alpha_3-3m(k-1)\alpha_3\geq er_0$, *where* $r_0\approx 0.546302$ *is the positive root of the equation* $r^2+2\cot(1)r-1=0$.
(*ii*) $\chi_f(z)\prec z+\sqrt{1+z^2}$ *and* $\alpha_1-\alpha_2-m^2\alpha_3-3m(k-1)\alpha_3\geq\sqrt{2}e$.
(*iii*) $\chi_f(z)\prec 1+\sin z$ *and* $\alpha_1-\alpha_2-m^2\alpha_3-3m(k-1)\alpha_3\geq e\sinh 1$.
(*iv*) $\chi_f(z)\prec 1+ze^z$ *and* $\alpha_1-\alpha_2-m^2\alpha_3-3m(k-1)\alpha_3\geq e^2$.
(*v*) $\chi_f(z)\prec 1+\sinh^{-1}z$ *and* $2(\alpha_1-\alpha_2-m^2\alpha_3-3m(k-1)\alpha_3)\geq\pi e$.
(*vi*) $\chi_f(z)\prec e^z$ *and* $\alpha_1-\alpha_2-m^2\alpha_3-3m(k-1)\alpha_3\geq e(e-1)$.

Acknowledgment. Neha Verma is thankful to the Department of Applied Mathematics, Delhi Technological University, New Delhi-110042 for providing Research Fellowship.

References

[1] J. Antonino and S. S. Miller, Third-order differential inequalities and subordinations in the complex plane, Complex Var. Elliptic Equ. **56** (2011), no. 5, 439–454.
[2] K. Arora and S. S. Kumar, Starlike functions associated with a petal shaped domain, Bull. Korean Math. Soc. **59** (2022), no. 4, 993–1010.
[3] S. Z. H. Bukhari and M. Nazir, Differential subordination and harmonic means for the Koebe type n-fold symmetric functions, Hacet. J. Math. Stat. **51** (2022), no. 6, 1630–1636.
[4] N. E. Cho, V. Kumar, S. S. Kumar and V. Ravichandran, Radius problems for starlike functions associated with the sine function, Bull. Iranian Math. Soc. **45** (2019), no. 1, 213–232.
[5] P. Goel and S. S. Kumar, Certain class of starlike functions associated with modified sigmoid function, Bull. Malays. Math. Sci. Soc. **43** (2020), no. 1, 957–991
[6] A. W. Goodman, Univalent functions. Vol. I, Mariner Publishing Co., Inc., Tampa, FL, 1983.
[7] W. Janowski, Extremal problems for a family of functions with positive real part and for some related families, Ann. Polon. Math. **23** (1970/71), 159–177.
[8] P. G. Krishnan, V. Ravichandran and P. Saikrishnan, Functions subordinate to the exponential function, Commun. Korean Math. Soc. **38** (2023), no. 1, 163–178.
[9] S. S. Kumar and P. Goel, Starlike functions and higher order differential subordinations, Rev. R. Acad. Cienc. Exactas Fís. Nat. Ser. A Mat. RACSAM **114** (2020), no. 4, Paper No. 192, 23 pp.
[10] S. S. Kumar and G. Kamaljeet, A cardioid domain and starlike functions, Anal. Math. Phys. **11** (2021), no. 2, Paper No. 54, 34 pp.
[11] S. Kumar and V. Ravichandran, Subordinations for functions with positive real part, Complex Anal. Oper. Theory **12** (2018), no. 5, 1179–1191.
[12] W. C. Ma and D. Minda, A unified treatment of some special classes of univalent functions, Proc. Confer. Complex Anal. (Tianjin, 1992), 157–169.

[13] V. Madaan, A. Kumar and V. Ravichandran, Starlikeness associated with lemniscate of Bernoulli, Filomat **33** (2019), no. 7, 1937-1955.
[14] R. Mendiratta, S. Nagpal and V. Ravichandran, On a subclass of strongly starlike functions associated with exponential function, Bull. Malays. Math. Sci. Soc. **38** (2015), no. 1, 365–386.
[15] S. S. Miller and P. T. Mocanu, Differential subordinations, Monographs and Textbooks in Pure and Applied Mathematics, 225, Marcel Dekker, Inc., New York, 2000.
[16] S. Mushtaq, M. Raza and J. Sokół, Differential subordination related with exponential functions, Quaest. Math. **45** (2022), no. 6, 889–899.
[17] A. Naz, S. Nagpal and V. Ravichandran, Starlikeness associated with the exponential function, Turkish J. Math. **43** (2019), no. 3, 1353–1371.
[18] R. K. Raina and J. Sokól, Some properties related to a certain class of starlike functions, C. R. Math. Acad. Sci. Paris **353** (2015), no. 11, 973–978.
[19] J. Sokół and J. Stankiewicz, Radius of convexity of some subclasses of strongly starlike functions, Zeszyty Nauk. Politech. Rzeszowskiej Mat. No. 19 (1996), 101–105.

Department of Applied Mathematics, Delhi Technological University, Delhi–110042, India
Email address: nehaverma1480@gmail.com

Department of Applied Mathematics, Delhi Technological University, Delhi–110042, India
Email address: spkumar@dce.ac.in

2023 2nd International Conference on Paradigm Shifts in Communications Embedded Systems, Machine Learning and Signal Processing (PCEMS) | 979-8-3503-1071-9/23/$31.00 ©2023 IEEE | DOI: 10.1109/PCEMS58491.2023.10136036

Implementing Chaos Based Optimisations on Neural Networks for Predictions of Distributed Denial-of-Service (DDoS) Attacks

Anisha Jha
Department of Applied Mathematics
Delhi Technological University
Delhi, India
2001anishajha@gmail.com

Avikal Goel
Department of Applied Mathematics
Delhi Technological University
Delhi, India
avikal.on.email@gmail.com

Divansh Mahajan
Department of Applied Mathematics
Delhi Technological University
Delhi, India
divanshmahajan09@gmail.com

Goonjan Jain
Department of Applied Mathematics
Delhi Technological University
Delhi, India
goonjanjain@dtu.ac.in

***Abstract*—A Distributed Denial-of-Service attack (DDoS) involves overwhelming a network with a large amount of traffic that aims to disrupt the normal functioning of a network. DDoS attacks can cause a variety of problems, such as website downtime, loss of revenue, and damage to a company's reputation. One of the main challenges in dealing with DDoS attacks is detecting them in a timely and accurate manner.**

Machine learning algorithms can be trained to recognize patterns in network traffic that are indicative of a DDoS attack, and they can also be used to distinguish between legitimate traffic and attack traffic. The paper discusses a method for improving the performance of neural networks by utilizing chaos-based algorithms for detection and prediction of DDoS attacks. Moreover, this paper talks about using chaos-based optimization to speed up the process of training a model using neural networks. This technique uses a chaotic sequence to set the initial weights and biases of the model, which can result in a wider range of random starting points. This can help the model to find the best solution faster.

***Keywords*—Distributed Denial of Service (DDoS), Chaos Theory, Chaos Genetic Algorithm (CGA), Chaos Based Back Propagation (CBP), Artificial Neural Networks**

I. INTRODUCTION

As a form of cyber attack, Distributed Denial of Service (DDoS) involves flooding a target website or online service with an overwhelming amount of traffic using a large number of compromised computers, called bots or zombies. The primary goal of this type of attack is to make the target website unavailable to legitimate users. In order to accomplish this, servers and network infrastructure are overloaded with information requests, rendering legitimate traffic impossible to process. This can cause significant disruptions to the targeted organization's operations and can result in significant financial losses.

979-8-3503-1071-9/23/$31.00 ©2023 IEEE

DDoS attacks can be launched from a single location, but are more often launched from a distributed network of compromised systems. This makes them difficult to block or mitigate, as the traffic is coming from multiple sources, making it difficult to identify and stop the attack. DDoS attacks can be used to target a wide range of organizations, including governments, financial institutions, and large corporations. The damage caused by DDoS attacks can range from minor disruptions to critical infrastructure failures, making them a serious threat to national security and economic stability.

To defend against DDoS attacks, various techniques have been proposed such as filtering, redirection and rate limiting. However, these methods are not always effective and can result in false positives. To address this problem, researchers have proposed the use of neural networks to predict DDoS attacks by analyzing network traffic patterns and identifying anomalies that may indicate an imminent attack. This can be done by training a neural network on historical data of normal network traffic, and then using this trained model to detect patterns in real-time network traffic that deviate from the expected normal patterns. The neural network can then be used to classify network traffic as either normal or potentially malicious, and take appropriate action to mitigate the attack.

In some recent papers, chaos-based optimization algorithms were used on neural networks to improve the optimization process by introducing randomness and increasing the chance of finding the global optimal solution by exploring a wider

Authorized licensed use limited to: DELHI TECHNICAL UNIV. Downloaded on June 14,2023 at 05:37:08 UTC from IEEE Xplore. Restrictions apply.

solution space. In complex systems, small changes in initial conditions can produce vastly different outcomes, which is the basis of chaos-based optimizers. The work presented in [1] surveys the recent developed DDoS detection approaches using the machine learning models. Authors of [2–4] proposed a DDoS detection system using Naïve Bayes model. On the other hand, the support vector machine model has been adopted in this works [5, 6] to detect the present of DDoS attacks. In addition, Decision Tree algorithm has also been adopted to detect the DDoS attacks, as presented in [7, 8]. By introducing randomness and allowing the algorithm to explore a wider range of the solution space, these optimizers can help the neural network find better solutions and improve its performance in identifying DDoS attacks.

II. RELATED WORK

A. Improved BP Neural Network Algorithm Model Based on Chaos Genetic Algorithm[9]

In this paper, Backpropagation neural networks have been designed to avoid local optimal problems and slow convergence speed by utilizing the ergodicity of chaos theory.. Mean error of the multimodal function based BP training was also observed to be the lowest when using the chaos genetic algorithm.

B. Study of chaos genetic algorithms and its application in neural networks[10]

Paper combined chaos theory and genetic algorithm and its use in training neural networks with the help of XOR Neural network.

C. Back-propagation with Chaos[11]

An examination of the effects of chaos on learning performance was presented in the paper. A new formula for updating the connection weights was proposed and then applied on 3 different datasets and performed better than traditional algorithms .

D. An new back propagation algorithm with chaotic learning rate[12]

This paper discusses an algorithm to improve the learning rate using chaos and how global optimal points can be achieved . The proposed method had a higher accuracy along with lesser iterations when compared with other algorithms like VLBP and SALBP.

E. Detection of known and unknown DDoS attacks using Artificial Neural Networks[13]

In this paper, among all other various existing machine learning models, artificial neural networks were used. The main aim of neural networks here was to detect TCP; UDP and ICMP. The system was then trained using both old and current datasets (patterns), and the results showed that it was successful at identifying both known (100%) and unidentified (95%) DDoS attacks that were comparable to those used to train it.

III. CHAOS BASED ALGORITHMS USED FOR NEURAL NETWORK OPTIMISATION

A. Chaos Genetic Algorithm (CGA)

Chaos Genetic Algorithm (CGA) is an optimization algorithm that combines the principles of genetic algorithms (GAs) and chaos theory. Like traditional GAs, CGA uses a population of candidate solutions that evolve over time through a process of selection, crossover, and mutation. However, CGA introduces chaotic elements into the genetic operators to increase the diversity and exploration of the population. Chaos Genetic Algorithm (CGA) can be used to improve the accuracy of a neural network by optimizing its parameters. The accuracy of neural networks is highly dependent on the parameters of the network, such as the weights and biases of the neurons, and small changes in these values can have a significant impact on the accuracy of the network. As a first step, a population of solutions is generated with random parameters for the neural network. The fitness of each solution is then evaluated by evaluating the neural network with the training data and measuring the accuracy of the network. The algorithm then iterates for the specified number of generations. In each generation, the best solutions from the population are selected for crossover. Random values for the logistic map function are generated. The new solutions are generated by applying crossover and mutation to the selected parents. The fitness of the new solutions is then evaluated when the accuracy of the neural network with the training data is being measured.

At the end of the generations, the solution with the best fitness is selected and the weights of the neural network are updated with the best solution's weights. The final optimized neural network is then returned.

By using CGA to optimize the parameters of a neural network, several advantages can be achieved :-

1) Exploration of the search space: CGA uses chaotic elements to increase the diversity of the population, which allows the algorithm to analyze and examine an even broader search space. This can help the algorithm to get to superior and more optimized solutions and improve the accuracy of the network.
2) Escape from local optima: CGA can escape from local optima by introducing chaos in the genetic operators, which can help the algorithm to find the global optimum.
3) Faster convergence: CGA can converge faster than traditional optimization methods, by combining the exploration capabilities of GAs and the fast convergence of chaos theory.
4) Handling complex optimization problems: The CGA algorithm can easily take into account the complex optimization problems that the conventional methods may struggle with, such as non-linear or multi-modal functions.

Authorized licensed use limited to: DELHI TECHNICAL UNIV. Downloaded on June 14,2023 at 05:37:08 UTC from IEEE Xplore. Restrictions apply.

B. Chaos Based Back-Propagation Algorithm (CBP)

Chaos-based backpropagation (CBP) is an optimization algorithm that combines the principles of backpropagation (BP) and chaos theory. Backpropagation is a method used to train artificial neural networks by adjusting the weights and biases of the neurons in order to minimize the error. It is based on the gradient descent algorithm and commonly used for training neural networks.

The chaotic optimization algorithm is implemented to enhance the performance of a neural network by utilizing the principles of chaos theory. It generates a sequence of random numbers through the use of a chaotic function called the logistic map, which is then employed to set the initial values of the model's weights and biases. By initializing the model with these random numbers, the algorithm aims to improve the model's ability to find good solutions to the problem. The model is then fit to the training data for a specified number of epochs and batch size. The logistic map is a simple mathematical equation that can generate a chaotic sequence of numbers. The "r" value is a parameter that controls the behavior of the logistic map, and when it is set to a value between 3.57 and 4, it generates a chaotic sequence of numbers. The algorithm uses this chaotic sequence of numbers to initialize the weights and biases of the model, which helps to improve the model's performance by avoiding local minima and helping the model to explore more of the solution space.

CBP can improve the accuracy of a sequential neural network in several ways:

1) Faster convergence: By introducing chaotic elements, CBP can increase the speed of convergence and help the network to find better solutions faster.
2) Escape from local optima: CBP can escape from local optima by introducing chaos in the learning rate and momentum, which can help the algorithm to find the global optimum.
3) Generalization ability: CBP can improve the generalization ability of the network, by avoiding overfitting which is a common problem in neural networks.
4) Handling complex optimization problems: CBP can handle complex optimization problems that traditional back propagation methods may struggle with, such as non-linear or multi-modal functions.
5) Better exploration of the parameter space: CBP can explore the parameter space more effectively by introducing chaos in the learning rate and momentum, which allows it to explore different areas of the space, thus finding better solutions.

IV. METHODOLOGY

The first step in this research is to collect and examine a dataset of network traffic data. This data is then utilized to train and evaluate a neural network-based machine learning model, which aims to differentiate between regular and malicious traffic. Machine Learning methods when exposed to data are capable of adapting independently and learning from earlier computations in order to interpret the available data for identifying hidden patterns.They have been known to classify network traffic [14], perform software metrics prediction [15], predicting software change proneness [16], Botnet detection [17], DDoS detection [18] etc. The research uses a simple neural network designed using the Keras library in Python which has two layers: an input layer with 32 neurons, and an output layer with 1 neuron. The input layer utilizes the sigmoid activation function, and the output layer also uses the sigmoid activation function. The model is fine-tuned using the Adam optimizer with a learning rate of 0.001 and is trained using binary cross-entropy loss. The training process is done on the provided X_train and y_train datasets for 100 epochs with a batch size of 16.

To improve the accuracy of the model, the research proposed the use of a chaos-based optimizer called the Chaos Genetic Algorithm (CGA) and Chaos backpropagation (CBP). CGA is an optimization algorithm that combines the principles of genetic algorithms (GAs) and chaos theory. Like traditional GAs, CGA uses a population of candidate solutions that evolve over time through a process of selection, crossover, and mutation. However, CGA introduces chaotic elements into the genetic operators to increase the diversity and exploration of the population. By using CGA to optimize the parameters of the neural network, several advantages can be achieved such as exploration of the search space, escape from local optima, faster convergence and the ability to find the global optimum.The Chaos-based backpropagation (CBP) algorithm improves neural network training by combining the principles of backpropagation and chaos theory. The algorithm incorporates chaotic elements to generate random numbers for fine-tuning the learning rate and momentum, which helps the network to bypass local optima and explore a broader range of possibilities for more effective optimization.

The last step of the methodology was to assess the effectiveness of the new CGA and CBP optimization method. The accuracy of the optimized neural network was measured and compared to that of the non-optimized neural network. The results indicated that the chaotic optimization method significantly enhanced the accuracy of the neural network. The study concludes that incorporating chaos-based optimization techniques like CGA and CBP can be an efficient way to enhance the performance of neural network models in network traffic prediction tasks.

V. EXPERIMENT

A. Dataset

The dataset that is being used is a labeled dataset related to Distributed Denial of Service (DDOS) attacks. The dataset contains 809361 rows and 49 columns, where each row represents a flow of network traffic, and each column contains various features that describe the properties of the

Authorized licensed use limited to: DELHI TECHNICAL UNIV. Downloaded on June 14,2023 at 05:37:08 UTC from IEEE Xplore. Restrictions apply.

traffic flow. The dataset includes various types of data related to the destination port, duration of flow, total amount of packets sent and received, statistics on packet lengths and flow, count of flags, and other relevant information.

The dataset includes columns that describe both forward and backward traffic, and it also includes statistics about the different flags and the length of the packets, which could be useful features to detect a DDoS attack. The dataset also includes columns that describe the flow statistics, such as the flow bytes per second and the flow packets per second, which may help in detecting abnormal traffic patterns.

The initial step in preparing the data for the model is to create a scaler object and fit it to the training data using the fit() method. Once the scaler has been fitted, it can then be applied to both the training and test data to standardize the features and make sure they are on the same scale. Normalizing the data can be beneficial in machine learning models as it allows for all features to have similar ranges which can enhance the model's performance.

Based on the parameters mentioned above, machine learning models are trained for DDoS attack detection, where the features in the dataset serve as input for the model, and the labels are used to distinguish between normal and attack traffic.

B. Training and Optimisation

After gathering and analyzing the dataset, the next step was to implement the neural networks machine learning model for predicting the normal traffic and the attack traffic. The neural network that is being used in this process has been created using the Keras library in Python. It has a simple structure, consisting of an input layer with 32 neurons and an input dimension of 77, and an output layer with 1 neuron. Both layers use the sigmoid activation function and it was optimized using Adam optimizer with a learning rate of 0.001, the model was trained using binary cross-entropy loss. The model was trained using the provided X_train and y_train data for 100 epochs and with a batch size of 16. The training process for this model is stored in a variable called "history" which can be used to plot the accuracy or loss of the model over the number of epochs.

The next step after building the neural network is to use the CGA Algorithm to optimize its performance. The function which implements the CGA algorithm needs the neural network, the data used for training X_train and y_train , and a set of parameters as inputs. These parameters include the number of iterations the algorithm should run for, the number of solutions in the population, and the range of values for the random numbers used in the logistic map. The function begins by generating a population of random solutions, then uses the evaluate() method of the neural network to determine the quality of each solution. The function repeatedly goes through a set number of iterations, choosing the most promising solutions for crossover and applying crossover and mutation to create new solutions. The fitness of the new solutions is evaluated, with the best one being chosen as the final output.

The second optimization that is being carried out on the neural network is the CBP Algorithm. In this model, a chaos function, logistic_map, is defined with a chaotic sequence generated using the logistic map with a parameter value of r = 4 and an initial value of x0. The chaotic sequence is utilized to set the initial weights and biases of the neural network model. Subsequently, the model is trained using the X_train and y_train data for 100 iterations, with a batch size of 32. The training progress is recorded in the "history3" variable which can be used to plot the accuracy or loss of the model against the number of iterations.

It's important to note that the machine learning model and the optimisations are not meant to be executed in sequence, but rather represent three alternative approaches to initializing the weights and biases of a machine learning model. Depending on the problem and the data, one approach may be more effective than the other, or they may not make a significant difference. It's also possible to combine the two approaches or use other methods for weight initialization.

C. Analysis

The accuracy of the neural network model on the training data is 83.799071119068%. The loss function used is binary_crossentropy. The loss values are negative because the optimizer is trying to maximize the log-likelihood of the model. Also, When training a neural network, there are several metrics that can be tracked and plotted against the number of epochs to help understand the performance of the model. The accuracy VS the epochs graph for this neural network suggests that the desired accuracy by the neural network is reached and the model does not learn further as the epochs are increased.

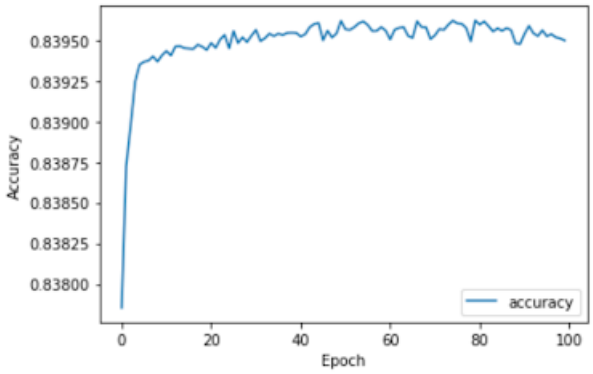

Fig. 1. Accuracy VS Epochs plot for the trained Neural Network

Furthermore, after applying the CGA optimisation and the CBP optimisation, we find that both methods achieve similar

Authorized licensed use limited to: DELHI TECHNICAL UNIV. Downloaded on June 14,2023 at 05:37:08 UTC from IEEE Xplore. Restrictions apply.

accuracy on the training data, with CGA achieving an accuracy of 83.91640782356262% and CBP achieving an accuracy of 83.9899212671066%. It's worth mentioning that the outcome of using this algorithm may differ based on the type of data and structure of the neural network being used. Also, for the CBP Algorithm, the training process is running for 100 epochs. At each epoch, the model is being trained on 25293 training examples. The loss is decreasing with each epoch and the accuracy is increasing. The final accuracy on training data is 83.83%. The accuracy of 83.83% is a good accuracy for a model and it can be considered as a good model.

Furthermore, for this model too, the accuracy VS the epochs graph is provided below.

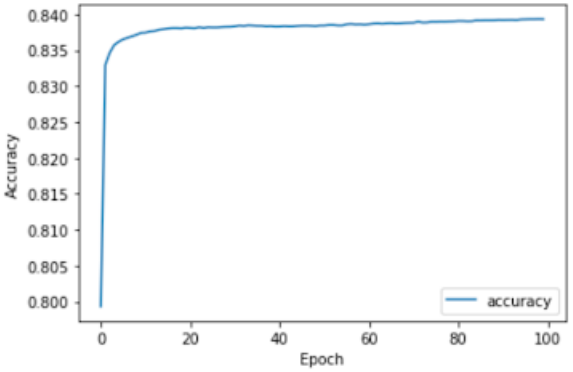

Fig. 2. Accuracy VS Epochs plot for the CBP Algorithm

In general, traditional machine learning models may take longer to train as they require multiple iterations to optimize the parameters and find the best fit for the data. This process involves computing the gradients of the loss function with respect to the parameters and adjusting them using an optimization algorithm, such as gradient descent or Adam. The time taken for this process can be reduced by using more powerful hardware, such as GPUs or TPUs.

On the other hand, chaos-based optimization aims to speed up the training process by using a chaotic sequence to initialize the weights and biases of the model. This initialization is expected to produce a more diverse and random starting point, which may lead to a faster convergence towards the optimal solution. However, the time taken for the chaotic sequence to generate may offset the benefits of the faster convergence. In our use case too the total time taken by the neural network is 5133 seconds, which approximates to 85.5 minutes for 100 epochs whereas the CBP optimiser takes only 2458 seconds, which approximates to 41 minutes for 100 epochs. The average time per epoch taken by neural network is 51 seconds whereas the average time taken by the CBP optimiser is 24 seconds.

VI. CONCLUSION

Detecting DDoS attacks is an important step in protecting networks and minimizing the impact of an attack. It helps network administrators to mitigate the attack, gather forensic information, respond to security incidents, identify security vulnerabilities, maintain business continuity, and comply with regulations. Hence in this paper, we first analyzed the use of an artificial neural network (ANN) as a method for distinguishing between normal traffic and attack traffic in the context of handling DDOS attacks and intrusion in conventional networks. The results of the ANN yielded an accuracy of 83.799071119068%. To improve upon this accuracy, we then applied two different chaos-based optimization techniques to the same neural network. The first optimization technique, called the CGA algorithm, resulted in an accuracy of 83.91640782356262%, while the second technique, called the CBP algorithm, resulted in an accuracy of 83.9899212671066%.

In conclusion, by utilizing the CGA algorithm, the performance of a neural network can be enhanced through optimization of its parameters. This is achieved by the CGA's ability to navigate a larger range of the search space, avoid getting stuck in local optima, reach an optimal solution faster and effectively tackle complex optimization challenges. On the other hand, the Chaos-based backpropagation (CBP) algorithm combines the principles of backpropagation and chaos theory to improve the performance of neural network training. By using chaotic elements to generate pseudo-random numbers to adjust the learning rate and momentum of the algorithm, the use of the CBP algorithm enables the network to avoid getting stuck in suboptimal solutions and instead explore a larger portion of the search space, leading to a more effective optimization process.

VII. FUTURE WORK

As a step further from this analysis, we can explore other chaos-based optimization algorithms for neural networks Exploring the potential benefits of using chaos-based optimization algorithms in conjunction with other machine learning approaches, specifically deep learning, to enhance the ability of neural networks to detect and mitigate DDOS attacks and intrusion attempts could be a valuable area of research.. We can also try to implement these algorithms on a real-time system to see how they perform under actual attack scenarios. Furthermore, researchers can also study the scalability of the CGA algorithm on big data and distributed systems. Additionally, we can investigate the use of these optimization techniques in other types of machine learning models and in other areas of network security.

References

[1] M. Arshi, M. Nasreen, and K. Madhavi, "A survey of ddos attacks using machine learning techniques," in *E3S Web of Conferences*, EDP Sciences, vol. 184, 2020, p. 01 052.

Authorized licensed use limited to: DELHI TECHNICAL UNIV. Downloaded on June 14,2023 at 05:37:08 UTC from IEEE Xplore. Restrictions apply.

[2] A. Bivens, C. Palagiri, R. Smith, B. Szymanski, M. Embrechts, *et al.*, "Network-based intrusion detection using neural networks," *Intelligent Engineering Systems through Artificial Neural Networks*, vol. 12, no. 1, pp. 579–584, 2002.

[3] J. K. Bains, K. K. Kaki, and K. Sharma, "Intrusion detection system with multi layer using bayesian networks," *International Journal of Computer Applications*, vol. 67, no. 5, 2013.

[4] M. Alkasassbeh, G. Al-Naymat, A. B. Hassanat, and M. Almseidin, "Detecting distributed denial of service attacks using data mining techniques," *International Journal of Advanced Computer Science and Applications*, vol. 7, no. 1, 2016.

[5] M. Salunke, R. Kabra, and A. Kumar, "Layered architecture for dos attack detection system by combined approach of naive bayes and improved k-means clustering algorithm," *International Research Journal of Engineering And Technology*, vol. 2, no. 3, pp. 372–377, 2015.

[6] T. Subbulakshmi, P. Parameswaran, C. Parthiban, M. Mariselvi, J. A. Anusha, and G. Mahalakshmi, "A unified approach for detection and prevention of ddos attacks using enhanced support vector machines and filtering mechanisms," *ICTACT Journal on Communication Technology*, vol. 4, no. 2, pp. 737–743, 2013.

[7] H. Waguih, "A data mining approach for the detection of denial of service attack," *IAES International Journal of Artificial Intelligence*, vol. 2, no. 2, p. 99, 2013.

[8] C. M. Rahman, D. M. Farid, N. Harbi, E. Bahri, and M. Z. Rahman, "Attacks classification in adaptive intrusion detection using decision tree," 2010.

[9] Q. Changxing, B. Yiming, and L. Yong, "Improved bp neural network algorithm model based on chaos genetic algorithm," in *2017 3rd IEEE International Conference on Control Science and Systems Engineering (ICCSSE)*, IEEE, 2017, pp. 679–682.

[10] Y. Yong, S. Wanxing, and W. Sunan, "Study of chaos genetic algorithms and its application in neural networks," in *2002 IEEE Region 10 Conference on Computers, Communications, Control and Power Engineering. TENCOM'02. Proceedings.*, IEEE, vol. 1, 2002, pp. 232–235.

[11] F. Fazayeli, L. Wang, and W. Liu, "Back-propagation with chaos," in *2008 International Conference on Neural Networks and Signal Processing*, IEEE, 2008, pp. 5–8.

[12] J. Ge, J. Sha, and Y. Fang, "An new back propagation algorithm with chaotic learning rate," in *2010 IEEE International Conference on Software Engineering and Service Sciences*, IEEE, 2010, pp. 404–407.

[13] A. Saied, R. E. Overill, and T. Radzik, "Detection of known and unknown ddos attacks using artificial neural networks," *Neurocomputing*, vol. 172, pp. 385–393, 2016.

[14] M. R. Parsaei, M. J. Sobouti, R. Javidan, *et al.*, "Network traffic classification using machine learning techniques over software defined networks," *International Journal of Advanced Computer Science and Applications*, vol. 8, no. 7, 2017.

[15] S. Jha, R. Kumar, M. Abdel-Basset, I. Priyadarshini, R. Sharma, H. V. Long, *et al.*, "Deep learning approach for software maintainability metrics prediction," *Ieee Access*, vol. 7, pp. 61 840–61 855, 2019.

[16] N. Pritam *et al.*, "Assessment of code smell for predicting class change proneness using machine learning," *IEEE Access*, vol. 7, pp. 37 414–37 425, 2019.

[17] X. D. Hoang and Q. C. Nguyen, "Botnet detection based on machine learning techniques using dns query data," *Future Internet*, vol. 10, no. 5, p. 43, 2018.

[18] M. Zekri, S. El Kafhali, N. Aboutabit, and Y. Saadi, "Ddos attack detection using machine learning techniques in cloud computing environments," in *2017 3rd international conference of cloud computing technologies and applications (CloudTech)*, IEEE, 2017, pp. 1–7.

Authorized licensed use limited to: DELHI TECHNICAL UNIV. Downloaded on June 14,2023 at 05:37:08 UTC from IEEE Xplore. Restrictions apply.

2023 2nd International Conference on Smart Technologies and Systems for Next Generation Computing (ICSTSN) | 979-8-3503-4800-2/23/$31.00 ©2023 IEEE | DOI: 10.1109/ICSTSN57873.2023.10151565

In-Silico medication of vitiligo by targeting 6AAH protein and riboflavin Ligand

Sakshi Rajesh Kumar
Department of Biotechnology
Delhi Technological University
New Delhi – 110042, India
Sakshikumar019@gmail.com

Firoz Tyagi
Department of biotechnology
Delhi Technological University
New Delhi – 110042, India
firoztyagi35@gmail.com

Yasha Hasija
Department *of biotechnology*
Delhi technological university
New Delhi - 110042, India
Yashahasija06@gmail.com

***Abstract*— Depigmentation of the skin is a primary symptom of the vitiligo disorder. By reducing their self-esteem and causing them psychological distress, it lowers patients' quality of life. The study made use of a number of computational tools, including Cyto Hubba, BioVia Discovery Studio through, Open babel, Drug bank, Avogadro, Auto dock, and Protein- Interaction Ligand profiler. The interaction between 6AAH and (Myristic acid, Heptadecanoic acid, Riboflavin, Propanol, 2,6-Dimethyl-7-octene-2,3,6-triol) has been examined in this study using Cyto Hubba and PILP clustering interactions, followed by Molecular Docking of Protein and Ligand. Due to its polygenic nature, vitiligo is frequently associated with a number of autoimmune or autoinflammatory disorders, including thyroid disease, psoriasis, atopic dermatitis, diabetes mellitus, and pernicious anaemia. Hence, it is conceivable to think about riboflavin as a possible drug for Vitiligo treatment. The findings imply that riboflavin laboratory tests reveal its inhibitory potential on skin depigmentation**

Keywords— gene expression, vitiligo, reversal gene, treatment, depigmentation, drugs.

I. INTRODUCTION

Depigmentation of the skin is brought on by the primary pigmentary disorder known as vitiligo. By reducing their self-esteem and causing them psychological distress, it decreases patients' quality of life. The prevalence varies widely by location and is between 0.5% and 2%. Due to a persistent loss of melanin, certain areas of the skin become depigmented. Melanocytes generate the pigment known as melanin. Melanocytes may stop producing melanin in vitiligo or they may even die.[1] An acquired autoimmune disorder is vitiligo. Celsus used the term "vitiligo" for the first time in his well-known Latin work De Medicina in the second century BCE. The Atharvaveda, an ancient work of Indian literature, also makes reference to this illness and describes the horrifying consequences of son-daughter marriage on those who have vitiligo.[2] Hindu writings also claim that stealing garments in a previous life is a potential cause of vitiligo.

Skin consists of three layers: the epidermis, dermis, and subcutaneous tissue. A type of cell found in the dermis is called a melanocyte. [3] These melanocytes create the pigment melanin. Keratinocytes take up melanin in their bodies. Whenever the immune system is activated, melanocytes are decreased or eliminated (autoimmune melanocyte death). Distal extremity tips, segmental, periorificial, and sites of friction are among the body parts where depigmented patches
can be found. [4] Occasionally, asymmetrical depigmented skin may also exist patches that develop on one axil after the other. Macule or patchy skin is described as having no pigment. Compared to a macule, which has a diameter of 10mm, a patch is a flat skin lesion that is larger. The five different kinds of vitiligo are focal, segmental, acro facial, generalized, and universal. Since normal skin and skin with pigmentation can be easily distinguished from one another, these might be easy to spot. Although the exact cause of vitiligo is unknown, there are various theories about how it arises. [5] Here are a few potential explanations: The first is genetics, where genes involved encode a part of the molecular network that controls the immune system and encourage melanocyte death. Second, the immune system of the body targets and destroys melanocytes as a result of an autoimmune response. The immune responses that occur after vitiligo are crucially triggered by oxidative damage. Stressed melanocytes produce DAMPs or autoantigens, which then activate innate immunity and adaptive immunity, leading to melanocyte malfunction and death via an inflammatory cascade Cellular proteins and membrane lipids are impacted by oxidative stress, which is brought on by an increase in reactive oxygen species (ROS) levels and subsequent decrease in antioxidant enzymes, in both lesioned and unlesioned skin.[6] The antioxidant system is therefore less active. Due to its polygenic nature, vitiligo is frequently associated with a number of autoimmune or autoinflammatory disorders, including thyroid disease, psoriasis, atopic dermatitis, diabetes mellitus, and pernicious anaemia. Risk factors include a long family history of vitiligo and genetic vulnerability to depigmentation.

In addition to other techniques, skin biopsies and blood tests can be used to diagnose vitiligo. The production of pigment can be induced by combining herbs Psoralean in pure form with UVA light, often known as PUVA treatment. A tiny area is treated with topical medications. Ultra- or potent topical steroids are used for lesions, whilst mid-potency steroids are used for children.[7] Systemic medications, which also include oral corticosteroid mini-pulses, converted steroid sparing agents, and antioxidants, are a different type of therapy. Another option for

Authorized licensed use limited to: DELHI TECHNICAL UNIV. Downloaded on June 28,2023 at 06:30:58 UTC from IEEE Xplore. Restrictions apply.

phototherapy is using a blacklight, also known as a Wood's lamp, which exposes skin to UV radiation. Similar to this, localised illnesses are treated using excimer laser therapy, which also uses another laser and additional lighting equipment. Surgical treatment is another option for grafting skin and tissue. [8].

Figure 1.Types of Vitiligo

II. Material and Method

A. Integration of Protein 6AAH-Ligand (Myristic acid, Heptadecanoic acid, Riboflavin, Propanol, 2,6-Dimethyl- 7-octene-2,3,6-triol)

The FASTA format of protein 6AAH and Myristic acid, Heptadecanoic acid, Riboflavin, Propanol, 2,6-Dimethyl-7-octene-2,3,6-triol were extracted from RCSB PDB (Protein Data Bank) RCSB PDB: Homepage. The PLIP (Protein – Ligand interaction Profiler) web-tool was then used to shows the PLI aggregation. All the ligands successfully bind with the protein showing residual values as 879A, 881B, 889B, 101B,959B respectively. Also find out the amino acids by which they binds are ARG, LEU, VAL, LEU, LEU respectively as above sequence.[9].

B. Docking procedure for proteins or ligands

The heteroatoms, polar hydrogen, and water molecules were carefully taken out. The KOLLMANN charges were received by the ligand and both receptors. The PDBQT file for the agonist or the PDB folder for the receptor were both stored for auto docking. A PDBQT file for agonist is required by auto dock, and this file was converted online using open babel.[10].

C. Used the Auto dock to bind proteins and ligands.

For pharmaceuticals and proteins, there is molecular docking software service. The web server was given the PDB files for the target and the medication, and docking was done by making a grid mapping. Launch the auto-grid file first, then the auto-docking.

D. Uses software called Bio via to do a structural evaluation of the docked protein-drug complex

The result downloads from the auto dock itself were analysed for structural interaction between protein and drug from BioVia Discovery Studio. Submit the complex of protein and ligand to BioVia Discovery Studio and see the interaction with the help of a 2D image. It also helps to analyse by which amino acid ligands bind to the receptor.

E. SWISS ADME examination of the Pharmacodynamic for the ligand.

Absorption, Dispersion, Metabolic activity, and Excretion are combined known as ADME. These variables are examined by adding canonical smiles to study the water solubility, Pharma kinetics, Physiochemical property, lipophilicity, and medical chemistry. These analyses provide evidence for the potency and efficacy of the drug. SWISS ADME (SwissADME). This online tool evaluates the agonist (drug) molecule using these parameters. For the evaluation, the canonical smiles add to sever and run. We can also find out whether the drug crosses the blood-brain barrier or not by seeing egg boiled figure whether the resides inside the yolk (BBB+) or in egg white (BBB-).[11]

III. Result and Discussion

A. Interaction between 6AAH and Ligand (Myristic acid, Heptadecanoic acid, Riboflavin, Propanol, 2,6-Dimethyl-7-octene-2,3,6-triol)

Significant relations between protein 6AAH and Ligand (Myristic acid, Heptadecanoic acid, Riboflavin, Propanol, 2,6-Dimethyl-7-octene-2,3,6-triol) have been observed. All the ligands successfully bind with the protein showing residual values as 879A, 881B, 889B, 101B,959B respectively. Also find out the amino acids by which they binds are ARG, LEU, VAL, LEU, LEU respectively as above sequence. Having hydrophic interaction distances as 2.93 3.83, 4.00, 3.65, 2.37.[12].

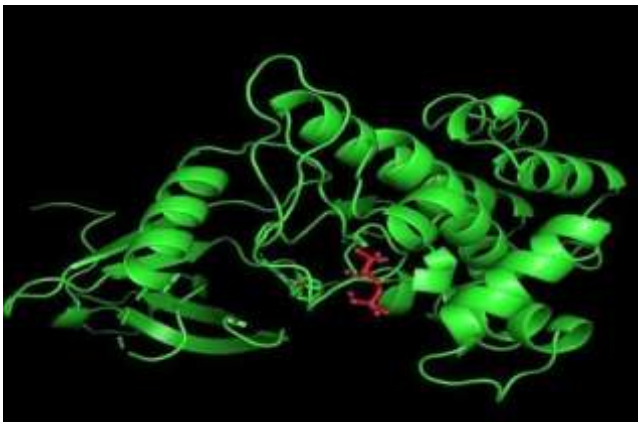

Figure 2. Interaction Of 6AAH and 2,6-Dimethyl-7-octene-2,3,6-triol

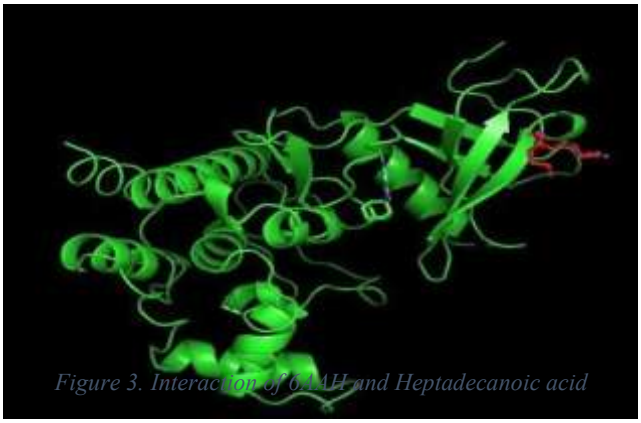

Figure 3. Interaction of 6AAH and Heptadecanoic acid

Authorized licensed use limited to: DELHI TECHNICAL UNIV. Downloaded on June 28,2023 at 06:30:58 UTC from IEEE Xplore. Restrictions apply.

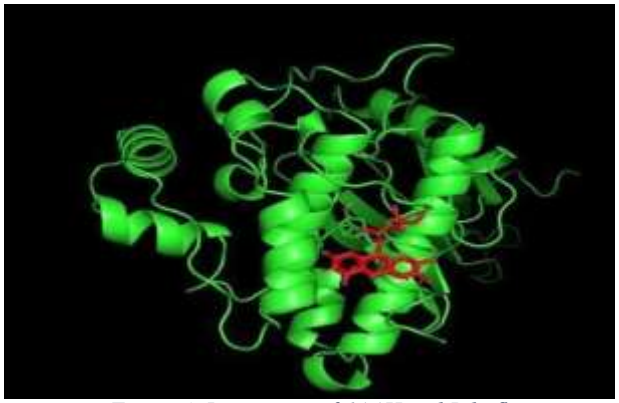

Figure 4. Interaction of 6AAH and Riboflavin

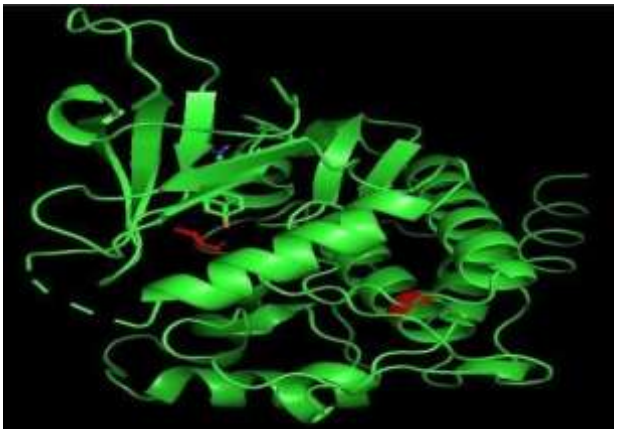

Figure 5. Interaction of 6AAH and Propanol

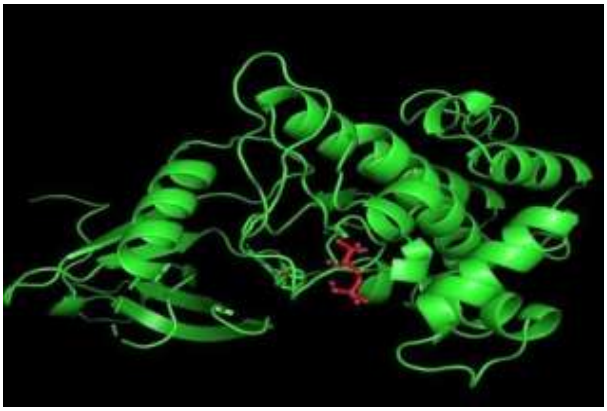

Figure 6. Interaction Of 6AAH and 2,6-Dimethyl-7-octene-2,3,6-triol

B. Interaction between 6AAH and Ligand (Myristic acid, Heptadecanoic acid, Riboflavin, Propanol, 2,6-Dimethyl7-octene-2,3,6-triol)

After docking was performed using Auto dock, The outcomes were positive, demonstrating a high level of interaction between 6AAH and Ligand (Myristic acid, Heptadecanoic acid, Riboflavin, Propanol, 2,6-Dimethyl-7- octene-2,3,6triol). The docking scores show that Ligand (Myristic acid, Heptadecanoic acid, Riboflavin, Propanol, 2,6-Dimethyl-7octene-2,3,6-triol) binds efficiently to the 6AAH protein complex. The binding energy is calculated as –4.00kcal/mol, -2.4kcal/mol, - 6.6kcal/mol, -3.6kcal/mol and -4.00kcal/mol respectively and the Cluster RMSD value is 0. This had been analysed via docking results. Docking was used to examine the topology of the molecules' interaction. The structure shows the target protein helical as a green in color consisting of A chain and B chain whereas the potential ligand is represented by the spheroid and the linear structure between the ribbons i.e., ligand. The geometry depicts the interactions of the ligand with the target protein's receptor site. [Fig.2, Fig,3, Fig.4, Fig.5, Fig6]

Table 1. Result of Protein interaction from Swiss

S.No.	Ranks	Ligands
1	Ist	Myristic acid
2	IInd	Heptadecanoic acid
3	IIIrd	2,6-Dimethyl-7- octene-2,3,6-triol
4	IVth	Propanol
5	Vth	Riboflavin

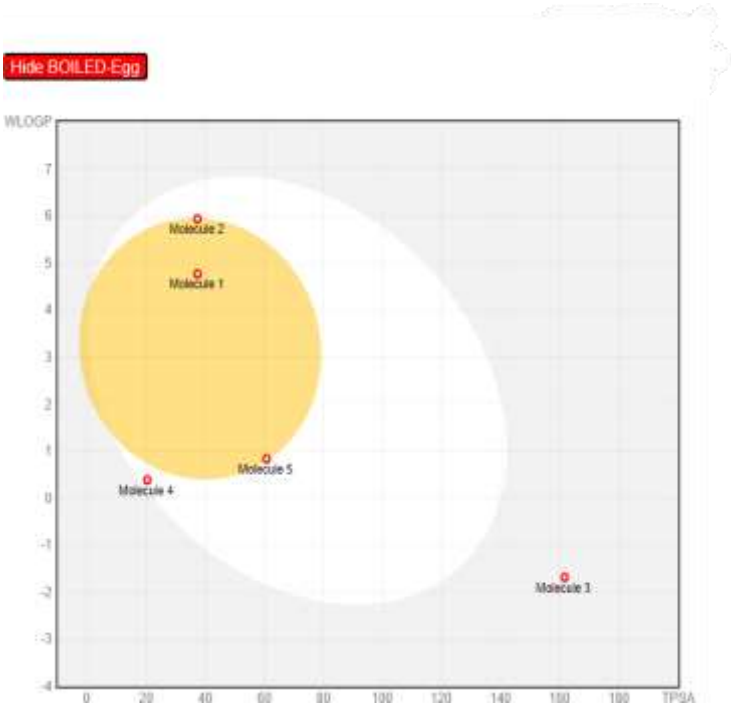

Figure 7. BBB (Blood brain barrier) crossing identified by the help of boiled egg

C. ADME analysis of the ligand

The skin permeation value (log Kp) is low, with values of - 3.35 cm/sec, -2.49 cm/sec, -9.63 cm/sec, -6.49 cm/sec, and - 7.14 cm/sec, respectively. (With Lipinski's value as required and has proven water solubility under logs (ESOL); logs (Ali), and logs (SILICOS-IT) categories with a value of -4.31, -5.37, -1.31, -0.30, -0.95; -6.67, -8.31, -1.43, -0.24, -1.28; - 4.51, 5.71, -2.62, -0.33, -0.72 respectively. The pharma kinetics score of 6.11, 7.69, -1.46, 0.25, and 0.44 and cast log P o/w (XLOGP3) were used to determine the drug's lipophilicity.[13]

IV. CONCLUSION AND FUTURE PROSPECTS:

The aim of this research was to ascertain how ligands and proteins interact. Protein-Ligand Interaction Profiler was utilized in the research. Find out precisely where the ligand attaches to the target protein by using bio to determine which

Authorized licensed use limited to: DELHI TECHNICAL UNIV. Downloaded on June 28,2023 at 06:30:58 UTC from IEEE Xplore. Restrictions apply.

amino acid is involved. With an estimated G value of -4.0, -2.4, -6.6, -3.6, -4.0kcal/mol, the docking research also demonstrated a notable relationship between protein and ligand value. As a consequence of its high binding values, this finding supports the notion that riboflavin is the best choice for the uses. Although myristic acid has average binding values, it successfully penetrates the blood–brain barrier. Therefore, according to the binding energy, we are able to determine that riboflavin is the greatest option out of all five ligands. We may consider this as a benefit for us and use it further as an experiment in the future since there is no best medication for this disorder.

REFERENCES

[1] Regazzetti, C., et al., Transcriptional analysis of vitiligo skin reveals the alteration of WNT pathway: a promising target for repigmenting vitiligo patients. Journal of Investigative Dermatology, 2015. 135(12): p. 3105-3114.

[2] Ning, X., et al., Evaluation of the Behavioral and Psychological Symptoms in Patients with Vitiligoin China. Psychology Research and Behavior Management, 2022: p. 2107-2116.

[3] Kitchen, H., et al., A Qualitative Study to Develop and Evaluate the Content Validity of the Vitiligo Patient Priority Outcome (ViPPO) Measures. Dermatology and Therapy, 2022. 12(8): p. 1907- 1924.

[4] Saeedinezhad, F., et al., The challenges facing with vitiligo: phenomenological research. International Journal of Pharmaceutical Research & Allied Sciences, 2016. 5(3).

[5] Yu, H.-S., C.-C.E. Lan, and C.-S. Wu, Segmental vitiligo: a model for understanding the recapitulation of repigmentation. Vitiligo, 2010: p. 306-310.

[6] Pun, J., et al., The impact of vitiligo on quality of life and psychosocial well-being in a Nepalese population. Dermatologic clinics, 2021. 39(1): p. 117-127.

[7] Shikhare, M.P. and N.B. Dudhe, VITILIGO-A REVIEW OF AN AUTOIMMUNE DISORDER AND PREVENTION IT'S NATURAL TREATMENT. 2021

[8] Bergqvist, C. and K. Ezzedine, Vitiligo: A focus on pathogenesis and its therapeutic implications. The Journal of dermatology, 2021. 48(3): p. 252- 270.

[9] Niu, C., D. Zang, and H.A. Aisa, Study of Novel Furocoumarin Derivatives on Anti-Vitiligo Activity, Molecular Docking and Mechanism of Action. International Journal of MolecularSciences, 2022. 23(14): p. 7959.

[10] Li, J., M. Yang, and Y. Song, Molecular mechanism of vitiligo treatment by bailing tablet based on network pharmacology and molecular docking. Medicine, 2022. 101(26).

[11] Chang, Y., et al., Pharmacological inhibition of demethylzeylasteral on JAK-STAT signaling ameliorates vitiligo. 2023

[12] Emir, C., G. Coban, and A. Emir, Metabolomics profiling, biological activities, and molecular docking studies of elephant garlic (Allium ampeloprasum L.). Process Biochemistry, 2022. 116: p. 49-59.

[13] Deng, Y., et al., Skin-care functions of peptides prepared from Chinese quince seed protein: Sequences analysis, tyrosinase inhibition and molecular docking study. Industrial crops and products, 2020. 148: p. 112331.

Authorized licensed use limited to: DELHI TECHNICAL UNIV. Downloaded on June 28,2023 at 06:30:58 UTC from IEEE Xplore. Restrictions apply.

Machine Learning Health Assessment Model To Project Long-Term Degradation For A Pack Of Micro Gas Turbines

Mr. Vaibhav Prasad[1*], Mr. Yash Prasad[2], Prof. (Dr.) R.S. Mishra[3]

[1*]Department of Mechanical, Production & Industrial and Automobile Engineering, Delhi Technological University, Email: vaibhavprasad_2k19ae063@dtu.ac.in
[2]Department of Mechanical, Production & Industrial and Automobile Engineering, Delhi Technological University, Email: yashprasad_2k19ae071@dtu.ac.in
[3]Department of Mechanical Engineering, Delhi Technological University, Email: rsmishra@dtu.ac.in

***Corresponding Author:** Mr. Vaibhav Prasad

*Department of Mechanical, Production & Industrial and Automobile Engineering, Delhi Technological University, Email: vaibhavprasad_2k19ae063@dtu.ac.in

Abstract:
Gas turbines are widely used for producing electricity, operating airplanes and for various industrial applications such as in refineries and petrochemical plants. Due to the low thermal efficiency of the fundamental gas turbine cycle, it is crucial to search for enhanced gas turbine-based cycles.

The availability and operating and maintenance expenses of tiny gas turbines can be considerably increased and decreased using predictive health monitoring. Predictive health monitoring techniques are often created for big gas turbines and frequently concentrate on a single setup. With this approach, the operational data from the turbine can be analysed to predict when maintenance is necessary, allowing for more efficient and cost-effective maintenance scheduling. This can also help prevent unexpected downtime and minimize the risk of equipment failure.

Overall, using operational metrics from actual installations, this research proposes a potential data-driven method for forecasting setup deterioration in micro gas turbines. The strategy employs linear regression techniques to estimate and anticipate deterioration and is not dependent on data from a reference setup. The method was evaluated on five distinct setups and showed consistent outcomes when compared to an existing technique that makes use of data from an analogous setup.

Index Terms: Deterioration, future forecasting, micro gas turbines, machine learning techniques.

1. INTRODUCTION

Estimating and predicting gas turbine performance deterioration is an essential component of condition-based maintenance since it enables dynamic planning that only reacts when necessary. It is possible to prevent time- and money-wasting unnecessary maintenance procedures, as well as unanticipated stops, by anticipating when a resource needs repair. The two primary factors contributing to the long-term performance reduction of gas turbines are fouling and erosion. It is challenging to predict unexpected or rapid failure mechanisms over long periods of time, such as bearing breakdown or breakage from external objects. If performance deterioration is not addressed, it may lead to increased fuel consumption, unproductive functioning, and a spike in emissions of greenhouse gases. In accordance with the current use case's experience, the short-term acute failures are less relevant for maintenance planning than the longer deterioration.

Technology advancement has previously mostly concentrated on the monitoring of both small- and large-scale gas turbines and further in the biologically anatomic ways. On the other hand, we see a time when networked and coordinated management of distributed groups of tiny gas turbines will make them more significant. The mini gas turbines are designed to be deployed in places like large homes,

multi-family dwellings, workplaces, educational institutions, and historic structures. The intention is to replace the local energy generation techniques now in use, such as coal combustion or other petroleum-based fuels.

In the case of the present investigation, turbines are positioned in a range of geographical locations, each with its own unique set of operating conditions, such as changes with respect to humid conditions, pressure of environment, and temperature of surrounding. A basic micro gas turbine would have a power output of under 10^5 W, and to keep construction economically efficient, it would preferably be built with automotive-related commercial-off-the-shelf (COTS) components. It is more challenging to diagnose medical problems when using commercially available components since there may be a greater performance gap between various gas turbines.

There aren't many existing sensors because of their small size and low price, therefore the development of new ones must be motivated by very outstanding efficiency or monetary incentives. As a result, each gas turbine may be monitored individually using a small number of sensor signals. Consequently, only a few sensor signals must be used to independently monitor each gas turbine.

It is critical to look for improved gas turbine-based cycles since the basic gas turbine cycle has a low thermal efficiency. We start off by talking about recent research in the area of condition-specific upkeep on compact gas turbines. Then, a comprehensive description of the MGTs under examination is provided, along with any additional background knowledge needed to understand this work. Then, both the issue we tackle and the information used in this effort are defined. The generated forecast model is then described, and the data-driven deterioration model is shown. In the concluding sections, we evaluate the techniques and provide some recommendations.

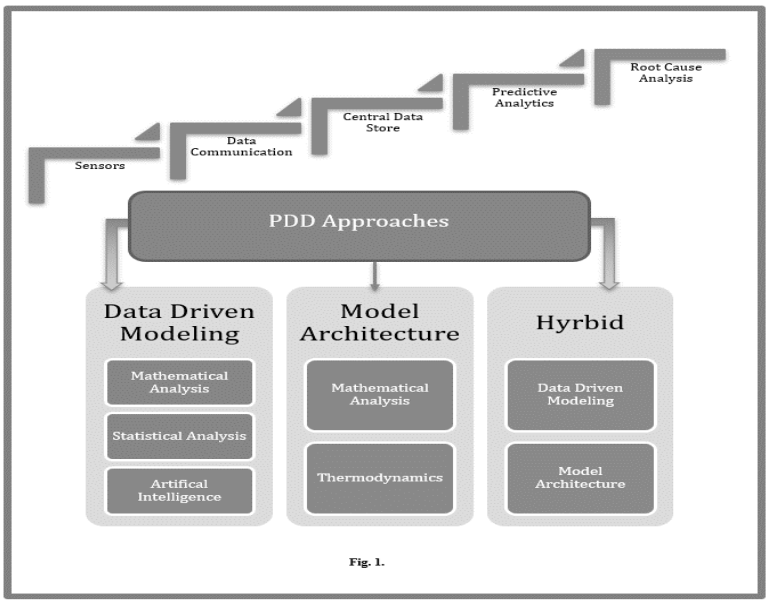

Fig. 1.

The method does not rely on data from a reference setup and instead uses operational data from actual installations. Two approaches were used to tackle the issue.

1. Calculating the deterioration from variables with a time dependence
2. Future projection utilising simply running hours. The estimate and forecasting of degradation both use the linear regression technique.

The technique was put to the test on virtually simulated setups, and the outcomes show that the conclusion corresponds r is greater than 0.8, which is with a prior approach that computes adjusted values based on information from a reference setup. Using merely operating hours as an input, the forecasting strategy likewise functioned comparable to the estimated model.

2. LITERATURE REVIEW

The creation of forecasting models for industrial deterioration and maintenance. The heart of Industry 4.0 consists of intelligent machines that organise themselves, cooperate with one another, and handle projects and deadlines.

According to the literature we studied, many experts concur that the following five elements are necessary for Industry 4.0 predictive maintenance:

1. **Sensors**: physical machines must have sensors installed for data gathering.
2. **Data communication**: Secure data transfer between the inspected asset and the consolidated database is made possible by this feature.
3. **Central data store**: data processing, on-site or cloud storage, and analysis take place
4. **Predictive analytics**: algorithms are used to discover patterns and produce helpful data for decision assistance;
5. **Whys technique**: Experts and engineers employ data analysis tools to determine the best course of action.

As components 1, 2, and 3 are already present in our case study, we will concentrate on finding solutions for components 4 and 5. So, within the current state of the art. In this section, we'll look at the models that are most useful for foreseeing deterioration and maintenance.

To further understand the issue, we will explore various degradation and maintenance models in addition to those applications linked to mGT (Micro Gas Turbines). The mGT has established itself as "an energy conversion technology, offering promising features like high fuel flexibility, low emissions level, and efficient co-generation of heat and power," which is why.

Three categories can be used to categorize the available methods:

- Data-driven strategies
- Model-based methods
- Hybrid techniques.

We will examine several degradation and maintenance models in addition to those applications related to Micro Gas Turbines in arrangement of understanding the reasonable issues.

The papers and applications for the diagnosis of mGT has increased recently. Due to its reputation as "an energy conversion technology, offering promising features like high fuel flexibility, low emissions level, and efficient co-generation of heat and power,"

Recently, an overview of the major degradation-based reliability estimate techniques was presented in [14]. The paper's authors analyzed the most widely used deterministic and stochastic degradation models according to be based on the Industrial Internet of Things (IoT) concept, the current state of the art, and offered a thorough strategical to develop based on degradation value and reliability forecast models.

A similar review was put forward in [26]. The authors have provided an in-depth review of the modern methods used for condition monitoring, diagnostics, and prognostics. The vast majority of the diagnostic/prognostic methods that make use of performance data gleaned from gas turbine operating systems were studied. The following categories were used to organize all of the described techniques:

- AI monitoring
- Offline assessment and monitoring
- Inadequate performance barriers
- Performance Bandwidth

Additionally, the provided list of the most frequently utilized indicators of performance, broken into both measurable and calculable ones, along with helpful explanations for each one. A comprehensive handbook of GT monitoring, diagnostics, and prognostics was issued in the paper [26], which included the most current and relevant research in the field of study. Fentaye et al. [2] presented a detailed assessment of the existing gas turbine defect diagnosis techniques, summarized their advantages and disadvantages, and identified difficulties and future research objectives. The recent work on AI (Artificial Intelligence) techniques were specifically emphasized by the authors due to their exceptional capacity for managing the current unforeseen defiance and the bulk of appealing qualities.

For PDD, machine learning has shown to be a useful technique [20, 4]. In [25], a deep learning approach for gas turbine combustors

to identify anomalies was put forward. This method, which early detects anomalous behaviours and upcoming faults, serves the purpose of an anomaly detection method as opposed to a maintenance forecast method. The authors proposed an approach using deep learning to detect combustion anomalies. In order to accomplish anomaly detection in the combustor, they first learned characteristics derived from temperature readings of the exhaust gas taken by the sensor being used. They then used the features they had learned as the input to a neural network classifier. [17] describes a methodology for gas turbine route analysis, using artificial neural networks to find, isolate, and assess problems during operational conditions. The method that was given employed a number of engine metrics as inputs and produced variations in component properties and flow rate.

In [1], a variety of machine learning methods for diagnosing gas turbines were assessed. The utilization of concepts of ANN and three different types of Support Vector Machine for determination of track of gas route diagnostics job was assessed in the paper. The article suggested a classification technique for variables that allows for very flexible changes to things like the sort of class being utilized, pattern numbers, fault severity, class amount, etc. Twelve fault classifications were generated by this technique, which the authors utilized to investigate the impact of classification structure on the final diagnostic precision.

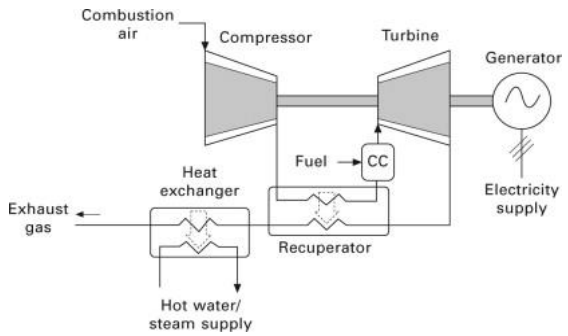

Fig2: archetypal layout of micro gas turbine.
Reference: Google Images

To evaluate the condition of gas turbines, Fentaye et al. [19] used a Bayesian network and an adaptive gas path analysis. By fusing a Bayesian network with correlation analysis, Zaccaria et al. [16] studied a hybrid technique for real-time defect detection of gas turbines. The hybrid approach demonstrated higher performance, with isolation rates ranging from 94% to 96% in the presence of one engine to the other engine variations and simulated AI changes, respectively.

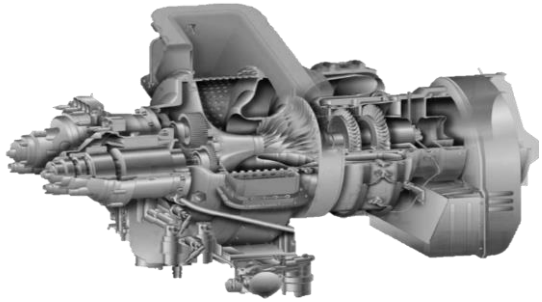

Fig3: micro gas turbine visualized model
Reference: https://www.mdpi.com/2504-186X/5/2/8

3. PRELIMANARIES

We lay out the foundational material in this section so the rest of our work can stand alone. First, we give a brief overview of the key characteristics and functionalities of the examined mGT. We conclude by looking at a type of regression where the coefficient estimates are constrained to zero, which serves as a foundation for comprehending the data-driven approach that will be discussed:

3.1. SIGNIFICANT MICRO GAS TURBINE TECHNOLOGIES

The forecasting approach also performed similarly to the estimation model using only running hours as an input.

This approach has the potential to greatly improve the maintenance scheduling of micro gas turbines, allowing for proactive maintenance rather than reactive repairs. Additionally, the use of operational data from actual installations provides a more accurate representation of system degradation compared to laboratory testing. Further research can be done to expand the approach to other types of systems and to improve the accuracy of the forecasting model. Overall, this data-driven approach presents a promising solution for predicting system degradation and improving the maintenance of micro gas turbines.

With a few exceptions of scale distinctions, lower compression ratios, and reduced combustion conditions, both micro gas turbines and large combustion turbines can run on the thermal cycle, and they both share many of the same basic components, such as combined units of turbines and types generators and regenerators, with heat exchangers, etc. When fuel is consumed in a thermodynamic cycle that describes the operation of certain heat engines that have air or some other gas as their working fluid, atmospheric air is heated and compressed. This heated and compressed air is then utilised to power the expansion turbine, which in turn drives the intake compressor and the drive shaft leading to the generator. Among the other research areas as priority research areas for future of micro gas turbines.

3.1.1. COMBUSTION CYCLE HAVING CONSTANT VOLUME

Combustion has a considerable impact on micro gas turbine combustion emissions, and restricting the range of alternate fuels utilised can significantly affect operating limitations [31]. Fuel injection technology, which aims to ensure full combustion without explosion by creating a steady flame, is the focus of early combustion research and development. In the last ten years, there has been a significant change in the international nitrogen oxide emission limiter, which has supported the advancement of micro gas turbine systems in the direction of pre-mixture design and, consequently, changed essential studies for stability of reacting body of gas, erratic combustion, and combustion chemistry with change in emissions.

In-depth study of the quasi-constant volumetric combustion cycle has also improved the dynamics of detonation waves and the transition from deflagration to detonation. It is possible to guarantee that the entire system can operate in an extreme temperatures and elevated pressures environment required for highly efficient cycles due to the specific percentage of multi-component mixed fuel by advancing the theoretical foundation research required for low-emission combustion systems, as well as advancements in closing rate, sporadic response, and speed.

3.1.2. USE OF COMPOSITE MATERIAL WITH A CERAMIC MATRIX AT EXTREMELY HIGH TEMPERATURES

The development of gas turbines depends heavily on structural components and coatings. By creating low-cost, high-quality silicon carbide fibre materials and the technology necessary to prepare ultra-high temperature ceramic matrix composite materials, it is possible to increase the path temperature of hot gas and improve combustion, which will increase efficiency by 10% and reduce fuel consumption by 2% [32]. The efficiency of single crystal rims and multi-crystal hole rotors of micro gas turbines can also be improved, and life cycle costs can be decreased, by using sophisticated superalloy materials such high-entropy alloys, high-temperature titanium alloys, cobalt-based superalloys, and refractory alloys [33].

3.1.3. THERMAL REGULATION

It is possible to increase the micro gas turbine's turbine inlet temperature, increase the cycle pressure ratio, decrease the cooling flow of the combustor and turbine, meet the gas turbine's lifetime requirements, and increase the thermal cycle's efficiency by developing advanced cooling strategies and swiftly and economically integrating them into the development and production of gas turbines. The usual approach is to raise the turbine inlet temperature while keeping the cooling flow constant, or to maintain the inlet temperature while decreasing the cooling flow [34].

That is, under conditions where the temperature of the metal parts of the turbine is constant, increasing the turbine inlet temperature and overall cooling efficiency simultaneously can increase the lifetime of the parts. Alternatively, under conditions where the temperature of the metal parts of the turbine is constant, improving the overall cooling efficiency can reduce the temperature of the metal parts and increase the lifetime by creating cutting-edge fully conjugate heat transfer technology and blade and turbine cooling configuration, the turbine inlet

temperature and cycle pressure ratio may be raised.

The waste heat of the gas generated by the turbine can also be successfully reused thanks to a a type of heat exchanger that has separate flow paths for each fluid throughout its passages and heat is transferred through the separating walls in the MGT (power 3x105 Watt). According to the results of thermal exchange, waste heat can be used to warm up the compressed chilly air, increasing the micro gas turbine's efficiency from the range of 20% and 30%. The process of the gas's heat exchange, however, moves slowly because of its low density and low thermal conductivity. Therefore, to increase the thermal conductivity of the gas, the plate-fin heat exchanger or main surface recuperator are frequently utilized.

3.1.4. PHYSICAL MODEL-BASED SIMULATION

Researchers used the large eddy simulation method ten years ago to produce a multi-ideal complete simulation of the combustor and diffuser of a gas turbine engine, and they computed the Reynolds average stress for rotating machinery [35]. The fast development of hydrodynamics and high-fidelity computing capabilities based on physical models have made it possible to gradually materialise the relation of interactive with any condition wherein a pump is required by the force of circumstances to deliver flows either in excess of or below the capacity at best efficiency and conditions of simulated gas turbine modules.

Researchers have thoroughly investigated the factors causing the combustion unpredictability of Ambient air is injected and pressurized in the compressor. In the recuperator, compressed air is preheated. The burning of fuel increases the heat in the combustion chamber. The heated, pressured gas expands in the turbine, giving the compressor and the generator mechanical power. The power generated by the generator is converted via a "inverter" to the 230V/50Hz voltage and frequency of the primary electrical grid. The recuperator's compressed air is heated by the expanding gas following the turbine. The heat exchanger converts the remaining heat still present in the recuperator outlet gas to water. The hot water is utilised as tap water or for central heating. This foundational work lays the groundwork for the test and calibration of standard single-module and multi-module configurations using high-precision numerical simulation tools, and for the improved degree for system coupling i.e., it synchronizes the solvers participating in a Multiphysics simulation [36].

3.2. COMBINING MACHINE LEARNING AND MICRO GAS TURBINES

A few kWe to over 500 kWe are the power output range for micro gas turbines, which are small-scale gas turbines [11]. Power production, electrical efficiency, and investment costs are all significantly impacted by downsizing [23]. Numerous advantages, such as small size, low weight per unit of power, simplicity of operation, high fuel flexibility, low maintenance, and lower levels of emissions are also brought about by it [3]. The mGT uses the well-known Brayton cycle, just like the large-scale gas turbine. An air compressor is used in a straightforward Brayton cycle to compress the air. At a generally constant pressure, the fuel and air are then mixed and combusted in a combustor. The compressor and high-speed generator are driven by the hot gases that are expanded in a turbine as a result. To decrease the consumption of fuel and boost cycle efficiency in mGTs, a recuperator is typically installed after the turbine heats the compressed air by preheating processes before to combustion. Additionally, a boiler is frequently used to collect exhaust heat, producing a high thermal efficiency [3]. Figure 2. depicts a typical arrangement for a mGT in a CHP (Combined Heat and Power) configuration.

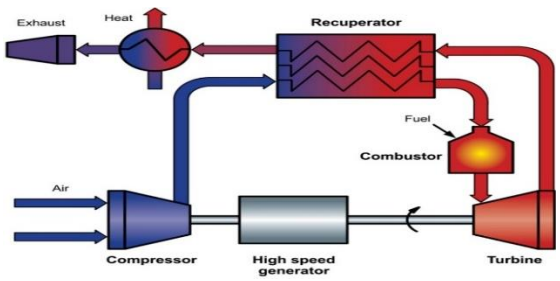

Fig 3.1: The micro-CHP system based on a micro turbine

Reference: https://www.tomkinsonheating.co.uk/enertwin-micro-chp

A is commercial (Fig 3.1) l micro-CHP built on mGT technology, and it is the subject of the research. The mGT unit was designed so that it provides 15kW of thermal power and 3.2kW of electrical power. Heating and the use of hot water from the faucet are intended uses for the thermal power. Because it is based on an automobile turbocharger technology, the mGT unit has a distinctive feature. Figure 3 shows the turbomachinery assembly of an MGT system. More information about the prototype of MGT setups and the maintenance intervals offered by the supplier is included in Appendix A.

3.2.1. LINEAR DEGRADATION

Gas turbine performance deteriorates with time and has a certain pattern and rate of deterioration, much like other types of material asset. Usually, the engine's overall degeneration is just the culmination of the degeneration of each of its constituent parts. Each component ages differently and follows a certain pattern of aging. There are two types of degradation associated with this one: recoverable and nonrecoverable.

Recoverable degradation is a type of performance decline that may be fixed using operational methods without the need for new hardware or intensive maintenance. Nonrecoverable degradation, on the other hand, is a performance decline that cannot be reversed without considerable repair or replacement of the damaged components [22]. Typically, this deterioration results in an increase in the tip clearance, a change in the blade geometry, and a roughening of the surface, all of which reduce power output and raise thermal energy losses [27].

The nonrecoverable performance degradation of gas turbines is plainly linear in character, according to Zagorowska et al. [10]. Fouling among recoverable degradation also exhibits a fairly linear decline in engine performance with time [13]. However, there is still no agreement among diagnostics researchers as to how linear gas turbine degradations are. The gas turbine degradation mechanism is said to have a retreating s-shape by Brotherton et al. in their study [29]. The rates of deterioration for gas turbines are rarely understood and unlikely to be linear, according to Saravaramuttoo and Maclsaac [18]. Every gas turbine design will also behave differently, which will be further influenced by the environment and location in which the gas turbine is used, as well as how brutally it is used (start-stop cycles, load change behavior, control techniques, etc.). Escher and Singh [9] and Li and Singh [27] asserted that the degradations in gas turbines are nonlinear in character and created a diagnostic method based on non-linear GPA. However, when designing diagnostic and prognostic approaches, many researchers thought that the linear depreciation of gas turbines was an acceptable assumption. Gas turbine degradation was thought to be a linear function of time by Puggina and Venturini [21]. In order to use a moving window approach for gas turbine performance prognostics, Tsoutsanis and Meskin [28] approximated deterioration to be locally linear within each window and made the assumption that degradation was monotonically rising. The leakage from the recuperator output to the ambient was simulated by Mahmood et al. [8] and was linear in character. Later, Kim et al. [15] investigated how internal leakage affected a micro gas turbine's performance and discovered that the impact is almost linear at constant speed.

3.2.2. REGULARIZED REGRESSION

Finding a function $f\ (\vec{x}\ )$ such that for observations x, y we obtain $y = f\ (\vec{x}) + e$ where e is a minor error is the challenge of supervised machine learning. . To make sure that $y = f\ (\vec{x}\ )$, we will use y to represent the projected y. The majority of the time, a specific set of operations is chosen on which f is parameterized by the parameters of w such way $y = f\ (\vec{x}\ ;\ \vec{w})$. It can contribute to the func. f being either linear or non-linear with functions including non-linearity of functions too, for example, artificial neural networks. The challenge then becomes figuring out w so that there is a minimal error between y and $f\ (\vec{x}\ ;\ \vec{w}\ )$

We shall just take into account linear functions in this work. Given independent and uniformly distributed observations, if the function is

linear and $f\ (\vec{x}\ ;\ \vec{w}\ ).= \vec{x}$ T $\vec{w}$ (with column vectors) and the error is the $l2$-norm, then we have linear regression, which minimizes the following error [24]:

$$\sum_i (\mathrm{y}_i\ -\ \vec{\mathrm{x}}_i^T\ \vec{w}\ )^2$$

Where total over i is for all observations of $\overrightarrow{\mathrm{x}_i}, \mathrm{y}_i$.

It is also feasible to direct the fit by giving different variables in $\vec{x}$ more or less weight by restricting the relevant coefficients in $\vec{w}$ to be near zero. This would increase the generalizing ability of the model described above while preventing excessive fitting of the data used for training. This can be accomplished through regularization, which adds a loss to Equation (1), for example using the l2 -norm:

$$\sum_i (\mathrm{y}_i\ -\ \vec{\mathrm{x}}_i^T\ \vec{w}\ )^2\ +\ C\ \times\ \sum_j |\overrightarrow{w_i}\ |^2$$

C variable is often chosen through cross-validation. Through the use of cross-validation, over fitting may be prevented and it ensures that the model that is produced generalizes to data that is not the training data. Ridge regression and lasso regression are the names given to the two types of regularized linear regression discussed above, respectively, when the l1-norm is used.

$$\sum_i (\mathrm{y}_i\ -\ \vec{\mathrm{x}}_i^T\ \vec{w}\ )^2\ +\ C\ \times\ \sum_j |\overrightarrow{w_i}\ |^2$$

While there are closed solutions for ridge regression and plain linear regression, lasso regression requires the use of additional techniques, such as gradient descent as the coefficients in $\vec{w}$ cannot have specific values, such as that they cannot be negative. Gradient descent is supported by several deep learning frameworks for a wide range of regularizations and constraints. In this study, we combine TensorFlow [12] and two deep learning packages, Keras [30]. The two libraries combine to create a general method for fitting any artificial neural network using gradient descent, including basic linear regression.

4. PROBLEM DEFINITION AND DATA

First, we outline our issue and our objective in this part. Next, we go over the data that were used in this study.

This research aimed to assess and forecast the deterioration of a group of mGTs before remedial intervention was required. The issue is that the degradation cannot be measured explicitly and must instead be inferred. In the current estimation of deterioration, corrected values are computed using a linear model that was developed using information from a reference system. The following relation is used to calculate the corrected power:

$$\mathrm{P}_{e_cor} = \mathrm{P}_e - \mathrm{a} * (\mathrm{T}_{ref} - \mathrm{T}_{ret}) - \mathrm{b} * (\mathrm{T}_{isa} - \mathrm{T}_0) + \mathrm{c} * (\mathrm{p}_{isa} - \mathrm{p}_0) + \mathrm{d} * (\mathrm{N}_{ref}\ - \mathrm{N}_1)$$

where P_e is the power generated, T_{ret} and T_{ref} are the inlet temperature and their respective ISA reference values, p_0 and p_{isa} are the ambient pressure and their respective scientific papers in ISA transactions format, N_1 and N_{ref} are the rotating speed of turbine and their respective referenced values, and the sustained values of a, b, c, and d are either determined empirically. The corrected power is shown by a yellow curve in Figure 4, which is an illustration of the current methodology but is not very smooth. Deterioration is identified by the yellow curve's downward tendency.

There are also relatively few sensors available due to the small scale of the gas turbine and the need to keep the system's cost low. We can only use the few available sensors, thus. The systems being evaluated are also test installations, and the data was collected while the system design was still being developed. Consequently, the fact that there are few systems and few breakdowns adds to the complexity.

Therefore, it is not possible to learn when a system fails using a conventional supervised machine learning approach.

1. Calculate the wear-related degradation in proportion to the optimal output power when inefficiencies or alterations brought on by external variables like weather are absent; a

2. Estimate deterioration that is substantially smoother than the current approach;
3. Make it simple to establish a general cut-off point for when a system needs to be maintained;
4. Make future deterioration predictions so that maintenance actions can be prepared in advance.

Use just data from actual systems and do away with the necessity for a reference system. The assumption of nearly linear deterioration is used to make long-term projections, which is also compatible with the explanation in Section 3.2.

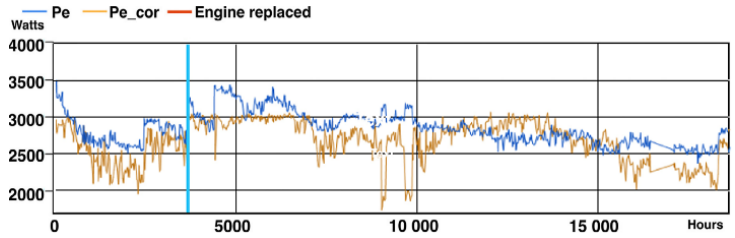

Fig. 4: Pe is measured power and Pe_cor is corrected power, and engine replacement indicates start of currently installed engine life

4.1. DATA

Five separate micro-CHP setups with the identifiers 1, 2, 3 4 and 5 provided the data for this study. The data were collected every minute; however, we've only used samples every other hour because it was thought to be sufficient for our job. We employ the parameters given in Table 1 that were chosen based on prior experience, this comprises both the data points that have shown their ability to predict the output power and the data points that were utilised to calculate the corrected values using the reference model (see Section 4.1).

Variable	Parameter	Unit/Type
forecasted factor (y)	- (Net electric) power generated - Measured return water temperature - Inlet air temperature - Ambient pressure - Ambient pressure at stand still	Watts Kelvin Kelvin bar bar
Ambient variable (x *vector*)	- Measured turbine speed - Turbine rotational speed set point - The internal point of adjustment of the turbine exits temperature and desired speed- Ambient pressure is missing	rpm rpm code dummy
Time dependent variable affecting the degradation trend (t *vector*)	- Total number of running hours - Total number of starts and stops	hours frequency count
Maintenance actions (M)	- Total number of running hours when action was taken	hours
The ideal output power per system (k)	- Net electric output power during installation	Watts

Table 1

These variables were selected because of their significance in this particular use case, which may not be typical for bigger gas turbines. For example, the cooling of the bearing housing on the turbine side is achieved through water. The amount of heat removed from the gas route surrounding the turbine is influenced by the temperature of the returning water. Given that the turbine outlet temperature remains constant for a given operating condition, variations in the return water temperature impact the heat extraction process and subsequently the temperature at the turbine inlet. As the temperature difference across the turbine has a significant effect on the output power, it is crucial to consider the return water temperature in the analysis.

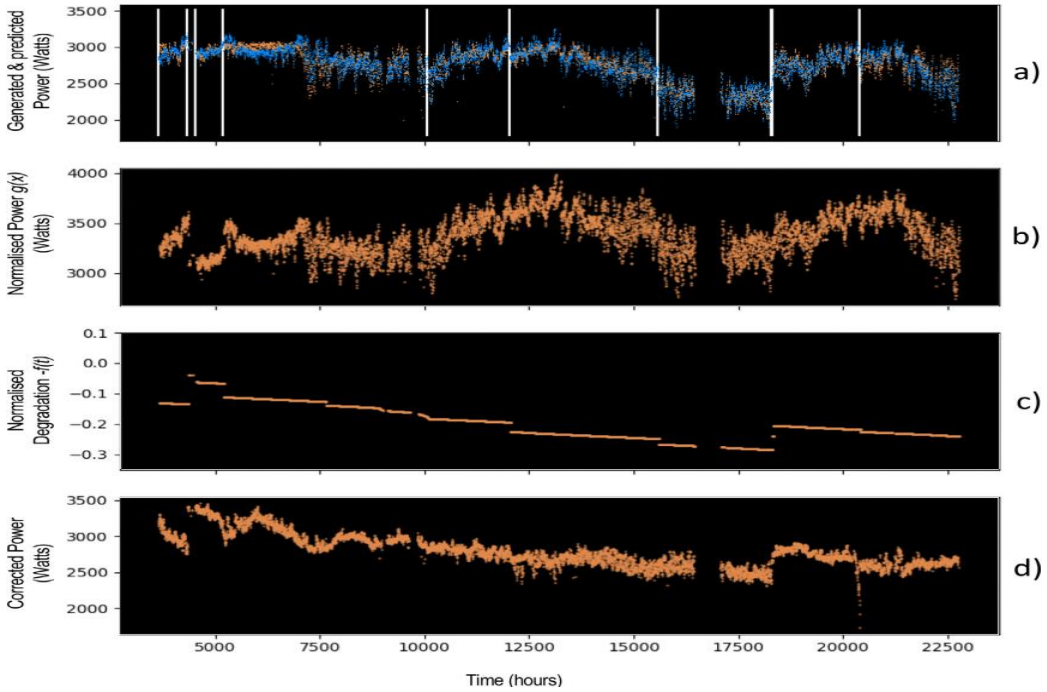

Fig. 5: System 1

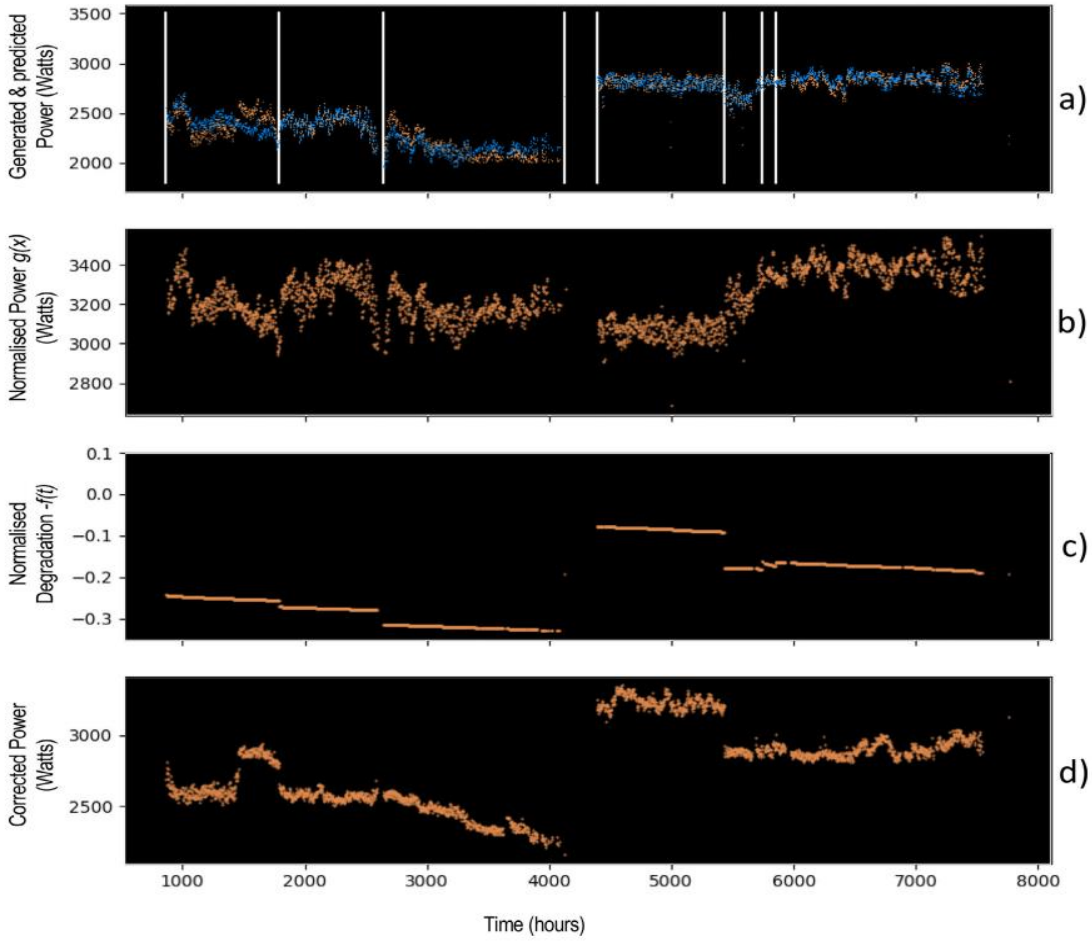

Fig. 6: System 2

5. METHOD: DATA-DRIVEN DEGRADATION MODEL

We break the issue down into two sequentially addressed subproblems, one for projecting future degradation merely using operating hours, and another for projecting future degradation based on data. The solutions to the two sub-problems are then discussed.

5.1. ESTIMATION OF DEGRADATION

Consider y as the output power, $\vec{x}$ as a column vector encompassing the recorded ambient parameters like temperature, pressure, and so on, $\vec{t}$ as a column vector comprising time-dependent variables, and n and m as the respective numbers of setups and maintenance periods (representing the duration between two maintenance actions or since the installation of a setup). It is important to note that $1 \leq i \leq n$ and $1 \leq j \leq m$ indicate a specific setup and maintenance period, respectively. Thus, the general degradation model can be formulated as follows:

$$y = k_i + g(\vec{x}) + e(\vec{t};\, i, j)$$

where, the constant value k_i denotes the ideal output power for a particular setup i. The function e depicts the deterioration over time brought on by the use and abuse of setup i during maintenance period j, whereas the function g indicates the impact of $\vec{x}$ on the power. As a result, our approach separates the signal into two parts: variation brought on by environmental factors and degradation produced by time-dependent variables, which results in a trend. Additionally, we assume that the ambient variables would behave consistently, whereas the degree of degradation will differ based on the particular setup and the period between maintenance intervals.

Also let:

$$f(\vec{t}\,;\, i, j) = -\frac{e(\vec{t}\,;\, i, j)}{k_i}$$

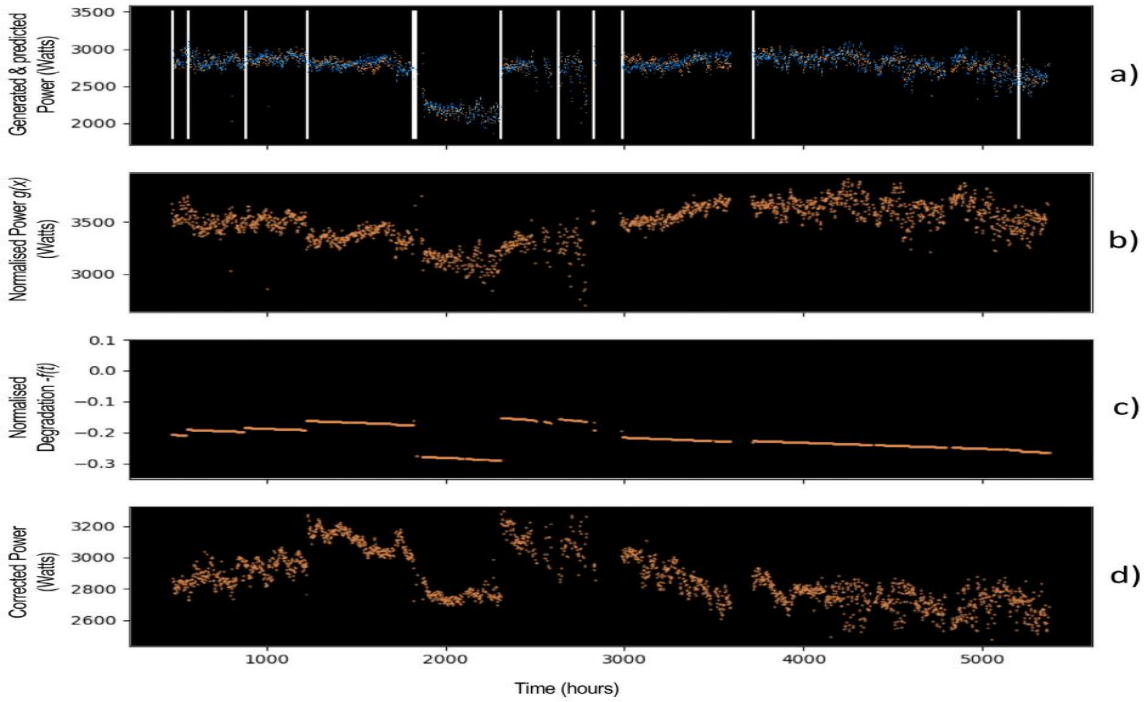

Fig. 7: System 3

be the normalised degradation over time, where $0 \leq f\ (\vec{t};\ i,\ j) \leq 1$denotes no degradation and $f\ (\vec{t};;\ i,j) = 0$ indicates there is no degradation. As a result, we can reformat Eq. 4 as follows:

$$y - g(\vec{x}) = k_i\ (\ 1\ - f\ (\vec{t}\,;\, i, j)\ )$$

In this context, the difference between the actual output power y and the power explained by the environmental variables $g(\vec{x})$ represents the degradation effect, which is multiplied by the ideal output power k_i.

Now, we can choose a cut-off point for when maintenance is necessary, for example:
Perform a corrective maintenance procedure if $f\ (\vec{t}) > 0.25$

You should be aware that choosing a threshold is not an easy task to resolve. It requires taking into account a variety of variables, including the cost of power, gas, subsidies, replacement costs, the kind of maintenance agreement, the setup's age, how much time is left on its expected lifespan, and customer expectations. We

assume that the topic can be chosen utilising expert knowledge even if it will not be further examined in this study.

Considering that g and e have linear functions, the following is true:

$$g(\vec{x}) = \vec{c}^{T}\,\vec{x}$$
$$e(\vec{t}\,;\,i,j) = a_i + b_j + \overrightarrow{e_0^T}\,\vec{t} + \overrightarrow{e_i^T}\,\vec{t}$$

In the given context, $\overrightarrow{e_0}$ and $\overrightarrow{e_i}$ represent column vectors with weights that quantify the degradation shared among all setup s and the degradation specific to individual setups, respectively. Meanwhile, $\vec{c}$ is a column vector with weights that account for the variation attributed to ambient conditions. The variables a_i and b_j denote the remaining degradation at the start of measurement or after a maintenance action for setup i and maintenance period j, respectively.

All things considered; Eq. 4 may be expressed as the matrix illustrated below:

$$\vec{y} = \vec{k}^{T}S + \vec{a}^{T}S + \vec{b}^{T}M + \vec{c}^{T}X + \vec{e}^{T}T$$

where:

- $\vec{y}$ is a column vector containing all power measurements
- X is a matrix containing all measurements of ambient variables
- $\vec{k}$ is a column vector containing all known k_i;
- $\vec{a}$ is a column vector with all a_i;
- $\vec{b}$ is a column vector containing all ai; b is a column vector containing all b_j;
- $\vec{c}$ is a column vector containing weights describing the variation caused by ambient variables;
- $\vec{e}$ is a column vector made up of several types of $\vec{e}_0$ and all $\vec{e}_i$ so that $\vec{e} = [\vec{e}_0, \vec{e}_1^{T}, \vec{e}_2^{T}, \ldots \vec{e}_n^{T}]^{T}$;

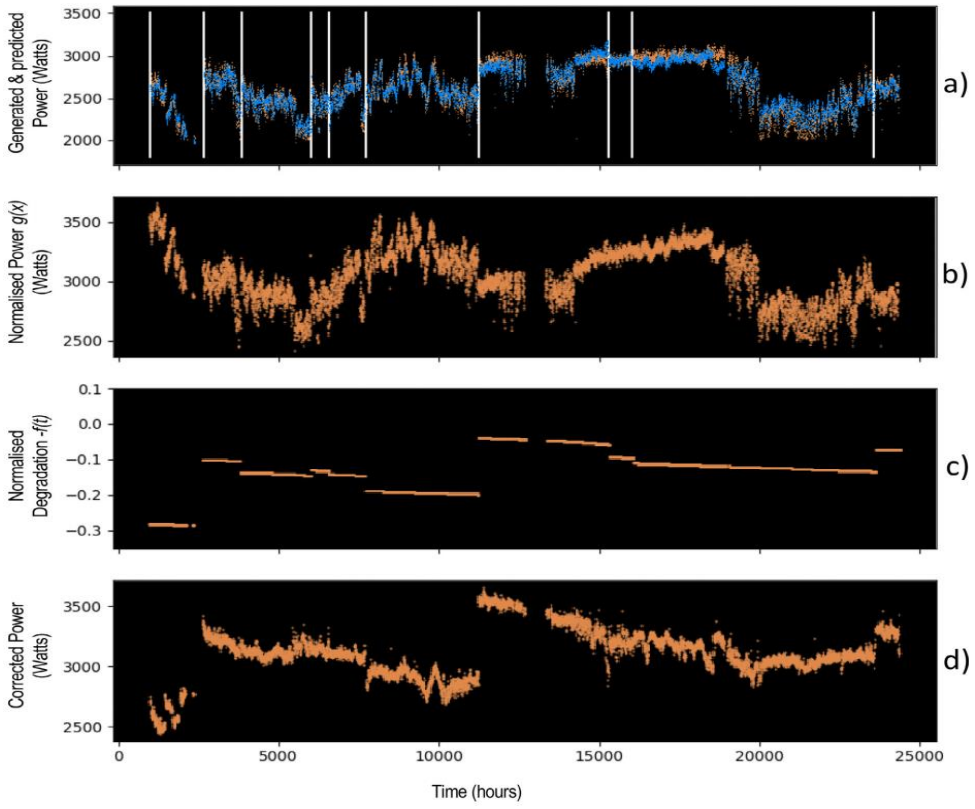

Fig. 8: System 4

- Matrix M consists of dummy variables representing all maintenance periods. Each column of M corresponds to a specific maintenance period and contains zeros except for a single element that is assigned the value of one to indicate the respective maintenance period.
- Matrix S is composed of dummy variables for all setups. Each column of S corresponds to a specific setup and is populated with zeros,

except for a single element that is set to one, indicating the respective setup.

- Each column in matrix T is organised as follows: it starts with t (representing $\vec{e}_0$), is followed by a zero vector, and then another t (representing $\vec{e}_i$ of a particular setup). The length of each column in matrix T is (1 + n) times the length of t. As a result, n extra zero vectors make up the column pattern's repetition. In conclusion, there are two examples of the t and n-1 zero vectors in each column.

If we blithely attempt to solve Equation 8 using an ordinary least squares approach, we will encounter issues and may arrive at a solution that is far from optimal as anticipated. As a result, we must use past information encoded as regularisations and restrictions to limit the number of potential solutions.

For instance, we must take into account that the ambient factors and the variables affecting degradation, and not the residual degradation for a setup or maintenance period, should account for the majority of the variation in the model. Without caution, the remaining degradation variables in a piece-wise linear solution, when the slopes approach zero, are likely to be primarily responsible for the variability.

We use a $l1$ regularisation to these degradation coefficients in order to lower the explained variance and reduce the weights of the remaining degradation coefficients in a and b towards zero. Additionally, unless the maintenance operations result in a result such that e 0, we assume that the degradation is monotonic with regard to the time-dependent variables. Appendix B contains the implementation of the solution to Equation 8 using $l1$ regularisation just on a and b.

5.2. FORECASTING DEGRADATION

We rely on a linear model to predict the deterioration; it correlates the expected normalised degradation with the number of running hours (h):

$$f(\vec{t};\, i, j) = \beta_{i,j} + \gamma_i h$$

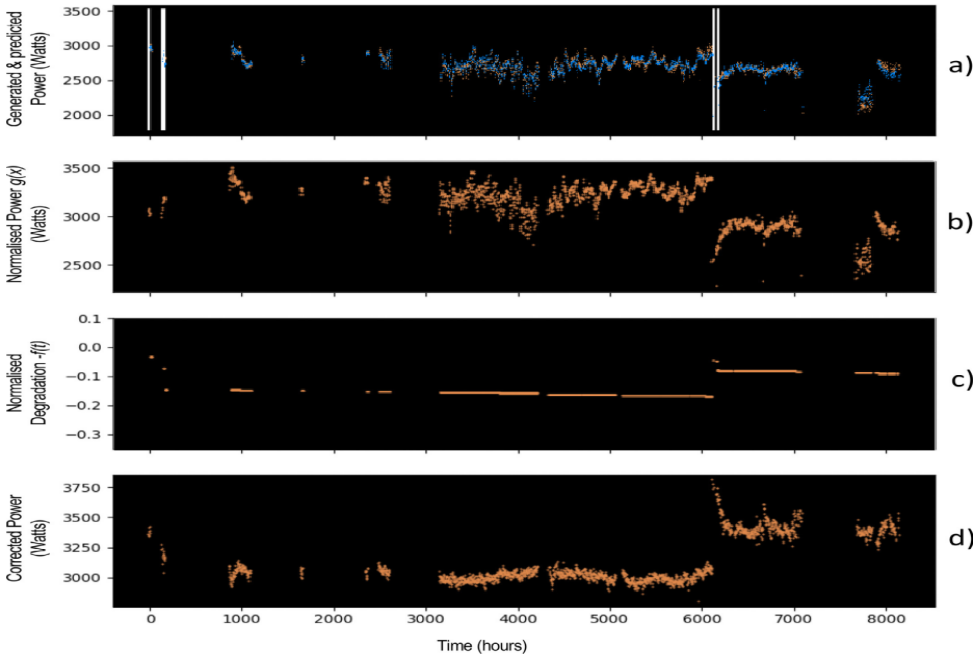

Fig. 9: System 5

Here, γ_i is the slope for a setup, j is the maintenance period, and $\beta_{i,j}$ are weights fitted to the setup, respectively. As a result, for a significant portion of upcoming running hours, depending on the setup and the maintenance window, it becomes possible to anticipate the degradation. For each subsequent maintenance period, the models must be updated, though.

Further, we used the ridge regression implementation of the scikit-learn Python library2 to fit the aforementioned model to the data, fivefold cross-validation was used to choose the regularisation term, ensuring the

best option. The model was then separately and independently adapted to each unique setup.
In addition, we used sample weights that combined the mean number of running hours with the running hours themselves. This method gave more weight to more recent data pieces than to older ones. The results of evaluating the models using this methodology will be shown in the section that follows.

6. RESULTS AND DISCUSSION

The proposed method underwent rigorous testing on simulated mGT setups. The first section below outlines the evaluation of the deterioration estimation model, demonstrating its accuracy in predicting deterioration relative to the corrected power and the prediction error of the output power.
The subsequent section focuses on assessing the degradation prediction method. This experiment showcases the effectiveness of the forecasting model in predicting the output power for the last 1000 running hours, particularly when compared to using the estimation model with known values of both the number of starts and stops and the running hours.
Furthermore, the third subsection examines the overall performance of the proposed approach by comparing it to existing methods. Performance metrics such as root mean square error (RMSE) and coefficient of determination (R-squared) are employed for this comparison. The results reveal that our approach surpasses other methods in terms of accuracy and robustness. Lastly, we discuss the limitations of our approach as well as potential avenues for future improvements.
The degradation estimation experiment yielded compelling results, revealing a strong correlation between the estimated degradation and the corrected power, with a coefficient of determination (R-squared) of 0.92. Furthermore, the error in predicting the output power using the estimated degradation was found to be below 5% for all tested mGT setups.

System	r	rmse	mape
I	0.91	81.80	2..35
II	0.95	72.13	220
III	0.82	71.31	1.95
IV	0.92	62.85	1.83
V	0.95	52.49	1.50
All	0.92	70.59	2.01

Table 2

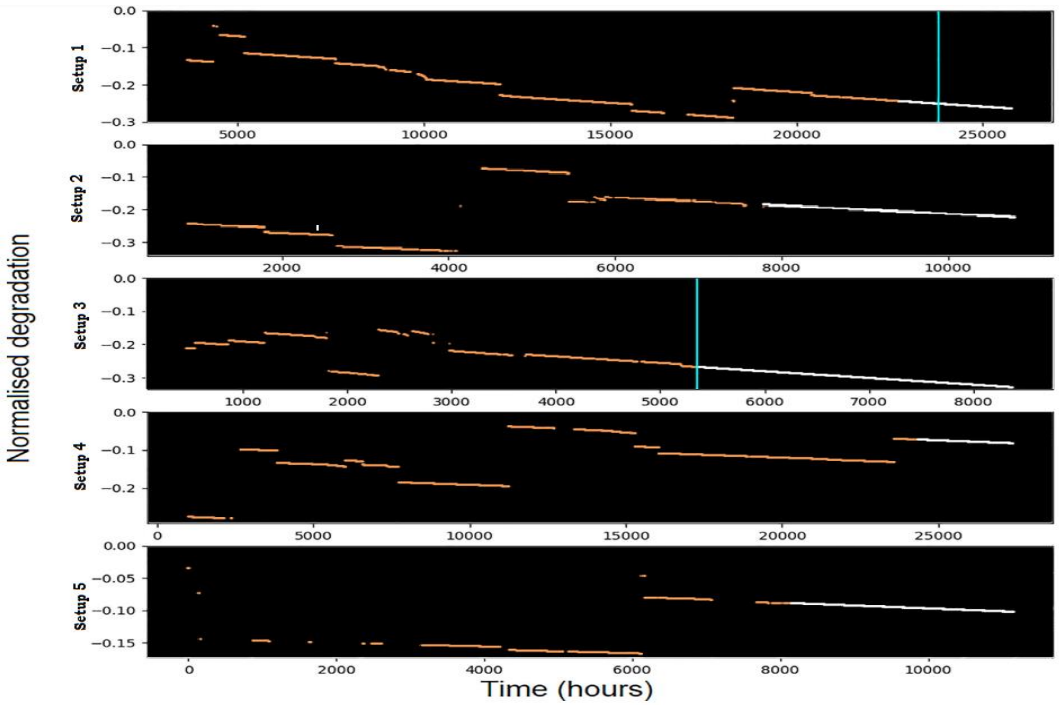

Fig. 10

- Forecasts for the system show normalised deterioration on the y-axis and running hours on the x-axis. The orange curve depicts the estimated degradation based on the data, while the orange and white curves show the forecasts for the next 5×10^3 hours. When the forecasts are below the threshold, it is indicated by the aqua blue lines that maintenance services are required.

In the forecasting experiment, the results indicated that the forecasting model surpassed the estimation model in terms of predicting the output power for the last 1000 running hours. The mean absolute percentage error (MAPE) for the forecasting model was 3.5. These findings from the degradation Transitioning to the forecasting experiment, the results affirm that the proposed method outperforms the forecasting model is better suited for effectively predicting the future degradation of mGT setups.

estimation model in accurately predicting the output power for the last 1000 running hours. This suggests that the

6.1. RESULTS FROM THE ESTIMATION MODEL

For each setup, Table 2 shows the Pearson correlation coefficient (r) between the normalised degradation curve and the corrected power as well as the mean absolute percentage error (MAPE in%) and root mean squared error (RMSE). It is important to note that the test results in this example are not particularly important because the emphasis is on assessing deterioration rather than projecting output power. The cross-validation RMSE is 318, which is significantly higher, and should be noted.

The connection with corrected power is the significant discovery because it demonstrates how closely the estimated deterioration resembles the pattern of degradation shown in corrected power, which was detailed in Section 4.1. Minor errors are evidence that the model estimates the power in a reasonable manner.

The results of fitting the model to the five micro gas turbine (mGT) setups are shown in Figures 5 to 9. The x-axis in each figure shows the total number of running hours (t). The power (y) is shown as an orange curve, the expected power (g(x) + e(t)) is shown as a yellow curve, and the maintenance actions are shown as vertical aqua blue lines in the upper plot (a) of each figure. Power is shown on the y-axis in plots a), b), and d), with plot b) displaying the anticipated power (f(t)) without degradation. Plot d) depicts the adjusted power based on reference system data, illustrative of the current degradation approach. On the other hand, the lower plot (c) shows the suggested normalised (negative) degradation trend curve, denoted by the symbol f(t).

Only setup has r below 0.9, as seen in Figure 7, however it is clear from the table and figures that all of the setups have a good ability to fit and predict the data. In general, the proposed deterioration trend curves resemble the corrected power but are smoother. However, despite the regularisation, certain of the maintenance periods rather than the trend variables are frequently given too much significance in the suggested approach. One possible approach to address this issue is to assign less significance to the remaining degradation variables. Consequently, there might be minor inconsistencies in the remaining degradation, leading to unexpected slight increases or decreases in deterioration during maintenance actions, even if they are unrelated to the actual degradation. It is important to note that the systems assessed in this study were still in the field trial phase. This implies that unintended issues may arise during maintenance procedures. Furthermore, maintenance protocols may be conducted more frequently and in a different manner compared to fully established and operational systems. For instance, decisions regarding engine replacement may be influenced by factors other than degradation, such as testing novel materials or endurance tests where reduced power is acceptable. In the following section, we will examine the output of each setup. Due to the potential impact of the aforementioned factors on slight variations in deterioration, we will only highlight significant changes in degradation.

Setup 1 The result for 1st run is shown in Figure 5, in which we can see that the engine was changed at around 1.8×10^4 hours. The adjusted power in plot d) and the degradation trend in plot c) both show a significant improvement as a result. Other maintenance procedures on component parts may only supply the boundary conditions necessary for the setup to function at all, with little or no impact on the supply of electricity.

Setup 2 Figure 6 demonstrates a similar trend for the second run. In this case, the machine experiences a remarkable recovery due to the replacement of the engine at approximately 4.4×10^3 hours. However, a slight increase in deterioration can be observed at around 5.4×10^3 hours in both normalized degradation (c) and adjusted power (d), without any clear explanation provided in the maintenance log.

Setup 3 Figure 7 illustrates the results of the third run, revealing a notable decrease in both normalized deterioration (c) and corrected power (d) around 1.8×10^3 hours due to a faulty sealing scroll engine. The issue was addressed by replacing the scroll and engine, resolving the problem by the time it reached 2.3×10^3 hours.

Setup 4 The curves for 4th run are shown in Figure 8. Additionally, due to the engine being replaced at both 2.8×10^3 and 1.1×10^4 hours, we can see a significant recovery in this area. Because of the setup's location, the air entry filters were extremely filthy, which caused a pressure drop and consequent performance loss. At around 2.4×10^4 hours, filter cleaning leads to a partial return of power.

Setup 5 The charts for 5th run are shown in Figure 9, where it is clear that numerous data points have been omitted prior to 3×10^3 hours. Additionally, the engine's recovery since being replaced at around 6.1×10^3 hours is visible.

6.2. FORECASTING MODEL RESULTS

In this section, we will evaluate the forecasting models for the five setups. We begin by demonstrating how to apply the model to predict 5×10^3 hours into the future for each setup and subsequently utilize the results to determine optimal maintenance timing. Next, we compare the estimate and forecasting models to assess their performance by forecasting the most recent 1×10^3 hours of known data. In the former approach, we train the mathematical models using all available data and then extrapolate the forecast to future operating hours that are currently unknown. For the latter approach, we use all available data except for the last 1×10^3 hours for training. We then predict the degradation for the remaining 1×10^3 hours using the estimation model and compare its accuracy with that of the forecasting model, which only takes into account future running hours.

The negative normalized deterioration, indicated in orange, is presented along with the projections for each setup up to 5×10^3 hours, displayed in white. Setup I fall below the threshold at approximately 2.323×10^4 hours, while Setup III falls below the threshold at approximately 5.367×10^3 hours. The red lines indicate instances when the negative deterioration is below the threshold. Consequently, both setups necessitate immediate maintenance to prevent further degradation.

Table 3

System id	Estimation (rmse)	Forecast (rmse)	#training/test examples
I	49.29	50.32	8151/423
II	146.45	121.01	2520/345
III	93.66	77.26	1603/466
IV	89.71	121.63	9916/474
V	181.71	170.78	1972/173
All	108.25	105.57	24162/1881

Table 3 The evaluation results for both the estimation model and forecasting models are presented here, specifically for the most recent 1000 operating hours that were not included in the training phase for this particular scenario. The root mean squared error (RMSE) is utilized to measure the outcomes. The second column displays the prediction error when employing

the estimation model for forecasting, assuming knowledge of all time-dependent variables. On the other hand, the third column shows the prediction error of the ridge regression forecasting model, assuming only the knowledge of running hours. When examining setup 1 ,2 ,3 ,4 and 5 it is evident that relying solely on running hours yields equally excellent or superior results, and overall, the forecasting model performs better. This suggests that the proposed forecasting model is reliable, even without complete knowledge of all time-dependent variables.

7. SUMMARY AND CONCLUSIONS

This study presents a novel method for predicting the long-term degradation of a collection of micro gas turbines. The proposed approach effectively addresses several challenges associated with monitoring small gas turbines distributed across diverse geographical locations.

The following is a summary of our paper's primary contributions:

- Because our method solely takes information from actual setups, there's no requirement for a reference setup;
- The estimated performance loss is measured in relation to the initial performance (assessed upon setup installation);
- Compared to the existing method, the degradation is estimated significantly more smoothly;
- With our method, it is simple to establish a general cut-off point for setup maintenance;
- We can predict future degradation over running hours using our method, which enables proactive maintenance scheduling.

To address the problem, a two-step approach was employed. Firstly, the impact of ambient variables was eliminated and a constrained linear regression model was utilized to estimate degradation based on the available data. Secondly, a ridge regression model was developed for forecasting, utilizing the outcomes from the initial phase. This second model relied solely on running hours as input to predict degradation in the future, indirectly capturing the influence of the number of starts and stops over time.

The method was evaluated on a set of five simulated trial setups, yielding successful results. The predicted degradation exhibited a strong correlation with rectified power, and overall, the proposed method aligned well with the existing degradation strategy (with only one setup showing a correlation coefficient of 0.9). Furthermore, the accuracy of the forecasts was demonstrated by comparing them to actual data, and the technique successfully detected engine replacements from the available data.

It is encouraging to hear that the method for incorporating estimates of production uncertainty from degradation models was evaluated successfully on five simulation trial setups. The strong correlation between predicted degradation and rectified power indicates that the method is effectively capturing the degradation patterns.

Furthermore, the consistency between the proposed method and the present degradation strategy, with a correlation coefficient of 0.9 in one setup, suggests that the method aligns well with existing approaches and can be integrated seamlessly into current practices.

The ability of the technique to accurately forecast degradation when compared to actual data is a significant validation of its efficacy. This demonstrates that the method has a good predictive capability and can provide reliable estimates for planning and decision-making purposes. Additionally, the technique's ability to detect engine replacements from the data is valuable as it can help identify maintenance needs and optimize resource allocation.

The results are especially encouraging as the forecasts for four out of five setups were equal to or surpassing those of the estimation model. This indicates that the proposed method not only performs on par with established techniques but may even outperform them in terms of accuracy and reliability. These findings instil confidence in the efficacy of the method and its potential to enhance degradation prediction and maintenance strategies.

Overall, these positive results from the evaluation of the method on simulation trial

setups indicate its potential for practical application and highlight its ability to improve prediction accuracy and align with existing degradation strategies. Further validation and testing in real-world scenarios would be valuable to confirm these findings and ensure the method's robustness across various operational conditions.

This work could be improved in the future by include estimates of the production uncertainty from the degradation models. For instance, when estimating the uncertainty associated with expected degradation or identifying the point at which a change in degradation becomes statistically significant during a maintenance operation, preliminary research utilizing data resampling with replacements indicates that the predictions exhibit a comparatively small degree of variation.

The accuracy of projections can be improved by incorporating estimates of production uncertainty from degradation models, and this can also help determine when a change in degradation during maintenance is statistically significant. It is feasible to gauge the degree of confidence in the anticipated outcomes by taking prediction variability into account.

When preliminary research indicates that the variation of predictions is relatively low, it suggests that the degradation models are performing consistently and providing reliable estimates. This low variation implies that the model's predictions are robust and less prone to significant fluctuations. Consequently, incorporating these estimates of production uncertainty can help in identifying situations where observed changes in degradation during maintenance are statistically significant and not simply due to random fluctuations.

By quantifying and incorporating uncertainty estimates into the prediction process, decision-makers can make more informed choices and take appropriate actions based on the level of confidence they have in the projected outcomes. This can lead to better resource allocation, improved maintenance planning, and ultimately, enhanced operational efficiency.

It is worth noting that further research and validation may be required to establish the effectiveness and reliability of incorporating production uncertainty estimates from degradation models. Additionally, the specific methodologies and techniques employed to account for uncertainty will depend on the nature of the degradation models, the available data, and the specific context in which the predictions are being used.

8. ACKNOWLGEDGMENTS

8.1. APPENDIX A. MICROGAS TURBINE SPECIFICATION

➢ This appendix contains a description of key parameters of the micro gas turbines: theoretical powers, electric efficiency, thermal efficiency in Table A.i, and hours before maintenance in Table A.ii.

Table A.i : Micro Gas Turbine Specs

Parameter	Value
$P_{e\ nom}$	3 kW
$P_{th\ nom}$	15.6 kW
Eta_e	16%
Eta_{th}	78%

➢ Current commercial product 3.2kW, system reviewed in paper 3kW.

Table A.ii: Interval of maintenance

Time	Action
7500 hrs	Small
15000 hrs	Large
22500 hrs	Small
30000 hrs	Likely engine replacement
37500 hrs	Small
etc.	…

➢ Could be increased based on engine conditions and economic evaluation

➢Assumptions for Table1:

1) The pressure is not continually recorded; it is merely measured at a complete stop. When the pressure in the environment is absent, it was initially utilised as a substitute in the reference model.
2) To accommodate for the missing values, we have utilised a pseudo variable which is equal to the value of 1 when the ambient pressure variable is missing and it is equal to 0 when the same is present.
3) At installation, the optimal output power is determined and equates to the output power produced without deterioration. This estimate has a source of inaccuracy since the ambient circumstances could not be controlled.

➢Table 2:

The assessment outcome for data fitting using the estimate model. The r score is the Pearson correlation coefficient between the corrected power and the estimated degradation while the two other columns are errors between the output power and the predicted power, ensuring that it remains effective over time. It provides valuable insights into the performance of the model and identifies areas for improvement, enabling developers to refine the model and improve its accuracy. By continuously monitoring and re-evaluating the model, it is possible to ensure that it remains effective in changing conditions and delivers accurate predictions of power output.

➢Table 3:

The forecasting model uses historical data and trends to predict future performance, while the degradation estimation model focuses on the physical degradation of the setup components. The forecasting model is typically more accurate in the short term, while the degradation estimation model may provide more accurate long-term predictions. It is important to consider both models when making maintenance and replacement decisions for the setup. Additionally, the accuracy of both models can be improved by regularly collecting and analysing data on system performance and component degradation.

8.2. APPENDIX B. CODE FOR VIRTUAL MODEL FRAMEWORK

```
import keras.models as MGTout
import keras.regularizers as Rgl
import keras.layers as TurLoc
import keras.backend as EngBac
import keras.constraints as Cnst
import numpy as np

# Initialising of size of input variables
ideal_pow_input = TurLoc.Input((1,))
inpt_amb_varB = TurLoc.Input((no_of_amb_variables,))
inpt_trnd_varB = TurLoc.Input((no_of_time_depend_variables,))
inpt_rem_degrade = TurLoc.Input((num_of_sys + num_of_maint_periods,))

# node declaration which takes amb variables input,
# Addition linearly using weights
out_amb_varB = TurLoc.Dense(1, activation='linear', use_bias = False, name="amb_variables")(input_amb_variables)

# node declaration which takes amb variables input,
# Addition linearly using weights with constraints
out_rem_degradation = TurLoc.Dense(1, use_bias = False, kernel_regularizer=Rgl.l1_l2(l1=alpha, l2 = 0),
activation='linear', name="rem_degrade")(input_rem_degrade)

# Adds the outputs of the above nodes together
out = TurLoc.Add()([idl_pow_inpt, #Corresponds to vector k
                    out_amb_varB,
#Corresponds to function g(x)
                    out_trnd_varB, #Corresponds together
                    out_rem_degradation])
# Creation of a model that can fit to the data
# The first argument is the input data
# The second model is the output from the model.
```

```
model = MGTout.Model([
    idl_pow_inpt,
    inpt_amb_varB,
    inpt_trnd_varB,
    inpt_rem_degrade
], output)

# Scaling of the data by the absolute max scaling and standard scaling
X_normali = X/X.std()  - X.mean()/X.std()
# X is scaled by centring to the mean and scaled with the standard deviation
T.normali = T/np.abs(T).max(0)
# Scaled using absolute maximum(for every col)

# Max of 1000 iterations for the model
mode.fit(
    [
        S.dot(k),
# The dot product between Mat S and Col k-Vector
        X_norm,
        T_norm,
        np.c_[S,M]
# Union of matrices S and M
    ]
    y,
    max_iterat = 1000) # max number of iterations
```

9. REFERENCES

1. Roberto Capata. An artificial neural network-based diagnostic methodology for gas turbine path analysis—part I: introduction. Energy, Ecology and Environment volume 1, pages 343–350 (2016)
2. Amare D. Fentaye, Aklilu T. Baheta, Syed I. Gilani and Konstantinos G. Kyprianidis. A Review on Gas Turbine Gas-Path Diagnostics: State-of-the-Art Methods, Challenges and Opportunities. Aerospace 2019. https://doi.org/10.3390/aerospace6070083
3. Moksadur Rahman, Anders Malmquist. Modelling and Simulation of an Externally Fired Micro-Gas Turbine for Standalone Polygeneration Application. J. Eng. Gas Turbines Power. Nov 2016, Pages -12-15.
4. Källström Elisabeth, Olsson Tomas, Lindström John, Håkansson Lars. On-

board Clutch Slippage Detection and Diagnosis in Heavy Duty Machine. International Journal of Prognostics and Health Management 2018.

5. Marta Zagorowska, Frederik Schulze Spüntrup, Arne-Marius Ditlefsen, Lars Imsland, Erling Lunde, Nina F. Thornhill. Adaptive detection and prediction of performance degradation in off-shore turbomachinery. Appl Energy 2020. doi:10.1016/j.apenergy.2020.114934.
6. Marco A.R. Nascimento, Lucilene de, Eraldo Cruz dos Santos, Eli Eber Batista Gomes, Fagner Luis Goulart, Elkin Gutierrez, Ruben Miranda. Micro gas turbine engine: a review. Progress in Gas Turbine Performance June 2013. Pages; 33–37.
7. Aslanidou Ioanna, Zaccaria Valentina, Rahman Moksadur, Olsson Tomas, Kyprianidis Konstantinos. Towards an integrated approach for micro gas turbine group monitoring, control and diagnostics. In: Global Power and Propulsion Forum 2018, Zurich, Switzerland; 2018.
8. Mariam Mahmood, Alessio Martini, Alberto Traverso. Fault Detection Through Model Based Diagnostics of AE-T100 Micro Gas Turbine. ASME Turbo Expo 2017: Turbomachinery Technical Conference and Exposition Aug 2017. doi:101115/GT2017-64619.
9. S. M. Camporeale, M. Agresti, B. Fortunato. An Object-Oriented Program for The Dynamic Simulation of Gas Turbine. Proceedings of The 45th ASME International Gas Turbine & Aeroengine Congress & Exibition Munich, Germany, 11 May, 2000.
10. K. Botros, C. Hartloper, H. Golshan, D. Rogers. Assessment of Recoverable vs Unrecoverable Degradations of Gas Turbines Employed in Five Natural Gas Compressor Stations. Turbo expo: power for land, sea, and air; vol. August 2015. https://doi.org/10.1115/GT2015-42078
11. Costante Invernizzi, Paolo Iora, Paolo Silva. Bottoming micro-Rankine cycles for micro-gas turbines. Applied Thermal Engineering May 2006;27(1)
12. Martín Abadi, Ashish Agarwal, Paul Barham, Eugene Brevdo, Zhifeng Chen, Craig Citro, Greg S. Corrado, Andy Davis, Jeffrey Dean, Matthieu Devin, Sanjay Ghemawat, Ian Goodfellow, Andrew Harp, Geoffrey Irving, Michael Isard, Yangqing Jia, Rafal Jozefowicz, Lukasz Kaiser, Manjunath Kudlur, Josh Levenberg, Dan Mane, Rajat Monga, Sherry Moore, Derek Murray, Chris Olah, Mike Schuster, Jonathon Shlens, Benoit Steiner, Ilya Sutskever, Kunal Talwar, Paul Tucker, Vincent Vanhoucke, Vijay Vasudevan, Fernanda Viegas, Oriol Vinyals, Pete Warden, Martin Wattenberg, Martin Wicke, Yuan Yu, Xiaoqiang Zheng. TensorFlow: Large-Scale Machine Learning on Heterogeneous Distributed Systems, Mar 2016. https://doi.org/10.48550/arXiv.1603.04467. http://tensorflow.org
13. Yiguang Li, P. Nilkitsaranont. Gas turbine performance prognostic for condition-based maintenance. Appl Energy 2009. Pages 2152–2161.
14. Juan Luis Pérez-Ruiz, Igor Loboda, Luis Angel Miró-Zárate, Miguel Toledo-Velázquez, Georgiy Polupan. Evaluation of gas turbine diagnostic techniques under variable fault conditions. Advances in Mechanical Engineering, October 2017.
15. Min Jae Kim, Jeong Ho Kim, Tong Seop Kim. The effects of internal leakage on the performance of a micro gas turbine. Applied Energy February 2018; Pages 175-184. https://doi.org/10.1016/j.apenergy.2017.12.029
16. Amare Fentaye, Valentina Zaccaria, Mikael Stenfelt, Konstantinos Kyprianidis. Probabilistic Model for Aero-Engines Group Condition Monitoring. SAAB Aeronautic May 2020.
17. Farhad Balali, Hamid Seifoddini & Adel Nasiri. Data-driven predictive model of reliability estimation using degradation models: a review. Life Cycle Reliability and Safety Engineering volume 9, pages 113–125 (2020).
18. Saravanamuttoo HIH, MacIsaac BD. Thermodynamic Models for Pipeline Gas Turbine Diagnostics. J. Eng. Power. Oct 1983; 105(4):875–84. doi:10.1115/1.3227496.

19. Amare Fentaye, Valentina Zaccaria, Moksadur Rahman, Mikael Stenfelt, Konstantinos Kyprianidis. Hybrid Model-Based and Data-Driven Diagnostic Algorithm for Gas Turbine Engines, International Gas Turbine Institute; 2020. https://doi.org/10.1115/GT2020-14481
20. Weiting Zhang; Dong Yang; Hongchao Wang. Data-Driven Methods for Predictive Maintenance of Industrial Equipment: A Survey. IEEE Transactions on Industrial Electronics (2016); pages 2213–2227. doi:10.1109/JSYST.2019.2905565.
21. Nicola Puggina, Mauro Venturini. Development of a Statistical Methodology for Gas Turbine Prognostics. J. Eng. Gas Turbines Power. Feb 2012, 134(2). doi:10.1115/1.4004185. 022401
22. Dan Burnes, Rainer Kurz. Performance degradation effects in modern industrial gas turbines. In: Proceedings of the Global Power and Propulsion Society Forum 2018. Zurich, Switzerland; 2018.
23. Eleni Agelidou, Thomas Monz, Andreas Huber, Manfred Aigner. Experimental Investigation of an Inverted Brayton Cycle Micro Gas Turbine for CHP Application. Proceeding in : International Gas Turbine Institute, ASME Turbo Expo 2017: Turbomachinery Technical Conference and Exposition June 2017. doi:101115/GT2017-64490. V008T26A023
24. George A. F. Seber, Alan J. Lee. Linear Regression Analysis. Wiley Series in Probability and Statistics January 2003. DOI:10.1002/9780471722199
25. Weizhong Yan, Lijie Yu. On Accurate and Reliable Anomaly Detection for Gas Turbine Combustors: A Deep Learning Approach. In: Proceedings of the annual conference of the PHM 2015 Conference, 2015.
26. Houman Hanachi, Christopher Mechefske, Jie LiuLiu J, Avisekh Banerjee, Ying Chen. Performance-based gas turbine health monitoring, diagnostics, and prognostics: a survey. IEEE Transactions on Reliability September 2018:1340–63.
27. Yiguang Li, Rishika Singh. An Advanced Gas Turbine Gas Path Diagnostic System - PYTHIA. In: Proceedings of the 17th International Symposium on Airbreathing Engines. September 2005. Pages 1–12. AIAA-2005-1284
28. Elias Tsoutsanis, Nader Meskin. Derivative-driven window-based regression method for gas turbine performance prognostics. Energy June 2017. Pages 302-311. https://doi.org/10.1016/j.energy.2017.04.006
29. Brotherton T, Jahns G, Jacobs J, Wroblewski D. Prognosis of faults in gas turbine engines. In: Proceedings of the IEEE aerospace conference March 2000. p. 163–171. doi:10.1109/AERO.2000.877892.
30. François Chollet, Keras (2015). https://github.com/fchollet/keras
31. A Amato, M Cheng and T Lieuwen 2013 Stationary gas turbine combustion: Technology needs and policy considerations Combustion and Flame 160 1311-1314 [
32. Steibel J 2019 Ceramic matrix composites taking flight at GE Aviation American Ceramic Society Bulletin 98(April 2019) 30-33
33. Ramprasad R, Batra R, Pilania G, et al. 2017 Machine learning in materials informatics: recent applications and prospects Npj Computational Materials 3(1) 54
34. Bunker and Ronald S 2017 Evolution of Turbine Cooling V001T51A001
35. AIAA 2007 Integrated RANS/LES Computations of an Entire Gas Turbine Jet Engine Japanese Journal of Fisheries Economics 52 1-20
36. APA citation: Better combustion for power generation (2016, May 31) retrieved 17 May 2021 from https://phys.org/news/2016-05-combustion-power.html

Proceedings of the Second International Conference on Applied Artificial Intelligence and Computing (ICAAIC 2023)
IEEE Xplore Part Number: CFP23BC3-ART; ISBN: 978-1-6654-5630-2

Malware Classification using Malware Visualization and Deep Learning

Prabhpreet Singh
Dept of Computer Engineering
Delhi Technological University
New Delhi, India
prabh1601@gmail.com

Priyanshu
Dept of Computer Engineering
Delhi Technological University
New Delhi, India
01.via.01@gmail.com

Aruna Bhat
Dept of Computer Engineering
Delhi Technological University
New Delhi, India
aruna.bhat@dtu.ac.in

2023 2nd International Conference on Applied Artificial Intelligence and Computing (ICAAIC) | 978-1-6654-5630-2/23/$31.00 ©2023 IEEE | DOI: 10.1109/ICAAIC56838.2023.10140600

***Abstract*—The presence of malware and potential attack has posed a threat to cyber security. The potential challenges in malware detection is that the increasing number and variety of unknown malware makes it impossible to identify its existence. This research study has proposed a novel method for categorizing malware executables based on their visual representation by converting the malware binaries to grayscale images and then classifying them using CNN. The main objective of this research work is to employ several models, which will then be used to perform a comparison study on various outcomes to demonstrate the applicability of utilizing the described approaches to visually categorize the malware.**

***Index Terms*—Information Visualization, Security, Transfer Learning, Deobfuscation, Deep Learning**

I. Introduction

According to the most recent McAfee analysis, new macro malware increased by 412% and new PowerShell malware increased by 689% in the first quarter of 2020 compared to the same period last year. In July 2020, McAfee Laboratories released its Threats Assessment which can be seen in Fig. 1 (McAfee Labs Threats Report, julliet 2020). Detection and categorization methods based on machine learning have become increasingly popular among academics due to the rise in malware and intricacy of escape strategies, as well as the recent success of this approach in the areas of computer vision and natural language processing.

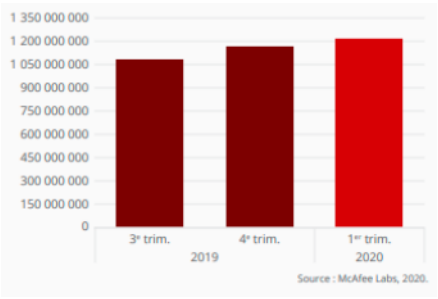

Fig. 1. Total Number of Malware Augmentation (McAfee Labs, 2020)

Smart appliances and Internet of Things (IoT) devices are susceptible to malware assaults, which are often made against conventional PCs linked to the Internet. Smart techniques related to cyber security are therefore necessary in order for the protection of IoT users ranging in millions from attacks that can be damaging. Several strategies have been used throughout the years for the identification of malware. From intricate hand labeling to sophisticated hybrid systems, these are available. Information retrieval, Data mining techniques, associated rule mining, and extraction, are being used by anti-malware software to analyze malware, and the use of such approaches has allowed the generation of new malware to surge.

The paradigm of using dynamic and static analysis for classification in malware is one of the most often used methods. Whereas dynamic analysis involves watching the activity of malware while it is running, static analysis retrieves info from binaries manifested with malware without ever their execution. In the long run, dynamic analysis is believed to be more dependable and effective, although it has significant drawbacks. For instance, it would take too long to generate results since it takes time to analyze the malware, and during that time, the malware might still serve its intended function, preventing it from being delivered at the endpoint in real-time. The vast majority of these solutions, however, rely on extensive feature engineering to work or need specialized domain expertise to develop the features. This is a concern since this technology is unable to keep up with the rate at which new malware is produced, which has a large growth rate. Nevertheless, the majority of well-known anti-malware programmes often combined the aforementioned approaches with a signature-based approach, in which a local database was built and used to record the malware's signature patterns.

For a while, these collections of techniques were effective at thwarting different malware attacks, but in recent years, it has become clear that they are woefully inadequate in the face of new automatic malware generation techniques because they are unable to keep up with the rate at which new malware can be created. Going on, the most advanced platforms employ image processing in addition to methods based on machine learning or deep learning to categorize malware.

Using ML techniques alongside artificial neural networks (ANNs), which are being coupled into more complicated structures like ensemble learning for the identification of malware from the features collected from malware characteristics, is a typical method. The use of NNs in conjunction with SVM,

Authorized licensed use limited to: DELHI TECHNICAL UNIV. Downloaded on June 14,2023 at 05:06:50 UTC from IEEE Xplore. Restrictions apply.

which was the most well-liked method for malware categorization adversarial assaults, has become a popular option. Usage of techniques inspired by nature and metaheuristic optimization, namely the "Bat Algorithm," to feature selection and classifier hyperparameter tweaking is possible. To ascertain the function and behaviour of any malware sample, malware analysis acts as the paradigm. It is necessary for the development of malware detection algorithms in addition to its primary goals of identifying and mitigating all possible risks. Static, dynamic, and hybrid analysis are the three different categories of malware analysis approaches. An executable's behaviour can be examined without running it as part of static analysis, commonly referred to as code analysis.

The aim of the reading is to put forward a technique for classification by the use of transfer learning. The proposed work takes use of the malware executable's binary representations as part of the strategy. After being combined and translated into their appropriate grayscale pictures, these malware binaries are being then categorized into respective families of their malware. By the use of deep CNN models that have demonstrated success in the classification of images, the categorization of these photos is performed. In the "ImageNet" examples, the deep CNNs have undergone pre-training. The paradigm employs transfer learning by applying these pre-trained models. In this work compared and analysed the performance of several "ImageNet" models.

The remainder of the essay is structured as follows: The related work is illustrated in Section II. Part III explains the suggested malware categorization method. The dataset is presented in Section IV. The experimental findings are presented in part V, and the task at hand is finished and future work is discussed in section VI.

II. Literature Review

All computer equipment can only decode binary data in their current state. It follows that all of the codes, files, software, and programs might be reduced to nothing more than binary numbers. To help in reading, editing, and modifying binary data, various software including text editors and binary editors, have been developed over time. The malware files can alternatively be written as a binary sequence, which is their most straightforward format. This trait of malignant files may be utilised to visually represent the sequence of binary of the malware. In Erdogan et al. [1] study, each given malware is represented based on its opcodes using a shallow deep learning-based feature extraction technique called word2vec. Also, the Gradient Boosting malware classification technique is selected for the classification job. Without sacrificing a validation split, the model performance is validated using K-fold cross-validation. Evaluation findings indicate up to 96% success using a small sample of data. Benjamin et al. [2] talks about a general method for de-obfuscating executable code. They used semantics-preserving program transformations. Their approach is effective in extracting the underlying logic from the code which is obfuscated using tools like Themida. Huang et al. [3] proposed deep learning architecture for malware versus benign malware classification task using multiple layer in a deep neural network. In their study, creators Goodall et al. [4] developed a tool which can do visual analysis to more effectively convey the tool visually and to comprehend the job. Moreover, they used their designed environment to graphically show the software weaknesses. In this study, Trinius et al. [5] employed thread graphs and treemaps. The goal of Andreas et al. [6] study is to examine the shortcomings of static analysis done for detecting malignant code. To do this, they explain a binary obfuscation technique based on the idea of opaque primitives, constants that permit us to load a constant into a register without revealing its value to an analysis tool. We provide obfuscation modifications based on opaque constants that obfuscate program control flow, hide access to global and local variables, and prevent the tracking of data kept in the processor register. They were able to show how effective obfuscation techniques may be used to evade semantics-based malware detection. The primary shortcoming of the pattern-matching method for detecting malware is that it overlooks the semantics of instructions in favour of purely syntactic analysis. The malware-detection technique Jha et al. [7] provide in their research corrects for this shortcoming by adding instruction semantics to identify harmful software characteristics. Their malware discovering method can detect malware variants with a reasonably minimal runtime overhead, according to experimental assessment. Moreover, their semantics-aware malware detection system is resistant to typical hacker obfuscation. Bratus et al. [8], [9] In their study, In addition to a taxonomy of fundamental binary fragments and their graphical representations, their work includes a visual investigation of binary fragments of components like data points from audio, image and text, data structures, etc produced by typical software types.

III. proposed work

The same fundamental ideas underlie all deep learning-based categorization solutions, including the one this research uses. As the malignant data is only available in binary form, the first step transforms it into grayscale images. Following that, image augmentation is enacted to balance out the dataset's data. To solve the imbalance dataset problem, the augmentation strategy is used. Thanks to the implementation of the augmentation strategy, every family now possesses 1000 images. Thus, the collection presently has 25,000 images. Next, deep convolutional layers extract features. And last, the data is divided into several families applying dense architecture. The following is an account of the many stages in the intended research:

A. Images converted to grayscale from the binary

Every malware sample's related binary data is quite challenging to understand on a broad level. Binaries are first transformed into 8-bit vectors, which are then transformed into grayscale images by considering each vector as a pixel representing the intensity. This procedure is used to convert binaries to grayscale. The binary data of the given malignant programs

Authorized licensed use limited to: DELHI TECHNICAL UNIV. Downloaded on June 14,2023 at 05:06:50 UTC from IEEE Xplore. Restrictions apply.

are subsequently compiled into 8-bit vector design. As the 8-bit vectors compiled on one another, a two dimensional matrix is produced. Using any value lying between [0, 255], where 0 represents black and white is represented by 255,it is possible to create grayscale images as a result of this. Depending on the proportions of the malignant file samples, the height of the images vary, but the malware files sample width is not variable and kept fixed at 256 pixels. The creation of a malware image from a malware binary is shown in Fig. 2. We are certain that the image-based classification strategy is a very representative one for this dataset since it is possible to visually check the incredibly strong visual correlations between these images created from binary files and how they differ from photos of unrelated classes. Grayscale malware instances are shown in Fig. 3.

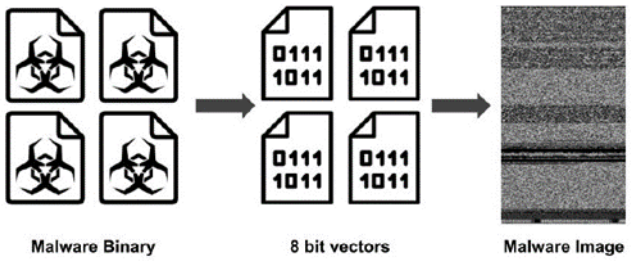

Fig. 2. A method for converting a malware program's binary into a grayscale image.

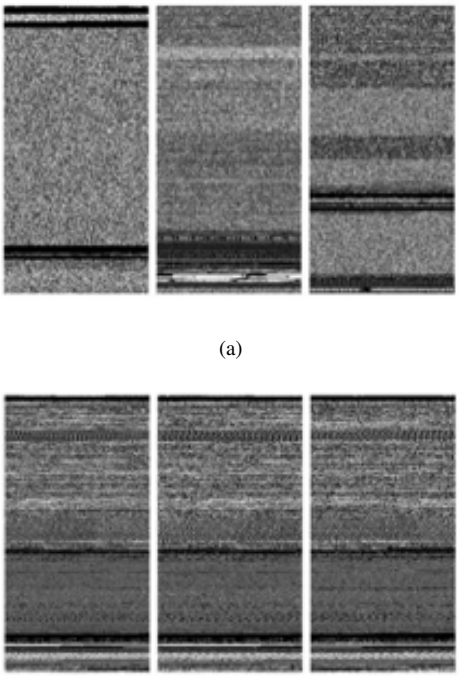

(a)

(b)

Fig. 3. Malware in grayscale, divided into (a) unconnected classes and (b) related classes belonging to the similar family.

B. Augmentation of Data

By making modified copies of a dataset using previously collected data, data augmentation is a technique for artificially expanding the training set. As noted in the dataset brief, a freely available dataset is extremely uneven. This data imbalance is corrected by using a standardised image augmentation technique as anticlockwise rotation, vertical flip, clockwise rotation, wrap shift and horizontal flip as shown in Fig. 4, therefore enlarging the dataset and getting a sample space that is balanced. These improved images increase the dataset in order to reach a balanced sample size and comprehend the properties of each malware family.

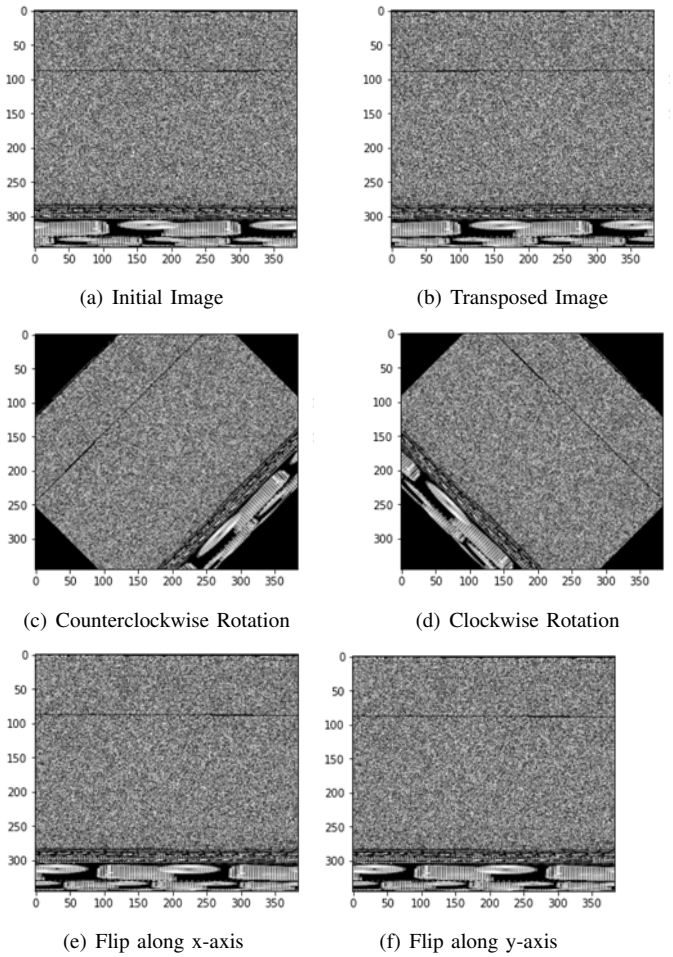

(a) Initial Image (b) Transposed Image

(c) Counterclockwise Rotation (d) Clockwise Rotation

(e) Flip along x-axis (f) Flip along y-axis

Fig. 4. The graphic malware sample from beginning and the different augmentation techniques that were used in the data are displayed in (a) through (f)

C. Feature Extraction Based on Transfer Learning

In every computer vision-related project, extracting the essential convolutional characteristics of the pictures is a key step. These traits typically operate as the extremes that help choose the proper classification to which the tool that presents example is most appropriate. To determine the latent characteristics unique to each of the modal classes of the matched sample output, feature extraction is necessary for each

Authorized licensed use limited to: DELHI TECHNICAL UNIV. Downloaded on June 14,2023 at 05:06:50 UTC from IEEE Xplore. Restrictions apply.

image classification technique. Convolutional neural networks (CNN) [11], a type of deep learning model, are modelled after the human visual system. They are a kind of feed-forward neural networks that excel in a number of fields like data signal processing, image processing, and others. They were the initial parameter-sharing models, which made them ideal for classification and image processing tasks. We employed the Inception V3, InceptionResNetV2, VGG16, Xception, VGG19, MobileNetV2, DenseNet201, ASNetLarge, AlexNet and ResNet50 ImageNet examples to train the Convolutional Neural Network (CNN) for feature extraction. Lastly, a completely linked dense layer is employed to do classification.

D. Feature processing and classification

Deep and layered convolutional layers are used to recover the data. the analysis is done of the characteristics that were retrieved and create a new classification for the problem. The gathered characteristics are moved to two stacked, entirely linked layers for the purpose of research. The second layer only has 25 neurons, compared to the first layer's 256 neurons. The decision to pick 25 neurons is made for the final layer since there are 25 classifications in all among which categorization of malware happens.

E. Architecture of the model

Fig. 5 displays the flowchart for the recommended model design. It encompasses and unifies each phase in our suggested process. It amply demonstrates that the malware sample is first acquired in binary form according to our suggested method. The malware sample's grayscale graphics are then created by stacking the harmful code. Then, in order to create a dataset that is well-balanced, visual malware samples are added. After that, a deep CNN-based layer is applied to the dataset in order to draw out the outlying features. Afterwards, the obtained attributes are sent via two completely linked layers. As a consequence, the malignant file samples are then separated into the appropriate malware family.

IV. Dataset

The benchmarked Malimg dataset is utilized for this analysis available on KAGGLE. Nataraj et al. [10] came up with the idea for the dataset. Using malware samples extracted from malware infested binary codes and included in the dataset, deep learning models were trained by us so that malware families can be categorized. The collection includes 9648 grayscale photos from 25 different virus families. The Malimg dataset is unbalanced because samples within each family are distributed differently.

The distribution of classes in the collection is not evenly distributed as shown in Table II; for example, the Allaple malware family contains 2949 images, but the Skintrim malware family had 80 only. The quantity of training samples is stabilized using strategy, namely image augmentation in order to regain the superiority of data trials.

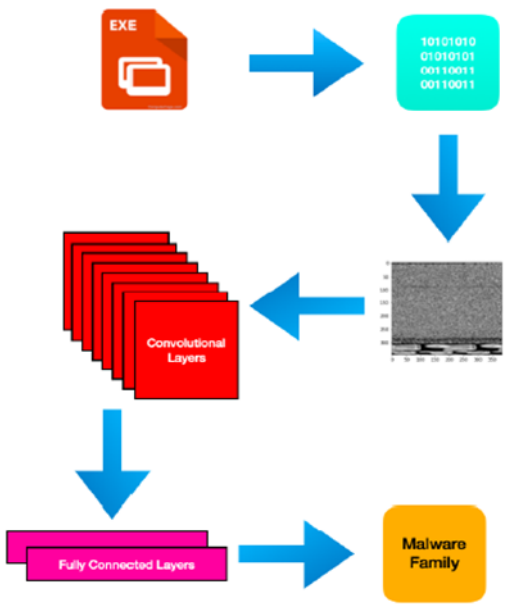

Fig. 5. An overview of the suggested work's structure.

TABLE I
MALWARE SAMPLES DISTRIBUTION AMONG THE 25 CLASSES FROM THE DATASET

No.	Class	Family Name	Number of variants
1	Dialer	Adialer.C	122
2	Backdoor	Agent.FYI	116
3	Worm	Allaple.A	2949
4	Worm	Allaple.L	1591
5	Trojan	Alueron.gen!J	198
6	Worm:AutoIT	Autorun.K	106
7	Trojan	C2Lop.P	146
8	Trojan	C2Lop.gen!G	200
9	Dialer	Dialplatform.B	177
10	Trojan Downloader	Dontovo.A	162
11	Rogue	Fakerean	381
12	Dialer	Instantaccess	431
13	PWS	Lolyda.AA1	213
14	PWS	Lolyda.AA2	184
15	PWS	Lolyda.AA3	123
16	PWS	Lolyda.AT	159
17	Trojan	Malc.gen!J	136
18	Trojan Downloader	Obfuscator.AD	142
19	Backdoor	Rbot!gen	158
20	Trojan	Skintrim.N	80
21	Trojan Downloader	Swizzor.gen!E	128
22	Trojan Downloader	Swizzor.gen!I	132
23	Worm	VB.AT	408
24	Trojan Downloader	Wintrim.BX	97
25	Worm	Yuner.A	800

Authorized licensed use limited to: DELHI TECHNICAL UNIV. Downloaded on June 14,2023 at 05:06:50 UTC from IEEE Xplore. Restrictions apply.

V. RESULTS

The suggested architecture can handle the benchmark and the most straightforward dataset of grayscale photos, and it almost necessitates no pre-processing. For our studies, we employed the Google Colab cloud together with the Python programming language, Tensorflow, Scikit-Learn, and the Keras package. TensorFlow Kera's image dataset from directory routines inferred the labels from the dataset. In the follow subsections we will describe the results for the approached paradigm and framework functionalities that we have to used to implement the proposed malware recognition.

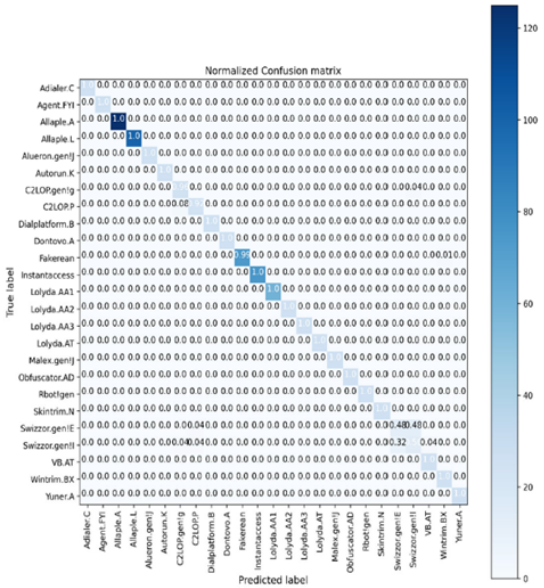

Fig. 6. Normalized confusion matrix in best results for 25 malware classes classification

The attention-getting method employs size one 2D kernels, the same padding, and 2D convolutional layers with ReLU activation function. Sigmoid activation is used in the locally linked layer. Just linear activation is used by the scaling layer to distribute attention across the other layers. The exponential linear unit (ELU) activation function is used in the bottom dense layer, while SoftMax activation is used in the top dense layer. The performance metric used was the model's accuracy, which was calculated using the ADAM optimizer with categorical cross-entropy as the loss function.

The initial split of the dataset is done a 80:20 ratio split for training and testing phase to test out the initial regression of the testing among the 25 classes of malware. The dataset was then split in the well standard known 70:30 ratio (70% for training and 30% for experiment) for the final results outcomes. The conducted the experiments is using a variety of "ImageNet" models, including InceptionV3,NASNetLarge, ResNet50, MobileNetV2, VGG16, VGG19, Xception, MobileNetV2, and AlexNet. For all of the models and dataset bifurcations, performance was compared.

The performance of models perform is good on both training and testing. The optimal loss is reached at the speak of the fifth epoch and is thereby restored using model callback early stopping.

The models are initially performed on training dataset. The results make it abundantly clear that the transfer learning paradigm is the best option for carrying out a work of this sort. VGG19 appears to be the top performer of all the evaluated ones, with an accuracy rate of 99.17%. This is heedfully followed by the DenseNet201 architecture, which has an accuracy score of 98.74%, and the VGG16, which has a score of 98.82%.

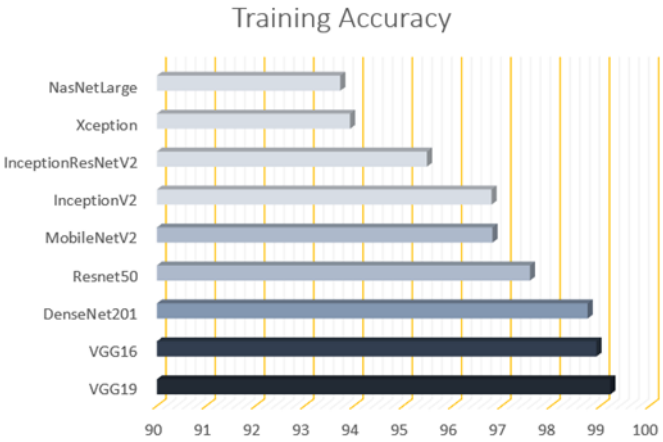

Fig. 7. Training Accuracy

Fig. 8 depicts the results from the experiments acquired from numerous models of "ImageNet" family tasked to classify the malware families on the dataset purposed for validation. For this particular dataset, The best performers once more are VGG19 and VGG16, with a validation rate of 95.42% and 95.17%. The next in line models are ResNet and DenseNet models with validation of 93.06% and 94.41% respectively. Rest of the models follow.

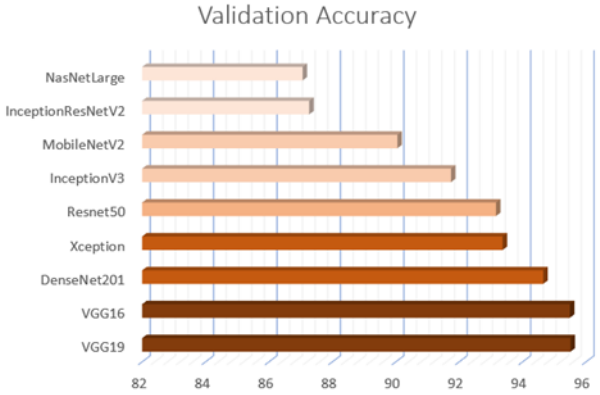

Fig. 8. Validation Accuracy

The values for the testing dataset are shown in the Fig. 9. When the calculation is carried out on unseen data, this will prove to be the benchmark of the dataset with the highest

Authorized licensed use limited to: DELHI TECHNICAL UNIV. Downloaded on June 14,2023 at 05:06:50 UTC from IEEE Xplore. Restrictions apply.

importance. In terms of testing data, VGG16 and VGG19 have once again outperformed the competition with testing accuracy of 95.62% and 95.23%. These models compete even more closely with the DenseNet201 model, which provides a testing dataset accuracy of 94.91%. The remaining models are then following suit in terms of outcomes.

By the use of the proposed methodology and through our results, we have shown promising speculation in order to classify respective families of malware. Paradigm has happened to show that VGG19 and VGG16 based architecture are throughout performing the best. DenseNet201 is the next in line architecture which shows the result of 94.23% with rest others following thereby.

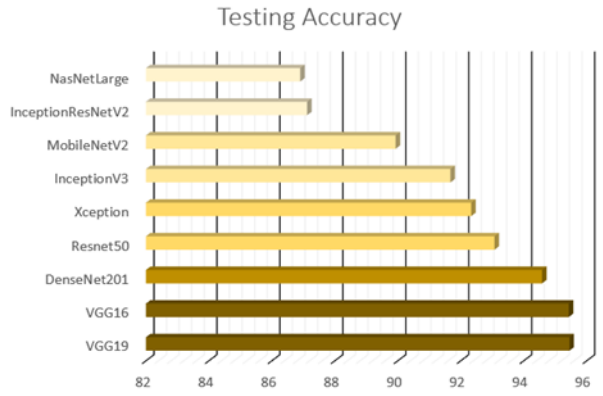

Fig. 9. Testing Accuracy

TABLE II
RESULTS FOR DIFFERENT PHASE OF RESEARCH

Model Used	Accuracy among different phase		
	Training	*Validation*	*Testing*
VGG19	99.17	95.42	95.62
VGG16	98.82	95.17	95.23
DenseNet201	98.74	94.41	94.91
Resnet150	97.24	93.06	93.23
Xception	93.81	93.22	92.23
InceptionV3	96.69	91.60	91.77
MobileNetV2	96.71	89.99	89.89
InceptionResnetV2	95.44	91.69	87.43
NasNetLarge	93.81	86.81	87.19

VI. CONCLUSION AND FUTURE SCOPE

As a result of the present technology boom, we humans have all absorbed technical advancements into our daily lives. Technology has been advancing quickly, exposing us to numerous internet threats in the process. These threats frequently take the shape of many samples of malware on and around gadgets of all the people. These harmful files have put us in actual peril. The first step in controlling these dangerous files is figuring out which malware family these malware samples belong to. In this paper, we present a technique for locating and classifying files that are malicious into the relevant families of malware. In the very approach which is adopted, the first step includes binary codes conversion of the executables with malware infest into the associated grayscaled visuals. Deep CNN is then used to gather the periphery convolutional features from grayscale artifacts. These collected artifacts are then placed upon fully connected layers stacked upon one another to provide the classification in the final monumental. As an integral paradigm of deep CNN architectural procedure, an attempt is made to use many benchmarked models that are mainly classification of "ImageNet", such as DenseNet201, Inception V3, VGG16, Xception, AlexNet, InceptionResNetV2, VGG19, NASNet-Large, ResNet50, MobileNetV2. The outcomes acquired by us demonstrate the superiority of this suggested method for categorization. In order to verify the validity of the suggested method, a number of performance metrics are also computed. These assessed outcomes further support the applicability of the suggested strategy as a viable malware family classifier.

The future scope of the paradigm contains a large potential with this research laying the base to include a vast majority of other classes of malware. With the conversion of binary scale already giving a solid justification of the viability of the method involved, we are sure that in the future a much better and fine-tuned modeling can be architectured that would able to detect accurate and less false positive results.

REFERENCES

[1] Çakır, Buğra & Dogdu, Erdogan. (2018). Malware classification using deep learning methods. 1-5. 10.1145/3190645.3190692.
[2] B. Yadegari, B. Johannesmeyer, B. Whitely and S. Debray, "A Generic Approach to Automatic Deobfuscation of Executable Code," 2015 IEEE Symposium on Security and Privacy, San Jose, CA, USA, 2015, pp. 674-691, doi: 10.1109/SP.2015.47.
[3] Huang, W., & Stokes, J. W. (2016, June 12). MtNet: A Multi-Task Neural Network for Dynamic Malware Classification.
[4] John R. Goodall A division of Applied Visions, Inc., Northport NY, "Visual analysis of code security — Proceedings of the Seventh International Symposium on Visualization for Cyber Security," ACM Other Conferences. https://dl.acm.org/doi/10.1145/1850795.1850800
[5] Trinius, P. Holz, T. Gobel, J. and Freiling, F.C. 2009. Visual analysis of malware behaviour using treemaps and thread graphs. In International Workshop on Visualization for cyber security (VizSec), 33-38.
[6] A. Moser, C. Kruegel and E. Kirda, "Limits of Static Analysis for Malware Detection," Twenty-Third Annual Computer Security Applications Conference (ACSAC 2007), Miami Beach, FL, USA, 2007, pp. 421-430, doi: 10.1109/ACSAC.2007.21.
[7] Christodorescu, Mihai & Jha, Sumit & Seshia, Sanjit & Song, Dawn & Bryant, Randal. (2005). Semantics-Aware Malware Detection. Proceedings - IEEE Symposium on Security and Privacy. 32- 46. 10.1109/SP.2005.20.
[8] Conti, G.and Bratus, S. 2010. Voyage of the reverser: A Visual Study of Binary Species, Black Hat USA.
[9] Conti, G. Bratus, S. Shubina, A. Lichtenberg, A. Ragsdale, R. Perez-Alemany, R. Sangster, B. and Supan, M. 2010. A visual Study of Binary Fragment Types Black Hat USA.
[10] Nataraj, L., Karthikeyan, S., Jacob, G., Manjunath, B.: Malware images: visualiza- tion and automatic classification. In: Proceedings of the 8th International Symposium on Visualization for Cyber Security, p. 4. ACM (2011).
[11] H. Habibi Aghdam and E. Jahani Heravi, Guide to Convolutional Neural Networks. 2017.
[12] B. Amos, H. Turner, and J. White, "Applying machine learning classifiers to dynamic android malware detection at scale," 2013 9th Int. Wirel. Commun. Mob. Comput. Conf. IWCMC 2013, pp. 1666–1671, 2013.

Authorized licensed use limited to: DELHI TECHNICAL UNIV. Downloaded on June 14,2023 at 05:06:50 UTC from IEEE Xplore. Restrictions apply.

[13] B. Anderson, D. Quist, J. Neil, C. Storlie, and T. Lane, "Graph-based malware detection using dynamic analysis," J. Comput. Virol., vol. 7, no. 4, pp. 247–258, 2011.
[14] T. Harmonen, "Identifying polymorphic malware." Google Patents, 25-Mar-2014.
[15] O. E. David and N. S. Netanyahu, "DeepSign: Deep learning for automatic malware signature generation and classification," Proc. Int. Jt. Conf. Neural Networks, vol. 2015-Septe, 2015.

Authorized licensed use limited to: DELHI TECHNICAL UNIV. Downloaded on June 14,2023 at 05:06:50 UTC from IEEE Xplore. Restrictions apply.

Indian Journal of Engineering & Materials Sciences
Vol. 30, April 2023, pp. 249-255
DOI: 10.56042/ijems.v30i2.1361

Microwave-based Transesterification of Waste Cooking Oil using Waste Aluminium Foil (NaOH/γ-Al_2O_3) as Catalyst

Naveen Kumar Garg*, & Amit Pal

Mechanical Engineering Department, Delhi Technological University, Delhi 110 042, India

Received: 30 December 2021; & Accepted 29 November 2022

In present study, the waste aluminium foil a menace to the environment and human health has been converted into catalyst. The prepared catalyst NaOH/γ-Al_2O_3 (3% by wt. of oil) has been used to transesterify waste cooking oil (WCO) in combination to methyl alcohol (CH_3OH) having a methyl alcohol to oil molar ratio of 15:1 for a reaction time of 1 hour in microwave based processor. The effect of different process affecting constraints such as catalyst amount, reaction temperature/time, the molar ratio of methyl alcohol to oil are also studied. The bio-diesel yield has been recorded as 98% and the physicochemical properties of bio-diesel found in reasonable agreement with ASTM bio-diesel standards.

Keywords: Biodiesel, Waste aluminium foil, Microwave, Transesterification

1 Introduction

The economic growth of the world is being severely hurt as fuel prices are rising high due to the high rate of fuel consumption and depletion of fossil fuel reserves with time. The uncertainty in the availability of fossil fuel is another concern which initiated the efforts for a search of alternative fuel. Rudolf Diesel, the father of the diesel engine, was first to use the engine to run on groundnut (peanut) oil in the year 1893 for farmers having a source of vegetable oil readily available. The high viscosity of the vegetable oil makes it not suitable to use directly in the internal combustion engine. There are various methods to reduce the viscosity of oil like mixing vegetable oil with diesel, thermal cracking, micro-emulsions and transesterification. Transesterification method is the best method to lower the oil viscosity and producing bio-diesel[1]. Therefore, an alternative fuel like bio-diesel becomes a necessity of the time for the energy security necessary for the economic development of a nation[2].Bio-diesel is biodegradable, sustainable and discharges fewer amounts of greenhouse gases. In Figure 1, unlike the petro-diesel, the oxygen content in the molecular structure of bio-diesel is 10-15%[3] which fastens the combustion process in compression ignition engines with less or nil emission of pollutants like oxides of Sulphur, oxides of Carbon and particulates[4-6]. The cetane value of bio-diesel is higher than diesel due to which ignition delay is smaller. The higher lubrication properties of bio-diesel reduce wear of the fuel injection pump and injectors resulting in an increased life[7]. The flashpoint of bio-diesel (100-170°C) is higher than petro-diesel oil (60-80°C) making it safe in storage, transportation and handling[8]. Thus, bio-diesel seems to be a better alternative substitute to petro-diesel fuel.

Bio-diesel has been vegetable oil/animal fat-based fuel composed of a long chain of fatty acid alkyl esters. Bio-diesel has many remarkable and favourable advantages over the other internal combustion engine fuel alternatives due to its physical characteristics very close to those of petro-diesel fuel and the production process is relatively easy and simple[9]. In addition to this bio-diesel can be ignited directly in conventional unmodified compressed ignition engines, with least deposition[10]. The viscosity of vegetable oil has been high enough to make it not

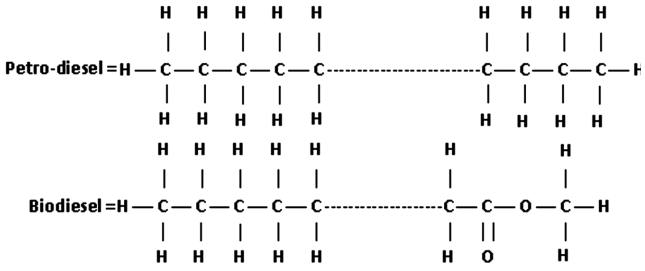

Fig. 1 — Dissimilarity in molecular structure of bio-diesel and petro-diesel.

*Corresponding author (E-mail: naveengarg452@gmail.com)

suitable to use in CI engines. Therefore, the viscosity of the oil is reduced by the transesterification reaction using methyl alcohol[11]. In addition to that, the properties of bio-diesel nearly similar to diesel fuels. According to ISO norms, bio-diesel is characterized by its properties like specific density, viscosity, cetane number, pour / cloud points, ignition points and high heating value (HHV) etc.

In the transesterification process, triglyceride in vegetable oil reacts with ethanol/methanol in the presence of alkaline catalysts as shown in Fig. 2. The use of a different type of catalyst in the transesterification reaction is a deciding factor in the conversion of triglycerides into bio-diesel. So the different types of catalysts are experimented to convert triglycerides into bio-diesel fuel. In general, there are two types of catalysts used to catalyze transesterification reaction i.e. homogeneous and heterogeneous catalysts. KOH and NaOH are popular base homogeneous catalysts soluble in methanol that give a higher yield of bio-diesel in transesterification reaction. But it generates a huge quantity of wastewater required for water-washing to neutralize and separate the catalyst from the methyl esters (bio-diesel). The byproduct of reaction i.e. glycerol is also obtained of poor quality due to the presence of water. These problems are easily rectified with the use of heterogeneous catalysts in the reaction due to its insolubility in methanol. The heterogeneous catalysts can be separated from the product of the reaction very economically. The recycling and reusability of the heterogeneous catalysts further make it more suitable than homogeneous catalysts leading to lower cost of production.

2 Materials and Methods

The vegetable oil after repeated frying becomes nonedible, is referred to here as waste cooking oil (WCO). On repeated frying of oil, total polar compounds (TPC) is formed in oil and the toxicity of TPC leads to diseases like hypertension, Alzheimer's diseases[12] and liver disease. A huge quantity of WCO is produced by caterers all over the world. Therefore it is essential to check the quality of vegetable oil during repeated frying[13]. As per the Food Safety and Standards Authority of India (FSSAI), the Total Polar Compounds (TPC) in vegetable oil should not be more than 25%. From 1st Jul 2018, all Food Business Operators (FBO) are required to monitor the quality of vegetable oil and comply with the regulations. In this work, WCO was collected from reputed caterers in kamla nagar, Delhi. WCO contains moisture and food particles. Food particles were removed by filtering through sieves and moisture was removed by heating the oil to 120°C. The WCO was then cooled and kept in an airtight glass container after filtration. FFA, iodine value, saponification, value, etc. of WCO were determined and recorded in table 1 by using standard methods. The Aluminium food wrap foil discarded from the lunch box was collected from local offices and educational institute, DTU in Delhi. The foil was used to convert into the catalyst required for the transesterification of WCO.

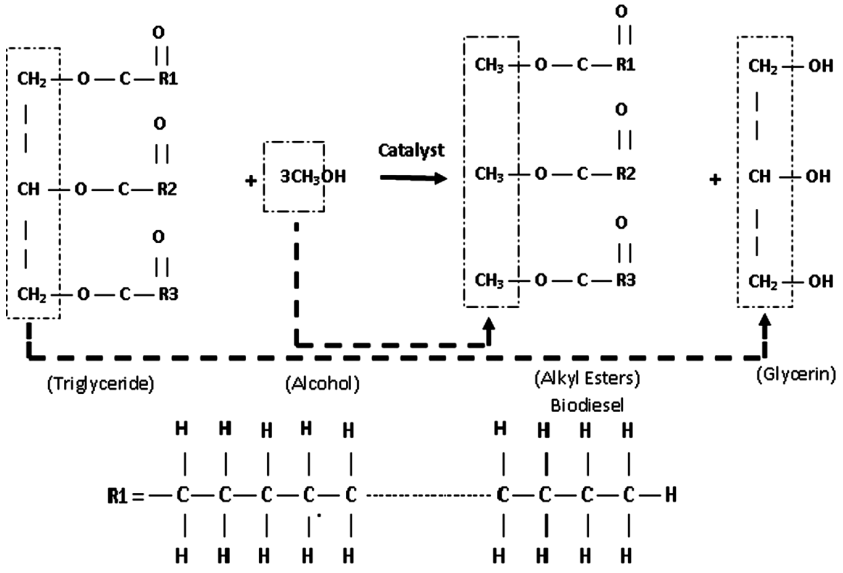

Fig. 2 — Transesterification reaction using alcohol and catalyst.

Table1 — Properties of WCO

Properties	Measured Value
Kinematic viscosity @ 40°C	51.5 mm^2/s
Acid Value	5.4 mg KOH/g
Iodine number	58.7 g I_2/100g
Saponification Value	203.7 mg KOH/g
FFA	1.04%

2.1 Catalyst from waste aluminium foil

Aluminium foil is emerging out as one of the most consumed aluminium products across the world due to its versatility and multiple uses. The demand of Aluminium foil may rise to 6.4 MMT by 2020. As per Aluminium Foils Market intelligence, aluminium foil is also used in the packaging of beverages and other liquids whose demand is also expected to grow at 4-5 percent by 2022. Growth in the consumption of aluminium foil is increasing due to the change in lifestyle and food habits. The high demand for ready to eat confectionaries and pharmaceutical products is also a reason for the growth of the aluminium foils industry. As per aluminium association, out of total aluminium foil produced in the world, more than 75% is used for food packaging which ends up in the local landfills Fig. 3.

The aluminium producing industries are optimistic to recover and recycle aluminium from the used foil. They want to get back all of the used metal at the expense of less energy than that is required to produce the pure metal. Industries are making significant efforts and investment to explore the different ways to recycle the aluminium from foil over several years. There are many companies in the world supplying the thin foils, used as laminates in drinks cartons. They have carried a feasibility study that shows the possibility to remove the aluminium from laminating material and return the used aluminium to produce more foil.

Aluminium oxide (Al_2O_3) known as alumina, is a compound of aluminium and oxygen. The oxides of aluminium are good in hardness, chemical inertness, high melting point, resistance to oxidation and corrosion, so broadly used in making ceramic refractory and abrasives[14]. The alumina as a catalyst is used in many chemical reactions. Aluminium oxide because of its properties like high dielectric constant, favourable thermal conductivity, excellent stability, low refractive index, and high hardness is used in electric batteries, thermal machinery, optics, and microelectronics. There are seven phases of polymorphs of transition alumina identified till now. These are named as phase γ (gamma), η (eta), δ (delta), θ (theta), χ (chi), κ (kappa), and ρ (rho). The phase-γ of transition alumina has a larger surface area in comparison to other phases and also has better structural stability. So it is widely used in industries for catalysis processes. The phase γ-alumina is formed conventionally by thermal dehydration of aluminium oxy-hydroxide above 450°C temperature. The γ-phase is a metastable phase which upon heating will form α-phase. The phase-γ of alumina is used as a catalyst in various processes due to its high surface area and mesoporous properties. Phase γ-alumina is usually used as a catalyst in various chemical processes such as ammonia synthesis, production of hydrogen gas, hydrogenation of oils, refining of petroleum, emissions control of automotive, etc.

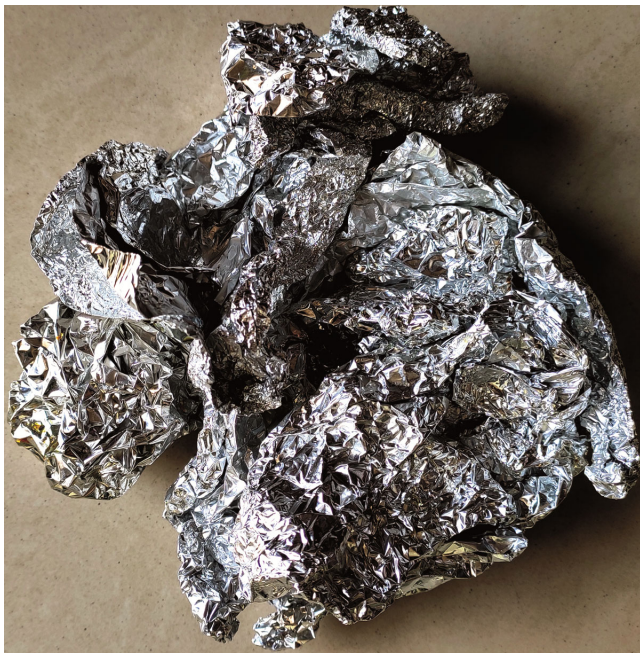

Fig. 3 — Waste Aluminium Foil.

2.2 Preparation of $AlCl_3.6H_2O$ from waste aluminium foil

Waste aluminium foil was cleaned using water and detergent to remove any dirt or oil. Dried foil was dissolved in a hydrochloric acid (HCl) solution containing 6 moles of hydrochloric acid. As aluminium being amphoteric, so can react with acid as well as with base. While reacting with acids, aluminium dissolves in hydrochloric acid to form solution of aluminium chloride and colourless gas hydrogen.

$$2Al + 6HCl = 2AlCl_3 + 3H_2$$

Aluminium chloride solution is kept for drying under desiccators to form crystalline aluminium

chloride hexahydrate ($AlCl_3.6H_2O$). These crystals were dissolved in distilled water and the solution is filtered to remove any soluble chloride. The solution is again dried to re-crystallize. The process of purifying the crystal is done 2-3 times. The complete removal of chloride was verified by adding a drop of silver nitrate ($AgNO_3$) in the sample of the solution. The presence of any chloride content will be indicated by a turbid solution. Finally, pure $AlCl_3.6H_2O$ is obtained.

2.3 Preparation of catalyst γ-Al_2O_3 from $AlCl_3.6H_2O$

The obtained precipitate of aluminium chloride hexahydrate was dispersed in distilled water. The pH value of the solution was regulated with ammonia solution NH_4OH drop by drop. The solution was stirred continuously at a speed of 200 rpm with a magnetic stirrer.

$AlCl_3(aq) + 3\ NH_4OH(aq) \rightarrow Al(OH)_3(s) + 3NH_4Cl\ (aq)$

The pale off-white precipitate of $Al(OH)_3$ was filtered, washed, and dried at 120°C. The substance was further calcined at 500°C and 600°C for a period of 2 hours in a muffle furnace to obtain γ-Al_2O_3.

2.4 X-Ray diffraction analysis

The crystalline phase was verified using X-ray diffraction (XRD) patterns, obtained with CuK radiation of λ = 1.54 A° in 2θ range varying from 20° to 80° at room temperature as shown in Fig. 4 and Fig. 5. The diffractograms for the samples at a calcination temperature of 500°C and 600°C have shown three distinctive reflections of 311, 400 and 440 at angle 2θs of 37.2°, 45.6°, and 66.8° respectively. These reflections are found in line with the gamma Al_2O_3 standards. The further increase in the calcination temperature did not have any effect in the position of peaks, therefore indicating no further change in the structure of γ-Al_2O_3.

2.5 Preparation of catalyst γ-Al_2O_3/NaOH/Na

The catalyst was prepared by employing the impregnation method using phase γ-Al_2O_3 and a solution of sodium hydroxide. The phase γ-Al_2O_3 was impregnated with 15 ml of sodium hydroxide solutions (50 wt.%). This impregnated γ-Al_2O_3 was then dried at a temperature of 120°C. The catalyst was then calcined at 650°C for 2 hours.

2.5.1 Transesterification of waste cooking oil (WCO)

a) A WCO sample was collected in a glass beaker. To eliminate any solid contaminants, it was filtered with a clean cloth. To eliminate any moisture existing in the oil, the oil was heated to 105°C. The oil was then allowed to cool to 60°C before being treated further.

b) The catalyst (γ-Al2O3 / NaOH) powder (3 % by weight of oil) was stirred in a molar ratio of 15:1 with heated methyl alcohol (CH_3OH) and poured into the glass beaker carrying oil.

c) 100 gm WCO sample was transferred to a round bottom flask. It has been treated with a CH_3OH solution and the prepared catalyst. The reactant mixture in the flask was treated in a microwave reactor[15]. The reaction temperature was recorded at 60°C. Throughout the reaction, the solution was constantly agitated. The speed of the turntable stirring was kept constant at 5 rpm throughout the process.

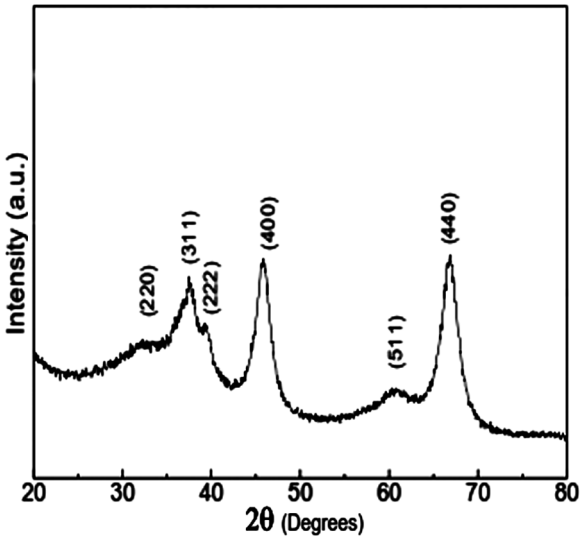

Fig. 4 — XRD pattern of γ-Al_2O_3 calcined at 500°C.

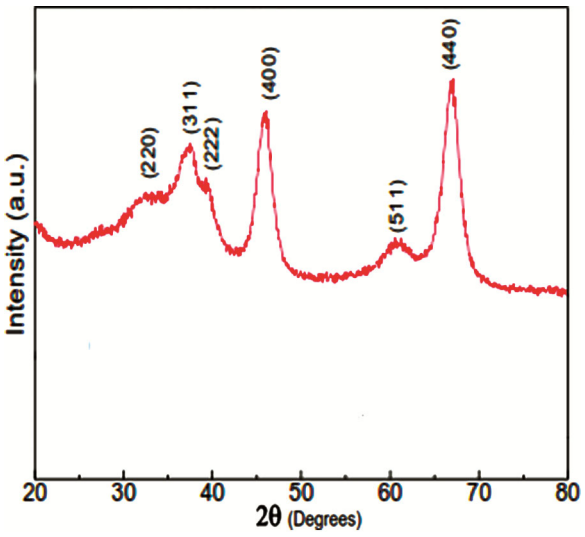

Fig. 5 — XRD pattern of γ-Al_2O_3 calcined at 600°C.

d) To avoid alcohol boiling, the reaction temperature of the solution was not allowed to increase over 60°C. The procedure was repeated for 60 minutes.
e) The reaction catalyst was removed from the reaction product. The remaining solution was allowed to settle in a separate funnel. The reaction products, bio-diesel, methyl alcohol, and glycerin, were separated based on their specific weight.
f) Because bio-diesel and methyl alcohol are lighter in weight, they settled on top of the solution, leaving glycerin at the bottom. The distillation procedure was used to extract the methanol from the bio-diesel.
g) Bio-diesel's physicochemical qualities were investigated. The bio-diesel's specific gravity (0.8849) and density (0.884 gm/cm^3) were determined using the DMA 4500 (Anton Paar) instrument, which was found to be in fair compliance with ASTM bio-diesel specifications. The product's kinematic viscosity was also determined to be 5.694 centistokes using a Stabinger Viscometer.

3 Results and Discussion

3.1 The Effect of Methanol/oil Molar Ratio

The molar ratio has been the most important element in the transesterification reaction, influencing both the bio-diesel output and the production cost. Three moles of methanol react stoichiometrically with one mole of triglyceride to form three moles of fatty acid methyl ester and one mole of glycerin. Because the reaction is seen as being reversible in nature, an excessive amount of methanol was required to drive the reaction towards the product side. The use of an excessive quantity of methanol in the process may increase the cost of bio-diesel, therefore it became critical to determine the ideal molar ratio to limit production costs. The addition of the methanol-oil molar ratio increased the bio-diesel output, as seen in the Fig. 6. A molar ratio of 15:1 produced the highest output. When the molar ratio exceeded 15, the yield % declined. This might be owing to an incomplete reaction and residual glycerol in the bio-diesel form.

3.2 The Effect of Catalyst Amount

The impact of catalyst loading on the reaction has been investigated. The method was evaluated by adjusting the amount of catalyst from 1 to 5 (wt%) of oil weight, and the effect on bio-diesel yield is shown in Fig. 7.

The yield increased when the catalyst was increased from 1 to 3 (wt %). A further increase in the amount of catalyst has lowered the yield. The addition of catalyst apparently made the liquid viscous enough to minimise the likelihood of reactants coming together for the reaction.

3.3 Reaction Time's Effect

For different samples, the reaction time ranged from 5 to 90 minutes. It was discovered that with a reaction period of 60 minutes, a maximum yield of 98 % was achieved. There was no apparent increase in yield afterwards.

3.4 The influence of Reaction Temperature

The transesterification reaction gets influenced by the reaction temperatures. The temperature of the reaction may vary depending on the type of alcohol and catalyst used. Figure 8 illustrates an example of the mixture prepared at five different temperatures. It can be noticed that the yield was decreased at a lower

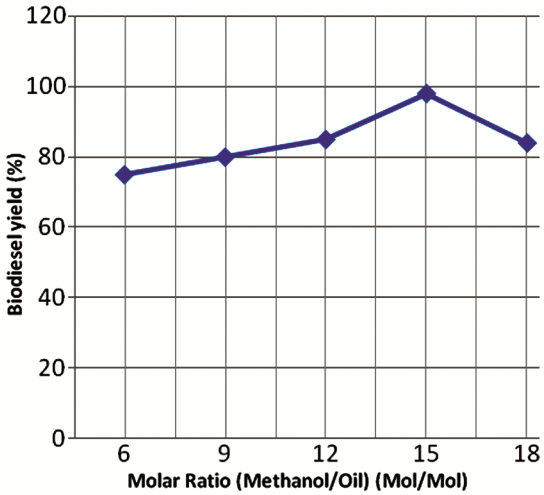

Fig. 6 — Impact of the molar ratio on yield.

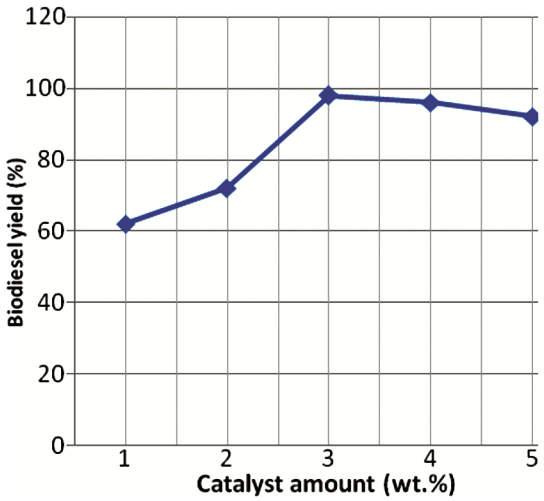

Fig. 7 — Impact of the catalyst on yield.

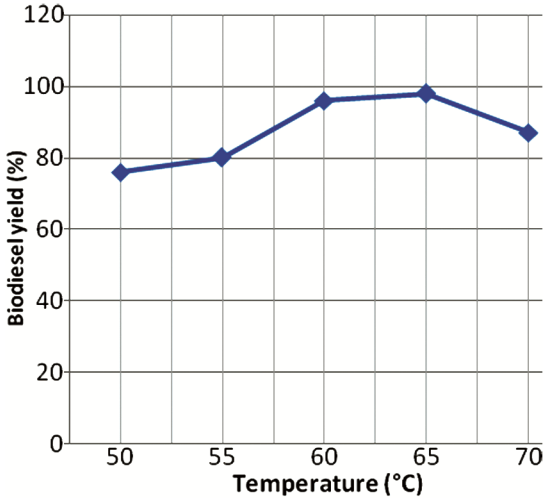

Fig. 8 — Impact of reaction temperature on bio-diesel yield.

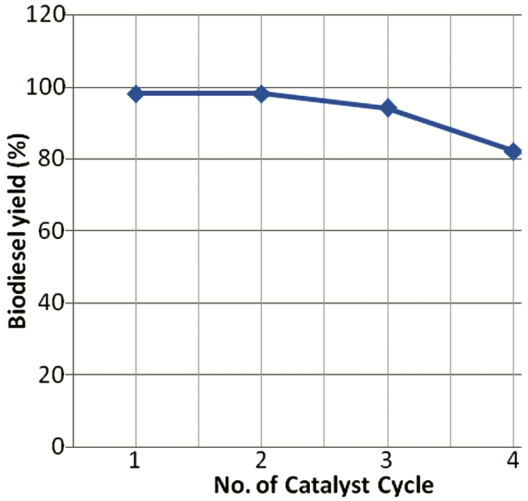

Fig. 9 — Reusability of catalyst.

temperature range of 50-55°C due to mass transfer and solubility issues.

The viscosity of the mixture was found to be reduced at higher temperatures, which is sufficient to increase the kinetic energy of the reactant and provide good mass transfer between oil and methanol to improve yield. The highest yield was found at reaction temperatures ranging from 60 to 65°C. Methanol began to boil at around 65°C, and methanol evaporate from the mixture, lowering the molar ratio and resulting in a reduced bio-diesel yield.

3.5 Reusability of catalyst

The cost of producing bio-diesel has been a determining element in bio-diesel manufacturing technologies. The cost of production can be lowered to some extent by reusing the same catalyst. The recovered catalyst γ-Al2O3 / NaOH has been washed with n-hexane and calcined again at 650°C temperature.

In the same experiment, the utilised and rejuvenated catalyst was employed in four successive transesterification reactions with similar regeneration strategies. No substantial loss of catalytic activity was seen in the first three consecutive uses of the catalyst, while catalytic activity was observed to be lowered in the fourth run of the experiment, as shown in Figure 9. This reduction of catalytic activity could be owing to the absorbed organic molecule blocking active sites on the catalyst surface, resulting in less surface area accessible for the reaction site.

3.6 Bio-diesel Properties and Their Significance

The characteristics of bio-diesel are mostly determined by the quality of the feedstock and the amount of free fatty acid present in it. In the laboratory of Delhi Technological University, the bio-diesel made from WCO has been tested for its chemical and physical attributes. As demonstrated in Table 2, the sample satisfies the ASTM D6751 standards.

Table 2 — Properties of bio-diesel produced

Parameter	Measured Value
Calorific Value	39MJ/kg
Flash point	146°C
Pour point	6°C
Kinematic viscosity @ 40°C	4.5 mm^2/s
Density at 30°C	0.884 g/cm^3
Specific gravity	0.8849
Acid value	0.77 mg KOH/g
Iodine number	86.4 g I_2/100g

The flash point would be a critical factor in the safe storage and handling of bio-diesel for fire safety. The minimal temperature at which the vapour of a liquid fuel forms an ignitable composition when mixed with air and produces a short flash in the presence of a small flame has been defined as the flash point. The flashpoint of bio-diesel produced in this study was determined to be 146°C, which is greater than the flashpoint of petro-diesel fuel (52 to 96°C)[16]. The pour point of fuel determines its ability to flow in the engine at lower temperatures. Fuels with a high pour point should not be used in engines at low temperatures[17]. When subjected to external forces, a fluid's resistance to flow is caused by internal friction. The viscosity of the fuel influences its atomization (spray properties and droplet volume). For the fuel injection system to function properly, the kinematic viscosity of the fuel should be close to that of petro-diesel[18]. At 40°C, the kinematic viscosity of the bio-diesel produced in this investigation was determined

to be 4.5mm^2/s. Bio-diesel with a higher density consumes more fuel, resulting in higher nitrogen oxide emissions. The higher the acid value of the fuel, the more likely it is to induce corrosion in the engine's fuel supply system. The acid value in this investigation was 0.77 mg KOH/g, which was close to the ASTM D-6751 norm of 0.8 mg KOH/g. The iodine number represents the occurrence of double bonds in bio-diesel, indicating the extent of unsaturation[19]. The iodine number has an effect on the oxidation stability of bio-diesel.

4 Conclusions

- Waste aluminium foil has been effectively employed to create a heterogeneous catalyst γ-Al_2O_3.
- The catalyst has been utilised to convert WCO into methyl ester, and a maximum yield of 98% is reached utilising a catalyst amount of 3 wt. %, a molar ratio of 15:1, and a reaction temperature of 60°C for 60 minutes.
- The catalyst has been optimally reutilized multiple (four) times in the bio-diesel conversion process.
- The microwave centred transesterification along with waste aluminium foil based catalyst has been effectively used to synthesize bio-diesel from WCO.
- The cost of bio-diesel production can be reduced to great extent by combination of microwave centred transesterification along with waste aluminium foil based catalyst and WCO.

References

1 Mythili R & Venkatachalam P & Subramanian P & Uma D, *Int J Energy Res,* 38 (2014) 1233
2 Alajmi FSMDA & Hairuddin AA & Adam NM & Abdullah LC, *Int J En Res*, 42 (2018) 885
3 Hwang J & Bae C & Gupta T, *Fuel* 176 (2016) 20
4 Anand K & Sharma RP &, Mehta PS, *Biomass Bioenergy,* 35 (2011) 533
5 Balat M & Balat H, *Applied Energy* 87 (2010) 1815
6 Kafuku G & Mbarawa M, *Applied Energy,* 87 (2010) 2561
7 Mofijur M &, Masjuki H, *Ren Sus Energy Rev,* 46 (2015) 51
8 Alagumalai A & Subramaniam D & Murugesan A (2014) *Ren Sus Energy Rev,* 29 (2014) 517
9 Kataria J & Mohapatra SK & Kundu K, *J Energy Inst,* 92 (2018) 1
10 Kumar R, & Dixit A, *J Ren Energy*, (2014) 1
11 Balasubramanian, D & Lalvani J & Murugesan P & Annamalai K *Energy Conv Mgmt,* 117 (2016) 466
12 Tetsumori Y, *J Alzheimers Dis Parkinsonism,* 7 (2017) 410
13 Farooq M & Ramli A & Naeem A & Perveen F, *Int J Energy Res,* 43 (2019)1
14 Itoh T & Uchida T, *Ceramics Int,* 41 (2015) 3631
15 Garg N & Pal A, *Proc Inst Mech Engr, Part E: J Pro Mech Engg,* 234 (2020) 394
16 Ismail S & Sinin H, *J Sci Tech Dev,* 31 (2014) 91
17 Lalvani J & Parthasarathy M, Ecotoxicol Environ Saf, 134 (2016) 336
18 Cataluna R & Silva R, *J Combustion,* (2012) 1
19 Verma P & Sharma & Dwivedi G, *Energy Rep*, 2 (2016) 8

2023 International Conference on Distributed Computing and Electrical Circuits and Electronics (ICDCECE)

Mining Twitter for Insights into ChatGPT Sentiment: A Machine Learning Approach

1st Shivam Sharma
Department of Computer Engineering
Delhi Technological University
Delhi, India
shivamvats4321@gmail.com

2nd Rahul Aggarwal
Department of Computer Engineering
Delhi Technological University
Delhi, India
rahul.aggarwal000005@gmail.com

3rd Manoj Kumar
Department of Computer Engineering
Delhi Technological University
Delhi, India
mkumarg@dce.ac.in

2023 International Conference on Distributed Computing and Electrical Circuits and Electronics (ICDCECE) | 979-8-3503-4745-6/23/$31.00 ©2023 IEEE | DOI: 10.1109/ICDCECE57866.2023.10150620

***Abstract*—In the past few years, ChatGPT has evolved into a powerful N.L.P. technology, with applications ranging from text generation to question resolution. However, there is still relatively little research on how the public perceives this technology. In this research, we use sentiment analysis techniques to assess the sentiment of tweets regarding ChatGPT. Users manually categorized a dataset of tweets mentioning ChatGPT as positive, negative, or indifferent based on their attitude. The overall sentiment of the tweets was therefore directly determined utilizing machine learning models including logistic regression and support vector machines. Our results show that the majority of tweets related to ChatGPT are neutral, while a smaller proportion are positive or negative. We also found that certain words and phrases, such as "AI" and "language model", are strongly associated with positive sentiment, while others, such as "bias" and "privacy", are associated with negative sentiment. These findings have important implications for the development and deployment of ChatGPT and other NLP technologies, as they suggest that public perception is influenced by factors such as trust, transparency, and ethical considerations. Overall, this paper highlights the importance of understanding public sentiment towards emerging technologies like ChatGPT, and the potential of sentiment analysis techniques to shed light on these issues**

Keywords—Algorithms, ChatGPT, Sentiment Analysis, Twitter, Machine Learning (ML), Emerging Technologies, Natural Language Processing (NLP).

I. INTRODUCTION

Since its launch in 2019, ChatGPT, an OpenAI-developed generative pre-trained transformer model, has made a splash in the NLP [17] field. With its impressive ability to generate coherent and natural-sounding text, ChatGPT has gained popularity among researchers and the general public alike. As ChatGPT increasingly gains momentum, it is essential to gain insight into the perception of this technology among the general public. Social media platforms, especially Twitter, provide a rich source of data that can be used to gauge public sentiment towards ChatGPT. Twitter is a microblogging platform that enables individuals to post tweets, or 280-character messages, with their thoughts and opinions. With over 300 million active users, Twitter is a valuable source of data for sentiment analysis, a subfield of NLP that involves analyzing text data to classify it as impartial, positive, or negative based on the sentiment expressed.

Sentiment analysis has been widely used to analyze social media data, including tweets [7], to understand how people feel about a particular topic or issue. In recent years, sentiment analysis has been applied to analyze tweets related to various technologies, such as self-driving cars, cryptocurrencies, and artificial intelligence (AI), among others. However, sentiment analysis of ChatGPT-related Twitter posts has been given little attention [8, 21].

The public's perception of ChatGPT is important for several reasons. First, understanding public sentiment can inform future research and development of ChatGPT and other NLP models. If the public perceives ChatGPT as a useful and beneficial technology, this could encourage further research and development in this area. On the other hand, if the public is skeptical or critical of ChatGPT, this could lead to a slower adoption of this technology and may require more effort to build trust. Second, public perception can also have an impact on the deployment of ChatGPT and other NLP models in various applications. For example, if the public is concerned about the potential misuse of ChatGPT, this could lead to regulations or restrictions on the use of this technology. Similarly, if the public is concerned about bias or fairness in ChatGPT, this could lead to efforts to address these issues and ensure that the technology is deployed in an ethical and responsible manner.

In this paper, we conduct a deep analysis of tweets related to ChatGPT using sentiment analysis techniques. Our goal is to uncover insights into how the public perceives this technology, and to identify any key factors that may influence their sentiment. We collected a dataset of tweets that mention ChatGPT and applied deep learning techniques to analyze their sentiment. Our study is motivated by the need to understand how the public perceives this technology, which can inform future research and development of ChatGPT and other NLP models. We believe that our study will contribute to a better understanding of the public's perception of ChatGPT, and provide insights into the factors that influence their sentiment. Our study has important implications for the development and deployment of NLP models, as it highlights the importance of understanding public sentiment towards these technologies, and the potential of social media data and sentiment analysis techniques to inform these efforts.

II. RELATED WORK

Several studies have focused on sentiment analysis of social media data, including Twitter data. For instance, [12] analyzed the sentiment of tweets related to the 2010 Haiti earthquake and found that machine learning techniques such as support vector machines (SVMs) and naive Bayes classifiers per- formed well in predicting the sentiment of tweets. Similarly, a study by [18] analyzed the sentiment of tweets related to the 2008 US Presidential election and found that a lexicon-based approach performed well in identifying sentiment-bearing words in tweets. The paper [15] used ChatGPT for sentiment analysis on movie reviews. The authors fine-tuned the model on a large dataset of movie reviews and found that it achieved high accuracy in classifying positive and negative reviews. In the context of sentiment analysis of tweets related to ChatGPT, several studies have been conducted. For example, a study by [8] analyzed the sentiment of tweets related to ChatGPT and found that most

979-8-3503-4745-6/23/$31.00 ©2023 IEEE

Authorized licensed use limited to: DELHI TECHNICAL UNIV. Downloaded on June 28,2023 at 04:48:32 UTC from IEEE Xplore. Restrictions apply.

tweets were neutral in sentiment. Similarly, a study by [15] analyzed the sentiment of tweets related to GPT- 2 (a similar language model to ChatGPT) and found that most tweets were positive in sentiment. However, these studies have largely focused on analyzing the sentiment polarity of tweets, without examining the factors that influence sentiment towards ChatGPT. The paper [25] used ChatGPT for sentiment analysis on social media text data. The authors proposed a new method of fine-tuning the model on human preferences to improve its performance on the task. The paper [1] used ChatGPT for sentiment analysis on Russian texts. The authors fine-tuned the model on a dataset of Russian social media posts and found that it achieved high accuracy in classifying positive and negative sentiments. Another area of research that is relevant to sentiment analysis of ChatGPT-related tweets is the study of bias in machine learning models. Several studies have shown that machine learning models can be biased towards certain groups, leading to inaccurate or unfair predictions. In the context of ChatGPT, there have been concerns raised about the potential for bias in the language model.

Several studies, including ChatGPT, have glanced into the application of pre-trained language models for sentiment analysis. For instance, a study by [24] proposed a novel approach for sentiment analysis that combines the strengths of pre-trained language models with traditional lexicon-based methods. The authors found that their approach outperformed traditional supervised learning approaches in sentiment analysis of movie reviews. In addition to sentiment analysis, several studies have focused on the use of ChatGPT for other NLP tasks such as text classification and question answering. For instance, a study by [5] proposed a method for multi-label text classification using ChatGPT and achieved state-of-the-art performance on several benchmark datasets. Similarly, a study by [2] demonstrated the ability of ChatGPT to answer complex questions in a conversational manner.

[8] and [3] both propose methods for sentiment analysis using machine learning algorithms, with the former focusing on Twitter data and the latter on customer reviews. [10] provides an overview of recent trends in sentiment analysis and emotion detection, while [11] proposes a specific approach to sentiment analysis using a convolutional neural network and term frequency-inverse document frequency based vectorization.

[19] explores the different types of sentiment analysis methods and their strengths and limitations, while [20] discusses the issue of overfitting in machine learning models and presents solutions to address it. Finally, [14] provides an overview of various machine learning algorithms, including supervised and unsupervised learning algorithms, connecting to the broader context of the papers' focus on sentiment analysis in the context of machine learning.

III. Data and Methods

A. Datasets

The datasets for this study was obtained from Kaggle. A ChatGPT sentiment analysis dataset typically consists of a collection of 217622 unique tweets related to ChatGPT, along with corresponding sentiment labels that indicate whether each post expresses a good, bad, or neutral sentiment towards ChatGPT. The subsequent dataset consist 49% bad, 26% good and 25% neutral labelled entries (refer figure 1).

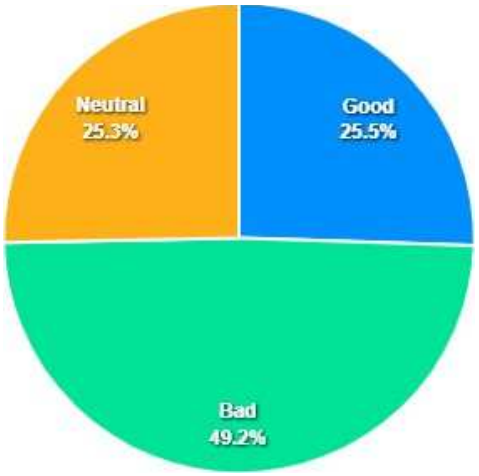

Fig. 1. Dataset Evaluation

B. Classification Algorithms and Techniques

To find the sentiment of the tweet, a variety of supervised learning classification algorithms are used such as Logistic Regression, Random Forest Classifier, k-Nearest Neighbors, Decision Tree Classifier and Gradient Boosting using TF-IDF and Bag of Words techniques.

Logistic Regression: Theoretically, the connection be-tween such a binary dependent variable and one or per- haps more independent variables can be modeled using logistic regression. The dependent variable often referred to as the outcome or response variable can have one of two potential values (e.g. "yes" or "no", "success" or "failure", "1" or "0"). Both continuous and categorical independent variables, typically referred to as predictors or explanatory variables, can be employed. By comparing the values of the independent and dependent variables, logistic regression attempts to assess the probability that the dependent variable will take on a particular value. The study [22] demonstrates the wide applicability of logistic regression for risk assessment, prediction, and classifi-cation in sectors including social sciences, banking, and marketing. General Mathematical Equation for Logistic Regression is given below.

$$p(y = 1|x, \beta) = \frac{1}{1+exp(-x^T\beta)} \quad (1)$$

The logistic function (2**Error! Reference source not found.** is used to transform the linear combination of input features and weights$x^T\beta$, into a probability value between 0 and 1.

$$\sigma(z) = \frac{1}{1+exp(z)} \quad (2)$$

K-Nearest Neighbors: K-nearest neighbor (KNN) is a non-parametric machine learning algorithm used for classification and regression. In KNN, data points are classified based on their proximity to other data points in a feature space. The algorithm works as follows: for a given test data point, it identifies the k nearest data points in the training set, where k is a user-defined parameter. The class or value of the test data point is then assigned based on the majority class or average value of the k-nearest neighbors in the training set. The research shows [9] KNN is considered a lazy algorithm because it does not make any assumptions about the distribution of the data and does not require training before making predictions. KNN is simple to implement and can work well with small to medium-sized datasets. However, it

Authorized licensed use limited to: DELHI TECHNICAL UNIV. Downloaded on June 28,2023 at 04:48:32 UTC from IEEE Xplore. Restrictions apply.

can be computationally expensive and is sensitive to the choice of k and the distance metric used to measure proximity.

Decision Tree Classifier: A well-liked machine learning approach for classification tasks is the Decision Tree Classifier. By constructing a tree-like model of choices based on input features, it functions. Based on the value of an input feature, the algorithm divides the data into progressively smaller subgroups until each subset only contains data from a single class. The final model is a tree-like structure where the nodes represent the input features, the branches represent the decision rules based on the values of those features, and the leaves represent the class labels. The algorithm can handle both numerical and categorical data, and is easy to interpret and explain, making it a popular choice for many applications. However, decision trees are prone to overfitting, which can be addressed by using ensemble methods like Random Forest [4].

Let X be a vector of input features, and let T be a decision tree with K leaf nodes. Then, the prediction of T for a new input x is given by:

$$T(x) = \sum_{k=1}^{K} y_k \cdot \prod x \in R_k \quad (3)$$

Where y_k is the output value associated with leaf node k, and R_k is the region of feature space corresponding to leaf node k. The indicator function $x \in R_k$ is defined as 1 if x falls within the region R_k, and 0 otherwise as in.

Random Forest Classifier: It is an ensemble learning method that builds a collection of decision trees and aggregates their predictions to make a final classification decision. It functions by constructing numerous decision trees, each trained on a haphazard subset of the input features and training data. The algorithm then combines the predictions of all the trees to make the final classifica- tion decision. Random Forest Classifier is a popular ma- chine learning algorithm for classification tasks because it can handle both categorical and numerical data, can handle missing values, and is resistant to overfitting. It is often used for high-dimensional datasets with many input features, and is known for producing accurate results. Additionally, Random Forest Classifier can pro- vide feature importance scores, which can be useful for identifying which input features are most important in making classification decisions [13].

Gradient Boosting: Gradient boosting is a popular machine learning algorithm that enhances the accuracy of existing models by iteratively adding weak learners to it. Early research on gradient boosting [16] focused on its application in regression and classification problems, where it showed high effectiveness in handling imbal- anced and noisy data. Recent research has explored variants of gradient boosting tailored for specific data types, such as categorical or sparse data, and for unsu- pervised learning tasks like clustering and dimensionality reduction. Gradient boosting finds practical applications in finance, marketing, and natural language processing, with the latter being used in text classification, sentiment analysis, and named entity recognition. It can handle complex, nonlinear relationships between variables and is used for both supervised and unsupervised learning tasks. Feature selection and dimensionality reduction are additional valuable features of gradient boosting.

Term Frequency-Inverse Document Frequency (TF-IDF): It is a technique used in natural language processing to rank the importance of words in a document based on their frequency and distribution across a corpus of documents [6]. Early research focused on its use in information retrieval, while recent research has explored extensions and modifications to the original algorithm, such as using TF-ICF and machine learning techniques.

TF-IDF has important practical applications in fields such as information retrieval, text classification, and informa- tion extraction.

$$tf - idf(t, d) = tf(t, d) \cdot idf(t) \quad (4)$$

where tf(t, d) as in (4**Error! Reference source not found.** is the term frequency of term t in document d, and idf(t) is the inverse document frequency of term t:

$$tf(t, d) = \frac{n_{t,d}}{\sum_k n_{k,d}} \quad (5)$$

$$idf(t) = log\left(\frac{N}{df_t}\right) \quad (6)$$

Where $n_{t,d}$ is the number of times term t appears in document (5) $d, \sum_k n_{k,d}$ is the total number of terms in document d, N is the total number of documents in the collection, and df_t is the number of documents in the collection that contain term t (6**Error! Reference source not found.**.

Bag of Words: It is a prevalent natural language processing technique that symbolizes text as an unordered collection of words. It has practical applications in var- ious fields, including information retrieval, text classi- fication, sentiment analysis, and information extraction. Recent research [23] has explored modifications to the original BoW algorithm, such as TF-IDF weighting and probabilistic models like LDA. BoW can be used in conjunction with other machine learning techniques, such as SVMs and neural networks, to improve performance on text analysis tasks.

IV. Proposed Methodology

This project aimed to analyze a dataset of tweets related to "chatgpt" from Kaggle. The dataset had a size of 219k, and it contained tweets from the last month. The tweets were classified into three categories: good, bad, and neutral, and there were 217,622 unique values in the dataset. To start the analysis, the project team performed basic preprocessing steps on the dataset. The first step was to remove URLs from the textual content of the tweets, as URLs do not contribute to the sentiment analysis of the text and could introduce noise to the dataset. Next, the team split the data into smaller subsets for better understanding. This could involve dividing the data based on various criteria, such as the date, source, or topic of the tweets. The team also replaced the labels of the sentiment categories with numerical values. The labels "good," "bad," and "neutral" were replaced with the numerical values 1, -1, and 0, respectively. This step was necessary to convert the categorical data into numerical form, which would be easier to process and analyze. Finally, the team used NLTK to remove stopwords from the tweets. Stopwords are typical words found in all languages that don't add much to a sentence's meaning and can be easily omitted without altering it. Removing stopwords can reduce the number of irrelevant words that the algorithm needs to process, which can improve the accuracy of the model.

After performing the preprocessing steps, the team implemented various techniques with different machine learning models to study the accuracy over this dataset. First, they used TF-IDF (Term Frequency-Inverse Document Frequency) to

Authorized licensed use limited to: DELHI TECHNICAL UNIV. Downloaded on June 28,2023 at 04:48:32 UTC from IEEE Xplore. Restrictions apply.

vectorize the different sentences and create a matrix. Using a max features value of 1000, they were able to convert all the textual data into numeric format. They then compared different machine learning models to evaluate the accuracy over this dataset. The group employed a variety of techniques based on machine learning, such as gradient boosting, decision trees, random forests, and logistic regression. The team evaluated the accuracy of each model using techniques such as cross-validation and plotted the results to identify the best- performing model. The results of this analysis can be used to gain insights into the sentiment of the tweets and to develop a model that can predict the sentiment of future tweets related to "chatgpt" (refer figure 2).

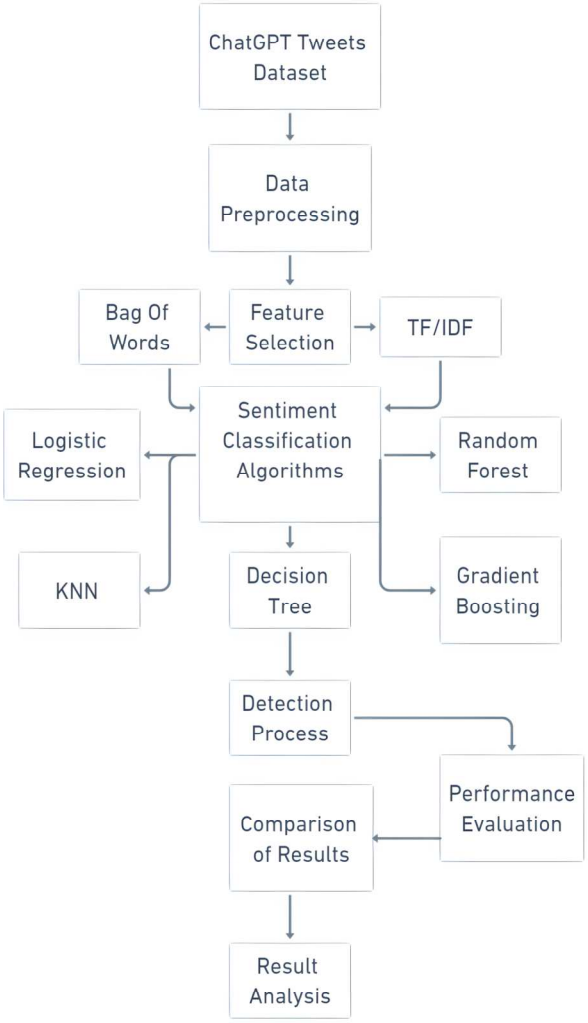

Fig. 2. Methodology for Sentiment Classification

Additionally, the team used various evaluation metrics to assess the performance of the machine learning models, such as precision, recall, and F1 score. These metrics help to understand the true positive, false positive, true negative, and false negative values of the predictions made by the model. The team also explored the concept of feature importance to identify the most significant words or phrases that contribute to the sentiment of the tweets. This information can be useful in understanding the underlying factors that drive the sentiment of the tweets. Furthermore, the project team explored deep learning models such as convolutional neural networks (CNN) and recurrent neural networks (RNN) to achieve higher accuracy in sentiment analysis. These models are known for their ability to capture complex relationships between words in a sentence and can perform better than traditional machine learning models in some cases.

Overall, the project aimed to analyze the sentiment of tweets related to "chatgpt" using various machine learning techniques and to develop a model that could predict the sentiment of future tweets related to this topic (refer table I). By leveraging the power of NLTK, TF-IDF, and machine learning algorithms, the team was able to analyze a large dataset of tweets and gain insights into the sentiment of the users towards "chatgpt".

TABLE I. PARAMETERS USED FOR DIFFERENT ALGORITHMS IN TF-IDF

Machine Learning Algorithms	Parameters Used
Logistic Regression	c=1.0, penalty='12', solver='newton-cg'
k-Nearest Neighbors	metric='manhattan', n neighbors=5, weights='distance'
Gradient Boosting	learning rates=0.1, max depth=3, n estimators=100, subsample=1.0
Decision Tree Classifier	criteria='gini', max depth=2
Random Forest Classifier	n estimators=1000, max features = 'log2'

Similarly we used Bag of words technique to convert the textual data into numeric format (refer table II).

V. EXPERIMENTAL RESULTS

The ChatGPT Sentiment Analysis dataset shows that, after contrasting all of the algorithms for the Term Frequency-Inverse Document Frequency and Bag of Words strategies, Logistic Regression in TF-IDF and Random Forest in BoW outperformed with accuracy rates of 75% and 71.8%, in both. Table III shows the exact accuracy of all machine learning approaches for both techniques. Closely followed by Random Forest with an accuracy of 74.98% and Logistic Regression with an average prediction accuracy of 70.9% in TF-IDF and BoW respectively.

K-nearest Neighbour and Decision Tree Classifier algorithm predicted to an average precision level of approximately 53% in TF-IDF and BoW. However, the Gradient Boosting Classifier performed sentiments prediction up to an average accuracy of just over 68% in TF-IDF and 65% in BoW. After applying the ML model (Random Forest or Logistic Regression), this model will analyze the tweets and will detect the sentiment associated with that. The entire model may have greater time and space complexity but none of the existing systems implement the combination of both these techniques. The Accuracy bar plot of different Machine Learning Model in TF-IDF and BoW techniques are presented in Figures 3 and 4 correspondingly.

TABLE II. PARAMETERS USED FOR DIFFERENT ALGORITHMS IN BAG OF WORDS

Machine Learning Algorithms	Parameters Used
Logistic Regression	c=1.0, penalty='12', solver='liblinear'
k-Nearest Neighbors	metric='euclidean', n neighbors=19, weights='distance'
Gradient Boosting	learning rates=0.1, max depth=3, n estimators=100, subsample=1.0
Decision Tree Classifier	criteria='gini', max depth=3
Random Forest Classifier	n estimators=1000, max features = 'sqrt'

Authorized licensed use limited to: DELHI TECHNICAL UNIV. Downloaded on June 28,2023 at 04:48:32 UTC from IEEE Xplore. Restrictions apply.

TABLE III. ACCURACY OF DIFFERENT ALGORITHMS ON TF-IDF AND BOW TECHNIQUES

Algorithm	TF-IDF (in %)	BoW (in %)
Logistic Regression	75	70.9
k-Nearest Neighbors	56.45	54.1
Gradient Boosting	68.71	65.74
Decision Tree Classifier	53.5	51.85
Random Forest Classifier	74.98	71.8

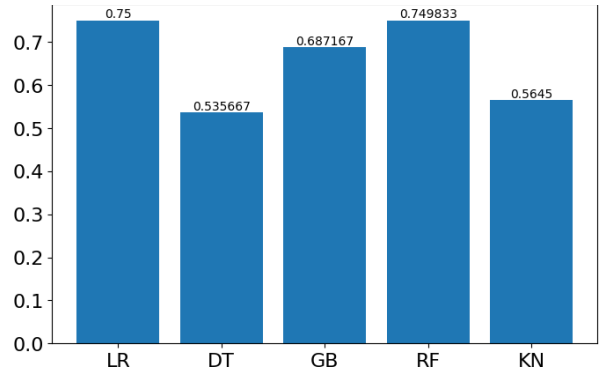

Fig. 3. TD-IDF Accuracy

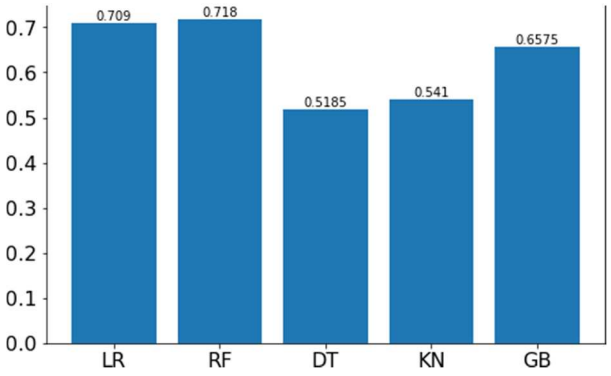

Fig. 4. BoW Accuracy

Classification matrices for TF-IDF and Bag of Words tech- nique are shown in table IV and tabel V respectively. Our machine learning algorithm achieved a highest average F1 score of 0.71 and a recall of 0.70 on the test set in TF-IDF technique, demonstrating its high accuracy in predicting sentiment for the three classes (good, bad, neutral). In case of Bag Of Words (BoW), a highest average F1 score of 0.69 and a recall of 0.69 is obtained. Calculation of different parameters of classification matrices can be done by (7) and (8).

$$F1 - score = \frac{2 \cdot Precision \cdot Recall}{Precision + Recall} \quad (7)$$

$$Recall = \frac{True\ Positive}{True\ Positive + True\ Negative} \quad (8)$$

The terms "True Positive," "False Positive," and "True Negative" in these equations reflect the proportion of accurate positive predictions, the proportion of inaccurate positive predictions, and the proportion of accurate negative predictions, respectively.

TABLE IV. CLASSIFICATION MATRICES OF DIFFERENT ALGORITHMS ON TF-IDF TECHNIQUES

Algorithm	Precision	Recall	F1- Score
Logistic Regression	72	69.6	70.6
k-Nearest Neighbors	63	45	43
Gradient Boosting	69	61	61
Decision Tree Classifier	55	40.6	35
Random Forest Classifier	72	70	71

TABLE V. CLASSIFICATION MATRICES OF DIFFERENT ALGORITHMS ON BOW TECHNIQUES

Algorithm	Recall	Recall	F1- Score
Logistic Regression	67	65	65
k-Nearest Neighbors	66	42	39
Gradient Boosting	64	57	57
Decision Tree Classifier	70	39	32
Random Forest Classifier	70	69	69

VI. CONCLUSION

From the above results it is clearly evident that Logistic Regression and Random Forests works better in both the techniques. The reason is that the output classes are a small number i.e 3. Random forests operate successfully with high-dimensional information since we are dealing with subsets of data. We can simply work with hundreds of attributes since we're only using a portion of the attributes in our model, which makes it simpler to train than decision trees. We generally got good results with Decision tree and KNN when the number of output classes are a bit large in number.KNN works well with a small number of input variables (p), but struggles when the number of inputs is very large. They tried to overfit in this case so we got better results with Logistic Regression here. Gradient boosting allows various hyperparameter tuning to obtain better accuracy but similarly it can lead to overfitting of data as well.

VII. FUTURE WORK

Till now we have tried five ML models with two techniques to classify the given data as good, bad or neutral. As classification is a very wide domain we can apply Deep learning techniques such as RNN and LSTM to check the performance of these algorithms over this dataset. Hyperparameter tuning can be performed to achieve better results. In addition to this, BERT is a highly popular technique in the field of natural language processing. BERT was originally inspired by pre-training contextual representations like semi-supervised sequence learning, generative pre-training, ELMo, and ULMFit. In contrast to prior models, BERT is a profoundly bidirectional, unsupervised language representation that's been exclusively trained on a corpus of plain text.

ACKNOWLEDGMENT

The technicians at the department's lab at DTU are gratefully acknowledged by the authors for their support in supplying the resources required to execute the study. The authors appreciate the peer reviewers' helpful comments as well. This study has been much enhanced and many mistakes have been avoided thanks to everyone's generosity and knowledge.

REFERENCES

[1] N. Alexandr, O. Irina, K. Tatyana, K. Inessa, and P. Arina, "Fine-Tuning GPT-3 for Russian Text Summarization," in R. Silhavy, P. Silhavy, Z. Prokopova, (eds) Data Science and Intelligent Systems: Proceedings of 5th Computational Methods in Systems and Software, CoMeSySo, 1st October 2021, online, Czech Republic, vol. 2, pp. 748–757. Springer Cham, https://doi.org/10.1007/978-3-030-90321-3_61.

[2] Y. Bang, S. Cahyawijaya, N. Lee, W. Dai, D. Su, B. Wilie, H. Lovenia, Z. Ji, T. Yu, W. Chung, Q. V. Do, Y. Xu, and P. Fung, "A multitask, multilingual, multimodal evaluation of chatgpt on reasoning, hallucination, and interactivity," arXiv:2302.04023, 2023, https://doi.org/10.48550/arXiv.2302.04023.

Authorized licensed use limited to: DELHI TECHNICAL UNIV. Downloaded on June 28,2023 at 04:48:32 UTC from IEEE Xplore. Restrictions apply.

[3] K. Barik, S. Misra, A. K. Ray, and A. Bokolo, "LSTM-DGWO-Based Sentiment Analysis Framework for Analyzing Online Customer Reviews," Computational Intelligence and Neuroscience, vol. 2023, p. 6348831, Feb. 2023, https://doi.org/10.1155/2023/6348831.

[4] A. Bayhaqy, S. Sfenrianto, K. Nainggolan, and E. R. Kaburuan, "Sentiment Analysis about E-Commerce from Tweets Using Decision Tree, K-Nearest Neighbor, and Naïve Bayes," International Conference on Orange Technologies (ICOT), 23-26 October 2018, Nusa Dua, Bali, Indonesia, IEEE, pp. 1-6, https://doi.org/10.1109/ICOT.2018.8705796.

[5] I. Chalkidis, M. Fergadiotis, S. Kotitsas, P. Malakasiotis, N. Aletras, and I. Androutsopoulos, "An empirical study on large-scale multi-label text classification including few and zero-shot labels," in Proceedings of the 2020 Conference on Empirical Methods in Natural Language Processing (EMNLP), November 2020, Online, pp. 7503–7515, Association for Computational Linguistics, https://doi.org/10.18653/v1/2020.emnlp-main.607.

[6] H. Christian, M. P. Agus, and D. Suhartono, "Single document automatic text summarization using Term Frequency-Inverse Document Frequency (TF-IDF)," ComTech: Computer, Mathematics and Engineering Applications, vol. 7, no. 4, pp. 285–294, December 2016.

[7] P. Gonçalves, M. Araújo, F. Benevenuto, and M. Cha, "Comparing and combining sentiment analysis methods," in Proceedings of the first ACM conference on Online social networks (COSN '13), Boston, Massachusetts, USA, 7-8 October, 2013, Association for Computing Machinery, NY, USA, pp. 27–38, https://doi.org/10.1145/2512938.2512951.

[8] M. U. Haque, I. Dharmadasa, Z. T. Sworna, R. N. Rajapakse, and H. Ahmad, ""I think this is the most disruptive technology": Exploring sentiments of ChatGPT early adopters using twitter data," arXiv:2212.05856, December 2022, https://doi.org/10.48550/arXiv.2212.05856

[9] S. Hota and S. Pathak, "KNN classifier based approach for multi-class sentiment analysis of twitter data," International Journal of Engineering & Technology, vol. 7, no. 3, pp. 1372–1375, July 2018, https://doi.org/10.14419/ijet.v7i3.12656.

[10] L. P. Hung and S. Alias, "Beyond Sentiment Analysis: A Review of Recent Trends in Text Based Sentiment Analysis and Emotion Detection," Journal of Advanced Computational Intelligence and Intelligent Informatics, vol. 27, no. 1, pp. 84–95, January 2023, https://doi.org/10.20965/jaciii.2023.p0084.

[11] B. Kabra and C. Nagar, "Convolutional neural network based sentiment analysis with tf-idf based vectorization," Journal of Integrated Science and Technology, vol. 11, no. 3, p. 503, January 2023.

[12] P. Liang and B. Dai, "Opinion mining on social media data," in 2013 IEEE 14th International Conference on Mobile Data Management, 03-06 June 2013, Milan, Italy, pp. 91–96. IEEE, https://doi.org/10.1109/MDM.2013.73.

[13] Y. Liu, Y. Wang, and J. Zhang, "New Machine Learning Algorithm: Random Forest," in B. Liu, M. Ma, J. Chang, (eds), Information Computing and Applications: Third International Conference, ICICA 2012, Chengde, China, September 14-16, 2012, pp. 246–252, Springer, https://doi.org/10.1007/978-3-642-34062-8_32.

[14] B. Mahesh, "Machine learning algorithms - A review," International Journal of Science and Research, vol. 9, no. 1, pp. 381–386, January 2020, https://doi.org/10.21275/ART20203995.

[15] L. Mathew and V. R. Bindu, "A review of natural language processing techniques for sentiment analysis using pre-trained models," in 2020 Fourth International Conference on Computing Methodologies and Communication (ICCMC), 11-13 March 2020, Erode, India, pp. 340–345. IEEE, https://doi.org/10.1109/ICCMC48092.2020.ICCMC-00064.

[16] A. Natekin and A. Knoll, "Gradient boosting machines, a tutorial," Frontiers in Neurorobotics, vol. 7, p. 21, December 2013, https://doi.org/10.3389/fnbot.2013.00021.

[17] A. A Patel and A. U. Arasanipalai, "Applied Natural Language Processing in the Enterprise," O'Reilly Media, Inc., 2021.

[18] H. Saif, Y. He, and H. Alani, "Semantic sentiment analysis of twitter," in P. Cudré-Mauroux, J. Heflin, E. Sirin, T. Tudorache, J. Euzenat, M. Hauswirth, J. X. Parreira, Jim. Hendler, G. Schreiber, A. Bernstein, E. Blomqvist (eds), The Semantic Web–ISWC 2012: 11th International Semantic Web Conference, Boston, MA, USA, November 11-15, 2012, Proceedings, Part I, Springer Berlin, Heidelberg, pp. 508–524, https://doi.org/10.1007/978-3-642-35176-1_32.

[19] C. Sindhu and G. Vadivu, "Sentiment analysis, The beginning," in Secure Data Management for Online Learning Applications, 1st Ed., CRC Press, 2023.

[20] C. Song, T. Ristenpart, and V. Shmatikov, "Machine Learning Models that Remember Too Much," in Proceedings of the 2017 ACM SIGSAC Conference on Computer and Communications Security, (CCS'17), Dallas Texas USA, 30th October 2017–3rd November 2017, Association for Computing Machinery, US, pp. 587–601, https://doi.org/10.1145/3133956.3134077.

[21] V. Taecharungroj, ""What Can ChatGPT Do?" Analyzing Early Reactions to the Innovative AI Chatbot on Twitter," Big Data and Cognitive Computing, vol. 7, no. 1, p. 35, February 2023, https://doi.org/10.3390/bdcc7010035.

[22] A. Tyagi and N. Sharma, "Sentiment Analysis using Logistic Regression and Effective Word Score Heuristic," International Journal of Engineering & Technology, vol. 7, no. 2.24, pp. 20–23, April 2018, doi: https://doi.org/10.14419/ijet.v7i2.24.11991.

[23] Y. Zhang, R. Jin, and Z.-H. Zhou, "Understanding bag-of-words model: a statistical framework," International Journal of Machine Learning and Cybernetics, vol. 1, no. 1–4, pp. 43–52, December 2010, https://doi.org/10.1007/s13042-010-0001-0.

[24] C. Zhou, C. Qiu, and D. E. Acuna, "Paraphrase Identification with Deep Learning: A Review of Datasets and Methods," arXiv:2212.06933, 2022.

[25] D. M. Ziegler, N. Stiennon, J. Wu, T. B. Brown, A. Radford, D. Amodei, P. Christiano, and G. Irving, "Fine-tuning language models from human preferences," arXiv:1909.08593, 2019.

Authorized licensed use limited to: DELHI TECHNICAL UNIV. Downloaded on June 28,2023 at 04:48:32 UTC from IEEE Xplore. Restrictions apply.

Journal of Scientific & Industrial Research
Vol. 82, June 2023, pp. 597-602
DOI: 10.56042/jsir.v82i06.1816

Modelling and Simulation of Crankcase Cover Manufacturing in the Automobile Industry

Sumit Chawla[1]* & Ranganath M Singari[2]

[1] Applied Science Department (Mechanical), Bharati Vidyapeeth's College of Engineering, Delhi 110 063, India

[2] Mechanical, Production, and Industrial Engineering Department, Delhi Technological University, Delhi 110 042, India

Received 28 October 2020; revised 13 November 2022; accepted 16 May 2023

The simulation creates the virtual production model which is exactly like the real environment, and it provides future insights before laying down the actual production plant layout. With the help of simulation, we can simulate the complex and costly manufacturing system without investing money physically and check the system's real-life behavior. In this study, for the first time, the modelling and simulation of two-wheeler crankcase cover manufacturing are done with the help of Flexsim. This study deals with the development of a simulation model for crankcase cover manufacturing systems in the automobile industry. Flexsim simulation tool is used as an optimization tool for analyzing the effect of varying the number of operators and process stations on system performance using various scenarios. The results indicate that scenario 2 is best for crankcase cover manufacturing which reduces the overall idle time of all process stations and optimizes the number of Die-Casting Machines (DCM) and Vertical Milling Center (VMC). These results are useful for all industries for simulating their process or product layout.

Keywords: Flexsim, Optimization, Plant layout, Production model, System performance

Introduction

Simulation helps in the analysis of the various manufacturing system. It solved the problems related to resource allocation, scheduling, shop floor, material handling, storage, and manufacturing. Nowadays the different company provides different simulation software. This software reduces production costs and provides effective resource allocation.[1]

The various simulation software available in the market are Flexsim, Arena, Simul8, Anylogic, Witness, and Promodel. Flexsim is discrete event simulation software used for complex optimization problems. Flexsim is a very powerful tool used for modelling and simulation. This tool can be effectively used for appointment booking analysis and manufacturing problems. It also helps the management in hiring employees for future projects and changing the work schedules. The simulation also highlights any inefficiency or bottleneck occurring in the system.[2]

The simulation approach can be effectively used in design, production planning, and scheduling problems. These approaches help in decision-making problems and in finding more realistic results based on the actual dynamic conditions.[3] Flexsim consists of the experimenter tab of the design of experiments used for optimizing the set of solutions and performance of the production plant.[4] Flexsim tool can solve multi-objective optimization problems and develop the hybrid simulation model which optimizes the various parameters such as makespan, due date, tardiness, work in process inventory and machine utilization, etc.[5] This tool provides a complete output report which can be analyzed for measuring the performance of the system.[6]

The study of simulation-based papers consisting of the problem type, parameter optimized, and types of simulation is represented in Table 1. Bjorklund *et al.*[1] solved the real-time forecasting problem with the help of Flexsim simulation software. Badri *et al.*[7] utilized the simulation modelling concept for effective operations in hospital emergency cells by minimizing the waiting time, and cost and increasing the throughput, resource utilization, and efficiency of the system. Cheng *et al.*[8] developed a simulation model for machined component manufacturing in a flexible manufacturing system. They optimized the routing sequence of operations. Peng *et al.*[9] applied the Flexsim simulation method for improving

*Author for Correspondence
E-mail: chawlasumit4@gmail.com

Table 1 — Study of simulation-based papers

Problem Type	Factors/Parameters	Type of Simulation
Real-time forecasting problem[1]	Machine failure times	Flexsim
FMS Scheduling problem[2]	Makespan	Flexsim
Warehouse logistic system problem[3]	Space utilization, use of equipment and tools, work safety	Flexsim, Arena, and Promodel
Parallel machine scheduling problem[4]	Makespan	Flexsim
Jobshop Scheduling[5]	Makespan and machine utilization	Agent-based simulation
Gantry crane scheduling problem[6]	Operator efficiency and waiting time	Flexsim
Health services scheduling problem[7]	Waiting time, cost, throughput, resource utilization, and efficiency	SLAMSYSTEM
FMS Scheduling problem[8]	Routing sequence of operations	Flexsim, OptQuest
Assembly line problem[9]	Productivity and reducing the cycle time	Flexsim
Assembly line problem[10]	Machine utilization rate, efficiency, and blockage rate	Flexsim
Micropump design problem[11]	Fabrication cost	INTELLISUITE
Pull system problem[12]	Work-in-process inventory	SIMAN
Appointment scheduling and resource allocation[13]	Resource overtime, patient waiting time, and waiting area congestion	Simulation-based heuristic algorithm
Trucks appointment scheduling problem[14]	Waiting time and productivity of container terminals	Flexsim
Trucks appointment scheduling problem[15]	Truck turn time and resource utilization	Flexsim
Machine shop operations scheduling problem[16]	Productivity and energy cost	Anylogic
Job shop scheduling problems[17]	Total processing time, machine utilization, and allocation of jobs	Flexsim
Production planning problem[18]	Uncertainty and robustness of production planning	GeneSim
Logistics system problem[19]	Production efficiency	Flexsim and Petri net

productivity and reducing the cycle time in the assembly line problem. Gong *et al.*[10] developed a simulation model for an automobile mixed assembly line. They increased the machine utilization rate and efficiency and reduced the blockage rate in the assembly line.

Chandika *et al.*[11] designed and simulated the micropump in the automobile industry using the INTELLISUITE software and optimized the fabrication cost. Kesan *et al.*[12] utilized the SIMAN simulation software for the analysis of the pull system to optimize the work-in-process inventory. Lin *et al.*[13] developed a simulation-based heuristic algorithm for appointment scheduling and resource allocation. Azab *et al*.[14] utilized the simulation approach for minimizing waiting-time and emissions of trucks and enhanced the productivity of container terminals. Krishna *et al.*[2] used the Flexsim simulation-based approach for analyzing the effect of buffers on a Flexible Manufacturing System (FMS) performance. Nathan Huynh[15] analyzed the effects of varying scheduling rules on truck turn time and resource utilization. Kim *et al.*[16] developed a simulation-based scheduling system for machine shop operations of the manufacturing industry of the USA to optimize productivity and energy cost. Jarernram *et al.*[4] solved the parallel machine scheduling problem using Flexsim simulation software and optimized the makespan. Rodrigues *et al.*[5] developed the hybrid simulation model and solved the multi-objective problems to optimize the makespan and machine utilization.

Nie *et al.*[6] optimized the operator efficiency and waiting time of the gantry crane using the simulation approach of Flexsim and find out the best operating scheduling mode for the gantry crane. Kumar *et al.*[17] optimized the total processing time, machine utilization, and allocation of jobs in job shop scheduling problems using the simulation approach based on Flexsim. Steinhauer *et al.*[18] presented a simulation approach for reducing the uncertainty for optimizing the quality and robustness of production planning in shipbuilding. Wang *et al.*[19] utilized the Flexsim and Petri net simulation model for optimizing the production efficiency of the logistics system of the automobile industry. Zhang *et al.*[20] developed the simulation truck–shovel system model using Flexsim. Marek Climent *et al.*[21] utilized the Flexsim tool for digital engineering elements application in innovation and optimization of production flows. Past studies show that most of the researchers have successfully utilized the Flexsim tool for modelling and simulation problems. It is also found from the literature review that the modelling and simulation of crankcase cover manufacturing in the automobile industry is an untouched area of research. This study initially aims

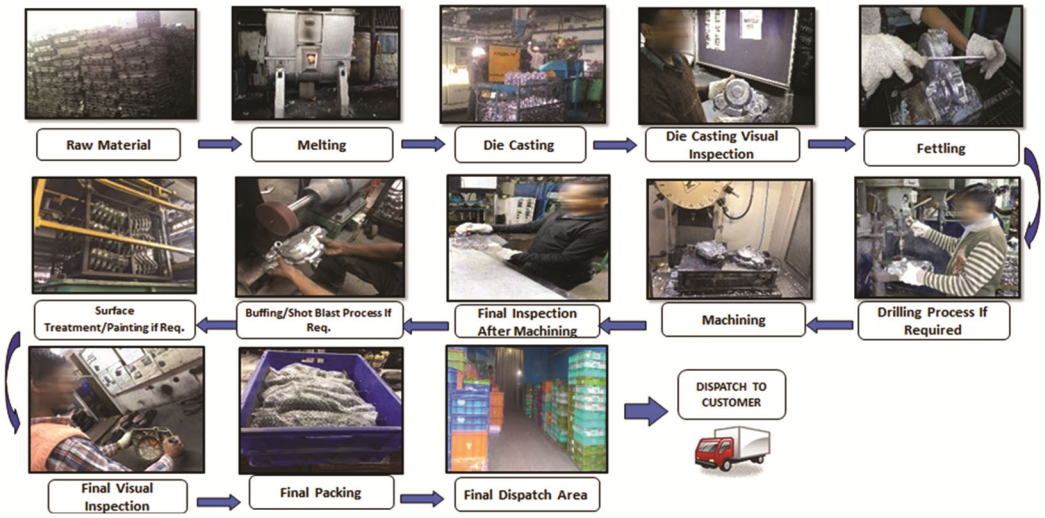

Fig. 1 — General process model for crankcase cover manufacturing

to develop the 3D simulation model based on the generic process model. Later, the experimenter function is utilized for selecting the best scenario for crankcase cover manufacturing and optimizing the number of process stations.

Materials and Methods

For simulating the layout of any industry, the first step is to analyze the process model. The next step is to convert this process model into a simulation model. Flexsim is a powerful tool for converting any chimerical process model into a realistic 3d simulation model.

Process Model

The crankcase cover manufacturing process consists of the processes such as the melting of raw material in the furnace, die casting process, fettling process, drilling process, machining process, buffing process, surface treatment, or painting process. The general process model for the crankcase cover manufacturing process is shown in Fig. 1. Our main aim of the study is to find out how the system performance varies with changes in the number of operators and the number of working process stations.

Flexsim Simulation Approach

Flexsim simulation software tool is used for developing a simulation model of the crankcase cover manufacturing process. Additionally, this tool generates models that are freely expandable, resulting in infinite space.[21] This tool provides a 3-D model that can be analyzed without establishing it in its physical form.[22]

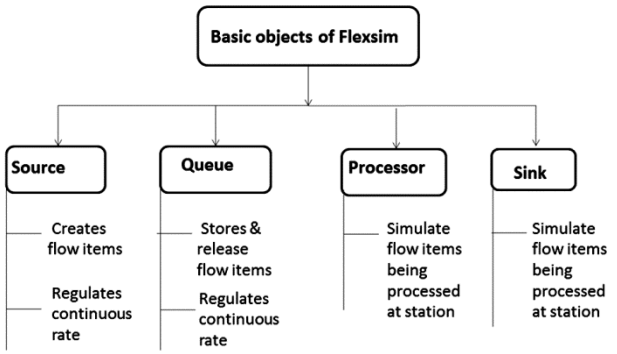

Fig. 2 — Basics objects of flexsim

Assumptions

The following assumptions are considered while developing a simulation model.

(i) There is no bottleneck present in the system.
(ii) All machines have enough capacity to operate.
(iii) The arrival rate of raw materials is assumed to be an exponential distribution with a location value of zero and a scale value of 4 minutes.
(iv) The setup time is assumed to be a triangular distribution with a min time of 0.05 minutes, a max time of 0.15 minutes but most commonly a time of 0.01 minutes.
(v) The processing time is also assumed to be triangular distribution.

Flexsim contains the four basic objects as shown in Fig. 2. These objects are a source, sink, processor, and queues.[22]

Simulation Model

There are generally 3 inputs of the simulation model which are arrival rate, processing time, and the

number of resources. The model output is generally measured in terms of throughput, utilization, and states. The flow items of this simulation model are crankcase covers. The fixed resources used in this simulation model are the source, queue, processor, and sink. Operators are also used for loading and unloading flow items. A dispatcher is used to coordinate the operators. Updating the virtual model is necessary using the company's real database system from time to time. The 3D simulation model of crankcase cover manufacturing is represented in Fig. 3. There is a need of defining the model parameters for running this simulation model. These model parameters are defined in Table 2 with their statistical distributions and values.

During the simulation, the reset and the run option are used in Flexsim for running the model, and the dashboard option provides all analysis of the manufacturing system in terms of various charts. Analysis of the virtual model eliminates any uncertainty present in the production system. The scheduling of all tasks on the processing stations is represented by the state Gantt chart in Fig. 4. This chart gives a visual representation of all the tasks scheduled on the various stations with object and state information.

Optimization

The scenarios option of Flexsim provides the option of adding variables for optimization. The two types of variables considered in this study are the operator group (dispatcher 1) and the processor group (processor group DCM & VMC). The three scenarios of simulation experiment control consisting of the various variable groups are shown in Fig. 5. Scenarios 1 include only one dispatcher, one DCM processor

Table 2 — Simulation model parameters

Model parameters	Distribution	Values (mins)
Arrival rate of raw materials	Exponential	4.00
Setup time	Triangular	0.01
Die casting machine (DCM)	Triangular	1.50
Manual fettling (MF)	Triangular	0.18
Drilling machine (DM)	Triangular	0.35
Vertical milling center (VMC)	Triangular	4.00
Buffing machine (BM)	Triangular	0.22
Painting Shop (PS)	Triangular	21.3

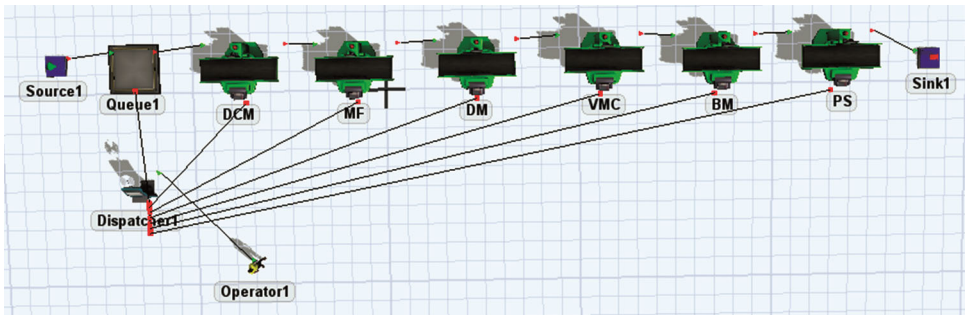

Fig. 3 — Simulation model of crankcase cover manufacturing

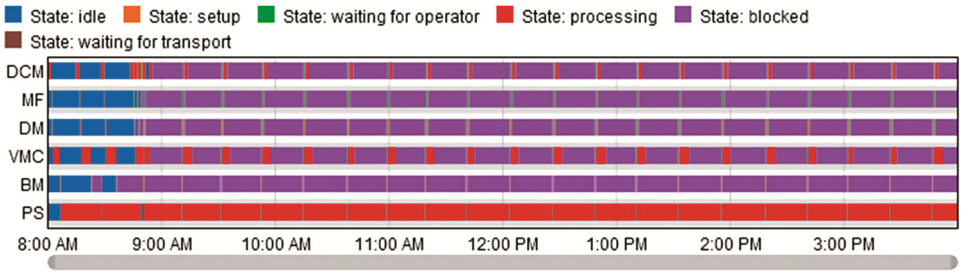

Fig. 4 — State gantt chart with the object and states information

	Variable	Scenario 1	Scenario 2	Scenario 3
Variable 1	Nr TEs in Team /Dispatcher1	1	2	3
Variable 2	Nr Objects in Processor group DCM	1	2	3
Variable 3	Nr Objects in Processor Group VMC	1	2	3

Fig. 5 — Various scenarios of simulation experiment control

group, and one VMC processor group, whereas scenario 2 and scenario 3 includes more than one dispatcher and processor groups.

Results and Discussion

In this study, we have taken processor groups of die-casting machines and vertical milling centers only. Because these machines are costly, industries can't afford many of these types of machines. So, there is a need of identifying the optimal number of these machines. A similar study had conducted by Marek Krynke[23] for optimizing the number of employees so that the production time for a single batch is the shortest. After adding all the variable groups with their numbers in this study, the experiment run tab is used for optimization. The statistical distribution of all the model parameters is identified from the expert Fit function of the Flexsim. The replications per scenario are 30 and this experiment is run for 3 days. The experimental conditions and running status are depicted in Fig. 6.

After running the simulation for 3 days, the processor and operator's state pie chart is obtained. The processor state pie chart represented in Fig. 7 shows the performance of all the processing stations in percentage terms of processing time, setup time, idle time, blocked time, operator waiting time, and transport waiting time. The results indicate the idle time for the painting shop and buffing machine is lowest for scenario 2, the idle time for the die casting machine is lowest for scenario 1, and the idle time for the drilling machine is lowest for scenario 2 and scenario 3. The idle time for the vertical milling center is the lowest for scenario 1.

The operator's state pie chart represented in Fig. 8 shows the effect of increasing the number of operators on the system performance in percentage terms of the

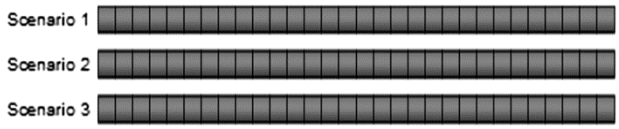

Fig. 6 — Experiment run window of simulation experiment control

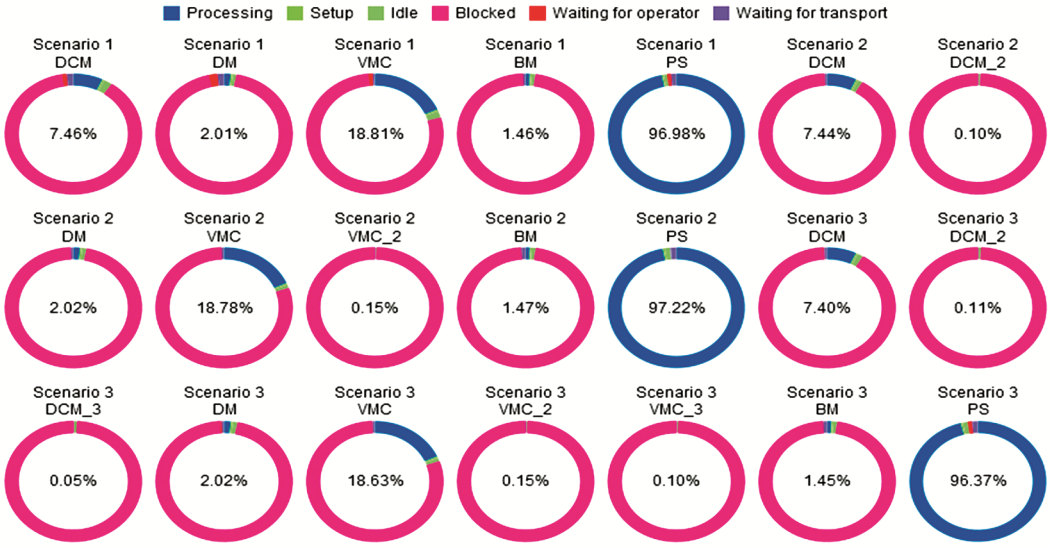

Fig. 7 — Processor state pie chart

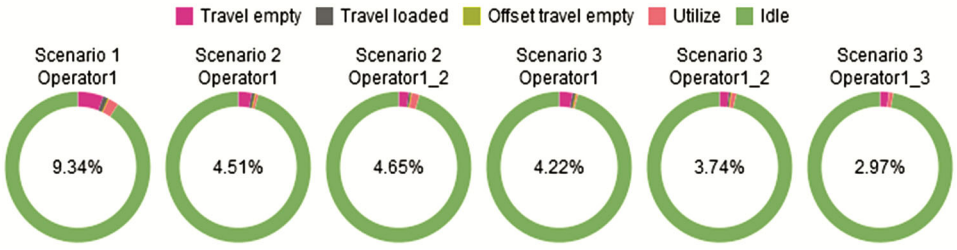

Fig. 8 — Operators state pie chart

parameters such as travel empty, travel loaded, offset travel empty, utilize time, and idle time. The operator's state pie chart shows that as the number of operators increased, overall idle time also get decreased.

Conclusions

With the rapid development in the automobile industry, effective operations and effective machines are the need of the hour. Simulation and modelling have changed the way of establishing new industries and always provide us the optimal results. This study deals with the simulation and modelling of crankcase cover manufacturing in the automobile industry to find out the optimal scenario with the Flexsim tool. The objective of this research was to analyze the effect of changing the number of operators and process stations on the system performance. The results show the percentage time of processing, blocked, idle, setup, waiting for the operator, and waiting for the transport. It is concluded from all the results that scenario 2 is best for crankcase cover manufacturing which reduces the overall ideal time and provides the optimal number of DCM and VMC required for crankcase cover manufacturing. These results are beneficial for all types of manufacturing industries. This developed simulation model is also helpful for the construction of new efficient production facilities for various industries.

Further study can also be extended by automatic updating of the database with company databases and using a global table with different part sets. The effects of adding the buffers on system performance within the layout of the processing stations can also be analyzed as a future study.

References

1 Bjorklund S, Yamani N & Lloyd T, Simulation software for real time forecasting as an operational support, *Proc Second World Conf POM and 15th Annual POM Conf* (Cancun, Mexico) 2004, 1–30.

2 Krishna L S R, Saketh T S S & Kumar M V S, A simulation based approach for studying the effect of buffers on the performance of an FMS, *Int J Eng Sci Invent*, **4(1)** (2015) 5–9.

3 Fauadi M, Azimi N Z, Anuar N I, Ali M M, Sued M K & Ramlan S, Simulation approach for logistical planning in a warehouse : a review, *Orient J Comput Sci Technol*, **11(4)** (2018) 201–208.

4 Jarernram J & Samattapapong N, Parallel machine scheduling using simulation software, *Proc ICMEIT* (Pattaya, Thailand) 2018, 150–155.

5 Rodrigues R P, Pinho A F D & Sena D C, Application of hybrid simulation in production scheduling in job shop systems, *Simul Trans Soc Model Simul Int*, **96(3)** (2019) 1–16.

6 Nie X & Wang L, Simulation process design for scheduling mode of railway container terminals based on Flexsim, *Proc J Phys: Conf Ser*, **1176(5)** (2019) 1–6.

7 Badri M A & Hollingsworth J, A simulation model for scheduling in the emergency room, *Int J Oper Prod Manag*, **13(3)** (1993) 13–24.

8 Cheng H C & Chan D Y K, Simulation optimization of part input sequence in a flexible manufacturing system, *Proc Winter Simulat Conf* (IEEE) 2011, 2374–2382.

9 Peng Y & Jiang Y C, Production process scheduling based on simulation with global optimization strategy: a case study, *Inf Technol J*, **12(5)** (2013) 983–989.

10 Gong L, Zou B & Kan Z, Modeling and optimization for automobile mixed assembly line in industry 4.0, *J Control Sci Eng*, **2019** (2019) 1–10.

11 Chandika S & Asokan R, Design and analysis of piezoactuated micropump for fuel delivery in automobiles, *J Sci Ind Res*, **70(6)** (2011) 448–454.

12 Kesen S E & Sert M, A simulation analysis of a serial line pull system producing orders with various part types and volumes, *Int J Model Simul*, **40(3)** (2019) 184–200.

13 Lin C K Y, Ling T W C & Yeung W K, Resource allocation and outpatient appointment scheduling using simulation optimization, *J Healthc Eng*, **2017** (2017) 1–19.

14 Azab A, Karam A, Eltawil A, Azab A & Karam A, A simulation-based optimization approach for external trucks appointment scheduling in container terminals scheduling in container terminals, *Int J Model Simul*, **40(5)** (2019) 1–18.

15 Huynh N, Reducing truck turn times at marine terminals with appointment scheduling, *Transp Res Rec J Transp Res Board*, **2100(1)** (2009) 47–57.

16 Kim S, Meng C & Son Y J, Simulation-based machine shop operations scheduling system for energy cost reduction, *Simul Model Pract Theory*, **77** (2017) 68–83.

17 Phani K, Kumar R, Kamala V & Kumar A, Simulation of job shop scheduling problem, *Int J Eng Res Technol*, **2(6)** (2013) 831–834.

18 Steinhauer D, Sikorra J N, Haux M A, Friedewald A & Lodding H, Processing incomplete data for simulation-based production planning in shipbuilding, *J Simul*, **11(1)** (2017) 30–37.

19 Wang Y R & Chen A N, Production logistics simulation and optimization of industrial enterprise based on Flexsim, *Int J Simul Model*, **15(4)** (2016) 732–741.

20 Zhang Y, Zhao Z, Bi L, Wang L & Gu Q, Determination of truck–shovel configuration of open-pit mine: a simulation method based on mathematical model, *Sustainability*, **14(19)** (2022) 12338.

21 Kliment M, Trojan J, Pekarcíková M, & Kronová J, Creation of simulation models using the Flexsim software module, *ALS - Theory Pract*, **16(1)** (2022) 41–50.

22 Kessel D, Jeon J, Jung J, Oh E & Kim C, Logistical simulation modeling for planning a soil remediation process, *Sci Technol Nucl Install*, **2019** (2019) 1–13.

23 Krynke M, Personnel management on the production line using the Flexsim simulation environment, *Manuf Technol*, **5** (2021) 657–67.

2023 IEEE IAS Global Conference on Emerging Technologies (GlobConET)
Loughborough University, London, United Kingdom. May 19-21, 2023

2023 IEEE IAS Global Conference on Emerging Technologies (GlobConET) | 979-8-3503-3179-0/23/$31.00 ©2023 IEEE | DOI: 10.1109/GlobConET56651.2023.10149950

Modified Mutation based Rao-3 Algorithm for Design Optimization of Surface Inset PMSM via Multi-Echelon Strategy

Monika Verma*, Saket Gupta, Prof. Madhusudan Singh, Prof. Mini Sreejeth, Prof. Narendra Kumar
* Electrical Engineering Department, Delhi Technological University, Delhi, 110085
* corresponding author email: monikaverma_phd2k17@dtu.ac.in

***Abstract*—The problem of design optimization of Surface Inset type of Permanent Magnet Synchronous Motor, or SI-PMSM, requires the consideration of large number of its design parameters. It arises the issue of making the decision about the design parameters, such as, what parameters should be optimized and what parameters can be left out. Due to this, the high computation time and cost is fostered. To address this problem, this paper presents a novel multi-echelon strategy (MES) based design optimization framework by introducing a new modified mutation based Rao-3 algorithm (MMRA) for the minimization of overall losses in the motor. For dividing various design parameters into three echelons, the proposed MES-MMRA technique employs Kendall correlation coefficient nalysis. The MES technique helps to separate significant and non-significant design parameters by analyzing the corresponding z-scores of all parameters statistically. It is shown that the newly introduced MMRA technique performs much better than other modern meta-heuristic algorithms. The proposed MES-MMRA technique has been able to perform well in solving the design optimization problem of SI-PMSM. As a result, the minimum loss obtained, by applying MMRA algorithm to the loss problem, is 136.215 W, leading to a saving of 29 % of the loss obtained from un-optimized initial model. Through this paper, the proposed mechanism can also efficiently improve the motor's overall electromagnetic performance. This results in the increase in the efficiency of the motor by 2.7 %. The technique of Finite Element Analysis, or FEA, is carried out to validate and verify the results.**

***Index Terms*—SIPMSM, Multi-echelon, modified mutation, Rao-3 algorithm, Kendall correlation coefficient.**

I. INTRODUCTORY WORK

Due to swift growth in electric vehicles (EVs) employing various electrical machines, the rapid extension in design optimization related research of such machines has been observed lately [1].

A. Motivation

Since EVs have to confront the various driving conditions which are complex to handle, the non-linear design optimization provision of traction motors becomes complicated [2]. It needs to examine large number of geometrical aspects like stator slot design, teeth design, stator inner radius, stator outer radius, rotor dimensions, magnet dimensions, length of air gap and other factors affecting its electromagnetic performance [3]. For simplifying this problem, it is advised to acquire the knowledge about distinguishing factors, for classifying various design parameters into different categories. This motivates the estimation of a precise mathematical explanation for assessment and generation of motor geometrical parameters.

In literature, it is found that the motor design optimization problems have been developed in the form of multi-level (ML) techniques in two types;

- The first one is multi-level based genetic algorithm called MLGA method. A ML based problem is outlined in [4] in matrix form in order to optimize geometry of PMSM. The matrix elements were computed using correlation analysis concept and thus MLGA architecture is implemented.
- The second one is multi-level based optimization via sensitivity test. In this, by dividing manifold geometrical parameters into separate levels, the sequential sensitivity test is carried out until the convergence is reached [5-7].

From this survey, the significance of ML based technique for improving motor performance is highlighted. However, these techniques lack in few considerations.

- First, such correlation analysis does not show the sufficient knowledge of describing standard deviations being at the distant from the moderate or average value. In the absence of this feature, it becomes difficult to differentiate the grades of various parameters. Further, if grades of parameters are not characterized, the complexity of solving high-dimensional optimization problem increases.
- Secondly, the knowledge of dependent and independent parameters is not addressed. Among various parameters, not all parameters are need to be included into the objectives. Variations in some parameters may pertain the variation in others. This ambiguity needs to be cleared before developing the required objectives.

For selecting the coefficient of correlation, the most common methods are Spearman, Kendall, and Pearson analysis [8]. Pearson and Spearman both provide correlation between data which is normally distributed but does not give the strength of corresponding correlation between the data. The Kendall's correlation analysis provides the quantitative results for strength of dependence of parameters. So, it is adopted for solving ML based shortcomings in this paper. It employs the z-score computation of various motor design

.

Authorized licensed use limited to: DELHI TECHNICAL UNIV. Downloaded on June 28,2023 at 06:38:17 UTC from IEEE Xplore. Restrictions apply.

parameters using statistical approach and provide aide to formulate the real world design optimization objectives with respect to the legitimate parameters.

B. Background

Various attempts, that have been made to optimize the motor geometry using different strategies, are shown in Table I. It is found that several meta-heuristic (MH) frameworks have lately emerged to address many real-world science and engineering problems [18]. However, the MH is random which involves the adjustment of specific parameters to obtain the best solution . This requires too much computational burden to find the global best solution. Also, if algorithm specific parameters are not tuned properly, they procure the premature convergence.

TABLE I. PRIOR RESEARCH WORK

Year, Authors	Strategy	Remarks/Gap
2018, Ebrahimi A. et. al. [9]	Multi-level Ant Stigmergy algorithm	Requires huge computation time.
2020, S. W. Baek et. al. [10]	Curve cutting technique	It explores the whole search region. But possibility of obtaining infeasible combination of design parameter increases.
2018, J. Hu. Et. al. [11]	Field circuit coupled FEM	Limited to only improving control performance of PMSM drive system.
2005, L. Jolly et. al. [12]	Response Surface methodology and Genetic Algorithm	Dependency of optimized motor performance is observed over parameters of algorithm.
2011, Abbaszadeh K. et. al. [13]	Magnet segmentation method	The approximated optimized values of parameters are obtained.
2015, L. Jain et. al. [14]	RSM along with LSM	It involves complexity in decision making of optimal values of coefficients in RSM to obtain minimum value of response.
2018, Q. Zhang et. Al. [15]	Considerable design factors sweep, appropriate pole-slot pair, superior design strategy and FEA validation scheme	The optimization is implemented to high power rating brushless DC (BLDC) motor. The parameters which are not considered may or may not affect the motor performance.
2012, F. Parasiliti et. al. [16]	Multi-aspect regression dissolution, Stochastic search algorithm	Dependency of optimized motor performance is observed over parameters of stochastic search algorithm.
2018, P. Asef et. al. [17]	RSM of dual grade, Booth algorithm	The parameters of Booth algorithm are found to be affecting the performance of optimized motor.

.

C. Contributions

The traditional Rao algorithms [19] is one of the population based methods. It has outstanding exploration capability but slower rate at exploitation stage in the search domain. It suffers with premature convergence while handling large dimensional non-linear problems.

In view of solving the limitation of traditional Rao algorithms, its cross-breeding with sine-cosine (SC) based mutation operation is performed. The efficiency of the proposed MMRA technique is checked and verified using benchmark functions, (i.e., total of 13 unimodal and multimodal type functions). The contribution of this work is listed as follows:

- An MES based real world non-linear problem is formulated to optimize the SIPMSM geometry, consisting of independent design parameters (obtained from Kendall correlation analysis).
- The novel hybrid mechanism, called MMRA, is proposed. It is formed by blending the Rao-3 algorithm and Sine-Cosine (SC) mutation- based strategy.
- Benchmark functions are utilized for testing the search potential of proposed MMRA technique. Performance of MMRA is compared with few similar techniques.
- The formulated design optimization problem is solved by the proposed MMRA algorithm, in order to minimize losses in motor.
- The comparison of initial model and optimized model with respect to their electromagnetic performances is presented for validation and verification.

II. FORMULATION OF PROBLEM BASED ON MES-MMRA TECHNIQUE

In this section, the formulation of design optimization problem and the proposed MMRA algorithm is presented.

A. MES based formulation of real world problem

In the proposed MES strategy, various design parameters (as shown in Fig 1) are categorized into three echelons; E_1, E_2 and E_3. Echelon E_1 represents stator design parameters: b_{so}= Slot aperture length, h_{s1}= Slot tip length, h_{s2}= Slot height, r_{si}= Stator inner radius, r_{so}= Stator outer radius, α_t= Tooth angular width. Echelon E_2 represents rotor design parameters: l_{ip}= Inter-polar length, r_{ri}= Rotor inner radius, w_m= Width of magnet, α_m= Magnetic angle. Echelon E_3 consists of auxiliary parameters: h_g= Gap length in air, p_e= Pole eccentricity.

By performing variations in motor design parameters to perform FEA experiments, the inter-related and independent design parameters of three echelons are separated. This step helps to identify the redundant design parameters while performing the formulation of objective functions.

Authorized licensed use limited to: DELHI TECHNICAL UNIV. Downloaded on June 28,2023 at 06:38:17 UTC from IEEE Xplore. Restrictions apply.

Then, the Kendall Correlation Coefficient (KCC) analysis computes the corresponding z scores for each design parameter of a particular echelon, by keeping parameters of other echelons constant. This step helps to identify the parameters to be optimized for that particular echelon.

For the computation of Kendall's Tau (τ) coefficient for m^{th} parameter, concordant (C_m) and discordant (D_m) pairs are computed statistically and thus the computation of corresponding z_m scores is carried out.

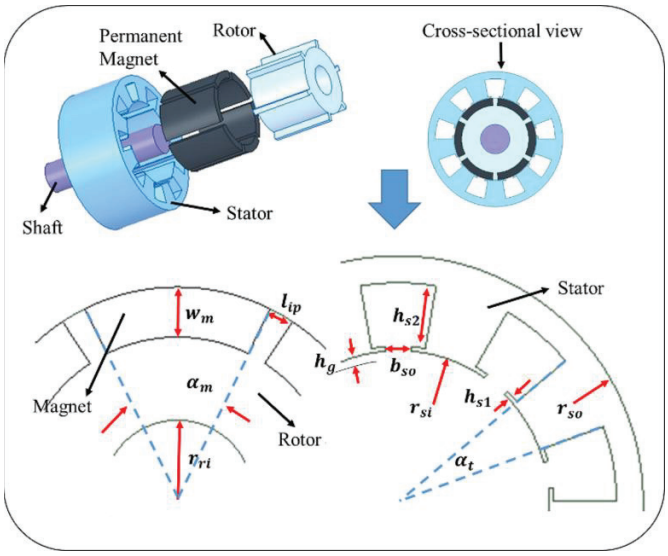

Fig. 1 Representation of various design variables of SIPMSM

For all parameters, τ_Y coefficient for Y objective is calculated by Eq. (1). The computation of z_m score is performed using Eq. (2). { x_m= value of m^{th} parameter, μ= Mean value in KCC, σ= Standard deviation in KCC}

$$\tau_Y = \frac{(C_m - D_m)}{(C_m + D_m)} \tag{1}$$

$$z_m = \frac{x_m - \mu}{\sigma} \tag{2}$$

The variation in z scores and KCC values of design parameters are presented in Fig. 2. As presented, the KCC gives the knowledge of z scores of design parameters of E_1 and E_2 independently. The z scores values are thus evaluated in the form of percentage using standard normal distribution z-table which yields the insight about the value of a particular parameter lying far or near its corresponding mean value. The more is the percentage z-score, the farther is the parameter from the average value and hence needs to be optimized.

Following are the observations via KCC analysis: -

- For E_1 (Fig. 2-(a)), parameters b_{so}, h_{s1} and r_{so}, have the highest values of 81%, 61% and 92% respectively.
- These are categorized as independent design parameters, for the formulation of loss objective function 1, i.e., l_s.
- While parameters h_{s2}, r_{si} and α_t are settled as inter-related design parameters since variations in other parameters directly influence the values of these three parameters.

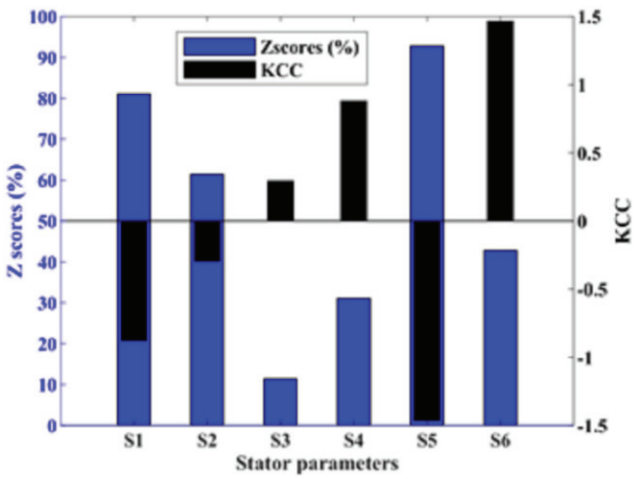

(a)

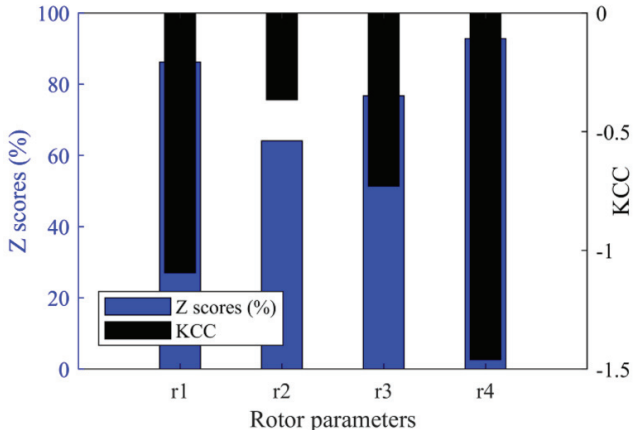

(b)

Fig. 2 Analysis results of KCC and z-scores of (a) stator design parameters: s1=b_{so}, s2=h_{s1}, s3=h_{s2}, s4=r_{si}, s5=r_{so}, s6=α_t; and (b) rotor design parameters: r1=l_{ip}, r2=α_m, r3=r_{ri}, r4=w_m

- Similarly, among rotor parameters (Fig. 2-(b)), parameters l_{ip}, r_{ri} and w_m have the largest z scores of 86%, 76% and 92% respectively.
- These are classified as independent design parameters for the formulation of loss function i.e., l_r.
- While α_m parameter is found to be inter-related to the variation in l_{ip} parameter.

The corresponding surrogate models of loss are developed (using FEA experiments) in terms of legitimate geometry parameters (identified via KCC analysis). For Design of Experiments (DOE) in surrogate modelling, the FEM model responses for different combinations of parameters are noted, in order to save loss results (The corresponding results are presented in supplementary document).

Thereafter, Least Square Method, or LSM, is used, to obtain coefficients related to Response Surface Models, or RSM, for the formation of the required non-linear design optimization problem. Hence, the formulated loss objectives, l_s (loss objective for echelon E_1) and l_r (loss objective for echelon E_2), are given by Eq. (3) and Eq. (4).

Authorized licensed use limited to: DELHI TECHNICAL UNIV. Downloaded on June 28,2023 at 06:38:17 UTC from IEEE Xplore. Restrictions apply.

$$l_s = 1e^3(2.5594 + 0.1305\, b_{so} - 0.1098\, h_{s1} - 0.0054\, rso - 0.0255\, bsohs1 - 0.0045\, bsorso + 0.0043\, hs1rso + 0.0124\, bso2 + 0.0081\, hs12 - 0.0006\, rso2 \quad (3)$$

$$l_r = 274.7576 - 27.1587\, l_{ip} - 34.7417\, r_{ri} + 53.7557\, w_m + 1.0058\, l_{ip} r_{ri} - 5.3784\, l_{ip} w_m + 2.404\, r_{ri} w_m + 1.4374\, {l_{ip}}^2 + 0.562\, {r_{ri}}^2 - 1.953\, {w_m}^2 \quad (4)$$

The error analysis is performed using Root Mean Square Error, or RMSE test, to check accuracy of the surrogate models. The difference between R^2 (Coefficient of determination) and its adjusted counterpart, R^2_{adj} (Adjusted coefficient of determination) is found to be ~0.00 after performing 14 experiments for E_1 and 12 experiments for E_2. This indicates that the non-significant terms are not in surrogate models [20]. The RMSE values for l_s and l_r are found to be 0.369 and 0.011 respectively (< 1), which indicates that no extra samples in FEA experiments are needed to be added [21]. The contour plots and residual plots represents the accurate fitting of the surrogate models (Fig. 3-(a)-(b)).

B. The proposed MMRA algorithm

The proposed algorithm starts with the aim of minimization (or maximization), having objective function of $f(x)$. For i^{th} iteration, if there are d decision variables, n number of solutions with population size $p = 1, 2, 3 \ldots . n$, this process stores the best solution ($f_b(x)$) and the worst solution ($f_w(x)$).

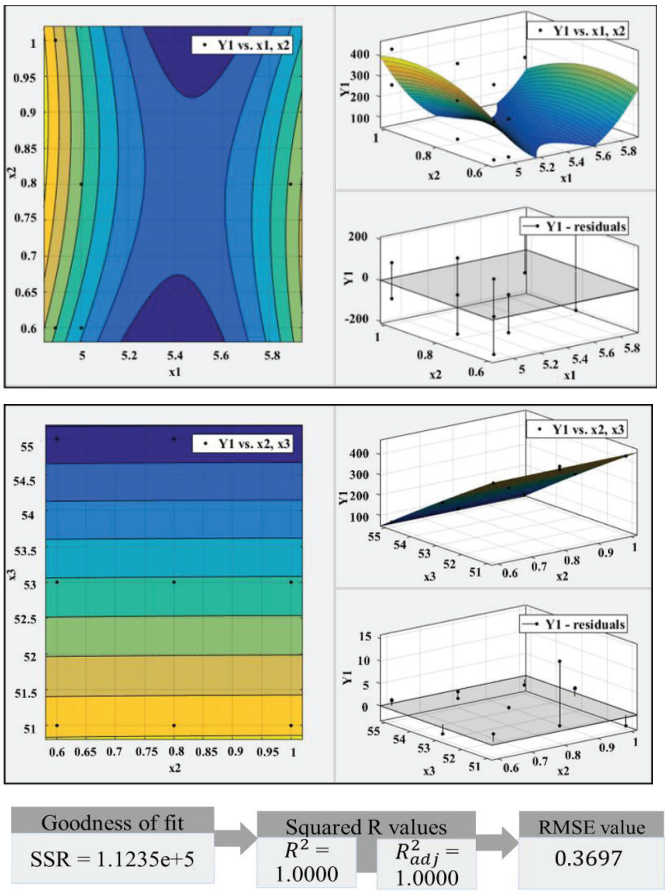

Goodness of fit	Squared R values		RMSE value
SSR = 1.1235e+5	R^2 = 1.0000	R^2_{adj} = 1.0000	0.3697

(a)

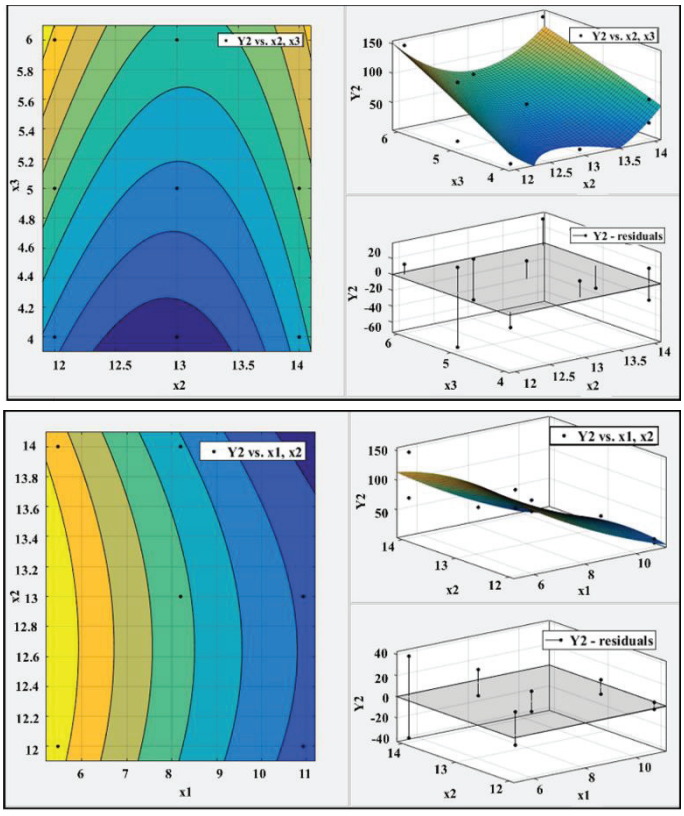

Goodness of fit	Squared R values		RMSE value
SSR = 8.8540e+4	R^2 = 1.0000	R^2_{adj} = 1.0000	0.0112

(b)

Fig. 3 The goodness of fit results of formulated real world objectives: (a) $Y1 = l_s$, $x1 = b_{so}$, $x2 = h_{s1}$, $x3 = r_{so}$ (b) $Y2 = l_r$, $x1 = l_{ip}$, $x2 = r_{ri}$, $x3 = w_m$; SSR: Sum of Squares due to Regression, R^2: Coefficient of correlation, R^2_{adj}: adjusted Correlation Coefficient and RMSE: Root Mean Square Error.

The value of j^{th} variable of k^{th} candidate at i^{th} iteration, $x^i_{j,k}$ is modified using Eq. (5). The modified SC based mutation is performed using Eq. (6). The parameter a is calculated using Eq. (7). Parameter b is varied between [0,2π] and $c \in [0,1]$ is random number respectively [22].

$$x^i_{j,k}{}' = x^i_{j,k} + r_1 \times \left(x^i_{j,best} - \left|x^i_{j,worst}\right|\right) + r_2 \times \left(\left|x^i_{j,k} \text{ or } x^i_{j,l}\right| - xj,lior\ xj,ki\right) \quad (5)$$

$$x^{i+1}_{j,k,new} = \begin{cases} x^i_{j,k_{c1}} + a \times sin(b) \times \left|c \times x^i_{j,k_{c2}} - x^i_{j,k_{c3}}\right| ; if\ r < 0.5 \\ x^i_{j,k_{c1}} + a \times cos(b) \times \left|c \times x^i_{j,k_{c2}} - x^i_{j,k_{c3}}\right| ; otherwise \end{cases} \quad (6)$$

$$a = 2 \times (1 - \tfrac{t}{T})^2 \quad (7)$$

The greedy selection operation is performed during SC mutation so that a consistent size of population can be

.

Authorized licensed use limited to: DELHI TECHNICAL UNIV. Downloaded on June 28,2023 at 06:38:17 UTC from IEEE Xplore. Restrictions apply.

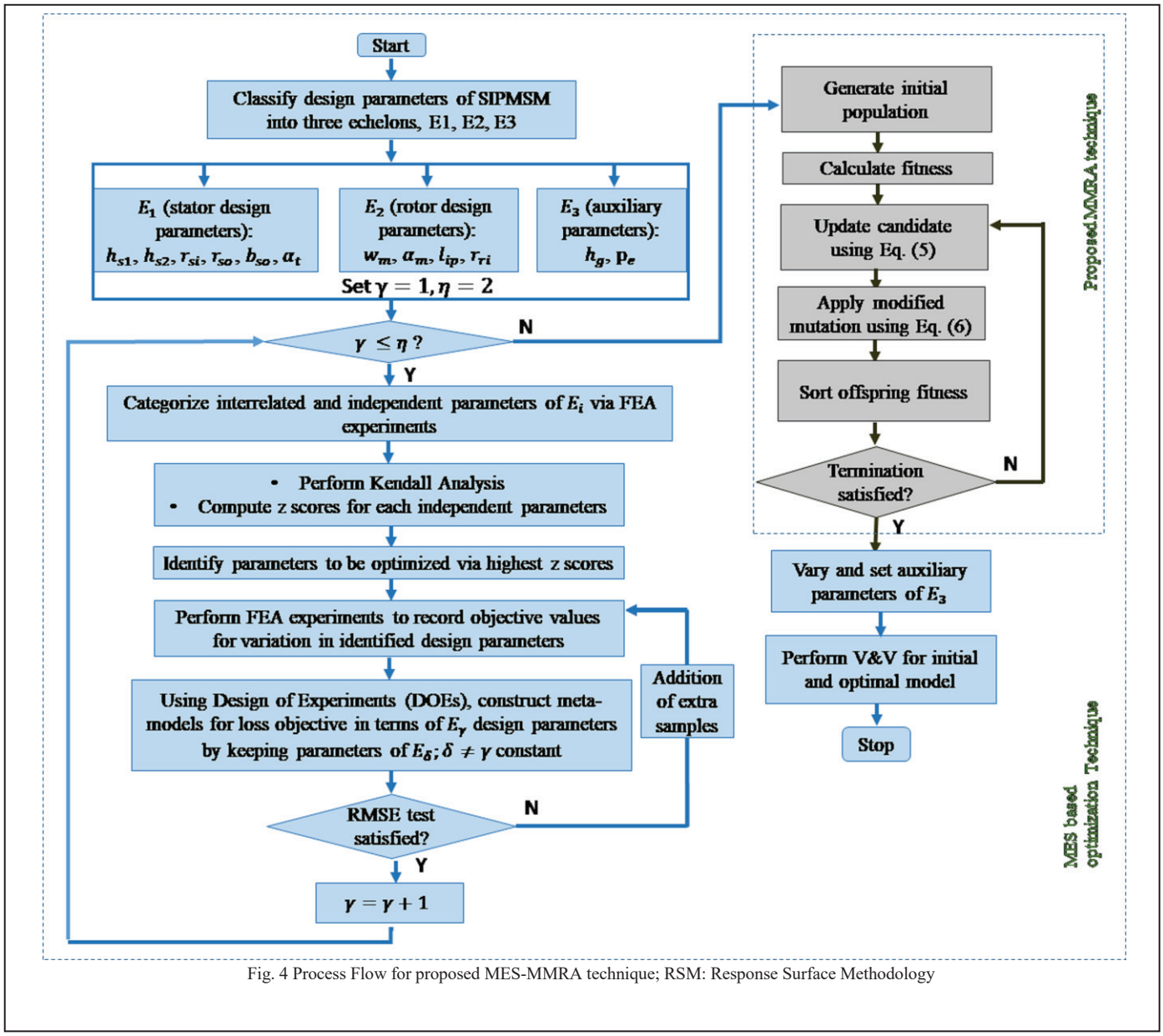

Fig. 4 Process Flow for proposed MES-MMRA technique; RSM: Response Surface Methodology

maintained. For this, if $f\left(x_{j,k,new}^{i+1}\right) < f(x_{j,k}^{i})$ condition is satisfied, the old candidate value $(x_{j,k}^{i})'$ gets replaced by $x_{j,k,new}^{i+1}$ value. Thus, Fig. 4 presents the process flow for the proposed MES based optimization technique using MMRA framework.

III. BENCHMARK, SCALABILITY AND VARIABILITY TESTS OVER MMRA

The thirteen Benchmarks, i.e., unimodal and multimodal functions, are used to examine potential of proposed MMRA technique; with dimension size = 10, 30; population size = 10, 50; maximum iteration = 1000. Note that, for proposed technique, only two features, i.e., population size and maximum iteration, are needed to be specified. For, real world non-linear problem, population size = 10 is taken with same maximum iteration setting. The search potential of proposed MMRA is compared with other state-of-the-art MH approaches [23-24]. Table II shows that MMRA technique is successful in achieving the better outcomes for most of the benchmark functions over 30 independent runs when it is compared with traditional state-of-the-art MH approaches.

As for F1, F2, F3, F4, F5, F7 (unimodal functions), and F8, F9, F11, F13 (multimodal functions), the proposed MMRA algorithm performs much better (mean value) solution than the other algorithms. However, for function F6, F10 and F12, MMRA algorithm finds difficulty to tune itself to reach the global optimum. From Table II, it is found that MMRA algorithm provides zero value of standard deviation (std) for F1-F4, F9, F11 and low value of std for F5-F7, F12, F13. *It specifies the robustness and superiority of MMRA algorithm over other reported methods.* The proposed method exhibits the convergence characteristics as displayed in Fig. 5.

.

Authorized licensed use limited to: DELHI TECHNICAL UNIV. Downloaded on June 28,2023 at 06:38:17 UTC from IEEE Xplore. Restrictions apply.

TABLE II. PERFORMANCE COMPARISON OF MMRA WITH OTHER ALGORITHMS FOR F1-F13 BENCHMARKS; DIMENSION=10, POPULATION=10

Function	MMRA		AGO	AO
	Mean	Std	Mean	Mean
F1	0.0000	0.0000	8.839E-35	1.770E-19
F2	3.0 E-165	0.0000	9.111E-23	1.554E-10
F3	0.0000	0.0000	3.831E-53	1.044E-19
F4	1.7E-163	0.0000	2.521E-62	9.034E-10
F5	0.00035	0.0063	8.222E-04	8.306E-04
F6	0.04504	0.0013	2.152E-25	4.556E-06
F7	0.00004	0.0001	5.318E-03	2.661E-03
F8	-4189.82	297.74	-413.586	-412.784
F9	0.0000	0.0000	1.294E-10	0.000E+00
F10	8.8E-16	0.0000	1.764E-16	8.881E-16
F11	0.0000	0.0000	1.775E-15	0.000E+00
F12	0.03070	0.0073	1.498E-06	1.505E-05
F13	1.3E-32	0.0035	1.537E-07	1.353E-06
Function	GOA	ABC	PSO	TLBO
	Mean	Mean	Mean	Mean
F1	2.509E-06	4.507E-11	1.715E-25	3.854E-33
F2	0.283E+00	2.879E-16	1.532E-12	1.020E-17
F3	1.633E-04	2.448E-10	2.912E-24	5.817E-32
F4	1.968E-04	5.199E-17	4.850E-12	4.703E-16
F5	1.011E+00	0.401E+00	0.000E+00	0.000E+00
F6	1.012E-09	0.500E+00	0.000E+00	4.264E-08
F7	5.812E-03	0.098E+00	3.292E-05	0.004E+00
F8	-417.336	-402.968	-408.229	-400.868
F9	4.682E+00	4.052E-10	0.000E+00	0.000E+00
F10	4.619E-05	4.148E-16	8.881E-16	8.881E-16
F11	0.096E+00	2.390E-05	0.000E+00	4.440E-15
F12	5.519E-06	1.000E+00	4.711E-03	4.326E-04
F13	1.327E-06	1.000E+00	1.349E-02	6.816E-03

* Aquila-Grasshopper- Optimization (AGO), Grasshopper optimization algorithm (GOA), Aquila optimizer (AO), Particle swarm optimization (PSO), Artificial bee colony algorithm (ABC), Teaching–learning-based optimization (TLBO)

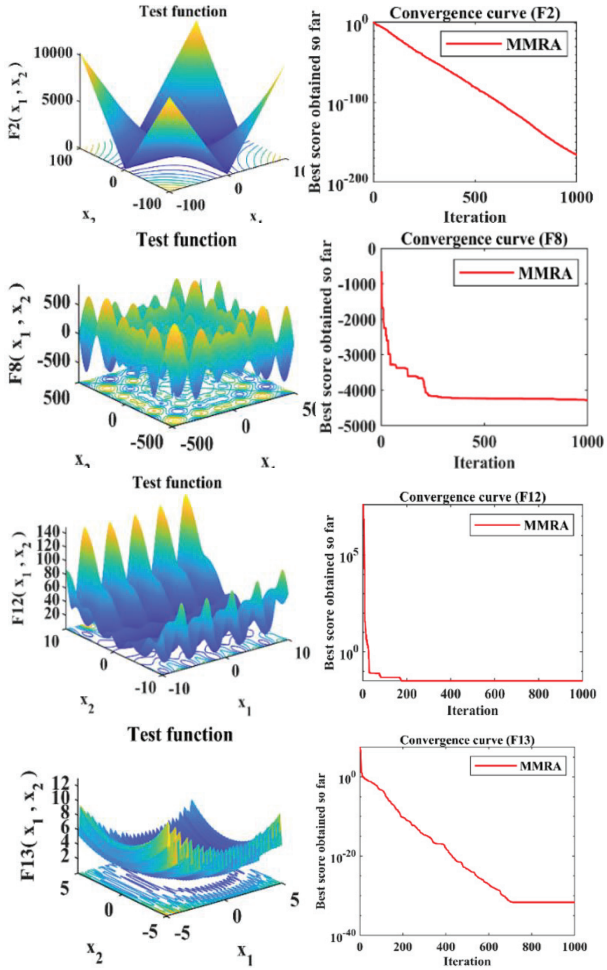

Fig. 5 Convergence of MMRA for few benchmark functions

To demonstrate the scalability of proposed MMRA algorithm, the Benchmark functions having 30-dimensional versions are solved. The candidate solutions (search agents) of 50 population size are selected for 1000 iterations. Table III presents the superior performance of MMRA for almost all Benchmarks, when compared to the most recent Inclined Planes Optimization, or IPO, and Gravitational Search Algorithm, or GSA.

To test the variability of MMRA, the performance of MMRA is examined with 30 separate trials with an increment of 250 in iteration numbers and increment of 10 in population with fixed dimension of problem (D=10).

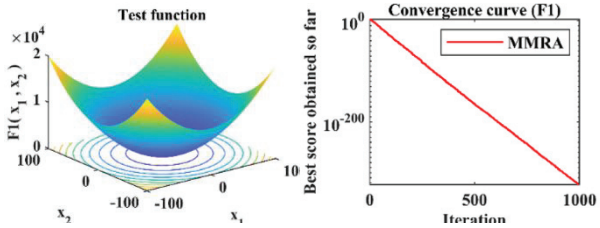

For unimodal functions, at lower iteration values (below 1000), the MMRA delivers lesser values of std. While beyond 1000 iterations, it delivers high values of std. However, number of iterations has no significant impact on its performance in case of multimodal functions (Table IV).

It is observed that as the population size is increased, there is a slight change in the outcomes. The clearer vision, for both the variability tests, is depicted in the form of box plot (in Fig. 6 and Fig. 7).

TABLE III. PERFORMANCE COMPARISON OF MMRA WITH IPO AND GSA ALGORITHMS FOR F1-F13 BENCHMARKS

Function	MMRA	IPO [25]	GSA [26]
	Mean	Mean	Mean
F1	2.57E-200	2.64E-20	2.1E-10
F2	2.10E-91	2.32 E-16	6.9 E-05
F3	1.63E-212	1.25E-04	0.16E+03
F4	8.48 E-90	2.99 E-03	8.5 E-06
F5	17.04	29.93	25.16
F6	1.27	0.00	2.6E-10
F7	2.7 E-4	1.27 E-02	0.533
F8	-10820.35	-10403.51	-1.1E+03
F9	0.0	3.59	15.32
F10	8.88 E-14	0.74	1.1E-05
F11	0.0	7.74 E-03	0.29
F12	5.7 E-02	6.22 E-02	0.01
F13	1.09 E-24	2.93E-03	3.2E-32

.

Authorized licensed use limited to: DELHI TECHNICAL UNIV. Downloaded on June 28,2023 at 06:38:17 UTC from IEEE Xplore. Restrictions apply.

TABLE IV. EFFECT OF DIFFERENT NUMBER OF ITERATION AND POPULATION SIZE ON THE MEAN VALUE OF OBJECTIVE FUNCTION

S. No.	Function	Number of iteration (population size=10)			
		500	750	1000	1250
1	F1	3.3E-150	2.5 E-210	0.0	0.0
2	F2	5.7E-70	4.0 E-110	3.0E-165	6.3E-180
3	F8	-4171.12	-4172.74	-4189.82	-4189.98
4	F10	2.6E-14	7.1E-15	8.8E-16	9.5E-16
S. No.	**Function**	**Population size (iterations=1000)**			
		10	**20**	**30**	**40**
1	F1	0.0	0.0	0.0	0.0
2	F2	3.0 E-165	1.3E-177	2.5 E-192	1.3E-183
3	F8	-4189.82	-4187.56	-4189.21	-4189.04
4	F10	8.8 E-16	2.5 E-15	9.6 E-16	3.4E-16

IV. REAL LIFE APPLIATION AND SIGNIFICANCE OF MES-MMRA FRAMEWORK

Here, the MMRA technique is implemented over the MES-based designed non-linear problem obtained in Section II. Thus, using MMRA, the optimal parameters of echelon E_1 are obtained as; b_{so}=5.27mm, h_{s1}=1mm, r_{so}=55mm, and of echelon E_2 as; l_{ip}=8.71mm, r_{ri}=12.19mm and ω_m=5.03mm with minimized loss of 136.215 W.

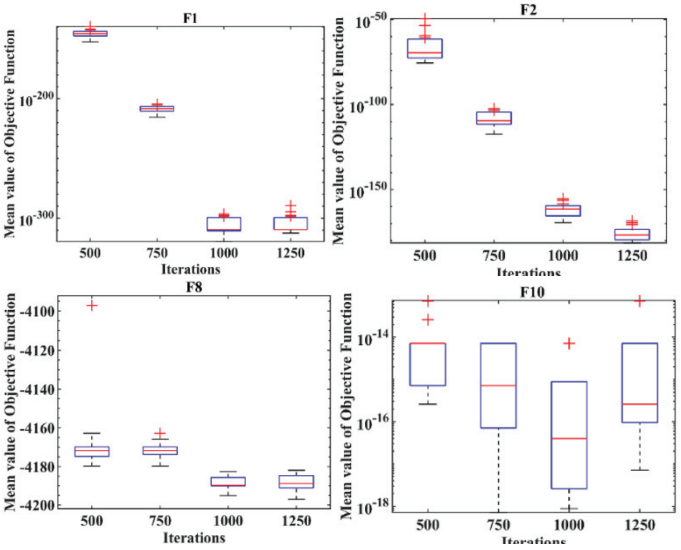

Fig. 6. Boxplots of MMRA with different values of Iterations on functions (F1, F2, F8 F10)

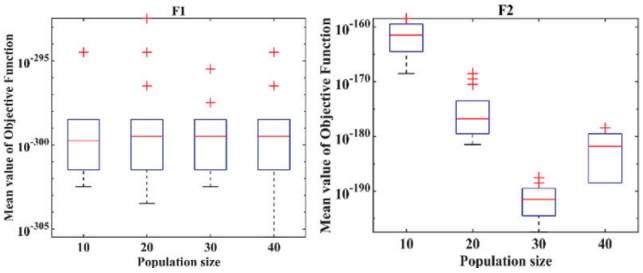

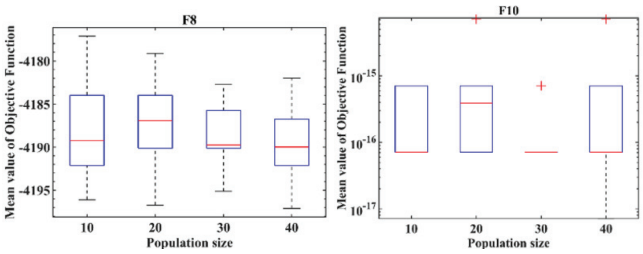

Fig. 7. Boxplots of MMRA with different values of population size on functions (F1, F2, F8 F10)

The variation in parameters of E_3 is tested by performing FEM experiments over the optimized model, for total ten samples of auxiliary parameters in the specified range: $h_g \epsilon [0.5 - 2.5]$ and $p_e \epsilon [0 - 4]$ variations. So, for E_3, the values of pole eccentricity ($p_e = 4\ mm$) and length of air gap ($h_g = 0.5\ mm$) are obtained. Thus, Fig. 8 shows that torque performance of final optimized model has improved along with lesser ripples than that produced by the initial model. The performance is compared on the basis of different indices of motor in Table V. It shows that not only unwanted ripples in torque, cogging torque and losses have fallen by considerable amount (~59%, ~29% and ~29%), but torque and efficiency of the motor are also improved by ~14% and ~2% respectively.

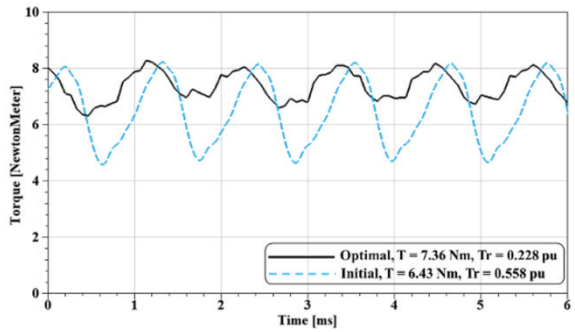

Fig. 8 Torque curves of initial and optimal models; T: Average Torque; T_r:Ripple in torque; pu: per unit

TABLE V. PERFORMANCE INDICES (PI) OF INITIAL AND OPTIMAL MODEL

Motor PI →	Losses (W)	Ripples in Torque (%)	Cogging Torque (Nm)	Efficiency (%)
Initial	192.468	55.8	0.790	91.4
Final	136.215	22.8	0.556	93.9
Remark	29% fall	59 % fall	29.6 % fall	2.7 % rise

Authorized licensed use limited to: DELHI TECHNICAL UNIV. Downloaded on June 28,2023 at 06:38:17 UTC from IEEE Xplore. Restrictions apply.

V. CONCLUSION

In this paper, as novel MES-MMRA technique is introduced for smoothening the complicated optimization procedure of SIPMSM. In addition to this, for resolving the complicated tuning issues of various parameter based optimization techniques, a parameter-less MMRA procedure is adopted. It is advisable to address the issues that has been resolved during execution of this technique. In the absence of MES-MMRA, to formulate objective meta-models via RSM, if three level values of each design parameter (total parameters = 12) are chosen, the overall design of parameters (DOEs) required 3^{12} FEM experimental results.

Firstly, it needs large estimation time and secondly, these results are fed to form the huge coefficient matrix. Due to this, coefficient matrix faces the controversial singularity issue. This makes the formulation of meta-models complicated and less effective due to large RMSE errors. Whereas, in the presence of MES-MMRA, the overall six independent design motor parameters are differentiated from overall twelve parameters. The echelon E_1 required 14 FEM experiments whereas E_2 needed 13 FEM experiments for the construction of required DOEs in surrogate modelling. Thereafter, computations for E_3 parameters is carried out via 10 samples and by comparing values of PIs of optimal model with that of initial one, the MES process flow is effectively realized through the use of parameter-less MMRA framework.

REFERENCES

[1] F. Momen, K. Rahman, and Y. Son, "Electrical propulsion system design of Chevrolet bolt battery electric vehicle," *IEEE Trans. Ind. Appl.*, vol. 55, no. 1, pp. 376–384, Jan./Feb. 2019.

[2] X. Sun, Z. Jin, S. Wang, Z. Yang, K. Li, Y. Fan, and L. Chen, "Performance improvement of torque and suspension force for a novel five-phase BFSPM machine for flywheel energy storage systems," *IEEE Trans. Appl. Supercond.*, vol. 29, no. 2, pp. 1–5, Mar. 2019.

[3] A. J. Sorgdrager, R. Wang, and A. J. Grobler, "Multi-objective design of a line-start PM motor using the Taguchi method," *IEEE Trans. Ind. Appl.*, vol. 54, no. 5, pp. 4167–4176, Sep./Oct. 2018.

[4] S.Wang *et al.*, "Multilevel optimization for surface mounted PM machine incorporating with FEM," *IEEE Trans. Magn.*, vol. 45, no. 10, pp. 4700–4703, Oct. 2009.

[5] X. Meng *et al.*, "Robust multilevel optimization of PMSM using design for six Sigma," *IEEE Trans. Magn.*, vol. 47, no. 10, pp. 3248–3251, Oct. 2011.

[6] G. Lei, C. Liu, J. Zhu, and Y. Guo, "Techniques for multilevel design optimization of permanent magnet motors," *IEEE Trans. Energy Convers.*, vol. 30, no. 4, pp. 1574–1584, Dec. 2015.

[7] G. Lei, W. Xu, J. Hu, J. Zhu, Y. Guo, and K. Shao, "Multilevel design optimization of a FSPMM drive system by using sequential subspace optimization method," *IEEE Trans. Magn.*, vol. 50, no. 2, pp. 685–688, Feb. 2014.

[8] L. Jantschi, 'Pearson versus Spearman, Kendall's Tau Correlation Analysis on Structure-Activity Relationships of Biologic Active Compounds', Leonardo journal of Sciences, Vol. 9, pp. 179-200, Dec. 2006: https://www.researchgate.net/publication/26449176.

[9] A. Ebrahimi, "Design Optimization of Permanent Magnet Synchronous Motors using Multilevel Ant Algorithm," *2018 14th International Conference on Power Electronics (CIEP)*, 2018, pp. 96-101, doi: 10.1109/CIEP.2018.8573399.

[10] Baek, Soo-Whang, and Sang W. Lee. 2020. "Design Optimization and Experimental Verification of Permanent Magnet Synchronous Motor Used in Electric Compressors in Electric Vehicles" Applied Sciences 10, no. 9: 3235. https://doi.org/10.3390/app10093235.

[11] J. Wu, J. Wang, C. Gan, Q. Sun and W. Kong, "Efficiency Optimization of PMSM Drives Using Field-Circuit Coupled FEM for EV/HEV Applications," in IEEE Access, vol. 6, pp. 15192-15201, 2018, doi: 10.1109/ACCESS.2018.2813987.

[12] Jolly, L., Jabbar, M.A., and Qinghua, L. Design optimization of permanent magnet motors using response surface methodology and genetic algorithms", IEEE Transactions on Magnetics, 41(10), pp. 3928- 3930 (2005).

[13] Abbaszadeh, K., Alam, F.R., and Saied, S.A. Cogging torque optimization in surface-mounted permanent magnet motors by using design of experiment", Energy Conversion and Management, 52(10), pp. 3075{3082 (2011).

[14] Jian, L., Shi, Y., Wei, J., et al. Design optimization and analysis of a dual-permanent-magnet-excited machine using response surface methodology", Energies, Vol. 8(9), pp. 10127-10140, 2015.

[15] Q. Zhang, S. Cheng, D.Wang, and Z. Jia, "Multi-objective design optimization of high-power circular winding brushless DC motor," IEEE Trans. Ind. Electron., vol. 65, no. 2, pp. 1740–1750, Feb. 2018.

[16] F. Parasiliti, M. Villani, S. Lucidi, and F. Rinaldi, "Finite-element-based multi-objective design optimization procedure of interior permanent magnet synchronous motors for wide constant-power region operation," IEEE Trans. Ind. Electron., vol. 59, no. 6, pp. 2503–2514, Jun. 2012.

[17] P. Asef, R. B. Perpiñà, M. R. Barzegaran, A. Lapthorn, and D. Mewes, "Multi-objective design optimization using dual-level response surface methodology and booth's algorithm for permanent magnet synchronous generators," IEEE Trans. Energy Convers., vol. 33, no. 2, pp. 652–659, Jun. 2018.

[18] A. Gogna and A. Tayal, "Metaheuristics: review and application, Journal of Experimental & Theoretical Artificial Intelligence," vol. 25, no. 4, pp. 503-526, 2013.

[19] Rao, R.V. Rao algorithms: Three metaphor-less simple algorithms for sol1ving optimization problems. Int. J. Ind. Eng. Comput. vol. 11, pp. 107–130, 2020.

[20] Y. Fujishima, et al, "Design optimization of PMSM by response surface methodology," J. Appl. Phys. vol. 91, pp. 8305–8308, 2002.

[21] S. Giurgea et al., "Multimodel optimization based on the response surface of the reduced FEM simulation model with application to a PMSM," IEEE Trans Magn. vol. 44, pp. 2153–2157, 2008.

[22] C. Zhou et al., "A sine cosine mutation based differential evolution algorithm for solving node location problem," International Journal of Wireless and Mobile Computing Vol. 13 (3), pp. 3, 2017.

[23] M. Verma, M. Sreejeth and M. Singh, "Integrated Taguchi method assisted polynomial metamodeling and genetic algorithm based optimization of surface inset permanent magnet synchronous motor for performance improvement", IET electrical system is transportation, pp. 1-10, Sep 2021.

[24] S. Mirjalili, "The ant lion optimizer" Advances in Engineering Software, vol 83, pp. 80–98, 2015.

[25] M. H. Mozaffari, H. Abdy, and S. H. Zahiri. IPO: An Inclined Planes System Optimization Algorithm. COMPUTING AND INFORMATICS, Vol. 35(1), pp. 222–240, 2016.

[26] E. Rashedi, H. Nezamabadi-Pour and S. Saryazdi. GSA: a gravitational search algorithm Information Sciences, Vol. 179 (13), pp. 2232-2248, 2009.

Monika Verma received her B. Tech. Degree in Electrical Engineering from G. B. Pant University of Agriculture & Technology, Uttarakhand, India in 2013, her M. Tech. Degree in Power Electronics and Drives from Vellore Institute of Technology, India in 2016, her Ph.D. degree in Electrical Engineering from Delhi Technological University, India in 2022. She is Institute of Electrical and Electronics Engineers (IEEE) student member, and Institution of Engineering and Technology (IET) associative member. **E-mail: monikaverma_phd2k17@dtu.ac.in**

.

Authorized licensed use limited to: DELHI TECHNICAL UNIV. Downloaded on June 28,2023 at 06:38:17 UTC from IEEE Xplore. Restrictions apply.

Saket Gupta obtained his M. E. degree in Industrial System & Drives from Madhav Institute of Technology and Science Gwalior, India in 2015. He received his Ph.D. degree from Delhi Technological University, New Delhi, India in 2022.
E-mail: sguptamits@gmail.com

Mini Sreejeth Born in Kerala, India, she received her B Tech. degree from Mahatma Gandhi University, Kerala, India; her M. Tech. degree from Calicut University, Kerala, India; and her Ph.D. degree from the University of Delhi, New Delhi, India. She joined Delhi College of Engineering (now DTU) as a Senior Lecturer in 2007, where she is presently working as a Professor in the Department of Electrical Engineering. Professor Sreejeth is a Life Member of the Indian Society for Technical Education, New Delhi, India; and a Senior Member of IEEE and WIE. **E-mail: minisreejeth@dce.ac.in**

Madhusudan Singh He received his Ph.D. Degree from University of Delhi, New Delhi, India respectively and is presently a Professor in the Department of Electrical Engineering at Delhi Technological University. Dr Singh is a fellow of the Institution of Engineers (IE), India and of the Institution of Electronics and Telecommunication Engineers, New Delhi, India. He is also a member of the IEEE (USA).
E-mail: madhusudan@dce.ac.in

Narendra Kumar received his B. Tech. degree in Electrical Engineering and M. Tech. degree in Power System and Drives from Aligarh Muslim University, Aligarh, India, in 1984 and 1987, respectively and Ph.D. in Electrical Engineering from University of Roorkee (Presently IIT Roorkee) India. He is currently working as a Professor at Delhi Technological University, New Delhi, India. He is Life Member Systems Society of India, Life Member Indian Society for Technical Education, Senior Member, IEEE, Fellow of Institution of Engineers India, Member Institution of Engineering and technology (IET, UK), Member IEEE USA. **E-mail: dnk_1963@yahoo.com**

.

Authorized licensed use limited to: DELHI TECHNICAL UNIV. Downloaded on June 28,2023 at 06:38:17 UTC from IEEE Xplore. Restrictions apply.

2023 International Conference on Computational Intelligence, Communication Technology and Networking (CICTN) | 979-8-3503-3802-7/23/$31.00 ©2023 IEEE | DOI: 10.1109/CICTN57981.2023.10140272

Multiple Replica Based Auditing of Outsourced Data: A Comprehensive Survey

Akhilesh Kumar Srivastava
(Computer Science & Engineering Department)
(Delhi Technological University)
Delhi, India
joinakhilesh@yahoo.com

Manoj Kumar
(Computer Science & Engineering Department)
(Delhi Technological University)
Delhi, India
mkumarg@dce.ac.in

Abstract—Due to its wide range of services, the cloud has amassed a significant number of consumers in the current environment. Data owners can keep any kind of data on the cloud server, and users can access it whenever they need it. The simplicity of using data that has been outsourced comes with many difficulties. Outsourced data's accuracy and confidentiality are at risk. Because cloud service providers occasionally lie, users have little faith in them. In order to evaluate and record the performance of their cloud vendor, a data owner conducts a cloud audit. Analyzing a cloud vendor's compliance with a predetermined set of controls is the aim of the audit. This article explores numerous cloud auditing techniques, their classifications, advantages, and disadvantages. The main focus of the study is the exploration of Multiple replica-based studies and their performance evaluation. The article discusses the way ahead in the field of multiple replica-based auditing research.

Index Terms—Auditing, Cloud Security, CSP, Data owner, multiple replicas

I. Introduction

For ICT firms in need of resources, data outsourcing is a cost-effective substitute. According to the data, outsourcing will expand 12.7% more in 2020–21 than it did in 2019. [1] [2]. By 2023, it is projected that the global market for data outsourcing will increase to 623.3 billion dollars. Around 94% of businesses utilize the cloud globally. The cloud receives about 30% of the total IT spend for businesses. The public cloud infrastructure is estimated to rise by 35% in 2021, and 100 Zettabytes of additional cloud data are anticipated to be added by 2025. A (CSP), the cloud storage service provider, is an entity outside the data owner's organization that offers outsourcing services (such as storage-as-a-service), whereas an enterprise that outsources its data to the CSP is known as Data owner (DO). Figure 1 depicts a simple data outsourcing scenario with two parties: DO and CSP. When data is outsourced, the CSP makes it available, and the DO is free to conduct any operation (read, write, or delete) on the data. The main benefit of such a scenario is complete control over all outsourced data, however, the absence of other users restricts the use of such settings in a corporate structure. The data owner is the lone user of the outsourced data in the two-party situation depicted in Figure 1. When access is granted, any activity (such as a read, write, or delete) may be carried out on the outsourced data. The main benefit of such a scenario is complete control over all outsourced data, however, the absence of other users restricts the use of such settings in a corporate structure. Figure 2 illustrates a typical enterprise

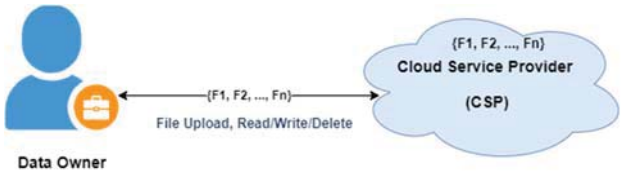

Fig. 1. Party Scenario arrangement for data outsourcing.

In such a configuration, in addition to the DO, end users can also access the data. There are two possible sorts of such settings:

- DO-write-user-read, where the users only read the data (For example, an electronic newspaper).
- User-read-write, where the DO allows end-users for a write operation, such as a blog where the user can read other blogs and write her own.

As a result, users that have write-authorization can write directly to data that has been outsourced. Although preventing direct write from users reduces the likelihood of data corruption, it worsens the bottleneck at the DO. As a result, such settings are inadequate for corporate setup. Users are registered with the DO in such a configuration. The end users receive authentication tokens (read or write) from the DO following successful registration. The end users can immediately read from or write to the outsourced data using these tokens. According to the 2-party scenario depicted in Figure 1, the data owner is the only one who uses the data that was outsourced to them. When access is granted, any activity (such as a read, write, or delete) may be carried out on the outsourced data. The main benefit of such a scenario is complete control over all outsourced data, however, the absence of other users restricts the use of such settings in a corporate structure. The organization that offers data storage as a service to the data owner is known as the cloud service provider (CSP). The individual asking for storage-as-a-service is the data owner. End-users are people who have been given permission by the database's owner to use a subset of the cloud data files. The data owner, who also gives access credentials to registered users, enforces data access control. Users who have permission from the data owners can directly access data files using their access credentials through the CSP. This considerably lessens the data owner's workload. If the data files are kept locally by the data owner, there will be a performance bottleneck due to constrained resources. The users try to access the data items directly from the CSP in order to get around this. Users may be granted read-only or write-only access permission.

Authorized licensed use limited to: DELHI TECHNICAL UNIV. Downloaded on June 14,2023 at 05:22:51 UTC from IEEE Xplore. Restrictions apply.

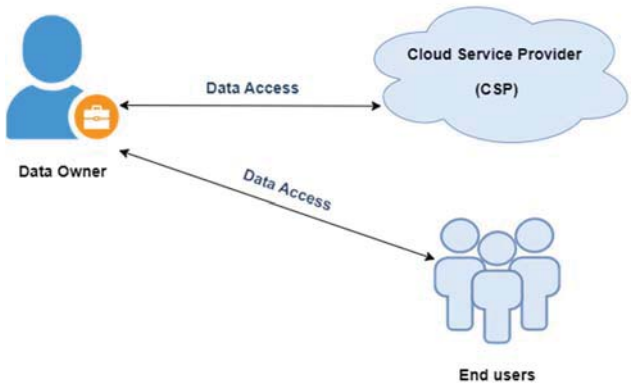

Fig. 2. Party Scenario

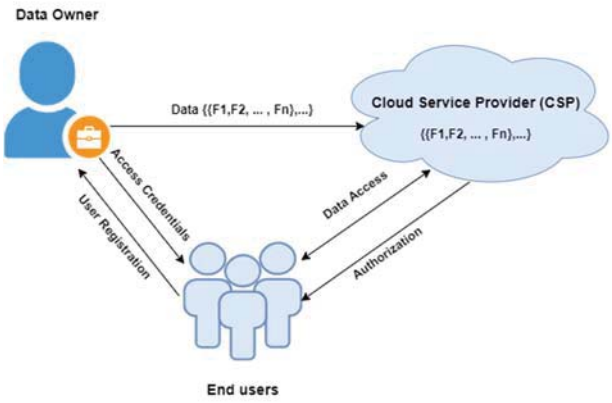

Fig. 3. 3-party system with access rights

A. *Types of 3-party scenario*

There may be two versions of write privileges possible. One of them is write with read [3] and write with or without read [4]. When it comes to the former type, read access is essential for a user in order to have write access, which allows her to examine and modify any pre-existing information. Google Docs, which enables numerous users to edit the same document at once, and blogging on social networking sites are two examples of this sort. Users in the second group are only permitted to write new files to the server and have write access; they are not permitted to read any files. One example of this kind of behavior is Dropbox: wherein it is allowed only to store the data files in the directory. Reading from Dropbox is not permitted.

B. *Considered outsourcing scenario*

We consider the following three parties in the scenario as given in Figure 3. The data that was outsourced belongs to DO. It gives the registered users the proper access credentials and distributes them. Later, it provides the CSP with a set of access credentials. Its data can be read, written to, deleted, and verified. Additionally, a preliminary Service-level Agreement (SLA) is created and communicated with the CSP. The provision of data storage as a service to the DO is given by CSP. It guarantees the accessibility of outsourced data and grants registered users access to such data. The SLA developed by the DO must be adhered to by the CSP. We take into account malicious-but-cautious CSP [5], which could include direct assaults on the outsourced data. End users have accounts with the DO. They get access codes from the DO, which can then be used to obtain data directly from the CSP. even though the final users are registered and known to the DO, they occasionally disregard the mission given by the DO in the interest of efficiency. Because of this, we only partially trust end users. Because CSP cannot be trusted, it might permit illegal data reading or alteration. There are the following security criteria in such an adversary setup:

II. Integrity Audit

Today, it is common practice for Internet apps and protocols to authenticate messages using cryptographic hash algorithms like MD5 or SHA. Despite being fairly simple to execute, these techniques often rely on ad hoc procedures without a careful security evaluation.

A. *Basic Integrity Audition Scheme*

Implementations of hash-based cryptographic message authentication mechanisms are suggested by Bellare et al. [6]. The security of these methods, NMAC and HMAC, has been proven, provided that the underlying hash function satisfies some suitable cryptographic features. Practically all of the hash function's security is preserved by the methods. The use of the hash function (or its compression function) as a "black box" enables simple implementation utilizing hardware or publicly available library code.

B. *2-Party*

Deswarte et al [7], in their work, have examined the integrity issues attached to the files located at the distant servers. Basis integrity examination on the storage servers are not trustworthy. This is because of several reasons. Some of them are as listed as under:

- For verification, the files are required to be downloaded at the DO which actually is not practical. The files were uploaded at the CSP with the reason that the DO did not have this much space.
- Storage servers are open to hackers for various kinds of attacks.
- The paper offered two challenge-response protocol-based integrity check methods:
- Protocol-1 makes several predefined sets of challenges to the servers and the integrity is checked based on the hash computation of the challenged file content.
- Protocol-2, the challenge is produced at random. The verifier already has the hash value for a file stored at the local system for each file.

The idea of provable data possession (PDP) had been developed by Ateniese et al. [8] and permits clients to check that the server actually has the original material without having to retrieve it, which is useful for users who have saved data on unreliable servers. By producing probabilistic proofs of possession from samples of random sets of server-side

Authorized licensed use limited to: DELHI TECHNICAL UNIV. Downloaded on June 14,2023 at 05:22:51 UTC from IEEE Xplore. Restrictions apply.

blocks, the method drastically reduces Input-Output costs. To validate the proof, the client keeps a constant quantity of metadata. By sending a modest, constant amount of data, By using the challenge/response protocol, N/W communication is reduced. Large data sets are thus made possible in distributed storage systems by the PDP paradigm for remote data validation. The PDP scheme's protocol is depicted in Figure 4.

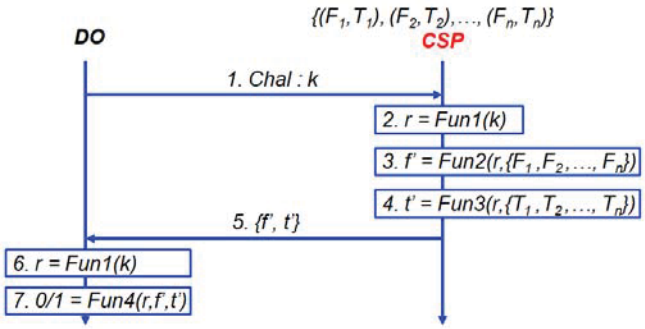

Fig. 4. Provable Data Possession scheme

Only static (or append-only) files are supposedly protected by the PDP systems, according to Erway et al. [9]. The PDP extended concept, named Dynamic Proven Data Possession (DPDP), was introduced by the authors of this article. They allowed verifiable updates on the uploaded data. Additionally, they provide a definitional framework and DPDP structures. They employ ranked authenticated dictionaries that are a new iteration. They have shown how to apply the DPDP approach using version control and external file systems. These solutions have a number of shortcomings.

- To start, because of the increased volume of data requests for the audit, DOs will incur large computing costs because the process of verification is completely handled by the DOs as the private auditing.
- Second, DOs are typically assumed to be entirely trustworthy based just on CSPs. The DO must admit that it cannot entirely rely on CSP. A CSP might, for example, conceal instances of data corruption in order to preserve its reputation.

C. 3-Party

Using Popa et al [10] Give a plan as an illustration. According to this system, each outsourced data file is assigned a probability (or priority) based on the degree of sensitivity. They claim that there are four different levels of sensitivity. Each audit cycle includes an audit of the sensitive data blocks. Consider the following data files: F1, F2, and F3. Since F2 is the most delicate of these, a high probability value is given to it. On the other side, F3 is the least sensitive and has a low probability value because of this. In the audits, file F2 will almost always be audited, whereas F3 will only seldom be audited. The data owner, CSP, and end users are the 3 stakeholders involved in this system. The read/write actions performed by end users cause the outsourced data file to be updated on a regular basis. Each time an R/W request is made, the CSP verifies the action by giving the reader their seal of approval (or writer). After receiving it, the end user sends the consent to the auditor. After obtaining all of the consents, the auditor verifies them and arranges them in order of their degree of sensitivity. The consent are now verified or audited because of how important the data files are. The benefit of this method is that it can manage dynamic data on the files. Its drawback is that it merely provides probabilistic evidence. The fact that it uses an asymmetric cryptosystem and requires a sizable amount of storage from the data owner in order to store the attestations is another drawback. Additionally, there is a high communication cost because the data owner receives each attestation. No one, not even the authorized user, should have unrestricted access to edit work that has been outsourced, according to Kumar et al. [11]. Additionally, the CSP should not be used to allow a user whose access has been revoked to alter the old written data files. The authors suggested two techniques based on audits to assure the data owner that no unauthorized writes have taken place.

D. Third Party Auditor

To get over the limitations, many researchers, including Nayak et al. [12], Li et al. [13], and Chavan et al. [14], have created a Third-Party-Auditor (TPA) to carry out public auditing. In Figure 5: Third-Party based integrity audit system architecture is given Yu et al [15]. The number of entities in the third-party-based data integrity audit is given as under:

- Users : DOs and authorized users are the two types of users (AUs). In a CSP, DOs can do dynamic data operations and store huge data on the CSP. An AU is a list of people authorized to perform data access on the stored data (by DOs at the CSP).
- T P A : A TPA may accept audit commands given by DOs and conduct audits on their behalf.
- CSP : Cloud Service provider gives the DOs ample space to store the data.

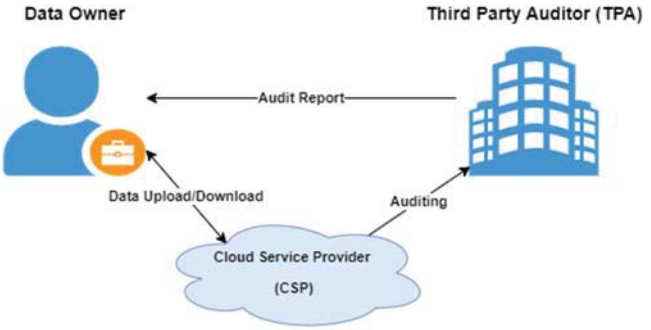

Fig. 5. Auditing of outsourced Data Integrity using TPA

In order to accept delegates from users with limited resources and complete outsourced computation in accordance with user requirements, it is anticipated that TPA has sufficient processing capacity. Furthermore, it is irrational to assume that the TPA is a devout and trustworthy organization in the context of real-world application. A TPA might even plan something with a CSP or DO. A centralized system like this also has the following two issues:

- Single point of failure: When the TPA is hacked or compromised, auditing mechanisms cannot operate as intended.
- A TPA's performance is constrained by its inability to meet the concurrent requests of multiple users for detailed audits.

Authorized licensed use limited to: DELHI TECHNICAL UNIV. Downloaded on June 14,2023 at 05:22:51 UTC from IEEE Xplore. Restrictions apply.

E. Blockchain based Audit

As the TPAs will be the single point of failure for the audit and so too the DOs (if they themselves perform the audit), and the TPAs cannot fully be trusted as they can collude with external entities, There are many researchers who suggested the Blockchain as the possible solution for the audit. Refer to Figure 6. Nakamoto 6 was the first one to introduce the blockchain. There are many unmatchable properties of blockchain [16], such as decentralisation, tamper − proofness, immutability, and traceability, which have had a significant impact on RDIA systems [17], [18], [19]. By utilizing the blockchain, many researchers have sought to increase the security and dependability of RDIA. An example of BC-oriented integrity audit architecture is shown in Figure 6. Specialized nodes on the blockchain network correspond to CSPs & DOs [20]. A third-party audit platform (Blockchain) that sits between the CSP & the user during the process of integrity audit, transmits and records the user and CSP contacts. When users submit a claim to the arbitration authority in a dispute with CSP, blockchain records may be used as a reliable form of evidence. All participants work together to maintain the blockchain network, and regular user and CSP behavior monitoring ensures the system runs smoothly.

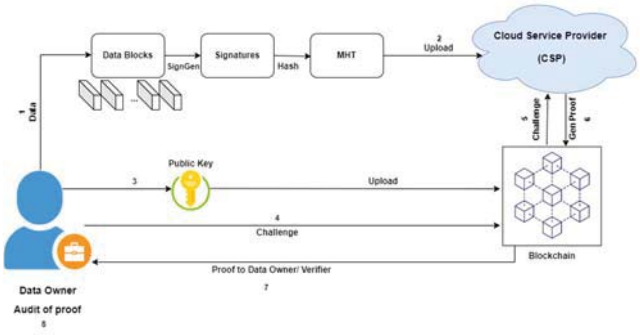

Fig. 6. Blockchain-based Integrity Audit

When compared to Third Party oriented integrity audit techniques, the following are a few ways why utilizing blockchain for integrity audits has advantages:

1) Decentralization : Instead of being managed by a single central entity, miner nodes maintain the distributed digital ledger known as the blockchain. Any miner can be given RDIA work by DOs. Upon receipt of instructions from DOs, a team of miners rather than a single TPA performs auditing functions. This significantly lowers the danger of a single point of failure.

2) T ransparency : Due to the public accessibility of blockchain records, authorized parties and miners can access them and verify the veracity of auditing findings.

3) Resistancetotampering : Blocks' hash value is stored in each block of a blockchain. To determine whether the data that was outsourced was altered, DOs can publicly check the hash value. This may make it difficult for CSP and TPA to work together to affect auditing results.

4) Non−repudiation : A blockchain is capable of recording data operations and auditing histories. When DOs may examine the logs to locate them, it is difficult for potential malevolent CSPs or auditors to refute their malicious activity. However, there are significant limitations to the BDIA proposals that should not be ignored. For instance, because each transaction must be checked by every minor to establish a consensus, increasing auditing delay, the efficiency of auditing is actually reduced.

F. Distributed Audit

Based on the presently distributed databases used in various applications in the real world, Dwivedi et al.'s [21] [22] suggestion for an auditing technique that audits in a distributed manner to achieve better efficiency. It can also make it simpler to quickly audit all of the files. The distributed audit has significant advantages, it eases the auditor's workload in terms of processing. The authors make the assumption that all secure channel communication takes happen between the CSP and auditor and that end users frequently access each outsourced data file. The outsourced data files are accessible to customers on demand in the scenario under discussion. With their authorization, they routinely perform read-and-write operations.

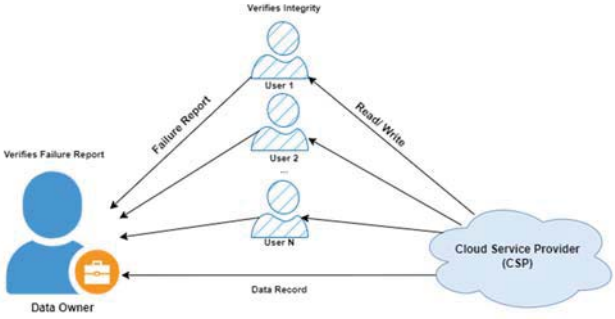

Fig. 7. Distributed and Lazy Audit

End users are the party outside the control, hence the data owner cannot fully rely on them. The writers took into account that end users are only partially trusted, which means that while they are obligated to obey the data owner's instructions, duties may get put off. Figure 7 shows the typical distributed audit. The protocol for the distributed audit technique is shown in Figure 8.

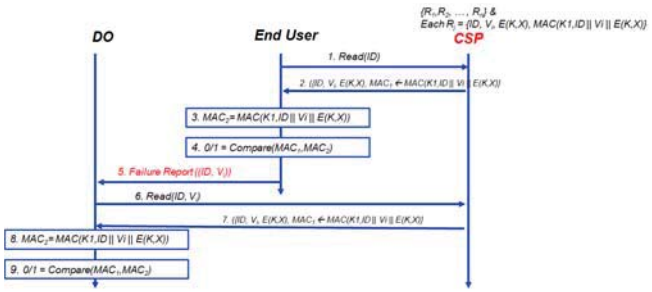

Fig. 8. Distributed Audit Timing Diagram

III. MOTIVATION FOR MULTIPLE REPLICAS

If the server's data becomes tainted in any way, the presence of data at multiple replicas will be helpful to restore the data. Another motivation gets generated from nature that we have considered i.e. malicious but cautious CSP. The write action is carried out in the current data outsourcing scenario in [8], [21] on any server that is close to the writer, and the CSP then replicates the data record on other servers. The data might not be replicated across all servers by an unreliable CSP. For instance, if there are k total servers, it might keep accurate data on server 1 close to the writer while corrupting or deleting the data record on the other k 1 servers for storage effectiveness or financial gain. The CSP will give data from the server

Authorized licensed use limited to: DELHI TECHNICAL UNIV. Downloaded on June 14,2023 at 05:22:51 UTC from IEEE Xplore. Restrictions apply.

where the data is properly stored after it receives the request for data access from authorized users. The user can experience a delayed response from the CSP in this situation. For all copies of an outsourced data record, the data owner, therefore, needs data rectification assurance.

IV. MULTIPLE REPLICA BASED AUDITING

Deswarte et al. [23] introduced data integrity audits in the distributed model for the first time. They gave a rudimentary checksum for integrity audit remotely utilizing distributed servers. The user will periodically ask the server to determine the checksum of the files. The user will then receive the checksum from the server. User will make a comparison of both checksums, one received from the server and another one saved on its local machine, Hash functions are required for checksum calculation. Thus, it is not yet possible to confirm the scheme's security. This conventional technique is also ineffective and open to numerous attackers. In order to prevent attacks, the verifier additionally needs to locally store a table of checksums on file contents, which increases the overall storage overhead. Additional criteria weren't stated in their paper than these two. Due to the fact that their protocol sends a modest, constant amount of data while the network communication is constrained, Ateniese et al. [24] also consider the distributed storage system. Their method is no longer used in multiple replicas protocols because it was later shown to be hazardous in the course of a multi-server collusion attack. In Curtmola et al [25] 's multiple replicas PDP (MRPDP) scheme, seceral copies of the data is made to get stored at multiple servers. The other copies can act as backups when a file on one server is corrupted. Computingly, storing several copies proved more effective than storing a single block. On the client side, the solution can result in more storage and communication overhead. Moreover, it did not support open auditing. They failed to meet any more criterion besides these. Hao et al. [26] suggested another protocol that makes MRPDP as the base and it provides public verifiability based on the work of MR-PDP [25]. They built the technique using homomorphic-authentication-tags which are BLS signaturebased. The protocol has been shown to be both secure and effective through security study and performance analysis. Data storage integrity auditing for a distributed hybrid-cloud was taken into consideration by Zhu et al. [27]. They combined the results from several servers into a single final result and provided it to the users using homomorphic verification response (HVR) and hash indexing (HIH) approaches. The experiment confirmed the potency of their remedy. They provided systems that supported both dynamic data modification and privacy protection. However, homomorphism may have prevented users from knowing whose server their file was on when some issues occurred. Their plan called for a negligible, constant level of communication overhead, but it ignored criteria like storage overhead and other requirements. The PDP system should be useable and secure in a collaborative cloud environment, and its communication and computing overhead should be lower than it would be in a non-cooperative environment, they then emphasized in the publication [28]. Bilinear mapping procedures were utilized in the work [28] to build a technique that permitted publicauditing however this scheme was not efficient for heavy-sized files. For distributed multiple replicas, He et al. [29] presented an innovative and effective data possession checking (DMRDPC) approach, for reducing the communication cost among the servers at various sites. This was done by making the check order scheduling of numerous data duplicates more effective. The computing overhead was the major factor on which they concentrated. In a distributed setting, more replicas and servers could lead to greater complexity. Users may also experience problems with data location transparency. Etemad et al. [30] suggested a method to solve this problem. Its complexity is independent of the servers counts and replica counts. They began by considering the many users scenario for tried and true version-control-systems (VCS). Computation cost was the only factor considered in their article. PDP Due to the public key architecture, protocol necessitates the distribution and administration of public key certificates, which added a significant cost. Using ID-based public key cryptography instead of cumbersome certificate maintenance could increase efficacy. Wang [31] presented an identity-based distributed verifiable data possession approach to offer ID-based authentication in distributed systems (ID-DPDP). It was a bilinear pairing-based security model that was demonstrated to be secure using the Diffie-Hellman presumption. Remaining criteria are not covered in this study; just computation efficiency and security are. Long et al. [32] A verifiable data possession strategy based on full-nodes of an AVL tree is described in this article as a way to safeguard its security. The suggested method first implements a Henon chaotic map for the node calculation of the AVL tree, after which the AVL tree verifies the data's placement in the cloud. An AVL tree can increase the search efficiency of the data block and shorten the authentication path because it can maintain balance even when many dynamic actions are performed on the cloud data. Analysis and simulation findings show that it is capable of achieving both high security and efficiency. The approach could facilitate dynamic operations on cloud-based data, increase search efficiency, and confirm the data's position by balancing AVL trees. It was demonstrated that this model may provide security with reduced storage and communication cost. This study enables dynamic operation and primarily focuses on measuring computation efficiency. Most PDP protocols believe that only one cloud storage server should hold all copies. Li et al. [33] offered an identity(ID)-based Provable data possession method of several copies of the same data on different CSS to improve security and effectiveness. These CSSs collaborate to produce the ondemand data. Storage and retrieval methods are similar in a way that collaboration among the CSSs is required in both. All copies can have their integrity checked simultaneously thanks to the homomorphic verifiable tags. They employ the computation Diffie-Hellman (CDH) hard problem to show how secure their system is. The system was shown effective through the experimental results and analysis by the authors. The primary drawback of Public Key Infrastructure is the enormous administrative burden of managing and computing certificates (PKI). Zhou et al. [34] suggested a certificateless signatures (referred to as MDSS). This eliminates the idbased signatures' key escrow issue as well as the costly certificate administration overhead. Additionally, They claim that by enhancing the conventional Merkle-Hash-Tree (MHT), they have made it possible for batch updates for multi-copy storage, enabling the communication cost. This enables the dynamic changes free from multi-copies. They suggested a variable replica number storage technique that would allow users to select the block's replica no. in order to satisfy the flexible storage need. They employed verification of signature to stop hostile TPAs of framing trustworthy CSPs in light of the possibility that auditors would do so. The random oracle model's security

Authorized licensed use limited to: DELHI TECHNICAL UNIV. Downloaded on June 14,2023 at 05:22:51 UTC from IEEE Xplore. Restrictions apply.

study concludes by demonstrating the security of this approach. The current public audit schemes still have a number of issues, despite allowing users to permit TPAs to confirm the accuracy of uploaded data. The majority of current solutions, to start, are built based on the conventional or ID-based PKI. Key escrow or certificate management are also key issues. Moreover, they do not allow user identity tracking and dynamic data updating for group users. Next, block's/file's replicas are kept on a CSS. Every replica will be harmed if the cloud server fails. TPA may conspire with cloud servers to mislead users or stray from the public audit protocol in real-world situations. Yang et al. [35], Miao et al. [36] proposed solutions to these issues. Their scheme was taking Blockchain as a base. Their solution provides the dynamically updating hash-table and modification-record-table in order to ensure the dynamic updations of user's data and ID tracking. As each duplicate is kept on a distinct cloud server, it is possible to simultaneously audit each replica's integrity. Also, they created fair challenge information using the unpredictable nature of blockchain blocks, prohibiting malevolent TPAs and CSPs from working together to fool users. Users may easily audit the behavior of TPAs because the blockchain records the audit results. Further analysis has shown that these schemes are very good with respect to the cost of Communication and the cost of computations. The schemes were proven secure too. The necessity of Electronic-Medical-Record (Cloud-based) System has been expounded upon by Zhou et al. [37]. Data ownership will be forfeited by the owner having uploaded the medical record-based information onto the CSP, and confidential information may be accessed or altered by unauthorized parties. For a cloud-based EMR system, they recommended the possession of several copies of verified data to solve the problem. The improved and dynamic structuring of the traditional Merkle-Hash-Tree (MHT) was proposed by the authors. This was done to record the data updates effectively. Their experiment used a random-masking method to produce distinct duplicate blocks of a single block. In comparison to current systems, the authors assert that their solution has lower communication and processing costs. Gudeme et al. [38] suggested another MR scheme for public auditing that was certificateless. Their plan makes use of the replica version table, a data structure, to support shared data dynamics. The revocation of untrusted/irresponsible users from ACL Group was also included in this study. They demonstrate that their system is provably safe against adversaries of types I, II, and III. For the integrity check of multi-copy data, users just need to run batch verification on the failure reports received from the TPAs. This stops malevolent TPA from falsifying auditing results. Another Blockchain based technique was introduced by Tian et al.[[39]]. to produce random and unrefutable challenge messages. Moreover, It is less expensive to store data when several replica files share a dynamic structure, as dynamic updates typically perform at O (1). This approach makes it possible to batch verify any number of replicas from numerous people, which improves the efficiency of auditing. Furthermore, when batch auditing fails, the recursive performance of the Lucas sequence can be used to find corrupted data files. Experimental results and theoretical analysis show that our design can successfully implement batch audits and dynamic updates. The study of Li et al [40] suggested a smart contractbased non-interactive multi-replica proven data possession scheme. Under the system, the smart contract takes the place of TPA and offers trustworthy conditions for integrity-test, making the verification process transparent, impervious to tampering, traceable, and periodically automatic. Transaction of a blockchain involves a fee. The idea of noninteractive is presented by authors in order to lower this fee carried on by the regular blockchain-based audit cycles. Smart contracts, also include payment regulations.

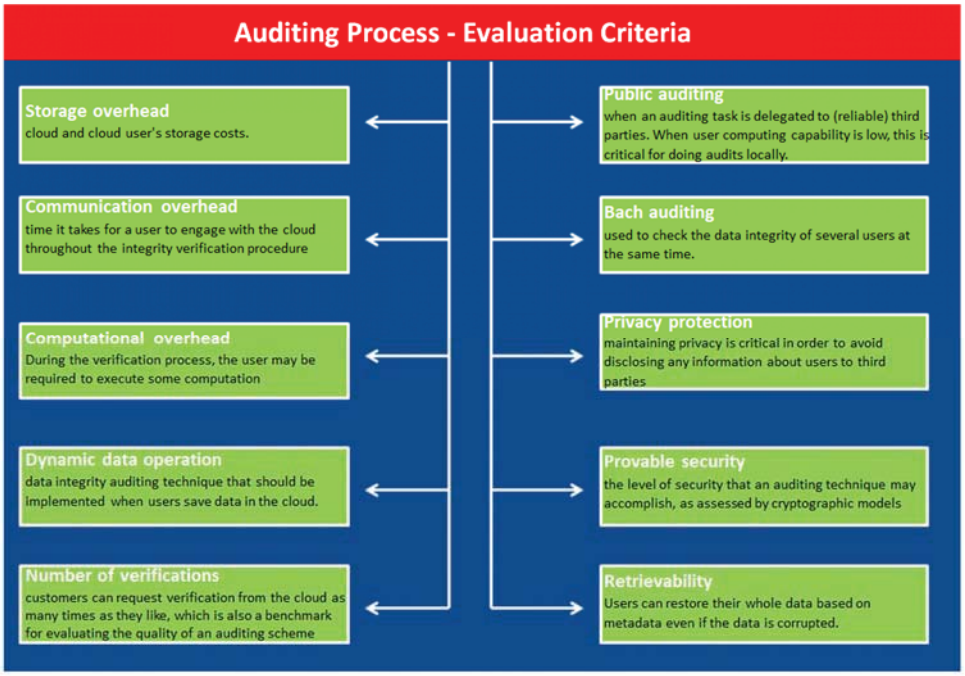

Fig. 9. Parameters of observation for auditing schemes

There are multiple criteria for the evaluation of auditing schemes. Some of these are listed as if figure 10. The table shows the comparative analysis of multiple replica-based auditing based on various parameters. The parameters which are studied for multiple replica-based auditing are listed as under:

Authorized licensed use limited to: DELHI TECHNICAL UNIV. Downloaded on June 14,2023 at 05:22:51 UTC from IEEE Xplore. Restrictions apply.

1. Low storage
2. Communication and computation efficiency
3. Dynamic data operation
4. Unlimitation of verification
5. Public auditing
6. Batch auditing
7. Privacy preservation
8. Provable security
9. Error Tracking

Fig. 10. Parameters of MR-based auditing

Paper	Year of Publication	Title	Low storage	Communication & computation efficiency	Dynamic data operation	Unlimitation of verification	Public auditing	Batch auditing	Privacy preservation	Provable security	Error Tracking
Deswarthe et al.	2003	Remote Integrity Checking	X	X						X	
Ateniese et al.	2011	Remote Data integrity checking using provable data possession		√						X	
Curtmola et al.	2008	Multiple Replica Provable Data Possession		X			X				
Wang et al.	2009	Ensuring data storage security in Cloud Computing			√		X			√	√
Zhu et al.	2010	Efficient Provable Data Possession for Hybrid Clouds		X	√		√		√		
He et al.	2012	Distributed Data Possession Checking for Securing Multiple Replicas in Geographically-dispersed cloud		√							
Basoum et al.	2012	Integrity Verification of Multiple Data Copies over Untrusted Cloud Servers					√			√	√
Etemad et al.	2013	Transparent, Distributed, and Replicated Dynamic Provable Data Possession		√							
Wang et al.	2015	Identity-Based Distributed Provable Data Possession in Multicloud Storage		√						√	√
Rakesh et al.	2017	Distributed Scheme to Authenticate Data Storage Security in Cloud Computing		√	√						√
Li et al.	2019	A Secure Privacy-Preserving Cloud Auditing Scheme with Data Deduplication		√	√						
Hao et al.	2010	A Multiple-Replica Remote Data Possession Checking Protocol with Public Verifiability		√			√			√	
Li et al.	2022	Efficient Identity-Based Provable Multi-Copy Data Possession in Multi-Cloud Storage	√	√	X		√	√			
Zhou et al.	2022	Efficient Certificateless Multi-Copy Integrity Auditing Scheme Supporting Data Dynamics	√		√					√	
Yang et al.	2020	Multi-Replica and Multi-Cloud Data Public Audit Scheme Based on Blockchain	X		√					√	
Miao et al.	2022	Blockchain assisted multi-copy provable data possession with faults localization in multi-cloud storage	X		√					√	
Zhou et al.	2021	Multicopy provable data possession scheme supporting data dynamics for cloud-based Electronic Medical Record system	X		√					√	
Gudeme et al.	2021	Certificateless multi-replica public integrity auditing scheme for dynamic shared data in cloud storage	√		√					√	
Tian et al.	2022	An efficient auditing scheme with a novel structure for multiple replicas	√		√					√	
Li et al.	2022	A Noninteractive Multireplica Provable Data Possession Scheme Based on Smart Contract	X		√					√	

Fig. 11. Comparison chart of MR Schemes

V. CONCLUSION

Due to its highly centralized system architecture, the cloud computing model is subject to the same security flaws as centralized data centers. In contrast to conventional data centers, the cloud also has issues with access control, privacy, trust, device management (multiple CSPs), user administration (including CSP management), and device management. Integration of blockchain with clouds could result in efficient solutions for cloud computing model security services. The system's overall scalability is increased by the cloud platform, which also enables significant analysis support. It is necessary to improve cloud computing's security and deal with its trust issues. The authors of this study have reported the results of numerous multiple replica based/ Distributed integrity auditing system approaches. Two distinct techniques of categorizing auditing schemes have been offered by the authors and are indepth examined in the paper. Several auditing implementation strategies for the three-party scenario have been provided by the authors, along with their benefits and drawbacks. The auditing plan should be chosen based on the necessity, and importance of the data, and the organization's budget. The accountability-based system was suggested in the survey as a way to hold the CSP accountable. The authors displayed the comparison table of designs and assessed them using the standards shown in Figure 5. In addition to the aforementioned, the authors also covered future integrity audit study directions in relation to the many described parameters.

REFERENCES

[1] Cloud adoption statistics for 2022. https://webtribunal.net/blog/cloudadoption-statistics/gref. Accessed on . Accessed: 22.11.2022.

[2] Take the 2021 state of european tech survey. https://www.orrick.com/en/News/2021/09/Take-the-2021-State-ofEuropean-Tech-Survey. Accessed: 22.11.2022.

[3] Sabrina De Capitani di Vimercati, Sara Foresti, Sushil Jajodia, Giovanni Livraga, Stefano Paraboschi, and Pierangela Samarati. Enforcing dynamic write privileges in data outsourcing. Computers & Security, 39:47–63, 2013. 27th IFIP International Information Security Conference.

Authorized licensed use limited to: DELHI TECHNICAL UNIV. Downloaded on June 14,2023 at 05:22:51 UTC from IEEE Xplore. Restrictions apply.

[4] Mariana Raykova, Hang Zhao, and Steven M. Bellovin. Privacy enhanced access control for outsourced data sharing. In Angelos D. Keromytis, editor, Financial Cryptography and Data Security, pages 223–238, Berlin, Heidelberg, 2012. Springer Berlin Heidelberg.

[5] Myrto Arapinis, Sergiu Bursuc, and Mark Ryan. Privacy-supporting cloud computing by in-browser key translation. Journal of Computer Security, 21(6):847–880, 2013.

[6] Hugo Krawczyk, Mihir Bellare, and Ran Canetti. Hmac: Keyed-hashing for message authentication. Technical report, 1997.

[7] Yves Deswarte, Jean-Jacques Quisquater, and Ayda Sa¨ıdane. Remote Integrity Checking, pages 1–11. Springer US, Boston, MA, 2004.

[8] Giuseppe Ateniese, Randal Burns, Reza Curtmola, Joseph Herring, Lea Kissner, Zachary Peterson, and Dawn Song. Provable data possession at untrusted stores. In Proceedings of the 14th ACM conference on Computer and communications security, pages 598–609. Acm, 2007.

[9] C. Chris Erway, Alptekin Kupc¸ ¨ u, Charalampos Papamanthou, and ¨ Roberto Tamassia. Dynamic provable data possession. ACM Trans. Inf. Syst. Secur., 17(4), apr 2015.

[10] Raluca Ada Popa, Jacob R. Lorch, David Molnar, Helen J. Wang, and Li Zhuang. Enabling security in cloud storage slas with cloudproof. In Proceedings of the 2011 USENIX Conference on USENIX Annual Technical Conference, USENIXATC'11, page 31, USA, 2011. USENIX Association.

[11] Naveen Kumar and Anish Mathuria. Improved write access control and stronger freshness guarantee to outsourced data. In Proceedings of the 18th International Conference on Distributed Computing and Networking, ICDCN '17, New York, NY, USA, 2017. Association for Computing Machinery.

[12] Sanjeet Kumar Nayak and Somanath Tripathy. Sepdp: Secure and efficient privacy preserving provable data possession in cloud storage. IEEE Transactions on Services Computing, 14(3):876–888, 2021.

[13] Aiping Li, Shuang Tan, and Yan Jia. A method for achieving provable data integrity in cloud computing. The Journal of Supercomputing, 75(1):92–108, 2019.

[14] Nikhil Sushil Chavan and Deepak Sharma. Secure proof of retrievability system in cloud for data integrity. In 2018 Fourth International Conference on Computing Communication Control and Automation (ICCUBEA), pages 1–5, 2018.

[15] Yong Yu, Man Ho Au, Yi Mu, Shaohua Tang, Jian Ren, Willy Susilo, and Liju Dong. Enhanced privacy of a remote data integrity-checking protocol for secure cloud storage. International Journal of Information Security, 14(4):307–318, 2015.

[16] Satoshi Nakamoto. Bitcoin: A peer-to-peer electronic cash system. Decentralized Business Review, page 21260, 2008.

[17] Yong Yu, Man Ho Au, Giuseppe Ateniese, Xinyi Huang, Willy Susilo, Yuanshun Dai, and Geyong Min. Identity-based remote data integrity checking with perfect data privacy preserving for cloud storage. IEEE Transactions on Information Forensics and Security, 12(4):767–778, 2017.

[18] Yong Yu, Yannan Li, Junfeng Tian, and Jianwei Liu. Blockchain-based solutions to security and privacy issues in the internet of things. Wireless Commun., 25(6):12–18, dec 2018.

[19] Yannan Li, Yong Yu, Geyong Min, Willy Susilo, Jianbing Ni, and KimKwang Raymond Choo. Fuzzy identity-based data integrity auditing for reliable cloud storage systems. IEEE Trans. Dependable Secur. Comput., 16(1):72–83, jan 2019.

[20] Haiyang Yu, Zhen Yang, and Richard O Sinnott. Decentralized big data auditing for smart city environments leveraging blockchain technology. IEEE Access, 7:6288–6296, 2018.

[21] Amit Kumar Dwivedi, Naveen Kumar, and Mayank Pathela. Distributed and lazy auditing of outsourced data. In International conference on distributed computing and internet technology, pages 364–379. Springer, 2020.

[22] Amit Kumar Dwivedi, Naveen Kumar, and Manik Lal Das. On accountable and distributed audit of outsourced data. In Intelligent Sustainable Systems: Selected Papers of WorldS4 2022, Volume 1, pages 663–673. Springer, 2023.

[23] Yves Deswarte, Jean-Jacques Quisquater, and Ayda Sa¨ıdane. Remote integrity checking: How to trust files stored on untrusted servers. In Integrity and Internal Control in Information Systems VI: IFIP TC11/WG11. 5 Sixth Working Conference on Integrity and Internal Control in Information Systems (IICIS) 13–14 November 2003, Lausanne, Switzerland, pages 1–11. Springer, 2004.

[24] Giuseppe Ateniese, Randal Burns, Reza Curtmola, Joseph Herring, Osama Khan, Lea Kissner, Zachary Peterson, and Dawn Song. Remote data checking using provable data possession. ACM Transactions on Information and System Security (TISSEC), 14(1):1–34, 2011.

[25] Reza Curtmola, Osama Khan, Randal Burns, and Giuseppe Ateniese. Mr-pdp: Multiple-replica provable data possession. In 2008 the 28th international conference on distributed computing systems, pages 411–420. IEEE, 2008.

[26] Zhuo Hao and Nenghai Yu. A multiple-replica remote data possession checking protocol with public verifiability. In 2010 second international symposium on data, privacy, and E-commerce, pages 84–89. IEEE, 2010.

[27] Yan Zhu, Huaixi Wang, Zexing Hu, Gail-Joon Ahn, Hongxin Hu, and Stephen S Yau. Efficient provable data possession for hybrid clouds. In Proceedings of the 17th ACM conference on Computer and communications security, pages 756–758, 2010.

[28] Yan Zhu, Hongxin Hu, Gail-Joon Ahn, and Mengyang Yu. Cooperative provable data possession for integrity verification in multicloud storage. IEEE transactions on parallel and distributed systems, 23(12):2231– 2244, 2012.

[29] Jing He, Yanchun Zhang, Guangyan Huang, Yong Shi, and Jie Cao. Distributed data possession checking for securing multiple replicas in geographically-dispersed clouds. Journal of Computer and System Sciences, 78(5):1345–1358, 2012.

[30] Mohammad Etemad and Alptekin Kupc¸ ¨ u. Transparent, distributed, and ¨ replicated dynamic provable data possession. In Applied Cryptography and Network Security: 11th International Conference, ACNS 2013, Banff, AB, Canada, June 25-28, 2013. Proceedings 11, pages 1–18. Springer, 2013.

[31] Huaqun Wang. Identity-based distributed provable data possession in multicloud storage. IEEE Transactions on Services Computing, 8(2):328–340, 2014.

[32] Min Long, You Li, and Fei Peng. Dynamic provable data possession of multiple copies in cloud storage based on full-node of avl tree. International Journal of Digital Crime and Forensics (IJDCF), 11(1):126–137, 2019.

[33] Jiguo Li, Hao Yan, and Yichen Zhang. Efficient identity-based provable multi-copy data possession in multi-cloud storage. IEEE Transactions on Cloud Computing, 10(1):356–365, 2022.

[34] Lei Zhou, Anmin Fu, Guomin Yang, Huaqun Wang, and Yuqing Zhang. Efficient certificateless multi-copy integrity auditing scheme supporting data dynamics. IEEE Transactions on Dependable and Secure Computing, 19(2):1118–1132, 2022.

[35] Xiaodong Yang, Xizhen Pei, Meiding Wang, Ting Li, and Caifen Wang. Multi-replica and multi-cloud data public audit scheme based on blockchain. IEEE Access, 8:144809–144822, 2020.

[36] Ying Miao, Qiong Huang, Meiyan Xiao, and Willy Susilo. Blockchain assisted multi-copy provable data possession with faults localization in multi-cloud storage. IEEE Transactions on Information Forensics and Security, 17:3663–3676, 2022.

[37] Lei Zhou, Anmin Fu, Yi Mu, Huaqun Wang, Shui Yu, and Yinxia Sun. Multicopy provable data possession scheme supporting data dynamics for cloud-based electronic medical record system. Information Sciences, 545:254–276, 2021.

[38] Jaya Rao Gudeme, Syam Kumar Pasupuleti, and Ramesh Kandukuri. Certificateless multi-replica public integrity auditing scheme for dynamic shared data in cloud storage. Computers Security, 103:102176, 2021.

[39] Junfeng Tian and Qianqian Song. An efficient auditing scheme with a novel structure for multiple replicas. The Journal of Supercomputing, 78(17):18994–19019, 2022.

[40] Zhengwen Li, Yang Xin, De Zhao, and Yixian Yang. A noninteractive multireplica provable data possession scheme based on smart contract. Security and Communication Networks, 2022, 2022.

Authorized licensed use limited to: DELHI TECHNICAL UNIV. Downloaded on June 14,2023 at 05:22:51 UTC from IEEE Xplore. Restrictions apply.

ResearchGate

See discussions, stats, and author profiles for this publication at: https://www.researchgate.net/publication/371158813

NUMERICAL MODELLING OF GEOSYNTHETIC REINFORCED RETAINING WALL

Conference Paper · May 2023

CITATIONS
0

READS
7

2 authors, including:

Nikhil Gautam
Delhi Technological University
1 PUBLICATION **0** CITATIONS

SEE PROFILE

All content following this page was uploaded by Nikhil Gautam on 30 May 2023.

The user has requested enhancement of the downloaded file.

NUMERICAL MODELLING OF GEOSYNTHETIC REINFORCED RETAINING WALL

Anil Kumar Sahu[1][0000-1111-2222-3333] and Nikhil Gautam[2][1111-2222-3333-4444]

[1] Professor, Dept. of civil engineering, Delhi Technological University, New Delhi, India
[2] Research scholar, Delhi Technological University, New Delhi, India
nikhilgautam19@gmail.com

Abstract. Recently, the use of retaining walls has been seen widely and are so much in use. The use of mechanically stabilized earth walls (MSE) has picked up pace in recent years. Practical uses of MSE walls are in making underpasses, to support bridges, in other civil engineering purposes. The present study focuses on the practicality of these walls and to design MSE walls reinforced with geotextile to give strength and long term stability to the structure. The objective of the present study is to perform a numerical analysis of geotextile reinforced MSE wall and to verify it via the theoretical approach using suitable methods available. This model is made on Plaxis 2d software and analyzed by changing the spacing and the lap length of the geotextile layers. It was found that using geotextile as a reinforced material in walls not only increases stability but also reduces cost of construction significantly. Different Layer combinations of geotextile in soil were made and studied and the suitable number of layers required to provide sufficient stability is concluded.

Keywords: Geosynthetic reinforced retaining wall, Plaxis 2D, Numerical modeling.

1 Introduction

The MSE wall is a composite structure and are widely used in civil engineering Projects. The use of geotextile in it gives an edge over the stability and reduced costs at a significant rate. Soil, especially granular, is relatively strong under compressive stresses. When reinforced, significant tensile stresses can be carried by the reinforcement, resulting in a composite structure which possesses wider margins of strength. This extra strength means that steeper slopes can be built. Geotextiles have been utilized in the construction of reinforced soil walls since the early 1970's. Geotextile sheets are used to wrap compacted soil in layers producing a stable composite structure. Geotextile-reinforced soil walls somewhat resemble the popular sandbag walls which have been used for some decades. However, geotextile-reinforced walls can be constructed to a significant height because of the geotextile's higher strength and a simple mechanized construction procedure.

2 Numerical Model and analysis

In this study, a retaining wall reinforced with geotextile is analyzed in plaxis 2d software. Eight phase simulation is carried out in the analysis. first phase is while constructing the foundation and remaining phases are after application of load with varying spacing. Plaxis is a finite element software. To investigate different stability, deformation, ground water flow etc. This software has been developed and used exceptionally in geotechnical, structural engineering.

2.1 Finite element material properties

This specific model generally requires five input parameters. They are Modulus of elasticity, poisson's ratio, angle of friction, cohesion and dilatancy angle. The properties of the backfill and the foundation soil are presented in Table 1. Length of the geotextile taken is 5m. With the mohr coulomb failure criterion, the mc model depicted a linearly elastic–perfectly plastic material; the characteristics for this model are stated in table 3.1.

Table 1. Material Properties (Kibria et al. 2014; Kong et al. 2013)

Properties	Backfill soil	Foundation soil
γ_{unsat} (kg/m^3)	19	16
γ_{sat} (kg/m)	20	16
Elastic Modulus E (kN/m^2)	12500	5500
Cohesion(kN/m^2)	1	8.45
Internal Angle of Friction φ (°)	34	27
Angle of Dilation ψ(°)	4	0

Table 2. Finite Element Plate Properties (Kibria et al. 2014; Kong et al. 2013)

Properties	Foundation block	Concrete panel
Flexural Rigidity EI (kN m^2/m)	3.7x10^5	1.1x10^4

Normal Rigidity EA (kN/m)	$1.8x10^7$	$5x10^6$
Weight W(kN/m/m)	0.15	38

Table 3. Properties of non woven geotextile (ASTM D5199)

Properties	
Mass (g/m^2)	200
Thickness, t (mm)	1.78
Apparent Opening Size, AOS (mm)	0.11
Permittivity, Ψ (s^{-1})	1.96
Cross-plane permeability, k (m/s)	3.5×10^{-3}
Ultimate tensile strength, T_{ult} (KN/m)	9.28

Note: The thickness was measured according to ASTM D5199. The first and second values of tensile properties correspond to the test results in longitudinal and transverses directions, respectively.

2.2 Configuration of the wall

The study has been conducted to investigate improvement of the stability of the retaining wall. So here we have taken height of the wall which is 4m. The wall considered in the present study is 4m high, reinforced with Non woven geotextile reinforcement of length 4m. The vertical spacing between the geotextile is first taken uniform then also taken 0.5m , 0.25m subsequently for further models and the facing panel of length 0.5m and thickness 0.15m is provided.

3 Results and Discussions

The PLAXIS 2D software has been applied to develop the numerical model in this study. PLAXIS is a finite element program. It can be used for the estimation of

deformation, stability, and flow in foundation engineering. A few simple graphical input procedures enable a quick generation of complex finite element models; also, the increased output facilities provide a clear representation of computational results in a visual presentation. Modeling sequences are as follows:
(a) Definition of soil stratigraphy with soil properties,
(b) Definition of an embankment and retaining wall,
(c) Mesh generation, and
(d) Performing calculation.

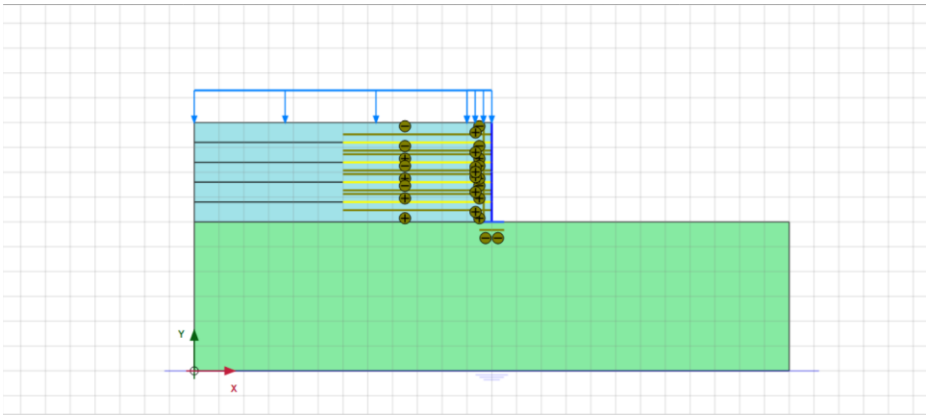

Fig 1. Geometry of 4 m retaining wall with 80 cm vertical spacing between geosynthetic reinforcement.

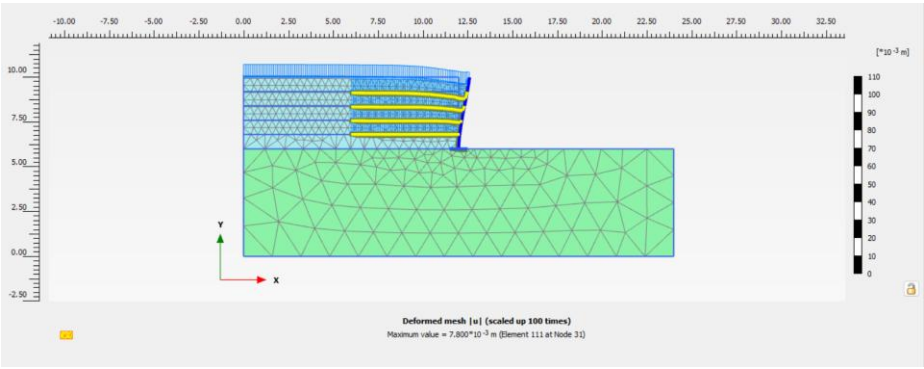

Fig. 2. Deformed mesh of 4 m retaining wall with 80 cm vertical spacing between geosynthetic reinforcement.

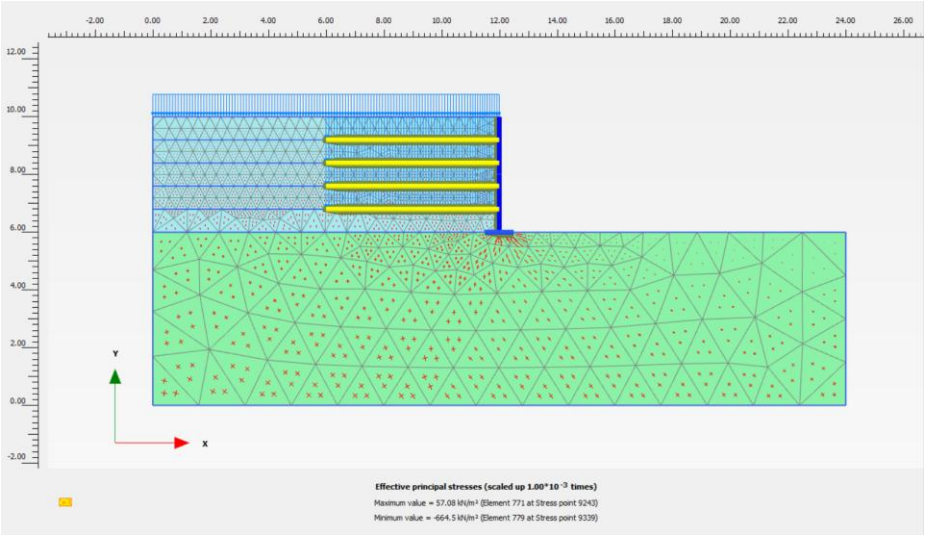

Fig. 3. Principal stresses of 4 m retaining wall with 80 cm vertical spacing between geosynthetic reinforcement.

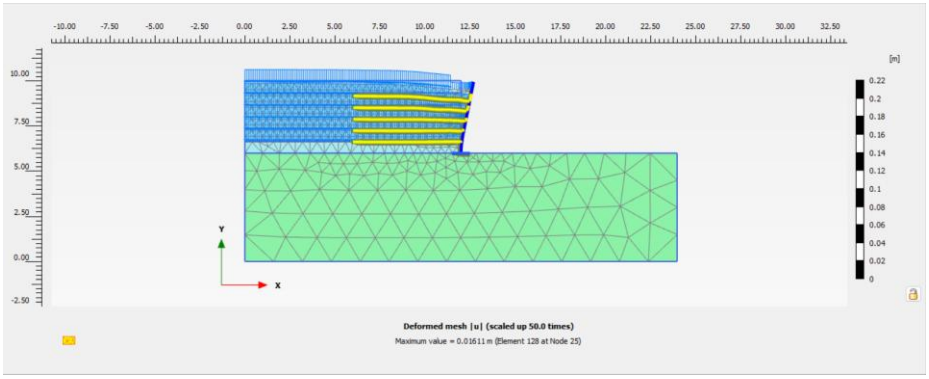

Fig. 4. Deformed mesh of 4 m retaining wall with 67 cm vertical spacing between geosynthetic reinforcement.

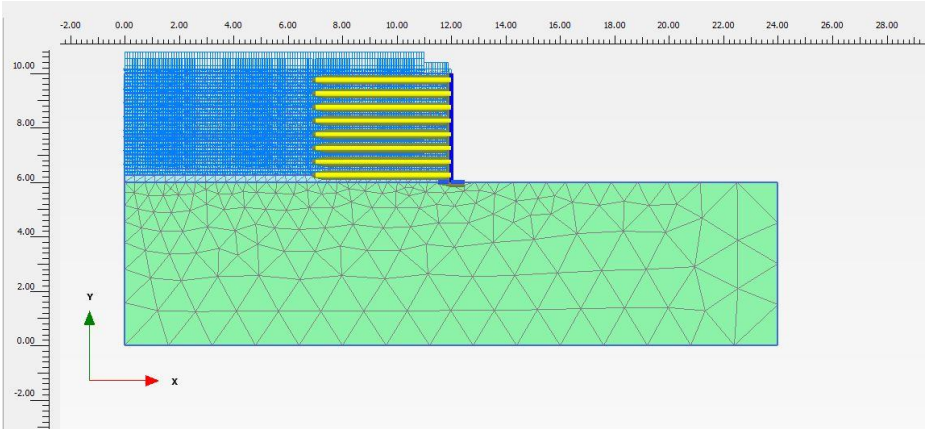

Fig. 5. Mesh of 4 m retaining wall with 25 cm vertical spacing between geosynthetic reinforcement.

Table 3. Different combinations of geotextile layering

Layer (No's.)	Spacing (m)	Lap Length (m)	Surcharge (kN/m^2)
5	0.80	1	100
6	0.67	1	100
8	0.50	1	100

3.1 Calculation of overlap length

The L*o* is the required overlap length (minimum is one meter)

$$L_o = \frac{S_V \sigma_h FS}{4(C_a + \gamma Z \tan\delta)} \qquad (1)$$

(Koerner, Robert M., 1933- Designing with geosynthetics / Robert M. Koerner.-5th ed. p.cm.)

Where, S_v = Vertical Spacing (lift thickness),

σ_h = total lateral pressure at depth considered,

FS = factor of safety,

C_a = soil adhesion between soil and Geotextile,

γ = unit weight of backfill soil,

Z = depth from ground surface,

δ = angle of shearing resistance between soil and Geotextile.

By putting the values we get L_o = 0.375m, but minimum length should be 1m.

Table 4. Total displacement and shear stress values of different geotextile layers

Spacing (m)	Layers (No's.)	Total displacement (m)	Cartesian shear stress max value (KN/m^2)	Cartesian shear stress min value (KN/m^2)
0.50	8	0.06296	541.3	-436.9
0.67	6	0.01611	200.2	-150.1
80	5	0.0078	125.9	-119.7

The observations taken from the table and model are studied and it is found that the Model 3 which is having 5 no. of layers is among the best suitable combination with lap length of 1 m which is uniform among all the rest models. Less displacement of wall means that the wall is having higher stability and chances of failure are less as compared to the other models.
In all models, the overall displacement of the retaining wall and the various forces acting on it are depicted as seen in figures 2, 4. These findings are crucial for the retaining wall's design. Active earth pressure operating on retaining walls is depicted as effective normal stresses acting on retaining walls in the PLAXIS output in figure 3. According to figure 4, the retaining wall's midpoint height is where the largest bending moment occurs. The middle height zone of retaining wall designs must therefore be constructed to support considerable bending moment, whereas bending moment near the top and bottom of the wall must be reduced.

4 Conlcusion

- An attempt is made to analyse the behaviour of Geotextile reinforced MSE wall of 4 meters by using FEM software. The deformation of wall of each model is compared to one another and the best suitable model is found out. The Geotextile is laid in wall by different combinations of spacing and overlap length.
- The use of Geotextile as reinforcement in soil retaining walls may offer benefits over the use of other types of reinforcement, such as metallic strips or geogrids. These include ease of construction, expediency, and significant cost reduction.
- A better understanding of the behavior of Geotextile reinforced soil structures could be gained by systematic monitoring of full-scale structures, combined with a thorough material characterization program.
- High stiffness Geotextile may be used to reinforce foundation soil to improve bearing capacity and reduce differential settlement.

References

1. Hossain, S.M., G. Kibria, M. S. Khan, J. Hossain, and T. Taufiq. : Effects of Backfill Soilon Excessive Movement of MSE Wall. J. Perform. Constr.

Facil. (26),793-802 (2012).
2. Chalermyanont, T., and Benson, C. H. : Reliability based design for internal stability of mechanically stabilized earth walls. J. Geotech. Geoenviron. Eng., 10.1061/(ASCE)1090-0241(2004)130:2(163), 163–177 (2004).
3. Chalermyanont, T., and Benson, C. H.: Reliability based design for external stability of mechanically stabilized earth walls." Int. J. Geomech., 10.1061/(ASCE)1532-3641(2005)5:3(196), 196–205 (2005).
4. Desai, C. S., and El-Hoseiny, K. E. : Prediction of field behavior of reinforced soil wall using advanced constitutive model. J. Geotech. Geoenviron. Eng., 10.1061/(ASCE)1090-0241(2005)131:6(729), 729–739 (2005).
5. Abdullah, A. B. M., A Hand book of Geotextiles Particularly natural goetextiles from jute and other vegetable fibers, FAO- (2000).
6. Gregory, R. N., Barry, C. R., Geotextiles in Transportation Applications, Featured Short Course, (1998).
7. Rankilor, P. R., Membranes in Ground Engineering, John Wiley and Sons, New York, (1981).
8. Koerner, R. M., Designing with Geosynthetics.
9. Han, J., and Leshchinsky, D. "Limit equilibrium and continuum mechanics-based numerical methods for analyzing stability of MSE walls." Proc., 17th ASCE Engineering Mechanics Conf., ASCE, Reston, VA. (2004).
10. Leshchinsky, D., and Han, J. "Geosynthetic reinforced multitiered walls." J. Geotech. Geoenviron. Eng., 10.1061/(ASCE)1090-0241(2004) 130:12(1225), 1225–1235. (2004).
11. Hatami, K., Bathurst, R. J., and Di Pietro, P. "Static response of reinforced soil retaining walls with non uniform reinforcement." Int. J. Geomech., 10.1061/(ASCE)1532-3641(2001)1:4(477), 477–506 (2001).
12. Ho, S. K., and Rowe, R. K. "Predicted behavior of two centrifugal model soil walls." J. Geotech. Engg., 10.1061/(ASCE)0733-9410 (1994)120:10(1845), 1845–1873. (1994).
13. Hossain, M. S., Kibria, G., Khan, M. S., Hossain, J., and Taufiq, T. "Effects of backfill soil on excessive movement of MSE wall." J. Perform. Constr. Facil., 10.1061/(ASCE)CF.1943-5509.0000281, 793–802. (2012).
14. Huang, B., Bathurst, R. J., and Hatami, K. "Numerical study of reinforced soil segmental walls using three different constitutive soil models." J. Geotech. Geoenviron. Eng., 10.1061/(ASCE)GT.1943- 5606.0000092, 1486–1497. (2009).
15. Kim, D., Bhowmik, S. K., and Willmer, J. L. "Acase history of MSE wall failure: Finite element modeling and evaluation." Proc., Geo-Florida 2010: Advances in Analysis, Modeling, and Design, Vol. 199, ASCE, Reston, VA, 2232–2242. (2010).
16. Chiang, J., K. Yang, Y. Chan, and C. Yuan . "Finite element analysis and design method of geosynthetic-reinforced soil foundation subjected to normal fault movement". Computers and Geotechnics 139,104412. (2021)
17. Linhares, R. M., S. H. Mirmoradi, and M. Ehrlich. "Evaluation of the effect of surcharge on the behavior of geosynthetic-reinforced soil walls". Transportation Geotechnics 31, 100634. (2021)
18. Guler, E., M. Hamderi, and M. M. Demirkan. "Numerical analysis of reinforced soil- retaining wall structures with cohesive and granular backfills". Geosynthetics International. 14(6), 330-345 (2007)

19. Hatami, K., R.J. Bathurst, and P. D. Pietro. “Static Response of Reinforced Soil Retaining Walls with Nonuniform Reinforcement”. T. Int. J. Geomechanics. 1(4), 477-506. (2001).
20. Fonseca, C. A. E., E. M. Palmeira, and E. C. G. Santos. “Numerical analysis of a geotextilereinforced retaining wall built with nonconventional backfill material”. 10th International Conference on Geosynthetics (ICG 2014).
21. Ling, H. I. (2003). “Finite element applications to reinforced soil retaining walls—Simplistic versus sophisticated analyses.” Proc., Geomechanics: Testing, Modeling, and Simulation, 1st Japan-U.S. Workshop on Testing, Modeling, and Simulation, J. A. Yamamuro and J. Koseki, eds., ASCE,Reston, VA, 77–94.
22. Jones, C. J. F. P., and Edwards, L. W. (1980). “Reinforced earth structures situated on soft foundations.” Geotechnique, 30(2), 207–213.
23. Huang, B., Bathurst, R. J., and Hatami, K. (2009). “Numerical study of reinforced soil segmental walls using three different constitutive soil models.” J. Geotech. Geoenviron. Eng., 135(10), 1486–1498.
24. Chida, S., and Nakagaki, M. (1979). “Test and experiment on a full-scale model of reinforced earth wall.” Proc., Int. Conf. on Soil Reinforcement,Vol. 2, Paris, 533–538.

View publication stats

ResearchGate

See discussions, stats, and author profiles for this publication at: https://www.researchgate.net/publication/371379437

Numerical Prediction of the Proximity Effects on Wind Loads of Low-Rise Buildings with Cylindrical Roofs

Article · April 2023

DOI: 10.12989/was.2023.36.4.277

CITATIONS
0

READS
49

3 authors:

Deepak Sharma
Delhi Technological University
2 PUBLICATIONS **0** CITATIONS
SEE PROFILE

Ritu Raj Ahirwar
Delhi Technological University
59 PUBLICATIONS **296** CITATIONS
SEE PROFILE

Shilpa Pal
Delhi Technological University
67 PUBLICATIONS **324** CITATIONS
SEE PROFILE

Some of the authors of this publication are also working on these related projects:

Recycled Aggregate Concrete View project

Investigation of Wind Effects on High Rise Buildings Having Varying Cross-sectional Shapes. View project

All content following this page was uploaded by Deepak Sharma on 09 June 2023.

The user has requested enhancement of the downloaded file.

Wind and Structures, *Vol. 36, No. 4 (2023) 277-292*
https://doi.org/10.12989/was.2023.36.4.277

Numerical prediction of the proximity effects on wind loads of low-rise buildings with cylindrical roofs

Deepak Sharma[a], Shilpa Pal[b] and Ritu Raj[*]

Department of Civil Engineering, Delhi Technological University, Delhi 110042, India

(*Received August 26, 2022, Revised December 6, 2022, Accepted April 1, 2023*)

Abstract. Low-rise structures are generally immersed within the roughness layer of the atmospheric boundary layer flows and represent the largest class of the structures for which wind loads for design are being obtained from the wind standards codes of distinct nations. For low-rise buildings, wind loads are one of the decisive loads when designing a roof. For the case of cylindrical roof structures, the information related to wind pressure coefficient is limited to a single span only. In contrast, for multi-span roofs, the information is not available. In this research, the numerical simulation has been done using ANSYS CFX to determine wind pressure distribution on the roof of low-rise cylindrical structures arranged in rectangular plan with variable spacing in accordance with building width (B=0.2 m) i.e., zero, 0.5B, B, 1.5B and 2B subjected to different wind incidence angles varying from 0° to 90° having the interval of 15°. The wind pressure (P) and pressure coefficients (C_{pe}) are varying with respect to wind incidence angle and variable spacing. The results of present numerical investigation or wind induced pressure are presented in the form of pressure contours generated by Ansys CFD Post for isolated as well as variable spacing model of cylindrical roofs. It was noted that the effect of wind shielding was reducing on the roofs by increasing spacing between the buildings. The variation pf Coefficient of wind pressure (C_{pe}) for all the roofs have been presented individually in the form of graphs with respect to angle of attacks of wind (AoA) and variable spacing. The critical outcomes of the present study will be so much beneficial to structural design engineers during the analysis and designing of low-rise buildings with cylindrical roofs in an isolated as well as group formation.

Keywords: ANSYS CFX; cylindrical roof; low-rise buildings; pressure coefficients; wind loads

1. Introduction

Low-rise buildings, which are utilized for commercial, industrial, residential, and other purposes, make up the vast majority of structures created across the world. These structures are built in a variety of terrain and topography, with a variety of plan styles (Uematsu and Isyumov 1999). For instance, the low-rise buildings with various types of roof shapes (dome, cylindrical, hip, pyramidal and mono-slope roof etc.) find its applications in hilly areas, coastal areas, rural areas and sub-urban areas etc., where the cyclonic attacks incidents take place many times throughout the year. During these cyclonic events the roofs of these low-rise structures are the most susceptible to the wind loads (Jagbir and Kumar 2021). The precinct ventilation zone concept provides a straightforward mechanism to characterise and distinguish the relationships between urban morphology and precinct ventilation performance. On the one hand, the precinct ventilation zone system may broaden awareness and understanding of wind in practical settings. Precinct ventilation zone concept, on the other hand, offers urban planners and decision-makers a simple framework for upcoming urban growth (He *et al.* 2019). Wind loads influence the lateral strength of structures in locations other than high seismic zones. This feature is especially apparent in areas with strong wind, such as coastal regions, open terrains, and hilltops.

The cylindrical roof represents the shape of an arched roof with a wide range of uses, including a recreation centre, Coliseum, and warehouse. Wind loads are an essential design issue, especially for mesh shells and stretchable membrane structures, as they are often lightweight and flexible. In such structures, the aerodynamics are highly dependent on the roof's curvature (Qiu *et al.* 2014).

Different codes of practise from various countries have provided the coefficient of external and internal pressure values for various low-rise roof types for varying wind orientations and varied slopes or roof angles. (Archit. Inst. 2015, ASCE/SEI 7-16 2011, New Zealand Standard and Australia 2016, ASCE 7-16 2017, Standards British Institution 2002, TCVN 2737-1995).

Stathopoulos provided similar results by examining the flat roof and the coefficients of three different roof slopes 1:12, 4:12, 12:12 in the area of the edges and ridges than the other roof slopes (Stathopoulos 1975, Davenport *et al.* 1977). It was also pointed out in that some standards do not specify high suction loads in ridge areas with moderate roof slopes. The fact that certain standards do not provide for

*Corresponding author, Assistant Professor
E-mail: rituraj@dtu.ac.in
[a]Ph.D.
[b]Associate Profeesor

Copyright © 2023 Techno-Press, Ltd.

ISSN: 1226-6116 (Print), 1598-6225 (Online)

Cylindrical Roof (Coolidge Municipal Airport, Arizona)

Multi-Span Cylindrical Roof Building (Beijing, China King Peng- Plastic film multi-span greenhouse)

Cylindrical Roofs Structures

significant suction loads in ridge regions with modest roof slopes was also brought up. The corners of the roof edge were discovered beneath a sizable suction peak at a roof slope of 12:12, with noticeably higher roof pressure coefficients.

Dome roofs fit this group of intricate roof forms. The roof form has also been altered in several investigations to increase aerodynamics. Domed roofs are used to cover large buildings such as mosques, churches and schools in Iran (Faghih and Bahadori, 2007).

The wind flow over a curving, sloping roof is more complicated than the wind flow around other roof forms, according to analytical, theoretical, and numerical studies of different roof types (depending on shape) (Mahdavinejad and Javanroodi 2016). Another experimental study of domed roofs revealed a complex recirculation flow around the roof (Rahmatmand & Yaghoubi, 2014).

Using the computational fluid dynamics (CFD) method, it is investigated how the wind would affect the low-rise structure with a cylinder roof at angles between 0° and 90° with a 15° interval. The findings of numerical simulation are validated by comparison with earlier wind tunnel tests and several international standards. To clearly understand the properties of the flow, CFD is utilised to examine the streamlines around the building models. To be able to completely comprehend the wind load dispositions that take place at various angles of incidence of wind, the distribution of local wind pressure on cylindrical roof building models is carefully analysed. Discussion of the pressure profile on the cylindrical roof seems fair.

The apex angle and attack angle for the highest turbulence intensity and maximum reattachment length were found in a numerical evaluation of the surface-mounted pyramid(Beura and Prasad, 2014). The wind angle has a major influence on the suction on the building model with setback (Debasish 2015, Kumar 2018). Another factor that influences wind load is aspect ratio. In an experimental examination of long-span, low-rise building models with a significant roof slope, the scientists discovered that as the aspect ratio increases, so does the suction on the leeward roof and on the wall (J.D. 2003). Numerous wind tunnel studies have been conducted on the flat and gable roof of low-rise buildings to find out the influence of apex angle. It was concluded that the wind induced pressure got highly affected if the roof angle is more than 20° (Satheeskumar *et al*. 2017) (Weerasuriya *et al*. 2018) (John *et al*. 2009) (Vickery 1976).

In addition to the characteristics (apex angle, attack angle, aspect ratio, etc.), there is the interference impact of surrounding buildings in both low-rise and high-rise structures. The comparative height of the upwind side building created an increase in wind stress on a low-rise structure in an interference wind tunnel investigation (Pindado Santiago 2011). Surrounding buildings were frequently found to be useful since they typically lesser suction on the roof (Surry and Lin 1995).

In practically all structures, wind loads result in positive pressure and negative pressure (suction), as well as shear force and torsional load. In a study of flat and gable roofs, it was shown that the gable roof had much higher shear force and torsional moment than the flat roof (Elsharawy 2011).

From the above literature work, it can be concluded that most of the past studies have been done either on gable roofs or flat roofs. Still other types of roofs i.e., mono-slope roof, cylindrical roofs, pyramidal roof, hip roof, etc. has got less attention from researchers. These roofs need to be investigated too for wind induced parameters. Also, the previous studies focused either on an isolated model or group of 2 or 3 buildings which is practically insufficient for the sake of wind load knowledge of low-rise building. Additionally, most of the wind load studies on low-rise and high-rise buildings have been performed using boundary layer wind tunnel (BWLT) which is sometimes not available and expensive too. Therefore, numerical investigation using CFD is very effective and reliable alternative source of BWLT.

Since it is well known fact that the values for pressure coefficients of cylindrical roof in Indian Standard (IS 875 Part 3 2015) are available only for isolated condition but not available for interfering condition. Therefore, it is necessary to investigation the disposition of pressure for interfering model also. In the present research, the investigation for pressure distribution over the roof of low rise building with cylindrical roof under isolated and interfering or proximity condition has been done. It will be very beneficial for the structural design engineers while designing the low rise building with cylindrical roofs arranged in rectangular pattern with variable spacing. The Photo 1 shows some of the structures with cylindrical roofs.

2. Methodology

In the present investigation, the numerical modeling has

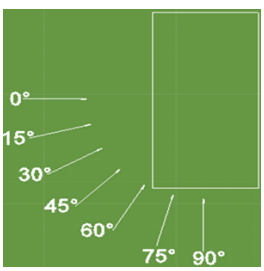

Plan View

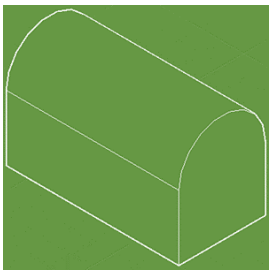
Isolated Model

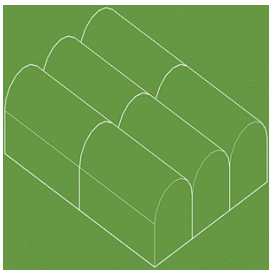
0 Spacing Model

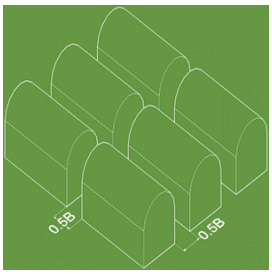

0.5B Spacing Model

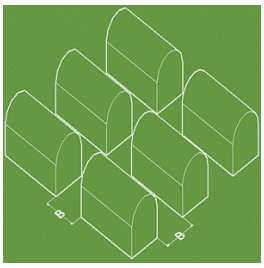

B Spacing Model

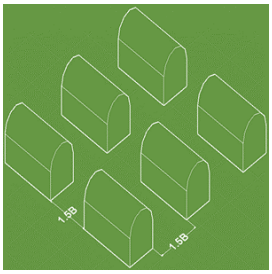

1.5B Spacing Model

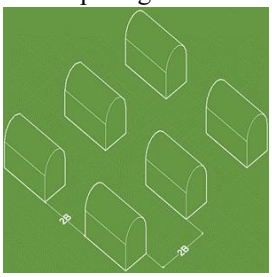

2B Spacing Model

Top A	Top B	Top C
Top D	Top E	Top E

Nomenclature of the roofs

Fig. 1 Different Models considered for the study

been done using ANSYS CFX to find out the proximity effects on wind loads of low rise building with cylindrical roofs arranged in rectangular pattern with the variable spacing.

2.1 Numerical modeling

Computation-based analysis carried out with computational fluid dynamics. The k-Ɛ turbulence model was used in the majority of earlier studies. This model has a well-documented capacity for prediction and has demonstrated stability and numerical dependability. With this approach, general-purpose simulations may be conducted with a precise balance of dependability. It is frequently used to imitate the properties of turbulent flow and is quite inexpensive. The answer is provided by the two transport equations, turbulent kinetic energy (k) and turbulent dissipation rate (ε), which make up the two-equation k- turbulence model. Being able to model without any geometry-related factors is a benefit. Two variables are added to the model's system of equations: turbulent kinetic energy and turbulence dissipation rate. The equations used in the present investigation are described as follows:

a) Navier stokes equation:

$$\frac{\partial(\rho u_i)}{\partial t} = -\frac{\partial(\rho u_i u_j)}{\partial x_j} - \frac{\partial P}{\partial x_j} + \frac{\partial}{\partial x_j}\left[\mu\left(\frac{\partial_{u_i}}{\partial_{x_j}} + \frac{\partial_{u_j}}{\partial_{x_i}}\right)\right] + F \quad (1)$$

b) Continuity equation:

$$\frac{\partial_\rho}{\partial_t} + \frac{\partial_{\rho_i}}{\partial_{x_i}} = 0 \quad (2)$$

The transportation equations for turbulence kinetic energy and dissipation for standard k- ε model are described as follows

$$\rho\frac{\partial k}{\partial t} + \rho\overline{u_\iota}\frac{\partial k}{\partial x_j} = \tau_{ij}\frac{\partial \overline{u_\iota}}{\partial x_j} - \rho\varepsilon + \frac{\partial}{\partial_{x_j}}\left[\left(\mu + \frac{\mu_t}{\sigma_\varepsilon}\right)\frac{\partial \varepsilon}{\partial x_j}\right] \quad (3)$$

c) Moment equatiom:

$$\frac{\partial(\rho U_i)}{\partial t} = -\frac{\partial(\rho U_i U_j)}{\partial x_j} - \frac{\partial P}{\partial x_i} + \frac{\partial}{\partial_{x_j}}\left[\mu_{eff}\left(\frac{\partial_{U_i}}{\partial_{x_j}} + \frac{\partial_{U_j}}{\partial_{x_i}}\right)\right] + S_M \quad (4)$$

2.2 Model computational domain and geometry

In this research, the study has been carried out using ANSYS CFX solver. The scale of the building model is taken as 1:50. CFD simulations were performed to investigate the influence of wind on the roof of a low-rise structure with a cylindrical roof of 150 mm eave height, 100mm rise and length of 400mm. This study discusses the fluctuation of wind induced coefficient of pressure (C_p) on the surfaces of roofs, and the models of buildings are illustrated in Fig. 1. To study the influence of wind direction, simulations were run with wind directions ranging from 0° perpendicular to the building's main axis (parallel to the roof profile) to 90° parallel to the roof's ridge line with a 15° gap. Streamwise velocity path lines are drawn along the central plan parallel to the wind direction to understand the influence of cylindrical roof form on wind flow above it. In the event of an isolated scenario, cylindrical roof forms cover a structure with a rectangular cross section of 20 m × 10 m and an eave height of 7.5 m. For multi-span cylindrical roof, the buildings are arranged in a rectangular plan with variable spacing i.e., 0, 0.5B, B, 1.5B and 2B where B is the width of the building.

Using CFD modelling, the impact of wind on the building model is examined. CFD works by splitting the location into a grid of many cells. The cell grid is surrounded by a space that simulates an opening and a surface that surrounds the boundary. The restraint pressure, and the movement of the air in the opening in the cell, are then adjusted to an initial state close to the actual the setting for wind tunnel experiment. For simulation purposes, the inlet, top, and sidewall boundaries are considered 5H from the model, and

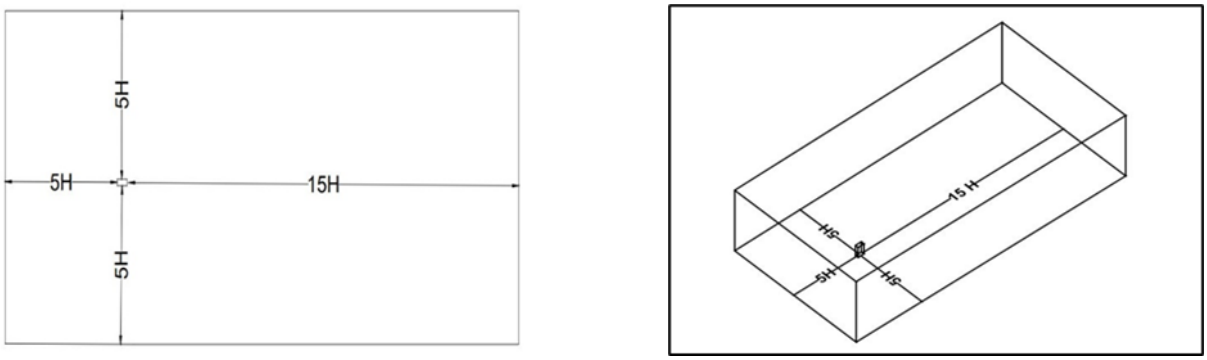

Fig. 2 Size of Domain used in CFD Simulation

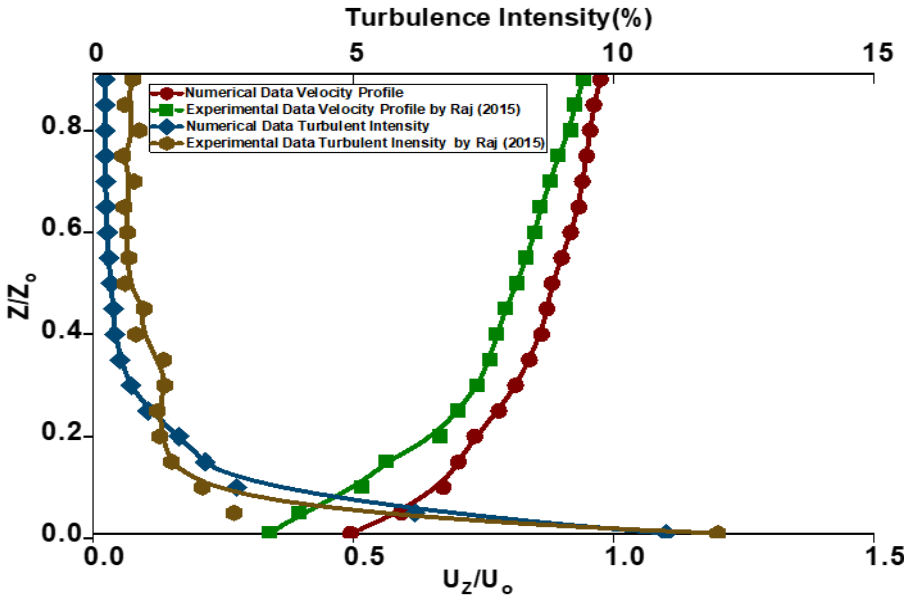

Fig. 3 Velocity and Turbulence Intensity w.r.t Height (Meena *et al*. 2022, IS: 875 Part-3 2015)

the exit boundaries are placed 15H behind the model recommended by Franke *et al*. (2007), Revuz *et al*. (2012) and Meng *et al*. (2018). Since the governing equation is a derivative and its solutions need to be integrated, when defining a problem that leads to a singular solution, you need to include the data of the dependent variable at the domain boundary. The premise is that the mathematical counterpart of a combination is constant, and its value is important for deriving a peculiar solution. Fig. 2 shows the domain. The side panels and ceiling remain in front of the CFX as free slips. During this investigation, the floor surface and building model will be treated as non-slip walls within the pre CFX configuration. No-slip describes a situation when the air velocity at the wall's edge and the air velocity at the entrance are same. The value of the velocity parallel to the wall is finite (calculated by the solver), but both the velocity perpendicular to the wall and the shear stress are set to zero. At the inlet, the free stream velocity is set to 10 m/s. The domain is designed according to Revuz *et al*. (2012). The velocity profile and turbulence intensity profile are plotted in Fig. 3 and compared with previous wind tunnel data by Raj (2015). Reynolds Number in the numerical simulation technique varies between 1.24×10^6 to 1.79×10^6.

2.4 Meshing

In numerical simulation, the meshing plays a vital role since the finer mesh may be not reliable for the results while the bad mesh will affect the results as well. So, it becomes very important to select the suitable mesh size which gives reliable results. The different meshing sizes were provided to the capture the flow characteristics around the critical zones. Since meshing is time consuming, it can be used to discretize domains by subdividing complex geometries. The meshing of present study is presented in Fig. 4. Domain meshes are provided as tetrahedral meshes because they require less resources to calculate the results. Building meshes are available in a range of sizes so that the solution can accurately depict the flow behaviour close to the building's surface. Flow characteristics can also be recorded using edge meshes that are more precise than other mesh sizes. To easily replicate the flow around the building model's geometry, inflation is offered. For simulation purpose, the size of the meshing is taken as 0.0125 m on the faces of buildings, 0.025 m on the edges of buildings, 0.05

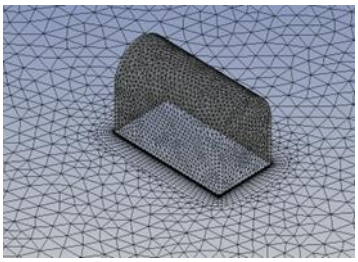

Isolated Model Mesh

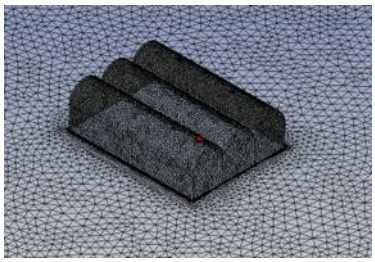

Multi-Span Model Mesh

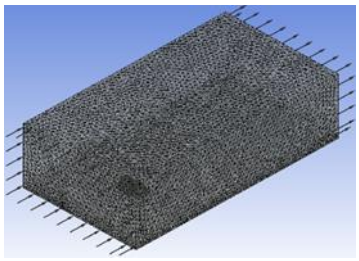

Domain Mesh

Fig. 4 Meshing of the Model

Table 1 Grid independence test result for isolated cylindrical roof

H/L	Values	IS 875 Part 3 (2015)	Coarse Mesh	Medium Mesh	Fine Mesh	Very Fine Mesh
0.5	C	-1.2	-1.36	-1.28	-1.23	-1.25
	C_2	+0.7	+0.85	+0.77	+0.73	+0.73
	Leeward Portion	-0.4	-0.63	-0.51	-0.43	-0.43

m at ground level and 0.1 m on all the faces of computational domain. The size of the computational domain is decided on the basis of recommendations given by Franke *et al*. (2007), Revuz *et al*. (2012) and Meng *et al*. (2018) as described in section 2.3 in boundary conditions.

2.4 Velocity and turbulence intensity profile

The boundary conditions used in the numerical simulation are similar to those used in Raj (2015). To achieve a good link between numerical simulations and wind tunnel experiments, the boundary conditions must be the same, especially for inflow boundary conditions. Changes in wind with altitude are usually expressed in logarithmic form.

$$U_z = \frac{u_0}{k} ln\left(\frac{Z}{Z_o}\right) \tag{5}$$

Where U_z is the wind speed at height z, U_o is friction velocity, Z_o is the characteristic height of surface roughness, k is a Karman constant with a value of 0.4 (Meena *et al*. 2022)

The boundary layer wind profile is governed by the power low equation

$$U_z = U_o \left(\frac{z}{z_o}\right)^n \tag{6}$$

Where U_z is the wind speed at height Z, U_o is the mean wind speed at a reference height Z_o, 'n' is a parameter that varies with ground roughness. The value of 'n' is taken as 0.16 for present study (IS: 875 Part-3 2015, Verma and Ahuja 2015).

In general, the eddy intensity of smooth terrain is less than the eddy intensity of rugged terrain. Eddy intensity is a dimensionless quantity derived from scattering and average wind speed.

$$I_z = \frac{\sigma_z}{U_z} \tag{7}$$

Where I_z is the turbulence intensity at height z, σ_z is the standard deviation of the wind speed at height z, U_z is the mean wind speed at reference height.

2.6 Pressure Coefficient (C_p)

It is defined as the ratio of pressure difference acting on the surface at a point and static pressure due to incident wind to the design wind pressure. After considering the geographical location, terrain conditions and shielding effect, the static and design wind pressure are measured at the height of the point considered.

$$C_p = \frac{p - p_o}{\frac{1}{2}\rho {U_Z}^2} \tag{8}$$

Where p is the pressure at needed point, p_o is static pressure at referred height, ρ is the density of air i.e., 1.225 kg/m^3, and U_z is wind average velocity at the referred height of the building.

2.7 Grid independence study

Disorganized grids can't condense mesh nodes, which leads in less precise computations. To provide grid independent numerical solutions, grid independent investigations are carried out. To minimise vortex diameters in wake zones and obtain accuracy in CFD simulation, the mesh must be separated into higher orders. The mesh dependency has been checked by using different types of meshing i.e., Coarse (total elements are 17508), Medium (total elements are 74485), Fine (total elements are 373458) and Very Fine mesh (total elements are 2139561) respectively. It is observed that simulations with a higher number of nodes produce better accuracy. The results obtained from all the types of meshing were compared with the data available for isolated curved roof in Indian Standards (IS 875 Part 3 2015). Nevertheless, a larger node count will entail a corresponding rise in simulation duration. According to the findings of a study on

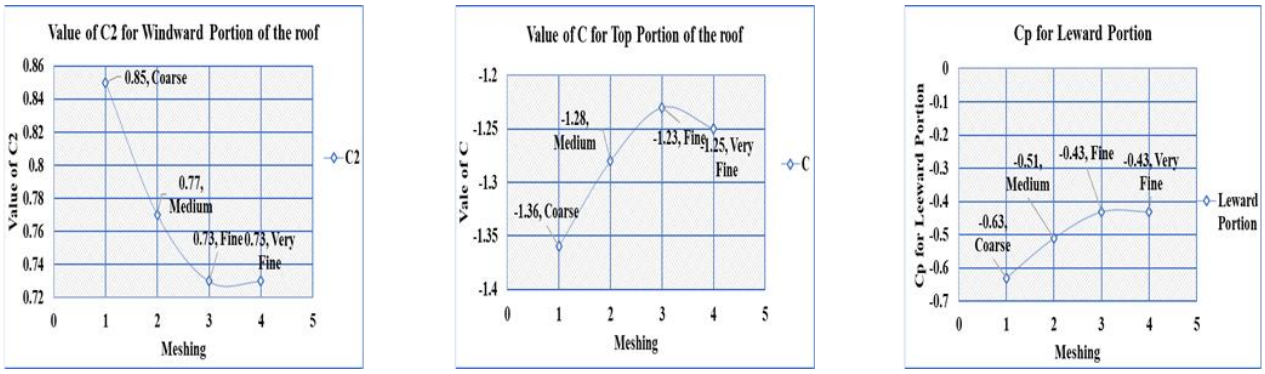

(a)

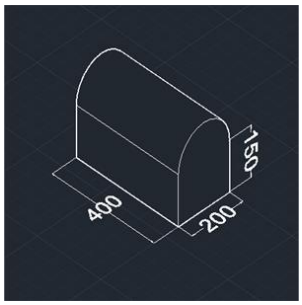

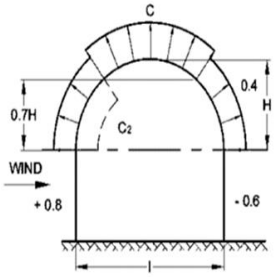

(b)

Fig. 5 (a) Grid sensitivity (b) Pressure coefficient for isolated cylindrical roof as per IS 875Part 3 (2015)

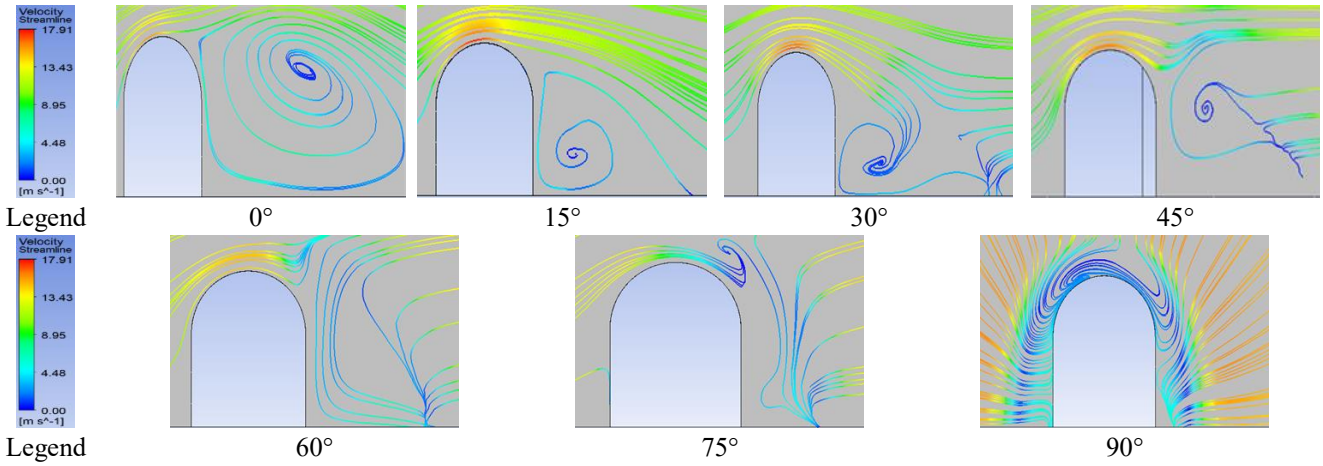

Fig. 6 Streamlines for Isolated Model at different wind incidence angles

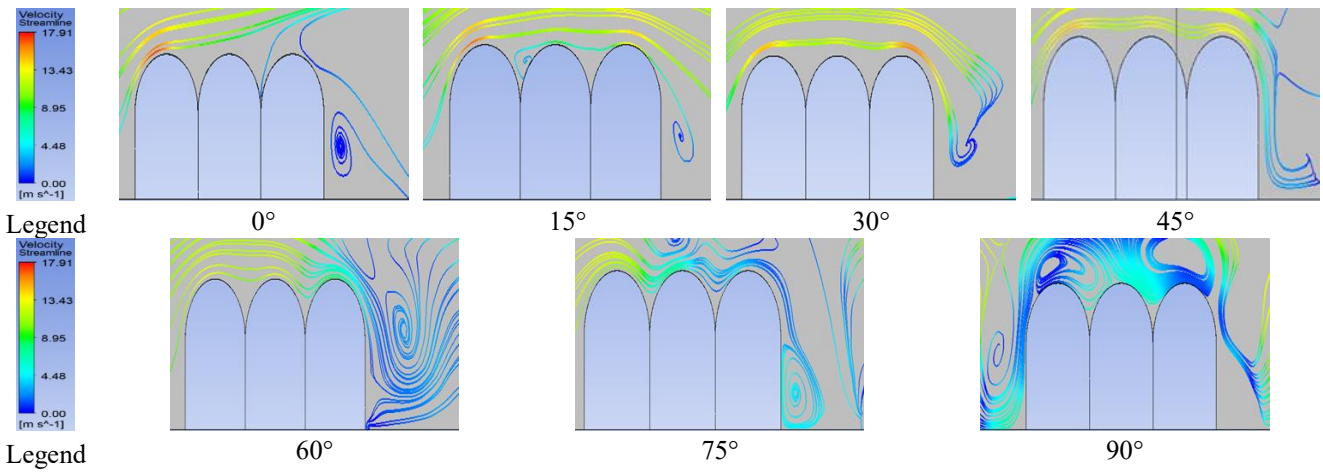

Fig. 7 Streamlines for Multi- Model at different wind incidence angles

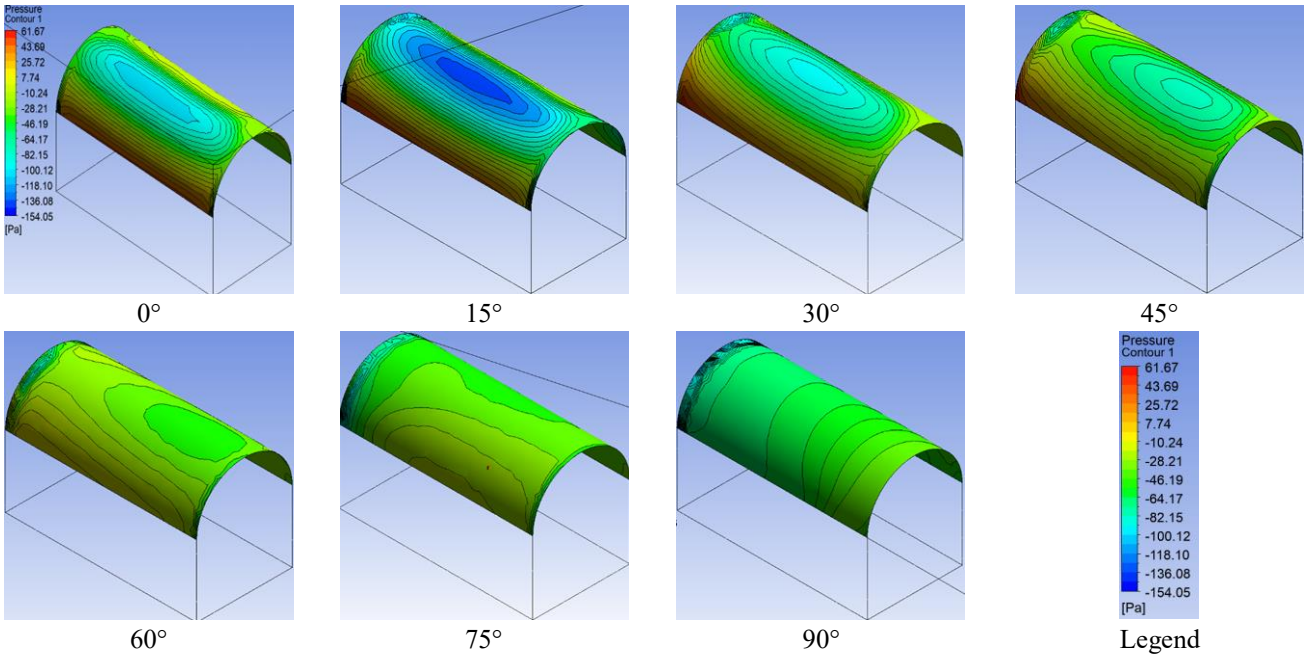

Fig. 8 Pressure contours for isolated cylindrical roof model

convergence for finer base sizing with constant face sizing and inflation, the mesh and outcomes are more closely converged in this scenario. The variation of wind coefficients for windward zone (C_2), top (C) and leeward zone (C_p) obtained from all the types of meshing are presented in Fig. 5. After conduction of grid dependence study, it was noted that results show very less variation in the pressure coefficients for coarse, medium, fine and very fine meshing respectively. The results obtained from the grid sensitivity are shown in Table 1. For the further simulation, the fine meshing is utilised, the size of which is mentioned in section 2.4.

3. Result and discussion

3.1 Flow patterns

The pressure distribution due to wind load is highly affected by certain factors for instance vortex, flow separation, stagnation, flow recirculation and flow reattachment. The wind flow streamlines for the isolated and multi-span cylindrical roof model are presented in the Fig. 6 and Fig. 7 respectively.

The change in pressure distribution and the emergence of vortices are caused by the building's geometric design. In case of the isolated cylindrical roof, the maximum reversible of flow was taking place when the wind incidence angle was from 15° to 45° due to which the maximum suction was generated. The flow pattern around multi-span cylindrical roof was quite similar to that of the isolated cylindrical roof for all the wind incidence angle. The leeward roof of multi-span model was mostly subjected to the flow reversible phenomenon which indicates that the maximum suction was acting on the leeward roof. When the wind is acting from 90° angle of attack, all the roofs of the multi-span model were under the suction.

3.2 Pressure distribution

For Isolated Cylindrical Roof: The pressure contours for single and multi-span cylindrical roof model are presented in Fig. 7 and Fig. 8 respectively for different wind incidence angle varying from 0° to 90° with having the interval of 15°. When a single span cylindrical roof was subjected to 0° to 45° wind occurrences, it was found that just a sliver of the windward edge was exposed to positive pressure while the rest of the roof was under suction. The maximum negative pressure was occurred during the wind angle of 30°.

It was observed from the Fig. 8 that the wind force was suction at every wind angle on the roof. The most unfavourable wind angle was 30° in case of isolated cylindrical roof. The cylindrical vortex was appeared near the windward edge in during 0° wind attack angle. The conical vortex was observed near the short leading edge when wind angle was ranging from 15° to 45° also the vortexes were disappeared in case of wind angle 45° to 90°. It was observed that wind direction of 15° to 45° was most unfavourable for suction and cylindrical vortex while the 45° to 90° wind angle was most unfavourable for conical vortex and suction.

For Multi-Span or Zero Spacing Model: We can also call this model as a model with 0 spacing. It was observed from the Fig. 8 that in case of 0° wind angle the suction on the leeward span is smaller than the suction on the upwind span, up to half the upwind span. The pressure distribution on windward span of multi-span roof was quite similar to that of the single span roof. The middle span was least subjected to suction when compared with windward and leeward span. In the wind pressure distribution of the leeward span, there is an advantage of the shield by the

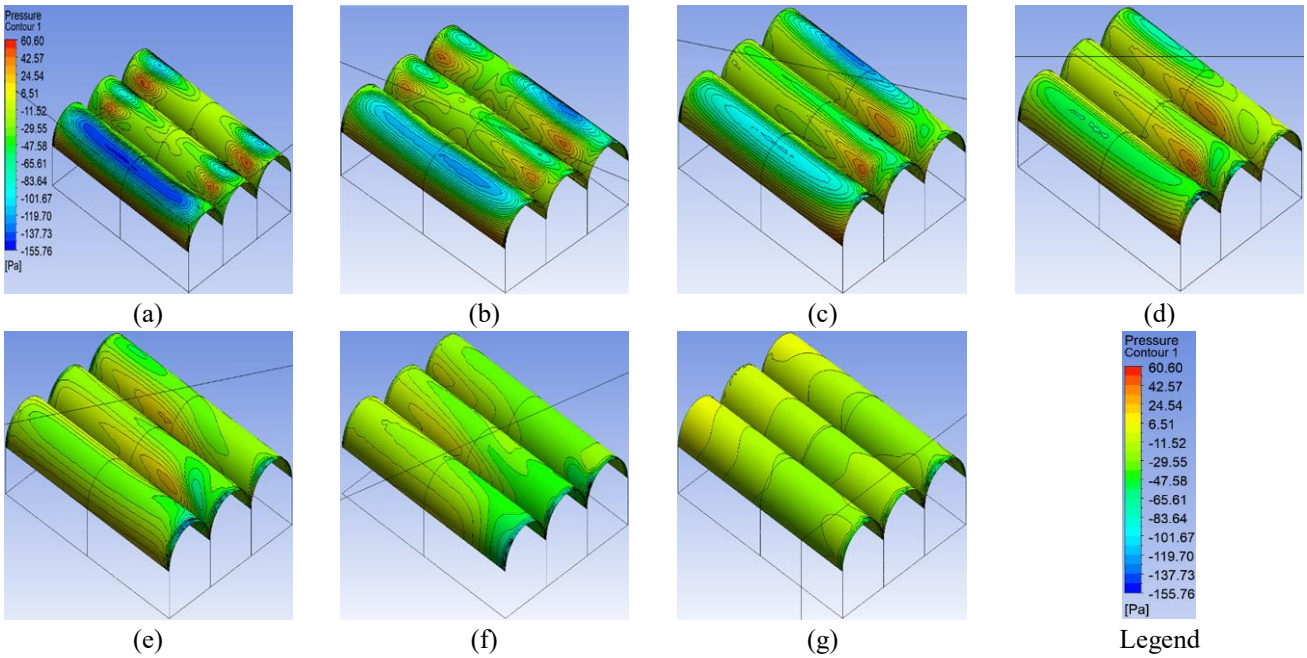

Fig. 9 Pressure Contours for Multi-Span model at (a) 0° (b) 15° (c) 30° (d) 45° (e) 60° (f) 75° (g) 90°

leeward span. During the 0° wind angle it was observed that the maximum negative pressure (suction) having approximately same magnitude was acting on the windward roofs A and D while other left roofs B, C, E and F were subjected to less negative pressure (suction) having the magnitude quite equal. The maximum negative pressure was recorded on the leeward roof C in case of 30° wind incidence angle. The pressure distribution on windward roofs A & D and middle roofs B & E was showing quite similar pattern with very less algebraic difference during wind incidence angle moving from 0° to 45° but it shows significant difference during the wind angle from 60° to 90°. But on the leeward roofs C & F it was observed that the pressure distribution was similar only for the wind angle of 0° and 60° otherwise it was having a noticeable difference for all other wind angles. The maximum negative pressure was observed on the leeward roof C during wind angle of 30°.

For the Interference Model of 0.5B Spacing: Numerous simulations run at variable spacings between the interfering and instrumented models as well as various angles of incidence of wind ranging from 0° to 180° at 15° intervals. In the current investigation, an interfering model is one that shares the same exterior dimensions as an instrumented model. The distance between the two models is adjusted according to the building's width (b=0.2m) while the instrumented model is kept immediately behind the interfering model, i.e., in full blockage state, at 0° wind incidence. The 0.5B, B, 1.5B, and 2B values for the 4 various spacing taken into consideration in this study are shown in Fig. 1. The Fig.10 shows the pressure contours for the models of 0.5B spacing.

Fig. 10(a) depicts the contours created by pressure brought on by the disposition of wind loads on low-rise structures with cylinder roofs that are placed in a rectangular pattern with 0.5B spacing between them during the wind incidence angle of 0°. It was noticed that the maximum negative (suction) pressure was acting on the top of windward roofs A & D. The windward roofs A & D were having similar kind of distribution of pressure. Furthermore, it was discovered that the negative pressure on windward roofs A & D of 0.5B spacing model was reduced when compared with zero spacing model. This implies that suction reduced on the windward roofs due to increase in the spacing between the buildings i.e., 0 to 0.5B. The middle roofs B & E were subjected to minimum negative pressure due to shielding effect. A very sliver portion of windward span of roof B & D was exposed to small magnitude of shielding effect. The negative pressure on leeward roofs C & F found greater than that of the middle roofs B & D. Although there is maximum shielding effect observed in the windward span of the roofs C & F. Fig. 10(b) represents the pressure contours for wind incidence angle of 15°. During 15° wind interval it was observed that the negative pressure on roofs A, B, E and F, reduced when compared with 0° incidence. On the other hand, the negative pressure on roofs C & D were increased when compared with 0° wind incidence. Shielding effect observed on windward span of middle and leeward roofs. The contours generated by the wind induced pressure at a 30° angle of wind attack are shown in Fig. 10(c). It can be inferred that the wind shielding effect started getting reduced on the middle and leeward roofs. The negative pressure on roofs A, B, E and F were not affected that much when compared with 15° wind incidence. But on the roofs D & C, the pressure was highly suction in nature. The maximum changes in the pressure observed during the wind incidence angle of 0° to 30°, after that the suction on the roofs started getting reduced on all the roofs. In Fig. 10(g), the side faces of the roofs A, B and C were directed towards the wind direction due to which the roofs D, E and F were acting as leeward roofs. The pressure distribution on these

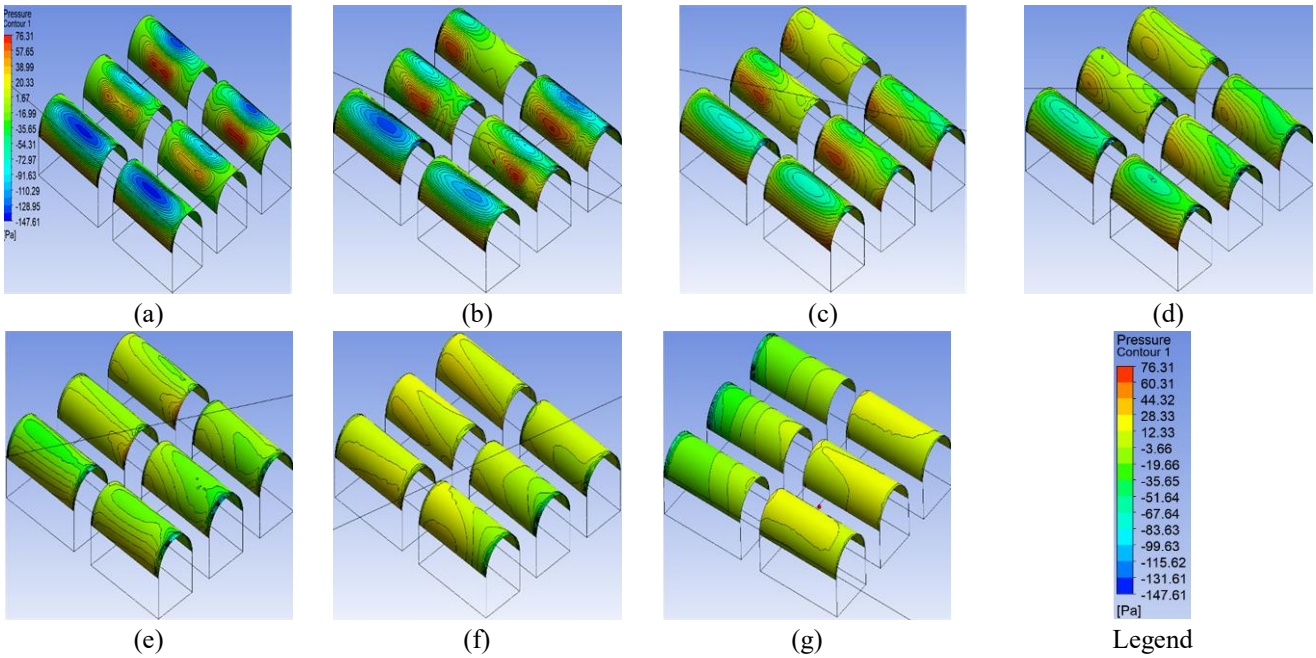

Fig. 10 Pressure Contours for 0.5B Spacing Model (a) 0° (b) 15° (c) 30° (d) 45° (e) 60° (f) 75° (g) 90°

leeward roofs found to be similar in nature and magnitude. Although the least suction noticed on these leeward roofs during 90° wind incidence angle when compared with all other wind incidence angles. It can be inferred from the Fig.10 that the maximum suction acting on the windward roof D at angle of 15° incidence and least suction observed on the roofs D, E and F during the wind incidence angle of 90°.

For Interference Model with B Spacing: Fig. 11 shows the pressure contours for the models of B spacing. Fig. 11(a) depicts the contours created by pressure brought on by the disposition of wind loads on low-rise structures with cylinder roofs that are placed in a rectangular pattern with B spacing between them during the wind incidence angle of 0°. It was noticed that the maximum negative (suction) pressure was acting on the top of windward roofs A & D. The windward roofs A & D were having similar kind of disposition of pressure. Furthermore, it was discovered that the negative pressure on all the roofs A, B, C, D, E and F of B spacing model was reduced when compared with zero and 0.5B spacing model. This implies that suction was reduced on all the roofs due to increase in the spacing between the buildings i.e., 0 to B. Fig. 11(b) represents the pressure contours for wind incidence angle of 15°. During 15° wind interval it was observed that the negative pressure on roofs A & F was reduced when compared with 0° wind incidence. On the other hand, the negative pressure on roofs B, C, D and E was increased when compared with 0° wind incidence. The effect of wind shielding was reduced on windward span of middle roofs (B & E) and leeward roofs (C & F). Fig. 11(c) shows the pressure contours for 30° wind incidence angle. Since the suction dramatically increases from a wind incidence angle of 0° to 30°, it has been noticed that the windward roof D is most impacted by negative pressure. In other words, we can say that the most critical wind incidence angle is 30°. The maximum changes in the pressure were observed during the wind incidence angle of 0° to 30°, after that the suction on the roofs started getting reduced on all the roofs. Fig. 11(g), the side faces of the roofs A, B and C were directed towards the wind direction due to which the roofs D, E and F were acting as leeward roofs. The pressure distribution on these leeward roofs was to be similar in nature and magnitude. Also, the least suction was noticed on these leeward roofs during 90° wind incidence angle when compared with all other wind incidence angles. It can be inferred from the Fig. 11 that the maximum suction was acting on the windward roof D at an angle of 30° incidence and least suction was subjected on the roofs D, E and F during the wind incidence angle of 90°.

For Interference Model with 1.5B Spacing: Fig. 12 shows the pressure contours for the models of 1.5B spacing. Fig. 12(a) depicts the contours created by pressure brought on by the disposition of wind loads on low-rise structures with cylinder roofs that are placed in a rectangular pattern. with 1.5B spacing between them during the wind incidence angle of 0°. It was noticed that the maximum negative (suction) pressure was acting on the top of windward roofs A & D. The windward roofs A & D were having similar kind of disposition of wind induced pressure. Furthermore, it was discovered that the negative pressure on all the roofs A, B, C, D, E and F of 1.5B spacing model was reduced when compared with zero, 0.5B and B spacing model. This implies that suction was reduced on all the roofs due to increase in the spacing between the buildings i.e., 0 to 1.5B. Fig. 12(b) represents the pressure contours for wind incidence angle of 15°. During 15° wind interval, there was drastic increase in the negative wind pressure on the windward roof D. It was observed that the negative pressure on roofs A & F was reduced when compared with 0° wind incidence. The leeward roof F was subjected to least negative pressure. On the other hand, the negative pressure

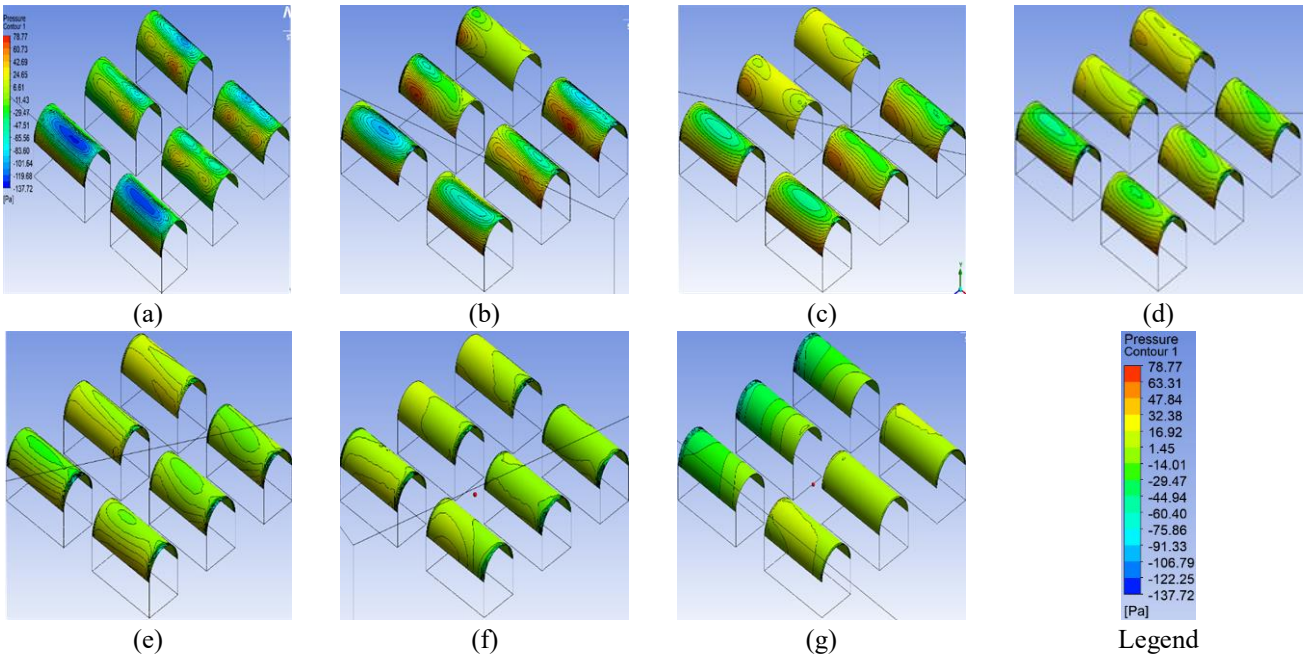

Fig. 11 Pressure Contours for B Spacing Model (a) 0° (b) 15° (c) 30° (d) 45° (e) 60° (f) 75° (g) 90°

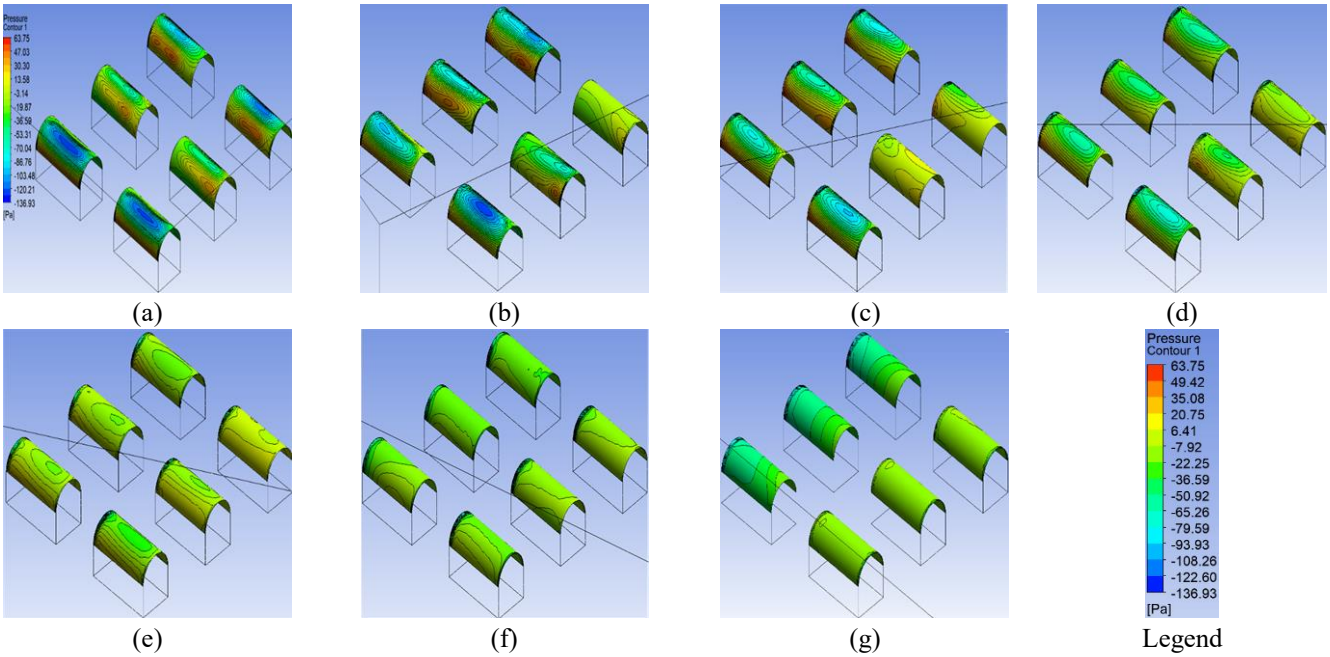

Fig. 12 Pressure Contours for 1.5B Spacing Model (a) 0° (b) 15° (c) 30° (d) 45° (e) 60° (f) 75° (g) 90°

on roofs B, C, D and E was increased when compared with 0° wind incidence. The effect of wind shielding was reduced on windward span of middle roofs (B & E) and leeward roofs (C & F). Fig. 12(c) shows the pressure contours for 30° wind incidence angle. Since the suction dramatically increases from a wind incidence angle of 0° to 30°, it has been noticed that the windward roof D is most impacted by negative pressure. In other words, we can say that the most critical wind incidence angle is 30°. The maximum increase in the suction pressure is observed during wind incidence angle of 30° for all the roofs except middle roof E. The maximum changes in the pressure were observed during the wind incidence angle of 0° to 30°, after that the suction on the roofs started getting reduced on all the roofs. Fig. 12(g), the side faces of the roofs A, B and C were directed towards the wind direction due to which the roofs D, E and F were acting as leeward roofs. The pressure distribution on these leeward roofs was to be similar in nature and magnitude. Also, the least suction was noticed on these leeward roofs during 90° wind incidence angle when compared with all other wind incidence angles. It can be inferred from the Fig. 12 that the maximum suction was acting on the windward roof D at an angle of 30° incidence and least suction was subjected on the roofs D, E and F during the wind incidence angle of 90°.

For Interference Model with 2B Spacing: Fig. 13

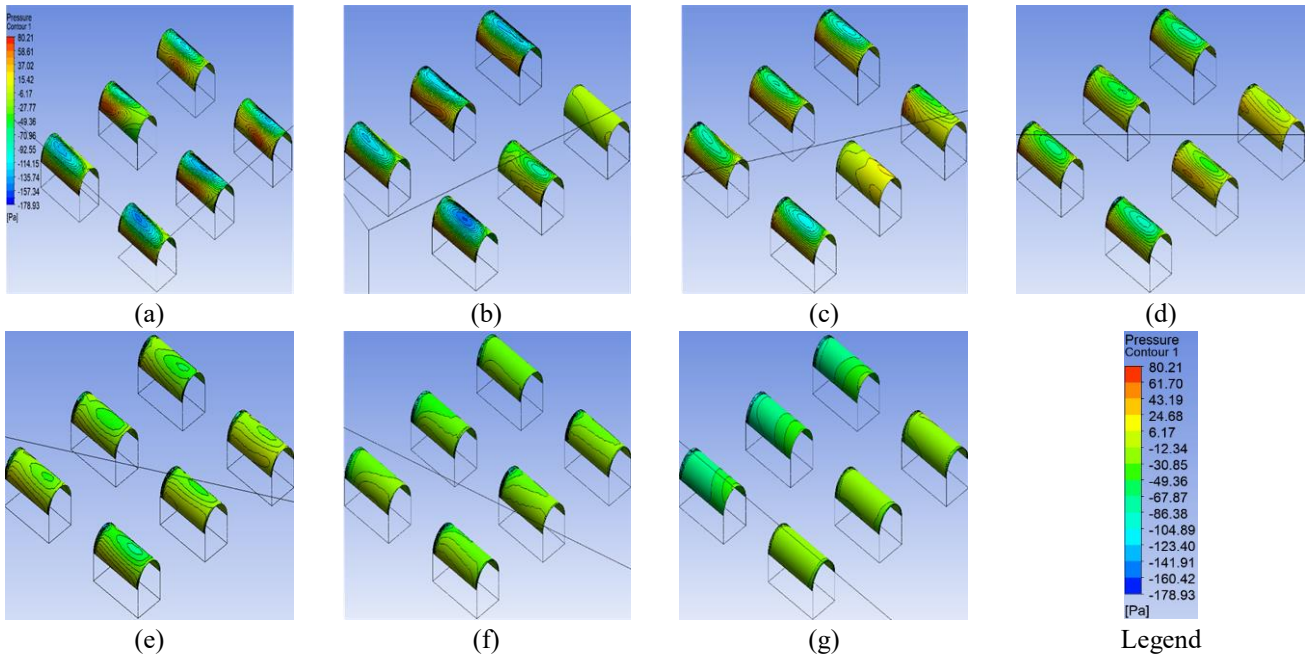

Fig. 13 Pressure Contours for 2B Spacing Model(a) 0° (b) 15° (c) 30° (d) 45° (e) 60° (f) 75° (g) 90°

shows the pressure contours for the models of 2B spacing. Fig. 13(a) depicts the contours created by pressure brought on by the disposition of wind loads on low-rise structures with cylinder roofs that are placed in a rectangular pattern with 2B spacing between them during the wind incidence angle of 0°. It was noticed that the maximum negative (suction) pressure was acting on the top of windward roofs A & D. The windward roofs A & D were having similar kind of distribution of pressure. Furthermore, discovered that the negative pressure on all the roofs A, B, C, D, E and F of 1.5B spacing model was reduced when compared with zero, 0.5B and B and 1.5B spacing model. This implies that suction was reduced on all the roofs due to increase in the spacing between the buildings i.e., 0 to 2B. Fig. 13(b) represents the pressure contours for wind incidence angle of 15°. During 15° wind interval, there was drastic increase in the negative wind pressure on the windward roof D. the windward roof D was subjected to maximum negative pressure as compared with other roofs. It was observed that the negative pressure on roofs A & F was reduced when compared with 0° wind incidence. The leeward roof F was subjected to least negative pressure. On the other hand, the negative pressure on roofs B, C, D and E was increased when compared with 0° wind incidence. The effect of wind shielding was reduced on windward span of middle roofs (B & E) and leeward roofs (C & F). Fig. 13(c) shows the pressure contours for 30° wind incidence angle. Since the suction dramatically increases from a wind incidence angle of 0° to 30°, it has been noticed that the windward roof D is most impacted by negative pressure. In other words, we can say that the most critical wind incidence angle is 30°. The maximum increase in the suction pressure is observed during wind incidence angle of 30° for all the roofs except middle roof E. The maximum changes in the pressure were observed during the wind incidence angle of 0° to 30°, after

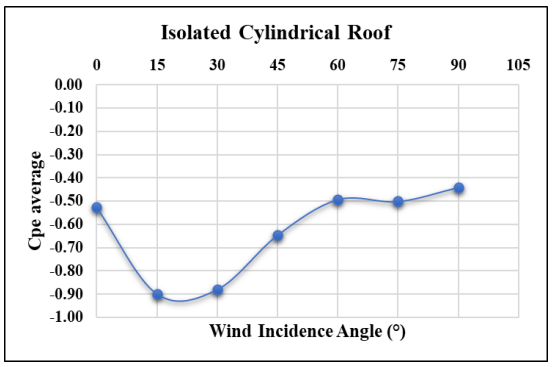

Fig. 14 Variation of C_{pe} average w.r.t wind incidence angle for isolated cylindrical roof

that the suction on the roofs started getting reduced on all the roofs. In Fig. 13(g), the side faces of the roofs A, B and C were directed towards the wind direction due to which the roofs D, E and F were acting as leeward roofs. The pressure distribution on these leeward roofs was to be similar in nature and magnitude. Also, the least suction was noticed on these leeward roofs during 90° wind incidence angle when compared with all other wind incidence angles. It can be inferred from the Fig. 13 that the maximum suction was acting on the windward roof D for 30° wind attack angle and least suction was subjected on the roofs D, E and F during the wind incidence angle of 90°.

3.4 External pressure coefficient

It is defined as the ratio of pressure difference acting on the surface at a point and static pressure due to incident wind to the design wind pressure. After considering the geographical location, terrain conditions and shielding

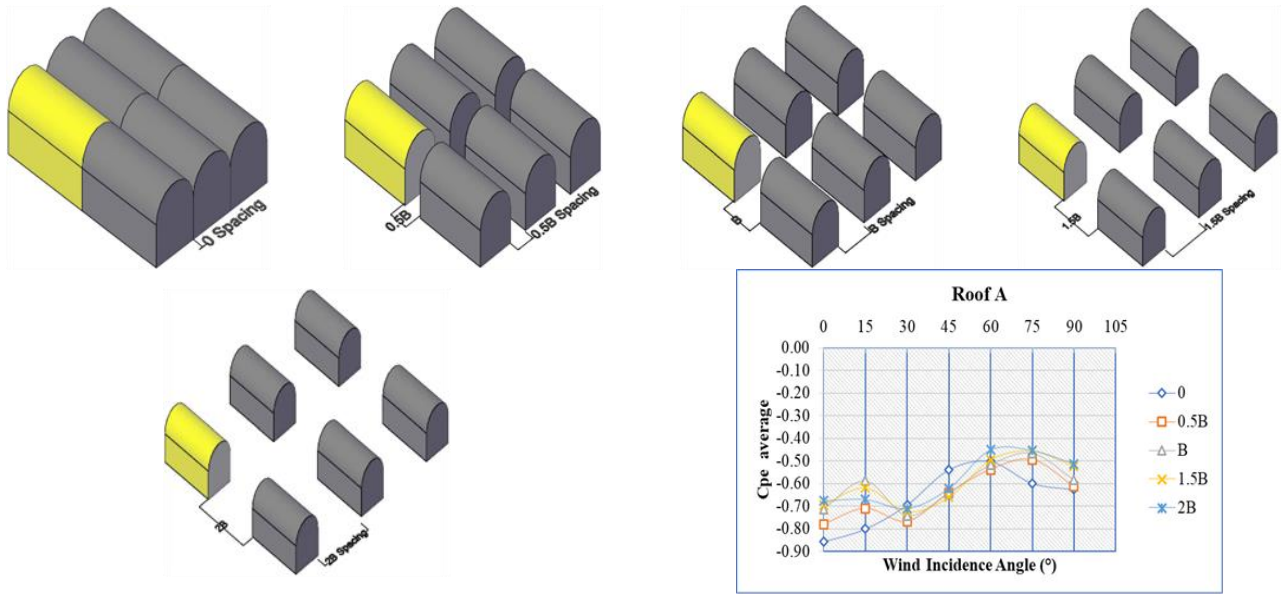

(a) Roof A

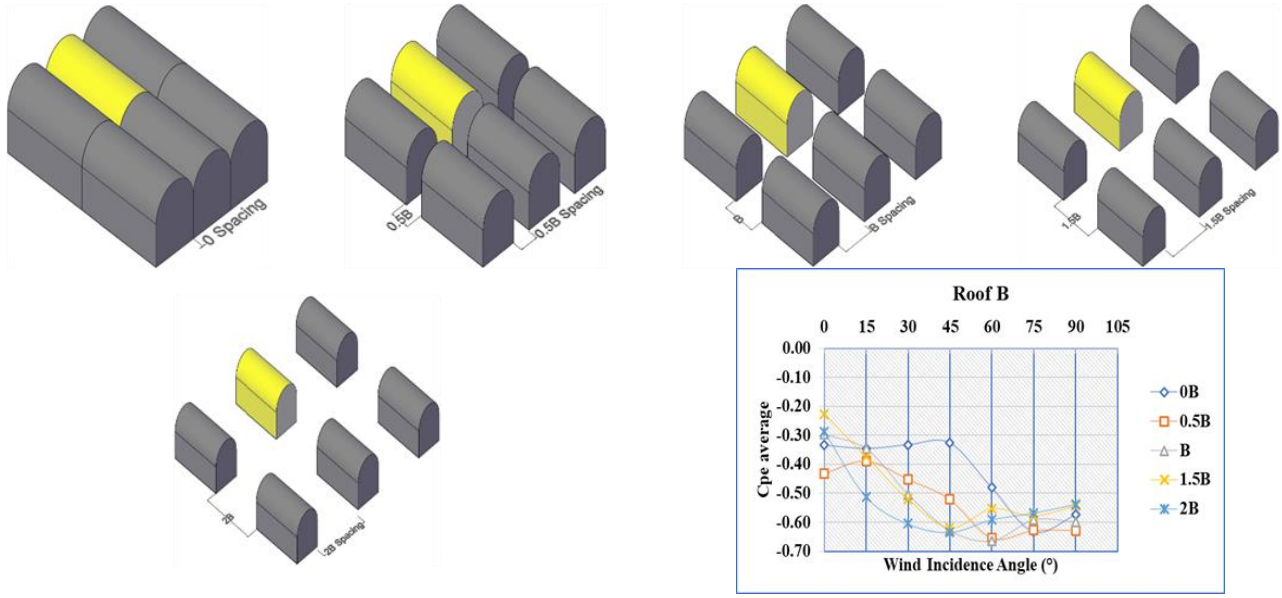

(b) Roof B

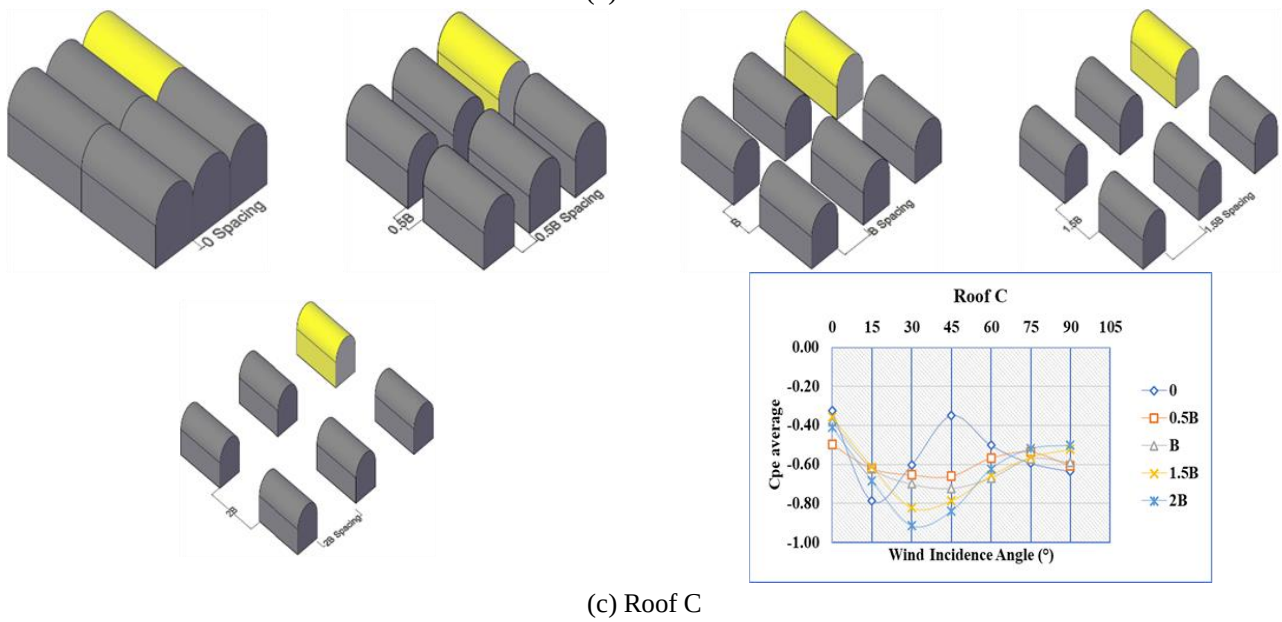

(c) Roof C

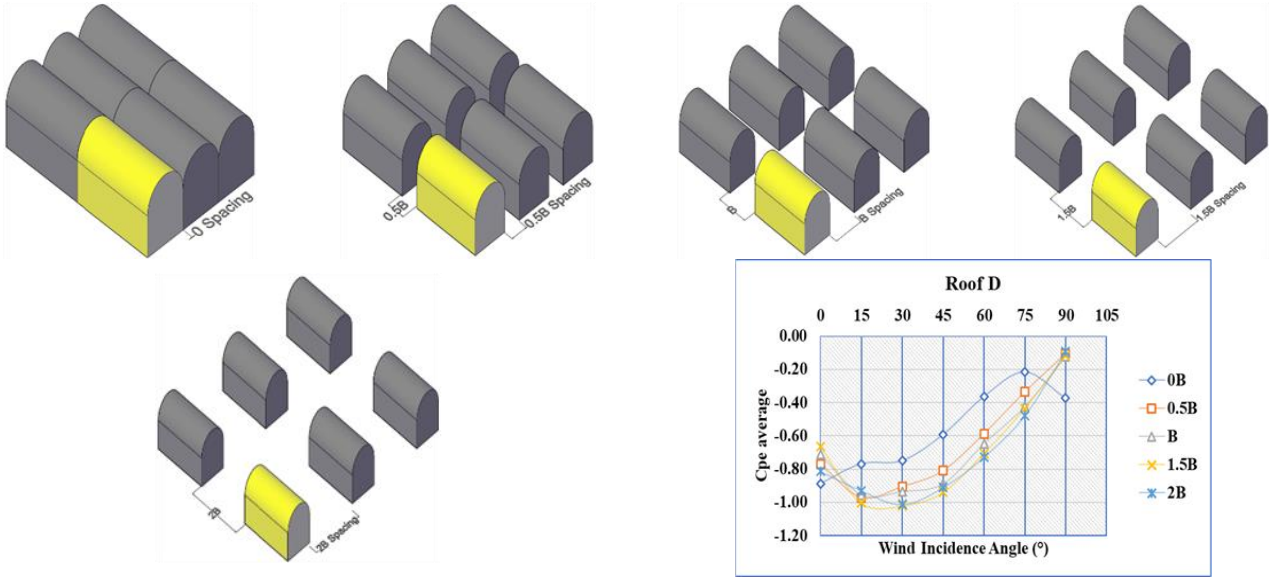

(d) Roof D

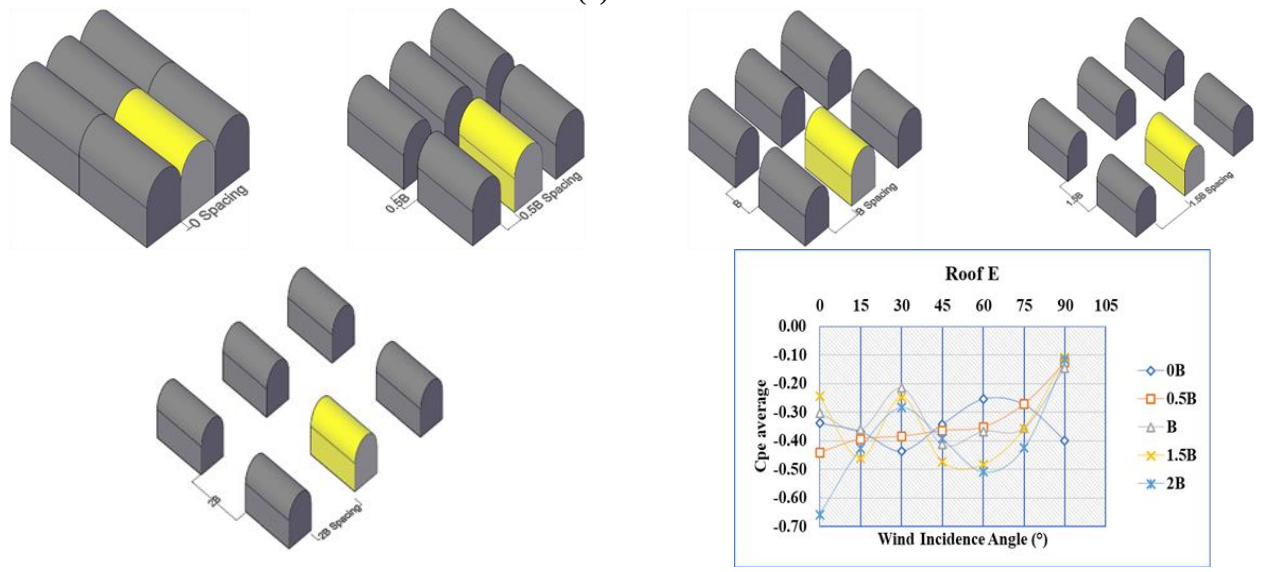

(e) Roof E

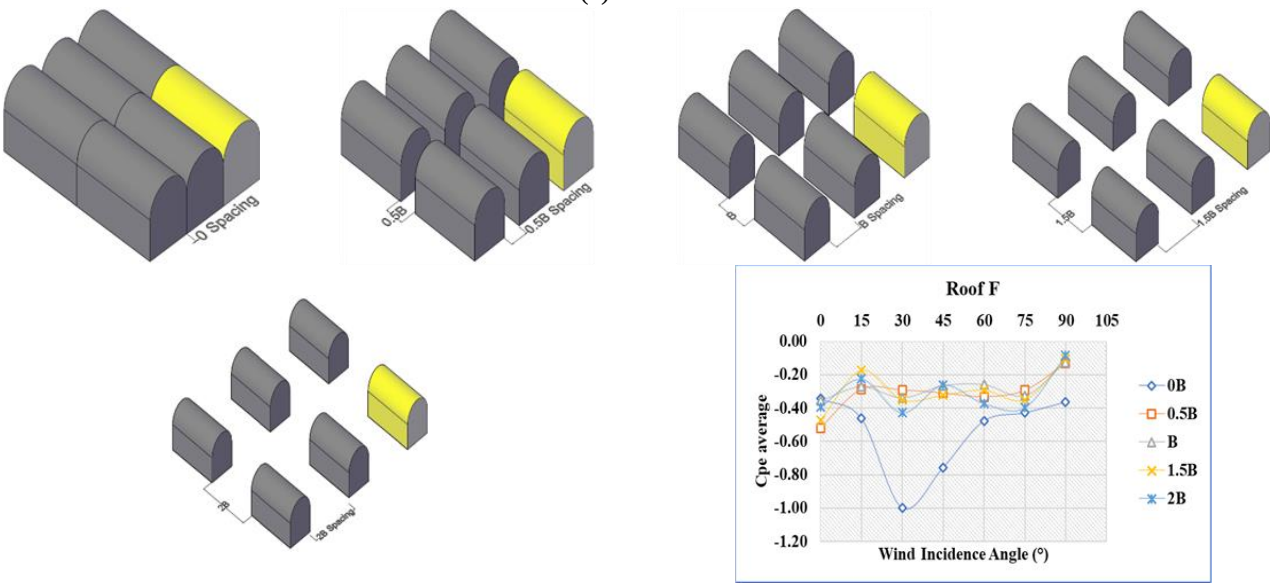

(f) Roof F

Fig. 15 Variation of average pressure coefficient having variable spacing with wind incidence angle

effect, the static and design wind pressure are measured at the height of the point considered.

$$C_{pe} = \frac{p - p_o}{\frac{1}{2}\rho {U_Z}^2} \quad (8)$$

For Isolated Cylindrical Roof: It was observed that a small portion of the isolated model near the windward edge is exposed to pressure when the angle of wind attack was ranging from 0° to 45° otherwise entire roof area will be under sucked condition. The maximum suction (- Cp) was occurring at the apex of the roof. During the wind angle of 15° and 30° respectively, it was noticed that there was maximum suction was acting i.e., C_{pe}=-0.90 at 15° wind incidence & -0.88 at 30° wind incidence. As the angle changes from 30° to 90°, the suction was reduced to the half of the magnitude. The minimum value of suction was observed as -0.44 at an angle of 90°. The variation of Cp for isolated cylindrical roof is presented in the Fig. 14.

Fig. 15 depicts the variation of average C_{pe} of all the roofs for different wind incidence angle i.e., 0° to 90° at 15° wind interval with variable spacing i.e., zero, 0.5B, B, 1.5B and 2B (where B=0.2 m).

From Fig. 15(A), it was observed that the variation of C_{pe} for roof A showed the similar trend of variation for all the types of interfering model i.e., C_{pe} was gradually decreasing which indicates that the suction was reducing due to the interfering buildings. The maximum negative value of C_{pe} on roof A was noticed during zero spacing interfering model at 0° wind interval i.e., C_{pe} = -0.86 and minimum negative C_{pe} was observed for 2B interfering model at 90° wind incidence angle i.e., C_{pe} = -0.45.

In Fig. 15(b), the variation of C_{pe} for roof B is shown for different interfering model w.r.t to different wind incidence angle. The value of C_{pe} was increasing in magnitude towards negative value which indicates that the suction on roof B was increased for all the types of interfering model. The minimum suction i.e., C_{pe} = -0.23 was noticed on roof B during 0° wind incidence angle having 2B spacing while maximum suction with C_{pe} = -0.63 was found at 0°, 45°, and 75° wind interval for zero, 2B and 0.5B spacing interfering model.

In Fig. 15(c), the variation of C_{pe} for roof C was quite similar for 0.5B, B, 1.5B and 2B interfering model except for zero spacing model. For zero spacing model, it shows reduction in C_{pe} for 15° to 45° wind incidence angles after onwards, it started increasing till 90° whereas for other interfering models, the value of C_{pe} was gradually decreasing. The maximum negative value of C_{pe} was -0.91during 30° wind incidence angle for 2B interfering model and minimum negative value of C_{pe} was observed to be -0.32 at 0° wind angle for zero spacing interfering model.

Fig. 15(d) shows the variation of C_{pe} for roof D with variable spacing models at different wind incidence angle. It can be inferred from the Fig. 15(d) that the value of C_{pe} was keep on decreasing in magnitude for all types of interfering models when wind angle changes from 0° to 90° at 15° wind interval. The minimum negative value of C_{pe} = 0.09 was found on the roof D at 90° wind angle for 2B spacing model and maximum negative value of C_{pe} = -1.02 was found at 30° wind angle for 1.5B spacing model.

The variation of C_{pe} for roof E is shown in Fig. 15(E). The maximum negative value of C_{pe} = -0.66 for 2B spacing model at 0° wind interval and minimum negative value of C_{pe} = -0.11 for 1.5B spacing model, were found respectively.

The maximum negative value of C_{pe} for roof F was found out to be -1.0 during 30° wind angle of incidence for zero spacing and minimum negative value of C_{pe} is -0.08 at 90° wind incidence angle for 2B interfering model, as shown in Fig. 15(f).

This paper presents the wind induced pressure contours and pressure coefficient on the roof of low-rise building with cylindrical roof during isolated and group conditions with variable spacing when subjected to various wind incidence angles between 0° to 90° at an interval of 15° using CFD simulation. It can be seen from the results that during isolated condition, the average pressure acting on the roof was negative in nature which creates suction on whole area of the roof. From all the wind incidence angle 0° to 90°, it was found that maximum suction was occurring during 15° and 30° wind angles. It was also discovered that the negative pressure on isolated roof started reducing after 30° wind incidence till 90°. Therefore, the minimum suction was occurring at 90° wind angle on isolated cylindrical roof.

In case of group formation of buildings in rectangular pattern with variable spacing, the windward roofs A&D were behaving as shield for middle roofs B&E and leeward roofs C&F respectively on windward portions of the roofs. Due to group formation of buildings, the pressure on the roofs got reduced when compared with isolated condition. The wind shielding effect was getting reduced with the increase in spacing between the buildings. At 90° wind incidence angle, the roofs A, B and C were behaving as a shield for roofs D, E and F respectively. The maximum negative value of C_{pe} on roof A was noticed during zero spacing model at 0° wind interval i.e., C_{pe} = -0.86 and minimum negative C_{pe} was observed for 2B spacing model at 90° wind incidence angle i.e., C_{pe} = -0.45. The minimum suction i.e., C_{pe} = -0.23 was noticed on roof B during 0° wind incidence angle having 2B spacing while maximum suction with C_{pe} = -0.63 was found at 0°, 45°, and 75° wind interval for zero, 2B and 0.5B spacing model. On roof C, the maximum negative value of C_{pe} was -0.91during 30° wind incidence angle for 2B model and minimum negative value of C_{pe} was observed to be -0.32 at 0° wind angle for zero spacing model. The minimum negative value of C_{pe} = 0.09 was found on the roof D at 90° wind angle for 2B spacing model and maximum negative value of C_{pe} = -1.02 was found at 30° wind angle for 1.5B spacing model. The maximum negative value of C_{pe} = -0.66 for 2B spacing model at 0° wind interval and minimum negative value of C_{pe} = -0.11 for 1.5B spacing model, were found respectively on the roof E. The maximum negative value of C_{pe} for roof F was found out to be -1.0 during 30° wind angle of incidence for zero spacing and minimum negative value of C_{pe} is -0.08 at 90° wind incidence angle for 2B spacing model.

4. Conclusions

In the present investigation, the variation of $C_{pe\ mean}$ has been studied due to presence of interfering buildings arranged in rectangular pattern with different spacing configurations in terms of width (B) of the building i.e., 0, 0.5B, B, 1.5B and 2B respectively. Some of the important outcomes of this study are as follows:

• A very sliver portion of the isolated model near the edge of windward side is exposed to pressure. On the other hand, the unified roof area will be sucked. In case of isolated cylindrical roof, the maximum change in flow pattern was observed during the wind incidence angle of 15° to 45° due to which there was generation of suction taking place. For the case of isolated building, the value of suction was increased when the wind angle changed from 0° to 30° after that the suction value stared decreasing from 45° to 90° wind incidence angle. The maximum value of suction was observed at a wind angle of 30° while minimum suction was observed during 90° wind angle for isolated cylindrical roof.

• Due to the presence of interfering buildings, there was reduction in Cpe mean values when compared with isolated cylindrical roof. This reduction in Cpe mean was due to the wind shielding effects because of the presence of windward roofs. As the direct entrance of the wind streamline is constrained with each increase in wind incidence angle, the Cpe mean values steadily decrease. As a result, after 90°of wind incidence, negative Cpe mean values are inevitable.

• It was observed that the almost whole cylindrical roof was subjected to the suction. The value of the suction was varying w.r.t to wind incidence angle for both isolated and interfering cylindrical roofs. The pressure distribution on windward roofs A & D for all the interfering models was similar to that of isolated cylindrical roof during 0° wind incidence angle.

• The maximum value of negative Cp was observed on the roof C during the wind incidence angle of 30° and minimum value of negative Cp was subjected on the roof A during the wind incidence angle of 75°.

• The shielding effect of the windward span benefits the wind pressure distribution of the leeward span. Also, the wind shielding effect was reducing by increasing the spacing between buildings.

• For multi-span cylindrical roof, the middle span was least subjected to the suction as compared to with windward and leeward span. The suction on the leeward span is smaller than the suction on the upwind span, up to half the upwind span.

• For the designing of low-rise buildings with cylindrical roofs by arranging them in rectangular pattern with variable spacing, at least we have to consider the three cylindrical roof model.

• The findings and recommendations made by this study would directly affect investigations of the various types of roofs. This study offers significant new knowledge on the impact of the roof's form and curvature on the pressure induced by the wind, coefficients of wind pressure (C_p), knowledge that may be applied to different forms of roofs. This would be helpful in the investigation of the structural soundness of various roof types under wind load circumstances, together with a cost-effective design.

Future work

In the present numerical investigation, the analysis of wind induced pressure and pressure coefficients has been done over the low-rise building with cylindrical roof in isolated as well as by arranging them in a rectangle pattern with variable spacing with respect to the width of the building using ANSYS CFX. There can be the possibility of study for wind effects on other types roof shapes by arranging them in different patterns.

References

ASCE/SEI 7-16, (2016), ASCE Standard, Wind Loads, In Minimum Design Loads and Associated Criteria for Buildings and Other Structures, Reston, American Society of Civil Engineers, 245-390.

Eurocode 1 (2010), *Standard*, *European*, *Actions on Structures - Part 1-4: General Actions - Wind Actions*, European Union.

Standard, New Zealand Standard and Australia (2011), *Structural Design Actions - Part 2: Wind Actions (AS/NZS 1170.2:2011)*, *Australian/New Zealand Standard*.

Architectural Institute of Japan (2015), *Architectural Institute of Japan*, *Chapter 6 Wind Loads*, *In AIJ Recommendations for Loads on Buildings*, *Tokyo*, *Architectural Institute of Japan.*

ASCE 7-16 (2017), *American Society of Civil Engineers*, *Reston Minimum Design Loads and Associated Criteria for Buildings and Other Structures*. Structural Engineering Institute of the American Society of Civil Engineering, Reston.

Bairagi, A.K. and Dalui, S.K. (2018), "Comparison of aerodynamic coefficients of setback tall buildings due to wind load, asian", *J. Civil Eng.*, **3**. https://doi.org/10.1007/s42107-018-0018-3.

Beura, M.S. and Mishra, D.P. (2014), "Effect of wall tapper and attack angle on mean flow structure around a pyramid", *Int. J. Emerg. Technol. Comput. Appl. Sci.*, **8**(6), 490-98.

Davenport, A.G., Surry, D. and Stathopoulos, T. (1977), "Wind loads on low-rise buildings", *Final Report of Phases I and II - Parts 1 and 2'*, *BL WT Report SS8-19 77*, The University of Western Ontario, London, Ontario, Canada.

Elsharawy M., Stathopoulos T. and Galal K. (2011), "Wind-Induced torsional loads on low buildings, journal of wind engineering and industrial aerodynamics", *J. Wind Eng. Ind. Aerod.* **104**(106), 349-359. https://doi.org/10.1016/j.jweia.2012.03.011.

Faghih, A.K. and Bahadori, M.N. (2009), "Experimental investigation of airflow over domed roofs", *Iran. J. Sci Technol.*, **15**, 207-16.

Franke, J., Hellsten, A., Schlünzen, H. and Carissimo, B. (2007), "Guideline for the CFD Simulation of Flows in the Urban Environment", *COST Action 732 Quality Assurance and Improvement of Microscale Meteorological Models*, *May*.

Ginger, J.D. and Holmes, J.D. (2003), "Effect of building length on wind loads on low-rise buildings with a steep roof pitch", *J. Wind Eng. Ind. Aerod.*, **91**(11), 1377-1400. https://doi.org/10.1016/j.jweia.2003.08.003.

He, B.J., Ding, L. and Prasad, D. (2019), "Enhancing urban ventilation performance through the development of precinct

ventilation zones: a case study based on the greater sydney, australia", *Sustain. Cities Soc.*, **47**, 101472. https://doi.org/10.1016/j.scs.2019.101472.
IS: 875 (2015), *Indian Standard Design Loads (Other than Earthquake) for Buildings and Structures-Code of Practice*, *Part 3(Wind Loads)*, *BIS*, *New Delhi*: 51.
Jagbir, S. and Roy A.K. (2021), 14 *Wind Loads on Roof of Low-Rise Buildings*.
Jana, D., Bhaduri, T. and Dalui, S.K. (2015), "Numerical study of optimization of interference effect on pentagonal plan shaped tall building", *Asian J. Civil Eng.* **16**(8), 1123-1153. https://doi.org/10.1016/j.jweia.2012.03.011.
John, A.D., Kotamrazu, Mohan, Gairola, A., Mukherjee, M. (2009), "Effect of architectural features on wind loads in low-rise buildings", *In 7th Asia-Pacific Conference on Wind Engineering*, *APCWE-VII*.
Mahdavinejad M. and Kavan J. (2016), "Impact of roof shape on air pressure, wind flow and indoor temperature of residential buildings", *Int. J. Sustain. Build. Technol. Urban Develop.*, **7**(2), 87-103. https://doi.org/10.1080/2093761X.2016.1167645 (2016).
Meena, R.K., Raj, R. and Anbukumar, S. (2022), "Effect of wind load on irregular shape tall buildings having different corner configuration", *Sadhana - Academy Proceedings in Engineering Sciences*, **47**(3), https://doi.org/10.1007/s12046-022-01895-2.
Meng, F.Q., He, B.J., Zhu, J., Zhao, D.X., Darko, A. and Zhao, Z.Q. (2018), "Sensitivity analysis of wind pressure coefficients on caarc standard tall buildings in cfd simulations", *J. Build. Eng.*, **16**, 146-58. https://doi.org/10.1016/j.jobe.2018.01.004.
Pindado, S., Meseguer, J. and Franchini, S. (2011), "Influence of an upstream building on the wind-induced mean suction on the flat roof of a low-rise building", *J. Wind Eng. Ind. Aerod.* **99**(8), 889-93. https://doi.org/10.1016/j.jweia.2011.06.003.
Qiu, Y., Sun, Y., Wu, Y. and Tamura, Y. (2014), "Modeling the mean wind loads on cylindrical roofs with consideration of the reynolds number effect in uniform flow with low turbulence", *J. Wind Eng. Ind. Aerod.* **129**, 11-21. https://doi.org/10.1016/j.jweia.2014.02.011.
Rahmatmand, A., Yaghoubi, M., Rad, E.G. and Tavakol, M.M. (2014), "3D experimental and numerical analysis of wind flow around domed-roof buildings with open and closed apertures", *Build. Simulation* **7**(3), 305-319. https://doi.org/10.1007/s12273-013-0157-0 (2014).
Raj, R. (2015), "Effects of cross-sectional shapes on response of tall buildings under wind loads", *Iit Roorkee*.
Revuz, J., Hargreaves, D.M. and Owen, J.S. (2012), "On the domain size for the steady-state cfd modelling of a tall building", *Wind Struct. An Int. J.*, **15**(4), 313-329.
Satheeskumar, N., Henderson, D.J., Ginger, J.D. and Wang, C.H. (2017), "Finite element modelling of the structural response of roof to wall framing connections in timber-framed houses", *Eng. Struct.* **134**, 25-36. http://dx.doi.org/10.1016/j.engstruct.2016.12.034.
Standards British Institution (2002), *Loading for Buildings: Part 2: Code of Practice for Wind Loads*.
Stathopoulos, T. (1975), *Wind Pressure Loads on Flat Roofs*, *BL WT 47 Rep. 3*, The University of Western Ontario.
Surry, D. and Lin, J. X. (1995), "The effect of surroundings and roof corner geometric modifications on roof pressures on low-rise buildings", *J. Wind Eng. Ind. Aerod.*, **58**(1-2), 113-38. https://doi.org/10.1016/0167-6105(95)00016-K.
TCVN 2737-1995 (1995), *Vietnamese Standard- TCVN 2737:1995 Loads and Actions*.
Uematsu, Y. and Isyumov, N. (1999), "Wind pressures acting on low-rise buildings", *J. Wind Eng. Ind. Aerod.*, **82**(1), 1-25. https://doi.org/10.1016/S0167-6105(99)00036-7.
Verma, A. and Ashok, K.A. (2015), "Wind pressure distribution on domical roofs", *Int. J. Eng. Appl. Sci.*, **2**(1).
Vickery, B. (1976), "Wind loads on low-rise buildings", *In DRC Seminar*, *Darwin*, *Australia*,
Weerasuriya, A.U., Hu, Z.Z., Zhang, X.L., Tse, K.T., Li, S. and Chan, P.W. (2018), "New inflow boundary conditions for modeling twisted wind profiles in cfd simulation for evaluating the pedestrian-level wind field near an isolated building", *Build. Environ.*, **132**, 303-318. https://doi.org/10.1016/j.buildenv.2018.01.047.

TK

View publication stats

Multimedia Tools and Applications
https://doi.org/10.1007/s11042-023-16078-2

Obscenity detection transformer for detecting inappropriate contents from videos

Kamakshi Rautela[1] · **Dhruv Sharma**[1] · **Vijay Kumar**[2] · **Dinesh Kumar**[1]

Received: 20 September 2022 / Revised: 12 June 2023 / Accepted: 18 June 2023
© The Author(s), under exclusive licence to Springer Science+Business Media, LLC, part of Springer Nature 2023

Abstract
With the availability of a wide range of images and videos on the Internet, classification and detection of inappropriate content has become a matter of serious concern. This type of content has a harmful impact on the minds of minors as well as on adults. Therefore, it is necessary to control and detect such content from images and videos. Recent research has focused on deep-learning-based automated pornographic detection, a bold move to replace humans in the time-consuming task of moderating online content. This paper is based on the idea that incorporating detailed information into a model helps solve the problem of mapping pornographic content. In this paper, a novel deep-learning transformer-based framework namely, Obscenity Detection Transformer (ODT) is proposed to detect and classify inappropriate or pornographic content from videos. The proposed transformer inputs video frames and leverages the vision transformer with the LSTM layer. LSTM embedding enables the network to extract more informative features. Also, GELU activation-based MLP is employed to classify pornographic and non-pornographic content. The advantage of leveraging transformer-based architecture is that these architectures improve efficiency and accuracy when compared with CNN-based models. To validate the efficiency and efficacy of the proposed model, extensive experiments are carried out on Pornography-2 k and Pornography-800 datasets. The proposed model outperforms the current state-of-the-art (CNN) in terms of computational efficiency and accuracy. The accuracies achieved for the two aforementioned datasets are 99.6% and 98.8%, respectively.

Keywords Transformer · Obscenity Detection · Pornography Detection · Deep-Learning · Obscenity Detection Transformer (ODT)

✉ Vijay Kumar
vijaykumarchahar@gmail.com

Kamakshi Rautela
rautelakamakshi11@gmail.com

Dhruv Sharma
dhruv.0906@yahoo.in

Dinesh Kumar
dineshkumar@dtu.ac.in

[1] Delhi Technological University, Delhi, India

[2] Dr B R Ambedkar National Institute of Technology, Jalandhar, India

1 Introduction

The advancement of technology has made it easy for one and all to have easy access to the Internet. People of every age can stumble upon inappropriate content available intentionally or unintentionally. The booming consumption of online media has made filtering sensitive media (pornography, brutality, abusive content, etc.) an important task. Pornographic content does have an adverse impact on mental and physical health specially on minors. Further, exposure to pornographic content at a young age may lead to aggression and negative attitude and behavior toward others [21]. The main issue here is how to prevent someone from uploading or accessing undesired content for certain demographics (e.g., minors), or environments (e.g., schools, workplace). for certain demographics (e.g., minors), or environments (e.g., schools, workplaces).

Pornography is a very subjective topic with no clear definition. It is really difficult to precisely define what constitutes pornography. For this research, pornography is defined as a visual depiction of sex organs or behaviors in the form of photos or movies, with the primary goal of simulating sexual excitation in a person. Adult video content is considered to be responsible for a major portion of Internet traffic [3, 7]. Pornography can be distributed in multiple forms on the Internet. Online pornography forms a non-negligible fraction of the total Internet traffic, with adult video streaming gaining significant traction among the most visited global websites [13, 26, 29, 31].

To detect pornography, a logical strategy is to first try to detect nudity [8–10, 32] before determining appropriate thresholds to further filter the content. Human skin characteristics such as color and texture, as well as human geometry, are frequently used in such solutions [4, 16, 17, 22]. The solutions discussed above are not reliable as people may reveal a lot of skin in activities other than sex (e.g., sunbathing, swimming, running, wrestling), resulting in a lot of false positives. Skin exposure is not a viable proxy for pornography detection in and of itself. Some sexual activities, on the other hand, involve very little skin exposure, resulting in unsatisfactory false negatives.

Despite the success of deep learning approaches in the field of computer vision, there is a paucity of research on pornography detection. The aforementioned methods had poor classification accuracy, poor detection speeds, and a time-consuming process. The motivation for this work is to deal with the aforementioned problems. As an outcome, there is a scope to develop solutions that are reliable, computationally less expensive, and quick to train and infer.

In this paper, we have proposed a transformer-based framework for obscenity detection namely Obscenity Detection Transformer (ODT). The proposed framework structure is presented in Fig. 1. ODT is used to detect and categorize the sequence of frames of pornographic videos without using motion information. In practical application scenarios,

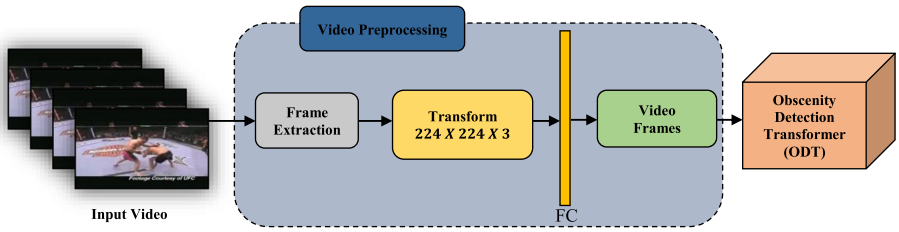

Fig. 1 The proposed Framework

this research can also be used to detect illegal videos on live broadcast platforms and can help in the intelligent detection of pornographic videos. To the best of our knowledge, the transformer-based deep learning framework, for the detection of inappropriate content in video frames, is being proposed for the first time. The main contributions are as under:

- An efficient transformer-based framework, Obscenity Detection Transformer (ODT) is proposed. It detects inappropriate content from preprocessed video frames.
- The proposed LSTM embedding enables the network to extract more informative features, thereby improving detection accuracy.
- The effectiveness of the proposed work is validated through experimentation on Pornography-800 [2] and the Pornography-2 K dataset [18].
- The proposed incremental learning strategy improves the generalization capability of the proposed model. The comprehensive experiments show that our model can achieve good performance on a new dataset while maintaining their performance on the previous dataset.

The organization of the rest of the paper is as follows: Section 2 presents the related work that covers both handcrafted and deep-learning features for obscenity detection. Section 3 discusses the proposed Obscenity Detection Transformer (ODT). Section 4 presents experimental analysis with its results whereas Section 5 presents the computational complexity. Further, in Section 6, we conclude the paper along with the future scope.

2 Related works

Obscenity detection in videos came into existence when researchers started recognizing the problems related to skin-based features [15] and nudity detection [28]. They used the process of creating color models for skin and non-skin categories involved using a dataset containing close to 1 billion pixels with corresponding labels. Classification of images and extraction of features from them is considered an important indicator for nudity if the input using CNN is one of the common methods. The human face is by far the most significant area of interest in detection. It includes an exceedingly massive area of skin. However, the face may not be the most obvious factor that impacts the output. As a result, the more difficult task is to discover the best method for comprehending video context.

Moustafa et al. [19] presented the first-ever approach for obscenity detection. To achieve the best classification results, [19] combined AlexNet and GoogLeNet features. A deep learning system is suggested to automatically examine images and video frames and classify their content as either regular or explicit. Further, Wehermann et al. [28] provided improvements in [19] by extracting features from various models of ResNet and processing them through RNN. A new and innovative deep learning architecture has been proposed by them, which combines convolutional neural networks and LSTM recurrent networks to detect adult content in videos. Perez et al. [20] extracted static and dynamic features from videos to classify them into pornographic or non-pornographic videos. They obtained the highest classification accuracy for adult videos and were the first to use motion information to classify videos. Further, [25] explored Convolution3D-based CNN architectures Conv3D layer to learn Spatiotemporal embeddings. Wang et al. [27] proposed a multimodal deep-learning framework to detect inappropriate content from videos with the help

of Bi-GRU. Though this approach performed better in terms of accuracy but possessed high computational complexity.

The attention mechanism is widely used in image classification, object identification, natural language processing, and other fields due to its many benefits [13]. Nonetheless, the use of attention mechanisms in the classification of obscene images is slowly growing. An innovative dot-product-based attention technique with a 92.72% accuracy for pornography detection was proposed [11]. A unique visual attention mechanism called CBAM and Scale Constraint Pooling (SCP) was used to create a moderate CNN called DOCAPorn, which had an accuracy of 98.41%. It also minimized same-class fluctuation and optimized the distance between classes [6].

Recently, Yousuf et al. [30] presented a deep-learning-based approach to detect inappropriate content from YouTube videos. This model employed EffiecentNet-B7 to extract the features from videos and Bi-LSTM is further employed for multiclass video classification. Also, Gautam et al. [12] proposed a ConvNet pipeline classifier to detect obscenity in videos without capturing the motion information. Further, Deep learning-based methods have been proven excellent performance in detecting pornographic images/videos flooded on social media. Samal et al. [23] utilized transfer learning and feature fusion and detected pornographic images. They propose a transfer learning-based feature fusion process (FFP) that eliminates the need for hyper-parameter tuning, improves model performance, and reduces the computational requirements of the desired model. FFP combines low-level and mid-level features from superior pre-trained models and applies the knowledge gained to guide the classification process. Also, Samal et al. [24] developed a deep learning model that could classify and label the obscene portion as an attention mechanism and a suitable pooling strategy. With the rapid development of online live broadcast, live broadcast has become an indispensable part of people's entertainment and enriches people's lives. Yuan et al. [14] proposed deep-learning framework-based detection of pornographic content from live broadcasting. The comparative analysis of various deep-learning techniques for obscenity detection is presented in Table 1.

Table 1 Comparative analysis of different state-of-the-art

Ref	Year	Model used	Dataset	Performance
[28]	2017	CNN, LSTM	NPDI	Acc = 95.3%
[20]	2018	CNN	Pornography-2 k, Pornography-800	Acc = 96.4%
[19]	2015	CNN	NDPI	Acc = 94.1%
[25]	2019	Spatiotemporal CNN	Pornography-800	Acc = 95.1
[27]	2020	CNN, Bi-GRU	BJUTSD_V2	Acc = 69.2%
[12]	2022	CNN, ConvNet	Pornography-2 k, Pornography-800	Acc = 98.25% (P-800) Acc = 97.15% (P-2 k)
[30]	2022	EfficientNet-B7	YouTube cartoon	Acc = 95.66%
[11]	2021	AttM-CNN	Pornographic-2 M Juvenile-80 k	Acc-92.72%
[6]	2020	DOCAPorn		Acc-98.41%
[23]	2023	Transfer Learning & Feature Fusion	NPDI Pornography-2 K GGOI	Acc-99.13% Acc-99.15% Acc-99.48%
[24]	2023	SBMY:v3	GLOI	Acc-99.26%

3 Proposed work

With the advancements made in transformer-based deep-learning architectures, the work in this paper focuses on the detection and classification of obscenity in videos using a modified vision transformer. Perhaps this is an initiative toward transformer-based obscenity detection and classification.

This section presents a proposed Obscenity Detection Transformer (ODT), as shown in Fig. 2. The proposed framework is created to develop a precise method of pornographic detection and classification. The details of the proposed work are as follows.

3.1 Data preprocessing

The datasets used for the detection and classification of inappropriate content are in the form of videos. These videos are first converted into frames and are further fed to the input of the ODT. To obtain the necessary information for better video classification, deep learning approaches play an important role in video preprocessing. In this work, a video V_M is initially represented as n short video clips $(s_1^i, s_2^i, \ldots\ldots\ldots, s_n^i)$ that are each one second long. These short clips are manually annotated, where any missing details or context are ignored. It is observed that each video clip contains information from the preceding clip of the same video in the first three to four frames after dividing and labeling the video clips. Because of this, each q^{th} video clip (s_j^i) is sampled at the frame rate of 28 fps by neglecting certain initial frames, based on an average video frame rate of 29–30 frames per second (fps). For all video clips that include fewer frames than the typical frame rate of a video, the last frame is replicated.

The overall representation of the frames is $q_1^{i,j}, q_2^{i,j}, \ldots\ldots, q_{28}^{i,j}$, where $q_n^{i,j}$ stands for the n^{th} frame of video clips$_j^i$. The next step is to rescale the chosen frames from each video clip to a fixed resolution of 124×124 pixels, which is the input to the ODT.

3.2 Obscenity detection transformer

The input video frames are first converted into a sequence of image patches to adapt to the input form of the transformer. Further, position embeddings are added to the patch

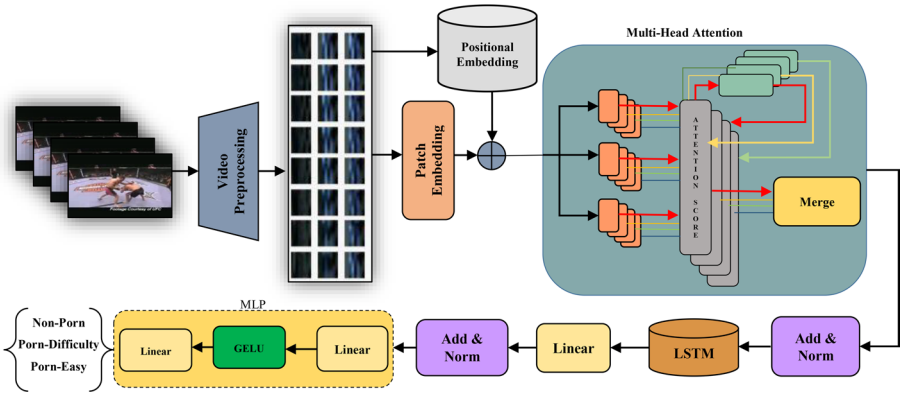

Fig. 2 Architecture of the proposed Obscenity Detection Transformer (ODT)

embeddings to retain positional information that yields a sequence of embedding vectors. Therefore, input is embedded into a feature vector, following a sequence of transformations The model therefore splits the images (video frames) into a series of positional embedding patches, which are processed by the transformer encoder given by:

$$\ddagger_0 = [\mathcal{X}_{class}; \mathcal{X}_p^1\mathcal{E}; \mathcal{X}_p^2\mathcal{E}; \ldots\ldots \mathcal{X}_p^N\mathcal{E}] + \mathcal{E}_{pos} \tag{1}$$

where, $\mathcal{E}_{pos} \in \mathbb{R}^{(N+1)\times D}$ represents trainable positional embedding vector and $\mathcal{E} \in \mathbb{R}^{(p^2.C)\times D}$ represents trainable embedding vector. Further, $\ddagger_0$ serves as input to the encoder. Let us consider Query $\mathbb{Q}$, Key $\mathbb{K}$, and Values $\mathbb{V}$ as the inputs to the transformer encoder. The multi-head attention module splits $\mathbb{Q}$, $\mathbb{K}$, and $\mathbb{V}$ parameters in N-ways and passes each split independently through a separate Head. All of these similar Attention calculations are then combined to produce a final Attention score. The multi-head attention module is represented in the form of equations:

$$[\mathbb{Q}, \mathbb{K}, \mathbb{V}] = \ddagger \cup_{\mathbb{Q},\mathbb{K},\mathbb{V}}, \cup_{\mathbb{Q},\mathbb{K},\mathbb{V}} \in \mathbb{R}^{D\times D_h} \tag{2}$$

$$A = softmax\left(\frac{\mathbb{Q}\mathbb{K}^T}{\sqrt{D_h}}\right)\mathbb{V}, A \in \mathbb{R}^{N\times N} \tag{3}$$

$$SA(\ddagger) = A\mathbb{V} \tag{4}$$

$$MSA(\ddagger) = \left[SA_1(\ddagger); SA_2(\ddagger); \ldots\ldots .SA_{\mathbb{K}}(\ddagger)\right] \cup_{msa} . \cup_{\mathbb{Q},\mathbb{K},\mathbb{V}} \in \mathbb{R}^{\mathbb{K}.D_h\times D} \tag{5}$$

The output from the multi-head attention module is normalized. Further, the normalized output is fed to the LSTM layer which provides a better joint modeling framework. This improves the detection performance by learning the hidden state of image features. This also leverages the modeling capability and provides a boost in accuracy by capturing the local temporal dependencies.

$$\mathcal{U} = norm(MSA(\ddagger)) \tag{6}$$

$$\mathcal{S} = LSTM(\mathcal{U}) \tag{7}$$

The LSTM output, after feeding to the Linear layer is again normalized. The MLP is implemented as two linear layers with GELU activation function to further transform features and classify the output as detected. Further, a consistent improvement in accuracy is observed when GELU is utilized in comparison to ReLU, and ELU. Also, GELU is smoother near zero and "is differentiable in all ranges, and allows to have gradients (although small) in the negative range.

$$\mathcal{S}^{'} = MLP(LN\left(\mathcal{S}^{'}\right)) + \mathcal{S}^{'} \tag{8}$$

$$y = LN(\mathcal{S}^{'}) \tag{9}$$

The algorithm for the proposed ODT is explained below:

Algorithm: Obscenity Detection Transformer

Input: **Learning rate ($\Re$) = 2 x 10^{-5}**
Epochs (ε) = 100
Batch size (β) = 50
Images in 1 batch (κ)
Output: **Model Accuracy (Ac_{epoch}), Loss (L_{epoch}), Precision (P_{epoch})**

Begin:
Prepare data:
Categories= [Porn, NonpornDifficult, NonpornEasy]
For i in categories
  Print {i}
  Define path=os.path.join(dir,i)
  X[p , :]=read_image(os.path.join(path,img))
  if i ==’Porn’
    Y[0 , p]= 2
    p=p+1
  elif i == ‘NonpornDifficult’
    Y[0 , p]= 1
    p=p+1
  elif i == ‘NonpornEasy’
    Y[0 , p]= 1
    p=p+1
  End If
End for
return X, Y
Prepare X_train, Y_train
  X_test, Y_test
Extract Features:
  for **epoch 0→100**
    for all α **←feature extraction**
  end for
Train Classifier:
  X→ np.array(α)
  Y→Transform
  Model→ Train classifier (X, Y)
  end for
  for **epoch 0→100**
    for all γ **←feature extraction**
  end for
Validate:
  X→ np.array(γ)
  Y→ Validation
  Model→ Test classifier (X, Y)
  end for
  for **epoch 0→100**
  Calculate: $Ac_{epoch}, L_{epoch}, P_{epoch}, R_{epoch}$
  end for
return $Ac_{epoch}, L_{epoch}, P_{epoch}, R_{epoch}$

4 Results and discussions

In this section, the observed experimental results for the proposed ODT model are discussed. The experiments are conducted on the two standard baseline datasets, Pornography-800 and Pornography-2 K datasets. The Pornography-800 dataset includes videos from two categories: non-pornographic and pornographic. Non-pornographic content is classified into two groups: easy and difficult. It has a total of 77 h of videos, of which 57 h are pornography videos and the rest is nonpornographic video. The pornography-2 K dataset is an expansion of the Pornography-800 dataset and is larger. It contains 140 h of content, with 1000 non-pornographic and pornographic videos. Videos range in length from 6 s to 33 min. Figure 3 shows the sample of the dataset. The diversity in the dataset is demonstrated in Fig. 3. The figure is divided into three rows, with the top row representing frames from pornographic videos and non-pornographic frames represented in the other two rows. The frames in the middle row are from difficult non-pornographic video scenarios.

4.1 Implementation details

To detect and extract image features from the video frames, we train our model in an end-to-end manner. The input images are resized to 124×124 resolution and the patch size is set to 9. The number of transformer layers is set to 12. The whole model is trained on both datasets with a learning rate of 2×10^{-5} with binary cross entropy loss and Adam optimizer. The number of epochs for the setup is set as 100. To evaluate the performance of the proposed work, the ROC and AUC curves are plotted and further accuracy is determined.

4.2 Performance comparison on pornography-800 dataset

The proposed framework on the Pornongraphy-800 dataset is evaluated using ROC-AUC curves, confusion matrix, training and validation accuracy, and training and validation loss. The classification results using the confusion matrix are presented in Fig. 4. Further, training-validation accuracy and training-validation loss are depicted in Figs. 5 and 6. From these

Fig. 3 Pornography -2 K Dataset frames showing difficulty and diversity in videos

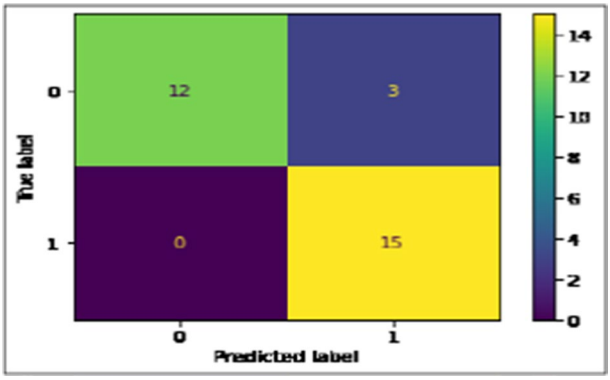

Fig. 4 Confusion Matrix for Pornography-800 Dataset

Figures, it is evident that ODT provides training and validation accuracies of 99.8% and 98.8% respectively while training and validation losses obtained are 0.01 and 0.06 respectively. Also, the performance of the proposed work is depicted by the ROC-AUC curve in Fig. 7 which gives $AUC = 99.39\%$ for the best-performing model. Furthermore, the model's performance is enhanced in detecting a specific video class (non-porn difficult, non-porn easy, and porn). Table 2 presents the comparison of the proposed ODT based on accuracy, AUC, and F-1 scores with various existing traditional and deep-learning techniques. From Table 2 it is evident that ODT provides an accuracy of 98.8%. Also, the AUC and F-1 scores reported for the proposed ODT are 0.9939 and 97.56 respectively. Hence, it is evident that transformer-based architecture surpasses other state-of-the-art techniques. Also, ODT achieves better accuracy than the best-performing techniques [1, 5, 12, 19, 20, 25].

4.3 Performance comparison on pornography-2 K dataset

The results of pornographic detection on the Pornography-2 K dataset using the confusion matrix are displayed in Fig. 8. When tested on the Pornography-2 K dataset, it is found that the model produces accuracy better than some other works even without human filtering due to the prevalence of substantial and diverse data. ROC-AUC curves, confusion matrix, training and validation accuracies, and training and validation losses are all used to evaluate the efficiency of the proposed method and are as shown in Figs. 8, 9, and 10. The

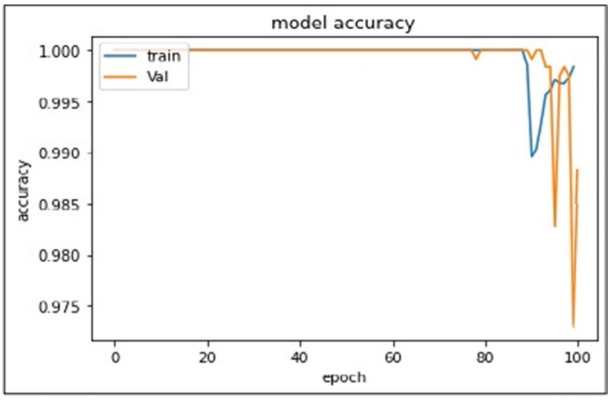

Fig. 5 Training and Validation Accuracy Curve for Pornography-800 Dataset

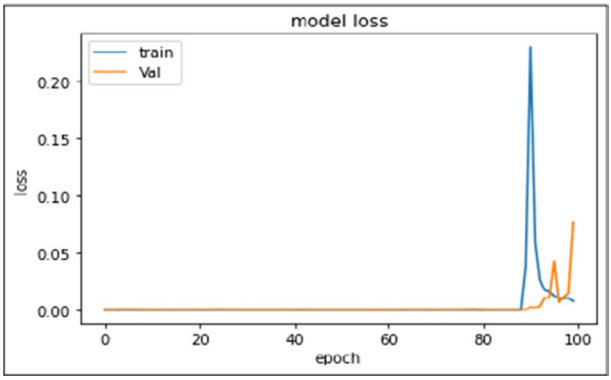

Fig. 6 Training and Validation Loss Curve for Pornography-800 Dataset

maximum overall test/validation accuracy and the minimum test/validation loss reported on this dataset are 0.0001 and 0.009 respectively. Further, the outstanding performance of the proposed ODT can also be seen in the ROC curve given in Fig. 11, where the AUC is 99.5%. Also, Table 3 presents a comparative analysis of the proposed framework with the state-of-the-art on Pornography-800 dataset. Table 3 reports accuracy, AUC, and F-1 scores for different state-of-the-art [12, 18, 20].

5 Computational comlexity

This section describes the computational complexity of the proposed Obscenity Detection Transformer. The time and space complexities are explained in sections 5.1 and 5.2.

5.1 Time complexity

- The initialization of the proposed model needs $\mathrm{O}\left(V_F(g \times h)\right)$ time. Where V_F represents, the frames captured from videos for detection, g and h are the numbers of rows and columns, respectively.
- Using Obscenity Detection Transformer, key (K_F) query (Q_F) and values (Va_F) are obtained as an input to multi-head attention $\mathrm{O}\left(K_F(g \times h)\right) + \mathrm{O}\left(Q_F(g \times h)\right) + \mathrm{O}\left(Va_F(g \times h)\right)$.

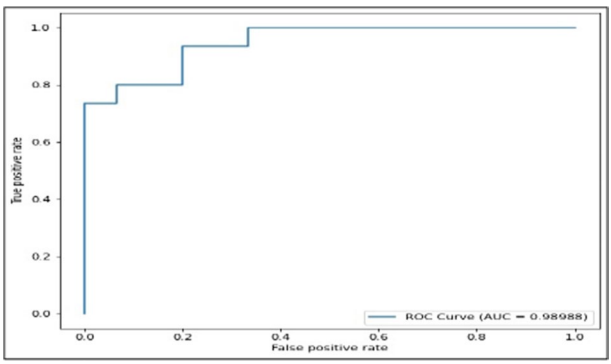

Fig. 7 ROC-AUC Curve for Pornography-800 Dataset

Table 2 Comparison Results of Proposed ODT on Pornography-800 Dataset with other State-of-the-art

Ref	Accuracy	AUC	F1 Score
Cateano et al. [5]	92.4 ± 1	0.976	-
Avila et al. [1]	87.1 ± 2	-	-
Caetano et al. [5]	92 ± 1	0.973	-
Mustafa et al. [19]	93.8 ± 2	-	-
Mustafa et al. [19]	94.1 ± 2	-	-
Silva et al. [25]	95.1 ± 1.7	-	-
Wehrmann et al. [28]	95.6 ± 1	0.99	-
Perez et al. [20]	97.9 ± 0.7	-	96.7
Gautam et al. [12] (8-Frame Sequence)	91.5 ± 1	0.975	-
Gautam et al. [12] (16-Frame Sequence)	92.37 ± 1	0.973	-
ODT (Proposed)	**98.8**	**0.9939**	**97.56**

The bold values indicate the best value of performance measures from the corresponding algorithm

- Time taken by training and testing of the proposed model is $\mathrm{O}\big(V_F(Train)\big) + \mathrm{O}\big(V_F(Test)\big)$
- Therefore, the overall time complexity of the proposed model is $\mathrm{O}\big(K_F(g \times h)\big) + \mathrm{O}\big(Q_F(g \times h)\big) + \mathrm{O}\big(Va_F(g \times h)\big) +$ $\mathrm{O}\big(V_F(g \times h)\big) + \mathrm{O}\big(V_F(Train)\big) + \mathrm{O}\big(V_F(Test)\big)$

5.2 Space complexity

The proposed network's space complexity is considered during the initialization.

- Space taken by training of the proposed model is $\mathrm{O}\big(V_F(Train)\big)$
- Space taken by testing of the proposed model is $\mathrm{O}\big(V_F(Test)\big)$
- The overall space complexity of the proposed approach is $\mathrm{O}\big(V_F(g \times h)\big) + \mathrm{O}\big(V_F(Train)\big) + \mathrm{O}\big(V_F(Test)\big)$

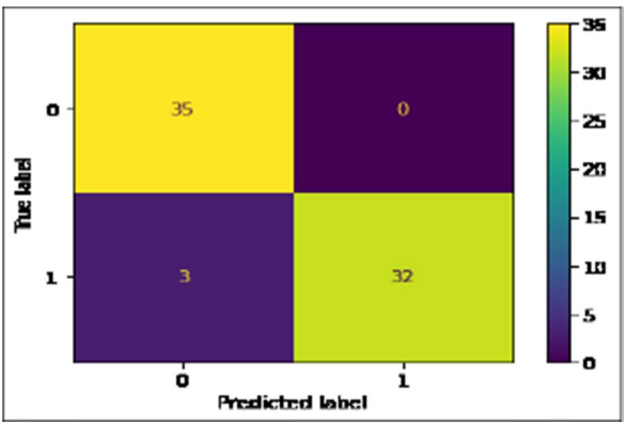

Fig. 8 Confusion Matrix for Pornography-2 k Dataset

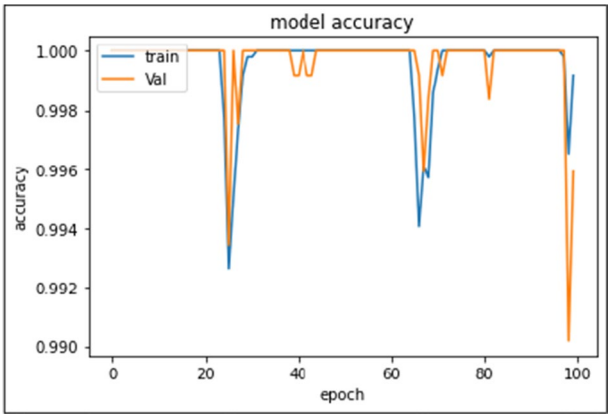

Fig. 9 Training and Validation Accuracy Curve for Pornography-2 K Dataset

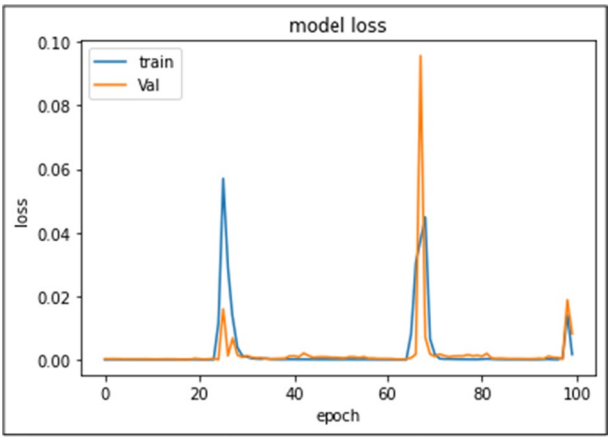

Fig. 10 Training and Validation Loss Curve for Pornography-2 K Dataset

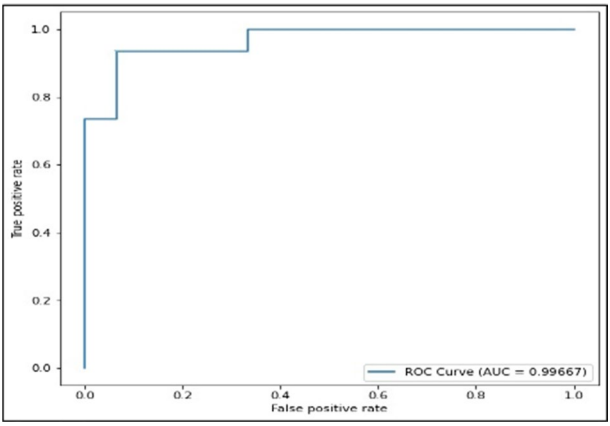

Fig. 11 ROC-AUC Curve for Pornography-2 K Dataset

Table 3 Comparison Results of Proposed ODT on Pornography-800 Dataset with other State-of-the-art

Ref	Accuracy	AUC	F1 Score
Moreira et al. [18]	95.6	-	-
Perez et al. [20] (Motion Vector)	96.4	-	95.3
Perez et al. [20] (Optical Flow)	96.4	-	92.0
Gautam et al. [12] (8-Frame Sequence)	97.15 ± 1	0.994	-
Gautam et al. [12] (16-Frame Sequence)	96 ± 1	0.992	-
ODT (Proposed)	**99.6**	**0.995**	**98.09**

The bold values indicate the best value of performance measures from the corresponding algorithm

6 Conclusions

The paper introduces the Obscenity Detection Transformer (ODT), a new framework that uses a transformer-based architecture to identify and categorize inappropriate content in videos. The framework includes a vision transformer with an embedded LSTM layer and a GELU-activated multi-layer perceptron (MLP). The GELU-activated MLP consistently outperforms ReLU and ELU activations in terms of test error rate, making it a promising alternative. In comparison to convolutional neural networks (CNNs), the proposed model is widely applicable and yields impressive results. The Pornography-800 and Pornography-2 K datasets were used in the experiments. The proposed ODT outperformed existing cutting-edge approaches with accuracy rates of 98.8% and 99.6% for the two datasets, respectively. Furthermore, transformers lack certain inherent biases found in CNNs and rely heavily on large datasets for extensive training which are overcome by incorporating LSTM and conducting extensive experiments on Pornography-800 and Pornography-2 K datasets. As a result, the quality of the data has a significant impact on transformers' ability to generalize and remain robust in computer vision tasks.

Data availability Data sharing not applicable to this article as no datasets were generated during the current study.

Declarations

Conflict of interest The authors declare that they have no conflict of interest.

References

1. Avila S, Thome N, Cord M, Valle E, De A (2011) BOSSA: Extended bow formalism for image classification. Proc - Int Conf Image Process. ICIP (1): 2909–2912. https://doi.org/10.1109/ICIP.2011.6116268
2. Avila S, Thome N, Cord M, Valle E, De A. Araújo A (2013) Pooling in image representation: The visual codeword point of view. Comput Vis Image Underst 117(5):453–465. https://doi.org/10.1016/j.cviu.2012.09.007
3. Bhatt R, Onyema EM, Almuzaini KK, Iwendi C, Band SS, Sharma T, Mosavi A. Assessment of dynamic swarm heterogeneous clustering in cognitive radio sensor networks. Wirel Commun Mob Comput. 2022. Article ID 7359210: 1–15. https://doi.org/10.1155/2022/7359210
4. Bouirouga H, El Fkihi S, Jilbab A, Aboutajdine D (2012) Skin detection in pornographic videos using threshold technique. J Theor Appl Inf Technol 35(1):7–19

5. Caetano C, Avila S, Schwartz WR, Guimarães SJF, de A. Araújo A (2016) A mid-level video representation based on binary descriptors: A case study for pornography detection. Neurocomputing 213:102–114. https://doi.org/10.1016/j.neucom.2016.03.099
6. Chen J, Liang G, He W, Xu C, Yang J, Liu R (2020) A pornographic images recognition model based on deep one-class classification with visual attention mechanism. IEEE Access 8:122709–122721
7. Farrelly B, Sun Y, Mahanti A, Gong M (2017) Video Workload Characteristics of Online Porn: Perspectives from a Major Video Streaming Service, 2017 IEEE 42nd Conference on Local Computer Networks (LCN), Singapore, pp. 518–519. https://doi.org/10.1109/LCN.2017.119
8. Fleck M, Forsyth D, Bregler C (1996) Finding naked people, in: Proceedings of the European Conference on Computer Vision (ECCV). 1065, pp. 593–602
9. Forsyth D, Fleck M (1996) Identifying nude pictures, in: Proceedings of the IEEE Workshop on Applications of Computer Vision. pp. 103–108
10. Forsyth D, Fleck M (1999) Automatic detection of human nudes. Int J Comput Vis 32(1):63–77
11. Gangwar A, González-Castro V, Alegre E, Fidalgo E (2021) AttM-CNN: Attention and metric learning based CNN for pornography, age and child sexual abuse (CSA) detection in images. Neurocomputing 445:81–104
12. Gautam N, Vishwakarma DK (2022) Obscenity detection in videos through a sequential ConvNet pipeline classifier. IEEE Trans Cogn Dev Syst 15(1):310–318
13. Guo MH, Xu TX, Liu JJ, Liu ZN, Jiang PT, Mu TJ, Zhang S-H, Martin RR, Cheng M-M, Hu S-M (2022) Attention mechanisms in computer vision: A survey. Computational Visual Media 8:1–38
14. Huang C, Yuan C, Zhang J (2020). Violation Detection of Live Video Based on Deep Learning, https://doi.org/10.1155/2020/1895341
15. Jones MJ, Rehg JM (1999) Statistical color models with application to skin detection. IEEE Computer Society Conference on Computer Vision and Pattern Recognition. (Cat. No PR00149), Fort Collins, CO, USA, pp 274–280. https://doi.org/10.1109/CVPR.1999.786951
16. Jones M, Rehg J (2002) Statistical color models with application to skin detection. Int J Comput Vis 46(1):81–96
17. Lee S, Shim W, Kim S (2009) Hierarchical system for objectionable video detection. IEEE Trans Consum Electron 55(2):677–684
18. Moreira D et al (2016) Pornography classification: The hidden clues in video space–time. Forensic Sci Int 268:46–61. https://doi.org/10.1016/j.forsciint.2016.09.010
19. Moustafa M (2015) Applying deep learning to classify pornographic images and videos. arXiv preprint arXiv:1511.08899
20. Perez M, Avila S, Moreira D, Moraes D, Testoni V, Valle E, Rocha A (2017) Neurocomputing 230: 279-293. https://doi.org/10.1016/j.neucom.2016.12.017
21. Quadra A, El-Murr A, Latham J (2017) The effects of pornography on children and young people: An evidence scan. Australian Institute of Family Studies
22. Rowley H, Jing Y, Baluja S (2006) Large scale image-based adult-content filtering, in: Proceedings of the International Conference on Computer Vision Theory and Applications (VISAPP), pp. 290–296
23. Samal S, Nayak R, Jena S et al (2023) Obscene image detection using transfer learning and feature fusion. Multimed Tools Appl. https://doi.org/10.1007/s11042-023-14437-7
24. Samal S, Zhang Y-D, Gadekallu TR, Nayak R, Balabantaray BK (2023) SBMYv3: Improved MobYOLOv3 a BAM attention-based approach for obscene image and video detection. Expert Systems e13230. https://doi.org/10.1111/exsy.13230
25. da Silva MV, Marana AN (2019) Spatiotemporal CNNs for pornography detection in videos. Lect Notes Comput Sci (including Subser. Lect. Notes Artif. Intell. Lect. Notes Bioinformatics) 11401 LNCS:547–555. https://doi.org/10.1007/978-3-030-13469-3_64
26. Song Y-D, Gong M, Mahanti A (2019) Measurement and Analysis of an Adult Video Streaming Service, 2019 IEEE/ACM International Conference on Advances in Social Networks Analysis and Mining (ASONAM), Vancouver, BC, Canada, pp. 489–492. https://doi.org/10.1145/3341161.3342940
27. Wang L, Zhang J, Wang M, Tian J, Zhuo L (2020) Multilevel fusion of multimodal deep features for porn streamer recognition in live video. Pattern Recogn Lett 140:150–157
28. Wehrmann J, Simões GS, Barros RC, Cavalcante VF (2018) Adult content detection in videos with convolutional and recurrent neural networks. Neurocomputing 272:432–438. https://doi.org/10.1016/j.neucom.2017.07.012
29. Wong C, Song YD, Mahanti A (2020) YouTube of porn: longitudinal measurement, analysis, and characterization of a large porn streaming service. Soc Netw Anal Min 10:62. https://doi.org/10.1007/s13278-020-00661-8

30. Yousaf K, Nawaz T (2022) A deep learning-based approach for inappropriate content detection and classification of youtube videos. IEEE Access 10:16283–16298
31. Yu R, Christophersen C, Song Y-D, Mahanti A (2019) Comparative analysis of adult video streaming services: characteristics and workload, 2019 Network Traffic Measurement and Analysis Conference (TMA), Paris, France, pp. 49-56. https://doi.org/10.23919/TMA.2019.8784688
32. Zheng H, Daoudi M (2004) Blocking adult images based on statistical skin detection. Electron Lett Comput Vis Image Anal 4(2):1–14

Publisher's Note Springer Nature remains neutral with regard to jurisdictional claims in published maps and institutional affiliations.

Springer Nature or its licensor (e.g. a society or other partner) holds exclusive rights to this article under a publishing agreement with the author(s) or other rightsholder(s); author self-archiving of the accepted manuscript version of this article is solely governed by the terms of such publishing agreement and applicable law.

Kamakshi Rautela , received M.Tech. degree from Graphic Era Hill University, Bhimtal, India, in 2017. She is currently pursuing the Ph.D. degree with the Department of Electronics and Communication Engineering from Delhi Technological University, New Delhi, India. Her current research interest includes machine learning, deep learning, computer vision, and medical image processing. She is also a reviewer in Computers in Biology and Medicine.

Dhruv Sharma , received his M.Tech. degree from Ambedkar Institute of Advanced Communication Technology & Research, New Delhi, India, in 2017. He is currently pursuing the Ph.D. degree with the Department of Electronics and Communication Engineering from Delhi Technological University, New Delhi, India. His current research interest includes machine learning, deep learning, computer vision, natural language processing and image captioning.

Vijay Kumar is Associate Professor in Information Technology Department, Dr B R Ambedkar NIT Jalandhar, Punjab. He received his Ph.D. degree from NIT Kuruksherta. Previously, he received M.Tech. and B.Tech. degrees from GJUS&T, Hisar and Kurukshetra University, Kurukshetra, respectively. He has 13 years of teaching and research experience in various reputed institutes such as NIT Hamirpur, Thapar Institute of Engineering & Technology Patiala, and Manipal University Jaipur. He completed 2 DST SERB and 01 CSIR sponsored research projects. He has published more than 170 research papers in International Journals/Conferences. He has many book chapters in international repute publishers. He has supervised many Ph.D. and M.Tech. thesis on Metaheuristics, Image Mining, and Data Clustering. He is the reviewer of several reputed SCI journals. He is member of ACM, CSI, International Association of Engineers, International Association of Computer Science and Information Technology, Singapore. His current research area is Soft Computing, Data Mining, Deep Learning, Steganography, and Pattern Recognition.

Dinesh Kumar received his B.Tech. (ECE) and M.Tech.(ECE) (Gold Medalist) form National Institute of Technology (NIT) Kurukshetra (erstwhile REC Kurukshetra) and received Ph.D. degree in the field of Biometrics (Face Recognition) from GGS Indraprastha University, Delhi. He has more than 30 years of teaching and research experience and currently working as Professor in the Electronics and Communication Engineering Department of Delhi Technological University, Delhi. He has research publications in National/International Journals and Conferences including IEEE, Elsevier, Springer, Wiley. His current research interests include image processing, biometrics, soft computing, clustering, biomedical imaging, machine learning, image captioning. He is on the panel of reviewers for IEEE, Elsevier and Springer journals/Transactions.

J Mater Sci: Mater Electron (2023) 34:1351

One step hydrothermal synthesis of MoS_2–SnO_2 nanocomposite for resistive switching memory application

Km. Komal[1], Mukhtiyar Singh[1], and Bharti Singh[1,*]

[1] *Department of Applied Physics, Delhi Technological University, Delhi 110042, India*

Received: 11 January 2023
Accepted: 28 May 2023
Published online: 15 June 2023

© The Author(s), under exclusive licence to Springer Science+Business Media, LLC, part of Springer Nature 2023

ABSTRACT

Resistive switching random access memory (ReRAM) where the resistance of the active semiconducting layer can be changed as a function of applied voltage has been becoming popular due to its simple structure and design. In the present study, we have used MoS_2–SnO_2 nanocomposite as a resistive switching material, where the effect of MoS_2 weight percentage (0, 5, 7, and 10 wt.%) have been evaluated in terms of the structural, optical, and electrical properties changes of resulting nanocomposite using X-ray diffraction, UV–Visible Spectroscopy, Scanning electron microscopy, and Transmission electron microscopy techniques. The nanocomposite samples were synthesized using a simple hydrothermal technique and are spin-coated on commercially available ITO-PET substrate. The top metallic electrode was deposited by thermally evaporating Aluminium through a shadow mask resulting in Al/SnO_2/ITO-PET and Al/MoS_2–SnO_2/ITO-PET (5%, 7%, 10%) based resistive memory devices. The measured current–voltage (I–V) characteristics over the fabricated devices having different MoS_2 wt. % showed the increase in I_{On}/I_{Off} ratio (3, 6, and 25) with an increase in MoS_2 concentration.

1 Introduction

Human society is getting more digitalised, every aspect of our everyday existence is surrounded by data produced by media, social networks, machines, historical archives, etc. The so-called significant data era has unquestionably arrived in the World of humans. Unfortunately, using the most recent technologies to process data is not without its difficulties. Probably the most important is the hardware. A new gadget called the resistive switching (RS) device combines computing and memory functions in a single cell. The discovery of negative differential resistance in binary oxide thin films (SiOx, Al_2O_3, Ta_2O_5, ZrO_2, TiO_2) in the year 1960s led to the beginning of the RS field of study [1]. Starting in 2008, RS devices gained popularity as a research area in academia and business. RS devices have been the subject of several studies on various topics, including physical mechanisms, materials, devices, and circuits.

Address correspondence to E-mail: bhartisingh@dtu.ac.in

https://doi.org/10.1007/s10854-023-10727-w

Due to its ability to function under low operating power [2], fast switching speed [3], high scalability [4], and non-destructive readout [5], resistive random-access memory (ReRAM) is regarded as one of the prospective candidates to replace the current flash-based memories. Further it may be mentioned that in addition to the negative differential resistance-based ReRAM device another aspirant based on the negative capacitance (NC) effect has also gained the attention of scientific community for reducing issues related to scaling, switching speeds and power consumption of existing electronic devices [6].It is to be noted that progress in electronics is always limited by power dissipation constraints which need to be addressed. In this direction HfO_2 and ZrO_2 based ferroelectric materials are promising for negative capacitance electronics due their compatibility with the modern semiconductor fabrication industry. The NC effect was first reported by Sayeef Salahuddin and Supriyo Datta in 2007 and it means that a change in charge causes the net voltage across a material to change in the opposite direction, so that a decrease in voltage leads to an increase in charge which is different from normal capacitor [7]. This NC effect is firstly reported in ferroelectric materials and is unstable, however it could be stabilized by connecting the ferroelectric material in series with a standard dielectric capacitor. The capacitance C of a parallel-plate capacitor with dielectric material between the plates can be expressed as:[8]

$$C = \varepsilon\left(\frac{A}{d}\right) = \varepsilon_0\varepsilon_r\left(\frac{A}{d}\right) = \frac{dD}{dE}\left(\frac{A}{d}\right) \quad (1)$$

where ε_0, A, d, D, and E denote vacuum permittivity, plate area, plate separation, electric displacement field, and electric field, respectively. Further for FE materials like HfO_2 the negative capacitance is due to negative permittivity and is expressed as:

$$\varepsilon_0\varepsilon_r = \frac{dD}{dE} = \varepsilon_0 + \frac{dP}{dE} \approx \frac{dP}{dE} \quad (2)$$

By applying the electric field larger than the coercive field, the polarization state can be changed and if the polarization occurs opposite to the applied field ($dP/dE < 0$), negative capacitance state is achieved. To make use of this effect for fabricating a transistor, the ferroelectric material layer is staked with gate of a metal-oxide- semiconductor field-effect transistor. It may be mentioned that with suitable design, a negative capacitance field-effect transistor (NC-FET) should, in principle, able to achieve a subthreshold swing below the 60 mV per decade thermionic limit, and with an on-current performance comparable to current devices. Many semiconductor industries such as GlobalFoundaries, Samsung have filed the patents in the mentioned field [9]. Despite the progress, the development of practical devices based on negative capacitance has been slow and may be attributed to the unclear mechanism and lack of theoretical and characterization support. However, for the present study we will only focus on ReRAM devices having more matured physics behind the resistive switching effect.

Further it has also been observed that binary transition metal oxides, such as HfO_2 [10] is not only a favoured materials for negative capacitance effect, has also been explored for ReRAM application as compared to ternary and quaternary oxide semiconductor films due to their ease of fabrication and compatibility with the CMOS industry. However, 2D transition metal dichalcogenides has superseded due to their layered structure, and distinctive physical and mechanical properties. Molybdenum disulfide (MoS_2) one of member of transition metal dichalcogenide (TMDs) family, is one of the most suitable materials for researchers [11]. It has been reported for use in transistors, photodetectors [12], lithium batteries [13], hydrogen evolution catalysts [14], and transistors [15], as well as these other devices. MoS_2, which has a layered structure akin to graphite and may be exfoliated to produce single or few-layer nanosheets, is made up of sandwiches units made of covalently coupled hexagonal planes of Mo and S atoms linked together by the weak van der Waals attraction [16]. To improve the performance of devices based on MoS_2, researchers are focusing on combining MoS_2 with other promising nanomaterials to create nanocomposites, such as reducing graphene oxide-MoS_2/TiO_2 heterostructures for photocatalytic actives and MoS_2/CdS heterojunction for H_2 evolution under light irradiation [17].

SnO_2 has attracted the interest of many researchers in various applications, which include gas sensors [18], photo catalysis [19], batteries [20], solar cells [21], etc. In addition to the mentioned applications, the SnO_2-based resistive memory device has also gained attention due to its tetragonal rutile structure and stoichiometry which is easy to synthesize than the multinary oxide materials. It has received a lot of attention from researchers working on ReRAM

devices because of its intriguing electrical and optical features. Nanocrystals, nanowires, nanobelts, and nanotubes are among the various nanostructures of SnO_2. Among these structures, nanocrystals are technologically essential for ReRAM devices owing to their size-dependent features [22]. However, the resistive switching phenomenon has not been much explored and therefore requires further effort to improve the switching parameters. In this regard, one of the ways for the modification is to make a nanocomposite based on semiconductor metal oxide and TMDs-based material such as molybdenum disulphide [23], MoS_2, WS_2, $MoSe_2$, etc.

Particularly, MoS_2 is the first and most actively researched transition metal dichalcogenides among the 2-D materials. Its composites have attracted considerable attention due to their strength to withstand mechanical stress, strain, and stretchable conditions, which are essential for a memristive device to be integrated with a flexible and wearable electronic system [24]. The outstanding properties of MoS_2, such as layer-specific surface area, fast electron transport at room temperature, and chemical functionalities, ensure that it can be combined with metal oxide for the fabrication of resistive memory [25]. Additionally, it has been observed that numerous papers are accessible for MoS_2-MO based nanocomposite for photocatalysis, gas sensors, electrochemical energy storage, etc. Here, we use MoS_2 and SnO_2 to create MoS_2–SnO_2 nanocomposite with various MoS_2 concentrations using an easy one-step hydrothermal approach. MoS_2 nanosheets can firmly attach to the SnO_2 nanoparticle surface in the produced nanocomposite sample. The growth of SnO_2 nanoparticles is somewhat affected by the amount of MoS_2 present. As compared to pure SnO_2, the results demonstrate that the composite samples have better resistive switching performance. The best resistive switching performance of them all is achieved by 10%MoS_2–SnO_2 nanocomposite. Further it may be mentioned that up to best of our knowledge there is no report available for MoS_2–SnO_2 based nanocomposite for the ReRAM application.

2 Experimental

2.1 Chemical reagents

The precursors utilized during the synthesis are Ammonium molybdate (99.98%), thiourea (>99.0%), sodium hydroxide (NaOH, 98%), tin (IV) chloride pentahydrate ($SnCl_4.5H_2O$, 98%), and ethanol (C_2H_5OH, 99.9%). Fisher Scientific and Sigma Aldrich supply all the chemicals. All the chemicals used in the synthesis processor are of Analytical-grade purity and are used without further purification.

2.2 Materials synthesis

MoS_2 was synthesized using a facile hydrothermal route [26–28]. Firstly, ammonium molybdate (2.48g) and thiourea (1.2 g) were dissolved into 72 mL of deionized (DI) water and subsequently stirred for 30 minutes at room temperature. Then the mixture was transferred into a 100 mL Teflon-lined stainless steel autoclave to react at 200 °C for 8 hours and then to cool down at room temperature. The product was rinsed with Di-water and two times ethanol centrifuged to collect black precipitates. Then the collected paste was dried in the vacuum oven at 60 °C for 12 hours [29].

2.3 Synthesis of 5%MoS_2–SnO_2, 7%MoS_2–SnO_2 and 10%MoS_2–SnO_2 nanocomposites

To synthesize 5%MoS_2–SnO_2, 7%MoS_2–SnO_2, and 10%MoS_2–SnO_2 nanocomposite, synthesized MoS_2 (200 mg, 280 mg, 400mg) with 4 ml DI water ultrasonicated for 1 hour. $SnCl_4{\cdot}5H_2O$ (2.10 g) and NaOH (1.68g) were added into 80 ml DI-water and magnetically stirred for 2 hours to get a homogenous solution [29]. Then finally, after 2 hours of stirring, the SnO_2 solution is added to the MoS_2 solution and stirred for 60 minutes. This prepared suspension was put into a 100 ml Teflon-lined autoclave made of stainless steel, shut up, and heated at 180 °C for 18 hours. The product underwent three centrifugal washes with ethanol and three centrifugal washes with di-water. The residue was dried in a vacuum oven at 70 °C for 6 hours [30]. Figure 1 depicts the two-step mentioned hydrothermal method of MoS_2–SnO_2 nanocomposite.

2.4 Film fabrication

The spin coating method has been used to deposit film, which includes the following steps: (1) ITO-PET substrates were cleaned before ultrasonic use by acetone, ethanol, and deionized water. (2) Using an

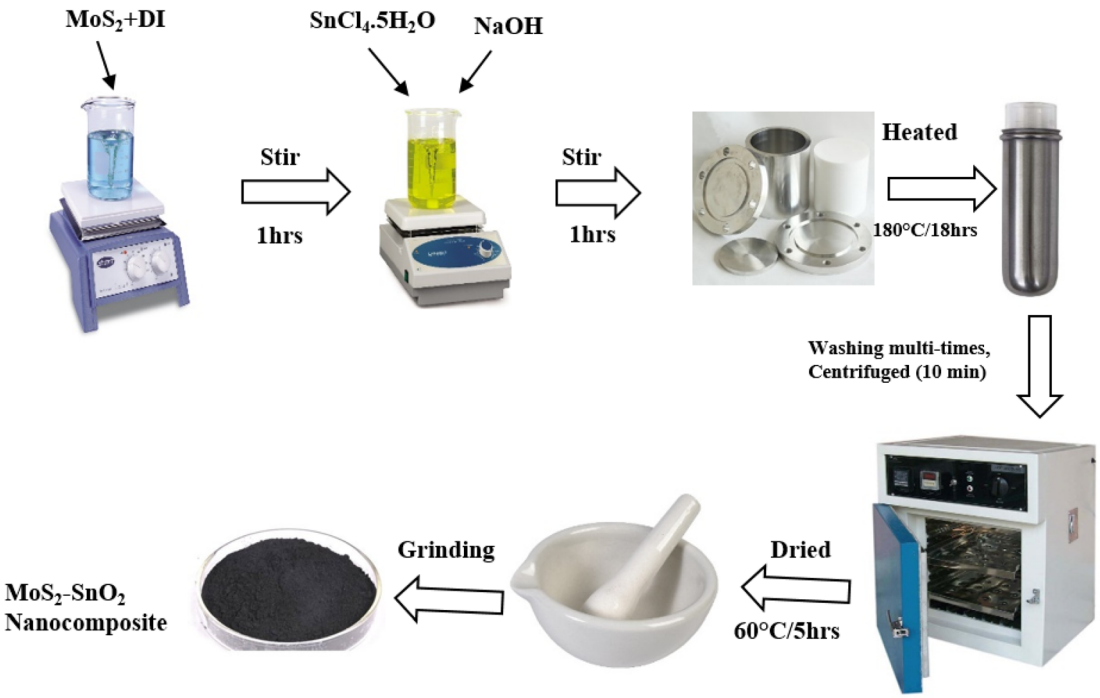

Fig. 1 A schematic depicts the two-step hydrothermal technique used to prepare the MoS_2-SnO_2 nanocomposite

ultrasonic bath to dissolve 50 mg of MoS_2–SnO_2 in 1.5 ml of ethanol for 30 minutes, four drops of the resulting solution were then deposited onto a piece of ITO-PET glass, which was then spun at 2000 rpm for 60 seconds. (2) For 10 minutes, a hot plate set to 90 °C was used to heat the coated sample. We then obtained a film of MoS_2–SnO_2 eight times by repeating this method. Through the use of the thermal evaporation technique and a pressure of 10^{-5} bar, the top aluminum electrode of a thickness of 100 nm was deposited. The schematic illustration for fabrication of different weight percentages of MoS_2, Al/5%MoS_2–SnO_2/PET, Al/7%MoS_2–SnO_2/PET, and Al/10%MoS_2–SnO_2/PET-based MIM device is shown in Figs. 2 and 3.

3 Results and discussion

Firstly, the crystal structure of the synthesized samples, MoS_2, SnO_2, and MoS_2-SnO_2 (5%, 7%, 10%) nanocomposites were investigated using an X-ray diffractometer (Bruker D8 Advance) with Cu Kα radiation source (1.54Å). The WiTec alpha 300RA Raman Spectrometer with a laser source of wavelength 530 nm was used to carry out the structural investigations. Further, the scanning electron microscope (SEM) was used to analyse the surface morphologies of the prepared materials MoS_2, SnO_2, 5%MoS_2–SnO_2, 7%MoS_2–SnO_2, and 10%MoS_2–SnO_2. A Keithley 2450 source meter was used to conduct (I–V) measurements on all constructed thin film-based memory devices (Al/SnO_2/ITO, Al/MoS_2–SnO_2/ITO). We initially covered the sample with silver paste on both sides and heated it at 160 °C for 2 hours to perform dielectric measurements using the capacitance method. An Agilent LCR meter (Model E4980A) was used to determine how frequency (10–10^6 Hz) affected the capacitance (C) and loss tangent (D = tanδ) measurements.

3.1 X-Ray diffraction (XRD)

The crystal structure, phase purity, and crystallite size of pure MoS_2, pure SnO_2, and MoS_2–SnO_2 (5%, 7%, 10%) nanocomposite are determined using the XRD technique. In Fig. 4, the XRD spectra of pure MoS_2, SnO_2, and various nanocomposites of MoS_2–SnO_2 (5, 7, and 10 wt. %) confirm the existence of MoS_2 and SnO_2 phases. The XRD results for the SnO_2 sample show diffraction peaks of SnO_2 observed at 2θ diffraction angles of 26.36°, 33.82°, 52.62°, and 65.21°, corresponding to (110), (101), (211), and (301) characteristic planes, respectively, indicating the

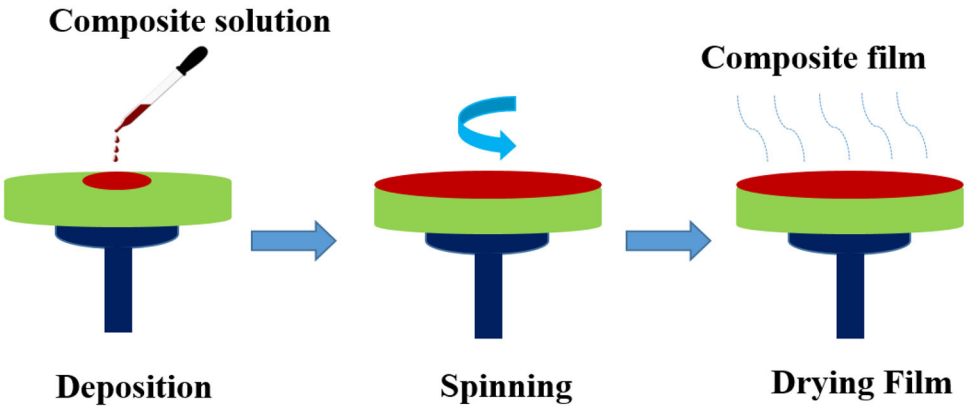

Fig. 2 A schematic illustration depicts the spin coating procedures used in the fabrication of resistive memory devices

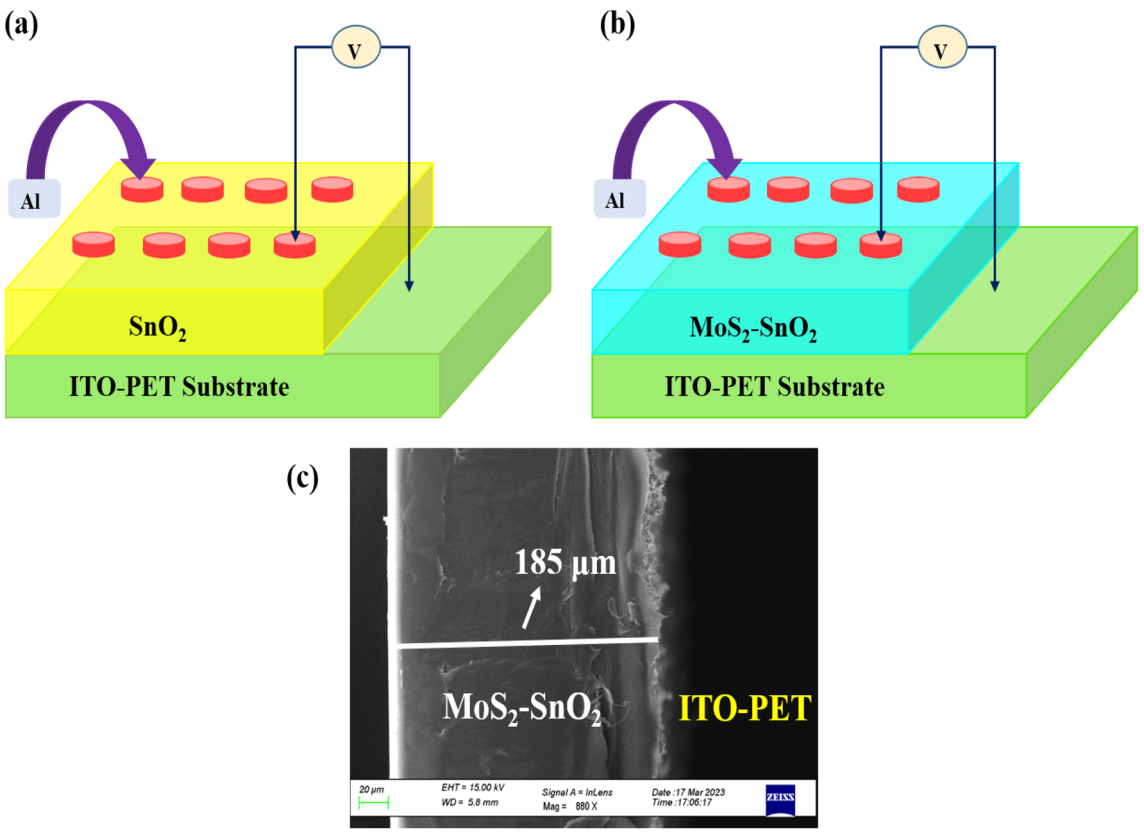

Fig. 3 A schematic of the **a** AI/SnO_2/ITO PET and **b** AI/MoS_2–SnO_2/ITO PET subtract-based MIM devices is shown. **c** Image captured using a cross-sectional FESEM of a MoS_2–SnO_2 nanocomposite layer on a PET substrate covered with ITO

tetragonal structure of SnO_2 [31]. The prominent and sharp diffraction peaks show the remarkable crystallinity of the SnO_2 nanoparticles. Similar to this, the primary MoS_2 diffraction peaks can be seen at 9.2°, 18.3°, 32.5°, 35.18°, 43.4°, and 57.32° which correspond to the (0 0 2), (004), (1 0 0), (101), (103) and (110) crystal planes of MoS_2, respectively [32–34]. The hexagonal MoS_2 phase is responsible for these peaks. Furthermore, the appearance of peaks at 26°, 34°, and 52° that correspond to the (110), (101), and (211) planes in the MoS_2-SnO_2 nanocomposite supports the existence of the tetragonal rutile phase of SnO_2. Because of the poor crystallinity of Mo, the peaks of pure MoS_2 cannot be seen in the case of the MoS_2–SnO_2 nanocomposite, which might be due to the low amount of molybdenum disulfide in the MoS_2–SnO_2 composites as well as the intense peaks of SnO_2. As crystallinity depends on crystallite size, the crystallite

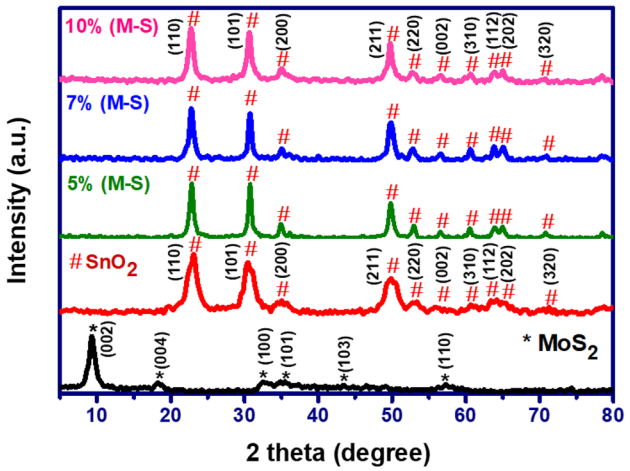

Fig. 4 XRD graph of pure MoS_2, pure SnO_2, and MoS_2–SnO_2 nanocomposite with a different weight percentage of 5%MoS_2–SnO_2, 7%MoS_2–SnO_2, and 10%MoS_2–SnO_2. The planes corresponding to MoS_2 and SnO_2 have been marked by (*) and (#), respectively

size was calculated by using Eq. 3 called the Scherrer's equation [35] for pure MoS_2, pure SnO_2, 5%MoS_2–SnO_2, 7%MoS_2–SnO_2, and 10%MoS_2–SnO_2 nanocomposite [36, 37];

$$D = K\lambda/(\beta\cos\theta) \tag{3}$$

where λ denotes the wavelength of X-ray, β denotes the broadening of the diffraction peak measured at full-width half maximum intensity (FWHM), θ denotes the angle corresponding to peak position, Crystallite size is D, and k denotes the shape factor (k=0.94). The calculated average crystal size for pure MoS_2, pure SnO_2, 5%MoS_2–SnO_2, 7%MoS_2–SnO_2, and 10%MoS_2–SnO_2 are found to be 6.52 nm, 12.68 nm, 13.4 nm, 12.26 nm, and 10.25 nm respectively. As the concentration of MoS_2 in SnO_2 is very small, therefore to complement the XRD results of nanocomposite formation a highly sensitive Raman technique will be used.

3.2 Raman spectroscopy

Raman scattering is a powerful tool for studying the structure of MoS_2-based materials, hence the structure of MoS_2–SnO_2 nanocomposites was explored further using this technique. Raman spectra of SnO_2 nanoparticles and MoS_2–SnO_2 composites with varying MoS_2 concentrations are shown in Fig. 5. The peak of SnO_2 nanoparticles has Raman peaks at 628 cm^{-1} corresponding to the A_{1g} vibration mode

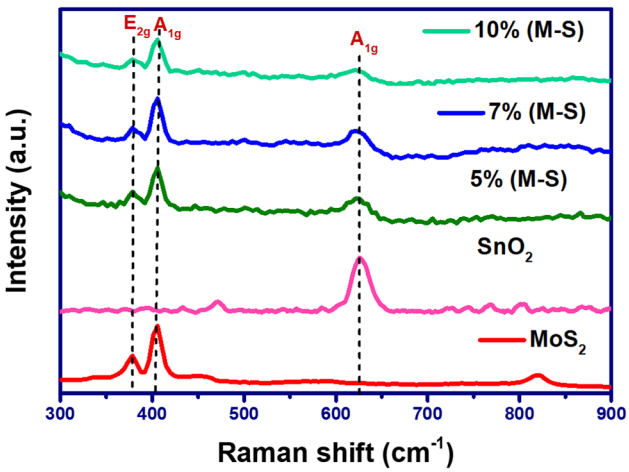

Fig. 5 Raman spectra of pure MoS_2, pure SnO_2 nanoparticles, 5%MoS_2–SnO_2, 7%MoS_2–SnO_2, and 10%MoS_2–SnO_2 nanocomposites

[31]. The typical peaks of MoS_2 are primarily found at 380 cm^{-1} and 406 cm^{-1}, which are associated with the E_{2g} mode (reverse vibration of two S atoms concerning Mo atoms) and A_{1g} mode, respectively (only S atoms vibrate in the outer plane in the opposite direction). This is also consistent with the previously reported Raman spectroscopy of MoS_2 [38]. Raman spectra of MoS_2–SnO_2 nanocomposite materials exhibit distinctive peaks caused by both MoS_2 and SnO_2 at different MoS_2 concentrations (5, 7, and 10%). For the 5%MoS_2–SnO_2 composite sample, the Raman spectrum is a simple superposition of the single vibration modes of MoS_2 and SnO_2, which is consistent with the literature [39]. The peak positions do not change, however, the peak intensities of the MoS_2 vibration modes E_{2g} and A_{1g} are dramatically reduced, With the increase of MoS_2 content, the peak intensity for the A_{1g} mode of SnO_2 decreases, indicating the successful fabrication of the nanocomposite substance with variable MoS_2 content.

3.3 UV–visible spectroscopy

The optical characteristics of the MoS_2, SnO_2, 5%MoS_2–SnO_2, 7%MoS_2–SnO_2, and 10%MoS_2–SnO_2 nano-composites are examined using the diffuse UV–vis reflection spectrum, as shown in Fig. 6. SnO_2 mostly absorbs ultraviolet light and has a relatively modest absorption in the visible spectrum (420–700 nm). The synthesized MoS_2 is black and exhibits no discernible absorption edges over the whole spectrum. As a result, MoS_2 exhibits strong absorption intensity throughout the whole range. The

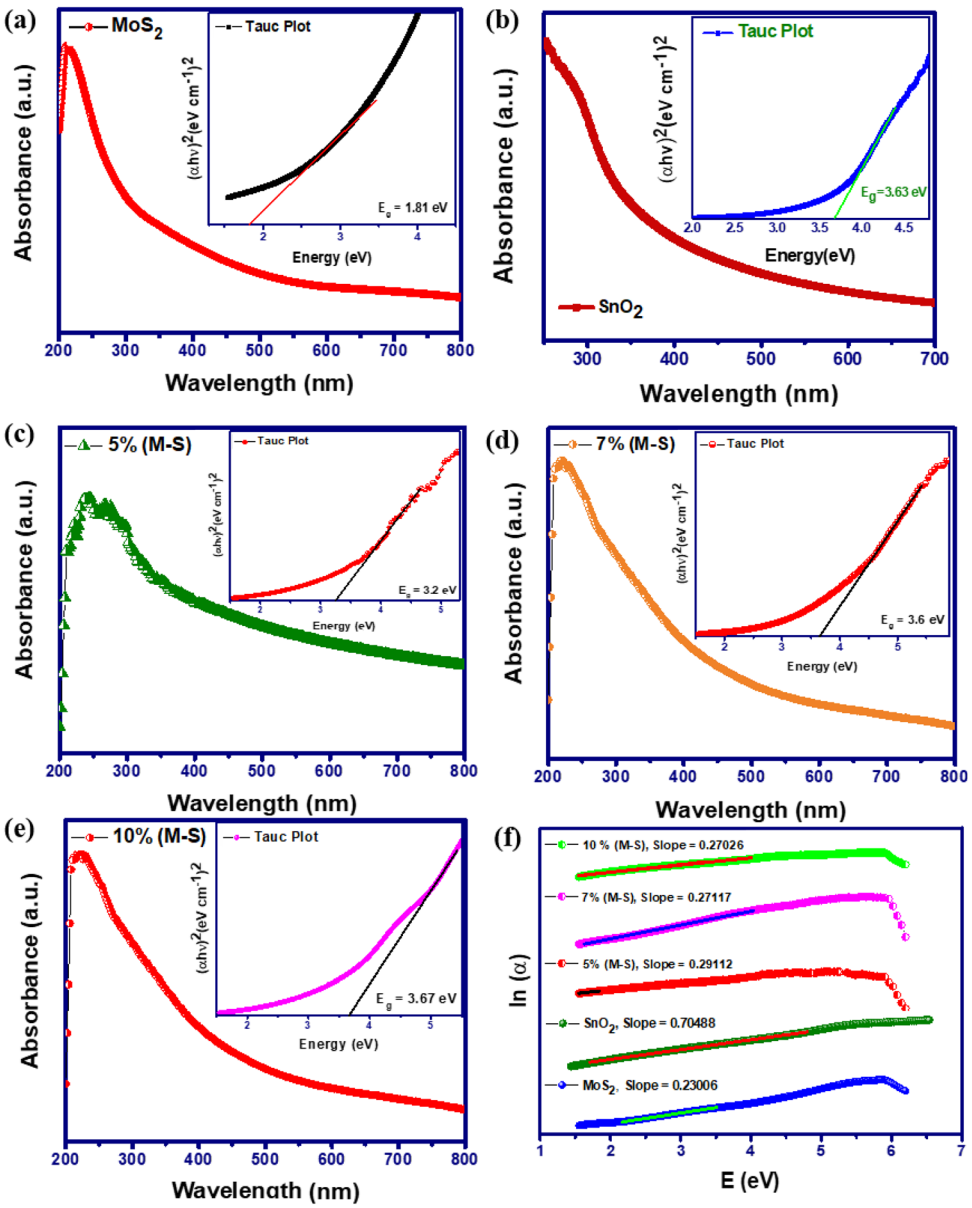

Fig. 6 UV–vis spectra with optical band energy (Eg) of **a** MoS_2 flakes, **b** SnO_2 nanoparticle, **c** 5%MoS_2–SnO_2, **d** 7%MoS_2–SnO_2 and **e** 10%MoS_2–SnO_2 nanocomposites. **f** Illustration of (lnα) vs photon energy (eV) for MoS_2, SnO_2, 5%MoS_2–SnO_2, 7%MoS_2–SnO_2, and 10%MoS_2–SnO_2 nanocomposites to determine Urbach energy

optical characteristics of MoS_2 have carried over to the 5%MoS_2–SnO_2, 7%MoS_2–SnO_2, and 10%MoS_2–SnO_2 composites, which have a substantially higher visible absorption capability. The increase in the optical band gap as the MoS_2 weight percentage is increased from 5 to 10% may be attributed to overall crystallite size reduction due to the quantum confinement feature of MoS_2 nanoparticles in the synthesized nanocomposites [40]. The results are also supported by XRD-based crystallite size calculation in Table 1.

The formula below has been used to determine the energy bandgap (Eg) and is given by Eq. 4 [10].

$$(\alpha hv) = A(h - Eg)^{1/2} \quad (4)$$

where A is a constant, Eg is the bandgap, and α is the absorption coefficient. The optical bandgap for pure SnO_2, pure MoS_2, 5%MoS_2–SnO_2, 7%MoS_2–SnO_2, and 10%MoS_2–SnO_2 nanocomposites were calculated by the plot between $(\alpha hv)^2$ vs hv. According to Table 2, the estimated bandgap energies for pure SnO_2, MoS_2, 5%MoS_2–SnO_2, 7%MoS_2–SnO_2, and 10%MoS_2–SnO_2 were 3.63 eV, 1.81 eV, 3.2 eV, 3.6 eV, and 3.67 eV, respectively. The absorption spectra hump changes continually to the lower wavelengths and the bandgap value increases in the MoS_2-SnO_2 nanocomposites after MoS_2 addition in the SnO_2 nanoparticles. To further understand the effect of MoS_2 weight

Table 1 XRD analysis of MoS_2, SnO_2, 5%MoS_2-SnO_2, 7%MoS_2-SnO_2 and 10%MoS_2-SnO_2 nanocomposites

Sample	Peak position (2θ)	Planes (*hkl*)	FW HM	Crystal size (nm)	Average crystal size (nm)
SnO_2	26.36	(110)	0.01035	13.76	12.68
	33.82	(101)	0.00887	16.34	
	52.62	(211)	0.00972	15.86	
	65.21	(301)	0.03455	4.77	
MoS_2	9.2	(002)	1.22142	6.52	6.52
5%MoS_2–SnO_2	26.57	(110)	0.68038	11.99	13.40
	34.02	(101)	0.52873	15.71	
	51.84	(211)	0.70678	12.49	
7%MoS_2–SnO_2	26.62	(110)	0.76659	10.64	12.26
	34.03	(101)	0.54595	15.21	
	51.86	(211)	0.80827	10.92	
10%MoS_2–SnO_2	26.56	(110)	0.80695	10.11	10.25
	33.93	(101)	0.81696	10.16	
	51.77	(211)	0.84346	10.46	

Table 2 Calculated optical bandgap and Urbach energy values

Sample	Bandgap (eV)	Urbach energy (eV)
SnO_2	3.63	1.41
5% MoS_2–SnO_2	3.2	3.43
7% MoS_2–SnO_2	3.6	3.68
10% MoS_2–SnO_2	3.67	3.70
MoS_2	1.81	4.34

percentage in the SnO_2, Urbach energy calculations have been carried which correlate the amount of disorder on the absorption properties shown in Fig. 6f. As a molecule absorbs a photon, an excited electron from the valence band moves through the energy gap and into the conduction band bottom. The density of electronic states, tails through the energy difference in the valence and conduction bands, if any disorder in the molecule exists throughout this transition process. [41]. The term "Urbach tail" describes the tail of the density of electronic states that penetrates the energy bandgap [42]. It is frequently interpreted as the width of the band tail caused by localized states linked to material disorder [43]. The exponential relationship between photon energy and the absorption coefficient is known as the Urbach rule and given by the Eq. 5.

$$\alpha = \alpha_0 \times \exp[E/E_u] \quad (5)$$

Here $E = h\nu$ is the energy of the incident photons, and E_u is the Urbach energy in this instance. The calculated value of Urbach energy is given in Table 2 and indicates that as we increases the MoS_2 weight percentage from 5 to 10% in SnO_2, the Urbach energy shows the enhancement from 3.43 to 3.70 respectively. This slight enhancement may be attributed to the rise in defects brought on by oxygen vacancies as a result of MoS_2 adding. It is possible to assume that the distortion advances with increasing MoS_2 content in the materials since this raises the Urbach energy in the material. The increase in distortion may be brought on by two factors: either the presence of MoS_2 in the system produces oxygen vacancies that raise levels near the conduction band, or the presence of MoS_2 in the system causes distortion in the lattice structure [44].

3.4 Scanning electron microscopy (SEM)

The morphology of the pure MoS_2, pure SnO_2, 5%MoS_2–SnO_2 (M-S), 7%MoS_2–SnO_2, and 10%MoS_2–SnO_2 nanocomposite was examined using the SEM technique. As seen in Fig. 7a, layered flakes can be seen on the surface of MoS_2 in the SEM image. Additionally, aggregated MoS_2 sheets are shown randomly. The SEM image of the nanocrystalline SnO_2 is also depicted in Fig. 7b. It demonstrates the homogeneous and uniform dispersion of SnO_2 nanocrystallites. Furthermore, as shown in Fig. 7c–e, the SEM picture of the MoS_2–SnO_2 (5%, 7%, 10%) nanocomposite shows that SnO_2 nanoparticles are uniformly attached to the surface of MoS_2 sheets. It indicates that hydrothermal treatment of MoS_2 and

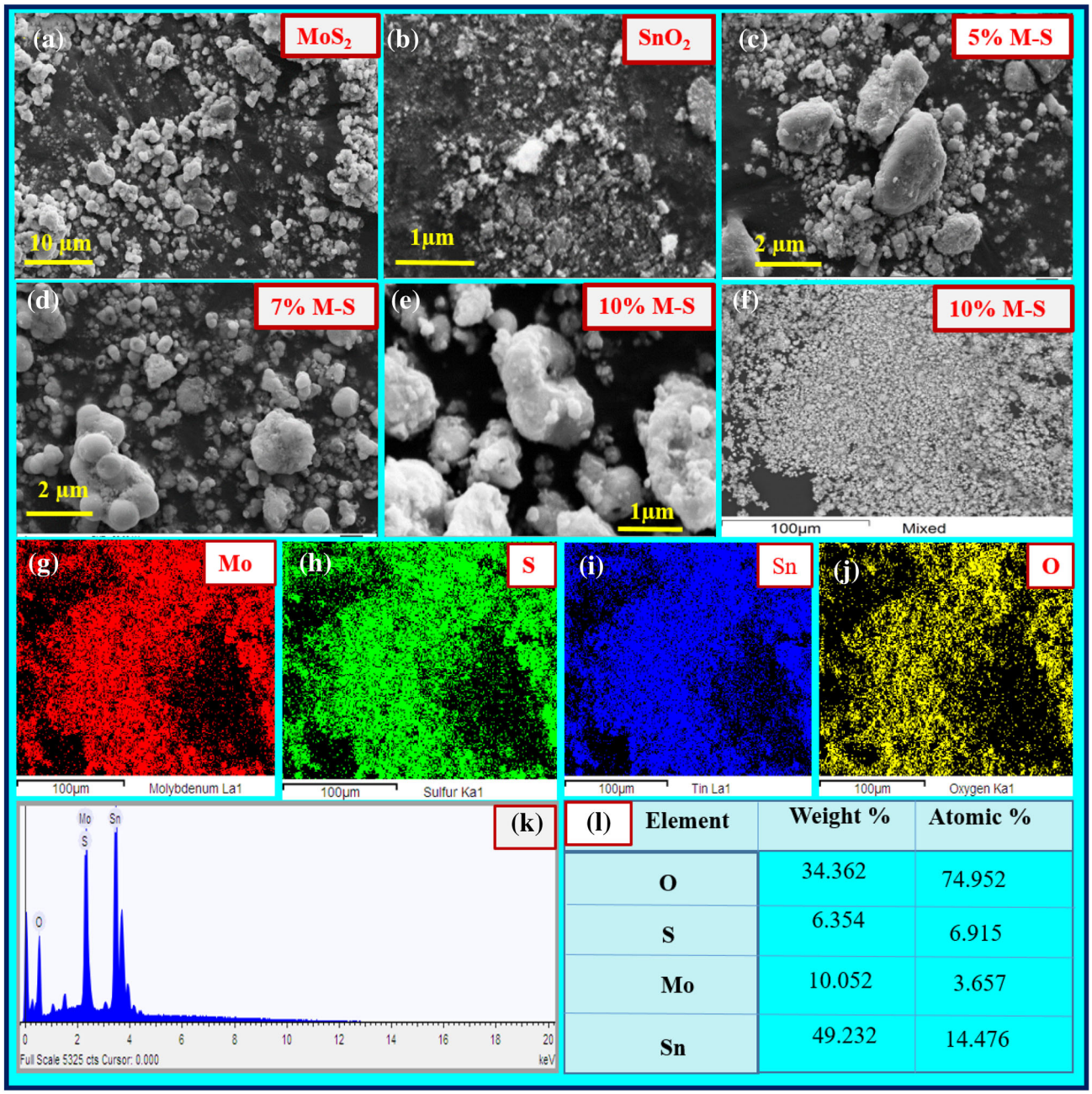

Fig. 7 SEM micrograph of MoS_2, SnO_2, and MoS_2–SnO_2 nanocomposites: **a** MoS_2, **b** SnO_2, **c** 5%MoS_2–SnO_2, **d** 7%MoS_2–SnO_2 **e** 10%MoS_2–SnO_2 **f**–**j** elemental mapping and **k**, **l** EDX spectra of the synthesized 10% MoS_2–SnO_2 nanocomposite showing the purity of the synthesized powder

$SnCl_4$ solution is a successful approach for the synthesis of the MoS_2–SnO_2 nanocomposite [45]. Further to check the purity of synthesized nanocomposite powder, Energy Dispersive X-ray Spectroscopy (EDAX) technique has been used. Fig. 7f–j shows the elemental mapping pictures of Mo, Sn, S, and O elements, respectively of 10% MoS_2–SnO_2 powder. EDAX spectra shown in Fig. (k) revealed no additional elements, thereby further demonstrating the purity of the produced nanocomposite samples. The corresponding weight % and atomic % of the various elements in the synthesized powder are also tabulated and are given in Fig. 7.

3.5 Transmission electron microscopy (TEM)

Transmission electron microscopy (TEM) and high-resolution transmission electron microscopy (HRTEM) techniques have been utilized to further describe the morphology of the synthesized nanocomposite powders and determine the lattice spacing, respectively. Fig. 8a shows the TEM image of synthesized MoS_2 flakes with a calculated lattice spacing of 0.68 nm by the HRTEM image of Fig. 8b. Furthermore, the planes of the hexagonal MoS_2 structure can be indexed to the SAED pattern shown in Fig. 8c. The morphology of SnO_2 nanoparticles is depicted in Fig. 8d, which makes the nanoparticles spherical shape abundantly obvious. The fact that SnO_2 nanoparticles can be seen, yet the identified particles from Fig. 8d are agglomerated and incoherently clustered. Fig. 8e predicts the lattice spacing of 0.36 nm in size corresponding to the (110) plane of the tetragonal SnO_2 phase [46]. The two prominent diffraction peaks of standard SnO_2 identified in the XRD investigation correlate to two crystal faces identified in the HRTEM images as (110) and (101), respectively. The SAED rings in Fig. 8f have been indexed with respect to the planes of the tetragonal rutile SnO_2 structure [47]. As shown in Fig. 8g, the morphological image of the MoS_2–SnO_2 nanocomposite contains both SnO_2 nanoparticles and MoS_2 nanosheets, with SnO_2 nanoparticles appearing to have uniformly stuck to MoS_2 surfaces. The fact that these observations and the SEM images are in strong agreement should be noted. In Fig. 8h, HRTEM images of MoS_2–SnO_2 lattice fringes can be observed in all their detail. According to Fig. 8i, the

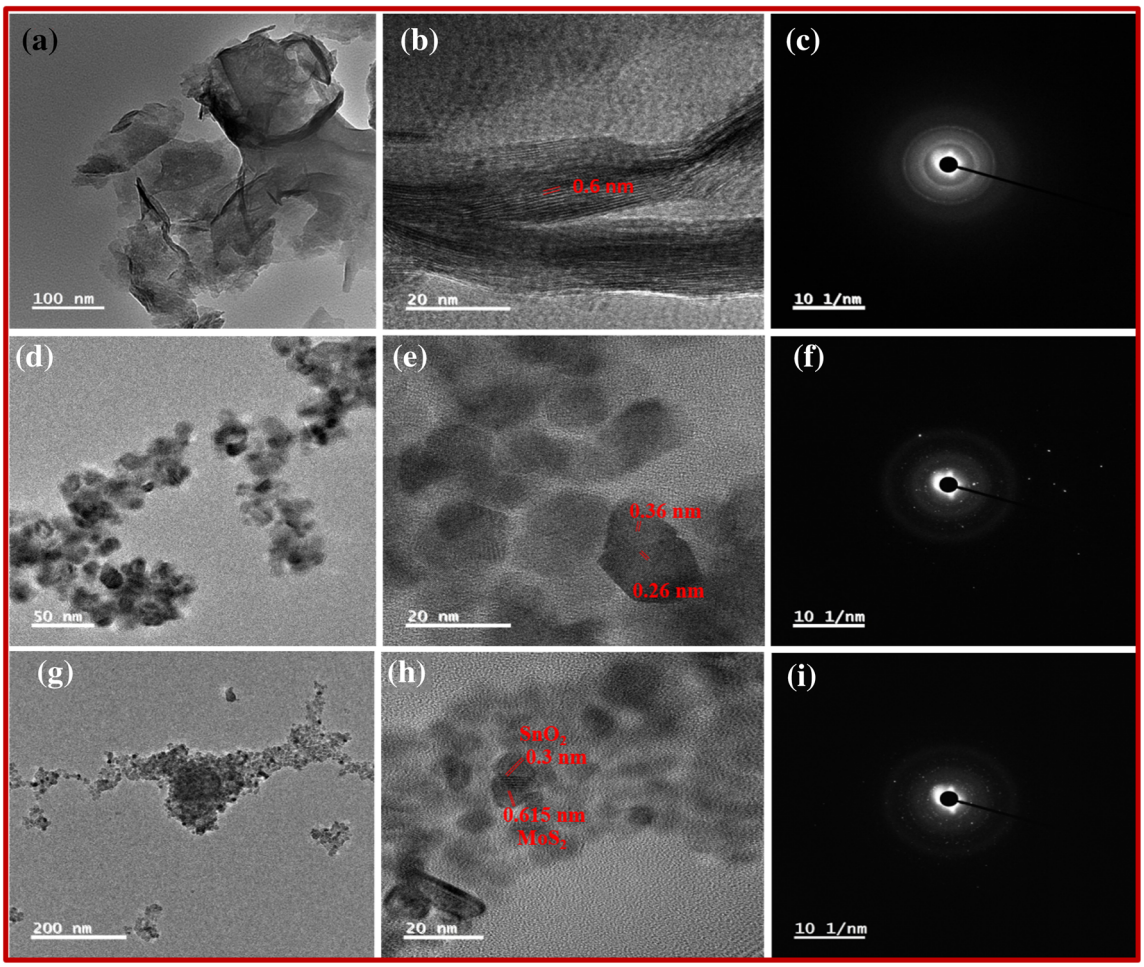

Fig. 8 displays TEM images of **a** Flakes of MoS_2 nanosheets, **b** the distance between two layers in MoS_2 nanosheets, (**c**) the SAED pattern of MoS_2 nanosheets, **d**, **e** as-synthesized SnO_2 nanosheets, **f** the SAED pattern of SnO_2 nanoparticles, and **g** hybrid MoS_2–SnO_2. HRTEM images of **h** MoS_2–SnO_2 and **i** the SAED pattern of the MoS_2–SnO_2 nanocomposite

fringe spacing for the SnO_2 (1 1 0) crystal plane and MoS_2 (0 0 2) crystal plane, respectively, is 0.33 nm and 0.62 nm. It demonstrates how MoS_2 and SnO_2 are joined to form nanocomposite powder with improved properties [30, 48, 49].

3.6 3.6 Switching characteristic of Al/SnO_2/ITO-PET, Al/5%MoS_2–SnO_2/ITO-PET, Al/7%MoS_2–SnO_2/ITO-PET, and Al/10%MoS_2–SnO_2/ITO-PET devices

The schematic diagram for the Al/SnO_2/ITO-PET, Al/MoS_2–SnO_2/ITO-PET-based memristive devices is shown in Fig. 3a, b, and Fig. 3c shows a cross-sectional FESEM picture of Al/MoS_2–SnO_2/ITO-PET. The MoS_2–SnO_2 active layer has a homogeneous thickness of 185 µm and is deposited on the ITO-PET. The cross-sectional FESEM image demonstrates that 10%MoS_2–SnO_2 is uniformly deposited as the active layer.

To understand the resistive switching behaviour, the current-voltage characteristics of the fabricated memory device in a metal-insulator-metal (MIM) structure have been performed and, are given in Fig. 9. Fig. 9a–d illustrates the current-voltage characteristics of the Al/SnO_2/ITO-PET and Al/MoS_2-SnO_2/ITO-PET (5%, 7%, 10%) based devices, respectively, within − 1 V to + 1 V. It can be seen that the device with MoS_2–SnO_2 based nanocomposite has non-linear behaviour in comparison to the pure SnO_2-based device. In order to observe the memory effect, the voltage is further raised in both directions. It has been noted that the Al/SnO_2/ITO-PET based device enters the SET state at 10.8 V, where the device switches from the high resistance state (HRS) to the low resistance state (LRS). However, as demonstrated in Fig. 9e, there is no transition from LRS to HRS when the voltage is increased further in the same direction. Since the voltage polarity must be reversed for the device to make the reset transition, it has been discovered that the reset transition occurs at − 9.6 V. The device exhibits bipolar resistive behaviour, as demonstrated by the polarity-dependent switching of the constructed structure. The lower hysteresis and higher switching voltages of the SnO_2-based memory device are not useful for practical application. Therefore, the device with MoS_2–SnO_2 nanocomposite as an active layer was studied further. To understand the effect of 2D MoS_2 in SnO_2 for memory device application, the different weight percentages of MoS_2 in SnO_2-based devices were fabricated and tested. All of the MoS_2–SnO_2 nanocomposite devices displayed bipolar resistive switching (BRS) characteristics, as shown in Fig. 9f–h (arrows indicate the voltage sweep direction). In addition, as shown in Fig. 9h, the memory phenomenon with 10 wt.% MoS_2–SnO_2 based nanocomposite has the largest ON/OFF current ratio. The nanocomposite-based device displays the HRS to LRS transition at a reduced voltage of 1.96 V and the LRS to HRS transition at − 1.52 V. The MoS_2–SnO_2 based device demonstrates an improved resistive switching behaviour. The I_{ON}/I_{OFF} ratios for pure SnO_2, 5%MoS_2–SnO_2, 7%MoS_2–SnO_2, and 10%MoS_2–SnO_2 based devices are 1, 3, 6, and 25, respectively. This demonstrates the improved resistive switching properties of the hybrid 10%MoS_2–SnO_2 device.

The enhanced resistive switching performance may be attributed to the increased oxygen vacancies in the nanocomposite-based structure, thus causing bipolar resistive switching with an improved ON/OFF ratio. Singh et al. have reported a similar type of enhanced resistive performance of GO and TiO_2-based memory devices [50]. In order to connect the top and bottom electrodes and initiate LRS, the oxygen vacancies in the active memory layer device line up with the voltage applied to the structure and create the filament inside the oxide-based matrix. Based on the magnitude of the applied voltage, oxygen vacancies are attracted to the electrode when changing the voltage polarity, which breaks the filament close to the electrode and causes the device to enter HRS. The memory phenomenon is reversible in nature and is repeated by the cyclic application of voltage.

3.7 Dielectric properties

The frequency dependence of the dielectric measurement provides important information regarding the relaxation mechanism within the material. It offers details on two crucial material physical properties: (a) electric permittivity (also known as the dielectric constant), and (b) dielectric loss. Due to a lag in polarisation known as “dielectric loss” (D = tanδ), charge carriers generate heat when an alternating field is applied across the sample. The combined actions of electrical conduction and dielectric relaxation result in dielectric loss inside a material [51]. Fig. 10a and b, depict the variation of the real (ε'_r) and imaginary (ε''_r) components of the dielectric

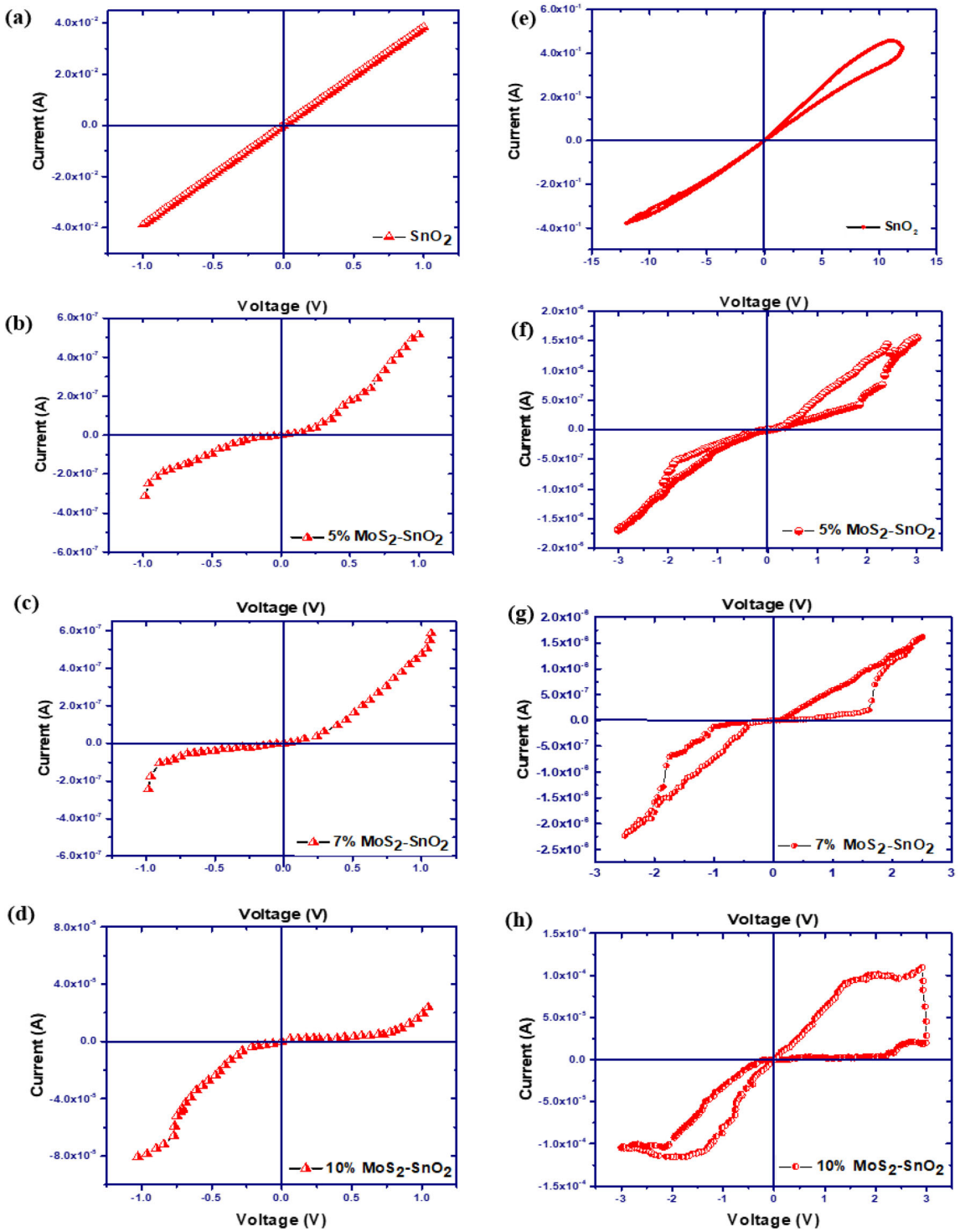

Fig. 9 I-V characteristic of **a** SnO_2 **b** 5%MoS_2–SnO_2, **c** 7%MoS_2–SnO_2 **d** 10%MoS_2–SnO_2 and resistive switching characteristic of **e** SnO_2 **f** 5%MoS_2–SnO_2, **g** 7%MoS_2–SnO_2 **h** 10%MoS_2–SnO_2 nanocomposite

constant (electric permittivity), with frequency. On the basis of the Maxwell-Wagner model, it can be seen that ε'_r decreases with increasing frequency of applied field for all samples [52]. Since oscillating nano-dipoles can easily orient themselves along the direction of the applied electric field, as a result of

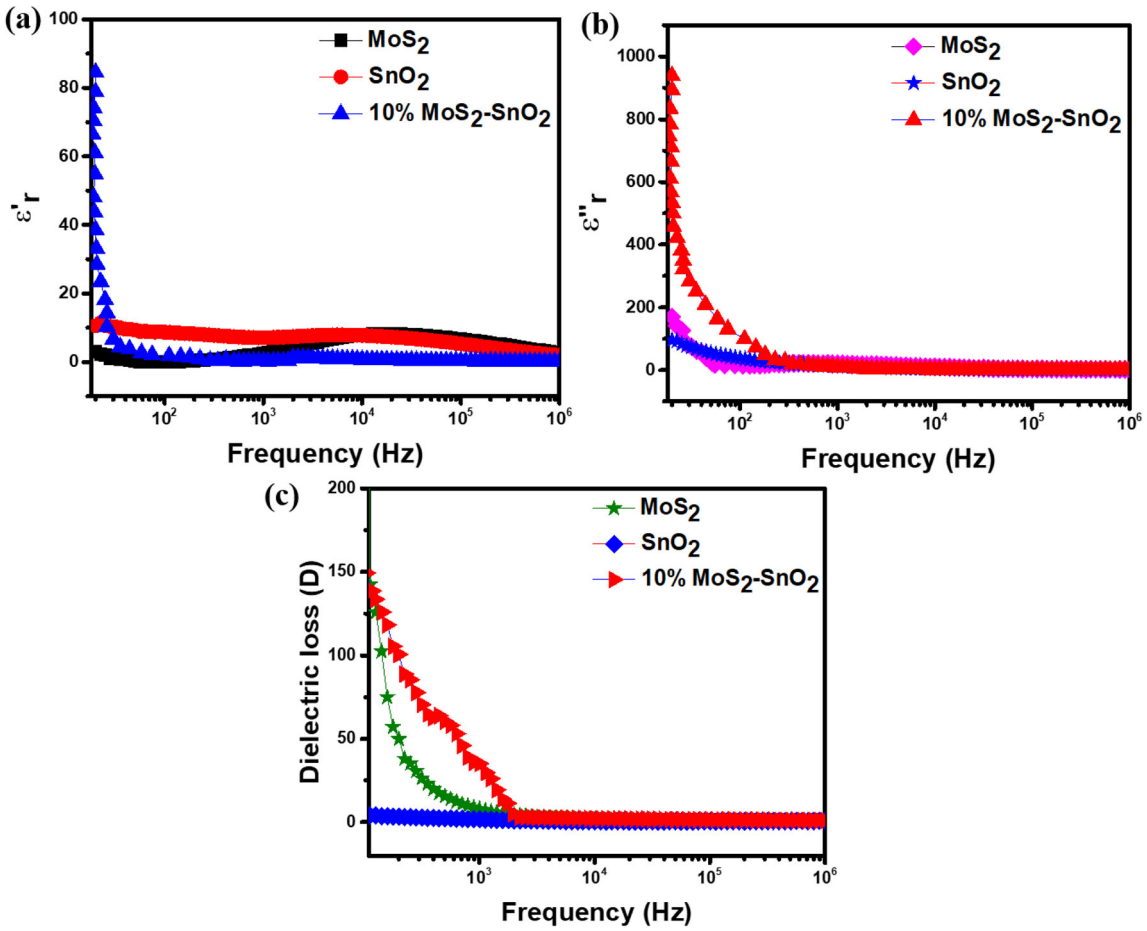

Fig. 10 Variation of dielectric constant **a** real and **b** imaginary part and Fig **c** dielectric loss for the pure MoS_2, SnO_2, and 10%MoS_2–SnO_2 nanocomposite as a function of the frequency

space charge polarization, thus a high value of ε'_r is observed in the low-frequency region as a result of space charge polarization. When the frequency is low, the dipoles have enough time to travel to the grain boundaries, where all the charge carriers accumulate and lead to strong polarization. At high frequencies, the field direction changes so quickly that the charge carriers are unable to align with it. As a result, carriers are unable to reach the grain boundaries, and as a result, no polarisations occur [53]. Due to the fact that composites have a larger surface area due to their small size (more grains), the dielectric constant in composites is higher than in pure SnO_2 and MoS_2 [54].

Energy is lost in the dielectric system through a process known as dielectric loss (tanδ). The dielectric loss for MoS_2, SnO_2, and 10%MoS_2–SnO_2 nanocomposite at room temperature is shown in Fig. 10c as a function of the frequency range of 10–10^6 Hz. Dielectric loss happens if the charge carriers in a dielectric media are unable to keep up with changes in the electric field. It is discovered that when the applied field frequency rises, dielectric losses for all samples decrease. Inhibition of domain walls causes magnetization to be forced to shift rotation, and lower dielectric losses are observed at higher frequencies. The lower values at higher frequencies may also be an indication of Maxwell-Wagner relaxation. Fig. 10c shows that the larger dielectric loss occurs at lower frequencies. This is caused by space charge polarisation, which can be explained by the Shockley-Read mechanism [55]. The dielectric loss tanδ of pure MoS_2 and SnO_2 is discovered to be considerably lower than that of the MoS_2–SnO_2 composite [56]. The increase in dielectric loss in the case of the MoS_2–SnO_2 nanocomposite may result from a significant leakage current caused by the direct connection of MoS_2 sheets above the percolation threshold [57].

In the high-frequency region, it is discovered that the variation of the dielectric constant (ε'_r) with the frequency of the MoS_2, SnO_2, and 10%MoS_2–SnO_2 samples follows the Cole–Cole relaxation. The following relation was used to fit the experimental ε'_r vs. f curve in the frequency range between 20 and 1.0×10^6 Hz.

$$\varepsilon\prime(w) = \varepsilon\prime_\infty + [(\varepsilon\prime_s - \varepsilon\prime_\infty)/(1 + (iwt)^{1-\alpha})] \quad (6)$$

where ε' denotes the real part of the dielectric constant, ε'_∞ denotes the value at the greatest frequency, ε'_s denotes the value at the lowest frequency, ω denotes the angular frequency, τ denotes the average relaxation time, and α denotes the spread. Fig. 11 shows experimental data with a Cole–Cole-fitted curve of MoS_2, SnO_2, and 10%MoS_2–SnO_2 samples. Table 3 demonstrates the values of α and τ for the MoS_2, SnO_2, and 10%MoS_2–SnO_2 samples derived from the Cole–Cole fitting [58, 59].

3.8 Impedance spectroscopy

To examine various electrical features, such as the impact of grain and grain boundaries on the total impedance, relaxation time distribution, and kind of relaxation mechanism [51], one can analyse the complex behaviour of total impedance with frequency. The following formula can be used to represent the total complex impedance:

$$Z^* = Z' + jZ'' \quad (7)$$

where the total impedance real (Z') and imaginary (Z'') components are given by Eq. 8

$$Z' = Z \times \cos\theta \text{ and } Z'' = Z \times \sin\theta \quad (8)$$

In this case, Z represents a total measured impedance for θ, which is the measured phase angle (in radians). Fig. 12a, b shows the variation in resistive or real part (Z'), and its capacitive or imaginary part with the frequency of the applied field. At lower

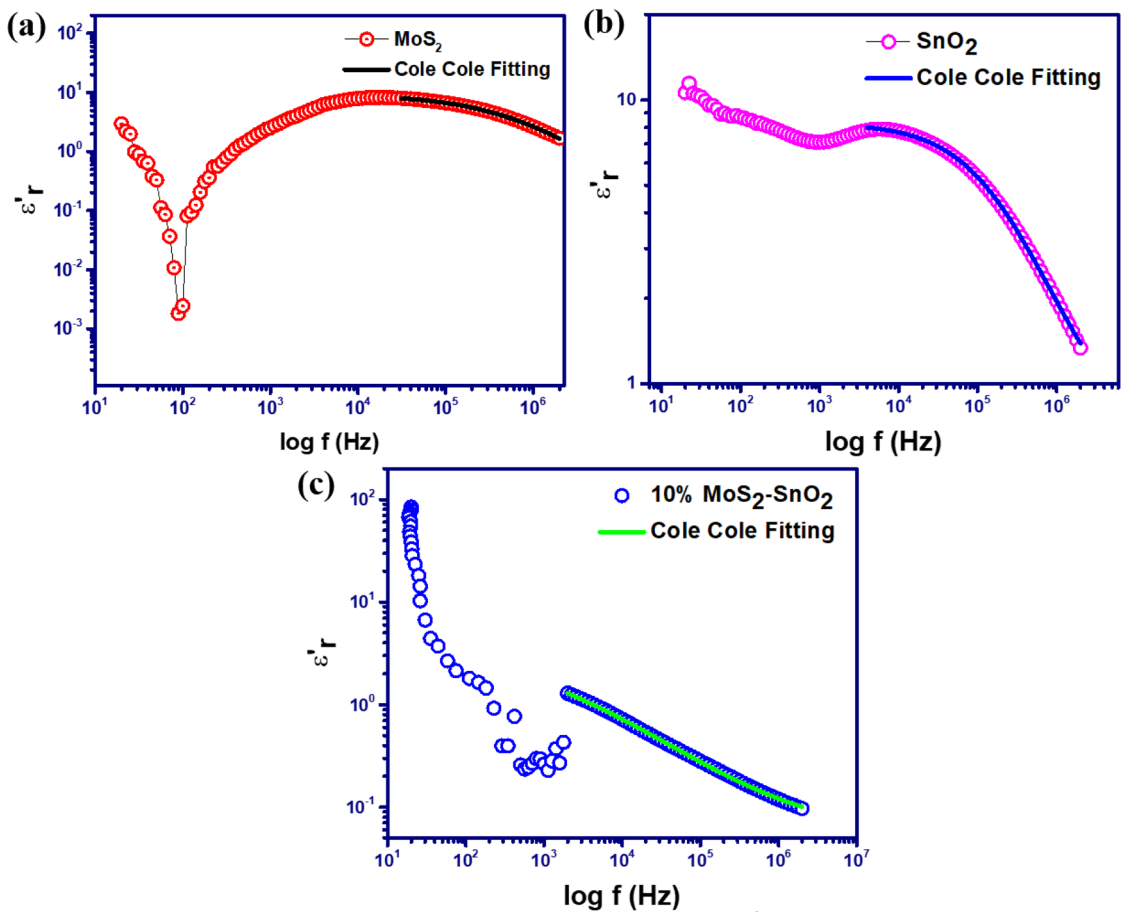

Fig. 11 **a** MoS_2, **b** SnO_2, and **c** 10%MoS_2–SnO_2 nanocomposite were fitted using a Cole–Cole fit to measure the frequency dependence of the dielectric constant (real part)

Table 3 Parameters extracted from Jonscher's power law and Cole–Cole fitting for all samples

Materials	Frequency exponents (s)	Pre exponent A	Spreading factor (α)	Relaxation time (τ)
MoS_2	0.805	2.92×10^{-10}	0.60	2.66×10^{-6}
SnO_2	0.698	4.46×10^{-12}	0.56	5.69×10^{-6}
MoS_2–SnO_2	0.467	2.00×10^{-9}	0.72	1.06×10^{-3}

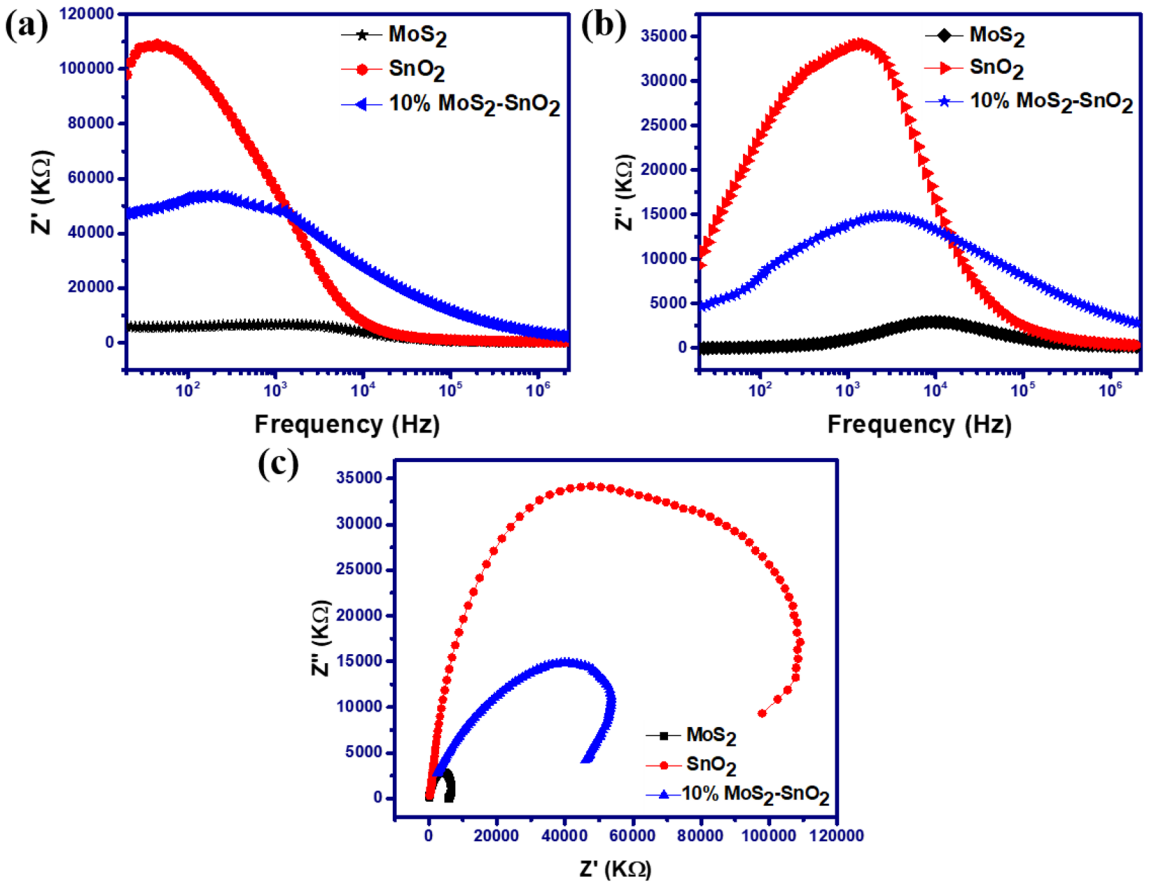

Fig. 12 Variation of impedance **a** real and **b** imaginary parts of impedance as a function of frequency (10–10^6 Hz) for the MoS_2, SnO_2, and 10%MoS_2–SnO_2 nanocomposite powder. **c** Nyquist plot of MoS_2, SnO_2, and 10%MoS_2–SnO_2 nanocomposite samples

frequencies, the impedance values are high, and they decrease as the frequency increases. Due to the dissipation of immobile charges and increased mobility with increasing frequency, impedance has decreased. At higher frequencies, there is a tendency for all the curves to merge due to a decrease in space charge and the cancellation of the dipole orientation effect [51]. At room temperature, Nyquist plots were utilised to separate the effects of the grains and grain boundary, as shown in Fig. 12c. Conducting grain boundaries is important at higher frequencies in MoS_2, SnO_2, and 10%MoS_2–SnO_2 nanocomposite materials, while resistive grain boundaries dominate at low frequencies. At low frequencies, the semicircle indicates highly resistant grain boundaries. The conducting grains produce the semi-circle at high frequency and low resistance value. In our situation, all of the samples display just one semicircle, which is caused by the contribution of the grain boundaries [57], as seen in Fig. 12c. Due to their higher resistance than the grain itself, grain boundaries are thought to play a significant role in impedance [60]. Due to the high conductivity of MoS_2, it is evident that the MoS_2–SnO_2 nanocomposite has lower resistance than SnO_2.

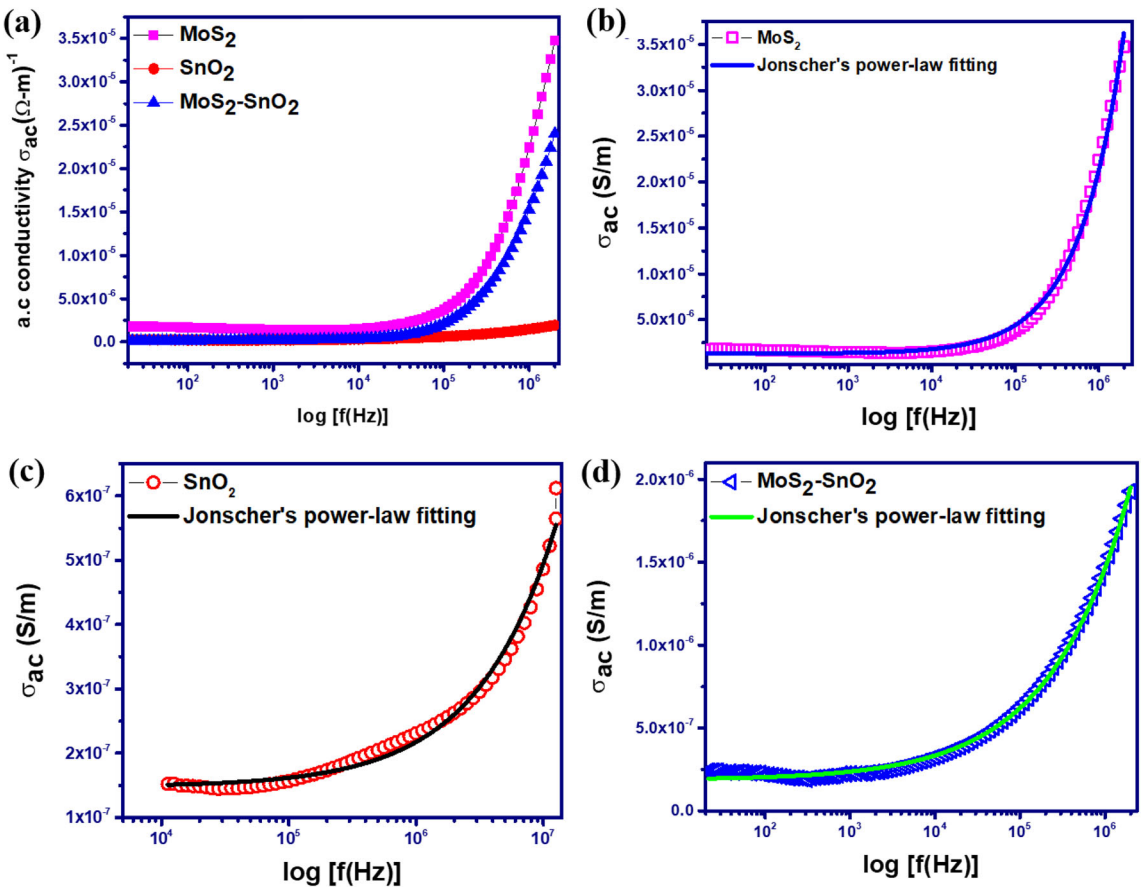

Fig. 13 **a** Ac conductivity (σ_{ac}) as a function of frequency. **b–d** The graphs of curve fitting by using Jonscher's power law for MoS_2, SnO_2, and 10% MoS_2–SnO_2 nanocomposite

3.9 AC conductivity

Frequency-dependent AC conductivity has been examined at room temperature in the frequency range of 10–10^6 Hz to analyse the conduction mechanism in synthesised MoS_2, SnO_2, and 10%MoS_2–SnO_2 nanocomposite samples. In an alternating field, carriers that are in phase with the applied field contribute to the electrical conduction. The contributions of free carriers and bound charge carriers add up to the total conductivity. It has been noted that when the conductivity decreases with an increase in frequency, the free charge carriers make the majority contribution, whereas when the conductivity increases with frequency, the bound charge carriers make the majority contribution [61]. Carriers are induced to hop from one defect condition to another by the alternating field across the sample. The calculated a.c. conductivity using the formula $\sigma(\omega) = \omega\varepsilon_0\varepsilon_r\tan\delta$ is shown in Fig. 13a. It demonstrates that conductivity increases with frequency, supporting the involvement of bound charge carriers and illuminating the behaviour of substantial frequency dependence. At lower frequencies, the carriers successfully hop for longer periods, resulting in long-range translational motion of the carriers that create frequency-independent conductivity. Due to the carrier's shorter durations, failed and successful hopping, two competing processes, happen at higher frequencies. The scattered behaviour in conductivity at higher frequencies is caused by the ratio of failed to successful hops. Jonscher's power law is used to fit the frequency dependence of a.c. conductivity data using Eq. 9 [51].

$$\sigma_{ac}(\omega) = \sigma_{dc} + A\,\omega^{s} \tag{9}$$

where A is the amount or strength of polarization, and s is an exponent describing the interaction

between the lattice and mobile ions depending on the frequency of the applied field, and where $\sigma_{ac}(\omega)$ is total measured conductivity, σ_{dc} is d.c. contribution (frequency-independent), and $A\omega^s$ describes the frequency-dependent contribution. The shift between the frequency-independent and frequency-dependent regions demonstrates the transformation from long-range hopping across barriers to the short-range motion of carriers [51, 62]. We notice a sharp increase in conductivity at higher frequency in the analysis of a.c. conductivity, suggesting the possibility of alternative conduction mechanisms, which is supported by Jonscher's power law. We used Jonscher's power law to fit the a.c. conductivity data, as shown in Fig. 13b–d, and the retrieved fitting parameters are listed in Table 3. It is clear from Fig. 13a that adding MoS_2 to SnO_2 causes the AC conductivity to increase.

4 Conclusion

In summary, the effect of the MoS_2 content on the resistive switching capabilities of MoS_2–SnO_2 composite film were investigated using a device designed as an Al/MoS_2–SnO_2/ITO-PET structure. Hydrothermal synthesis is used to successfully synthesize the 5%MoS_2–SnO_2, 7%MoS_2–SnO_2, and 10%MoS_2–SnO_2 nanocomposite sample, with average particle sizes of 13.40 nm, 12.26 nm, and 10.25 nm. The composite formation is supported by the XRD and Raman studies. The dielectric measurement shows that the 10%MoS_2–SnO_2 nanocomposite exhibited high dielectric constant, and dielectric loss in comparison to pure SnO_2 and MoS_2 material The reduction in space charge polarisation account for how impedance changes with frequency. The Nyquist plots have just one semicircle, which can be attributed to a result of the contribution of the grain boundary to the conduction process. The a.c. conductivity data confirms the involvement of bound charge carriers and is fitted with the Jonscher's power law. The Al/MoS_2–SnO_2/ITO-PET memory device displays the bipolar resistive switching phenomenon. The I_{On}/I_{Off} ratio for the fabricated Al/10%MoS_2–SnO_2/ITO-PET device was 25 times greater than that of Al/SnO_2/ITO-PET device. The filamentary model, based on the movement of oxygen vacancies between the electrodes, was used to explain the behaviour of bipolar resistive switching. The findings of the current study are valuable for understanding the importance and effect of MoS_2 addition on the structural and transport characteristics of the nanocomposite. The MoS_2–SnO_2 nanocomposite has the potential to be used in resistive random-access memory (ReRAM) applications and high-frequency electromagnetic devices due to its low losses and hysteresis loop type behaviour of Current–Voltage (I–V) behaviour. The current work unequivocally demonstrates that composite-based devices have better performance and, as a result, presents a novel technique for modifying the devices performance.

Acknowledgements

The CSIR, Government of India, and the Advance Instrumentation Centre, Department of Applied Physics, Delhi Technological University are both acknowledged by the authors as sources of support for their work.

Author contributions

KK: methodology, conceptualization, investigation, data curation, writing—original draft. BS: methodology, conceptualization, writing—review & editing at different stages, supervision. MS: visualization, revising the manuscript critically for important intellectual content.

Funding

The funding was received from Human Resource Development Group,08/133(0025)/2018-EMR-I,Km. Komal.

Data availability

The data that support the findings of this manuscript are available in this article.

Declarations

Conflict of interest The authors declare that there is no conflict of interest.

References

1. T. Shi, R. Wang, Z. Wu, Y. Sun, J. An, Q. Liu, Small Struct. **2**, 2000109 (2021)
2. W. Banerjee, Electronics **9**, 1029 (2020)
3. K. Ando, S. Fujita, M. Hayashikoshi, Y. Fujimori, Normal.-Off Comput. (2017). https://doi.org/10.1007/978-4-431-56505-5_3
4. A. Chen, Solid-State Electron. **125**, 25 (2016)
5. M.-J. Lee, C.B. Lee, D. Lee et al., Nat. Mater. **10**, 625 (2011)
6. MS Islam, AAM Mazumder, C Zhou, C Stampfl, J Park, CY Yang (2023) IEEE Journal of the Electron Devices Society.
7. S. Salahuddin, S. Datta, Nano Lett. **8**, 405 (2008)
8. M. Hoffmann, S. Slesazeck, T. Mikolajick, APL Mater. **9**, 020902 (2021)
9. R Galatage, S Bentley, PH Suvarna, Z Krivokapic. Google Patents, (2019)
10. K. Komal, G. Gupta, M. Singh, B. Singh, J. Alloy. Compd. **923**, 166196 (2022)
11. W. Choi, N. Choudhary, G.H. Han, J. Park, D. Akinwande, Y.H. Lee, Mater. Today **20**, 116 (2017)
12. O. Lopez-Sanchez, D. Lembke, M. Kayci, A. Radenovic, A. Kis, Nat. Nanotechnol. **8**, 497 (2013)
13. H. Hwang, H. Kim, J. Cho, Nano Lett. **11**, 4826 (2011)
14. T.F. Jaramillo, K.P. Jørgensen, J. Bonde, J.H. Nielsen, S. Horch, I. Chorkendorff, Science **317**, 100 (2007)
15. H. Qiu, L. Pan, Z. Yao, J. Li, Y. Shi, X. Wang, Appl. Phys. Lett. **100**, 123104 (2012)
16. K.F. Mak, C. Lee, J. Hone, J. Shan, T.F. Heinz, Phys. Rev. Lett. **105**, 136805 (2010)
17. Y. Liu, Y.-X. Yu, W.-D. Zhang, J. Phys. Chem. C **117**, 12949 (2013)
18. M.A. Andio, P.N. Browning, P.A. Morris, S.A. Akbar, Sens. Actuators, B Chem. **165**, 13 (2012)
19. M. Periyasamy, A. Kar, J. Mater. Chem. C **8**, 4604 (2020)
20. P. Sun, Y. Cai, S. Du et al., Sens. Actuators, B Chem. **182**, 336 (2013)
21. J. Yang, S. Wang, L. Zhang, R. Dong, Z. Zhu, X. Gao, Sens. Actuators, B Chem. **239**, 857 (2017)
22. N. Van Hieu, Sens. Actuators, B Chem. **150**, 112 (2010)
23. S. Kumar, V. Pavelyev, P. Mishra, N. Tripathi, P. Sharma, F. Calle, Mater. Sci. Semicond. Process. **107**, 104865 (2020)
24. T. Wang, S. Chen, H. Pang, H. Xue, Y. Yu, Adv. Sci. **4**, 1600289 (2017)
25. K. Kalantar-zadeh, J.Z. Ou, T. Daeneke, A. Mitchell, T. Sasaki, M.S. Fuhrer, Appl. Mater. Today **5**, 73 (2016)
26. N. Chaudhary, M. Khanuja, S. Islam, Sens. Actuators, A **277**, 190 (2018)
27. S. Kumari, R. Gusain, N. Kumar, O.P. Khatri, J. Ind. Eng. Chem. **42**, 87 (2016)
28. H. Miao, X. Hu, Q. Sun et al., Mater. Lett. **166**, 121 (2016)
29. D. Zhang, Y. Sun, P. Li, Y. Zhang, ACS Appl. Mater. Interfaces **8**, 14142 (2016)
30. X. Ni, C. Chen, Q. Wang, Z. Li, Chem. Phys. **525**, 110398 (2019)
31. K. Komal, G. Gupta, M. Singh, B. Singh, J. Alloys Compds. **923**, 166196 (2022)
32. V. Singh, B. Singh, J. Alloys Compds. **941**, 168850 (2023)
33. Y. Zhang, W. Zeng, Y. Li, J. Alloy. Compd. **749**, 355 (2018)
34. W. Ding, L. Hu, J. Dai et al., ACS Nano **13**, 1694 (2019)
35. U. Holzwarth, N. Gibson, Nat. Nanotechnol. **6**, 534 (2011)
36. D. Zhang, H. Chang, R. Liu, J. Electron. Mater. **45**, 4275 (2016)
37. P. Tyagi, A. Sharma, M. Tomar, V. Gupta, Sens. Actuators, B Chem. **248**, 980 (2017)
38. K.C. Bogaert, Massachusetts Institute of Technology, (2019)
39. A Konopatsky, VV Kalinina, DV Barilyuk, et al. Available at SSRN 4188529.
40. G. Muthulakshmi, M.M. Ismail, R. Ramya, M. Arivanandhan, S. Arjunan, A. Bhaskaran, Inorg. Chem. Commun. **143**, 109802 (2022)
41. J. Tauc, Amor. Liquid semicond. (1974). https://doi.org/10.1007/978-1-4615-8705-7_4
42. N. Sharma, K. Prabakar, S. Ilango, S. Dash, A. Tyagi, Adv. Mater. Proc. **2**, 342 (2017)
43. N. Ahmad, S. Khan, M.M.N. Ansari, Ceram. Int. **44**, 15972 (2018)
44. P. Chetri, B. Saikia, A. Choudhury, J. Appl. Phys. **113**, 233514 (2013)
45. N Hidayah, WW Liu, CW Lai, et al., AIP Conference ProceedingsAIP Publishing LLC, (2017)
46. J. Wang, S. Liu, X. Cao et al., Appl. Phys. A **126**, 1 (2020)
47. S. Wu, H. Cao, S. Yin, X. Liu, X. Zhang, J Phys Chem C **113**, 17893 (2009)
48. S. Cui, Z. Wen, X. Huang, J. Chang, J. Chen, Small **11**, 2305 (2015)
49. E.H. Umukoro, N. Kumar, J.C. Ngila, O.A. Arotiba, J. Electroanal. Chem. **827**, 193 (2018)
50. R. Singh, R. Kumar, A. Kumar, D. Kumar, M. Kumar, Mater. Res. Express **6**, 105621 (2019)
51. R. Meena, R.S. Dhaka, Ceram. Int. **48**, 35150 (2022)
52. Y. Song, T.W. Noh, S.-I. Lee, J.R. Gaines, Phys. Rev. B **33**, 904 (1986)
53. R. Khan, Y. Yuan, Z. Iqbal et al., J. Mater. Sci.: Mater. Electron. **28**, 4625 (2017)
54. S. Khan, T. Khan, R. Khan, M. Khan, S.A. Khattak, G. Khan, J. Mater. Sci.: Mater. Electron. **30**, 10202 (2019)
55. S. Mehraj, Sci. Adv. Mater. **4**, 1258 (2012)
56. Y. Guo, J. Tan, J. Zhao, Ceram. Int. **48**, 17795 (2022)

57. A. Ahmed, M.N. Siddique, T. Ali, P. Tripathi, Adv. Powder Technol. **29**, 3415 (2018)
58. M. Kamran, M. Anis-ur-Rehman, Ceram. Int. **48**, 16912 (2022)
59. N. Bhakta, P. Chakrabarti, Appl. Phys. A **125**, 1 (2019)
60. M. Kamran, M. Anis-ur-Rehman, J. Alloy. Compd. **822**, 153583 (2020)
61. S. Sumi, P.P. Rao, M. Deepa, P. Koshy, J. Appl. Phys. **108**, 063718 (2010)
62. S. Nasri, A. Oueslati, I. Chaabane, M. Gargouri, Ceram. Int. **42**, 14041 (2016)

Publisher's Note Springer Nature remains neutral with regard to jurisdictional claims in published maps and institutional affiliations.

Springer Nature or its licensor (e.g. a society or other partner) holds exclusive rights to this article under a publishing agreement with the author(s) or other rightsholder(s); author self-archiving of the accepted manuscript version of this article is solely governed by the terms of such publishing agreement and applicable law.

Biomedical Engineering Letters
https://doi.org/10.1007/s13534-023-00296-6

ORIGINAL ARTICLE

Optimized deep neural network models for blood pressure classification using Fourier analysis-based time–frequency spectrogram of photoplethysmography signal

Pankaj[1] · Ashish Kumar[2] · Manjeet Kumar[3] · Rama Komaragiri[1]

Received: 17 February 2023 / Revised: 28 May 2023 / Accepted: 9 June 2023
© Korean Society of Medical and Biological Engineering 2023

Abstract
Appropriate blood pressure (BP) management through continuous monitoring and rapid diagnosis helps to take preventive care against cardiovascular diseases (CVD). As hypertension is one of the leading causes of CVDs, keeping hypertension under control by a timely screening of subjects becomes lifesaving. This work proposes estimating BP from motion artifact-affected photoplethysmography signals (PPG) by applying signal processing techniques in realtime. This paper proposes a deep neural network-based methodology to accurately classify PPG signals using a Fourier theory-based time–frequency (TF) spectrogram. This work uses the Fourier decomposition method (FDM) to transform a PPG signal into a TF spectrogram. In the proposed work, the last three layers of the pre-trained deep neural network, namely, GoogleNet, DenseNet, and AlexNet, are modified and then used to classify the PPG signal into normotension, pre-hypertension, and hypertension. The proposed framework is trained and tested using the MIMIC-III and PPG–BP databases using five-fold training and testing. Out of the three deep neural networks, the proposed framework with the DenseNet-201 network performs best, with a test accuracy of 96.5%. The proposed work uses FDM to compute the TF spectrogram to accurately separate the motion artifacts and noise components from a noise-corrupted PPG signal. Capturing more frequency components that contain more information from PPG signals makes the deep neural networks extract better and more meaningful features. Thus, training a deep neural network model with clean PPG signal features improves the generalized capability of a BP classification model when tested in realtime.

Keywords Arterial blood pressure · Hypertension · Photoplethysmography · Fourier decomposition method · Time–frequency spectrogram · Deep learning · Transfer learning

1 Introduction

Continuous high blood pressure (BP) in a subject causes heart complications and increases the risk of heart attack and stroke. According to WHO reports [1], hypertension (HYP) is a major cause of untimely death. Around 1.28 billion in the age group of 30–79 years are affected by hypertension. Out of these, approximately 46% of adults are unaware they are suffering from hypertension [2]. Many do not receive the needed treatments because they feel no symptoms [3]. There is a known correlation between hypertension and cardiovascular diseases (CVD) [4]. CVD can be prevented through early diagnosis and control of hypertension. However, no proper and adequate means are available as the formation of HYP has no common or unified reasons. Only continuous BP monitoring and treatment can help to stabilize the BP at normal levels [5]. Reducing the frequency of HYP by 33%

✉ Manjeet Kumar
manjeetchhillar@gmail.com

Pankaj
er.pankaj08@gmail.com

Ashish Kumar
akumar.1june@gmail.com

Rama Komaragiri
rama.komaragiri@gmail.com

[1] Department of Electronics and Communication Engineering, Bennett University, Greater Noida, India

[2] School of Electronics Engineering, Vellore Institute of Technology, Chennai, Tamil Nadu, India

[3] Department of Electronics and Communication Engineering, Delhi Technological University, Delhi, India

Published online: 24 June 2023

up to 2030 is one of the global targets for non-communicable diseases [6].

In their daily routine, most people tend to ignore their health status due to many obligations. If a subject suffering from HYP fails to check the health status and is untreated, the risk of vision loss, stroke, heart failure, and other serious health problems increases significantly [7]. BP classification using a wearable device helps users know their BP condition timely and can provide an early warning system for potential patients. Thus, the research on the identification of HYP in real-time is increasing. Hence, the demand for reliable wearable healthcare devices that continuously monitor BP and promptly flag the BP state as normotension (NT), pre-hypertension (PH), or hypertension (HYP) is increasing.

During a heart cycle, when the heart pumps blood into the body, the pressure in the arteries is denoted by systolic BP (SBP). Diastolic BP (DBP) denotes the pressure in the arteries between heartbeats [8]. The oscillography and Korotkoff's sound method are commonly used to measure BP. These methods rely on building and releasing cuff pressure to detect SBP and DBP. However, the requirement of an arm cuff makes these techniques unsuitable for prolonged and continuous monitoring [9]. To continuously measure BP in realtime, the research is inclined toward designing wearable devices using PPG sensors [10]. The PPG technique uses a photo-electric sensor to extract the pulse wave signal due to blood volume changes during the systolic and diastolic phases [11].

During the systolic and diastolic phases, arterial blood pressure (ABP) depicts the pressure details of blood pumped out by the heart. Similarly, during a cardiac cycle, the PPG signal depicts a change in blood volume. Therefore, in recent years, the use of PPG signal to extract ABP signal information has emerged, as PPG signal has a high correlation with ABP in both time and frequency domains.

Accurate detection and early diagnosis of HYP are vital in preventing CVDs. In the past decade, the parameters extensively studied to estimate and classify BP are pulse transit time (PTT) and pulse wave velocity (PWV) [12].

Measuring PTT and PWV requires two sensors, thus having an increased system complexity. Further, PTT and PWV require calibration of sensors with different physiological conditions of subjects, thus unsuitable for real-time monitoring [13]. A pulse wave analysis (PWA) approach is proposed in [14] to classify BP by overcoming the need for two sensors.

Handcrafted features shown in Fig. 1 are extracted using PWA. These handcrafted features train a machine learning (ML) classification model [15]. In [16], an ML framework is trained using the first and second derivatives of a PPG signal and is proposed to classify BP. Training an ML model using handcrafted features is unreliable as these features vary significantly among subjects and are usually noise-sensitive. Also, the changes in the shape of PPG signals due to various diseases make it hard to extract the features accurately [17]. BP classification requires an accurate methodology that requires less or no intervention, making the ML-based models redundant for realtime BP classification in wearable devices. To overcome the person-specific morphological feature-based classification, deep learning-based BP classification approaches are recently becoming popular in the healthcare industry. The deep learning method consists end-to-end learning approach for BP classification. The end-to-end learning approach takes a 2-D image as input and captures the temporal and spectral information of a PPG signal. A deep neural network implicitly obtains features and correlates those features with actual values, allowing the network to perform better classification [18].

A two-class BP classification model is proposed using the cascade approach of CNN–LSTM [19]. A hybrid approach of CNN and the gated recurrent unit (GRU) for BP classification is proposed in [20]. A parallel convolutional layer network architecture is proposed to extract the features from PPG and ECG signals [21]. The studies mentioned above showed that acquiring PPG and ECG signals simultaneously is mandatory to achieve better accuracy and classify the BP using a deep neural network. The need for two sensor signals increases the system's complexity, which motivates single PPG sensor-based BP classification.

In [22], a pre-trained GoogLeNet deep neural network-based PPG signal classification is proposed. The reported work creates a PPG signal spectrogram using continuous

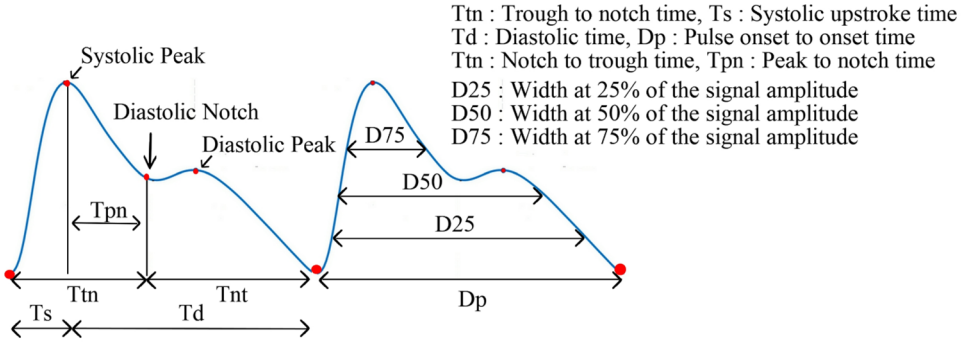

Fig. 1 Morphological features of PPG signal for BP estimation

wavelet transform (CWT) to train and test the GoogLeNet network. A CWT spectrogram and pre-trained deep neural network-based approach have been proposed [23]. In [24], a method based on wavelet transforms is proposed to improve the accuracy of the CNN model to predict and classify BP.

In [25], a hybrid LSTM-ANN model is proposed for BP classification using a PPG signal. In [26], a synchrosqueezing transform and a pre-trained deep neural network-based approach is proposed to classify BP automatically from a PPG signal. In [27], wavelet scattering transform (WST) and pre-trained neural network-based approach is proposed to classify the BP using PPG signal.

A convolutional neural network (CNN) model based on the mean impact value and genetic algorithm is proposed to desolate the statistical morphological-based process and predict the BP class [28]. The CNN and LSTM layer-based approach is proposed in [29]. The LSTM layer estimates the BP value based on the Eigenvalues extracted using the CNN layer. The work proposed in [30] introduced a multilayer perceptron neural network-based classification model to classify high blood pressure. A cascade approach of residual network CNN and bidirectional long short-term memory (BILSTM) is proposed to classify the BP into different classes [31]. This work obtains a high training accuracy but lacks test accuracy.

A 2-D convolutional neural network based on the Hilbert Huang Transform (HHT) framework is proposed to classify the BP state [32]. A personalized approach is applied to deep neural network transfer learning-based architecture to improve the classification accuracy of the model [33]. In [34], using various features of a PPG signal, a classifier is proposed to indicate the BP class.

The TF-based PPG signal analysis using a CNN-based model improves BP classification accuracy [35]. The method has a tradeoff in frequency resolution at high frequencies. Thus, exploring other TF analysis-based approaches for BP classification using a PPG signal is possible.

This work proposes a deep neural network-based classification methodology to classify three BP conditions: normotension (NT), pre-hypertension (PH), and hypertension (HYP). The proposed framework uses the potential of the Fourier decomposition method (FDM) to transform a 1-D PPG signal into a 2-D time–frequency (TF) spectrogram. The ability of the FDM method to provide fine spectral and temporal details of a non-stationary signal is used in this work to analyze the PPG signal.

The key highlights of the proposed work are given as follows.

(1) A Fourier series-based FDM technique is proposed for the first time to classify BP obtained using a PPG signal into multiclass.
(2) The FDM TF spectrogram decomposes the entire signal into a set of distinct frequency bands called Fourier intrinsic band functions (FIBFs), helping the model extract relevant features for accurate and reliable classification.
(3) This work investigates the performance of different pre-trained deep neural network models to differentiate between normal and hypertensive subjects based on PPG signal.
(4) The proposed work does not require additional ECG signals and manual PPG morphological feature extraction steps.

The organization of the rest of the paper is as follows. Section 2 describes the materials and methods of the proposed work. Section 3 presents the results obtained with the proposed framework, and Section 4 discusses a comparison with the state of art methods. Section 5 concludes the proposed work.

2 Material and methods

This section shows a detailed description of all blocks present in the proposed framework. A block diagram of the proposed work is shown in Fig. 2.

2.1 Data acquisition

The first stage of the proposed block diagram is related to the data collection stage. The multiparameter intelligent monitoring in intensive care (MIMIC-III) waveform database [36] is a publicly available dataset used in this work.

The MIMIC-III dataset contains multiple parameter recordings of more than 10,000 subjects.

The PPG and ABP signals are recorded at a sampling frequency of 125 Hz. A recording containing PPG and ABP signals is only considered for analysis.

The PPG signal is normalized using zero mean unit variance to get meaningful data. After normalization, the signal passes through the fourth-order Butterworth bandpass filter with a cutoff frequency [0.4–8] Hz. After filtering, the PPG signal is passed through the Hampel filtering stage to remove the outliers. The ABP signal is passed through the Hampel filtering stage to remove the outliers and then subjected to a peak detection algorithm to obtain true SBP and DBP values. The ABP signals are classified into NT, PH, and HYP BP labels, as per the seventh report of the Joint National Committee (JNC7).

The figshare dataset contains PPG signals acquired from 219 subjects aged between 21 and 86 years. The figshare database consists of a total of 657 PPG waveform segments. The dataset includes PPG, SBP, and DBP information from

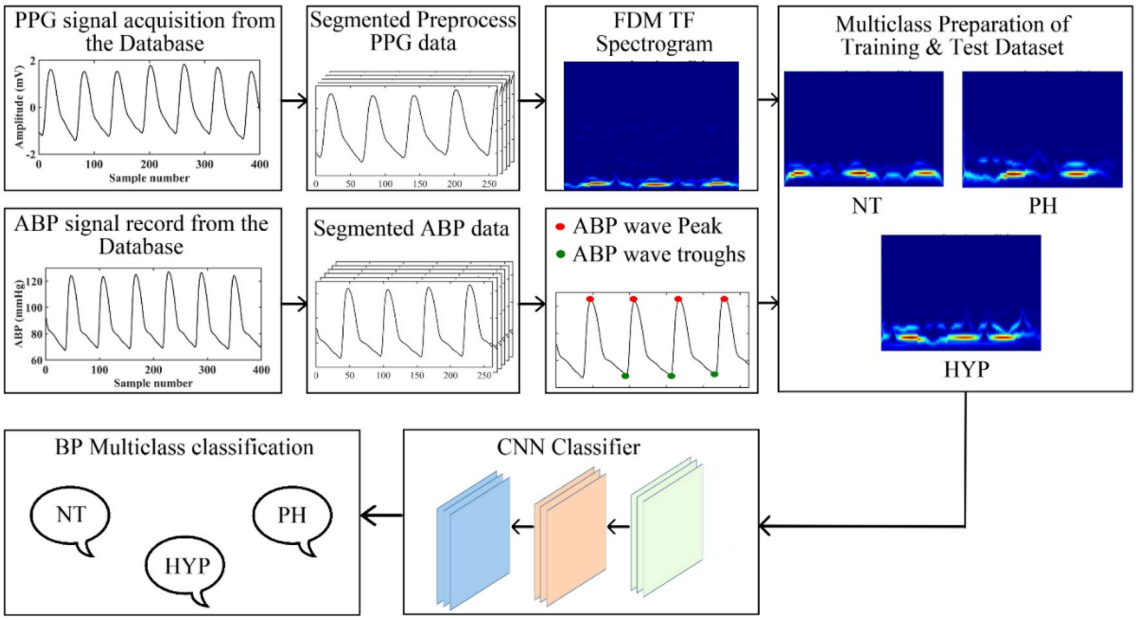

Fig. 2 Block diagram of the proposed method

the subjects diagnosed with NT, PHT, and HYP classes. The PPG signals are acquired in three segments per subject, each duration of 2.1 s. Each segment has 2100 samples at a sampling frequency of 1 kHz.

2.2 Mathematical background of Fourier decomposition method

FDM is a recently proposed valuable technique for analyzing non-stationary signals. FDM maps the sine and cosine basis function of the Fourier series into a finite number of band-limited analytic Fourier intrinsic band functions (FIBFs). The instantaneous frequencies of the FIBFs yield the TF distribution of any signal. Thus, FDM demonstrates its efficacy in analyzing non-stationary signals [37]. The FDM is an adaptive time-series method based on zero-phase filtering. FDM decomposes an input non-sinusoidal signal into a constant and a set of band-limited FIBFs. These energy-preserving FIBFs have a zero mean and are adaptive. FDM provides a clear time–frequency–energy (TFE) distribution of 1-D signal that discloses the time–frequency structure of the signal. The advantage of the FDM method is that it allows decomposing a signal into a desired number of FIBFs with varying amplitude and frequency in time [38].

Figure 3 shows the enhanced TFE representation of raw PPG signal indulged with noises and other undesired frequency components. The FDM method provides precise TFE analysis and effectively separates frequency bands during the signal decomposition, as shown in Fig. 3a.

The obtained FIBFs are adaptive and data-driven as a change in the input data changes these FIBFs. Each of the FIBFs obtained from the FDM contains a single frequency component.

The FDM-based TF is a 2-D graph representation of a 3-D spectrogram in which the amplitude (third dimension) is represented by color intensity. The spectrogram visually depicts the PPG signal strength over time at various frequencies present in the PPG waveform. The TF spectrogram represents the change in PPG signal amplitude over time. Along the horizontal axis in Fig. 3a, time runs from left to right. The vertical axis represents frequency, and the amplitude of a particular frequency at a particular time is represented using a color scale, with dark blues corresponding to low amplitudes and brighter colors up through red corresponding to progressively stronger amplitudes.

Figure 3b shows the FDM TF spectrogram of a preprocessed PPG signal divided into three different BP classes. The proposed method uses the 2-D TFE distribution as input to the pre-trained model.

2.3 Proposed methodology

The proposed framework is shown in Fig. 2. A PPG signal collected from the MIMIC database is first segmented into a consecutive window of 2.1 s. This segmentation process increases the number of PPG-BP categories of NT, PH, and HYP. After segmentation, each 2.1-s window is passed through the FDM block to compute a 2-D TF spectrogram. In the proposed framework, 2181 2-D TF spectrogram

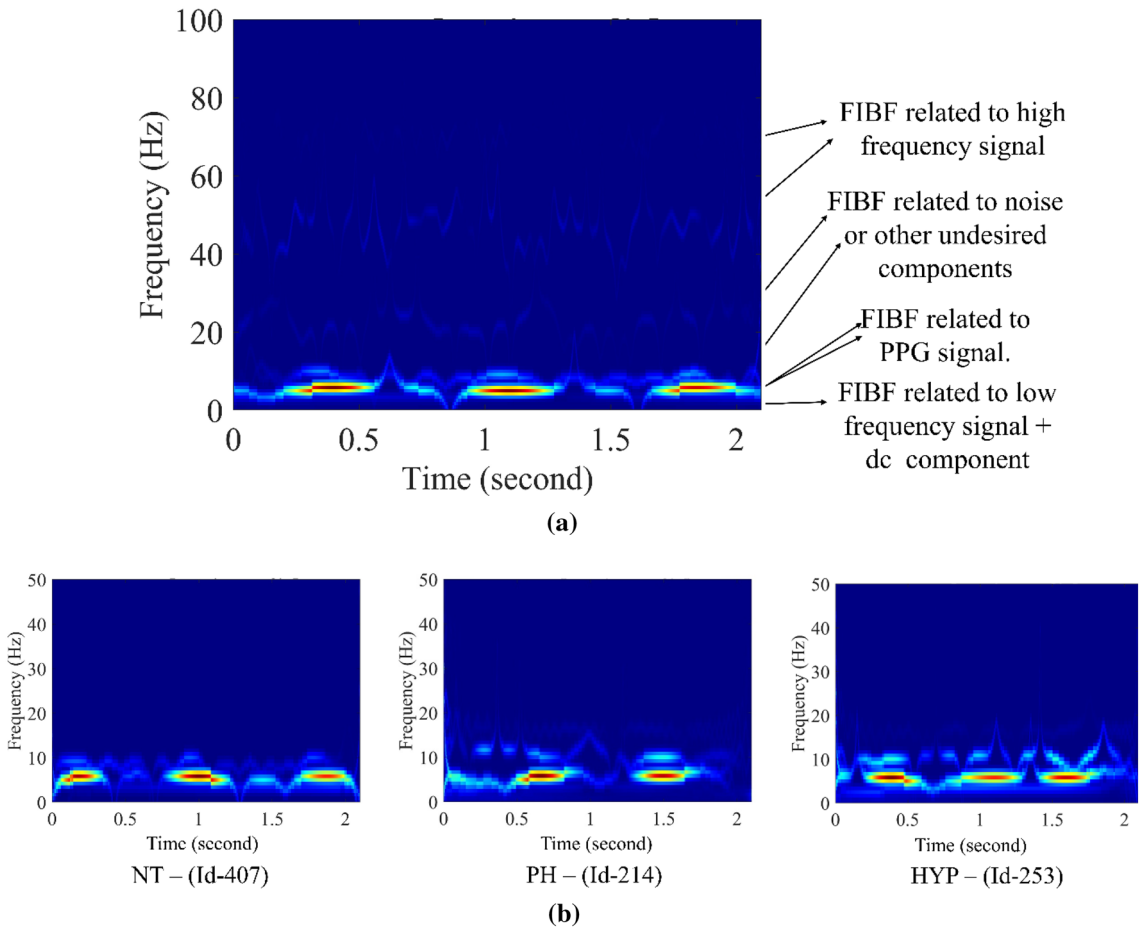

Fig. 3 **a** TFE representation of a PPG signal obtained using FDM, 3 **b** The FDM TF spectrogram cases of the three different BP categories. (Color figure online)

Table 1 JNC7 guidelines for BP classification

Classification type	SBP (mmHg)		DBP (mmHg)
NT	< 120	And	< 80
PH	120–139	Or	80–89
HYP	> 140	Or	> 90

images are obtained using the FDM algorithm belonging to NT, PH, and HYP classes.

ABP signals are segmented into the same window duration to label the BP levels and analyze the accuracy of the classifier. Table 1 lists the BP classes as per the American College of Cardiology/American Heart Association (ACC/AHA) 2017 Hypertension Guidelines [39].

For an ABP window, the mean of all synchronous wave peaks shown by the red dots in Fig. 2 are used to calculate SBP. The mean of the synchronous wave trough shown by the green dots are used to calculate the DBP.

In the proposed framework, each BP class has 650 images, out of which 97 are used to validate the classifier. A set of 231 images consisting of 77 images from each class are used to test the classifier. This work introduces the pre-trained deep neural network model to classify the PPG signal. Three neurons in the last fully connected layer classify BP into three classes. Parameters like initial learning rate, validation frequency, solver, batch size, and learning rate drop factor of the classifier are optimized to obtain the best classification accuracy.

2.4 Deep neural network classifier

Transfer learning is one of the important aspects of a deep neural network. The deep neural network is initially trained on a larger image dataset in transfer learning. These pre-trained deep networks can be used directly to classify thousands of categories. The strong in-depth characteristics of a pre-trained model allow network generalization by transfer learning [40].

Thus, transfer learning can be used for many applications if the input signal to the model is of type 2-D images. In this work, the updated weight of the pre-trained network is transferred to classify the new dataset. GoogLeNet, DenseNet, and AlexNet deep neural networks are fine-tuned and trained based on the MIMIC-III dataset to solve the problem of BP multiclass classification.

GoogLeNet is a pre-trained CNN framework variant of the Inception architecture [41]. Input to the GoogLeNet is a $224 \times 224 \times 3$ sized 2-D image. In this work, the GoogLeNet architecture uses a dropout layer with a dropout factor of 0.4 to prevent the model from overfitting during training.

DenseNet is a pre-trained neural network in which each layer is connected to every layer except itself, thus also called a Densely connected neural network [42]. For an L-layer DenseNet network, there are $L\ (L+1)/2$ direct connections. In DenseNet, the feature map obtained with $(L-1)th$ layer is fed as input to the Lth layer. The feature map of the Lth layer is fed as an input for each subsequent layer. DenseNet-201 [43] is a version of DenseNet used in the proposed work to classify the PPG signals.

AlexNet consists of eight layers; the first five are convolutional layers. The remaining three are fully connected layers. The AlexNet has an average pooling and rectified linear unit (ReLU) layer between two consecutive convolutional layers [44]. The use of the ReLU layer makes the model learning process faster. The output of the last fully connected layer is passed through the activation function softmax to predict the class of the input images.

3 Result analysis

3.1 Performance metrics

The metrics used to check the performance of the proposed framework are accuracy, specificity, precision, sensitivity, and F1-score, shown in Eq. (1). These metrics are estimated by using true positives (TP), false positives (FP), true negatives (TN), and false negatives (FN).

$$\begin{aligned} Accuracy &= \frac{TP+TN}{TP+TN+FP+FN} \times 100 \\ Specificity &= \frac{TN}{TN+FP} \times 100 \\ precision &= \frac{TP}{TP+FP} \times 100 \\ Sensitivity &= \frac{TP}{TP+FN} \times 100 \\ F1-Score &= \frac{2 \times precision \times sensitivity}{precision + sensitivity} \end{aligned} \tag{1}$$

3.2 Simulation results

The pre-trained neural network automatically extracts features from the input 2-D TF spectrogram. The pre-trained neural network correlates different classes with the extracted features to recognize the class when a new dataset (test dataset) is fed as an input to the network. This work compares the performance of the three pre-trained neural networks, GoogleNet, DenseNet, and AlexNet, to classify BP into three classes. The pre-trained GoogLeNet architecture with 144 layers is trained to classify the PPG records in the proposed method. The last three layers in the GoogLeNet architecture are replaced to categorize the new images. The input PPG spectrogram is resized to 224×224 to fulfill the input image size requirement of the GoogLeNet. An initial learning rate of 0.001 with a batch size of 40 and validation frequency of 40 is fixed for this work. The GoogLeNet resulted in 94.92% training accuracy and 94.81% testing accuracy. Figure 4 shows the confusion matrix for the training and test dataset.

The DenseNet-201 pre-trained neural network is used for BP classification. The input PPG spectrogram is resized to 224×224 to fulfill the input image size requirement of the DenseNet-201. The parameter of the last three layers is optimized to recognize the three PPG signal classes. An initial learning rate of 0.001 with a batch size of 40 and Adam optimizer are used to train the proposed DenseNet-201 network. The DenseNet resulted in 96.92% training accuracy and 96.51% testing accuracy. Figure 5 shows the confusion matrix for the training and test datasets.

In the AlexNet network, the input spectrograms are resized to $227 \times 227 \times 3$. In this proposed work, the parameters of the last three layers are optimized to obtain the best results. Adam optimizer trains the AlexNet model with an initial learning rate of 0.001 and a batch size of 40. A validation frequency of 40 is fixed for this work. The AlexNet resulted in 95.51% training accuracy and 95.21% testing accuracy. Figure 6 shows the confusion matrix for the training and test dataset.

To analyze the performance of this work, the performance metrics (Accuracy, precision, sensitivity, specificity, and F-1 score) are calculated from the training and test datasets. Tables 2, 3 and 4 show the performance analysis of GoogleNet, DenseNet-201, and AlexNet on the test dataset and demonstrate the potential of the proposed FDM-TF-based classification.

The proposed FDM-TF-based method is compared with various works from the literature. For a fair comparison, three classification experiments are examined from the confusion matrix: NT versus PH, NT versus HYP, and NT + PH versus HYP. The F1-score obtained for NT versus PH, NT versus HYP, and NT + PH versus HYP with the proposed work using GoogLeNet, DenseNet-201 and for AlexNet are shown in Tables 2, 3 and 4.

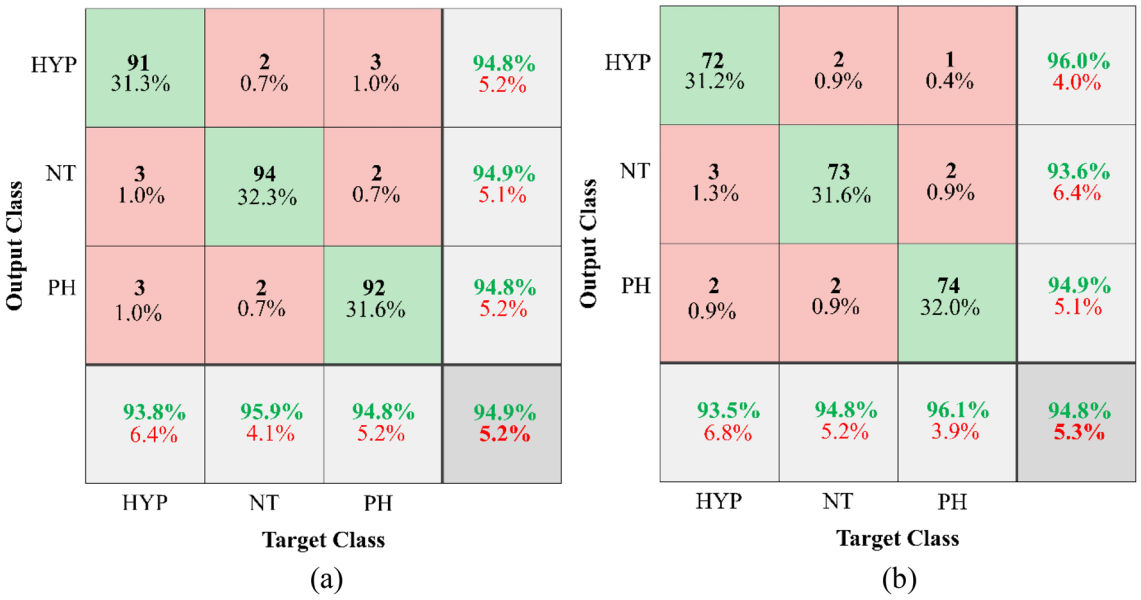

Fig. 4 Confusion matrix of the **a** training dataset and **b** the testing dataset obtained using GoogLeNet

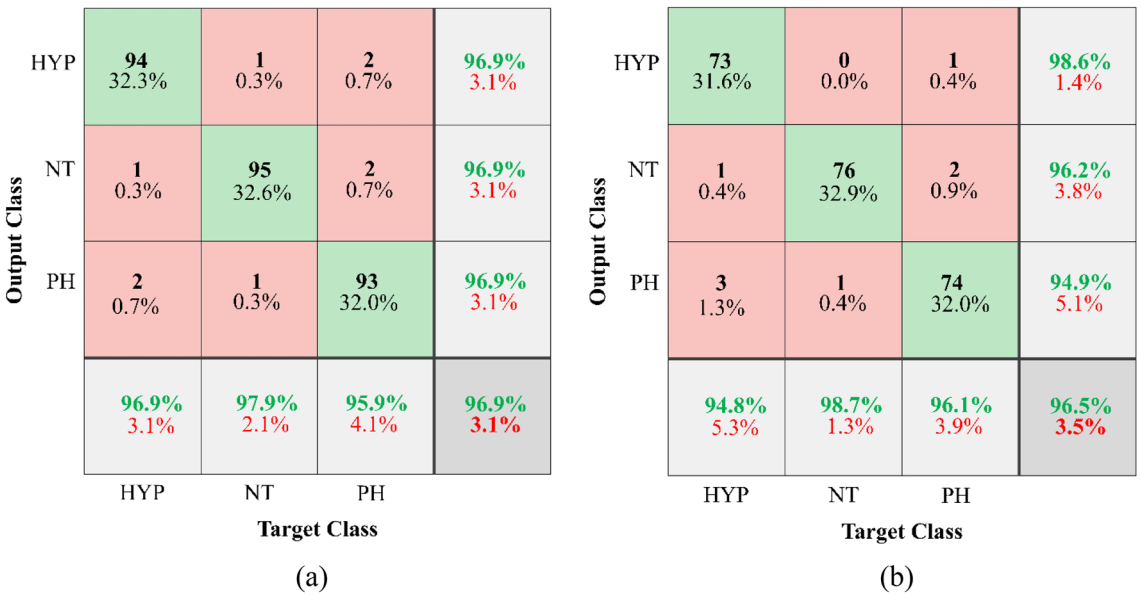

Fig. 5 Confusion matrix of the **a** training dataset and **b** the testing dataset obtained using DenseNet-201

Out of the three deep neural networks, the DenseNet-201 and AlexNet performed better than the GoogLeNet model. Thus, we tested both models further using the figshare dataset. The F1-score obtained using DenseNet-201 for NT versus PH, NT versus HYP, and NT + PH versus HYP is 98.06, 99.34 and 97.40 respectively. The AlexNet obtained a F1-score for NT versus PH, NT versus HYP, and NT + PH versus HYP is 97.61, 98.15 and 96.80 respectively. The F1-score is higher for the proposed FDM-TF-based method tested using Densenet-201.

A fivefold cross-validation approach is used for better utilization of the dataset and to improve the robustness of the optimized deep neural network model. The model performance is evaluated five times, where each fold out of fivefold acts as a test dataset, and the remaining four folds are fed to train the model. The final performance of the model is evaluated by averaging the accuracy obtained in all five trials.

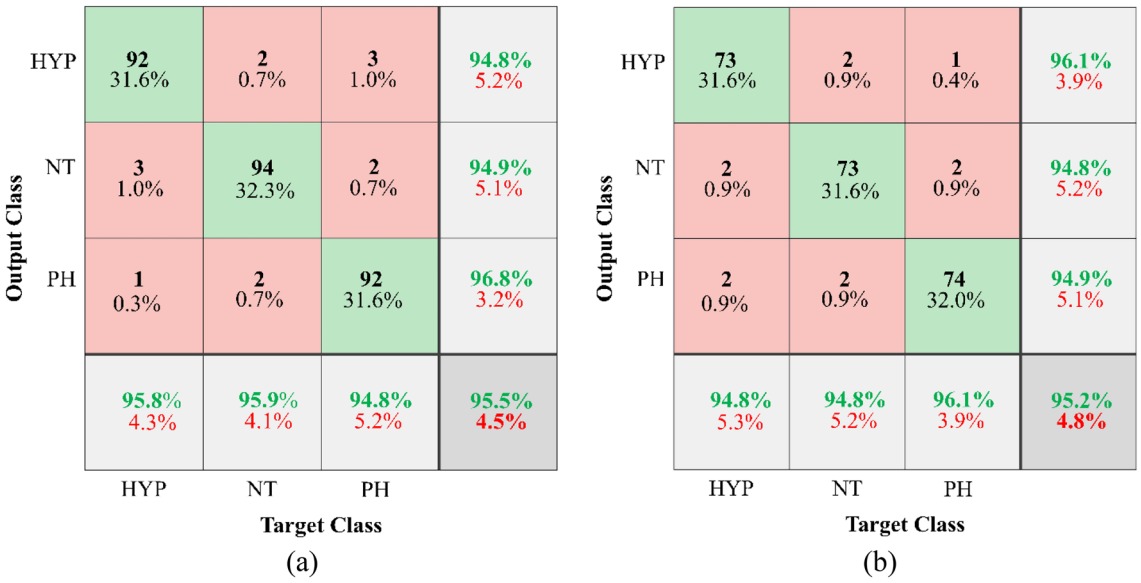

Fig.6 Confusion matrix of the **a** training dataset and **b** the testing dataset obtained using AlexNet

Table 2 Performance Analysis of FDM TF method using GoogLeNet

	TP	FP	FN	TN	Accuracy	Precision	Sensitivity	Specificity	F1-Score
HYP	72	5	3	147	96.47	93.5	96	96.71	94.73
NT	73	4	5	146	96.05	94.8	93.58	97.33	94.19
PH	74	3	4	145	96.9	96.1	94.87	97.97	95.48
NT versus PH	73	2	2	74	97.35	97.33	97.33	97.36	97.33
NT versus HYP	73	2	3	72	96.67	97.33	96.05	97.29	96.68
(NT + PH) versus HYP	147	3	9	72	94.8	98	94.23	96	96.07

Table 3 Performance analysis of FDM TF method using DenseNet-201

	TP	FP	FN	TN	Accuracy	Precision	Sensitivity	Specificity	F1-Score
HYP	73	4	1	150	97.8	94.8	98.64	97.4	96.68
NT	76	1	3	147	98.23	98.7	96.2	99.32	97.43
PH	74	3	4	149	96.95	96.1	94.87	98.02	95.48
NT versus PH	76	1	2	74	98.03	98.7	97.43	98.67	98.06
NT versus HYP	76	0	1	73	99.33	100	98.7	100	99.34
(NT + PH) versus HYP	150	1	7	73	96.53	99.33	95.54	98.64	97.4

Table 4 Performance analysis of FDM TF method using AlexNet

	TP	FP	FN	TN	Accuracy	Precision	Sensitivity	Specificity	F1-Score
HYP	73	4	3	147	96.91	94.8	96.05	97.35	95.42
NT	73	4	4	147	96.49	94.8	94.8	97.35	94.8
PH	74	3	4	146	96.91	96.1	94.87	97.98	95.48
NT versus PH	73	2	2	74	97.35	97.33	97.33	97.36	97.33
NT versus HYP	73	2	2	73	97.33	97.33	97.33	97.33	97.33
(NT + PH) versus HYP	147	3	8	73	95.23	98	94.83	96.05	96.39

The average test accuracy of the proposed framework with fivefold cross-validation using GoogLeNet, DenseNet, and AlexNet is 95.12%, 96.71%, and 95.28%, respectively. These results are similar to accuracy values obtained without using the fivefold cross-validation approach shown in Figs. 4, 5 and 6.

Table 5 compares the overall accuracy obtained with the optimized pre-trained neural network with other existing methods. The results indicate that BP classification using DenseNet + FDM achieves better accuracy than the methods listed in Table 5.

4 Discussion

The proposed method has the potential to detect the BP level in realtime accurately. This method only uses a raw PPG signal and replaces the cuff-base and PPG morphology feature extraction process for BP classification.

This paper presents an optimized deep neural network framework to classify the BP into multiple classes: NT, PH, and HYP. The proposed framework explores the potential of the FDM TF spectrogram to classify BP in realtime only by using a PPG signal. The acquired 1-D PPG signal is transformed into a 2-D TF spectrogram using the FDM method. FDM decomposes the acquired preprocessed PPG signal into desirable FIBF with varying amplitude and frequency with time. FDM provides better TF estimation and separates FIBFs related to the clean and noise signals.

In recent times, with the introduction of artificial intelligence, the estimation and classification of BP using wearable devices have emerged. BP classification using a wearable device helps the user to know their BP condition timely and acts as an early warning system.

Therefore, this work used FDM based TF spectrogram of PPG signals to train and test the deep neural network to accurately classify PPG signals into three BP classes per the criterion given by ACC/AHA hypertension guidelines 2017.

The proposed framework demonstrated a classification accuracy of BP in multiclass for three optimized pre-trained deep neural network models trained and tested using MIMIC-III and figshare datasets. The proposed framework obtained 95.12%, 96.71%, and 95.28% accuracy for GoogLeNet, DenseNet, and AlexNet, respectively.

The work proposed in [16] shows a significant performance with an F1-score of 97.51% for the classification of NT versus HYP. However, the performance of the framework report in [16] requires first derivative PPG and second derivative PPG in addition to the PPG signal for model training. The work reported in [49] shows significant results compared to the proposed work. However, the performance of this work relies on the feature value extracted manually from the TF spectrogram of the PPG signal. The value of the features strongly depends on the morphological structure of the PPG signal, which can change due to noise and disease. The work proposed in [21] obtained an accuracy of 95% for classifying BP in five classes. However, this work concatenates the feature extracted from the PPG and ECG signals. Thus, the need for the PPG signal and the ECG signal for feature extraction increases the computational complexity of the system.

Most of the techniques in the literature require an additional PPG sensor or an ECG signal to extract features from the PPG signal to train the machine-learning model. Thus,

Table 5 Performance comparison of the proposed work with the existing work

Author	Method	Number of classes	Overall accuracy (%)
LaFreniere et al. 2017 [45]	Feedforward neural network	2	82.00
Patnaik et al. 2018 [46]	Support vector machine	2	80.23
Luo et al. 2018 [47]	CNN	2	89.95
Fitriyani et al. 2019 [48]	Ensemble machine learning model	2	85.73
Tjahjadi et al. 2020 [49]	Bidirectional long short-term memory + CWT	3	93.00
Wu et al. 2021 [24]	CNN + CWT	2	90.36
Wu et al. 2021 [24]	GoogLeNet + CWT	2	84.54
Yen et al. 2021 [31]	ResNetCNN + BiLSTM	4	76%
Fuadah et al. 2022 [21]	Concatenated 1-D CNN	5	95%
Kuzmanov et al. 2022 [20]	ECG + PPG	3	78%
Martinez et al. 2022 [50]	WST + SVM	2	71.4%
Zhang et al. 2023 [51]	STFT + CNN	2	75%
Proposed work	GoogLeNet + FDM	3	95.12
Proposed work	DenseNet-201 + FDM	3	96.71
Proposed work	AlexNet + FDM	3	95.28

the performance of these techniques relies on the requirement of two signals. Moreover, the synchronization between the two signals in realtime is challenging.

The work proposed in [32] shows a comparable performance for NT versus PH classification, but the reported work does not provide good results for other classification types. The performance of the reported work [32] depends on the feature extracted from three signals (PPG, first derivative PPG, and second derivative PPG signal).

Further, the main hurdle associated with realtime acquired PPG signal is the effect of motion artifacts which degrade the algorithm's accuracy. Thus, removing motion artifact components from a PPG signal is also a factor to consider while designing a wearable device. Most of the work reported in the literature used features extracted from a raw PPG signal to train and test the model. Training a machine learning model with features acquired from the corrupted PPG signal reduces the generalized capability of the model when tested in realtime, as the effect of motion artifacts is random. Notably, a deep neural network has the potential to automatically extract relevant features and map these features with the target class. It is assumed that training a model with a corrupted PPG signal consisting of random and irregular peaks degrades the generalized capability of the model when tested in realtime. Thus, the proposed work trains the deep neural network model using an FDM-based TF spectrogram to increase the model's accuracy.

The parameters of the pre-trained neural network are optimized to improve the accuracy of the classifier. The model accuracy on the test dataset is evaluated using the performance metrics accuracy, specificity, sensitivity, precision, and the F1-score.

5 Conclusion and future scope

A deep learning-based approach to analyzing PPG signals helps improve classification accuracy. The proposed study is tested using publicly available MIMIC-III and figshare datasets. A new framework by combining FDM-based TF spectrogram and deep neural network architectures is proposed so that the same can be used in smart wearable healthcare devices for early diagnosis of hypertension to reduce the mortality rate.

This work uses PPG signals from the MIMIC-III database as an input to produce a 2-D TF spectrogram from a 1-D PPG input signal by applying FDM. The obtained TF spectrogram is used as an input image database of the pre-trained deep neural network. FDM TF spectrogram accurately separates the motion artifacts and other unwanted frequency components from the PPG signal. Thus, the model training becomes more robust and accurate. This work considered three pre-trained deep neural networks: GoogLeNet, DenseNet, and AlexNet. In this work, the parameter of the last three layers of the pre-trained network are optimized to meet the classification needs. Out of the three pre-trained networks used in this work, the DenseNet-201 provides the highest classification accuracy of 96.71%. The confusion matrix shows the potential of DenseNet-201 to successfully classify the PPG spectrogram into multiclass (NT, PH, and HYP). For BP classification, each class is equally important to provide the BP state of a user in realtime. Thus, the overall performance of the classifier is measured using the F1-score that combines precision and recall. A high F1 score indicates the model's efficiency in accurately classifying BP. After analysis of computational time taken by all proposed deep neural network, it is found that DenseNet-201 training time, testing time, and model complexity is higher than the GoogLeNet and AlexNet. Although DenseNet-201 provides better accuracy than the AlexNet and the GoogLeNet, indicating that there is a tradeoff between system complexity and system performance.

This work is performed over a non-GPU device; thus, the training and testing time are high. For future studies, we plan to increase the dataset and train and test the pre-trained model on a GPU-based workstation.

Author contributions P: Conceptualization, Methodology, Software, Data Curation, Investigation, Writing—Original draft preparation. AK: Conceptualization, Investigation, Visualization, Writing-Reviewing and Editing, Supervision. MK: Investigation, Visualization, Writing-Reviewing and Editing, Supervision. RK: Investigation, Visualization, Writing-Reviewing and Editing, Supervision.

Funding No funding Received.

Declarations

Conflict of interest All Authors of this work declare no conflict of interest.

Ethical approval This article does not contain any studies with human participants or animals performed by any of the authors.

References

1. Health topic, cardiovascular disease, world health organization. 2023. https://www.who.int/health-topics/hypertension. Accessed 31 Mar 2023.
2. Hypertension, key facts, world health organization. 2023. https://www.who.int/news-room/fact-sheets/detail/hypertension. Accessed 31 Mar 2023.
3. Meyerovitz CV, et al. Social determinants, blood pressure control, and racial inequities in childbearing age women with hypertension, 2001 to 2018. J Am Heart Assoc. 2023;12(5):e027169.
4. Fuchs FD, Whelton PK. High blood pressure and cardiovascular disease. Hypertension. 2020;75:285–92.

5. Song K, Chung KY, Chang JH. Cuffless deep learning-based blood pressure estimation for smart wristwatches. IEEE Trans Instrum Meas. 2020;69(7):4292–302.
6. Al-Makki A, et al. Hypertension pharmacological treatment in adults: a world health organization guideline executive summary. Hypertension. 2022;79(1):293–301.
7. Haghi M, Thurow K, Stoll R. Wearable devices in medical internet of things: scientific research and commercially available devices. Healthc Inform Res. 2017;23(1):4–15.
8. Pankaj, Kumar A, Komaragiri R, Kumar M. A review on computation methods used in photoplethysmography signal analysis for heart rate estimation. Arch Comput Methods Eng. 2022;29(2):921–40.
9. Kachuee M, Kiani MM, Mohammadzade H, Shabany M. Cuffless blood pressure estimation algorithms for continuous healthcare monitoring. IEEE Trans Biomed Eng. 2017;64(4):859–69.
10. Kumar A, Ashdhir A, Komaragiri R, Kumar M. Analysis of photoplethysmogram signal to estimate heart rate during physical activity using fractional Fourier transform–a sampling frequency independent and reference signal-less method. Comput Methods Programs Biomed. 2023;229:107294.
11. Pankaj, Kumar A, Kumar M, Komaragiri R. STSR: spectro-temporal super-resolution analysis of a reference signal less photoplethysmogram for heart rate estimation during physical activity. IEEE Trans Instrum Meas. 2022;71:1–10.
12. Esmaelpoor J, Moradi MH, Kadkhodamohammadi A. A multistage deep neural network model for blood pressure estimation using photoplethysmogram signals. Comput Biol Med. 2020;120:103719.
13. Li Z, He W. A continuous blood pressure estimation method using photoplethysmography by GRNN-based model. Sensors. 2021;21(21):7207.
14. Teng XF, Zhang YT Continuous and noninvasive estimation of arterial blood pressure using a photoplethysmographic approach. 2003. pp. 3153–3156
15. Tjahjadi H, Ramli K. Noninvasive blood pressure classification based on photoplethysmography using K-nearest neighbors algorithm: a feasibility study. Information (Switz). 2020;11(2):93.
16. Hu X, et al. Blood pressure stratification using photoplethysmography and light gradient boosting machine. Front Physiol. 2023;14:231.
17. Evdochim L, Dobrescu D, Halichidis S, Dobrescu L, Stanciu S. Hypertension detection based on photoplethysmography signal morphology and machine learning techniques. Appl Sci (Switz). 2022;12(16):8380.
18. Schrumpf F, Frenzel P, Aust C, Osterhoff G, Fuchs M. Assessment of non-invasive blood pressure prediction from PPG and RPPG signals using deep learning. Sensors. 2021;21(18):6022.
19. Kuzmanov I, Bogdanova AM, Kostoska M, Ackovska N Fast cuffless blood pressure classification with ECG and PPG signals using CNN–LSTM models in emergency medicine. In: 2022 45th Jubilee international convention on information, communication and electronic technology (MIPRO). 2022; pp. 362–7.
20. Kuzmanov I, Kostoska M, Bogdanova AM. Blood pressure class estimation using CNN-GRU model. In: 2022 The 19th International Conference on Informatics and Information Technologies, CIIT 2022. In 2021 IEEE Computing in Cardiology, CinC 2021. 2021;Vol. 48; pp. 1–4.
21. Fuadah YN, Lim KM. Classification of blood pressure levels based on photoplethysmogram and electrocardiogram signals with a concatenated convolutional neural network. Diagnostics. 2022;12(11):2886.
22. Liang Y, Chen Z, Ward R. Photoplethysmography and deep learning: enhancing hypertension risk stratification. Biosensors. 2018;8:101.
23. Cano J, Bertomeu-González V, Fácia L, Zangróniz R, Alcaraz R, Rieta JJ. Hypertension risk assessment from photoplethysmographic recordings using deep learning classifiers.
24. Wu J, Liang H, Ding C, Huang X, Huang J, Peng Q. Improving the accuracy in classification of blood pressure from photoplethysmography using continuous wavelet transform and deep learning. Int J Hypertens. 2021;9938584:2021.
25. Faris Ali N, Atef M. An efficient hybrid LSTM-ANN joint classification-regression model for PPG based blood pressure monitoring. Biomed Signal Process Control. 2023;84:104782.
26. Tanc YH, Ozturk M. Hypertension classification using PPG signals. In: 2022 medical technologies congress (TIPTEKNO). IEEE; 2022. pp. 1–4.
27. Martinez-Ríos EA, Montesinos L, Alfaro M. A comparison between wavelet scattering transform and transfer learning for elevated blood pressure detection. In: 2022 BMEiCON. IEEE; 2022. pp. 1–5.
28. Tanveer MS, Hasan MK. Cuffless blood pressure estimation from electrocardiogram and photoplethysmogram using waveform based ANN-LSTM network. Biomed Signal Process Control. 2019;51:382–92.
29. Tazarv A, Levorato M. A deep learning approach to predict blood pressure from PPG signals. In 2021 IEEE 43rd Annual international conference of the IEEE engineering in medicine & biology society (EMBC), 2021;pp. 5658–5662.
30. Kwong EWY, Wu H, Pang GKH. A prediction model of blood pressure for telemedicine. Health Inform J. 2018;24(3):227–44.
31. Yen CT, Chang SN, Liao CH. Deep learning algorithm evaluation of hypertension classification in less photoplethysmography signals conditions. Meas Control (UK). 2021;54(3–4):439–45.
32. Sun X, Zhou L, Chang S, Liu Z. Using CNN and HHT to predict blood pressure level based on photoplethysmography and its derivatives. Biosensors (Basel). 2021;11(4):120.
33. Schrumpf F, Serdack PR, Fuchs M. Regression or classification? Reflection on BP prediction from PPG data using deep neural networks in the scope of practical applications. In: 2022 Proceedings of the IEEE/CVF Conference on Computer Vision and Pattern Recognition, 2022; pp. 2172–2181
34. Riaz F, Azad MA, Arshad J, Imran M, Hassan A, Rehman S. Pervasive blood pressure monitoring using Photoplethysmogram (PPG) sensor. Futur Gener Comput Syst. 2019;98:120–30.
35. Mansouri SR, Lowe A, Gholamhosseini H, Baig MM. Blood pressure estimation from electrocardiogram and photoplethysmography signals using continuous wavelet transform and convolutional neural network. Conf-Irm 2019, 28;2019. https://aisel.aisnet.org/confirm2019/28
36. Johnson AEW, et al. Data descriptor: MIMIC-III, a freely accessible critical care database. Scientific data 2016;3(1):1–9.
37. Singh P, Joshi SD, Patney RK, Saha K. The Fourier decomposition method for nonlinear and non-stationary time series analysis. Proc R Soc A Math Phys Eng Sci. 2017;473(2199):20160871.
38. Pankaj, Kumar A, Komaragiri R, Kumar M. Reference signal less Fourier analysis based motion artifact removal algorithm for wearable photoplethysmography devices to estimate heart rate during physical exercises. Comput Biol Med. 2022;141:105081.
39. Whelton PK, et al. 2017 ACC/AHA/AAPA/ABC/ACPM/AGS/APhA/ASH/ASPC/NMA/PCNA guideline for the prevention, detection, evaluation, and management of high blood pressure in adults: a report of the American College of Cardiology/American Heart Association task force on clinical practice guidelines. J Am Coll Cardiol. 2018;71(19):e127–248.
40. Alzubaidi L, et al. Review of deep learning: concepts, CNN architectures, challenges, applications, future directions. J Big Data. 2021;8(1):1–74.
41. Szegedy C, et al. Going deeper with convolutions. Sep. 2014, Online. Available at http://arxiv.org/abs/1409.4842

42. Huang G, Liu Z, van der Maaten L, Weinberger KQ. Densely connected convolutional networks. Aug. 2016, [Online]. Available at http://arxiv.org/abs/1608.06993
43. Li T, Jiao W, Wang LN, Zhong G. Automatic DenseNet sparsification. IEEE Access. 2020;8:62561–71.
44. Krizhevsky A, Sutskever I, Hinton GE. ImageNet classification with deep convolutional neural networks. [Online]. Available at http://code.google.com/p/cuda-convnet/
45. Lafreniere D, Zulkernine F, Barber D, Martin K. Using machine learning to predict hypertension from a clinical dataset. In: 2016 IEEE symposium series on computational intelligence, SSCI 2016, 2017.
46. Patnaik R, Chandran M, Lee SC, Gupta A, Kim C. Predicting the occurrence of essential hypertension using annual health records. In: 2018 2nd International Conference on Advances in Electronics, Computers and Communications, ICAECC 2018; vol. 13, pp. 1–5:2018.
47. Luo Y, Li Y, Lu Y, Lin S, Liu X. The prediction of hypertension based on convolution neural network. In: 2018 IEEE 4th international conference on computer and communications, ICCC 2018. pp. 2122–2127;2018.
48. Fitriyani NL, Syafrudin M, Alfian G, Rhee J. Development of disease prediction model based on ensemble learning approach for diabetes and hypertension. IEEE Access. 2019;7:144777–89.
49. Tjahjadi H, Ramli K, Murfi H. Noninvasive classification of blood pressure based on photoplethysmography signals using bidirectional long short-term memory and time-frequency analysis. IEEE Access. 2020;8:20735–48.
50. Martinez-Ríos E, Montesinos L, Alfaro-Ponce M. A machine learning approach for hypertension detection based on photoplethysmography and clinical data. Comput Biol Med. 2022;145:105479.
51. Zhang C, et al. Video based cocktail causal container for blood pressure classification and blood glucose prediction. IEEE J Biomed Health Inform. 2023;27(2):1118–28.

Publisher's Note Springer Nature remains neutral with regard to jurisdictional claims in published maps and institutional affiliations.

Springer Nature or its licensor (e.g. a society or other partner) holds exclusive rights to this article under a publishing agreement with the author(s) or other rightsholder(s); author self-archiving of the accepted manuscript version of this article is solely governed by the terms of such publishing agreement and applicable law.

Phase Transition Material Modulated Hyper FET for Digital Applications

Ritika Sorot
Electronics & Communication Engineering
Delhi Technological University
New Delhi, India
ritika.sorot@gmail.com

Anubha Goel
Electronics & Communication Engineering
Maharaja Agrasen Institute Of Technology
New Delhi, India
anubhagoel5@gmail.com

Sonam Rewari
Electronics & Communication Engineering
Delhi Technological University
New Delhi, India
rewarisonam@gmail.com

2023 IEEE Devices for Integrated Circuit (DevIC) | 979-8-3503-4726-5/23/$31.00 ©2023 IEEE | DOI: 10.1109/DevIC57758.2023.10134819

***Abstract*—In this paper, a Phase Transition Material Modulated Hyper-FET has been proposed for Digital Applications. It has been examined by implementing a Spice model of Phase Transition Material with the source of 32nm MOSFET and later a comparison is drawn with 32nm MOSFET. In our proposed device, Iso-I_{OFF} transfer characteristics and Output Characteristics of 32nm Hyper-FET reveal approximately 104 times higher ON current. The metallic resistivity, insulating resistivity, insulating to metallic current density, metallic to insulating current density, and geometry of Phase Transition Material are varied to study the effect on transfer characteristics of Hyper-FET in order to optimize the parameters for proper operation of the device.**

Keywords—Phase Transition Material(PTM), Hybrid Phase Transition FET(Hyper-FET), steep slope, insulating to metallic current density, insulating to metallic state transition, I_{ON}/I_{OFF} Ratio

I. INTRODUCTION

Hyper-FET is designed by integrating Phase Transition Material(PTM) with the source of MOSFET as shown in Fig. 1 [1], [2]. A wide variety of Phase transition Materials like VO_2, V_2O_3, VO, TiO, doped chalcogenide, Cu-doped HfO_2 are available [3]. Field Effect Transistors with a steep sub-threshold slope have been designed using Ag/AgTe/Tio_2/TiN as threshold Selector(TS) [4]–[8].

Phase Transition Material (PTM) is capable of being in an insulating state and metallic state. Without any electrical stimulation, a PTM stays in an insulating state. It requires a critical current density, $J_{C\text{-}IMT}$(Insulating to Metallic Current Density) for switching to Metallic State. Similarly, it can switch back to an insulating state if the current density falls below $J_{C\text{-}MIT}$(Metallic to Insulating Current Density) [9]. When the MOSFET is off, drain current density is less than $J_{C\text{-}IMT}$, and PTM stays in an insulating state. For a fixed value of V_{DS} (Drain to Source Voltage), if the Gate to Source Voltage (V_{GS}) of the device is increased, the current density of MOSFET is increased. The V_{GS} at which current density becomes equal to $J_{C\text{-}IMT}$ is defined as $V_{GS\text{-}IMT}$ (Gate to Source Voltage at which PTM switches from insulating to metallic state).

At $V_{GS\text{-}IMT}$ there is a steep rise in the drain current flowing through the MOSFET. The steep rise is proportional to the difference in insulating and metallic state resistivity values. Similarly, if we decrease the values of V_{GS}, the value of Gate to Source voltage at which current density falls below $J_{C\text{-}MIT}$, is defined as $V_{GS\text{-}MIT}$. Likewise, for fixed values of V_{GS}, there will be some critical values of V_{DS} for which the transition of insulating to metallic state happens and vice-versa ($V_{DS\text{-}IMT}$ and $V_{DS\text{-}MIT}$). Trade-offs between different parameters can be used for designing low-power circuits using Hyper-FET [10]. PTM can be used to design Low-Power Dynamic Circuits [11]. In the emerging new hybrid device, the Phase transition of VO_2 can be combined with the negative capacitance effect for use in digital devices and memories. [12].

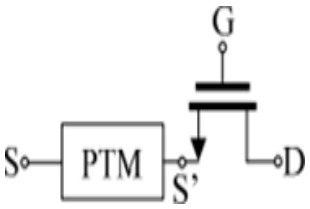

Fig. 1. Hyper-FET

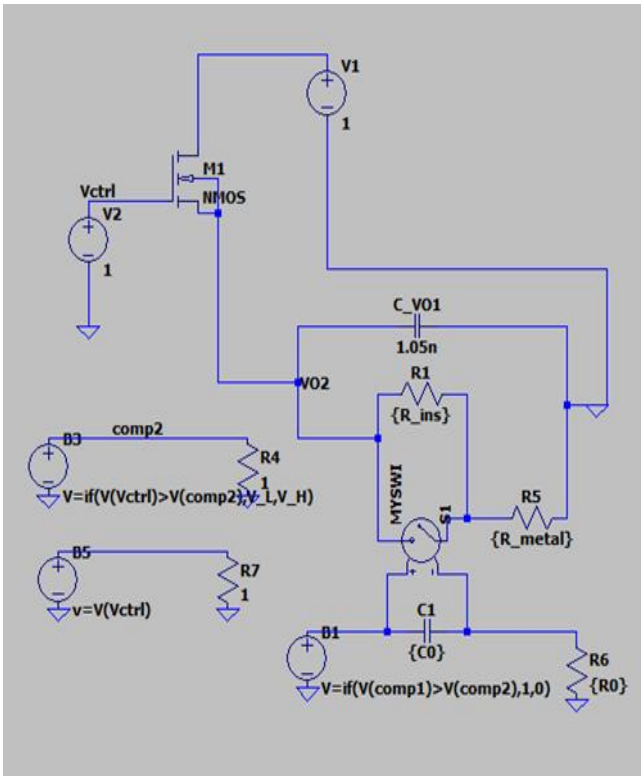

Fig. 2. Schematic Of Hyper-FET

979-8-3503-4726-5/23/$31.00 ©2023 IEEE

Authorized licensed use limited to: DELHI TECHNICAL UNIV. Downloaded on June 01,2023 at 06:00:39 UTC from IEEE Xplore. Restrictions apply.

II. Device Structure And Simulation Of Hyper-FET

Fig. 2 shows the Spice Schematic for Hyper-FET. The source of MOSFET is connected with VO_2 which is modeled using a Voltage Controlled Switch. The effective resistance of the Switch is equal to R_{INS} when the voltage across it is less than $V_{C\text{-}IMT}$. The effective resistance of the switch is reduced to R_{METAL} when the voltage is greater than $V_{C\text{-}IMT}$. The voltage-controlled switch makes use of the following behavioral equations of PTM [3].

$$V_{C-IMT} = I_{C-IMT} * R_{INS} \quad (1)$$

$$V_{C-MIT} = I_{C-MIT} * R_{MET} \quad (2)$$

TABLE I. The spice Netlist for simulating Hyper-FET is given in Fig. 17 at the end of this paper. The designed Hyper-FET was simulated for varying values of PTM parameters [13]. The optimized values for the design of 32nm Hyper-FET are listed in Table 1.

TABLE I. Optimized Parameters Of PTM For 32nm Hyper-FET

S.NO	Parameters Of PTM	Values Of Parameters
1.	$J_{C\text{-}IMT}$	520 A/cm^2
2.	$J_{C\text{-}MIT}$	8000 A/cm^2
3.	ρ_{INS}	149 Ωcm
4.	ρ_{METAL}	0.00149 Ωcm
5.	R_{INS}	22.6 MΩ
6.	R_{METAL}	226 Ω
7.	L_{PTM}	32 nm
8.	A_{PTM}	64*33nm^2

For the selected parameters of Hyper-FET (Table 1), the device turns on around the threshold voltage of 32nm MOS-FET and satisfies the constraint required for switching from the OFF state to the ON state and vice-versa. Fig. 3 shows the transfer characteristic curve of Hyper-FET for different Drain- to-Source voltages (V_{DS}) when V_{GS} is gradually increased. The value of $V_{GS\text{-}IMT}$ increases if the value of V_{DS} is less. This happens because the current flowing through a MOSFET is decreased by reducing V_{DS}. A steep transition is observed from the OFF state of the MOSFET to the ON state, thus increasing the value of the sub-threshold slope [2], [14]. There is a value of V_{DS}, below which the drain current of Hyper-FET is insufficient for transition to metallic state in the operating window of V_{GS}. PTM never reaches the metallic state, and device does not turn ON. The range of V_{DS} for which the device does not make a transition to a metallic state is known as the ”dead Zone”. Fig. 4 depicts the Transfer Characteristics of Hyper-FET for decreasing values of V_{GS} at different values of V_{DS}. If V_{DS} is less, then MIT will occur at a higher value of V_{GS}. This happens due to reduced drain current at lower V_{DS}. At higher values of V_{DS}, there may be cases where the device does not return to an insulating state. Such voltage ranges should be avoided while designing circuits. Fig. 5 combines the IMT and MIT transition for Hyper-FET at different Drain to source Voltages.

A comparison is drawn between Hyper-FET and MOSFET in Fig. 6, Fig. 7, and Fig. 8. I_{ON}/I_{OFF} ratio is approximately 104 times higher for Hyper-FET as it shifts to metallic state at $V_{GS\text{-}IMT}$ leading to a steep rise in current. The OFF current for Hyper-FET is much lower because it reverts to an insulating state at $V_{GS\text{-}MIT}$.

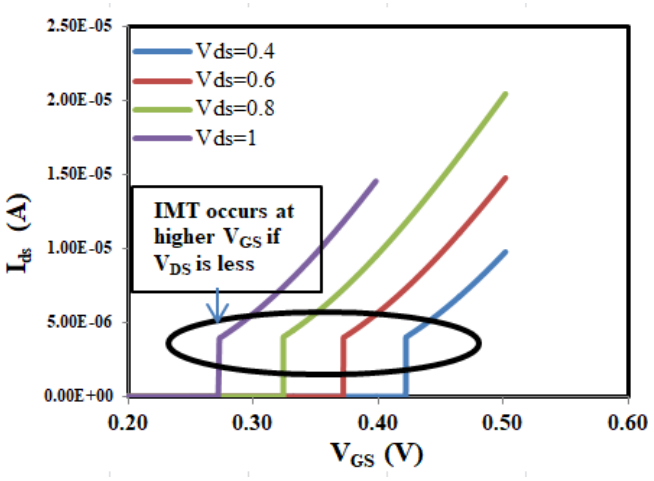

Fig. 3. Transfer Characteristic Curve depicting IMT for increasing values of V_{GS} at different values of V_{DS}

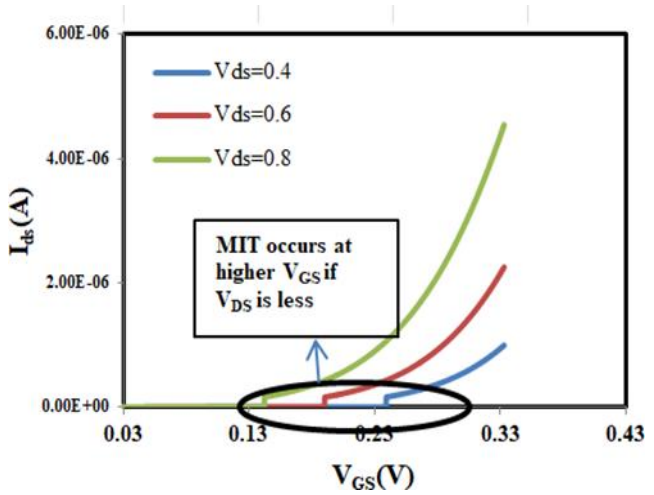

Fig. 4. Transfer Characteristic Curve depicting MIT for decreasing values of V_{GS} at different values of V_{DS}.

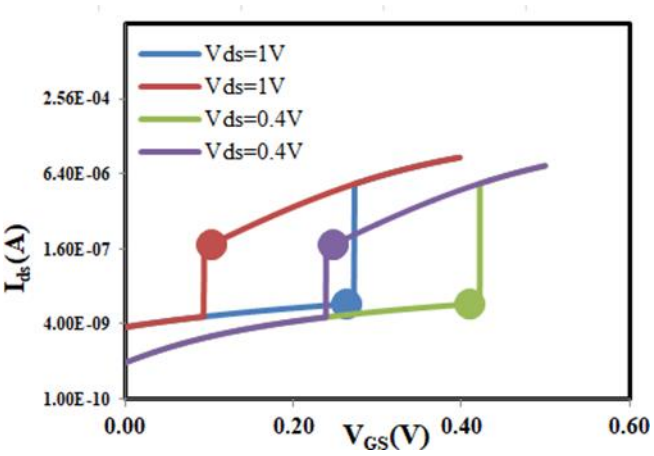

Fig. 5. Transfer Characteristic Curve depicting transition to metallic state as well as insulating state at different values of V_{DS}.

Authorized licensed use limited to: DELHI TECHNICAL UNIV. Downloaded on June 01,2023 at 06:00:39 UTC from IEEE Xplore. Restrictions apply.

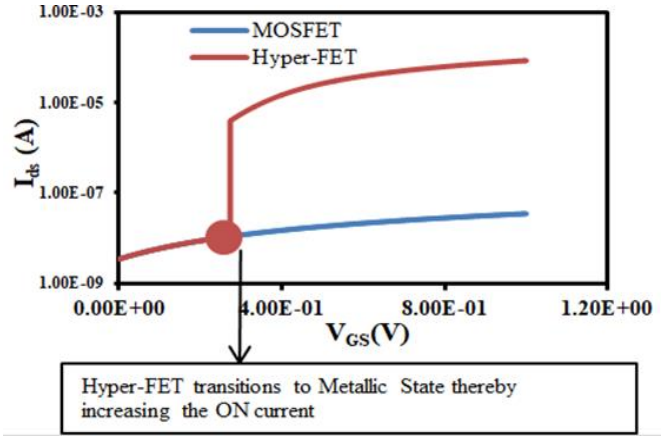

Fig. 6. Iso-OFF comparison for Hyper-FET and MOSFET

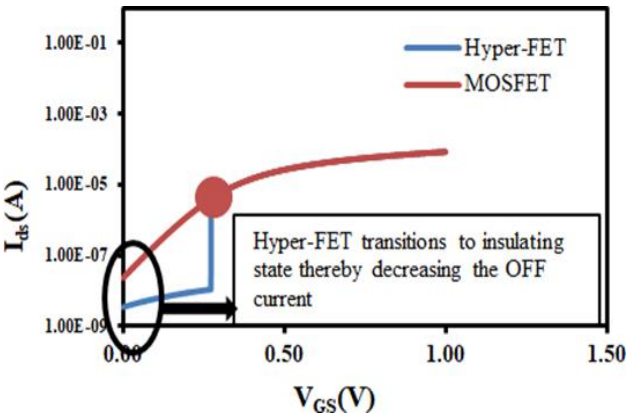

Fig. 7. Iso- ON comparison for Hyper-FET and MOSFET

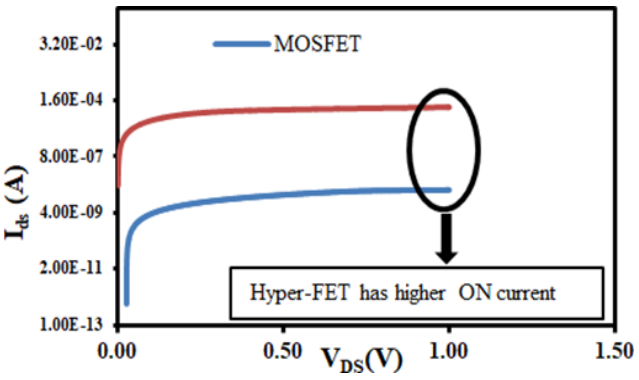

Fig. 8. Output characteristic curve depicting the Iso-OFF comparison for Hyper-FET & MOSFET

III. Impact Of PTM Parameters

The transfer Characteristic curve as shown in Fig. 9 is plotted by varying Metallic State Resistivity keeping V_{DS}=1V. As seen in the curve, the ON current reduces and $V_{GS\text{-}IMT}$ decreases on increasing the Metallic State Resistivity. This happens because the effective resistance of the MOSFET in the ON state increases if Metallic State Resistivity is increased. Fig. 10 depicts the transfer characteristic curve for varying values of Insulating Resistivity. The value of $V_{GS\text{-}IMT}$ increases with increasing Insulating State Resistivity. This happens because the effective OFF state resistance of MOSFET increases and a greater V_{GS} is required to generate the current required for switching to the metallic state. The Insulating State Resistivity should be so chosen that $V_{GS\text{-}IMT}$ lies approximately near the threshold voltage of MOSFET so that a steep sub-threshold curve is obtained. It should not be greater than the threshold voltage to take advantage of a higher I_{ON}-I_{OFF} ratio for digital applications. Metallic state Resistivity should be so chosen that $V_{GS\text{-}MIT}$ is less than $V_{GS\text{-}IMT}$ and greater than zero. It should be carefully selected so that negative hysteresis is avoided and PTM reaches a stable state.

The transfer Characteristic curve for varying values of $J_{C\text{-}IMT}$ and $J_{C\text{-}MIT}$ is plotted in Fig. 11 and Fig. 12 respectively. A large value of $J_{C\text{-}IMT}$ will prevent the device from switching to the metallic state within the desired voltage range of V_{DS} because the value of current for transition to metallic state ($I_{C\text{-}IMT}$) increases with an increase in $J_{C\text{-}IMT}$ and hence $V_{GS\text{-}IMT}$ also increases. The threshold value of current required for the transition to an insulating state is more if $J_{C\text{-}MIT}$ is more. This decreases $V_{GS\text{-}MIT}$ further. Therefore, a large value of $J_{C\text{-}MIT}$ prevents the device from returning to the insulating state within operating window of Gate to Source voltage. Further, it can be concluded that the ratio of current densities should be of the same order of magnitude as single crystal VO_2 for higher I_{ON}/I_{OFF} ratio [3]. $J_{C\text{-}IMT}$ is less than $J_{C\text{-}MIT}$ since the device current in the metallic state is greater than that in the insulating state.

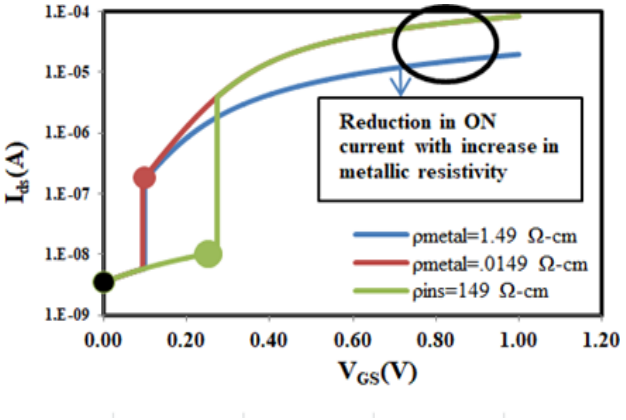

Fig. 9. Transfer Characteristic Curve for varying values of Metallic State Resistivity at fixed Insulating State Resistivity.

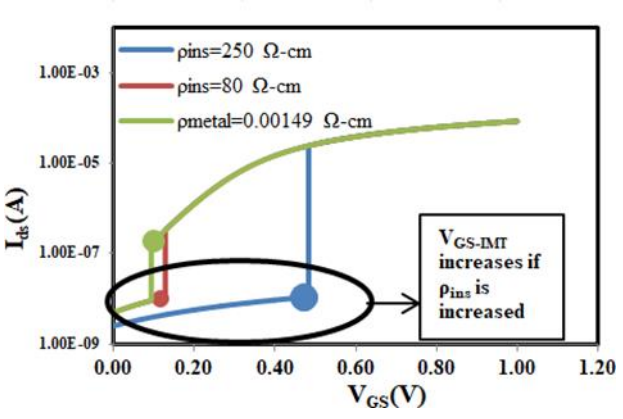

Fig. 10. Transfer Characteristic Curve for varying values of Insulating State Resistivity at fixed Metallic State Resistivity.

Authorized licensed use limited to: DELHI TECHNICAL UNIV. Downloaded on June 01,2023 at 06:00:39 UTC from IEEE Xplore. Restrictions apply.

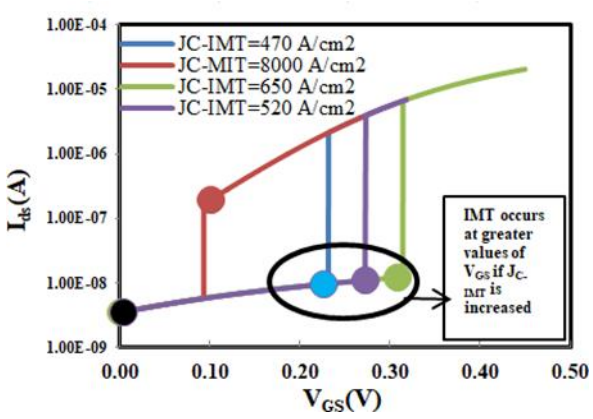

Fig. 11. Drain current for varying $J_{C\text{-}IMT}$ at fixed $J_{C\text{-}MIT}$

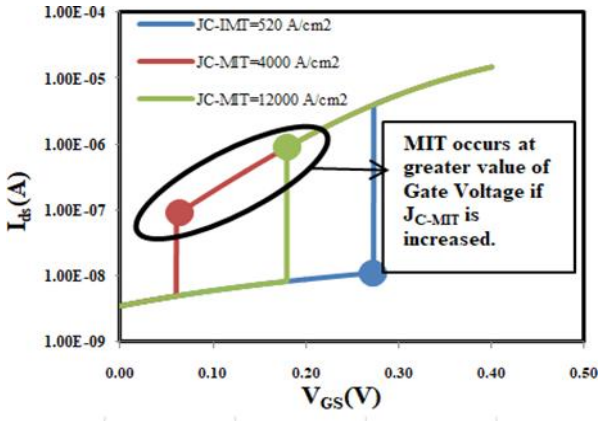

Fig. 12. Drain current for varying $J_{C\text{-}MIT}$ at fixed $J_{C\text{-}IMT}$

Fig. 13 and Fig. 14 depict that the increase in the area of PTM leads to an increase in the value of $I_{C\text{-}IMT}$ and $I_{C\text{-}MIT}$. At the same time, the effective resistance of metallic and insulating states increase. The combined effect is such that the values of $V_{GS\text{-}IMT}$ and $V_{GS\text{-}MIT}$ initially increase with the increasing area and after some critical value, they start to decrease. Care must be taken that the value of the area of PTM is so chosen that $V_{GS\text{-}MIT}$ is not negative and $V_{GS\text{-}IMT}$ does not go beyond the highest operating value of V_{DS}. Also, it should be made sure that $V_{GS\text{-}IMT}$ is always greater than $V_{GS\text{-}MIT}$. As seen from the curve in Fig. 15 and Fig. 16, at greater values of Length of PTM, $V_{GS\text{-}IMT}$ is always greater than $V_{GS\text{-}MIT}$. But at smaller values of Length, the two are approximately near. The constraint for the critical values should be satisfied by proper Length selection.

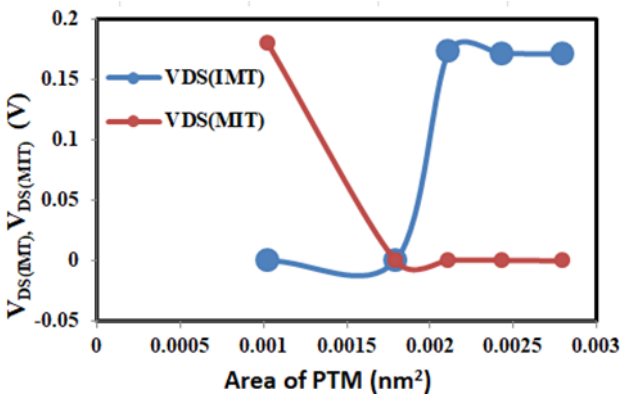

Fig. 13. Variation of of $V_{DS\text{-}IMT}$ and $V_{DS\text{-}MIT}$ with area of PTM

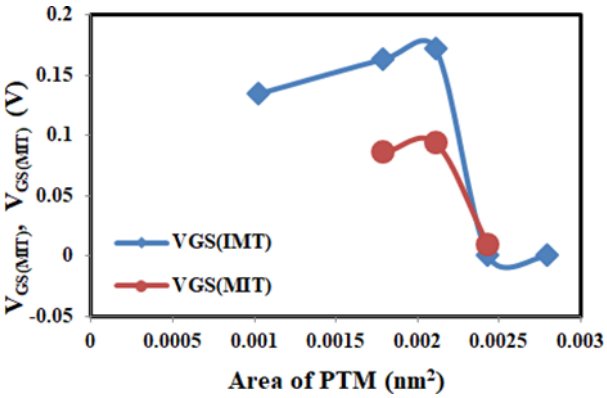

Fig. 14. Variation of of $V_{GS\text{-}IMT}$ and $V_{GS\text{-}MIT}$ with area of PTM

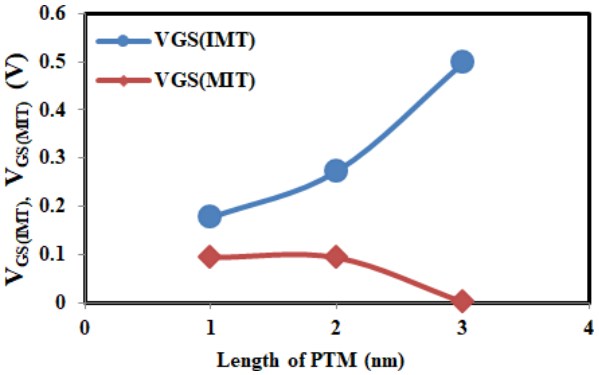

Fig. 15. Variation of of $V_{GS\text{-}IMT}$ and $V_{GS\text{-}MIT}$ with Length of PTM

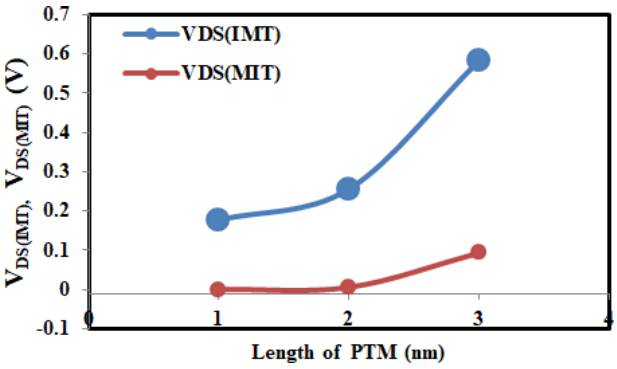

Fig. 16. Variation of of $V_{DS\text{-}IMT}$ and $V_{DS\text{-}MIT}$ with Length of PTM

CONCLUSION

In this paper, Phase Transition Material Modulated Hyper-FET is analyzed and compared with the conventional device for digital applications by studying I_{ON}/I_{OFF} ratio in particular. It is to be noted that percentage change in Drain current at $V_{GS\text{-}IMT}$ is approximately 99.9%. The impact of PTM parameters like $J_{C\text{-}IMT}$, $J_{C\text{-}MIT}$, Area of PTM, Length of PTM, insulating resistivity, and metallic resistivity is also studied. Percentage change in the value of $V_{GS\text{-}IMT}$ with respect to percentage change in various parameters is as depicted in Table II.

Hyper-FET achieves a steep sub-threshold curve that may be used for designing low-power digital circuits. This paper provides insights to properly select PTM parameters to

Authorized licensed use limited to: DELHI TECHNICAL UNIV. Downloaded on June 01,2023 at 06:00:39 UTC from IEEE Xplore. Restrictions apply.

avail full benefits. The utility and constraints of 32nm Hyper-FET for low-power digital computation should be examined in detail.

TABLE II. VARIATION OF VGS-IMT WITH VARIOUS PARAMTERS

S.NO	Name of Parameter	Change in Parameter	Change in $V_{GS\text{-}IMT}$
1.	$J_{C\text{-}IMT}$	10.6%	18%
2.	ρ_{INS}	212.5%	159%
3.	A_{PTM}	21.32%	75%
4.	L_{PTM}	45%	55.11%

```
* C:\Users\ABCD\Documents\LTspiceXVII\hyperFET final.asc
R1 VO2 Vctrl {R_ins}
R2 Vctrl 0 {R_metal}
C_VO1 0 VO2 1.05n
S1 Vctrl VO2 N003 0 MYSWI
M1 N001 N002 VO2 VO2 NMOS l=32nm w=72nm
V1 N002 0 1
V2 N001 0 1
C1 0 N003 {C0}
B1 N003 0 V=if(V(comp1)>V(comp2),1,0)
B2 comp1 0 v=V(VO2)
R3 comp1 0 1
B3 comp2 0 V=if(V(VO2)>V(comp2),V_L,V_H)
R4 comp2 0 1
.model NMOS NMOS
.model PMOS PMOS
.lib C:\Users\ABCD\Documents\LTspiceXVII\lib\cmp\standard.mos
.model MYSWI SW(Ron=1 Roff=10000000000 Vt=15.86m Vh=0.0005)
.param V_L=2.04m
.param V_H=15.86m
.param R0=1
.param C0=10n
.param R_metal=226
.param R_ins=22600000
```

Fig. 17. Spice Netlist For Simulating Hyper-FET

REFERENCES

[1] N. Shukla, A. V. Thathachary, A. Agrawal, H. Paik, A. Aziz, D. G. Schlom, S. K. Gupta, R. Engel-Herbert, and S. Datta, "A steep-slope transistor based on abrupt electronic phase transition," Nature commu- nications, vol. 6, no. 1, pp. 1–6, 2015.

[2] E. Ko, J. Shin, and C. Shin, "Steep switching devices for low power applications: Negative differential capacitance/resistance field effect transistors," Nano Convergence, vol. 5, no. 1, pp. 1–9, 2018.

[3] A. Aziz, N. Shukla, S. Datta, and S. K. Gupta, "Steep switching hybrid phase transition fets (hyper-fet) for low power applications: A device- circuit co-design perspective–part i," IEEE Transactions on Electron Devices, vol. 64, no. 3, pp. 1350–1357, 2017

[4] J. Song, J. Park, K. Moon, J. Woo, S. Lim, J. Yoo, D. Lee, and H. Hwang,"Monolithic integration of agte/tio 2 based threshold switching device with tin liner for steep slope field-effect transistors," in 2016 IEEE International Electron Devices Meeting (IEDM). IEEE, 2016, pp.25–3.

[5] J. Song, J. Woo, S. Lee, A. Prakash, J. Yoo, K. Moon, and H. Hwang, "Steep slope field-effect transistors with ag/tio 2-based threshold switch- ing device," IEEE Electron Device Letters, vol. 37, no. 7, pp. 932–934, 2016.

[6] J. Song, J. Woo, A. Prakash, D. Lee, and H. Hwang, "Threshold selector with high selectivity and steep slope for cross-point memory array," IEEE Electron Device Letters, vol. 36, no. 7, pp. 681–683, 2015.

[7] Q. Hua, G. Gao, C. Jiang, J. Yu, J. Sun, T. Zhang, B. Gao, W. Cheng, R. Liang, H. Qian et al., "Atomic threshold-switching enabled mos2 transistors towards ultralow-power electronics," Nature communications,vol. 11, no. 1, pp. 1–10, 2020.

[8] J. Shin, E. Ko, and C. Shin, "Analysis on the operation of negative differential resistance finfet with pb (zr 0.52 ti 0.48) o 3 threshold selector," IEEE Transactions on Electron Devices, vol. 65, no. 1, pp. 19–22, 2017

[9] M. J. Avedillo and J. Núñez, "Insights Into the Operation of Hyper-FET-Based Circuits," in IEEE Transactions on Electron Devices, vol. 64, no. 9, pp. 3912-3918, Sept. 2017.

[10] M. Jiménez, J. Núñez and M. J. Avedillo, "An Approach to the Device- Circuit Co-Design of HyperFET Circuits," 2020 IEEE International Symposium on Circuits and Systems (ISCAS), Seville, Spain, 2020,pp. 1-5.

[11] Islam, Md Mazharul, et al. "Low-Power Dynamic Circuit Design With Steep-Switching Hybrid Phase Transition FETs (Hyper-FETs)." IEEE Transactions on Electron Devices (2022).

[12] Yadav, Sameer, et al. "Ferroelectric negative-capacitance-assisted phase-transition field-effect transistor." IEEE Transactions on Ultrasonics, Ferroelectrics, and Frequency Control 69.2 (2021): 863-869.

[13] Jiménez, Manuel, Juan Núñez, and María José Avedillo. "Hybrid-Phase-Transition FET Devices for Logic Computation." IEEE Journal on Exploratory Solid-State Computational Devices and Circuits 6.1 (2020): 1-8.

[14] Frougier, J., et al. "Phase-transition-FET exhibiting steep switching slope of 8mV/decade and 36% enhanced ON current." 2016 IEEE Symposium on VLSI Technology. IEEE, 2016.

Authorized licensed use limited to: DELHI TECHNICAL UNIV. Downloaded on June 01,2023 at 06:00:39 UTC from IEEE Xplore. Restrictions apply.

Plant-based phytochemical mediated inhibition of breast cancer by targeting PLAT: An in-silico study

Akash Rana
Department of Biotechnology
Delhi Technological University Delhi, India
Rana30aakash@gmail.com

Amit
Department of Biotechnology
Delhi Technological University
Delhi, India
Amit9912pal@gmail.com

Navneeta Bharadvaja
Department of Biotechnology
Delhi Technological University
Delhi, India
navneetab@dce.ac.in

2023 2nd International Conference on Smart Technologies and Systems for Next Generation Computing (ICSTSN) | 979-8-3503-4800-2/23/$31.00 ©2023 IEEE | DOI: 10.1109/ICSTSN57873.2023.10151458

***Abstract*—Cancer refers to a group of diseases in which some cells of the body start growing abnormally and in an uncontrolled manner causing deaths in millions worldwide. Tumor cells spread or invade to other parts of body or tissue and the process is called metastasis. Genetic and environmental factors like arsenic, alcohol, and tobacco cause cancers in the human body. Studies show antioxidants have potential anticancer effects and are used to design therapeutic tactics to fight cancer. Several computational tools, including Autodock Vina, Pymol, Protein Drug Bank, and PILP, are used in this study. (Protein-Interaction Ligand Profiler). By using PILP and molecular docking of the protein and ligand, the interactions between Tissue type Plasminogen-Activator and plant phytochemicals are investigated. Drug discovery is facilitated by research into protein and ligand interactions. The purpose of this study is to identify the most effective plant phytochemicals that have demonstrated promise in preventing cancer in humans.**

Keywords— Bioinformatics, Drug discovery, Pymol, ProteinLigand Interactions, Docking, Computational biology.

I. INTRODUCTION

Breast cancer a serious threat to human health. It mostly affect women worldwide, also affect men. There are several proteins that are upregulated (i.e., increased in expression) in breast cancer, Estrogen receptor, Progesterone receptor,p53,Ki-67. Breast cancer can start in different parts of the breast, such as the milk ducts, lobules, or other breast tissue[1]. Risk factors for breast cancer include being a woman, getting older, having a family history of breast cancer, having certain gene mutations, having dense breast tissue, being overweight or obese, drinking alcohol, and not having children or having children after age 35.Symptoms of breast cancer may include a lump or thickening in the breast or armpit, a change in the size or shape of the breast, nipple discharge or inversion, redness or swelling of the breast, or skin changes on the breast. Early detection and treatment are important for improving the chances of survival from breast cancer. Screening tests such as mammograms can help detect breast cancer before symptoms appear. Treatment options for breast cancer may include surgery, radiation therapy, chemotherapy, hormone therapy, or targeted therapy, depending on the type and stage of the cancer. There are several proteins that are upregulated (i.e., increased in expression) in breast cancer. Estrogen receptor (ER) - This is a protein that is present on the surface of some breast cancer cells. ER-positive breast cancers depend on estrogen to grow and are typically treated with hormone therapy. Progesterone receptor (PR) - This is another protein that is present on the surface of some breast cancer cells. PR-positive breast cancers also depend on hormones to grow and are typically treated with hormone therapy. Ki-67- This is a protein that is present in the nucleus of dividing cells. t's important to note that there are many other proteins that may be upregulated in breast cancer, and the specific proteins that are involved can vary depending on the individual tumor. Plasminogen activator tissue (tPA) is a protein utilized in the degradation of blood clots. It is produced by various cells in the body, including cancer cells. In breast cancer, tPA protein suggest role in tumor growth, invasion, and metastasis. tPA able to activate plasminogen, a precursor protein, which then converts to plasmin, an enzyme that can break down the extracellular matrix and other proteins that hold cells together. This process is important for cancer cells to invade and spread to other parts of the body.

Phytochemicals in cancer prevention

Resveratrol - Resveratrol has been studied for its potential health benefits, particularly in relation to its antioxidant and anti-inflammatory properties. In laboratory studies, resveratrol has been shown to have anti-cancer effects, such as inhibiting the growth of cancer cells and inducing apoptosis (cell death) in cancer cells. However, its efficacy in humans is still under investigation and more clinical studies are needed to confirm its anti-cancer properties. Resveratrol is also known for its potential anti-aging effects. It has been shown to activate a protein called SIRT1, which is involved in cellular aging and may help to protect against age-related diseases[2]. However, its effects on human lifespan are not yet clear. Resveratrol is available in supplement form and is also found in foods such as red wine, grapes, berries, and peanuts. It is important to note that while resveratrol has shown promise in laboratory studies, its long-term effects and safety in humans are still being investigated, and it should not be used as a replacement for conventional medical treatment.

Silymarin - Silymarin obtained from Silybum marianum. It is commonly used as a dietary supplement for its potential health benefits, particularly for liver health[3]. Silymarin is believed to exert its beneficial effects through several mechanisms, including antioxidant, anti-inflammatory, and

Authorized licensed use limited to: DELHI TECHNICAL UNIV. Downloaded on June 28,2023 at 06:30:02 UTC from IEEE Xplore. Restrictions apply.

hepatoprotective (protective of liver cells) properties. It is thought to help protect liver cells from damage caused by toxins, drugs, and alcohol, and to promote liver regeneration. Silymarin has been studied for its potential therapeutic effects in a variety of liver diseases, including hepatitis, cirrhosis, and non-alcoholic fatty liver disease. It has been shown to improve liver function tests and reduce inflammation in some clinical trials, although results have been mixed and more research is needed to confirm its efficacy. Silymarin is available in supplement form and is generally considered safe when used as directed.

Mitomycin C - Mitomycin C is a drug that is used to treat cancer, including breast, lung, stomach, and bladder cancer. It induce DNA damage in cancer cells, so that they can not divide and multiply. Mitomycin C is typically administered intravenously and is often used in combination with other chemotherapy drugs. It is generally reserved for use in advanced or metastatic cancers, or in cases where other treatments have been unsuccessful. Mitomycin C is a potent chemotherapy drug and must be used with caution. It is important for patients to discuss the potential benefits and risks of this treatment with their healthcare provider before beginning therapy[4].

Berberine - Berberine is a natural alkaloid compound found in a variety of plants, including the barberry plant, Oregon grape, and goldenseal. It has been used in traditional Chinese medicine and Ayurvedic medicine for centuries to treat a variety of conditions, including diarrhea, diabetes, and infections. Berberine has been studied extensively in recent years for its potential health benefits[5]. It has also been shown to have effects on blood sugar levels and cholesterol and may have potential benefits for cardiovascular health. Some studies have suggested that berberine may be effective in treating certain conditions, such as type 2 diabetes, metabolic syndrome, and high cholesterol. It may also have potential benefits for cognitive function and neurological disorders. Berberine is available as a dietary supplement and is generally considered safe when used as directed.

Andrographolide - Andrographolide is a bioactive compound derived from the leaves and stems of the Andrographis paniculate plant, also known as the "king of bitters". It has been used in traditional medicine in Asia for centuries to treat a variety of conditions, including infections, inflammation, and digestive disorders. Andrographolide has been studied for its potential health benefits, and it has been found to have a number of pharmacological effects, including antiinflammatory, antioxidant, and immunomodulatory properties. Andrographolide is available as a dietary supplement and is generally considered safe when used as directed[6].

Hesperidin - (3,5,7 – trihydroxyflavanone 7-rhamnoglucoside) was first isolated in 1828 by chemist from france named lebreton, it is isolated from inner white peel of oranges(citrus). Hesperidin is reported for various biological and pharmacological effects, such as anticancer, anti-oxidant, anti-inflammation properties. Hesperidin and it's aglycone hesperitin, possesses anticancer activity and reported effective against various cancers like breast cancer,liver cancer, colon cancer, gastric cancer, lung cancer and Prostate cancer[7].

II. Material and Methodology

A. Materials

A 10th generation i6 core with 8.0 GB of RAM and a 64bit operating system are needed for in-silico study of proteins and ligands. Protein of plasminogen activator (tissue type) with receptor structure found in protein databank (pdb). A docking utility called Auto Dock 1.6.3 is needed. The interaction of protein-ligand is visualized using PLIP and the protein and ligand are generated and converted into pdbqt format in Open Babel GUI..

B. Methodology

1. Protein and ligand (phytochemicals) selection from the IMPPAT database
2. After receiving the protein's structure from the Protein Data Bank, make the protein. The protein was created using the auto dock 1.6.3 tools, and then the water molecules were removed, Kolman's charge was added, and polar hydrogen was added before the file was saved in the pdbqt format.
3. Protein and ligand molecular docking is initiated by formatting the x, y, and z centers in 6.084, 45.738, and 38.252 points, respectively. This is done by Auto Dock Vina 1.4.6. X, Y, and Z are each 40, 40, 40 in size. In auto dock vina software, all phytochemicals (ligands) are docked with proteins.
4. Analysis: Using the auto dock vina tools, an output file is created. This output is then run via the pymol software to create a pdb file, and the results are analyzed using PLIP. On the basis of binding energy, the protein and phytochemical (ligand) and protein and conventional inhibitor (ligand) were compared and chosen.

III. Results

Table 1. molecular docking showing binding energy of phytochemicals against PLAT

S. No	Phytochemical	Binding Energy (kcal/mol)	Amino Acid	Distance
1	Hesperidin	-8.5	190A	3.80
2	Silymarin	-8.5	192A	3.66
3	Berberine	-7.7	213A	3.78
4	Resveratrol	-6.7	215A	3.67
5	Mitomycin c	-6.8	190A	3.80
6	Andrographolide	-6.8	192A	3.66
7	Tranexamicacid (standard inhibitor)	-5.0	215A	3.78

Authorized licensed use limited to: DELHI TECHNICAL UNIV. Downloaded on June 28,2023 at 06:30:02 UTC from IEEE Xplore. Restrictions apply.

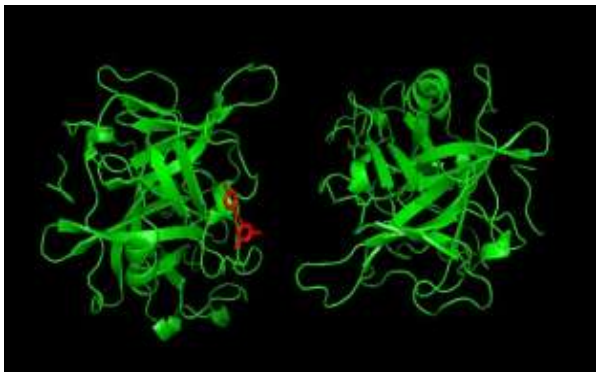

Figure 1 Interaction Between protein (PLAT) and ligand Hesperdin in pymol

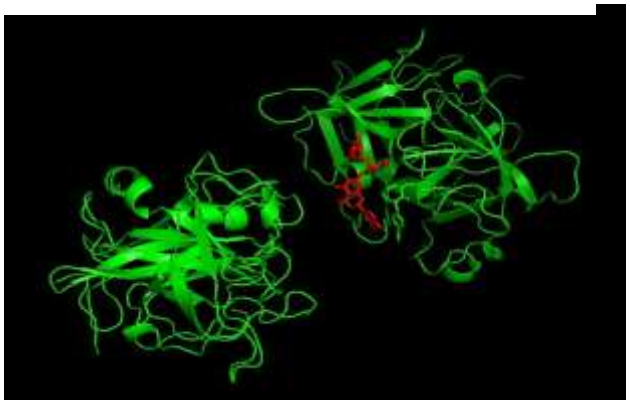

Figure 2 Interaction Between Protein (PLAT) and Ligand (Silymarin) in pymol

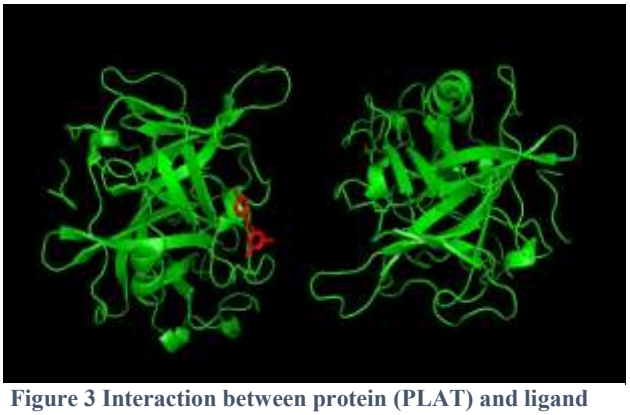

Figure 3 Interaction between protein (PLAT) and ligand Berberine in pymol

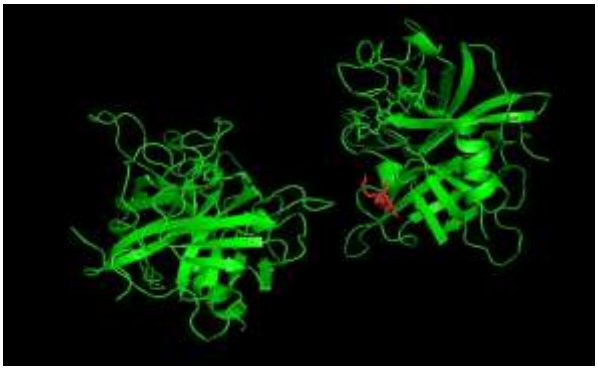

Figure 4 Interaction between Protein (PLAT) and ligand (resveratrol) in pymol

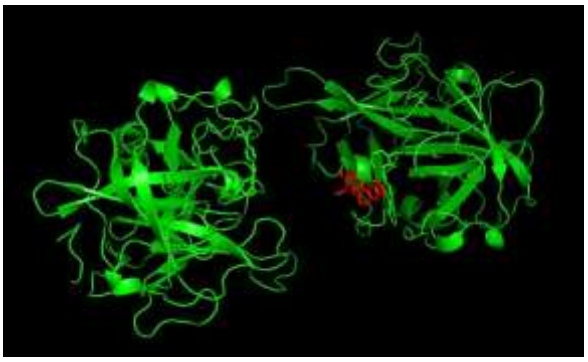

Figure 5 Interaction between protein (PLAT) and ligand (Mitomxin-c) in pymol

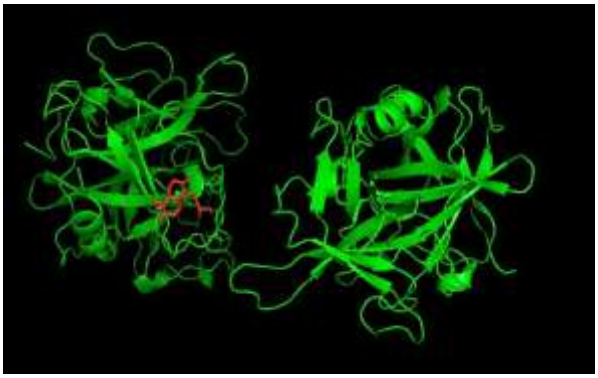

Figure 6. Interaction between protein (PLAT) and ligand (Andrographolide) in pymol

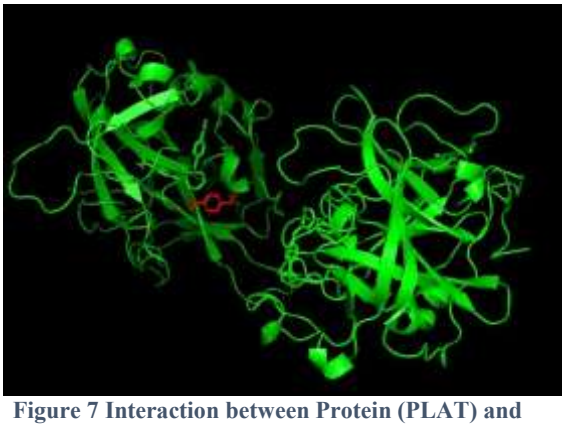

Figure 7 Interaction between Protein (PLAT) and Ligand (Tranexamic acid) in pymol

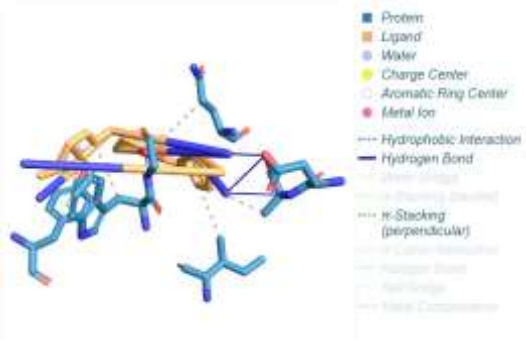

Figure 8. Interaction of protein (PLAT) and ligand (Tranexamic acid) in Protein-Ligand Interaction Profiler PLIP

Authorized licensed use limited to: DELHI TECHNICAL UNIV. Downloaded on June 28,2023 at 06:30:02 UTC from IEEE Xplore. Restrictions apply.

Figure (1–7) are images obtained in pymol, a software which require pdb file and show interaction of protein with ligand in visual form. Green (protein) and Red (ligand) in these figures, depicts interactions between them. Figure 8 obtained from online tool also show interactions among them.

IV. OBSERVATION

The most energetic molecules for binding are chosen. Hesperidin and silymarin in table 1 exhibit maximum binding energy (-8.5 kcal/mol), allowing for their usage in the development of drugs that inhibit the PLAT protein in breast cancer and function as therapeutic agents for the disease

V. CONCLUSION

Studies have shown that high levels of tPA expression are linked with poor prognosis in breast cancer patients, indicating that it can be used as biomarker agent for predicting disease outcome. Additionally, inhibition of tPA by ligand inhibitor have been shown to reduce growth of cancer cells and metastasis in breast cancer models, suggesting that targeting tPA may be a potential therapeutic strategy for treating the disease. Overall, the role of tPA in breast cancer appears to be significant, and further research is needed to understand its mode of action and potential as a therapeutic target. Targeting multiple targets enhance the quality data and utilized in drug design.

REFERENCES

[1] A. Braden, R. Stankowski, J. Engel, and A. Onitilo,"Breast Cancer Biomarkers: Risk Assessment, Diagnosis, Prognosis, Prediction of Treatment Efficacy and Toxicity, and Recurrence," CurrPharm Des, vol. 20, no. 30, pp. 4879–4898, Aug.2014, doi: 10.2174/1381612819666131125145517.

[2] S. Galiniak, D. Aebisher, and D. Bartusik-Aebisher, "Health benefits of resveratrol administration," Acta Biochim Pol, vol. 66, no. 1, pp. 13–21, 2019, doi: 10.18388/abp.2018_2749.

[3] T. Koltai and L. Fliegel, "Role of Silymarin in Cancer Treatment: Facts, Hypotheses, and Questions," J Evid Based Integr Med, vol. 27, Jan. 2022, doi: 10.1177/2515690X211068826.

[4] W. T. Bradner, "Mitomycin C: A clinical update,"Cancer Treat Rev, vol. 27, no. 1, pp. 35–50, 2001, doi: 10.1053/ctrv.2000.0202.

[5] K. Wang, X. Feng, L. Chai, S. Cao, and F. Qiu, "The metabolism of berberine and its contribution to the pharmacological effects," Drug Metab Rev, vol. 49, no. 2, pp. 139–157, Apr. 2017, doi: 10.1080/03602532.2017.1306544.

[6] Y. Peng et al., "Andrographolide inhibits breast cancer through suppressing COX-2 expression and angiogenesis via inactivation of p300 signaling and VEGF pathway," Journal of Experimental and Clinical Cancer Research, vol. 37, no. 1, Oct. 2018, doi: 10.1186/s13046-018-0926-9.

[7] C. Li and H. Schluesener, "Health-promoting effects of the citrus flavanone hesperidin," Crit Rev Food Sci Nutr, vol. 57, no. 3, pp. 613–631, Feb. 2017, doi: 10.1080/10408398.2014.906382.

Authorized licensed use limited to: DELHI TECHNICAL UNIV. Downloaded on June 28,2023 at 06:30:02 UTC from IEEE Xplore. Restrictions apply.

Proceedings of the Second International Conference on Applied Artificial Intelligence and Computing (ICAAIC 2023)
IEEE Xplore Part Number: CFP23BC3-ART; ISBN: 978-1-6654-5630-2

Predicting Next Quarter Nifty 50 Price using Genetic Algorithm and Support Vector Regression

Mohit Beniwal
Delhi School of Management
Delhi Technological University
Delhi, India
mohitbeniwal@dtu.ac.in

Archana Singh
Delhi School of Management
Delhi Technological University
Delhi, India
archanasingh@dtu.ac.in

Nand Kumar
Department of Humanities
Delhi Technological University
Delhi, India
nandkumar@dce.ac.in

2023 2nd International Conference on Applied Artificial Intelligence and Computing (ICAAIC) | 978-1-6654-5630-2/23/$31.00 ©2023 IEEE | DOI: 10.1109/ICAAIC56838.2023.10140439

***Abstract*—The stock market is difficult to predict due to uncertainty and complexity. Still, several methods are utilized to predict stock prices, such as fundamental analysis, technical analysis, and statistical and machine learning methods. Most of the studies, which use daily historical price, predicts next-day price. However, next-day price is not so useful for investors or short-term traders. In this study, genetic algorithm optimized support vector regression (GA-SVR) predicts next quarter's Nifty 50 index price using daily historical close price. Further, the study compares the GA-SVR prediction with Support Vector Regression (SVR) based on Root Mean Square Error (RMSE). The result shows that GA-SVR improves the prediction of SVR.**

***Index Terms*—Genetic Algorithm, Support Vector Regression, Stock Price, Prediction, Stock Index, Long-Term**

I. INTRODUCTION

Predicting stock prices is challenging due to several factors, such as market complexity, uncertainty, human behavior, and market manipulation. The stock market is influenced by numerous factors, including economic news, global events, company news, and investor sentiment, making it difficult to predict the market accurately. Additionally, unexpected events such as natural disasters and geopolitical tensions can significantly impact stock prices. Human behavior and investor sentiment also play a significant role in the stock market.

Several methods are used to predict the stock market, including fundamental analysis, technical analysis, and machine learning. Fundamental research focuses on a company's financial and economic indicators, such as earnings and revenue, to predict its future stock performance. Technical analysis, on the other hand, involves using charts and past market data to identify patterns and make predictions about future market trends. Machine learning methods use models and algorithms to analyze large amounts of market data and predict future market trends. Some investors also use these methods to make informed investment decisions. However, no single approach is foolproof, and market predictions can never be made with certainty. Further, past performance is not always indicative of future results. Hence, investing in the stock market involves a certain degree of risk.

The efficient market hypothesis (EMH) [1] argues that it is impossible to predict future stock prices based on past market trends or other available information. EMH argues that all public information is already reflected in stock prices. Similarly, the random walk hypothesis (RWH) [2] is a subset of the EMH and states that stock prices follow a random walk, meaning that they change randomly and unpredictably over time. Both these theories are widely accepted in academia. Other researchers argue that the stock market can be predicted to some extent. Machine learning methods can be used to predict stock market trends by identifying patterns that are difficult to detect generally. Machine learning algorithms such as Artificial Neural Networks (ANNs), Long Short-Term Memory (LSTM), and Support Vector Regression (SVR) are commonly used in stock market forecasting. ANNs are modeled after the structure of the human brain and can be trained on market data to make predictions about future stock prices. However, ANNs are ineffective in handling sequential data. LSTMs are well-suited for sequential data. Hence, LSTMs are widely used for time series prediction problems, such as stock market prediction, and can analyze time series data to identify patterns in stock price trends over time.

Similarly, SVR is useful in stock market prediction because it can handle non-linear relationships between stock prices. Further, it is easier to interpret and useful when the number of features is small. Genetic algorithms (GA) are evolutionary algorithms used for optimization. Genetic algorithms mimic the process of natural selection. Genetic algorithms can be applied to a wide range of problems such as function optimization, parameters optimization, or feature selection. In this study, a genetic algorithm is used for hyper-parameter tuning. The study predicts the Nifty 50 index using a genetic algorithm-optimized support vector regression (GA-SVR). The result of (GA-SVR) is compared with SVR using Root Mean Square Error (RMSE). The main contributions of the paper are as follows:

- A comparison of GA-SVR and SVR performance to predict the Nifty 50 index price. The result shows genetic algorithm improves SVR prediction.

Authorized licensed use limited to: DELHI TECHNICAL UNIV. Downloaded on June 14,2023 at 05:02:03 UTC from IEEE Xplore. Restrictions apply.

- Most of the studies focus on next-day prices [3]–[5]. This paper predicts the next quarter's Nifty 50 index price rather than a next-day price.
- The parameters of SVR are automatically selected using the genetic algorithm to eliminate bias.

II. Literature Review

Most of the studies predict next-day prices. Siddique and Mohanty [3] used a hybrid support vector regression model (SVR) and particle swarm optimization (PSO-SVR). They predicted the next day's price. Their result showed that PSOSVR outperformed SVR. Similarly, Zhang et al. [4] predicted the next day's price. They proposed modified firefly algorithm support vector regression (SVR-MFA) to predict stock prices. They compared SVR-MFA with SVR, GASVR, Firefly Algorithm-SVR, particle swarm optimization SVR, ANN, and LSTM. They concluded that the proposed SVR-MFA model is superior. In another study, Dash et al. [6] proposed Fine Tuned Support Vector Regression (FT-SVR) to predict stock prices. The SVR was optimized by the grid search method. The FT-SVR was compared with ANN, and it was found that FT-SVR is more accurate than other compared models.

Pun and Shahi [7] used SVR to predict different sectors of the Nepal Stock Exchange. They compared the result with ANN and found that SVR outperformed ANN for most of the sectors. Rustam and Kintandani [8] also proposed a hybrid model using SVR, PSO, and technical indicators. They created an accurate model to predict stock prices in Indonesia. Huang et al. [9] proposed a strategy of investment in the stock market using modified support vector regression. They compared their model with ANN and found that their model's accuracy is more stable in terms of Root Mean Square Error (RMSE) and Mean Absolute Percentage Error (MAPE). Yeh et al. [10] used the SVR hyper-parameter manually. However, manually selecting the hyper-parameter of machine learning methods may not optimize the algorithm.

Li and Sun [11] used Support Vector Machine (SVM) to develop an intelligent investment strategy. They used mesh search, genetic algorithm, and particle swarm optimization to optimize SVM hyper-parameters and kernels. Their result shows that GA-optimized SVM predicted prices were closer to the real value of the stock market. Kazem et al. [12] proposed a model based on chaos-mapping, firefly algorithm, and SVR (SVR-CFA). They chose three stock market time series: Intel, Microsoft, and National bank share from NASDAQ. They compared their model with chaotic genetic algorithm based SVR, firefly based SVR, ANN, and adaptive neuro-fuzzy inference system. Their proposed model performed best based on root mean square error (RMSE) and mean absolute percentage error (MAPE).

The literature review suggests that there is a gap in predicting long-term, such as quarterly prediction using support vector regression. Further, this study optimizes the SVR prediction using a genetic algorithm. This paper fills this gap

III. Methodologies

A. Data

The Nifty 50 index data is downloaded from yahoo finance. It is daily data of around one year from the period of 1-Jan2022 to 31-12-2022. Fig. 1 shows the Nifty 50 daily prices.

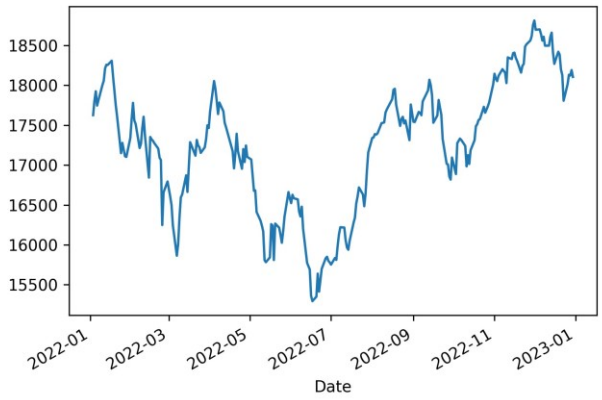

Fig. 1. Nifty 50 Daily Data

There are 248 trading days in the year 2022. The Nifty 50 index price first falls from around 18500 to the 15500 level and then again rises to the 18500 level.

B. Genetic Algorithm (GA)

Genetic algorithms are a type of optimization algorithm that are nature inspired based on the principles of natural selection and genetics. They imitate the process of evolution to find the optimum solution to complex problems. The potential solutions are evaluated based on a fitness function. The top solutions are recombined in crossover and further mutated to generate new solutions, and the process continues until an optimal solution is found. Fig. 2 shows the flow chart of the genetic algorithm. In this study, a genetic algorithm is used to tune the parameters of the SVR.

Authorized licensed use limited to: DELHI TECHNICAL UNIV. Downloaded on June 14,2023 at 05:02:03 UTC from IEEE Xplore. Restrictions apply.

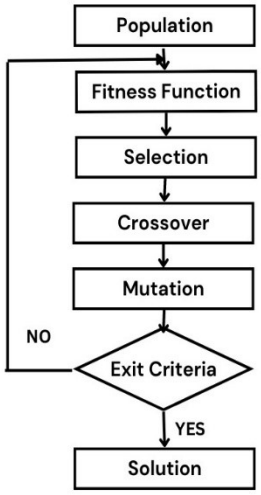

Fig. 2. Genetic Algorithm

C. *Support Vector Regression (SVR)*

Support Vector Regression (SVR) is a type of support vector machine (SVM) [13], developed by Vapnik in 1995, that is used for regression. The SVR algorithm finds the best map between input and output. Hence, the goal of SVR is to find the best line that can predict the continuous value of the target variable based on the input features. SVR attempts to find the narrowest tube around the hyperplane and minimize the prediction errors. The SVR algorithm is helpful for non-linear data and prediction. Further, it can handle noisy data. In this study, the dates are converted into integers and used as an input variable. The close prices are used as the target. A genetic algorithm is used to find the hyper-parameters "C" and epsilon of the SVR algorithm. The "C" parameter penalizes the data points falling outside the insensitive epsilon tube. The balance between these parameters ensures that the model is not overfitting or under-fitting.

In this study, the data is first pre-processed to drop data that is missing. Further, the close prices are scaled from 0 to 1. In contrast, dates are converted into integers and not scaled. The dates as integers are used as input to the SVR model, and close prices are the target. Fig 3 shows the flow of the prediction algorithm.

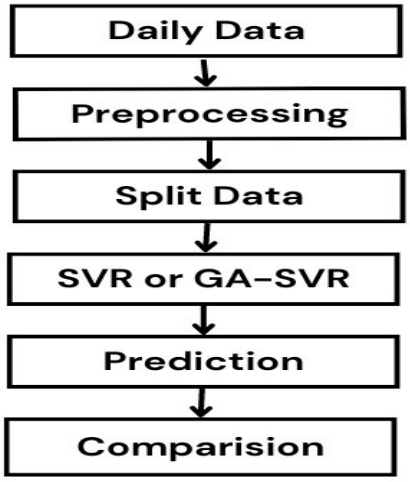

Fig. 3. Genetic Algorithm

IV. RESULTS

According to the academic literature, SVR is a robust algorithm for noisy data. Further, it avoids over-fitting. However, the value of "C" and epsilon can lead to over-fitting and under-fitting. This study uses a genetic algorithm to eliminate the problem of over-fitting and under-fitting. 1-year of Nifty 50 data is taken and spitted into a 75:25 ratio. Twenty-five percent of 1-year is equivalent to 3 months or one quarter. Predicting for the period of one quarter using a daily frequency of data is quite difficult if lagged prices are used. Finally, the performance of GA-SVR is compared with SVR using RSME.

Fig. 4 shows the prediction of the SVR model with default parameters. The Radial Bias Function (RBF) kernel is used in the default configuration. The value of "C" and epsilon is 1 and 0.1, respectively. The green line is the actual price for the next quarter, whereas the red line is the prediction by the SVR algorithm for the next quarter.

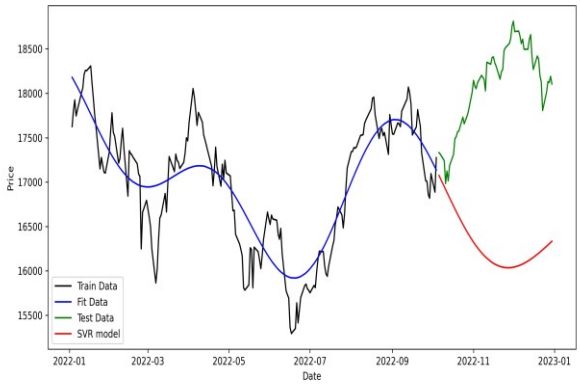

Fig. 4. SVR prediction for next quarter

Authorized licensed use limited to: DELHI TECHNICAL UNIV. Downloaded on June 14,2023 at 05:02:03 UTC from IEEE Xplore. Restrictions apply.

In contrast to SVR, the GA-SVR selected the hyperparameters from the population of the solution containing values for "C" and epsilon. The population containing the initial solution is the pairwise combination of "C" and epsilon from table I. The fitness function sorts the solutions based on their RMSE value. The best solution, having minimum RMSE, are recombined and mutated to produce more potential solution. This cycle continues until exit criteria are met.

TABLE I
PAIRWISE COMBINATION - POPULATION

Genetic Algorithm Population	
C	0.001, 0.01,0.1
Epsilon	0.15,0.2,0.25

Fig. 5 shows the prediction by the genetically optimized SVR. In contrast to the SVR, the predicted prices are closer to the actual prices.

Table II compares the models using RMSE.

TABLE II
RMSE OF MODELS

Model	Train RMSE	Test RMSE
SVR	350.2	1940.861
GA-SVR	447.38	1108.17

Meesad and Rasel [14] used MAPE to compare models. This study also uses RMSE only, as MAPE will be redundant. The train RSME of the SVR model is the lowest, but the test RMSE is the highest. This indicates that there is over-fitting in the train data without the hyper-parameter optimization. In contrast, the RMSE of GA-SVR during training is greater than

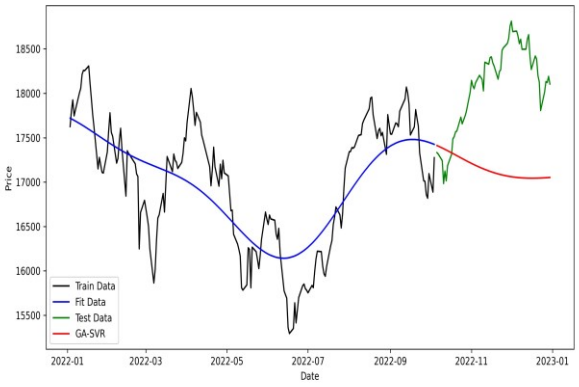

Fig. 5. GA-SVR prediction for next quarter

the SVR model but lower in test data. This indicates that the GA-SVR avoids over-fitting.

V. CONCLUSION

Predicting Stock price is a tricky task. Developing a model that handles the noise in time series without over-fitting and under-fitting is important in the stock market. Machine learning models also suffer from over-fitting or under-fitting problems if they are not handled carefully. An evolutionary algorithm, such as a genetic algorithm, helps find the optimum hyper-parameters of the machine learning algorithms. In this study, the stock prices are forecasted for the next quarter using daily frequency data. A hybrid model using a genetic algorithm and support vector regression (GA-SVR) is used to predict the Nifty 50 index prices. Further, the model is compared with the base model SVR with default hyper-parameters. This study uses only one input parameter, date as integers, to forecast the close prices.

The genetic algorithm creates an initial population of solutions. These solutions are evaluated using a fitness function. The top solutions are selected and recombined using a crossover function. These solutions are further mutated randomly. Again, top solutions are evaluated using the fitness function. This cycle continues until the optimum solution is found.

The result showed that GA-SVR is able to optimize the hyper-parameters of the SVR model. By creating population, selection and crossover, and mutation, the genetic algorithm helps avoid the over-fitting problem of the SVR. Hence, it can be concluded that in the stock market, evolutionary algorithms such as genetic algorithms can improve the machine learning algorithm performance by finding the optimum hyper-parameter. In future work, we would further experiment with bigger data and different market conditions such as low volatility, high volatility, and bear or bull market.

REFERENCES

[1] Fama, E. F. Efficient Capital Markets: A Review of Theory and Empirical Work. J Finance 25, 383–417 (1970).
[2] Malkiel, B. G. A Random Walk Down Wall Street. Norton & Co, New York (1973).
[3] Siddique, M. & Mohanty, S. A Hybrid Forecasting Model For Prediction
Of Stock Value Of Tata Steel Using Support Vector Regression And Particle Swarm Optimization. International Journal of Pure and Applied Mathematics 119, (2018).
[4] Zhang, J., Teng, Y. F. & Chen, W. Support vector regression with modified firefly algorithm for stock price forecasting. Applied Intelligence 49, 1658–1674 (2019).
[5] Huang, W., Nakamori, Y. & Wang, S. Y. Forecasting stock market movement direction with support vector machine. Comput Oper Res 32, 2513–2522 (2005).
[6] Dash, R. K., Nguyen, T. N., Cengiz, K. & Sharma, A. Fine-tuned support vector regression model for stock predictions. Neural Comput Appl (2021) doi:10.1007/s00521-021-05842-w.
[7] Pun, T. B. & Shahi, T. B. Nepal Stock Exchange Prediction Using
Support Vector Regression and Neural Networks. in 2018 Second International Conference on Advances in Electronics, Computers and Communications (ICAECC). IEEE (2018).
[8] Rustam, Z. & Kintandani, P. Application of Support Vector Regression in Indonesian Stock Price Prediction with Feature Selection Using Particle Swarm Optimisation. Modelling and Simulation in Engineering 2019, (2019).
[9] Huang, C. H., Yang, F. H. & Lee, C. P. The strategy of investment in the stock market using modified support vector regression model. Scientia Iranica 25, 1629–1640 (2018).
[10] Yeh, C. Y., Huang, C. W. & Lee, S. J. A multiple-kernel support vector regression approach for stock market price forecasting. Expert Syst Appl 38, 2177–2186 (2011).

Authorized licensed use limited to: DELHI TECHNICAL UNIV. Downloaded on June 14,2023 at 05:02:03 UTC from IEEE Xplore. Restrictions apply.

[11] Li, X. & Sun, Y. Stock intelligent investment strategy based on support vector machine parameter optimization algorithm. Neural Comput Appl 32, 1765–1775 (2020).

[12] Kazem, A., Sharifi, E., Hussain, F. K., Saberi, M. & Hussain, O. K. Support vector regression with chaos-based firefly algorithm for stock market price forecasting. Applied Soft Computing Journal 13, 947–958 (2013).

[13] Vapnik, V. The Nature of Statistical Learning Theory. The Nature of Statistical Learning Theory (Springer Verlag, 1995).

[14] Meesad, P. & Rasel, R. I. Predicting stock market price using support vector regression. in 2013 International Conference on Informatics, Electronics and Vision, ICIEV 2013 (2013). doi:10.1109/ICIEV.2013.6572570.

Authorized licensed use limited to: DELHI TECHNICAL UNIV. Downloaded on June 14,2023 at 05:02:03 UTC from IEEE Xplore. Restrictions apply.

Section A-Research paper
ISSN 2063-5346

PREDICTION OF SURFACE ROUGHNESS IN ADDITIVELY MANUFACTURED SAMPLES IN PLA+ POLYMER MATERIAL THROUGH MACHINE LEARNING

Anuj Saxena[a]*, Qasim Murtaza[a], Paras Kumar[a]

[a]Department of Mechanical Engineering, Delhi Technological University, India 110042
*E-mail address: engg.anujsaxena@gmail.com

Abstract. Both artificial intelligence and additive manufacturing are excellent and revolutionary technologies. The main aim of this research paper is to predict surface roughness in additively manufactured processes in Poly Lactic Acid+ polymer material through different machine learning algorithms like support vector machine, linear regression, and two ensemble learning techniques Xtremegradient boosting and randomforest regressor. All machine learning is trained and tested. Predictive model of surface roughness is developed and machine learning behaviour is analyzed. Taguchi's Design of the Experiment was used to make L25 orthogonal array sample datasets. The machine model works on five parameters that influence layer geometries: layer height, infill density, printing speed, and nozzle temperature with a 0-degree raster angle. By applying all machine learning algorithms, random forest regression is best model, which gives 94.85% accurate results in datasets with minimum mean squared error of approximate 0.1255 and maximum r2 score of approximate. 0.9685.

Keywords: Additive Manufacturing, Poly lactic acid (PLA+) material, fused deposition modelling, Machine learning.

1. Introduction

According to recent studies, the implementation of machine learning (ML) methods may provide both improved speculate performance and increased productivity in the industrial sector. Additive manufacturing (AM) is an auspicious technology to manufactured components with intricate geometries. It can produce complex parts with minimum price and take time and without using special tooling system like molds compared to traditional manufacturing technologies.

Nomenclature

ML	Machine learning	AM	Additive manufacturing
FDM	Fused deposition modelling	3D	Three-dimensional
PLA	Poly lactic acid	RMSE	Root mean square Error
Ra	Surface roughness (μm)	DoE	Design of experiments
ASTM	American Society for Testing and Materials	AI	Artificial intelligence
FFF	Fused filament fabrication	ABS	Acrylonitrile butadiene styrene
CAD	Computer-aided design	MSE	Mean Squared Error

Additive manufacturing, also referred to as AM, is the method of joining the material (layer-by-layer deposition) with the help of 3D models. In comparison with subtractive manufacturing techniques, AM is defined by the ASTM as "a process of incorporating materials to create 3D objects from 3D model data, generally layer upon layer deposition [1]. FDM is “a material extrusion process that is used to make polymer material parts by the heating of material filaments and the deposition of material layer by layer and make 3d objects” [2].

The roughness of a surface plays a significant role in machining processes because it has a direct impact on the functional specifications of the machined parts. [3], [4]. According to a survey, FDM is the most frequently utilized AM technology at the present time. One of the main areas of focus for enhancing FDM part quality has been the development of predictive models that link process factors (i.e., machine settings) and material qualities with the printed part properties [5]. Shaha et al [6], the DoE method was used to examine the impact of machine parameters on printed component surface roughness. The researcher determined that layer height was a significant determinant, but that there was no significant relationship between surface roughness and nozzle temperature. The investigation detailed in reference number [7] demonstrates how different machine configurations affect surface roughness. It was discovered that the height of the slice and the width of the raster have an impact on surface roughness. Meanwhile, P.K. Rao et al. [8], [9] conducted experiments to determine the machine settings that result in the

smoothest surface finish, which is associated with high temperatures, thin layers, and a high feed/flow rate ratio. Similarly, R. Anitha et al. [9] reports on similar research where the thickness of the deposited filament, layer height, and extrusion speed were found to affect surface roughness. Popescu et al.[10] discussed that due to the various types of 3D printers, materials, and slicing software available, experimental methods may not be able to produce consistent results that accurately reflect the material's behavior in reality. To address this issue, theoretical modeling and finite element analysis were used to connect the mechanical properties of 3D-printed samples with material and process parameters[11]. However, the complex microstructure of 3D-printed parts, such as irregular pores and surface interactions, make it difficult to accurately model and simulate. Therefore, the accuracy and reliability of these methods are uncertain. To overcome these challenges, ML techniques, as a form of AI, can learn patterns between input features and output results automatically based on training data, without explicit programming [12]. In the context of the ME-AM process, the use of ML may provide effective solutions to the aforementioned issues [13]. The quality of parts produced by FFF can be impacted by variations in the thermal influence between layers during the layer-by-layer material deposition process. Such variations can cause issues like surface roughness, microstructural defects, and poor mechanical properties [14]. To address this, Boschetto et al.[15] developed a predictive modeling strategy to evaluate the surface roughness of FFF-printed items, and this strategy was demonstrated through a series of experiments. Boschetto and Bottini [16] also developed a model that can predict surface roughness of FFF-printed parts that underwent barrel finishing. Reeves and Cobb [17] created an analytical model that examined the effects of layer thickness, surface angle, layer profile angle, and layer composition on the surface roughness of stereolithography-printed parts. Meanwhile, Ahn et al. [18] developed a technique for predicting the surface roughness of 3D-printed parts using geometric data from an STL file. They fabricated multiple specimens on an SLA 3500 machine and measured their surface roughness with a profilometer.

Mishra and colleagues [19], [20] conducted experiments to examine how six different process parameters affect the mechanical strength of parts produced by FDM). The parameters included air gap, part orientation, layer thickness, raster angle, contour number, and raster width. The significance of each process parameter was determined using an analysis of variance. The study's findings revealed that air gap, contour number, and part orientation had the most substantial impact on the parts' strength. Bharat and colleagues [21] examined how various process parameters, such as layer thickness, air gap, road width, build orientation, and model temperature, affect the surface finish of FDM-built parts. The study employed a fractional factorial design with two levels for each factor. The results indicated that part orientation and layer height had the main impact on surface quality, with a part orientation of 70° and layer thickness of 0.007" yielding the best surface finish. Model temperature, air gap, and road width had minimal effect on the surface finish of FDM parts. In a similar study, Garg et al. [22] investigated the effects of part orientation on the dimensional accuracy and surface finish of FDM ABS P430 parts at seven different angles (0°, 15°, 30°, 45°, 60°, 75°, and 90° about the Y-axis). They found that part orientation had a considerable influence on both dimensional accuracy and surface finish, with the most desirable outcomes obtained at a 45° angle. The impact of model temperature, layer thickness, and part fill style on the surface roughness of FDM-built parts was studied by Daniel Horvath et al. [23]. All factors were found to have a significant effect on surface roughness, with layer thickness having the greatest impact. Reducing the layer thickness resulted in decreased roughness. Peârez et al. [24] also investigated surface roughness and dimensional accuracy in ABS P400 parts, creating four prototypes with different slope variations. Past studies have primarily concentrated on creating different methods for estimating surface roughness in AM processes. However, there has been minimal research on predicting surface roughness in AM utilizing heterogeneous sensors and data-driven techniques. To fill this void in research, a new data-driven predictive modeling technique fitted in machine learning has been introduced to predict the surface roughness of AM components using FFF.

2.1. Overview of Fused Deposition Modelling

FDM is a 3D printing technology that works by extruding a thin strand of molten material, typically thermoplastic, through a heated nozzle. The nozzle is mounted on a movable arm, which moves in the X, Y, and Z directions according to the design specifications of the 3D model [25]. The material is deposited layer by layer, with each layer fusing to the previous one to create a solid object. The FDM process with the components (see Fig 1)

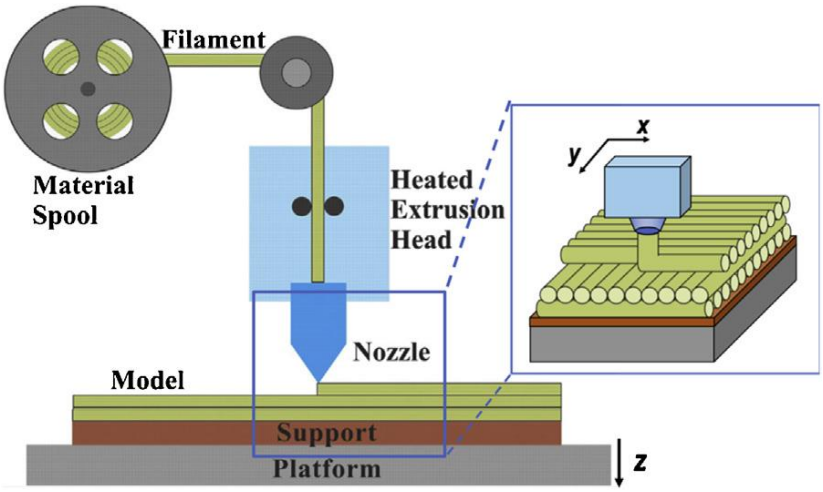

Fig. 1. FDM procedures of the 3D printing [25].

The process starts with the design of a 3D model using CAD software. The 3d model design is then convert into a format that can be read by the 3D printer, typically an STL file. The 3D printer software then analyzes the design and creates a toolpath, which is a set of instructions that tell the printer where and how to deposit the material to create the object.
The material used in FDM is typically a filament, which is a long, thin strand of thermoplastic material, such as ABS or PLA. The filament is fed into the printer through a spool and is heated to a melting point. The melted material is then extruded through the nozzle in a controlled manner, forming the object layer by layer. During the printing process, the object is supported by a platform, which can be either fixed or movable, depending on the printer design. As each layer is deposited, the platform is lowered or moved, allowing the next layer to be added. FDM 3D printers can produce objects with a high level of detail and accuracy, making them useful for a variety of applications, from rapid prototyping to producing end-use parts.

3. Experimental work

3.1 Material

PLA and PLA+ are two types of 3D printing filaments that are widely used. PLA is a biodegradable and environmentally friendly material that is typically derived from corn starch or sugarcane. On the other hand, PLA+ is an advanced version of PLA that boasts enhanced physical properties like increased strength, durability, and heat resistance. Numakers Company procures the PLA+ material for all experimental work.

PLA is crafted from natural and renewable resources such as sugarcane or cornstarch. To enhance its strength and durability, PLA+ is created by adding substances like carbon fiber, metal particles, or other polymers. The result is a stronger and more durable material that can withstand higher stresses without breaking or cracking. PLA+ is particularly useful for printing objects that require more strength, durability, and resilience, and it retains its shape and physical properties even at temperatures up to 90 degrees Celsius. Its improved adhesion properties make it less prone to warping and ideal for printing large objects. Additionally, PLA+ has best layer sticking and less shrinkage with less warpage than PLA, which change to a printed object that is closer to the same size and shape, with less warping or distortion during the 3D printing. Finally, PLA+ has a matte finish due to the natural additives in the material [26]–[28].Both PLA and PLA+ are great options for 3D printing. PLA is suitable for general-purpose printing, whereas PLA+ is more appropriate for printing objects that require greater strength, durability, and resistance to heat. PLA+ has enhanced properties compared to PLA, such as improved strength, durability, and heat resistance, making it the preferred material for printing high-performance objects. However, it is slightly more difficult to print with than PLA, and it is also more expensive due to the added additives. PLA+ is a thermoplastic polymer that is commonly utilized in fused deposition modeling. It is an eco-friendly material that is fully biodegradable and produced from renewable resources obtained from corn starch fermentation. Additionally, it is cost-effective and offered in a range of colors. [29], [30] provides information on the properties of PLA. In FDM, the print quality can be impacted by several process parameters, including layer thickness, nozzle temperature, ,print speed, infill density, print orientation, shell thickness, and printing pattern. Only the parameters that directly affect surface roughness and mechanical properties are considered, which includes layer thickness, infill density, and nozzle temperature. These parameters, along with their corresponding levels for an FDM 3D printer with a 0.4 mm nozzle diameter, are chosen using trial-and-error models. Table 1 presents the selected process parameters.

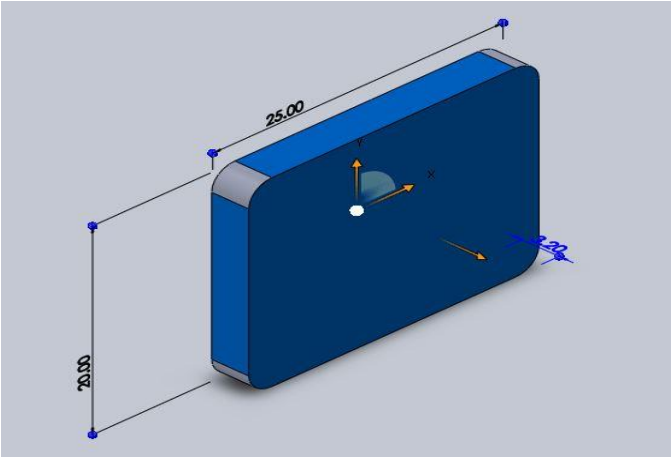

Fig 2. Schematic Diagram of 3D sample parts with Geometry 25x20x3.2 mm³.

The experiment keeps all other parameters at a constant value while focusing on layer thickness, infill density, and nozzle temperature as the main process parameters. The printing speed, traveling speed, printing pattern, and shell thickness are also set to predetermined values. No supports are needed for printing the CAD models, so they are disabled. An orthogonal array (OA) is generated using MINITAB L25 software, which uses a 5-level Taguchi design with 5 factors. The L25 design is selected, resulting in a 5x5 array presented in Table 1. The specimens developed in a SolidWorks CAD model have dimensions of 25*20*3.2 mm³. (see in fig 2)

3.2 Taguchi Method

Genichi Taguchi developed the Taguchi method, which aims to reduce process variation through a robust design of experiment and produce very high-quality products at a low cost for manufacturers. The method involves using a taguchi orthogonal array to organize the parameters that affect the process and the dimensions at which they are varied. The Taguchi method differs from the factorial design in that it only tests pairs of combinations, rather than all possible combinations. This approach is useful for identifying which factors have an impact on product quality while minimizing the amount of experimentation required, thereby saving time and resources. The proposed experimental design by Taguchi is discussed in reference [31].

The Taguchi Orthogonal Array (OA) design is a fractional-factorial model that ensures all levels and factors are equally considered. This allows for independent evaluation of factors, despite the functionality of the design. The Taguchi orthogonal array design L25 chosen in Table 1 shows the orthogonal array selected for the parameters and levels.

Table1: Control factors and different levels used for the Experiments

Parameters	L1	L2	L3	L4	L5
Printing Speed	50	60	70	80	90
Nozzle Temperature	200	207.5	215	222.5	230
Infill Density %	35	40	45	50	55
Layer Height	0.12	0.14	0.16	0.18	0.20

3.3 Fabrication and experimental setup

A total of 25 samples were printed according to the Taguchi L25 orthogonal array, as illustrated in Figure 4. These samples were printed using an Ender 3 3D printer, which is see in Figure 3. The specifications of this 3D printer are provided in Table 2. To test the surface roughness of the PLA+ material printed part, the Taylor Hobson surface roughness tester equipment was used. The components that were fabricated underwent testing using the Taylor Hobson machine shown in Figure 5, which has a range of approximately 0.05 to 12.25 um and is used in battery connectivity operations. Before testing the fabricated parts, it was necessary to check whether the diamond tip connected to the stylus was straight or not. Additionally, the surface roughness of the given sample base plate, which measured 6 um, was examined. Surface roughness was tested in three different positions of the sample parts, and the average of all three positions was taken to determine the final surface roughness (Avg), as shown in Table 3.

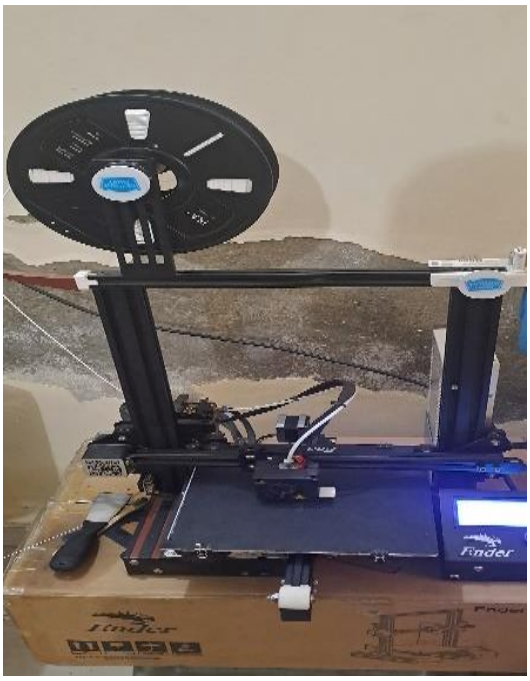

Fig 3. Ender-3 3D printer machine

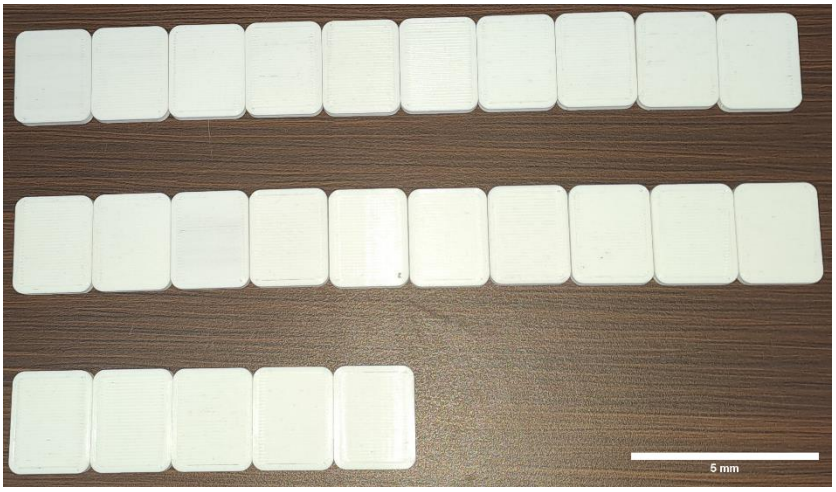

Fig 4. 3d Printed sample parts

Fig 5. Taylor Hobson surface roughness tester with printed sample parts

Table 2: Specification of Ender-3 3D printer.

S.No.	Parameter	Type/Size
1	Bed size	235 * 235
2	Bed type	Heated
3	Max travel	X= 235, Y = 235. Z = 250
4	Nozzle size	0.4 mm
5	File supported	G code
6	Material Supported	PLA, PLA+, ABS
7	Display size	2.5 Inch
8	Max speed	120 mm/s
9	Power supply	220 – volt AC, 240Watt

Table 3: Experimental Result of surface roughness in different Parameters Taguchi L25 orthogonal array.

Exp No.	Printing Speed	Nozzle Temperature	Infill Density	Layer height	SR (Ra1)	SR (Ra2)	SR (Ra2)	SR Average
1	50	200	35	0.12	4.24	4.3	4.08	4.20
2	50	207.5	40	0.14	5.72	5.86	5.25	5.61
3	50	215	45	0.16	6.50	6.31	6.21	6.34
4	50	222.5	50	0.18	7.21	7.88	7.46	7.51
5	50	230	55	0.2	9.54	9.36	8.94	9.28
6	60	200	40	0.16	6.44	7.1	6.32	6.62
7	60	207.5	45	0.18	7.31	7.84	8.44	7.86
8	60	215	50	0.2	8.41	8.19	8.75	8.45
9	60	222.5	55	0.12	4.12	4.365	4.62	4.4
10	60	230	35	0.14	5.84	5.7	5.81	5.78
11	70	200	45	0.2	8.89	9.12	9.4	9.13
12	70	207.5	50	0.12	4.14	4.68	4.84	4.55
13	70	215	55	0.14	5.94	5.34	6.24	5.84
14	70	222.5	35	0.16	6.34	6.84	6.94	6.70
15	70	230	40	0.18	8.154	8.54	8.21	8.30
16	80	200	50	0.14	6.25	6.32	6.05	6.20
17	80	207.5	55	0.16	7.45	7.64	6.84	7.31
18	80	215	35	0.18	8.54	8.89	8.24	8.55
19	80	222.5	40	0.2	7.55	7.3	7.95	7.6
20	80	230	45	0.12	5.15	5.89	5.25	5.43
21	90	200	55	0.18	9.32	9.75	8.95	9.34
22	90	207.5	35	0.2	10.25	9.98	9.84	10.02
23	90	215	40	0.12	7.1	6.84	6.35	6.76
24	90	222.5	45	0.14	6.65	6.9	6.25	6.6
25	90	230	50	0.16	8.21	8.75	8.1	8.35

3. Result and discussion

The generated machine learning model considers a total of four input parameters, with surface roughness measurement serving as the output. The input data or features consist of the following printing parameters: printing speed, Infill Pattern (IP), nozzle temperature, and Layer Thickness (LT), with a raster angle of 0 degrees. These parameters were obtained through the experimental procedure outlined in the experimental work, which was then used to calculate the surface roughness output of the 3D printed sample parts. Figure 6 displays the correlation between the input and output variables of the experimental datasets, while Figure 7 shows the Heatmap correlation created using Python programming.

3.1 Effect of printing parameter in surface roughness

ISSN 2063-5346

Layer height. Printing speed, nozzle temperature and Infill density all the four parameters shown different impact on the surface roughness which is shown in the figure 6.

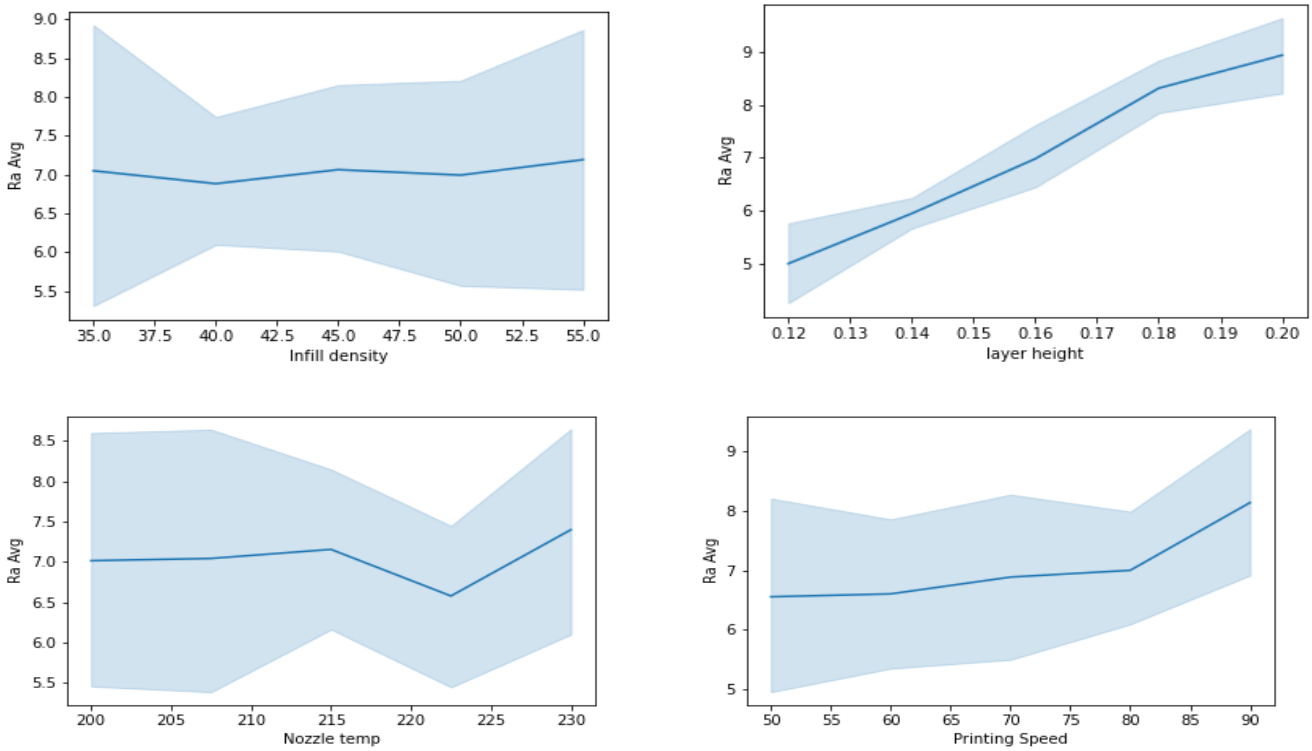

Fig. 6. show variation of different parameters with surface roughness (Ra)

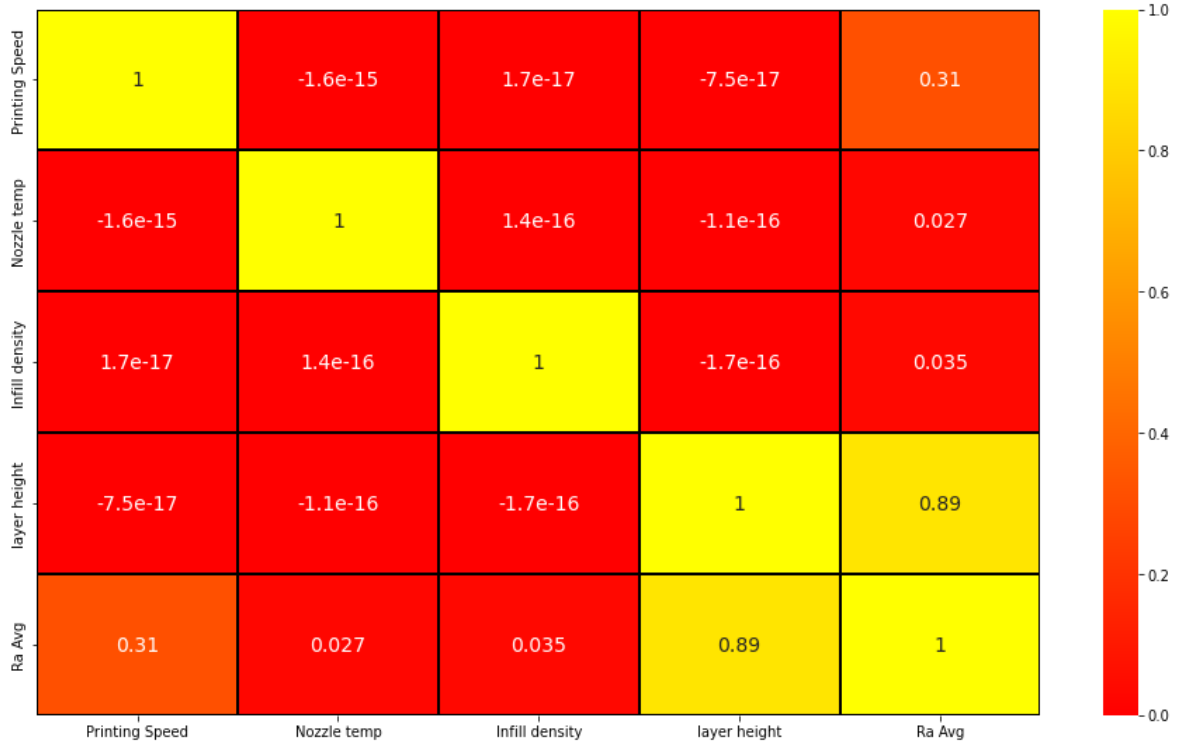

Fig. 7. Heatmap of correlation with surface roughness with other parameters

This heatmap gives the percentage of correlation of input features to the output features(Surface Roughness). This heatmap gives the correlation in percentage which is given below

1. Printing speed is 31% corr. With Ra
2. Nozzle temperature is 2.7% corr. with Ra
3. Infill density is 3.5% corr. with Ra
4. Layer height is 89% corr. With Ra

The correlation analysis reveals that layer height has a very strong correlation with surface roughness, at approximately 89%. Conversely, infill density and nozzle temperature have the least correlation with surface roughness. Infill density primarily affects tensile strength rather than surface roughness, as it fills the inside of the material in 3D printed parts. Nozzle temperature also has minimal correlation, as the melting temperature of the PLA+ polymer used in the experiment is around 200-230 degrees Celsius, as indicated on the filament coils purchased from the Numkers company. Given these findings, we eliminated the two least correlated parameters, nozzle temperature and infill density, and focused on the highly correlated layer height parameter. The dataset was then split into training and testing sets, with 75% allocated for training and 25% for testing. The machine learning model was applied to the datasets.

3.2 ML modelling

The specimens were manufactured with FDM 3D printing and tested for surface roughness on a Taylor Hobson surface roughness tester. Different machine learning is used to predict the surface roughness of the 3D printed parts, which show different results in the training and testing datasets . Working procedure of the ML is shown by the flow chart in the figure 8.

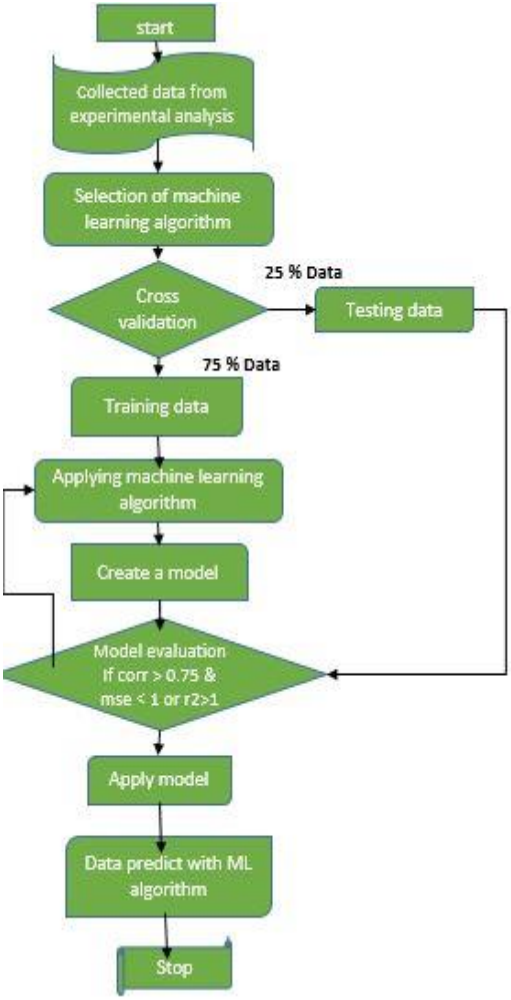

Fig 8. Working procedure of different ML created by flow chart

Table 5. Training and testing result in different Ml algorithm

Machine Learning algorithm	Training score (%)	Testing score
Linear regression	85.0	84.29

Support vector machine	3.08	-3.099
Random forest repressor	94.45	95.45
Gradient Boosting regression	98.871	36.67

Random forest regression shows a better-fitted algorithm on training and testing datasets, which is shown in the above table 5 all over the machine learning I am also checking the evaluation of all 4 algorithms. To determine whether a machine learning regression model is good or not, you can use various evaluation metrics, such as MSE: which measures the average squared difference between the predicted and actual values. A lower value of MSE indicates a better model. R-squared (R2) score: It represents the proportion of variance in the target variable that is explained by the independent variables. A higher value of R2 indicates a better model. RMSE: It is the square root of MSE and represents the average distance between the predicted and actual values. A lower value of RMSE indicates a better model.

Random forest regressor is minimum mse 0.1255 and maximum r2_Score with 0.9685 as compared to the linear regression and the other two algorithms give more error as compared to the random forest, the overall best algorithm is random forest regressor because it has better training accuracy, testing accuracy, less mean squared error and also great r2_score of all the ML algorithm. After applying the best ML model make a user interface to predict the surface roughness by using the saved model.

All the actual and predicted data are shown by the graph in Figure 9 in different machine learning algorithms. This graph shows a graphical representation of all detailed understanding of the actual and predicted data.

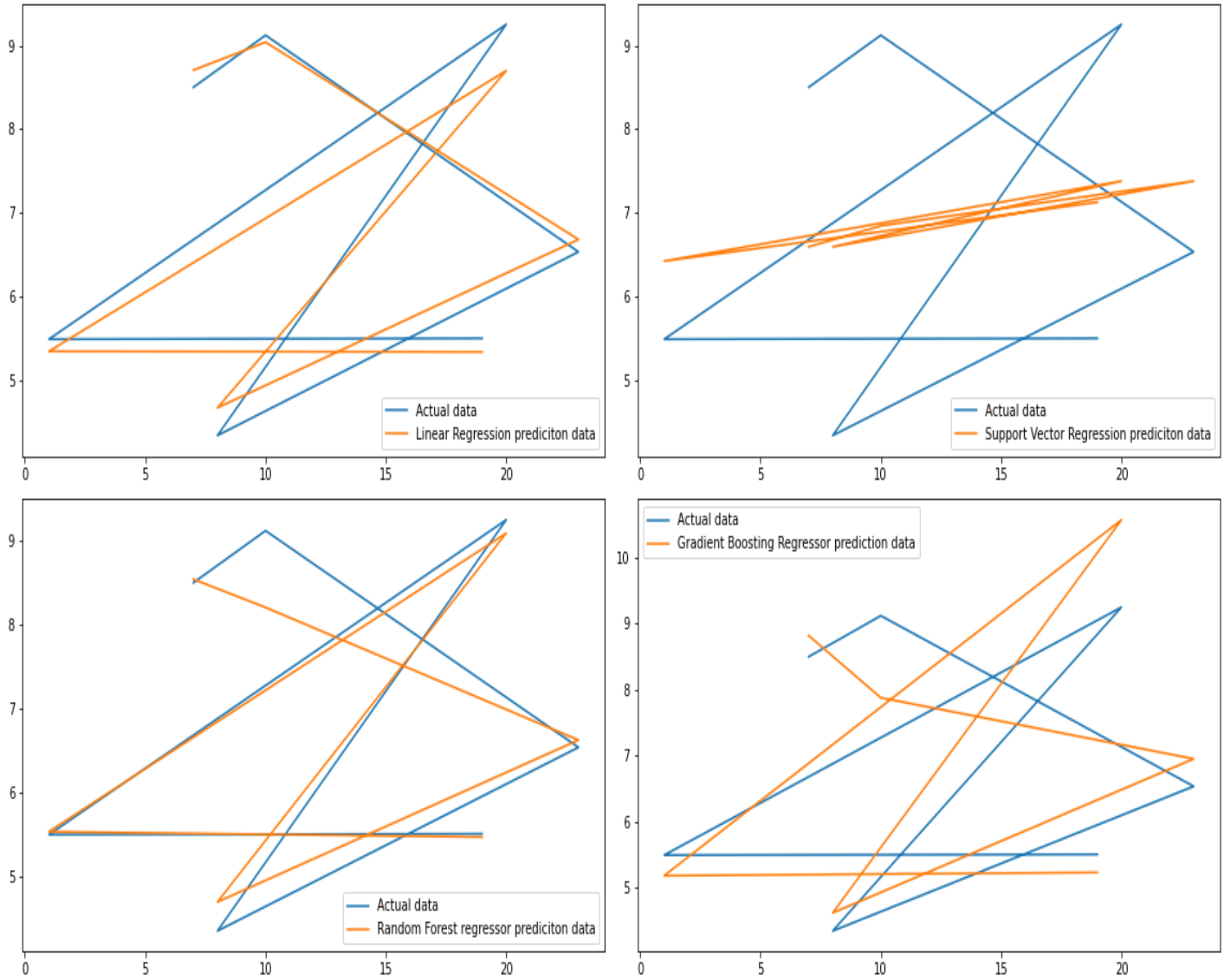

Fig 9. Graphical representation of actual data and predicted data of different machine learning algorithm

Random forest regression algorithm gives the prediction result of the experimental data with minimize error, overall all the 4 machine learning algorithm. All the code of the machine learning is written in jupyter notebook and fig. 9 is coding generated graphical representation of all machine learning

5. Conclusions and future works

The surface roughness was measured and 3D samples were fabricated successfully using the L25 orthogonal array. The study proposed a data-driven framework that utilized machine learning to predict surface roughness and dimensional accuracy, and obtain optimal process parameters. Verification experiments showed that the optimized results were consistent with experimental results, indicating the effectiveness and feasibility of the proposed method. The study concluded that using machine learning to study process parameters and obtain optimal settings for surface roughness is a viable approach.

1. Surface roughness is directly depend on the parameters of layer height and printing speed, With the increase of layer height, Printing speed, that directly effect to increase the surface roughness of the 3d printing parts. Layer height is 89% positive correlation with the surface roughness and printing speed is 30% correlation with the surface roughness. Surface roughness is minimum gives less wear with the meshing parts
2. Infill density and nozzle temperature gives constant relation between the surface roughness's does not gives any type of effect in the surface roughness. Its approx. 0.030 % correlation with the surface roughness.
3. An ensemble machine learning algorithm random forest repressor is less MSE approx. 0.1255 and maximum r2_Score approx. 0.9685 in all the used machine learning algorithm, with training accuracy is 94.45 and testing accuracy 0.9685 which is also shown in the visualization graph in the figure number 9.

Upcoming work involves collecting more data to increase the robustness of the models. Furthermore, new input parameters such as nozzle diameter will be incorporated. Additionally, experimental data will also be utilized in conjunction with or in lieu of numerically generated data to enhance the predictive models.

References:

[1] "IannGibsonn· DaviddRosen BrenttStucker Additive Manufacturing Technologies 3D Printing, Rapid Prototyping, and Direct Digital Manufacturing Second Edition."

[2] S. Ford and M. Despeisse, "Additive manufacturing and sustainability: an exploratory study of the advantages and challenges," *J Clean Prod*, vol. 137, pp. 1573–1587, Nov. 2016, doi: 10.1016/j.jclepro.2016.04.150.

[3] Y. Deshpande, A. Andhare, and N. K. Sahu, "Estimation of surface roughness using cutting parameters, force, sound, and vibration in turning of Inconel 718," *Journal of the Brazilian Society of Mechanical Sciences and Engineering*, vol. 39, no. 12, pp. 5087–5096, Dec. 2017, doi: 10.1007/s40430-017-0819-4.

[4] D. Wu, Y. Wei, and J. Terpenny, "Surface Roughness Prediction in Additive Manufacturing Using Machine Learning," 2018. [Online]. Available: http://www.asme.org/about-asme/terms-of-use

[5] B. N. Turner, R. Strong, and S. A. Gold, "A review of melt extrusion additive manufacturing processes: I. Process design and modeling," *Rapid Prototyping Journal*, vol. 20, no. 3. Emerald Group Publishing Ltd., pp. 192–204, 2014. doi: 10.1108/RPJ-01-2013-0012.

[6] U. Shaha, "Optimizing Process Parameters of FDM Printer using Design of Experiments Method," *International Research Journal of Engineering and Technology*, 2021, [Online]. Available: www.irjet.net

[7] F. Lavecchia, M. G. Guerra, and L. M. Galantucci, "Chemical vapor treatment to improve surface finish of 3D printed polylactic acid (PLA) parts realized by fused filament fabrication," *Progress in Additive Manufacturing*, vol. 7, no. 1, pp. 65–75, Feb. 2022, doi: 10.1007/s40964-021-00213-2.

[8] P. K. Rao, J. Liu, D. Roberson, Z. Kong, and C. Williams, "Online Real-Time Quality Monitoring in Additive Manufacturing Processes Using Heterogeneous Sensors," *Journal of Manufacturing Science and Engineering, Transactions of the ASME*, vol. 137, no. 6, Dec. 2015, doi: 10.1115/1.4029823.

[9] R. Anitha, S. Arunachalam, and P. Radhakrishnan, "Critical parameters in¯uencing the quality of prototypes in fused deposition modelling."

[10] D. Popescu, A. Zapciu, C. Amza, F. Baciu, and R. Marinescu, "FDM process parameters influence over the mechanical properties of polymer specimens: A review," *Polym Test*, vol. 69, pp. 157–166, Aug. 2018, doi: 10.1016/j.polymertesting.2018.05.020.

[11] M. Domingo-Espin, J. M. Puigoriol-Forcada, A. A. Garcia-Granada, J. Llumà, S. Borros, and G. Reyes, "Mechanical property characterization and simulation of fused deposition modeling Polycarbonate parts," *Mater Des*, vol. 83, pp. 670–677, Oct. 2015, doi: 10.1016/j.matdes.2015.06.074.

[12] S. Nasiri and M. R. Khosravani, "Machine learning in predicting mechanical behavior of additively manufactured parts," *Journal of Materials Research and Technology*, vol. 14, pp. 1137–1153, Sep. 2021, doi: 10.1016/j.jmrt.2021.07.004.

[13] M. A. Mahmood, A. I. Visan, C. Ristoscu, and I. N. Mihailescu, "Artificial neural network algorithms for 3D printing," *Materials*, vol. 14, no. 1. MDPI AG, pp. 1–29, Jan. 01, 2021. doi: 10.3390/ma14010163.

[14] S. K. Everton, M. Hirsch, P. I. Stavroulakis, R. K. Leach, and A. T. Clare, "Review of in-situ process monitoring and in-situ metrology for metal additive manufacturing," *Materials and Design*, vol. 95. Elsevier Ltd, pp. 431–445, Apr. 05, 2016. doi: 10.1016/j.matdes.2016.01.099.

[15] A. Boschetto, V. Giordano, and F. Veniali, "3D roughness profile model in fused deposition modelling," *Rapid Prototyp J*, vol. 19, no. 4, pp. 240–252, 2013, doi: 10.1108/13552541311323254.

[16] A. Boschetto and L. Bottini, "Roughness prediction in coupled operations of fused deposition modeling and barrel finishing," *J Mater Process Technol*, vol. 219, pp. 181–192, 2015, doi: 10.1016/j.jmatprotec.2014.12.021.

[17] P. Reeves and ac Cobb, "REDUCING THE SURFACE DEVIATION OF STREOLITHOGRAPHY USING AN ALTERNATIVE BUILD STRATERGY."

[18] D. Ahn, H. Kim, and S. Lee, "Surface roughness prediction using measured data and interpolation in layered manufacturing," *J Mater Process Technol*, vol. 209, no. 2, pp. 664–671, Jan. 2009, doi: 10.1016/j.jmatprotec.2008.02.050.

[19] S. B. Mishra, R. Malik, and S. S. Mahapatra, "Effect of External Perimeter on Flexural Strength of FDM Build Parts," *Arab J Sci Eng*, vol. 42, no. 11, pp. 4587–4595, Nov. 2017, doi: 10.1007/s13369-017-2598-8.

[20] S. B. Mishra, K. Abhishek, M. P. Satapathy, and S. S. Mahapatra, "Parametric Appraisal of Compressive Strength of FDM Build Parts," in *Materials Today: Proceedings*, Elsevier Ltd, 2017, pp. 9456–9460. doi: 10.1016/j.matpr.2017.06.203.

[21] M. R. Henderson, B. Vasudevarao, D. Prakash Natarajan, M. Henderson, and A. Razdan, "Sensitivity Of Rp Surface Finish To Process Parameter Variation," 2000. [Online]. Available: https://www.researchgate.net/publication/2467464

[22] A. Garg, A. Bhattacharya, and A. Batish, "On Surface Finish and Dimensional Accuracy of FDM Parts after Cold Vapor Treatment," *Materials and Manufacturing Processes*, vol. 31, no. 4, pp. 522–529, Mar. 2016, doi: 10.1080/10426914.2015.1070425.

[23] D. Horvath, R. Noorani, and M. Mendelson, "Improvement of Surface Roughness on ABS 400 Polymer Using Design of Experiments (DOE)," *Materials Science Forum*, vol. 561–565, pp. 2389–2392, Oct. 2007, doi: 10.4028/www.scientific.net/msf.561-565.2389.

[24] C. J. Luis Pérez, "Analysis of the surface roughness and dimensional accuracy capability of fused deposition modelling processes," *Int J Prod Res*, vol. 40, no. 12, pp. 2865–2881, Aug. 2002, doi: 10.1080/00207540210146099.

[25] J. Zhang, P. Wang, and R. X. Gao, "Deep learning-based tensile strength prediction in fused deposition modeling," *Comput Ind*, vol. 107, pp. 11–21, May 2019, doi: 10.1016/j.compind.2019.01.011.

[26] R. A. Ilyas *et al.*, "Natural Fiber-Reinforced Polylactic Acid, Polylactic Acid Blends and Their Composites for Advanced Applications," *Polymers*, vol. 14, no. 1. MDPI, Jan. 01, 2022. doi: 10.3390/polym14010202.

[27] R. A. Wach, P. Wolszczak, and A. Adamus-Wlodarczyk, "Enhancement of Mechanical Properties of FDM-PLA Parts via Thermal Annealing," *Macromol Mater Eng*, vol. 303, no. 9, Sep. 2018, doi: 10.1002/mame.201800169.

[28] F. Yu, T. Liu, X. Zhao, X. Yu, A. Lu, and J. Wang, "Effects of talc on the mechanical and thermal properties of polylactide," *J Appl Polym Sci*, vol. 125, no. SUPPL. 2, Sep. 2012, doi: 10.1002/app.36260.

[29] B. Wittbrodt and J. M. Pearce, "The effects of PLA color on material properties of 3-D printed components," *Addit Manuf*, vol. 8, pp. 110–116, Oct. 2015, doi: 10.1016/j.addma.2015.09.006.

[30] M. F. Gonzalez, R. A. Ruseckaite, and T. R. Cuadrado, "Structural Changes of Polylactic-Acid (PLA) Microspheres under Hydrolytic Degradation," 1999.

[31] O. Y. Venkatasubbareddy, P. Siddikali, and S. M. Saleem, "Improving the Dimensional Accuracy And Surface Roughness of Fdm Parts Using Optimization Techniques," *IOSR Journal of Mechanical and Civil Engineering*, vol. 16, no. 053, pp. 18–22, Dec. 2016, doi: 10.9790/1684-16053041822.

Proceedings of the Second International Conference on Applied Artificial Intelligence and Computing (ICAAIC 2023)
IEEE Xplore Part Number: CFP23BC3-ART; ISBN: 978-1-6654-5630-2

Recoloring Grayscale Images using GAN

Aeshita Mathur
Department of Computer Engineering
Delhi Technological University
Delhi, India
aeshitamathur@gmail.com

Ameesha Dabas
Department of Computer Engineering
Delhi Technological University
Delhi, India
ameeshadabas2002@gmail.com

Parikshit Rana
Department of Computer Engineering
Delhi Technological University
Delhi, India
parikshitrana123@gmail.com

Sanjay Kumar
Department of Computer Engineering
Delhi Technological University
Delhi, India
sanjay.kumar@dtu.ac.in

2023 2nd International Conference on Applied Artificial Intelligence and Computing (ICAAIC) | 978-1-6654-5630-2/23/$31.00 ©2023 IEEE | DOI: 10.1109/ICAAIC56838.2023.10140749

***Abstract*—In this paper, we intend to develop an efficient method for Colorizing Grayscale Images such that the output images are close to their real colors. The main objective is to produce a precise image should be produced, which means that the output image should be as close to its natural color as possible. In colorization, there is no aim to recover the ground truth color; rather, the aim is to create a plausible colorization that is useful to the user, even if it differs from the ground truth color.In order to solve this problem, we use Convolutional Neural Networks (CNN) and a variety of deep learning techniques. Instead of using vectors drawn at random from the probability distribution, we employ Conditional Generative Adversarial Networks (GAN). This will enable it to extract different features and understand the correlations between them in order to predict colored images.**

***Index Terms*—Deep Learning, Colorization, Gray-scale, Generative Adversarial Network, Convolutional Neural Networks, Feature Extraction, Transfer Knowledge,image-to-image translation**

I. Introduction

Colorization is the technique of adding colour to a gray scale image or video with the help of a computer. The procedure for adding colour to a grayscale image entails giving an image with just one dimensional variation three dimensional (RGB) pixel values. The mapping between intensity and colour is not unique, and colorization is ambiguous in nature, needing some level of human input or outside information since distinct colours might have the same luminance/ intensity value but differ in hue or saturation [1]. The purpose of colorization, it is vital to remember, is not to recreate the real ground truth colour, but rather to create a believable colorization that the user finds helpful, even if the colorization deviates from the actual ground truth colour. Considering how much information is lost when a colour image is reduced to its underlying grayscale representation (two out of the three colour dimensions), colorization might appear to be a daunting undertaking. Numerous hints for sound colorization are provided by the semantics of a picture scene. Because it uses scene semantics for picture categorization and object recognition, deep learning is a successful method for colorization. Note that the human eye would attempt to discern distinctions between two images if a true colour image and an artificial one were side-by-side. In recent times, machine learning and deep learning techniques have produced improved results for many real-life problems like computer vision, image processing, fake news detection, online social networks, and many others [2]–[7].

This paper intends to create an effective technique for ”colourizing grayscale images using Deep learning methods that will provide output images that are fairly accurate representations of their actual hues.

- The final image needs to be precise. Precise refers to how closely the colours in the produced image should match their actual natural state.
- It is crucial to remember that colorization's objective is to create a believable colorization that the user finds helpful even if the colorization deviates from the ground truth colour rather than to retrieve the actual colour of the ground truth.

A. Motivation

The task of colourizing a grayscale image is challenging. There is frequently no ”right” achievable hue given a certain visual. Due to how much information is lost when a colour image is converted to its underlying grayscale representation (two out of the three colour dimensions), colorization might appear to be a daunting undertaking. By enabling colorization of ancient, black-and-white photos and films and improving interpretation of CCTV camera footage, astronomical photography, and electron microscopy, uses of such a system offer a new kind of entertainment. Deep learning, which already makes use of scene semantics for picture categorization and object recognition, has the potential to be an effective tool for colorization. A manual method of colorization dates back to the early 19th century [8].The theories and techniques created in the area of colourizing grayscale photographs have been applied to improve the effectiveness of object detection systems. Motivations for Deep Architectures:

- Insufficient depth can hurt- The number of nodes in the graph that are necessary for shallow architecture (SVM, NB, KNN, etc.) calculations and parameter learning may

Authorized licensed use limited to: DELHI TECHNICAL UNIV. Downloaded on June 14,2023 at 05:01:30 UTC from IEEE Xplore. Restrictions apply.

increase significantly. Many functions that are efficiently represented in deep architectures cannot be efficiently represented in shallow ones.

- The brain has a deep architecture- Signals go from one part of the visual cortex to the next as it displays a series of regions, each of which includes a representation of the input. Be aware that brain representations fall somewhere between densely dispersed and entirely local. Only 1% of the brain's neurons are simultaneously engaged.
- Cognitive processes seem deep- Human conceptions and ideas are arranged hierarchically. It is in our fundamental nature to first master more basic notions before combining them to express more complex ones.

B. Goals

Generative Adversarial Networks(GAN) are used to colourize photos with the goal of minimising the designer's labor-intensive manual colorization of the grayscale images. For the same objectives, earlier systems employed basic regression and other related techniques. Precision is the second significant issue that we address in our dissertation. Our aim was to design a Web Application that receives a grayscale image as input and creates a colourful image as output. The process of colouring grayscale photographs is a very challenging one. In actuality, there have been several methods used throughout history that have not produced positive outcomes.

In this thesis, we provide a fully automated colorization method that generates accurate hues. We embrace the underlying ambiguity of the problem by expressing it as a classification job and leverage the class rebalancing training time to boost the diversity of colours in the output . The achieved colorization results are excellent and bright. Additionally, because the process is totally mechanical, there is no need for human involvement; all that is required of the user is the input to be coloured.

II. Related Work

A comprehensive study by Žeger et. al. [9] has been done on algorithms with various architectures and levels of user guidance, taking into account objective image quality metrics as well as colorization.time. Due to the combination of human effort and technological advancements regarding neural networks, the user-guided colorization neural network from Zhang et al. [10] provided the most visually convincing results. It was found, however, that the colorization method required extensive human intervention and a great deal of time.

In their method, Nazeri et. al. employed a conditional Deep Convolutional Generative Adversarial Network (DCGAN) in a completely generalized colorization operation [11]. CIFAR10 and Places365 datasets were used for training the network. A comparison was made between the results of the generative model and those of a conventional deep neural network.

In 2014, Goodfellow et. al. introduced Generative Adversarial Networks (GANs) as a novel kind of generative model [12]. During the discussion, it was mentioned that a GAN consists of two smaller networks, the generator and the discriminator. The generator's job is to produce unrecognizable results. The discriminator problem consists of identifying whether the sample belongs to the model distribution generated by the generator, or to the original data distribution. Both subnetworks are trained simultaneously until the generator reliably produces results that the discriminator cannot categorize.

With no manual intervention, Wan et. al. opted for an innovative method of colorizing grayscale photographs [13]. A neural network was used to train the colorization model for the training set by selecting interest points based on SLIC superpixels. In order to colorize input grayscale images, the trained model should first colorize the interest points and propagate the color to the entire image.

Using 3D Printed Low-Index Nanopillars, Wang et. al. created full-color and grayscale paintings [14]. As a result of their study, two-photon polymerization lithography-based 3D printing gave users access to a complete 3D color spectrum with control of hue, saturation, and brightness, as well as producing grayscale shades by adjusting the height, diameter, and spacing of nanopillar arrays [15]

For the colorization process, Zhong et. al. proposed a GECNet-based model based on colorization [16]. As part of the training samples, GECNet converted the input visible images into grayscale images. To retain the features of the original infrared image as well as the rich texture and semantics provided by the visible version, the researchers proposed a feature fusion module. Through cross-modal image generation, their method effectively addressed the modality gap issue in VI-ReID.

A dissertation by Jiancheng An examined the ability to automatically colorize grayscale images using VGG-16 and CNN [17]. In their study, they concluded that color rebalancing is sometimes useful in correcting saturated colors in certain images. Jiancheng proposed to utilize the VGG-16 CNN model based on classification with loss of cross-entropy next year in accordance with the same study [18]. This model produced efficient results.

III. Proposed Methodology

The flowchart shown in Fig. 1 illustrates the method we used to complete the work.

A. Upload Grayscale Image

In order to properly run the model, a grayscale picture is uploaded to the website and further processed by a Python script to change its dimensions.

B. Pre-processing of the uploaded image

The uploaded image is transformed during this stage into a format that may be altered during following stages.

- Rotate- By rotating the image, the model ensures it does not depend on the image slope for prediction.
- Contrast stretching- The pixel intensity values are stretched to cover the desired range of values using full contrast stretching.
- Histogram Equalization- This technique distributes pixels over a wide range of intensities by utilizing non linear,

Authorized licensed use limited to: DELHI TECHNICAL UNIV. Downloaded on June 14,2023 at 05:01:30 UTC from IEEE Xplore. Restrictions apply.

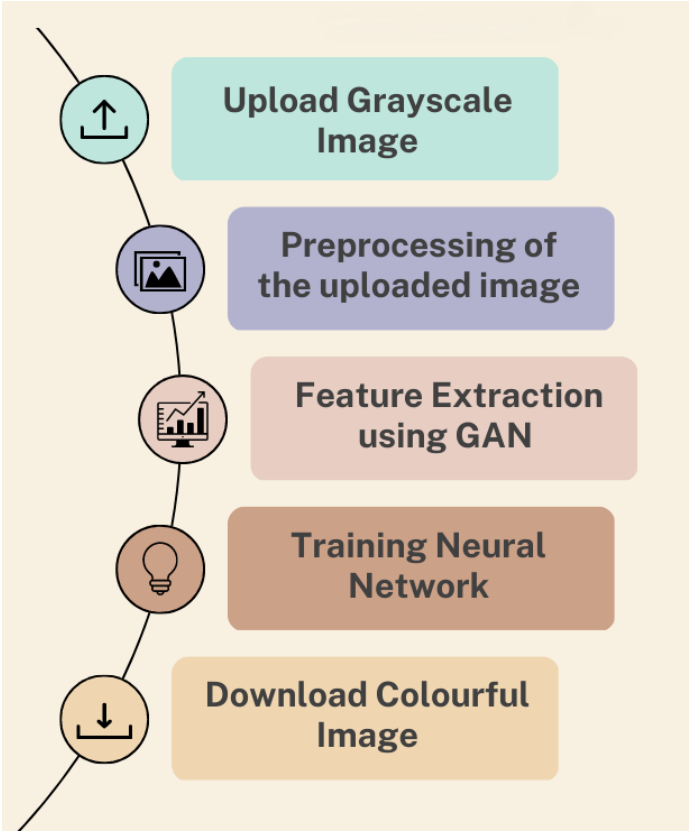

Fig. 1. Flowchart of Methodology applied.

non monotonic transfer functions. This parameter changes the intensity histogram's shape.

C. Feature Extraction using GAN

Randomly produced noise vectors serve as the generator network's input in GANs. Nevertheless, such a GAN will not be effective in the job of picture colorization since our GAN is not intended to create images from random vectors but rather to add colours to already-existing photographs containing only one channel (Black and white). So, adding three RGB channels with appropriate intensities for each colour channel is the fundamental challenge for our GAN. This problem is solved by using conditional GANs, which have one intensity channel and accept black and white pictures as inputs (technically, G(0z—x)). A modified discriminator input is also required for conditional GANs.

Grayscale image and produced image, as well as grayscale image and original picture, are the two inputs that the discriminator accepts. Next it decides if the pairs are bogus or real.

1) Method: The issue that we're working to resolve falls under the umbrella of image-to-image translation with high-dimensional input to high-dimensional output mapping. Regression is really being done at the pixel level with an output condition whose structure is comparable to the input. Hence, the network must have very high spatial similarity between input and output, as well as offer information on each pixel's colour in the original grayscale image.

2) GAN Architecture: This model's network is built using "fully connected networks". Convolutional layers are used in the Generator. Instead of pooling layers, the image is downscaled till it is a vector with a size of 2x2 pixels. The compressed portion is then expanded via upsampling to bring it up to the dimension of the input set of 32 x 32 pixels. A specific kind of deep networks termed encoder-decoder networks, which incorporate encoding and decoding networks for contracting and expanding, and therefore rebuilding the input, are what inspired this approach. This method facilitates network training without using a lot of memory.

The Generator accepts X as an input, which is a dimensioned black and white picture (32 x 32 x 1). The downsampling starts with kernels that have size as 1 and stride as 1. Furthermore, it is then compressed to an image of size (2x2) using a kernel and stride size of 2. After the first layer, this is repeated four more times to create a matrix of dimensions 2 by 2 by 512. With the exception of the last layer, the expansion phases include upsampling the matrix using kernel size 2 and strides 2. To preserve the structural integrity of the image, I and n-i layers were concatenated. For Generator's robust training, 0.5 scale dropouts are performed in the first and second expanding layers.

For improved training, batch normalisation is performed. LeakyReLU with a slope of 0.2 was employed in our model since it performed better than ReLU activation function. Convolution with a kernel size of 1 and a stride of 1 is performed in the last layer to create the picture dimensions (32 x 32 x 3). We utilize the "tanh" activation function since it has been shown to be more effective than linear activation functions. It produces results in the form of a matrix with values ranging from -1 to 1. During training, the model minimizes the cosine distance between the original image and the predicted image.

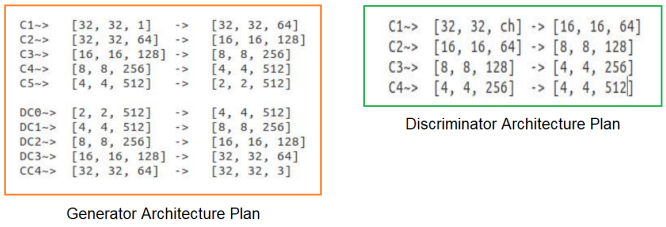

Fig. 2. Generator and Discriminator Architecture Plan.

In order to create the coloured picture for the discriminator, we foremost combine the grayscale image, forecast grayscale image, and ground truth image on the channel axis. Using a convolutional layer with a filter size of 2 x 2 and strides of 2, we downscale the matrix sequentially. Every layer does Batch Normalization, and each layer has a Leaky ReLUactivation function with a slope of 0.2. The final layer is flattened after which a hidden layer consisting of 128 units and an output layer comprising units are linked. The last layer's activation

Authorized licensed use limited to: DELHI TECHNICAL UNIV. Downloaded on June 14,2023 at 05:01:30 UTC from IEEE Xplore. Restrictions apply.

function, known as a ”sigmoid,” estimates the likelihood that the input picture belongs to the anticipated or actual image.

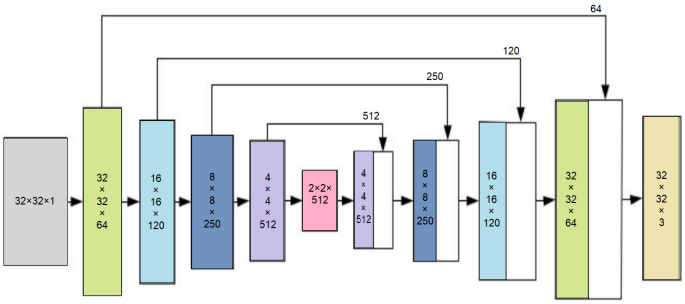

Fig. 3. Generator Network visualization.

D. Training Neural Network

We have used Adam’s optimizer to our model. The optimizer’s learning rate is held to 0.0001. For the implementation of our model, we used the free and open-source Python libraries Tensorflow and Keras. We used the free GoogleCoLabGPU to train the model. Our batch consists of 50 photos.

1) Batch Normalization: The ‘Mode collapse’ phenomena is thought to make the GAN challenging to train. The generator was successful in tricking the discriminator into accepting the same produced output as true throughout the model collapse10 phase. As a result, the generator consistently produces similar outputs, which makes the generation lack variation. This behaviour is an undesirable situation during the GANs’ training phase. We employ batch normalisation, which has been shown to lower the likelihood of mode collapse, to prevent the aforementioned problem. Nevertheless, as indicated by, batch normalisation is avoided in the discriminator and generator’s first layer as well as its final layer.

2) All Convolutional Net: Strided convolutions are utilised rather than spatial pooling. Hence, strided convolutions enable the model to learn its own upsampling and downsampling rather than relying on predetermined downsampling and upsampling. This method has been demonstrated to improve training efficiency and aid in the network’s learning of key invariances using only convolutional layers.

3) Leaky ReLu Activation Function: We have employed the LeakyReLU activation function whenever activation function is used since it performs better than conventional ReLU.

4) Mode Collapse avoidance strategy: In our work, we discovered that the generator produced images utilising the same colour scheme and colour grids at various points during the training. This was the result of ”mode collapse,” as it was previously described. In addition to batch normalisation, we employed a cutting-edge strategy in which we trained the generator to avoid utilising the same colours repeatedly. In a way, this serves as the generator’s ”reverse training,” as we instinctively instruct it to steer clear of consistently employing the same colours.

E. Generate Output

We have a grayscale layer as input once model training is complete, and we anticipate the model to forecast an RGB image as output.

IV. Result

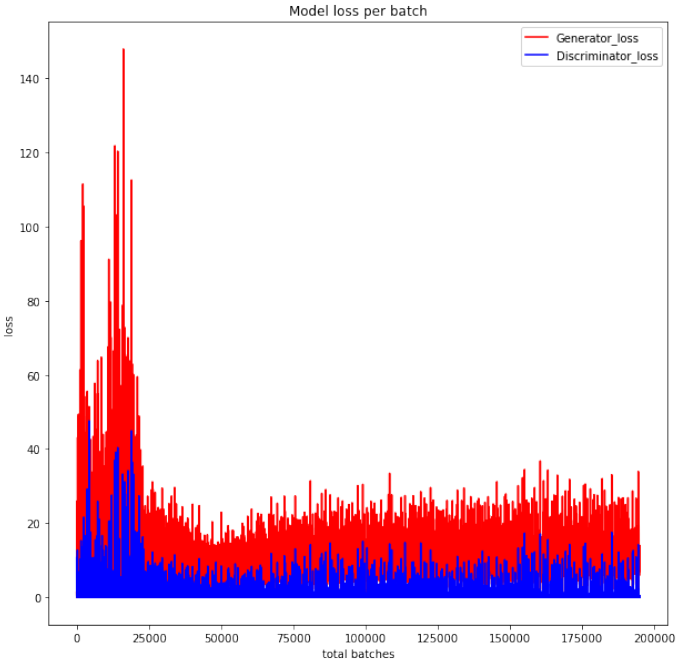

Fig. 4. Graphical representation of model loss per batch.

Fig. 4 shows the losses of both the generator and the discriminator of the implemented model. As can be observed from the graph, initially the generator loss is very high while the discriminator loss is very low thereby signifying the convergence failure problem and thus showing that the discriminator was winning at the start. As the number of batches increases, it can be seen that a state of near-equilibrium is achieved as the losses of both generators and discriminators seem to achieve a low value, and their relative difference also decreases.

We can deduce the following from observations collected from Fig. 5:

- In addition to producing promising results, the software provides some useful insights.
- Even though the output images may not represent the ground truth colors, they are vivid and accurate.
- In terms of performance, the software was able to handle a variety of images, such as human life, infrastructure, nature, etc.
- As the random inputs demonstrate, overfitting is not present.

V. Conclusions

The accuracy of the images mainly depends on the architecture of the model used and the training of the model, and

Authorized licensed use limited to: DELHI TECHNICAL UNIV. Downloaded on June 14,2023 at 05:01:30 UTC from IEEE Xplore. Restrictions apply.

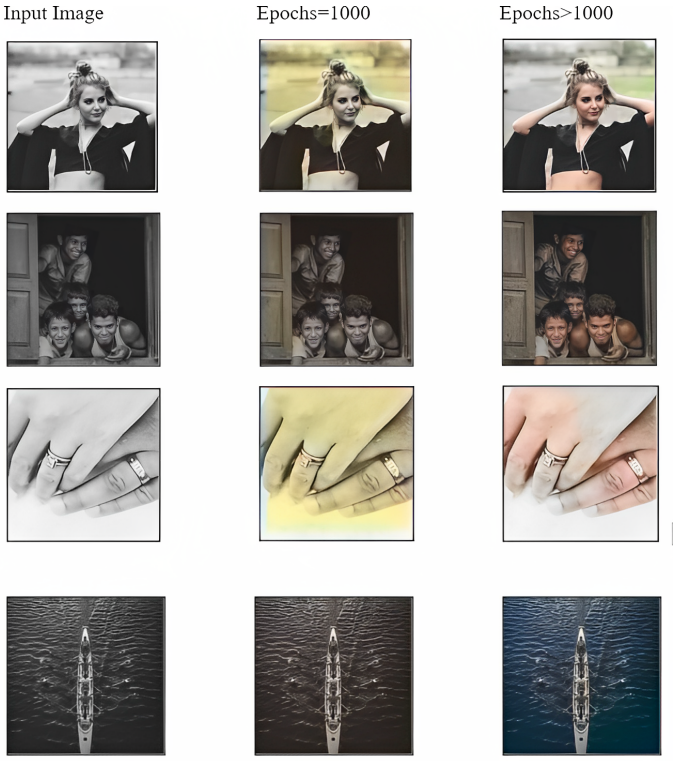

Fig. 5. Colorization of input image with respect to epochs.

as you can see the more promising results were obtained as the number of epochs increased. With the help of generative adversarial networks, we were able to successfully automatically colourize grayscale photos to a visually acceptable level. The GAN-created synthetically coloured images resembled the source pictures rather well. Not only is increasing the number of epochs sufficient, but we also need a large dataset to avoid overfitting problems. Efficient use of resources saves time and improves accuracy. For example, using the system GPU instead of the CPU saves hours. Adding more convolutional layers makes the model more accurate. Even after adding a significant number of convolutional layers, the output size is still large enough for efficient processing. In this case, pooling or downsampling is a good candidate to further compress the output of the convolutional layer without significant loss of information. Although our model can be used effectively for coloring small images, they are not reliable because it takes a long time to work with large images under normal conditions and increases the cost requirements.

VI. Future Scope

- Color Precision - Although the results provided by the color accuracy model were satisfactory, the still needs more model training to improve accuracy.
- With the advent of better deep learning methods, such as DCGAN (Deep Convolutional Generative Adversarial Network), models can be further refined to improve color accuracy.
- The ideas proposed in this paper can be extended to coloring in images, old movies, videos, and CCTV footages.
- We also want to add more convolution and pooling layers to make the model more accurate.

References

[1] Vivek George Jacob, Sumana Gupta. "Colorization of grayscale images and videos using a semiautomatic approach" , 2009 16th IEEE International Conference on Image Processing (ICIP), 2009.
[2] S. Kumar, M. Kumar," A study on the image detection using convolution neural networks and TenserFlow". International Conference on Inventive Research in Computing Applications (ICIRCA) (pp. 1080-1083), 2018, IEEE.
[3] A. Bhowmik, S. Kumar, & N. Bhat,"Evolution of automatic visual description techniques-a methodological survey". Multimedia Tools and Applications, 80(18), 28015-28059 (2021).
[4] S. Kumar, & R. Hanot (2021) "Community detection algorithms in complex networks: A survey", In Advances in Signal Processing and Intelligent Recognition Systems, 6th International Symposium, (2020), Springer Singapore.
[5] A. Mallik, A. Khetarpal, & S. Kumar,"ConRec: malware classification using convolutional recurrence". Journal of Computer Virology and Hacking Techniques, 18(4), 297-313, (2022).
[6] S. Anand, A. Mallik, & S. Kumar, "Integrating node centralities, similarity measures, and machine learning classifiers for link prediction". Multimedia Tools and Applications, 81(27), 38593-38621, (2022).
[7] S. Kumar, A. Mallik, & B. S. Panda,"Influence maximization in social networks using transfer learning via graph-based LSTM". Expert Systems with Applications, 212, 118770, 2023
[8] A. Weltz. The Basics of Hand-Coloring Black-and-White Prints. Accessed: 2020. [Online]. Available: https://www.bhphotovideo.com/explora/photography/tips-and-solutions/the-basics-of-hand-coloringblack-and-white-prints.
[9] I. Žeger, S. Grgic, J. Vuković and G. Šišul, "Grayscale Image Colorization Methods: Overview and Evaluation," in IEEE Access, vol. 9, pp. 113326-113346, 2021, doi: 10.1109/ACCESS.2021.3104515.
[10] R. Zhang, J.-Y. Zhu, P. Isola, X. Geng, A. S. Lin, T. Yu, and A. A. Efros, "Real-time user-guided image colorization with learned deep priors," ACM Trans. Graph., vol. 36, no. 4, pp. 111, Jul. 2017.
[11] Kamyar Nazeri, Eric Ng, and Mehran Ebrahimi. 2018. Image Colorization using Generative Adversarial Networks. In book: Articulated Motion and Deformable Objects, pp.8594.
[12] I. Goodfellow, J. PougetAbadie, M. Mirza, B. Xu, D. WardeFarley, S. Ozair, A. Courville, and Y. Bengio, "Generative adversarial nets," in Advances in Neural Information Processing Systems 27, Montreal, Quebec, Canada, 2014, pp. 26722680.
[13] S. Wan, Y. Xia, L. Qi, Y. H. Yang and M. Atiquzzaman, "Automated Colorization of a Grayscale Image With Seed Points Propagation," in IEEE Transactions on Multimedia, vol. 22, no. 7, pp. 17561768, July 2020, doi: 10.1109/TMM.2020.2976573.
[14] Hao Wang, Qifeng Ruan, Hongtao Wang, Soroosh Daqiqeh Rezaei, Kevin T. P. Lim, Hailong Liu, Wang Zhang, Jonathan Trisno, John You En Chan, and Joel K. W. Yang, "Full Color and Grayscale Painting with 3D Printed Low-Index Nanopillars", Nano Letters 2021 21 (11), 4721-4729.
[15] N. Bhat, N. Saggu, & S. Kumar S," Generating visible spectrum images from thermal infrared using conditional generative adversarial networks". In 2020 5th International Conference on Communication and Electronics Systems (ICCES) (pp. 1390-1394),. 2020, IEEE
[16] X. Zhong, T. Lu, W. Huang, M. Ye, X. Jia and C. -W. Lin, "Grayscale Enhancement Colorization Network for Visible-Infrared Person Re-Identification," in IEEE Transactions on Circuits and Systems for Video Technology, vol. 32, no. 3, pp. 1418-1430, March 2022.
[17] J. An, K. K. Gagnon, Q. Shi, H. Xie and R. Cao, "Image Colorization with Convolutional Neural Networks," 2019 12th International Congress on Image and Signal Processing, BioMedical Engineering and Informatics (CISP-BMEI), Suzhou, China, 2019, pp. 1-4.
[18] An, J., Kpeyiton, K.G. & Shi, Q. Grayscale images colorization with convolutional neural networks. Soft Comput 24, 4751–4758 (2020).

Authorized licensed use limited to: DELHI TECHNICAL UNIV. Downloaded on June 14,2023 at 05:01:30 UTC from IEEE Xplore. Restrictions apply.

ResearchGate

See discussions, stats, and author profiles for this publication at: https://www.researchgate.net/publication/370406845

Small signal and noise analysis of T-gate HEMT with polarization doped buffer for LNAs

Article · April 2023

DOI: 10.1016/j.micrna.2023.207593

CITATIONS
0

READS
32

3 authors:

Megha Sharma
Delhi Technological University
14 PUBLICATIONS **32** CITATIONS
SEE PROFILE

Bhavya Kumar
Delhi Technological University
19 PUBLICATIONS **109** CITATIONS
SEE PROFILE

Rishu Chaujar
Delhi Technological University
255 PUBLICATIONS **2,278** CITATIONS
SEE PROFILE

Some of the authors of this publication are also working on these related projects:

Novel Mosfet Design for Digital Applications View project

Modelling and Simulation of GAA FinFET View project

All content following this page was uploaded by Bhavya Kumar on 09 May 2023.

The user has requested enhancement of the downloaded file.

Micro and Nanostructures 180 (2023) 207593

Contents lists available at ScienceDirect

Micro and Nanostructures

journal homepage: www.journals.elsevier.com/micro-and-nanostructures

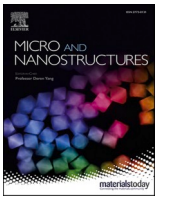

Small signal and noise analysis of T-gate HEMT with polarization doped buffer for LNAs

Megha Sharma, Bhavya Kumar, Rishu Chaujar *

Department of Applied Physics, Delhi Technological University, Delhi, India

ARTICLE INFO

Keywords:
Heterostructure
Polarization
Noise
Small signal
T-shaped gate

ABSTRACT

Small signal behavior and RF noise performance of T-gate InAlN/GaN HEMT with polarization doped buffer (PDB-HEMT) have been examined in this paper and compared to conventional HEMTs at GHz frequency range. Enhancement mode operation is possible in the PDB-HEMT device, which has a recessed T-gate structure with a gate length of 10 nm and delivers the threshold voltage (V_{th}) of 0.9 V and a high transconductance of 1.55 S/mm. This study examines the auto/cross-correlation factor, minimum noise figure, reflection/transmission coefficients, noise conductance, and optimal noise resistance and reactance. The enhanced transconductance of PDB-HEMT has resulted in a considerable increase in the forward transmission coefficient and a decrease in the input/output reflection coefficient compared to traditional HEMTs. It has also been shown that the PDB- HEMT has a lower noise figure and noise conductance than the GaN buffer HEMT by 57% and 20%, respectively. This research demonstrates that the T-gate polarization doped buffer (PDB-HEMT) structure is an excellent choice for Low Noise Amplifiers (LNA) operating at higher frequencies.

1. Introduction

In every wireless communication system, Low Noise Amplifiers (LNAs) are the building blocks. LNA is used to enhance extremely weak signals that are picked up by an antenna. Regarding LNA design, there are four key considerations: gain, noise figure, non-linearity, and impedance matching. One of the most critical aspects of a low-noise amplifier's performance is its noise figure [1]. Thus, we can determine which LNA best suits a certain application. When a Low Noise Amplifier (LNA) does not have a high gain, noise in the LNA circuit might impact the signal and even attenuate it. Gain and noise figures are balanced via input-matching circuits. Through the use of scattering parameter analysis, the circuit's gain, noise figure, and stability circle were all calculated. The initial stage of the amplifier must have a high amplification level to reduce the amount of noise.

GaN-based HEMTs are a particularly ideal choice for such applications because of unique material properties like greater bandgap energy, higher electron saturation velocity, higher electron density, and higher breakdown voltage [2,3] when compared to existing materials such as gallium arsenide (GaAs). In addition, the polarization property of GaN material led to the formation of a 2DEG at the AlGaN/GaN junction [4]. Because of this improvement in electron mobility, the GaN device became a fantastic option for use in high-power settings applications. The superior microwave properties of the AlGaN/GaN HEMT [5–12], together with its low noise and high power microwave performance, as well as its high current drive capabilities, drew attention to its use in low noise applications. In

* Corresponding author.
E-mail addresses: meghasharma_phd2k18@dtu.ac.in (M. Sharma), bhavyakumar_phd2k18@dtu.ac.in (B. Kumar), chaujar.rishu@dtu.ac.in (R. Chaujar).

https://doi.org/10.1016/j.micrna.2023.207593
Received 13 November 2022; Received in revised form 7 April 2023; Accepted 26 April 2023
Available online 29 April 2023
2773-0123/© 2023 Published by Elsevier Ltd.

the context of wideband robust receiver applications, various AlGaN/GaN HEMT-based LNAs were created [13–15]. GaN HEMTs have made significant progress in their development for usage in LNAs, with results showing NF_{min} values of 1.6 dB at 30 GHz [16] and 1.2 dB at 20 GHz [17] when using a gate length of 100 nm. Shinohara et al. reported a good NF_{min} of around 0.5 dB at 30 GHz, which exhibited the cut-off frequency (f_T) of 400 GHz and maximum oscillation frequency (f_{max}) of 500 GHz using 20-nm T-gate AlGaN/GaN HEMTs [18]. Although AlGaN/GaN HEMTs have seen a large rise in operating frequency, they still suffer from strain issues [19]. When the thickness of the AlGaN barrier is decreased, there is an inevitable strain produced at the junction of AlGaN and GaN. This problem is effectively minimized by using a lattice-matched InAlN layer [20]. The HEMTs that are based on InAlN and AlN make it possible for the device to scale aggressively, which increases the f_T and decreases the short-channel impact (SCE) [21]. Though the InAlN/AlN T-Gate HEMTs claimed to have numerous benefits, they also had one significant drawback: 2DEG spilling from the channel into a buffer, which lowers the device's mobility and reliability [22]. Therefore, the performance of InAlN HEMTs has to be made more resilient by implementing creative buffer engineering. Polarization doping, which may be achieved by grading the AlGaN layer, has recently gained popularity and is seen as a superior option [23]. This has already been shown in our prior study that implementation of polarization doping in the buffer region of InAlN/AlN T-gate HEMT significantly enhances the f_T and f_{max} of the device [24].

The small-signal behavior and noise FOMs of InAlN/AlN T-gate HEMT with polarized doped buffer are investigated in this study by employing the ATLAS SILVACO simulator. The following subheadings constitute the various sections of this article: Section 2 analyses the simulation models and device construction; Section 3 and 4 addresses the feasibility of fabrication of the device and the performance of the device in terms of small signals and noise; and Section 5 provides a conclusion to the article.

2. Device design and simulation models

Fig. 1(a and b) depicted the conventional GaN-HEMT and proposed PDB-HEMT's schematic structure. The dimensions of both devices are the same. The proposed device consists of a 1 μm AlGaN buffer layer with a linear reduction in aluminum concentration from 0.2 to 0 in the (0001) direction, a 20 nm GaN channel layer, a 1 nm AlN spacer layer, and 6 nm lattice-matched InAlN barrier layer. The smaller foot length and bigger gate area of the T-shaped construction (gate length = 10 nm, gate width = 50 μm) reduce gate resistance and capacitance. Reduction in contact resistance is achieved by doping source and drain regions with Silicon. The spacing between the source-drain region is 1 μm. To minimize parasitic capacitance and improve the device's RF characteristics, the circuit is passivated by the 20 nm SiN layer. Silvaco TCAD software was used to simulate the device [25]. The high and low field mobility model, polarization, and SRH recombination models have been used in the simulation procedure [25].

3. Experimental calibration and fabrication feasibility

Fig. 2 shows how the physical models match the experimental results [26]. The acceptor and donor-like traps with energy levels 0.5eV, 0.42eV, and trap density $5 \times 1016\ cm^{-3}$, $3.86 \times 10^{13}\ cm^{-3}$ are considered below the conduction band to fit the experimental 2DEG density. The agreement between the simulated and experimental outcomes is remarkable. Fig. 3 depicts the proposed structure's fabrication process. Two fabrication methods exist for the proposed structure.: top-down and bottom-up. The epitaxial stack is fabricated via molecular beam epitaxy (MBE) [27]. The InAlN/AlN/GaN/AlGaN epitaxial stack is grown utilizing the bottom-up technique on the SiC substrate. To create the n++ GaN ohmic source/drain regions, MBE is utilized with a SiO_2 growth mask [28]. By using plasma-enhanced chemical vapor deposition (PECVD), the passivation layer is deposited on top of the epitaxial stack. Following are the stages involved in making the T-gate. To define the gate, electron beam lithography (EBL) is employed and partly recessed the gate foot into the barrier layer by dry etching [29].

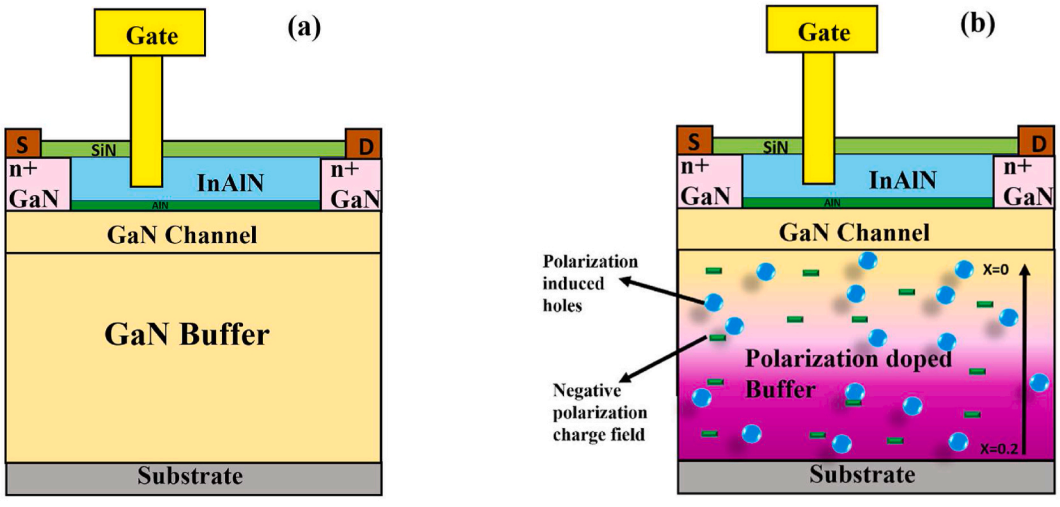

Fig. 1(a). GaN-HEMT (b) PDB-HEMT

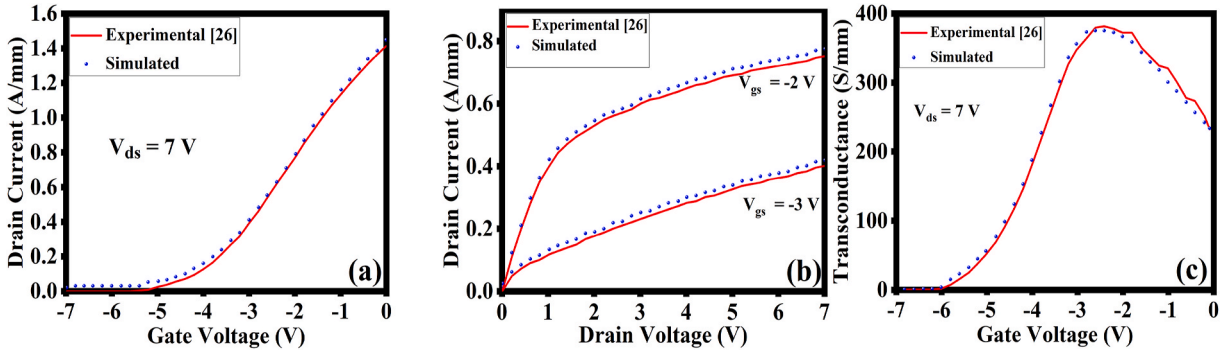

Fig. 2. Comparison of simulated and experimental data.

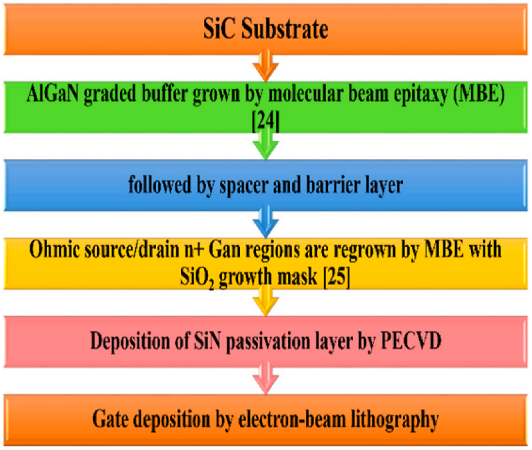

Fig. 3. PDB-HEMT calibration process.

4. Results and discussion

Fig. 4 depicts the transfer characteristics of the proposed polarized doped buffer HEMT (PDB-HEMT) and conventional GaN-HEMT. In comparison to the conventional ones, the PDB-HEMT exhibits a lower drain current (2.56 A/mm) and a greater transconductance peak (1.55 S/mm) at $V_{gs} = 1.4$ V. The suggested structure exhibits a dramatic increase in transconductance at the pinch-off area, which shows the lower subthreshold current in the device.

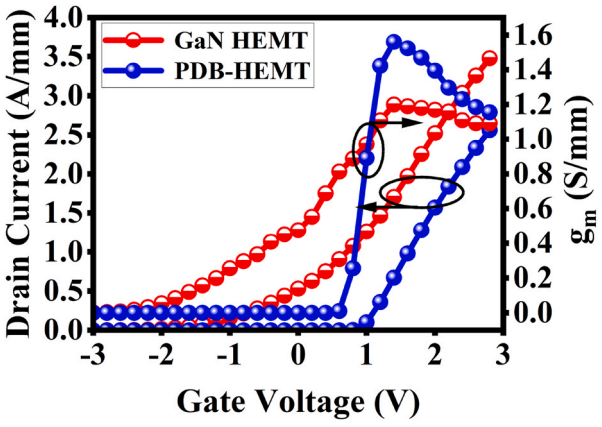

Fig. 4. Transfer characteristics for both the structure.

4.1. Small signal analysis

The scattering (reflection and transmission coefficients) properties of PDB-HEMT at $V_{gs} = 1.4V$ and GaN-HEMT at $V_{gs} = 1.8V$ are examined at fixed drain bias voltage of 3V. We have chosen these gate voltages because the transconductance peak is observed for PDB-HEMT at $V_{gs} = 1.4$ V and for GaN buffer at $V_{gs} = 1.8$ V as shown in Fig. 4.

One of the greatest ways to look into the high-frequency small-signal behavior of HEMTs is via measurements of their S-parameter. Networks that operate at microwave frequencies often use S-parameters because it is simpler to compute signal power and energy at radio and microwave frequencies than currents and voltages. The input/output reflection coefficient is defined as [30].

$S11 = \frac{\text{reflection wave at port 1}}{\textit{Incident wave at port 1}}$, where port 2 terminated on the characteristic impedance

$S22 = \frac{\text{reflection wave at port 2}}{\textit{Incident wave at port 2}}$, where port 1 terminated on the characteristic impedance

These parameters evaluate the matching between the terminating impedance and the port. For RF circuit design, matching is required, and a perfectly matching condition occurs when the reflection coefficient reduces to zero [31]. Hence, a lower value of S11 and S22 is required for better RF performance. In Fig. 5(a and b), the lower value of S11 and S22 is obtained for the PDB-HEMT. The reduction of the S11 parameter in PDB-HEMT is due to the reduction of source resistance and gate resistance in PDB-HEMT, which is 27.7% and 67.6% lower than the Gan-HEMT as shown in Fig. 6(a and b). The lower value of gate and source resistance increases the coupling between the input and output port and decreases the S11 parameter. The higher value of drain resistance, transconductance, and lower channel resistance reduce the S22 parameter. However, in PDB-HEMT lower drain resistance is observed which is 13% lower than the Gan-HEMT as exhibited in Fig. 6(c), and higher channel resistance is observed which is 7% higher than the GaN-HEMT as shown in Fig. 7(b), which lead to increase the S22 parameter, but the higher transconductance is observed in Fig. 6(d) which is 30% higher than the GaN-HEMT and reduced the S22 parameter.

The amount of feedback an amplifier receives from its output to its input is measured by the reverse isolation parameter S12, which affects the amplifier's supremacy in terms of its stability at high frequency. The magnitude and phase change of the reverse and forward transmission coefficients (S12, S21) for both devices is exhibited in Fig. 5 (c, d). For better RF performance, the S21 parameters should be high and the S12 parameter should be as low as possible to reduce the feedback of the output signal to the input port. Fig. 5(c) shows the improvement in the S21 parameter for PDB-HEMT which is 69% higher than the GaN-HEMT. This enhancement is due to the polarization-doped buffer engineering in the proposed structure. The polarization-doped buffer engineering caused a negative polarization field in the buffer, which limited the electrons to a shallower depth range and enhanced gate

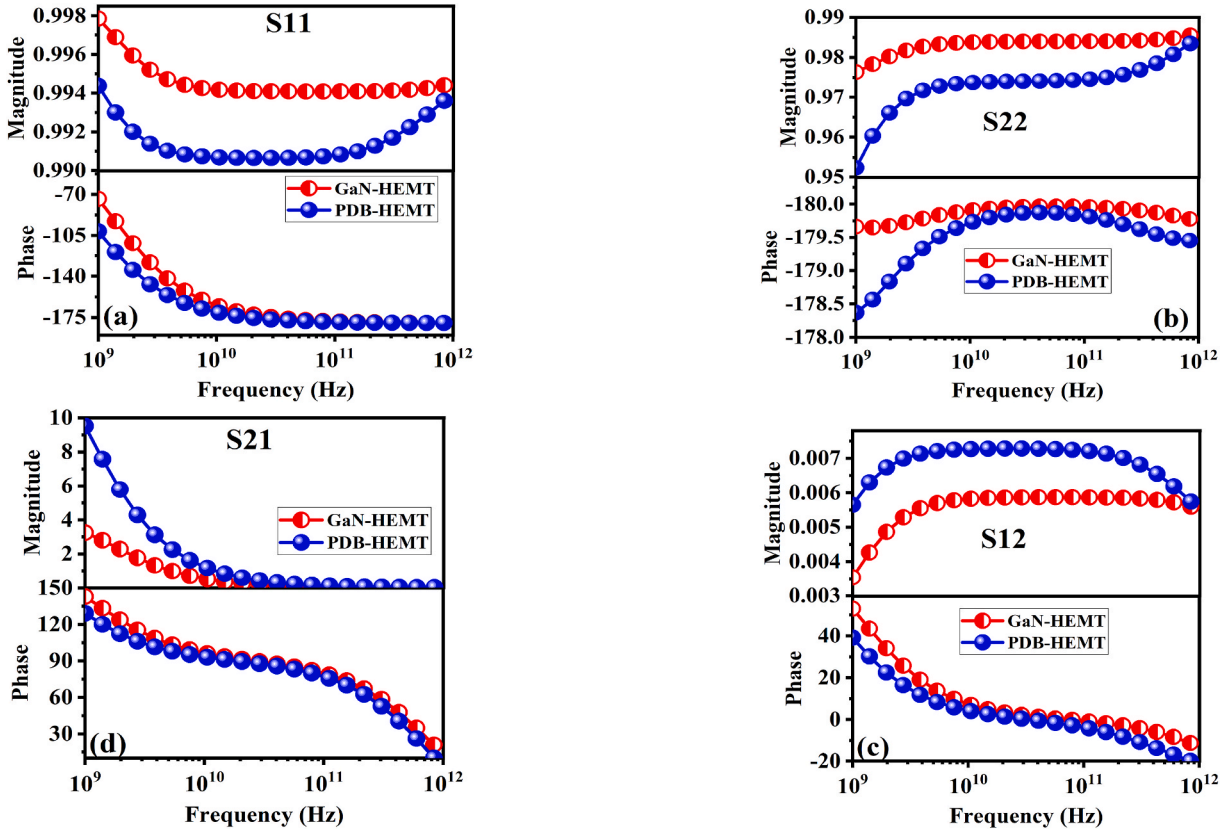

Fig. 5. Variation of magnitude and phase of (a) input (b) output reflection coefficient (c) forward (d) reverse transmission coefficient.

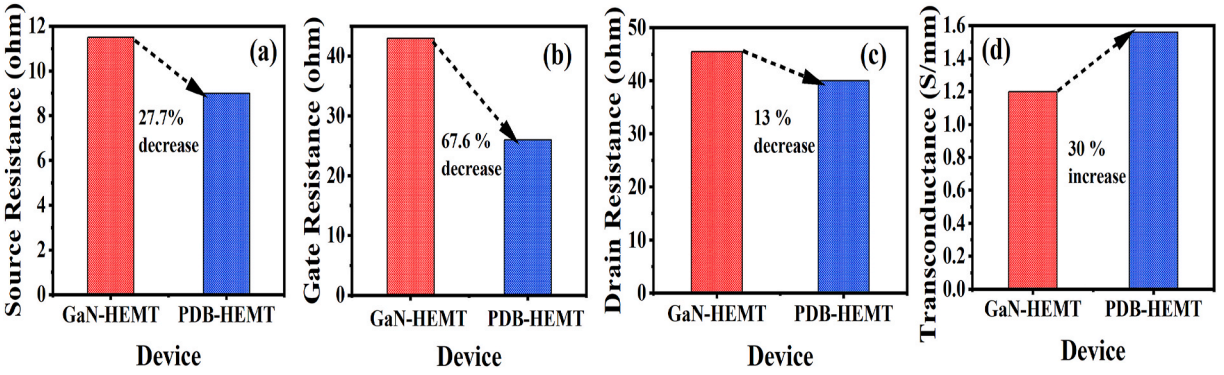

Fig. 6. Bar graph of (a) Source resistance (b) Gate resistance (c) drain resistance (d) Transconductance for both the devices.

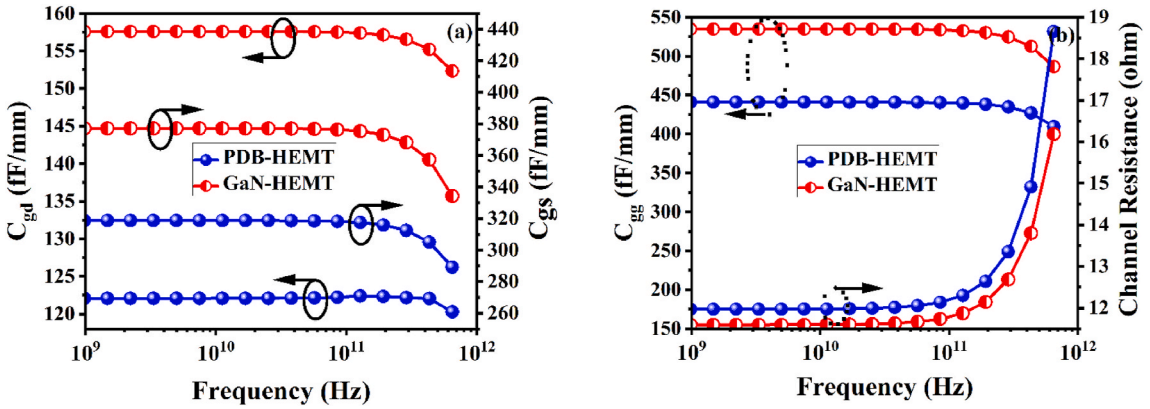

Fig. 7. Variation of (a) gate to drain and source capacitance (b) gate capacitance and channel resistance for both the structures.

controllability. Because of this, the transconductance increases, which ultimately leads to an improvement in the S21 parameter. However small increment in the S12 parameter is also observed for PDB-HEMT which is 8% higher than the GaN-HEMT.

Fig. 7(a and b) exhibits the graph of parasitic capacitance i.e., gate to source capacitance (C_{gs}), gate to drain capacitance (C_{gd}), gate capacitance, and gate capacitance (C_{gg}) for both devices. The lower value of parasitic capacitances is observed for PDB-HEMT which enhances cut off frequency (f_T) and maximum oscillation frequency (f_{max}) of the device. Fig. 7(b) exhibits the graph of channel resistance for both devices. It has been observed that in PDB-HEMT channel resistance increases by 7% as compared to GaN-HEMT. This enhancement of channel resistance is due to the lower 2DEG density in PDB-HEMT. However, enhancement in channel resistance adversely affects the f_{max} of the device but a higher value of transconductance and lower parasitic capacitance overcome this effect.

When the device's current and unilateral power gain are both unity, the device's f_T and F_{max} are calculated. The PDB -HEMT's f_T (583 GHz) and f_{max} (840 GHz) are displayed in Fig. 8(a and b), and they are 40% and 75% more efficient than the conventional device.

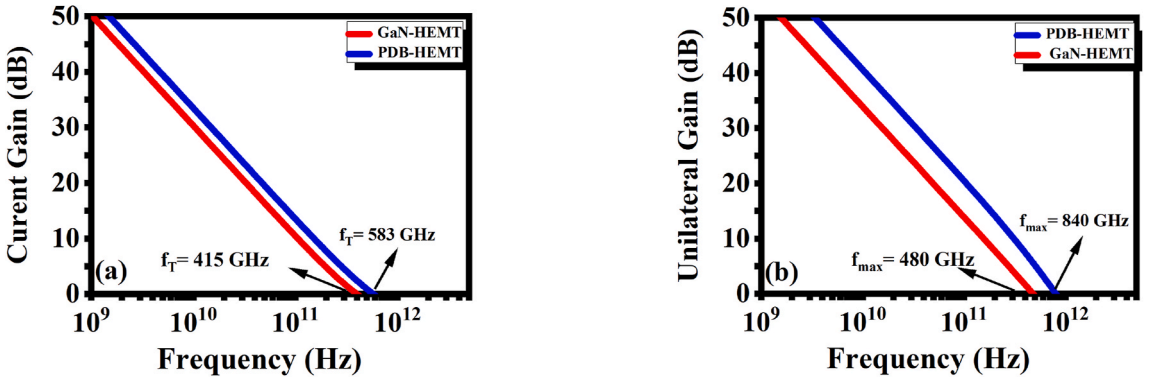

Fig. 8. Variation of (a) current gain (b) unilateral power gain for both the structures.

4.2. Noise analysis

The two-port noisy network is often required to investigate internal sources of noise [32], as seen in Fig. 9. It is possible to replace a linearly noisy two-port network with a noise-free network having a noise current and voltage source. There is a correlation between these two noise sources in real devices [33]. The noise parameters of the general circuit are obtained from the measurement conducted on two-port networks. The noise performance of the PDB-HEMT is examined with the help of the two port circuits by using the following parameters: NF_{min} (the least noise figure), the noise conductance (G_n), optimum source impedance (Z_{opt}), and the auto/cross-correlation function. The optimum source impedance (Z_{opt}) is the impedance that gives the minimum noise figure [34]. Z_{opt} is a complex number that has both real and imaginary values, as expressed in Eqn. (1).

$$Z_{opt} = R_{opt} + jX_{opt} \tag{1}$$

The real value of Z_{opt} is optimum source resistance (R_{opt}), and the imaginary part of Z_{opt} is optimum reactance (X_{opt}) as expressed by Eqn. (2) and (3) [35]. Where P and R are the noise coefficient and Cr is the correlation factor [36].

$$R_{opt} = \frac{1}{\omega C_{gs}} \sqrt{\frac{g_m\left(R_{gs} + R_s\right) + R\left(1 - C_r^2\right)}{P}} + \sqrt{\omega^2 C_{GS}^2 \left(R_{gs} + R_s\right)^2} \tag{2}$$

$$X_{opt} = \frac{1}{\omega C_{gs}} \left(1 - C_r \sqrt{\frac{R}{P}}\right) \tag{3}$$

Fig. 10(a) depicts the variation of R_{opt} and X_{opt} with frequency for both devices. The optimum source resistance and reactance value drop with increasing frequency and become saturated at a higher frequency. The impact of gate voltage on optimum source resistance (R_{opt}) and optimum reactance (X_{opt}) is depicted in Fig. 10(b and c). The optimum source resistance increases with gate voltage due to the enhancement of carrier concentration at the channel region. Moreover, R_{opt} is constant at the MHz frequency region and decreases at a greater frequency region, as depicted in Fig. 10(b). The inset graph of Fig. 10(b) exhibited the optimum source resistance at a higher frequency region. The optimum reactance versus frequency for.

different gate voltages are exhibited in Fig. 10(c). At the lower

frequency range, the optimum reactance increases with the frequency due to the recombination of charge carriers [37], and a higher peak of X_{opt} is observed for $V_{gs} = 1.4$V; after that, there is a downward swing in X_{opt}. The inset graph of Fig. 10(c) shows the value of X_{opt} at a higher frequency range.

One of the essential metrics used to evaluate the performance of a low-noise amplifier (LNA) is noise conductance (G_n), expressed by Eqn. (4). Where S_I is the drain current noise spectral density, and T_a is the reference temperature 290K.

$$G_n = \frac{S_I}{4K_B T_a |Y_{21}|^2} \tag{4}$$

The power spectral densities of noise current generators are often estimated using noise conductance. RF and low-noise amplifiers (LNAs) need low-noise conductance [38]. The fluctuation of noise conductance with frequency for both devices is shown in Fig. 11(a). At 583 GHz frequency, the PDB-HEMT exhibits a lower noise conductance, which is 20% lower than the GaN-HEMT. Fig. 11(b) shows how the gate voltage affects the noise conductance. The flat G_n response is observed at the lower frequency region and linearly increases at a higher frequency. The lower noise conductance is observed at $V_{gs} = 1.4$ V.

The mathematical expression of the noise figure for a two-port network is depicted by Eqn. (5) [39].

$$NF = NF_{min} + \frac{R_n}{G_s}\left(G_s - G_{opt}\right)^2 + \frac{R_n}{G_s}\left(B_s - B_{opt}\right)^2 \tag{5}$$

The optimal source susceptance and conductance are expressed by G_{opt} and B_{opt} [40]. The minimum noise figure (NF_{min}) is

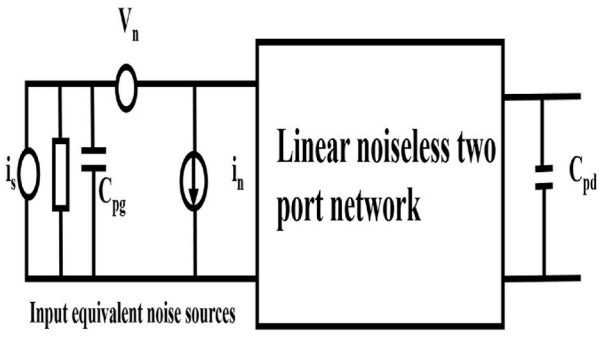

Fig. 9. The equivalent noise circuit.

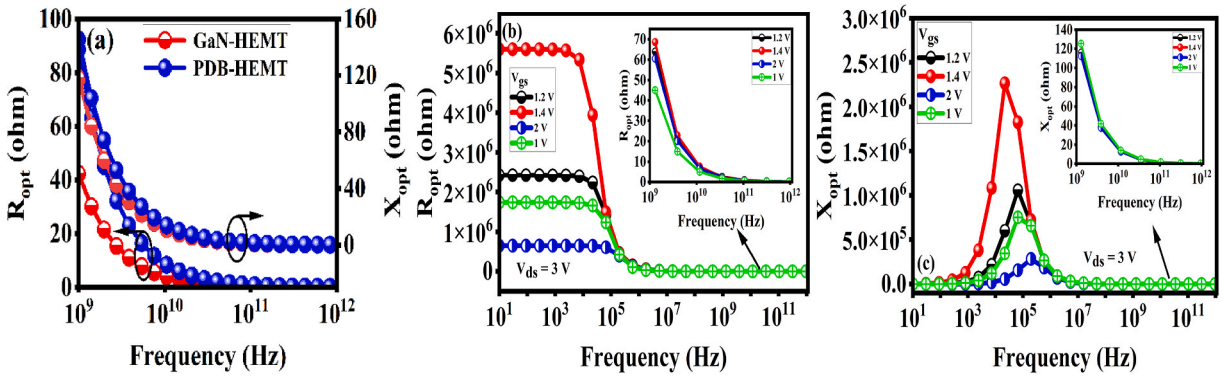

Fig. 10. (a) optimum source resistance and reactance for PDB-HEMT and GaN-HEMT (b) optimum noise resistance (c) reactance for different V_{gs}.

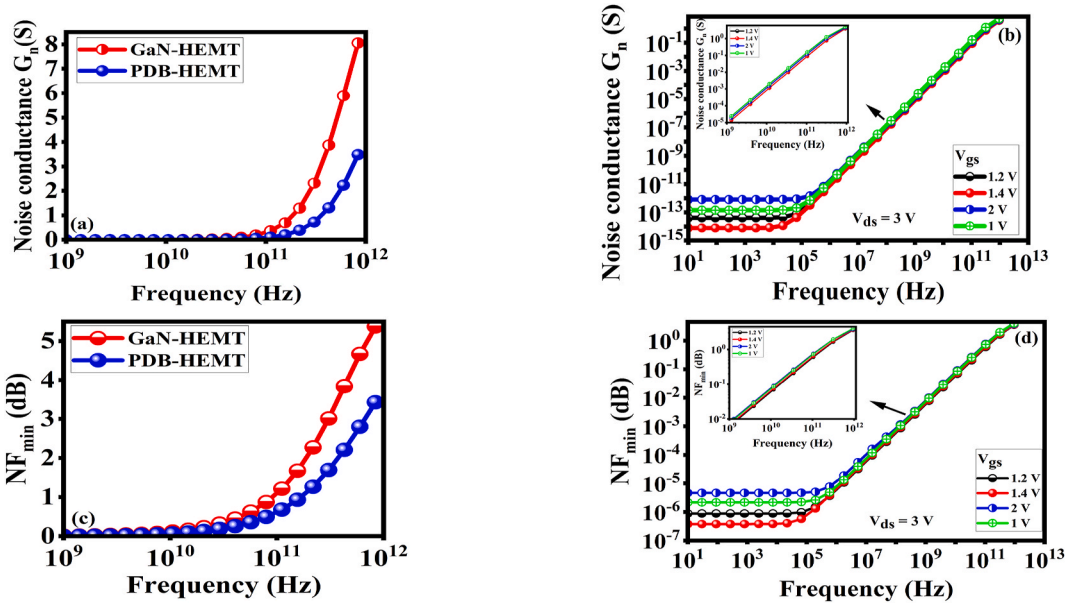

Fig. 11. Noise conductance (a) PDB-HEMT and GaN-HEMT (b) variable gate voltage; NF_{min} (c) PDB-HEMT and GaN-HEMT (d) variable gate voltage.

obtained when $G_s = G_{opt}$ and $B_s = B_{opt}$. The frequency-dependent fluctuation of NF_{min} for both devices is shown in Fig. 11(c). The reduction in NF_{min} is noticed for PDB-HEMT compared to the conventional HEMT. The NF_{min} is inversely proportional to the transconductance. In PDB-HEMT, the graded buffer engineering caused a negative polarization field in the buffer, which limited the electrons to a shallower depth range and enhanced gate controllability. Because of this, the transconductance increases, leading to an improvement in the low noise figure compared to the conventional HEMT. The impact of gate voltage on the noise figure is exhibited in Fig. 11(d). It has been observed that at the MHz frequency range, NF_{min} is constant; at the GHz region, NF_{min} linearly increases with frequency. The NF_{min} value decreases with an increase in the gate voltage from 1 V to 1.4 V; the afterward higher value of NF_{min} is observed for $V_{gs} = 2V$. This variation in NF_{min} is basically due to the transconductance variation with gate voltage, as exhibited in Fig. 4. The NF_{min} is the inverse of the transconductance. It is observed from Fig. 4 that transconductance increases with an increment in gate voltage from 1 V to 1.4 V, and a higher peak of transconductance is observed at $V_{gs} = 1.4V$ afterward downward swing is observed.

Fig. 12 depicts the HEMT as a two-port device, with V1 representing noise generated at the gate and V2 representing noise received at the output [41]. A little statistical analysis is required for this study since noise is a random event. These two ports are examined in terms of autocorrelation and cross-correlation of their voltages. Fig. 13(a and b) shows the cross-correlation (V1. V2) and autocorrelation between the input (V1. V1) and output voltages (V2. V2) for both structures. In contrast to the GaN-HEMT, the PDB-HEMT has a stronger auto/cross-correlation. The polarization-doped buffer in PDB-HEMT significantly bends the conduction band of the buffer layer upwardly convex. This enhances the carrier confinement in the channel and prevents the channel electrons from interacting with the traps in the buffer layer to reduce the trapping effects, which attribute to the enhancement of electron mobility and reduces the scattering. Therefore, the scattering mechanism in PDB-HEMT is inefficient in disrupting the correlation among the gate and drain

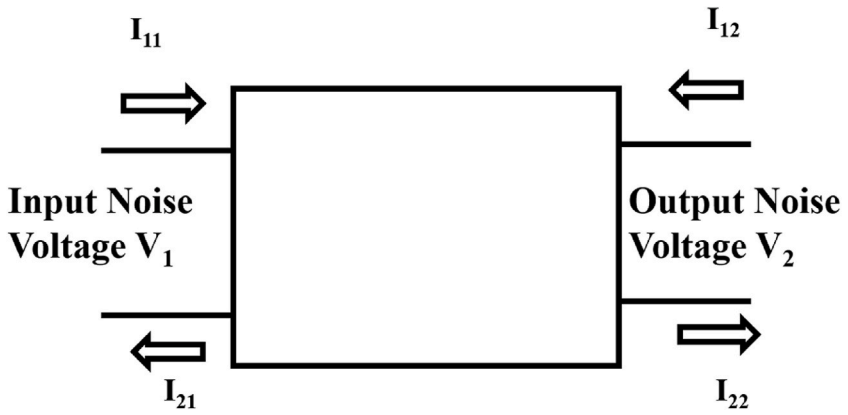

Fig. 12. Two-port device.

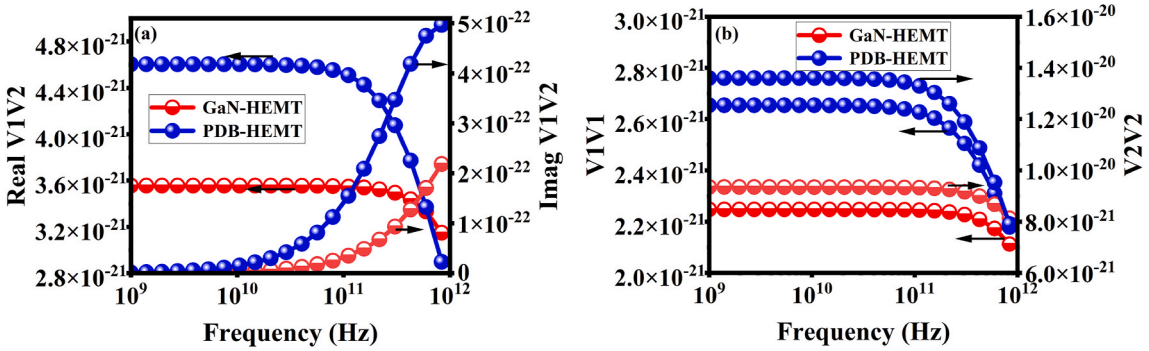

Fig. 13. (a) Cross-correlation (b) autocorrelation for both the structures.

current, significantly enhancing the auto/cross-correlation between them.

The real and imaginary part of the cross-correlation of PDB-HEMT for $V_{gs} = 1V$, 1.2V, 1.4V, and 2V is exhibited in Fig. 14(a and b). The real part of cross correlation remains constant in the frequency range 1 GHz–100 GHz after that linear reduction is observed in the THz frequency region shown in Fig. 14(b). Furthermore, the cross-correlation function decreases with increasing gate voltage. Fig. 14 (c) depicts the fluctuation of the auto-correlation function concerning the variation of the gate voltage (V_{gs}). The autocorrelation function falls linearly with lower order frequency (MHz) and stays constant with higher order frequency (GHz). The autocorrelation function reduces as the gate voltage (V_{gs}) of the PDB-HEMT increases. Hence, this work's results show that using the polarized doped buffer in T-gate InAlN/GaN HEMT devices may achieve extremely low noise levels via improved structural design.

5. Conclusion

This study presents a comprehensive investigation of the small-signal behavior and noise analysis of PDB-HEMT operating in the GHz frequency range. The simulated results suggest that the introduction of the polarization-doped engineering scheme into the buffer region results in a reduction in the reflection coefficient and an increment in the transmission coefficient in comparison with traditional GaN buffer HEMT. Even at high frequency, the PDB-HEMT device has a minimum noise figure of $NF_{min} = 1.62$ dB, lower noise conductance, and stronger auto/cross-correlation. These outstanding results show that PDB-HEMT is suitable for creating microwave amplifiers and oscillators. These findings make it abundantly evident that the T-gate PDB HEMT structure is an excellent candidate for high-performance RF applications and LNAs.

Authors statement

Megha Sharma: Conceptualization, Methodology, Software, Data Curation, Writing-Original draft preparation. **Bhavya Kumar**: Conceptualization, Methodology, Software, Data Curation, Writing-Original draft preparation. **Rishu Chaujar**: Supervision, Reviewing, and Editing.

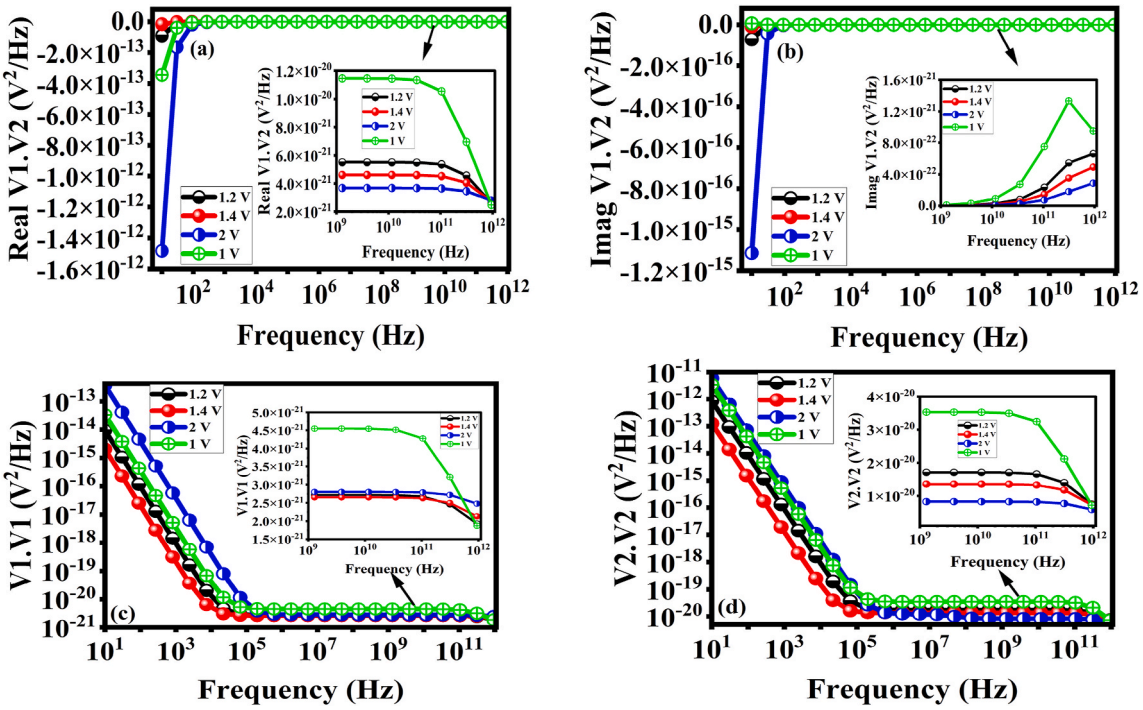

Fig. 14. For different gate voltage (a) real part of cross-correlation (b) imag part of cross-correlation (c) input (d) output autocorrelation.

Declaration of competing interest

The authors declare that they have no known competing financial interests or personal relationships that could have appeared to influence the work reported in this paper.

Data availability

No data was used for the research described in the article.

References

[1] A. Mohanbabu, R. Saravana Kumar, N. Mohankumar, Noise characterization of enhancement-mode AlGaN graded barrier MIS-HEMT devices, Superlattice. Microst. 112 (2017) 604–618, https://doi.org/10.1016/j.spmi.2017.10.020.

[2] Y. Zhang, K. H Teo, T. Palacios, Beyond thermal management: incorporating p-diamond Back-barriers and cap layers into AlGaN/GaN HEMTs, IEEE Trans. Electron. Dev. 6 (2016) 2340–2345, https://doi.org/10.1109/TED.2016.2553136.

[3] S. Prasad, A.K. Dwivedi, A. Islam, Characterization of AlGaN/GaN and AlGaN/AlN/GaN HEMTs in terms of mobility and subthreshold slope, J. Comput. Electron. 15 (2016) 172–180, https://doi.org/10.1007/s10825-015-0751-8.

[4] H. Xiao-Guang, Z. De-Gang, J. De-Sheng, Formation of a two-dimensional electron gas at AlGaN/GaN heterostructure and the derivation of its sheet density expression, Chin. Phys. B 24 (2015), 067301, https://doi.org/10.1088/1674-1056/24/6/067301.

[5] K. Liu, R. Wang, C. Wang, X. Zheng, X. Ma, J. Bai, B. Cheng, R. Liu, A. Li, Y. Zhao, Y. Hao, The influence of lightly doped p-GaN cap layer on p-GaN/AlGaN/GaN HEMT, Semicond. Sci. Technol. 37 (2022) 268–1242.

[6] S.P. Kumar, A. Agrawal, R. Chaujar, M. Gupta, R.S. Gupta, Analytical modeling and simulation of subthreshold behavior in nanoscale dual material gate AlGaN/GaN HEMT, Superlattice. Microst. 44 (2008) 37–53, https://doi.org/10.1016/j.spmi.2008.01.023.

[7] S.P. Kumar, A. Agrawal, R. Chaujar, M. Gupta, R.S. Gupta, Device linearity and intermodulation distortion comparison of dual material gate and conventional AlGaN/GaN high electron mobility transistor, Microelectron. Reliab. 51 (2011) 587–596, https://doi.org/10.1016/j.microrel.2010.09.033.

[8] D. Chen, P. Yuan, S. Zhao, S. Liu, Q. Xin, X. Song, S. Yan, Y. Zhang, H. Xi, W. Zhu, W. Zhang, Wide-range-adjusted threshold voltages for E-mode AlGaN/GaN HEMT with a p-SnO cap gate, Sci. China Mater. 65 (2022) 795–802.

[9] S. Chatterjee, M. Mukherjee, Band-engineered quasi-AlGaN/GaN high-electron-mobility-avalanche-transit-time (HEMATT) oscillator: electro-optical interaction study in the sub-mm frequency domain, Eur. Phys. J. Plus 137 (2022) 1–5.

[10] S. Qu, X. Wang, H. Xiao, C. Wang, L. Jiang, Analysis of transconductance characteristic of AlGaN/GaN HEMTs with graded AlGaN layer, Eur. Phys. J. Appl. Phys. 66 (2014), 20101, https://doi.org/10.1051/epjap/2014130368.

[11] J. Liu, Y. Zhou, J. Zhu, Y. Cai, K.M. Lau, K.J. Chen, DC and RF characteristics of AlGaN/GaN/inGaN/GaN double-heterojunction HEMTs, IEEE Trans. Electron. Dev. 54 (1) (Jan. 2007) 2–10, https://doi.org/10.1109/TED.2006.887045.

[12] O. Fathallah, M. Gassoumi, B. Grimbert, C. Gaquière, H. Maaref, Parasitic effects and traps in AlGaN/GaN HEMT on sapphire substrate, Eur. Phys. J. Appl. Phys. 51 (1) (2010), 10304.

[13] O. Fathallah, M. Gassoumi, B. Grimbert, C. Gaquière, H. Maaref, Wideband AlGaN/GaN HEMT MMIC low noise amplifier, IEEE MTT-S International Microwave Symposium Digest (IEEE Cat. No.04CH37535) 1 (2004) 153–156, https://doi.org/10.1109/MWSYM.2004.1335828.

[14] K.W. Kobayashi, An 8-W 250-MHz to 3-GHz decade-bandwidth low-noise GaN MMIC feedback amplifier with > +51-dBm OIP3, IEEE J. Solid State Circ. 47 (10) (2012) 2316–2326, Oct, https://doi.org/10.1109/JSSC.2012.2204929.

[15] J.-S. Moon, J. Kang, D. Brown, R. Grabar, D. Wong, H. Fung, P. Chan, D. Le, C. McGuire, "Wideband Linear Distributed GaN HEMT MMIC Power Amplifier with a Record OIP3/Pdc", IEEE Topical Conference on Power Amplifiers for Wireless and Radio Applications (PAWR), 2016, pp. 5–7, https://doi.org/10.1109/PAWR.2016.7440127.
[16] H. Sun, A.R. Alt, H. Benedickter, C.R. Bolognesi, High-performance 0.1- μm gate AlGaN/GaN HEMTs on silicon with low-noise figure at 20 GHz, IEEE Electron. Device Lett. 30 (2) (Feb. 2009) 107–109, https://doi.org/10.1109/LED.2008.2010339.
[17] C.-T. Chang, H.-T. Hsu, E.Y. Chang, C.-I. Kuo, J.-C. Huang, C.-Y. Lu, Y. Miyamoto, 30-GHz low-noise performance of 100-nm-Gate-Recessed n-GaN/AlGaN/GaN HEMTs, IEEE Electron. Device Lett. 31 (2) (Feb. 2010) 105–107, https://doi.org/10.1109/LED.2009.2037167.
[18] K. Shinohara, D.C. Regan, Y. Tang, A.L. Corrion, D.F. Brown, J.C. Wong, J.F. Robinson, H.H. Fung, A. Schmitz, T.C. Oh, S.J. Kim, P.S. Chen, R.G. Nagele, A. D. Margomenos, M. Micovic, Scaling of GaN HEMTs and Schottky diodes for submillimeter-wave MMIC applications, IEEE Trans. Electron. Dev. 60 (10) (2013) 2982–2996, Oct, https://doi.org/10.1109/TED.2013.2268160.
[19] M. Higashiwaki, T. Mimura, T. Matsui, Gallium Nitride Materials and Devices III, vol. 6894, International Society for Optics and Photonics, 2008, pp. 293–301.
[20] M. Neuburger, T. Zimmermann, E. Kohn, Unstrained InAlN/GaN HEMT structure, Int. J. High Speed Electron. Syst. 14 (3) (2004) 785–790, https://doi.org/10.1142/S0129156404002831.
[21] H. Sun, H. Benedickter, 205-GHz (Al,In)N/GaN HEMTs, IEEE Electron. Device Lett. 31 (9) (Sept. 2010) 957–959, https://doi.org/10.1109/LED.2010.2055826.
[22] M.A. Khan, J.N. Kuznia, J.M. Van Hove, N. Pan, J. Carter, Observation of a two-dimensional electron gas in low-pressure metalorganic chemical vapor deposited GaN-AlxGa1-xN heterojunctions, Appl. Phys. Lett. 60 (24) (1992) 3027–3029, https://doi.org/10.1063/1.106798.
[23] D. Jena, S. Heikman, D. Green, D. Buttari, R. Coffie, H. Xing, S. Keller, Realization of wide electron slabs by polarization bulk doping in graded III-V nitride semiconductor alloys, Appl. Phys. Lett. 81 (23) (2002) 4395–4397, https://doi.org/10.1063/1.1526161.
[24] M. Sharma, R. Chaujar, Ultrascaled 10 nm T-gate E-mode InAlN/AlN HEMT with polarized doped buffer for high power microwave applications, Int. J. RF Microw. Computer-Aided Eng. 32 (4) (2022), 23057, https://doi.org/10.1002/mmce.23057.
[25] ATLAS User's Manual, SILVACO International, CA, USA, 2016.
[26] T. Han, S. Dun, Y. Lü, G. Gu, X. Song, Y. Wang, P. Xu, Z. Feng, 70-nm-gated InAlN/GaN HEMTs grown on SiC substrate with fT/fmax > 160 GHz, J. Semiconduct. 37 (2) (2016) 4–8, https://doi.org/10.1088/1674-4926/37/2/024007.
[27] D. Jena, et al., Realization of wide electron slabs by polarization bulk doping in graded III-V nitride semiconductor alloys, Appl. Phys. Lett. 81 (23) (2002) 4395–4397, https://doi.org/10.1063/1.1526161.
[28] J. Guo, et al., MBE-regrown ohmic in InAlN HEMTs with a regrowth interface resistance of 0.05 Ωmm, IEEE Electron. Device Lett. 33 (4) (2012) 525–527, https://doi.org/10.1109/LED.2012.2186116.
[29] M. Micovic, et al., GaN DHFETs having 48% power added efficiency and 57% drain efficiency at V-band, IEEE Electron. Device Lett. 38 (12) (2017) 1708–1711, https://doi.org/10.1109/LED.2017.2763940.
[30] A. Kumar, M.M. Tripathi, R. Chaujar, In_2O_5Sn based transparent gate recessed channel MOSFET: RF small-signal model for microwave applications, AEU - Int. J. Electron. Commun. 93 (1434–8411) (2018) 233–241, https://doi.org/10.1016/j.aeue.2018.06.014.
[31] N. Gupta, R. Chaujar, Influence of gate metal engineering on small-signal and noise behavior of silicon nanowire MOSFET for low-noise amplifiers, Appl. Phys. A 122 (2016) 1–9, https://doi.org/10.1007/s00339-016-0239-9.
[32] A. van der Ziel, Representation of noise in linear two-ports, Proc. IEEE 57 (6) (June 1969) 1211, https://doi.org/10.1109/PROC.1969.7203, 1211.
[33] K. Hartmann, M.J.O. Strutt, Changes of the four noise parameters due to general changes of linear two-port circuits, IEEE Trans. Electron. Dev. 20 (1973), https://doi.org/10.1109/T-ED.1973.17761.
[34] A. K Gupta, A. Raman, N. Kumar, Design considerations and optimization of electrostatic doped ferroelectric nanotube tunnel FET: analog and noise analysis, Silicon (2022), https://doi.org/10.1007/s12633-022-01720-9.
[35] S. K Dubey, M. Mishra, A. Islam, Characterization of AlGaN/GaN based HEMT for low noise and high-frequency application, Int. J. Numer Model 35 (2022), https://doi.org/10.1002/jnm.2932.
[36] T. Takahashi, S. Hatsushiba, S. Fujikawa, H.I. Fujishiro, Comparative study on noise characteristics of as and Sb-based high electron mobility transistors, Phys. Status Solidi A 214 (2017), 1600599, https://doi.org/10.1002/pssa.201600599.
[37] A.M. Ivanov, G.V. Nenashev, A.N. Aleshin, Low-frequency noise and impedance spectroscopy of device structures based on perovskite-graphene oxide composite films, J. Mater. Sci. Mater. Electron. 33 (2022) 21666–21676, https://doi.org/10.1007/s10854-022-08955-7.
[38] R. Poornachandran, N. Mohankumar, R. Saravanakumar, et al., Analysis of microwave noise in an enhancement-mode dual-quantum-well InAs HEMT, J. Comput. Electron. 18 (2019) 1280–1290, https://doi.org/10.1007/s10825-019-01365-9.
[39] S. Lee, K. J Webb, V. Tilak, L. F Eastman, Intrinsic noise equivalent-circuit parameters for AlGaN/GaN HEMTs, IEEE Trans. Microw. Theor. Tech. 51 (2003) 1567–1577.
[40] Y. Zhu, C. Wei, O. Klimashov, B. Li, C. Zhang, Y. Tkachenko, Gate Width Dependence of Noise Parameters and Scalable Noise Model for HEMTs, European Microwave Integrated Circuit Conference, Amsterdam, 2008, pp. 298–301.
[41] A. Agarwala, R. Chaujar, "Investigation of Frequency-dependent Noise Performance Matrices for Gate Electrode Work Function Engineered Recessed Channel MOSFET,", Technical Proceedings of the 2012 NSTI Nanotechnology Conference and Expo, 2012.

View publication stats

Solar PV fed Non-Isolated DC-DC Multiport Converter

1st Kumood
CoE for Electric Vehicle and Related Technologies
Department of Electrical Engineering
Delhi Technological University
Delhi, India
kumood_2k19ee143@dtu.ac.in

2nd Krishan Kumar
CoE for Electric Vehicle and Related Technologies
Department of Electrical Engineering
Delhi Technological University
Delhi, India
krishankumar_2k19ee137@dtu.ac.in

3rd Jatin Dalal
CoE for Electric Vehicle and Related Technologies
Department of Electrical Engineering
Delhi Technological University
Delhi, India
jatindalal_2k19ee124@dtu.ac.in

4th Mayank Kumar (*SM IEEE*)
CoE for Electric Vehicle and Related Technologies
Department of Electrical Engineering
Delhi Technological University
Delhi, India
mayankkumar@dtu.ac.in

2023 International Conference on Power, Instrumentation, Control and Computing (PICC) | 979-8-3503-3446-3/23/$31.00 ©2023 IEEE | DOI: 10.1109/PICC57976.2023.10142411

***Abstract*— Multiport converters (MPC) design is promising from the point of view of centralized control and compact packaging. The basic bidirectional switching cells present several possibilities for constructing a multiport converter. This paper discusses a technique which is termed as switched-boost action, it produces two controlled ports using time-multiplexing of switches. This technique permits regulation and control of all the outputs while utilising comparatively fewer switches. An alternative to traditional DC-DC topology, multiple-output converters with a single input source are now being researched in order to increase power density in small powered multiload appliances. With the help of a switched boost MPC, a solar panel with battery storage system and household loads are connected. The battery is connected to the 12 V bus. The converter's functionality is tested with solar PV, which feeds a 12 V battery and a 36 V load bus. The converter automatically switches to a mode in which the 12 V battery powers the loads on the 36 V bus when solar power is absent.**

Keyword: dc-dc non-isolated converter, multiport converter, solar PV, switched-boost action.

I. Introduction

One input supply and many outputs at various voltage levels make up a converter which is defined in the literature as single input multiple output converter. The block diagram of multiport converter (MPC) is shown in Fig.1, where input and output ports have bidirectional property. Some of the primary applications of the MPCs are explored as consumer electronic devices due to their smaller size and cost factor [1-3], electrical supply for consumer household appliances [4-6], integration of solar PV system in household applications [7-8], and electric vehicles [9]. MPCs can be categorized into two types of converters either isolated or non-isolated, which is shown in Fig. 2. To interact with various loads, the isolated type MPCs employs a transformer with multiple secondary winding. Only one of the outputs is strictly-regulated while remaining outputs are associated with extra secondary winding. In non-isolated type MPCs there is no galvanic separation between separate ports. Further it can also be classified based on the number of inductors like single-inductor multiport converter (SI-MPC) and multiple inductor multiport converter (MI-MPC) [10-11]. Irrespective of the type of MPCs under ideal conditions, the power conservation must obey. Therefore, with reference to Fig.1, the sum of input power must be equal to output power, the same is represented

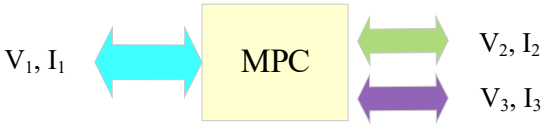

Fig. 1. Multiport converter block diagram.

mathematically in (1) given as follows:

$$V_1 I_1 - V_2 I_2 - V_3 I_3 = 0 \qquad (1)$$

In the above equation, it is assumed that the current in all the ports is in the positive direction of the voltage at that port. At any instant of time, if port 1 is source, then $V_1 \times I_1$ is positive; and if port 2 and 3 are load ports then $V_2 \times I_2$ and $V_3 \times I_3$ are negative. If the input voltage to be made constant and the output power supply to be increased then input current will also increase to satisfy power balance equation. This makes the input current to be higher than the current at boost side.

Only MPCs of the non-isolated category are studied in this article. Generally, when creating various kinds of non-isolated MPCs, the passive and active parts of a non-isolated DC-DC converter are often swapped. A converter consists of '*N*' number of switch can control '*N*' number of output. Although, only one of the outputs may be fully controlled if just one switch is used to control several outputs. The other outputs would then continue to be partially controlled. As a result, choosing MPC essentially involves balancing the requirement to regulate outputs against a simpler converter architecture with fewer controlled switches.

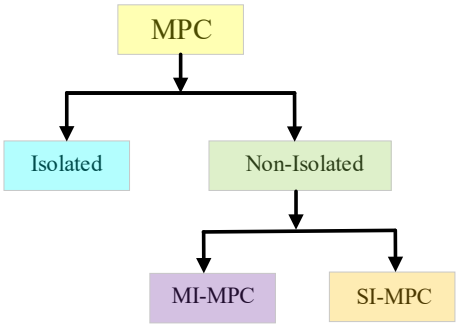

Fig. 2. Different MPCs are categorised depending on magnetics.

979-8-3503-3446-3/23/$31.00 ©2023 IEEE

Authorized licensed use limited to: DELHI TECHNICAL UNIV. Downloaded on June 14,2023 at 05:01:01 UTC from IEEE Xplore. Restrictions apply.

In modern devices, various voltage levels are needed which can be lower or higher than the supply input. Likewise, in renewable applications, boost converter is integrated to a solar panel to utilize a lower supply voltage. Boost converter takes lower input voltage and increase and delivers high output voltage. Thus, it enables lower voltage to be used. Consequently, boost topology is considered as significant choice for MPCs. An inductor is also connected to source which makes DC input current to be continuous.

This paper discusses MPCs obtained from boost topology. A control approach for providing gating signals for three-port converter by time multiplexing switching in modified boost topology is called switched boost MPC. This approach is explained in detail in Section-III. The application of switched boost MPC is discussed with Solar photovoltaic (PV) in Section IV.

II. Solar PV Characteristics

As the price of fossil fuels increases, renewable energy is quickly becoming a more important source of energy. The most plentiful energy source is solar energy. The energy comes from the sun is in the form of electromagnetic radiation. The expanding need for energy, the ongoing depletion of fossil fuel reserves, and the growing concern about environment contamination have propelled humans to research new methods for producing electrical energy from clean, renewable sources, such as solar energy, wind energy, and others. Solar energy has considerable potential for transformation into electric power, able to provide a significant portion of the world's electric demand. It is one of the non-conventional renewable energy sources. It is readily available almost limitless and emits no harmful byproducts or greenhouse gases.

A solar cell, commonly referred to as PV cell, this is a type of electrical device that uses the photovoltaic effect to transform light energy into electrical energy. A solar cell is composed of a p-n junction. Its electrical properties, such as voltage, current or resistance change in response to the light. A solar panel is a module made up with individual solar cells. A maximum open-circuit voltage is around 0.5 to 0.6 volts may be generated by a typical silicon single junction solar cell. Significant amount of renewable energy may be produced when solar cells are joined to form a huge solar panel. The photovoltaic cell's front edge is shielded by a transparent varnish covering. The voltage-current (V-I) and power-voltage (P-V) characteristics are shown in Fig. 3.

As soon as light intensity falls on solar cell, the solar energy present in the light is absorbed by semi-conductor. Due to this absorbed energy, the electron gets free from the atom and produces external DC current. Photovoltaic cells are made up of semiconductor like silicon. Silicon consists of 14 electrons arranged in three different shells. Two shells are completed filled and last shells contains valance electrons. To complete its octet, it shares electron with four different atoms. Phosphorus contains five electrons in valance shell. Therefore, when it combines with silicon, one electron remains free. When a pure silicon gets energy from photon then it causes four electrons to break their bonds and leave their atoms but in case of impure silicon with phosphorus atom it takes less energy to free the electrons as a result doping having a lot freer electrons. The parameters of PV panel are given in Table I.

TABLE-I Electrical Parameters of Solar Panel

Parameters	Values
Maximum power (P_{max})	180 W
Voltage at P_{max} (V_{mpp})	34.4 V
Current at P_{max} (I_{mpp})	5.23 A
Open-circuit voltage (V_{oc})	43.2 V
Short-circuit current (I_{SC})	5.81 A
Temperature coefficient of V_{oc}	-(80±10) mV/ºC
Temperature coefficient of I_{sc}	(0.065 ± 0.015)% /ºC
Temperature coefficient of power	-(0.05 ± 0.015)% /ºC
Operating temperature	45 ± 2 ºC
Maximum system voltage	1000 V DC
Power tolerance	± 5 %

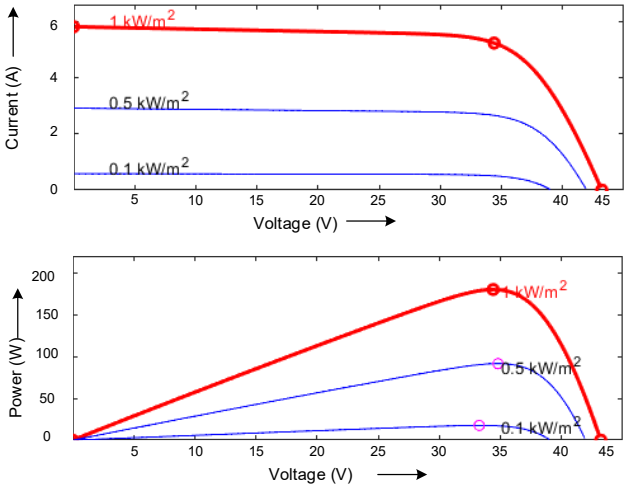

Fig. 3. I-V and P-V characteristics solar photovoltaic module.

III. Switched-Boost Action

The functioning of this approach for manufacturing an MPC, which was created for low to moderate power applications, is outlined below. In this instance, the goal is to minimize the number of switch while achieving multiple output and maintain converter's fundamental property [12-13]. The time- multiplexing control concept for this approach is illustrated by Fig. 4 (a). A synchronous buck converter is used in place of the boost switch to implement an MPC using this theory.

In this case, the boost action is achieved by activating S_1 and S_2 simultaneously. This will cause source current to find a low resistive path, so it makes diode (D_1) reverse biased meanwhile inductor (L_1) charging take place. When both S_1 and S_2 are turned off simultaneously, then it makes diode (D_1 forward biased and inductor current i_{L1} routes through diode (D_1) and inductor current (i_{L2}) freewheels through S_2 anti-parallel diode. If S_1 is turned-on keeping S_2 off, the current of the inductor is routed to V_{out1} and V_{out2} , it makes $V_{sw1} = V_{out1}$. In this case V_{sw1} act as an input voltage for buck structure which is equal to V_{out1}, so in this interval input of buck converter depends on output of boost converter (V_{out1}), this concept is known as switched boost action. By using a diode, the converter structure is made able to three-way energy flows between V_{out1}, V_{out2}, and V_{in}. The output voltages and relation between V_{g1}, V_{g2}, V_{sw1}, V_{sw2} with respect to output voltages is presented in Fig. 4 (b); V_{g1}, V_{g2} are gate voltages to S_1 and S_2, respectively.

Authorized licensed use limited to: DELHI TECHNICAL UNIV. Downloaded on June 14,2023 at 05:01:01 UTC from IEEE Xplore. Restrictions apply.

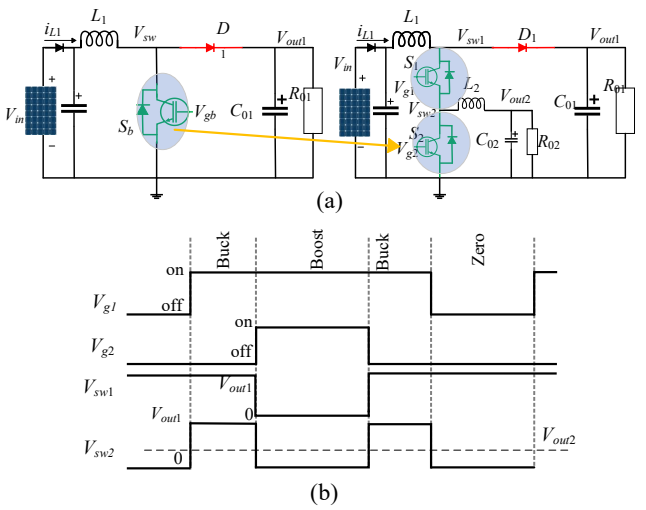

Fig. 4. (a) Switch boost action based multiport converter, (b) waveforms.

IV. Test-Case: An Application of Switched Boost MPC

A. Setup Overview

Multi-output boost converter with switched boost actions can be used in rural roof-top solar power distribution. This section designs and verifies a dual output power supply using a 24 V input as a test case. Typical household loads are interfaced via a 36 V bus. A battery is interfaced to a 12 V output. There are two ways that the power processing unit can function:

(i) Mode A: The renewable energy source acts as an input source for 36 V bus and battery (Fig. 5 (a)).

(ii) Mode B: The 36 V bus is powered by the 12 V battery while the input source is cut-off (Fig. 5 (b)).

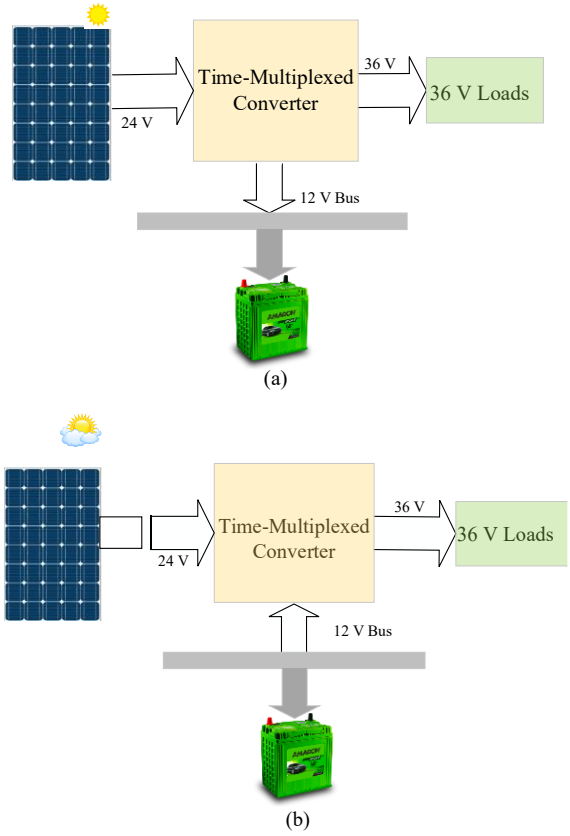

Fig. 5. System setup with solar power source; (a) *Mode A*: availability of renewable energy source (b) *Mode B*: non-availability of renewable energy source.

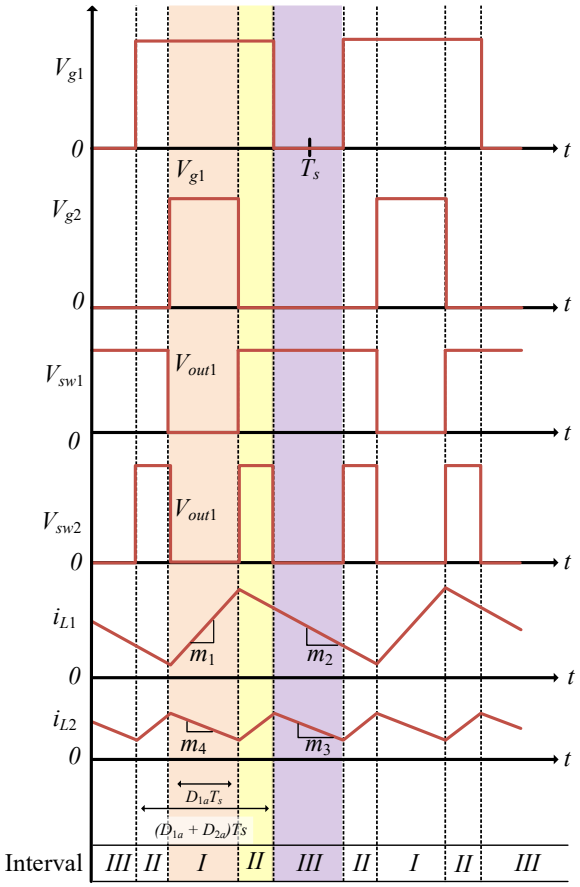

Fig. 6. Converter waveforms for mode-A at steady state

B. Design Parameters

B1. Inductor L_1: For time, $0 < t < D_{1a}T_s$; $V_{L1}=V_{in}$, here V_{L1} is inductor voltage ,V_{in} is source voltage and D_{1a} represents fraction of time in which S_1 and S_2 are activated for same time. The current of L_1 charges from I_{min} to I_{max}. It can be written as follows:

$$\frac{L_1\left(I_{\max}-I_{\min}\right)}{D_{1a}\times T_s}=V_{in}\Rightarrow\frac{L_1\Delta I_{L1}}{D_{1a}\times T_s}=V_{in} \tag{2}$$

$$L_1=\frac{D_{1a}\times V_{in}}{\Delta I_{L1}\times f};\quad \text{where } f=1/T_s \tag{3}$$

$$L_1=\frac{(1/3)\times 24}{0.53\times 10^5}\Rightarrow L_1=150\mu H \tag{4}$$

B2. Capacitor C_{01}: For time, $0 < t < D_{1a}T_s$; $i_c = -I_0$, here i_c is capacitor current and I_0 is the load current.

$$\frac{C_{01}\left(V_{\min}-V_{\max}\right)}{D_{1a}\times T_s}=-I_o\Rightarrow\frac{-C_{01}\Delta V_o}{D_{1a}\times T_s}=-I_o \tag{5}$$

$$C_{01}=\frac{D_{1a}\times I_o}{\Delta V_o\times f} \tag{6}$$

$$C_{01}=\frac{(1/3)\times 1.44}{0.0072\times 10^5}\Rightarrow C_{01}=660.6\mu F \tag{7}$$

Authorized licensed use limited to: DELHI TECHNICAL UNIV. Downloaded on June 14,2023 at 05:01:01 UTC from IEEE Xplore. Restrictions apply.

C. Intervals of operations of Mode A

Solar power acts as input source to the 12 V port connected to the battery and the output port delivers to the load at 36 V. Battery (12 V) takes energy from renewable source. Mode A operation comprises of three intervals. Fig. 6 shows the steady state waveforms during the process. The duty of operation when both the switches S_1 and S_2 are ON is defined as D_{1a}; when switch S_1 is ON and S_2 is OFF is defined as D_{2a}. The switching time period is defined as T_s.

C1. Interval-I: The switches S_1 and S_2 are activated simultaneously to make up the converter operation. The current in the L_1 inductor goes up at a slope of m_1 which is equal to V_{in} / L_1. The current inductor i_{L2} freewheel through switch S_2 and has a slope of m_4 which is equal to -(V_{out2} / L_2). During this interval, the voltages of the v_{sw1} and v_{sw2} switching nodes are shorted to ground. Fig. 7 displays the analogous circuit during this time period.

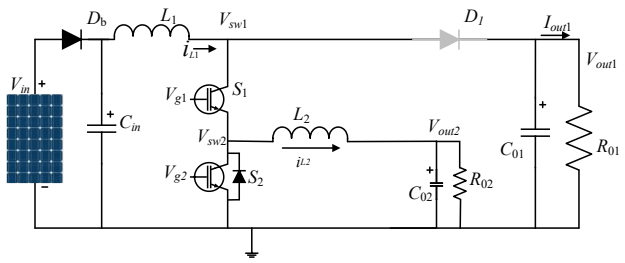

Fig. 7. Operation of MPC under Mode-A: Interval – I.

C2. Interval-II: A short period for switch S_1 is activated and switch S_2 is deactivated and diode (D_1) is forward biased. The source inductor (L_1) gets discharge and the buck side inductor (L_2) gets charged with buck operation at battery side. Slope of inductor current i_{L1} follows m_2 i.e., $\frac{(V_{in}-V_{out1})}{L_1}$ and inductor current i_{L2} follows m_3 i.e., $\frac{(V_{out1}-V_{out2})}{L_2}$. The voltages V_{sw1} and V_{sw2} are fixed to V_{out1}. It is to be observed that here the input of buck converter is constant and nearly equals to V_{out1}. The corresponding equivalent circuit can be found in Fig. 8.

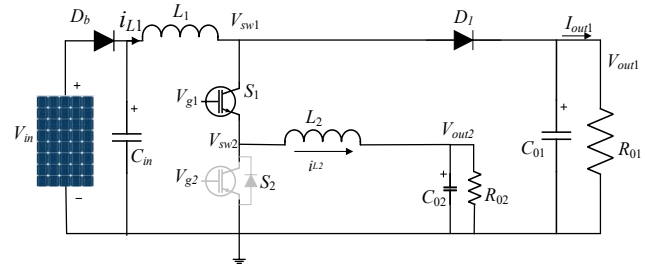

Fig. 8. Operation of MPC under Mode-A: Interval – II.

C3. Interval-III: In this time period switch S_1 is deactivated. This time period resembles the freewheeling action of a traditional buck converter as shown in Fig. 9. The diode (D_1) remains in forward bias. Freewheeling action of buck inductor current i_{L2} take place through anti-parallel diode of S_2, it follows a slope of m_4 which is equal to -(V_{out2} / L_2).

C4. Mathematical modelling of Mode A: In this segment, relationship between input and output is obtained for both the ports. The waveforms are illustrated in Fig. 6. Volt-second balance is applied across source inductor L_1. Mathematically, it can be written as in (8).

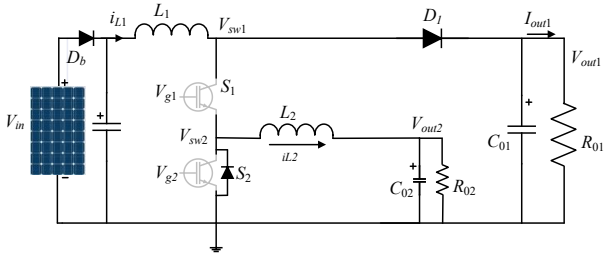

Fig. 9. Operation of MPC under Mode-A: Interval – III.

TABLE-II ELECTRICAL PARAMETERS OF MPC

Parameters	**Values**
Input voltage V_{in}	24 V
Inductor L_1	150 µH
Inductor L_2	110 µH
Filter capacitor at 36V C_{o1}	660 µF
Filter capacitor at 12V C_{o2}	440 µF
Switching frequency (f_{sw})	100 kHz
Output maximum power (W)	200 W
Filter capacitor C_{in}	200 µF

$$V_{in}D_{1a} + (V_{in} - V_{out1})(1 - D_{1a}) = 0 \tag{8}$$

Here, D_{1a} represents fraction of time in which S_1 and S_2 are activated for same time. Thus, output voltage at boost side is given as follows:

$$V_{out1} = \frac{1}{1 - D_{1a}} V_{in} \tag{9}$$

Volt-sec balance is applied across buck inductor L_2 for deriving voltage at buck side given as follows:

$$V_{out2}D_{1a} - (V_{out1} - V_{out2})D_{2a} + V_{out2}(1 - D_{1a} - D_{2a}) = 0 \tag{10}$$

Here, D_{2a} is the fraction of interval when only S_1 is ON and S_2 is OFF. Thus, the steady state expression for V_{out2} is given as follows:

$$V_{out2} = \frac{D_{2a}}{1 - D_{1a}} V_{in} \tag{11}$$

Since, V_{in} = 24 V, D_{1a} = 0.333 and D_{2a} = 0.333,

$$V_{out1} = \frac{24}{1 - 0.333} = 36\text{V}; \quad V_{out2} = \frac{24 \times 0.33}{1 - 0.333} = 12\text{V}$$

D. Simulation results of Mode A

The output voltage at boost side of the converter (V_{out1}) is shown in Fig. 10 (a). The voltage is ranges from 35.994 V to 36.004 V and the output voltage at buck side of the converter (V_{out2}) is shown in Fig. 10 (b). The voltage is ranges from 11.9993 V to 11.99965 V. The current at source side inductor (i_{L1}) is shown in Fig. 10 (c) and the current at buck side inductor (i_{L2}) is shown in Fig. 10 (d).

E. Interval of operation of Mode B

The unavailability of a DC input source results in Mode-B functioning. The boost side 36 V gets power from the 12 V battery supply. Hence the gate pulses of switches are revised to get the boost output. In this mode S_1 become deactivated only S_2 switch is operated. Waveforms are shown in Fig. 11.

Authorized licensed use limited to: DELHI TECHNICAL UNIV. Downloaded on June 14,2023 at 05:01:01 UTC from IEEE Xplore. Restrictions apply.

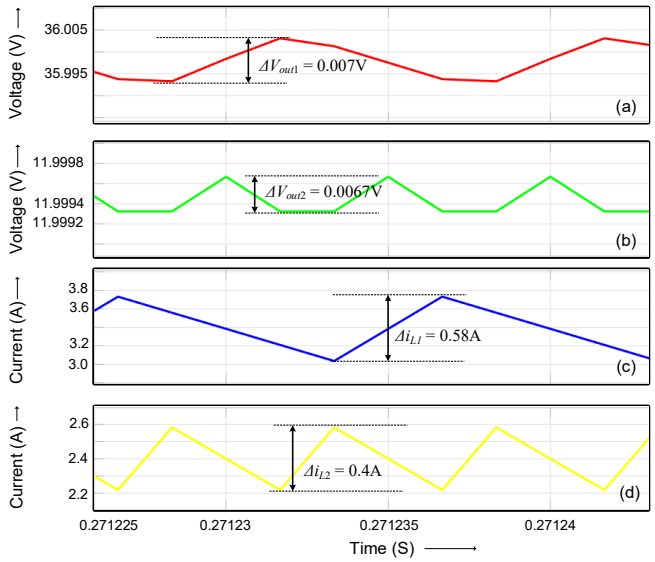

Fig. 10. Output voltage and current for Mode-A; (a) boost side output voltage (b) buck side output voltage; (c) current in source side inductor i_{L1}; (d) current in buck side inductor i_{L2}.

E1. Interval-I: The circuit diagram for this time period is represented below in Fig. 12. In this time period switch S_2 is activated. The inductor (L_2) at buck side gets charged with a slope of m_5 i.e., V_{out2} / L_2. This operation is similar to discharging of battery under boost mode.

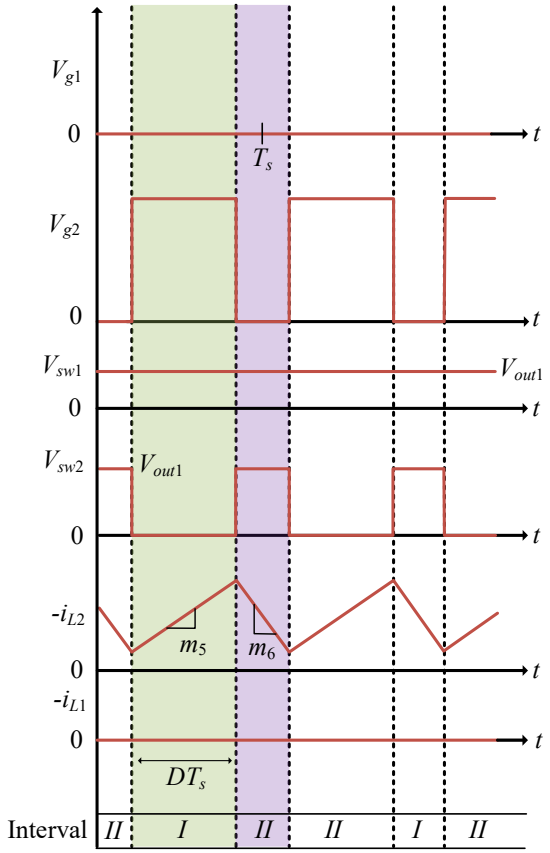

Fig. 11. Converter waveforms for Mode-B at steady state.

E2. Interval-II: The equivalent circuit diagram is shown below in Fig. 13. As C_{in} is connected parallel to V_{out1}. Hence under the steady state condition the inductor current i_{L1} becomes zero.The switch S_2 is deactivated in this period. The inductor at buck side L_2 start transfering energy to boost side with a declining slope of m_6 i.e., $\frac{(V_{out1}-V_{out2})}{L_2}$.

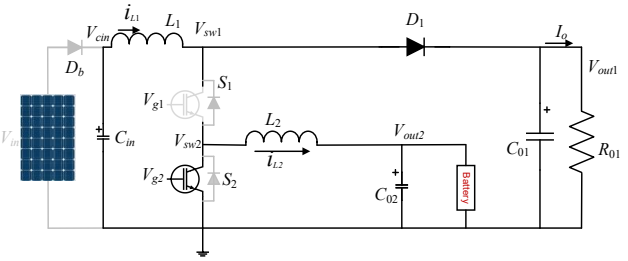

Fig. 12. Operation of MPC under Mode-B: Interval – I.

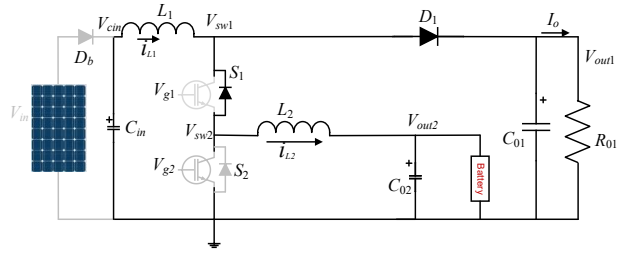

Fig. 13. Operation of MPC under Mode-B: Interval – II.

F. *Mathematical modelling of Mode B*

In this sub-section, the relationship between V_{out1} and V_{out2} is derived. Volt-second balance is applied across L_2. Waveforms are shown in Fig. 11.

$$-V_{out2}DT_s + (V_{out1} - V_{out2})DT_s = 0 \tag{12}$$

Here, D is the duty ratio of switch S_2. Thus, the output voltage at boost side is given as

$$\frac{V_{out1}}{V_{out2}} = \frac{V_{out1}}{V_{battery}} = \frac{1}{1-D} \tag{13}$$

G. *Calculation for Mode B*

$$V_{out1} = \frac{1}{1-D} V_{out2} \tag{14}$$

Since, V_{out2} = 12 V and D = 0.667

$$V_{out1} = \frac{12}{1-0.667} = 36\text{V}$$

H. *Simulation result of Mode B*

The output voltage at boost side of the converter V_{out1} is shown in Fig. 14 (a). The voltage is ranges from 35.987 V to 36.003 V and the current in buck side inductor (i_{L2}) is shown in Fig. 14 (b).

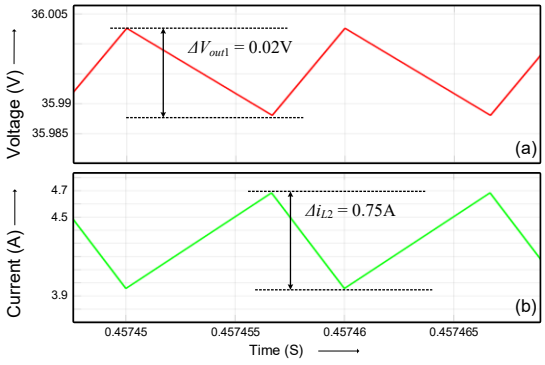

Fig. 14. Output voltage and current for Mode B; (a) boost side output voltage (b) current in buck side inductor i_{L2}.

Authorized licensed use limited to: DELHI TECHNICAL UNIV. Downloaded on June 14,2023 at 05:01:01 UTC from IEEE Xplore. Restrictions apply.

V. Conclusion

MATLAB/Simulink is used to simulate the time-multiplexing control strategy in open loop for three-port dc-dc converter. Converter's components are taken ideal. The converter is tested with a 24V input. Theoretical and simulation findings are almost identical. This converter allows for both step-up and step-down input voltage conversion at various ports. For automotive applications, such as hybrid electric vehicles, the converters can be utilized with a battery, a solar system and/or a fuel cell system.

Acknowledgment

This research supported by the Science and Engineering Research Board (SERB), Department of Science & Technology, Government of India, under the SERB sanction order number SRG/2021/001640.

References

[1] P. Patra, A. Patra, and N. Mishra, "Single-inductor multiple-output switcher with simultaneous buck, boost, and inverted outputs," *IEEE Trans. Power Electron.*, vol. 27, no. 4, pp. 1936- 1951, April 2012.

[2] D. Ma, W.-H. Ki, C. Y. Tsui, and P. K. T. Mok, "Single-inductor multiple- output switching converters with time-multiplexing control in discontinuous conduction mode," *IEEE J. Solid-State Circuits*, vol. 38, pp. 89–100, Jan. 2003.

[3] Hyun-Chang Kim, Chang Soo Yoon, Deog-Kyoon Jeong, and Jaeha Kim, "A Single-inductor, multiple-channel current-balancing LED driver for display backlight applications," *IEEE Trans. Ind. Appl.*, vol. 50, no. 6, pp. 4077-4081, Nov. 2014.

[4] Kumar Modepalli and Leila Parsa, "A scalable N-color LED driver using single inductor multiple current output topology," *IEEE Trans. Power Electron.*, vol. 31, no. 5, pp. 3773-3783, May 2016.

[5] Rajiv Damodaran Prabha and Gabriel A. Rincón-Mora, "Battery-assisted and photovoltaic-sourced switched-inductor CMOS harvesting charger– supply," *IEEE Int. Symposium Circuits and Systems,* pp. 253-256.

[6] H. Shao, X. Li, C. Y. Tsui, and W. H. Ki, "A novel single-inductor dual- input dual-output DC-DC converter with PWM control for solar energy harvesting system," *IEEE Trans. VLSI Syst.*, vol. 22, no. 8, pp. 1693- 1704, Aug. 2014.

[7] Y. Qian, H. Zhang, Y. Chen, Y. Qin, D. Lu, and Z. Hong, "A SIDIDO DC– DC converter with dual-mode and programmable-capacitor-array MPPT control for thermoelectric energy harvesting," *IEEE Trans. Circuits and Systems II: Express Briefs*, vol. 64, no. 8, pp. 952-956, Aug. 2017.

[8] S. K. Mishra, K. K. Nayak, M. S. Rana and V. Dharmarajan, "Switched-boost action based multiport converter," *IEEE Trans. Ind. Appl*., vol. 55, no. 1, pp. 964-975, Jan.-Feb. 2019, doi: 10.1109/TIA.2018.2869098.

[9] Nahavandi A, Hagh M T, Sharifian M B B, et al. "A non-isolated multi-input multioutput DC–DC boost converter for electric vehicle applications," *IEEE Trans. Power Electron*., vol. 30, no. 4, pp. 1818-1835, 2015.

[10] Benfei Wang, Xinan Zhang, Member, Jian Ye, Hoay Beng Gooi, "Deadbeat control for single-inductor multiple-input multiple-output DC-DC Converter," *IEEE Trans. Power Electron*., *Early Access*, 2018.

[11] T. Kerekes, M. Liserre, R. Teodorescu, C. Klumpner, and M. Sumner,"Evaluation of three-phase transformer-less photovoltaic inverter topologies," *IEEE Trans. Power Electron*., vol. 24, no. 9, pp. 2202–2211, Sep. 2009

[12] Santanu Mishra and Olive Ray, "Advances in nanogrid technology and its integration into rural electrification in India," *Proc. IEEE IPEC-ECCE Asia*, Hiroshima, Japan, May 2014.

[13] Olive Ray, Anil Prasad, Santanu Mishra, and A. Joshi, "Integrated dual output converter," *IEEE Trans. Ind. Electron*., vol. 62, no. 1, pp. 371-382, Jan 2015.

Authorized licensed use limited to: DELHI TECHNICAL UNIV. Downloaded on June 14,2023 at 05:01:01 UTC from IEEE Xplore. Restrictions apply.

Journal Pre-proof

Structural and photoluminescence properties of Sm^{3+} ions doped Strontium Yttrium Tungstate Phosphors for Reddish-orange Photonic device applications

Sheetal Kumari , A.S. Rao , R.K. Sinha

PII: S0025-5408(23)00274-X
DOI: https://doi.org/10.1016/j.materresbull.2023.112419
Reference: MRB 112419

To appear in: *Materials Research Bulletin*

Received date: 25 November 2022
Revised date: 21 June 2023
Accepted date: 23 June 2023

Please cite this article as: Sheetal Kumari , A.S. Rao , R.K. Sinha , Structural and photoluminescence properties of Sm^{3+} ions doped Strontium Yttrium Tungstate Phosphors for Reddish-orange Photonic device applications, *Materials Research Bulletin* (2023), doi: https://doi.org/10.1016/j.materresbull.2023.112419

This is a PDF file of an article that has undergone enhancements after acceptance, such as the addition of a cover page and metadata, and formatting for readability, but it is not yet the definitive version of record. This version will undergo additional copyediting, typesetting and review before it is published in its final form, but we are providing this version to give early visibility of the article. Please note that, during the production process, errors may be discovered which could affect the content, and all legal disclaimers that apply to the journal pertain.

© 2023 Published by Elsevier Ltd.

Journal Pre-proof

Highlights

- Solid state reaction method employed to prepare Sm^{3+} doped $Sr_9Y_2W_4O_{24}$ phosphors.
- XRD studies reveal tetragonal structure with an $I4_1/a$ space group for the titled phosphors.
- Dexter theory reveal dipole-dipole type interaction responsible for concentration quenching.
- The calculated CIE coordinates for as-synthesized $Sr_9Y_2W_4O_{24}$ phosphor lies in reddish-orange region.
- The optimised phosphor gives an External Quantum Yield of 86.64%.

Journal Pre-proof

Journal Pre-proof

Structural and photoluminescence properties of Sm^{3+} ions doped Strontium Yttrium Tungstate Phosphors for Reddish-orange Photonic device applications

Sheetal Kumari, A.S. Rao*, R. K. Sinha

Department of Applied Physics, Delhi Technological University, Bawana Road, New Delhi 110 042, India

ABSTRACT

In the present research work, Sm^{3+} ions doped Strontium Yttrium Tungstate ($Sr_9Y_2W_4O_{24}$) phosphors entitled to emit reddish-orange light have been synthesized using the conventional solid-state reaction method and analysed their structure and phase using X-ray diffraction (XRD) patterns. The diffraction peaks of the $Sr_9Y_2W_4O_{24}$ phosphor matches very well with the standard JCPDS pattern with card no. 49-0568. The morphological behaviour of the as synthesized phosphor has been studied using scanning electron microscopy (SEM). Different vibrational bands present in the titled phosphor have been examined using Fourier Transform Infrared (FT-IR) spectroscopy. The optical band gap values of the as synthesized phosphors have been measured using diffuse reflectance spectra (DRS). The photoluminescence (PL) spectral features recorded for the Sm^{3+} ions activated $Sr_9Y_2W_4O_{24}$ phosphor under 405 nm excitation reveal show strong visible reddish-orange emission at 604 nm pertaining to the $^4G_{5/2} \rightarrow {}^6H_{7/2}$ transition of Sm^{3+} ions. Also the PL spectra show concentration quenching at 2 mol% of Sm^{3+} ions doped in to them. From the recorded PL spectra, the CIE chromaticity coordinates estimated for $Sr_9Y_2W_4O_{24}$:2.0mol% of Sm^{3+} phosphor are falling in deep visible reddish orange region. The PL decay spectral profiles recorded at 604 nm emission under 405 nm excitation are showing double exponential behavior and the experimental lifetimes are found to be decreasing with increase in Sm^{3+} ions concentration in the as synthesized phosphors. The temperature-dependent PL (TD-PL) measurements demonstrate relatively better thermal stability for the as synthesized phosphor. All the investigations carried out finally allows us to contemplate the suitability of Sm^{3+} ions doped $Sr_9Y_2W_4O_{24}$ phosphor for reddish-orange photonic device applications.

Corresponding author: E-mail : drsrallam@gmail.com (Prof. A.S. Rao)
Tel+ :91 85860 39007, Fax+ :91 01127871023

Keywords: XRD; Sm^{3+} ions; Tungstate; Photoluminescence: PL Decay

Journal Pre-proof

Journal Pre-proof

1. Introduction

Energy is crucial in many areas of the modern digitized universe that affect social and economic development. A lot of public utilization of energy results in irreversible changes to the environment. It became a challenging task to fulfil the world's ever increasing energy demand. The scientists worldwide are paying lot of attention to address this challenging problem by realizing the light sources having relatively high efficacy [1–5]. Quite recently, solid-state lighting (SSL) devices have certain superior qualities such as longer lifespan, lower production cost and environment friendly nature than the conventional fluorescent and incandescent lights sources. The main building block of SSL technology is a combination of a phosphor coted epoxy excited by a forward-biased p-n junction semiconductor diode [6–10]. At present the most popular commercial w-LEDs are realised by the combination of yellow light emitting $Y_3Al_5O_{12}:Ce^{3+}$ (YAG: Ce^{3+}) phosphor with blue LED semiconducting chip. However, the white light coming out of such combination of blue and yellow light lacks the red component. This red color lacking results in various issues such as low color rendering index (CRI) and high correlated color temperature (CCT) value (7750 K). This has prompted the scientist to put more efforts in preparing a variety of phosphors doped with different rare earth (RE) ions which emit red or reddish-orange light [11–16]. Green, red, and blue-emitting phosphors on n-UV chips were developed as a viable alternative technique that can be adapted to the creation of w-LEDs [17,18]. Usage of these strategies relatively improves the CRI and CCT values when compared with the usage of yellow phosphor with blue LED chip. Apart from this, white light can also be produced by using a combination of RGB phosphors excited with n-UV LED. However, this technique is not frequently utilized because the commercial red phosphor (Y_2O_2S: Eu^{3+}) employed in it does not effectively absorb light generated by the n-UV semiconductor chip. Moreover, the Y_2O_2S: Eu^{3+} phosphor has poor lifespan under n-UV excitation and chemically unstable. This necessitates the exploration of red/reddish-orange emitting phosphors having relatively high luminous efficiency and chemical stability doped with Sm^{3+} ions which can be excited by either blue or by n-UV light [19–22].

RE ions are widely known for their superior performance as activator ions in host matrices and have been used in a wide variety of optical devices. Due to f-f transitions, RE ions are very significant for visible luminescence. When RE ions are incorporated in the specific crystal lattice as a dopant, these f-f transitions result in luminescent sharp emission [23–27]. Additionally, these RE ions are readily energized by absorbing n-UV radiations, and thereby emitting light in the visible region by the process known as downshifting/down-conversion. Among the various RE ions, Sm^{3+} ions are the most effective activators with good radiation

stability to emit efficient red or orange-red color with high color purity [11,15,28]. Also, white light can be generated using Sm^{3+} ions when co-doped with Tb^{3+} ions (reddish-orange + cyan = white) having a better CRI and color tenability[29]. Numerous Sm^{3+} ions doped phosphors have already been reported, such $Ba_3La(PO_4)_3$, $Ca_2Gd_8Si_6O_{26}$, $Sr_2CaMoWO_6$, and $Ba_5Zn_4Y_8O_{21}$: Sm^{3+}, which provide a high absorption in the n-UV region and emit intense reddish-orange light.

Currently, there is a great diversity of host materials that can be doped with RE ions, including phosphates, silicates, fluorides, ceramics, and tungstate's. The tungstate phosphor is also a typical self-activated luminescent material that exhibiting great optical characteristics, strong mechanical strength, high chemical and thermal stability, and environmental friendliness. Tungstate is considered as suitable host for the phosphors because of its low phonon energy which can avoid very competitive non-radiative decay for doped rare earth ions and better luminescence [30–33]. Single tungstate and di-tungstate with Scheelite structures are more prevalent for preparing phosphors suitable for SSL devices. The usage of poly tungstate matrix is rather uncommon despite having excellent luminescence characteristics, physical and chemical stability. However, Zeng et al. [34] reported that $Sr_9Eu_2W_4O_{24}$ phosphors had significant red emission under 395 and 465 nm excitation wavelength and the intensity increases further with increase in Sm^{3+} ion concentration. Recently Shi et al. [33] examined the PL characteristics of $Sr_9Y_2W_4O_{24}$: Mn^{4+} phosphors and discussed their usage in indoor plant cultivation. Eu^{3+} activated tetrahydro-tungstate $Ca_9Gd_2W_4O_{24}$, $Sr_9Eu_2W_4O_{24}$ and di-tungstate $SrLa_2Mg_2W_2O_{12}$ phosphors have also been explored to understand their usage in SSL devices [35–37]. However, to the best of our knowledge, no research has been done on $Sr_9Y_2W_4O_{24}$ phosphor doped with Sm^{3+} ions to understand its usage in w-LEDs.

The primary goal of this research work is to create white light with better luminescence and CCT. Sm^{3+} doped tungstate phosphors were synthesized using the high temperature solid-state reaction technique. To understand the feasibility of using these phosphors in photonic device applications, various techniques such as XRD, SEM, DSC-TGA, FT-IR, UV-vis absorption and PL have been employed. XRD and SEM are used to understand the structural and morphology of the as synthesized phosphor. FT-IR and DSC-TGA studies were conducted to understand the functional groups present in the phosphor and their thermal stability respectively. UV-vis absorption, PL excitation, PL emission, and PL decay studies were conducted to understand the optical and spectroscopic properties of the as synthesized tungstate phosphor doped with different concentrations of Sm^{3+} ions.

Journal Pre-proof

2. Preparation and characterization of the Sm^{3+} ions doped Strontium Yttrium Tungstate Phosphors:

The traditional solid-state reaction method is used to synthesize samarium doped $Sr_9Y_2W_4O_{24}$ phosphors at various concentrations of Sm^{3+} ion (i.e. 1.0, 1.5, 2.0, 2.5, and 3.0 mol%). Starting powders such as pure $SrCO_3$ (99.0%), Y_2O_3 (99.99%), WO_3 (99.99%), and Sm_2O_3 (99.99%) were procured from Sigma-Aldrich have been weighed as per the stoichiometric ratio were crushed for one hour in an agate mortar. Acetone was used as a wetting medium while griding the chemical mix. After through mixing, the mixture was placed into an alumina crucible and sintered for five hours at 1300°C in a programmable muffle furnace. The sample was then left to naturally cool down to the ambient temperature. The sintered sample was collected and again regrind into a fine powder before using it for various characterizations. Fig.1 depicts a flow chart of all the steps that are involved in the synthesis process.

The XRD of the synthesized samples were recorded in the 2θ range from 15° to 60° using the Bruker Model D8 Advance instrument assembled with Nickel filtered Cu-Kα radiation (0.154nm). SEM recordings were done for surface morphology by using JEOL 7610 F Plus machine. The FT-IR spectrum for an un-doped as synthesized phosphor has been recorded in the range 450 to 4000 cm^{-1} using Perkin-Elmer Frontier FT-IR spectrometer. A JASCO model V-923 UV-Vis-NIR spectrophotometer having a spectral resolution of 2 nm was employed to record the diffuse reflectance spectra for all the Sm^{3+}-doped titled phosphors in the wavelength range 200-1800 nm. PL excitation and PL emission spectra were recorded for all the Sm^{3+}-ions doped titled phosphors using JASCO FP-8300 spectrofluorometer having a resolution of 1.0 nm under Xenon excitation source. An Edinburgh FL920 Fluorescence Spectrometer was utilized to read the PL decay profiles. Ocean optics Flame-S-XR1-ES spectrometer was used to conduct TD-PL investigations. Except for the TD-PL studies, all the measurements were taken at an ambient temperature.

3. Result and discussion

3.1. XRD analysis

XRD patterns were used to analyse the crystalline structure and phase purity of both the un-doped and Sm^{3+} doped $Sr_9Y_2W_4O_{24}$ phosphors. Fig. 2 (a) shows the XRD patterns recorded for $Sr_9Y_2W_4O_{24}$: x Sm^{3+} (x = 0.0, 1.0, 1.5, 2.0, 2.5, 3.0 mol%) phosphors along with the suitable standard JCPDS database. All of the peaks were found to be closely matched with the standard JCPDS database card No. 49-0568, which has the lattice parameters a=11.642Å, b=11.642Å, and c=16.465Å, as well as the space group $I4_1/a$ [33,38]. The XRD diffraction patterns of

Journal Pre-proof

$Sr_9Y_2W_4O_{24}$:xSm^{3+} (x = 0.0, 1.0, 1.5, 2.0, 2.5, 3.0 mol%) phosphor compatible with the aforementioned JCPDS database demonstrated that $Sr_9Y_2W_4O_{24}$: Sm^{3+} phosphors have been synthesized successfully with high degree of purity. This allows us to contemplate that, the as synthesized phosphors doesn't contain any impurity phases with the addition of Sm^{3+} ions. This demonstrates that due to their close proximity in ionic radii, Y^{3+} ions (ionic radii 104 pm) are successfully replaced with Sm^{3+} ions (ionic radii 110 pm). Strong and precise diffraction peaks show that the synthesized phosphors have great crystallinity, which is an ideal condition for relatively better luminescence. Furthermore, the right shift observed in XRD patterns with increase in Sm^{3+} (110 pm) ions concentration might be due to the replacement of some of the Sr^{2+} (132 pm) ion sites with Sm^{3+} ions. Thus, Sm^{3+} ions in the as synthesized phosphors might be occupying the two potential positions and resulting a phosphor with double luminescence centres. Major diffraction peaks of the recorded XRD data were taken into account while calculating the crystallite size using the traditional Debye-Scherrer formula shown below [39]:

$$D = \frac{k\lambda}{\beta cos\theta} \qquad (1)$$

where λ, θ denotes the X-ray wavelength (1.54 nm), and diffraction angle, β denotes full width at half maxima (FWHM), k is the form factor (0.94) and, D represents the crystallite size. From the XRD patterns, the requisite values of FWHM and Bragg's diffraction angle were taken to calculate crystallite size. The crystalline size for $Sr_9Y_2W_4O_{24}$: x Sm^{3+} (0.0, 1.0, 1.5, 2.0, 2.5 and 3.0 mol%) phosphors using the Debye-Scherer relation was determined to be 52.54, 53.09, 55.13, 56.93, 59.64 and 60.89 nm respectively.

To study the crystal structure and phase of the $Sr_9Y_2W_4O_{24}$ phosphors, the Rietveld refinement was performed using software from the Full-prof suite. The pseudo-Voigt function has been used to define the profile shape refining. Fig. 2(b) depicts the Rietveld refinement pattern of an un-doped $Sr_9Y_2W_4O_{24}$ phosphor. Black line with dot represents the calculated data pattern and the red solid line with cross represent the experimental data patterns. The Bragg angles (2θ) for $Sr_9Y_2W_4O_{24}$ phosphor are represented by the green short vertical lines. The difference between calculated and experimental patterns is shown by the blue line [40]. The parameters for the crystal structure have finally been improved, and are shown in Table1. It was determined that the obtained goodness of fit ($\chi 2$) was 1.86. This result shows that $Sr_9Y_2W_4O_{24}$ phosphor sample with tetragonal structures can produce pure phases without any secondary phases.

Journal Pre-proof

3.2. Morphological studies from SEM

FE-SEM images of an un-doped and 2.0mol% of Sm^{3+} ions doped $Sr_9Y_2W_4O_{24}$ phosphor are taken for better understand the information related to the morphology and particle size of the as-synthesized phosphors. Fig.3 reveals that $Sr_9Y_2W_4O_{24}$ powder phosphors exhibit irregular polyhedron shape and uneven particle size. Additionally, certain phosphor particles also exhibit very little agglomeration due to manual grinding and the high-temperature reaction process. The majority of commercial phosphor particles on the market today range in size from 2-10 μm. Particle size for an un-doped and 2.0mol% of Sm^{3+} ions doped $Sr_9Y_2W_4O_{24}$ phosphor fall in the range of 5-8 μm. Therefore, the particle size of samples is in the micrometer range, making them ideal for coating in display devices and white LEDs [33].

3.3. Thermogravimetric analysis (TGA) and differential thermal analysis (DTA)

The weight loss and identification of the weight loss processes of the powder precursors to form pure $Sr_9Y_2W_4O_{24}$ phosphor phase were determined using the TGA and DTA curves. The weight loss and associated DTA curve, which has many endothermic peaks from 100 to 1100ºC as shown in Fig. 4. The TGA curve shows 15.88% weight loss over two distinct stages. The first stage (409 - 771ºC), which displays a weight loss of 5.01 % and an endothermic peak at 433ºC and 489º C on the DTA curve, can be attributed to the evaporation of water and acetone utilized in the synthesis of the material [41]. The second stage (771-1028ºC), with a weight loss of 10.87% and an endothermic peak at 754ºC on the DTA curve, represents the exhaustion and decomposition of residual oxides in the sample [42,43]. Finally, no weight loss seen after 1028ºC would indicate the beginning of pure phase formation of $Sr_9Y_2W_4O_{24}$ phosphor.

3.4. FT-IR Spectral analysis:

Infrared spectroscopy (IR) investigation was performed to understand the nature of bonding in un-doped $Sr_9Y_2W_4O_{24}$ phosphor. Fig.5 shows the FT-IR spectrum of an un-doped $Sr_9Y_2W_4O_{24}$ phosphor in the range 450-4000 cm^{-1} which represents the several vibrational bands. The FT-IR spectrum has bands near 547, 853, 1067, 1242, 1402, 2907, 2986, and 3665 cm^{-1}, shown in Fig. 4. The metal-oxygen (Y-O) bond vibrations are attributed to the peaks in the region 445-800 cm^{-1}, while the W-O-W stretching vibration mode may be represented by the band cantered at 853 cm^{-1} [44]. The asymmetric stretching vibration of the W-O bond is considered to be responsible for the peak at around 1067 and 1242 cm^{-1} [45].The presence of Sr-O gives rise to an IR band near 1402 cm^{-1} [46]. The existence of the hydroxyl radicals may be represented by the band seen at 2907 cm^{-1} and the antisymmetric stretching of adsorbed water molecules is accredited to the band at 2986 cm^{-1}. The stretching peak of the hydroxyl group is responsible

for the band seen at 3665 cm^{-1} [47]. As a result, the distinct bonding identified in the synthesized $Sr_9Y_2W_4O_{24}$ phosphors was confirmed by FT-IR spectrum.

3.5. Diffuse reflectance spectra and optical band gap determination

The optical band gap (*E*g) is an important parameter for phosphors that are used in WLEDs. Fig. 6 displays the diffuse reflectance spectra (DRS) recorded for $Sr_9Y_2W_4O_{24}$: x Sm^{3+} (x = 1.0, 1.5, 2.0, 2.5, and 3.0 mol%) phosphors in the 200-1800 nm region. The spectra exhibit transition from the ground level $^6H_{5/2}$ to the excited levels $^3H_{7/2}$, $^4F_{7/2}$, $^4I_{11/2}$, $^6F_{11/2,}$ $^6F_{9/2}$, $^6F_{7/2}$, $^6F_{5/2}$, $^6H_{13/2}$ and $^6H_{11/2}$ at wavelengths of 305, 406, 474, 948, 1082, 1231, 1382, 1483 and 1549 nm respectively. All the aforesaid band assignments were confirmed by Carnall et.al [48]. The optical band gap was calculated by converting the DRS spectral data into the Kubelka-Munk function by using the equation given below [49].

$$F(R) = \frac{(1-R^2)}{2R} = \frac{\alpha}{S} \qquad (2)$$

Here, α denotes absorption coefficient, R represents the reflectance of samples and S stands for scattering coefficient. The relationship between energy bandgap (E_g) and absorption coefficient (α), which is determined by the tauc equation, is seen below [50]:

$$\alpha h\nu = C(h\nu - E_g)^n \qquad (3)$$

Here hυ represent photon energy, C denotes energy independent constant (in current case, = 1), and depending on the type of transition, n can have values 2 and 1/2, which correspond to indirect and direct transitions, respectively [51]. F (R) is directly proportional to α, hence the above equation can be written as follows [50]:

$$F(R)h\nu = C(h\nu - E_g)^n \qquad (4)$$

A tauc plot was drawn between the $[F(R)h\nu]^{1/2}$ and hν to compute the bandgap for the $Sr_9Y_2W_4O_{24}$: Sm^{3+} phosphor. Extrapolating the line based on the linear data yields the optical band gap (E_g). The band gap of $Sr_9Y_2W_4O_{24}$:x Sm^{3+} (x =1.0, 1.5, 2.0, 2.5, 3.0) doped phosphors are 5.47, 5.49, 5.51, 5.54, and 5.55 eV, respectively, as shown in Fig.7**.** The increment in the bandgap is due to the formation of the intermediate energy levels of the RE ions (Sm^{3+}) in the $Sr_9Y_2W_4O_{24}$ host lattice. A little expansion of the unit cell caused by adding the dopant in the

Journal Pre-proof

host tends to make the conduction band and valence band narrower, which leads the band gap to widen.

3.6. PL spectral analysis

To analyse the PL characteristic of Sm^{3+} ions doped $Sr_9Y_2W_4O_{24}$ phosphors, PL spectral features were studied at ambient temperature. The PL excitation spectra of the as-synthesized phosphors in the 325-500 nm spectral range captured at a 604 nm emission wavelength is shown in Fig. 8. Samarium ion concentration varies in $Sr_9Y_2W_4O_{24}$ lattice from 1.0 to 3.0mol%. The spectra consist of the ten excitation bands corresponding to transitions from $^6H_{5/2}$ to $^4D_{5/2}$, $^4D_{3/2}$, $^6P_{7/2}$, $^4G_{11/2}$, $^4F_{7/2}$, $^4M_{19/2}$, $^4I_{13/2}$, $^4I_{11/2}$, $^4M_{15/2}$, and $^4I_{9/2}$ with corresponding wavelengths at 347, 363, 379,392, 405, 428, 462, 471, 478, and 492 nm respectively [52–55]. The strongest peak among these excitation peaks is at 405 nm which is considered to be the optimal excitation wavelength for recording the PL emission spectra. Several excitation peaks observed in n-UV region of the PL excitation spectra indicates the suitability of the $Sr_9Y_2W_4O_{24}$: Sm^{3+} phosphors for the fabrication of white LEDs having their excitation in n-UV light.

Fig. 9 displays the PL emission spectra for $Sr_9Y_2W_4O_{24}$: xSm^{3+} (x=1.0, 1.5, 2.0, 2.5, and 3.0) phosphor upon excitation at 405 nm. PL emission spectra consists of four distinct sharp peaks in the range of 500-750 nm of Sm^{3+} ions, which are attributed to the $^4G_{5/2}$ to $^6H_{5/2}$, $^6H_{7/2}$, $^6H_{9/2}$, and $^6H_{11/2}$ transitions having wavelengths 566, 604, 651 and 711 nm respectively [15]. Among these transitions, the transition analogous to $^4G_{5/2} \rightarrow {}^6H_{7/2}$ (604 nm) is considerably more potent as compared to the other transitions of $Sr_9Y_2W_4O_{24}$ phosphor. Thus, Sm^{3+} will also have two potential positions in the matrix to occupy, providing this kind of phosphor double luminescence centres. This might be the cause of the splitting in the PL emission spectra ascribed to stark splitting in the host lattice [56].

It is generally known that the emission peak at 651 nm which is caused by the $^4G_{5/2} \rightarrow {}^6H_{9/2}$ transition, is entirely an electric dipole transition ($\Delta J \leq 6$; J or J′=0, whether J=2, 4, or 6), while the emission peak at 566 nm which is caused by the $^4G_{5/2} \rightarrow {}^6H_{5/2}$ transition, is entirely a magnetic dipole transition ($\Delta J=0, \pm 1$) and the emission peak at 604 nm which is caused by the $^4G_{5/2} \rightarrow {}^6H_{7/2}$ transition, is partially electric and partially magnetic [57]. In 4f-4f transitions, electric dipole transitions are prohibited. The ratio of the electric dipole to magnetic dipole transitions gives information on the surroundings of the optical active ion within the lattice. The stronger electric-dipole transition leads to the asymmetric nature, and vice versa [18]. The lattice under investigation exhibits the electric-dipole transition corresponding to $^4G_{5/2} \rightarrow {}^6H_{9/2}$ transition at 651 nm wavelength, which is more potent than other magnetic-dipole transitions

Journal Pre-proof

and suggests the presence of Sm^{3+} in the high asymmetry lattice site. The outcome is compatible with the spectral features of the Sm^{3+} doped $Sr_9Y_2W_4O_{24}$ phosphor, which show a strong electric-dipole $^4G_{5/2} \rightarrow {}^6H_{9/2}$ transition. The highly asymmetric environment surrounding Sm^{3+} enables the generation of bright red phosphor with high color purity.

Fig. 10 show the energy level diagram of the as synthesized phosphor, which includes the emission, excitation, energy transfer, and cross-relaxation channels mechanisms (CRC**).** These CRC processes take place at levels which have a slight energy difference. The Sm^{3+} ions are excited to higher energy levels instantly coming back to a $^4G_{5/2}$ meta-stable state via a non-radiative decay mechanism. Since non-radiative transitions that bring the electrons to the $^4G_{5/2}$ metastable state instantaneously release some of the energy. The Sm^{3+} ions return from $^4G_{5/2}$ to the lower levels of $^6H_{5/2}$, $^6H_{7/2}$, $^6H_{9/2,}$ and $^6H_{11/2}$ by radiative decay process. The resonant energy transfer (RET) between Sm^{3+} - Sm^{3+} ions cause this decrease in intensity, which explains self-quenching and CRC processes. In Sm^{3+} ions doped as prepared phosphor, the possible RET channel ($^4F_{9/2} \rightarrow {}^6H_{15/2}$) and CRC accountable for non-radiative energy transfer mechanism such as [39,58]:

CRC 1: ($^4G_{5/2}$+ $^6H_{5/2} \rightarrow {}^6F_{5/2}$+ $^6F_{11/2}$),

A first Sm^{3+} ion relaxes from the level $^4G_{5/2}$ to the intermediate level $^6F_{5/2}$, and a second Sm^{3+} ion is stimulated from the level $^6H_{5/2}$ ground state to the level $^6F_{11/2}$.

CRC 2: ($^4G_{5/2}$+ $^6H_{5/2} \rightarrow {}^6F_{7/2}$+ $^6F_{9/2}$),

A first Sm^{3+} ion relaxes from the level $^4G_{5/2}$ to the intermediate level $^6F_{7/2}$, and a second Sm^{3+} ion is stimulated from the level $^6H_{5/2}$ ground state to the level $^6F_{7/2}$.

CRC 3: ($^4G_{5/2}$+ $^6H_{5/2} \rightarrow {}^6F_{9/2}$+ $^6F_{7/2}$)

A first Sm^{3+} ion relaxes from the level $^4G_{5/2}$ to the intermediate level $^6F_{9/2}$, and a second Sm^{3+} ion is stimulated from the level $^6H_{5/2}$ ground state to the level $^6F_{7/2.}$

CRC 4: ($^4G_{5/2}$+ $^6H_{5/2} \rightarrow {}^6F_{11/2}$+ $^6F_{5/2}$)

As a last, first Sm^{3+} ion relaxes from the level $^4G_{5/2}$ to the intermediate level $^6F_{11/2}$, and a second Sm^{3+} ion is stimulated from the level $^6H_{5/2}$ ground state to the level $^6F_{5/2.}$

The spectral intensities of the bands in the PL spectra were increased with Sm^{3+} ions concentration up to 2.0mol % and subsequently decreased as the Sm^{3+} ions concentration increased further. Because of the energy transfer between Sm^{3+} - Sm^{3+} ions, the intensity of PL bands decreased beyond 2.0mol% of the Sm^{3+} ion concentration and concentration quenching was achieved. As the Sm^{3+} concentration rises, the distance between the two closest Sm^{3+} ions rapidly reduces, strengthening the interaction between the adjacent Sm^{3+} ions which leads to

Journal Pre-proof

non-radiative energy transfer. Concentration quenching is caused by the exchange contact, radiation re-absorption, and multipole-multipole interaction between the activator ions.

To understand the type of interaction between Sm^{3+} ions, the critical distance (R_c) is evaluated. The critical distance R_c is calculated using Blasse's equation [59]:

$$R_c \approx 2\left[\frac{3V}{4\pi X_c N}\right]^{1/3} \qquad (5)$$

where X, N, V stands for the critical concentration, the number of cations in a unit cell, and the volume of the unit cell respectively. The critical distance of the Sm^{3+} ions doped $Sr_9Y_2W_4O_{24}$ phosphor is determined to be 37.63Å. If the R_c value is greater than 5Å, an electric multipolar interaction occurs in the energy transfer between the Sm^{3+} ions.

Dexter theory, which implies a relation between change in PL intensity and doping ions concentration, has been used to identify the type of multipolar interaction, using the following relation [60]:

$$log\left(\frac{I}{x}\right) = logf - \frac{slog(x)}{d} \qquad (6)$$

where A denotes a constant, d denotes the dimensions of the compound (= 3)[61] and I is the emission intensity. The value of s describes the types of interactions for dipole-dipole, dipole-quadrupole, and quadrupole-quadrupole interactions that have a value closer to 6, 8 & 10 respectively. The slope of the linear fitted curve between log(I/x) and log(x) is used to calculate the (s/d) value, shown in Fig. 11. The calculated s value is 5.09, which is very close to 6 indicates the reason for concentration quenching between the Sm^{3+} ions is dipole-dipole in nature in $Sr_9Y_2W_4O_{24}$ phosphors.

3.7. Colorimetric analysis

To understand the colorimetric performance of $Sr_9Y_2W_4O_{24}$: xSm^{3+} ions (x = 1.0, 1.5, 2.0, 2.5, 3.0mol %) phosphor, the CIE chromaticity coordinates were obtained using the emission spectral data (at λ_{ex} = 405 nm). Table 2 shows the evaluated CIE coordinates (x, y) for the as-prepared Sm^{3+} ions doped $Sr_9Y_2W_4O_{24}$ phosphor. Fig. 12 represents the calculated CIE coordinates for all of the as-synthesized $Sr_9Y_2W_4O_{24}$ phosphors at λ_{ex} = 405 nm and λ_{em} = 604 nm. The CIE coordinates marked in Fig. 12 show that, the coordinates of the as synthesized Sm^{3+} doped $Sr_9Y_2W_4O_{24}$ phosphors lie in the reddish-orange region. This reveals the suitability of Sm^{3+} ions doped $Sr_9Y_2W_4O_{24}$ phosphors for plasma display panels and solid-state lighting devices.

Journal Pre-proof

Color Purity (CP) is another critical factor in colorimetric calculations used to investigate color saturation. The following formula can be used to estimate CP[62]:

$$\text{Color purity} = \frac{\sqrt{(x-x_{ee})^2+(y-y_{ee})^2}}{\sqrt{(x_d-x_{ee})^2+(y_d-y_{ee})^2}} \quad (8)$$

where, (x_{ee}, y_{ee}) stands for equal energy point, (x, y) is color coordinates of the $Sr_9Y_2W_4O_{24}$ phosphor, and (x_d, y_d) denotes points of dominant wavelength.

Under 405 nm excitation, it is discovered that the Sm^{3+} (x = 2.0 mol%) ions doped $Sr_9Y_2W_4O_{24}$ phosphor has 97% colour purity which is high than the previous studies[63]**.** Due to its high degree of color purity, the Sm^{3+} (x = 2.0 mol%) ions doped $Sr_9Y_2W_4O_{24}$ phosphor may be employed as an orange-red emitting component in w-LEDs when excited by n-UV or blue light.

3.8. PL decay profile analysis

Fig. 13 demonstrates the PL decay profiles for $Sr_9Y_2W_4O_{24}$: x Sm^{3+} (x = 1.0, 1.5, 2.0, 2.5, and 3.0 mol%) ions phosphor under λ_{ex} = 405 nm and λ_{ex} = 604 nm at room temperature. The decay curves were fitted to different exponential equation but the best fit was observed for bi-exponential equation for all the concentration of Sm^{3+} ions which indicates the significant interaction between dopant ions and energy transfer between the excited Sm^{3+} ion (donor) to unexcited Sm^{3+} ion (acceptor) and the RE ions in the host lattice are likely to occupy two diverse crystallographic sites.

The luminous intensity can be represented by the equation below [64]:

$$I = I_0 + A_1 * \exp\left(-\frac{t}{\tau_1}\right) + A_2 * \exp\left(-\frac{t}{\tau_2}\right) \quad (9)$$

where, I_0 is the intensity at t = 0 & I is the intensity at time t, A_1 & A_2 are the amplitudes of decay constants and τ_1 & τ_2 are the luminescence decay lifetimes, respectively.

The τ_{exp} values were estimated by using the following formula[39,65]:

$$\tau_{exp} = \frac{A_1\tau_1^2 + A_2\tau_2^2}{A_1\tau_1 + A_2\tau_2} \quad (10)$$

The τ_{exp} values of the as synthesized $Sr_9Y_2W_4O_{24}$: x Sm^{3+} (x = 1, 1.5, 2, 2.5, and 3.0 mol%) phosphor is 610, 578, 554, 535 and 451µs, respectively. The values of τ_{exp} was found to be decreasing with increase in the concentration of Sm^{3+} ions in the titled phosphors. This could occur as a result of energy transfer between Sm^{3+}-Sm^{3+} ions itself at a shorter distance.

3.9. TD-PL spectral analysis

To investigate the thermal quenching behaviour, the TD-PL spectra of $Sr_9Y_2W_4O_{24}$: 2.0 Sm^{3+} phosphor were recorded at an excitation wavelength 405 nm within 30ºC to 150ºC temperature range. From the TD-PL spectra of $Sr_9Y_2W_4O_{24}$: 2.0 Sm^{3+} phosphor, it was observed that with

Journal Pre-proof

rise in temperature, the intensities of PL bands decrease without changing its peak position, as shown in Fig.14.

The thermal quenching of phosphors can be described by the non-radiative transition mechanism. Fig. 14 demonstrates the normalized intensity of the $^4G_{5/2} \rightarrow {}^6H_{7/2}$ transition as a function of temperature, with the maximum emission intensity at 30ºC considered as 100 %. The emission intensity drops to 71% at 150ºC, indicating that $Sr_9Y_2W_4O_{24}$: x Sm^{3+} (x = 2.0mol%) phosphor is relatively more stable thermally.

In addition, the activation energy (ΔE) was also evaluated to analyse the thermal properties of the as-synthesized phosphor sample. Using the Arrhenius equation, the value of ΔE was determined by applying the following formula[66]:

$$I_T = \frac{I_0}{1 + C \exp\left(-\frac{\Delta E}{K_B T}\right)} \quad (11)$$

Where I_0 and I_T are the intensity of PL at temperature 30ºC and temperature T (in Kelvin) respectively, K_B is the Boltzmann constant (8.617×10^{-5} eV/K) and C is the arbitrary constant. The value of ΔE is obtained by the slope of a linear fitted graph between ln $[(I_0/I_T)-1]$ and $1/K_BT$ as shown in Fig.15. The calculated value of ΔE for $Sr_9Y_2W_4O_{24}$: x Sm^{3+} (x = 2.0mol%) phosphor comes out to be 0.325 eV which is higher than the other reported lattices i.e., $Ba_3ZrNb_4O_{15}$: Sm^{3+} (ΔE = 0.191 eV), $Lu_{1.93}Ge_2O_5$: $0.06Bi^{3+}$, 0.01 Sm^{3+} (ΔE = 0.114 eV), $SrBi_2B_2O_7$: Sm^{3+} (ΔE = 0.15 eV),[67–69]. Relatively high activation energy value signifies that the synthesized phosphor is relatively more stable thermally. The TD-PL analysis finally allows us to declare that $Sr_9Y_2W_4O_{24}$: x Sm^{3+} (x = 2.0 mol%) phosphor is relatively more stable thermally and demonstrates its suitability in preparing visible photonic devices.

4. Conclusions

In summary, the present work Sm^{3+} ions doped $Sr_9Y_2W_4O_{24}$ phosphors were prepared by using solid state reaction method and investigated their structural, morphological, and PL characteristics. The phase purity of the as synthesized phosphors was confirmed by the XRD profile, and an average crystallite size which was computed using the Debye-Scherer method was found in the 50-65 nm range. $Sr_9Y_2W_4O_{24}$: Sm^{3+} crystallized in a tetragonal structure with an $I4_1/a$ space group. The SEM micrographs show the irregular polyhedron shape and mild agglomeration as well as the particle size falling in the micro-range suited to fabricate w-LEDs. The FT-IR spectrum demonstrates a variety of molecular bonds that are present in the structure. The band gap value was given by the linear fitting of the tauc plot of Sm^{3+} in the $Sr_9Y_2W_4O_{24}$ host which was found to be in range of 5.47-5.55 eV and illustrates the uses of synthesized

Journal Pre-proof

phosphors as photonic devices. According to the PL investigations, the as synthesized phosphors contain four emission bands, the strongest of which is at 604 nm for the $^4G_{5/2} \rightarrow {}^6H_{7/2}$ transition when pumped from $^6H_{5/2} \rightarrow {}^4F_{7/2}$ at 405 nm excitation wavelength. The effect of the Sm^{3+} ion concentration on the PL properties of $Sr_9Y_2W_4O_{24}$ phosphor reveals the concentration quenching at 2.0 mol% of Sm^{3+} ions concentration. The dipole-dipole interaction between Sm^{3+} ions is explained by the applied Dexter theory. The CIE coordinates of the optimized sample at λ_{ex} = 405nm is (0.595, 0.402) which is near the amber LED NSPAR 70BS (0.570, 0.420) produced by Nichia Corporation. The PL decay profile exhibits bi-exponential behaviour for the decay curves with decay times found in the range of microseconds. Due to energy transfer between Sm^{3+} - Sm^{3+} ions, the calculated τ_{exp} values decrease as the Sm^{3+} ion concentration rises. TD-PL examination revealed the thermal stability of the titled phosphors. All the aforementioned studies finally allows us to declare the superior nature of the Sm^{3+} ions doped $Sr_9Y_2W_4O_{24}$ phosphor in fabricating the photonic devices like w-LEDs.

Acknowledgement:

One of the authors Ms. Sheetal Kumari is very much grateful to CSIR-UGC for the award of Junior Research Fellowship (UGC Ref. 1431/ CSIR-UGC NET JUNE 2019) to her. We are very much thankful to the Department of Chemistry, Dayalbagh Eduactional Institute, Deemed University, Agra to avail their SEM facility. The authors are thankful to the authorities of Delhi Technological University, Delhi, India for providing the necessary infrastructure facilities in our MASR lab to carry out the present work.

References:

[1] R.K. Tamrakar, K. Upadhyay, Photoluminescence behaviour of Gd_2SiO_5 phosphor, Optik (Stuttg). 127 (2016) 5204–5206. https://doi.org/10.1016/j.ijleo.2016.02.059.

[2] N.L. Jobbitt, J.P.R. Wells, M.F. Reid, Energy transfer between Sm^{3+} ions in Y_2SiO_5 crystals, J. Lumin. 224 (2020) 117302. https://doi.org/10.1016/j.jlumin.2020.117302.

[3] Y. Zhang, C. Lu, L. Sun, Z. Xu, Y. Ni, Influence of Sm_2O_3 on the crystallization and luminescence properties of boroaluminosilicate glasses, Mater. Res. Bull. 44 (2009) 179–183. https://doi.org/10.1016/j.materresbull.2008.03.004.

Journal Pre-proof

[4] S. Kaur, A.S. Rao, M. Jayasimhadri, Enhanced red down-conversion luminescence and high color purity from flux assisted Eu^{3+} doped calcium aluminozincate phosphor, J. Lumin. 202 (2018) 461–468. https://doi.org/10.1016/j.jlumin.2018.06.015.

[5] S. Kaur, N. Deopa, A. Prasad, R. Bajaj, A.S. Rao, Intense green emission from Tb^{3+} ions doped zinc lead alumino borate glasses for laser and w-LEDs applications, Opt. Mater. (Amst). 84 (2018) 318–323. https://doi.org/10.1016/j.optmat.2018.07.020.

[6] J. Mu, W. Sun, F. Li, Y. Guan, X. Zhou, J. Li, L. Chen, Upconversion luminescent perovskite $CaTiO_3:Yb^{3+}/Er^{3+}$ nanocubes, J. Alloys Compd. 797 (2019) 1002–1006. https://doi.org/10.1016/j.jallcom.2019.05.181.

[7] G.H. Li, N. Yang, J.G. Guo, Z.L. Wang, G.M. Cai, X.J. Wang, Efficient and stable $Sr_3Eu_2B_4O_{12}$ red phosphor benefiting from low symmetry and distorted local environment, Dalt. Trans. 49 (2020) 3260–3271. https://doi.org/10.1039/c9dt04769g.

[8] Z. Xia, Z. Xu, M. Chen, Q. Liu, Recent developments in the new inorganic solid-state LED phosphors, Dalt. Trans. 45 (2016) 11214–11232. https://doi.org/10.1039/c6dt01230b.

[9] Y. Wang, C. Yu, Y. Zhou, E. Song, H. Ming, Q. Zhang, Mn^{4+} doped narrowband red phosphors with short fluorescence lifetime and high color stability for fast-response backlight display application, J. Alloys Compd. 855 (2021) 157347. https://doi.org/10.1016/j.jallcom.2020.157347.

[10] G.L. Bhagyalekshmi, D.N. Rajendran, Luminescence dynamics of Eu^{3+} activated and co-activated defect spinel zinc titanate nanophosphor for applications in WLEDs, J. Alloys Compd. 850 (2021) 156660. https://doi.org/10.1016/j.jallcom.2020.156660.

[11] X. Jin, Y. Xie, R. Tang, X. Geng, J. Che, L. Lou, W. Chen, B. Deng, R. Yu, Novel double perovskite $Sr_3WO_6:Sm^{3+}$, Na^+ orange-red emitting phosphors with high thermal stability for white LEDs, J. Alloys Compd. 899 (2022) 162739. https://doi.org/10.1016/j.jallcom.2021.162739.

[12] S. Shu, Y. Wang, Y. Ke, B. Deng, R. Liu, Q. Song, J. Wang, R. Yu, $NaCaTiTaO_6:Sm^{3+}$: A novel orange-red-emitting tantalate phosphor with excellent thermal stability and high color purity for white LEDs, J. Alloys Compd. 848 (2020) 156359. https://doi.org/10.1016/j.jallcom.2020.156359.

Journal Pre-proof

[13] Y. Xie, X. Geng, J. Guo, W. Shi, Q. Lv, J. Kong, Y. Li, B. Deng, R. Yu, Luminescence of a novel double-perovskite $Sr_2InSbO_6:Eu^{3+}$ orange-red-emitting phosphor for white LEDs and visualization of latent fingerprints, Mater. Res. Bull. 146 (2022) 111574. https://doi.org/10.1016/j.materresbull.2021.111574.

[14] Z. Xu, B. Devakumar, N. Ma, W. Li, X. Huang, High-brightness cyan-emitting Eu^{2+}-activated orthophosphate phosphors for near-UV-pumped white LEDs, J. Lumin. 243 (2022) 118640. https://doi.org/10.1016/j.jlumin.2021.118640.

[15] L. Zhang, J. Che, Y. Ma, J. Wang, R. Kang, B. Deng, R. Yu, H. Geng, Luminescent and thermal properties of novel orange-red emitting $Ca_2MgTeO_6:Sm^{3+}$ phosphors for white LEDs, J. Lumin. 225 (2020) 117374. https://doi.org/10.1016/j.jlumin.2020.117374.

[16] Chu-Yao Zhong, Ladi Li, Qing Chen, Kai-Zhe Jiang, Fa-tang Li, Zhao-Qing Liu, and Yibo Chen, Enhanced Exciton-to-Mn^{2+} Energy Transfer in 3D/0D Cesium–Lead–Chloride Composite Perovskites, Adv. Optical Mater. 2023, 11, 2202321.

[17] M. Peddaiah, C. Salma, B.H. Rudramadevi, Structural and an orange-red emission studies of Sm^{3+} doped $Ba_3La_2 (BO_3)_4$ phosphor for solid state lighting application, Optik (Stuttg). 244 (2021) 166695. https://doi.org/10.1016/j.ijleo.2021.166695.

[18] R. Yu, Y. Guo, L. Wang, H.M. Noh, B.K. Moon, B.C. Choi, J.H. Jeong, Characterizations and optical properties of orange-red emitting Sm^{3+}-doped Y_6WO_{12} phosphors, J. Lumin. 155 (2014) 317–321. https://doi.org/10.1016/j.jlumin.2014.06.041.

[19] Y. Zhang, J. Xu, Q. Cui, B. Yang, Eu^{3+} -doped $Bi_4Si_3O_{12}$ red phosphor for solid state lighting: Microwave synthesis, characterization, photoluminescence properties and thermal quenching mechanisms, Sci. Rep. 7 (2017) 1–12. https://doi.org/10.1038/srep42464.

[20] L. Zhang, B. Sun, C. Shao, F. Zhen, S. Wei, W. Bu, Q. Yao, Z. Jiang, H. Chen, Preparation, band-structure and luminescence of double perovskite $Ba_2MgMoO_6:Eu^{3+}$ orange-red phosphor for white LEDs, Ceram. Int. 44 (2018) 17305–17312. https://doi.org/10.1016/j.ceramint.2018.06.192.

Journal Pre-proof

[21] Y. Li, X. Liu, Sol-gel synthesis, structure and luminescence properties of $Ba_2ZnMoO_6:Eu^{3+}$ phosphors, Mater. Res. Bull. 64 (2015) 88–92. https://doi.org/10.1016/j.materresbull.2014.12.041.

[22] Liang Jing, Qingmei Cen, Qi Pang, and Jin Zhong Zhang, Enhancing Photoluminescence and Stability of Mn-Doped $Cs_2InCl_5 \cdot H_2O$ Microcrystals with Introduced Bi^{3+} Ion, J. Phys. Chem. C 2023 127, 5, 2448-2455 . https://doi.org/10.1021/acs.jpcc.2c08308

[23] G.B. Nair, H.C. Swart, S.J. Dhoble, A review on the advancements in phosphor-converted light emitting diodes (pc-LEDs): Phosphor synthesis, device fabrication and characterization, Prog. Mater. Sci. 109 (2020) 100622. https://doi.org/10.1016/j.pmatsci.2019.100622.

[24] V. Balaram, Rare earth elements: A review of applications, occurrence, exploration, analysis, recycling, and environmental impact, Geosci. Front. 10 (2019) 1285–1303. https://doi.org/10.1016/j.gsf.2018.12.005.

[25] R.S. Kumar, V. Ponnusamy, Phase formation and photoluminescence properties of Sm^{3+} doped Al_5BO_9 phosphor, Optik (Stuttg). 126 (2015) 1224–1227. https://doi.org/10.1016/j.ijleo.2015.03.006.

[26] D. Halmurat, T. Yusufu, Q. ling Wang, J. He, A. Sidike, Rare earth ion Tb^{3+} doped natural sodium feldspar ($NaAlSi_3O_8$) Luminescent properties and energy transfer, Sci. Rep. 9 (2019) 1–8. https://doi.org/10.1038/s41598-019-51171-3.

[27] S. Kumari, Anu, A. Prasad, P. Rohilla, A.S. Rao, Prospective applications of thermally stable Dy3+ doped potassium zinc strontium borate (KZSB) glasses in w-LEDs, J. Mater. Sci. Mater. Electron. 34 (2023). https://doi.org/10.1007/s10854-023-10272-6.

[28] N. Deopa, B. Kumar, M.K. Sahu, P.R. Rani, A.S. Rao, Effect of Sm^{3+} ions concentration on borosilicate glasses for reddish orange luminescent device applications, J. Non. Cryst. Solids. 513 (2019) 152–158. https://doi.org/10.1016/j.jnoncrysol.2019.03.025.

[29] Q. Ren, Y. Zhao, X. Wu, O. Hai, The color tunable of Tb^{3+}/Sm^{3+} co-doped phosphors through $Tb^{3+} \rightarrow Sm^{3+}$ energy transfer, Polyhedron. 192 (2020) 114862. https://doi.org/10.1016/j.poly.2020.114862.

Journal Pre-proof

[30] P. Du, L. Wang, J.S. Yu, Luminescence properties and energy transfer behavior of single-component $NaY(WO_4)_2:Tm^{3+}/Dy^{3+}/Eu^{3+}$ phosphors for ultraviolet-excited white light-emitting diodes, J. Alloys Compd. 673 (2016) 426–432. https://doi.org/10.1016/j.jallcom.2016.02.245.

[31] E. Kaewnuam, J. Kaewkhao, Synthesis-temperature effect on the luminescence under light and UV excitation of Eu^{3+} doped lithium lanthanum borate phosphor, Mater. Today Proc. 5 (2018) 15086–15091. https://doi.org/10.1016/j.matpr.2018.04.062.

[32] J. Xie, L. Cheng, H. Tang, X. Yu, Y. Wang, C. Wang, X. Mi, Q. Liu, X. Zhang, Synthesis and photoluminescence properties of $NaBi(WO_4)_2:Eu^{3+}$ red-emitting phosphor for NUV-based WLEDs, J. Lumin. 219 (2020) 116841. https://doi.org/10.1016/j.jlumin.2019.116841.

[33] L. Shi, Y. jie Han, H. xin Wang, D. chen Shi, X. yu Geng, Z. wei Zhang, High-efficiency and thermally stable far-red emission of Mn^{4+} in double cubic perovskite $Sr_9Y_2W_4O_{24}$ for plant cultivation, J. Lumin. 208 (2019) 307–312. https://doi.org/10.1016/j.jlumin.2018.12.065.

[34] Q. Zeng, P. He, X. Zhang, H. Liang, M. Gong, Q. Su, $M_9Gd_2W_4O_{24}:Eu^{3+}$ (M^{2+} = Ca^{2+} and Sr^{2+}) red phosphors for NUV and blue InGaN-based WLEDs, Chem. Lett. 38 (2009) 1172–1173. https://doi.org/10.1246/cl.2009.1172.

[35] C. Qin, Y. Huang, H.J. Seo, The thermal stability and structural site-distribution of Eu^{3+} ions in the red-emitting phosphors $Ca_9Eu_2W_4O_{24}$ and $Sr_9Eu_2W_4O_{24}$, J. Alloys Compd. 534 (2012) 86–92. https://doi.org/10.1016/j.jallcom.2012.04.034.

[36] S. Long, J. Hou, G. Zhang, F. Huang, Y. Zeng, High quantum efficiency red-emission tungstate based phosphor $Sr(La_{1-x}Eu_x)_2Mg_2W_2O_{12}$ for WLEDs application, Ceram. Int. 39 (2013) 6013–6017. https://doi.org/10.1016/j.ceramint.2013.01.013.

[37] Q. Zeng, H. Liang, M. Gong, Preparation of tetra-tungstate red phosphors and corresponding white light-emitting diodes, Asian J. Chem. 25 (2013) 5971–5974. https://doi.org/10.14233/ajchem.2013.14206.

Journal Pre-proof

[38] F. Zhou, M. Gao, Y. Shi, Z. Li, G. Zhu, S. Xin, C. Wang, Structure identification and strongly enhanced luminescence of $Sr_9Y_2(WO_6)_4$: Mn^{4+} phosphors by co-doping Mg^{2+} ions for plant growth LEDs, J. Lumin. 223 (2020) 117235. https://doi.org/10.1016/j.jlumin.2020.117235.

[39] S. Kaur, A.S. Rao, M. Jayasimhadri, Spectroscopic and photoluminescence characteristics of Sm^{3+} doped calcium aluminozincate phosphor for applications in w-LED, Ceram. Int. 43 (2017) 7401–7407. https://doi.org/10.1016/j.ceramint.2017.02.129.

[40] S. Kaur, A.S. Rao, M. Jayasimhadri, Color tunability and energy transfer studies of Dy^{3+}/ Eu^{3+} co-doped calcium aluminozincate phosphor for lighting applications, Mater. Res. Bull. 116 (2019) 79–88. https://doi.org/10.1016/j.materresbull.2019.04.022.

[41] K. Maheshwari, A.S. Rao, Down-shifting photoluminescent properties of Tb^{3+} doped phosphate glasses for intense green-emitting devices applications, Opt. Mater. (Amst). 137 (2023) 113533. https://doi.org/10.1016/j.optmat.2023.113533.

[42] S. Kaur, A.S. Rao, M. Jayasimhadri, B. Sivaiah, D. Haranath, Synthesis optimization, photoluminescence and thermoluminescence studies of Eu^{3+} doped calcium aluminozincate phosphor, J. Alloys Compd. 802 (2019) 129–138. https://doi.org/10.1016/j.jallcom.2019.06.169.

[43] N. Kaczorowska, A. Szczeszak, S. Lis, Synthesis and tunable emission studies of new up-converting $Ba_2GdV_3O_{11}$ nanopowders doped with Yb^{3+}/Ln^{3+} (Ln^{3+} = Er^{3+}, Ho^{3+}, Tm^{3+}), J. Lumin. 200 (2018) 59–65. https://doi.org/10.1016/j.jlumin.2018.03.085.

[44] T. Yang, Q. Xiang, L. Feng, C. Dong, X. Zhang, Z. Ning, X. Lai, D. Gao, Yttrium-based metal-organic frameworks: Controllable synthesis, growth mechanism and the phase transformation to Y_2O_3:Eu^{3+} phosphors, J. Lumin. 214 (2019) 116567. https://doi.org/10.1016/j.jlumin.2019.116567.

[45] V. Chaudhary, A. Kaur, Enhanced room temperature sulfur dioxide sensing behaviour of in situ polymerized polyaniline-tungsten oxide nanocomposite possessing honeycomb morphology, RSC Adv. 5 (2015) 73535–73544. https://doi.org/10.1039/c5ra08275g.

Journal Pre-proof

[46] V. Dubey, J. Kaur, S. Agrawal, Effect of europium doping levels on photoluminescence and thermoluminescence of strontium yttrium oxide phosphor, Mater. Sci. Semicond. Process. 31 (2015) 27–37. https://doi.org/10.1016/j.mssp.2014.10.052.

[47] N.S. Kuriyan, M. Sabeena, Luminescence studies of Eu^{3+} doped calcium magnesium silicate phosphor prepared at different annealing temperatures for fine color tunability, J. Lumin. 249 (2022) 119038. https://doi.org/10.1016/j.jlumin.2022.119038.

[48] W.T. Carnall, P.R. Fields, K. Rajnak, Electronic energy levels of the trivalent lanthanide aquo ions. IV. Eu^{3+}, J. Chem. Phys. 49 (1968) 4424–4442. https://doi.org/10.1063/1.1669893.

[49] P. Phogat, S.P. khatkar, V.B. Taxak, R.K. Malik, Sm^{3+} doped $Bi_4MgO_4(PO_4)_2$:crystal and optoelectronic investigation of the solution combustion derived bright orange emanating novel nanophosphor for SSLs, Mater. Chem. Phys. 276 (2022) 125389. https://doi.org/10.1016/j.matchemphys.2021.125389.

[50] P. Rohilla, A.S. Rao, Synthesis optimisation and efficiency enhancement in Eu^{3+} doped barium molybdenum titanate phosphors for w-LED applications, Mater. Res. Bull. 150 (2022) 111753. https://doi.org/10.1016/j.materresbull.2022.111753.

[51] L. Wang, H.M. Noh, B.K. Moon, S.H. Park, K.H. Kim, J. Shi, J.H. Jeong, Dual-Mode Luminescence with Broad Near UV and Blue Excitation Band from Sr_2CaMoO_6:Sm^{3+} Phosphor for White LEDs, J. Phys. Chem. C. 119 (2015) 15517–15525. https://doi.org/10.1021/acs.jpcc.5b02828.

[52] C.B.A. Devi, K. Swapna, S. Mahamuda, M. Venkateswarlu, M.V.V.K.S. Prasad, K. Siva Rama Krishna Reddy, N. Deopa, A.S. Rao, Spectroscopic studies and lasing potentialities of Sm^{3+} ions doped single alkali and mixed alkali fluoro tungstentellurite glasses, Opt. Laser Technol. 111 (2019) 176–183. https://doi.org/10.1016/j.optlastec.2018.09.051.

[53] B. Han, J. Ren, P.P. Teng, J.B. Zhu, Y. Shen, Z.A. Li, X. Zhu, X. Yang, Synthesis and photoluminescence properties of a novel double perovskite Ca_2LaSbO_6:Sm^{3+} phosphor for w-LEDs, Ceram. Int. 48 (2022) 971–980. https://doi.org/10.1016/j.ceramint.2021.09.182.

Journal Pre-proof

[54] N. Deopa, S. Kaur, A. Prasad, B. Joshi, A.S. Rao, Spectral studies of Eu^{3+} doped lithium lead alumino borate glasses for visible photonic applications, Opt. Laser Technol. 108 (2018) 434–440. https://doi.org/10.1016/j.optlastec.2018.07.010.

[55] P. Shahab Khan, B.C. Jamalaiah, M. Jayasimhadri, H. Kaur, N. Madhu, P. Raghupathi, K. Pavani, Deep reddish-orange emitting $Sr_3Gd(PO_4)_3$: Sm^{3+} phosphors via modified citrate-gel combustion method, J. Mol. Struct. 1255 (2022) 132428. https://doi.org/10.1016/j.molstruc.2022.132428.

[56] K. Nanda, R.S. Kundu, I. Pal, R. Punia, N. Kishore, Concentration dependence of intensity parameters and radiative properties of Sm^{3+} ions doped in BaO -ZnO-B_2O_3 glasses, J. Alloys Compd. 676 (2016) 521–526. https://doi.org/10.1016/j.jallcom.2016.03.112.

[57] I. Kumar, A.K. Gathania, Photoluminescence and quenching study of the Sm^{3+}-doped $LiBaPO_4$ phosphor, J. Mater. Sci. Mater. Electron. 33 (2022) 328–341. https://doi.org/10.1007/s10854-021-07301-7.

[58] G. Ouertani, M. Ferhi, K. Horchani-Naifer, M. Ferid, Effect of Sm^{3+} concentration and excitation wavelength on spectroscopic properties of $GdPO_4$:Sm^{3+} phosphor, J. Alloys Compd. 885 (2021) 161178. https://doi.org/10.1016/j.jallcom.2021.161178.

[59] S. Chen, Y. Wang, B. Zhao, B. Deng, Y. Liu, S. Chen, J. Wang, G. Wang, R. Yu, Luminescence properties of novel orange-red-emitting Gd_2InSbO_7 : Sm^{3+} phosphor with high color purity for W-LEDs, J. Lumin. 237 (2021) 118148. https://doi.org/10.1016/j.jlumin.2021.118148.

[60] J. Xie, L. Cheng, H. Tang, X. Yu, Z. Wang, X. Mi, Q. Liu, X. Zhang, Synthesis and photoluminescence properties of NUV-excited $NaBi(MoO_4)_2$: Sm^{3+} phosphors for white light emitting diodes, Opt. Laser Technol. 147 (2022) 107659. https://doi.org/10.1016/j.optlastec.2021.107659.

[61] P. Du, X. Huang, J.S. Yu, Facile synthesis of bifunctional Eu^{3+}-activated $NaBiF_4$ red-emitting nanoparticles for simultaneous white light-emitting diodes and field emission displays, Chem. Eng. J. 337 (2018) 91–100. https://doi.org/10.1016/j.cej.2017.12.063.

Journal Pre-proof

[62] P. Dixit, V. Chauhan, S.B. Rai, P.C. Pandey, Realization of neutral white light emission in $CaMoO_4$:4Dy^{3+} phosphor via Sm^{3+} co-doping, J. Alloys Compd. 897 (2022) 162820. https://doi.org/10.1016/j.jallcom.2021.162820.

[63] J. Zhao, S.X. Huang, D. Zhao, C.H. Huang, M.J. Ma, R.J. Zhang, Y.C. Fan, B.Z. Liu, J.W. Gao, Q. Zong, Y.P. Yu, Sm^{3+} doped $K_3Gd_3B_4O_{12}$: An orange-emitting phosphor for white light-emitting diodes, Optik (Stuttg). 159 (2018) 115–122. https://doi.org/10.1016/j.ijleo.2018.01.043.

[64] N. Deopa, M.K. Sahu, P.R. Rani, R. Punia, A.S. Rao, Realization of warm white light and energy transfer studies of Dy^{3+}/Eu^{3+} co-doped Li_2O-PbO-Al_2O_3-B_2O_3 glasses for lighting applications, J. Lumin. 222 (2020) 117166. https://doi.org/10.1016/j.jlumin.2020.117166.

[65] V. Uma, M. Vijayakumar, K. Marimuthu, G. Muralidharan, Luminescence and energy transfer studies on Sm^{3+}/Tb^{3+} codoped telluroborate glasses for WLED applications, J. Mol. Struct. 1151 (2018) 266–276. https://doi.org/10.1016/j.molstruc.2017.09.053.

[66] X. Zhang, Z. Zhu, Z. Guo, Z. Sun, L. Zhou, Z. chao Wu, Synthesis, structure and luminescent properties of Eu^{3+} doped $Ca_3LiMgV_3O_{12}$ color-tunable phosphor, Ceram. Int. 44 (2018) 16514–16521. https://doi.org/10.1016/j.ceramint.2018.06.069.

[67] G. Zhu, Z. Li, F. Zhou, C. Wang, S. Xin, A novel temperature sensitive Sm^{3+} doped niobate orange-red phosphor : The synthesis and characteristic luminescent property investigation, J. Lumin. 196 (2018) 32–35. https://doi.org/10.1016/j.jlumin.2017.12.014.

[68] Q. Li, S. Zhang, W. Lin, W. Li, Y. Li, Z. Mu, F. Wu, A warmwhite emission of Bi^{3+}-Eu^{3+} and Bi^{3+}-Sm^{3+} codoping $Lu_2Ge_2O_7$ phosphors by energy transfer of Bi^{3+}-sensitized Eu^{3+}/Sm^{3+}, Spectrochim. Acta Part A Mol. Biomol. Spectrosc. (2019) 117755. https://doi.org/10.1016/j.saa.2019.117755.

[69] L. Wu, Y. Bai, L. Wu, H. Yi, Y. Kong, Y. Zhang, J. Xu, Sm^{3+} and Eu^{3+} codoped $SrBi_2B_2O_7$: A red-emitting phosphor with improved thermal stability, RSC Adv. 7 (2017) 1146–1153. https://doi.org/10.1039/c6ra26752a.

Journal Pre-proof

Figure Captions:

Fig. 1. Flow chart of the steps involved in the synthesis of $Sr_9Y_2W_4O_{24}$ phosphor.

Fig. 2. (a) XRD patterns of $Sr_9Y_2W_4O_{24}$: xSm^{3+} (x= 0.0, 1.0, 1.5, 2.0, 2.5, and 3.0 mol%) phosphors along with the standard diffraction pattern of $Sr_9Y_2W_4O_{24}$ phosphor (b) Reitveld refinement pattern of an un-doped $Sr_9Y_2W_4O_{24}$ phosphor.

Fig. 3. SEM images recorded for (a) an un-doped (b) 2.0 mol% of Sm^{3+} ions doped $Sr_9Y_2W_4O_{24}$ phosphor.

Fig. 4. TGA and DTA curve for $Sr_9Y_2W_4O_{24}$ phosphor.

Fig. 5. FT-IR spectrum of an un-doped $Sr_9Y_2W_4O_{24}$ phosphor.

Fig. 6. Diffuse reflectance Spectra of $Sr_9Y_2W_4O_{24}$: xSm^{3+} (x= 1.0, 1.5, 2.0, 2.5, and 3.0 mol%) phosphors.

Fig. 7. Tauc plot for direct optical band gap of Sm^{3+} ions doped $Sr_9Y_2W_4O_{24}$ phosphors at different concentrations.

Fig. 8. Excitation spectra of Sm^{3+} ions doped $Sr_9Y_2W_4O_{24}$ phosphors under 604 nm emission wavelength.

Fig. 9. PL emission spectra of Sm^{3+} ions doped $Sr_9Y_2W_4O_{24}$ phosphors at λ_{ex} = 405 nm.

Fig. 10. Partial energy level diagram and possible cross-relaxation channels of Sm^{3+} ion doped $Sr_9Y_2W_4O_{24}$ phosphor.

Fig. 11. Plot of log (I/x) with log(x).

Fig. 12. CIE chromaticity coordinates of Sm^{3+} ions in $Sr_9Y_2W_4O_{24}$ phosphors.

Fig. 13. PL decay profiles of Sm^{3+} ions doped $Sr_9Y_2W_4O_{24}$ phosphors at λ_{ex} = 405 nm wavelength.

Fig. 14. TD-PL emission intensity variation for 2.0 mol% Sm^{3+} ion doped $Sr_9Y_2W_4O_{24}$ phosphor at λ_{ex} = 405 nm with temperature from RT to 150ºC.

Fig. 15. Linear relationship of ln $[(I_0/I_T) - 1]$ versus $1/K_BT$ plot to calculate the activation energy of 2.0mol% Sm^{3+} ions doped $Sr_9Y_2W_4O_{24}$ phosphors.

Journal Pre-proof

Fig. 1

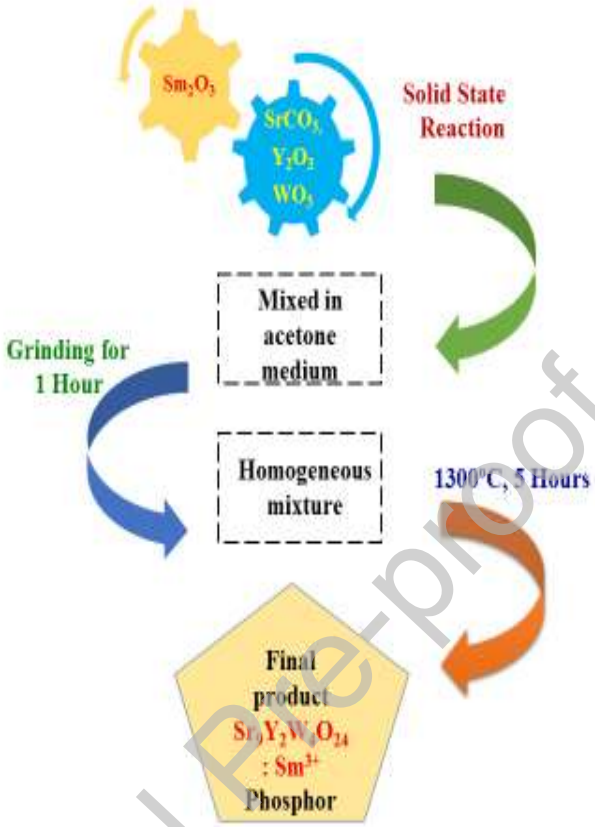

Journal Pre-proof

Fig. 2(a)

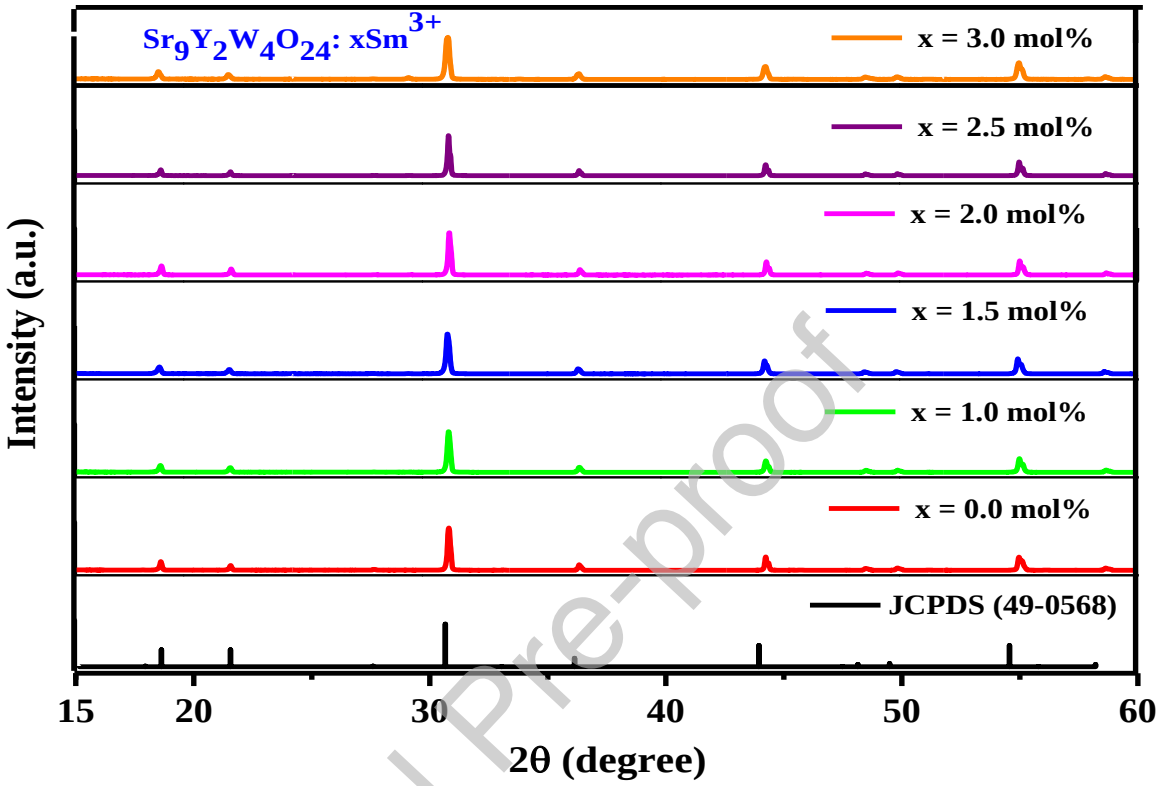

Journal Pre-proof

Fig. 2(b)

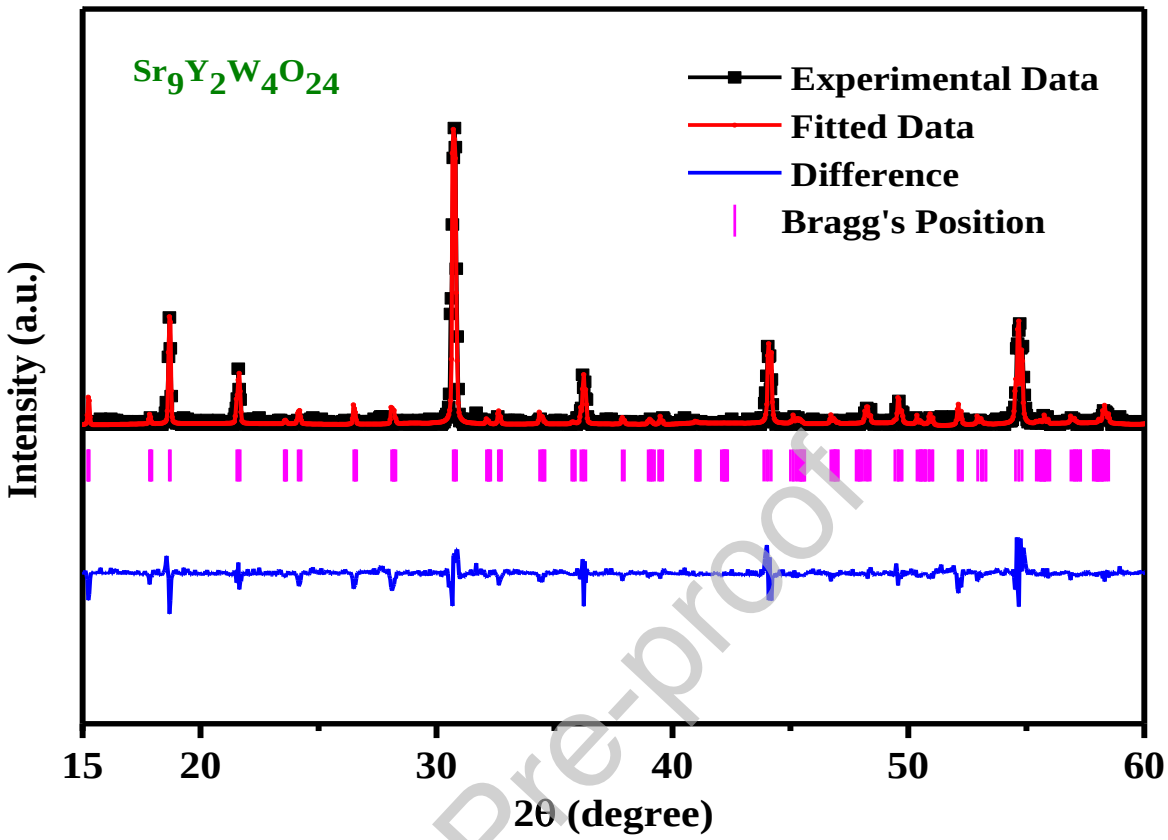

Journal Pre-proof

Fig. 3

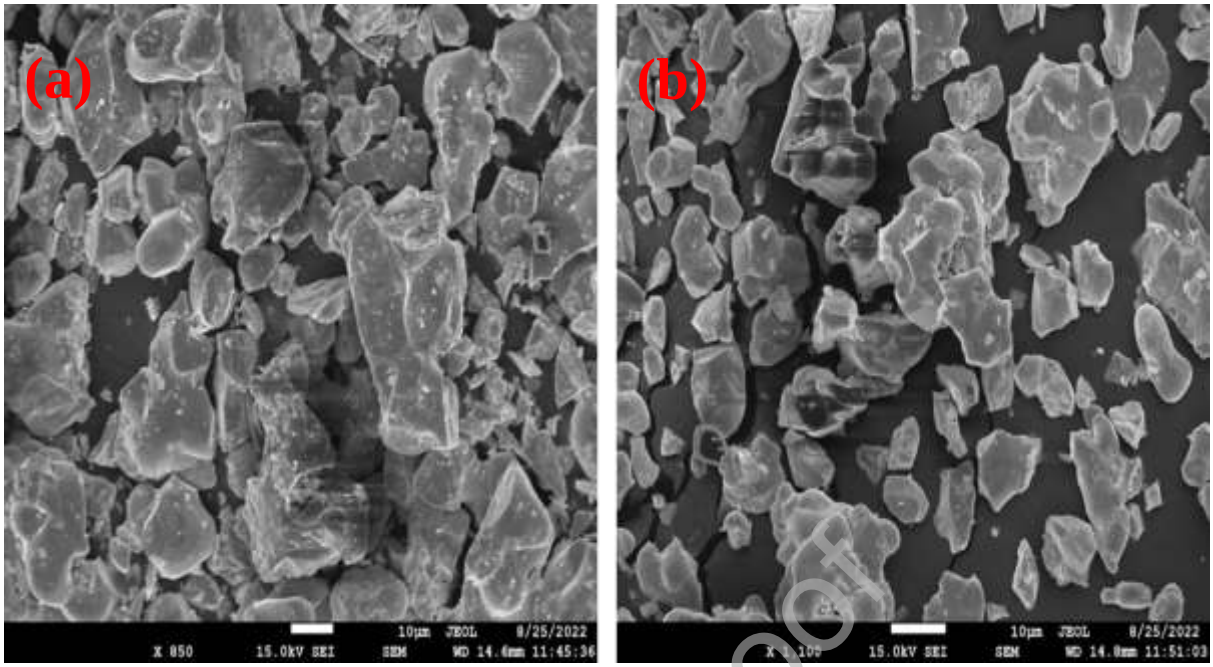

Fig.4

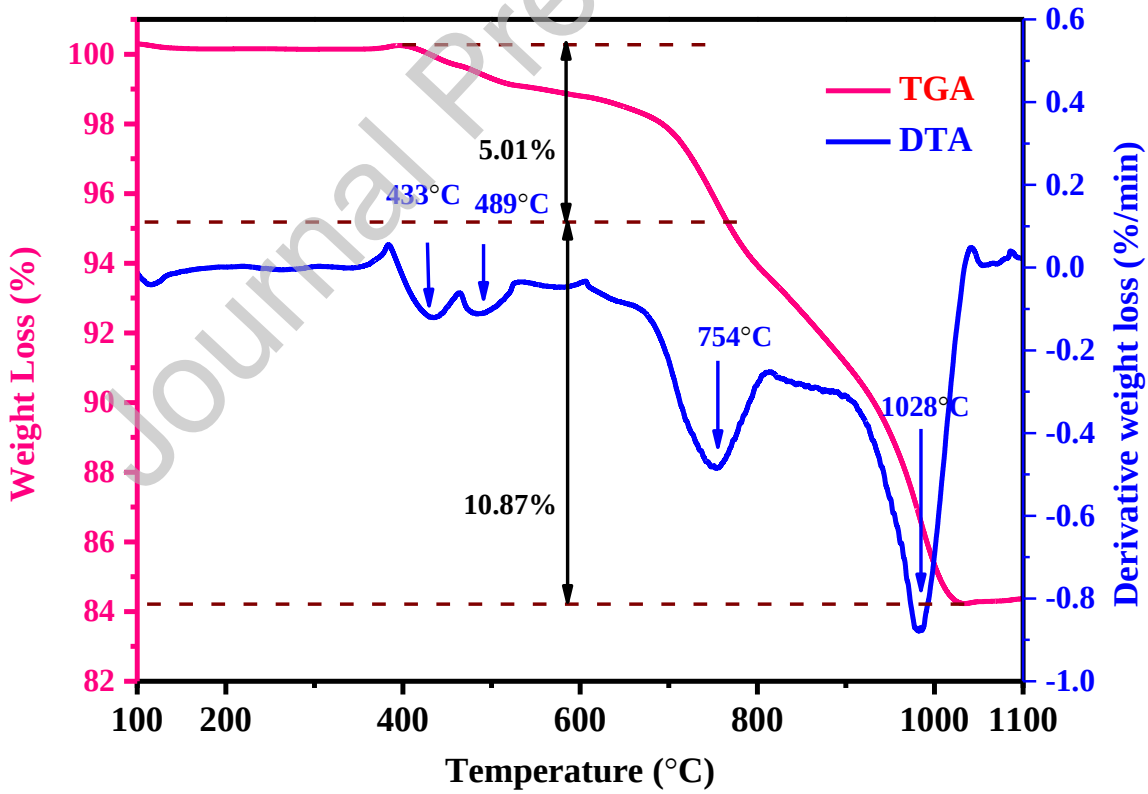

Journal Pre-proof

Fig.5

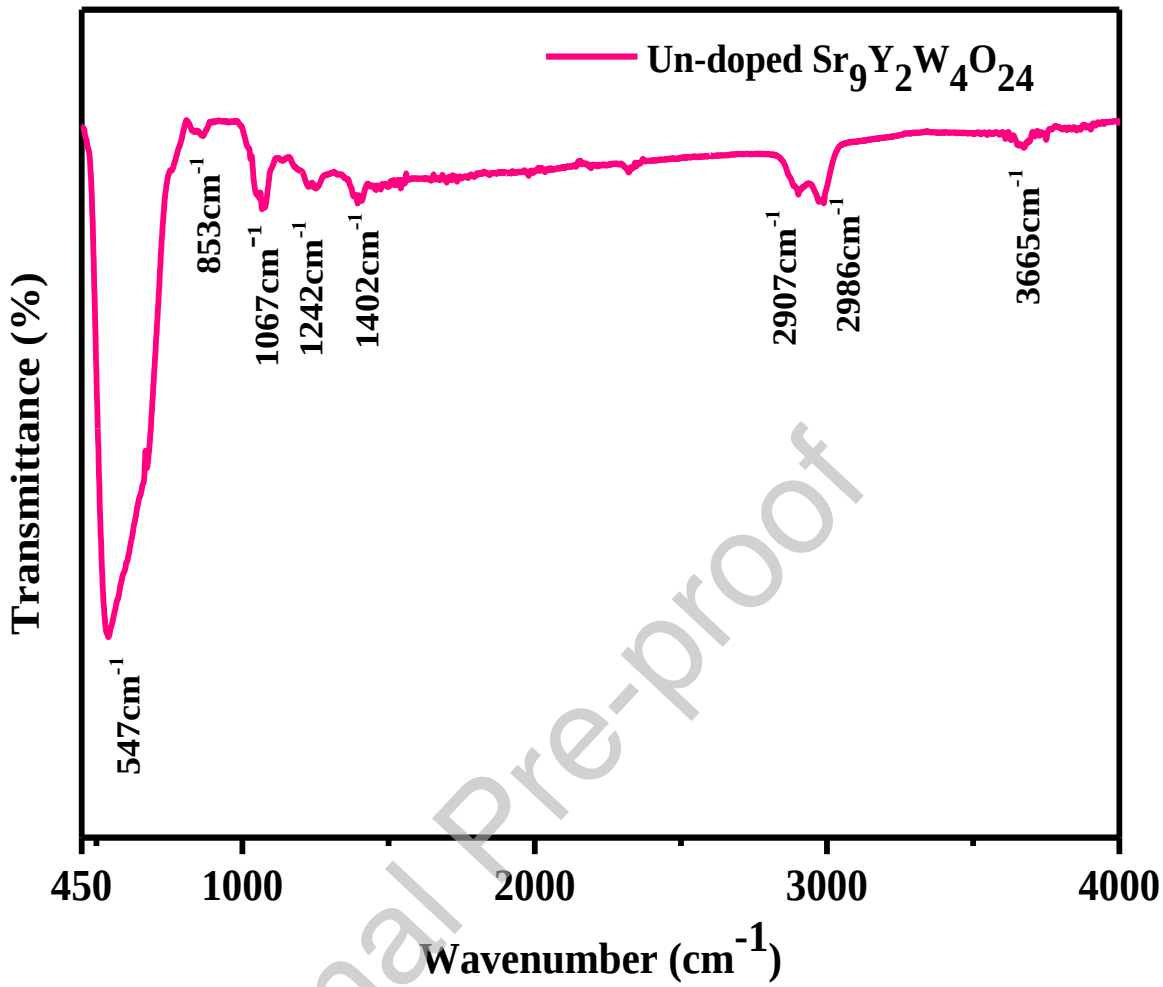

Journal Pre-proof

Fig.6

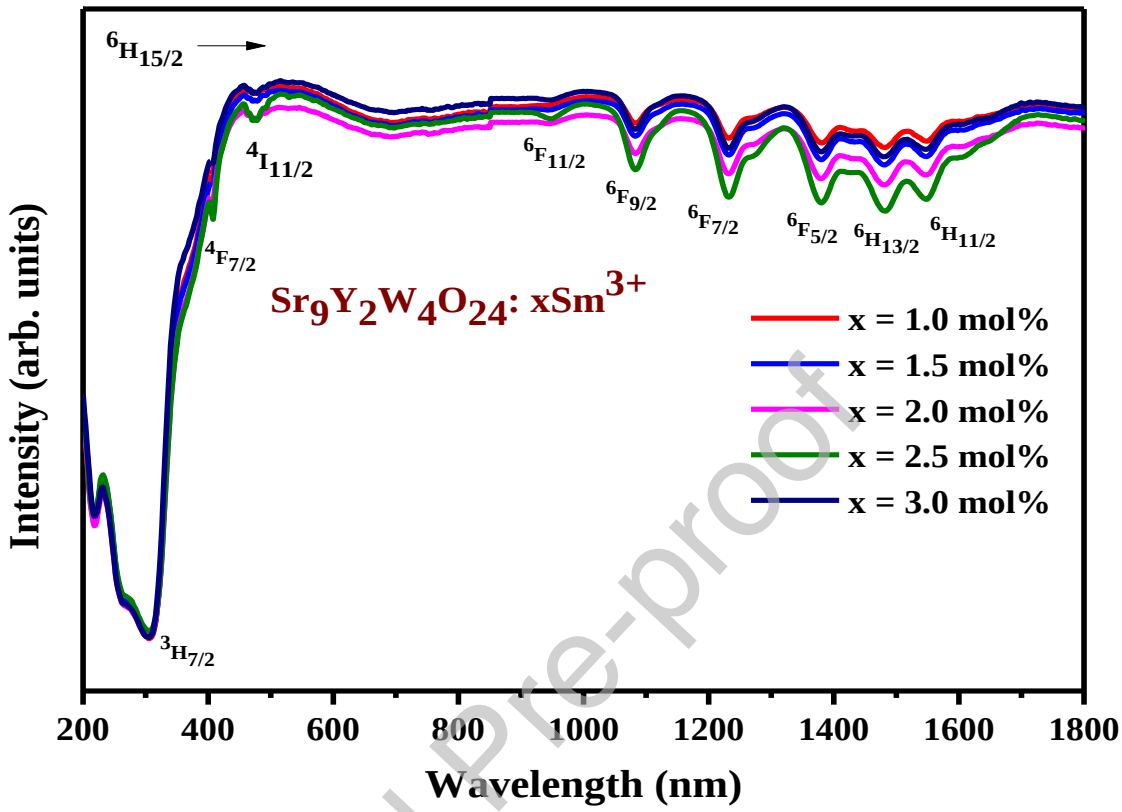

Journal Pre-proof

Fig.7

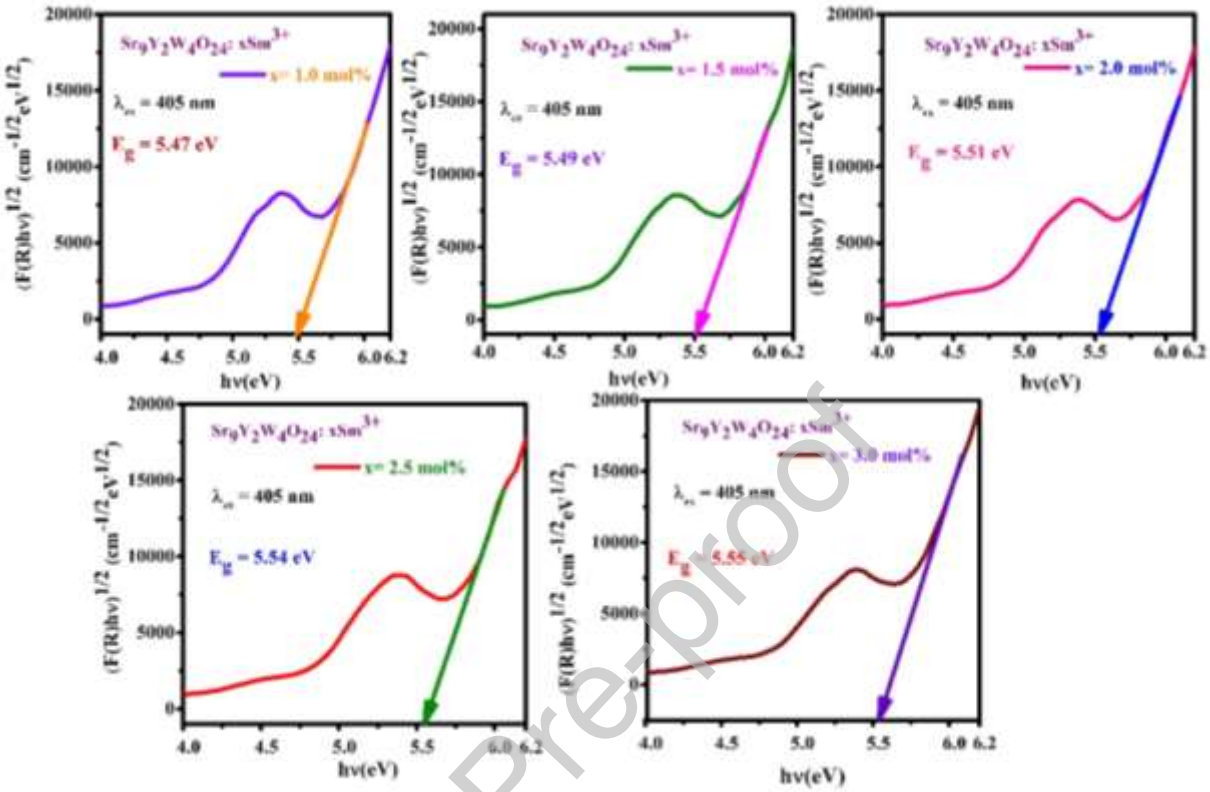

Journal Pre-proof

Fig.8

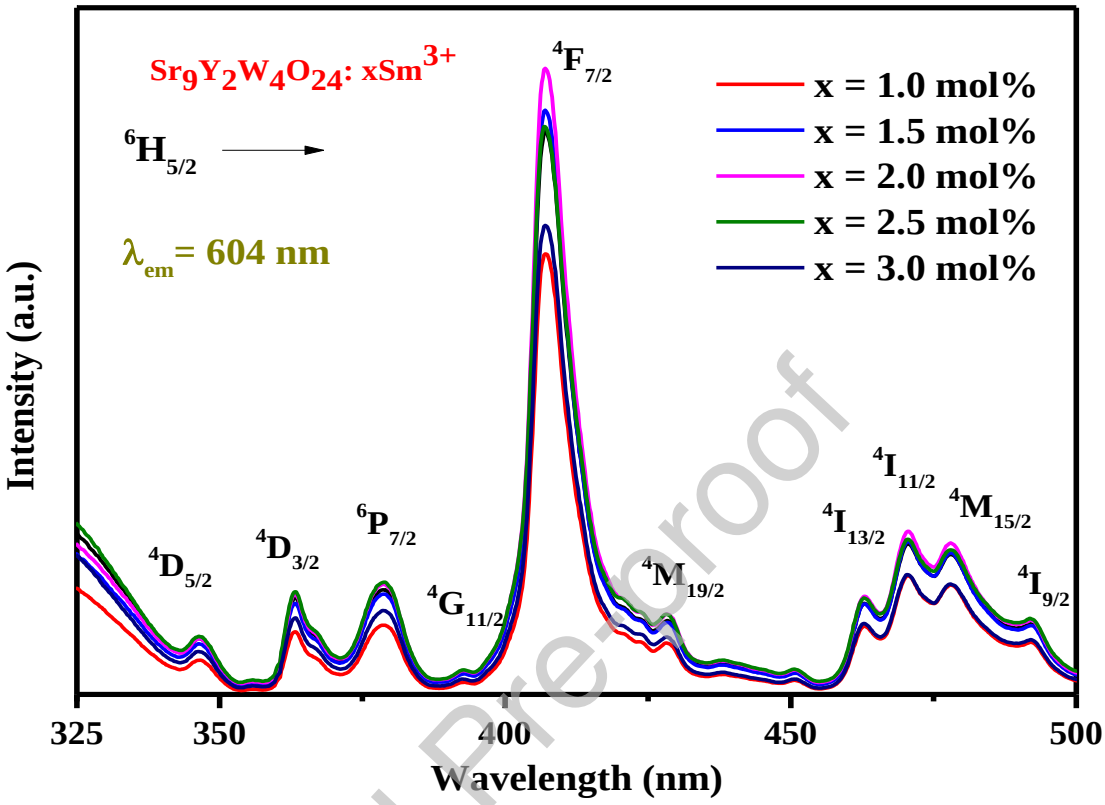

Journal Pre-proof

Fig.9

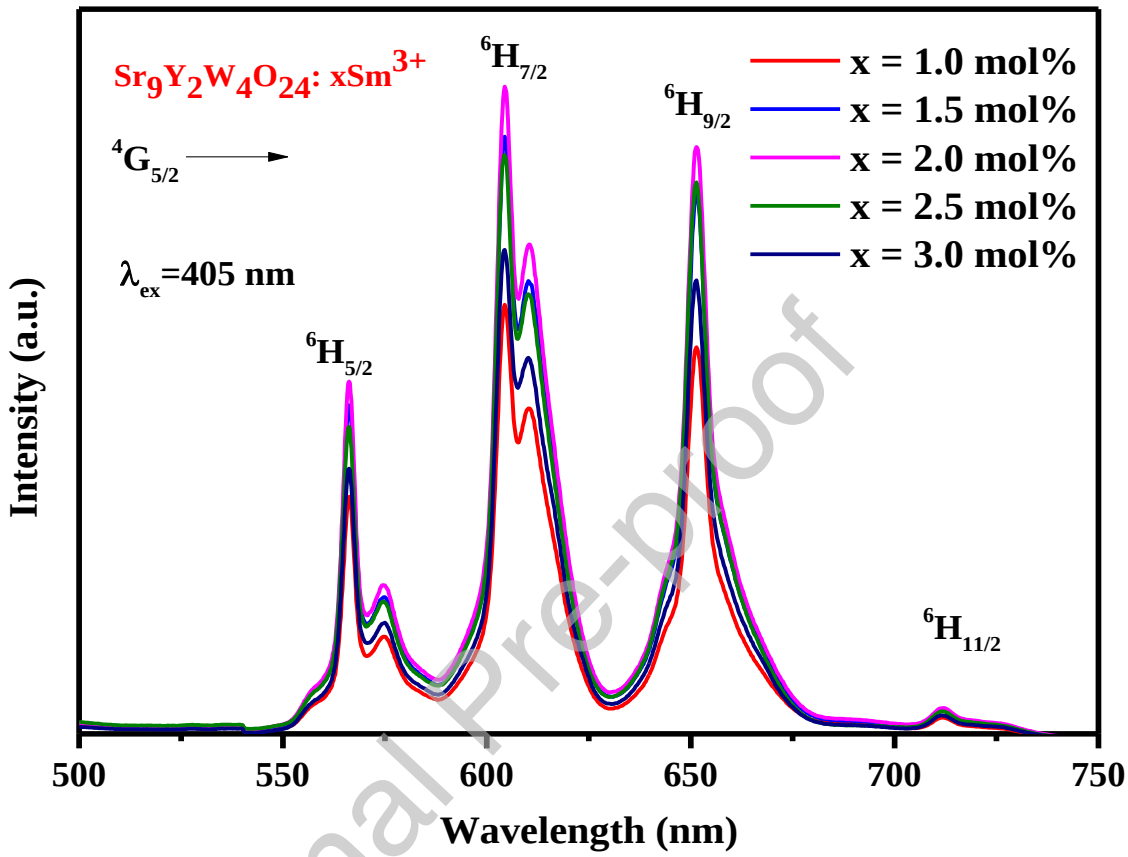

Journal Pre-proof

Fig.10

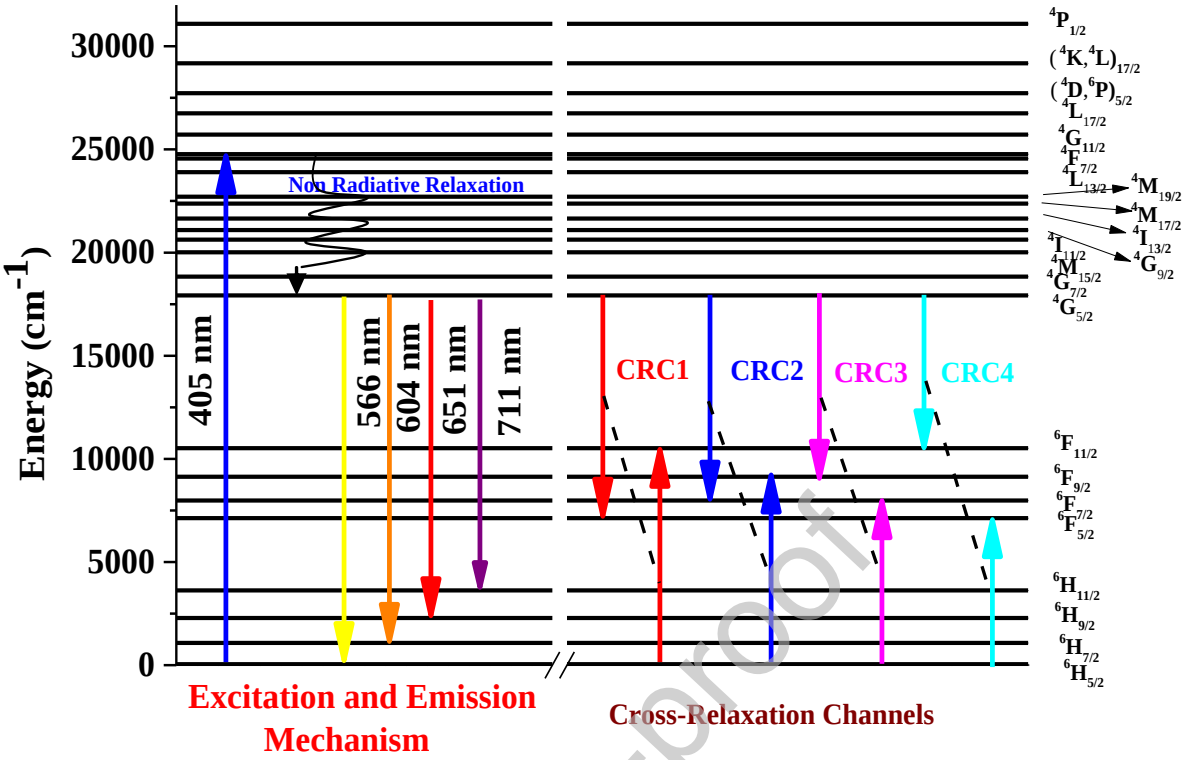

Journal Pre-proof

Fig.11

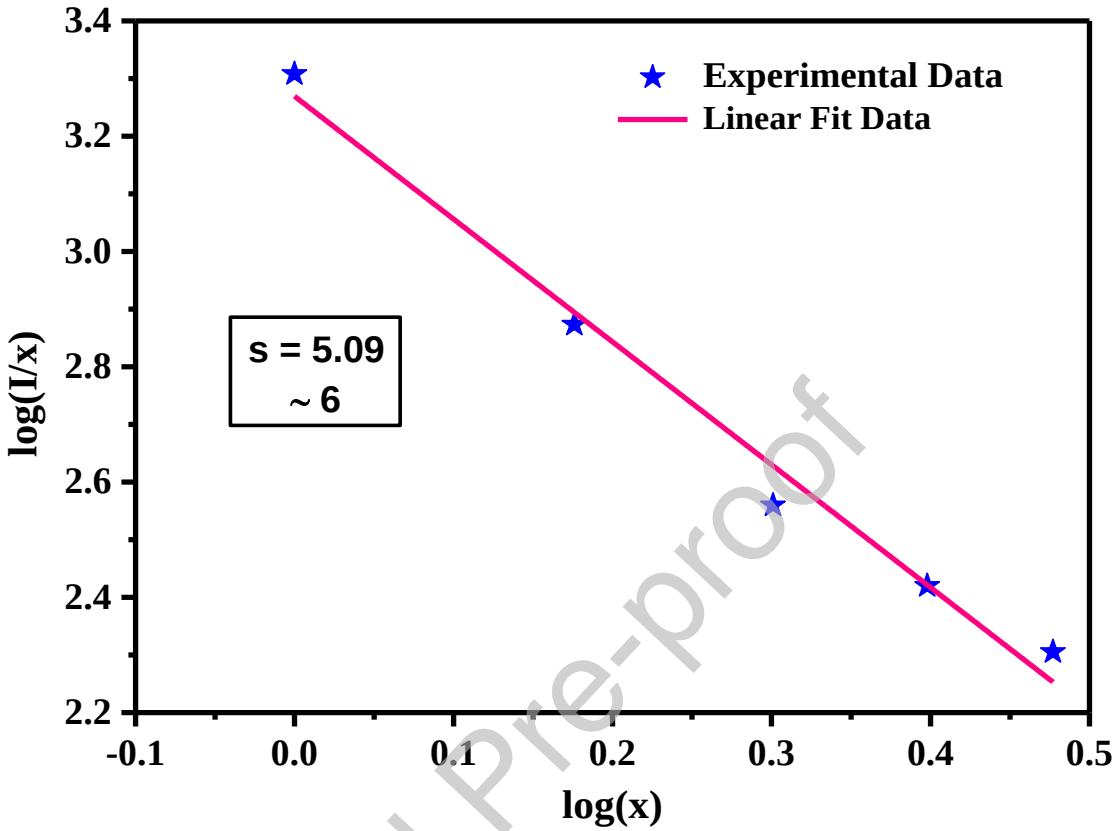

Journal Pre-proof

Fig.12

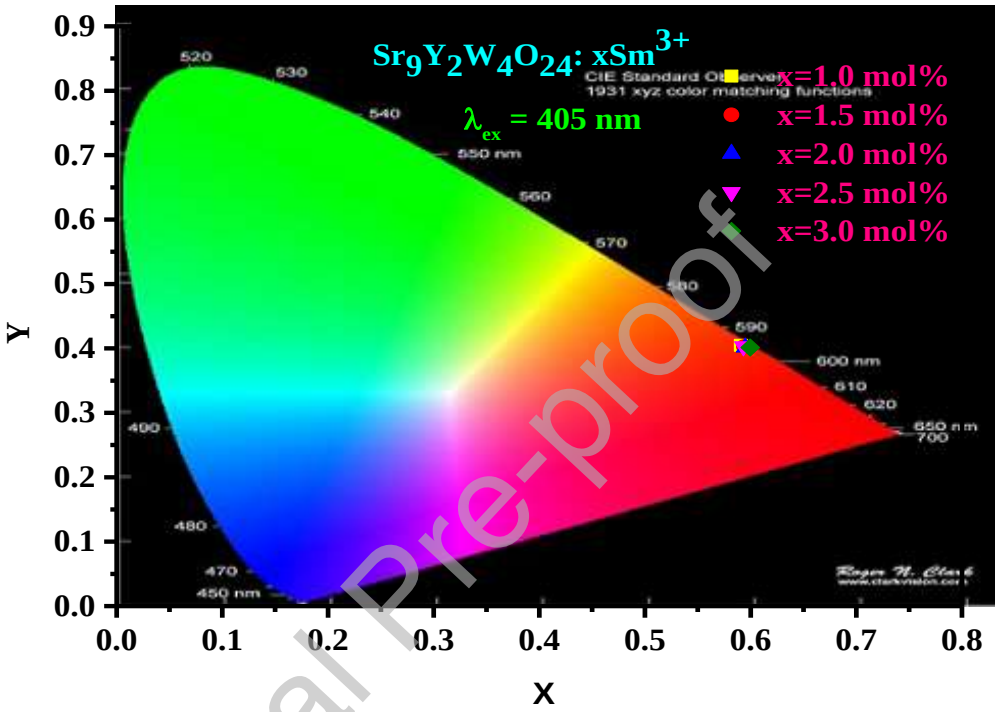

Journal Pre-proof

Fig.13

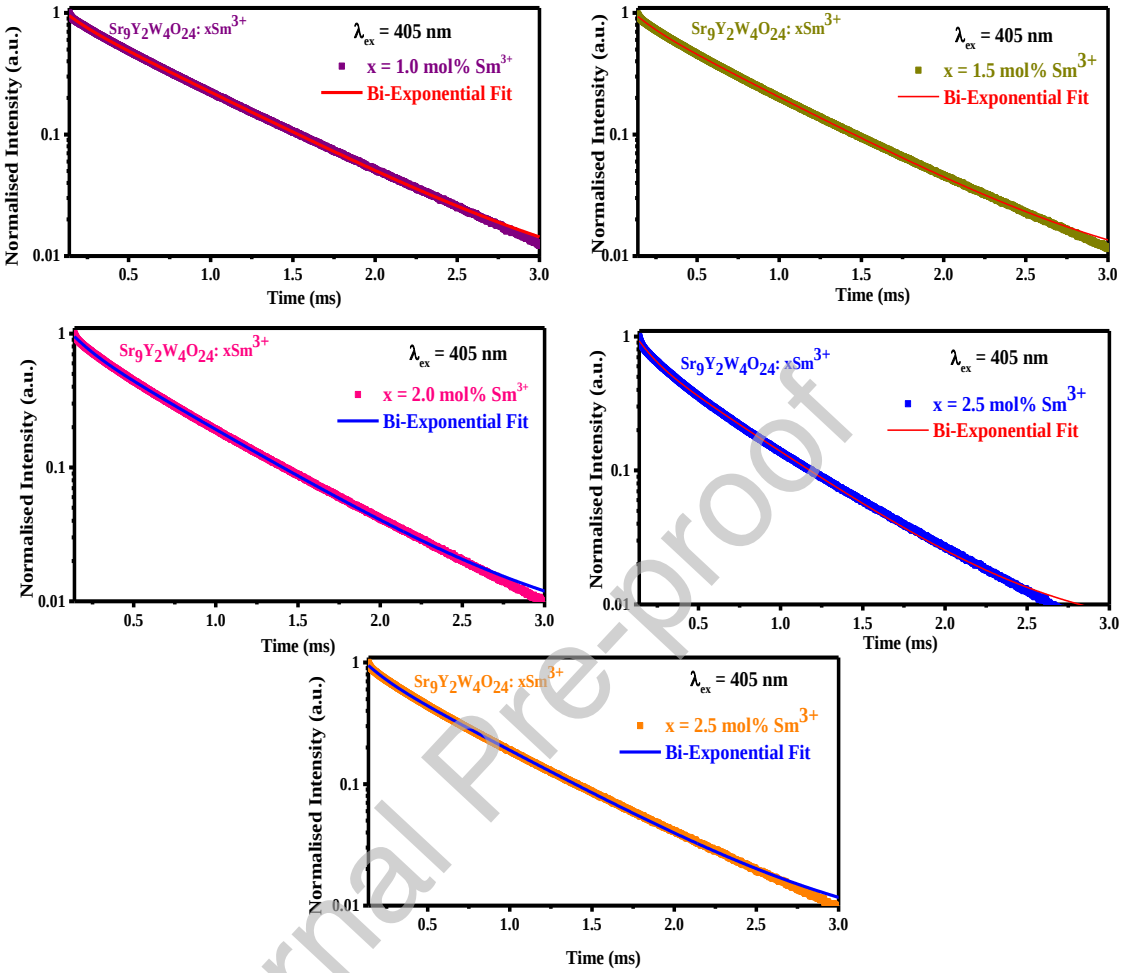

Journal Pre-proof

Fig.14

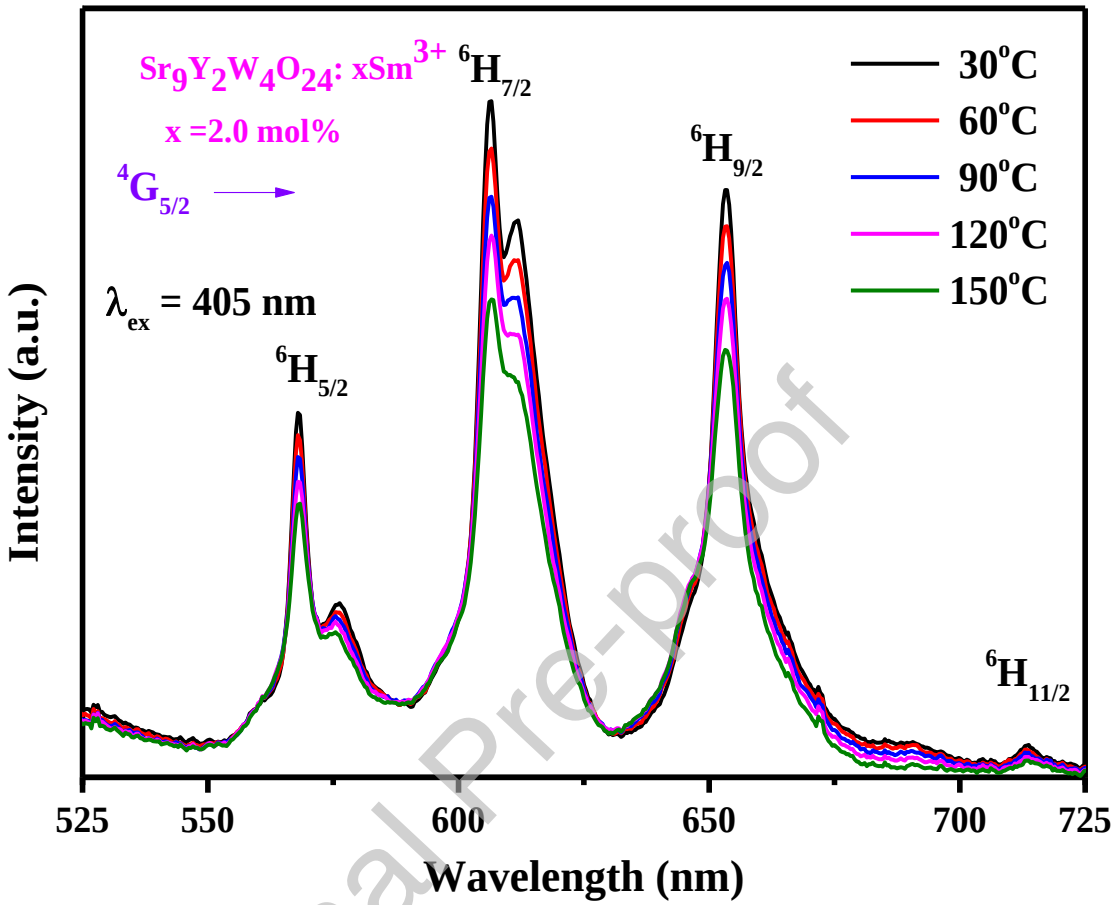

Journal Pre-proof

Fig.15

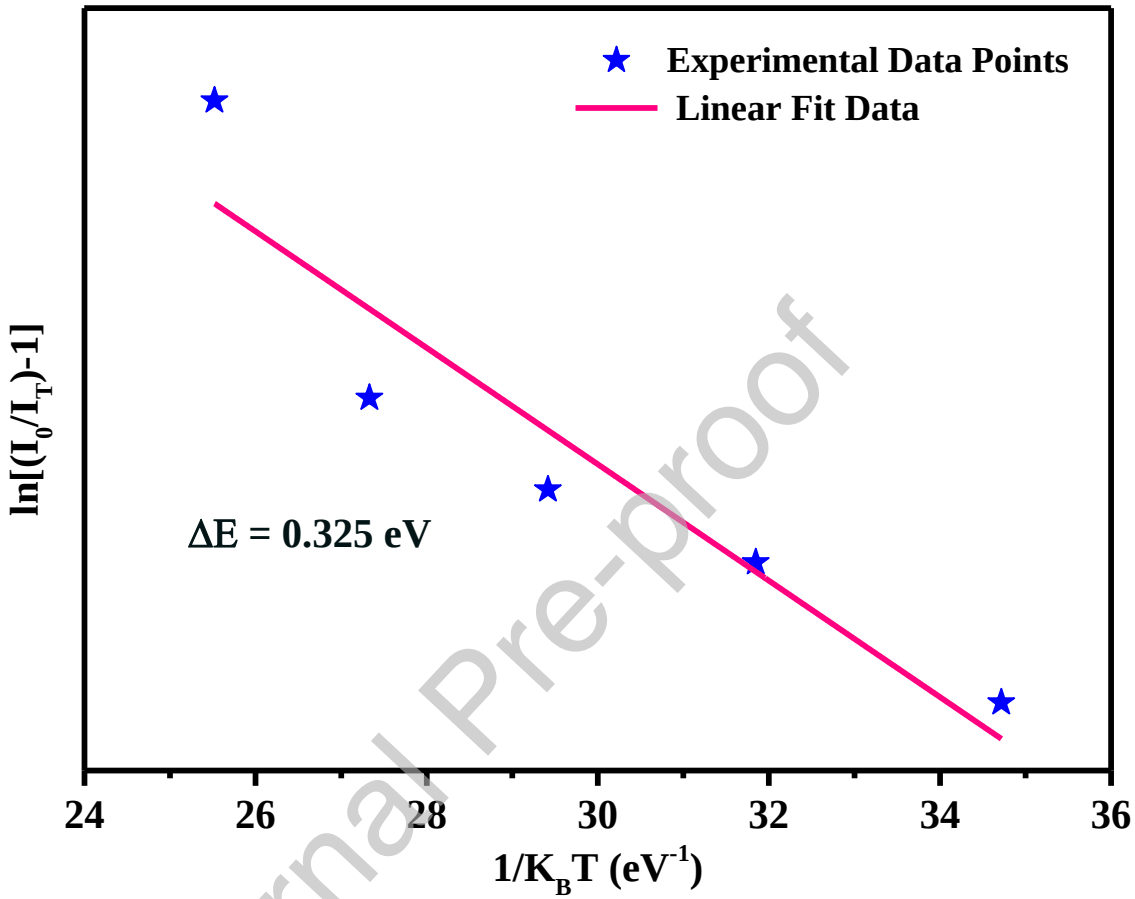

Journal Pre-proof

Graphical abstract

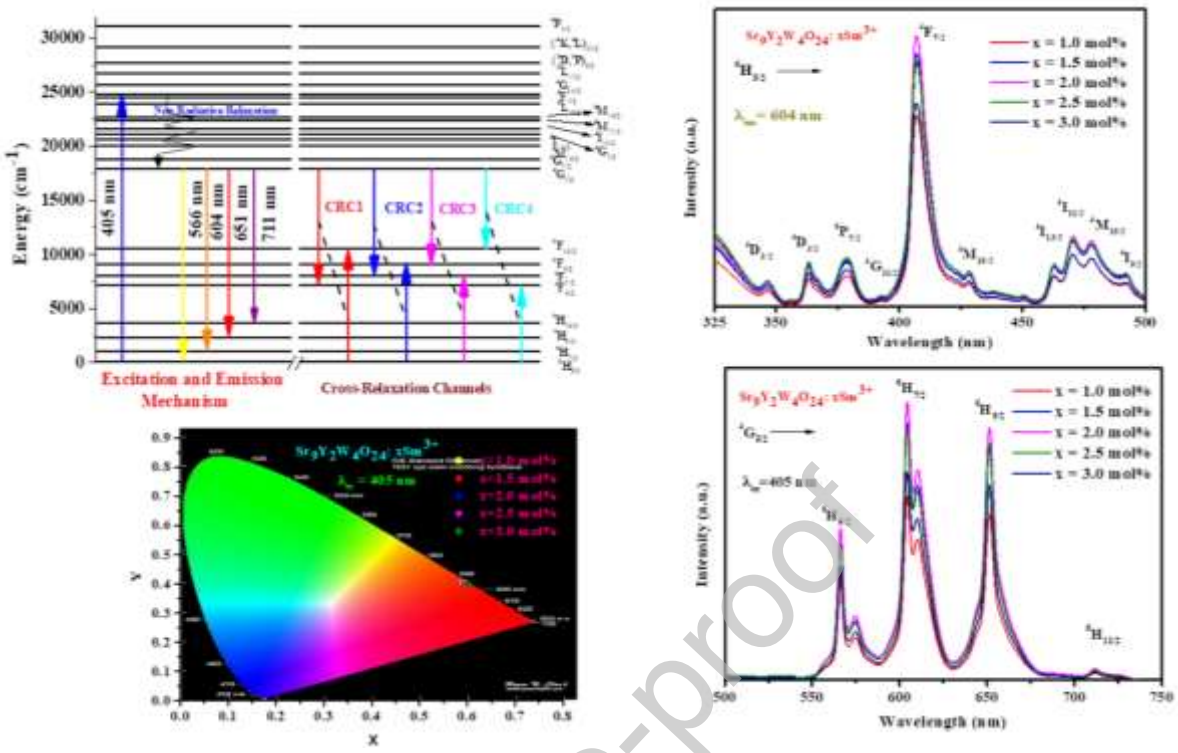

Graphical abstract showing the photoluminescence studies (excitation & emission spectra) of Sm^{3+} doped $Sr_9Y_2W_4O_{24}$ phosphors and their corresponding CIE points. Energy level diagram showing the various excitation and emission states involved in this mechanism.

Credit author statement

Ms. Sheetal Kumari: work plan, experiments, calculation and writing the manuscript

Prof. A.S. Rao: work plan, supervision, validation, correction of manuscript.

Journal Pre-proof

Table 1. Rietveld refinement parameters along with JCPDS data for an un-doped $Sr_9Y_2W_4O_{24}$ phosphor.

Parameters	**Standard data JCPDS (49-0568)**	**$Sr_9Y_2W_4O_{24}$ (Un-doped)**
a(Å)	11.642	11.614
b(Å)	11.642	11.614
c(Å)	16.465	16.496
$\alpha = \beta = \gamma$ (º)	90	90
χ^2	–	1.86
Cell Volume ($Å^3$)	2231.60	2225.06

Table 2

CIE chromaticity coordinates and CCT values for the as synthesized Sm^{3+} ions doped $Sr_9Y_2W_4O_{24}$ Phosphors.

Sample	**CIE chromaticity coordinates (x, y)**
1.0mol% Sm^{3+}	(0.5907, 0.4049)
1.5mol% Sm^{3+}	(0.5937, 0.4027)
2.0mol% Sm^{3+}	(0.5949, 0.4018)
2.5mol% Sm^{3+}	(0.5931, 0.4031)
3.0mol% Sm^{3+}	(0.5954, 0.4013)

Journal Pre-proof

Conflict of Interests Statement

The authors declare that they have no known competing financial interests or personal relationships that could have appeared to influence the work reported in this paper.

(Prof. A.S. Rao)
Corresponding Author

Journal Pre-proof